

https://dspace.org/

# Primary uranium mineralisation of the central Damara Orogen, Namibia: a petrographic, geochemical and mineralogical account of the granite - hosted uranium deposits situated along the Swakop- and Khan River valleys: Primary uranium mineralisation of the central Damara Orogen, Namibia

**Freemantle, Guy George**

**2017**

http://hdl.handle.net/10539/23612

Freemantle, Guy George (2017) Primary uranium mineralisation of the central Damara Orogen, Namibia: a petrographic, geochemical and mineralogical account of the granite - hosted uranium deposits situated along the Swakop-and Khan River valleys

Downloaded from a DSpace repository. https://dspace.org/

# PRIMARY URANIUM MINERALISATION OF THE CENTRAL DAMARA OROGEN, NAMIBIA

A petrographic, geochemical and mineralogical account of the granite - hosted uranium deposits situated along the Swakop- and Khan River valleys.

A thesis submitted to the Faculty of Science

In fulfilment of the requirements for the degree of Doctor of Philosophy

At the School of Geosciences University of the Witwatersrand,

Johannesburg

September 2015

By

Guy George Freemantle

…….

## PERMISSION TO USE

In presenting this thesis in partial fulfilment of the requirements for a Postgraduate degree from the University of the Witwatersrand, I agree that the Libraries of this University may make it freely available for inspection. I further agree that permission for copying of this thesis in any manner, in whole or in part, for scholarly purposes may be granted by the professor who supervised my research work or, in their absence, by the Head of the School of Geosciences or the Dean of the Faculty of Science. It is understood that any copying or publication or use of this thesis or parts thereof for financial gain shall not be allowed without my written permission or written permission from the University of the Witwatersrand. It is also understood that due recognition shall be given to me and to the University of the Witwatersrand in any scholarly use which may be made of any material in this thesis.

Requests for permission to copy or to make other use of material in this thesis in whole or part should be addressed to:

Head of the School of Geosciences
University of the Witwatersrand
1 Jan Smuts Avenue
Johannesburg
2050
South Africa

Dean
Faculty of Science
University of the Witwatersrand
Johannesburg
2050
South Africa

## Abstract

Namibia, the 6th largest producer of uranium globally, has produced uranium from Pan African granite-hosted (primary) deposits since 1976, and from palaeochannel deposits since 2007; exporting 3 472 tonnes U in 2016. The large granite-hosted deposits at the Husab Mine are expected to add over 5 700 tonnes U/year at peak, while three large primary-hosted deposits remain in various stages of development at Goanikontes, the Ida Dome, and Valencia. This study presents a comprehensive geological, geochemical and uranium mineralogical appraisal of four of the major primary-hosted uranium deposits, all situated within the southern Central Zone (sCZ) of the polydeformational ($D_1$-$D_3$) Damara Belt. The sCZ comprises highly deformed Neoproterozoic sediments, unconformably draped over rheologically competent granite-gneiss domes and inliers of a Palaeoproterozoic basement. A suite of fractionated sheeted leucogranites (SLGs) are a characteristic of the final stages of Orogenic deformation; while most SLGs appear to precede $D_3$ deformation and metamorphism (ca. 510 Ma); most of the mineralised SLGs across the region invade reduced-facies sediments in pressure shadows formed in the hinges and limbs of upright $D_3$ antiforms, proximal to basement inliers. A pre-existing, six-fold, alphabetised SLG classification scheme is revised and extended to categorise distinctive and consistent field and petrographic characteristics of the SLGs across the region. Discriminating SLG sub-types is less consistent in standard geochemical diagrams, except where high field-strength (HFS) and rare-earth elements (REE) are concerned. REE profiles in pre-$D_3$ SLGs reflect abundances, or paucities, of characteristic accessory mineral assemblages; while REE profiles show relative REE enrichment, prominent REE-fractionation and -ve Eu anomalies in the uraniferous SLGs, reflecting lower-percentage partial melts in the more uraniferous samples. The overwhelming majority of primary uranium mineralisation is in magmatic uraninite, followed by coffinite which predominate as a replacement phase of uraninite, and more rarely as solid solution with thorite. The refractory minerals betafite and brannerite are rare, but are locally abundant in discrete, magmatic textures within uraniferous SLGs of some deposits. Hydrated uranyl silicates predominate in the supergene portions of the orebodies across the region. An electron microprobe study presents the first comprehensive assessment of uraninite compositions in the region, while Husab deposit betafite and brannerite compositions allow for a well-rounded comparison with refractory minerals from the Rössing deposits.



Key Words

Primary Uranium, Granite, Orogenic, Damara, Namibia, Rare Earth Elements, Mineralisation, Fractionation, High-grade Metamorphism, Economic Geology, Mining, Processing, Uraninite, Coffinite, Etango, Goanikontes, Husab, Ida Dome, Rössing, Valencia

## Declaration

I declare that this Dissertation is my own, unaided work. It is submitted for the degree of Doctor of Philosophy at the University of the Witwatersrand, Johannesburg. It has not been submitted before for any degree or examination in any other university.

_____day of _____ at _____

_____

Guy George Freemantle

## Acknowledgements

First and foremost, I must thank Prof. Judith Kinnaird and Dr. Paul Nex, whose guidance has steered me through a testing Honours Project. And, for her near endless patience and great faith in my abilities and who has inspired me to take this on with new vigour when I needed it.

To my Family, Mom and Dad, without your support and encouragement this would not be possible. Thank you both so much for everything. To my brother, Neil and sister Lauren, for being my friends, and telling me to hurry up and finish

To Natasha, your tenacious commitment to make things work out in Namibia during the latter, most challenging part, of getting this project finished is truly inspirational and worthy of more praise than can be expressed in this medium. Thank you from the bottom of my heart.

To both Judith and Paul for all the discussions of Namibian geology, for helping to get my head around some of the most complex structural, metamorphic and igneous conundrums.

I would also like to thank the external and internal examiners for giving their time to reading and reviewing this thesis.

I would like to thank Dr Roger Laine and Valencia Uranium Ltd. Who have provided funding without which this project could not take place, for this I am especially grateful. To the Valencia Team thanks for rock-cutting, driving and sampling help.

To Bannerman Mining Resources, thank you for the use of your 'beach house' on weekends during field seasons, logistical support and the use of the laundry were much appreciated. This particular support essentially made trips economically viable. Thanks also to Martin Spence and Peter Batten (field season one) and Jamie, Bernie, Andrew (field season two). Thanks, must also go to Bannerman Mining Resources for providing core samples and for providing funding for expensive analytical work.

To Extract Resources, Swakop Uranium, thank-you Barry Parker and Martin Spivey for use of camping facilities at the 'old' and 'new' camps and for the geological discussions, for which I am grateful. Some special thank you to Andrew Penkethman and Martin Spivey for organising funds for analytical work and encouraging me to join the Swakop Uranium team.

At Wits, Alex Mathebula for preparing and polishing a seemingly endless chain of thin sections. Crushing and milling of some samples by graduate students., The guidance and advice from Joe Aphane in sample preparation and heavy mineral separation at the Bernard Price Institute. Sharon Turner ran the XRF and XRD facilities at BPI, where most of the geochemical work took place. Setpoint Laboratories processed 143 samples, thanks to Deidre Hatton and the team.

Luke Longridge for unfolding limbless hinges and explaining why '0, 1 and 2' subscripts are so important in S- and L- tectonites. Essential for explaining the abundant structural complexities of the Central Zone.

Thanks to Brandon Youlton for processing all the QEMSCAN samples, and providing the excellent mineral deportment statistics and supporting mineral imagery.

This thesis is dedicated to my family

To Mom and Dad, Lauren, Neil,

Natasha, thank you for endless patience and encouragement, and putting up with melt downs and technology failures

Thank you all so very much for everything

## Contents

List of Figures ..... viii
List of Tables ..... xix
Glossary of Abbreviations ..... xxiii
Appendix Volume ..... xxiv

**Chapter 1 INTRODUCTION TO PRIMARY URANIUM MINERALISATION IN CENTRAL WESTERN NAMIBIA ..... 1**

1.1 Introduction ..... 1
Historical Context ..... 2
1.2 Research Outline ..... 3
1.3 Exploration and Mining Interest ..... 7
1.4 Namibian and World Uranium Production ..... 8
1.5 Global Influences on Exploration and Mine Development ..... 9
Uranium Exploration in the Damara Orogen ..... 11
1.6 Summary ..... 14

**Chapter 2 THE DAMARA OROGEN, CENTRAL ZONE GEOLOGY, AND URANIUM MINERALISATION ..... 16**

2.1 Introduction ..... 16
2.2 Stratigraphy of the Central Zone of the Damara Orogen ..... 18
Central Zone Stratigraphy Summary ..... 18
Southern Central Zone Stratigraphy Summary ..... 20
2.3 Structural evolution of the southern Central Zone ..... 23
2.4 Magmatism in the Central Zone ..... 25
2.5 Sheeted Leucogranites in the Southern Central Zone ..... 31
2.6 Regional Metamorphism ..... 34
Contact Metamorphism ..... 37
2.7 Discussion ..... 38
2.8 Summary ..... 39

**Chapter 3 GEOLOGICAL SETTING OF THE CENTRAL ZONE PRIMARY - HOSTED URANIUM DEPOSITS ..... 41**

3.1 Introduction....41
3.2 Introduction to the Granitoid rocks at the Central Zone uranium deposits....42
Salem Granite....42
Red Granite....43
Grey Granite....43
3.3 Sheeted leucogranites....44
Distribution of the uraniferous sheeted leucogranites....47
3.4 Controls on mineralisation....51
Entrained metasediments....53
Oxidation halos and supergene alteration....55
D-types vs. E-types....59
3.5 The Rössing Deposit....65
Stratigraphy....66
Structure....68
Magmatism....69
Mineralisation....69
Rössing Summary....71
3.6 Goanikontes area....73
Introduction....73
Stratigraphy....75
Magmatism....76
Mineralisation....77
3.7 Hildenhof....78
Introduction....78
Stratigraphy....79
Structural Setting and Associated Magmatism at Hildenhof....79
Mineralisation....82
3.8 The Ida Dome Deposits....84
Introduction....84
Stratigraphic - Structural Setting at the Ida Dome....86
Ida Dome Intrusives....87
Ida Central and Garnet Valley Deposits....89
Holland's Dome Deposit....98
Uranium Distribution in Leucogranites at The Ida Dome....102
3.9 The Husab Deposit....103
Introduction....103
Husab Exploration and Mining History....104
Geophysical signature....105
Deposit Description....107
Husab Stratigraphic Succession....108
Khan - Rössing Transition at Husab....113
Structural Setting at Husab....115
Intrusive Rocks at Husab....118
Husab Mineralisation....119

3.10 The Valencia Deposits ..... 125
Introduction ..... 125
Valencia Stratigraphy ..... 129
Structural Setting at Valencia ..... 133
Metamorphism ..... 135
Magmatism ..... 137
Mineralisation ..... 138
3.11 Field Relationships of granite populations at the primary deposits ..... 141
Salem Suite ..... 141
Grey Granites ..... 143
3.12 Sheeted leucogranites ..... 144
A- and B-Type Sheeted Leucogranites ..... 145
C-Type Sheeted Leucogranites ..... 149
3.13 Uraniferous Leucogranites - The Alaskites ..... 157
Goanikontes Alaskites ..... 158
Hildenhof Uraniferous Sheeted Leucogranites ..... 161
Ida Dome Alaskites ..... 161
Ida Dome E-Type Sheeted Leucogranites ..... 162
3.14 Central Zone Primary Uranium-Deposits Discussion ..... 165

**Chapter 4 PETROGRPAHY OF THE GRANITIC ROCKS THAT HOST THE URANIUM DEPOSITS OF THE CENTRAL ZONE ..... 175**

4.1 Introduction ..... 175
4.2 Background of Granite Classification in the Southern Central Zone ..... 176
4.3 Sheeted leucogranites and Associated Granitoids at the Central Zone deposits 177
4.4 Aims and Objectives ..... 179
4.5 Methodology and Sampling ..... 179
4.6 Salem, Red and Grey Granite Petrography ..... 189
Salem Suite at Valencia - Thin Section Petrography ..... 189
4.7 Thin section petrography of A- and B-type sheeted leucogranites ..... 196
4.8 C-type Sheeted Leucogranite Thin Section Petrography ..... 199
Goanikontes C-type Sheeted Leucogranites ..... 199
Hildenhof C-type Sheeted Leucogranites ..... 205
Ida Dome Area C-type leucogranites ..... 208
Husab C-type leucogranite thin section petrography ..... 212
Valencia C-types ..... 214
4.9 Uraniferous Sheeted Leucogranites- The Alaskites ..... 217
Rock-Forming and Accessory Minerals of Uraniferous Leucogranites ..... 217
Ore Mineral Petrography Samples ..... 218

Mineralisation ..... 221
Alteration of the Uraniferous Sheeted Leucogranites ..... 226
D- and E-type Sheeted Leucogranites at Goanikontes ..... 231
Goanikontes E-Type Sheeted Leucogranites ..... 234
Hildenhof Uraniferous Sheeted Leucogranite Petrography ..... 237
Goanikontes and Hildenhof Ore Mineral Petrography ..... 239
Ida Dome Uraniferous Sheeted Leucogranite Petrography ..... 244
Ida Dome Ore Mineral Petrography ..... 250
Husab Alaskite Petrography ..... 254
Alteration of the Husab Uraniferous Sheeted Leucogranites ..... 266
Husab Ore Mineral Petrography ..... 267
Valencia Uraniferous Sheeted Leucogranite Petrography ..... 277
Valencia Ore Mineral Petrography ..... 283

4.10 Petrography Summary ..... 286
Petrogenesis implications of the non-uraniferous leucogranites ..... 286
Summary of petrographic characteristics of the sheeted leucogranites ..... 289
Origins of the sheeted leucogranites ..... 291

4.11 Concluding Remarks ..... 296

**Chapter 5 GEOCHEMISTRY OF THE GRANITIC ROCKS AT THE PRIMARY-HOSTED URANIUM DEPOSITS ..... 299**

5.1 Introduction ..... 299

5.2 Methodology ..... 300
Major Elements ..... 302
Trace Elements ..... 303
Hand - Held XRF Assay ..... 303
Rare Earth Elements ..... 304

5.3 Sampling andAims ..... 304

5.4 Major Element Trends ..... 307

5.5 Rock Classification using Major Elements ..... 310
Q'-Anor ..... 311
The Granite System Ternary Diagram ..... 319
Discussion of the Granite Eutectics ..... 322

5.6 Aluminium Saturation Index ..... 323
Aluminium Saturation Indices of Uraniferous Leucogranites ..... 327
The Modified Alkali-Lime Index - MALI ..... 330
Fe Classification of the Central Zone Leucogranites ..... 333
Maficity ..... 335
Debon and Le Fort Binary Classification ..... 339

5.7 Major Element Summary and Discussion ..... 342

5.8 Trace Elements ..... 343
Low Field Strength Trace Element Trends ..... 345
Mobile Trace Element Discrimination Diagrams ..... 352
5.9 High Field Strength Elements ..... 355
Trace Element Indicators of Granite Source Affinity ..... 359
Discrimination Diagrams ..... 362
Transition Metals ..... 370
5.10 Uranium and Thorium ..... 371
U, Nb, and Ti Discrimination Plots ..... 377
5.11 Alternative Geochemical Techniques: Hand-Held XRF ..... 380
Background ..... 380
Drill Hole RDD373 Geochemical Profile ..... 381
Evaluation of Geochemical Data from a Portable XRF Profile of RDD373 Drill Core 381
Uranium Mineralisation in the RDD373 Drill Hole ..... 382
Discussion of Handheld XRF Survey Results ..... 389
5.12 Geochemistry Results Discussion and Petrogenesis Implications ..... 391
Major Elements Discussion ..... 392
Trace Elements Discussion ..... 394
Classification Schemes ..... 396
5.13 Geochemical Conclusions ..... 397

**Chapter 6 RARE EARTH ELEMENT GEOCHEMISTRY ..... 398**

6.1 Introduction ..... 398
Samples ..... 400
6.2 REE Analysis Results ..... 402
6.3 REE Trends of the Goanikontes Sheeted Leucogranites ..... 405
6.4 REE Trends of the Husab Sheeted Leucogranites ..... 407
6.5 REE Trends of the Ida Dome Granites ..... 410
6.6 REE Trends of the Valencia Sheeted Leucogranites ..... 413
6.7 REE Discussion ..... 420
Rare Earth Element Fractionation ..... 420
Monazite Geochemistry ..... 431
6.8 Summary of The REE Trends of The Central Zone Uranium Deposits ..... 436

**Chapter 7 URANIUM MINERALISATION AND URANIUM MINERALOGY OF THE PRIMARY DEPOSITS ..... 438**

7.1 Introduction....438
Previous Uranium-Bearing Mineral Studies in The Central Zone.... 440
Uranium in Refractory Minerals in the Central Zone .... 442
7.2 Uranium Mineral Speciation and Deportment Study - QEMSCAN ....443
7.3 QEMSCAN Results ....444
7.4 QEMSCAN Mineral Maps of Central Zone Deposits....448
Goanikontes and Hildenhof Mineral Maps .... 448
Ida Dome Mineral Maps.... 454
Ida Dome and Holland's Dome Surface Sample Mineral Maps .... 458
Husab Deposit Mineral Maps.... 459
Uranium Mineral Textures of The Husab Deposits .... 462
Uranium-Bearing Refractory Minerals and Textures In Husab Drill Core RDD373465
Valencia Uranium Mineral Maps.... 472
Valencia Surface Samples.... 479
7.5 QEMSCAN Discussion....481
Mineralisation Trends.... 481
Secondary Uranium Minerals.... 486
Betafite and Brannerite Occurrences at Husab.... 489
Speciation and Refractory Mineral-Hosted Uranium.... 491

**Chapter 8 URANIUM MINERAL DESCRIPTION AND COMPOSITONS AT THE PRIMARY DEPOSITS.... 495**

8.1 Introduction....495
Previous Work .... 497
Approach .... 498
The Significance of Uraninite Composition in The Granite-Hosted Mineral Systems.... 498
Replacement and Contamination Trends in Uraninite .... 500
Industrial Application .... 500
8.2 Samples and Methodology....501
Uranium Mineral Compositions By EPMA.... 502
Stoichiometry Formulae Recalculation .... 503
8.3 EPMA Analysis Results....504
8.4 Goanikontes U-Mineral Compositions....511
Goanikontes Uraninite and Coffinite.... 512
Goanikontes Uranophane-, and Monazite-Hosted Uranium Mineralisation ..... 516
8.5 Hildenhof Uraninite Compositions....521
8.6 Ida Dome U-Phase Compositions....524
Ida Dome U- and Fe-Mineral Relationships and Coffinite andThorite Compositions.... 524

8.7. Valencia Uraninite and Coffinite Compositions ....527
Coffinite and Thorite Calculations .... 529
8.10. Husab Uranium Mineral Compositions ....532
Husab Uranium Mineralogy Sample Descriptions.... 533
8.11. Husab Uraninite Composition Analysis ....535
Weakly Altered Uraninite .... 535
Altered Uraninite .... 536
Husab Uraninite Compositional Variation.... 539
8.12. Primary Uraninite Compositional Variation - Discussion....541
Rare Earth- and Trace Element Abundances in Uraninite.... 546
8.13. Other Primary Uranium Phases – The Husab Betafite and Brannerite Examples549
Betafite .... 549
Brannerite.... 554
Specimen Descriptions and Analyses .... 554
8.14. Mineral Element Mapping ....556
8.15. Compositional Variation and Trends in Betafite and Brannerite....561
8.16. Alteration of Primary Uranium Minerals ....566
8.17. Concluding Remarks on Composition Analysis Findings....572

**Chapter 9 SUMMARY AND Conclusions.... 581**

9.1 Introduction....581
9.2 Geological Context ....581
9.3 Discussion of Petrographic, Geochemical and Rare Earth Element Findings ...592
Conclusions on Sheeted Leucogranite Classification .... 596
9.4 Classification of The Central Zone Sheeted Leucogranites....602
Conclusions on Sheeted Leucogranite Classification .... 613
9.5 Mineralisation ....616
Uranium Mineralisation Conclusions .... 624
9.6 Comparisons with Other Orogenic Belts and Uranium Mineralisation Provinces628
9.7 Recommendations for Further Work....637
References .... 639

## *List of Figures*

### Chapter 1

Figure 1.1 The various domes of the Central Zone and their associated primary uranium deposits. ..... 4

Figure 1.2 Photographs illustrating primary, secondary, and refractory uranium minerals specimens. ..... 7

Figure 1.3 World uranium production by country for 2014. ..... 10

Figure 1.4 World production of the top fifteen uranium mines in metric tons of metal (tU) for the 2015 year. 10

Figure 1.5 Major Central Zone primary-hosted uranium deposits. ..... 13

### Chapter 2

Figure 2.1 The Pan-African Damara Orogen of Central, Namibia. ..... 17

Figure 2.2 Sheeted leucogranite intrusions in the Khan Formation, Khan River Gorge near the Valencia deposit. ..... 32

Figure 2.3 Polished slab of alaskite from the Stone Africa Quarry, SE of the Rössing Mine. ..... 33

Figure 2.4 Map of metamorphic grades and age date distribution of the western part of the Damara Orogen. 35

### Chapter 3

Figure 3.1 Early Damaran granites in the CZ include the Red and Salem Suite monzogranite. ..... 44

Figure 3.2 Diagram of sheeted leucogranite intrusion styles at the major Central Zone uranium deposits. ..... 49

Figure 3.3 Examples of wall rock assimilation in Husab granites. ..... 53

Figure 3.4 Examples of anomalous radioactivity associated with country rock entrainment. ..... 54

Figure 3.5 Sedimentary protolith indicators. ..... 55

Figure 3.6 Oxidation halos in sheeted leucogranites of the Central Zone. ..... 57

Figure 3.7 Varieties of oxidation halos in barren and mineralised leucogranites. ..... 58

Figure 3.8 Late stage vein minerals. (a) Fluorspar in breccia vein. ..... 61

Figure 3.9 Late granitic veins and U-remobilisation in brittle fractures ..... 62

Figure 3.10 Magnetite in alaskite and other leucogranites. ..... 64

Figure 3.11 The Rössing Mine area. ..... 66

Figure 3.12 Stratigraphic succession at the Rössing Mine. ..... 66

Figure 3.13 Features of the Rössing Uranium Mine. ..... 72
Figure 3.14 The geology of the Goanikontes area west of the Goanikontes Dome. ..... 74
Figure 3.15 Leucogranite sheets of the Goanikontes area. ..... 78
Figure 3.16 Stratigraphic and structural features of the Hildenhof area. ..... 80
Figure 3.17 Features of the Hildenhof Deposit Alaskites and metasediments. ..... 81
Figure 3.18 The Hildenhof Anomaly ground radiometric survey ..... 83
Figure 3.19 The Ida Dome deposits. ..... 85
Figure 3.20 The Zebraberge syncline structure, looking northwest from the southern end of the Ida Dome. ..... 87
Figure 3.21 Dykes and sills of sheeted leucogranite pervading Khan metasediments. ..... 88
Figure 3.22 View looking west over the Ida Dome from the old Copper Mine. ..... 89
Figure 3.23 View looking south up Garnet Valley, towards a large E-W dolerite dyke. ..... 90
Figure 3.24 Cross-section of the Rössing Formation on the eastern side of the Ida Dome. ..... 91
Figure 3.25 Field-scale examples of C-type sheeted leucogranite varieties in the Ida Dome area. ..... 94
Figure 3.26 Radiometric anomalies on surface in the vicinity of the Ida Cu Mine. ..... 97
Figure 3.27 Aerial view of the Holland's Dome deposit. ..... 99
Figure 3.28 Local features at Holland's Dome. ..... 102
Figure 3.29 Uranium distributions in the three main categories of rock type at the Ida deposits ..... 103
Figure 3.30 The Husab Mine Project Area. ..... 107
Figure 3.31 The Damara Supergroup at Husab. ..... 109
Figure 3.32 Typical Rössing Formation lithologies observed in Zone 1 drill core specimens. ..... 112
Figure 3.33 Typical Khan - Rössing transition succession lithologies observed in Zone 1 core specimens. ..... 114
Figure 3.34 Cross-sections of the Husab Zone 1 and Zone 2 deposits. ..... 117
Figure 3.35 Uranium distributions in the three main categories of rock type at the Husab deposits. ..... 122
Figure 3.36 Simplified stratigraphic log of a portion of RDD373. ..... 124
Figure 3.37a Schematic section of the Khan Syncline and its relationship with the Valencia Deposit. ..... 127
Figure 3.38 The Valencia stratigraphic succession, looking southwest. ..... 129
Figure 3.39 Examples of Major Damaran Formations present at Valencia. ..... 133
Figure 3.40 Bedding and fold hinge exposures at Valencia. ..... 134
Figure 3.41 Photograph illustrating the deformation of megacrystic Salem monzogranite. ..... 135

Figure 3.42 Migmatised Etusis Formation at the Valencia deposit. ..... 136

Figure 3.43 Schematic diagram of the large 'Z' folds into which the majority of mineralised granite has intruded. ..... 140

Figure 3.44 Salem Suite granites at Valencia. ..... 142

Figure 3.45 Grey granites at Hildenhof. ..... 143

Figure 3.46 Grey granite varieties at the Ida Dome. ..... 144

Figure 3.47 A-type and B-type sheeted leucogranites at Hildenhof. ..... 146

Figure 3.48 A- and B-types at Valencia. ..... 147

Figure 3.49 Early sheeted leucogranite varieties at the Ida Dome. ..... 148

Figure 3.50 C-type leucogranites at the Etango deposit. The sample set also includes C-type sheet sampled at surface north of the Swakop River. ..... 150

Figure 3.51 Euhedral magnetite and tourmaline in Cm- and Ct-type sheeted leucogranite. ..... 151

Figure 3.52 C-type leucogranite sheet crosscutting bedding and inheriting compositional banding. ..... 152

Figure 3.53 Examples of common sheeted leucogranites of the Husab Deposits. ..... 153

Figure 3.54 Ct-type sheeted leucogranites at Valencia. ..... 156

Figure 3.55 Magnetite-type leucogranites at Valencia. ..... 157

Figure 3.56 The common varieties of uranium-bearing granites observed in core from the Goanikontes Deposit. ..... 159

Figure 3.57 Typical Goanikontes (Etango) E-type core sample, DH019 71.74-72.18. ..... 160

Figure 3.58 Magnetite in barren and mineralised core from Goanikontes hole DH025. ..... 160

Figure 3.59 Typical mineralised sheeted leucogranite texture at Hildenhof. ..... 161

Figure 3.60 D and E-type leucogranites at Ida Dome. ..... 162

Figure 3.61 Mineralised sheeted leucogranite from Ida Central with typical E-type oxidation. ..... 163

Figure 3.62 Core samples from diamond hole HDD027 at Ida Central. ..... 164

Figure 3.63 Cross–cutting relationships of Khan Formation–hosted leucogranites. ..... 166

Figure 3.64 Schematic diagram of the Central Zone deposits within the context of the Damara stratigraphic succession. ..... 169

Figure 3.65 Major global uranium deposits, with Namibian deposits for comparison. ..... 171

**Chapter 4**

Figure 4.1 Sheeted leucogranites at the CZ deposits. ..... 178

Figure 4.2 Localities of Etango A drill hole collars at Goanikontes. ..... 183

Figure 4.3 Ida Dome sample localities. ..... 185

Figure 4.4 Location map of the Husab mine project on ML171. ..... 187

Figure 4.5 Valencia Hand samples and drill core collar locations on Valencia EPL 1496. ..... 188

Figure 4.6 Photomicrographs of Salem Suite features at Valencia. ..... 191

Figure 4.7 Photomicrographs illustrating features of the Grey granite varieties from Hildenhof. ..... 194

Figure 4.8 Photomicrographs of B-type sheeted leucogranites at Valencia ..... 198

Figure 4.9 Photomicrographs of the A-types at Ida Dome. ..... 198

Figure 4.10 Tourmaline in C-type sheets from Goanikontes. ..... 200

Figure 4.11 Textural features of the C-type sheeted leucogranites sampled from Goanikontes core ..... 202

Figure 4.12 Magnetite in grey type-3 from Hole DH012, in mineralised sheeted leucogranite from Hole DH019 and Cm-type from Hole DH022. ..... 204

Figure 4.13 Common features in C-type sheets at Hildenhof ..... 207

Figure 4.14 Ct-type Sheeted leucogranites at Ida Dome. ..... 210

Figure 4.15 Photomicrographs of Cm type leucogranites from the Ida Central Area. ..... 211

Figure 4.16 Examples of common sheeted leucogranites of the Husab Deposits. ..... 213

Figure 4.17 Photomicrographs of Ct-type Sheeted leucogranites at Valencia. ..... 216

Figure 4.18 Petrographic features of Magnetite-type sheeted leucogranites at Valencia. ..... 217

Figure 4.19 Magnetite-haematite-ilmenite and sulphide textures in Central Zone leucogranites. ..... 220

Figure 4.20 Magnetite at reaction contact between sheeted leucogranite and a metasediment. ..... 221

Figure 4.21 Entrained sulphides at Ida Central and Valencia. ..... 222

Figure 4.22 Two textures of pyrite and molybdenite younger than uraninite, in Husab alaskite. ..... 223

Figure 4.23 Early high temperature alteration features. ..... 229

Figure 4.24 Late high temperature and low temperature alteration features. ..... 230

Figure 4.25 Petrographic characteristics of Goanikontes D-type sheeted leucogranites. ..... 234

Figure 4.26 Features of altered D and E-type sheeted leucogranites. ..... 236

Figure 4.27 Features common to the majority of mineralised sheeted leucogranites at Hildenhof ..... 239

Figure 4.28 Examples of accessory phases in mineralised Sheeted leucogranites at Hildenhof. ..... 240

Figure 4.29 Uraninite, magnetite and uranophane associations in Goanikontes sample DH025 353.60-354.03. ..... 241

Figure 4.30 Photomicrographs of uranium mineralisation in D type ores from 350 m depth, at Goanikontes. 243

Figure 4.31 Uranium mineral features in the surface sample HILG21 from the Hildenhof anomaly. ..... 244

Figure 4.32 Features of mineralised sheets from the Ida Dome area. ..... 247

Figure 4.33 Features in oxidised and unaltered portions of E-type leucogranite at Ida Dome. ..... 249

Figure 4.34 Features of mineralised samples with skarn and host rock interaction. ..... 250

Figure 4.35 Uranium mineral associations in core specimens from HDD025. ..... 251

Figure 4.36 Alteration features of mineralised granites at Ida Dome. ..... 253

Figure 4.37 Uraninite and uranophane in Ida Dome Leucogranites. ..... 254

Figure 4.38 Examples of primary uraniferous sheeted leucogranite at the Husab Deposits. ..... 257

Figure 4.39 Pegmatitic uraniferous sheeted leucogranites at the Husab Deposit, Zone 1. ..... 259

Figure 4.40 Petrographic features of typical D-type alaskites at Husab. ..... 261

Figure 4.41 Brannerite- and betafite-bearing uraniferous leucogranite samples from drill hole RDD373. ..... 263

Figure 4.42 Petrographic features of brannerite- and betafite-hosting sheeted leucogranites. ..... 265

Figure 4.43 Fluorite and F- associated alteration. ..... 267

Figure 4.44 Primary uraninite textures and mineral relationships at the Husab deposits. ..... 269

Figure 4.45 Sulphide and uraninite textures in the Husab sheeted leucogranites. ..... 270

Figure 4.46 Accessory mineral textures in Husab alaskites. ..... 273

Figure 4.47 Alteration and remobilization of uranium at Husab. ..... 276

Figure 4.48 Typical post D3 sheeted leucogranites at Valencia. ..... 278

Figure 4.49 Unaltered D-type sheeted leucogranites and mineralised apophyses at Valencia. ..... 280

Figure 4.50 Oxidised D-type sheeted leucogranite from Valencia. ..... 282

Figure 4.51 The common primary uranium mineralisation textures and ore mineral associations in Valencia alaskites. ..... 284

Figure 4.52 Secondary uranium mineral textures at Valencia ..... 285

**Chapter 5**

Figure 5.1 Major element wt.% ranges of the Central Zone leucogranites and equigranular Grey and Salem suite granites. ..... 309

Figure 5.2 Major element abundances of the uraniferous leucogranite populations at the Goanikontes, Hildenhof, Ida Dome, Husab, and Valencia Deposits. ..... 309

Figure 5.3 Or-An-Ab normative plots (after Barker, 1979) of Salem, Grey, and leucogranite suites of the Central Zone uranium deposits. ..... 311

Figure 5.4 Q'-ANOR diagrams of Central Zone uranium deposit granites. ..... 313

Figure 5.5 Q'-ANOR of the pre- and post-D3 leucogranite type populations of the Central Zone U deposits. .. 314

Figure 5.6 Q-ANOR of uraniferous leucogranites. ..... 315

Figure 5.7 Q'-ANOR diagram for mineralised leucogranites from Etango deposit (on Farm Goanikontes) diamond drill core. ..... 316

Figure 5.8 Q'-ANOR diagram of Hildenhof mineralised sheeted leucogranite. ..... 316

Figure 5.9 Samples from the Central, Garnet Valley and Holland's Dome deposits. ..... 317

Figure 5.10 Q'-ANOR diagram of selected Husab mineralised leucogranites (alaskites). ..... 318

Figure 5.11 Valencia mineralised sheeted leucogranites. ..... 318

Figure 5.12 Normative orthoclase-quartz-albite ternary plots of Grey and Salem granites of the CZ uranium deposits. ..... 320

Figure 5.13 Normative orthoclase-quartz-albite ternary plots of sheeted leucogranites of the CZ uranium deposits. ..... 321

Figure 5.14 Aluminium saturation diagrams of the granite suites at the Central Zone primary uranium deposits. ..... 325

Figure 5.15 Aluminium saturation diagram of sheeted leucogranites from the Goanikontes, Hildenhof, Husab, Ida Dome and Valencia deposits. ..... 326

Figure 5.16 Aluminium saturation diagram of the Valencia leucogranite suite. ..... 328

Figure 5.17 Aluminium saturation diagrams of uraniferous sheeted leucogranites. ..... 328

Figure 5.18 Modified alkali-lime index diagrams of the Ida Dome and Husab leucogranite suites. ..... 331

Figure 5.19 Modified alkali-lime index diagrams of the Goanikontes and Valencia leucogranite suites. ..... 332

Figure 5.20 Fe* vs. $SiO_2$ diagrams of the leucogranite suite at Valencia and Goanikontes. ..... 334

Figure 5.21 Fe* vs. $SiO_2$ diagrams of the leucogranite suite at the Ida Dome and Husab. ..... 335

Figure 5.22 Total $Fe_2O_3$ + MgO (wt.%) of Central Zone granites. ..... 336

Figure 5.23 Maficity diagrams of Central Zone Grey, Red and Salem granites and sheeted leucogranites. ..... 338

Figure 5.24 Maficity diagrams of Central Zone sheeted leucogranites at Valencia. ..... 339

Figure 5.25 A-B diagrams of Debon and Le Fort (1983) of Central Zone sheeted leucogranites. ..... 340

Figure 5.26 P-Q plot of Goanikontes, Ida and Valencia A, B, and F-types. ..... 341

Figure 5.27 Bar graph plots of aluminium saturation of the sheeted leucogranites. ..... 343

Figure 5.28 $K_2O$ wt.% vs. Rb ppm of Central Zone sheeted leucogranites. ..... 346

Figure 5.29 Rb and K relationships in the Central Zone U-deposit leucogranite suites. ..... 347

Figure 5.30 Sr content of Central Zone granites relative to $SiO_2$. ..... 349

Figure 5.31 CaO vs. Rb/Sr of granites at the Central Zone uranium deposits. ..... 349

Figure 5.32 Plot of SiO2 vs. Rb/Sr ppm of Valencia and Goanikontes granites. ..... 350

Figure 5.33 Relationships between Ba and $K_2O$, and Ba and CaO in Central Zone leucogranites. ..... 351

Figure 5.34 Ba vs. Sr in the SLGs. ..... 352

Figure 5.35 Ternary plots of Ba, Rb and Sr and Na, K and Ca proportions of the Central Zone deposits. ..... 354

Figure 5.36 La vs. Ce in Central Zone sheeted leucogranite. ..... 357

Figure 5.37 Ce and Y content of mineralised sheeted leucogranite and photomicrographs of phosphate minerals. ..... 358

Figure 5.38 Graph of U vs. Zr of the Central Zone uraniferous SLGs. ..... 358

Figure 5.39 Trace element trends of pre-D3 sheeted leucogranites and uraniferous sheeted leucogranites as indicators of I- or S-type affinity. ..... 361

Figure 5.40 Discrimination plots of (Ce+Nb+Y+Zr) in CZ granite types, ..... 363

Figure 5.41 Ga/Al and major element discrimination plots of Central Zone leucogranites, Salem, and Grey granites. ..... 365

Figure 5.42 $FeO_{tot}$/MgO ratios of SLGs at the CZ primary U deposits. ..... 366

Figure 5.43 Y - Nb and Rb discrimination diagrams of Central Zone uranium deposit granites with fields from Pearce et al. (1984). ..... 368

Figure 5.44 Y and Nb, and Yb - Ta and Rb discrimination plots with fields from Pearce et al. (1984). ..... 369

Figure 5.45 Transition metal trends in the Central Zone alaskites. ..... 371

Figure 5.46 U vs. A/NK and U vs. A/CNK of the Central Zone sheeted leucogranites. ..... 372

Figure 5.47 Plots of Th vs. U of Grey, Salem, and uraniferous leucogranite suites of Central Zone U deposits. 374

Figure 5.48 Uranium and thorium concentrations in Central Zone leucogranites and associated metasediments. ..... 376

Figure 5.49 Graph of Th vs. U of Central Zone skarn and country rock xenoliths. ..... 377

Figure 5.50 Nb vs. U for ICP-MS samples. ..... 378

Figure 5.51 Plots of Ti vs. U and Ta vs. U for the ICP-MS samples. ..... 379

Figure 5.52 Key to lithology codes used in the RDD373 geochemical- and petrographic collages. ..... 383

Figure 5.53 Brannerite textural varieties identified in thin sections of samples from RDD373. ..... 383

Figure 5.54 RDD373-64 m specimens in hand sample with thin section localities. ..... 384

Figure 5.55 The RDD373 124-125 m sample with thin section locality and handheld XRF assay data. ..... 386

Figure 5.56 The RDD373 124-125 m sample with thin section locality and handheld XRF assay data. ..... 387

Figure 5.57 Thin section and SEM imagery of sample RDD373-93C. ..... 388

Figure 5.58 Uranium assay by ICP-MS comparison with hand held XRF assay. ..... 390

Figure 5.59 Nb (ppm) vs. Ti (ppm) of brannerite- and betafite-bearing intervals in drill hole RDD373. ..... 391

**Chapter 6**

Figure 6.1 REE plots for Grey and Salem Suite granites at Valencia, Holland's Dome and Hildenhof. ..... 402

Figure 6.2 REE plots for sheeted leucogranites from Etango, Husab, Ida Dome and Valencia. ..... 403

Figure 6.3 REE plots of mineralised leucogranites/ alaskites from Etango, Husab, Ida Dome and Valencia. ..... 404

Figure 6.4 Uranium content vs. ∑HREE from Tb through Lu. ..... 405

Figure 6.5 REE plots of leucogranite samples from the Etango Deposit at Goanikontes. ..... 406

Figure 6.6 REE plots of Rössing Formation-hosted alaskites from the Zone 1 deposit at Husab. ..... 409

Figure 6.7 REE plots of magnetite C-types from Zone 1, Husab. ..... 409

Figure 6.8 REE abundances of Ida Central and Holland's Dome Grey granites. ..... 412

Figure 6.9 REE abundances of the Ida Central and Garnet Valley C-type, and Cm-type sheeted leucogranites. ..... 412

Figure 6.10 REE plots of Ida Dome Area leucogranite and alaskite. ..... 413

Figure 6.11 Rare earth element plots of sheeted leucogranite and Salem granites at the Valencia deposit. ..... 416

Figure 6.12 The Khan Formation-hosted Salem suite and leucogranites at Valencia. ..... 418

Figure 6.13 The Kuiseb Formation-hosted sheeted leucogranites at Valencia. ..... 418

Figure 6.14 Uraniferous sheeted leucogranites at Valencia. ..... 419

Figure 6.15 X-Y plot illustrating systematic behaviour of HREE abundances vs. Zr. ..... 420

Figure 6.16 HREE vs Y of Central Zone sheeted leucogranites. ..... 421

Figure 6.17 LREE fractionation trends of selected CZ granites. ..... 422

Figure 6.18 HREE fractionation trends of selected CZ granites. ..... 424

Figure 6.19 REE ratios as discriminators between sheeted leucogranite types. ..... 426

Figure 6.20 U in ppm vs. Non-chondritic Y/Ho of CZ granites. ..... 428

Figure 6.21 Monazite specimens in backscatter imagery. ..... 432

Figure 6.22 Compositional variation of monazite from Valencia and Husab. ..... 433

Figure 6.23 Ce-Ca-Th ternary plot of CZ monazite. ..... 434

Figure 6.24 Nd-Ce-La ratios of the Valencia and Husab monazite samples. ..... 434

Figure 6.25 Monazite compositions on a ternary diagram of Y-Th-Ce with temperature fields of Gratz and Heinrich (1997). ..... 435

**Chapter 7**

Figure 7.1 Summary map of the Central Zone geology and locations of the study areas. ..... 439

Figure 7.2 Uranium-mineral speciation charts of samples from the Central Zone primary uranium deposits. . 446

Figure 7.3 Uranium-mineral deportment statistics chart. ..... 446

Figure 7.4 Key to mineral particle maps in the QEMSCAN section. ..... 447

Figure 7.5 Mineral map features of DH025 43.13-43.49 from the Etango Deposit at Goanikontes. ..... 449

Figure 7.6 Mineral map of DH025 334.91-335.25 and DH025 353.60-354.03 from diamond hole 25 at the Etango deposit, Goanikontes. ..... 451

Figure 7.7 Mineral map features of CZ14-1, surface sample E-type from Rabbit Valley. ..... 452

Figure 7.8 Mineral map features of HILG 21. ..... 453

Figure 7.9 Uranium deportment statistics of Goanikontes and Hildenhof samples. ..... 454

Figure 7.10 Uranium deportment of the Ida Dome QEMSCAN samples. ..... 454

Figure 7.11 Mineral map features of HDD027 samples. ..... 457

Figure 7.12 Mineral map features of IDAG 08 from Ida Central. ..... 458

Figure 7.13 Mineral map features of IDAG 43 from Holland's Dome. ..... 459

Figure 7.14 Uranium deportment of the Husab QEMSCAN samples from Zone 1 and Zone 2. ..... 460

Figure 7.15 QEMSCAN mineral maps of uraninite and coffinite textures in Husab Zone 1 and Zone 2 samples. ..... 463

Figure 7.16 QEMSCAN mineral maps of uranium mineral textures in Husab Zone 1 and Zone 2 samples. ..... 464

Figure 7.17 Uranium-bearing refractory mineral textures in samples from hole RDD373, Husab. ..... 467

Figure 7.18 Graphical representations of the RDD006 sample intervals. ..... 468

Figure 7.19 QEMSCAN derived mineral maps illustrating uranium mineral textures of RDD006 specimens. ... 470

Figure 7.20 QEMSCAN derived mineral maps illustrating uranium mineral textures of RDD006 specimens continued. ..... 471

Figure 7.21 Uranium deportment statistics of the Valencia QEMSCAN samples. ..... 473

Figure 7.22 Ortho-photo with lithological overlay at Valencia with localities of samples submitted for QEMSCAN analyses. ..... 474

Figure 7.23 Mineral maps of samples from the Va26 113 diamond drill hole at Valencia. ..... 476

Figure 7.24 Mineral map features of Va26 141 diamond drill hole at Valencia. ..... 478

Figure 7.25 Mineral map features of VALG 11. ..... 480

Figure 7.26 Mineral map features of VALG26. ..... 480

Figure 7.27 Uraninite, coffinite, and thorite phase distribution and relationships of the Central zone primary deposits. ..... 487

Figure 7.28 Uraninite, coffinite, and uranophane phase distribution and relationships of the Central zone primary deposits. ..... 489

Figure 7.29 U-deportment between brannerite and betafite. ..... 490

Figure 7.30 Primary uraninite-thorite-brannerite-betafite relationships with mobile U. ..... 494

**Chapter 8**

Figure 8.1 Uranium and thorium ternary diagram of 43 uraninite specimens from selected Central Zone primary deposits. ..... 506

Figure 8.2 Compositional ranges of primary uraninite specimens from the Etango, Hildenhof, Husab, Ida Dome, and Valencia localities. ..... 508

Figure 8.3 Four binary plots of uraninite compositional variables, U oxides, Th, REE and Y, Ca, and Si. ..... 509

Figure 8.4 Uraninite and coffinite in sample DH025-43m and DH025-353m. ..... 513

Figure 8.5 Uraninite compositional variation in the Etango DH025 drill hole samples. ..... 515

Figure 8.6 Secondary uranium minerals and uraninite inclusions in Etango samples. ..... 517

Figure 8.7 Uranium and magnetite relationships in Etango drill hole DH025 samples at 43 m and 353 m. ..... 519

Figure 8.8 Composite mineral grains from sample DH025_353 m. ..... 520

Figure 8.9 Backscatter and element map imagery of Hildenhof uraninite specimens from surface sample HILG21. ..... 522

Figure 8.10 Compositional summaries of 5 uraninite specimens in Hildenhof sample HILG 21. ..... 523

Figure 8.11 Next page. Mineral maps of Holland's Dome U phases ..... 525

Figure 8.12 Core samples from Va26 113 and Va26 141 NQ drill holes at Valencia. ..... 527

Figure 8.13 Backscatter images of Valencia deposit uraninite specimens. ..... 528

Figure 8.14 Uraninite compositional variations in specimens of drill core and from surface. ..... 531

Figure 8.15 Coffinite replacement of uraninite U1 from Va26 113 225m. ..... 532

Figure 8.16 Uraninite specimens from the Husab Zone 1 and Zone 2 deposits. ..... 536

Figure 8.17 Composition and texture of uraninite U7, hosted in biotite of sample RDD373-125 m. ..... 538

Figure 8.18 Uraninite specimens from the RDD008 and RDD006 drill cores, Zone 1 and Zone 2, respectively. 540

Figure 8.19 $UO_2$ vs. $ThO_2$ of granite-hosted uraninite. ..... 543

Figure 8.20 $U_{tot}$ vs. $ThO_2$ wt% in uraninite of the Central Zone primary uranium deposits, with comparative orogenic granite-hosted uraninites. ..... 544

Figure 8.21 Uranium and thorium concentrations in uraninite and in corresponding whole-rock samples ..... 546

Figure 8.22 Uranium vs. total REE wt.% for primary uraninite. ..... 548

Figure 8.23 Betafite from diamond hole RDD373_115m, Zone 1 Deposit, Husab ..... 551

Figure 8.24 Mineral map of a detailed area in an altered brannerite specimen. ..... 557

Figure 8.25 Mineral map with line scan spectra for selected major and trace elements of euhedral brannerite from 93 m in hole RDD373. ..... 558

Figure 8.26 Normalised cationic proportions of Husab betafite and Rössing Mine betafite. ..... 563

Figure 8.27 Binary plot of Husab RDD373-115m betafite (purple) data points pyrochlore-euxenite-samarskite mineral group classifications. ..... 563

Figure 8.28 Bivariate plots of betafite and brannerite compositions. ..... 565

Figure 8.29 Uranium vs PbO wt.% for the Central Zone uraninite. ..... 568

Figure 8.30 $UO_2/ThO_2$ vs. PbO of Central Zone uraninite. ..... 569

Figure 8.31 Pb distribution in Valencia uraninite. ..... 570

Figure 8.32 $UO_3$ +$UO_2$/$ThO_2$ vs. CaO wt.% from analyses of betafite and brannerite from drillhole RDD373. .. 571

Figure 8.33 Simplified mineralisation sequence for the primary uranium deposits. ..... 577

**Chapter 9**

Figure 9.1 Textural and compositional inhomogeneity in the leucogranites. ..... 586

Figure 9.2 Schematic diagram of the Central Zone deposits within the context of the Damara stratigraphic succession. ..... 591

Figure 9.3 Textural varieties of garnetiferous leucogranite. ..... 593

Figure 9.4 Average REE abundances of selected Central and Southern Zone granite groups. ..... 599

Figure 9.5 HFS elements vs. FeOtot/MgO wt.% granite- discrimination plot. ..... 607

Figure 9.6 10000*Ga/$Al_2O_3$ wt.% vs $K_2O$/MgO plot with discrimination fields of Whalen et al. (1984). ..... 608

Figure 9.7 Tectonic discrimination diagrams of the Central Zone granites. ..... 610

Figure 9.8 Simplified schematic diagram of the mineralisation sequence in the Central Zone primary deposits. ..... 623

## *List of Tables*

**Chapter 1**

Table 1.1 Reserves and Resources of the uranium deposits described in this study. ..... 14

**Chapter 2**

Table 2.1 Simplified stratigraphic section of the Damara Supergroup in the Central Zone. ..... 21

Table 2.2 Ages of granitic rocks of the southern Central Zone. ..... 27

Table 2.3 Average U-content of Damaran granitoids and metasediments. ..... 28

Table 2.4 Granitic rocks of the southern Central Zone. ..... 30

**Chapter 3**

Table 3.1 Revised Central Zone sheeted leucogranite classification after Nex (1997). ..... 50

Table 3.2 The SLG sequence at Goanikontes ..... 77

Table 3.3 Estimated percentages of ore material by rock type of the Husab Mine Project. ..... 121

Table 3.4 Central Zone uranium deposit geological characteristics. ..... 170

**Chapter 4**

Table 4.1 Summary of samples and their locations. ..... 180

Table 4.2 Thin section characteristics of Salem Suite samples from Valencia ..... 189

Table 4.3 Key petrographic features of type-2 and type-3 Grey granites at Hildenhof ..... 193

Table 4.4 Key petrographic features of Red granites at Hildenhof. ..... 195

Table 4.5 Petrographic characteristics of A and B-type sheeted leucogranites from Valencia ..... 196

Table 4.6 Petrographic characteristics of C-type leucogranites from the Goanikontes area. ..... 199

Table 4.7 C-type granite samples from the Hildenhof Anomaly (U and Th content by XRF, in ppm). N/A no analysis. ..... 206

Table 4.8 Petrographic characteristics of C-type sheeted leucogranites from the Ida Dome areas ¼ NQ core. 208

Table 4.9 Petrographic characteristics of Valencia C- and F- type sheeted leucogranites ..... 214

Table 4.10 Petrographic characteristics of D- and E-type leucogranites from the Goanikontes area. ..... 232

Table 4.11 Petrographic characteristics of mineralised sheeted leucogranite thin sections from Hildenhof. ... 238

Table 4.12 Petrographic characteristics of alaskite thin sections cut from core samples from Ida Central and hand specimen from the Holland's Dome deposit. ..... 245

Table 4.13 Petrographic characteristics of the Husab alaskites. ..... 255

Table 4.14 Thin section characteristics of uraniferous sheeted leucogranites from the Valencia deposit. ..... 277

Table 4.15 Revised Central Zone sheeted leucogranite classification after Nex (1997). ..... 295

**Chapter 5**

Table 5.1 Summary statistics of 244 major element XRF analyses of Central Zone granite and metasediment samples. ..... 302

Table 5.2 Trace elements summary of the granitic samples collected for this study, all values in ppm, analysed by XRF fusion ..... 303

Table 5.3 Rare-earth, trace-, and major elements analysed at the Bernard Price Institute ICP-MS laboratory. 304

Table 5.4 Summary total of samples analysed for major and trace elements by XRF fusion and/or pressed pellet analyses. ..... 305

Table 5.5 Major Element averages of Central Zone granites in this study (all XRF fusion). ..... 308

Table 5.6 Summary of the $Al_2O_3$, CaO, $Na_2O$ and $K_2O$ wt.% values of the outlying sample, with U in ppm (XRF). ..... 326

Table 5.7 Molar proportions of Al, Ca, Na and K at the Ida Dome Deposits. ..... 326

Table 5.8 Summary of handheld XRF chemical analyses. ..... 389

**Chapter 6**

Table 6.1 Collar positions of diamond holes sampled for REE analyses. X and Y are in UTM (WGS84- 33S). Samples represent 1 m intervals of granite (alaskite). ..... 401

Table 6.2 Positions of surface samples submitted for REE analyses. X and Y are in UTM (WGS84- 33S). ..... 401

Table 6.3 Summary of REE trends of refractory-bearing and uraniferous sheeted leucogranites at the Husab Zone 1 deposit. ..... 407

Table 6.4 of REE trends of Grey granites, leucogranites and mineralised leucogranites (alaskite) of the Ida Dome area sample set. ..... 411

Table 6.5 Summary of REE trends of Grey granites, leucogranites and mineralised leucogranites (alaskite) of the Valencia sample set. ..... 415

Table 6.6 REE fractionation summary of the SLGs, Grey-, and Salem granites in this study. ..... 426

**Chapter 7**

Table 7.1 Summary of QEMSCAN study samples and locations ..... 444

Table 7.2 Common abbreviations used in Chapter 7. ..... 445

**Chapter 8**

Table 8.1 Average compositions of Central Zone primary uranium deposit uraninite, as determined by EPMA analyses. ..... 507

Table 8.2 Composition of coffinite specimen U7 of sample DH025_43m. ..... 516

Table 8.3 Summary of uraninite analyses undertaken by EPMA on 11 uraninite specimens from Valencia. ..... 529

Table 8.4 The recalculated non-stoichiometric formulae of uraninite, coffinite and thorite from the Valencia deposit. ..... 530

Table 8.5 Husab uraninite, coffinite, brannerite, and betafite composition summary. ..... 534

Table 8.6 Recalculated mineral formulae for Husab uraninite specimens. ..... 537

Table 8.7 Cation corrections for all betafite analysis spots from sample RDD373_115m. ..... 552

Table 8.8 Cation proportions of the RDD373_115A Betafite, normalised to 8.31 oxygen. ..... 553

Table 8.9 Brannerite formulae from EPMA analyses of sample RDD373 – 64m. ..... 555

Table 8.10 Brannerite formulae from EPMA analyses of sample RDD373 – 93m. ..... 555

Table 8.11 Results of formula recalculation of the RDD373 64 m brannerite specimen. ..... 559

Table 8.12 Results of formula recalculation of the RDD373 64 m brannerite specimen. ..... 560

Table 8.13 The A site cation proportions of the Husab betafite. ..... 562

**Chapter 9**

Table 9.1 Central Zone uranium deposit geological characteristics ..... 590

Table 9.2 Major and trace element abundances in the pre-D3 and the uraniferous leucogranites. ..... 596

Table 9.3 Revised classification scheme for the sheeted leucogranites. ..... 616

Table 9.4 Comparative table of uraniferous sheeted leucogranites and their respective geological settings ... 633

## Glossary of Abbreviations

| General Abbreviations | |
|---|---|
| **BSE** | Backscatter electron |
| **CZ** | Central Zone |
| **D1, D2, D3, *D4*** | Major Damaran Deformational Events (1-4) |
| **DH** | Downhole |
| **Fm.** | Formation |
| **ll** | Parallel |
| **Ma** | Million years before present |
| **ND** | No Data |
| **NQ** | 47.6 mm Diamond Drill Core |
| **sCZ** | Southern Central Zone |
| **SLG** | Sheeted Leucogranite |
| **U** | Uranium, Uranium-bearing |

| Analytical Techniques | |
|---|---|
| **EPMA** | Electron Probe Microanalysis |
| **Ppl** | Plane-polarised Light |
| **QEMSCAN** | Automated Scanning Electron Microscope |
| **Rfl** | Reflected light |
| **SEM** | Scanning Electron Microscope |
| **TS** | Thin Section |
| **Xpl** | Crossed Polarised Light |
| **XRD** | X-Ray Diffraction |
| **XRF** | X-Ray Fluorescence |

| Measurements | |
|---|---|
| **µm** | Micro metre ($m^{-6}$) |
| **mm** | Millimetre ($m^{-3}$) |
| **cm** | Centimetre ($m^{-2}$) |
| **m** | Metre |
| **g** | Gram |
| **kg** | Kilogram ($g^3$) |
| **t** | Metric tonne |

| Sample Nomenclature | |
|---|---|
| **GOAG** | Goanikontes Granite |
| **GOAG** | Goanikontes Granite |
| **GOAV** | Goanikontes Vein |
| **DH_** | Goanikontes Core Sample |
| **HILG** | Hildenhof Granite |
| **HILM** | Hildenhof Metasediment |
| **Hu** | Husab Fluorite Mine Sample |
| **IDAG** | Ida Dome Granite |
| **IDAM** | Ida Dome Metasediment |
| **HDD_** | Ida Dome Core Sample |
| **GDD_** | Garnet Valley Core Sample |
| **HDDD** | Holland's Dome Core Sample |
| **RDD_** | Husab Core Sample |
| **VALB** | Valencia Salem Granite |
| **VALG** | Valencia Granite |
| **Va26_** | Valencia Core Sample |
| **Jo** | Joly Zone Core Sample |
| **Vs** | Valencia Salem Granite/Grey Granite |

| Common Mineral Abbreviations | | | |
|---|---|---|---|
| **Ab** | Albite | **Mp** | Microcline-perthite |
| **All.** | Allanite | **My** | Myrmekite (texture) |
| **An** | Anorthite | **Mz** | Monazite |
| **And** | Andalusite | **Msp** | Meso-perthite |
| **Ap** | Apatite | **Ol** | Oligoclase |
| **Bt/B** | Biotite | **P** | Plagioclase |
| **Bf** | Betafite | **Py** | Pyrite |
| **Br** | Brannerite | **Pyr** | Pyrrhotite |
| **Ca** | Calcite | **Mc** | Microcline |
| **Cf** | Coffinite | **Mo** | Molybdenite |
| **Czo** | Clinozoisite | **Se/** | Sericite |
| **Ep** | Epidote | **Sil** | Sillimanite |
| **Fl** | Fluorite | **Ss** | Saussurite |
| **Gn** | Garnet | **Tm** | Tourmaline |
| **H** | Haematite | **U** | Uraninite |
| **I** | Ilmenite | **Up (β-U)** | Uranophane (beta) |
| **Ksp** | K feldspar | **Xe** | Xenotime |
| **M** | Magnetite | **Zo** | Zoisite |
| **Ms** | Muscovite | | |

## Appendix Volume

Appendix A Uranium Production Statistics ..... 1
Appendix B Central Zone Uranium Deposit Locations ..... 4
Appendix C1 Radiometric mapping ..... 5
Appendix C2 Hildenhof radiometric map data points ..... 6
Appendix C3 Ida Central radiometric map data points ..... 8
Appendix C4 Spivey 2011 geological map ..... 15
Appendix C5 Smith 1965 Structural geology map ..... 16
Appendix C6 Geological Map of the Valencia Deposit ..... 17
Appendix C7 Structural data for Kink fold at Valencia ..... 18
Appendix C8 Sample Localities ..... 19
Appendix D1 Thin Section Petrography Summary ..... 25
Appendix D2 Ore petrography notes ..... 47
Appendix E1 Analytical Facilities and Apparatus ..... 48
Appendix E2 Methodology for Whole Rock Geochemical Analyses (XRF) ..... 49
Appendix E3 Methodology for Hand Held XRF ..... 50
Appendix E4 Methodology for ICP-MS Analyses ..... 51
Appendix E5 XRF Laboratory Calibration Standards and Detection Limits ..... 51
Appendix E6 ICP-MS Calibration Standards and Conditions ..... 57
Appendix E7 XRF Accuracy and Precision Testing ..... 64
Appendix E8 Hand Held XRF Accuracy and Precision Testing ..... 68
Appendix E9 ICP-MS Accuracy and Precision Testing ..... 75
Appendix E10 XRF Laboratory Major and Trace Element Data ..... 81
Appendix E11 Handheld XRF Data ..... 99
Appendix E12 REE Sample Descriptions ..... 105
Appendix E13 ICP-MS Data for REE Samples ..... 108
Appendix F1 QEMSCAN History and description ..... 112
Appendix F2 QEMSCAN sampling summary ..... 114
Appendix F3 QEMSCAN Sample Preparation ..... 115
Appendix F4 QEMSCAN Data validation and bulk mineralogy ..... 116
Appendix F5 Deportment statistics ..... 123
Appendix F6 Descriptive Tables of QEMSCAN and EPMA Samples ..... 125
Appendix F7 Photographs of samples submitted for QEMSCAN analyses ..... 131
Appendix F8 QEMSCAN mineral map collages (original data) ..... 143
Appendix G1 Electron Probe Microanalyser Operating Conditions and Calibration standards . 166
Appendix G2 Formulae recalculation procedures ..... 166
Appendix G3 Weight Percentage Portions of Raw EPMA Data Sheets ..... 170
Appendix G4 Appendix G12 Etango Calculated Mineral Compositions ..... 176
Appendix G5 Appendix G12 Hildenhof Calculated Mineral Compositions ..... 179
Appendix G6 Husab Calculated Mineral Analyses ..... 180
Appendix G7 Ida Dome Calculated Mineral Compositions ..... 183
Appendix G8 Valencia Calculated Mineral Compositions ..... 184
Appendix G9 Husab Monazite mass% raw data ..... 188
Appendix G10 EPMA Calculated Analyses for Uranophane species ..... 190

# CHAPTER 1 INTRODUCTION TO PRIMARY URANIUM MINERALISATION IN CENTRAL WESTERN NAMIBIA

## 1.1 Introduction

Over thirty proven occurrences of uranium mineralisation exist in Namibia, most of which occur within the western extent of the Pan-African Damara Orogen. These range from geologically recent calcrete-hosted deposits in the northern and central regions (Hambleton-Jones, 1984) through late Pan African-aged, granite-hosted primary deposits in the central west (Jacob, 1975) and older still, Neoproterozoic granite-hosted deposits in the Gariep and Namaqua Belts in the south of the country (e.g. Andreoli *et al.*, 1992)[1].

The most prolific occurrences of uranium mineralisation are located in the southern Central Zone (sCZ) of the Damara Orogen. As such, Brynard and Andreoli (1988) describe the Central Zone as a 'Large Uranium Province'. Rio Tinto majority owns and operates the Rössing Uranium Mine, the region's premier mine, established in the mid 1970's, it was also the only operating mine to extract uranium from granite for much of its existence. A second producer, Paladin Energy, opened the Langer Heinrich Mine in 2006, which exploits a sedimentary palaeochannel deposit. The recently discovered Husab deposits, which are owned by Swakop Uranium[2], are located near Rössing Mine and the open pit operation is set to become Namibia's largest producer with peak annual production expected to be 15 Mlbs. or ~7 000 tonnes $U_3O_8$. The first product is expected by end 2016, and the nameplate capacity of drummed yellow cake should double Namibian uranium production.

[1] Warmbad Uranium Prospect in Namibia and Steenkampskraal Monazite Deposit, South Africa.
[2] China General Nuclear Resources owns 90 % of Swakop Uranium, the Epangelo Mining Company of Namibia owns 10 %.

### *Historical Context*

Uranium mineralisation in Namibia was first noted by G.P. Louw in 1928, near the site of the Rössing Mine. The world entered the Nuclear Age after the Second World War, and the global search for uranium intensified. It was not until 1955 that detailed prospecting for source minerals commenced in Namibia (Berning *et al.*, 1976). As nuclear power demands increased and the arms race between the United States and Russia developed, exploration for uranium intensified globally, with Namibia and South Africa dominating southern African exploration. Increasing insecurity in the oil producing areas of the Middle East during the nineteen-sixties and nineteen-seventies also contributed to the search for alterantive energy sources.

The demand and price subsequently declined during the early nineteen-eighties, coinciding with a global downturn in U prices as the fuel fell out of public favour in the Cold War era. The surge uranium discoveries in Namibia and the world at large is coincident with the advent of the Nuclear Power Age after World War II, subsequently helped along by oil shortages during OPEC's embargo in the nineteen-seventies. Uranium, like no other metal, is affected by public sentiment, not surprisingly because of the far-reaching consequences, perceived and real, of nuclear war and nuclear waste, respectively.

A revival of the uranium exploration industry in the early 2000's prompted a dramatic increase in exploration licence applications in Namibia. Prices were driven to high levels (over $120/lb) primarily on the back of ambitious speculation and an anticipated shortfall of world production vs. world consumption[3]. Revived exploration programs focussed around historic occurrences at localities such as Valencia, the Ida Dome and Farm Goanikontes, Langer Heinrich, and Trekkopje. The latter two are hosted in recent sediments, whereas the former are all primary deposits; comprising structurally-controlled sheeted leucogranite dykes, sills and stocks that intruded particular sequences of highly metamorphosed Neoproterozoic metasediments.

[3] A common impression at the time was that the finite number of Cold War warheads being dismantled for fuel rod downgrades was coming to an end, in truth, the "Warheads for Fuel" agreement between The Russian Federation and the United States camecomes to its end in 2013.

Uranium mineralisation at most primary deposits is dominated by uraninite. The localised occurrences of abundant uranium silicates; coffinite, and the $U^{6+}$ secondary products boltwoodite, uranophane, and its dimorph β-uranophane within primary deposits is also known well-known. The potassium-uranium-vanadate, carnotite is the main U constituent at palaeochannel-hosted deposits such as Trekkopje (Youlton, 2007).

The uranium-bearing refractory minerals betafite and brannerite are known to occur in localised concentrations exceeding that of uraninite and the U-silicates combined. Occurrences of refractory mineralisation in proximity to the Rössing Mine are well documented in technical literature as well as detailed academic research. Cuney (1980a) and Cuney (1980b), Herd (1996), Nex *et al.* (2002) and Nex *et al.* (2003), and Abraham (2009) present detailed accounts of betafite at the Rössing Mine area and adjacent deposits. In this regard the appreciation of uranium speciation for new projects, whether embarking on further exploration endeavours or undertaking advanced mine feasibility studies, is potentially very important.

To date, no systematic account of the uranium mineral populations encompassing the major uranium deposits of the region is available. This dissertation addresses the need for information in a detailed account of the primary uranium mineralisation trends in the region around the Rössing Mine, and provides new data of uranium mineral compositions and uranium mineral deportment.

## 1.2 Research Outline

As with any large, low-grade deposit type, primary uranium deposits require stringent planning and detailed geological and mineral resource models, as is normal practice they are modelled from data collected in extensive drilling and sampling programs. However, understanding of geological controls on uranium distribution in the host-rocks, geochemical controls on uranium mineral crystallisation, and local variations in host mineral speciation contribute to the refining of such resource models. Four large deposits within the southern Central Zone (sCZ) of the Damara Orogen are considered in this thesis at; Husab on the Welwitschia Plains, Etango on Farm Goanikontes, Valencia on Farm Valencia, and at the Ida

Dome, which comprises several deposits within relative proximity along the eastern flank of the dome structure. A fifth showing of mineralisation at Farm Hildenhof, in the Swakop River valley, is included as an interest case between Etango and the Ida Dome. All of the Primary-hosted deposits occur in folded Damaran metasediments, near prominent dome-like structures. Figure 1.1 illustrates the present-day distribution of the basement dome structures in the west of the southern Central Zone and deposits that occur near them.

Chemical analyses for over 220 leucogranites and whole-rock rare earth element analyses of over 39 granite samples provide a petrological characterisation for the leucogranites at the major primary uranium deposits. Uranium mineral populations of the Ida Central, Holland's Dome, Garnet Valley, Etango deposits at Farm Goanikontes, Onkelo Deposit at Farm Hildenhof, The Husab Mine, and Valencia are presented from automated electron microscope analyses (QEMSCAN). Quantitative analyses of selected uranium mineral phases from each of the main deposit areas are presented from Electron Probe Microanalyses (EMP).

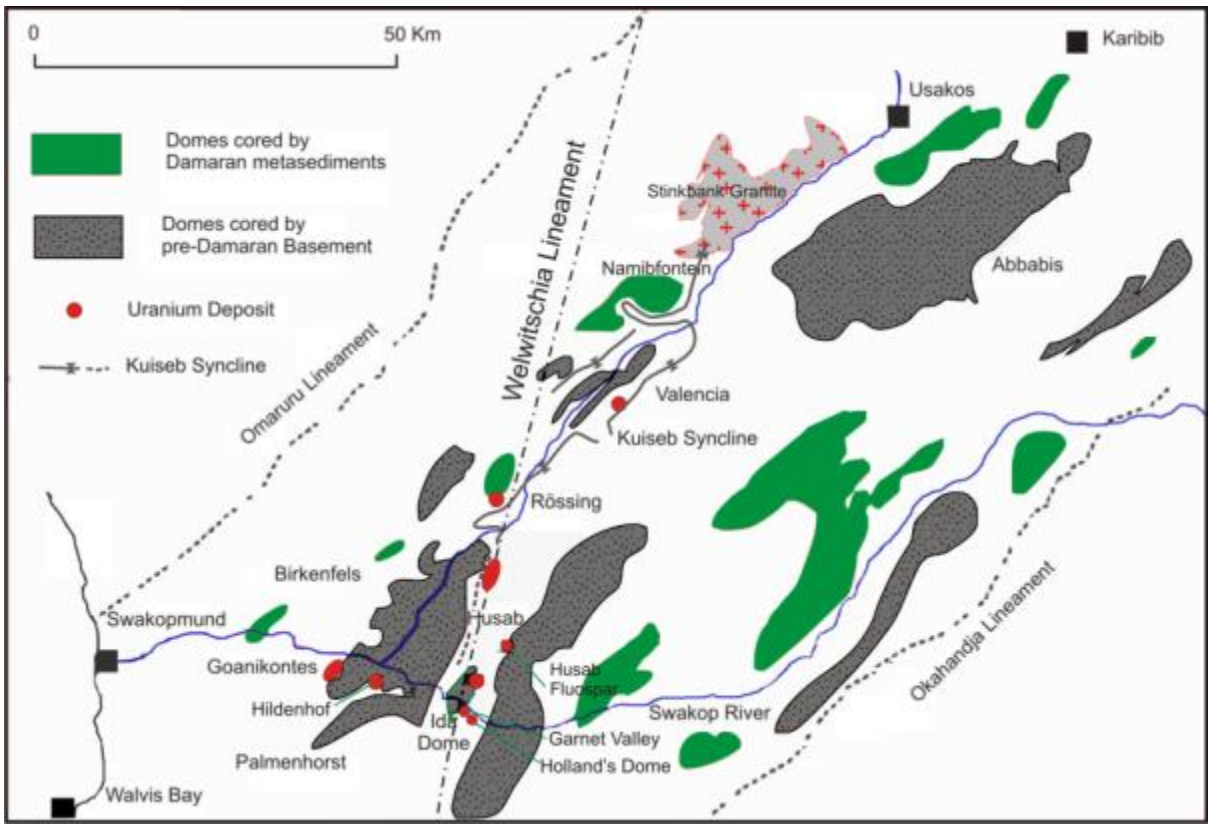



Figure 1.1 The various domes of the Central Zone and their associated primary uranium deposits. The Welwitschia Lineament is a regional magnetic trend produced by late kinematic movement which truncates

and postdates D3 structures. Data sources: Corner (1981; 1983); Eberle *et al.* (1995); Anderson and Nash (1997); Basson and Greenway (2004) and Kinnaird and Nex (2007).

Of the four major deposit areas, only the Husab deposits currently occupy a mine-development stage, while the Etango deposit at Goanikontes has undergone a definitive feasibility study and recently completed column leach tests[4]. The Ida Dome area is currently being revisited while Hildenhof remains a low priority target for both Bannerman and Swakop Uranium.

Projects such as those at Etango, the Ida Dome, and Valencia were explored in the past while the Husab deposits and the Hildenhof Anomaly were not. Their respective histories and near-recent exploration programs are outlined in Rösener and Schreuder (1994), Kinnaird *et al.* (2008) and in Kinnaird and Freemantle (2009). They are discussed in further detail in Chapter 2.

The speciation of the uranium minerals is also an important consideration for new prospects (Figure 1.2). Although the detailed uranium mineralogy of the deposits is presented in Chapter 7 it is necessary to make a brief comment here before describing each of the major deposits in detail. Whilst uraninite is the dominant primary U-bearing phase (Figure 1.2a) sporadic occurrences of the refractory mineral, betafite (Figure 1.2b and 1.2c) brannerite, and davidite are locally abundant at Rössing and Husab. Secondary uranium minerals include β-uranophane (Berning, 1986) at Rössing, and uranophane and boltwoodite at Husab (Spivey, et al., 2010, Townend, 2009) which is often associated with fluorite-present hydrothermal alteration (Figure 1.2d). Company reports of test work conducted by the exploration companies in the region during the 1970's indicated that the dominant mineral species are acid leachable U- silicates and oxides but it is therefore important to assess what percentage of the uranium population is not amenable to acid leaching.

Small percentage changes in refractory uranium mineral deportment are amplified in cost-of-loss, by the scale and size of production, especially where large mines such as Husab are

[4] www.bannermanresources.com.au/etango-project/heap-leach-demonstration-plan. (2015)

expected to process upwards of 15M tonnes/annum of ore[5]. Essentially, modern open pit hard-rock uranium mining operations continually aim to improve mining and extraction efficiencies; from employing large-capacity mining equipment to complex run-of-mine and stockpile classification and management principles to investigating auxiliary mineral processing circuits.

There is thus, a drive to not only understand and quantify the nature, variability, and distribution of the uranium-bearing phases for mining and grade control purposes, but also to describe and quantify the compositional variations in the uranium minerals for processing and metallurgical concerns. Within the context of mineral distribution, metallurgy and mining are not mutually exclusive. Greater efficiencies and environmental concerns are the key drivers for exploiting lower-grade, high-tonnage uranium deposits (after Bhargava *et al.*, 2015). Additionally, the variable ratios of hexavalent- and tetravalent uranium, and thorium, may contribute to optimised grade control techniques and efficient use of processing reagents in multiple- ore-mineral uranium deposits.

A systematic approach to mineral population assessment, within the context of regional and local geological setting and petrographic and geochemical observations will add useful knowledge to an ever-increasing Namibian uranium knowledge base. The intention in future is to use the understanding of the controls of refractory uranium mineral distribution within primary uranium deposits to better assess the potential for developing these projects into viable mining prospects.

Of the key deposits in the Central Zone, the Husab, Goanikontes and Valencia deposits are of variable economic interest and are at present, at differing stages in their mining project development. These projects, from an industrial perspective, require detailed mineralogical characterisations in order to assess economic potential accurately, uranium resource geological modelling, and manage mining and processing efficiencies.

[5] Swakop Uranium, Definitive Feasibility Study, 2011

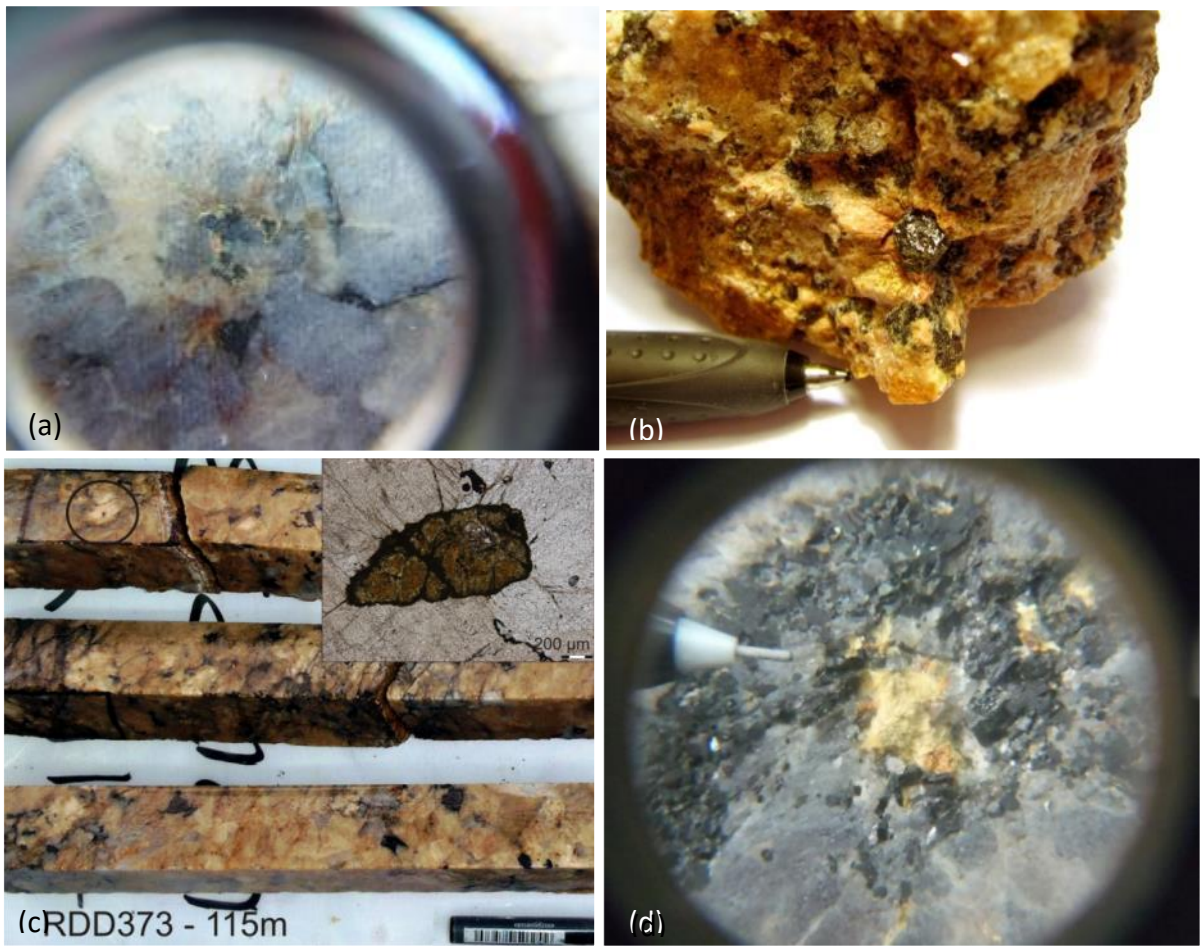



Figure 1.2 Photographs illustrating primary, secondary, and refractory uranium minerals specimens. (a) Uraninite cluster in coarse- textured, uraniferous sheeted leucogranite (alaskite). Note the halo of yellow secondary U minerals, scale: uraninite grains <1 mm, Husab Deposit. (b) Uranophane/boltwoodite in a vug between cubic fluorite, hydrothermally altered, uraniferous sheeted leucogranite (alaskite) Husab Deposit. (c) Brannerite from the Rössing SH Deposit and (d) 1.6 mm betafite grain from the Husab Zone 1 Deposit. In the Husab example Betafite grows across a quartz-feldspar grain boundary. *Images from a- Freemantle (2011); and b- Freemantle (2006).*

## 1.3 Exploration and Mining Interest

Understanding uranium deposition in magmatic systems, particularly in the Central Zone, has in the past focussed on the Rössing Deposit (Jacob, 1974(a); Cuney, 1980a and 1980b; Berning; 1986; Jacob *et al.*, 1986; Herd, 1996; Nex *et al.*, 2003; Basson and Greenway, 2004; Abraham, 2009); and the deposits in the Goanikontes area (Mouillac et al., 1986; and Nex, 1997) which hosts the Etango deposits of Bannerman Resources. Exploration companies also undertook minor studies during the late 1970's and 1980's at the Ida Dome deposits and the Valencia deposit which is also discussed in McDermott (1986).

The exploration industry's awareness of refractory U-mineralisation around Rössing Mine prompted exploration companies at the Ida Dome, Goanikontes and Valencia deposits to investigate the U-mineralogy of their respective targets.

The potential for variable uranium mineral hosts within the Central Zone U-deposits necessitates a systematic investigation of the deposits and individual systems within the larger metamorphic and magmatic contexts of the Damara Orogen. This is especially important for projects wishing to develop into mining operations, such as at Husab, Etango (Goanikontes) and Valencia, where uncertainties in variables such as mineralogy need to be mitigated in order to increase confidence in mining and subsequent process plant performance.

## 1.4 Namibian and World Uranium Production

The demand for uranium is a key driver in the exploration for, and discovery of, new uranium deposits. The global trends in production and consumption are an important consideration for a producer nation like Namibia, in which the mining industry is a significant contributor to the economy. The International Atomic Energy Agency (Hanly, 2014) has reported that uranium production has seen year-on-year increases, despite the persistent global economic downturn. The increased production is, in part, driven by anticipated demand from long-term nuclear power generation projects and improved efficiencies in bulk mining and extraction techniques have made previously uneconomic deposits viable.

The Rössing Mine was, until 2007, Namibia's sole uranium producer since its inception in 1976, and is currently the world's largest uranium producer from primary sources, and 3rd largest by production overall[6]. Figure 1.3 and Figure 1.4 illustrate the supply share percentages of the major producing countries and the largest uranium mines in the world, respectively. All data is from the World Nuclear Association Website, and is up to date to the end of 2015. According to the World Nuclear Association, 2015 mine production accounts

[6] www.world-nuclear.org, 2015

for 75 % of world demand; 56 252 tonnes of uranium (tU) produced vs. 65 908 tU consumed. The deficit is largely made up from down-grading weapons stockpiles and re-enriching spent fuel rods.

Between 2008 and 2009 the world production from mining, in metric tons, increased from 43 853 t(U) to 53 663 t(U); a 22% increase. The global production between 2014 and 2013 decreased 6 %, however, Namibian production decreased by 25 % from 4 315 t(U) to 3 255 t(U) in the same period. It is expected to increase dramatically as Swakop Uranium's Husab Mine enters final product production in 2016. The mine will ramp up to a peak of 15 Mlbs per annum (~7,000 tons U) at name plate capacity before 2020.

Thirteen developed nations generate at least one quarter of their electrical power capacity from nuclear power plants. The world combined power generation capacity is 377,728 megawatts (MW) from 437 reactors, or 11% of the total electricity generation. The projected capacity based on the known and forecast power plant projects globally is between 559,000 MW and 1,087,000 MW[7]. As of January 2015, the International Atomic Energy Agency lists 70 reactors under construction (for 73,514 MW with 49 % in China) and a further 183 reactors planned or on order which should add 203,580 MW of capacity.

## 1.5 Global Influences on Exploration and Mine Development

The boom in uranium exploration accompanied the global commodities boom of the early 2000's, which prompted speculators to predict global power production to increase in future, coupled with assumptions that warhead stockpiles were diminishing at a rate that would be overtaken should new nuclear fuel supplies not be located. Despite these factors that would encourage higher uranium prices, the spot price of $U_3O_8$ has steadily declined in the wake of global economic slow-down after 2009. A resurgence between 2009 and 2011 saw the price rise from US$40/lb to US$70/lb only to drop dramatically shortly after the Fukushima disaster. Spot prices today are below US$20/lb.

[7] World Nuclear Century Outlook, 2012, World nuclear Association Publications.

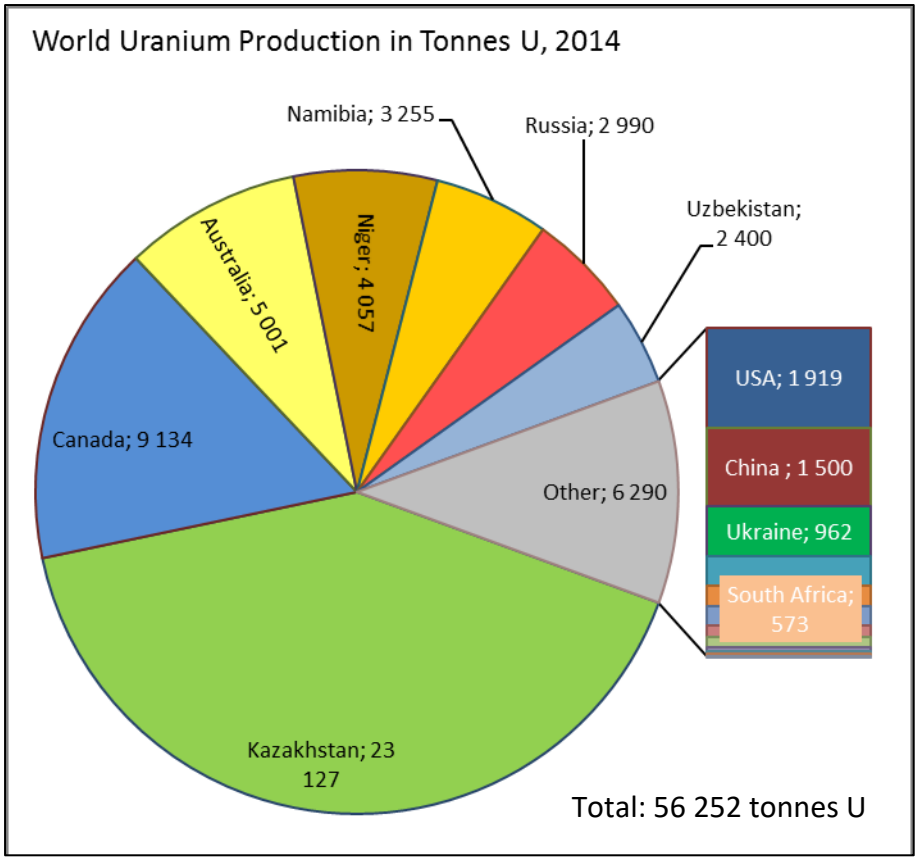



Figure 1.3 World uranium production by country for 2014. Combined with Langer Heinrich, Namibia's Rössing Uranium Mine produces 8% of world uranium production. The 2013 total of 59 673 tU accounted for 90 % of world demand. The deficit is made up of recycling of spent fuel, dismantling of spent fuel rods, and stockpiles. (Statistics from: The World Nuclear Association, 2015)

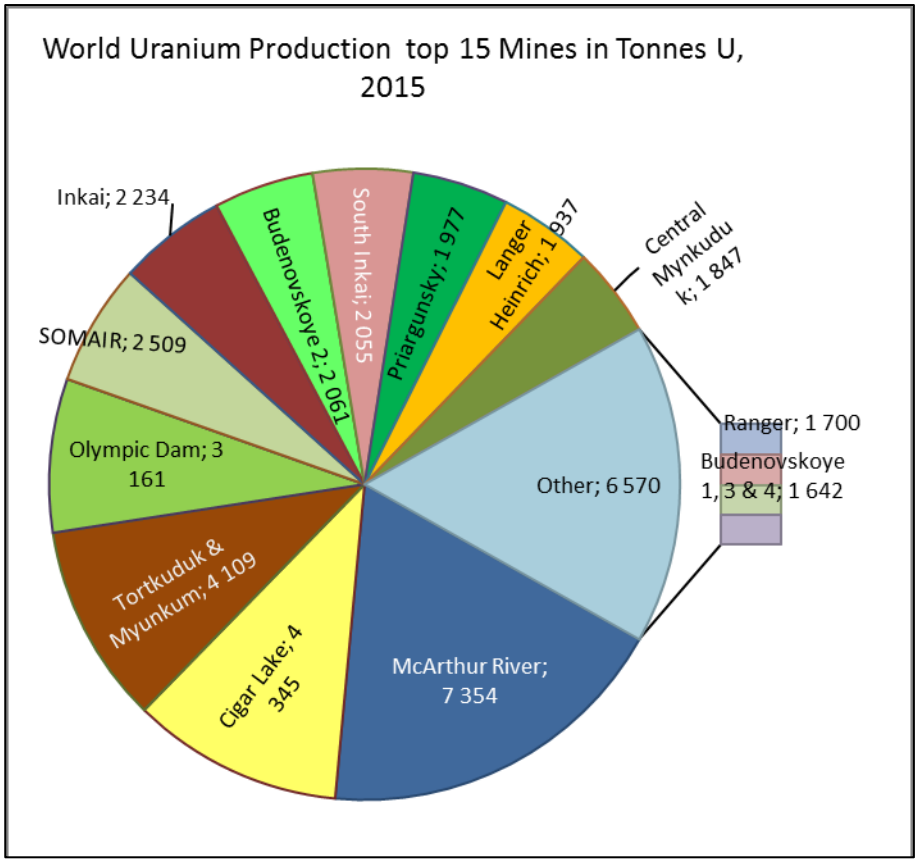



Figure 1.4 World production of the top fifteen uranium mines in metric tons of metal (tU) for the 2015 year. The combined fifteen account for 67 % of world supply (40 159/59 939 tU). The Rössing Mine is out of the top 15, however it still produced 1 057 tU, or ~1.8 % of the world total. (Production statistics from: The World Nuclear Association, February 2016).

The construction of new reactors does however ensure a long-term demand, at least for contracted suppliers to the nuclear power producers. Despite guaranteed demand from the existing and anticipated new power stations, the events of the past 5 years have exposed uranium to be as susceptible to global economics and popular perception (Fukushima, Chernobyl, and Three-Mile Island) as it was to the geo-political climate during the cold war and the oil crisis of the late 1970's.

Japan, for example, shut down all its nuclear power plants after the Fukushima disaster in 2011, but has refrained from selling any of its stockpiled fuel. A reactor was turned on temporarily in 2013, and in August 2015 a reactor at Sendai went into production, which can only be viewed as a positive outlook for the nuclear fuels industry.

The agreement between the United States and the Russian Federation that facilitated the downgrading of warheads to fuel rods came to a halt in 2013, which essentially increased the amount of commercial uranium required by the USA. This may be seen as a positive development, however, exploration and production in North America also experienced the surge of the mid 2000's and the supply shortfall did not meet expectations. The spot price is not anticipated to reach the highly speculative levels seen between 2008 and 2009[8]. As such the depressed prices, have seen large projects such as the Areva-owned Trekkopje Mine be put on care and maintenance. Further development of large primary-hosted projects such as Bannerman Resource's Etango deposit requires not only reliable forecasting of demand but increased levels in confidence of the ore body and the uranium mineral deportment, especially where marginal grades are concerned. Statistical summaries for production and resources are presented in Appendix A and are all sourced from the World Nuclear Association.

### *Uranium Exploration in the Damara Orogen*

Primary uranium prospects and mines are limited to the western portion of the southern Central Zone in the Damara Orogen. For the most part these deposits are exposed on surface

[8] Roger Murray of Fuel Cycle Week, pers. comm., 2013.

by the incised erosion profiles around the Khan and Swakop River gorges (Figure 1.5). The Husab deposits are almost completely concealed beneath Quaternary Namib desert calcrete and gravels, while a large proportion of the Etango deposit is also buried beneath the Namibia peneplain south of the Swakop River Gorge (Figure 1.1).

The Rössing Mine, which has produced the most uranium of any mine globally, was the sole producer from primary sources until 2016 and is currently undertaking expansion of its existing pit. It has also undertaken exploration of two satellite deposits, the SH deposit to the southwest and the SK deposit to the northeast of the main SJ pit. During 2008, Extract Resources encountered significant U intercepts during reconnaissance drilling at what is now known to be the northern end of a very large alaskite system, under cover of the Namib Desert peneplain.

Namibia has a progressive mining and exploration charter that, combined with favourable markets, facilitated the renewed interest in previously abandoned targets during the 2006 to 2009 boom. Exploration for uranium in Namibia had been so intensive between 2004 and 2010 that the Ministry of Mines and Energy placed a moratorium on the issuing of nuclear fuel exploration licences. The areas in this study were explored from 2006 and occur along the Swakop and Khan River valleys, except the Husab deposit which is located below the Namib Desert plains. These exploration studies included:

- Bannerman Mining Resources explored the Etango deposit on Farm Goanikontes and conducted a definitive feasibility study in 2011.
- Extract Resources' (Swakop Uranium, Namibia) explored the deposits at the Ida Dome and Husab areas. They successfully applied for a mining licence, shortly before 99% of the project was acquired by the China Guangdong Nuclear Power Corporation (CGNPC).
- The Valencia deposit was explored by Valencia Uranium (Ltd) as a local subsidiary of Canada's Forsys Metals Corporation and was awarded a mining licence in August of 2008.

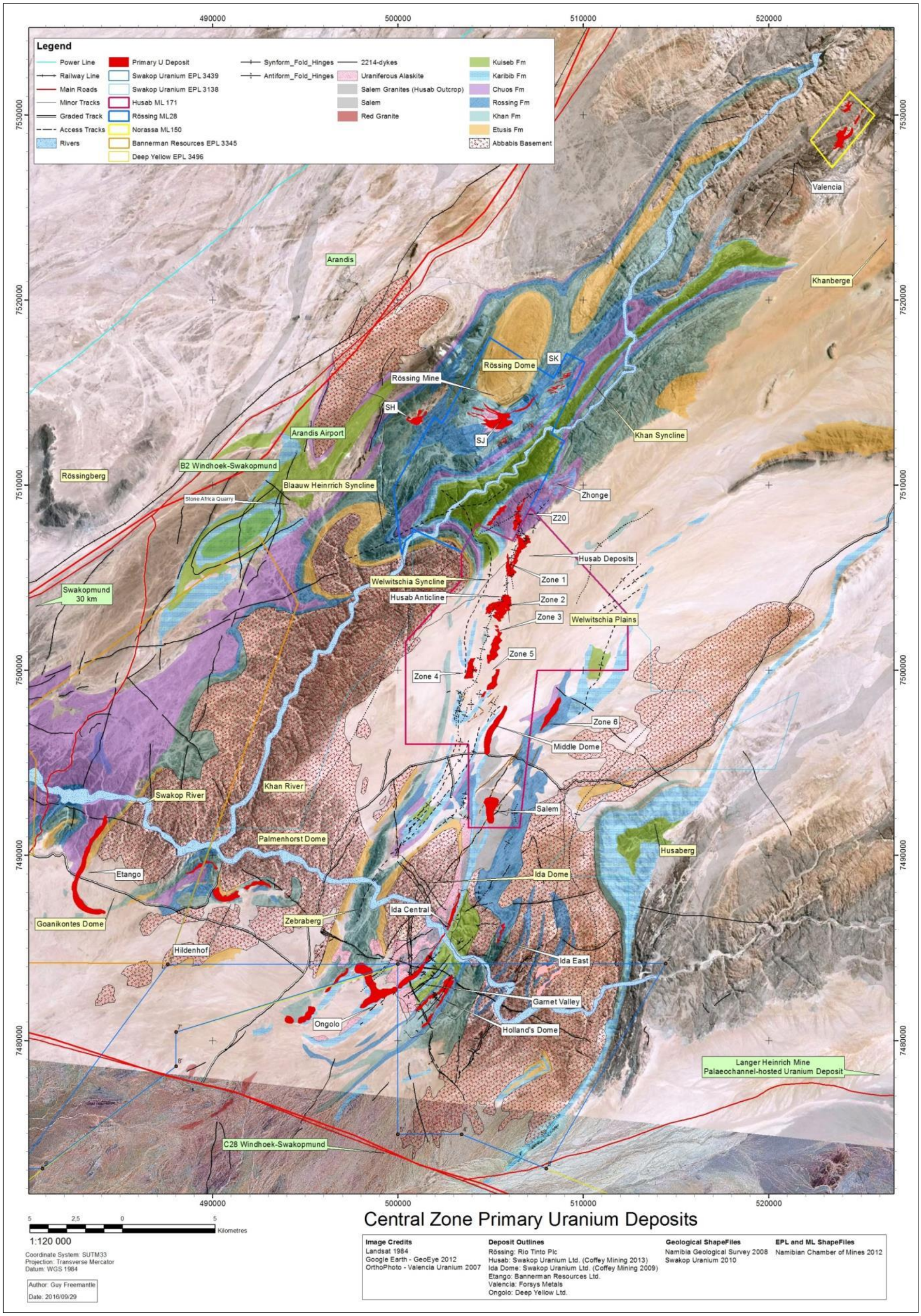



Figure 1.5 Major Central Zone primary-hosted uranium deposits. Most primary hosted U deposits occur within ~40 km of the Rössing Mine and include significant, economically viable projects at Etango and at Husab. The samples of this study are obtained from Hildenhof (Onkelo) on Bannerman Resources EPL 3345 and from drill core at the Etango Deposit. Ida Dome surface samples were collected at Ida Central, Garnet Valley and Holland's Dome. A limited number of core samples were sourced from Ida Dome and Garnet Valley for REE analyses. All of the Husab samples are sourced from diamond core. The Valencia sample population is a combination of surface and core material. The geological coloration overlay is traced from the Walvis Bay Map sheet- 2214 of the Namibian Geological Survey. The deposit locality shapes are traced from information available courtesy of Bannerman Mining Resources, Namibia (2009); Extract Resources (2012) and Valencia Uranium, Namibia (2010). Satellite Imagery is courtesy of Landsat™ (1990) and GeoEye (Google Earth, 2013).

## 1.6 Summary

The Central Zone of the Damara Orogen hosts the Rössing and Husab deposits, two world-class uranium mines, while the Etango deposit is potentially a third large-scale open pit mine. The Husab deposit is set to surpass Rössing's annual production, and likely be one of the top-three of global uranium mines. Proven resources at the Etango deposits at Goanikontes are the 4$^{th}$ largest in the region, albeit at a lower overall grade (Table 1.1). Renewed interest in alternative power sources and a global attitude toward reducing carbon emissions, means that previously un-economic uranium anomalies will become targets of exploration and eventual mine development in the near future.

Table 1.1 Reserves and Resources of the uranium deposits described in this study. Data sourced from the latest available Technical Reports

| **Deposit and technical report (date)** | **Reserves - proven** | **Grade (cut-off in ppm)** | **Measured** | **Indicated** | **Inferred** |
|---|---|---|---|---|---|
| | Tonnes U | % U | Tonnes U | | |
| Rössing ML028 (2015) | 5 699 | 0.027 (150 ppm) | 1 866 | 17 554 | 801 |
| Valencia ML149 (2014) | 2 731 | 0.017 (100 ppm) | 2 692 | 26 538 | 1 923 |
| Etango EPL3345 (2014) | 5 385 | 0.017 (150 ppm) | 5 538 | 57 769 | 40 808 |
| Ida Dome EPL3138 (2009) | | 0.021 (100 ppm) | | 118 | 9 420 |
| Husab Zone 1 (2012) | 10 346 | 0.041 (150 ppm) | 13 483 | 29 552 | 7 801 |
| Husab Zone 2 (2012) | 19 923 | 0.053 (150 ppm) | 25 440 | 27 808 | 6 322 |
| Husab Total in ML171 (2012) | 30 269 | 0.52 (150 ppm) | 38 923 | 57 360 | 14 123 |

The IAEA anticipates that the growth in nuclear power generation in the next 15 to 20 years will surpass the current production from mining. The economic assessment of new and existing targets is especially important in countries with large, low-grade deposits such as Namibia. In addition, the technological developments in modern, large-scale open pit mining

allows the extraction of increasingly lower grade ore, in many of the world's major commodities.

The profit margins on large, low-grade deposits requires careful assessment of metallurgical variables, uranium ore mineralogy being one of the most critical in the early stages of project feasibility studies. A solid mineralogical foundation can only be improved by a systematic and thorough investigation of the deposits and the geological systems on a regional and local scale.

This thesis presents an account of the major structural and stratigraphic settings of the Central Zone magmatic deposits as a backdrop to a detailed and systematic investigation of petrographic, geochemical (including rare earth elements) and quantitative and semi-quantitative mineralogical characteristics of the Central Zone deposits. The results show consistencies on a regional, macroscopic and chemical level, as well as anomalies that warrant further investigation of the nature of magmatic uranium systems.

# CHAPTER 2 THE DAMARA OROGEN, CENTRAL ZONE GEOLOGY, AND URANIUM MINERALISATION

## 2.1 Introduction

The Pan-African Damara Orogen resulted from a "Wilson Cycle" oblique collision between the Kalahari Craton in the south and the Congo Craton in the north (Kennedy, 1964; Stanistreet *et al.*, 1991). It comprises the Kaoko Belt, a coastal branch that extends along Namibia's north coast into Angola, and an inland branch, the Damara Belt, stretching from the Namibian coast northeastwards through to the Lufilian Arc in Zambia/Democratic Republic of Congo. The Gariep Belt, in southern Namibia and the Northern Cape of South Africa is of similar age. The collisions that generated the two mobile belts have resulted in the juxtaposition of sedimentary rocks from varied depositional environments, with later regional metamorphism and magmatism overprinting the sedimentary and intrusive histories (Barnes and Sawyer 1980; Miller, 1983a; Jasper *et al.*, 1992; Jasper *et al.*, 2000). The boundaries between the zones are characterised by faults, shear zones, and thrusts, or simply prominent stratigraphic boundaries (Miller, 1983a). A large collection of detailed geologic and geophysical studies of the Damara Orogen are collated and presented in Miller (2008). There is an overall increase in P-T° grades to granulite facies southeastwards toward the more deeply eroded coastal region (Goscombe *et al*., 2003a; Ward et al., 2008; Longridge, 2012). Miller (1983a) and Hoffman (1983) have divided the Inland Branch of the Damara Orogen along NE-SW trending tectono-stratigraphic lineaments into a series of Zones (Figure 2.1):

- A Northern Platform (containing the foreland basin of the Orogen)
- The Northern Zone (NZ),
- Central Zone (CZ)
- Okahandja Lineament Zone (OLZ)
- Southern Zone (SZ)
- Southern Marginal Zone (SMZ)
- Southern Foreland (SF)

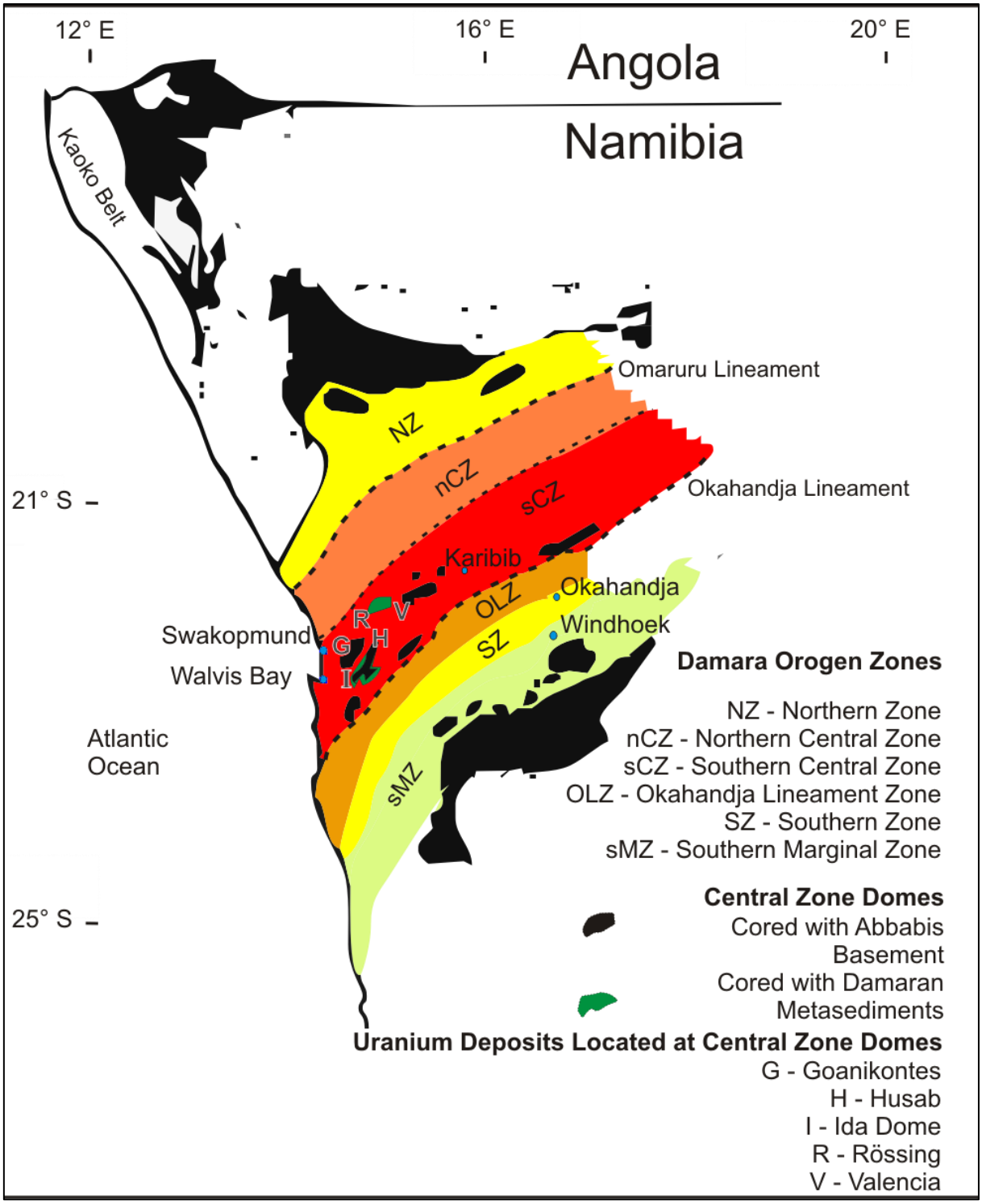



Figure 2.1 The Pan-African Damara Orogen of Central, Namibia. The regional orogen is divided into a number of tectono-stratigraphic zones, bounded by major lineaments. The four deposit areas that are investigated in this research are; Goanikontes (G) Husab (H) the Ida Dome (I) and Valencia (V). Zones and structural features from Miller (1983a and 1983b, 2008) and Kinnaird and Nex (2007).

The Damara Succession, which was deposited unconformably onto the Abbabis Metamorphic Complex, is a variably thick sequence of metasediments. Sedimentation began

from ~750 Ma (Hoffman et al., 1996) and continued during and after the opening and closing of a potential ocean basin, beginning in the mid-Proterozoic (Kröner, 1982; Miller, 1983a and 1983b; 2008). The depositional sequence represents a variety of environments; from early rift sediments, and meta-rhyolites, fluvial deposits to cyclic sequences of shallow-water carbonate shelves and reefs, to deep water sediments (mechanical and chemical) and abyssal flysch sequences (Miller, 1983a; Henry, 1992; de Kock, 2001). Cap carbonates above the marine sediment sequences, include glacial diamictite deposits (Hoffmann, 1987(a); Henry, 1992). Rifting terminated with the Matchless Member, an amphibolite schist-dominated sequence that is believed to represent a mid-ocean ridge as it contains deformed pillow basalt, it is however, a continued topic of debate (Finnemore, 1978; Kröner, 1982; Miller, 1983b; 2008).

The ~2 Ga Abbabis Metamorphic Complex (AMC), named from the type locality on Farm Abbabis (after Miller, 1983, 2008), is a schist-gneiss-granite package that forms the basement to the Neoproterozoic Damaran sequence. The AMC lithologies typically show amphibolite to granulite facies metamorphism, and are extensively invaded by pegmatite and other granites. Both the Abbabis basement and the unconformable Damaran sedimentary rocks were subsequently metamorphosed during the Neoproterozoic Damaran orogeny (Nash, 1971; Jacob, 1974a; and Sawyer, 1981).

In the Central Zone, the oblique closure of the Damara Ocean during the Neoproterozoic orogeny resulted in a northeast-southwest trending fold belt, punctuated by dome and inlier structures of the older basement lithologies. Klein (1980) has shown that the Central Zone is separable into distinct blocks, each with characteristic syn-tectonic to late- or post-tectonic granites.

## 2.2 Stratigraphy of the Central Zone of the Damara Orogen

### *Central Zone Stratigraphy Summary*

Granite-hosted uranium deposits and the Damaran stratigraphy are near inseparable when describing mineralisation models; except perhaps at the Goanikontes area, where the

Rössing Formation that hosts the bulk of uraniferous granites at the deposits elsewhere, is largely absent. The following is a greatly abridged summary to the sedimentary history. Damaran sedimentation commenced during rifting in the Neoproterozoic, from ≥750 Ma (Kröner, 1984; Hoffman, 1983; Brandt, 1985). The oldest volcanic rocks in the rifting stage are meta-rhyolites in the Etusis Formation, dated at 748 ± 3 Ma (De Kock *et al.*, 2001; Hoffman *et al.*, 1996). The basal stratigraphic sequence includes fluviatile sediments that coincided with the onset of rifting; evolving to deeper water marine sediments as the rift widened (Stanistreet *et al.*, 1991); later cyclical cap carbonates were deposited and diamictite was formed during global ice-age events (Henry, 1992). Rifting culminated with what is, in some interpretations, the remnants of an oceanic ridge; the Matchless Amphibolite Belt (Finnemore, 1978; Kröner, 1982; Miller, 1983b; Schmidt and Wedepohl, 1983; Miller, 2008). Martin and Porada (1977) propose a failed rift setting, comprising continental crust; however, Kukla and Stanistreet *et al.,* (1991) refute this with interpretations of the Khomas Hochland as an accretionary prism. Detailed accounts of the stratigraphic variation in the Central Zone are presented in Smith (1965) for the western Central Zone; Hoffman (1983 and 1987a) for the Southern Central Zone; whilst for the Central Zone Henry (1992) has discussed the stratigraphy at Farm Valencia, Central Zone; Barnes (1981) at the Ida Dome, Brandt (1985) for the Central Zone; and Anderson and Nash (1997) at the Rössing Mine.

Damaran sedimentation must have ceased at ~650 - 600 Ma, before craton convergence (Miller, 1983) while magmatism is believed to have commenced at ~580 Ma with the Goas Suite (Milani *et al.*, 2014). Continental collision is believed to have taken place from ca. 560-550 Ma (Haack *et al.*, 1980) and marked by a regional NW-dipping tectonic fabric (Sawyer, 1981; Hoffmann, 1983; Kukla, 1992). The Central Zone of the Damara Orogen contains two main stratigraphic groups which roughly divide it into the southern (sCZ) and northern Central Zones (nCZ) that are dominated by the lower- Nosib Group and upper Swakop Group, respectively.

### *Southern Central Zone Stratigraphy Summary*

The Abbabis Metamorphic Complex (A.M.C.) forms the oldest suite of rocks in the region and occurs as cores to the numerous domes that characterise the deeply-eroded southern Central Zone (sCZ, Figure 2.1). The complex consists of poly-deformed and poly-metamorphosed metasedimentary rocks, paragneisses, orthogneisses, pegmatites and orthoamphibolites (Smith, 1965; Jacob *et al.*, 1978; Marlow, 1981). The AMC gneisses are dated at ~2 Ga (Jacob *et al.*, 1978; Kröner *et al.*, 1991; Jacob *et al.*, 2000; de Kock *et al.*, 2000; Tack *et al.*, 2002; Longridge *et al.*, 2009; Longridge, 2012). Younger U-Pb SHRIMP Grenvillian ages of 1038 ± 58 Ma (Kröner *et al.*, 1991) may represent a ca. 1 Ga event overprinted on the older Abbabis rocks (Rainaud *et al.*, 2005a; Longridge, 2012). Recent studies of amphibolite in the AMC have yielded a U-Pb SHRIMP age of 2027 ± 2.3 Ma (Longridge, 2012); and are considered to be the oldest rocks in the basement, which are confirmed in Tack *et al.* (2002) and at the Abbabis Inlier (Jacob et. al., 1978). The basic stratigraphic sequence that overlies the basement complexes in the Southern Central Zone is summarised in Table 2.1.

The base of the stratigraphic succession in the southern Central Zone is occupied by the Nosib Group, comprising arenaceous, shallow- and deep-water clastic, and calcsilicate rocks (Table 2.1). The Nosib Group is sub-divided into the Etusis Formation, which comprises coarse fluviatile quartzite, arenites, and arkose (De Kock and Botha, 1989), and the Khan Formation, consisting mainly of siliciclastic to schistose rocks, and calcsilicates with a clastic component that led to the formation of gneisses and schists during subsequent metamorphism (Smith, 1965; Henry, 1992). Khan Formation rocks at the uranium deposit localities tend to be progressively calcic with mafic minerals (diopside and amphibole) in the younging direction, reflecting progressively anoxic deposition conditions.

The Swakop Group unconformity overlies the Nosib Group according to Miller, (1983) although at some locations transition to a cyclical carbonate sequence is not particularly abrupt, such as at Husab (this study). Historic work at the Rössing Mine, though reports an unconformity between the Rössing marbles and underlying Khan Formation of the Nosib Group (Jacob, 1974a; Henry, 1992; Anderson and Nash, 1997; De Kock *et al.*, 2000). The area surrounding the mine has recently been mapped in detail by Gray (2015).

The lower Swakop Group commences with the Rössing Formation which comprises a series of cyclical carbonate units with intercalated siliciclastic, pelitic metasediments, and pyritic quartzites toward the top (Nash, 1971; Miller, 1983; Anderson and Nash, 1997). The formation varies greatly in thickness within the Central Zone; the most complete package described is along the Khan River, south of the Rössing Mine. The upper Swakop Group was deposited in a passive margin setting as the rift evolved into a full seaway, where carbonate platforms were deposited to form shelves and peri-platforms at the edge of an abyssal plain (Walker et al., 1983; Martin *et al*, 1983; Badenhorst, 1992; de Kock, 2001).

Table 2.1 Simplified stratigraphic section of the Damara Supergroup in the Central Zone. Typical succession after, Smith, 1965; Nash, 1971; Miller, 1983a; Hoffmann, 1987(a); Henry, 1992; Hoffmann and Prave, 1996); Anderson and Nash, 1997; Nex 1997; Miller, 2008.

| **Damara Supergroup in the Central Zone** | | | | |
|---|---|---|---|---|
| Group | Subgroup | Formation | Lithologies | Thickness (m) |
| Swakop | Khomas | Kuiseb | Biotite-rich quartzo-feldspathic schist, biotite-garnet-cordierite schist, minor amphibolite schist, quartzite, calcsilicates and marble: basal graphitic schist with calcsilicate rock lenses (Tinkas Member) | 3000 |
| | | Karibib | Marble, dolomite, biotite schist, quartz schist, calcsilicate rocks, shale. | 700 |
| | | *Ghaub Diamictite* | Siliciclastics with drop stones, shales and mudstones, volcanic rocks, | <100 m |
| | | *Arandis Member* | Schist, calcsilicate, marble, pelitic gneiss, quartzite | 100 |
| | | Chuos | Mixite, diamictite, pebble- and boulder-bearing schist, minor quartzite, shale-BIF, schist. | 700 |
| | Discordance | | | |
| | Ugab | Rössing (Reducing Lithologies)[9] | Very variable: marble, quartzite, conglomerate, meta-greywacke, biotite schist, biotite-cordierite schist and gneiss, aluminous gneiss, biotite-hornblende schist, calcsilicate rocks. | 200 |
| Conformable transition with recognised REDOX boundary | | | | |
| Nosib | | Khan (some reducing Lithologies) | Pyroxene-amphibole feldspathic quartzite, amphibole-pyroxene gneiss, aluminous gneiss, biotite-hornblende schist, calcsilicate rocks. | 1100 |
| | | Etusis | Pink-grey well-bedded feldspathic quartzite, arkoses, conglomerate, quartzo-feldspathic gneiss; minor biotite schist, marble, amphibolite, meta-rhyolite and calcsilicate rocks. | 3500 |

[9] The Rössing Formation at Husab hosts over 90% of the known ore- bearing leucogranite tonnage, there are very few instances of mineralisation pervading Khan or Chuos lithologies. The pelitic, sulphide-bearing gneiss units consistently host high grades, while marble and calcsilicate units form localised granite traps, Spivey (2010).

Sedimentation above the Rössing Formation is unconformable and comprises glacial-marine deposits of the Chuos Formation, wich took place after after primary rifting in the Basin (after Hoffmann, 1987(a); Henry, 1992; Hoffmann and Prave, 1996; De Kock, 2001). Banded iron formations characterise the top of the Chuos Formation. The glacial deposits correlate with the world-wide, Snowball Earth - Sturtian Glaciations (after 748 ± 3 Ma age of the Etusis Formation, and before the Marinoan Glaciation at 635 ± 1.2 Ma, Hoffmann and Prave, 1996; Hoffmann *et al.*, 2004). A thin cap-carbonate is observed locally at the Valencia deposit, directly beneath the Karibib marble package. It is not observed at any of the other deposits investigated in this study.

The Arandis Member comprises carbonates, calcsilicates and pelitic sediments and is restricted in its distribution beneath the Karibib Formation. The Arandis Member is present in the Husabberg to the east of Husab and locally along the Khan Syncline south of the Rössing pit, usually in hinge zones of secondary folds. The Formation has similarities to the Rössing Formation in that it is largely reduced, has a cyclical carbonate sequence and is metalliferous (Fe, Cu).

Locally above the Arandis Member, is the Ghaub diamictite, which includes drop stones in thinly bedded siliciclastic rocks that are succeeded by basic volcanic rocks (Hoffmann *et al.*, 2004; Miller, 2008). The Ghaub rocks have been correlated with the world-wide Marinoan glacial event at 635.5±1.2 Ma (Hoffman *et al.*, 2004). It may be present in the vicinity of the Husab deposit, where the Arandis Member hosts uraniferous leucogranite intrusions, but has not been confirmed in the area studied for this thesis. The thick shelf carbonates of the Karibib Formation that followed the Ghaub glaciation, were deposited along a slumping peri-platform (De Kock, 2001) during rifting.

The youngest formation of the southern Central Zone is the Kuiseb Formation, which was deposited during down-warping associated with an active margin. It is a pelitic metasedimentary package which consists primarily of cordierite garnet schists, with locally developed metamorphosed siltstone, sandstone and mudstone intercalations. There are remnants of original bedding at localities around Farm Valencia 122, and the Kuiseb Formation is interpreted to have been deposited as thin beds of on the abyssal plain (after Porada and Wittig, 1983).

Henry (1992) presents a comprehensive account of the Swakop and Nosib groups in the Central Zone. Remote-sensed interpretations of the lithologies (as well as structures) around the Rössing Mine area are presented by Anderson and Nash (1997) and by Gray (2015). The Chuos, Karibib and Kuiseb Formations are poorly represented in the area of the Ida Dome south of the Swakop River, but are significantly thicker and more extensive north and north-eastwards toward Karibib and Windhoek (De Kock, 1989; Hoffmann, 1990; De Kock, 2001). The distribution of the Damara Supergroup in the southern Central Zone is depicted in Figure 1.5 which also places the primary uranium deposits in spatial-stratigrapahic context.

## 2.3 Structural evolution of the southern Central Zone

A protracted continent-continent collision, with at least 4 discernible major deformation events is represented in the well-defined tectono-stratigraphic zonation of the Damara Orogen described by Miller (1983). Of these zones, the Southern Central Zone (sCZ) contains the highest metamorphic grades (e.g. Hartmann *et al.*, 1983; Masberg *et al.*, 1992; Goscombe *et al*., 2003a).

Miller (1983) describes at least three major Damaran deformational events ($D_1$ to $D_3$) that occurred in the Central Zone; the second and third, together with a potential fourth (Barnes, 1981; Anderson and Nash 1997) play an important role in the timing of the majority of mineralisation events in the Damara.

The sCZ is characterised by numerous, prominent dome structures, with characteristic negative magnetic anomalies in the overlying metasediments along the NNE-SSW Welwitschia Lineament of Corner (1981) helping to define the structures below a Quaternary cover. The domes are commonly cored by pre-Damaran gneisses of the Abbabis Metamorphic Complex (Smith 1965; Jacob *et al.*, 1986). The most recent accounts of southern Central Zone Abbabis- and Damara sediment-cored domes around the Khan-Swakop River confluence are given in Longridge *et al.* (2009), Longridge (2012), and Longridge *et al.* (2014). The geometries, ages, metamorphic and petrological features, and genesis are described in detail and refer to previous work in Smith (1965), Barnes (1981),

Kasch (1983b), Kröner (1984), Oliver (1994, 1995), Oliver and Kinnaird (1996), Nex (1997) and Kisters *et al.* (2004).

Variably thick packages of Damaran metasediments overlie, and are infolded into the dome structures (e.g. Smith, 1965; Barnes, 1981; Oliver and Kinnaird, 1996; Longridge, 2012). The contacts between the domes and the Damara Supergroup are sometimes characterised by a shear zone interface (Jacob *et al.*, 1983) and are the site of later voluminous sheeted leucogranite intrusions. At Valencia, for example, the prominent shearing crosscuts Salem granite which has developed uraniferous partial melts along conjugate shear sets. Interpretations of the formation of the domes in the Damara belt include:

- Fold interference (Smith, 1961, 1965);
- Sheath folding in shear zones (Coward, 1983);
- Ballooning of basement-derived granite (Kröner, 1984); and
- Ductile mid-crustal detachment (Oliver, 1994).

Oliver and Kinnaird (1996) have noted that the Rössing Dome is cored by Etusis Formation quartzites rather than basement lithologies, and, Oliver (1994) postulates that the cover was detached from the basement during extension towards the southwest during NW-SE compression. This observation discounts the notion of interference folding as a mechanism for dome formation. There are however, no large shear zones such as the Khan River Detachment recognised at the Ida Dome between basement and cover, thus a basement cover contact detachment may not be a uniform cause of doming at all localities.

Anderson and Nash (1997) note the importance of a D4 episode in the Rössing area as being responsible for creating dilation sites suitable for SLG emplacement. Basson and Greenway (2004) produced a rotation model for the Rössing Dome, which opened up the southern end of the dome cover contact, allowing for a swarm of sheets in the SJ area (current pit) of the Rössing area and en-echelon sheet emplacement along the east of the dome at the SK Deposit. Marlow (1981) and Nex (1997) showed that emplacement of mineralised leucogranite sheets are preferentially emplaced in a high-strain zone along the western lobe of the Goanikontes dome.

More recently, Longridge (2012) and Longridge *et al.* (2009) reinterpreted the fold interference interpretation of Smith (1965) and give evidence that structures such as the Ida Dome and Khan Inlier are km-scale folds, where the Khan Dome Inlier (sometimes simply the Khan Inlier) comprises numerous instances of refolded Damaran rocks. Longridge (2012) therefore supports a fold-interference model over the mid-crustal detachment model of Oliver (1994) and the basement ballooning diapiric dome model of Kröner (1984). These interpretations of Longridge (2012) are more compatible with those of Smith (1961; 1965) and Coward (1983).

Two prominent orogen-scale structural features dominate the region in the study area.

The first feature is an extensive synformal structure, the Khan Syncline, which has folded the Damaran metasedimentary sequence. It is exposed for over 50 km on surface along a NE - SW axis that divides the distribution of the primary uranium deposits in the region between east and west. The NW end of the syncline exposure on surface terminates at the Stinkbank granite, near Usakos, and south of the Husab deposit at its most southwestern exposure (Figure 2.2).

The second feature is the Welwitschia lineament, a geophysical feature first described by Corner (1961) who identified the regional magnetic trend which extends from the Northern Zone south southwestward beyond the shoreline (Figure 1.1 demarcates the lineament trace in the Central Zone). It is interpreted as being produced by late kinematic movement which truncates and postdates the late Damaran deformational structures, and forms a boundary between the southern Central Zone and the Southern Zone (Corner, 1981; 1983).

## 2.4 Magmatism in the Central Zone

The stratigraphic sequence of the southern Central Zone is intruded by a variety of syn-tectonic and post-tectonic intrusive rocks that crop out over 74 000 $km^2$ of the Central Zone (Miller, 1983). The main intrusive suites in the southern Central Zone are the Red Granites; the Salem Suite; the Grey or equigranular granites; and the sheeted Leucogranites (SLG's).

The intrusives are dated between 633 ± 39 Ma (Downing and Coward, 1981) and 458 ± 8 Ma (Hawkesworth *et al.*, 1983).

The earliest magmatism is recorded by the Goas Diorite Suite-a series of small disconnected quartz diorite plutons in the area south of Karibib (Milani *et al.*, 2014) that often display a strong fabric. The oldest significant age (U-Pb single zircon SHRIMP) is 564 ± 5 Ma for a quartz diorite (Jacob *et al.*, 2000) and more recently Milani *et al.* (2014) suggest the earliest mafic intrusives invaded at ca. 560 Ma (laser-ablation ICP-MS). Diorite, quartz diorite and syenogranite were emplaced between 560 Ma and 540 Ma (Jacob *et al.*, 2000; de Kock *et al.*, 2000; Kisters *et al.*, 2004; and Milani *et al.*, 2014).

A suite of "Grey" granitoids vary from biotite granite to granodiorite in composition, which are locally present in variable volumes are later than the Goas Suite. They usually have a foliation and are sometimes thorium-enriched. Grey granites are ubiquitous in the thesis areas and intruded ~520.4 ± 4.2 Ma (Longridge (2012), which coincides with peak metamorphism ages of Jung *et al*. (2000a); Jung *et al.* (2001); Jung and Mezger (2003a; 2003b); and Longridge *et al.* (2014).

The uraniferous syn- to post-tectonic sheeted leucogranites, locally referred to as alaskites when hosting anomalous concentrations of uranium, are some of youngest intrusives in the southern Central Zone. The youngest ages are 506.1 ± 8.1 Ma for zircon (SHRIMP) in uraniferous leucogranite at Valencia (Longridge *et al.*, 2009); and 496.1 ± 4.1 Ma for uraninite (EPMA on euhedral uraninite) in uraniferous alaskites from the Husab deposits (Cross *et al.*, 2009). The Husab uraninite specimens appear to be euhedral, thus representing primary mineralisation, rather than post magmatic crystallisation. Younger pegmatites, based on field observations, occur in the Khan and Swakop River Valleys. These are localised, and described in Nex (1997) and Longridge (2012). Table 2.2 summarises the ages of Central Zone granitoids that are relevant to this study.

The Central Zone intrusives and most of the metasediments contain appreciable concentrations of uranium, with respect to typical crustal averages of ~2.5 ppm U or averages for felsic igneous rocks of ~4.0 ppm U (Rogers and Adams, 1969 and Taylor & McLennan, 1985). Table 2.3 summarises the average uranium and Th contents of the Central

Zone rock groups, highlighting the U-enriched nature of the metasediments and leucogranites. The granitic rocks, as described in this thesis are summarised in Table 2.4.

Precursor rocks of many of the metasedimentary rocks of the Damara are likely to have recycled appreciable proportions of the Abbabis metamorphic assemblages; essentially crustal recycling in a rifting environment. If the leucogranites are products of basement melting alone, the sheets are still products of material that has undergone uranium-enriching crustal processes, as the Abbabis has a metamorphic history that predates the Damara sedimentation and thus the orogeny (after Sawyer, 1981). The recycling of refractory minerals such as zircon may have contributed to the metasedimentary U content. While typical partial melt and fractionation processes of weakly uraniferous metasedimentary and mixed-source lithologies provided the mechanisms for uranium enrichment in the leucogranites, they do not fully explain the great range of uranium concentrations (U is reported in 10 000's ppm in this study). Nex (1997) showed that the uraniferous granites post-dated the other varieties of sheeted leucogranites, with the major $D_3$ deformation event separating the earlier weakly-mineralised from the late uraniferous varieties.

Table 2.2 Ages of granitic rocks of the southern Central Zone. Data compiled from various sources; Longridge, 2012; Miller, 2008; Kinnaird and Nex, 2007; Nex, 1997 and Miller 1983. * Zircon, ** Monazite.

| Granite | Age (Ma) | Method | Reference | Reference Interpretation |
|---|---|---|---|---|
| Husab Alaskite | 496±4.1 | SHRIMP | Cross *et al.*, 2009 | Post $D_3$ D-type SLG |
| Valencia U - leucogranite | 506±8.1* | SHRIMP | Longridge, 2012 | Syn- to Post $D_3$ D-type |
| Goanikontes 'Alaskite' | 508±2 and 509±1 | Concordant monazite | Briqueu *et al.*, 1980 | Post $D_3$ |
| Ida 'F-type' | 515±10* | SHRIMP | Longridge, 2012 | Post $D_3$ likely not 'F-type' |
| Grey 2 (Hildenhof) | 519.1 ± 4.2 * | SHRIMP | Longridge, 2012 | Syn to post $D_3$ |
| Pegmatite | 518±2 | Titanite | Kinny *et al.*, 1994 | Khan pegmatite - C-type |
| B-type (garnet granite, Ida Dome) | 520.3 ± 4.6*, 514.1 ± 3.1** | SHRIMP | Longridge, 2012 | Pre $D_3$ |
| Grey 1 (Hildenhof) | 520.4 ± 4.2* | SHRIMP | Longridge *et al.*, 2009 | Syn to post $D_2$ |
| Ida Dome syeno - monzogranite | 526±17 | U - Pb single zircon | Tack *et al.*, 2002 | Late to post D3 |
| Red Granite | 517±7 | U-Pb zircon | Briqueu *et al.*, 1980 | Pre $D_3$ |
| Red (Khan River Gorge, Khan Mine) | 539 ± 17*, 535.6 ± 7.2** | SHRIMP | Longridge *et al.*, 2009 | Pre $D_2$ |
| Grey (Ida Dome) | 542±6 | U - Pb single zircon | Tack *et al., 2002* | Late to post $D_2$ |
| Salem (Stinkbank) | 549±11 | U-Pb zircon | Johnson *et al.*, 2006 | $D_1$ |
| Basement (Ida Dome) | 2038±5 | U - Pb single zircon | Tack *et al.*, 2002 | Pre Damaran metamorphic complex |
| Basement (Khan R. Gneiss) | 2164±6 | U - Pb single zircon | Kröner *et al.*., 1991 | Pre Damaran metamorphic complex |

Table 2.3 Average U-content of Damaran granitoids and metasediments. Data from various sources including: Jacob *et al.,* (1986); Haack *et al.,* (1983); Herd, (1996); Nex (1997) and Kinnaird & Nex, (2007). Values for the Red/Grey Granites, Pre- and Post-$D_3$ leucogranites and Skarns (in bold and pink) are exclusively from this study.

| **Lithological Unit** | **Average U (ppm)** | **Th (ppm)** | **U / Th** |
|---|---|---|---|
| Upper Continental Crust (*Taylor & McLennan, 1985)* | 2.8 | 10.7 | 0.26 |
| Average Granite *(Rogers and Adams, 1969, Taylor & McLennan, 1985)* | 3-4.5 | 8.5-18 | 0.16-0.52 |
| Post $D_3$ sheeted leuco-granites | **356.25** | **72.68** | **4.90** |
| Pre $D_3$ sheeted leuco-granites | **29.39** | **19.56** | **1.50** |
| Red / Grey granites | **27.96** | **36.20** | **0.77** |
| Skarns (Holland's Dome, Garnet Valley, Ida Central, Valencia and Hildenhof) * | **826.64** | **155.77** | **5.31** |
| Chuos Formation** | 14 | 14 | 1 |
| Rössing Formation** | 12 | 25 | 0.48 |
| Khan Formation** | 7 | 17 | 0.41 |
| Etusis Formation** | 2 | 12 | 0.17 |
| Abbabis Basement** | 3-5 | 20-50 | 0.13 |

*The skarn samples are a selection of mineralised skarn material from the deposits. Skarns tend to have abnormally high U grade relative to the alaskites which surround them. ** Various sources including publicly available technical reports of the Husab, Etango, Ida Dome, Rössing, and Valencia deposits.

Table 2.4 Granitic rocks of the southern Central Zone. The divisions below follow those of Smith; 1965; Marlow, 1983; Brandt, 1985; and McDermott, 1986. The sheeted leucogranites were first subdivided and classified by Nex (1997). CPS: - counts per second on handheld scintillometer, BG: - background counts per second.

| Suite | Type | Description | Locations | CPS vs. BG |
|---|---|---|---|---|
| **Pegmatite** | White | White, pegmatitic, clear quartz, no accessories visible in core or hand-specimen. Intrudes most other granites, sporadically spread throughout the deposits, accessory tourmaline, often in quartz - tourmaline segregations. | Ubiquitous, throughout CZ | low |
| **Quartz pods** | Quartz segregations | Sporadic, usually only a few centimetres wide, found in most granite types and in some metasediments. | Ubiquitous, throughout CZ | High |
| Sheeted leucogranite | A-type | Thin, very light pink to white, bedding parallel, very few accessories, often folded and boudinaged within Damaran Metasediments | Valencia, Goanikontes | low |
| | B-type | White, as well as light pink, medium-grained and homogeneous often bedding parallel, folded and boudinaged. Garnet is a distinctive accessory and occurs in clusters or as disseminated grains mostly < 1 cm in size. Poikilitic textures are noted at Valencia with 5 cm garnet porphyroblasts. | Valencia, Ida Dome, Goanikontes | low |
| | C-type (indistinct) | Extensive sheets or coalescences of sheets, predominantly in upper Nosib and Swakop Groups, white to light pink in colour, variably coarse-grained, minimal accessories except entrained biotite. | Ubiquitous, throughout CZ | low |
| | C-type (magnetite) | Distinctive pink and white colour, medium- to coarse-grained as well as pegmatitic in patches, accessory magnetite clusters or disseminated. These may also have accessory tourmaline accompanied by clear quartz. Typically occur in structurally - controlled arrangements of parallel sheet swarms | Husab; Ida Dome, Goanikontes, Hildenhof, Valencia, | Low-high in patches |
| | C-type (tourmaline) | May be light pink or white, mostly coarse-grained with clusters of massive tourmaline. The massive tourmaline can often be as large as 5 - 6 cm across. Occur as parallel to bedding sheets in Kuiseb and Khan schists and gneisses. | Valencia, Ida Dome | low |
| | D-type | White, medium to coarse-grained, smoky quartz (black) typically minimal biotite, occasionally biotite is host to U in pegmatitic examples. May host yellow uranium secondary phases on exposed surfaces and on joint planes. | Ubiquitous, Goanikontes, Husab, Ida Dome, Valencia | very high |
| | E-type | Variably oxidised, deep pink amorphous veins and fingers of granite, which intrude pelitic metasediments and crosscut the earlier sheets. These have a high biotite content and smoky quartz. **This study does not recognise the E-type as a separate generation of granite, and follows existing interpretations that they result from autohydration-derived alteration during emplacement of D-types.** | Ubiquitous, Goanikontes, Hildenhof, Ida Dome | High- very high |
| | F-type | Deep red pink, pegmatitic, milky quartz, cross cuts most features and granites | Goanikontes, Valencia, Ida Dome | low |
| **Grey Granites** | Grey Type 1 | Dark grey, fine- to medium-grained, homogeneous texture, biotite-rich, white feldspar. Displays a prominent foliation. | Hildenhof, Ida Dome | low |
| | Grey Type 2 | Lighter shade of grey than 'Type 1'. Has distinctive porphyroblasts of white/pink feldspar, typically < 1 cm in size. May have high Th. | Hildenhof, Ida Dome | low |
| | Grey Type 3 | Lighter grey than Type 2, found intruding the type 2, often accompanied by a white pegmatite in the form of thin veins which finger into the host lithologies | Ida Dome, Hildenhof | low |
| **Red Granite** | Red Th granite | Red to light pink, fine- to medium-grained, anomalous Th content, intrudes Basement and parts of Nosib Group, heterogeneous and homogeneous textures, accessory sillimanite in some examples. | Hildenhof, Valencia | Med-high |
| **Salem Suite** | Salem 1 | Dark grey, high % biotite, High Ca (~$An_{35}$) foliated, fits descriptions of Jacob (1974a). Quartz – plagioclase dominant. Th > U. | Valencia | Low-med |
| | Salem 2 | Lighter grey, subtle foliation, less Ca (~$An_{25}$) large megacrysts of white and pink K feldspar (up to 5 cm) high % biotite. Th > U | Valencia | moderate |
| **Basement Granites and Gneisses (oldest)** | Granite | Large bodies, many tens of metres across, constitute a large proportion of the basement lithologies. White, to very-light pink, fine - grained, minimal accessories with the exception of biotite. High Th content relative to U. | N. of Valencia, Ida Dome, Goanikontes | low |
| | Porphyritic Granite - Gneiss | Dark grey with distinctive white feldspar porphyroblasts (augen) up to 2 cm long. Also, characterised by numerous pink partial - melt. | N. of Valencia, Ida Dome, Goanikontes | low and high |
| | Basement Gneiss | Light grey, coarsely banded gneiss, with distinctive leucocratic and mafic (biotite) segregation, also with pink partial melt throughout. | Ida Dome, Goanikontes | low and high |

## 2.5 Sheeted Leucogranites in the Southern Central Zone

Leucogranite intrusions of the Damara Orogen are most prevalent in the Central Zone, particularly around the Welwitschia Lineament. Mineralised varieties occur in discrete locations, while several generations of weakly-mineralised or barren leucogranites occur over a broad area. The sheeted leucogranites intruded a limited stratigraphic range of the metasedimentary packages, typically into lithologies within 100 m to 200 m above and below the Nosib-Swakop Group contact. Uranium mineralisation in the granites is frequently close to the lower Swakop Group carbonates (Rössing Formation and locally within the Arandis Member). They are characterised by vein-, sill-, and dyke-like or anastomosing forms, although locally more massive or plug-like occurrences are known at Valencia and the SH area of Rössing Mine. The oldest sheeted leucogranite ages in the area are the garnetiferous varieties from east of the Ida Dome, that intruded between 520 Ma and 514 Ma (Longridge, 2012).

The structural control on leucogranite emplacement, in all the areas of this thesis, is the provision of space through a range of pressure shadow-type mechanisms. Husab and Valencia deposits clearly occupy variations of typical saddle-reef emplacement, where alaskites occupy bedding-parallel spaces in the hinge zones of $D_3$ folds, while portions of the Husab deposits and the majority of alaskite at the Ida Dome occupy planar features parallel to bedding-parallel fabrics in quartzo-feldspathic lithologies of the upper Khan Formation and lower Rössing Formation. There is a distinct lack of evidence at locations of this study for displacement of Damaran metasediments by aggressive intrusion of alaskites. Overall, the sheeted leucogranites appear to have had a passive emplacement at most of the locations in this study, reflecting observations first made by Jacob (1974a) near the Rössing deposit. Pooling or coalescence of sheets tends to be controlled by impermeable silicic and carbonate rock units, whereas in schists and gneisses, S0-S1 oblique granite dykes and bedding-parallel dykes alternate as the dominant arrangements of sheeted intrusives. Figure 2.3 illustrates S0-S1 parallel leucogranite sheets joined by oblique veins of leucogranite in Khan Formation banded gneiss in the Khan River Gorge near the Valencia deposit.

The parallel sheets often show boudinage (Figure 2.2). Large masses of sheeted leucogranite appear to cross cut the parallel sheets and exploited pre-existing structural

features, such as local shear bands. The tendency for some sheets to cross-cut pre-existing structural features suggests that in some cases the magma invasion may be more aggressive in these areas. An example of this is at the Ida Dome where rafts of Khan Formation occur within large volumes of leucogranite. Sheeted leucogranite invaded the Basement through the Damara Supergroup to the Kuiseb Formation.

The sheeted leucogranites were locally referred to as alaskites at Rössing by Hiemstra (1967); Hiemstra and Beukes (1969); Jacob (1974(a), 1974b); Berning *et al*. (1976); Jacob *et al*. (1986) and at Goanikontes by Mouillac *et al.* (1986); and Briqueu *et al.* (1980). The definition of the term alaskite in Johannsen (1931) refers to granite that contains less than 5% mafic minerals. The more recent Le Maître (1989) definition terms an alaskite as a leucocratic variety of alkali feldspar granite consisting almost entirely of quartz and alkali feldspar.

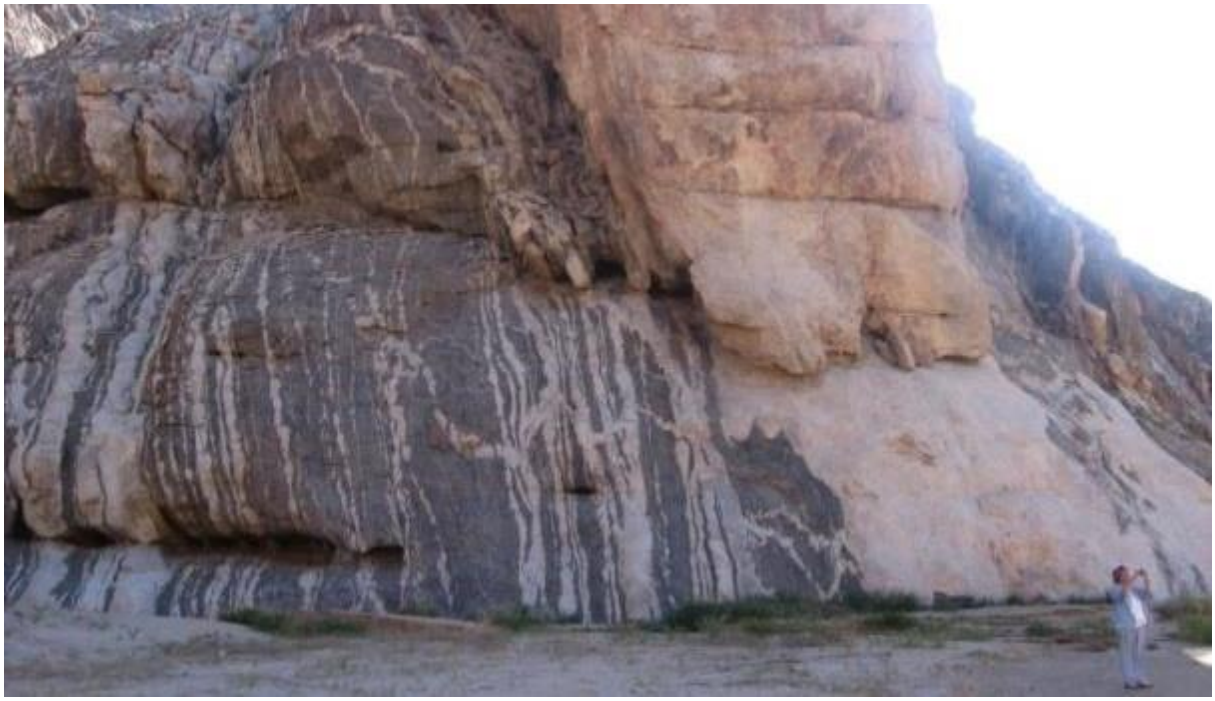


Figure 2.2 Sheeted leucogranite intrusions in the Khan Formation, Khan River Gorge near the Valencia deposit. The thin, parallel sheets are the older generation at this locality and show boudinage as a result of strain, post intrusion. A younger, large mass of sheeted leucogranite cross cuts the narrower parallel sheets which appear to be deformed with the sediments immediately adjacent to the larger sheet. These granites invade the underlying Abbabis basement rocks at this location, and downstream in the vicinity of the Husab Mine. Location (UTM) 512448E 7520771N

The most comprehensive account of the sheeted leucogranites outside of studies at Rössing is the in-depth study by Nex (1997) of the tectono-metamorphic settings of the sheeted

leucogranites in the Goanikontes area. The research produced a nomenclature for the SLG's, which is based on colour, texture, structural setting, timing of emplacement, and style of uranium mineralisation. It is supported by detailed petrographic observation and geochemical analyses. The work also showed that though a specific generation of leucogranite sheets are U-enriched, others have undergone U-enhancement by later processes. A typical example of a weakly mineralised alaskite from a dimension stone quarry near the Rössing Mine is shown in Figure 2.3. The granite shows a typically pegmatitic texture and the symptomatic smoky quartz coloration that distinguishes mineralised generations from barren sheets.

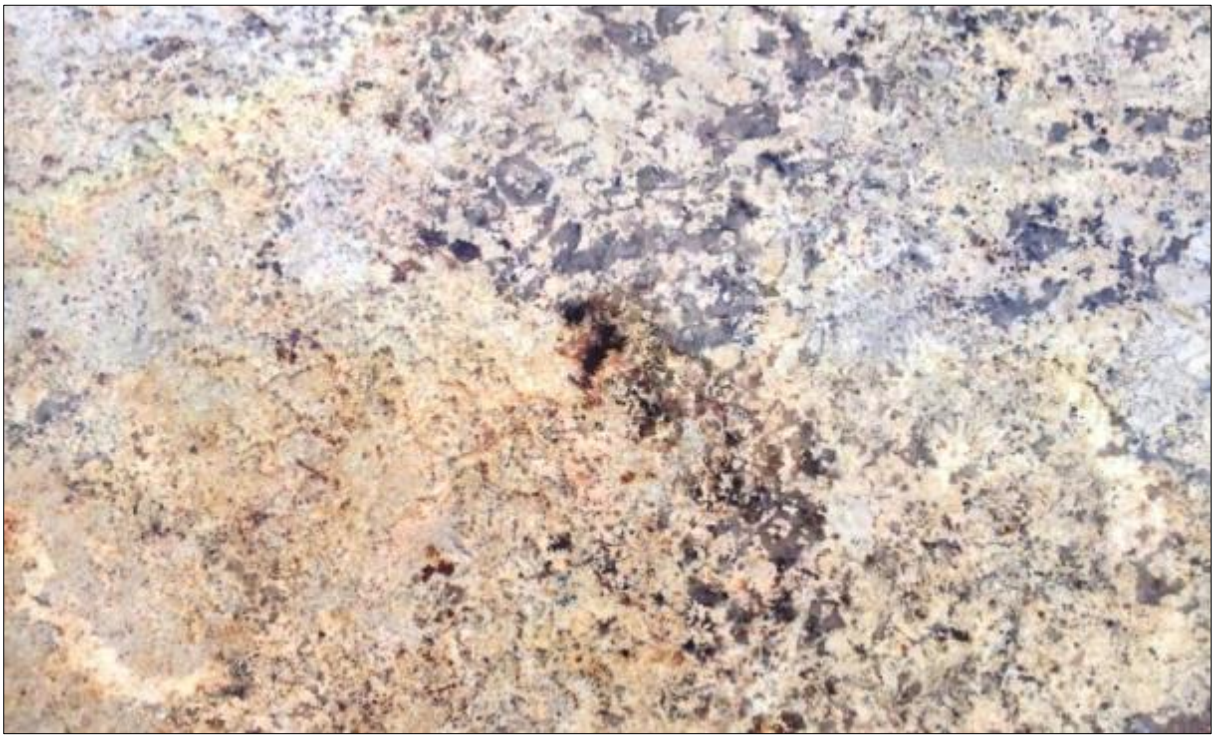


Figure 2.3 Polished slab of alaskite from the Stone Africa Quarry, SE of the Rössing Mine. Frequent local examples show more homogeneous, but coarse-grained textures that characterise most occurrences of mineralisation. Quartz is smoky as a result of radioactive disruptions to the quartz. Quartz coloration ranges from light grey (as above) to jet black, and is usually a fair indication of the U content. Field of view is approximately 50 cm.

All of the coarse-grained and pegmatitic granite veins fall into the category of sheeted leucogranite, whereas the term alaskite is used informally as a term meaning uranium-bearing sheeted leucogranites. Typically, an alaskite is a felsic intrusive with less than 5 % mafic minerals (Johannsen, 1931), however many of the sheeted leucogranites, whether

uranium-bearing or not, possess mafic mineral proportions that deviate a great deal from the 5 % threshold. Modal abundances of plagioclase place the uraniferous types outside of the alkali-feldspar granite category of Le Maître (1989) or the United States Geological Survey. Studies at Rössing (Freemantle, 2006) and Goanikontes (Nex, 1997) in particular report highly variable plagioclase abundances. So, for the purposes of continuity, alaskite refers to any of the uraniferous sheeted leucogranites at an economically prospective deposit, recognising that the actual rock is not an alkali-feldspar granite sensu-stricto. Sheeted leucogranite is reserved more specifically to the pegmatitic-textured granite veins that also occur at the deposit areas, but do not contain appreciable uranium (typically having low 10's of ppm U and Th).

## 2.6 Regional Metamorphism

Present day erosion levels expose a systematic increase in metamorphic grade from northeast to southwest, resulting from progressively deeper exposure down the stratigraphic sequence from east to west. Thus, the lowermost Damaran metasediments show the highest metamorphic grades and are exposed in the western portion of the sCZ. They are draped over the Mesoproterozoic Abbabis basement-cored domes (and occasionally the Nosib Group-cored domes, e.g. Rössing Dome) and fold structures that dominate the regional structure.

The metamorphosed pelitic and semi-pelitic rocks of the sCZ have undergone granulite facies metamorphism at medium- (Masberg, 2000) to low-pressure (Masberg *et al*., 1992) with a relatively uniform metamorphic gradient. Even at the highest grades (granulite) the P-T-t path is considered one of low-pressure, high-temperature (Hartmann *et al*., 1983; Masberg, 1992; Nex *et al*., 2003; Goscombe et al., 2003a; Longridge, 2012). The map of metamorphic grade shown in Figure 2.4 illustrates the metamorphic gradient as summarised by Goscombe *et al.* (2003a).

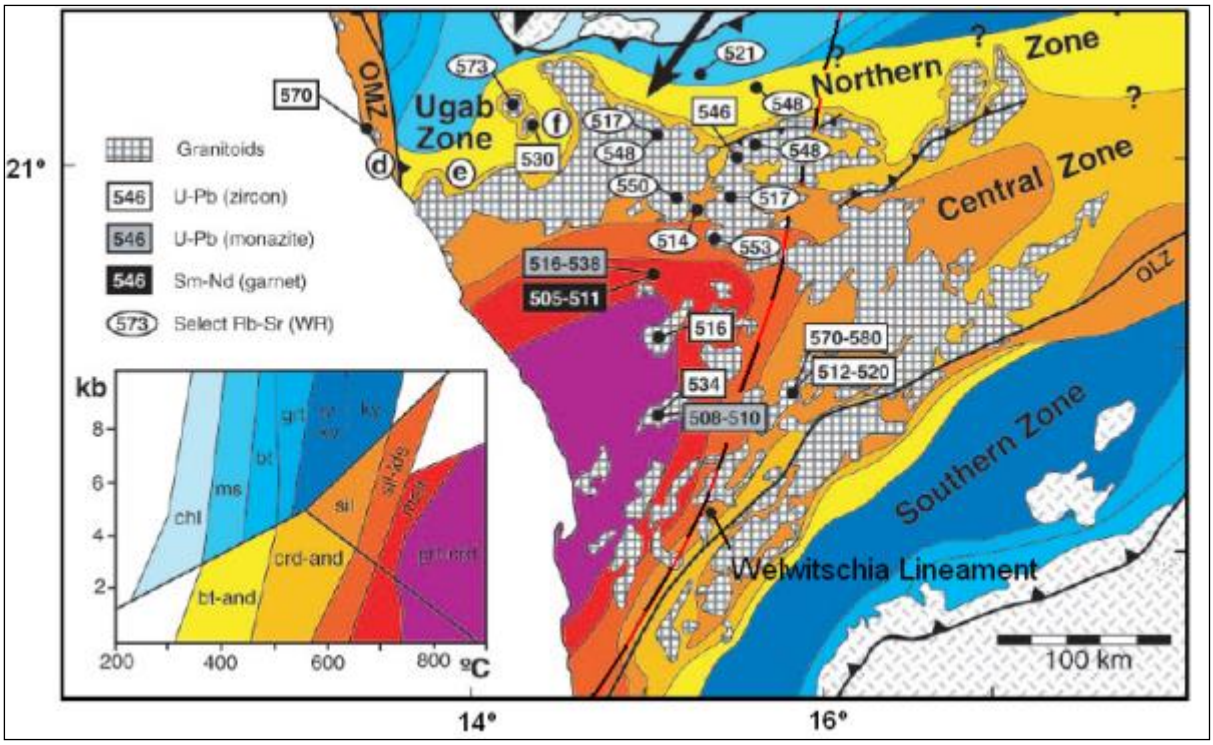



Figure 2.4 Map of metamorphic grades and age date distribution of the western part of the Damara Orogen.The map is a summarised interpretation of Central Zone metamorphic conditions by Goscombe *et al*. (2003a) after Hoernes and Hoffer (1979). Rb-Sr (whole-rock) and U-Pb zircon ages are magmatic. The Welwitschia Lineament is added, and shows that the majority of metamorphic assemblages west of it are in the upper amphibolite to granulite facies.

Peak metamorphic temperatures in the metasediments are 570–650 °C (Hoernes and Hoffer, 1979) but may be as high as 750°C as presented by Ward *et al*. (2008). Early metamorphic ages range from 540 ± 4 Ma (Sm-Nd, garnet, Jung *et al., 2000*) to garnet ages 525 ± 5 Ma through to ages of 504 ± 3 Ma at peak metamorphic conditions (U-Pb monazite and Sm-Nd, respectively, Jung and Mezger, 2003).

The metamorphic grade corresponds with overall structural trends east and west of the Welwitschia Lineament (Figure 2.4). The area east of the Welwitschia Lineament is dominated by lower amphibolite facies rocks, with dome structures showing a northeast vergence (Kisters *et al.*, 2004). This is in contrast with the amphibolite facies metamorphism and a strong trend of southwest, orogen-parallel extension of the lower Damara (Coward, 1983; Oliver, 1994; Poli and Oliver, 2001).

Regional contact metamorphism ($M_1$) in the early stages of the orogeny (540-535 Ma) is suggested to be the result of intrusion of Salem granite and the Goas suite, and took place

prior to the second episode of deformation ($D_2$), Longridge *et al.* (2014). Heat from the granitic intrusives may also have provided heat for the second, peak T°, episode of metamorphism ($M_2$) between 520 Ma and 510 Ma (Jung *et al.*, 2000b; Jung *et al.*, 2001; Jung and Mezger, 2003a; 2003b; Longridge *et al.*, 2011; Longridge, 2012). Peak temperature, and possibly the amount of heat required to reach the granulite facies metamorphism often described for the southwestern Central Zone, may have coincided with the large volume of high heat-producing uraniferous leucogranites that intruded between 510 Ma and 495 Ma.

The evidences of varying metamorphic conditions observed in the sCZ are explained by a number of processes, namely:

- Contact metamorphism in the metasediments as a result of heat from the large number of intrusions (Kröner and Hawkesworth, 1977);
- Crustal stacking accompanied by the intrusion of granites (Kröner, 1984);
- Doubling of the crust in a classic subduction setting (Kasch, 1983b; Miler, 1983);
- Internal heat production from radioactive isotopes (Haack *et al.*, 1983);
- Temperatures were not uniformly distributed during orogeny and heat was generated by a combination of extensional tectonics and granite intrusion Jung *et al.*, 2000a, 2000b, 2001; Jung and Mezger, 2001); and
- The regional metamorphism is overprinted by a contact metamorphism peak brought about by the locally abundant intrusion of late- post-orogenic granite intrusions (Nex, 1997; Jung and Mezger, 2003a).

The age of peak metamorphism in Longridge (2012) at ca. 520 Ma is similar to the ages of sheeted leucogranites intrusives and quartz-diorite rocks, e.g. Briqueu et al, 2003a. Longridge (2012) proposes a PT-t path from the onset of recumbent folding, as follows:

- Pressure and temperature increased between ca. 560 Ma and ca. 540 Ma, coinciding with the first major deformation event, intrusion of diorite granites and anatexis of the Abbabis lithologies;
- Peak pressure was reached at ca. 540 Ma, while temperature continued to rise with the intrusion of more evolved granites;

- Slow pressure increases and sharp temperature increases occurred between ca. 520 Ma and ca. 510 Ma where T° reached a peak of over 800 °C; finally
- Cooling ensued until at least 480 Ma.

Longridge (2012) suggested that this explanation is contentious, and the selective emplacement of the uraniferous granites ensured heterogeneous distribution of a late, contact metamorphic overprint. The debate as to whether peak metamorphism was a result of granite intrusion, or the granite intrusion coincided with the onset of peak metamorphism is not yet resolved.

### *Contact Metamorphism*

It is reasonable to assume that in the Central Zone the volumes of granite that are present must have contributed to the regional heat budget in certain areas. Field observations tend to show that contact metamorphism is localised, and though metamorphic minerals exist in pelitic units in many localities, metamorphic assemblages are not always apparently coincident with granite intrusion.

Generally, unequivocal evidence of contact metamorphism related to sheeted leucogranite intrusion at localities across the southwestern Central Zone tends to be limited to the most reactive country rocks, particularly the Rössing Formation carbonates, and to a lesser extent in the Nosib Group calcsilicates and gneisses where it is common to have Fe-Ti-Ca mineral porphyroblasts developed at intrusive-metasediment contacts.

Large volumes of leucogranite intrude the Kuiseb Formation at locations such as Valencia, where the schists have a significant amount of garnet-bearing melt as well as intrusive leucogranites, described in detail by Ward *et al.* (2008). Leucogranite sheets intrude rocks with a pre-existing fabric, defined for the most part by textures of biotite wrapping cordierite. Thus, the granite population is a representation of melt migration at the deposit as well as a reflection of sufficient metamorphic grade to produce partial melting, as described by Ward *et al.* (2008).

## 2.7 Discussion

Petford *et al.* (1993) and Petford *et al.* (2000) suggest that granites do not rise up as carrot-shaped diapirs, or as balloons rising from the lower crust, rather they tend to be well-controlled dyke- and sill-like bodies. Cross-sections of dome structures along the Swakop River support this concept and show that domes such as that at Ida, actually consist of sub-horizontal gneiss toward the core, with steep to sub-vertical Damaran metasediments along the margins.

The Central Zone leucogranites appear to be well-exposed examples of such structurally controlled, passive intrusions at the majority of the uranium prospects. The leucogranite sheets conform largely to a local combination of bedding/fabric-parallel-, fold hinge-, and axial planar orientations, at the Valencia and Holland's Dome (Ida Dome Area) deposits in particular. The nature and controls of granite sheet geometries at the Rössing deposit are described in Jacob *et al*, 1986; and Basson and Greenway (2004). The most comprehensive account of the structural controls of leucogranites at Goanikontes is given in Nex (1997). The structural settings and controls of the leucogranites are localised, and contrast somewhat from deposit to deposit. The relative abundances of dykes vs. sills of leucogranites and the uraniferous alaskite types at each deposit, and are therefore a function of local conditions of emplacement. This variation is covered for each deposit of this study in Chapter 3.

Furthermore, the Central Zone domes and inliers consist of rocks of different ages and compositions, and in addition to this, Klein (1980) has shown that the Central Zone is separable into distinct blocks with their own characteristic nontectonic to late- or post tectonic granite suites.

The preponderance of intact country rock xenoliths, containing metamorphic assemblages also suggests that the country rocks had cooled to some extent prior to the invasion of leucogranites. The collision between the cratons comprises a protracted series of ‘peak-events’, some of which are coincident with granite formation while others developed metamorphic assemblages without the presence of large volumes of melt to contribute heat in a contact metamorphic setting.

## 2.8 Summary

The Damara Orogen represents a Wilson Cycle event of rifting, ocean-opening, ocean-closing, mountain-building, and finally, orogenic collapse. Oceanic rifting, for example, may be preserved in the Matchless Amphibolite Belt[10], as suggested by Finnemore (1978); Kröner (1982); Miller (1983b); Schmidt and Wedepohl (1983); and Miller (2008) but is a realtively inconsequential concept for this thesis as there is no evidence of basaltic contributions, even to the oldest intrusives in the western Central Zone (after Milani et al., 2014).

The depositional history and evolution of the Central Zone lithologies are recorded locally in the Damara Supergroup, which follow a northeast-southwest zonation and unconformably overlie the 2 Ga Abbabis metamorphic complex (Miller, 1983). As rifting began, rhyolites were erupted and fluviatile and shallow water sediments of the Etusis Formation were deposited. The evolving depositional environment included cyclical carbonates, turbidites and abyssal facies, interspersed with unconformable contacts has essentially created an inhomogeneous stratigraphic column.

The rheological contrasts between the variable lithologies of the Damara Supergroup and between the relatively more competent Abbabis basement created areas that suited the intrusion of localised networks of leucogranites in pressure shadows of variable geometries, for example;

- Emplacement as saddle-reefs at the Husab deposit (Spivey et al., 2010, this study) and Valencia (this study)
- Rotation of a competent dome structure at Rössing (Basson and Greenway, 2004)
- Emplacement of sheeted granites perpendicular to extension directions at the margin of the Ida Dome (Kruger and Kisters, 2016; Longridge et al., 2009; Longridge, 2012, this study)
- En-echelon emplacement geometry of sheeted leucogranites at a brittle-ductile structural transition (High-strain Zone of Nex, 1997).

[10] The Matchless amphibolites are not present at the deeply eroded western Central Zone, but do appear further inland at higher stratigraphic levels.

These areas are the sites of focussed sheeted leucogranite intrusion and occur consistently around eastern, western and southern edges of Basement- and/or lower Damara Supergroup-cored dome and inlier structures:

- Sheared Basement with disharmonic folding - Damara Supergroup contacts (Valencia, this study);
- Sheared antiforms in complex synformal structures and dilation associated with Dome rotation (Rössing, Basson and Greenway 2004);
- Ductile and brittle transition at high - strain zones (Etango – Goanikontes, Nex, 1997, and Ida Dome, this study);
- Basement – with infolded antifoms of Damaran packages (Hildenhof, this study); and
- Northeast - southwest upright $D_3$ antiform hinges and limbs (Holland's Dome and Husab, Spivey et al., 2010 and this study).

Heat is a function of the conditions that generated upper amphibolite to granulite facies metamorphism, while dilation associated with deformation facilitated melt formation and migration away from source and into the reactive Damara lithologies.

The interaction between sheeted leucogranite intrusions and the differing compositions of the units of the Damara Supergroup has had a profound influence on the focussing of uranium mineral crystallisation in the invading sheeted leucogranites (Cuney, 1980b; Herd, 1996; Nex *et al.*, 2003; Abraham, 2009). Where sheeted leucogranites have invaded the cyclic carbonate, calcsilicate, pelitic, and sulphide-bearing sequences of the Rössing Formation and Arandis Member, uranium minerals have crystallised to form the economic deposits that characterise western central Namibia today. The detailed geology of the major prospects and the controls on mineralisation are the topic of the next chapter.

# CHAPTER 3 GEOLOGICAL SETTING OF THE CENTRAL ZONE PRIMARY - HOSTED URANIUM DEPOSITS



View from the cab of a CAT6060 hydraulic face shovel. The view looks northeast toward Swakop Uranium's Husab Deposits; the Zone 1 and Zone 2 orebodies extend continously for 5.5 km of strike, up to 100 m below the Quaternary cover. Mining commenced in March 2014 and expects to produce up to 7 500 tons of $U_3O_8$ per year, for the next 20 years, eventually excavating to 410 m below surface. The Husab resource drilling project advanced rapidly from a reconnaissance prospect in 2007 to mine feasibility study in 2010-2011, and is the first primary-hosted uranium mining project in Namibia since the opening of the Rössing Mine in 1976.

## 3.1 Introduction

The primary uranium deposits of Namibia occur in two regions, namely those in the Namaqua Belt near the Orange River border with South Africa, and those near the Atlantic coast in the Erongo Region within the Damara Orogen. The presence of radioactive minerals in the Damara Orogen has been known since 1910, and in 1928, Captain Pieter Louw and his wife conducted an autoradiography test on a sample collected 12 km from the present day Rössing Uranium Mine (from Nield, 2002).

Sheeted leucogranites or (SLG's) host the primary uranium occurrences in the southern Central Zone. The term 'alaskite' is used to describe the uraniferous varieties, though these may not necessarily be true alaskite in composition (<5 % mafics, after Johansen, 1922). The granite-hosted deposits occur within a northeast-southwest tectono-stratigraphic zone, within 80 km of the Namibian coast. The majority of the uranium prospects investigated during the 1970's and 1980's, as well as the present-day mines are all located within ~50 km of the Welwitschia Lineament (Corner, 1983). The majority of uranium mineralisation occurrences are bound in the north by the Okahandja Lineament and in the south by the Omaruru Lineaments (Figure 1.1, Chapter 1, and Figure 2.1, Chapter 2). The primary, granite-hosted deposits formed within the high-temperature / low-pressure region as outlined in Goscombe (2003a). Brief geological, exploration, and economic summaries of most of the known uranium deposits in the region are presented in Rösener and Schreuder (1994).

## 3.2 Introduction to the Granitoid rocks at the Central Zone uranium deposits

The section below introduces the granite rock types in the general vicinity of the primary uranium deposits; this study presents detailed field relationships of the equigranular (Grey) granites and leucogranites at specific deposit locations, and Salem granitoids, where present.

The Abbabis basement and lower Damara metasediments host sheeted leucogranites (SLGs) in the obliquely exposed western Central Zone, between the town of Usakos and the Atlantic coast. The primary uranium deposits of the Erongo Region are the largest and most numerous in the country. Mineralised sheeted leucogranites have preferentially intruded a uranium-prospective interval in the metasedimentary sequence, where structural controls have facilitated amalgamations of intrusives sufficient to warrant low-grade, open pit mining.

### *Salem Granite*

A number of authors (Jacob, 1975; Marlow, 1983; Brandt, 1985; McDermott, 1986; McDermott *et al.*, 1996; McDermott *et al.*, 2000; Johnson *et al*., 2006; and Miller, 2008)

describe the Salem Suite granites; the term refers to diorite to monzogranite composition intrusives that occur at a number of Central Zone locations. A range of textures and compositions of diorite, monzogranite and adamellites are described in detail in Marlow (1981). According to age data for the Salem Suite (Johnson *et al*., 2006), the Stinkbank intrusions near the town of Karibib are a nontectonic example of granite magmatism, coincident with the main Congo-Kalahari collision event at ca. 549 Ma.

The Salem megacrystic monzogranite and foliated diorites observed at Valencia (Figure 3.1a) and south of the Husab deposits do not occur at the Goanikontes or Hildenhof deposits. Instead, biotite-bearing, equigranular-textured granites of ca. 520 Ma are interpreted as pre-$D_3$ intrusives in Longridge *et al.*, 2009 and Longridge, 2012. The composition and tectonic interpretations of equigranular textured granites, similar to the examples at Hildenhof and the Ida Dome are described for the Goanikontes area in Nex (1997). Prominent megacrystic feldspars define the Salem type granites and give the granite a recognisable texture. A large outcrop of Salem type granites (a megacrystic textured biotite granite) and two varieties of Grey (biotite) granites intrude the Rössing Formation roughly midway between the Husab deposits and the Ida Dome on the Welwitschia Plains (Figure 1.5), and are in turn intruded by alaskite (Spivey *et al.*, 2010).

### *Red Granite*

The Red granites at Goanikontes and Hildenhof are characterised by their pink to red colour, homogeneous texture, and tectonic foliation (after Longridge, 2012). At Hildenhof, the Red granites intrude the Nosib lithologies and the samples collected are homogeneous with occasional fibrolite/sillimanite clusters.

Figure 3.1a andFigure 3.1b illustrates the Red granite and the Salem granite, respectively.

### *Grey Granite*

Nex *et al.* (2001a) describe equigranular granites in terms of three groups; Red, Grey and basement-hosted. The Grey granites referred to in this- and subsequent chapters fall into the equigranular and basement-hosted categories of Nex *et al.* (2001a); McDermott (1986); and

Marlow (1983). Several facies of Grey granite are recorded and sampled at Hildenhof and observed at the Ida Dome; the oldest is foliated and melanocratic and is intruded by two facies, each of succeeding lighter colour.

The Grey granites intrude the basement and Nosib lithologies and occasionally the Swakop Group (only observed at Hildenhof, Holland's Dome and on the Welwitschia Plains) and range in size from centimetric xenoliths in sheeted leucogranites to thousands of square metres of pavement outcrop. In addition to decreasing mafic content, the three generations at Hildenhof and at Ida Dome are locally distinguishable from each other by crosscutting relationships, and supported by dating of the grey varieties at Hildenhof by Longridge (2012). A single sample of Grey granite at Valencia fits the description of the youngest grey generation occurring along the Swakop River.

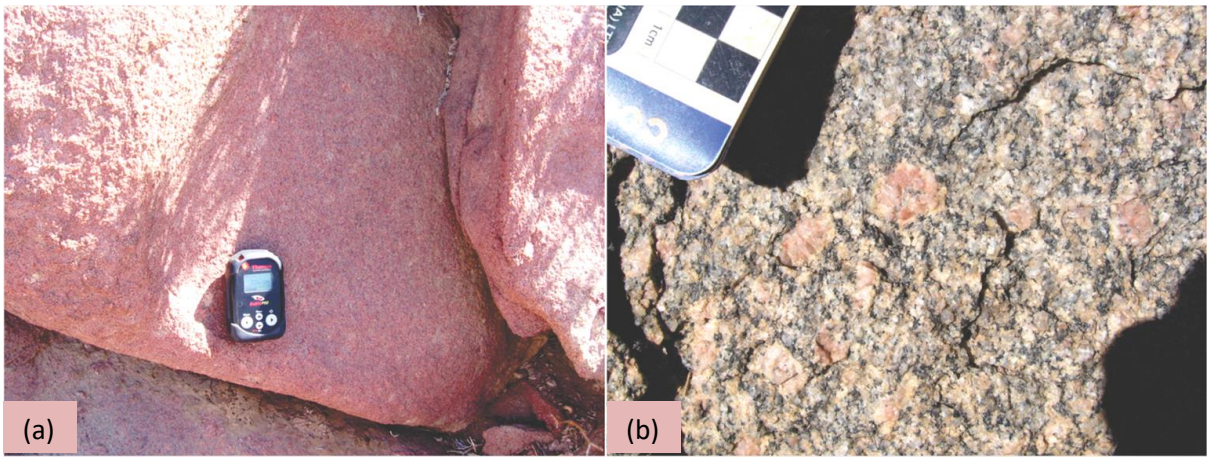



Figure 3.1 Early Damaran granites in the CZ include the Red and Salem Suite monzogranite. (a) The Red granites at Hildenhof are distinctive in colour and homogeneous texture, accessory fibrolite expresses itself as cm scale nests (white spots on surface). (b) The megacrystic Salem granites at Valencia have distinctive 2 – 3 cm K-feldspars in a biotite rich matrix.

## 3.3 Sheeted leucogranites

The term, sheeted leucogranite was introduced in the Namibian context to subdivide the Goanikontes leucogranites, and in the broader sense the CZ granites into six field types (Nex and Kinnaird, 1995; Nex, 1997). In this study, field-based subdivision of these granites considers host-rock relationships; feldspar assemblage (1- or 2-feldspar-type granites);

colour; size of intrusive body; relationship to structural features (local and regional); and accessory mineral assemblages. Descriptions follow the methodology employed by Nex and Kinnaird (1995) and Nex (1997) in the Swakop River Valley. The scheme uses an alphabet prefix from A to F to denote the subtypes of sheeted leucogranites, A-type, B-type, C-type through to F-type. This nomenclature is not to be confused with the traditional 'Granite Alphabet' of I and S type granite type classification system of Chappell and White (1974a and 1974b) much less the A type granites of Loiselle and Wones (1979).

Description of the sheeted leucogranites at the primary uranium deposits of the Central Zone retains a hyphenated A- to F- field type descriptions for ease-of-referencing purposes with the definitive work in Nex and Kinnaird (1995) and Nex (1997). References to I, S, and A type granites will drop the hyphen for the purposes of this study. Despite the vast distances between deposits, certain varieties of colour, texture, feldspar assemblage, and stratigraphic level of intrusion are remarkably consistent across the study region. Thus, direct comparison and contrast to the Nex (1997) classification at Goanikontes is possible for many of the locations and sheeted leucogranite populations because of these consistencies.

The sheets that appear unique to certain deposits necessitate a location - specific means of classification, with respect to the sub-type of leucogranite, which at the same time can provide a way to compare the deposits with each other directly.

Field identification of sheeted leucogranites that do not contain appreciable U (<50 ppm U) and the uraniferous alaskite varieties is primarily based on hand-held scintillometer (Thermo RADEYE™) readings; the single-channel device does not differentiate between the gamma radiation spectra of K, Th, and U. Thus, for most of the samples, U, Th, and K was obtained by whole-rock analyses by conventional XRF (43 samples were twinned with ICP-MS analyses) at a later stage. Field relationships of the sheeted leucogranites at each deposit in this study are given in detail in Chapter 4; the sections below summarises the distribution of the different A- to F- subtypes of sheeted leucogranite at the primary uranium deposit locations within the study area.

The A- and B-type sheeted leucogranites are rather limited in exposure, with the most abundant occurrences of the garnet-bearing B-type sheeted leucogranites found at Valencia

(this study, Ward et al., 2008) and at the Goanikontes area around the Etango deposits (as described first in Nex and Kinnaird, 1995).

The C-type sheeted leucogranites are the most voluminous type, they are often bedding-parallel, occasionally crosscutting B-type sheets and with variable host rock interaction. The most massive examples of outcrop occur along the Khan and Swakop River valleys. It is possible to subdivide the C-type into three distinctive varieties, because the accessory assemblages are more often than not consistent with the stratigraphic level of intrusion:

1. A relatively accessory-free type (C) is extensive in length and parallel sided. These sheets are typically coarse-grained and commonly have patches of graphic quartz-feldspar. Biotite is the most abundant accessory; however, it is predominantly in the form of sparsely-spread entrained laths and consumed ghost bedding;
2. A magnetite-bearing type ($C_m$), which occurs primarily in the Khan Formation is the most distinctive variety. They are coarse-grained, variably textured distinctly pink and white, containing significant accessory magnetite, especially when intruded into the Khan Formation. However, they do also occur at some localities within the Chuos Formation and may occasionally have accessory tourmaline (DH022 59.00 -59.24 at Valencia for example); and
3. A tourmaline-bearing type ($C_t$) that tends to intrude higher up in the Swakop Group succession. They are medium- to coarse-grained or pegmatitic and may have a subtle foliation inherited from entrained biotite. Accessory tourmaline occurs in quartz–tourmaline nests or as euhedral or massive accumulations of crystals up to cm-scale in size. Feldspars are generally pink or white; combinations of pink or white are not as widespread as in the $C_m$ variety.

The uraniferous sheeted D-type leucogranites, or alaskites as they will be referred to in this and subsequent chapters are limited in extent to specific areas at each of the primary uranium deposits. They may form the bulk of granitic intrusive in localised settings, but are generally less voluminous, relatively, than the C-type sheeted leucogranites.

There are at least five textural-mineralogical varieties of sheeted leucogranite recognised at Valencia, whereas at the Ida Dome and Hildenhof, fewer distinctive varieties occur. There are at least four distinctive varieties of leucogranite at Husab; and these appear to have a stratigraphic distribution, based entirely on observation of diamond drill core from the Etango, Husab, Ida Dome, and Valencia deposits:

1. Magnetite-bearing sheeted leucogranites occur almost exclusively within the Khan Formation diopside gneiss and are almost always pegmatitic in texture (relatively consistent approximation to a footwall to the mineralisation), the presence of magnetite implies these are oxidised at the time of crystallisation;
2. Uraniferous leucogranites, or alaskites, occur within the cordierite gneiss and in close association with carbonate and siliciclastic units of the Rössing Formation. These often host sulphides, implying they were more reduced at the time of crystallisation;
3. Garnetiferous sheeted leucogranites are rare and recorded in a few instances within the Rössing and Chuos Formations. Garnetiferous SLGs are abundant in the Kuiseb Formation, and are considered to be melts of the host metapelites (after Ward *et al*., 2008); and
4. Accessory mineral-free, coarse-grained leucogranite occur within the Rössing and Chuos Formations, as sills and dykes approximating to the C-type of Nex (1997) at Goanikontes.

***Distribution of the uraniferous sheeted leucogranites***

Regional scale distribution of the primary uranium deposits is largely foccussed within or below the Rössing Formation. The deposits at Goanikontes, the Ida Dome, and Rössing are also all in close proximity to an Abbabis basement inlier (most of the Rössing Dome, as previously illustrated, is competent Etusis metaclastics) The map in Figure 1.1 detailed the locations of the major uranium deposits of the Central Zone with respect to each other and the general Central Zone geological setting. An enlarged version is given in Appendix B. The

Valencia deposit is located on the northern limb of the Khan syncline; and the Rössing and Husab deposits occupy synformal and antiformal structures immediately adjacent to the north and south limbs of the Khan syncline, respectively (Figure 1.5).

The Ida Dome deposits occupy sheared structures immediately east of the basement-cored Ida Dome anticline, and an upright anticline at the Holland's Dome deposit (also see Figure 1.5 in Chapter 1). The Goanikontes deposits occupy a high-strain zone immediately to the west of the Khan Dome basement inlier. Prior to the early 2000's, most of the known primary uranium deposits were largely exposed at surface, and usually located within the area of erosion networks that surround the two major rivers in the area, the Khan and the Swakop. All of the primary uranium deposits are hosted in a suite of sheeted leucogranites, of which the younger generation(s) hosts the least uranium. Nex (1997) showed that at Goanikontes (now named Etango) the most uraniferous leucogranite sheets postdate the third major Damaran deformation event ($D_3$) of Miller (1983). Leucogranites with relatively low (<50 ppm U) or average uranium content (50 ppm to 100 ppm U) commonly show signs of deformation and are crosscut by younger leucogranites, and described as syn- to post-$D_2$ in terms of relative timing.

Spatially, uranium mineralisation preferentially occurs within sheets that intrude the prospective sedimentary boundary between the Nosib and Swakop Groups. The prospective interval essentially comprises the upper Nosib Group and lower Swakop Group lithologies. Studies at the Rössing deposits (Jacob, 1974) first noted the correlation between the stratigraphy and the mineralisation, which was later studied in an attempt to quantify the chemical reactions between the intrusives and associated fluids and the reactive units of the Rössing Formation by Cuney (1980a and 1980b). Essentially it is reactive units within the Khan and Rössing Formations that provide the REDOX buffers necessary for $U^{6+}$ reduction and consequential primary uraninite $(U^{4+},U^{6+})O_2$, crystallisation. Figure 3.2 illustrates a schematic form of the major primary U deposits and their positions of mineralised SLG emplacement relative to the Damara Supergroup.

In summary, mineralisation occurs in granites intruded within the Khan Formation and Chuos Formations at Etango and within the Khan- and Rössing Formations at Rössing, and predominantly within the Rössing Formation at the Husab mine. The Valencia deposit is

characterised by exposures of uraniferous leucogranite that truncate most of the units of the upper Nosib- and formations of the lower Swakop Group.

Modification of the original A- to F- classification of Nex (1997) is required to accommodate sub-varieties in the voluminous C-type sheets and to remove the E-types as a separate granite type. The new classification should include the A- and B-types; the C-types (C, Cm and Ct); the D-types and the late sporadic F-type and is presented in Table 3.1. Table 3.2 summarises the former SLG suite of the Central Zone devised by Nex and Kinnaird (1995) and Nex (1997). Table 2.2 summarised the geochronology of granitic and crust-derived intrusives of the Central Zone.

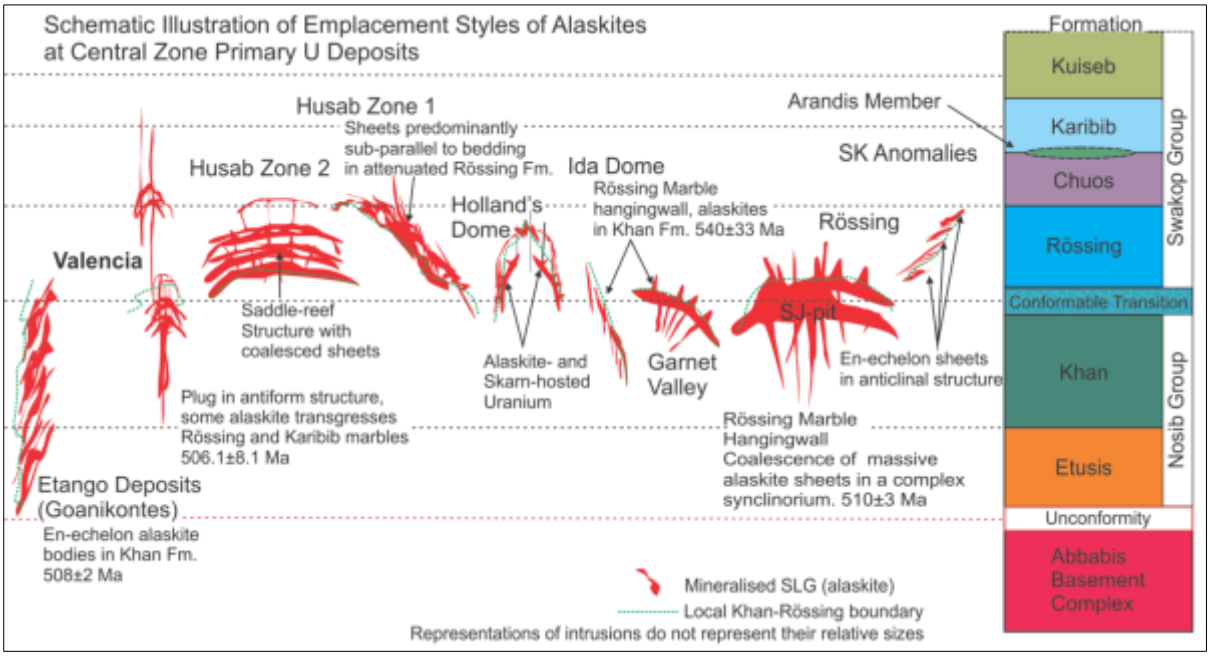



Figure 3.2 Diagram of sheeted leucogranite intrusion styles at the major Central Zone uranium deposits. The deposits primarily occur within the upper Nosib Group and lower Swakop Group. The Rössing Formation is a key assemblage of reactive metasediments at the Rössing Mine and is host to the bulk of uranium-bearing leucogranites at Husab, though its presence is not essential, the Etango deposit at Goanikontes for example is hosted almost entirely within the Khan- and Chuos Formations.

A number of researchers have published papers that include proposals for granite petrogenesis: Corner (1982) and Ward *et al.* (2008) included samples from the Valencia area, Barnes (1981); and McDermott (1986) sampled the suites at the Ida Dome. Many of the geological attributes of the deposits at Rössing are summarised from work by previous authors including Jacob (1974a; 1974b), Jacob (1975); Cuney (1980b); Miller (1983a); Berning

(1986); Jacob *et al.* (1986); Oliver (1994); Oliver and Kinnaird (1996); Goscombe (2003a); Basson and Greenway (2004); and Abraham, (2009). Because more has been written on Rössing than any of other deposits, it is included in this thesis as the reference example against which other deposits in the Central Zone can be compared and contrasted. The complex dome and basin deposit formation setting and complex deformational history combine to produce variable litho-stratigraphy accounts at each deposit that differentiate them from each other and the Rössing setting.

Table 3.1 Revised Central Zone sheeted leucogranite classification after Nex (1997). Goanikontes refers to the location on farm Goanikontes of the Etango Deposit, Husab refers to the Zone 1 and Zone 2 deposits within ML171, Ida Dome refers to the area that encompasses the Ida Central (EPL3138), Garnet Valley and Holland's Dome Deposits (both EPL3439), Hildenhof refers to the portion of the anomaly on Farm Hildenhof that lies within EPL3345 (Bannerman Resources, 2014).

| Type | Description | Locations | CPS vs. BG |
|---|---|---|---|
| A-type | Thin, very light pink to white, bedding parallel, very little accessories, often folded and boudinaged within Damaran Metasediments, limited extent. | Goanikontes, Valencia | low |
| B-type | White as well as light pink, medium-grained and homogeneous, often bedding parallel, folded and boudinaged. Garnet is a distinctive accessory and is found in clusters or as disseminated grains mostly < 1 cm in size. Examples at Valencia may be anatectic granites from Kuiseb Formation melt, as described in Ward *et al*. (2008). | Goanikontes, Ida Dome, Valencia (Husab – not certain) | low |
| C-type (accessory-free) | Extensive sheets or coalescences of sheets, predominantly in upper Nosib and Swakop Groups, white to light pink in colour, variably coarse-grained, minimal accessories except entrained biotite. May be a B-type at Valencia, as they are crosscut by tourmaline SLG's. | Throughout CZ | low |
| $C_m$-type (magnetite) | Distinctive pink and white colour, medium to coarse as well as pegmatitic in patches, accessory magnetite clusters or disseminated throughout. These may also have accessory tourmaline accompanied by clear quartz. Recognisable by being parallel to bedding/cleavage/foliation. | Goanikontes, Hildenhof, Husab, Ida Dome, Valencia, | Low-high in patches |
| $C_t$-type (tourmaline) | May be light pink or white, mostly fairly coarse-grained with massive tourmaline, often in clusters. The massive tourmaline can often be as large as 5 - 6 cm across. Sheets occur as parallel to bedding sheets in Kuiseb and Khan schists and gneisses. | Ida Dome, Valencia | low |
| D-type | White, medium to medium - coarse-grained, smoky quartz (black) and very little accessory biotite. May have yellow uranium secondary phases on exposed surfaces and on joint planes | Goanikontes, Husab, Ida Dome, Valencia | very high |
| Altered D-type | Highly oxidised deep pink amorphous veins and fingers of granite intruding a range of other granites. These have a high biotite content and smoky quartz. Hydrothermal alteration of D-types has resulted in the colour and texture seen as the E-type by Nex (1997). | Goanikontes, Hildenhof, Husab, Ida Dome | High-very high |
| F-type | Deep red pink, pegmatitic, milky quartz, cross cuts most features and granites | Goanikontes, Valencia, Ida Dome | low |

Exploration companies have successfully applied the deposit descriptions and regional mineralisation trends described by Jacob (1974b); Berning (1980); Corner (1981); Jacob *et al.* (1986); Nex and Kinnaird (1995); and Nex (1997) to their drilling campaigns and have expanded known resources and discovered new deposits:

- Exploration drilling at Valencia focussed on the preferential intrusion of leucogranites down the plunge of a fold hinge;
- The Etango Deposits' resources at Goanikontes were expanded by tracing the edge of the Palmenhorst-Khan Dome structure under the Namib peneplain;
- In the Garnet Valley and Ida Dome areas, exploration focussed on tracing a Rössing marble hanging wall trap; and

Interpretation of regional geophysical features under the Welwitschia Plains south of Rössing mine played a crucial role in the discovery of the very large Husab deposits (>360 Mlbs measured and Indicated U3O8)[11]

## 3.4 Controls on mineralisation

There are a number of factors that are common to each uranium prospect. Timing of emplacement is important as uranium mineralisation is associated with post-$D_3$ leucogranite sheets, which range in composition from tonalite to alkali-feldspar granite (Berning, 1986; Nex 1997; Freemantle, 2006; and Kinnaird and Nex, 2007).

There is a structural control as mineralised sheeted leucogranites were emplaced during the transition from ductile to brittle deformation (Oliver, 1994; Nex, 1997; Basson and Greenway, 2004; and Kinnaird and Nex, 2007). Sheeted leucogranites predominantly intrude along existing fractures, faults, bedding planes, axial planes and axial-planar cleavages, but also show some signs of deformation such as persistent fabrics and strain extinction in quartz. The rheological contrast between competent gneiss to ductile marble has had a

[11] June 2012 resource update for the Husan Uranium Project, Coffey Mining, 2012

strong influence on the preferential emplacement at the Khan-Rössing contact (Basson and Greenway, 2004).

The preferential emplacement of sheets close to the stratigraphic intervals where REDOX contrasts between the magma and fluids and the country rocks existed plays the most significant role in $U^{6+}$ reduction, and subsequent uraninite crystallisation. Important REDOX intervals include the boundary between the Khan and Rössing Formations (Jacob *et al.*, 1986; Marlow, 1981; Berning *et al.,* 1976; Nex and Kinnaird, 1995; and Nex, 1997), or the Khan-Chuos boundary where the Rössing Formation is attenuated or absent (Nex, 1997 and Kinnaird and Nex 2007). Similarly, the sulphide-bearing, reduced metasediments of the Arandis Member, below the Karibib Formation, host uraniferous sheeted leucogranites at the Z19 deposit of Rössing Uranium. Mineralisation is mostly limited to the Rossing Formation and marginally in the upper Khan and lower Chuos Formations at the Husab deposits.

Fluid composition controls also may have been important. The de-carbonisation reaction $CaCO_3 + SiO_2 = CaSiO_3$ (diopside, skarns) + $CO_2$, where $CO_2$ increases, the melt liquid/$H_2O$ equilibrium had to adjust by raising the silicate melt solidus to higher temperatures, thus forcing the alaskite to crystallise within or below significant marble layers (after Cuney, 2009). However, the lack of significant marble at Goanikontes and at Valencia indicates that this mechanism is not of universal importance.

REDOX changes at the Khan-Rössing Formation boundary is the strongest influence on uranium precipitation and deposition (Cuney 1980a; Kinnaird and Nex, 2007; and Cuney 2009). The Khan Formation becomes progressively reducing up-stratigraphy, sulphide mineralisation is prevalent in the upper Khan, and the most obvious evidence is the numerous Cu-sulphide showings in the Central Zone, especially at the Ida Dome (defunct Ida Mine), Khan Mine and Valencia (defunct Kainkaghas Mine). Such reducing units would have promoted $U^{4+}$ and uraninite precipitation. A suitable reduction agent (or combination of agents) must be present in the reactive rocks. Given the amount of biotite, pyrite and variable magnetite and pyrite present at locations such as Goanikontes (magnetite) and Husab (pyrite-pyrrhotite) $Fe^{2+}$ is a strong candidate for the dominant reducing agent. In addition, there are local controls at the various granite-hosted uranium deposits of the

Central Zone, as noted by Kinnaird and Nex (2007). Each of these are discussed for the individual deposits in the next section.

***Entrained metasediments***

The margins to entrained metasediment xenoliths, where some incorporation of the host rock fragments has taken place, tend to show elevated CPS when measured on surface. Figure 3.3a andFigure 3.3b illustrates similar examples of wall rock entrainment, at the Husab Deposits.

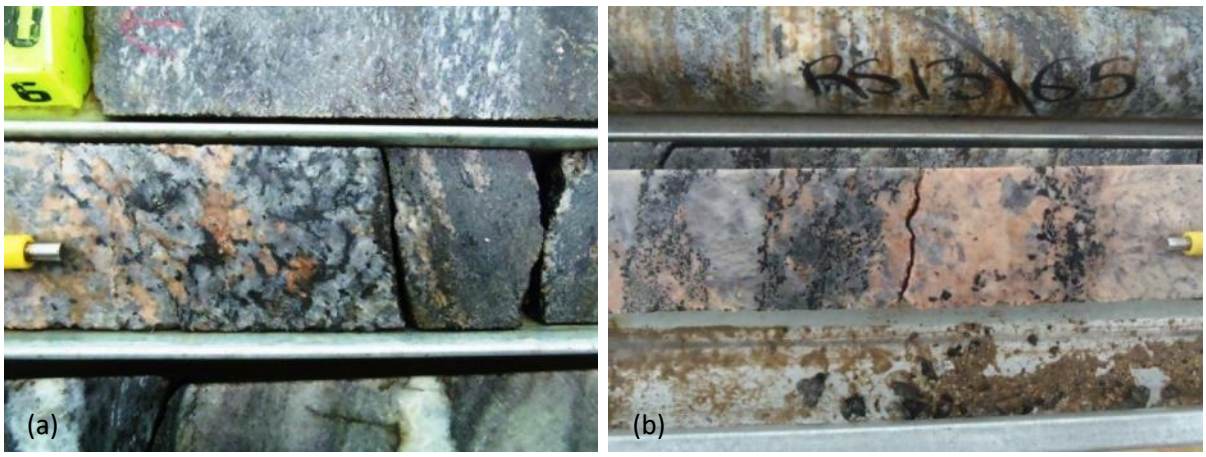



Figure 3.3 Examples of wall rock assimilation in Husab granites. (a) Alaskite contact with Rössing schist, where the contact is characterised by quartz and coarse biotite and elevated CPS, RDD051 - 440 m. (b) Streaks of remnant metasediments in leucogranite, RDD113 - 404 m.

The larger sheets (> 10 m wide) and amalgamations of multiple leucogranite sheets at Goanikontes and the Ida Dome preserve original textures of host rocks in xenoliths; suggesting that the host rocks retained these sedimentary and metamorphic features at temperatures similar to the intruding leucogranites (Figure 3.4a and 3.4b). The localised U concentration is likely to have been the result of host rock influence on U solubility in the intruding magma and associated fluids as there is no evidence of any externally - sourced- or late stage U mobilisation. Barren to weakly mineralised sheeted leucogranites at Valencia (Figure 3.4c) contain laths and ghost bedding of consumed diopside Khan Formation gneisses, where elevated cps (up to 10 times background- ~400 cps) accompanies haematite-discoloration of the granite.

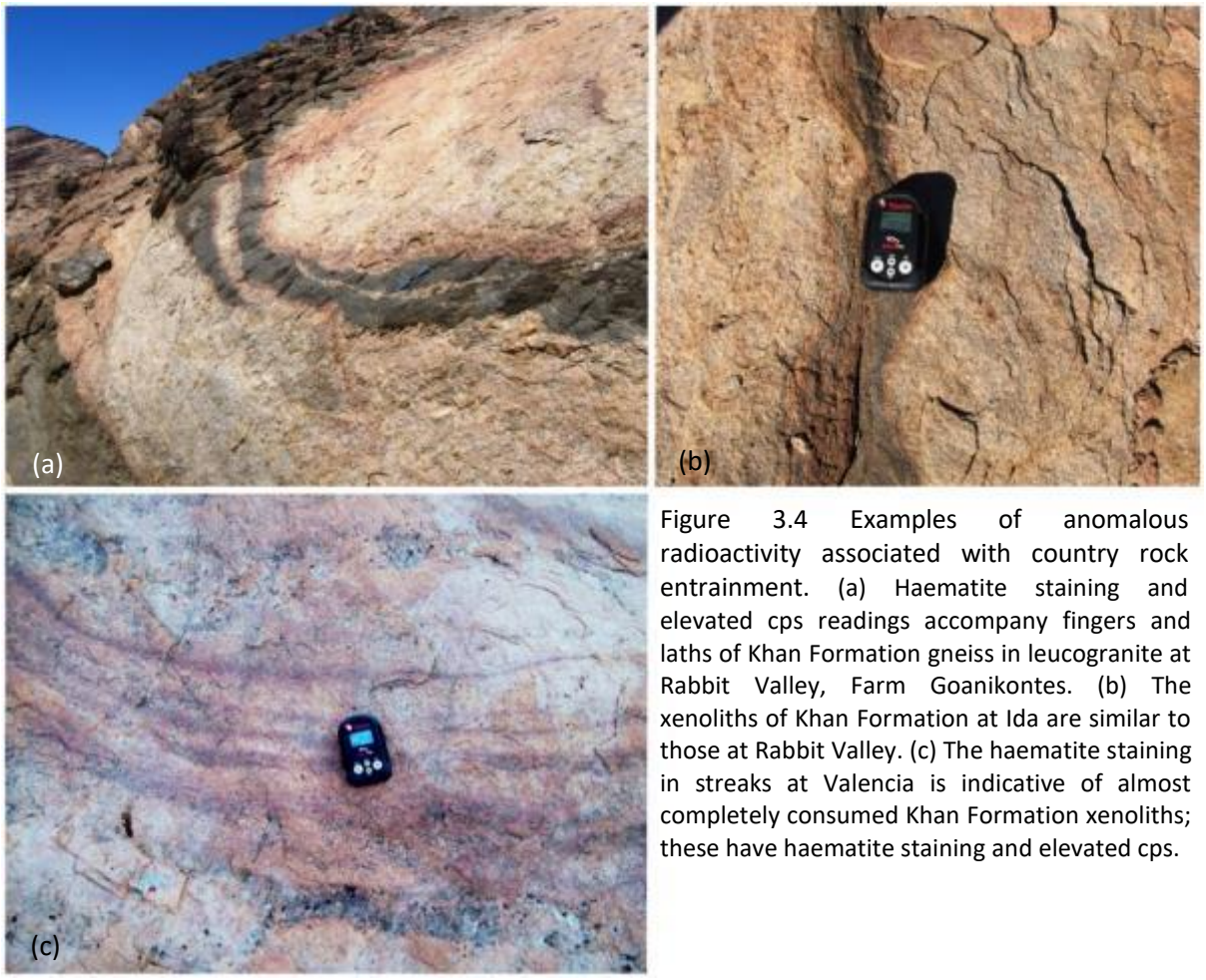



Figure 3.4 Examples of anomalous radioactivity associated with country rock entrainment. (a) Haematite staining and elevated cps readings accompany fingers and laths of Khan Formation gneiss in leucogranite at Rabbit Valley, Farm Goanikontes. (b) The xenoliths of Khan Formation at Ida are similar to those at Rabbit Valley. (c) The haematite staining in streaks at Valencia is indicative of almost completely consumed Khan Formation xenoliths; these have haematite staining and elevated cps.

Peraluminous phases such as sillimanite, garnet, muscovite and tourmaline should be absent in the sheeted leucogranites. However, they often occur as nests or skeletal blades (Figure 3.5a and 3.5b). Polycrystalline quartz clasts are infrequent in most of the barren sheeted leucogranites resulting from the incorporation of Damaran metasediment into the leucogranite, or possibly transported from a Basement metasediment. Polycrystalline quartz occurs in some pre-$D_3$ sheeted leucogranites, and is likely to have been sourced from a metasediment (Figure 3.5c). The variability in volumes of sheeted leucogranite intrusions during emplacement and interaction with the metasediments has resulted in a range of metasediment incorporations; from intact xenoliths of country rock fully consumed remnants of biotite-rich laths and ghost bedding. These observations support the observations of Berning (1986) regarding timing of the metamorphic textures at Rössing. Sites of partial assimilation of reduced metasediments are important locations for U deposition:

*Larger sedimentary xenoliths of predominantly Khan Formation gneisses are intact, apart from reactive margins and near-consumed ghost bedding. This infers that in order to explain the metamorphic textures, present in xenoliths; the metasediments had to have been deformed prior to any granite emplacement and had cooled by the time the mineralised sheets had intruded. Alternatively, the metasediments melt at a higher temperature than the invading, fractionated melts.*

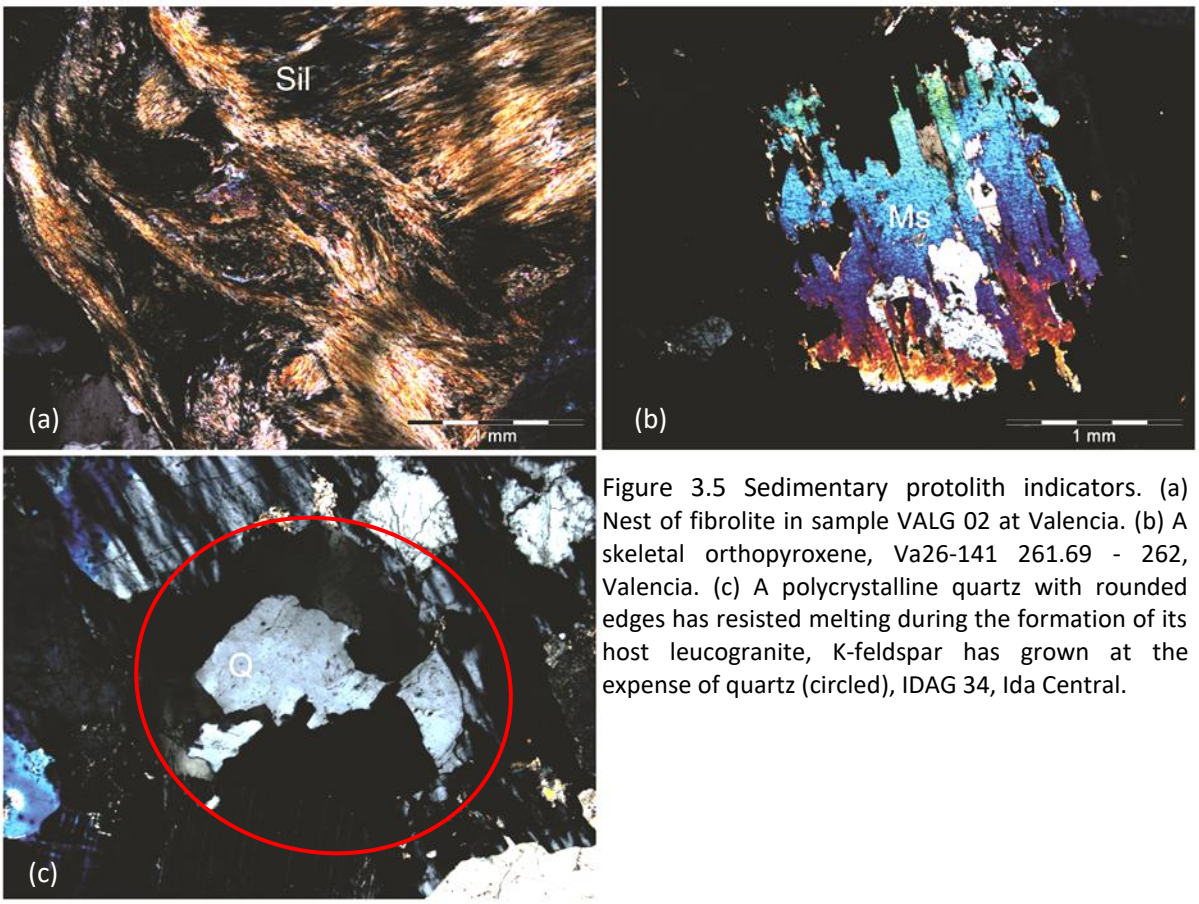



Figure 3.5 Sedimentary protolith indicators. (a) Nest of fibrolite in sample VALG 02 at Valencia. (b) A skeletal orthopyroxene, Va26-141 261.69 - 262, Valencia. (c) A polycrystalline quartz with rounded edges has resisted melting during the formation of its host leucogranite, K-feldspar has grown at the expense of quartz (circled), IDAG 34, Ida Central.

***Oxidation halos and supergene alteration***

Typically, oxidation halos are rounded or ellipsoid in shape and may comprise multiple coronas, (Figure 3.6a). Pavements and faces of interconnected amoeboid-shaped halos occur along the Khan River at Goanikontes and at locations along the east periphery of the Ida Dome (Figure 3.6b - Garnet Valley and Figure 3.6c - Ida Central). The average thickness of a halo is within the cm- range, often accentuated by surface weathering. The oxidation halos

are common at Goanikontes and the Ida Dome and these are interpreted by Corner (1983) as resulting from CZ–wide chemical alteration that occurred in post-Damaran time (Corner, 1983).

Valencia and Hildenhof locations do not exhibit examples of typical oxidation halos on surface. Haematite red-coloured patches occur near the Khan-Rössing boundary at Valencia, but do not resemble the core and rim halo types at typical Goanikontes and Ida Dome localities. The discoloration is instead, usually a product of interaction and partial consumption of Fe - bearing skarn. Iron staining occurs at depths of over 200 m in core samples from Ida, Etango (at Goanikontes) and at Valencia (Figure 3.6d and e, respectively). Large pavements at the Ida Dome and Goanikontes illustrate the distinctly lighter shade of pristine alaskite within the oxidised, surrounding granite (Figure 3.6d, Ida Dome).

The core from Goanikontes (Figure 3.6f) preserves a pristine white and black leucogranite. The cores of the halos preserve Damaran-age palaeo-magnetism, while the surrounding orange-coloured alteration halo does not (Corner, 1981). Thus, the inner portion of the halo was interpreted as the unaltered granite, in most cases. Large feldspars cross-cut halos, which supports a perception of a singular granite generation inside and outside the halo.

Nex (1997) recognised two basic types of halo at Goanikontes; those with distinctive oxidation fronts and inner constituents with D-type leucogranite appearances, and another, less abundant type, with amorphous shape and distinct reddening (and occasional yellowing) of feldspars. The inner portion of the coronas preserves a higher grade of U than the surrounding granite at Goanikontes. Halos observed at the Ida Dome area do not always indicate mineralisation. For example, the photographs in Figure 3.7a to 3.7d illustrate that halos with almost identical appearance may have vastly different cps readings and correspondingly variable U content. Coloration of the cores of the halos varies from light grey-white to dark-grey (Figure 3.7a and b) and cores tend to be darker in barren halos. Oxidation patches (rather than halos) are also characteristic of mineralised and occasionally barren sheeted leucogranites; in Figure 3.7c and Figure 3.7d, two types of oxidation patch contrast in coloration, the deep-red mineralised examples appear to be consumed magnetite-skarn rather than altered granite.

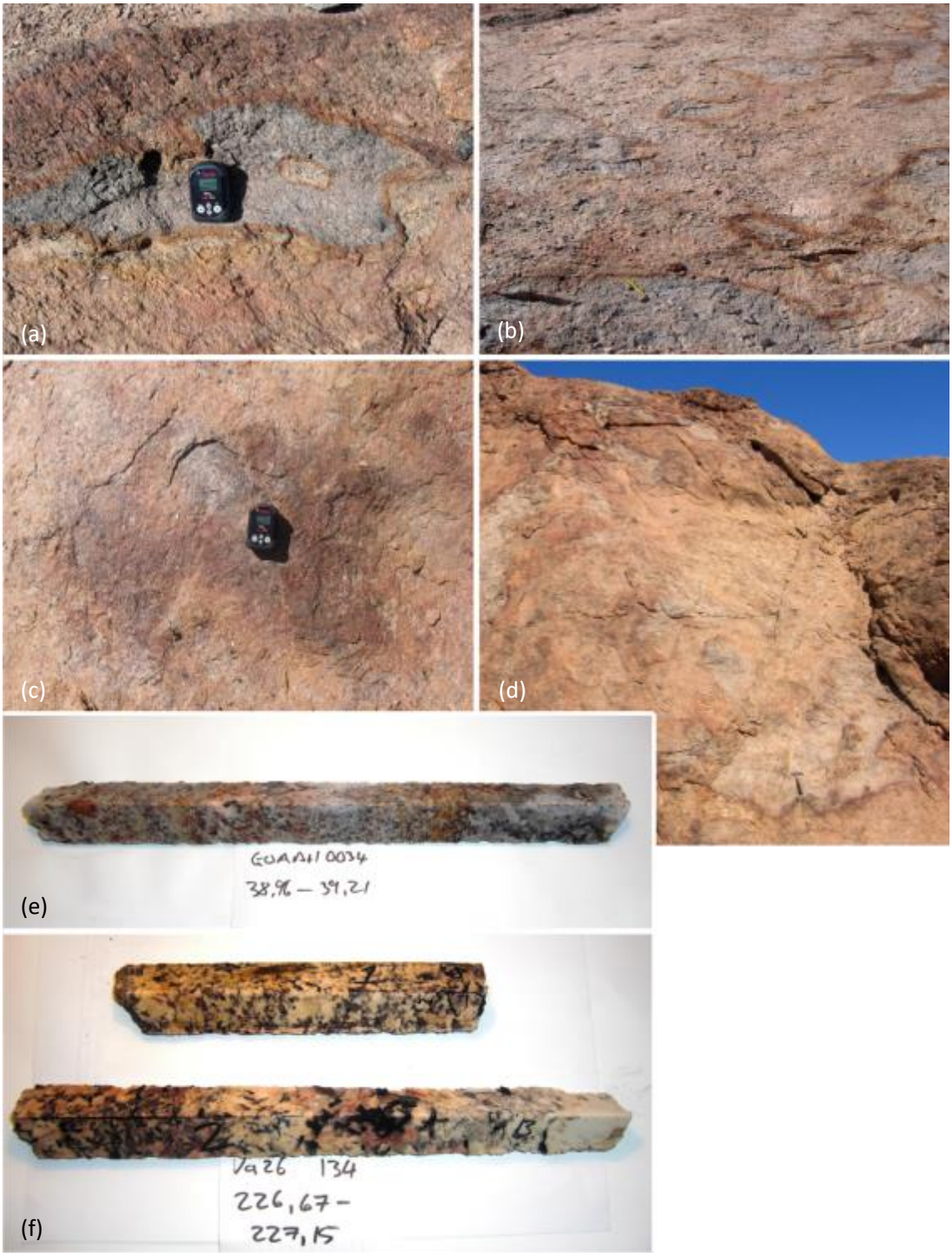



Figure 3.6 Oxidation halos in sheeted leucogranites of the Central Zone. Fe dominated discoloration is characteristic of many of the mineralised leucogranites from the Central Zone.(a) A composite halo at Ida Central, two oxidation fronts are clear; a red coloured massive halo surrounds a smaller grey-coloured core, which in turn surrounds a white coloured core. (b) Pavement exposure of oxidation halos at Garnet Valley. (c) Patch of haematite staining at Valencia, these are not but discolouration associated with magnetite and biotite alteration accompanied by elevated cps readings. (d) E-type sheeted leucogranite locality with characteristic oxidation halos, at Ida Central. (e) Haematite stained patches occur in fresh core samples from Valencia, but distinctive halos are not present. (f) The halos are present in relatively fresh material from Goanikontes, the core of the halo and its haematite-limonite rim are clearly visible.

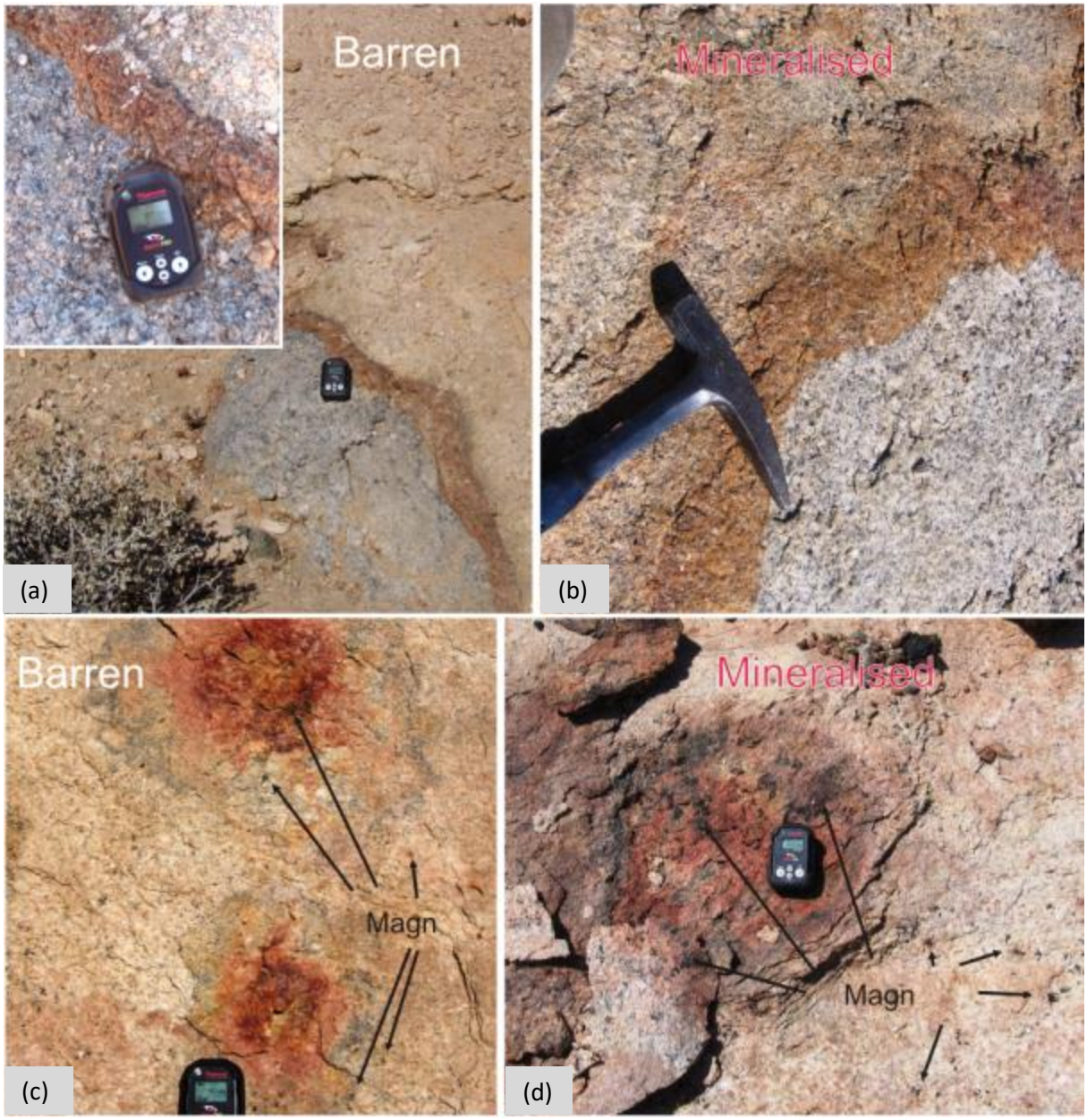



Figure 3.7 Varieties of oxidation halos in barren and mineralised leucogranites. (a) A barren halo at Ida Central is characterised by limonite-brown staining and a deep blue-grey core. The granites are only weakly radioactive and occur lower down in the Khan succession than the more mineralised varieties, at both Garnet Valley and Ida Central. (b) An unaltered mineralised core and halo at Holland's Dome appears near identical to the barren variety, it does however have a slightly lighter grey core. (c) Barren haematite stains in magnetite-bearing C-type granite near the core of the Ida Dome, note the limonite coloration in the cores. (d) A haematite stain at Holland's Dome, the large magnetite porphyroblasts and deep red-pink colour discriminates it from the U-barren stains. It is adjacent to a skarn pod and is itself actually the remnant of a skarn fragment.

The regional distribution of the typical orbicular halos appears to be restricted to the Ida Dome and Goanikontes deposits, there is of course haematite staining at Husab and Valencia but the development of corona-shaped halos is far more limited at these deposits. The halos,

as noted by Nex (1997) appear to be a late magmatic feature. This interpretation is supported at Garnet Valley in particular, where the most prominent halos occur in the granite pavements at some distance from the reactive marbles and skarns. This implies that reduction of the oxidised magmatic fluids by reaction with the sediments was incomplete and portions remained in circulation during granite crystallisation.

***D-types vs. E-types***

The uraniferous sheeted leucogranite varieties were divided into two types by Nex (1997) in a classification scheme based primarily on observable petrographic characteristics and supported by interpretation of geochemical evidence. The D- and E-types, in general, are different in physical appearance. The most apparent difference between the two is the prominence of orbicular haematite-limonite oxidation halos that characterise the E-type.

The D-type uraniferous granites are recognisable throughout the Central Zone, besides their anomalous gamma radiation, by the following macroscopic features:

- Distinct black and white coloration (smoky quartz and feldspar, respectively);
- They are texturally unique, smoky quartz forms semi-continuous chains and large clusters, with little to no milky quartz component;
- Generally greater quartz proportion than barren granite sheets; and
- Secondary mineral textures are visible in macroscopic observation, particularly microclinisation and albite rims around coarse plagioclase feldspars.

Uranium mineralisation shows tendencies for the following features, which are not universally applicable to all the Central Zone deposits:

- Abundant biotite, usually corresponding to very high grades of uranium (sub wt. % metal enrichment at Husab, for example); and
- Intensive interaction with the metasedimentary host rocks, usually with localised U precipitation.

Nex (1997) found, at Goanikontes, that the E-type was consistently lower in uranium content than the D-type. D-type textures vary between exposed localities at the Central Zone deposits and the following summarise each locality's D-type surface exposures:

- Goanikontes D-types are medium to coarse-grained and inhomogeneous, with patches of quartz-rich and feldspar-rich granite varying within tens of centimetres;
- Ida Dome D-types are very similar in texture to Goanikontes, where textures range from medium to coarse-grained equigranular granites to pegmatitic and quartz-dominated pegmatite varieties;
- Valencia D-types are more or less equigranular, and range from medium- to coarse-grained. The texture is described locally as 'salt and pepper' granite; and
- Husab has no prominent surface exposure of alaskite. A shallow box cut at the north end of Zone 1 reveals pegmatitic alaskite with a higher biotite component, relative to the deposits along the Swakop River Valley. The near surface exposure is pervasively weathered. The box cut is not representative of the entire deposit and core observations highlight a great variety of textures.

Late brittle features in the sheeted leucogranites and country rocks have formed faults and breccia zones. These planes are filled with a variety of secondary vein minerals; which have leached minerals including uraninite where fluorspar veins and breccia - fills remain behind (Figure 3.8a). Fluorspar is observed in varying abundances at all the deposits in this study; the Husab drill core in particular, contains prominent fluorspar veining. Hydrofluoric fluid percolation through whole units of metasediment and partially through sheeted leucogranites has leached uranium from intervals of otherwise high grade ore. Quartz-calcite-fluorite vein systems tend to carry mobile uranium complexes that form boltwoodite and the dimorphs of uranophane, which elevate the uranium content in the otherwise barren pegmatites or host metasediments (Figure 3.8b).

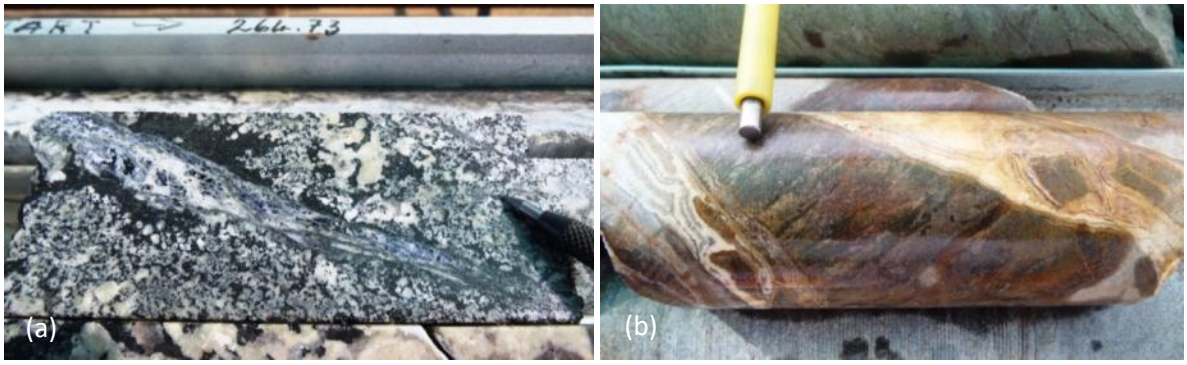



Figure 3.8 Late stage vein minerals. (a) Fluorspar in breccia vein. The fluorspar is purple in colour, which is indicative of U content. Invariably sheeted leucogranites with prominent fluorspar veining tend to show lower than expected U grades, RDD193 - 261 m. (b) Calcite - quartz veins often accompany intense weathering of the host rocks, but carry elevated grades of mobile U, RDD373 - 68 m.

The Holland's Dome and Garnet Valley areas preserve a number of late-magmatic features in the exposed pavements of granite that characterise the area. The pavements comprise predominantly weakly mineralised/barren leucogranite swarms with a uniform, subtle northeast - southwest foliation, that are large masses of the C-type variety of Nex (1997). Veins of coarse-grained granite with smoky quartz and anomalous radiation occur in straight-sided veins within these masses of barren granite. The veins range from 1 cm to over 50 cm in width, and metre- to tens of metres in length. Numerous crosscutting veins may occur in a single outcrop and the distribution of these veins is patchy and sporadic, with some areas completely devoid of any. Locations such as the Holland's Dome have abundant examples of leucogranite pavements that host xenoliths of biotite-rich Grey granite and Khan Formation schists. Figure 3.9(a) illustrates a coarse-grained, mineralised granite vein cutting a xenolith of Grey granite. The xenolith is hosted in a mass of C-type leucogranite, while the vein is a mineralised type, as indicated by smoky quartz. Often these sites have veins of mineralised granite that appear to terminate at/propogate from the margins of metasediment xenoliths (Figure 3.9b). Pavements of uraniferous D-type - textured leucogranite are always in close proximity to these straight-edged mineralised veins/fractures.

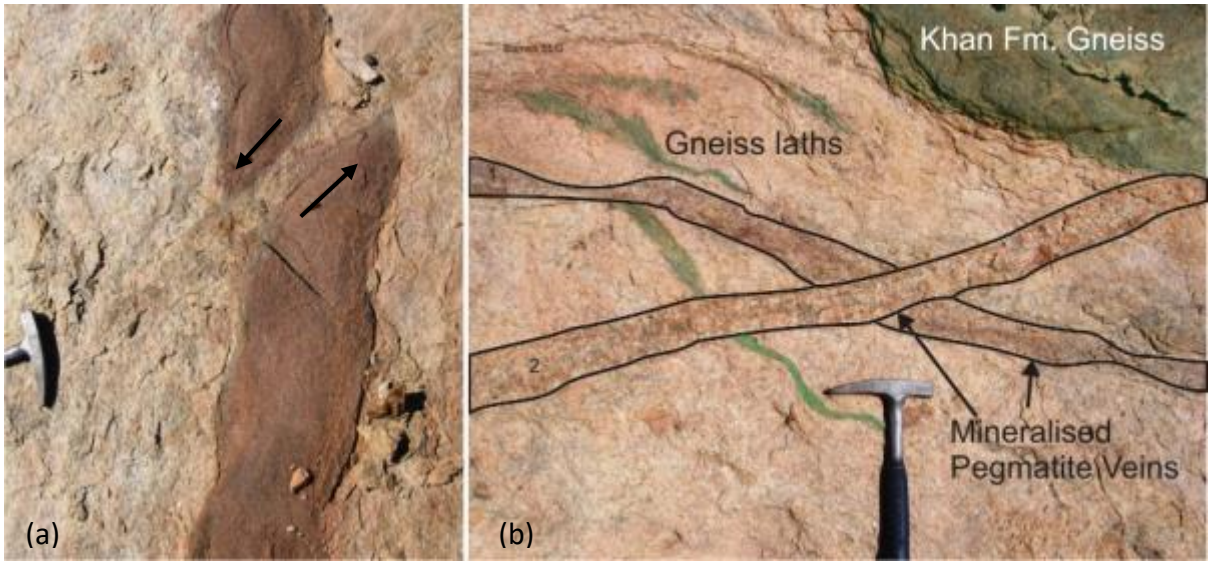



Figure 3.9 Late granitic veins and U-remobilisation in brittle fractures (a) Melts crystallise as coarse-grained granite with smoky quartz and are highly variable in size, but always straight edged. The example is a tension-gash shape between two parts of Grey granite xenolith. (b) Multiple generations of coarse-grained granite veins occur in the massive C-type sheets at Holland's Dome; these propagate from the contacts of gneiss xenoliths and from the edges of patches of D-type sheeted leucogranite. They and have elevated cps readings and usually are accompanied by some discoloration of the older granite.

Magnetite-bearing sheeted leucogranites occur in two locations within the stratigraphic succession. The lower suite contains magnetite-ilmenite porphyroblasts within the granite, and shows little evidence of subsequent alteration and does not show prominent reaction textures at contact margins. The upper suite appears to be comprised of variably uraniferous sheets awhere the magnetite is very often oxidised by some later hydrothermal event that has altered the host granite and metasedimentary rocks. It usually has more textural evidence of granite-metasediment reaction than the lower suite. Sheeted leucogranites that intrude a banded gneiss unit of the Khan Formation are characterised by disseminated 1 mm - 5 mm magnetite porphyroblasts that increase in abundance toward the sedimentary contacts. Locations at Valencia, Holland's Dome, and Etango (at Goanikontes) provide type-examples of sheeted leucogranite and reactive metasediment contacts.

At Valencia, a black mass of magnetite porphyroblasts occurs in a migmatised sediment matrix (Figure 3.10a); the greatest densities of such porphyroblasts are located at intrusive contacts predominantly within the local upper Khan Formation (Figure 3.10b). Holland's Dome, where skarn pods are well developed, hosts examples of magnetite porphyroblasts in sheeted leucogranites that have developed to large sizes (Figure 3.10c) and are associated with haematite discoloration of the host rocks (Figure 3.10d). Similarly, magnetite with

associated U-enhancement occur in mineralised core specimens from Goanikontes, characteristically surrounded by haematite staining and occasional secondary U-phases (Figure 3.10e) despite coming from depths in excess of 200 m. Garnet valley sheeted leucogranites contain minor base–metal sulphides, entrained into granites along with larger, massive magnetite (Figure 3.10f).

Sheeted leucogranites that have invaded calcareous horizons such as the Ida Dome area have produced calcsilicate and skarns that are U-enriched, particularly at Holland's Dome and to a lesser extent, the Hildenhof Anomaly and the Valencia area has localised skarns, some of which are Th-enriched. The U enhancement of these metasediments coupled with prominent base metal sulphide entrainment in the sheeted leucogranites indicates significant interaction between the sheets and the host rocks, which has influenced on the sheeted leucogranite geochemistry, particularly with respect to mobile major elements such as Ca.

Observations at the Ida Dome and Valencia deposits strongly suggest that host-rock mineralogy, pre-determined structural pathways, and contact metamorphism interaction strongly influenced the textural and mineralogical characteristics of the barren and mineralised varieties. The hydrothermal alteration has resulted in some sheets attaining vivid Fe-oxidation staining and the addition of yellow $U^{6+}$ species in fractures and between grain boundaries. Although surface - derived weathering emphasises the colour contrast between oxidation fronts and the surrounding leucogranite, this oxidation is not the same as similar-looking alteration that occurs at depths in excess of 300 m. The observations presented in this Chapter tend to show that local conditions rather than temporally different generations (D- and E-types) may be responsible for the variations in the uraniferous leucogranite textures, petrographic character and probably chemistry.

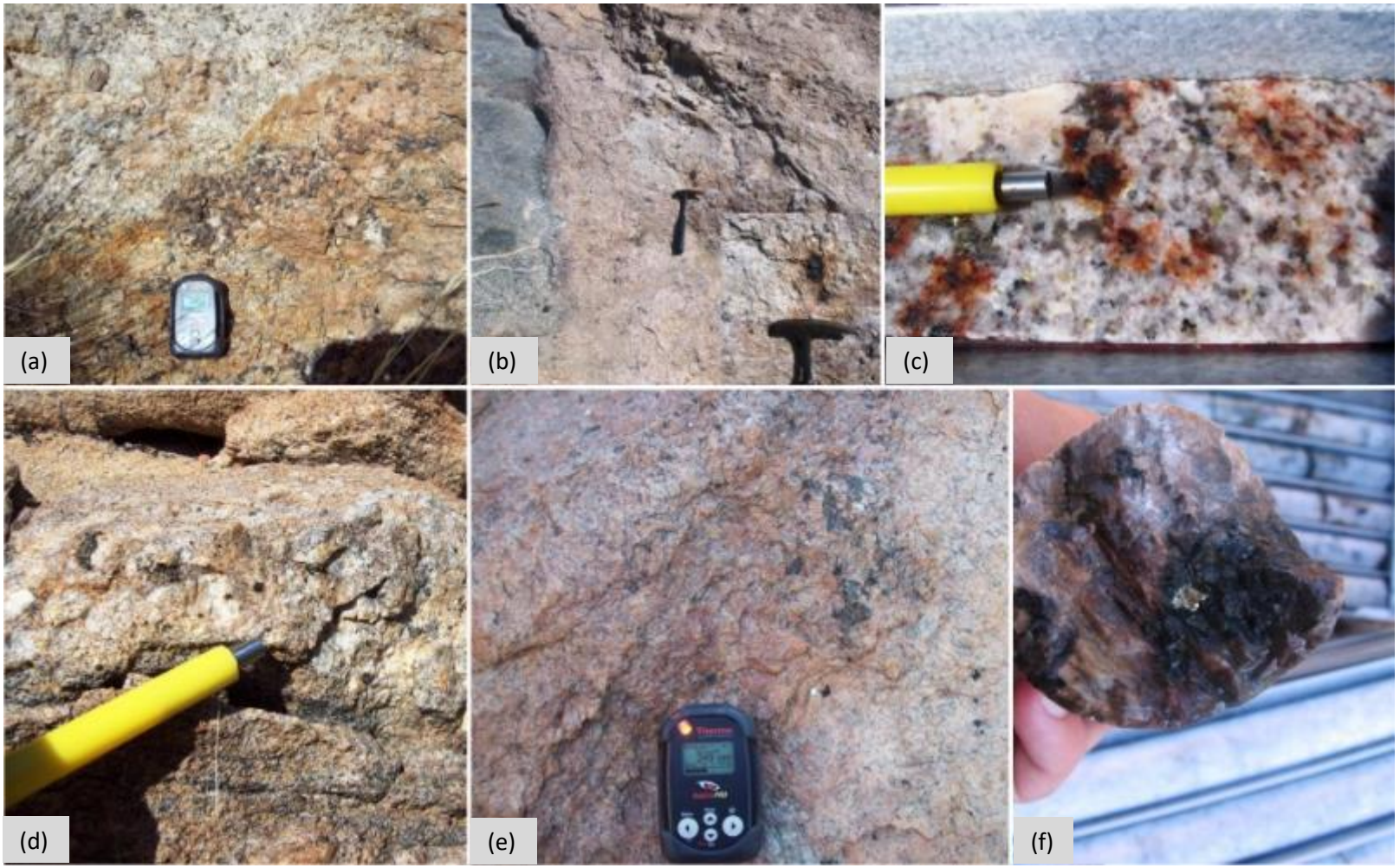
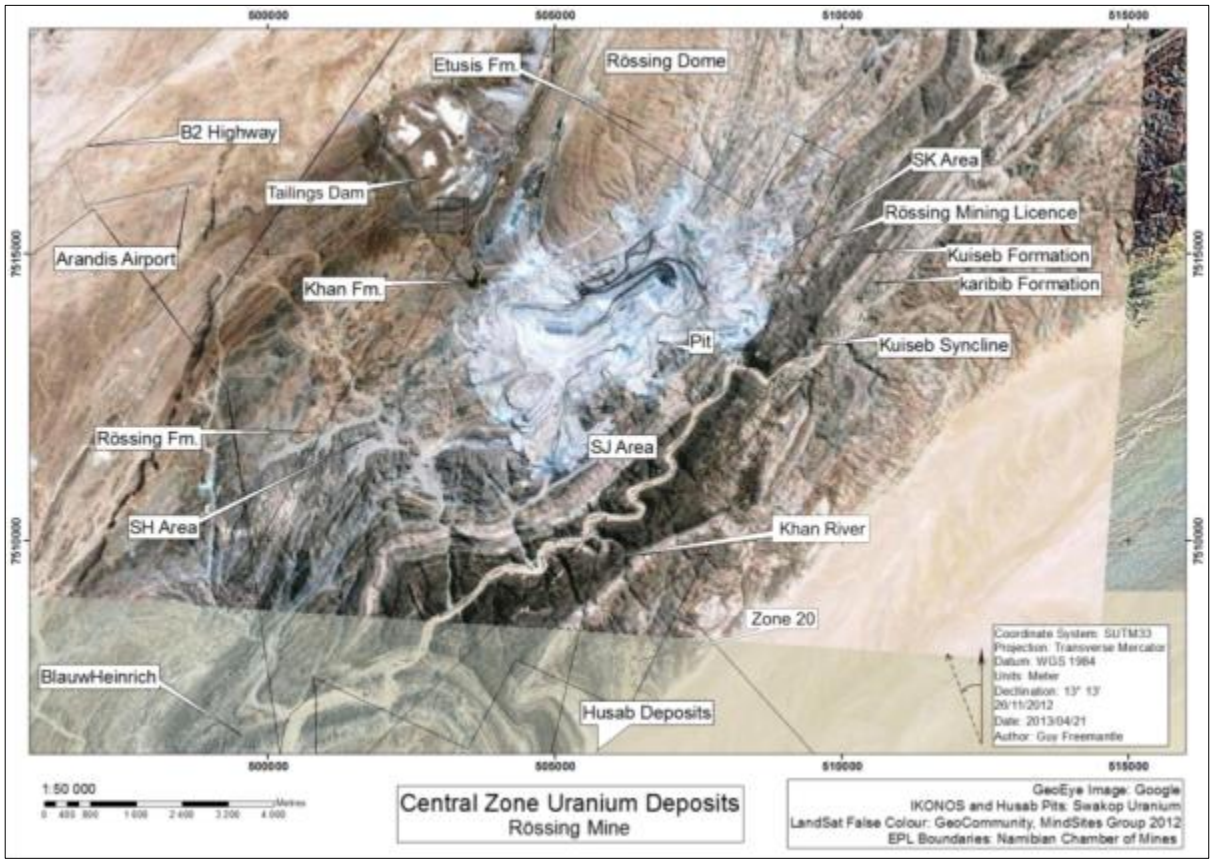



Figure 3.10 Magnetite in alaskite and other leucogranites.(a) Fine - grained magnetite porphyroblasts in banded gneiss of the lower Khan Formation. (b) Magnetite has developed in migmatised Khan Formation units at Valencia. (c) Magnetite associated with skarn development grow larger; Fe-oxide staining accompanies all the magnetite at Holland's Dome. (d) Magnetite cluster associated with elevated cps, Holland's Dome. (e) At Goanikontes, fresh samples show haematite staining surrounding magnetite in mineralised leucogranite, alteration halos do not surround magnetite in nearby, non-mineralised leucogranites. (f) The magnetite at Garnet Valley is also associated with interaction between leucogranite and skarn and/or calcsilicates, accessory ore minerals are often well developed and relatively large sized sulphide phases occur in the granite.

## 3.5 The Rössing Deposit

The Anglo American Corporation commenced prospecting in the area surrounding the Rössing Mine in 1956. In 1966 it was re-investigated by Rio Tinto, who have seen the project through to the world class producer it is today and currently retain a 52 % stake in the globally strategic operation. Mine preparation and plant construction began in 1974 and by 1976; the Rössing Mine was in production (Jacob, 1976). Large sheeted leucogranites (locally alaskite) host the majority of the mineralisation with a highly variable proportion of secondary uranium found in the host rocks (Abraham, 2008). The sheets are highly variable in width and extent, some of which have coalesced into a >90 m wide dykes. The Rössing Mine is currently the largest $U_3O_8$ producer from primary sources in the world[12]. The pit is over 3 km long and over 1 km wide and Figure 3.11 shows the mine in a satellite image segment.




[12] www.worldnuclear.org

Figure 3.11 The Rössing Mine area. The main SJ deposit is a large open pit, over 3 km long, and processed by conventional oxidant – acid leach. The neighbouring SK and SH areas contain large volumes of leucogranite, but host mineralogy is dominated by the refractory phase, betafite.

### *Stratigraphy*

The Damara Supergroup at Rössing comprises mostly Nosib Group and lower Swakop Group lithologies. The stratigraphic succession of the Rössing Mine presented below is an abridged summary of research work by Nash (1971), SACS (1980), Coward (1983), Downing (1983), Martin (1983), Lehtonen *et al.* (1996) and Nex (1997) and personal communication with Timothy Gray of Rio Tinto. The summarised succession is presented in Figure 3.12. Because the stratigraphic sequence has been described in most detail at Rössing, it forms a basis for comparison for all other new mining interests in the Central Zone. The sequence is described in Nash (1971), Henry (1992), Lehtonen *et al.* (1996); Anderson and Nash (1997); and Gray (2015) the latter having integrated remote sensing and geophysical techniques to refine the lithostratigraphy.

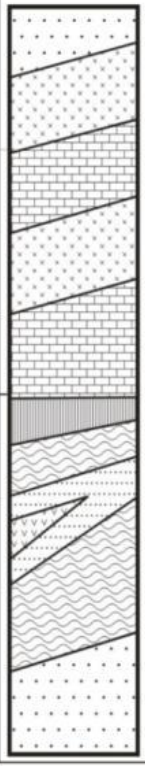
| Group | Formation | Unit | Thickness (metres) | | Lithology |
|---|---|---|---|---|---|
| Swakop | Rössing | Quartzite | < 100 |  | Medium-grained quartzite, gritty near base |
| | | Upper pelitic gneiss | 40-50 | | Diopside-biotite(-scapolite) gneiss with thin inter-bedded quartz grit and marble near base; grading upwards into cordierite-biotite gneiss |
| | | Upper marble | 50-70 | | Serpentine marble and diopside-quartz marble with inter-bedded biotite-diopside granofels and cordierite-biotite gneiss. Conglomerate-grit at base. |
| | | Lower pelitic gneiss | 30-40 | | Migmatised cordierite-biotite-sillimanite gneiss, locally garnet-bearing, grading into biotite-diopside granofels and pelitic schist. |
| | | Lower Marble | 20-50 | | Serpentine marble and subordinate graphite marble, with irregular intercalations of biotite-diopside granofels and pelitic schist |
| Nosib | Khan | Para-amphibolite and conglomerate | 10-20 | | Amphiobole-biootite schist containing local pebble bands |
| | | Upper basic gneiss | 70-120 | | Strongly migmatised amphibole and pyroxene gneiss |
| | | Pyx-gnt gneiss | 0-120 | | Migmatised pyroxene-garnet gneiss; local concordant bodies of hornblende-oligoclase orthoamphibolite |
| | | Orthoamphibolite Pyx-gnt gneiss | | | Strongly banded, partially migmatised pyroxene-amphibole gneisses |
| | | Lower basic gneiss | 70-150 | | Strongly migmatised quartzofeldspathic gneisses with numerous biotite foliae. |
| | Etusis | Psammitic gneiss | > 300 | | |

Figure 3.12 Stratigraphic succession at the Rössing Mine. The succession is a summary of work by Nash (1971), SACS (1980), Downing (1983), Martin (1983), Lehtonen *et al.* (1996) and Nex (1997).

The stratigraphy is well exposed in the open pit; the north high wall comprises predominantly Khan Formation lithologies and the south wall of Rössing Formation. The upper Nosib Group and lower Swakop Group metasediments are draped over the Etusis-cored dome, and dip roughly 60° to the south southwest (Basson and Greenway, 2004). The Rössing Formation is greatly thinned along the margins of the Dome, and is significantly thinner than the Karibib Formation higher up in the stratigraphy, as illustrated in Figure 3.13a and 3.13b.

The Etusis Formation comprises migmatised cross-bedded fluviatile sandstones and shales and represents the basal units of the Damara Supergroup at the Rössing area, composing the bulk of the Rössing Dome. The Etusis Formation locally consists of a lower biotite schist member, a lower meta-quartzite member, an upper biotite schist member and an upper meta-quartzite member (Nash, 1971; Lehtonen et al., 1996; Oliver and Kinnaird, 1996)

The local Khan Formation succeeds the Etusis Formation with banded pyroxene-amphibole gneiss with well-defined banding. The package is over 450 m thick and contains variably thick, if present, orthoamphibolite and pyroxene (diopside - hedenbergite) gneiss. Amphibole-biotite schist with deformed pebbles marks the uppermost package of the local Khan Formation. The local marker unit between the top of the Khan and bottom of the Rössing Formations is a distinctive, dark grey-black amphibole-biotite ± garnet schist, which shares the local top-of the Khan Formation with a meta-conglomerate. The evidence for an unconformity at this level would be the two contrasting marker units (conglomerate and para-amphibolite) below the first marble, as shown in the stratigraphic columns of Anderson and Nash (1997).

The lower units of the Rössing Formation comprise an intercalated package of impure, serpentine and graphite marble, with schists and calcsilicate units. The package varies between 20 m and 50 m in thickness (Nash, 1971). The lower pelitic gneiss includes sillimanite biotite gneiss with local biotite-garnet schist intervals which grades into cordierite- to garnet-dominated pelitic schist. The upper marble package has a locally gritty quartzite base, succeeded by serpentine- and graphite-bearing marble, with intercalated biotite-diopside granofels and distinctively textured cordierite-biotite gneiss (cordierite may be centimetric in size with a biotite fabric wrapping the porphyroblasts and a persistent

chlorite alteration overprint). The top of the Rössing Formation is locally a pyritic quartzite, which is variably gritty.

***Structure***

The area is characterised by the Rössing Dome, a feature that is ~7 km long northeast-southwest, and ~3 km across. It is cored by migmatised Etusis Formation meta-quartzites and metapelites (Oliver and Kinnaird, 1996). There is a synclinorium with sheared antiforms at the southern end of the dome with an accompanying antiform structure at the immediate southwest, and a sheared sequence of Khan Formation gneiss along the south-eastern flank of the dome. This synclinorium hosts the greatest concentration of sheeted leucogranite dykes and sills. Marbles and semi-pelitic rocks, are thickened at the southwest end of the Dome by tight folding and 'pooling' at the nose of the dome, while attenuation along the eastern and western flanks of the dome has left the Rössing Formation thinned and sometimes non-existent.

The Rössing SJ deposit occurs in a complex synclinorium, cored by Rössing Formation marble with an axial plane that trends approximately E-W, (Figure 3.13a). The synclinorium itself wraps around the southwestern nose of the Rössing dome in an arc shape. Stratigraphic sequences may vary significantly because of folding, shearing and attenuation along strain axes (Berning 1986).

Basson and Greenway (2004) present a model of granite intrusion and uranium mineralisation closely associated with a 4$^{th}$ phase of deformation that deformed the $D_3$ synclinorium. The model describes sinistral rotation of the dome structure with southward overall movement, generating sufficient dilation and low pressure for the leucogranite sheets to have invaded the synclinorium relatively unhindered and form the main SJ ore body, as well as invading en-echelon at the eastern flank to form the mineralised ore bodies at the SK area.

### *Magmatism*

The Rössing area is intruded by structurally controlled granites and pegmatites, described in Downing (1983); Jacob *et al.* (1986); Tack and Bowden (1999); and Oliver and Kinnaird (1996). The contrasting interaction between the competent Khan and Rössing gneiss units and less competent Rössing carbonate lithologies around the Rössing Dome during the late stage rotation of the Dome opened up space for the SLG's at the southeast nose of the dome. The sheets intruded oblique-to-bedding structures in the 'brittle' gneissic units of the Khan and Rössing Formations (after Basson and Greenway, 2004). The intimate way in which stratigraphic and structural characteristics of the deposit have combined to control and localise the granite sheets and uranium mineralisation makes it difficult to separate the effects of the two controls.

### *Mineralisation*

Mineralisation at Rössing occurs close to the Khan-Rössing Formation boundary. In addition, the impermeable marble barrier has acted as a local trap for magmatic fluids, promoting recirculation of uranium-bearing fluids during- and immediately after granite intrusion (Berning et al, 1986). Uranium minerals are hosted in D-type and E-Type leucogranite sheets, distributed throughout the pit and surrounding deposit areas and targets (Figure 3.13b).

The host mineral population is varied, but is dominated by sub - millimetric crystals of uraninite and accounts for ~55 % of the U in the deposit, the remainder comprising ~40 % U-silicates (uranophane, boltwoodite, coffinite) and ~5 % refractory betafite (after Hiemstra, 1969 and Berning, 1986). The feed-to-mill grade is between 300 ppm and 350 ppm U with resource-definition cut-off grade typically ~150 ppm.

Prior to the more recent studies, a number of authors have contributed to the understanding of the Rössing U-mineralogy distribution since the first systematic assessments during mine feasibility studies. Hiemstra (1967) investigated the Th content of uraninite in Rössing alaskite. Hiemstra *et al*. (1968) and Hiemstra and Beukes (1969) indicated that uraninite occurs as singular grains and in clusters surrounded by alteration halos of secondary uranium phases. Hiemstra (1968) investigated the relative amounts of

primary and secondary uranium phases by optical identification; Hiemstra et al. (1968) unsuccessfully attempted to assess relative amounts of primary and secondary phases. However, their team did identify leucoxene, which they described as a product after ilmenite and betafite, an oxide comprising variably proportioned Ca, Na, Nb, Ta, U, and REE. Hiemstra and Beukes (1969) described in detail the U-minerals of the Rössing deposit borehole composites, highlighting the presence of the refractory phase betafite.

The Rössing Mine and its surrounds are well-documented examples (Cuney, 1980b; Herd, 1996; and Nex et al. 2001a) where primary uranium mineralogy contrasts dramatically on a local scale. Although the dominant uranium species in the Rössing pit is uraninite, in the nearby SH area, 90% of the uranium is carried by the Nb-Ti pyrochlore, betafite (Kinnaird and Nex, 2007) These betafite-dominated sheets in the SH are believed to be resultant of the influence of the antiformal fold structure and local chemistry of the Rössing Formation on the magma and associated fluids (after Cuney, 1980b; Herd, 1996; Nex et al., 2002; and Nex et al., 2003). Abraham (2008) showed that granite sheets that have intruded the Khan Formation at the nearby SK area also contain high proportions of betafite.

The mineral properties of betafite are described in detail in Hogarth (1977) and its occurrences in carbonatites in Hogarth (1989). Descriptions and detailed studies of betafite in the Rössing area are given in Herd (1996) and Nex *et al.* (2003).

Fluid inclusion studies by Cuney (1980a, 1980b) indicated that a difference in fluid compositions in the granites may have been responsible for contrasting primary phases. This difference in fluid composition is attributed to the presence of a Na-rich evaporite layer in an antiformal structure, contributing to high $CO_2$ and thus promoting pyrochlore or betafite over uraninite. Fluid extraction studies by Nex *et al.* (2002) performed on quartz in the granites at Rössing and pyrochlore mineralogy studies (Nex *et al.,* 2003) included bulk fluid extractions, which also found contrasts in the fluid compositions of betafite- and uraninite-bearing granites.

The significance of betafite occurrence is also emphasised in quantitative mineralogical analysis of betaphite and pyrochlore from the SH area by Nex *et al.* (2003) and in semi-quantitative mineralogical analysis of the SK deposit by Abraham (2009). These studies show that betafite at Rössing may hold in excess of 30 wt. % U (higher than the 26 wt. % and 27 wt. % $UO_3$ given by Hogarth, 1961, and Mazzi and Munno, 1983). Essentially the physio-

chemical controls of the contorted, heterogeneous Rössing Formation lithologies (Figure 3.13c) has prevented $U^{6+}$ from reducing and crystallising in uraninite, and instead it has been incorporated into complex Nb-Ta-Ti-Fe-Ca phases such as betafite, and to a lesser extent brannerite.

### *Rössing Summary*

Mineralisation at the Rössing deposit resulted from a number of controls; however, partial melting in the source is regarded as the most important means of concentrating incompatible elements and of transporting uranium metal as outlined by Robb (2005) for the Central Zone. Late magmatic fluid percolation and supergene enrichment has contributed significantly to the economic viability of the mine (Jacob, 1986 and Berning, 1986).

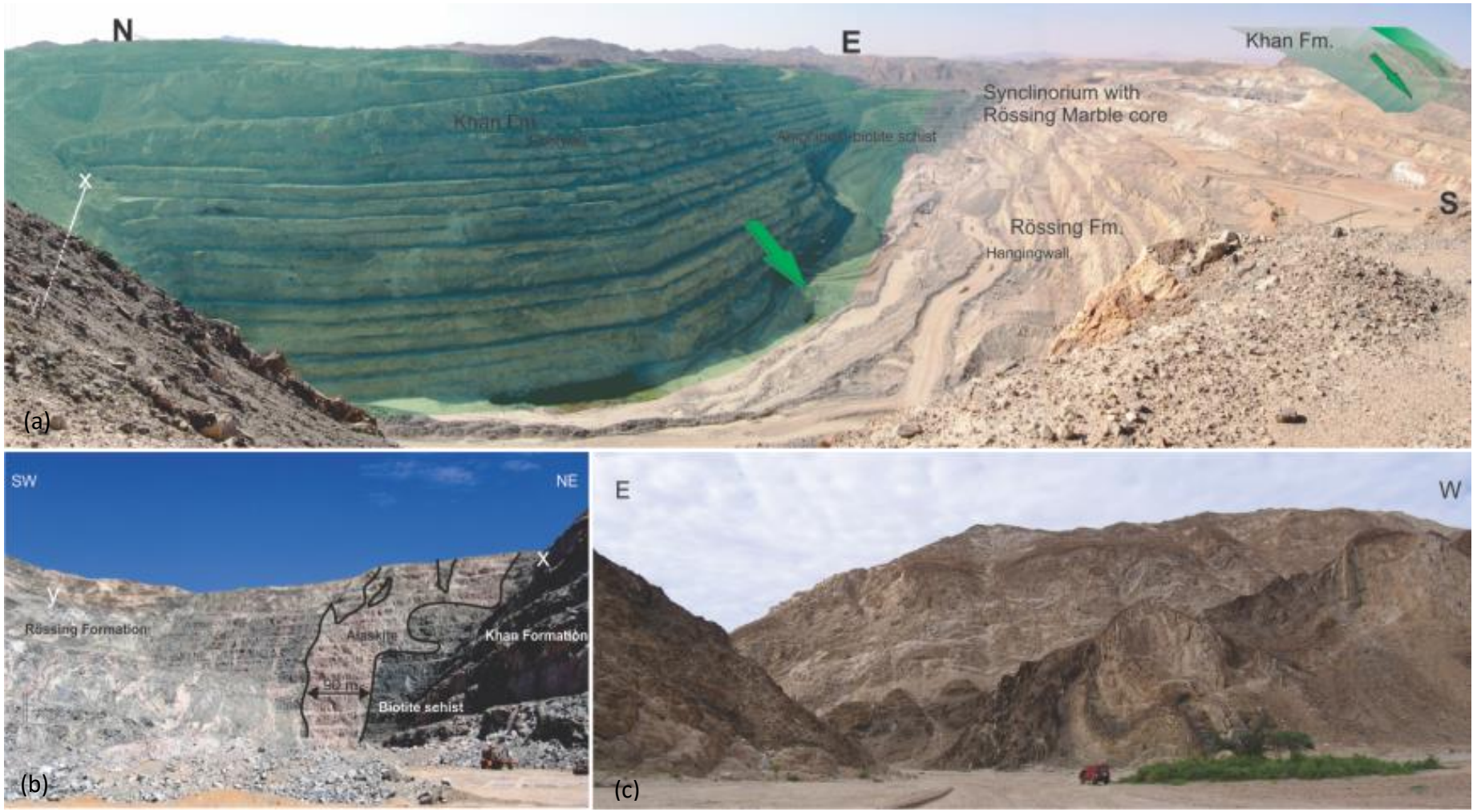



Figure 3.13 Features of the Rössing Uranium Mine. (a) Ninety-metre wide dyke of coalesced SLG's in Khan Formation on the western wall of the Rössing open pit. Rafts of Khan Formation gneiss engulfed in mineralised SLG's are highlighted in green and the alaskite is highlighted in pink. The X-Y section corresponds to the high wall photo in Figure 2.5b. (b) The open pit looking east is >3 km long and >1 km wide. The Rössing marble-dominated south wall is cut back at a lower angle than the north wall for stability. The north wall consists of Khan Formation gneisses and schists where most of the SLG's have intruded the brittle structures (cleavage planes). (c) The Panner Gorge outcrop of Rössing Formation, looking southeast. The Rössing succession is folded in the foreground and measures ~70m in thickness. It is bound by Khan Formation diopside gneiss of the Nosib Group at the base and succeeded by Chuos Formation schist above. The thick succession of marble in the background is Karibib Formation on the western limb of the Khan Syncline.

## 3.6 Goanikontes area

### *Introduction*

The Goanikontes deposits are located 30 km east of the coastal town of Swakopmund, and about 40 km south of the Rössing Mine[13]. Historical prospecting was undertaken between 1976 and 1978 by Elf Aquitaine South West Africa, in a joint venture with B & O Minerals named Omitara Mines. From 1976 to 1978 Omitara Mines drilled 224, mostly vertical, percussion drill holes totalling 13 383 m on a reconnaissance grid of 400 m north by 75 m to 100 m east along the western edge of Palmenhorst Dome[14]. In addition, nine diamond drill holes were drilled for a total of 2 100 m. The programme included airborne radiometric and magnetometer surveys and 6.8 km of excavation channels to expose alaskites beneath the Namib peneplain (Mouillac *et al.,* 1986).

As at other deposits in Namibia, exploration activity was spurred on by the elevated uranium price and encouraging mining activity at the newly opened Rössing Mine. Western Mining (Ltd.) undertook exploration along the Swakop River from 1982 to 1986 on what was then their 'Swakop Project'. The program included 22 percussion drill holes totalling 1 017 m and regional scintillometer surveys[15]. A resource was estimated in 1986 but no further activity took place. Barbour (1980) and Barbour (1983) record the exploration activities on the nearby licences M46/3/600 east of the Goanikontes Dome along the Swakop River from 1977 to 1983. Fifteen significant anomalies were identified over a 37-km strike-continuous anomaly during the 1970 to 1986 exploration period[16]. Figure 3.14 illustrates the location of the Etango project of Bannerman Resources at Goanikontes.

[13] Figure 2.1 and Appendix B give the localities of all the deposits in this study

[14] Kisters refers to the Palmenhorst - Goanikontes Dome complex as the Khan Dome, which extends north to where Damara sediments converge in the Blauer Heinrich - Khan and Welwitschia Syncline complex south of the Rössing Mine, pers. comm., 2013.

[15] Unpublished reports by Barbour (1980) and Barbour (1983) of activities on Prospecting Grant M46/3/600 which covers ground within Bannerman Resources EPL3345

[16] www.bannermanresources.com

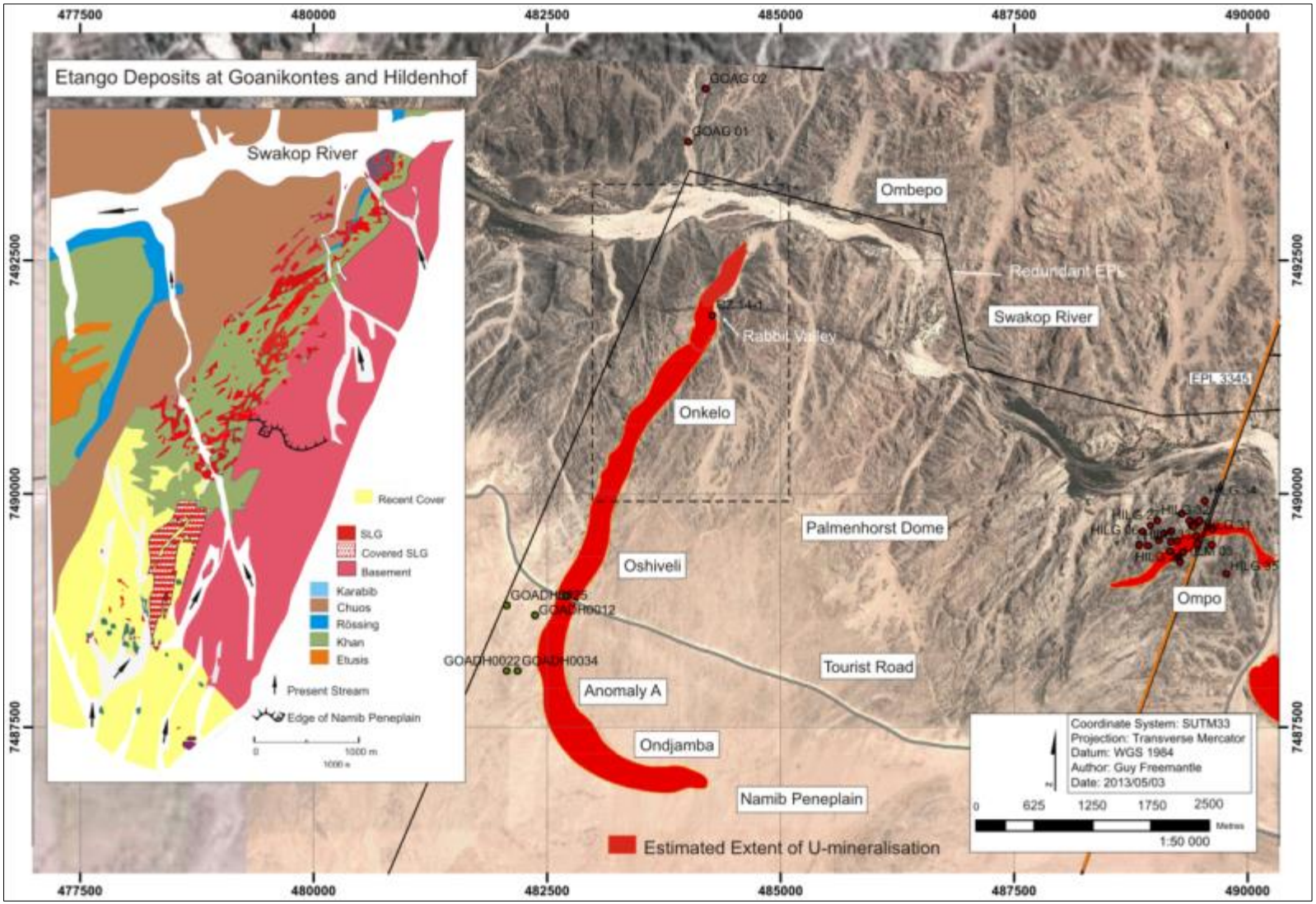



Figure 3.14 The geology of the Goanikontes area west of the Goanikontes Dome. The map shows the sheeted leucogranites predominantly intruding the Khan and Chuos Formations, Bannerman Mining Resources' Etango Project 'Anomaly A' (from Nex, 1997 modified after Mouillac *et al.,* 1986 and Marlow, 1983, colour-altered Quickbird® image after Google Earth®).

The prospecting rights around the original 15 anomalies, including the Goanikontes Deposits, were acquired by Bannerman Resources of Australia in 2006. The anomalies occur within the southern portion of exclusive prospecting licence EPL 3345. Bannerman subsequently renamed Goanikontes the 'Etango Project' in respect of the local nomenclature for the area. An intensive drilling programme began shortly after the licence was granted and the surrounding U-anomalies are now collectively referred to as the Rössingberg Anomalies, six of which, Anomaly A, Oshiveli, Ompo, Ondjamba, Onkelo, and Ombepo are renamed from historical targets of the 1970 to 1986 exploration programmes.

The basic layout of the Etango deposit and the estimated extents of mineralisation are presented on the map in Figure 3.14. The 2009 Indicated Resource estimate was calculated from all suitable historic drill data and from 527 RC and 64 diamond holes, totalling 165 311 m, to maximum depths of 480 m to 520 m for RC and NQ core holes respectively (after Lindskog and Inwood, 2009). The Indicated estimate is calculated from conventional 50 m x 50 m grid spacing. A further 1 600 m was drilled in 40 holes and the revised Indicated Resources for the 2009 National Instrument 43-101 report was a total of 146.2 Mt containing 75.4 Mlbs $U_3O_8$ (>30 000 tU) at 234 ppm $U_3O_8$. A Definitive Feasibility Study concluded a Measured and Indicated Resource of 149 Mlbs $U_3O_8$ with an additional 64 Mlbs of $U_3O_8$ Inferred Resources at the Etango Deposits, excluding Ompo. In 2012 Bannerman presented the feasibility study of an open pit operation with heap leach processing facilities. The anticipated mining operation would include a 16-year mine life, producing between 6- and 9 Mlbs $U_3O_8$ per year[17].

### *Stratigraphy*

The Etango deposits lie on both sides of the Swakop River, most of which lie on, or near, Farm Goanikontes. Mouillac *et al.* (1986) first described the area in detail and noted that augen gneiss, which is typical of the pre-Damaran Basement, is unusually absent from the Goanikontes Dome and also that the cover sequence is comprised solely of Khan, and Chuos Formations. Detailed mapping by Nex and Kinnaird (1995) and Nex (1997) have shown that

[17] Bannerman Resources Annual General Meeting Presentation. www.bannermanresources.com, November 2012. Note that there is some rounding of the figures.

the cover succession of the area, actually comprises Etusis, Khan, Rossing, and Chuos Formation metasediments and that these are in tectonic contact with older pre-Damaran basement, with only intermittent and attenuated portions of the Rössing Formation in outcrop (Nex, 1995). Longridge (2012) showed that the Khan Inlier comprises significantly less Abbabis type rocks than originally mapped, which would, in part, explain the lack of augen gneiss observed in prior studies. The Etusis and Rössing Formations are attenuated and mostly absent on surface north of the river (Figure 3.15a). South of the River the Damara lithologies wrap around the southern lobe of the inlier, the Palmenhorst Dome, and the Damaran Formations are thicker than along the dome margin.

### *Magmatism*

A high-strain zone was preferentially exploited by leucogranites. The Goanikontes area leucogranites take on an en-echelon pattern of emplacement in relationship to the NNE-SSW basement – meta-sediment contact and strain is approximately parallel to the contact.,as is well documented in Nex and Kinnaird (1995) and Nex (1997).

Intrusions in the area are numerous, and these have been categorised into early intrusions and sheeted leucogranites. The following description is taken from Nex (1997): -

> *"Granitoid intrusions are extremely well exposed in the area, and these are dominated by leucogranite sheets which intrude both basement and Damaran metasediments. Red and Grey granite emplacement was followed by these* sheeted leucogranite *intrusions which were preferentially located within the high-strain zone."*

The area on and around Farm Goanikontes is the type locality for the classification of the six leucogranite sheet types by Nex and Kinnaird (1995) as shown in Table 3.2 The SLG sequence at GoanikontesTable 3.2. The classification scheme divides the six sheet types into roughly two groups; three types that intruded before at least one major deformation event ($D_3$) and those that intrude post-event, the mineralisation occurs in SLG's that post-date the $D_3$ event (after Nex, 1997).

The intrusions only occasionally crosscut the Abbabis gneisses and there are fewer granitic intrusions on surface south of the Khan River because of the poor outcrop on the Namib peneplain. The high-grade Onkelo anomaly (formally Rabbit Valley, Nex, 1997) is an exception and occurs on the southern bank and has excellent exposures of the E-type granites described by Nex (2007) as well as earlier non-uraniferous sheets intruding the Khan and Chuos Formations in the high - strain zone (Figure 3.15a and b).

Table 3.2 The SLG sequence at Goanikontes consists of six types, the oldest is the A-type and the D and E-types are U-mineralised. Counts by hand held scintillometer on surface are in the first column; with maxima in parenthesis. Width refers to the average width of the leucogranite sills and dykes. Data from Nex *et al.* (2001a).

| **Type (cps)** | **Width (m)** | **Diagnostic Structural Features** | **Diagnostic Mineralogical Features** |
|---|---|---|---|
| A<br>< 20 | < 0.75 | Infrequent occurrence, irregular form, weak foliation, boudinaged and folded by $D_3$, only occurs within the high - strain zone. | Pale pink, fine-medium grain size, homogeneous saccharoidal texture, and weak foliation. |
| B<br><20 | 1 - 4 | Common outside the high - strain zone, fine-grained weakly-foliated sheets, frequently boudinage and occasionally folded by $D_3$. | White, fine to pegmatitic, typically garnet-bearing, infrequent abundant biotite and tourmaline. |
| C<br>10-20<br>(200) | 0.5 - 10 | Most frequent type of sheet within the typical cover sequence, occasionally boudinaged, occurs in $F_3$ fold flexures. | Pale pink-cream, medium-pegmatitic grain size, hypersolvus with interstitial clear quartz, magnetite, ilmenite and tourmaline. |
| D<br>100<br>(400) | 1 - 7 | Irregular and anastomosing, restricted to the high - strain zone and the Khan-Rössing boundary. | White, medium-coarse grain size, granular texture, white feldspar with characteristic smoky quartz, frequently visible beta-uranophane and occasional betafite. |
| E<br>30<br>(300) | 1 - 10 | The dominant type of SLG within the high - strain zone. Generally tabular, occasionally bifurcating generally emplaced parallel to the prominent gneissosity. | Extremely variable colour and grain size, contains "oxidation haloes" (Corner and Henthorn, 1978). |
| F<br>< 20 | 0.5 - 3 | Tabular with straight parallel sides, occurring throughout the area, crosscuts all structural features. | Distinctive red colour, coarse-pegmatitic grain size, pink perthitic feldspar and milky-coloured quartz. |

### *Mineralisation*

Regionally, the ore deposits are situated on the west and southwestern sides of the Goanikontes Dome; a lobe of the larger, complex Khan Inlier that is cut east to west by the Swakop River and Figure 3.6 illustrates the extent of mineralisation around the lobe. Elevated U grades predominate where SLG's intrude the Khan-, Rössing-, and Chuos Formations, with a noticeable drop in grade where sheets intrude Etusis and basement gneisses (Bannerman Resources, personal communication, 2009). Mouillac *et al.,* (1986) published data on the deposit and highlighted that, despite the lack of significant Rössing

lithologies, mineralisation still occurs at the top of the Khan and in the lower Chuos Formations.

The timing of primary mineralisation of the SLG's and their emplacement are indistinguishable, both occurred between 509 Ma and 508 Ma ago, according to U-Pb geochronology studies by Briqueu *et al.,* (1980). This remains the definitive age at Goanikontes, and is comparable to the 506.1 ± 8.1 Ma age at Valencia (Longridge *et al.*, 2009). It is considerably younger than the 542 ± 33 Ma Rb-Sr age for the Ida Dome 'alaskite' but older than the 496±4.1 Ma (Cross *et al.*, 2009) and 458±8 ages (Marlow, 1983) for the Husab and Rössing alaskites, respectively.

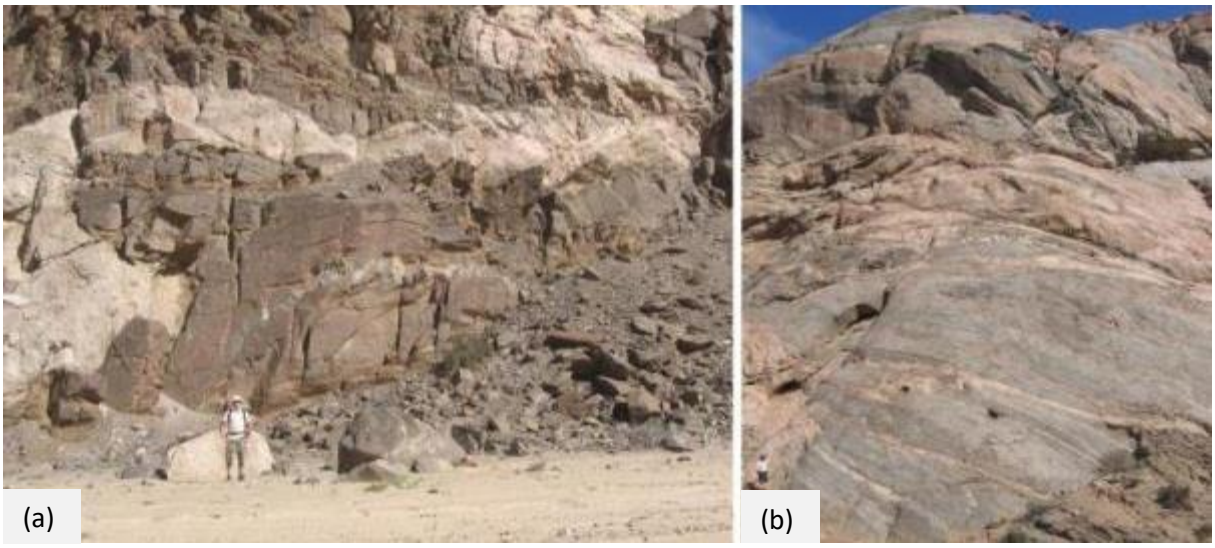



Figure 3.15 Leucogranite sheets of the Goanikontes area. (a) Pre $D_3$ folded SLG intruding the Chuos Formation north of the Swakop River. (b) E-type SLG's intruding the Khan Formation at the Onkelo section of the Etango deposits, south bank of the Swakop River, looking west.

## 3.7 Hildenhof

### *Introduction*

The Hildenhof Anomaly is situated on Farm Hildenhof, southeast of the Khan and Swakop River confluence. It is hosted within an antiformal structure between lobes of the regional Khan Inlier; essentially it is located on the eastern edge of the same lobe as Etango. Leucogranite sheets have intruded parallel to steep north-verging $D_2$ structures, along

bedding and cleavage planes (after Longridge *et al.*, 2009). Mineralisation extends discontinuously away from the antiform along a stratigraphic boundary (Khan – Rössing) to the east onto EPL 3138 of Swakop Uranium and to the west-southwest toward the Etango deposits. This zone has a roughly east-west strike, over ~5 km, and is less than 250 m wide.

### *Stratigraphy*

The Khan, Rössing, and Chuos Formations are the main stratigraphic units present at Hildenhof, with minor Etusis units in the vicinity. The Khan Formation includes banded diopside gneiss, typical of most deposits in the region. The Rössing Formation comprises at least two packages of attenuated marble and calcsilicates. A quartzite unit, with minor sulphides, occurs near the contact with the Chuos Formation, which is relatively thin in comparison to the sequence on the western side of the Khan Dome at Goanikontes. Second order folding attenuates sediments at the limbs and duplicates the ductile Rössing marbles, with vergence towards the main body of the Khan Dome in the north (Figure 3.16a). Boudins and brittle-ductile contrasts in diopside Khan Formation units (Figure 3.16b) reflect attenuation parallel to the strike of the $D_3$-antiform limbs.

### *Structural Setting and Associated Magmatism at Hildenhof*

The area is characterised by a large north-westward-verging $D_3$ antiform (Longridge *et al.*, 2009) with a distinct, stratigraphically-bound mineralised zones trending parallel to the contact between the Khan and Rössing Formations. The antiform has an open structure and a ~N-S axial trace, and on surface the limbs wrap eastward and westward around the two lobes of the Dome Structure. The upright $D_3$ synform between the antiformal lobes of the Khan Inlier infact, refolds the tight-folded north-verging $D_2$. The refolding resulted in a repeated sequence of the distinctive Khan Formation banded diopside gneiss (Longridge, 2012). Strain directions are parallel to $S_1/S_0$ which varies from NNE-SSW in the west to NW-SE in the east (on either limb of the main antiform). There is localised repetition of the Rössing Formation in the carbonate units, which have formed abundant second-order folds within the main structure (Figure 3.16c). The calcsilicate units in the Rössing Formation are

competent relative to the marbles and the pelitic sediments, and have developed brittle dilation features (Figure 3.16d).




Figure 3.16 Stratigraphic and structural features of the Hildenhof area. (a) Tight folding within ductile carbonates of the Rössing Formation. (b) Brittle and ductile deformation in Khan Formation diopside gneiss. c) North verging secondary folds in Rössing Formation marble, with bedding parallel SLG. A SLG has also intruded along the axial plane of the antiform. (d) SLG intruding between the Rössing (lower) and Chuos Formations (upper). Note the SLG sheet is at an oblique angle to the dilatational features in the Rössing calcsilicate. Locations: (a) and (c) 489331E 7489434N and (b) and (d) 488824E 7489479N.

Figure 3.17a is viewed east across the Khan-Rössing-Chuos succession that comprises the main antiform. The structure has a core of Chuos diamictite and a mirrored succession of Rössing marbles and calcsilicates, and banded diopside gneisses of the upper Khan Formation on the north and south limbs. Local-scale folds tend to verge northward parallel to the thrust direction (Figure 3.17b). Local scale thrusts shear-out the second order antiforms and synform structures in the ductile carbonate sequences. The sheet of uraniferous leucogranite in Figure 3.17c is at least 3 to 5 m thick and broad in horizontal extent.

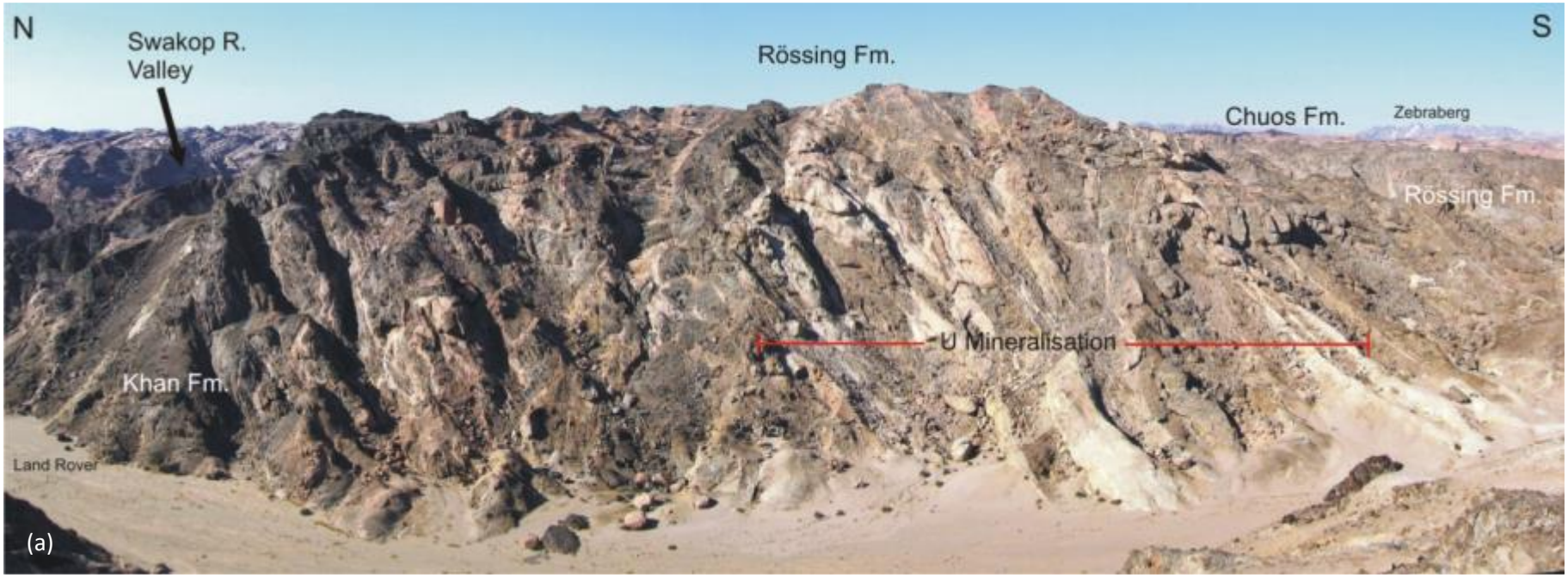






Figure 3.17 Features of the Hildenhof Deposit Alaskites and metasediments. (a) The Hildenhof area looking east and folded Rössing Formation to the south of the anomaly. In the background are the Zebraberge of the Ida Dome. The Khan diopside gneiss verges to the north as does the Rössing Formation. (b) The north verging D2 folding has resulted in a repeated sequence of Rössing marble which outcrops to the south of the mineralised zone. Note the sheared-out synform at right. (c) Thick, bedding-parallel alaskite sheet with ghost bedding forming bands of mafic minerals.



*Magmatism*

Th-rich red granites occur in the vicinity, preceding at least two of the three generations (types-1, 2 and 3) of equigranular Grey granite. The Red granite contains fibrolite, alluding to its anatectic, S-type, generation. The Grey granites vary in mafic content, from a biotite-rich quartz-diorite through to leucocratic monzogranite, syenogranite, and alkali-feldspar granite. Dilation structures have developed syn-deformational melts with the growth of Ca-pyroxene both in the Khan and Rössing Formations. Sheeted leucogranites have intruded at the contacts between calcsilicates and less competent lithologies, such as the Chuos Formation discordance with the Rössing Formation. Leucogranites and mineralised alaskites also tend to intrude structures that crosscut bedding, such as axial planes, shear bands and dilation features.

Bedding parallel sheets (predominantly sills) and some crosscutting dykes intrude into calcareous Khan Formation metasediments and thin repeated sequences of tightly folded Rössing Formation marbles, quartzites, and gneisses (Chapter 2.2). There does not appear to be a $D_3$ overprint on the U - deficient sheets. Mineralised sheets focus at the Khan- contact with minor occurrences in the upper Khan and lower Chuos Formations. C-type and minor A-type sheets intrude in the Khan and Etusis Formations north of the mineralised zone and in the Chuos Formation to the south.

The sheeted leucogranite suite within the Hildenhof area is not as varied as the suites described at Goanikontes, the Ida Dome area and Valencia. A-types are scarce and limited in size, and garnetiferous B-types or E-types with oxidation halos are absent. Types- C, -D and oxidised mineralised sheeted leucogranites (analogous to the E-type) are the most abundant, however, crosscutting relationships between the barren and mineralised sheets are rare, because of intrusion of the granites into pre-existing $D_2$ structures.

***Mineralisation***

The majority of sheets have intruded the relatively brittle Khan and Chuos Formations, and wollastonite-diopside-scapolite skarn pods have developed where they are in contact with

Rössing Fm. marbles and calcsilicates. Mineralisation tends to be more prevalent within the Rössing Formation but may occur to a limited extent in the Khan Formation (Figure 3.18)[18].

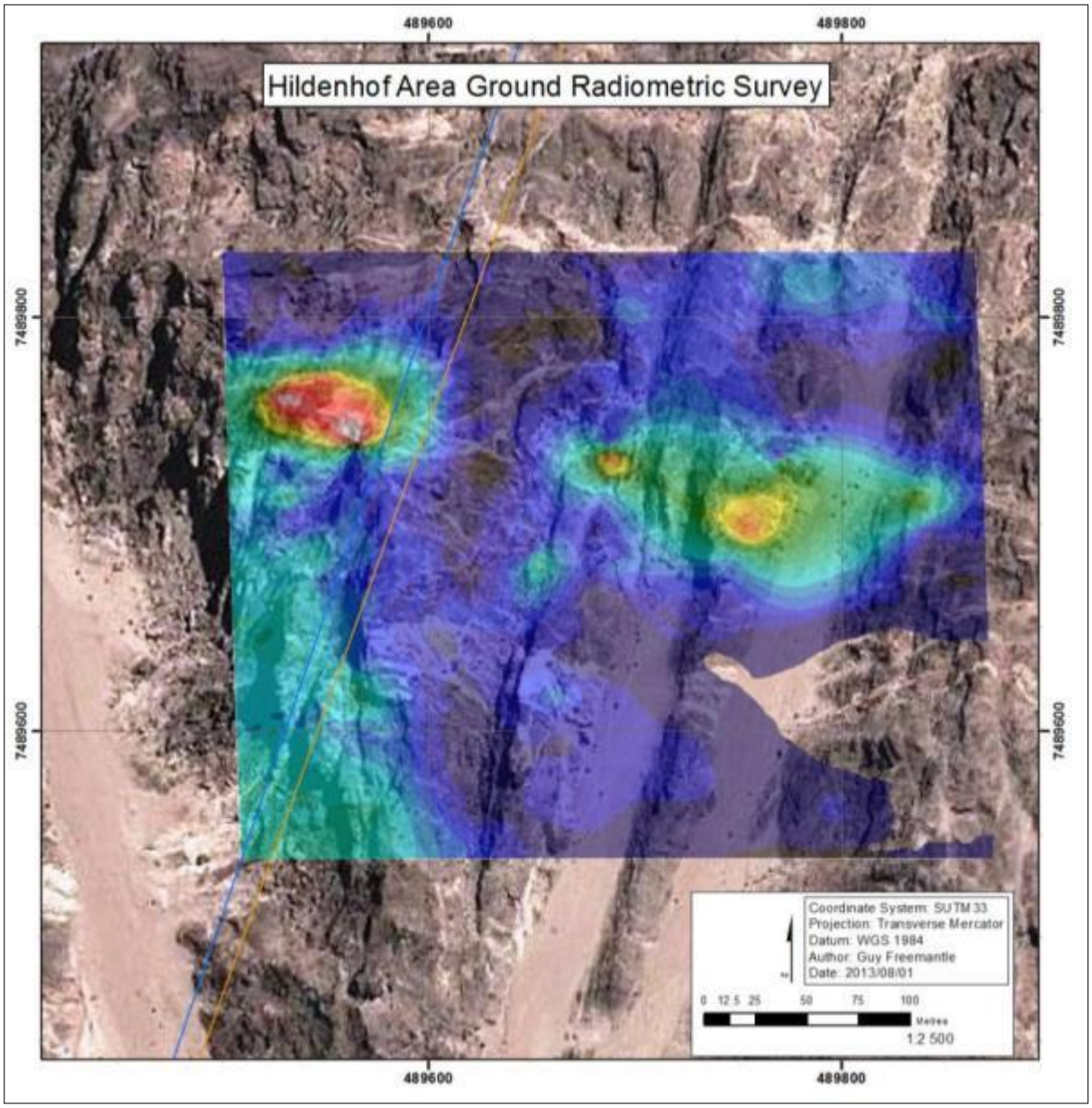



Figure 3.18 The Hildenhof Anomaly ground radiometric survey. The deposit is situated in an antiform adjacent to the southeast of the Goanikontes Dome. The bedding parallel mineralised sheets are confined to an east-west zone 100 m to 200 m wide. (Quickbird™ image from Google Earth™). Count readings taken at relatively constant waist-height of 1 m. Device: THERMO RadEye personal radiation detector.

[18] The ground radiometric diagram was produced by synchronising a RADeye™ scintillometer and a Garmin Etrex CS™ GPS receiver. Detailed method description is in Appendix C1 and data are in Appendix C2

## 3.8 The Ida Dome Deposits

### *Introduction*

The Ida Dome is a prominent geological feature in the Namib Desert. It is ovoid in shape with the long axis trending roughly north-northeast and roughly bisected east to west by the Swakop River Valley. There are three main deposit areas in the vicinity of the Ida Dome structure: Garnet Valley and Ida Central along the eastern flank of the dome, south and north of the river, respectively; and the Holland's Dome deposit in an antiform adjacent to a sheared synform immediately east of the Ida Dome (Figure 3.19). The Ida Dome deposits presently occur on two of Swakop Uranium's exclusive prospecting licence areas, EPLs- 3138 and 3439, situated 52 km east of the resort town of Swakopmund. The dome comprises Abbabis augen and banded gneiss, with rafts of pre-Abbabis amphibolite (after Longridge, 2013). It is intruded by at least three successively felsic biotite-granites (Grey granites) and swarms of leucogranite, which give the false-appearance of a leucogranite-cored dome from the air. The Dome is flanked by a thick, folded succession of Khan diopside gneiss. A thin sliver of Etusis quartzites along the western flank, is in contrast to the eastern side which is bound by a thick succession of Khan Fm. Gneiss and Rössing Fm. marbles, quartzites and garnet-biotite gneiss. The uranium deposits at the Ida Dome were first described in the late 1950's when the Tsumeb Corporation undertook a re-investigation of the copper potential of the old Ida Mine. During this survey uranium mineralisation was noted in the country rocks surrounding alaskitic intrusives and the radioactive minerals schröckingerite[19] and gummite were subsequently reported (from Söhnge, 2001). During 1975, the Anglo American Corporation, operating as Swakop Exploration (PTY) Limited, had an active uranium exploration programme in the Husab Area[20] immediately north of the Ida Dome. At the same time, the Trekkopje Mining and Exploration Company, a subsidiary of Gold Fields South Africa, undertook exploration at the area known as Holland's Dome and Garnet Valley and Ida Central anomalies.

[19] $NaCa_3(UO_2)(SO_4)(CO_3)_3F.10H_2O$

[20] GSN-2, Communication between Swakop Exploration (PTY) Ltd and Trekkopje Mining and Exploration Company, 1975.

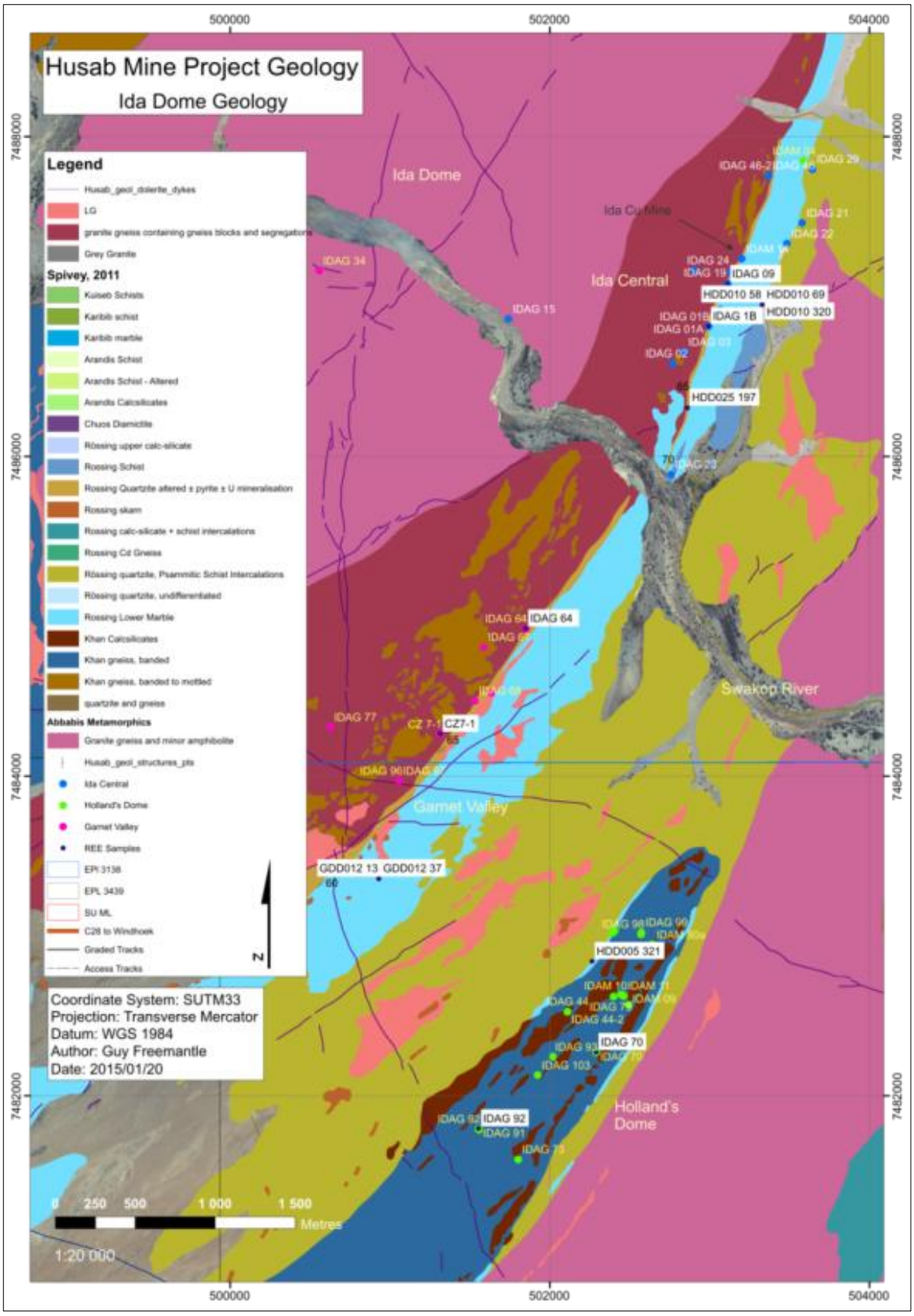



Figure 3.19 The Ida Dome deposits. The exploration area consists of two EPL's, 3138 and 3439, which combined cover an area of ~630 km2. The Ida Dome deposits span the boundary between the two EPL's, Holland's Dome is on 3439 and Ida Central lies on 3138. Geological map reproduced after Spivey (2012). The ground survey radiometric map area at Ida Central is enlarged in Figure 3.26.

The Garnet Valley and Ida Central deposits occur along the eastern flank of the Dome, in the same stratigraphic packages of Khan and Rössing Formation gneiss and schist. The Holland's Dome deposit occupies a tight, upright antiform with a shallow northeast axial plunge, separated from the south-eastern flank of the Ida Dome by an isoclinal-fold package of Rössing marble.

Core samples from Garnet Valley and from Ida Central were sampled specifically for REE analyses. Holland's Dome and Garnet Valley extend into the neighbouring licence area of Reptile Uranium Namibia, directly south of the Dome. The Garnet Valley and Holland's Dome areas are under reinvestigation by Swakop Uranium as of 2012, following on from the results highlighted by intensive exploration undertaken by the Company during 2006 to 2009.

### *Stratigraphic - Structural Setting at the Ida Dome*

Sawyer (1978) and Barnes (1981) mapped the Dome with an Abbabis gneiss core on Map Sheet 2214 – Walvis Bay. Smith (1965) had interpreted the structures to be the result of interference folding caused by $D_2$ and $D_3$ events, which were re-interpreted by Barnes (1981) and Longridge (2012) who refined the interference folding geometries.

The structural geology of the basement, amphibolite, and unconformable cover sequence is described in Barnes (1981); Longridge *et al.* (2009); Longridge (2012); and Longridge *et al.* (2014). It is intruded by at least three successively felsic biotite granites and swarms of leucogranite, which give the false-appearance of a leucogranite-cored dome from the air.

From east to west, steeply east-dipping Khan- and Rössing Formation rocks flank the Ida Dome, including a thick carbonate package at the base of the Rössing; the core of the dome is exposed to Abbabis gneiss level and the western flank is dominated by a tightly folded Khan Formation gneiss and Etusis meta-quartzite. The tightly folded sequence on the western flank is the adjoining synform to the dome antiform and forms the prominent Zebraberge Syncline ridge (Figure 3.20). Local structural features at Garnet Valley – Ida Central and Holland's Dome are described in the sections that follow.




Figure 3.20 The Zebraberge syncline structure, looking northwest from the southern end of the Ida Dome.Two-feldspar pink sheeted leucogranites intrude a thick, folded package of Khan Formation metasediments at the Ida Dome west flank. The Zebraberge has formed along the southwest edge of the Ida Dome. A regional-scale outcrop of Abbabis Metamorphic Complex (Abbabis Com.) granite-gneiss, which dominates the Khan Inlier, borders the west side of the Zebraberge. The westerly dip of the Khan Formation on the western edge of the dome is in the foreground. The photograph was taken looking west-northwest from the southern end of the Ida Dome. Position: 500382E 7484668N.

### *Ida Dome Intrusives*

The Basement gneisses, Nosib- and lower Swakop Group sediments are invaded by leucogranite sheets, which in the Khan Formation display a strong tendency to stack sub-horizontally, at high angles (usually) to the steeply east-dipping bedding/schistocity. Subordinate granite sheets crosscut the dominant gneissic fabric in what appear to be local-scale shear displacements, often linking between the larger leucogranite dykes (Figure 3.21 illustrates the large sub horizontal sheets invading sub-vertical metasediments). A detailed account of the sheeted leucogranite volume and orientations and their relationships to the $S_0/S_1$ orientations of the metasediments, as well as the relationship between melt volume and proximity to the basement contact is given in Toch (2013).

There are three biotite-bearing granites that intrude the basement and Nosib Group rocks; each successively more felsic. The intermediate generation is most distinguishable by a porphyritic texture and often entrains xenoliths of the more mafic first generation. These fit into the leucogranite suite of Miller (2008) and Longridge (2012). The oldest is a quartz diorite and the youngest is a fine-grained quartz diorite with distinctively less mafic minerals

than the older generation. The suite has a overall homogenous texture, with a fabric highlighted by ≥5 % biotite in hand specimen. These granites tend to be constrained within the gneissic units of the Basement and Khan Formations, but they do also occur as xenoliths in larger leucogranite masses that transgress Nosib- into the lower Swakop Group metasediments at Holland's Dome.



Figure 3.21 Dykes and sills of sheeted leucogranite pervading Khan metasediments. The locality is on the eastern portion of the Ida Dome within ~2 km of the eastern basement contact. Outcrop shows that sheets predominantly intrude at oblique angles to bedding, and occasionally parallel to $S_0$ and $S_1$ (bedding and secondary foliation). Sheets take advantage of outcrop-scale $F_2$ antiform hinges. The thin black dykes are dolerite and intruded during Karoo-aged extension. View is to the north. Position: 502409E 7486134N.

The Basement lithologies, the Damaran metasediments and the early Damaran granites, are all variably invaded by sheeted leucogranites with mineralised varieties confined to the southern and eastern flanks of the Dome where the Rössing Formation is best represented. The barren sheeted leucogranites are predominantly magnetite-bearing or relatively accessory-free, axial planar-parallel dykes at high angles to bedding, or sub - vertical sills which appear to be the main granite pathways. Tourmaline-bearing varieties intrude Swakop Group metasediments to the east of the Holland's Dome- and Ida Central Deposits. The Central and Garnet Valley sheeted leucogranites intrude below a Rössing marble

hanging wall with localised skarn associated with the contact metamorphism. At least two mineralised varieties dominate the Ida Dome- the typical D-type and the oxidised variety described as E-type (Nex, 1997) at Goanikontes.

### *Ida Central and Garnet Valley Deposits*

The Ida Central deposit is located about 1 km north of the Swakop River, and extends for at least 3 km along the eastern flank of the Ida Dome. The Khan Formation consists of diopside gneisses and dips sub-vertically to the east and southeast on a ~185° to ~200° strike. Extension along 180° to 220° produced boudins characterised by quartz-feldspar-diopside leucosomes at their necks. Mineralisation occurs along the Khan-Rössing boundary, with granite predominantly intruding the Khan Formation and seldom extending through the marble hanging wall. Sub-vertical, north-south striking faults have created pathways and deposition sites for remobilised uranium, as evidenced by secondary phases are present on joint surfaces and slickenside planes. Old copper workings have exposed oxidised Cu-sulphide mineralisation lending a rust coloration, as is typical of metalliferous units in the Rössing and Khan Formations (Figure 3.22). The Cu workings date back to the 1920's (Söhnge, 2001).



Figure 3.22 View looking west over the Ida Dome from the old Copper Mine. Rust-coloured gneiss and cream-coloured marble of the Rössing Formation are in the foreground. Dark green rafts of the Khan Formation, swamped by flat lying lit-par-lit leucogranite sheets, extend west to the Zebraberge on the centre horizon. Position: 503391E 7487474N.

Garnet Valley is located west of Holland's Dome, and is characterised by differential erosion caused by a Karoo-age dolerite dyke that crosses it at right angles near the head of the valley

(Figure 3.23). The name derived from the abundance of andradite garnet skarns that occur as chocolate-block type boudin arrangements or pods within massive leucogranite bodies along the length of the deposit.




Figure 3.23 View looking south up Garnet Valley, towards a large E-W dolerite dyke. The anomaly is similar to the Ida Central Anomaly in that the mineralisation is predominantly in Khan Formation below a Rössing marble hanging wall (inset). The metasediments dip steeply to the east southeast; thus, the leucogranites in the right of the image are dykes, perpendicular to a sub-vertical strain direction. Position: 501641E 7484535N.

*Ida Central and Garnet Valley Stratigraphy Summary*

The local stratigraphy of the Ida Dome area is very similar to that found at Rössing, with basal Etusis succeeded by Khan-, Rössing- and Chuos Formation lithologies. On either side of the Ida Dome the Damara Supergroup is steeply dipping away from the Dome, though it can be argued that the eastern side is at a slightly shallower angle than the western side as presented in Barnes (1981). The Zebraberge Mountains were also interpreted by Barnes (1981) as a reflection of eastward vergence of the interference fold structures responsible for the formation of the Ida Dome.

The Etusis Formation is not apparent to any extent on the eastern edge of the dome, but represented by a thin quartzite at the base of the Khan Formation. The Khan Formation is relatively thick and steeply dipping along the east and west sides of the dome, with $S_1/S_0$ dips much shallower toward the core of the Dome. It consists of quartzites and pelitic gneisses at the base and diopside gneiss, schist, and calcsilicates close to the Rössing marble contact.

The Rössing Formation forms a steeply east-dipping hanging wall to the Cu and U mineralisation in the upper Khan Formation along the east side of the Ida Dome. It is not present on the west side. It forms prominent ridges of the Geurtel Hills Syncline north of the Zebraberge. There are two attenuated marble packages sandwiching rust-coloured metalliferous gneiss. The sequence is preceded by evaporite lithologies, quartzite and calcsilicates along the eastern edge of the dome (Figure 3.24). The entire lower carbonate package is less than 100 m thick and intensely folded at the Ida Central location; the Chuos Formation is present to the northeast of the dome, but absent from the immediate vicinity of the deposit.



Figure 3.24 Cross-section of the Rössing Formation on the eastern side of the Ida Dome. The Swakop River valley at the eastern edge of the Ida Dome exposes folds in the attenuated Rössing Formation package of marbles, gneiss and calcsilicates. The photograph was taken looking north. Position: 502703E 7485879N.

Garnet Valley is the strike-parallel extension of the Ida Central deposits, and occurs along the southeastern edge of the Ida Dome. Although the Khan Formation is completely invaded by leucogranite, it is estimated that the banded diopside gneiss succession is close to 600 m thick on surface; considering the steep dip, a true thickness of <500 m is realistic. Major

units include banded diopside gneiss, intermittent quartzo-feldspathic units with compositional banding and minor calcsilicate units toward the top of the sequence.

The combined package of marbles and quartzo-feldspathic units is over 1.2 km thick between Garnet Valley and Holland's Dome. The marbles contain serpentine and graphite bearing units. There are essentially two packages, divided by a pelitic schist of at least 50 m thickness. The best exposures are along the Swakop River. The marbles are considerably thicker than the package north of the Swakop River at Ida Central because of folding. This thickening of the marbles at the southeastern edge of the dome is reminiscent of the thickened marbles at the Rossing SJ deposit.

Khan and Rössing Formation lithologies form the respective foot- and hanging walls and the Chuos Formation appears to be missing in the region. The stratigraphic succession of the area consists of:

- A thick footwall of Khan Formation diopside gneiss, striking northeast-southwest and dipping steeply to the southeast, unconformably overlying the Abbabis basement granite-gneiss of the Dome;
- A discontinuous skarn and calcsilicate package ranging from metre-scale pods of garnet to lenses of calcsilicate tens of metres long; and
- A considerably thickened package of Rössing marbles, with repetition due to folding between the Holland's Dome antiform and the Ida Dome.

*Garnet Valley and Ida Central Structure*

Garnet Valley consists of steeply, southeast-dipping Damara sediments, unconformably overlying the Abbabis Complex granite-gneiss of the Ida Dome. Dips are shallower toward the dome and become considerably steeper toward Holland's Dome in the southeast. The Khan Formation at Garnet Valley is sub-vertical, while the tightly refolded Rössing Formation reflects a range of steep bedding orientations. The strike orientation is consistent northeast to southwest, and local dip directions vary between southeast and northwest, revealing the tight folding within the more ductile carbonate units. Repetition of contrasting graphite and serpentine marble units also confirm marble duplication by folding between the southeastern edge of Ida Dome (Garnet Valley) and the Holland's Dome antiform. This

considerably thickened marble package is comparably thicker than the marble sequence at Ida Central and provided a thick impenetrable barrier to the sheeted leucogranite emplacement higher in the stratigraphy. The comparatively brittle Khan Formation has stronger cleavage and bedding consistency than the marbles, which is emphasised by the granite intrusives, as they appear to have pooled below the marbles as a large mass (Figure 3.23) and as sheets, oblique to bedding in the banded gneiss.

*Garnet Valley and Ida Central Intrusives*

There is some contrast in the volume and number of granite sheets intruding the Khan and Rössing Formations between Garnet Valley and Ida Central. The Khan Formation gneiss is overwhelmed by massive sheets of relatively low-grade leucogranites that have intruded at high angles to bedding with numerous crosscutting sheets, some sub-parallel to $S_1$ foliations. The granite sheets in the Khan Formation are light pink in colour and show localised U-mineralisation around gneiss and calcsilicate/skarn xenoliths.

*C-type SLGs*

Magnetite Variety

The magnetite type of sheeted leucogranite dominates the Khan Formation, and is particularly abundant in the upper units, near the contact with the Rössing Formation. Patches of D-type, U-mineralised, leucogranite occur throughout the largest C-type outcrops, particularly within the vicinity of exposed calcareous host rocks. These C-type and D-type mixes of sheeted leucogranite blur the distinction between pre D3 and post D3 timing that separates the barren from mineralised types at Goanikontes. Magnetite spots in some C-types show elevated scintillometer cps at Holland's Dome and near the marble contacts at Ida Central and Garnet Valley.

Tourmaline Variety

Large sheets of tourmaline-bearing sheeted leucogranite occur at the eastern edge of the Ida Dome, near Ida Central and to the east of Holland's Dome. They intrude the pelitic units

of the Khan Formation, the Rössing Formation gneiss and calcsilicates and the diamictite of the Chuos Formation. The largest sheets may have a combination of massive and euhedral tourmaline. Examples of typical C-type sheeted leucogranites in the field are shown in Figure 3.25a toFigure 3.25c, with Figure 3.25(d) illustrating euhedral tourmaline.




Figure 3.25 Field-scale examples of C-type sheeted leucogranite varieties in the Ida Dome area. (a) C-type sheet exposed at the Ida Cu Mine. The parallel fracture planes may be related to faulting, which is evident in slickenside surfaces in most of the exposed historical workings along the eastern edge of the Dome. (b) Narrow, bedding-parallel $C_m$-type sheets intrude the Khan Formation gneisses, with the typical pink and white feldspar assemblage, accessory magnetite and low quartz content. (c) A large tourmaline-bearing sheet with a massive tourmaline cluster (circled) intruding the Chuos Formation to the east of Holland's Dome. (d) Tourmaline occurs as stringers and clusters of euhedral individual crystals, intruding the Khan Formation near the contact on the eastern edge of the Holland's Dome antiform.

*D-type and E-type SLGs*

The majority of the uranium-mineralised granite sheets occur as coalesced masses beneath the marbles; these sheets have overwhelmed the country rock (gneiss, calcsilicate and skarn) and surface exposures are dominated by un-rotated blocks of diopside gneiss. The sheets also display the prominent oxidation halos described for the Ida Dome area in Corner

(1982) and at Goanikontes in Nex (1997). Drilling results reported by Swakop Uranium show a strong tendency for mineralisation to follow the dip of the sediment package beneath the marbles at depth.

Granite ages have been shown to overlap within error to such an extent that the relative timing of mineralised and barren leucogranites are indistinguishable in the field. Previous dates of mineralisation by Marlow (1983) appear to be too old when compared to the latest available data. The Ida Dome alaskites were assigned a whole-rock age of 542 ± 33 Ma (initial $^{87}Sr/^{86}Sr$ = 0.724 ± 2 – Marlow, 1983). More recently, Longridge *et al.* (2011) give ages for pre mineralisation granites of:

- Garnet-bearing leucogranite- 520.3 ± 4.6 Ma (zircons) and 514.1 ± 3.1 Ma (monazite);
- Early melanocratic Grey granite- 520.4 ± 4.2 (zircon) to leucocratic biotite granite 519.1 ± 4.2 (zircon) ages for pre-leucogranite diorite and monzogranite respectively; and
- Pegmatites believed to be post mineralisation of 515 ± 10 (zircon).

The pegmatite is described as an F type in the classification scheme of Nex (1997) and with the error of ~10 Ma the age overlaps the Goanikontes uraniferous leucogranite age of 508 ± 2 Ma of Briqueu et al. (1980) and the 506.1 ±10 Ma age at Valencia in Longridge (2012).

*Garnet Valley and Ida Dome Mineralisation*

Copper-bearing Khan Formation gneiss packages occur along most of the strike length of the northern 2/3 of the east flank of the Ida Dome. The copper was exploited at the Ida Cu-Mine (Figure 3.26) during the 20$^{th}$ Century, and is associated with some variably uraniferous leucogranites. The abandoned mine occurs below the transitional contact between the upper Khan Formation and the lower marble package of the Rössing Formation. The contact between the Khan and Rössing Formations is semi-continuous for over 9 km with the bulk of uraniferous leucogranite emplacement focussed at the southeast of the dome.

The Garnet Valley and Ida Central anomalies south and north of the Swakop River respectively, are typical examples of the stratigraphic influence on uranium mineralisation. Ground and airborne radiometric surveys show that mineralisation consistently follows the prospective Khan-Rössing contact for over 6 km of the 9-km strike length along the Dome's eastern flank. The Rössing Formation is absent from the western flank, and so too is any significant uranium mineralisation, reiterating the importance of stratigraphic and structural integration in the mineralisation model. The majority of the sheeted leucogranites intrude the relatively brittle, upper-Khan Formation gneiss and calcsilicate units and coalesce against the steep-dipping, thick package of serpentine and graphite marbles. The granites immediately below the marble units tend to host the highest grades of uranium, particularly where andradite skarn xenoliths occur.

A ground-based radiometric survey, conducted as part of this research, over a 1.5 km x 0.5 km area of the anomaly shows the surface expression of mineralisation; concentrated in a 200-m wide, strike-parallel zone below the marble hanging wall (Figure 3.26). The ground radiometric survey was carried out in strike-parallel ~1.5 km lines. The aim was to reflect radioactivity at surface (non-quantitatively) as an indication of radioactivity distribution (uranium, thorium, potassium). The complete dataset of positions and readings is presented in Appendix C3.

An important consideration is that the old copper workings and ore heaps have brought radioactive material to surface, resulting in increased surface exposure and therefore elevated scintillometer readings. Radiometric surveys do not penetrate more than a few tens of centimetres into solid rock; artificially-exposed mineralisation at old workings has placed a bias on the readings, this consideration has application across the Central Zone.

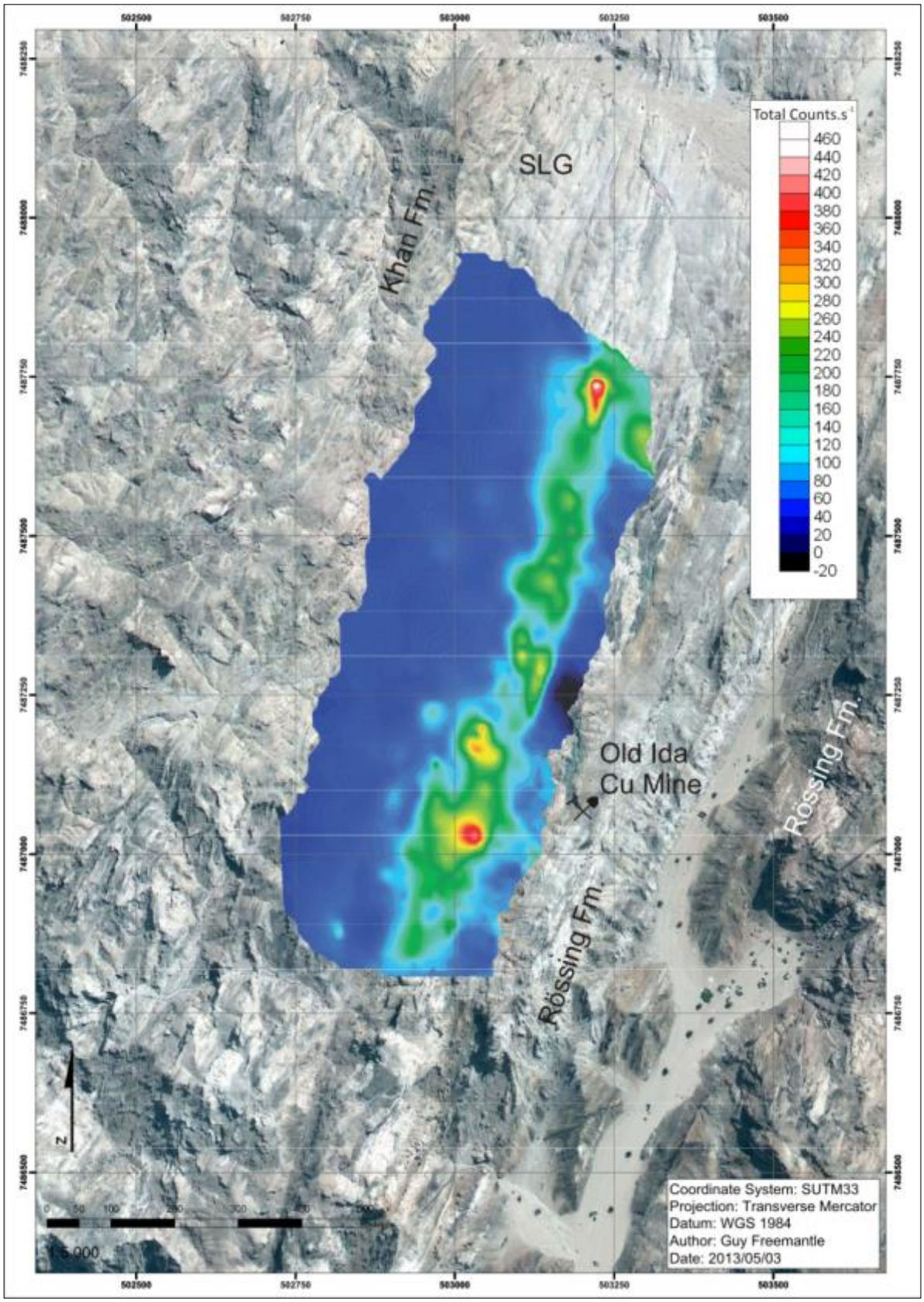



Figure 3.26 Radiometric anomalies on surface in the vicinity of the Ida Cu Mine. A handheld scintillometer survey was conducted over a portion of Ida Central, along the contact between the overhanging Rössing marbles and the underlying diopside gneiss of the Khan Formation. The majority of the granite intrusions do not transgress the marble barrier, and Cu and U mineralisation tend to concentrate along strike beneath the marble units. SLG: - sheeted leucogranite.

### *Holland's Dome Deposit*

The Holland's Dome deposit is located south of the Swakop River on the southeastern flank of the Ida Dome. The Dome is in fact an upright anticline with a NNE - SSW axial trace and cored by banded Khan Formation gneiss with Rössing Formation at the limbs. Figure 3.27 is a map segment containing remote-sensed imagery that illustrates the axial-planar nature of the sheeted leucogranite intrusives. The Holland's Dome deposit is thus, an example of a local-scale antiform-type structural control on granite intrusion. The structure essentially comprises the east limb, a core and a west limb of an anticline.

#### *Holland's Dome Stratigraphy*

The Holland's Dome is an upright anticline structure, which has an eroded hinge zone, thus the surface expression comprises a steeply east dipping, and northwest-verging repeated sequence as follows:

The Etusis Formation comprises migmatised, magnetite-bearing meta-quartzites with well-developed s-c fabrics and is exposed at the eastern limb and contacts an Abbabis basement inlier. It is <50 m thick and >250 m long in outcrop; completely surrounded by, and therefore interpreted as infolded by Abbabis gneiss. The Khan Formation outcrops in the core of the anticline, and contacts the basement to the east. It comprises a succession of banded and augen textured diopside gneiss, with intermittent schist units. The amphibole-biotite schist that characterises the top of the formation at the Ida Dome appears to be absent in outcrop, thus the top of the Khan Formation is seen as the first appearance of skarn lithologies.

The Rössing Formation comprises andradite – diopside – calcite – wollastonite ± magnetite skarn at the base, with serpentine marble outcropping on the western limb only. The carbonates are succeeded on the western limb by a calcsilicate-schist-quartzite package and a thick marble package, the eastern limb is in tectonic contact with the Abbabis gneiss, with the calcsilicate and quartzite typical of the Rössing deposit, all but absent.

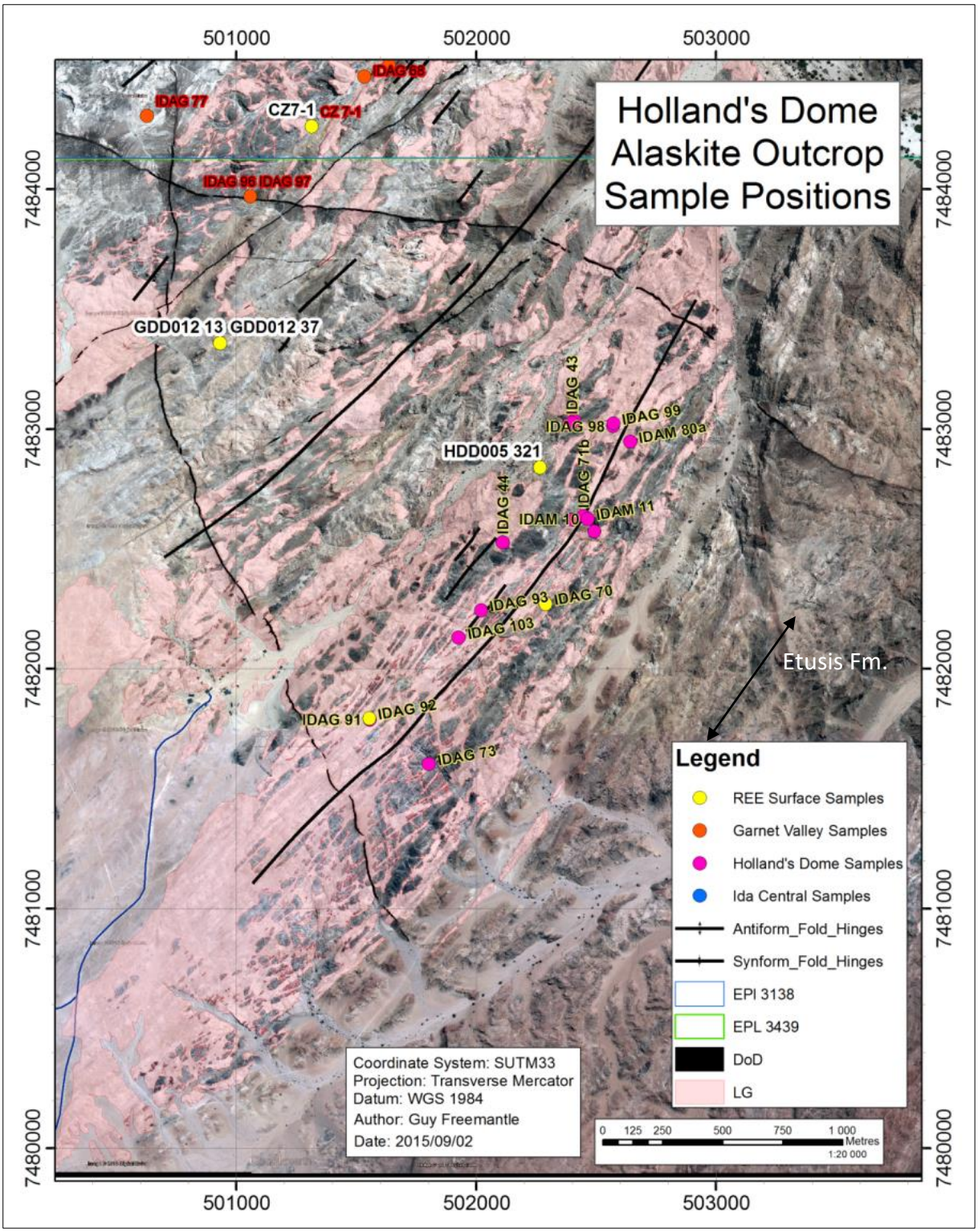



Figure 3.27 Aerial view of the Holland's Dome deposit. The Holland's Dome structure is an antiform, immediately adjacent to the Garnet Valley deposit on the south-eastern flank of the Ida Dome. The Garnet Valley deposit occupies a synform between the Ida Dome and Holland's Dome. The structure is bound by discontinuous marbles of the Rössing Formation at the limbs. Mineralisation occurs above and below the marble units and occurs in association with the calcsilicate-garnet-diopside-amphibole skarn pods. The axial planar-parallel leucogranite sheets (code LG) are conventional, but had to have intruded after folding. Late, Cretaceous dolerite dykes criss-cross the area (code DoD). Drill core samples come from the 'GDD' and HDD prefix samples.

*Holland's Dome Structure*

The Ida Central and Garnet Valley deposits occur along the same strike, within a monoclinal structural setting, whereas the Holland's Dome deposit occurs along the limbs of an upright box fold. The structure is separated from the Ida Dome by a shear zone[21].

Secondary folds on the antiform indicate a shallow axial plunge to the north-northeast. Bedding is mostly sub-vertical. Intersection lineations parallel to the main fold hinge line plunge northwards between -24° and -30° on 018° - 028° azimuths. The orientation of the roughly upright fold is consistent with the regional, southeast - northwest compression direction. Essentially, surface exposure comprises a pair of north-northeast - south-southwest striking limbs bounding a core of diopside gneiss with vertically plunging axial planar cleavage planes. The hinge zone of the fold has eroded leaving the ~1 km - wide predominantly Khan Formation diopside gneiss core section. Toward the northeast, the gap between the limbs does narrow but does not converge on surface. Skarn pods in a staggered boudin arrangement delineate the limbs on surface, and are interspersed with serpentine marble lenses. Drill data shows that the skarn pods are in a chocolate block boudin arrangement, parallel to strain in the vertical direction and parallel to NNE – SSW strain along the limbs.

*Holland's Dome Intrusives*

Emplacement is strongly controlled by the upright axial planar cleavage of the fold structure, and by dilation in the vertical direction. Exposed faces that give cross-section views between the limbs of the antiform show sheeted leucogranites invading as horizontal dykes exploiting dilation in the vertical direction. Toward the limbs of the antiform, more competent, brittle and reactive calcareous metasediments are overwhelmed by relatively structure-less coalesced leucogranite masses that form ~50% of the outcrop often containing xenoliths of the earlier biotite granites. The leucogranite sheets show a clear preference for axial planar cleavages and for dilation structures perpendicular to the southeast-northwest regional compression. Metasediments rarely show any indication of rotation within and between

[21] Kruger, 2014 pers. comm.

intrusive bodies, indicating a passive sequence of granite intrusion. Thus, there is very little clear evidence of crosscutting relationships between the uraniferous, and barren leucogranites at the Holland's Dome deposit.

In terms of classification within the deformational timeframe, the Holland's Dome granites in particular provide little visible support for separating supposedly older C-types from the younger mineralised sheets. Radiogenic dating of U-barren sheets give an age of ca. 514 Ma (Kruger and Kisters, 2016) which contradicts the 542 ± 6 Ma, and 542 ± 33 Ma ages for 'Ida Dome alaskite' (U-Pb, zircon, Tack et al., 2002; and Rb-Sr; Marlow, 1983, respectively). Intrusions at Holland's Dome and the Ida Dome show evidence of passive emplacement with very little rotation of country rocks, even when completely enveloped.

*Holland's Dome Mineralisation*

Uranium at Holland's Dome occurs in two main categories; the predominant uranium deposition is in the leucogranites and in the contact aureoles around the reactive skarn pods. The contrast in uranium grade between the skarn-contact granites and the vertical and horizontal sheets is sharp and uranium concentrations in granites drop abruptly within a few tens of metres of the skarn pods.

Figure 3.28a illustrates the vertical sheets with skarn pods on the west and east limbs, looking southwards. The granites host uraninite and uranophane, while the skarns contain uranophane on fracture planes and in dissolution cavities. The sheets and masses of leucogranite around the skarns are mineralised in uranium with up to 4 wt% U-metal. Coarse-grained titanite, diopside and garnet typify the contact aureoles (Figure 3.28b).

The second category is in the form of coarse-grained patches of leucogranite, with typical D-type texture and colour that occur within relatively uranium-free leucogranite masses, usually at a distance from the more prospective skarn and contact metamorphism aureoles. These appear to be the last-to-crystallise melt portions; the mineralised granite portions have pegmatitic texture and occasionally contain visible uranophane in cavities and along fractures. A potential third category exists as sporadic patches of consumed skarn, where Fe-stained $<1m^2$ areas host appreciable grades of uranium within low U-concentration leucogranite (Figure 3.28c).

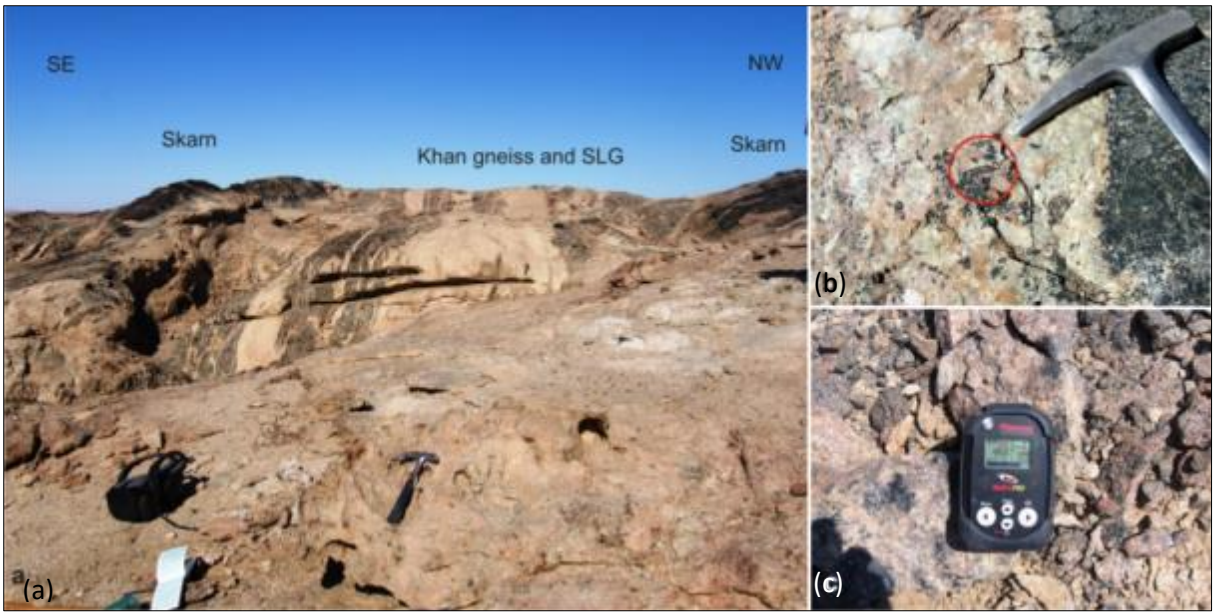



Figure 3.28 Local features at Holland's Dome. (a) View of Holland's Dome looking towards the southeast. The majority of bedding-parallel sheets intrude Khan Formation gneisses, while contact metamorphism at the Khan-Rössing contact has produced uranium-bearing skarns. Position: 502457E 7482718N (b) Euhedral sphene (titanite) is abundant in the Holland's Dome skarns; the assemblages of these localities are similar to the classic titanite localities in the Khan River Gorge south of Rössing. Position: 502066E 7482452N. (c) An example of the high-count rates on magnetite-bearing calcsilicates intruded by mineralised leucogranite. Position: 502645E 7482996N.

### *Uranium Distribution in Leucogranites at The Ida Dome*

Uranium concentrations in leucogranites and country rocks range from sub-economic ~100 ppm to over 40 000 ppm U at the Ida Dome (Figure 3.29). The sampling procedure has biased the database to include samples >100 ppm U, however there is a noticeable increase in sample frequency in the 2 000 - 4 000 ppm U category. The grade bin accounts for 2.5 % of all samples and 100 - 200 ppm U samples represent 59 % of all samples. There is at present no explanation for the spike in sample frequency above 2 000 ppm U. One possible interpretation is that unaltered leucogranite may host 2 000 ppm to 4 000 ppm U at maximum concentrations. The ≥100 ppm U sample frequency statistics at Ida Dome area (Holland's Dome, Garnet Valley, Ida Central – combined) are classified, the histogram presentation is proportionately accurate though.

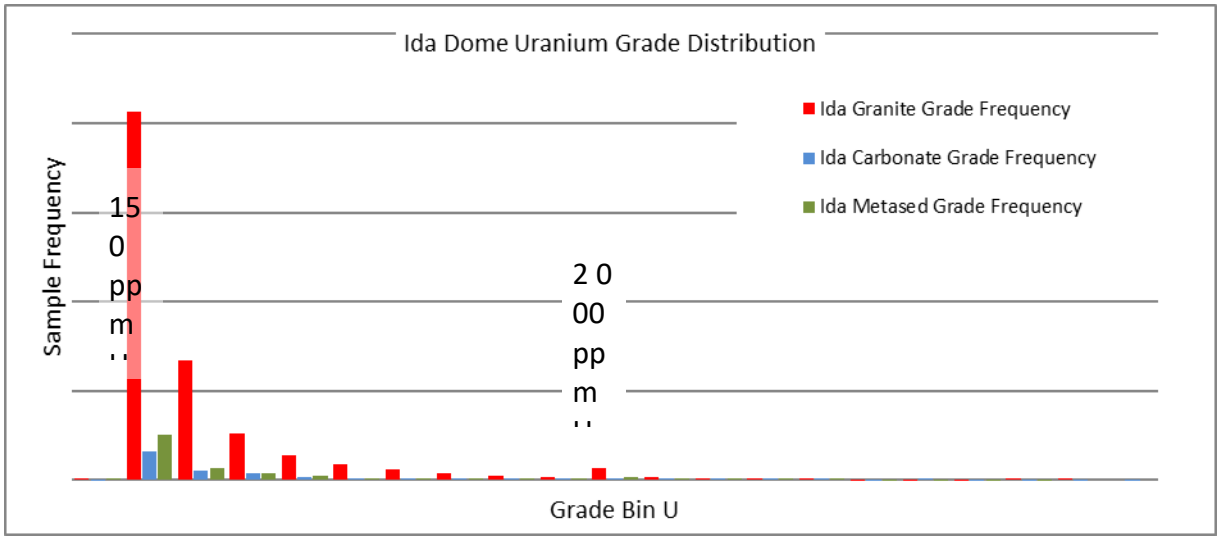



Figure 3.29 Uranium distributions in the three main categories of rock type at the Ida deposits. The Ida Dome deposits constitute a smaller dataset than Husab, but there is an increase in sample frequency at ~2000 ppm U, reflecting the pattern observed in the Husab samples, despite being over 20 km apart from each other. The cut-off at the low end is 150 ppm, but for confidentiality purposes the grade distribution can only be delivered qualitatively.

## 3.9 The Husab Deposit

### *Introduction*

The Husab Deposit is located ~5 km south of the Rössing Mine (Figure 3.30). The area is dominated by a large flat plain, north of the Swakop River and is bound to the east by the Khan River gorge watershed, and to the west by the Welwitschia Plains, named for the dense population of *Welwitschia Mirabilis*[22] that occur in the drainage patterns. It is the most significant granite-hosted deposit find in recent history and is set to double Namibia's uranium output[23]. It is one of the largest uranium deposits globally, developed or undeveloped, and is only challenged in size on the African Continent by the Areva - owned Imouraren Deposit in Niger. Globally it is the third largest proven uranium resource after McArthur River in Canada and Olympic Dam in Australia. The deposits were discovered by Extract Resource's geologists in late 2007. The company operated as Swakop Uranium in Namibia until early 2012. CGNPC-URC, through a Hong Kong subsidiary Taurus Minerals (60% CGNPC, 40% China-Africa Development Fund), took over Kalahari Minerals PLC and

[22] **Welwitschia** is a monotypic gymnosperm genus, comprising solely the very distinct Welwitschia mirabilis.
[23] www.swakopuranium.com.na

then Extract Resources Ltd, giving it ownership of the Husab project, at the time holding 137,700 t U in measured and indicated resources and a further 50,000 t U of inferred resources. The cost to Taurus Minerals for the entire Extract Resources' shareholding was about $2.2 billion[24].

The Welwitschia Plains area is dominated by Quaternary cover consisting predominantly of calcrete and silica lenses and covered in a thin veneer of recent aeolian sands (Smith, 1965). The Damara Supergroup is traceable through sub-outcrops of Khan, Rössing, Chuos, Karibib, and Kuiseb Formation lithologies, which were originally mapped by Smith (1965) and Barnes (1981) and more recently by (Kruger, 2016). The metasediments are only intermittently exposed, and there is little to no indication of U mineralisation on surface. Uranium is hosted in primary uraninite, secondary coffinite and a host of $U^{6+}$ minerals, including uranophane and boltwoodite. Uranium-bearing refractory minerals constitute a minor proportion of the measured uranium mineral population, and include brannerite and subordinate betafite.

### *Husab Exploration and Mining History*

Given the prospective nature of the Khan - Rössing boundary, the first drill targets were pegged in late 2007 at the northern end of what was to become Zone 1 of the Husab deposits, where uraniferous leucogranites are exposed at the contact between the two Formations. The Zone 1 mineralisation trend is in fact continuous with the large Z20 anomaly on the adjacent Rössing Uranium Mining Licence (Figure 3.30). The deposits occur in a north-south anticline that adjoins the Welwitschia Syncline of Smith (1965), which is in tectonic contact with the northeastern lobe of the Khan Inlier (after Spivey *et al.*, 2010). The initial investigation focussed on low-level uranium anomalies in the vicinity of the Z20 deposit. Shallow drilling to 40 m below semi-consolidated conglomerates, calcrete and gravel cover material intersected uranium in the bedrock, in leucogranite. Subsequent reconnaissance drilling began in late 2007 with a line of 3 RC holes, which returned very promising assay results in early 2008. Radiometric surveys ha d not revealed any evidence of the deposits because of the thick cover of recent sediments.

[24] World Nuclear Association, 2016

***Geophysical signature***

The Khan and Etusis Formations both contain Fe-Ti phases, which are fine-grained, except where intrusives have re-crystallised magnetite and haematite at contact margins. The fine-grained Fe-phases in these Formations have contributed to preserving a strong remnant magnetism, which is manifest as a -55° magnetic low (from Corner, 1981).

The Khan Formation is therefore traceable through various filters of processed Total Magnetic Intensity (TMI) survey data. Given the prospective nature of the Khan-Rössing Formation boundary at other U deposits in the vicinity, Swakop Uranium made use of TMI as the primary geophysical exploration aid. The remnant magnetism in the Khan Formation responded well to a 10-m altitude, 50 m line spacing aeromagnetic survey conducted in 2009. The Formation is continuous as a magnetic low extending from the northernmost exposure (3 km east of Blauer Heinrich Syncline) for approximately 22 km southwestwards to the Zebraberge hills that flank the western edge of the Ida Dome.

The discovery precipitated a large drill program involving a fleet of over 17 RC and diamond rigs at peak. The campaign lasted over 4 years, and remains in a state of active exploration outside of the proven Reserves areas. Over 600,000 m of reverse circulation and diamond drill core were bored between 2008 and 2012; with peak drilling in 2010, averaging 30 880 m/month; in comparison, pit-definition drilling at the large Rössing deposit peaked at 10 000 ft. (3 050 m) in August 1969, and accumulated drilling for that year was ~81 000 ft. (24 688 m)[25]. The resource definition drilling was undertaken on a 25-m grid to delineate measured resources, and at a 50-m grid-spacing to delineate the indicated and inferred resources. Extract Resources announced Zone 1 as a potential deposit in 2008 and between announcement and 2011, six zones of U mineralisation were discovered, with the northern two holding the highest grades and tonnages nearest to surface. The six mineralised zones were discovered systematically as exploration drilling expanded southward between 2008 and 2011.

[25] Husab Data sourced by Guy Freemantle at Swakop Uranium, Rössing Exploration statistics sourced from Berning *et al*. (1976).

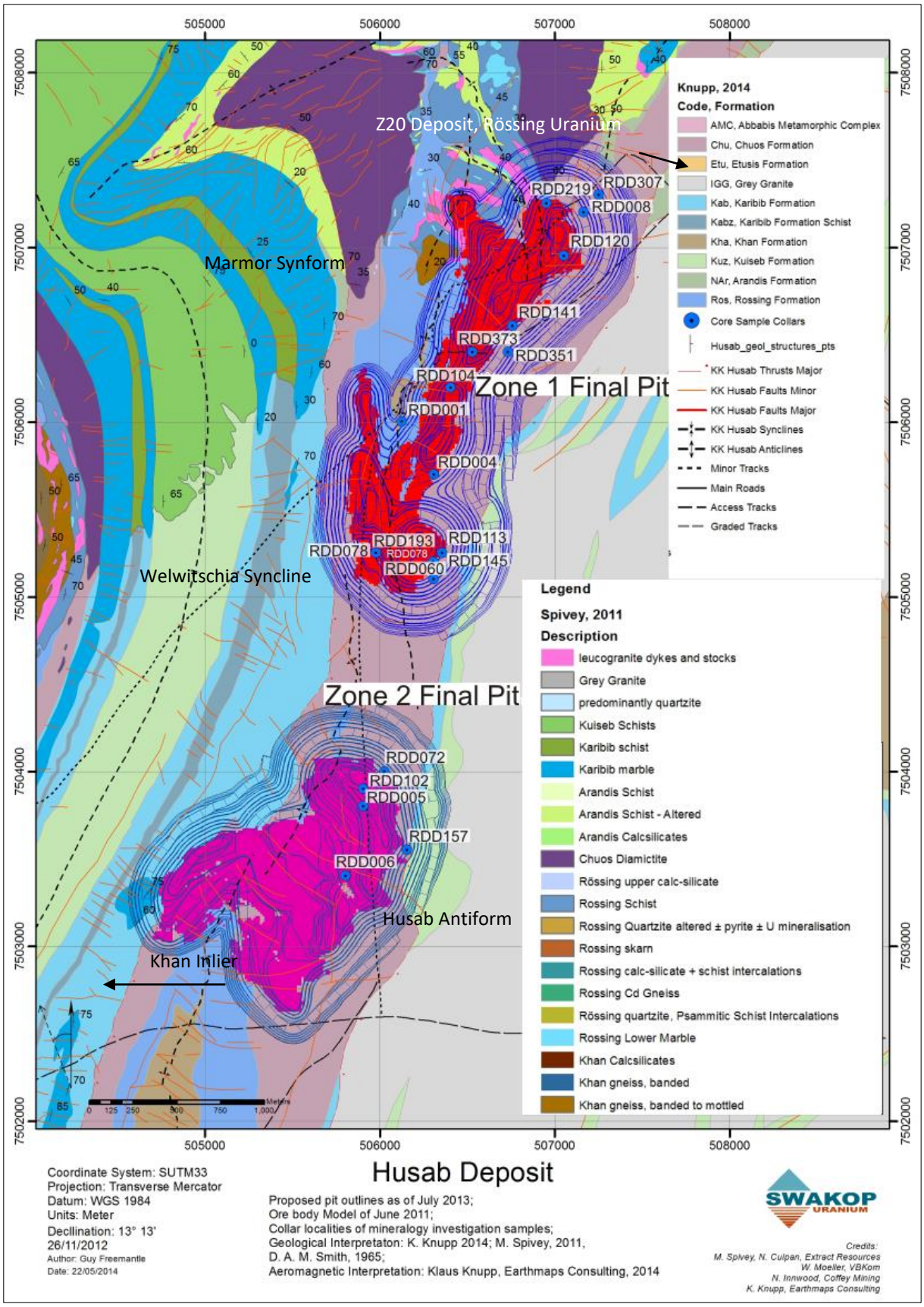

Z20 Deposit, Rössing Uranium
Marmor Synform
Welwitschia Syncline
Zone 1 Final Pit
Zone 2 Final Pit
Husab Antiform
Khan Inlier
RDD219
RDD307
RDD008
RDD120
RDD141
RDD373
RDD351
RDD104
RDD001
RDD004
RDD193
RDD078
RDD113
RDD145
RDD060
RDD072
RDD102
RDD005
RDD157
RDD006
Knupp, 2014
Code, Formation
AMC, Abbabis Metamorphic Complex
Chu, Chuos Formation
Etu, Etusis Formation
IGG, Grey Granite
Kab, Karibib Formation
Kabz, Karibib Formation Schist
Kha, Khan Formation
Kuz, Kuiseb Formation
NAr, Arandis Formation
Ros, Rossing Formation
Core Sample Collars
Husab_geol_structures_pts
KK Husab Thrusts Major
KK Husab Faults Minor
KK Husab Faults Major
KK Husab Synclines
KK Husab Anticlines
Minor Tracks
Main Roads
Access Tracks
Graded Tracks
Legend
Spivey, 2011
Description
leucogranite dykes and stocks
Grey Granite
predominantly quartzite
Kuiseb Schists
Karibib schist
Karibib marble
Arandis Schist
Arandis Schist - Altered
Arandis Calcsilicates
Chuos Diamictite
Rössing upper calc-silicate
Rossing Schist
Rossing Quartzite altered ± pyrite ± U mineralisation
Rossing skarn
Rossing calc-silicate + schist intercalations
Rossing Cd Gneiss
Rössing quartzite, Psammitic Schist Intercalations
Rossing Lower Marble
Khan Calcsilicates
Khan gneiss, banded
Khan gneiss, banded to mottled
505000
506000
507000
508000
7508000
7507000
7506000
7505000
7504000
7503000
7502000
Coordinate System: SUTM33
Projection: Transverse Mercator
Datum: WGS 1984
Units: Meter
Declination: 13° 13'
26/11/2012
Author: Guy Freemantle
Date: 22/05/2014
Husab Deposit
Proposed pit outlines as of July 2013;
Ore body Model of June 2011;
Collar localities of mineralogy investigation samples;
Geological Interpretaton: K. Knupp 2014; M. Spivey, 2011,
D. A. M. Smith, 1965;
Aeromagnetic Interpretation: Klaus Knupp, Earthmaps Consulting, 2014
SWAKOP URANIUM
Credits:
M. Spivey, N. Culpan, Extract Resources
W. Moeller, VBKom
N. Innwood, Coffey Mining
K. Knupp, Earthmaps Consulting

Figure 3.30 The Husab Mine Project Area. *previous page* The pit outlines were produced by a consulting company from the 2012 resource models of the ore bodies, defined by over 2,000 drill holes. The drill holes were sampled as part of a mineralogy study headed by Guy Freemantle in 2011 and 2012. Surface geology was re-interpreted by M. Spivey between 2008 and 2011 and is in bold colour. The pastel shaded lithologies are geophysical interpretations (aeromagnetic) of the subsurface geophysical interpretation by K. Knupp of Earthmaps Consultants in 2014. The Khan River is 4 km to the north, and the Rössing Mine is beyond on the north bank of the gorge. The magenta and red shapes delineate the ore bodies as of April 2013, with life of Mine pits superimposed, Zone 1 will terminate at 410 m below surface.

The five ore zones form a semi-continuous north to south chain for ~8 km from the northernmost surface exposure to the southernmost discoveries beneath the Welwitschia Plains. Depth to the palaeo-surface beneath Quaternary cover increases from the exposure in the north to over 100 m in the southernmost zones. Mine development commenced in April 2013 and as of mid-2014 the two largest, and nearest to surface mineralised sections, Zone 1 and Zone 2, began mining by conventional open pit operation. The first uranium drums were sealed at the final product recovery building in December 2016. The positions and shapes of two open pits are presented in Figure 3.30. The excavations will expose the largely stratiform granite bodies that occur within the Rössing Formation. Mineralisation is open ended beyond depths of over 400 m below surface at both Zones 1 and 2. Appendix C4 presents the most comprehensive geological map of the area; it was produced by Spivey et al. (2010) and covers the entire Ida Trend area, from the Ida Dome 20 km to the south through to the Z20 deposit.

### *Deposit Description*

The Husab deposit as a minable resource is divided into two zones; Zone 1 is the northernmost and outcrops at the crest of the Khan River Gorge- 6.5 km south-southeast of the SJ pit at Rössing. Zone 1 extends for over 3 km from north to south, and is divided from the 2.5 km x 2 km-wide Zone 2 deposit by a saddle structure in the NE-SW antiform hinge, and vertical fault displacement. Drill core observation shows that the granite sheets occur as centimetric- to >50-metre-thick dykes, intruded at variable angles to bedding/schistosity. The ore bodies are constructed at set grade intervals using assays from over 1500 reverse circulation, and over 500 diamond-drill holes. The end product shows very clearly the

tendency for uranium to concentrate in the mineralised SLG's bodies, and shows these granites to intrude at an oblique angle to the bedding of the metasediments in the steeply dipping Zone 1 deposit, but filling a saddle-reef arrangement in Zone 2. Essentially the Husab deposits comprise uraniferous leucogranites that have invaded the hinge zone and tension structures in the limbs of a regional scale antiform, the Husab Anticline. Erosion has removed the hinge zone of much of Zone 1, and thus mineralisation tends to occur on the limbs of the fold structure. Zone 2 occupies the antiformal hinge zone with palaeo-erosion levels having reached the Chuos Formation and thus preserving the Rössing Formation. Consequently, the uraniferous leucogranites at Zone 2 are arranged in a sub-horizontal zone over 200 m thick. South of Zone 2, the Zone 3, 4 and 5 deposits occur on the same anticline structure, but are buried beneath a considerably thicker Damara succession, as the palaeo-erosion surface has only progressed to through to the Karibib Formation.

### *Husab Stratigraphic Succession*

The Damara Supergroup at Husab is observed almost entirely in diamond core sections although the surrounding area hosts representatives of the typical Central Zone succession from Etusis through to Kuiseb Formations. The Rössing succession that hosts the majority of the uraniferous sheeted leucogranites is comparable to the succession described for the Rössing Mine in Anderson and Nash (1997). Figure 3.31 illustrates the Damara succession at the Husab deposits; a variety of upper Nosib and the lower Swakop Group metasediments are represented at the Zone 1 and Zone 2 deposits, including Arandis Member and lower Karibib Formation limestone.

The Etusis is shown, as exposure is limited to the basement contact to the Khan inlier of the recumbent Welwitschia Syncline (Smith, 1965) and is within the vicinity of the deposits. It is dominated by migmatised quartz-dominant sediments, but not represented in the Husab deposit drill core library, which is focussed at the Husab anticline

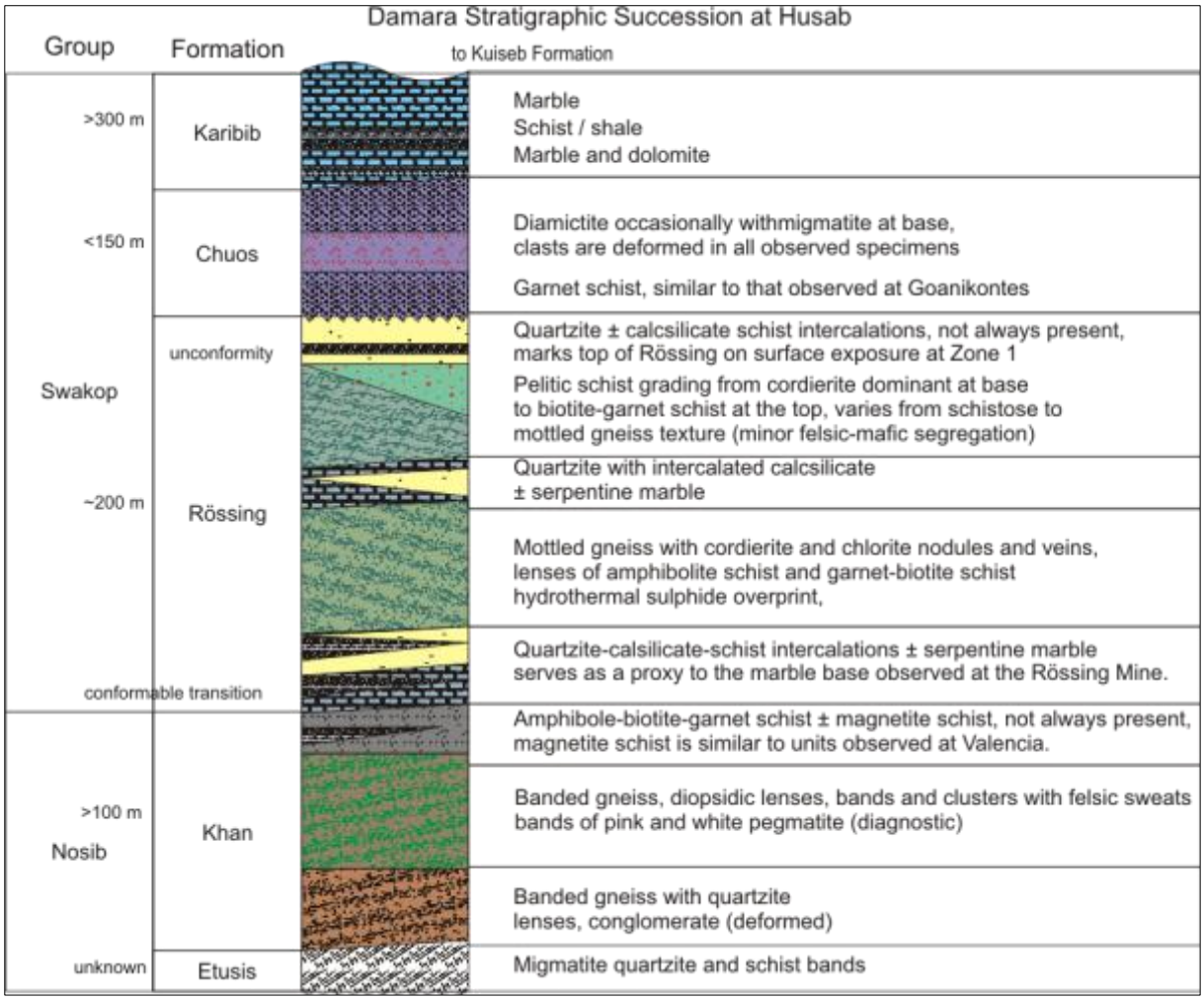



Figure 3.31 The Damara Supergroup at Husab. The Khan Formation forms a sharp footwall contact of banded diopside gneiss, which is succeeded by a calcareous mix of finely laminated quartzite and calcsilicate units. Marble is intermittently present in the lower carbonate package. The lower pelitic gneiss is mottled with coarse cordierite porphyroblasts and chlorite overprint, which is cut by sulphide veins. The upper carbonate package is similar to the lower, but tends to have thicker marble units. The upper pelitic gneiss is more schistose than gneiss and grades from cordierite-dominant at the base to garnet-dominant toward the upper quartzite and schist that underlie unconformable Chuos diamictite. The Arandis Member, as amphibolite and calcsilicates, is noted in field exposures at the north end of Zone 1, but is not included in the core logs.

The upper Swakop Group, also shown, is present south of Zone 2, and forms the hanging wall succession with the Chuos Formation to the Zone- 3, 4 and 5 deposits The overall succession at the mine includes the Khan Formation of the upper Nosib; and the Rössing-, and Chuos Formations of the lower Swakop Group. The Khan Formation, from top to the lowest units, as intercepted in drill core, comprises:

- <40 m of conglomeratic mudstone often with intermittent units of 1 m to 2 m thick biotite schist;

- 15 m to 20 m of biotite schist with amphibole and magnetite; up to 35 m of meta-greywacke (not always present);
- 50 m to > 100 m of banded gneiss with well-developed mafic - felsic segregation sub-parallel to $S_0$; and
- Biotite schist with sparse leucosomes of pink and white feldspar and quartz.

Rössing Formation lithologies at Husab are variably attenuated at Zone 1 and the Rössing succession is less consistent than the Khan Formation, particularly with regard to the marble units. Garnet-biotite schist (± amphibole and magnetite) is located between the banded gneiss of the Khan Formation and the first appearance of the Rössing Formation carbonates. The Rössing Formation is characterised, on surface at the north of Zone 1, by variably thick (metre-scale) marble packages, with serpentine and graphitic units. Their appearance places these within the lower Rössing succession described by Anderson and Nash (1971). The Rössing Succession from top to bottom is commonly represented as follows:

- >20 m of meta-greywacke, locally schistose and gneissic textured, may be a unit of the Chuos Formation, but clasts are less varied in size than in typical Chuos diamictite; >10 m of biotite schist, locally garnetiferous;
- <15 m of intercalated calcsilicate, quartzite, and schist constituting the Upper Quartzite package; > 30 m of augen- to mottled-textured gneiss, intensely chloritised, locally garnetiferous and dominated by accessory cordierite, constituting the Upper Pelitic gneiss;
- ~20-25 m Upper Carbonate of intercalated calcsilicate, marble, quartzite and schist/shale units, local contact metamorphism to skarn, serpentine and graphitic marbles and minor gneissic textured units (Figure 3.32a and 3.32b);
- >40 m of Cordierite gneiss. The package is intensely chloritised, and locally sulphide-bearing (Figure 3.32c). It contains sillimanite- and garnet dominant metapelites (Figure 3.32d and 3.32e) and is invaded by large percentages of uraniferous sheeted leucogranite, often constituting >50 % of total thickness; and

- The lower carbonate package, as described in the Khan - Rössing transition section below.

The Chuos Formation comprises, from the Rössing contact up, pebble-bearing sediments, metamorphosed shale/mudstone and diamictite. The diamictite has responded to deformation to develop an augen gneiss texture (often with garnet porphyroblasts, analogous to those described by Nex, 1997, at Goanikontes). The succession above the Chuos includes Arandis member calcsilicate and amphibolite schist units which are immediately succeeded by the Karibib Formation marbles and dolomites. Some local mineralisation in pegmatites is associated with the Arandis Member on surface, north of Zone 1.




Figure 3.32 Typical Rössing Formation lithologies observed in Zone 1 drill core specimens. (a) The upper units of the Rössing Formation are eroded away in parts of Zone 1; the intercalated diopside gneiss, quartzite and calcsilicates shown from RDD373 at ~100 m depth correlate to the upper marble sequence at the Rössing Mine. (b) The impure upper marble typically contains serpentine - diopside carbonates, quartzites and occasional skarns where intrusives have provided heat ± fluids. Intercalated gneiss and calcsilicates typify the package. (c) The dominant pelitic unit(s) include a thick ~10 - >100 m thick cordierite gneiss, which is variably metamorphosed and contains conspicuous amounts of hydrothermal sulphide mineralisation. The typical units include chloritic, migmatised cordierite gneiss, banded and augen garnetiferous gneiss and calcsilicates. (d) Lower pelitic units usually are separated by a carbonate unit(s) from the upper cordierite gneiss. These are distinguished by darker colour, significantly less prominent chlorite and a prominent garnet porphyroblasts (e - inset). The examples shown above are from diamond drill holes RDD373 and RDD351.

### *Khan - Rössing Transition at Husab*

The Khan Rössing boundary is marked by conglomeratic units of the upper Khan Formation and the appearance of the first calcsilicate-quartzite-marble package (Figure 3.35a). It is not always present, and when absent, the magnetite-bearing amphibole-biotite schist serves as the marker.

In comparison, the base of the Rössing Formation at the nearby Rössing deposit area is usually marked by the appearance of the lower marble of Anderson and Nash (1997) and a unit of distinctive amphibole-biotite-schist (hornfels) that bisects the Mine's SJ deposit. The Khan Formation below the transition comprises diopside gneiss and calcsilicate units, occasionally with magnetite-garnet-diopside skarn pods. Figure 3.33a and 3.33b illustrate examples of the meta-conglomerate and banded diopside gneiss respectively. The banded gneiss has developed a mottled localised texture, where centimetric diopside porphyroblasts define the units (Figure 3.33c).

The lower carbonate package of the Rössing Formation succeeds the Khan Formation, and is consistently represented by an intercalated package of fine-grained metasediments (mudstone and shale precursors) quartzite, and calcsilicates. The marbles, typical of the Rössing Formation at the Rössing mine are inconsistently represented and often occur as thin components of the lower quartzite-calcsilicate packages. Figure 3.33d represents part of the lower carbonate package of the Rössing Formation, and Figure 3.33e illustrates a thin, impure serpentine marble lens within the package.

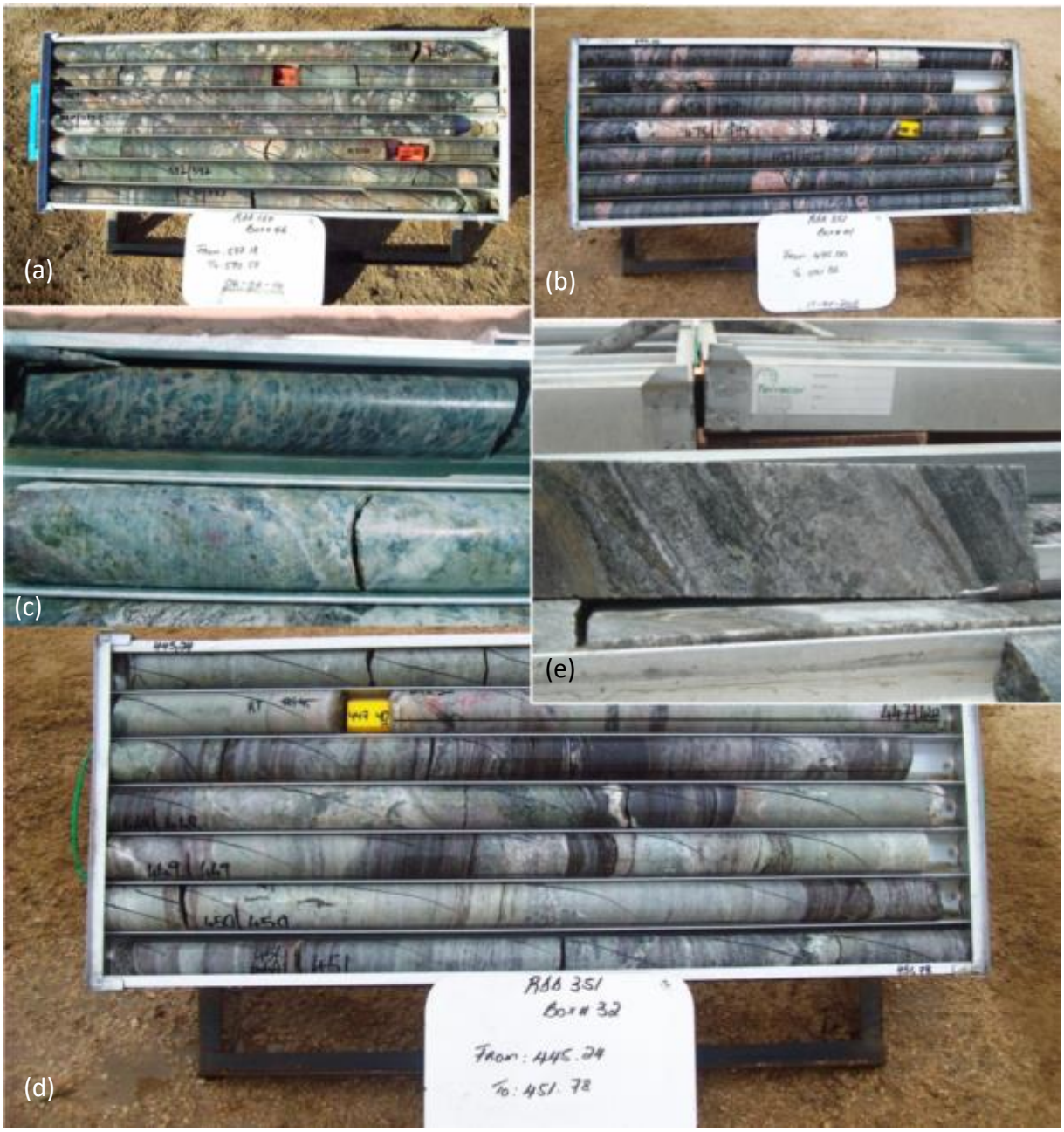



Figure 3.33 Typical Khan - Rössing transition succession lithologies observed in Zone 1 core specimens. (a-b) The upper Khan Formation meta-conglomerate (a) and banded gneiss becomes progressively less calcareous and retains pronounced compositional banding with depth (b). The banded gneiss is invaded by granitic leucosomes and veins (C-type of Nex, 1997). Core trays from drill holes RDD164 and RDD373, respectively. (c) Biotite is typically black and shows localised chloritic alteration, RDD373. (d) The lower Rössing carbonate package in RDD351 (southern section of Zone 1) is an intercalated package of green serpentine marbles which reach considerable thicknesses in some parts of Zone 1 and Zone 2. RDD351 (e) Close-up of the serpentine marble, showing fine banding, RDD373.

***Structural Setting at Husab***

Smith (1965) described the structural geology and named the major fold structures of the area, these are shown on a local map in Appendix C5. The major structural features that dominate the local area around the Husab deposits are: -

- The regional Khan Syncline that extends from the northeast to the southwest;
- The Blauer Heinrich Syncline, where the hinge line changes direction through ~90° from NE-SW to NW-SE;
- The Khan Syncline that wraps around the northeast flank of the Khan inlier of Abbabis basement, where the hinge line direction curves from NW-SE through to a NW-SE orientation;
- The Welwitschia Syncline that occurs along the eastern flank of the Khan Inlier; and
- The Husab antiform that extends north to south against the Welwitschia syncline.

The Husab deposits occur within the regional-scale Husab antiform that adjoins the eastern limb of the Welwitschia Syncline, and appears to be linked directly with the synclines directly south, in the Geurtel Hills (Figure 3.30). A section view is shown in Figure 3.34 at Zone 1 and Zone 2. A comprehensive 3D model of the geological units and major fault structures was managed and produced by Neal Culpan of Extract Resources. The geological model is constructed from >2 000 drill hole intercepts in conjunction with regional mapping interpretations by Martin Spivey aided under cover by geophysical interpretations of high resolution magnetic data (50 m helicopter-borne survey flown in 2010).

The eastern limb of the Welwitschia Syncline is overturned and refolded and was first described in Smith (1965). The western limb of the Husab structure should correspondingly also be overturned. (A limited portion of the Husab-Rössing area is illustrated in Figure 3.30. Detailed representations of the fold system described by Smith, 1965 are in Appendix C5.

The geological model describes the Husab antiform as a regional scale, upright to northwest verging antiform with a south plunging hinge line. The map segment in Figure 3.19 illustrates

the underlying Damaran sequence, where the hinge line forms the spine down the middle of the north-south oriented ore zones. Husab deposits comprise sheeted leucogranite intrusions occupying the hinge zone and limbs of the Husab antiform. The structure has eroded obliquely exposing the Khan Formation fold core at Zone 1. The fold shape fits that of an inclined D3 class anticlinal fold[26] and at Zone 2 where erosion only reaches the Chuos Formation, the fold is open to a D2 shape [25].

A pronounced fault structure between Zone 1 and Zone 2 divides the two main deposits by downward displacement (>400 m below surface) of the ore zone in a ~700 m wide east-west zone, located between 7504250N and 7505000N (Figure 3.30). Geophysical imagery shows the regional scale fault extending in a northwest direction from the Husabberg, cutting between Zone 1 and Zone 2 and extending on through to the Welwitschia Syncline.

The core of the Welwitschia Syncline comprises tightly folded Kuiseb Formation schists bound by Karibib marble and dolomite packages, which are divided by a laminated shale unit. The overturned eastern limb of the syncline comprises steeply north- to east-dipping Karibib marble-dolomite packages, which are overlain by Arandis Member schists and calcsilicate units. Surface exposures of the Husab deposit lithologies lie directly northeast of the exposed Welwitschia Syncline, and are limited to outcrop at the western and northern end of Zone 1[27].

The Husab antiformal structure is continuous for more than 5 km below surface and is confirmed by drill intersections, to intrude the limb of the fold at Zone 1 (Figure 3.36a) and the hinge zone of the fold at Zone 2 (Figure 3.36b). Closure of the Husab antiform and the Welwitschia Syncline are apparent on surface in the form of Karibib, Chuos, Rössing and Khan Formations of the Geurtel Hills folds, located between the eastern flank of the Khan Inlier and the north-western edge of the Ida Dome.

The structural geology interpretation of Spivey *et al.* (2010) places a prominent fault between the overturned eastern limb of the Welwitschia Syncline and the corresponding western limb of the adjoining Husab antiform. The eastern limb of the Husab Antiform is not

[26] Huddleston (1973) fold classification.

[27] The Welwitschia Syncline has a N-S hinge and joins the Blauer Heinrich and Khan Synclines immediately north of the Husab Anticline. Appendix C4 shows the structural map of Smith, 1965 that illustrates the junction of these regional fold structures.

entirely overturned according to Extract Resources interpretations of over 2 000 drill logs, but is rather sub-vertical with a slight northwest vergence.

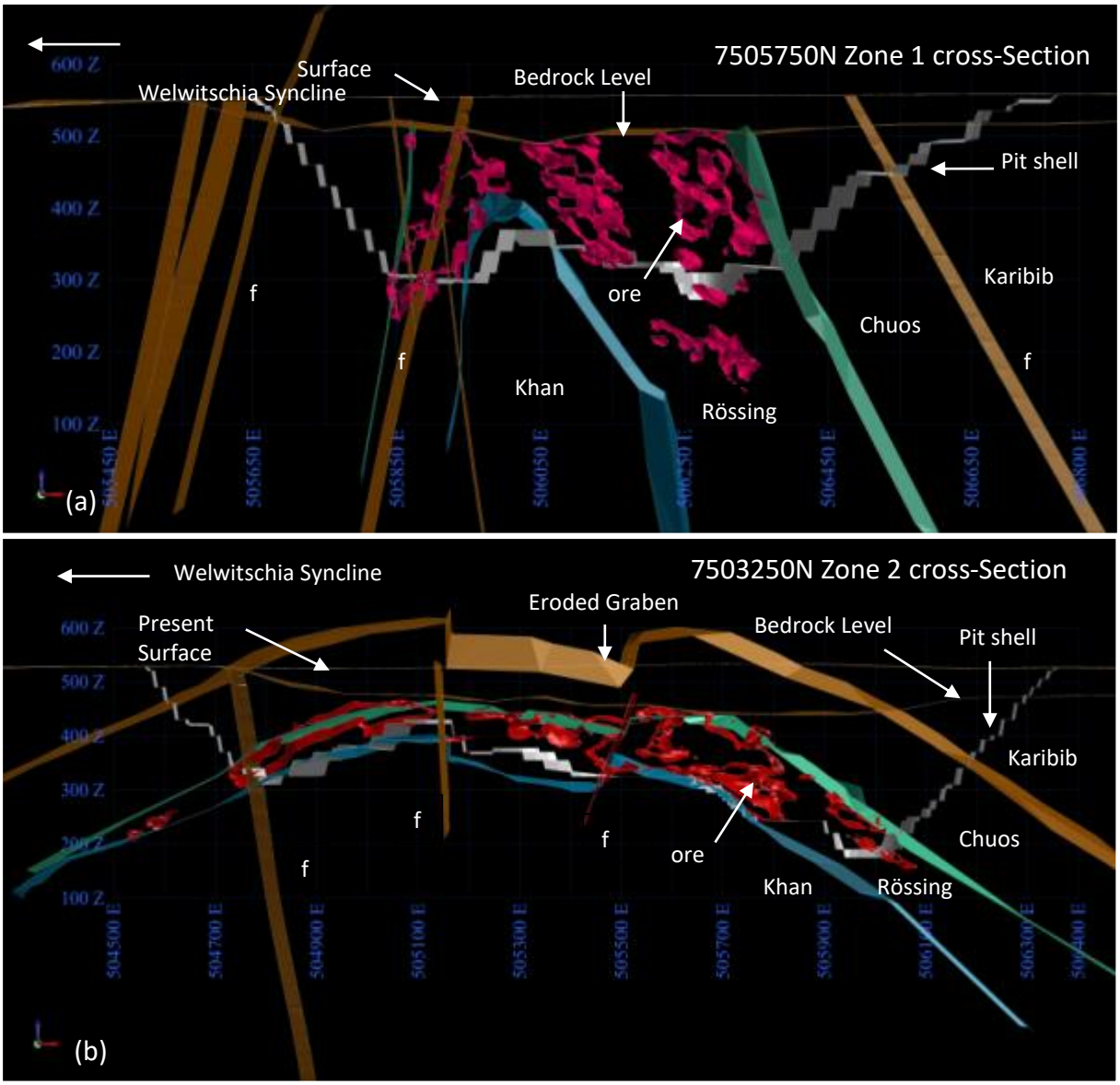



Figure 3.34 Cross-sections of the Husab Zone 1 and Zone 2 deposits. Both views look north with "Z" representing altitude above sea level and "E" representing Eastings in UTM (WGS84). Colour codes: Magenta - Mineralised leucogranite ore zones (Zone 1); Red - Mineralised leucogranite ore zones (Zone 2); Tan - Base of the Karibib Formation; Light Green - Base of the Chuos Formation; Blue - Base of the Rössing Formation; Brown - Fault Planes; Light Grey - Planned Pit Shells. (a) Mineralisation occurs in granites confined to the Rössing Formation in the limbs of the Husab Antiform at Zone 1, where the hinge is lost to erosion. (b) The Zone 2 section of the deposit occurs where the antiform hinge is preserved, the fold structure is more open and mineralised sheets conform more closely to the host rock bedding orientations. Geological Interpretation by Neale Culpan of Extract Resources, 2008 to 2012.

***Intrusive Rocks at Husab***

The oldest intrusion in the area is the Salem-type granodiorite that occurs intermittently within the Husab area. Immediately to the east of the Husab antiform, a large area of uniform magnetic response is interpreted as Salem type granite (Figure 3.30, from Knupp, 2014) and its extent is supported predominantly by sub-crop mapping and geophysical interpretation (magnetic). The Salem type granite is exposed on surface southwest of the Zone 3 and Zone 5 deposits, and confirms the magnetic interpretations. It invades and overwhelms Khan and Rössing Formation lithologies, and in turn intruded by sheeted leucogranite veins.

Grey biotite-bearing granites that are younger than the Salem granites are exposed on surface in the north of Zone 1 predominantly in the Khan Formation. The granites are also observed in cores, where they may be crosscut by veins of pegmatitic sheeted leucogranites.

The earliest generation of sheeted leucogranites appears to be the magnetite-bearing $C_m$-type sheets that preferentially intrude the Khan Formation. This generation of sheeted leucogranites appears consistently at Goanikontes; at the Ida Dome deposits; at Valencia, and at the Hildenhof anomaly and numerous Khan Formation outcrops along the Swakop- and Khan River Valleys. They are analogous to the C-type granites described in Nex (1997). The sheets seem to occur in elongate zones sub-parallel to bedding ($S_0$) and parallel to the dominant $S_1$ orientations, thick metre-scale sheets have intruded at oblique angles to the host rock fabric. Intrusions appear to be parallel to the compositional banding in the Khan Formation gneiss' (which is predominantly parallel to $S_1/S_0$). They vary in thickness from a few centimetres to a few metres in core intersection. They are distinctly parallel-sided and continuous for great lengths at other deposits, and it appears to be so in outcrop near Husab Mine's Zone 1 deposit. Sheets also intrude perpendicular to the bedding/compositional banding, exploiting brittle features at right angles to the NW - SE compression direction.

The Husab deposits comprise at least one generation of uraniferous leucogranites (alaskites) that have preferentially invaded the Rössing Formation strata in a regional scale antiform that adjoins the eastern limb of the northwest-verging Welwitschia Syncline. Uraniferous leucogranites intrude the Khan, Rössing and Chuos Formations, with the majority of mineralisation within the Rössing package. The Khan Formation consistently serves as a

footwall to mineralisation, though localised mineralised SLG's have intruded into the uppermost gneiss units. The succession of metamorphic and deformation events has attenuated the Nosib and Swakop Group sediments between the Welwitschia Syncline and Husab Antiform at Zone 1.

The intrusive rocks at Zone 2 have largely conformed to a saddle-reef type arrangement in the hinge zone of the more open fold and their emplacement thicknesses gradually thin, but are open ended in the limbs to the east and to the west. Pegmatitic leucogranite veins occur throughout the local Damara succession, and appear to be crosscut by mineralised leucogranite veins in the Rössing Formation, but in far more localised occurrences within the Chuos and Kahn Formations.

### *Husab Mineralisation*

Uraninite from the Husab deposit is dated at 496.1 ± 4.1 Ma by Cross *et al.* (2011) which will imply that the age of sheeted leucogranite intrusion at the site is at least this old.

Mineralisation predominantly occurs within at least one generation of the SLG's that intrude the Rössing Formation and upper units of the Khan Formation, and occasionally up into the Chuos Formation. The uraniferous leucogranites have a number of distinctive textures, that are similar to those described for Goanikontes by Nex (1997) and for Rössing alaskites by Berning *et al.* (1986):

- Pristine D-type sheets comprise white feldspar, a coarse to pegmatitic texture and grey to black smoky quartz;
- Prominent intervals of metre-scale biotite nests and quartz-biotite pods often occur near or at metasedimentary contacts, especially in the most pegmatitic textured sheets;
- The mineralised sheets also show prominent Fe-coloured alteration textures, particularly near the palaeo surface and resemble the E-type described at Goanikontes; and alteration near fault zones tends to be sericite - chlorite dominated.

A number of satellite occurrences of mineralised SLG's intrusion occur 2 - 3 km south, southwest and west of the abandoned Husab Fluorite Mine. These consist of Salem granodiorite intruded locally by pegmatites, some of which are mineralised wherever slivers of mafic-rich metasediment occur in the granite mass.

The most consistent high grades occur in the sheeted leucogranites invading sulphide-bearing, metalliferous (Cu, Ni, Mo) cordierite gneiss units between the upper and lower carbonate packages of the Rössing Formation. The diopside banded gneiss that characterises the Khan Formation in this region of the Central Zone forms a consistent footwall to the mineralisation, and the Chuos Formation diamictite is consistently the hanging wall.

Most of the primary U-mineralisation occurs within the intrusives; ~66 % of the ore feed comprises mineralised leucogranite (alaskite, Table 3.3). Uraniferous sheeted leucogranites tend to intrude the sulphide-bearing Rössing Formation gneiss packages, between the lower and upper carbonate packages. Common sulphides in metalliferous Rössing Formation gneiss include pyrite (in multiple generations); chalcopyrite; pyrrhotite; pentlandite, and molybdenite. The strong association with the sulphide-bearing units reflects the crucial role of REDOX buffering by reduced sediments on the crystallisation of uraninite. The sheets also invade above the upper carbonates, and into the lower Chuos Formation, particularly in the Zone 2 deposit. Uraniferous sheets occur within the Khan Formation, close to the lower carbonate package, in both Zone 1 and Zone 2. Minor occurrences of uranium mineralisation are reported in the lower Khan Formation, but do not carry sufficient grade, and are unlikely to be mined because of the great depth (over 600 m vertical from surface).

Secondary uranium mineralisation, which accounts for 44 wt% of the measured uranium budget, occurs in sheeted leucogranites within the Rössing Formation gneiss, schists and marbles, and calcsilicates in both deposits. The dominant secondary phase is coffinite, with sporadic observations made of uranophane and/or boltwoodite in both zones. The secondary uranium budget contrasts with the Rössing deposit, and attributed to the relatively thin marble units at Husab, with respect to the type locality.

Within the vicinity (SE) of the Husab deposits uranium mineralisation is hosted in Salem type granite, which has invaded and overwhelmed the local Khan and Rössing Formations. Large pavements of granite occur on the peneplain and host xenoliths and rafts of Rössing

Formation calcsilicate rocks. Sheeted leucogranites have intruded the older Salem granite, forming networks of <1 m wide dykes and $S_1$-parallel veins. Where leucogranite and Rössing Formation xenoliths coincide, uranium mineralisation is usually present.

Table 3.3 Estimated percentages of ore material by rock type of the Husab Mine Project. Zone 1 and Zone 2 show similar proportions of alaskite but differ in calcsilicate and Chuos Formation tonnages. (Data from Swakop Uranium Husab Project Definitive Feasibility Study, 2011). Note figures are rounded for confidentiality

| **Zone 1** | **Zone 2** | | **Average %** | **Ore Classification** |
|---|---|---|---|---|
| Ore (Mt) | Ore (Mt) | Total Tons | % of Ore | |
| 12 | 21 | | 10.44 | Calcsilicate |
| 26 | 29 | | 17.62 | Rössing Formation |
| 92 | 114 | | 66.05 | Alaskite |
| 12 | 4 | | 5.28 | Chuos Formation |
| 1.6 | 0.2 | | 0.61 | Khan Formation |
| 143.6 | 168.2 | **~312 Mt** | 100 | Total |

The Husab deposits are defined by the largest number of uranium assays, outside of the Rössing deposit, in the Central Zone. Uranium distribution analysis is calculated by dividing the assay database into three categories; 1- granite which included all varieties of granitic sheets; 2- pelitic rocks which include pelitic and semi-pelitic rocks of the Khan, Rössing and Chuos Formations; and 3- carbonate-clastic rocks, which include marble, calcsilicate and quartzite type lithologies.

. Figure 3.35 illustrates the distribution of the uranium grades in the Zone 1 and Zone 2 deposits; showing the highest sampling frequencies between 100 and 200 ppm in the granitic samples, which decreases almost exponentially toward the 2 000 - 3 000 ppm category. Between the 2 000 ppm and 4 000 ppm U there is an abrupt increase in sample frequency, accounting for 14.2 % of all sample assays of granitic rocks at Husab (Figure 3.35). The pelitic and carbonate-clastic rock categories mirror the granitic grade distribution. The Ida Dome 2 000 - 4 000 ppm U category accounts for 2.5 % of all samples and 100 - 200 ppm U samples represent 59 % of all samples. The 2 000 - 4 000 ppm samples also show an

abrupt increase in frequency from the consistent decline in sample frequencies with increasing grade.

The grade distribution in granites essentially represents three categories of uranium mineralisation in granites, representing the relative proportions of; primary uranium concentration in granite, the uranium-depleted granites, and the concentration of uranium-enhanced granites. The latter two categories essentially represent leucogranites that have had uranium leached, or had uranium added by a sub-solidus process. Such a process would be by late magmatic fluid circulation through the system during initial deposit formation.

Sixty five percent of the uranium grade in the alaskite rock at Husab fall within the 100 - 500 ppm category; twenty eight percent in the 500 ppm to 2 000 ppm categories; and two percent of uranium grades in the 0.5- to 4.0 % grade category. The high-grade cluster between 2 000- and 4 000 ppm U, which comprises 14 % of all assays may represent the highest grades that can be expected in leucogranites at the Husab deposits, while the exceptional 2 % of samples with 0.5 - 4 wt. % U and those below 2 000 ppm representing enhanced and average uranium grades, respectively[28].

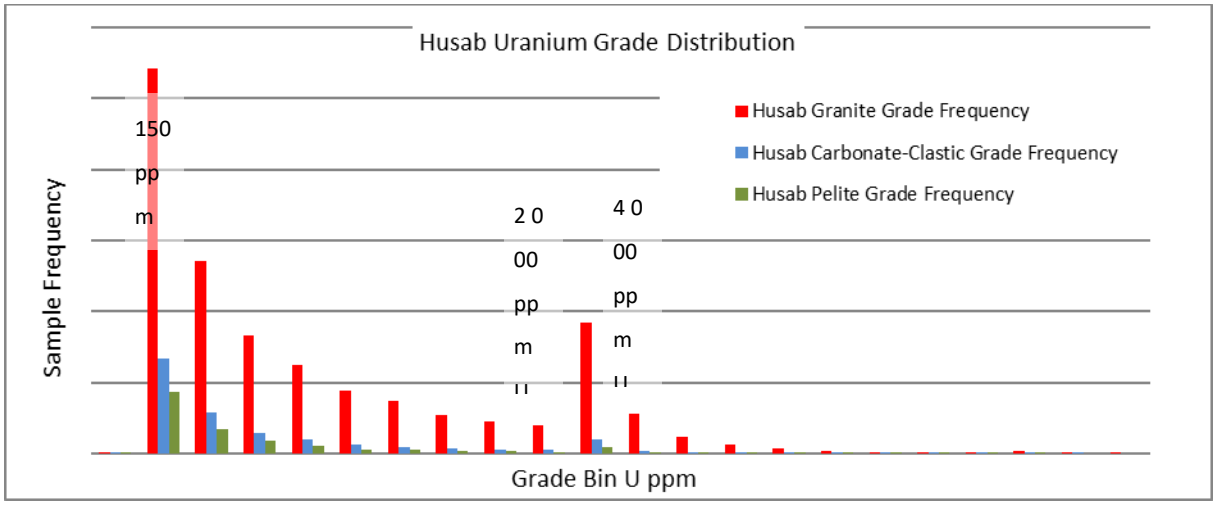



Figure 3.35 Uranium distributions in the three main categories of rock type at the Husab deposits. Uranium in granitic rocks appears to have a bimodal distribution, which may represent the average grade in the lower cluster, and perhaps the highest possible un-enhanced, granite-hosted grades in the upper 2 000- 4 000 ppm U cluster. The cut-off at the low end is 150 ppm, but for confidentiality purposes the grade distribution can only be delivered qualitatively.

[28] This data represents a portion of the Husab deposits and does not represent the whole. It is advised that this be treated as indicated trends rather than a representation of the published 2011 resource update.

*Husab Uranium Minerals*

Swakop Uranium commissioned ANSTO Minerals of Australia and Guy Freemantle of the University of the Witwatersrand to identify and quantify uranium minerals and U-deportment in selected samples, in 2009. The studies identified uraninite as the primary host phase of uranium at the Husab deposit, as well as brannerite being the dominant refractory U-phase in an extensive metallurgical study. Extract Resources commissioned a mineralogical study by Guy Freemantle in early 2011 to improve the understanding of the distribution of the refractory minerals at the Husab Deposit. This study found that uraninite and coffinite are the dominant uranium ore minerals (Freemantle, 2012). Locally, the mineral boltwoodite is the dominant $U^{6+}$ secondary phase. It occurs in fractures and along fault planes, as well as between sheets in large biotite books (Townend, 2009). Boltwoodite nests also occur in leached silicate cavities of altered granite, occasionally in metasediments and in cavities within late, crosscutting quartz-calcite veins that crosscut the deposits.

Uranium-bearing refractory minerals in Husab leucogranites include brannerite and betafite. Brannerite is the dominant refractory phase at the deposits, and locally hosts up to 40 wt.% of the uranium budget in Zone 1 (Freemantle, 2011 and Johnson, 2011). In comparison, the Rössing SH and SK deposits are dominated by betafite (Herd, 1996; Nex *et al.*, 2003; and Abraham, 2009). Quantifying the distribution of refractory minerals is an ongoing investigation for the mine owners, and indications are that the uranium-bearing refractory minerals occur within leucogranites that invade the upper unit of the Rössing succession.

The RDD373 drill hole provides all the samples for this study, where five discrete leucogranite dykes host brannerite and betafite, along with uraninite and coffinite. The Rössing succession contains upper and lower carbonates and a collection of pelitic gneiss and schist units (Figure 3.36). The sequence resembles the lower Swakop Group succession described at the Rössing mine in Anderson and Nash (1997).

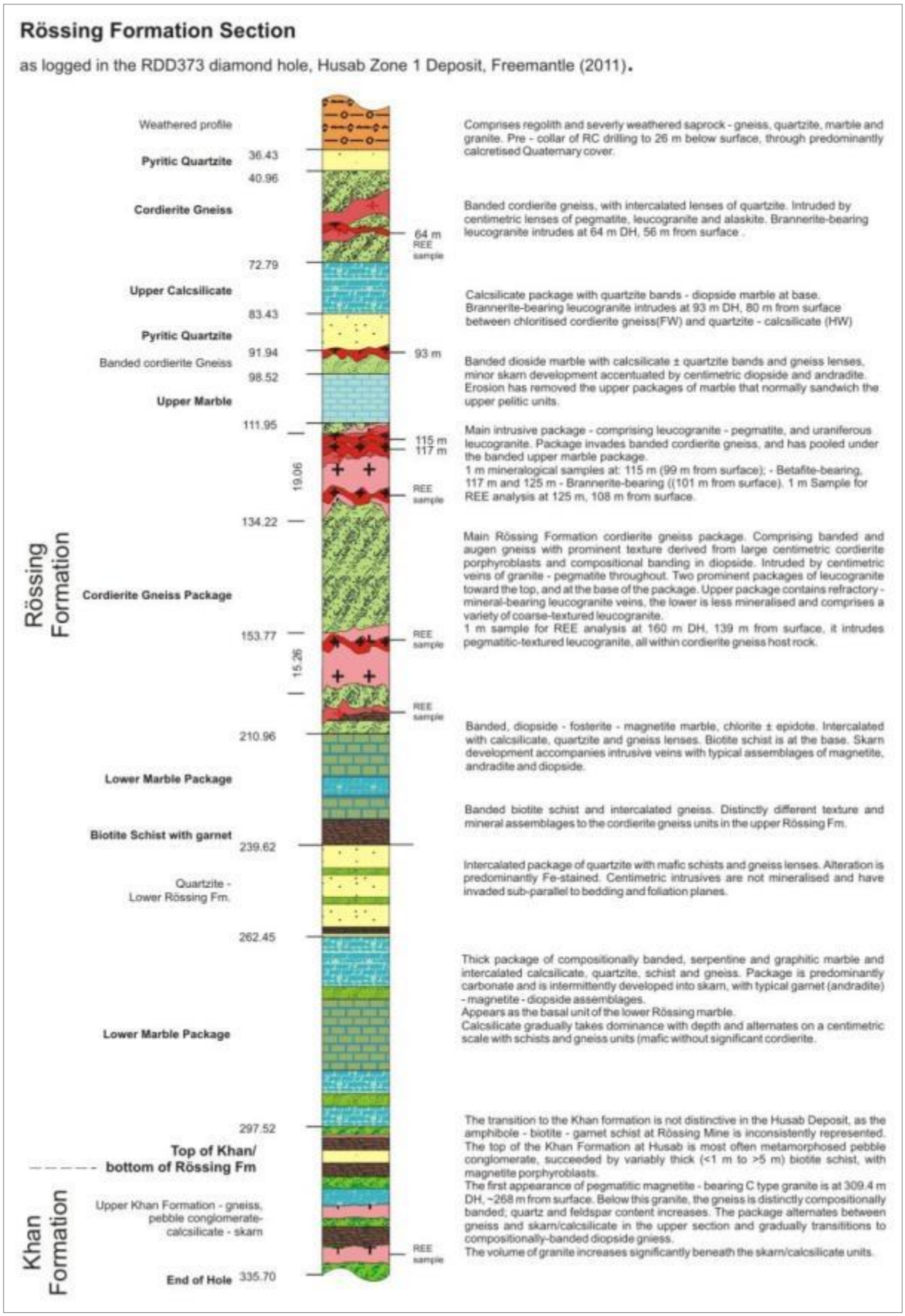



Figure 3.36 Simplified stratigraphic log of a portion of RDD373. Refractory - bearing alaskites are included in the section, with thicknesses approximately to scale. DH = down hole (bore -60°/270°).

The detailed description of samples from drill hole RDD373 provides the basis for uranium mineral speciation studies and discussion in Chapter 7 and Chapter 8 of this thesis. In summary, the 330-m deep RDD373 hole comprises the following key elements from top to bottom and summarises the general geological profile of the Zone 1 deposit, and to a certain extent, Zone 2:

- Cordierite gneiss and a banded-textured pelitic gneiss (garnet, cordierite) above the upper marble;
- An upper diopside marble;
- Banded gneiss below the upper marble;
- Intercalated gneiss, calcsilicate, schist and quartzite;
- Lower banded marble;
- A calcsilicate and quartzite package at the top of the Khan Formation;
- 7 packages of variably mineralised uraniferous sheeted leucogranites and leucogranites; and
- 5 packages containing discrete intervals of refractory uranium-bearing uraniferous sheeted leucogranite.

## 3.10 The Valencia Deposits

### *Introduction*

The Valencia Deposit of the southern Central Zone is situated 55 km west of Arandis by road and 27 km northeast of the Rössing uranium mine via the Khan River. The deposit covers an area of ~8.5 $km^2$ and lies within the boundaries of Farm Valencia 122.

Uranium mineralisation is hosted in sheeted leucogranites that have coalesced to form a stock-like body in a secondary fold structure on one of the limbs of the regional-scale Khan Syncline, ~7 km east of the Khan River Valley. Norassa Corporation (formerly Valencia Uranium) holds mining licence ML149 which was issued in August 2008, the Valencia deposit, the Namibplaas deposit, and a satellite deposit to the Valencia ore body were previously located within EPL 1493 and EPL 3638 (Namibplaas). The Namibplaas deposit used to be the Joly Zone before 2013, this study retains the Joly Zone naming. '

The Trekkopje Exploration and Mining Company (Pty) Ltd (Trekkopje Exploration) (Greenway, 2007) undertook the first significant exploration of the uranium mineralisation at Valencia. It was a subsidiary of Goldfields Namibia, between 1973 and 1977 and Bertram (1982b) provides further records of ownership up until July 1982. Prior to private field exploration activities, the South African Government flew an airborne radiometric survey in 1968, followed by a drilling and mapping programme with chemical analyses of selected surface and drill samples.

A bulk sample test was undertaken in 1979, followed by a renewal of exploration in 1988 (Department of Economic Affairs, 1988) and feasibility studies in 1989. The Tsumeb Corporation Limited (TCL) acquired a mineral deposit retention licence in 1994, which was later turned over to Ongopolo Mining Limited in 2000.

The Tsumeb Exploration Company Limited (TECO) acquired a retention licence in 2005, which it converted to an exclusive prospecting licence (EPL1496). TECO became Valencia Uranium Limited in November 2007 and successfully applied for a mining licence in 2008. The Valencia deposit amalgamated in 2012 with newly discovered anomalies within the mine licence area to become the newly formed Norassa Corporation, which owns the Norassa Project (Valencia- and Namibplaas deposits). Technical reports given in the Valencia 2009 Resource Update (Andrew, 2009) detail the results of the resource drill programmes Exploration and research projects have produced a number of maps for the Valencia Deposit and the information is compiled with more recent mapping and presented in the 1:4 000 geological map in Appendix C6.

Observations and interpretations made in Henry (1992) and De Kock (2001) provide details of the geological setting and history of the surrounding area. Henry (1992) presents the stratigraphic evolution of the Damara Orogen along the Khan River Valley, mostly west of Valencia, and De Kock (2001) reappraises the area from Usakos to the Windhoek Graben, essentially the area east of Valencia. Less-detailed accounts of the stratigraphic sequence at Valencia are also given in Labuschagne (1979) and Smith (1965).

The deposit area is the eastern- and northernmost of the deposits described in this study. The Nosib- and Swakop Group conglomerates and quartzites are similar to the units described in Smith (1965) near the Blauer Heinrich Syncline, and the stratigraphic range from Etusis to Kuiseb Formations characterise the deposit within the study group. Structurally it is

located on the northern side of the regional Khan syncline, as is the Rössing deposit, and is within the vicinity of the Usakos Horst described in Porada and Wittig (1983). The deposit occupies a secondary fold on the attenuated northern limb of the Khan syncline, while the overturned southern limb shows less-intense deformation (Figure 3.37a).

Figure 3.37b is an oblique, northeast-directed view of the deposit area; with portions of the colour-shaded geological boundaries taken from Smith (1965); Henry (1992); Rösener and Schreuder (1994); and undisclosed historical company reports. The overlay was produced for this study from field mapping during 2007 to 2009.

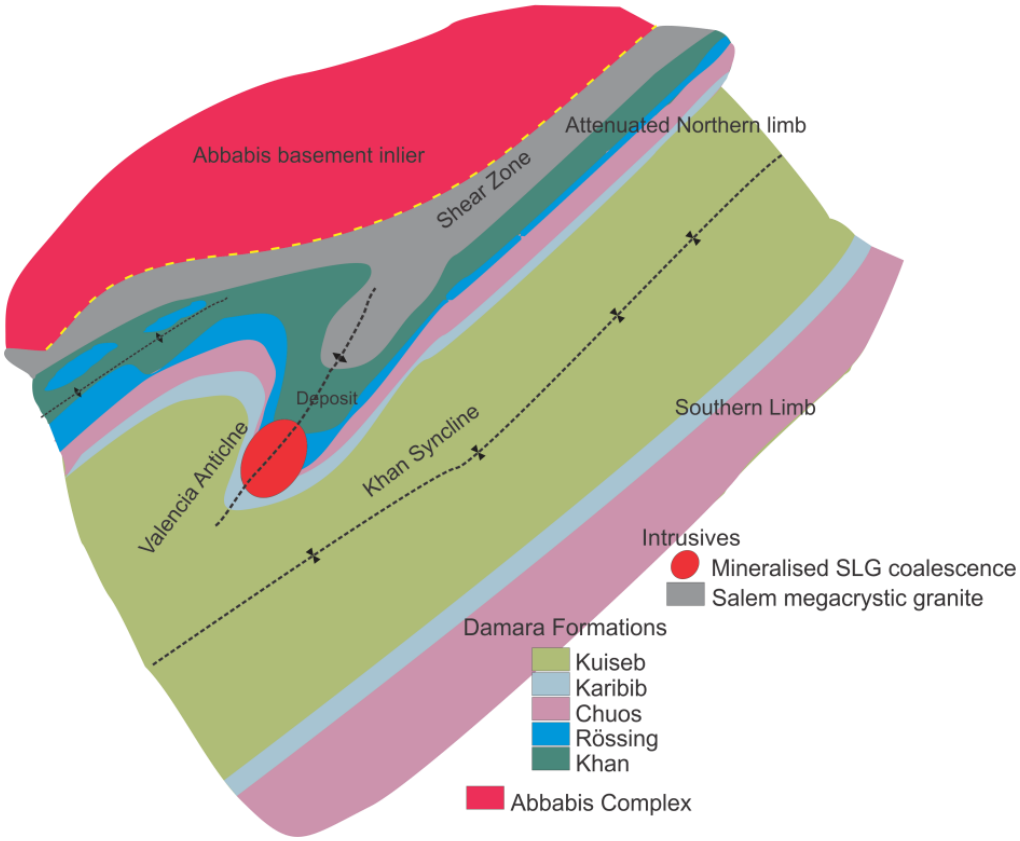



Figure 3.37a Schematic section of the Khan Syncline and its relationship with the Valencia Deposit.The syncline is a regional scale fold with a core of refolded Kuiseb schists. The fold hinge trends NE-SW. The synform is refolded south of the Rössing deposit (southeast of the Blauer Heinrich Syncline) where the hinge trend changes to roughly N-S. The eastern limb of the syncline at Valencia is attenuated and a secondary fold has played a role in focussing the mineralised intrusives in a saddle-reef style.

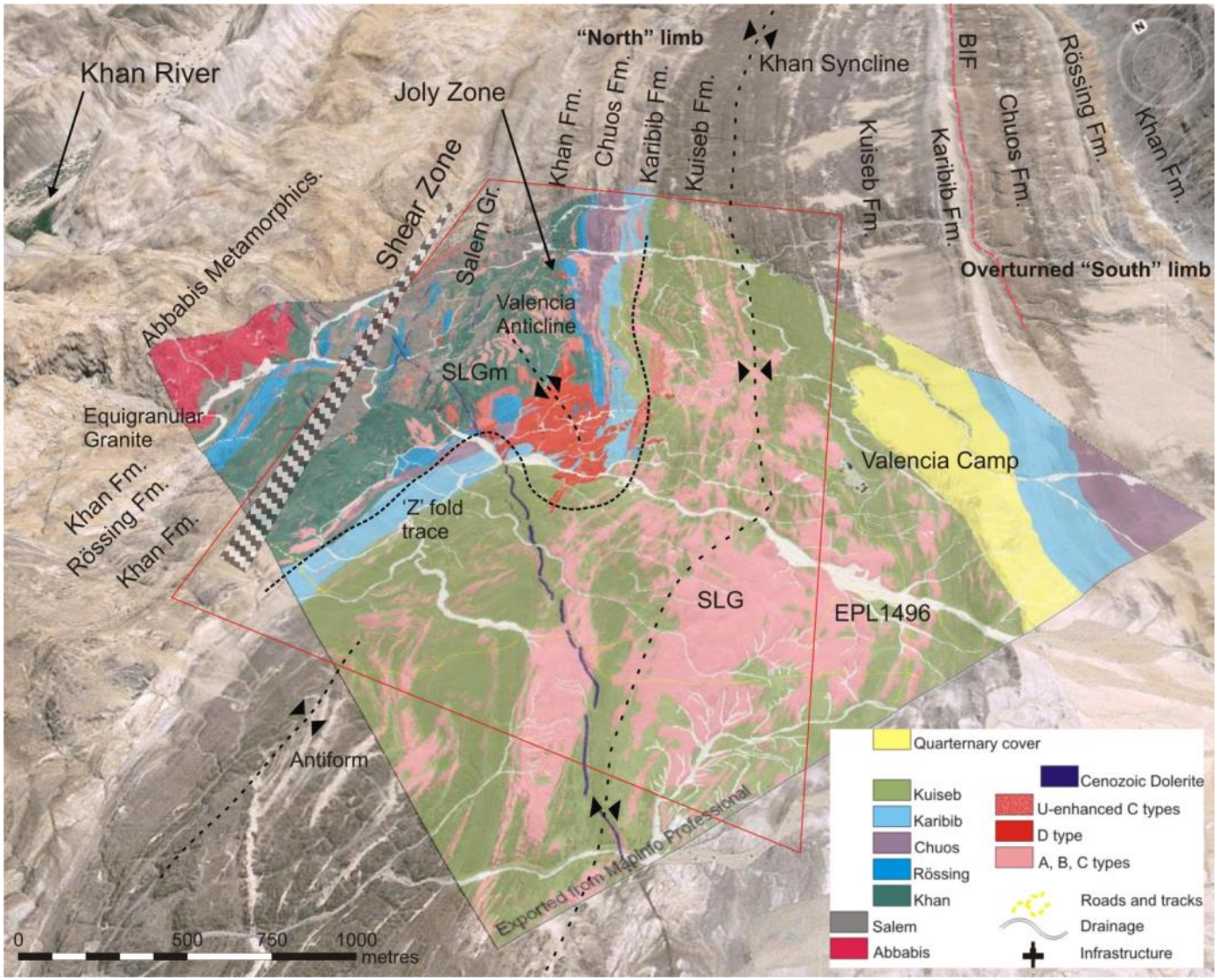



Figure 3.37b Geological map draped over an oblique-view satellite image of the Valencia area. The viewing direction is oriented parallel to the axial trace of the Khan Syncline. The deposit occurs where an area of structural disturbance has resulted in a number of secondary folds on the limbs of the main syncline. Note also, that a repeated sequence of Khan and Rössing Formation occurs adjacent to the Abbabis inlier, on the western side where the sequence is overturned and mirrors the east. Conjugate shear bands and mylonite occur in the lower Nosib units adjacent to the basement inlier. The Khanberge is located to the east of the deposit (top right of figure) and consists almost entirely of Khan Formation metasediments. The underlying remote sensing is 2 m resolution SPOT imagery sourced from Google Earth. A full-size map is presented in Appendix C5.

### *Valencia Stratigraphy*

Mapping of the Valencia deposit area describes the most complete Damaran stratigraphy of the deposits in the study region of this study. It includes well-defined boundaries between the Etusis-, Khan-, Rössing-, Chuos-, Karibib- and Kuiseb Formations. The major regional Khan syncline has affected stratigraphic thicknesses on the north-, and overturned, south limbs. The image in Figure 3.38 summarises the stratigraphic sequence on the northern limb, the photograph is taken on the northern limb looking southwest toward the main ore body at the Valencia deposit.

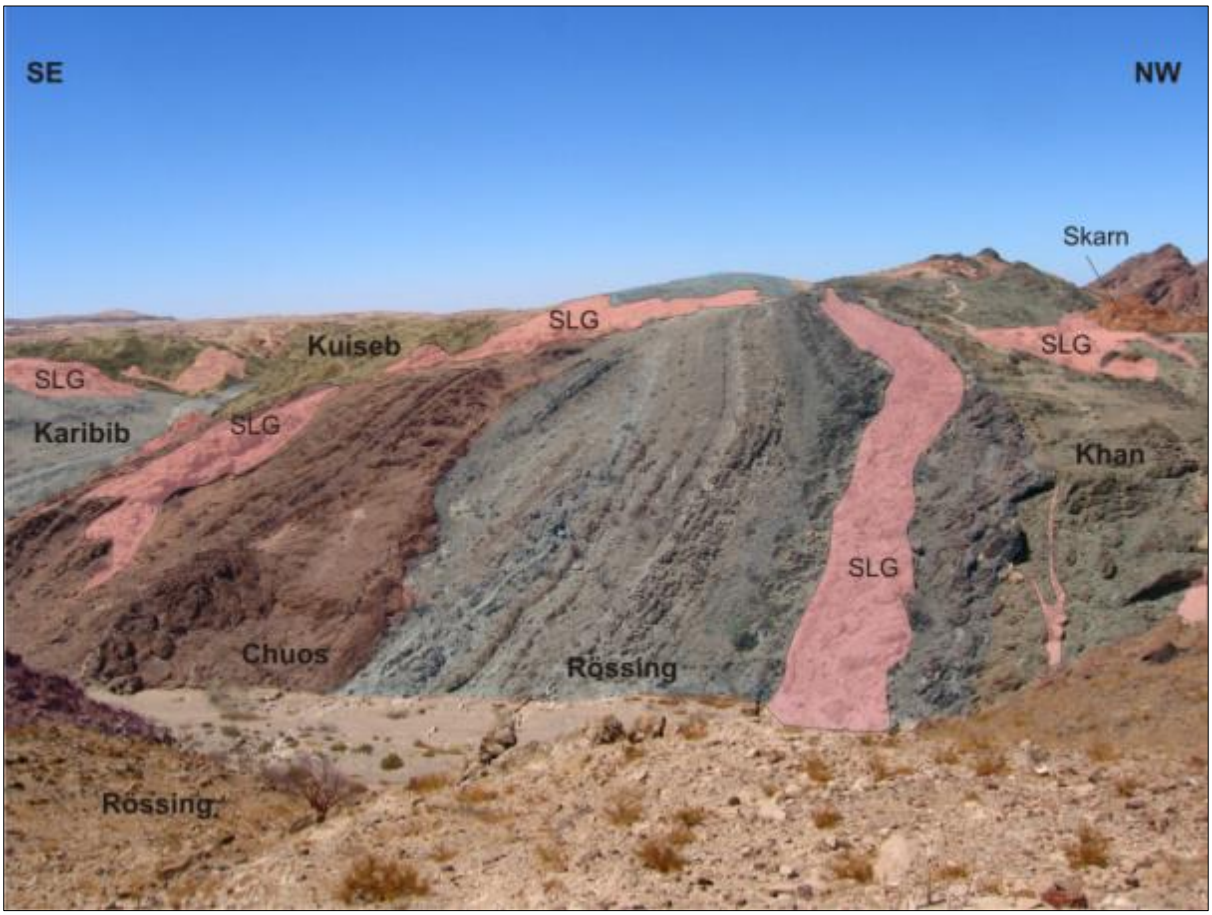



Figure 3.38 The Valencia stratigraphic succession, looking southwest. The northern limb of a regional scale synform contains narrow slivers of Etusis mylonite, and Damara Succession units from diopside gneisses of the Khan through cordierite-garnet schists of the Kuiseb Formation. SLG - sheeted leucogranite.

The lowermost Damara metasediment present at Valencia is the Etusis Formation, which forms the cross-bedded quartzites of the Khanberge Hills on the overturned southern limb

of the Khan Syncline, and is a sporadically distributed as attenuated lenses, some of which of mylonite in high-strain portions of the north limb. Prominent magnetite occurs along fore-sets in the cross-bedded quartzite of the south limb, and defines $S_1$ in the north limb exposures of the unit (Figure 3.39a).

The Khan Formation metasediments are typically dark grey-blue- to green-coloured banded gneiss, which are increasingly calcareous upwards, diopside defines prominent compositional bands on the northern limb exposures. Magnetite, diopside and titanite porphyroblasts have developed in the more deformed units. Partial-melt bands, particularly shear-associated types, and leucosomes occur adjacent to granite intrusions, which are most abundant on the north limb. The succession is considerably thicker on the south limb of the Khan syncline, and comprises well-preserved shallow water sediments that include conglomerates (Figure 3.39b) and quartzites

The Rössing Formation is discontinuous and attenuated on the north limb, forming 100 m-scale boudins along strike. It consists of at least two marble units separated by cordierite gneiss in a succession that is analogous to that near the Rössing Mine, as described by Nash (1971). On the overturned south limb of the syncline, the Rössing Formation is also attenuated, but considerably more continuous along strike and significantly thicker. The lower marble contains serpentine and has lenses of grey-coloured marble/limestone with a conglomerate at the base. The upper marble unit also contains serpentine and succeeds an intercalated schist and pelitic gneiss package, analogous to the lower pelitic sediments in the Rossing Mine succession. An upper quartzite is present on the south limb and forms the contact with the Chuos Formation. This upper sequence roughly equates to the upper Rössing package of Nash (1971) while the lower garnet-biotite granofels described in the Rössing Mine stratigraphy is largely absent at Valencia. Figure 3.39c illustrates a surface section of the Rössing Formation on the north limb of the Khan Syncline. This section is a >200 m long boudin that preserves the two distinct marble packages, intermediate cordierite gneiss, upper quartzite, and calcsilicate units.

The Chuos Formation is discontinuous along strike on the north limb and varies in thickness from <20 m to >50 m. The Chuos Formation comprises diamictite, pelitic units (shale and mudstones) and a distinct iron-shale formation at the top of the sequence. The

pelitic units on the north limb have developed metamorphic assemblages of garnet- and sillimanite-bearing schists. The diamictite contains larger and more rounded clasts than any observed at the Ida Dome, Rössing, Husab or Goanikontes deposits with the clast population comprising Nosib lithologies and Abbabis granite gneiss. On the more attenuated north limb clasts are deformed in a semi-pelitic schist matrix. Drop stones are visible continuously along strike on the south limb. Diamictite (Figure 3.39d) and iron shale in particular, are well preserved and relatively undeformed in the foothills to the Khanberge to the east of the deposit on the south limb of the Khan Syncline (inset in Figure 3.39c).

The Arandis Member is not present in the Valencia area; typically, it would occur below the cap carbonate of the Karibib Formation. Rather, there is an Fe-shale unit capping the Chuos Formation diamictite on the south limb, this unit is poorly preserved at other primary U deposits in the Central Zone and thus a characteristic feature of the Valencia deposit area.

The Karibib Formation is less than 75 m thick on the north limb, and is in two distinct packages of laminated dolomite-marble, with at least 20 m of finely laminated shale and meta-greywacke between. The Karibib Formation is significantly thicker (>150 m) in the foothills of the Khanberge, and the meta-greywacke between the dolomites (and marbles) is at least 50 m thick. The whole package forms prominent, continuous NE-SW parallel ridges. (Figure 3.39e) illustrates the SE-dipping marbles with the shale unit between them giving an erosion contrast. The Karibib marble and dolomite packages are prominent north and south of the mineralised body, however only remnants remain where granite has truncated the Damara Succession.

The Kuiseb Formation is the uppermost Formation within the Swakop Group at Valencia. It is comparatively thick due to its location within the core of the Khan Syncline. Bedding is highly transposed and is considerably less apparent than the compositional banding that biotite-, garnet-, and cordierite-dominant assemblages define, the southern flank of the fold core shows lithological- and compositional banding more distinctly than the attenuated and transposed norther portion which is nearer the basement inlier. The units comprise finely laminated shale/siltstone units, intercalated with pelitic schists with remnants of fine-grained mudstone and deep water sediments that give way entirely to porphyroblastic, cordierite ± garnet-bearing schist units from south to north (Figure 3.39f and 3.39g).


(a)
(b)
Khan Formation
Lower marble
Pelitic schist
Upper marble
Quartzite
Chuos Formation
(c)
(e)
(d)
(f)
(g)

Figure 3.39 Examples of Major Damaran Formations present at Valencia.*Previous page* (a) Cross bedding of Fe minerals in the Etusis Formation, foothills of the Khanberge, south limb of the Khan Syncline. (b) Conglomeratic unit in the Khan Formation on the south limb of the Khan Syncline. (c) View to the southwest of the Rössing Formation, between the Chuos and Khan Formations, dipping steeply to the southeast on the north limb of the Khan Syncline. Deposit-scale boudins have largely preserved the succession in 100 - 200 m long segments along strike. (d) A large granitic clast in undeformed Chuos diamictite at the foothills of the Khanberge to the south of the deposit. e) The upper marble package of the attenuated Karibib Formation on the north limb. The laminated shale separates upper and lower carbonate packages of the ~75 m thick Formation. (f) The distinctive surface texture of the cordierite schist that dominates the Kuiseb Formation at Valencia. (g) The Kuiseb at Valencia consists of laminated shale units and pelitic schists with well-developed biotite-wrapped cordierite porphyroblasts (hand specimen inset).

### *Structural Setting at Valencia*

The Khan syncline is a major regional structure which Smith (1965) showed to be recumbent south of the Rössing deposit, where the junction between the Khan-, Blauer Heinrich- and Welwitschia synclines occurs (map segment from Smith, 1965). The syncline is traceable northeastwards from the Rössing area, roughly parallel to the Khan River, to well-beyond Valencia where the vergence of top to the northwest upper Damara metasediments is described in detail around the Karibib Dome by Kisters *et al.* (2004). The axial trace strikes northeast southwest within a core of Kuiseb Formation schists, with the axial plane plunging steeper than -30° on a 110° to 130° direction. The overall orientation of the Khan Syncline axial plane at Valencia is estimated from $S_0$ dip angles of ~25° to 70° on 137°to 140.5° directions for the overturned south limb; and 50° to 80° $S_1/S_0$ dip angles on 137.5°to 164° dip directions for the deformed north limb metasediments[29].

Attenuation of lithologies is prominent on the north limb, although a near-complete sequence of Formations is still reasonably preserved. Toward the north and northwest of the Valencia deposit the Khan and Rössing Formations are in repeated sequence, as a result of tight folding against the irregular shaped basement inlier. The strike of the south limb changes to a southward direction toward the Valencia farmstead, and the metasediments disappear below the Quaternary cover.

[29] The $S_1$ and $S_0$ readings were taken on gneiss and schist units of the Kuiseb Formation, and gneiss, shale and quartzitic units of the Khan and Rössing Formations.

Evidence of early $D_1$ folding occurs in the Kuiseb Formation and although abundant cordierite and compositional banding overwhelms the original sedimentary bedding, there are finely laminated shale and mudstone units preserved at certain localities. These include bedding to axial planar cleavage intersections and limbless fold hinges, (Figure 3.40a) Original bedding is tightly folded and the limbs taper until they disappear from surface. The fold axes plunge 32° towards 030°. The intersection lineation ($S_2$) in Figure 3.40b plunges 10° toward 212°. The dominant fabric that overprints sheared Salem granites at the deposit are parallel to most fold axes and intersection lineation in the metasediments, indicating their early intrusion relative to the leucogranites.

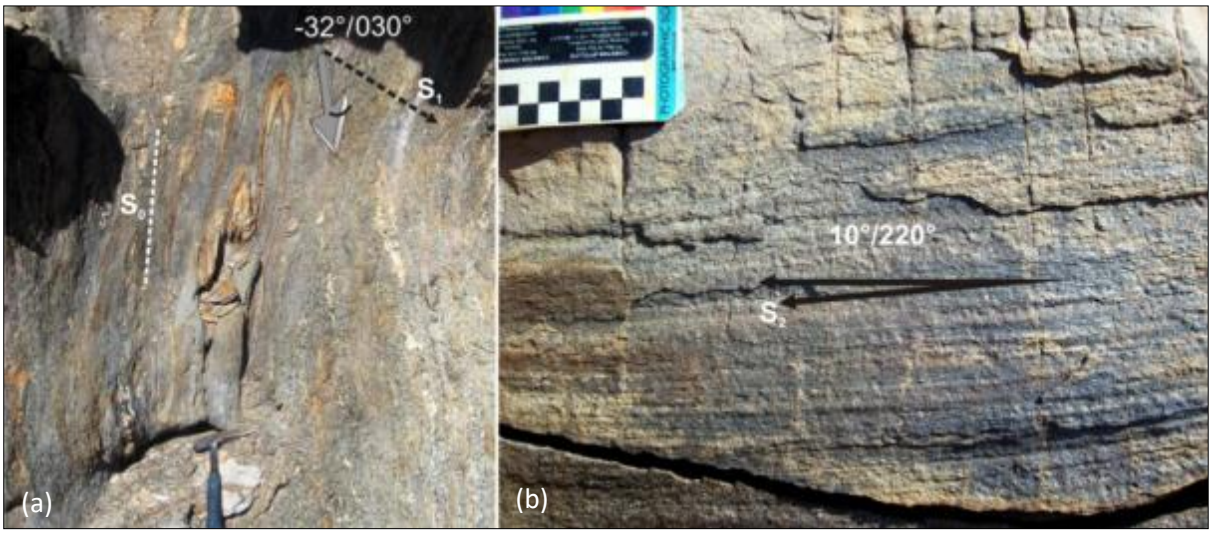



Figure 3.40 Bedding and fold hinge exposures at Valencia. Bedding ($S_0$)- Axial plane ($S_1$)- Intersection lineation (S2) relationships in the Kuiseb Formation east northeast of the main deposit, Valencia. (a) Limbless folds in the secondary fabric of transposed bedding ($S_1$) translate into well-developed $S_0$-$S_1$ intersection lineation ($S_2$) illustrated in (b).

The Khan- and Rössing Formations are locally duplicated by tight folding between the north limb of the Khan Syncline and the sheared contact with Abbabis basement to the north of the deposit. Shearing occurs along the length of the Damara-Abbabis unconformity and takes the form of prominent conjugate shear banding in the Salem megacrystic granites and as mylonite in the lower Nosib units. The orientation of shear bands in the Kuiseb Formation give a $\sigma_3$-estimation of the extensional direction, approximately -35° on 215°, coincident with the foliation in the megacrystic Salem granites at the basement contact. Figure 3.41 illustrates the prominent foliation that has developed. The inset shows a comparison to granite in a less deformed area near the deposit. The strain direction is roughly parallel to

pre-$D_3$ fold axes observed in the Kuiseb Formation (shown in Figure 3.40a). The orientations of structural features at two localities are presented in Appendix C7.

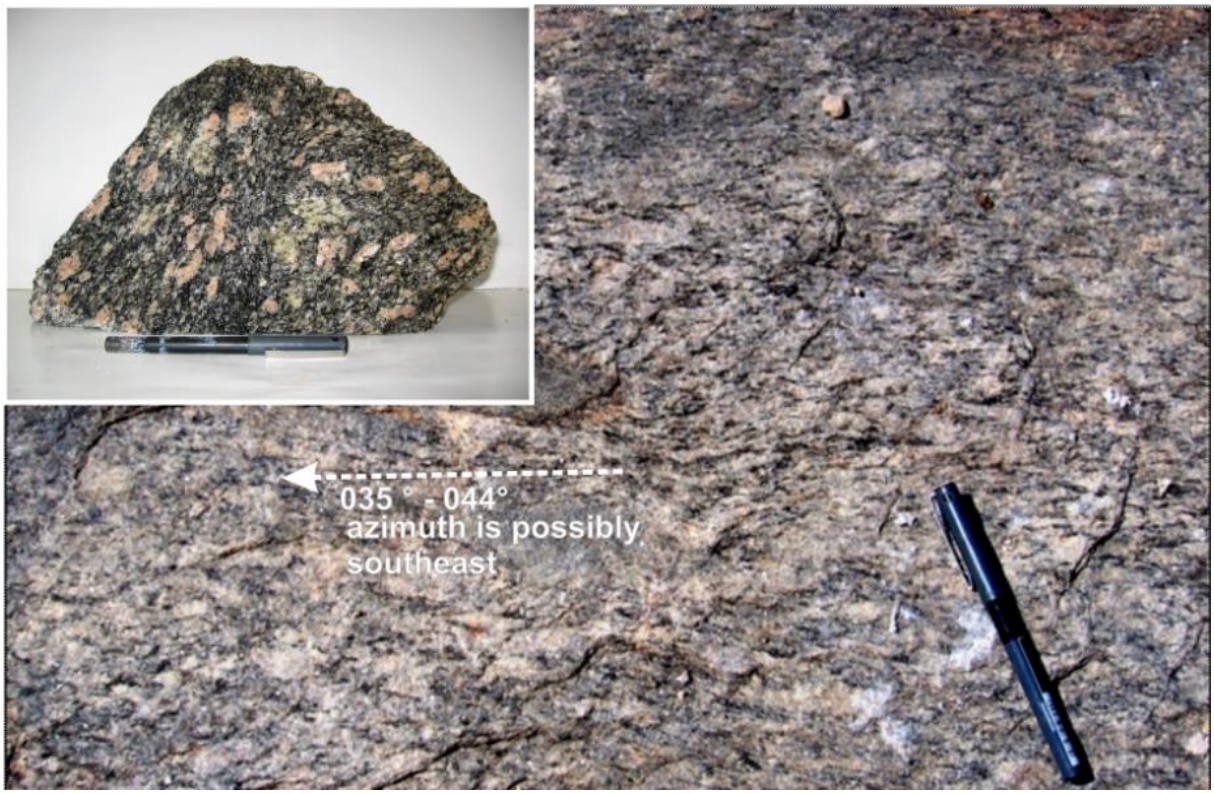



Figure 3.41 Photograph illustrating the deformation of megacrystic Salem monzogranite. The granite has acquired a gneissic texture. The fine-grained granite is of an older Salem diorite. The foliation is parallel to early, NW - SE fold axes in the nearby Kuiseb schists. The orientations of shear bands in the deformed Salem granite give a $\sigma_3$-direction of ~35° -44°/ 215° -224° which is roughly parallel to the SW extension direction elsewhere in the Central Zone (Miller, 1983b; Longridge, 2012 and references therein).

***Metamorphism***

Metamorphic assemblages and textures developed progressively in the Damara units toward the basement contact. In the Chuos Formation, garnet and cordierite porphyroblasts are abundant near to the ore deposit, and wrapped by biotite in a prominent shistose fabric, porphyroblasts become progressively less prominent northwards along strike, further from the main granitic intrusions. In the Kuiseb schists, the varying Al content has resulted in banding of cordierite, biotite and garnet. The minerals are aligned in a strong foliation and wrapped by fine (<1 mm) biotite. The well-developed cordierite porphyroblasts, increase in size from southeast to northwest across the hinge of the Khan Syncline, essentially reflecting an increasing local metamorphic gradient toward the basement contact. The amount of partial melt and the volume of invading leucogranite sheets and size of

cordierites increase and decrease systematically toward the deposit and toward the basement contact. The texture is aligned with $D_2$ metamorphism (Miller 1983a) and since the cordierite is wrapped around by the biotite the cordierite must have formed during or potentially before D2.

To the immediate northwest and west of the main deposit the Khan and Rössing Formation units occur in a folded, repeated sequence, with oblique shearing against the basement inlier best evident in the Khan and remnants of the Etusis (Figure 3.42). There is sillimanite-bearing schist and a quartz-rich mylonite (with magnetite rich layers) below the Khan which may represent remnant Etusis rocks or at least the base of the Khan Formation.

$D_2$ structures pre-date the bulk of the sheeted leucogranites, but post-date the diorites and megacrystic-textured Salem granites. The bulk of the uraniferous sheets invade pre-existing $D_3$ fold hinges, and transgress the stratigraphy via axial planar-parallel brittle structures. The most abundant evidence of contact metamorpshism occurs between the mineralised alksites and the upper Khan Formation, where skarns and magnetite porphyroblasts characterise the calcareous and psammitic units, respectively. The Rossing Formation, of course, hosts abundanct alaskites with interactive contacts occurring between the intrusives and the semi-pelitic, and calcareous units.

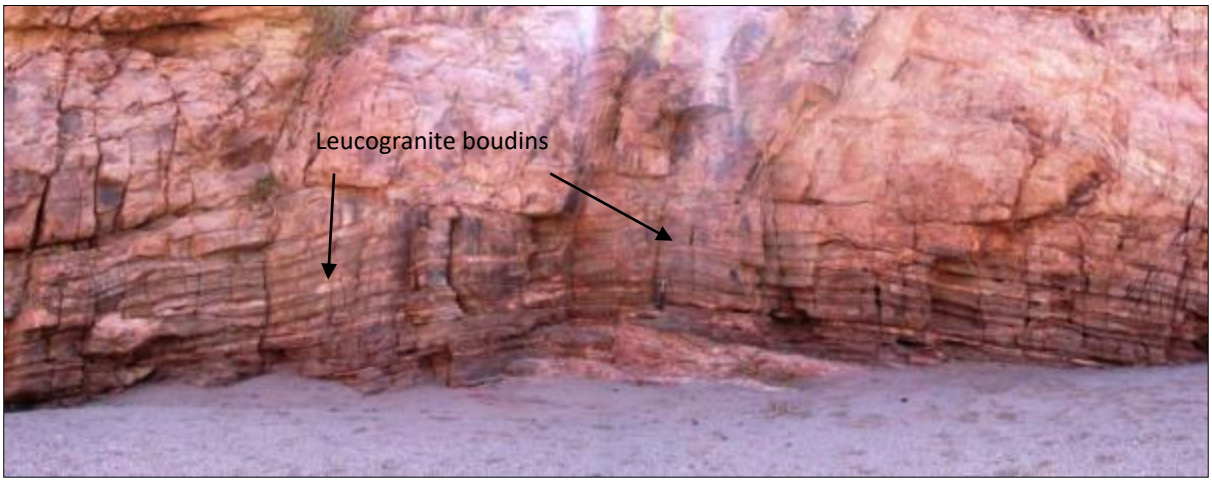



Figure 3.42 Migmatised Etusis Formation at the Valencia deposit. The location is northwest of the main deposit where the Nosib Group unconformably contacts the Abbabis inlier. The banding is predominantly compositional ($S_0$) while strain has developed boudins in leucogranite sills.

***Magmatism***

A large volume of megacrystic granite of the Salem Suite intrudes between- and into the basement lithologies and the overlying, folded and attenuated Nosib Group quartzites and gneisses, and into the Rössing Formation carbonate units. The Salem granites fit the descriptions of the Salem Suite described by Smith (1965); Jacob (1974) and in Miller (1983a, 2008). The megacrystic type intrudes (actually near completely engulfing) medium-grained, mafic-rich tonalite (possibly older granitoids of the same calc-alkaline suite). The granitoids occur, primarily, in folded (occasionally sheared) Khan Formation and within basement lithologies to the north and northeast of the mineralised body, but do not outcrop on the southern limb. The equigranular granite described at Valencia fits descriptions of McDermott (1986), McDermott *et al.* (1996), and McDermott *et al.* (2000) and Nex *et al.* (2001a and 2001b).

The leucogranites intrude synform- and antiform hinge zones in the repeated sequence and are themselves sheared and deformed to a gneissic texture between the Nosib Group - Abbabis basement contact north of the deposit. The area immediately around the uranium deposit consists of a variety of at least four generations of leucogranites in the surrounding, attenuated, Damara metasediments.

The sheeted leucogranite varieties at Valencia are similar to those in the Goanikontes area as described by Nex (1997). Sheeted leucogranites have coalesced into a stock-like body in saddle-reef type spaces in disharmonic Z-shaped fold hinges (Figure 3.37). The majority of these sheets are weakly mineralised or barren. They consistently show axial planar cleavage fractures and strong foliation and intruded prior to the folding event that produced the large ‘Z’ fold. There are five main leucogranite types (three pre-date the mineralised sheets, and one post-dates) and are named according to the established nomenclature (Nex, 1997) for the sheeted leucogranites:

1. A-type; accessory-free, folded with axial planar cleavages parallel to host sediments and with foliation.
2. Two textural varieties of garnetiferous B-type; one is foliated with local boudinage and the other is massive and pegmatitic, these varieties will be shown to be chemically distinguishable (Chapter 4).

3. Three C-types; an accessory-free variety (C) widespread but limited in local sheet size; massive, widespread tourmaline-bearing sheets ($C_t$); and less abundant, predominantly Khan Formation - hosted magnetite-bearing sheets ($C_m$).
4. Uraniferous sheeted leucogranites (D-type) are typically black (smoky quartz) and white in colour with variable biotite content. A relatively homogeneous but coarse grain size loosely characterises the Valencia mineralised sheets.
5. A brick red F-type, or late pegmatite; K-feldspar dominated with characteristic milky white quartz.

***Mineralisation***

The upper Khan and Rössing Formations host low grade Cu-sulphide bearing carbonate and gneiss units that were worked in the mid- 1900's at the abandoned Kainkaghas Mine. These deposits are similar to those at the Ida- and Khan mines to the south and southwest, respectively. Most uranium mineralisation occurs stratigraphically near the Khan- Rössing Formation transition, and minor covellite and secondary copper-carbonates are clearly visible in hand specimen.

The main uranium ore deposit is situated about 500 m south of the contact between the Salem granite and the basement inlier on the northern limb of the Khan Syncline. Mineralisation is concentrated in granites that intrude through the Nosib and lower Swakop rocks and into the lower Kuiseb schists. The sheets have exploited preferred pathways created by $D_2$ and $D_3$ folding and have coalesced in the antiformal hinge zone of a 1 km-wavelength 'Z' fold on the north limb of the Khan Syncline.

The Salem megacrystic granite envelops 100 m-scale segments of Khan and Rössing Formation toward the north and northwest of the Valencia deposit, and invade up and into the lower Swakop Group at the Joly Zone (now Namibplaas deposit). Where the megacrystic Salem granites have overwhelmed the calcareous units of the Khan and Rössing Formations, metre-scale slivers of wollastonite-scapolite-garnet ± magnetite skarn have developed in a similar style to those at Holland's Dome, Garnet Valley and localities near the Khan Mine site southwest of Rössing. Pegmatitic leucogranite veins that invade the Salem granite

where Rössing metasediments are present contain appreciable scintillometer counts and were the basis for the Joly Zone exploration program.

Competency contrasts between the Rössing marbles and the highly attenuated Chuos and the Karibib Formations in this tightly folded area have created the necessary space for the intrusions and the fold structure is accentuated by the swarm of bedding-parallel SLGs in the Kuiseb Formation (Figure 3.43). In 2007 a radiometric showing of mineralisation about 500 m northwest of the main mineralised body was investigated and named the Joly Zone during follow-up prospecting activities. It is hosted in leucogranite veins and Salem type granites that have invaded the Khan- and Rössing Formation metasediments.

The main lithology is megacrystic Salem Suite granite, which envelops >10 to 100 m scale laths of metasediment, and is in turn invaded by leucogranite sheets. The mineralisation is in pink-coloured apophasis of leucogranite distributed sporadically throughout a narrow band that follows the NE-SW trend of the rafts and slivers of Khan and Rössing Formation, hosted within the mass of Salem granite. The target was drilled and modelled between 2009 and 2013 and is referred to as the Namibplaas deposit

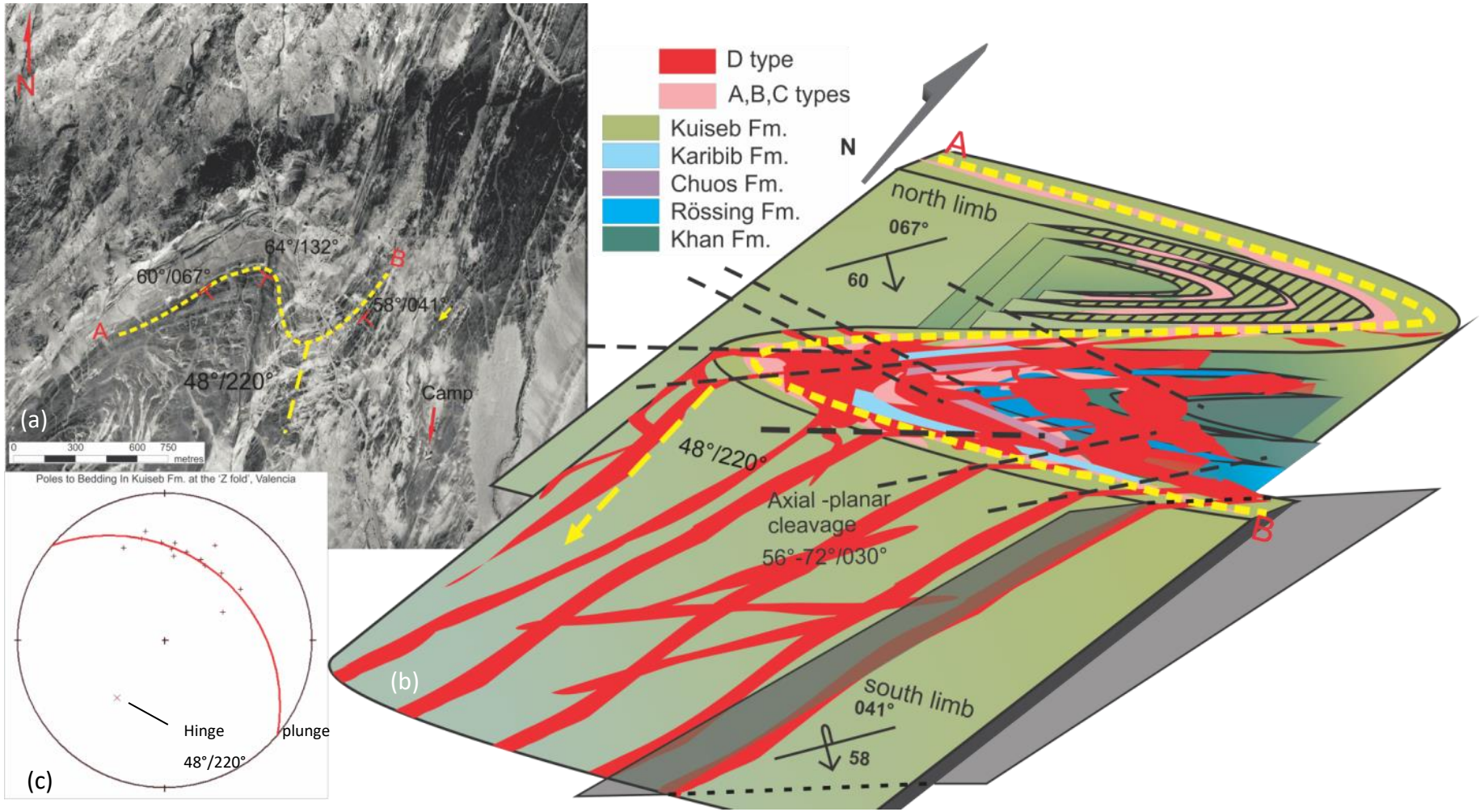



Figure 3.43 Schematic diagram of the large 'Z' folds into which the majority of mineralised granite has intruded. (a) The attenuation of the Rössing- and Karibib Formation marble units and the axial planar-parallel structures in the Chuos and the Khan Formation pelitic units has allowed the leucogranite sheets to invade up to the Kuiseb Formation. (b) Disharmonic folding has duplicated the Kuiseb and created voids at the antiformal hinge into which granite has coalesced in a saddle reef fashion. (c) Structural data in Appendix C7 quantifies fold hinge line orientation. The ortho-photo is courtesy of Valencia Uranium Namibia Ltd.

## 3.11 Field Relationships of granite populations at the primary deposits

### *Salem Suite*

The sample suite includes two Salem granite generations; the oldest Salem variety at Valencia is dark grey, medium-grained and homogenous-textured with a prominent foliation, emphasised by the high percentage of biotite and fits the quartz-diorite description given in Miller (1983a). The younger variety is distinguishable by its prominent megacrystic texture, highlighted by pink or white K-feldspar crystals up to 55 mm long, with biotite the main mafic mineral, in distinctly lower abundance than in the older variety. There is a clear contrast in the degree of mafic-felsic segregation in the more leucocratic younger Salem granite. Figure 3.44 illustrates hand specimen and field relationships.

The older variety occurs as minor intrusions into the Khan Formation to the north of the mineralised sheets and in the Joly Zone to the northeast of the main ore body. It also occurs as xenoliths within the younger megacrystic varieties. Sigmoidal quartz-feldspar leucosomes, oblique to the main fabric, have developed from dilation during shearing (Figure 3.44a). These tension features are present at most localities along the basement-lower Nosib contact zone and have their long axes perpendicular to $\sigma_3$ (indicated locally in a pervasive NE-SW fabric). The younger generation of Salem granites are distinctive by the abundance of pink or white K-feldspar crystals. Certain locations north of the main ore body expose NE-SW oriented xenoliths of Rössing Formation metasediments, the orientation suggest passive intrusion that largely preserved the orientation of $S_1/S_0$. Veinlets/apophasis of quartz- K-feldspar that intrude within proximity to- and crosscutting the xenoliths contain appreciable concentration of uranium. The apophyses is a local example of uranium deposition related to granite-Rössing Formation interaction.

The Salem granites in the Valencia area have a distinctive texture, the megacrysts may exceed 50 mm - 60 mm in size; thus, petrographic observation (described in Chapter 4) has focussed on the matrix component. Figure 3.44b illustrates afield exposure with quartz- K-feldspar melt apophasis and Figure 3.44c gives detail of the distinctive megacrystic texture. Shearing has occurred within the lower Khan Formation and within the megacrystic granite, and gives a relative timing of the Salem to be at least pre-$D_2$. The resultant banded gneiss is

locally radioactive, where Th-rich K-feldspar melts form. Figure 3.44d illustrates a >220 ppm Th sample). The shear zone is characterised by distinctive augen-gneiss textures with prominent conjugate shear-bands (Figure 3.44e).

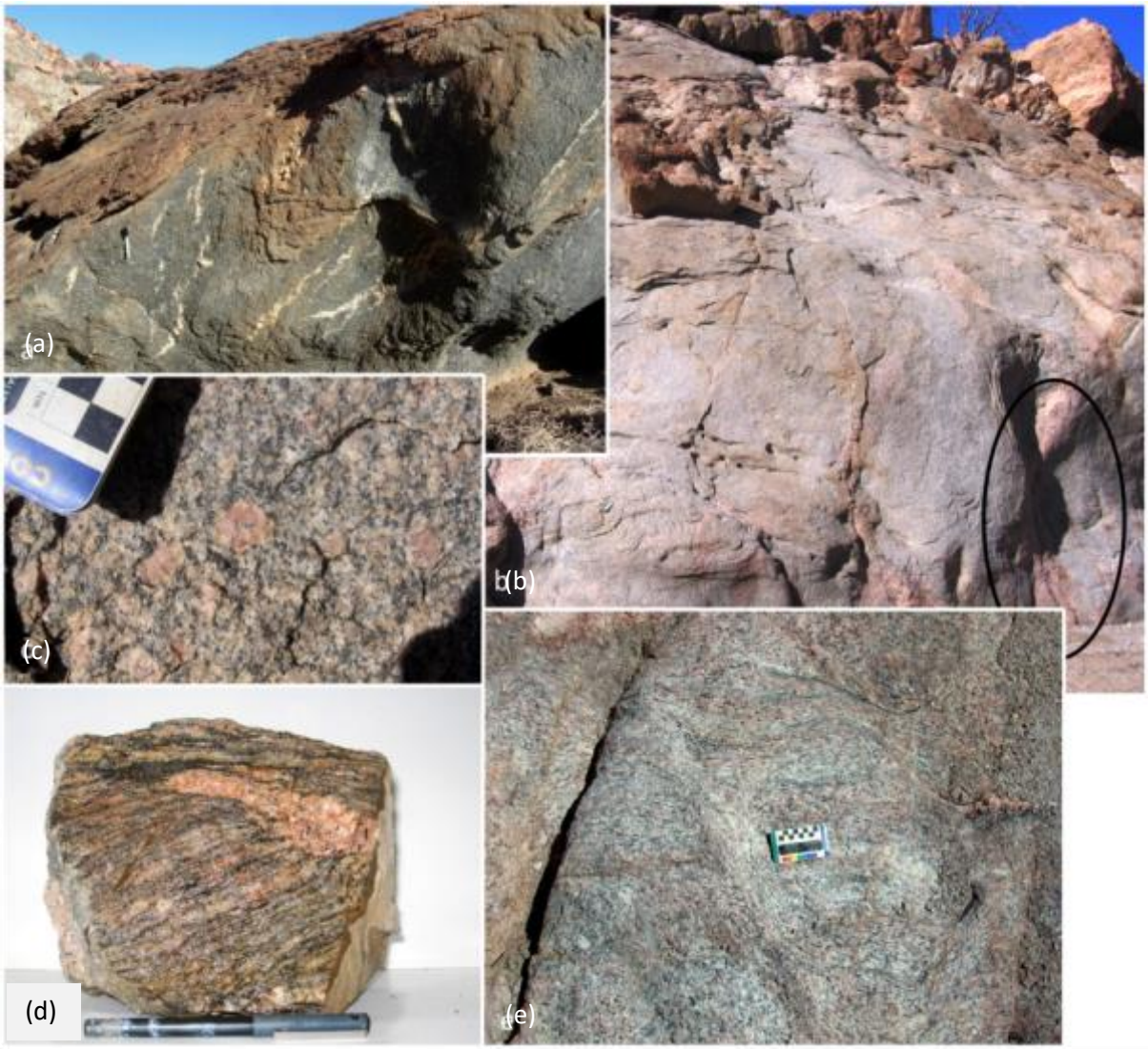



Figure 3.44 Salem Suite granites at Valencia. (a) The first generation of Salem-type granite is characterised by high biotite content and strong foliation. Subsequent quartz-feldspar leucosomes developed sub-parallel to the foliation. Position 524549E 7530330N. (b and c) Salem type-2 with characteristic K-feldspar megacrysts, U-mineralised melt apophyses, circled in (b). Position: 524002E 7528840N. (d) Partial melt vein oblique to foliation in Salem type-2, the sample in picture has elevated U concentrations. Position: 523092E 7530183N. (e) Conjugate shear bands in Salem type-2, the megacrystic granite has been strained to the extent that it has an augen gneiss texture. Note that some of the shear bands are oblique to the gneissic texture. The partial melts tend to have elevated U values. Position: 523113E 7530125N.

### *Grey Granites*

The oldest generations of grey granite are diorite in appearance and labelled as type-1 at all the deposits where examples are observed. Ages published by Longridge *et al* (2009) for Grey granites predate the leucogranites at ~520 Ma. They are foliated, homogeneous in texture with a strong fabric in biotite and the youngest is the most leucocratic with, fine-grained biotite (<1 mm) oriented in a fabric and occur at the Hildenhof and Ida Dome deposits in limited exposure (Figure 3.45a). An intermediate generation of Grey granite is porphyritic in texture with a slightly coarser grain size than the older and younger generations, and is characterised by ≤1 cm feldspar megacrysts. The younger generation occurs in less abundance and intrudes the older Grey granites. The youngest Grey granite is subsequently intruded by-, or incorporated as xenoliths within some sheeted leucogranites. Figure 3.45b illustrates dark Grey generation 1 xenoliths within a mass of porphyritic-textured second generation Grey granite, which is in turn intruded by veins of third generation, leucocratic Grey granite.

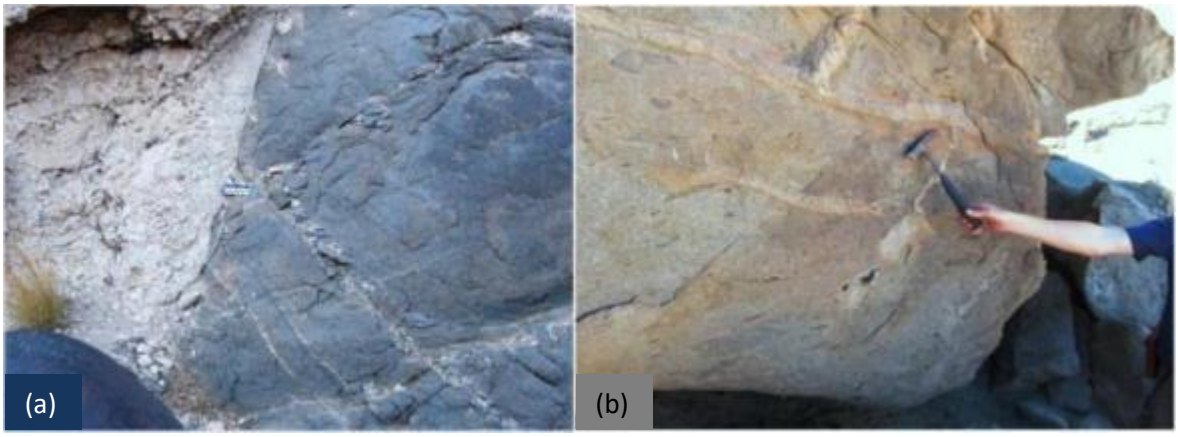



Figure 3.45 Grey granites at Hildenhof. (a) The type-1 Grey granite is melanocratic, foliated, medium to fine-grained and intruded by pre $D_3$ sheeted leucogranite. (b) The type-2 Grey granite contains less biotite than the type-1 and is characterised by megacrysts of K-feldspar. Thin veins of type-3 Grey granite frequently crosscut the type-1 and type-2 Grey granites. Position: 489345E 7490052N.

There are at least three generations of Grey granite intruding Nosib Group metasediments close to the basement contact at the Ida Dome. These granites exhibit crosscutting relationships that clearly illustrate age relationships between all three varieties; the porphyritic type-2 hosts xenoliths of the melanocratic type-1 (illustrated in Figure 3.46a).

The youngest generation (leucocratic Grey granite) is the only variety of significant proportion in proximity to a mineralised area and therefore sampled from Holland's Dome for geochemical comparisons. The youngest Grey granites at the Ida Dome are fine-grained, usually aplitic in texture with a subtle fabric defined by a low percentage of biotite. Xenoliths of this leucocratic Grey granite occur within the massive swarm of C-type sheets that have invaded the Holland's Dome antiform. The contacts are often characterised by oxidised staining and entrainment of biotite, in the sheeted leucogranite margins, from the aplitic Grey granite (Figure 3.46b).

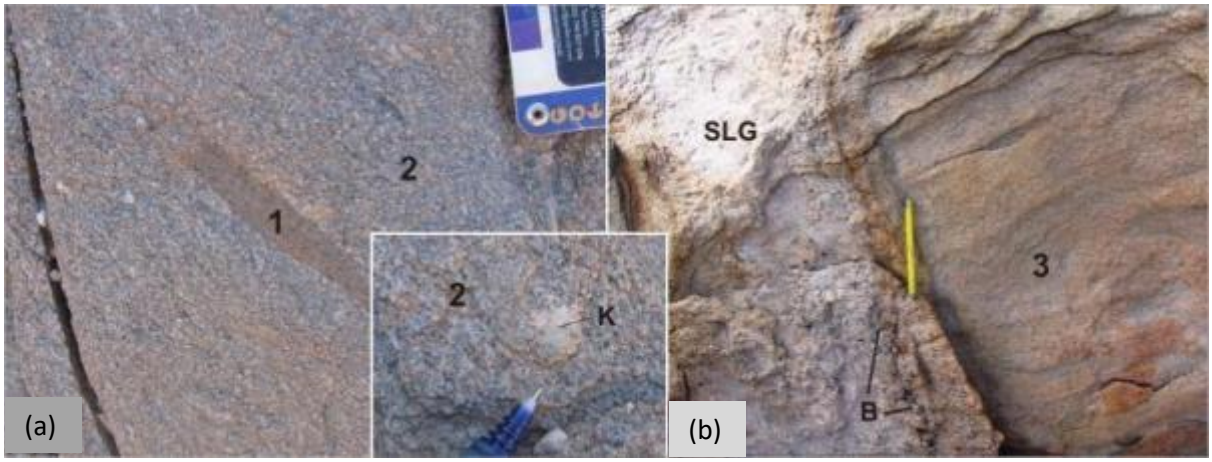



Figure 3.46 Grey granite varieties at the Ida Dome. (a) The type-1 and type-2 Grey granites found near the core of the exposed dome illustrate the contrast in mafic content between the older grey type-1 (1) xenolith and the porphyritic lighter grey type-2 (2). Inset: Large K–feldspar porphyroblasts (occasionally megacrysts) are characteristic of the type-2. Position: 502247E 7486268N. (b) The type-3 Grey granite occurs as xenoliths in sheeted leucogranites, where biotite and oxidation stains characterise the contacts. Position: 501907E 7482058N.

## 3.12 Sheeted leucogranites

The sheeted leucogranite suites of the deposits presented in this study represent a period of late-stage, episodic granite intrusion, which was strongly controlled by pre-existing structural features that formed during the protracted deformation periods of the orogen.

All of the leucogranites intrude the Nosib and lower Swakop Group metasediments, and more rarely, such as at Valencia and the Husab deposits, leucogranites have intruded into the Kuiseb Formation. Throughout the region, anomalously uraniferous pegmatitic granite

dykes and sills invade the Abbabis metamorphic inliers and dome structures near the primary uranium deposits, with their relationship to Damaran deformation events being less apparent. In addition to the regional litho-stratigraphic and structural consistencies, colour, textural, and accessory mineral assemblage variation is more-or-less predictable for the leucogranite suites, which appear to be closely reated to the stratigraphy. This section gives detailed accounts of the leucogranite varieties observed at the Etango, Hildenhof, Husab, Ida Dome area and Valencia deposits.

### *A- and B-Type Sheeted Leucogranites*

The A and B-type sheeted leucogranites are defined in this study as sheets that exhibit at least one of the following features: tight, upright and recumbent folding, limbless hinges, crosscut by axial-planar cleavages that transgress metasediment–leucogranite contacts, pinch and swell, and strong foliation parallel to $S_1/S_2$ in the metasediments.

The Hildenhof A-type sheets are discontinuous, folded (Figure 3.47a), and are cross cut by the larger B- and C-type sheets. They are predominantly sub-parallel to bedding. The B-type sheets are also discontinuous, but do appear to cross cut at least one phase of deformation, Figure 3.47b illustrates a sheeted leucogranite crosscutting folded bedding planes in deformed Chuos Formation diamictite.

A-type sheeted leucogranites at Valencia are narrow, usually less than 1 m wide, pale cream to white, strongly foliated, predominantly folded parallel to $S_0$ and show boudinage along $\sigma_2$. Most examples intrude the Chuos- and Kuiseb Formation schist packages, with many examples of concurrent folding with metasediments during $D_2$ and $D_3$ deformation, particularly the sheets that intruded sub-parallel to $S_0/S_1$. Additional evidence to boudinage of their early, the pre- syn-deformation timing of intrusion is supported by axial planar cleavages that cross cut the metasediment and the granites. Minor occurrences of A or B-type leucogranites that are crosscut by C-type sheets occur in the Khan Formation (Figure 3.48a and b) and are classified as A-types, because of the relative age relationship. The only visible accessory phase is minor skeletal biotite at sheet margins, essentially schlieren entrained from the host metasediments.

These are comparable to the peritectic melts described in Ward et al. (2007); and Ward et al. (2008), where fluid present melting at low granulite facies metamorphism and pre-existing structure pathways facilitate large volume granite melt sheet formation. The fact that one generation is clearly deformed and one is not, suggests that the pelitic source rock composition is suitable for multiple episodes of melt generation. Essentially, there are two distinct textures of the garnet bearing, B-type, leucogranite observed at Valencia:

1. The less abundant variety (VALG 13, 22) is coarse to pegmatitic, light pink to cream coloured and characterised by abundant garnet. The garnets mostly occur as prominent 1 mm - 5 mm porphyroblasts disseminated throughout large 10 m scale granite bodies; though in some the garnet occurs in dense nests of 1 mm to 2 mm individual dodecahedra, or as massive poikilitic masses >10 mm across (Figure 3.48c).
2. The more common variety (VALG 01) occurs as narrow 1 m- scale bodies often folded and boudinaged with a prominent foliation. Garnet is the distinguishing accessory phase and is in spots and clusters of 1 mm - 2 mm porphyroblasts (Figure 3.48d).

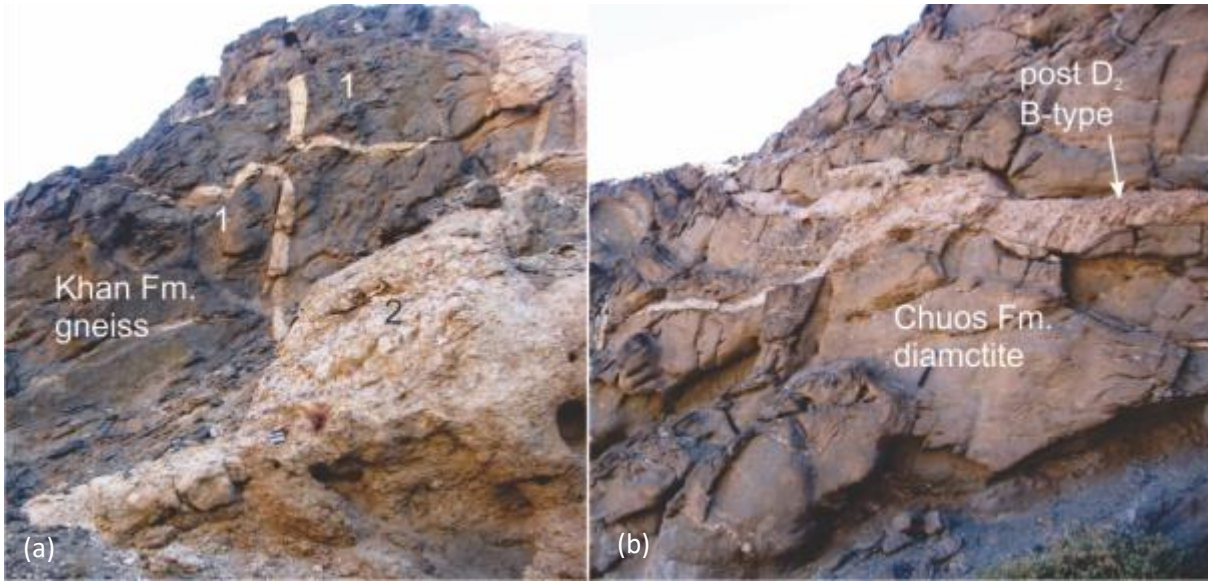



Figure 3.47 A-type and B-type sheeted leucogranites at Hildenhof. (a) Narrow discontinuous sheets are folded with the metasediments, these are crosscut by a later mineralised pegmatitic granite (foreground). (b) Post $D_2$ sheet intrudes bedding-parallel as well as crosscutting, note granite may appear folded as in (a).

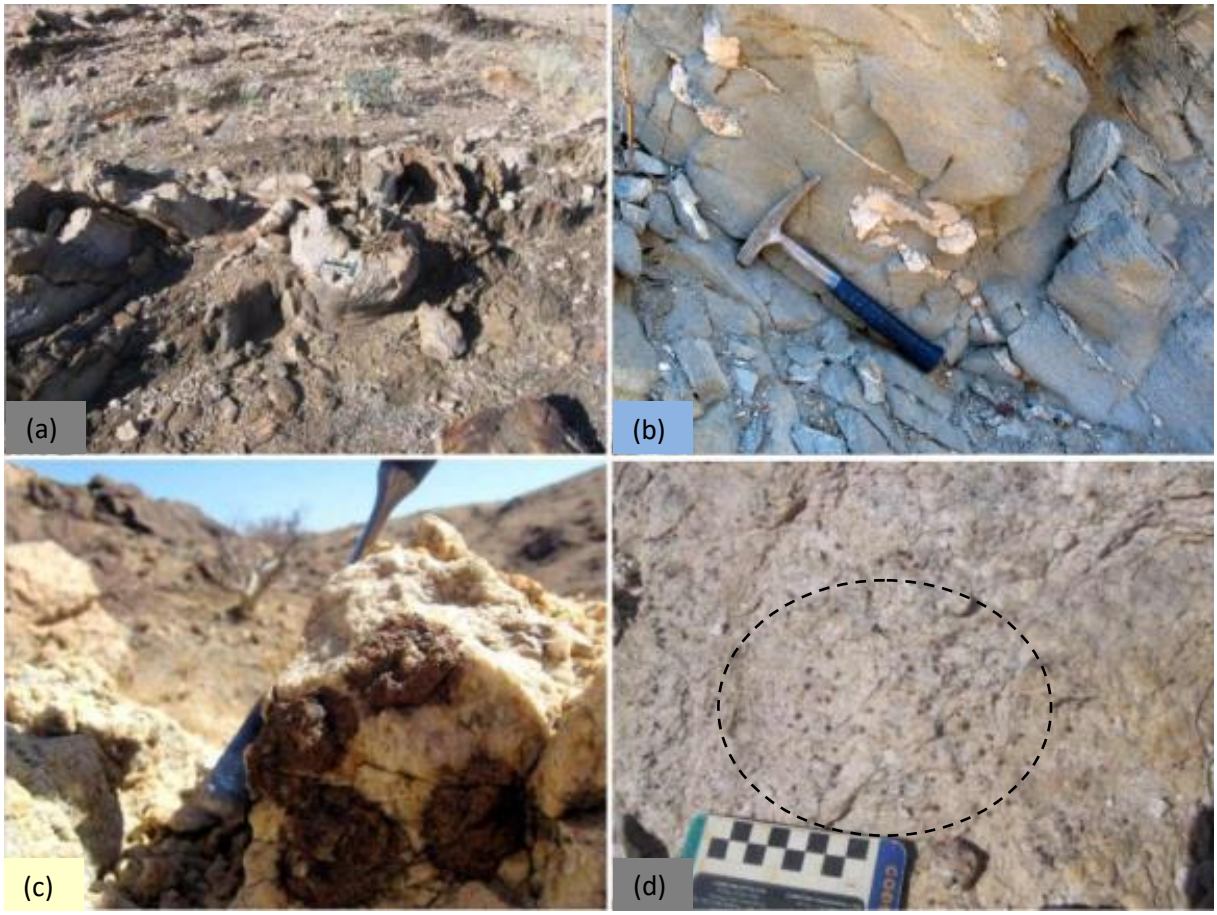



Figure 3.48 A- and B-types at Valencia. (a) The oldest sheets at Valencia are tightly folded and are common in the Kuiseb schists. (b) A-type sheets in the Khan Formation are highly attenuated and tightly folded. (c) Garnets (circled) are poikilitic and up to 3 cm across in some pegmatitic-textured B-type sheets. (d) Garnet bearing, foliated B-type leucogranite with a coarse to pegmatitic texture and disseminated 1 - 5 mm garnets throughout.

Easily recognisable early generations of sheeted leucogranite are scarce at the Ida Dome and just three examples were sampled. It is not immediately clear whether they are directly comparable with A- or B-types at Valencia or Goanikontes. Typically, they are folded granites with limbless hinges; often with boudinage and/or foliation, which differentiate them from the less deformed (younger) sheeted leucogranite types. These early granite sheets intrude the Nosib- and Swakop Groups, and preserve $D_2$ deformational features. Tight, upright folds have hinges sub-parallel to the NNE - SSW orientation of the Dome; where the folding of the metasediment is especially tight or transposed, the granites may resemble boudins, and in some locations. The true pinch and swell trends of the granite is evident in long sections of the Dome, where exposed faces are parallel to $\sigma_3$ (Figure 3.49a). A-type leucogranites in the Nosib Group tend not to host accessory phases, and B-type sheets that intrude the Swakop

Group tend to contain peraluminous phases, most typically garnet (Figure 3.49b) or other accessory phases such as tourmaline. Relative timing places the B-types at pre-$D_3$ time; as these granites also show recumbent folding (Figure 3.49c), limbless hinges, and irregular thickness that are crosscut by the same axial planar cleavage as the sediments.




Figure 3.49 Early sheeted leucogranite varieties at the Ida Dome. The highly deformed early sheeted leucogranites and garnet bearing varieties are scarce compared to the C-types and mineralised sheeted leucogranites. (a) A string of boudins and tightly folded leucogranite within the Khan Formation, located on the eastern edge of the Ida Dome. (b) A garnetiferous leucogranite intruding the Chuos Formation on the eastern edge of the Ida Dome, north of the Ida Cu mine. (c) An early leucogranite intruding along D2 structures in A-type-1 Grey granite within the Ida Dome.

### *C-Type Sheeted Leucogranites*

The C-types described in this study refer specifically to the voluminous sheets that intrude the Khan, Rössing, Chuos, and Kuiseb Formations within the study areas. These sheets crosscut A- and B-type SLGs but may host a fabric, do not unanimously occupy $D_3$ structures, and so temporally fit a syn- or post $D_2$ in the Nex (1997) classification scheme. There are however, some C-type SLGs that do not show prominent evidence of pre $D_3$ deformation. The C-type leucogranites tend to intrude parallel to $S_1$ or bedding in antiform hinges and at higher angles to $S_0$ and $S_1$ within the limb zones of regional scale $D_2$ and $D_3$ antiforms. The geometries are not strictly applicable and appear to be controlled by local structural features from deposit to deposit. Locations such as the Holland's Dome, which is a $D_3$ antiform, suggest that C-type intrusion is syn to post $D_3$ as the granites are strongly controlled by pre-existing fold related structures. Essentially the suite comprises large volumes of dyke and sill type intrusives, with a strong structural influence on geometry at the Ida Dome, Goanikontes and Valencia.

There is a wide range in textural- and accessory mineral variety in the C-type group; In addition, alteration or pegmatoidal textures that resemble the uraniferous varieties occur throughout the deposit area. An example of an altered pegmatitic-textured leucogranite and a sample that resembles a D-type are given in Figure 3.50a and 3.50b. The sample contains abundant, coarse biotite, but does not carry appreciable uranium grade. Tourmaline-dominant and magnetite-dominant varieties tend to be the most abundant varieties, at all deposits (Figure 3.50c and 3.50d). Colour, texture and accessory assemblages of C type sheets show strong consistency between deposits and most contain very weakly anomalous U. Hand specimen sample GOAG01 is a coarse-grained texture and accessory biotite (Figure 3.50e).Biotite is not considered an accessory phase, as many leucogranites contain in excess of 5 % modal biotite, and a reasonable proportion of this is contributed by host rock schlieren or assimilation. Thus, any granite which is comparable in size and extent to the large sheets that intrude the upper Nosib Group and the Swakop Group formations, which does not host a distinctive accessory phase, apart from biotite is classified in this study as the ‘Accessory-free C-type’.




Figure 3.50 C-type leucogranites at the Etango deposit. The sample set also includes C-type sheet sampled at surface north of the Swakop River. (a) DH019 100.50-100.93 is an example of hydrothermally altered sheet with pink feldspars, minimal accessories other than primary biotite books. (b) An example of a pegmatitic C-type from within the Khan Formation that displays the typical pink and white coloration to the feldspars and coarse texture. Coarse biotite is common and is a combination of primary biotite books, and skeletal entrained blades, DH034 226.29-226.63. It has typical smoky quartz of the D-type, but is not anomalous in U (c) A magnetite bearing C-type, these typically intrude the Khan Formation, DH022 59.00-59.24. (d) Pink and white feldspars with quartz-tourmaline segregation patch in a C-type, DH012 198.58-198.77. (e) Surface sample from within the Chuos Formation, GOAG 01.

*The Ida Dome C-type leucogranites*

There are three recognisable textural varieties of the wide-spread C-type sheeted leucogranite at the Ida Dome deposits, these include: a distinctive magnetite-bearing variety and a tourmaline-bearing pegmatitic leucogranite (Figure 3.51a and b, respectively). A third variety is similar to the accessory-free variety at Goanikontes.

Primary accessory minerals appear to be limited to magnetite, tourmaline, ilmenite, xenotime, and zircon. Certain metasediments within the Khan Formation are more reactive than others, and entrained metamorphic minerals such as diopside and titanite may constitute the bulk of contaminant mineral populations; Figure 3.52 illustrates a typical C-type sheet crosscutting the bedding ($S_0$ and compositional banding concurrently) with entrained diopside porphyroblasts maintaining the compositional banding of the host rock. This is an example of the main accessory assemblages being inherited from the host rock, and is widespread among the Ida Dome deposits. The distribution of accessory minerals is relatively consistent with the succession of host rocks, and thus contributes to a scheme of classifying the sheeted leucogranites by their intrusion within the local stratigraphic sequences. Magnetite-bearing leucogranite intrusions are limited to the Khan Formation, titanite-diopside bearing sheets in the upper Khan Formation, garnet- and tourmaline-bearing sheets in the Rössing and Chuos Formations.

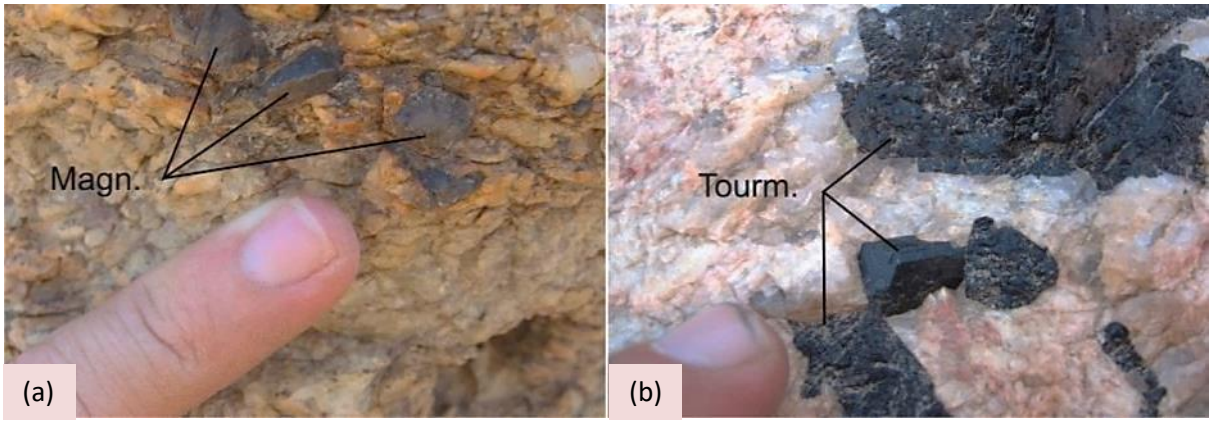



Figure 3.51 Euhedral magnetite and tourmaline in Cm- and Ct-type sheeted leucogranite. (a) Magnetite is euhedral at a number of localities, most notably at Holland's Dome where skarn development is most prominent. (b) Tourmaline-bearing sheets are scarce in the Khan Formation, but occur in the upper Rössing Formation and in the Chuos Formation on the eastern edge of the Ida Dome.



Figure 3.52 C-type leucogranite sheet crosscutting bedding and inheriting compositional banding. The host rock is diopside gneiss of the Khan Formation, with well - developed leucosomes in bands of light pink K-feldspar within a quartz - feldspar - diopside matrix. The granite has inherited accessory diopside, almost in parallel to the compositional banding.

*Husab C-type sheeted leucogranites*

The Husab deposit contains C-type leucogranites, which intrude within the Khan-, Rössing, and Chuos Formations, however, the abundance and focus of uraniferous granite in the Rössing overwhelms the non-uraniferous varieties in most drill intercepts. They do not show evidence of folding but do preserve some fabric at most deposits, supporting the pre-$D_3$ timing described in Nex (1997).

There are at least three varieties of pre - mineralisation leucogranites at the Husab deposits:

1. A typically coarse-grained and accessory-free variety that is present in the Rössing- and Chuos Formations (Figures 3.55a and b);
2. Magnetite-bearing sheets that intrude the Khan Formation - these are the most ubiquitous and serve as a footwall marker (Figures 3.55c and d); and
3. Garnetiferous and tourmaline-bearing pegmatitic sheeted leucogranites - these are encountered in a small number of holes (Figures 3.55e, f, and g).




Figure 3.53 Examples of common sheeted leucogranites of the Husab Deposits. (a) An example of typical, pegmatitic textured sheeted leucogranite pegmatite that intrudes a quartzite - calcsilicate package. (b) An example of an early sheeted leucogranite, invaded by quartz - rich uraniferous granitoid. The quartz in the barren granite is distinctively milky and light coloured compared to the dark grey - black smoky quartz of the younger intrusive. (c) Magnetite - bearing leucogranite - pegmatite intruding at a low angle to bedding in Khan Formation diopside gneiss; subsequent hydrothermal fluids have altered the more porous host rocks, but much less so in the granite sheets. (d) Magnetite - bearing granite veins with characteristic pink and white feldspars and magnetite porphyroblasts. The host rock is banded diopside gneiss, Khan Formation










Figure 3.53 (e) and (f) Coarse-grained leucogranite with minor accessory biotite, intruded by a high - grade uraniferous quartz - biotite vein; and a granitic vein sandwiched between a banded quartzite and a quartz pegmatite (alaskite). (g) Pegmatitic sheeted leucogranite with accessory tourmaline and entrained chlorite - diopside clusters.

C-type examples in this study are limited to sampling material taken from intervals within mineralised intersections, where mineralised granite has intruded between or within older C-type pegmatitic leucogranites. The drill sampling resolution at Husab is metre-to-metre, and this often includes intervals of barren C-type granite with centimetric veins of mineralised granite, and/or final crystallisation fractions with elevated U. Swakop Uranium maintains a detailed photographic record of each diamond core tray. The library of core specimens serves as a reference to some of the macroscopic observations presented in this section.

The relative ages of the barren sheet varieties are not easily determined, as they seldom occur together. It is clear though, that in some core samples the mineralised sheets crosscut the barren pegmatitic leucogranites; and certain barren varieties have foliation- consistent with pre-deformation intrusion (potentially pre $D_2$ when compared to other deposits). This section therefore limits discussion and interpretation of this aspect and rather describes the granites as observed.

The magnetite-bearing granite intrusions at Husab appear confined to the Khan Formation banded gneiss, the diopsidic units in particular. The stratigraphic limitations of these granites are such that it is the most recognisable footwall indicator to U - mineralisation at the Husab Deposits. The granites, as at other CZ deposits, are pegmatitic with distinctive pink and white coloration to the feldspars, the presence of haematite in the feldspar and in magenetite indicates Fe in variable oxidation states.

The accessory-free leucogranites at Husab are predominantly coarse-grained to pegmatitic textured granite sheets. These range from centimetric veins to sheets over 5 m thick. This classification encompasses a large volume of the leucogranite population recorded in the geological logging database of the Husab Mine. Quartz and feldspars appear in roughly equal proportions, with graphic intergrowth patches among larger rock-forming phases highlighting the often-pegmatitic nature of the sheets. Occasionally biotite occurs as fine disseminations or as altered laths at the margins of the intrusives.

Tourmaline-bearing leucogranites occur as sub - metre scale in core section within the Rössing Formation gneiss (cordierite) units. The granites are typically coarse-grained or

pegmatitic and relatively accessory - free. Tourmaline occurs in nests with quartz. The garnetiferous varieties occur in the lower Rössing Formation, and intrude mafic - rich biotite - garnet schist, similar in appearance to the dark amphibole - biotite schist described for the Rössing Deposit in Nash (1970). The sheets intrude at variable angles, often sub - parallel to the host - rock fabric; they range in thickness from centimetric to over 10 meters.

*Valencia Deposit C-type leucogranites*

The Valencia deposit is characterised by large volumes of granite intruding the Damara Supergroup, sheets have preferred to intrude the gneiss units of the Khan Formation and the schists of the Kuiseb Formation. There are three varieties of the C-type, magnetite, tourmaline and accessory-free, as at the Etango (Goanikontes) and Ida Dome areas.

The pegmatitic tourmaline-bearing granites occur in the Kuiseb-, Rössing-, and Khan Formations. They are light-pink to off-white coloured sheets that are extensive in length, parallel to $S_1$ and $S_0$, often 2 m - 5 m across, or larger (Figure 3.54a). The prominent accessory tourmaline occurs as both massive and euhedral crystals in clusters (Figure 3.54b) and as finer-grained symplectic intergrowths with quartz.




Figure 3.54 Ct-type sheeted leucogranites at Valencia. (a) C-type and Ct-type sheets predominantly intrude the Kuiseb Formation and intrude parallel to the bedding/foliation planes. Sheets may be wider than 10 m. (b) Tourmaline occurs as massive and euhedral crystals in mm- to cm-scale sizes within feldspar and quartz.

The sheeted leucogranites have, predominantly, intruded as extensive dykes and sills in the Kuiseb Formation, with minor intrusions in the lower Swakop- and upper Nosib Groups. The granite is coarse-grained to pegmatitic and has graphic-textured patches throughout the localities observed.

*Magnetite C-types*

Magnetite porphyroblasts serve as the distinguishing feature in this variety. It is often coarse-grained with prominent pink and white coloration to the feldspars, displaying minimal foliation. Less commonly, it is uniformly light pink, medium- to coarse-grained with a subtle foliation. The granite sheet geometries show strongly localised controls and intrude parallel to $S_1$ (Figure 3.55a) and oblique to foliation (Figure 3.55b).

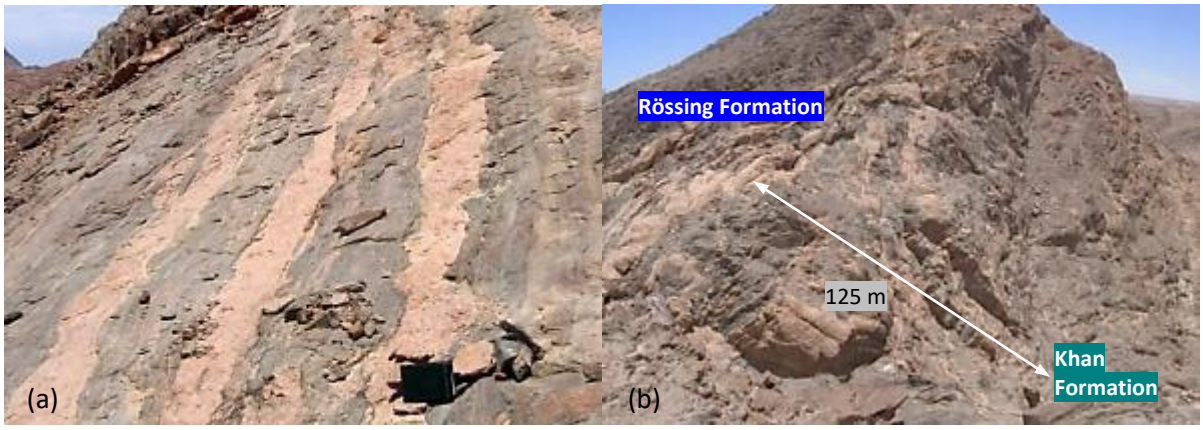



Figure 3.55 Magnetite-type leucogranites at Valencia. (a) Bedding parallel sheets in the Khan Formation, magnetite porphyroblasts are visible on surface. (b) Magnetite granite sheet volumes increase toward the Rössing Formation contact. Sheets display less ordered geometry in the upper Khan and have overwhelmed the metasediments, but have not enforced significant rotation of the metasedimentary xenoliths.

## 3.13 Uraniferous Leucogranites - The Alaskites

The Central Zone is an enriched uranium domain, where recycling of crustal material has produced metasedimentary and igneous host rocks containing uranium in concentrations sufficient to elevate their average U content above even the average granite (3.5 ppm U given in Taylor & McClennan, 1985). Uranium-enriched leucogranites occur in a very broad

range of geographic and stratigraphic locations; they intrude the Abbabis granite gneiss complexes; and as high up in the Damara Supergroup as the Kuiseb Formation in locations throughout the Khan–Swakop River valleys.

The term mineralised sheeted leucogranite is somewhat ambiguous, in that all the sheeted leucogranites contain some uranium, the known range of uranium concentration ranges from <9 ppm (XRF detection limit) to over 230 000 ppm in sporadic concentrations at the Husab deposits[30].

The mineralised sheeted leucogranites in this study contain at least 10 times more uranium than the typical A-, B-, or C-type sheeted leucogranites already described. Instead this section will utilise uraniferous leucogranite to differentiate uranium-bearing samples from weakly- or non-uraniferous leucogranites, these are the D- and E-types of Nex (1997). It appears that in areas such as the Ida Dome and Valencia deposits, determining the timing relationships is not uniformly applicable, as both C-types and uraniferous leucogranites carry parallel foliation.

### *Goanikontes Alaskites*

Goanikontes D- and E-types have undergone sericitisation and chloritisation at fault zones and limonite staining occurs in the subsurface to depths exceeding 40 m masking- or giving the incorrect impression of an originally D-type alaskite being an E-type (Figure 3.56a). Oxidation also occurs as a direct product of contact reaction with the wall-rock (Figure 3.56b). Fault-zone alteration is intense and samples rarely exhibit 'D-type' features, some are uranium-enriched therefore examples are included in this section (Figure 3.56c). Typically, the D-type texture is dominated by jet-black smoky quartz, with quartz- and feldspar-dominated patches interchanging in hand specimen scale (Figure 356d). Mineralisation is also associated with streaks of biotite that occur near alaskite contacts with gneissic host rocks (Figure 3.56e).

[30] Youlton and Coetzee (2012) Confidential mineralogical report no. MIN0512/091 prepared for Swakop Uranium.

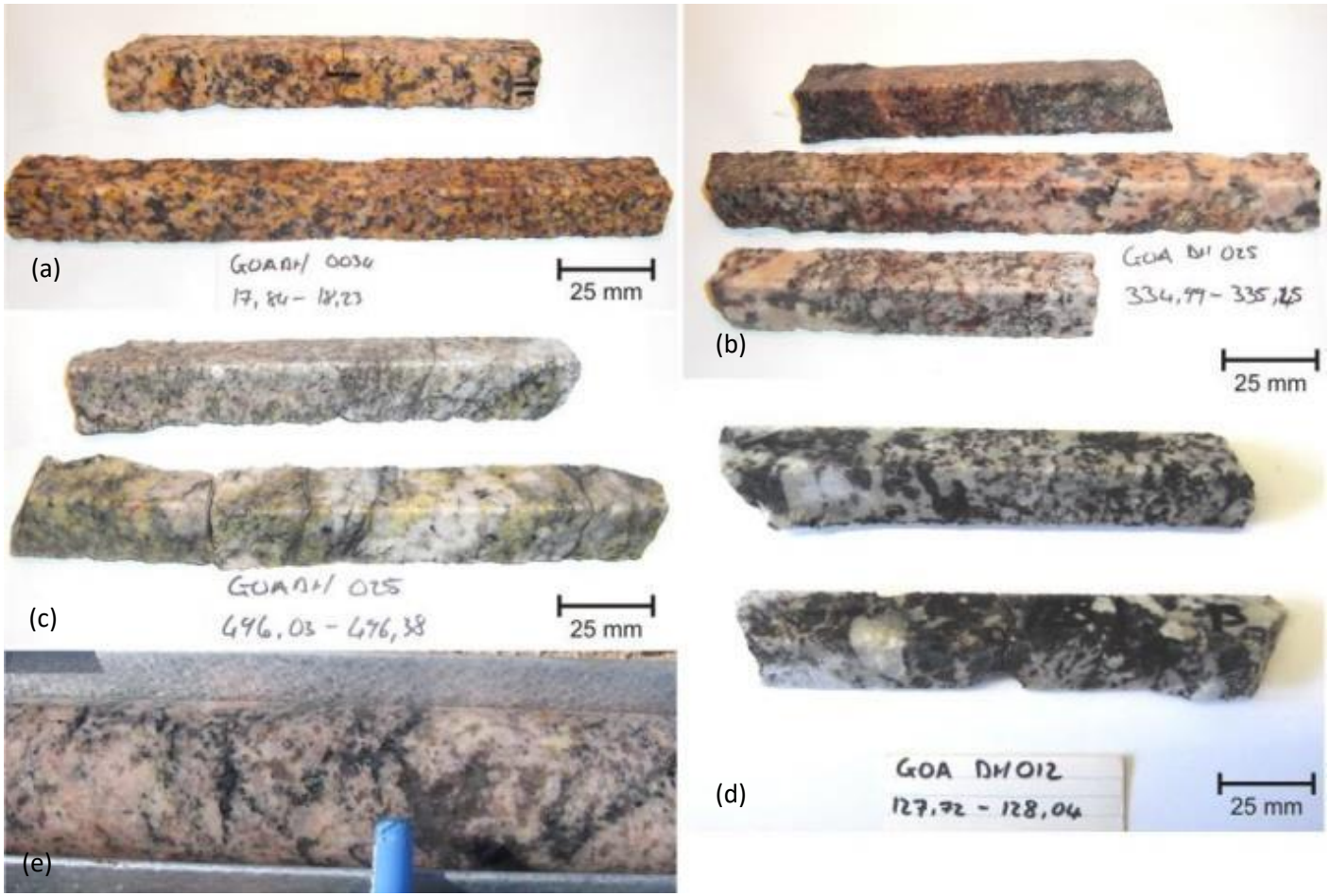



Figure 3.56 The common varieties of uranium-bearing granites observed in core from the Goanikontes Deposit. (a) Medium to coarse, homogeneous, limonite and haematite stained E-type sheeted leucogranite with accessory magnetite, alteration is attributed hydrothermal fluids. Being a shallow sample, there is likely to have been a later meteoric component. (b) Typical E-type of Nex (1997) with prominent haematite and limonite staining adjacent to unaltered granite, alteration is hydrothermal. (c) Altered sheeted leucogranite, showing sericitisation of feldspars, minor magnetite, chlorite streaks and veins, with biotite, inhomogeneous texture and brecciation, potential for alteration fluid migration along fault pathways. (d) Typical D-type of Nex (1997) with variable coarse texture, jet black smoky quartz and white feldspars. (e) Significant reaction with surrounding biotite-rich metasediment causes a margin of biotite entrainment, with streaks and laths of biotite, highly variable texture, with smoky quartz patches and haematite staining associated with elevated cps.

Certain E-type textured samples (DH019 71.74-72.18) have been purposefully selected to illustrate the difference between the oxidation halo (corona) and the supposedly unaltered granite (Figure 3.57). Comparison between magnetite in the C-types (Figure 3.58a) and magnetite in the E-type (Figure 3.58b) sheeted leucogranite specimens highlights the evidence of post-crystallisation magmatic-hydrothermal alteration in the mineralised types. The fluids associated with the uraniferous leucogranites appear to be more oxidising, and more abundant than in the barren C-types which tend to show very little wall rock interaction or internal alteration.




Figure 3.57 Typical Goanikontes (Etango) E-type core sample, DH019 71.74-72.18. There are distinctly oxidised portions (brick-red and black) and relatively unaltered portions in this sample (black and white colour).

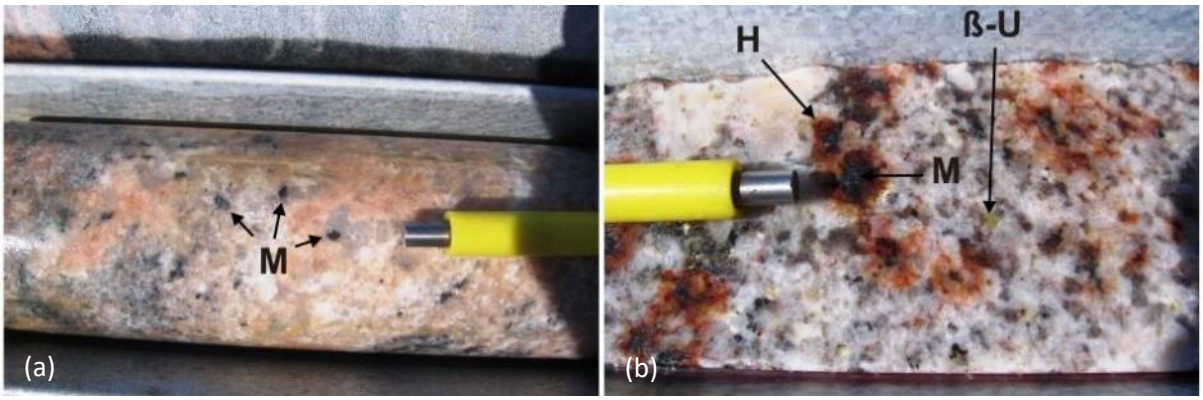



Figure 3.58 Magnetite in barren and mineralised core from Goanikontes hole DH025. (a) Magnetite (M) crystals up to 1 cm across occur in barren, magnetite-bearing C-type sheeted leucogranites at Goanikontes. Note that there are no halos of haematite around the magnetite crystals. (b) Haematite (H) halos surround magnetite in mineralised sheets, often accompanied by β-uranophane (β-U).

### *Hildenhof Uraniferous Sheeted Leucogranites*

The Hildenhof mineralised suite consists of a narrow zone (~100 m) of sheets that anastomose, coalesce, and diverge, occasionally cutting older C-types. The mineralised sheets are pegmatitic- to coarse-grained, inhomogeneous alkali feldspar dominated granites. Although there are no distinct examples of E-type sheeted leucogranites displaying the diagnostic oxidation halos of the Etango localities, the Hildenhof mineralised specimens show similar Fe-coloration. The variance in alteration colours is due, in part, to highly variable amounts of entrained biotite in some samples, which is often associated with haematite staining (Figure 3.59).



Figure 3.59 Typical mineralised sheeted leucogranite texture at Hildenhof. Mineralised Sheeted leucogranites at Hildenhof are coarse to pegmatitic with highly variable biotite content. The sheets intrude pelitic metasediments, and biotite laths at the margins reflect the orientation of the sediments.

### *Ida Dome Alaskites*

The Ida Dome alaskite sheets intrude biotite-garnet-magnetite schists and skarn-forming carbonate units of the upper Khan Formation. They constitute three deposits on the eastern and southern sides of the Ida Dome and fit two broad categories;

One is characterised by granite coalescence and pooling beneath impermeable Rössing marble at Garnet Valley and Ida Central (Chapter 2); and the other represents the interaction

of invading sheeted leucogranites with brittle-deformed calcsilicate units of the Khan- and Rössing Formation at the Holland's Dome deposit.

Coalescence of multiple leucogranite sheets at Ida Central and Garnet Valley is such that individual sheets are no longer recognisable in some areas. As such, the Ida Dome alaskites do not show clear crosscutting relationships with the older leucogranites. Distinctive D-type textured alaskites occur sporadically at all three Ida deposits and are analogous to the D-type of Nex (1997) at Goanikontes and comprise white feldspar and black smoky quartz veinlets (Figure 3.60a). The majority uraniferous leucogranites constitute altered alaskites showing the same characteristic halos as the E-type (Figure 3.60b). The halos are also present at Holland's Dome but are less abundant. This sample set includes typical D-types and E-types, in addition, a number of mineralised samples have deformation features and a number of alteration features similar to those seen at Goanikontes. Sizeable biotite books and magnetite crystals occur where sheets are in contact with the Khan Formation; magnetite may reach over 10 mm (occasionally cm-scale) and biotite books are often >5 cm-scale length.

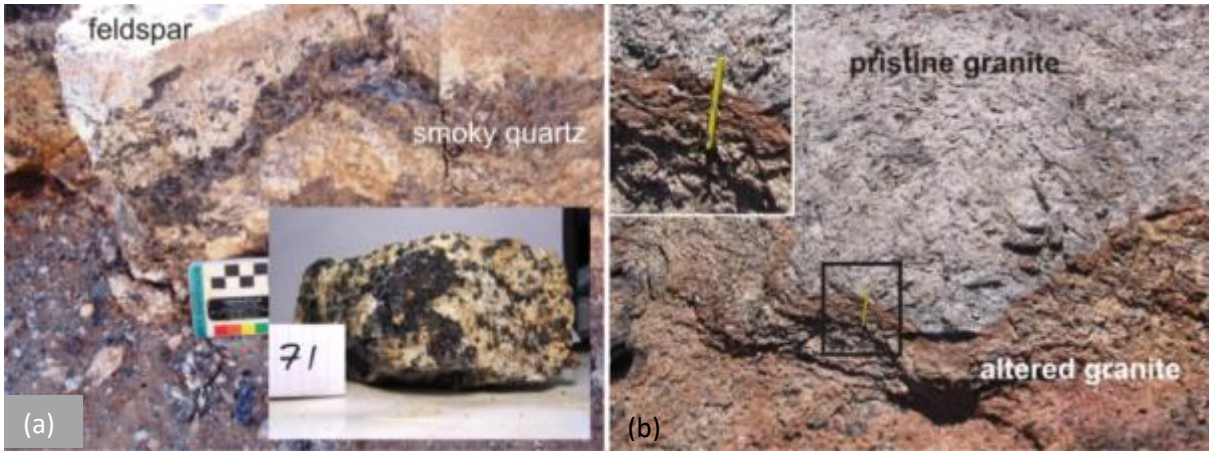



Figure 3.60 D and E-type leucogranites at Ida Dome. (a) D-types are typified at the Holland's Dome area by thick quartz veinlets and an inhomogeneous coarse-grained texture. (b) Garnet Valley and Ida Central pavements are covered with oxidation halos; the cores are unaltered and have a D-type colour and texture.

### *Ida Dome E-Type Sheeted Leucogranites*

Hand specimen sample IDAG 05 contains a section of haematite-stained oxidation halo and a portion of unaltered material as illustrated in Figure 3.61. In the fresh material, sericitisation of plagioclase is limited to the grain boundaries, whereas in the oxidised samples all

feldspars are sericitised. Minimal secondary U-phases correspond with the lower U detected in chemical analyses and provide evidence of U-oxidation and remobilisation. Samples with lower U content (100 to 300 ppm U) are characterised by sericite, albite rims, vein quartz and chloritised biotite, indicative of hydrothermal alteration.

Mobile Fe and clay alteration is enhanced by meteoric water circulation. The Fe stained samples appear to have more biotite than the D-type, which occurs within the oxidised portions of a given sample and is the most likely source of $Fe_2O_3$ from chloritisation. Pleochroic halos in biotite are abundant and surround ~0.5 mm metamict radioactive inclusions; the damage to the mica structure will have played a role in releasing Fe to the magmatic fluid system. Sulphide mineralisation and uranium grade show a strong correlation at the Ida Central deposit, where the high grades occur in sheets that intrude the cupriferous Khan Formation (after Söhnge, 2001). Alteration and host rock interaction are best represented in the core samples from HDD027 (diamond drill hole 27, Ida Central, Figure 3.62a to 3.62d) where sheeted leucogranites intrude predominantly calcareous upper Khan- and lower Rössing Formation lithologies.

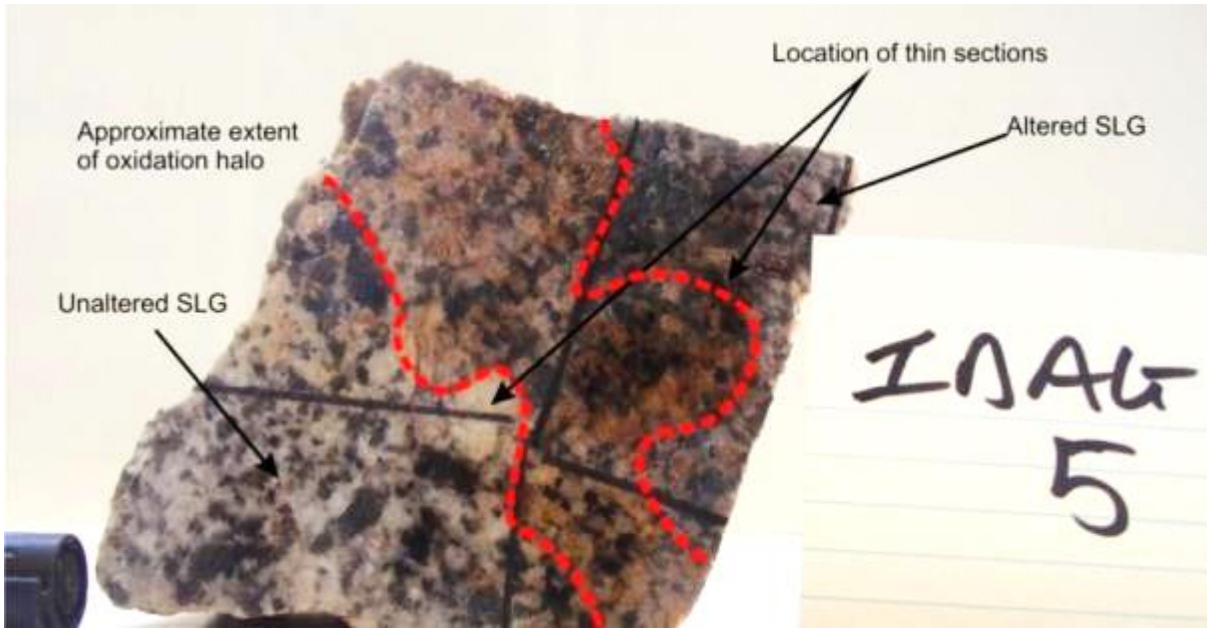



Figure 3.61 Mineralised sheeted leucogranite from Ida Central with typical E-type oxidation. The unaltered portion has typical D-type 'black and white' coloration, while the feldspars on the outside of the halo (top left of sample) have a distinct pink coloration. The unaltered leucogranite is examined in thin section IDAG 05a and the altered in section IDAG 05b (thin section slides are in Figure 4.34).

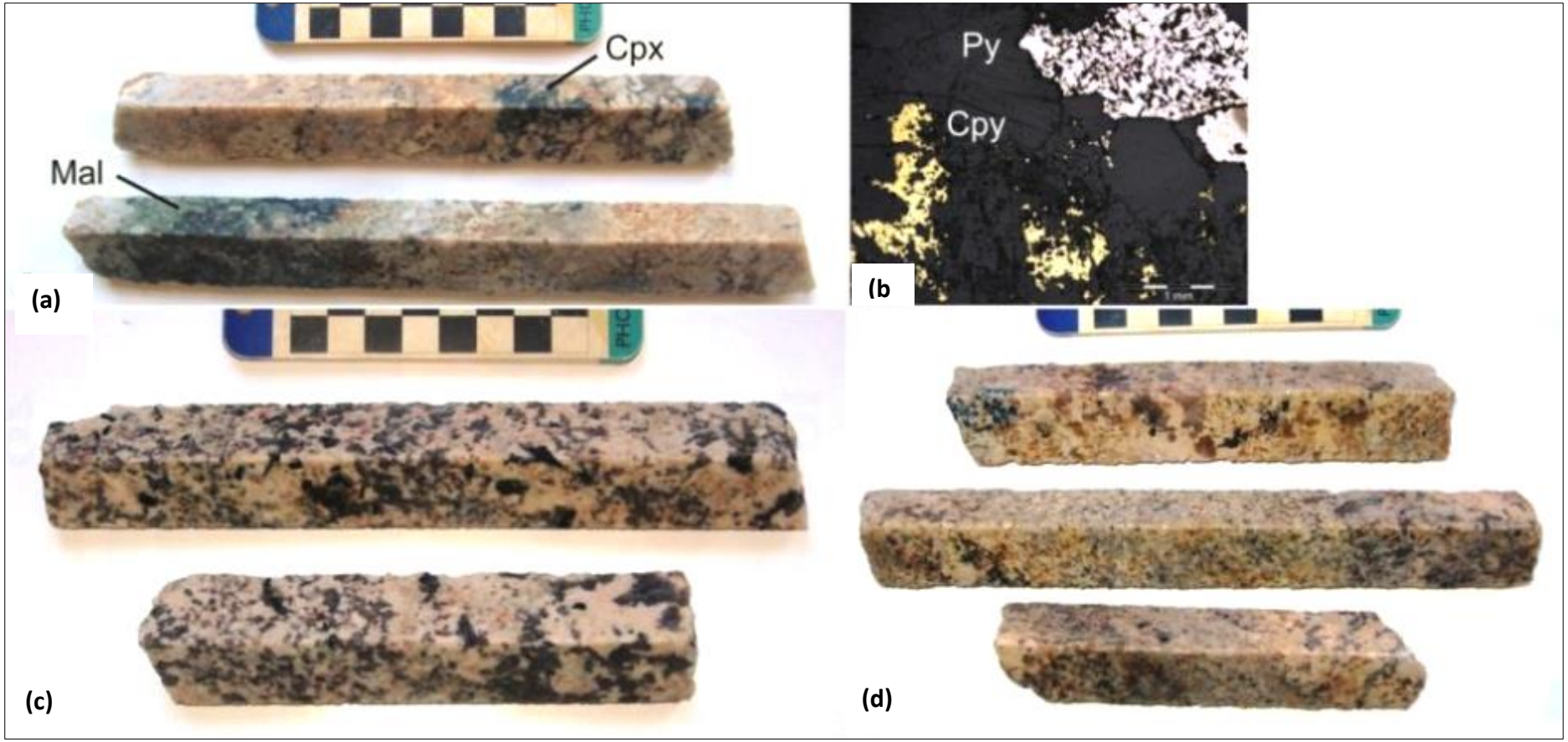



Figure 3.62 Core samples from diamond hole HDD027 at Ida Central. The samples reflect the influences of the host rock on sheeted leucogranite texture and colour. (a) Cu-mineralisation (malachite- Mal) from the Khan Formation stains the granite a green colour around a lath of metasediment. Associated epidote is light green and clinopyroxene is deep green, HDD27 122.90-123.22. (b) Thin sections reveal skeletal interstitial Cu-sulphides, HDD27 122.90-123.22, rfl. (c) The typical D-type texture, with chains of vermicular smoky quartz, has a cream to white-pink colour, HDD27 104.36-104.70. (d) Some samples display inhomogeneous texture, due to the interaction with- and entrainment of fine – grained Khan Formation gneiss, HDD027 89.47-89.95.

## 3.14 Central Zone Primary Uranium-Deposits Discussion

Across the sCZ there is some consistency in that two distinct marble packages of the Rössing Formation are divided by a package of reduced metapelite unit(s). The two carbonate packages and cordierite-bearing gneiss are present at the Ida Central, Garnet Valley, Husab, and Valencia deposits. The Khan Mine, occurs in metalliferous, sulphide-bearing units of the upper Khan Formation and is the type locality for pegmatite associated copper mineralisation in the Central Zone. Khan Formation-hosted Cu mineralisation similar to the Khan Mine occurs at the Valencia area, and at the Ida Copper Mine at the Ida Dome.

Structurally, the Rössing Deposit is marginal to a competent dome, whose post $D_3$ rotation has opened up space close to the Khan-Rössing transition that allowed for sufficient intrusion and coalescence of uranium bearing sheeted leucogranites (Basson and Greenway, 2004). Similarly, at the other deposits, the coincidence of ideal structural and stratigraphic settings has resulted in the formation of granite-hosted uranium deposits that today, are economically viable. Table 3.4 summarises these deposits and the comparisons- and contrasts to the deposits at the Rössing mine locality. Granite pegmatite sheets exploiting antiformal structures in the Khan Formation further up the Khan River are described by Kisters *et al.* (2004). The Valencia deposit is an example further north that clearly exploits the hinge zone of an anticline structure.

The Grey granites intruded the Damara Supergroup at ca. 520 Ma (Longridge, 2012) and the late uranium mineralised sheets at ca. 508, 506, and 495 Ma (Briqueu, 1986; Longridge, 2012; and Cross *et al.* 2009, respectively). The period between the early granites (Grey) and the late, uraniferous sheeted leucogranites (D-types) gives a time-span of 12- to 25 million years within which to have intruded and deformed leucogranite sheet types A-C prior to the intrusion of the mineralised SLGs.

The relationships of **B** cutting **A**, **F** cutting **C** or **B** and **E** cutting **B**, described in Nex (1997) are also observed, with some inference, at other deposits of this study. The sheeted leucogranite suite at Valencia provides examples of early generation sheeted leucogranites (**A-type**) that have undergone folding with the metasediments; sheeted leucogranites that are foliated, but not folded (**B-type**) and are crosscut by granites that pre-date the mineralised sheets (**C-type**).

The Ida Dome deposits comprise at least four varieties of leucogranite; garnetiferous sheets (analogous to the **B-type**) that carry a fabric not recorded in magnetite and tourmaline bearing sheets (Analogous to **C-type**). The most common crosscutting relationships are those between tourmaline-bearing **C-types** and garnetiferous **B-types**, and between the pristine and oxidised mineralised sheeted leucogranites and the C-types, particularly the tourmaline and magnetite varieties. At the Ida Dome and Holland's Dome deposits, the mineralised leucogranites appear to be coarse-grained segregations within the larger C-type masses.

Cross – cutting relationships do occasionally prove problematic, where in some locations, the older vs. younger granite is not easily determined. For example, Figure 3.63 illustrates two generations of magnetite – bearing leucogranite in the Khan Formation at the Ida Dome. The older generation (1) appears crosscut by a finer-grained sheet (2) intruding parallel to a displacement plane. However, tracing the veins that extend from the main sheets shows that they cross – cut in contradiction to what is expected (circled).




Figure 3.63 Cross–cutting relationships of Khan Formation–hosted leucogranites. The Leucogranites of the Khan Formation predominantly form conjugate sets of sheets that host magnetite ± entrained diopside as the primary accessory phases. Determining the temporal relationships between the sheets is not always possible within the same host Formation. As illustrated by the two contradictory cross–cutting relationships.

The primary-hosted uranium deposits of the Central Zone all occur within the stratigraphic transition between the upper Nosib and lower Swakop Groups, with the exception of the Valencia deposit, where uranium mineralisation occurs as high in the sequence as the Kuiseb Formation (Figure 3.66). Although uranium in uraninite, coffinite, and uranophane is primarily hosted in leucogranite sheets, a certain proportion is found in the surrounding metasediments (e.g. Rössing, Jacob 1974; Holland's Dome, Culpan, 2011, Husab, Freemantle, 2011).

The Khan Formation hosts the majority of the uraniferous alaskites at Rössing (Jacob, 19744; Berning, 1986); The Rössing Formation is absent south of the Swakop River at Goanikontes, and mineralisation is bound within the Khan- and Chuos Formations; The Rössing marble package forms an impermeable barrier on the east of the Ida Dome structure, trapping the invading leucogranites in the underlying Khan Formation gneiss. The Rössing Formation hosts the majority of uraniferous leucogranite at the Husab deposits, with <20 %[31] of the uranium hosted by leucogranites in the Khan- and Chuos Formation, foot- and hanging-walls, respectively.

The nature of the Valencia deposit geometry limits any accurate assessment of the relative volumes of sheeted leucogranite within each stratigraphic formation. Positions of drill collars and depths to mineralisation combined with surface mapping indicate the majority of mineralised granite is hosted within the Khan- and Rössing Formations, with a significant proportion of weakly mineralised dykes intruding through the Chuos-Karibib-Kuiseb succession.

Mineralisation in the Husab Deposit occurs almost exclusively within granites that intrude the Rössing Formation (Spivey *et al.*, 2010). The Khan Formation diopside gneiss forms a prominent footwall boundary. The Rössing Formation is attenuated, with most mineralisation occurring within- or in close proximity to the metalliferous (Cu, Mo, Ni, Fe) Swakop Group gneiss, carbonate lenses, and skarns. Hydrothermal alteration features are more prominent in extent and intensity in the Husab deposit than in any of the other deposits in this investigation. Similarly, U-mineralised leucogranites at the Ida Dome area

[31] Swakop Uranium Husab Project NI43-101 Resource Update, 2012

concentrate in metalliferous (Cu, Mo, Ni, Fe) units of the Nosib Group. A prominent marble hanging wall barred most mineralised SLG's from intrusion higher in the stratigraphic sequence. Barren leucogranites intrude $F_2$ and $F_3$ structures at the Holland's Dome deposit, these sheets should be classified as C-types (Nex, 1997) based upon their observable characteristics. They do, however, appear to have intruded at within the same structures and display the same deformational features (fabrics) as the uraniferous granites.

The following key points emphasised comparative granite varieties and respective ages that link the deposits within the Central Zone:

- Quartz diorites with ages of 520 ± 4 and 519.1 ± 4.2 Ma and sheeted leucogranites of 520.3 ± 4.6 to 514.1 ± 3.1 Ma (monazite) ages occur at the Ida Dome (Longridge, 2012);
- Mineralised leucogranite (alaskite) ages are distinctly younger and roughly correlate with the younger metamorphism ages of Jung and Mezger (2003a), these range from 496 ± 4.1 Ma at Husab (Cross *et al.*, 2009, uraninite); 506.1 ± 8.1 Ma at Valencia (Longridge, 2012, zircon) to 508 ± 2 Ma and 509 ± 1 at Goanikontes (Briqueu *et al.*, 1980, monazite and uraninite respectively[32]);
- The major granite intrusions of diorite and sheeted leucogranite post - date (within error) the CZ metamorphic peak at ~525 Ma described by Jung and Mezger (2003a); in addition
- There are granites observed and interpreted to have intruded late in the granite sequence (by crosscutting relationships) throughout the western portion of the sCZ which show no evidence of being derived from the sediments into which they intrude, but contain no appreciable uranium enrichment.

[32] Given the predominantly fractured and silicified nature of uraninite crystals observed at all the major U-deposits described in this thesis, the accuracy of the errors of ±1 and ±2 Ma given by Briqueu *et al*. (1980) is very low even by modern standards.

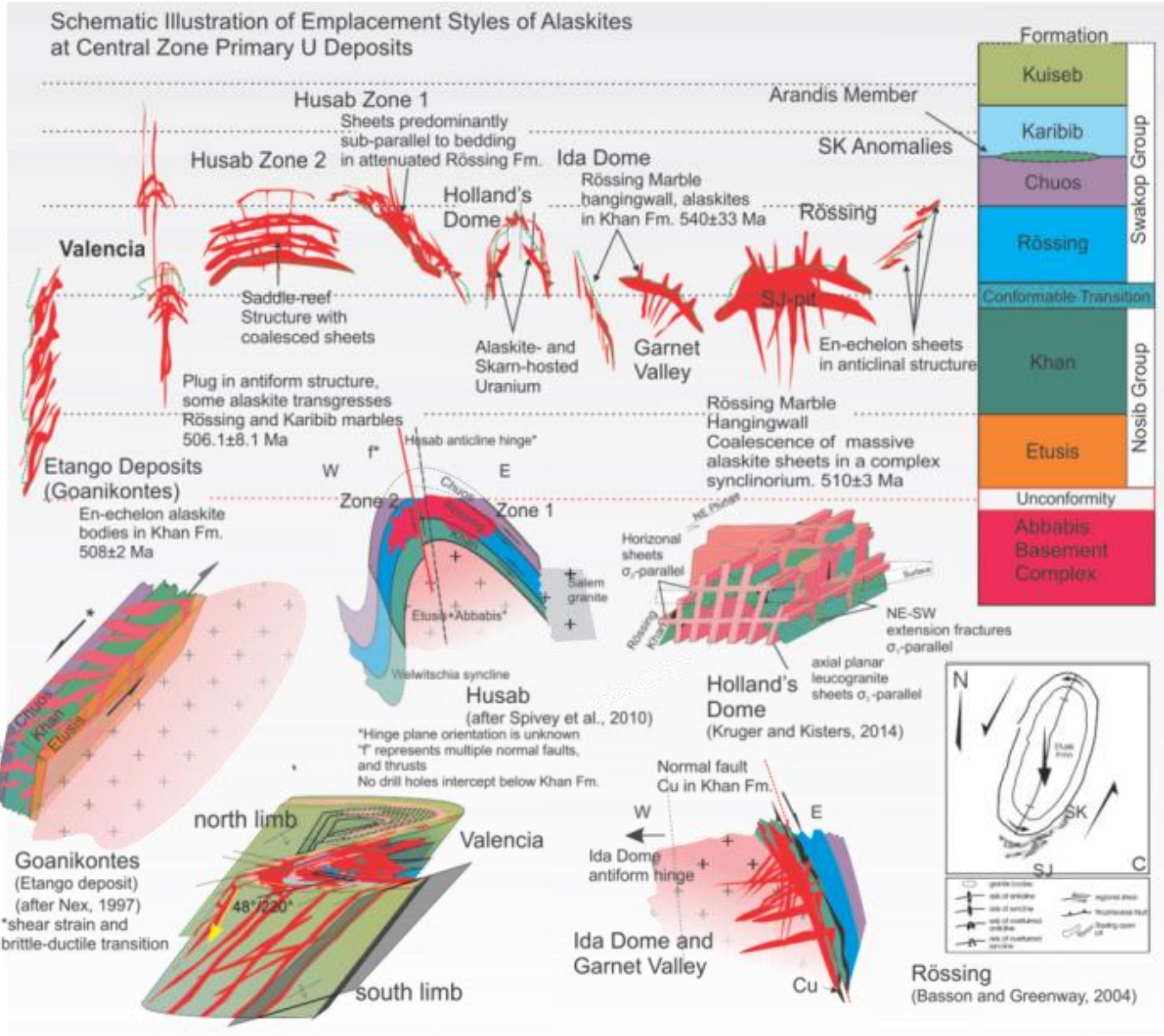



Figure 3.64 Schematic diagram of the Central Zone deposits within the context of the Damara stratigraphic succession. Tectonic processes have prepared certain sites within the Central Zone where relatively ductile sediments occur at an unconformable contact with relatively competent basement rocks. Local-scale rheological contrasts produce pressure shadows within shears, primary- and secondary folds, and associated extensional features, into which regionally significant volumes of leucogranite have invaded, in a more or less passive fashion. Interactions between U-bearing granite contact margins and reactive, predominantly reduced, metasedimentary rocks have played the most crucial role in deposit formation. The interaction zone between the granites and sediments is essentially a REDOX boundary, promoting $U^{6+}$ reduction to insoluble $U^{4+}$ and resultant uraninite precipitation. While the cyclic carbonate sequences at most deposits have provided a physical barrier to retain granite mass within focussed areas, essentially increasing tonnage.

Table 3.4 Central Zone uranium deposit geological characteristics.

| Deposit | Stratigraphic Formations | Stratigraphic Location of Mineralised SLG's | Prominent Structures and Emplacement Characteristics | Nex (1997) SLG Generations | Other Granites |
|---|---|---|---|---|---|
| **Etango** | Etusis, Khan ± Rössing, Chuos | Etusis-Khan and Khan ± Rössing, most mineralised sheets intrude the Khan Formation. | High-strain Zone (Nex, 2007) brittle-ductile transition. Goanikontes lobe of Palmenhorst Dome. | A, B, C, D, E, F | Grey, Red |
| **Hildenhof** | Khan, Rössing, Chuos | Khan-Chuos and Khan-Rössing contacts. | Roughly parallel to bedding and $D_2$ verging fold hinges. Antiform is infolded between lobes of the Palmenhorst Dome. | C, D, E, F | Grey, Red |
| **Husab** | Khan, Rössing, Chuos, (Arandis) Karibib, Kuiseb | Rössing Formation with minor volumes of sheets in the Chuos and Khan Formations. | Antiform, possibly overturned, verging northwest and adjoins the Welwitschia Syncline of Smith (1965). Hinge Zone of a regional antiform (Husab Anticline). | C, D, E | Grey, Salem Suite, pegmatite |
| **Ida Central** | Khan, Rössing | Upper Khan-Rössing, Rössing marble hanging wall. | Cleavage-controlled, oblique to bedding, coalescence below marble. Steeply dipping Marble and gneiss package on east flank of the Ida Dome structure. | A, B, C, D, E | Grey |
| **Garnet Valley** | Khan, Rössing | Upper Khan-Rössing, duplicated Rössing marble hanging wall. | Cleavage-controlled, oblique to bedding, coalescence below marble. Steeply dipping Marble and gneiss package on east flank of the Ida Dome structure. | B, C, D, E | Grey, pegmatites |
| **Holland's Dome** | Khan, Rössing | Upper Khan-Rössing, prominent skarn influence on mineralisation in the Khan Formation | Upright anticline between Garnet Valley and the Basement to the east. Axial planar, oblique to bedding and occasionally bedding-parallel. Extension in two directions creates space. | C, D, E | Grey, pegmatites |
| **Valencia** | Minor Etusis, Khan, Rössing, Chuos, Karibib, Kuiseb | Upper Khan-Rössing-Chuos-Karibib-Kuiseb, mineralisation prominent at Khan-Rössing transition. | Secondary antiform on a limb of the Khan Syncline– saddle reef type. Narrow folded basement inlier, Localised disharmonic hinges of secondary folds. | A, B, C, D, F | Salem, Grey-diorite, pegmatites |
| **Rössing** | Etusis-Khan-Rössing-Chuos | Khan-Rössing contact strongly influenced by thick marble units and distinctly zoned either side of biotite-amphibole-garnet schist. | Dome rotation and shearing against southeast of dome (Basson and Greenway, 2004). Etusis-cored Rössing Dome. | C, D, E | Grey |

Considering the history of exploration and the extent of the Central Zone, some potential exists to significantly add to Namibia's collection of known granite-hosted uranium resources, particularly in light of the recently discovered Husab deposits, which lay concealed beneath Namib sands and gravels until late 2007. The consistencies and contrasts in geological character between the deposits in this study provide a comprehensive information base with which prospecting for new deposits may approach north central Namibia for uranium exploration.

The deposits described in Chapter 2 are globally significant hard rock-hosted U resources. The sediment-hosted deposits at Langer Heinrich and Trekkopje are also included for

comparison in Figure 3.65. The plot illustrates the position of the Husab, Etango and Valencia deposits in terms of average resource grade and tonnage of contained metal. Husab is one of the largest untapped uranium resources in the world and has ~38 500 tU of measured reserves[33].

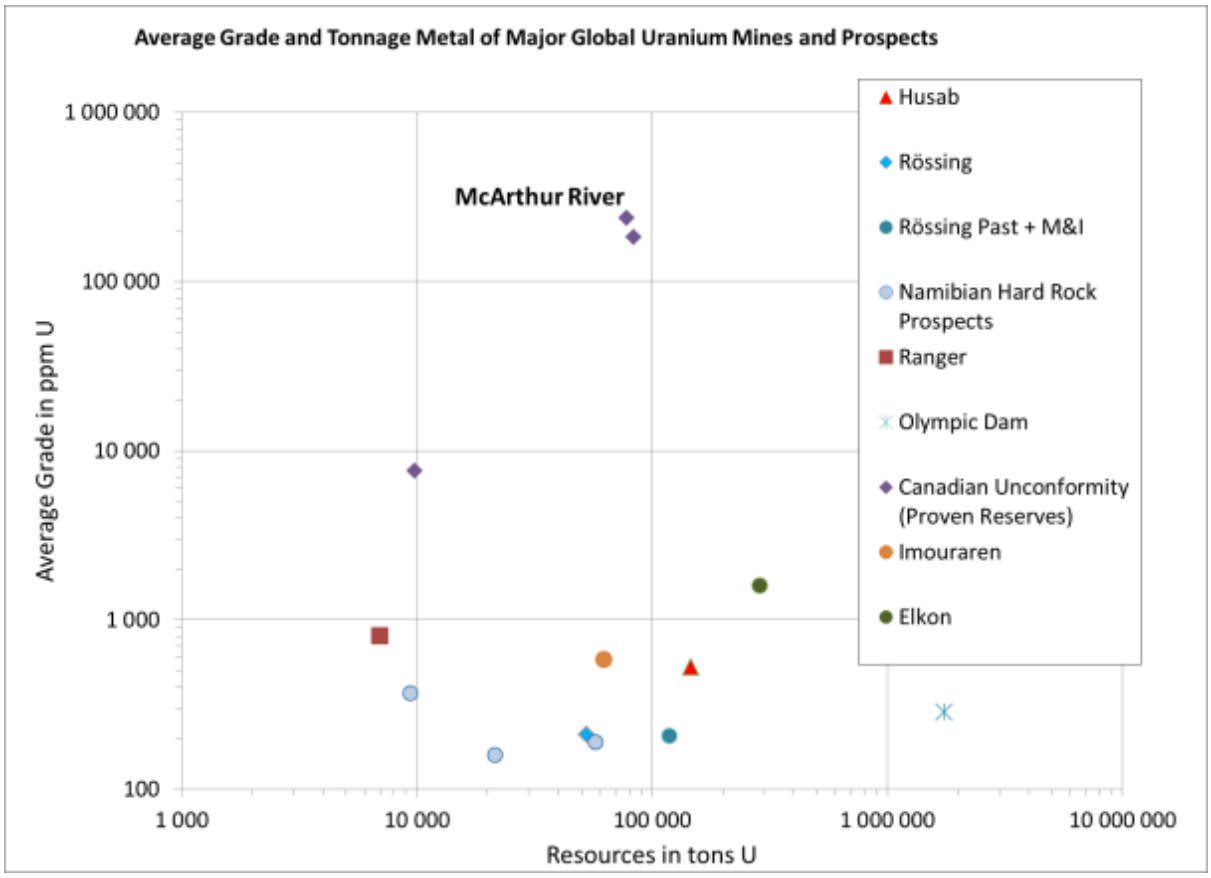



Figure 3.65 Major global uranium deposits, with Namibian deposits for comparison. Both axes are in $Log_{10}$ scale with tons U taken from the latest available resource estimations. Valencia, Etango and Husab are granite-hosted and the Rössing Deposit occurs at the only operational granite-hosted U mine in Namibia. The Canadian deposits (black circles) are exceptionally high grade, but have lower tonnages than the lower grade deposits from Namibia, Niger and Australia. The poly-metallic Olympic Dam Deposit is by far the largest resource in the world. All resource data is taken from the World Nuclear Association, combining the latest available figures as of 2012 and 2013.

The Rössing mine historically produced 101,123 t U to the end of 2011 and contains 57 700 t U in measured and indicated resources[34]. The large tonnage of uranium occurs, on average, at fractions of a percentage metal grade; thus, correspondingly large volumes of granite are required to accumulate, and react sufficiently with the reactive metasedimentary packages.

[33] Wolfe, 2012 – Swakop Uranium August 2012 Resource Report, Coffey Mining Australia.
[34] http://www.world-nuclear.org

Such coincidences should be rare; however, at least two comparably large deposits (Etango and Husab) are proven, and located within 50 km of the Rössing mine.

Primary uranium deposits in Namibia are classified as low-percentage partial melt deposits in Cuney (2014) and who draws on the work of Berning *et al.* (1976); Cuney (1980a, 1980b); Cuney and Kyser (2008) to support the classification. The type example at Rössing has grades of 0.01 - 0.05 % U, or between 100 ppm and 500 ppm.

Mineralisation at the Rössing deposit is a result of a number of controls; however, partial melting is regarded as the most important means of concentrating incompatible elements and therefore, of uranium metal transport as outlined by Robb (2005) for the Central Zone. Late magmatic fluid percolation and supergene enrichment are the next most significant means of uranium enrichment, especially at Rössing where it has contributed significantly to the economic viability of the mine (Jacob, 1986 and Berning, 1986).

Certain localities such as Ida Dome and Valencia provide cross-sections of the Basement-Damara Supergroup interface that support a basement- derived source for the sheets.

Granite-melt, and therefore uranium mineralisation pathways are varied and appear to be pre-existing at all deposits. Berning *et al.* (1986) describe how gneiss blocks in leucogranite show little to no rotation; Nex (1997) describes the invasion of a high strain zone, where the uraniferous sheets have invaded late or after the major deformation period(s); the Holland's Dome and Valencia deposits probably illustrate the clearest examples of fold-related structural control on surface; and the Husab deposits drill database indicates the granites occupy structures associated with a regional-scale antiform. The major uranium-bearing ore zones at all deposits tend to comprise amalgamations of sheet-like bodies ranging in size from centimetric to tens of metres in width. Secondary uranium deposition occurs in fractures and joint planes within the SLG's, in the surrounding metasediments and in older (or younger) intrusives.

In addition to the structural pathways, interaction with reducing metasediments is the most crucial influence on the deposition of uranium from the predominantly oxidised state in the silicate melt and fluids (after Cuney, 1980). Regional variation in the sedimentary sequence prior to deformation, combined with subsequent, localised folding and

metamorphic conditions result in deposit-by-deposit variations of the structural - REDOX uranium depositional model.

Primary chemical barriers exist where sulphide bearing gneiss, schist: calcsilicate rocks have interacted through localised contact metamorphism with the sheeted leucogranites. Physical barriers exist where the marbles are considerably thickened by tectonic process, the Rössing Deposit and the Ida Central and Garnet Valley deposits are essentially variations of the same category of impermeable metasediment barrier to granite and associate fluids.

Secondary chemical barriers exist at the Holland's Dome deposit, where calcareous metasediments and skarn pods are enriched in uranophane and other $U^{6+}$ species, where the primary control appears to be neutralisation of U-bearing solutions.

Uranium-bearing refractory minerals occur in the Husab deposit, where know distribution indicates the leucogranites that intrude the upper units of the Rössing Formation tend to host more brannerite and betafite than the leucogranites lower down in the sequence. The comparable position of the SH area suggests that controls favouring uranium-bearing refractory mineral crystallisation described in Cuney (1980); Herd (1996); Nex *et al.* (2003) and Kinnaird and Nex (2007) may have existed in localised sections of the Husab deposits.

The uranium mineralisation associated with these sheeted leucogranites within the poly-deformed, amphibolite facies southern Central Zone represent the some of the highest-temperature- and highest-pressure regimes for economic uranium mineralisation globally (after Kyser and Cuney, 2008). The nearest U occurrences with any similarity are the ~1030 Ma granite hosted uranium deposits in metamorphosed rocks of the Namaqualand Belt, described by Andreoli *et al.* (2006).

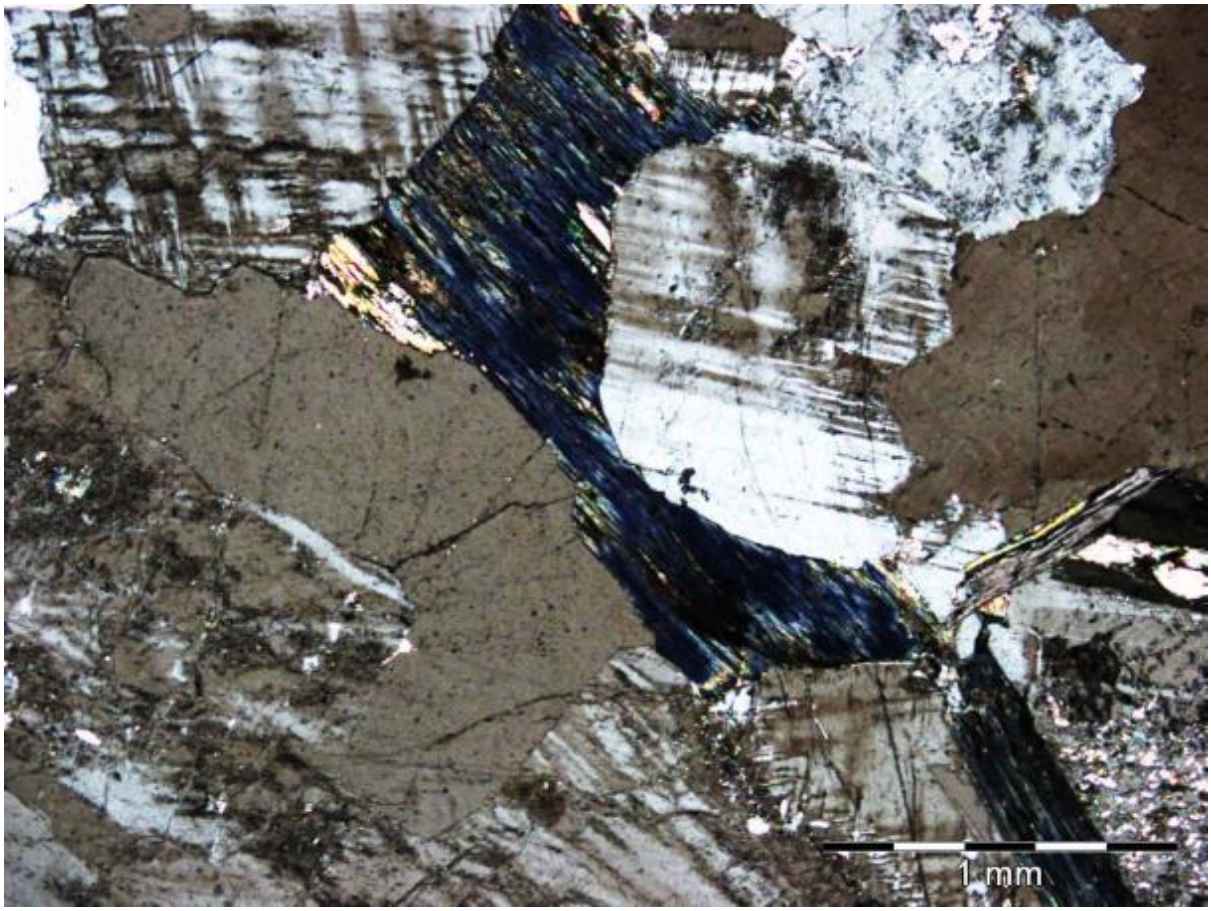
Granite-hosted U-mineralisation of economic potential occurs only in certain parts of the world, particularly Neo- to Mesoproterozoic and Palaeozoic orogenic belts. Examples include those of Pan-African age; The Rössing Deposit, Namibia, The Tranamaro and Betafo deposits, Madagascar; and the Neo- to Mesoproterozoic Grenville Province, Quebec; and Natal – Namaqua Belt, South Africa/Namibia.

The term "Erlank Paradox" was coined by Andreoli *et al.* (2003) which described the Namaqua Belt alaskite occurrence in terms of pressure and high temperature specific regimes. High U-grade alaskites occur in granulite-facies terrains, of largely low U-grade

gneisses and schists. Unlike the charnockite rocks described by Andreoli *et al.* (1992) in the Namaqua region, the alaskites in the Central Zone tend to contain contaminant clinopyroxene rather than orthopyroxene.

In Chapter 4 the petrography of both barren and mineralised sheeted leucogranites is investigated to determine any mineralogical- and compositional contrasts that may further discriminate the deposits. Particular emphasis is placed on systematically describing the petrographic characteristics of the granitic suites, as these reflect the local structural and contact interactions. With respect to uranium-bearing sheets, the local deposit-forming conditions prevalent at the individual deposits should be recorded in the rock-forming and accessory mineral assemblages.

# CHAPTER 4 PETROGRPAHY OF THE GRANITIC ROCKS THAT HOST THE URANIUM DEPOSITS OF THE CENTRAL ZONE




Tartan-twinned microcline (top); Centre – anhedral, albite twinned oligoclase replaced by quartz and biotite (chloritised); microcline perthite (lower left); myrmekite (lower centre); and strained quartz (right); rune – shaped quartz (left); and sericite-replaced plagioclase (lower right) in E-type alaskite, Etango Deposit at Goanikontes, diamond hole DH019 at 71 m downhole, 10x, xpl. The rock-forming minerals rarely preserve original features and display prominent replacement and/or recrystallisation textures, particularly in the uraniferous varieties.

## 4.1 Introduction

At least three distinct varieties of sheeted leucogranite (SLG) precede the mineralised types (locally termed, "alaskites"). The sheeted leucogranites are preceded by at least three generations of successively leucocratic, fine-grained biotite granite, while at the Valencia deposit a megacrystic Salem monzogranite and one variety of quartz diorite precede the

leucogranites, respectively. The Valencia area appears to have three distinctive generations of leucogranite that precede the mineralised sheets.

The categorisation of these granite suites is compiled by geochemistry (Miller, 1983a), mineralisation (Marlow, 1981) and isotopic characterisation (McDermott, 1986) and are summarised in Brandt (1985). Nex (1997) undertook the most comprehensive account of the sheeted leucogranite suite of the Central Zone in a study that focussed on the area around Farm Goanikontes and culminated with a temporal-structural context to six sub-types of SLG.

The study placed the granites into six distinctive varieties within the context of the complex deformational history recorded in the lithologies and structures of the western portion of the southern Central Zone (sCZ). The characterisation of the Central Zone granites has in the past, been addressed with respect to the metamorphic history with which they are so closely associated. Masberg *et al*. (1992); Masberg (2000) and Goscombe *et al*. (2003a) have presented detailed metamorphic observations and interpretations, while Basson and Greenway (2004) have also placed the granite generations (at Rössing) into the structural and metamorphic context. This was followed by Gray (2015) at Rössing and its surrounds.

## 4.2 Background of Granite Classification in the Southern Central Zone

The granite suites of the Central Zone are categorised in work by Miller (1983); Marlow (1983); McDermott (1986); Oliver (1994); Nex and Kinnaird (1995); Oliver and Kinnaird (1996); and Nex (1997). Subsequent work by Tack and Bowden (1999) McDermott *et al*. (2000); Nex *et al*. (2001b); Nex *et al*. (2002) Nex *et al*. (2003) also refer to the different granite generations. Longridge *et al*. (2009) Kisters *et al*. (2012) and Longridge (2012) place emphasis on the tectonic event(s) producing the local metamorphic and structural conditions that govern the nature of the granite emplaement throughout the Central Zone, and as such, present less detail on the variety of leucogranites specific to the various uranium deposits of the southern Central Zone.

## 4.3 Sheeted leucogranites and Associated Granitoids at the Central Zone deposits

The Central Zone granitoids are subdivided into four suites, as described in Miller (1983a and 1983b, revised in 2008) and include; the Salem Suite, the Red gneissic granites, the equigranular-textured Grey granites and the sheeted leucogranites. The D and E-type sheeted leucogranites (Nex, 1997) are described as 'alaskites' in previous reports by Hiemstra (1967); Hiemstra *et al*. (1968); Berning et al. (1976); Berning *et al*. (1976); *Jacob et al. (1986)*; and Mouillac *et al*. (1986).

There are eight textural varieties of sheeted leucogranite which are easily and consistently recognised between the primary deposits in this study, essentially expanding upon the Nex and Kinnaird (1995) and Nex (1997) classification. The populations of leucogranite at each deposit, have consistent characteristics in terms of colour, texture, and litho-stratigraphic position, which are all observed from one primary uranium deposit to another in the western Central Zone.

Recent dating studies of different granites (Longridge, 2012) and Kruger and Kisters (2016) has refined the classification of the intrusive sequence and shown schematically in Figure 4.1.

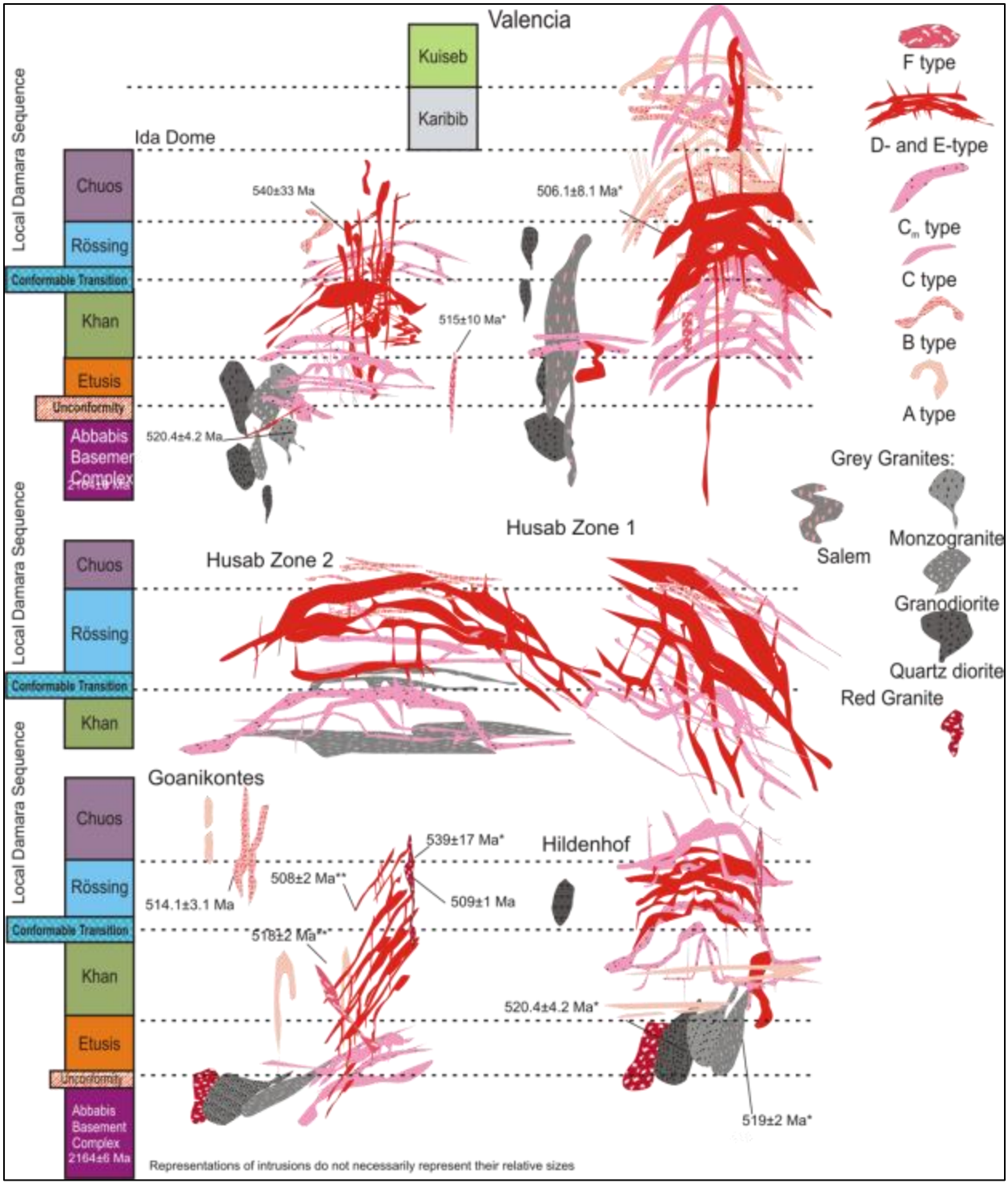



Figure 4.1 Sheeted leucogranites at the CZ deposits. Upper: Schematic diagram of the Ida Dome grey and sheeted leucogranite types and the Salem and sheeted leucogranite types found at Valencia. Middle: Schematic diagrams of the Husab Zone 1 and Zone 2. Lower: Schematic diagrams of the Etango and Hildenhof deposits and anomalies. The mineralised sheets intrude basement gneisses, except at Husab, and at Valencia. Mineralised granites occur, sporadically, in the Kuiseb Formation schists. Age data sources- Longridge (2012); Tack *et al*. (2002) and Marlow (1983). Symbols: * - Zircon; ** - Monazite.

## 4.4 Aims and Objectives

This chapter presents summaries of petrographic observation of sheeted leucogranites in hand-specimen and in microscopic scale from each of the Husab deposits, the deposit areas at Goanikontes (Etango) including Hildenhof, three deposit areas at the Ida Dome, and the Valencia deposits.

The primary aim of making a detailed petrographic comparison of leucogranites at the primary uranium deposits is to place these into a new context of sheeted granite classification, which will build on the foundation of classification presented in Nex (1997). The objective of this chapter is to present a comprehensive, descriptive account of the sheeted leucogranite populations at four of the primary uranium deposits in the western portion of the southern Central Zone. Exposed outcrop, exploration cuttings, trenches, and a comprehensive selection of NQ-size diamond core intervals from all but the Hildenhof anomaly provided the samples for the petrographic studies. The revised classification based on observations made in this study and presented in the discussion takes cognisance of the considerable amount of metamorphic, structural, and igneous research undertaken between 1997 and 2014.

Biotite- and Salem suite granites at the Hildenhof, Ida Dome, and Valencia areas supplement the leucogranite sample suites collected at each deposit and provide a means of comparing the younger leucocratic sheets with the older mafic mineral-bearing varieties. The observations presented in this study places emphasis on first accounting for the granites, describing them in hand specimen and within their geological position, in detail, and comparing them to existing work where necessary.

## 4.5 Methodology and Sampling

This study sources samples from the Etango (Goanikontes), Hildenhof, Holland's Dome, Husab, the Ida Dome area, and Valencia deposits. The large distances (up 50 linear km between Valencia and Ida Central) between the sampling areas, and the sizes of the

sampling fields (up to tens of km's at the Ida Dome area) presents a challenge to the categorisation of the granites between deposits, thus the granite suites at each deposit are described individually and then comparatively between sampling areas. Surface samples of the various leucogranites and older undifferentiated varieties were collected at each deposit. The NQ-size core collection comprises a large proportion of samples at the Valencia Deposit, and comprises the entire sampling collection at Husab. Appendix C8 contains a complete list of all samples and their locations at each deposit, in UTM-WGS84 Z33S, Y metres north and X metres east coordinates. Core specimens have names assigned by their respective Hole-ID prefixes and a depth interval suffix.

The mineralised leucogranites dominate the Husab sample suite in particular as the core drill campaign intentionally targeted the mineralised packages, with reverse circulation drill pre-collars through the Karibib and Chuos Formations, stratigraphically and physically above the Rössing- and the upper Khan Formations. Varieties of barren leucogranite and Grey granites are scarce and not considered as important as sampling the great variety of mineralised granites available to this study. The summary table below (Table 4.1) compares all the samples of granites and metasediments at each deposit in this study.

Table 4.1 Summary of samples and their locations. Core samples are listed in parentheses in the Total column. All Husab samples are from diamond drill core.

| Rock Type / Area | Salem Granite | Grey Granite | Red Granite | Sheeted leucogranites | Pegmatites and Quartz pods | Calcsilicates | Skarns | Skarn Xenoliths | Total |
|---|---|---|---|---|---|---|---|---|---|
| **Goanikontes** | | 1 | | **40** | | | | | **41 (38)** |
| **Hildenhof** | | 5 | 2 | **20** | 2 | 1 | | | **30** |
| **Ida Central** | | | | **27** | 1 | | | | **28 (4)** |
| **Garnet Valley** | | | | **7** | | | | | **7** |
| **Holland's Dome** | | 3 | | **18** | | 4 | 2 | 1 | **28** |
| **Valencia** | 9 | 1 | | **55** | 2 | | | 2 | **69 (25)** |
| **Husab** | | | | **66** | | | | | **(66)** |
| **Husab Fluorite** | | | | | | | 1 | | **1** |
| **Namib Pb-Zn** | | | | **1** | | | | | **1** |
| **Control** | | | | **5** | | | | | **5** |
| **Duplicates** | | 1 | | **12** | | | 1 | | **14** |
| **Total** | **9** | **11** | **2** | **185** | **5** | **5** | **4** | **3** | **290(133)** |

Drill core was made available from the Etango deposit at Goanikontes, the Ida Central and Holland's Dome deposits at the Ida Dome, Zone 1 and 2 of the Husab mine, and the Valencia and Joly Zone (now Namibplaas) deposits. The entire sample suite comprises 290 samples, most of which have at least one polished thin section for transmitted- and reflected-light petrographic study. All hand specimens and core samples are described in hand specimen detail, noting: prominent rock-forming minerals, accessory phases, alteration characteristics, any visible ore phases, and textural variations. Appendix D1 tabulates descriptive summaries of thin-sectioned samples in alphabetical order, by sample label. Digital versions of descriptive tables for all samples are in Digital Appendix 2

The Husab deposit is intersected by 453 diamond core holes, most plunge at -60° on 270° to intersect east dipping strata. The footwall at the deposits is consistently the Khan Formation diopside gneiss, with only sporadic occurrences of mineralisation extending down into the Nosib Group.

*Goanikontes and Hildenhof*

Sampling at Goanikontes includes two weakly uraniferous, surface-sampled C-types, sourced from within the Chuos Formation. One example (white in colour) has intruded bedding-parallel and along $D_2$ fold planes and the other (pink and white in colour) has intruded parallel to transposed, sub-horizontal bedding. Both varieties are accessory-free apart from biotite laths and streaks at the edges. Five drill holes- DH012, DH019, DH022, DH025 and DH034 provided the bulk of sample material of mineralised and barren samples. All the sampled drill holes are on the south-western edge of the Farm Goanikontes Lobe of the Palmenhorst Dome structure (Figure 4.3). The bores plunge at -70° on 105°, into attenuated Khan and Etusis units which dip roughly 40°- to 45° west to west-northwest; at these orientations bedding intersections are >75°.

The Hildenhof Anomaly is located between the Ida and Goanikontes domes ~1 km south of the Khan-Swakop confluence, it has not previously been described or sampled in detail. Mouillac et al. (1986) and Nex (1997) and a number of company reports give a brief mention

of the occurrence. The anomaly occupies a relatively small area within the Bannerman Resources Exploration Licence (EPL 3345) and has extensions to the east into the Swakop Uranium Ltd. licence (EPL 3138) where slivers of Rössing Formation and continuous Khan Formation are in-folded and unconformably overly the basement gneisses. All of the samples in this study come from EPL 3345.

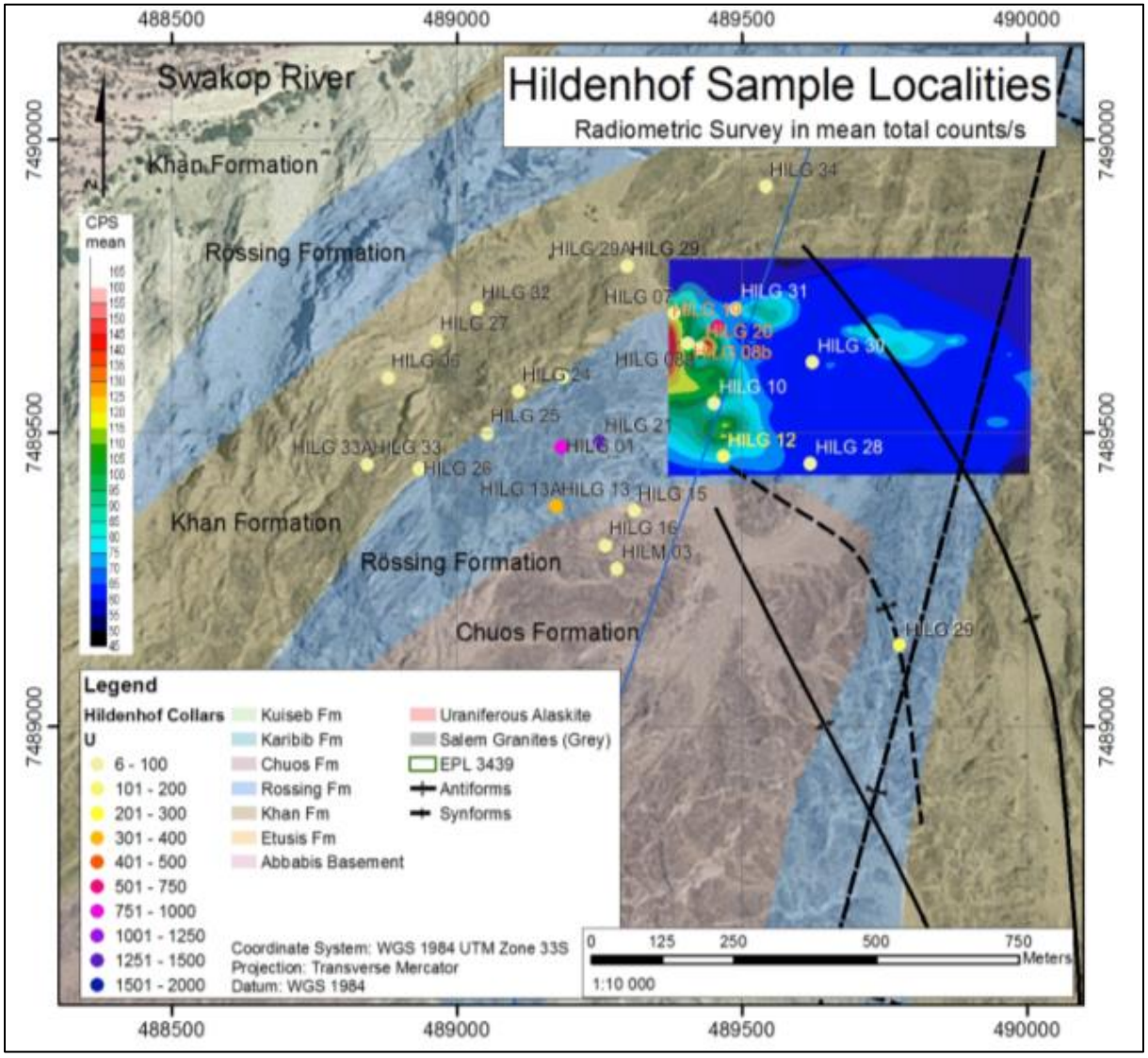



Figure 4.2 Illustrates the Hildenhof sampling locations, all of which occur within the Bannerman Resources EPL. The sampling collection comprises surface samples from the mineralisation trend and the granite assemblages in the surrounding metasediments. The collection includes three varieties of pre-D3 sheeted leucogranites, D- and E-type uraniferous leucogranites and a variety of late pegmatite granites. Three varieties of grey granite and a single red granite example were sampled.

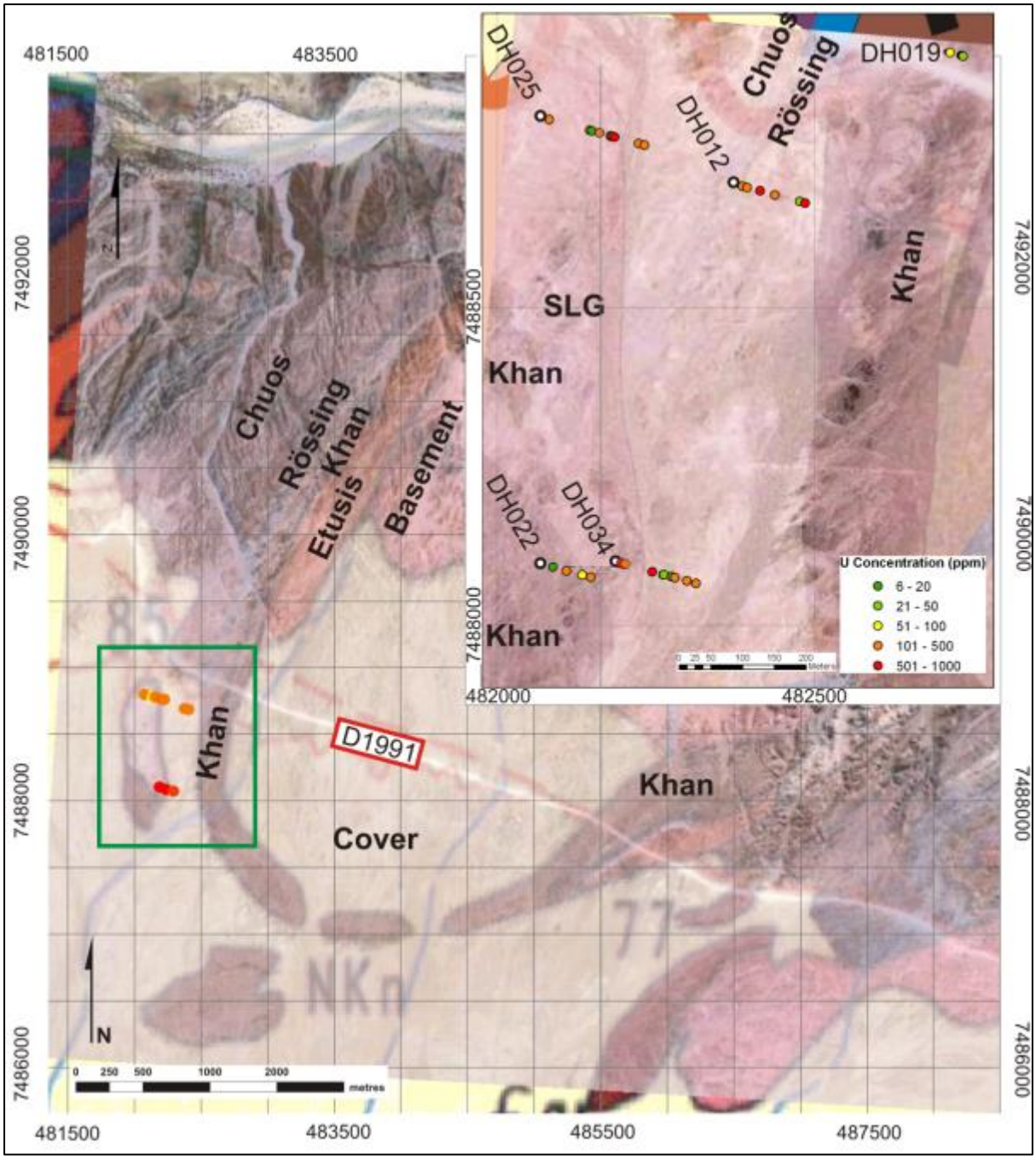



Figure 4.3 Localities of Etango A drill hole collars at Goanikontes. The drillholes dip uniformly at ~70° to the east-southeast. Vertical projections to the map surface of intersections show high-grade samples close to surface and at depth. The Etango deposit is on Farm Goanikontes and located within EPL3345 of Bannerman Resources. The colour overlay is from the Geological Survey of Namibia, Walvis Bay Map sheet 2214 and remote sensed image is geo-referenced from Google Earth™ (Quickbird™).

*Ida Dome*

Sampling in the Ida Dome area includes both mineralised- and barren varieties of sheeted leucogranite from the three main deposit areas; Ida Central, Garnet Valley, and Holland's Dome areas. Figure 4.4 illustrates the positions of drill collars and surface samples; Samples

for petrographic study were collected from Ida Central area core, while Garnet Valley and Holland's Dome have provided 1/4- or 1/2- NQ core material for REE analyses. The surface samples described in this Chapter come from all three of the main deposits of the Ida Dome.

There are few occurrences of A- and B-type SLGs at the deposits, and thus there are only two A-type samples collected from the Ida Central locality. This chapter presents petrographic studies for thirteen pre-mineralisation (and likely pre-$D_3$) Ida Dome area SLG*s*, the majority of which are from the Ida Central deposit. The sampled granite varieties include; three A-type, three C-type, five magnetite-bearing C-type, one tourmaline-bearing C-type and a single sample of the core of a U-barren oxidation halo. Ca-, Ti-, Mg-, and Fe-contaminated (entrained Fe-Mg-Ca phases) samples were collected in addition to the accessory-free, magnetite- and tourmaline-bearing varieties. Mineralised sheeted leucogranite samples include those that intrude the skarns, and Khan Formation.

Two surface samples, IDAG 08 and IDAG 43, represent two contrasting uraniferous leucogranite textures from Ida Central and Holland's Dome deposits, respectively. Three Ida Central core samples from HDD027 provide representative material from a ~40 m wide interval of intermittent uranium mineralisation; the intrusives being hosted in the biotite schist package of the upper Khan Formation. The two surface samples and three core samples (HDD027: 89.47-89.95 m, 104.36-104.70 m, and 122.90-123.22 m) are are analysed by QEMSCAN for the uranium deportment study in Chapter 7, and IDAG 43 provides uranium mineral specimens for the EPMA study in Chapter 8.

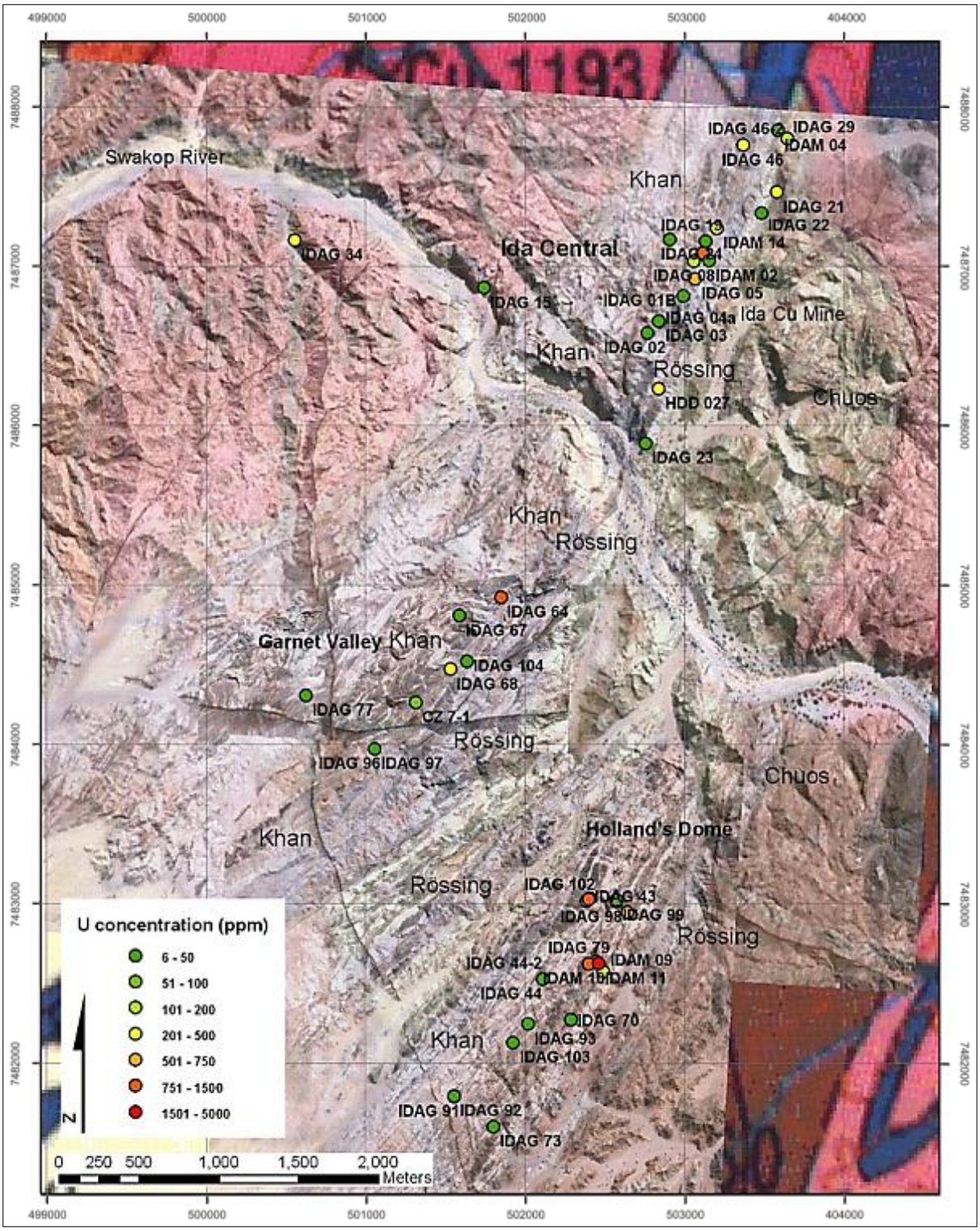



Figure 4.4 Ida Dome sample localities. The eastern portion of the Ida Dome comprises a core of Abbabis granite and augen gneiss, overlain by steeply east-dipping Khan- and Rössing Formation rocks. The bulk of Damaran intrusives occur above the Abbabis-Damara unconformity and comprise sub-horizontally-oriented barren C-type sheets in the Khan Formation, and uraniferous types below- and within the Rössing Formation (pink coloration). The Holland's dome is a north plunging antiform with limbs of upper-Khan and lower-Rössing Formation and cored by diopside Khan Formation gneiss. The Garnet Valley and Holland's Dome deposits occur within EPL3439 (S of Swakop River) and Ida Central is within EPL3138 (N of Swakop River). The colour overlay is from Geological Survey of Namibia, Walvis Bay Map sheet 2214 and the satellite image is taken from Google Earth™ (Quickbird™) and georeferenced in Arc Map v9.1 to WGS1984 UTM Zone 33 S.

*Husab*

Most mineralised leucogranites at Husab intrude the Rössing Formation, and all are closely associated with sulphide bearing units, thin marbles, calcsilicates, and a cordierite gneiss with prominent, remobilised sulphide veining being the most obvious mineralisation associations. The sulphide overprint has resulted in sulphide veins parallel to- and cross-cutting schist fabric and forming centimetric blebs and nuggets of pyrite, pyrrhotite, and chalcopyrite in the contact margins of the intruding leucogranites; this is a feature of contact metamorphism during $D_2$ and $D_3$ related magmatism.The descriptions in this Chapter include twenty-seven samples sourced from the Zone 1 and Zone 2 deposits (collars illustrated in Figure 4.5) and range in depth from 100 m to over 400 m, down hole. A systematic hand-specimen and thin section study identified the refractory uranium minerals, betafite and brannerite in the intervals of sheeted leucogranite. The search was aided by comparing intervals to results of test work on the twin hole, RRC028.

*Valencia*

The Valencia deposit granite population comprises a series of Salem Suite tonalite and monzogranite, at least one variety of Grey granite and at least five visually discernible, generations of sheeted leucogranite. Within the local SLG suite, the C-type is subdivided into three sub-types. All the sampled leucogranite types occur within close proximity (~500 m) to a mass of mineralised sheets that constitute the main uranium deposit. The deposit thus, provides the best opportunity (within the scope of this study) to compare and contrast the various SLG sub-types. The Valencia granite suite displays a strong stratigraphic distribution of granite varieties; Chuos Formation and Kuiseb Formation host the A-type sheeted leucogranites; the garnet-bearing varieties; and the majority of the massive, accessory - free and tourmaline - bearing C-type varieties; while the magnetite-bearing C-types appear to be restricted to the Khan Formation. Eleven barren sheeted leucogranites were used in the Valencia petrographic study, these include; one A-type, three B-types, three magnetite-bearing C-types (Cm) three tourmaline-bearing C-types (Ct) and one F-type. Figure 4.6 shows the localities of the samples and core-specimen drill hole collar positions.

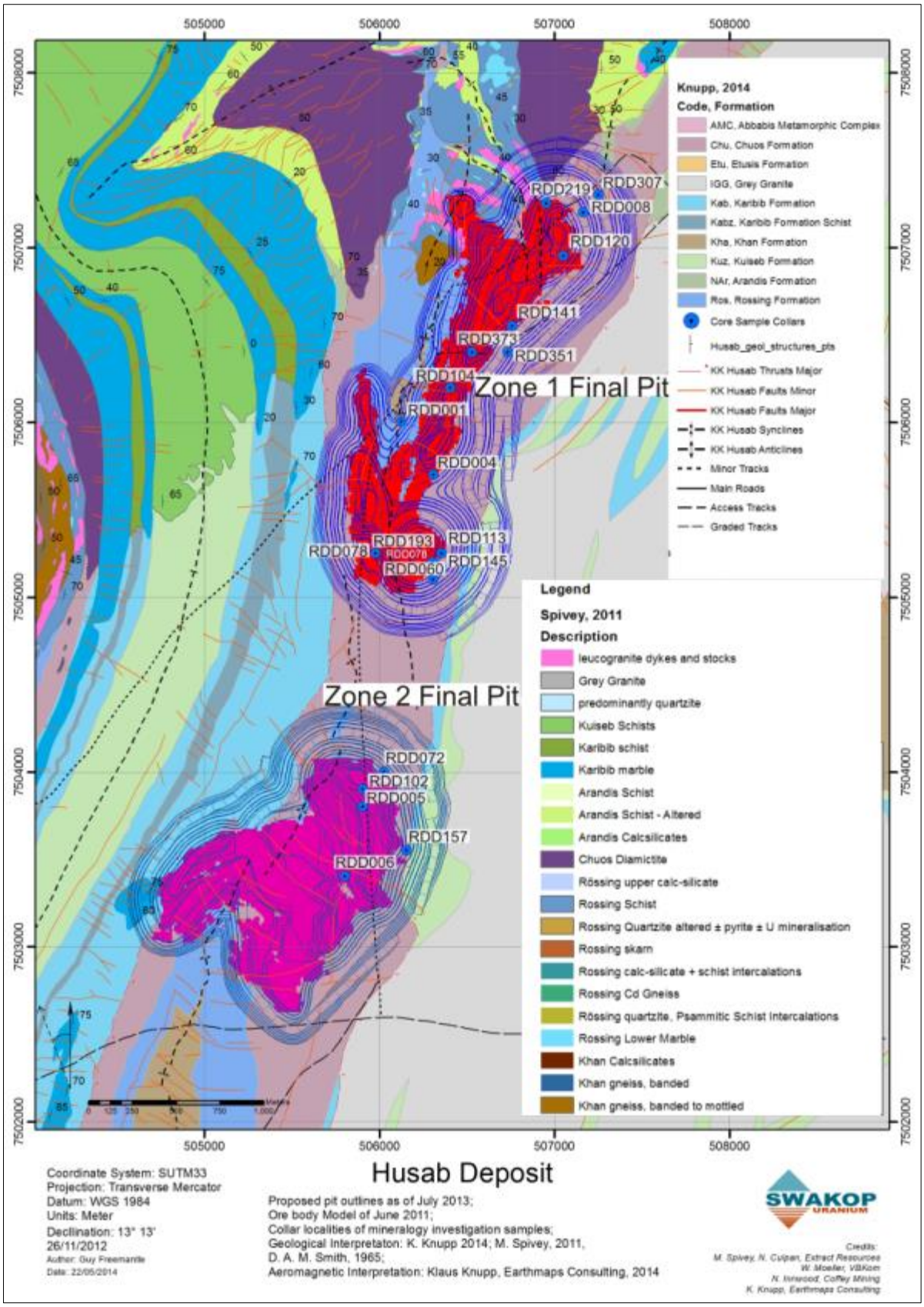



Figure 4.5 Location map of the Husab mine project on ML171. The blue circles locate the collar positions of drill core that provided petrographic, geochemical, and mineralogical sample material.

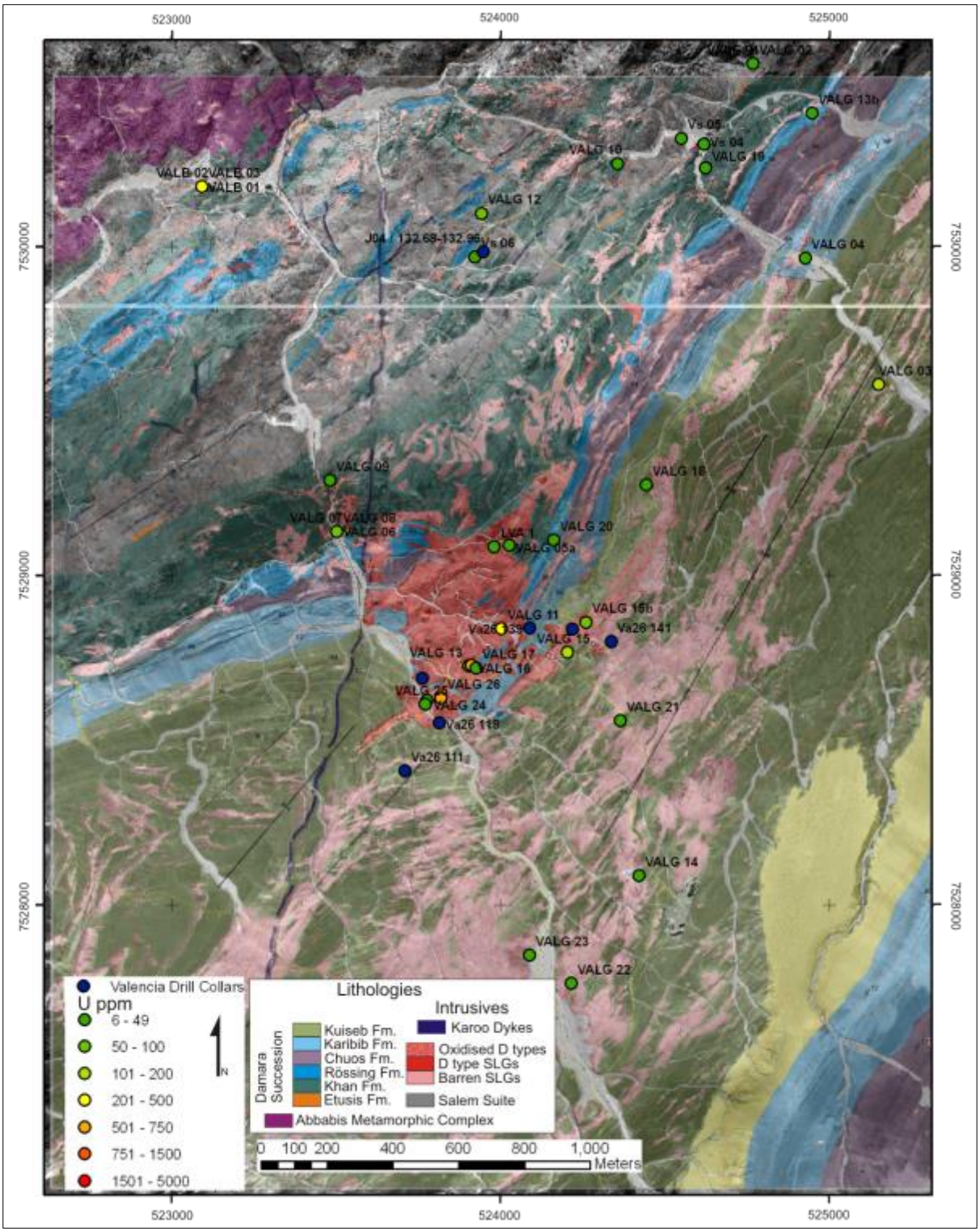



Figure 4.6 Valencia Hand samples and drill core collar locations on Valencia EPL 1496. U values are in ppm (by XRF) as indicated in the legend. Blue circles represent drill-hole collar localities. Lithological interpretation and coloration are from mapping during 2007 and 2008 and the underlying ortho-photo and contour lines are courtesy of Valencia Uranium Ltd.

## 4.6 Salem, Red and Grey Granite Petrography

### *Salem Suite at Valencia - Thin Section Petrography*

The Salem Suite sample set at Valencia comprises five polished thin sections including; a single, biotite-hornblende variety (quartz-diorite, cross-cut by the megacrystic Salem type); three, megacrystic varieties (monzogranite) and one sheared monzogranite. The older generation of Salem granite contains anhedral and euhedral, 1 mm - 6 mm plagioclase (oligoclase-andesine). 0.2 mm – 2 mm tan- to light green (chloritised) biotite blades dominate the type 1 thin section, and Table 4.2 summarises the sample set. The average An contents in carlsbad-twinned subhedral plagioclase grains gives oligoclase-andesine composition, compared to the albite-twinned grains, which give oligoclase extinction angles (Figure 4.7a). In addition, previous work summarised in Miller (2008) shows that the Salem granite plagioclases have higher An than the equigranular granites. The older Salem granites at Valencia are andesine ($An_{36}$ to $An_{44}$) dominant whereas oligoclase ($An_{25}$ to $An_{29}$) dominates in the younger megacrystic variety. Quartz occurs as globular inclusions and as vermicular textures, quartz inclusions tend to be <0.5 mm in plagioclase, and the vermicular grains may be even finer. Coarse grains match the feldspars in size range, most are <1 mm and strain extinction is variable but present in most. Microcline (≤1 mm), is subordinate, anhedral and sparsely disseminated throughout. It is also the only Valencia grey/Salem granite sample observed in this study with prominent green hornblende (Figure 4.7b).

Table 4.2 Thin section characteristics of Salem Suite samples from Valencia (U and Th content by XRF, in ppm).

| **Sample** | **Type** | Colour | **Grain size** | **Texture** | **Biotite** | **Dominant Feldspar** | **Plag.** | **Th** | **U** |
|---|---|---|---|---|---|---|---|---|---|
| Vs04 | Salem type-1 | Dark grey | Coarse | Homogeneous, foliated | V. high %, strong fabric | Oligoclase-Andesine | $An_{26-31}$ | 9 | 6 |
| VALB 03 | Salem type-2 | Intermediate grey and pink | V. coarse | Inhomogeneous | High %, gneissic fabric | Oligoclase | $An_{14-18}$ | 18 | **271** |
| J04 42.53-43.00 | Salem type-2 | Intermediate grey and pink | V. coarse | Inhomogeneous | High %, gneissic fabric | Oligoclase | $An_{17}$ | 18 | 7 |
| J04 96.06-96.57 | Salem type-2 | Intermediate grey and pink | V. coarse | Inhomogeneous | High %, gneissic fabric | Microcline | $An_{18}$ | 16 | 6 |
| VALB 01 | Sheared Salem type-2 | Intermediate grey and pink | Coarse | Inhomogeneous | High %, gneissic fabric | Microcline | $An_{17}$ | **155** | 28 |

Oligoclase is the dominant feldspar phase in the observed thin sections of megacrystic samples and represents >30% of the matrix area in two of the three sections. Oligoclase grain size is relatively coarse, >4 mm, and predominantly euhedral. Smaller anhedral grains are occasionally included in larger K-feldspars though. Sericite-cored grains are common and clusters of sericite with quartz rims are in two of the sections. Sericite textures appear cleavage-controlled; myrmekite has developed at altered plagioclase grain boundaries, when in contact with microcline.

Microcline is the dominant phase in one of the three sections, and in all three, quartz is the subordinate mineral. The size-distribution of microcline grain sizes is bimodal; euhedral ~15 mm megacrysts dominate sections and some contain (~1 mm) inclusions of biotite, globular quartz and rounded oligoclase textures (Figure 4.7c). Fine – grained microcline, quartz, and plagioclase form a finer-grained matrix that surrounds the K-feldspar megacrysts. Flame perthite is cleavage-parallel in J04 96.06-96.59, and in all thin sections, tartan-twinned microcline is the dominant K-feldspar.

Quartz is minor in all samples and is present in three textural generations; primary globular inclusions in feldspars, such as large (4 mm) plagioclase, secondary, interstitial chains between feldspars, and fine-grained myrmekite growths at oligoclase-microcline feldspar grain boundaries. Quartz strain extinction is variable in all sections and is strongest in large polycrystalline clusters and chains. Sample J04 42.53-43.00 shows older quartz inclusions in younger quartz, but not in feldspars, a texture which is not observed in any other section in this sample collection.

Micrographic (0.2 mm – 0.5 mm) quartz runes are prominent in the megacrystic sample VALB 03 as are wart-like myrmekite growths into K-feldspars in the similar-textured Joly Zone sample J04 96.06-96.59 (Figure 4.7d). Quartz has embayed boundaries with most feldspars, and in J04 42.53-43.00, this texture is the most prevalent. Biotite shows a subtle foliation and wraps some feldspar crystals. Blades are large (>2 mm) and most are chloritised. Colours range from pistachio green to deep grass green; however, there are red-brown grains with characteristic pleochroic halos around zircons with radioactive inclusions (Figure 4.7e). Minor accessories also include magnetite and skeletal muscovite.

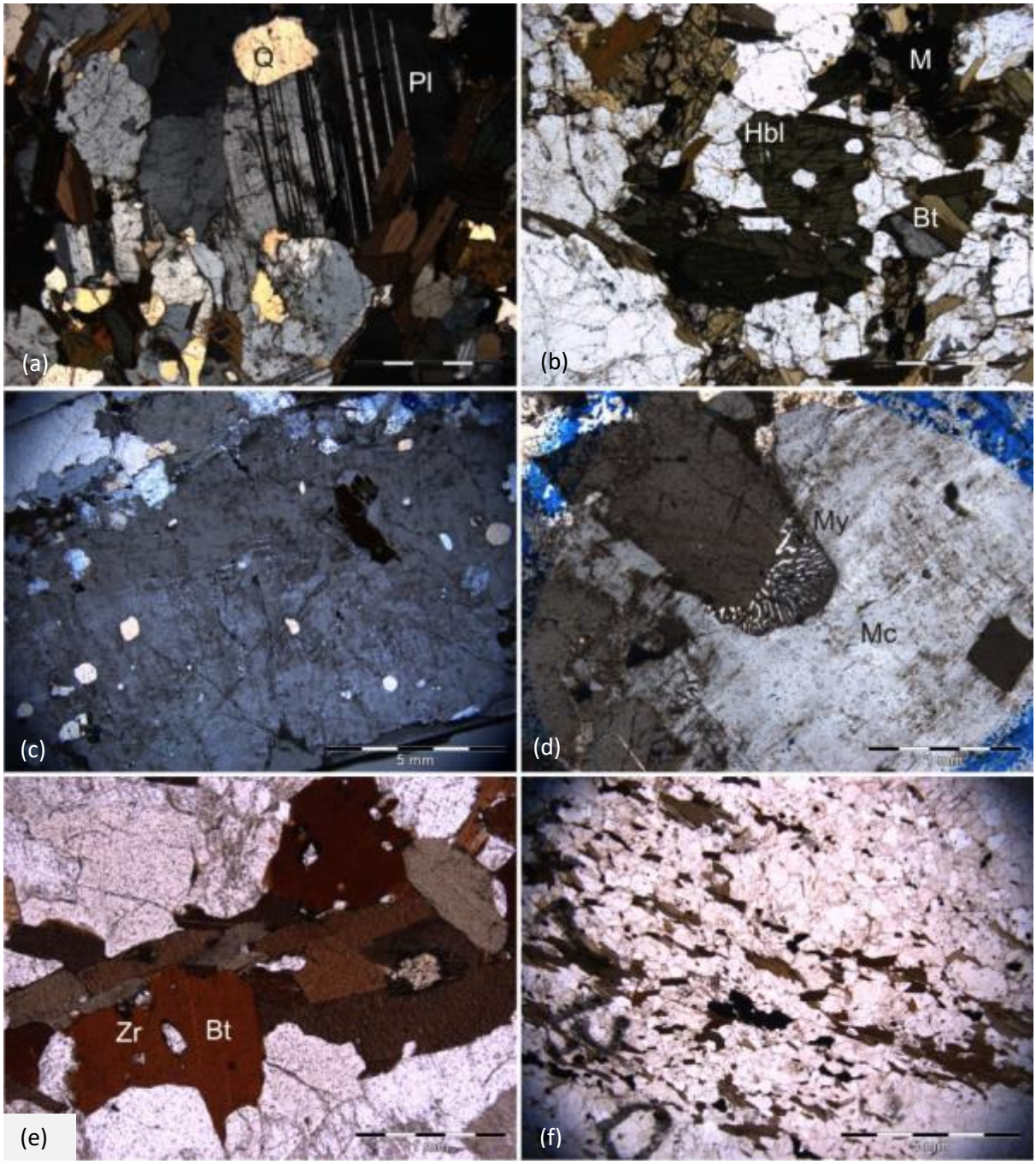



Figure 4.7 Photomicrographs of Salem Suite features at Valencia. (a) Plagioclase (Pl) is the most abundant rock-forming mineral, quartz (Q) is finer grained and anhedral, Vs04, xpl. (b) Magnetite is associated with abundant hornblende (Hbl) and biotite (Bt) Vs04, ppl. (c) Large microcline megacrysts exceed 15 mm in Salem type-2 monzogranite; the globular quartz inclusions are a common feature in all pre D3 granites, J04 96.06-96.59, xpl. (d) Myrmekite occurs where microcline (Mc) overgrows anhedral, rounded plagioclase, J04 96.06-96.59, xpl. (e) Zircon (Zr) is often in biotite and at the cores of pleochroic halos, secondary U is found at the ragged ends of biotite blades that contain zircon inclusions, J04 42.53-43.00, ppl. (f) Fabric defined by biotite reflects the shearing in megacrystic Salem suite monzogranite, VALB 01, ppl.

Deformation is a prominent feature in the megacrystic variety of Salem granite in a number of localities along a northwest strike length (parallel to the Abbabis-basement inlier contact). Conjugate extensional-shear bands are common and well exposed in the dry riverbeds and

strongly foliated localities have a banded gneissic appearance. The orientations of the shears, highlighted by partial melt veinlets of K-feldspar-quartz-biotite up to 3 cm wide, are roughly-parallel to $D_2$ shearing directions described in Longridge 2012 for the Central Zone.

The partial melts (Figure 3.44, Chapter 3) are characterised by elevated scintillometer counts and XRF analyses, summarised in Table 4.2, confirming that Th and probably K are the dominant radionuclide elements. At sites of prominent partial melting readings on the RADEye hand held scintillometer are often over 400 cps (examples of anomalously radioactive Salem granites in thin section in Figure 4.7d and 4.7e). Mineralisation is evident in thin section as β-uranophane clusters at biotite edges, particularly those with zircon inclusions, suggesting U sourced from the radioactive inclusions.

The dominant rock-forming mineral is microcline, it is predominantly euhedral, and clusters with microcline-perthite. Quartz grains are less-abundant but commonly show 120° grain boundary junctions. Exceptionally large tartan - twinned K-feldspars (>5 mm) are amoeboid to subhedral in shape. The matrix comprises smaller-sized feldspar grains that average ≤1 mm in size. Quartz is fine – grained (~0.5 mm) and predominantly anhedral and interstitial to the more euhedral K-feldspars. Inclusions of globular and subhedral quartz are found in K-feldspars but not in plagioclase. Oligoclase is scarce in the sheared Salem granite thin sections; examples display evidence of strain in lenticular albite twinning. Most grains are anhedral and are in sparse, disseminated distribution. Biotite alignment in thin section mirrors that of hand specimen textures, defining the deformation fabric (illustrated in Figure 4.7f). The common accessories include colloform haematite, a result of magnetite alteration and millimetric-scale magnetite porphyroblasts; muscovite, and zircon allude to a probable metasedimentatry source rock.

*Grey granite thin section petrography*

Thin section observations were made on specimens of Grey granite from the Hildenhof and Goanikontes deposits. Table 4.3 summarises the key features of the Grey granite sections of Hildenhof samples. The Goanikontes sample feldspar population comprises predominantly anhedral microcline (≤2.5 mm in size) and minor oligoclase. Quartz is subordinate and occurs in three main textural varieties: Coarse-grained, subhedral specimens exceeding 2.5 mm,

intermediate grains in chains and clusters between feldspar with an average grain size of <1 mm, and fine-grained, early quartz inclusions in some of the larger feldspars. Oligoclase (average of $An_{12}$) is variably sericitised, skeletal or rounded and scarce throughout, with rare larger grains containing globular quartz inclusions. Biotite is fine-grained (<0.5 mm), skeletal, chloritised and arranged in a subtly aligned fabric.

Table 4.3 Key petrographic features of type-2 and type-3 Grey granites at Hildenhof (U and Th content by XRF, in ppm). The red blocks highlight samples with the highest U and Th concentrations.

| Sample | Type | Colour and Texture | Dominant Feldspar | Plag. | Th | U |
|---|---|---|---|---|---|---|
| HILG 16 | Grey 2 Monzogranite | Intermediate grey porphyritic, coarse, subtle foliation | Oligoclase | $An_{11}$ | 26 | <9 |
| HILG 10 | Grey 3 Syenogranite | Light grey, foliated, medium | Oligoclase | $An_{15}$ | 14 | 6 |
| HILG 20 | Grey 3 Syenogranite | Light grey, foliated, medium-coarse | Microcline | $An_{15}$ | 43 | **32** |
| HILG 28 | Grey 3 Alkali-Feldspar granite | Light grey, foliated, medium | Microcline | $An_{11}$ | 13 | <9 |

Oligoclase and quartz are in roughly-even proportions (35-40 %) throughout the Hildenhof Grey granite thin sections. Oligoclase, quartz and K-feldspar occur in grain sizes between 0.5 mm - 2 mm, quartz grain sizes are more varied, from <0.05 mm to occasional >5 mm subhedral to euhedral grains. Larger (>1 mm) euhedral quartz grains are common and intermediate sized (<1 mm) quartz often has 120° junctions. Microcline is the dominant feldspar in the type-3 Grey granites, while oligoclase is dominant in the intermediate, type-2, varieties at Hildenhof. Plagioclase feldspars in the older generations are oligoclase in composition, and display albite twinning with albite rims. Myrmekite is associated with K-feldspar (microcline) contact boundaries, forming a wart-like growth as a reaction to the younger K-feldspar crystal growth. Figure 4.8a and 4.8b illustrate the textures and alteration features observed in Grey granite oligoclase-bearing specimens.

Biotite is more abundant in the type-2 Grey granite (~15 %) than the type-3, and variable alteration has resulted in two textural varieties of the mica. Grain size is varied from 0.2 mm-2 mm. The alteration of biotite reflects various stages of chloritisation, and in both chloritised, and relatively unaltered varieties radioactive inclusions are surrounded by pleochroic halos. Variable orientations have some bearing on the colour differences, but the interpretation is of a single generation with varied degrees of retrograde chloritisation

(euhedral blades in Figure 4.8c and anhedral variably chloritised laths in 4.8d). Very fine (< 0.05 mm) fluorite occurs in clusters, as a marker of fluid alteration. Accessory phases in the type-2 and type-3 Grey granites at Hildenhof include zircon, monazite, and magnetite.

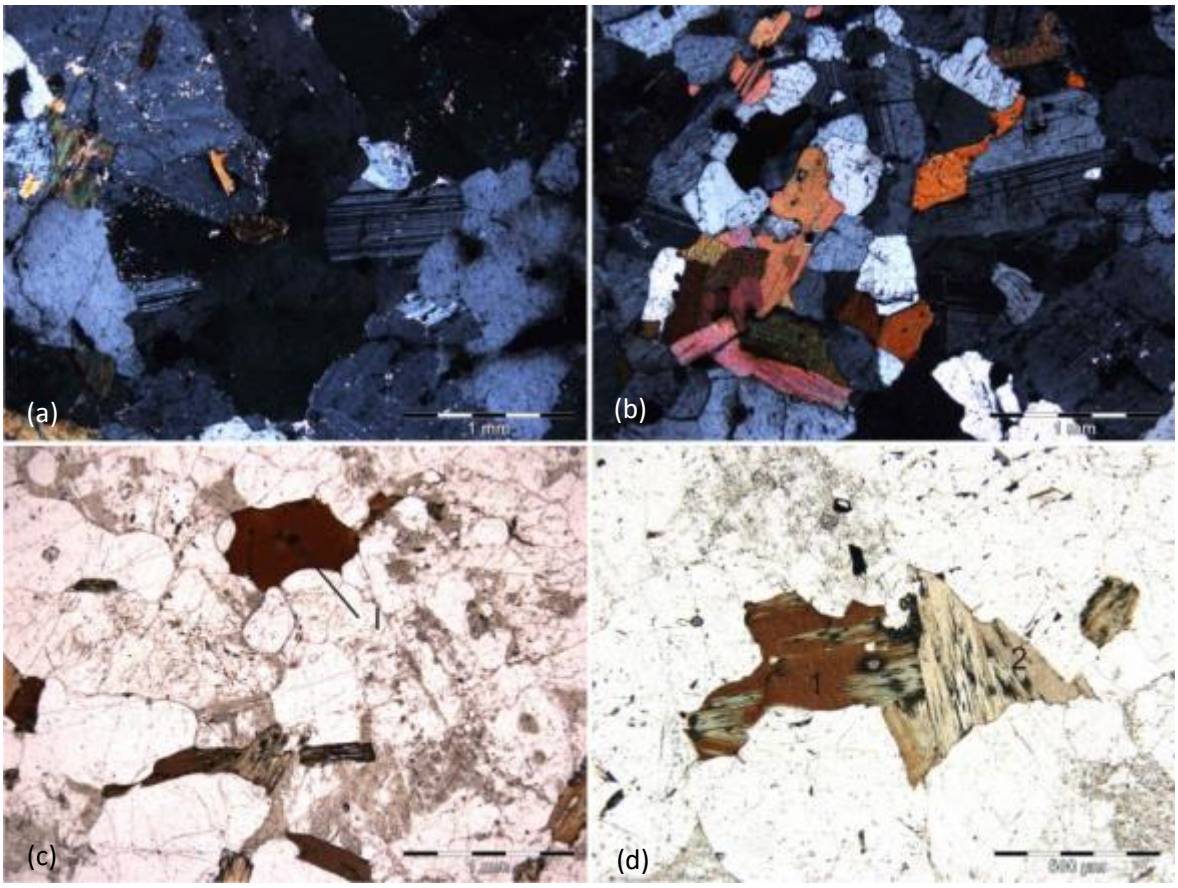



Figure 4.8 Photomicrographs illustrating features of the Grey granite varieties from Hildenhof. (a) Rounded plagioclase between strained quartz grains, note also the high order interference colours of the biotite, HILG 10, xpl. (b) The dominant feldspar is plagioclase, many grains are euhedral with irregular boundaries at later quartz boundaries, HILG 16, xpl. (c) Biotite contains prominent radioactive inclusions (I) HILG 20, ppl. (d) Well - cleaved, partially chloritised biotite contains zircon inclusions (1). Cleavage-parallel view shows alteration along the planes (2) HILG 20, ppl.

Two of the Ggrey type-3 thin sections show oligoclase as the most abundant feldspar (>35 %). Average grain sizes range from 20 µm to > 5 mm, in contrast to the overall 1.5 mm to 2 mm average in quartz and K-feldspars. Sericite occurs in the majority of the oligoclase, and in the microcline-dominated sample. Albite rims around most feldspar may represent sub-solidus reaction. Microcline-perthite is the dominant K-feldspar in two of the sections and in one, tartan-twinned microcline dominates the section (typically 0.5 mm -1 mm across in the thin section specimen).

There are three prominent quartz textures: The oldest is fine globular inclusions in feldspar. The intermediate texture is relatively fine-grained with irregular feldspar contacts and is predominantly in interstitial chains and clusters of subhedral grains with variable strain extinction; and the youngest variety is in strings of fine, late quartz that appears to cut the larger grains and is occasionally in graphic intergrowth with K-feldspars.

The blades of biotite in the younger granite are sparsely distributed relative to the older generations, and occasionally define a recognisable fabric or preferred orientation in some sections and are rarely larger than 1 mm in length. As with the older Grey granites, the biotite in the younger type host pleochroic halos around radioactive inclusions of zircon and monazite.

*Red Granites*

The Red granite variety at Hildenhof is observed in two thin sections; the details are summarised in Table 4.4. Both show a foliation, a light red to pink colour, and contain remnant, metasedimentary aluminous minerals, primarily sillimanite and skeletal muscovite, alluding to their anatectic nature.

Table 4.4 Key petrographic features of Red granites at Hildenhof. The red blocks highlight samples with the highest U and Th concentrations. (U and Th content by XRF, in ppm)

| Sample | Type | Colour and Texture | Dominant Feldspar | Plag. | Th | U |
|---|---|---|---|---|---|---|
| HILG 06 | Red | Brick red, fine-medium, foliated, sillimanite patches | Microcline | $An_{11-17}$ | **123** | <9 |
| HILG 30 | Red | Brick red, fine, foliated | Microcline | $An_{12}$ | 25 | <9 |

Tartan-twinned microcline dominates the Red granite thin sections (>40 % modal) and forms a matrix of 0.5 mm-2 mm, sub- to euhedral grains. Microcline-perthite is minor in both samples and perthite development is present in a small proportion of the microclines. Plagioclase is minimal and occurs as fine (<1 mm) anhedral grains, occasionally euhedral, of albite - oligoclase composition. Quartz is sub- to euhedral and finer grained than feldspar, it occurs as 0.1 mm-1 mm grains; the fine - grained portion includes sparse, globular inclusions in feldspar and the majority of the larger grains are in chains and clusters, mostly interstitial

to the feldspar and rarely in micrographic intergrowth. Biotite is a minor component (<10 %) and is partially chloritised. Bladed grains with pleochroic halos range in size from 1 mm - 2 mm, with minor skeletal grains observed in both sections. Fine, sparse sillimanite is the most prominent accessory phase along with retrogressive and entrained muscovite.

## 4.7 Thin section petrography of A- and B-type sheeted leucogranites

A-type leucogranites that were sampled at the Valencia and Ida Dome areas were examined in thin section, and summarised in Table 4.5.

Table 4.5 Petrographic characteristics of A and B-type sheeted leucogranites from Valencia (U and Th content by XRF, in ppm).

| Sample | Type | Colour | Grain size | Texture | Biotite | Main Feldspar | Plag. | Th | U |
|---|---|---|---|---|---|---|---|---|---|
| VALG 23 | A | V. light grey | Fine | Foliated, aplitic | Prominent streaks | Microcline-perthite | $An_{12-15}$ | **14** | 7 |
| VALG 01 | $B_a$ | Light pink | Medium-fine | Aplitic with foliation | Minimal, skeletal | Microcline-perthite | $An_{12-17}$ | 9 | 7 |
| VALG 13 | $B_p$ | Cream-white | V. coarse | Pegmatitic | Minimal, skeletal | Oligoclase | $An_{17}$ | 9 | 6 |
| VALG 22 | $B_p$ | Light pink-white | Coarse | Inhomogeneous | Minimal, skeletal | Oligoclase | $An_{12}$ | 9 | 6 |
| IDAG 01A | A/B | White | Fine and coarse | Inhomogeneous, foliation | Disseminated, skeletal | Albite-oligoclase | $An_{15}$ | <12 | <9 |
| IDAG 01B | A/B | White | Medium-coarse | Inhomogeneous, foliation | Disseminated, skeletal | Microcline-perthite | Seric. | <12 | <9 |
| IDAG 09 | A/B | White | Fine-medium | Homogeneous, foliation | Fine streaks | Albite-oligoclase | $An_{16}$ | <12 | 12 |

Microcline-perthite dominates the Valencia A-type thin sections. It has two generations of perthite, albite overprints older microperthite. Grain sizes are 1 mm to 2 mm and most K-feldspars are anhedral. Quartz grains cluster, some with straight 120° junctions, while individual grains have embayed edges. Fine, globular quartz occurs in K-feldspars throughout the section and occasionally in oligoclase. Strain is not uniform in all quartz, as there is clearly a later generation associated with the anhedral feldspars.

Sericite occurs in most oligoclase inclusions as well as in grains that are in contact with microcline, which also tend to develop minor vermicular quartz or myrmekite at the boundaries.

The aplitic B-type variety (VALG 01) has prominent tartan-twinned microcline which can be as large as 5 mm and contains a high % of globular quartz inclusions as well as anhedral (0.5 mm) zoned oligoclase with consistent twinning from core to rim. The finer plagioclase forms interstitial clusters with similar sized quartz between large amoeboid quartz.

Most quartz is anhedral in both textural varieties (Figure 4.9a). Grain sizes in the pegmatitic varieties ranges from 1 - 3 mm grains to <0.05 mm amoeboid inclusions. Euhedral quartz (1-3 mm) clusters do occur in the pegmatitic variety, but are not abundant. Quartz in the aplitic type show strain extinction. The aplitic textured B-type has entrained metasedimentary muscovite in large (up to 4 mm) skeletal, sheets. It often wraps the edges of garnets or is interstitial to larger feldspars and quartz. Distinctive nests and laths of sillimanite occur in the pegmatitic sample thin sections (Figure 4.9b).

Oligoclase is the main feldspar in the pegmatitic varieties and grainsize varies from ~1 mm to >8 mm; myrmekite development is scarce because there is comparatively little K-feldspar with which to react. What microcline there is present usually contains quartz inclusions. Plagioclase alteration is characterised by cleavage-parallel sericite and coarse clay minerals, grouped epidote (zoisite/clinozoisite).

Three thin sections of A-type granites from the Ida Dome area show the following common features: Tartan-twinned microcline or microcline-perthite as the main feldspar phases (>40 % of sample) and oligoclase as the subordinate; oligoclase is predominantly in subhedral texture with grains >2 mm across being common. Skeletal or rounded oligoclase crystals are observed between- or included in K-feldspar and quartz.

Oligoclase that is observed as inclusions in microcline has reacted to form myrmekite at the edges (Figure 4.10a). Oligoclase grains often display zoning, where albite rims form in the subsolidus. The zoned oligoclase grains have higher An in their cores than grains with no zoning, potentially there are early and late plagioclase growths associated with deformation ($D_3$). Large, euhedral (1-2 mm) oligoclase also tends to have a lower An content than the smaller skeletal and rounded grains.

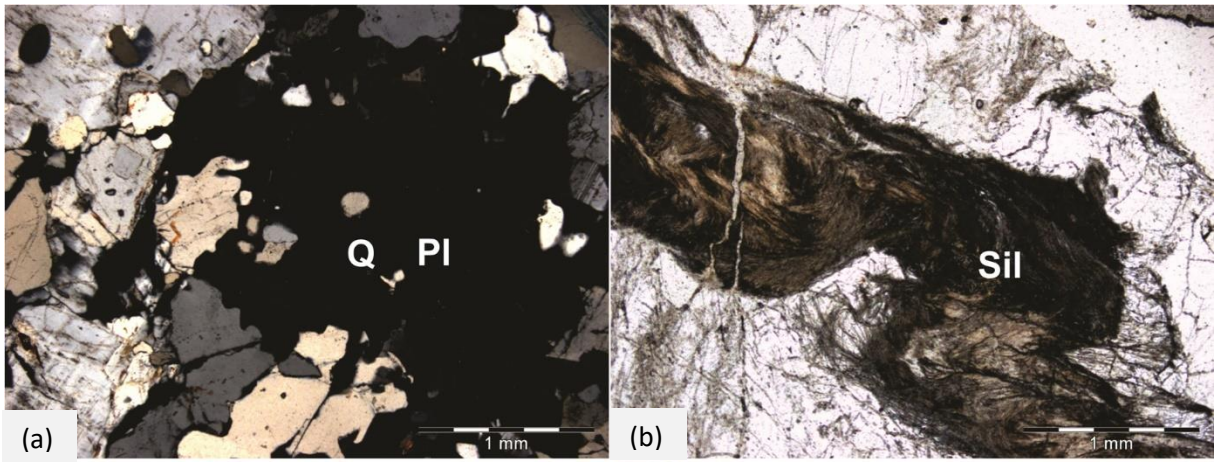



Figure 4.9 Photomicrographs of B-type sheeted leucogranites at Valencia. (a) Examples of quartz textures; globular and amoeboid - shaped quartz inclusions occur in plagioclase. VALG 01, xpl. (b) Laths of entrained sillimanite are characteristic of pegmatitic B-types, VALG 13, ppl.

Quartz occurs in three generations; the oldest is amoeboid and globular textured inclusions in millimetric feldspars (both plagioclase and K-feldspar), and larger anhedral, and younger euhedral grains are found in clusters or chains throughout the samples, in varied grain sizes and proportions. Late stage quartz veinlets cross cut the feldspars to varying degrees in all samples. Biotite is fine-grained (sub- 1 mm) bladed and skeletal, and often with pleochroic halos surrounding zircon inclusions. The SLG has incorporated sillimanite, skeletal quartz, and polycrystalline quartz from the metasediment dominant source (Figure 4.10b).

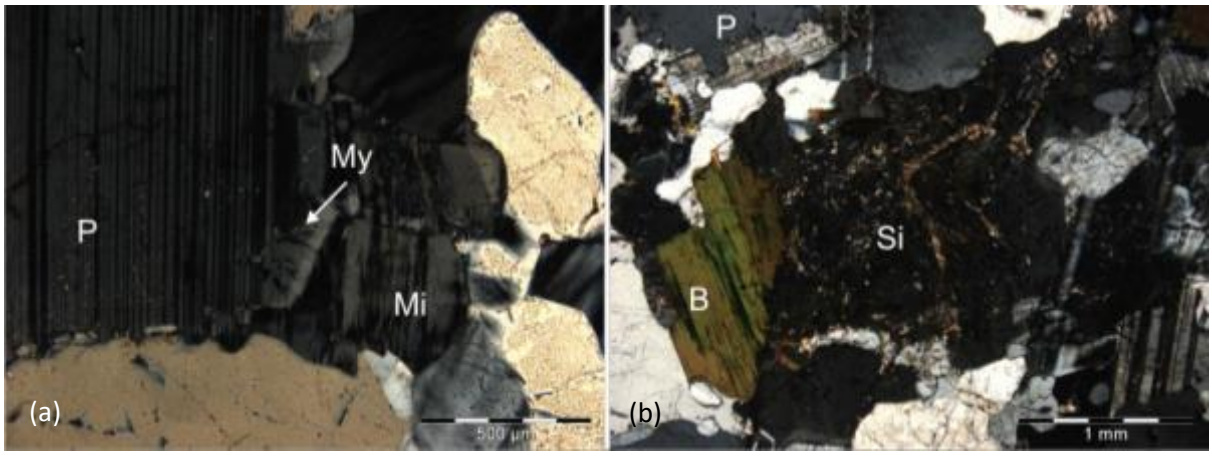



Figure 4.10 Photomicrographs of the A-types at Ida Dome. (a) Plagioclase (P) occurs as skeletal or rounded inclusions between or in K feldspar and quartz. Biotite (B) is bladed and skeletal often with pleochroic halos, sillimanite (Si) is a common accessory when remnant laths of metasediment are present, IDAG 01A, xpl. (b) Large plagioclase (P) grains tend to have lower An than their skeletal and rounded counterparts, margins in contact with K-feldspar (Mi) have myrmekite development, IDAG 09, xpl.

## 4.8 C-type Sheeted Leucogranite Thin Section Petrography

### *Goanikontes C-type Sheeted Leucogranites*

The C-type SLGs tend to show accessory mineral dominance that correlates with stratigraphic level of intrusion, a pattern consistent from deposit to deposit in the study region. However, there are some inconsistencies observed in assessing the accessory assemblages in thin section. For example, DH022 59.00-59.24 is a magnetite-dominated leucogranite in hand-specimen but contains a millimetric nest of skeletal quartz-tourmaline (Figure 4.11a) as an inclusion within a larger microcline cluster (Figure 4.11b). The sample is dominated by coarse (5 mm) magnetite-ilmenite clusters. Table 4.6 summarises the thin section observations of the Goanikontes C-type samples.

Table 4.6 Petrographic characteristics of C-type leucogranites from the Goanikontes area. Uranium occurs in biotite and refractory minerals such as zircon. Phosphates such as apatite, monazite and xenotime are abundant in the Goanikontes (Etango) area, and are the U and Th hosts, in addition to thorite. (U and Th content by XRF, in ppm)

| Sample | Colour | Grain size | Texture | Biotite | Plag. comp. | Th | U | Type |
|---|---|---|---|---|---|---|---|---|
| DH012 66.41-66.79 | Pink and white | Medium-coarse | Homogeneous, graphic | Large entrained laths | $An_{12-12}$ | 33 | **371** | C |
| DH022 59.00-59.24 | Light pink | Coarse | Inhomogeneous | Minor, disseminated | $An_{5}$ | 9 | 6 | $C_m$ |
| DH019 67.09-67.54 | Pink and white | Medium | Homogeneous | Minor, disseminated | $An_{12}$ | 52 | 10 | $C_m$ |
| DH019 76.39-76.67 | Pink and white | Medium-coarse | Homogeneous | Minor, disseminated | $An_{5-17}$ | 18 | 37 | $C_m$ |
| DH012 198.58-198.77 | Pink and white | V. coarse | Pegmatitic | Large laths | $An_{5-15}$ | **203** | **278** | $C_t$ |
| DH012 315.67-315.93 | White | Coarse | Inhomogeneous | Minor, disseminated | $An_{5-10}$ | 24 | 24 | $C_t$ |
| DH019 100.50-100.93 | Pink | V. coarse | Pegmatitic | Skeletal blades | Too altered | <12 | <9 | F |

### *Accessory-free C-type*

Accessory-free C-type sheeted leucogranites at Goanikontes tend to have graphic quartz in large microcline grains (Figure 4.12a) and microcline inclusions in larger microcline–perthite.

Perthite is less prominent in the tourmaline-bearing varieties and microcline inclusions in quartz are not present. Euhedral quartz inclusions in plagioclase are found in most C types; accessory-free DH022 59.00-59.24 and DH012 66.41-66.79 for example (Figure 4.12b).

Quartz occurs in more than one generation- early inclusions and entrained skeletal grains are common in all sections, larger quartz grains are euhedral in the coarse tourmaline varieties and anhedral and vermicular in the magnetite-bearing varieties. Coarse-grained quartz often envelops feldspars (Figure 4.12c) and forms quartz-dominant clusters, visible in hand specimen.

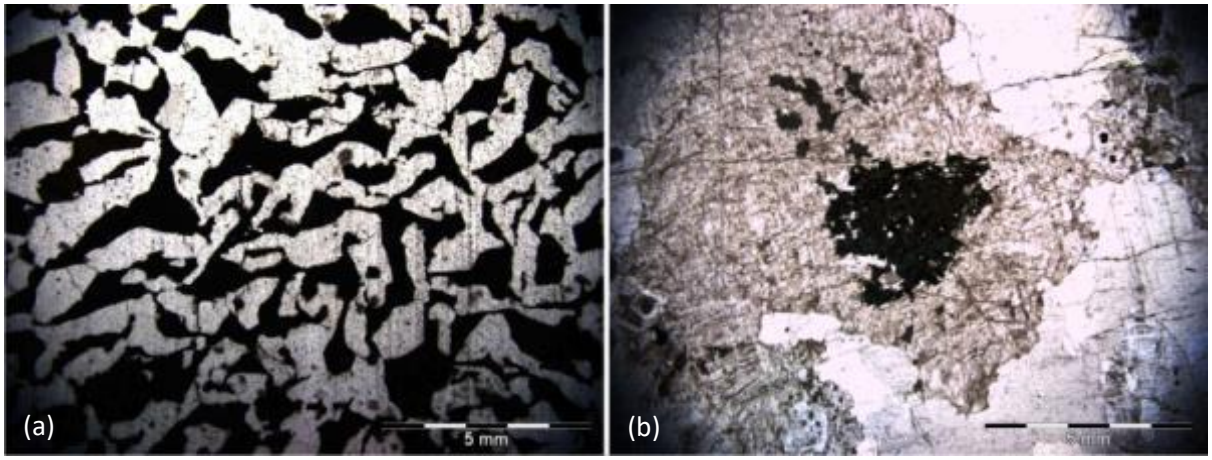



Figure 4.11 Tourmaline in C-type sheets from Goanikontes. (a) Quartz – tourmaline nests are common in very coarse and pegmatitic C-type leucogranites- in very coarse samples individual prismatic tourmaline crystals are visible in hand-specimen, DH012 198.58-198.77, ppl. (b) Massive-textured tourmaline is more common, and occurs as inclusions in feldspars or interstitial to large quartz and feldspar crystals, it is found in samples from all the deposits in this study, DH022 59.00-59.24, ppl.

*Tourmaline -bearing C types*

Tourmaline occurs in cm-scale nests with vermicular quartz. The nests comprise distinctly finer-grained crystals relative to the surrounding rock texture. These granites are pegmatitic in texture, and form roughly $S_1/S_0$-parallel sheets in surface expression; some may be several metres thick. They are comparable to similar sheets at Valencia and the Ida Dome.

Plagioclase feldspar constitutes <10 % of most of the thin sections of the Etango $C_t$-types; grain size and abundance are significantly biased to the potassic feldspars. Oligoclase specimens are often no more than sub-mm rounded, zoned inclusions or anhedral clusters between large quartz and microcline. Occasionally large grains up to 4 mm across are present. Sample DH012 66.41-66.79, is an exception to the K-feldspar dominated sample set and comprises at least 30% fine - grained (≤0.5 mm) oligoclase. The An content of the plagioclase inclusions varies from $An_5$-$An_{20}$ and is on average >$An_{12}$. The plagioclase composition is bimodal, the larger often euhedral plagioclase compositions rarely exceed $An_{10}$ and in the finer component, An is consistently >10 %. In comparison, plagioclase compositions recorded for Goanikontes surface samples by Nex (1997) report an oligoclase composition of $An_{20}$-$An_{30}$ which is higher than the maximum of $An_{20}$ observed in this study of core samples.

Sericitisation of oligoclase is persistent throughout and many have albite rims with myrmekite that occasionally continues into the cores of some grains. Zoned oligoclase (Figure 4.12d) should be distinctly albite composition at the rim, while the older cores, more oligoclase, however, twin extinction angles are consistent between cores and rims. This suggests simple recrystallization of the same material in the subsolidus. Myrmekite tends to be in the outer rim, overprinting any reaction textures that may have been hosted on the original grain boundary.

Myrmekite growth occurs where oligoclase contacts K-feldspar rims (Figure 4.12e) and where it is included in microcline, the whole grain may be myrmekite. Another typical observation in the $C_t$-types is graphic-textured quartz-microcline growth (Figure 4.12f) which is a distinguishing feature between the earlier $C_t$-type and later mineralised D-type. The alteration observations in these samples are consistent with the more comprehensive sample observations presented in Nex (1997).

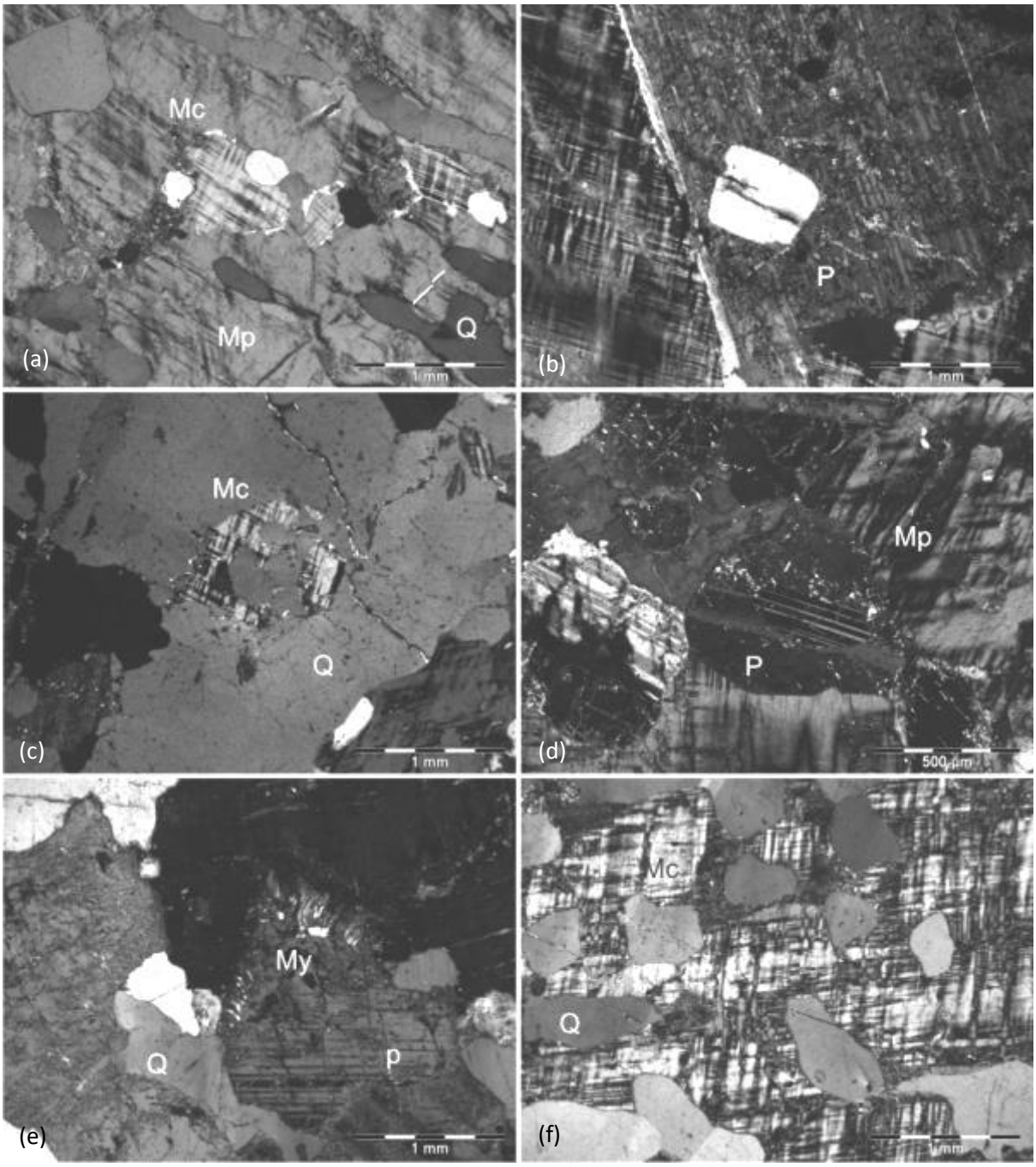



Figure 4.12 Textural features of the C-type sheeted leucogranites sampled from Goanikontes core. (a) Tartan microcline, euhedral and vermicular quartz (Q) in microcline – perthite (Mp) in an accessory-free C-type, DH012 66.41-66.79, xpl. (b) Euhedral quartz included in euhedral plagioclase in a magnetite C-type, which coincidently also has tourmaline (Figure 4.11b) DH022 59.00-59.24, xpl. (c) A magnetite-bearing C-type, in which microcline is surrounded by later quartz, DH019 67.09-67.54, xpl. (d) Zoned plagioclase in a tourmaline C-type; the grain resembles a plagioclase overgrowth more than a zoned single grain. The inner plagioclase has ~$An_5$ composition, DH012 315.67-315.93, xpl. (e) Myrmekite develops at plagioclase – K-feldspar grain boundaries, and is rarely observed in the cores of the feldspars, DH019 76.39-76.67, xpl. (f) Typical pegmatite with graphic quartz growth in large (>10 mm) microcline, DH019 100.50-100.93, xpl.*Magnetite-bearing C-types*

The $C_m$-type sheeted leucogranites on the Etango project primarily intrude the Khan Formation, although this interpretation may be biased by the drilling targets that avoid the overlying Chuos Formation rocks. As such, the magnetite-bearing samples are the most abundant non-mineralised SLGs in core specimen, for this study.

Biotite is often the only accessory phase in the pegmatitic varieties, it occasionally contributes to anomalous U, as a host to inclusions. The accessory assemblages do overlap to some extent, however, magnetite is predominantly limited to sheets in the Khan Formation, while tourmaline occurrences are more often observed in sheets intruding semi-pelitic Chuos Formation units. All of the samples of this study that were sourced from within the Khan Formation at Goanikontes contain magnetite porphyroblasts. It occurs as singular euhedral porphyroblasts and as interstitial mm-scale blebs between large feldspars and quartz. The majority of the $C_m$-types in the Goanikontes cores comprise pink and white feldspars in excess of quartz; a coarse but relatively homogeneous texture, minimal biotite and significant amounts of accessory magnetite.

Thin sections show more than one generation of microcline in some of the magnetite bearing $C_m$-type sections. The older is tartan twinned and included in larger microcline-perthite. Feldspar grain sizes range from <0.2 mm to >10 mm, with microcline-perthite in the larger grains. Magnetite textures are variable in the $C_m$ types and show evidence of sub-solidus mobilisation and formation[35]. Figure 4.13a and 4.13b illustrate rare magnetite with straight grain edges between quartz and feldspar. Note magnetite propagation into fine space between the grains. Figure 4.13c and 4.13d shows magnetite filling a void between tartan microcline and microcline-perthite as well as cross-cutting the microcline-perthite. Ilmenite is also a common accessory and occurs as skeletal grains (Figure 4.13e) and as exsolution lamellae in magnetite (Figure 4.13f).

[35] It also occurs in Grey granites though more scarce and usually between crystallised quartz-feldspars instead of the more euhedral porphyroblasts observed in the leucogranites.

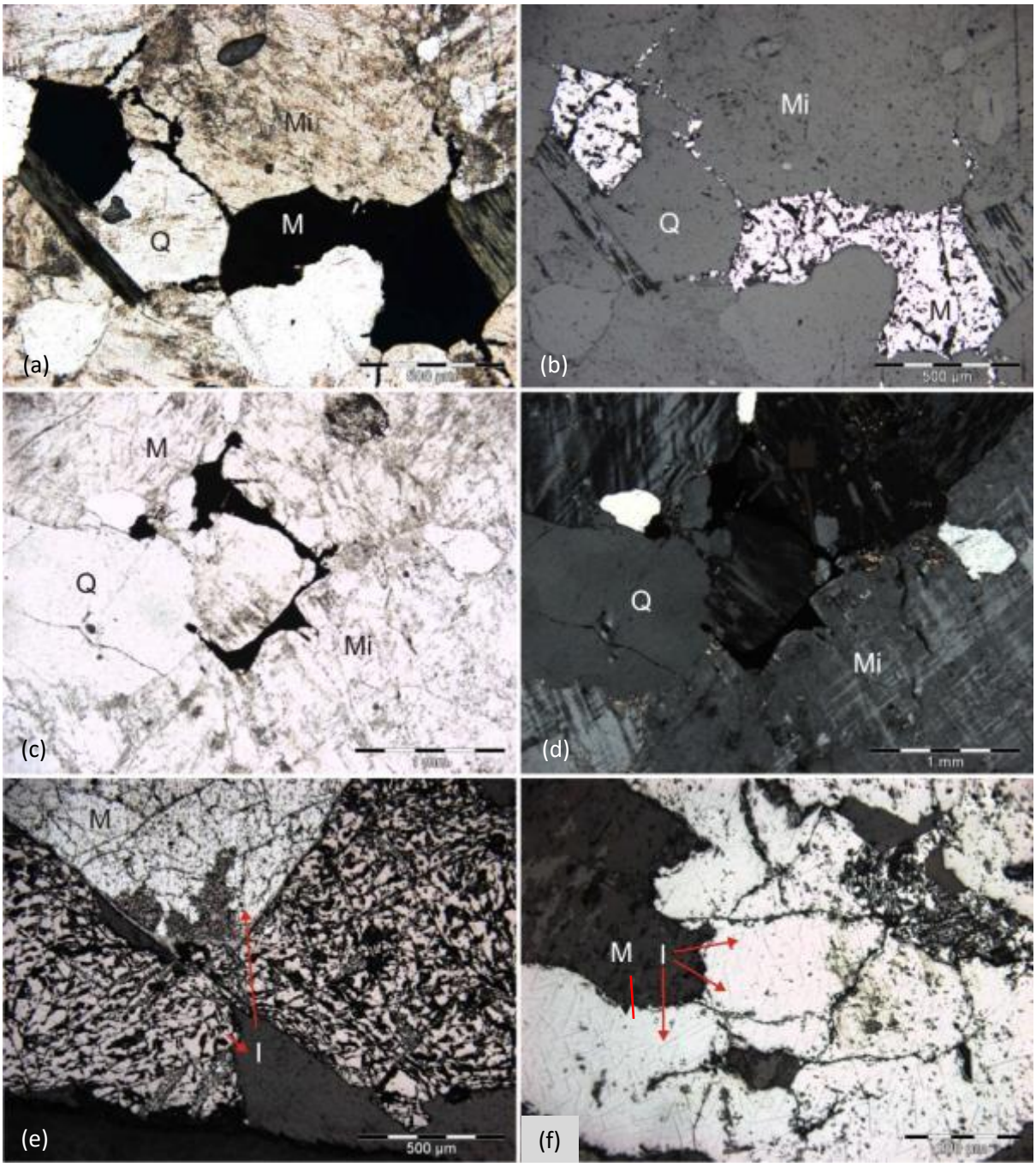



Figure 4.13 Magnetite in grey type-3 from Hole DH012, in mineralised sheeted leucogranite from Hole DH019 and Cm-type from Hole DH022. (a) and (b); Euhedral magnetite (M) surrounds a quartz (Q) crystal, magnetite permeates between the euhedral quartz and adjacent microcline as well as in fractures of the feldspar (Mi) DH012 197.04-197.35, ppl and rfl. (c) and (d); Magnetite (M) bisects a microcline-perthite grain and also permeates into fractured quartz (Q) and microcline (Mi) DH019 71.74-72.18, ppl and xpl. (e) and (f); Magnetite (M) often occurs with exsolved ilmenite (I) however ilmenite occasionally does occur on its own and is usually adjacent to magnetite, DH022 59.00-59.24, both rfl.

Biotite is a minor accessory, rarely >0.5% - 1% in all samples and is partially or completely chloritised with prominent FeO along cleavages. Textures range from disseminated blades and skeletal grains to laths and clusters with a very broad range in grain sizes of fine and coarse booklets (0.05 - 2 mm). Pleochroic halos around zircons and/or phosphates and uraninite are common and best observed in sections parallel to the biotite x-axis.

Muscovite is skeletal and associated with biotite when entrained with quartz; it has also developed from plagioclase breakdown during metasomatism. The common accessories such as zircon, monazite, xenotime, apatite, muscovite and occasional fluorite (particularly with biotite) occur in most C-type samples. Inclusions of phosphates, zircon and biotite-associated accessory mineral assemblages would explain anomalous Ce, La, Th, U and Y identified in the C-types (Chapter 5).

***Hildenhof C-type Sheeted Leucogranites***

The subdivision into three varieties (either; pink or white, or a combination) of the C-type sheets at Hildenhof is based, primarily on coloration of the feldspars (white, pink or both), and on the accessory mineralogy in the limited variety of samples observed and collected. Table 4.7 summarises the features observed in C-type samples from Hildenhof. In terms of accessoruy mineral classification, the Hildenhof C-types are either magnetite-bearing or accessory-free, tourmaline is rare.

The white variety is homogeneous, coarse-grained and relatively free of biotite and other accessory phases. The pink varieties are medium- to coarse-grained, with variable biotite abundances and tend to have lower quartz content. The deep pink coloration evident in many surface samples is a result of a later episode of alteration. The third variety is less abundant and characterised by distinctive pink and white feldspar combinations, as observed in the magnetite bearing samples from the Etango, Valencia and Ida Dome areas. It typically intrudes within the Khan Formation.

Table 4.7 C-type granite samples from the Hildenhof Anomaly (U and Th content by XRF, in ppm). N/A no analysis.

| Sample | Colour | Grain size | Texture | Biotite | Main Feldspar | Plag. comp. | Th ppm | U ppm |
|---|---|---|---|---|---|---|---|---|
| HILG 22 | Pink | Coarse | Homogeneous | Entrained ghost streaks | Microcline | Seric. | N/A | N/A |
| HILG 24 | White | Medium | Inhomogeneous | Minimal, fine, disseminated | Microcline-perthite | $An_{12}$ | <12 | <9 |
| HILG 25 | White | Medium | Homogeneous | Minor, clustered | Microcline | $An_{12}$ | <12 | **15** |
| HILG 26 | Pink | Medium-Coarse | Inhomogeneous | Minor, clustered | Microcline | $An_{10}$ | <12 | <9 |
| HILG 27 | Pink and White | Medium | Inhomogeneous | Fine, disseminated, throughout | Microcline | $An_{15}$ | <12 | <9 |
| HILG 31 | Pink | V. coarse | Inhomogeneous | Minor, clustered | Microcline | Seric. | 9 | 6 |

Quartz is concertal, embayed and occasionally euhedral to subhedral. Fine micro-veinlets and myrmekite growth with plagioclase are common in all slides (Figure 4.14a). The majority occurs in chains and beaded strings of <1 mm subhedral grains. Most display strain extinction, particularly the large polycrystalline grains. Quartz shows variable extinction but is not interpreted to represent a significant strain component (Figure 4.14d). Accessory minerals are scarce but include some euhedral examples of common primary minerals such as monazite, apatite, and zircon (Figure 4.14 e).

Microcline and microcline-perthite are the dominant feldspars, and tartan-twinning dominates in all samples. The majority of samples are coarse-grained and many grains exceed field-of-view (~4 mm).

Plagioclase reveals a complex history to the granite, early-formed plagioclase is anhedral and included in microcline (Figure 4.14b); it either represents an entrained component, or partial resorption prior to final crystallisation of the granite. Zoned, anhedral plagioclase on the other hand, may represent multiple growth phases, with a final resorption prior to final crystallisation (Figure 4.14c). The latter is consistent with the multiple phases of granite sheet injection to form thick composite sheets (described in Nex, 1997 at Goanikontes for example). Twinning planes that cross-cut the zones support an interpretation of crystallisation from a consistent granite magma composition with time.

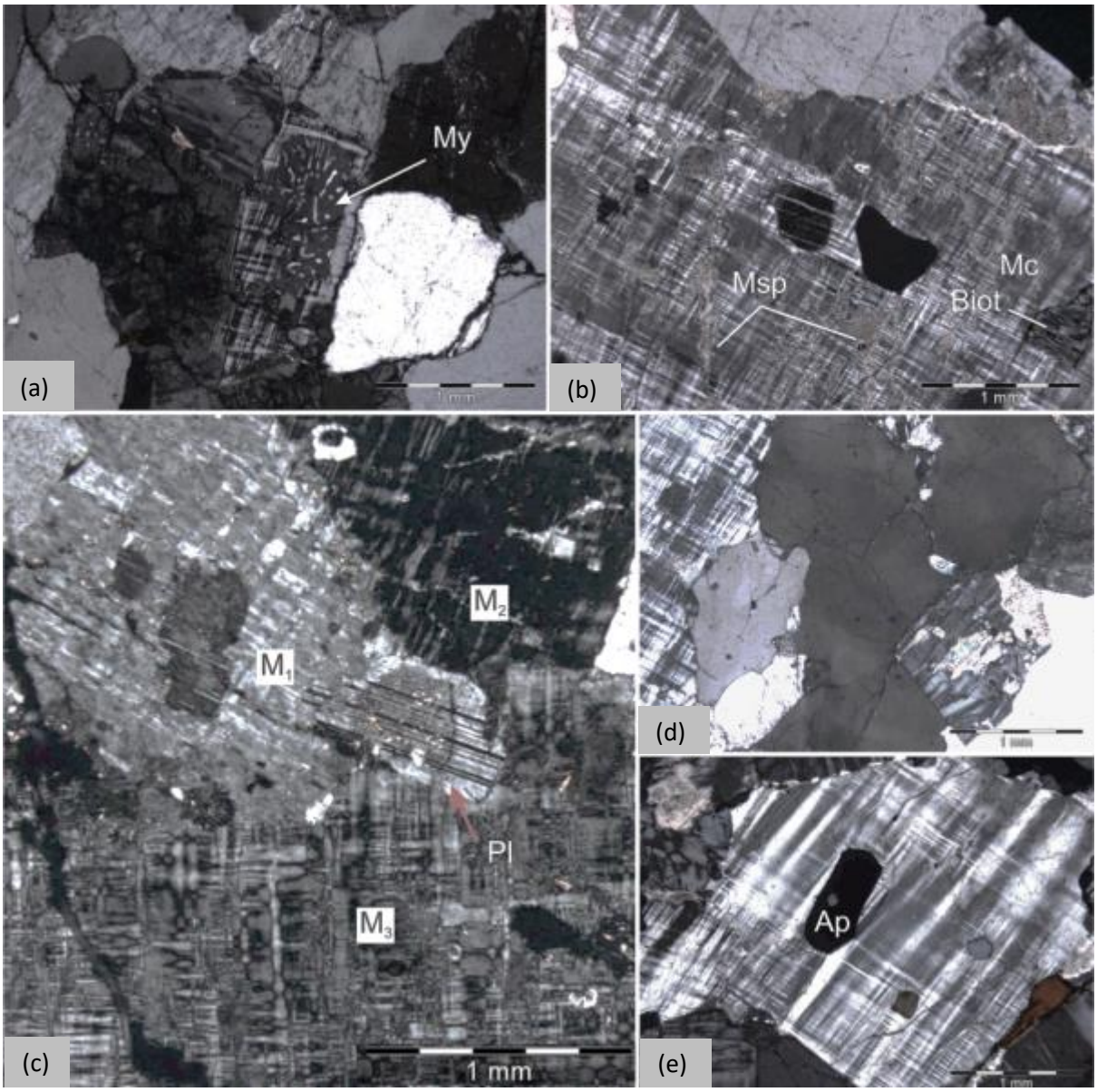



Figure 4.14 Common features in C-type sheets at Hildenhof. (a) Myrmekite in a plagioclase inclusion within microcline, HILG 27, xpl. (b) Zoned plagioclase inclusions in microcline, HILG 25, xpl. (c) Zoned plagioclase at a junction of three microcline grains, note the round quartz inclusions in microcline (bottom right), HILG 26, xpl. (d) Strained quartz embayed with microcline, muscovite inclusion in microcline (bottom right) and euhedral plagioclase adjacent to quartz (centre right) HILG 27, xpl. (e) Apatite (Ap), biotite and quartz inclusions in microcline, accessories are scarce in the U-barren sheets at Hildenhof, HILG 22, xpl.

### *Ida Dome Area C-type leucogranites*

The Ida Dome area is characterised by voluminous C-type intrusives that have invaded the U-prospective Nosib - Swakop Group transitional contact. Table 4.8 summarises the petrographic samples.

Table 4.8 Petrographic characteristics of C-type sheeted leucogranites from the Ida Dome areas ¼ NQ core (U and Th content by XRF, in ppm).

| Sample | Colour | Grain size | Texture | Biotite | Dominant Feldspar | Plag. | Th | U | Type |
|---|---|---|---|---|---|---|---|---|---|
| IDAG 07 | Light pink | Coarse | Inhomogeneous | Minimal | Microcline-perthite | $An_{12-15}$ | 16 | <9 | C |
| IDAG 19 | Pink and white | Coarse | Homogeneous | Minimal | Microcline-perthite | $An_{17}$ | <12 | 18 | C |
| IDAG 23 | White | Medium-coarse | Subtle foliation | Disseminated, sparse | Microcline-perthite | Seric. | <12 | <9 | C |
| IDAG 02 | Pink | Medium | Homogeneous | Entrained, booklets | Microcline | $An_{10-17}$ | 9 | 6 | $C_m$ |
| IDAG 08 | Pink and white | Medium | Homogeneous | Minimal | Microcline | $An_{12}$ | **73** | **128** | $C_m$ |
| IDAG 15 | Pink | Medium | Homogeneous | Disseminated, fine | Albite-oligoclase | $An_{10}$ | <12 | <9 | $C_m$ |
| IDAG 24 | Pink | V. coarse | Pegmatitic | Minimal, entrained | Albite-oligoclase | $An_{10}$ | <12 | <9 | $C_m$ |
| HDD 027 142.01-142.31 | White | Medium-coarse | Inhomogeneous | Entrained streaks | Microcline/ oligoclase | **$An_{12-18}$** | no data | no data | $C_m$ |
| IDAG 22 | V. light pink | Medium | Homogeneous | Minimal, entrained | ~Plagioclase | $An_{17}$ | <12 | <9 | $C_t$ |
| IDAG 04 | Light pink | Coarse | Inhomogeneous | Minimal, skeletal | Microcline-perthite | $An_{16}$ | 10 | 31 | Barren halo |

The dominant rock-forming phase is microcline, as observed in ten thin sections of ten C-type granites. A rough modal estimate is >35 % - 45 % based on grain counts. Microcline-perthite is a minor phase and is present in all samples. Microcline grain sizes average ≤3 mm and exceed 8 mm in two of the samples. Observations in most sections show microcline forming after plagioclase, and a replacement texture is shown in Figure 4.15a; usually as pseudo-inclusions formed in plagioclases along fractures, e.g. in IDAG 22 (Figure 4.15b). Quartz occurs in multiple generations; the oldest variety comprises globular and skeletal inclusions in feldspar (microcline); intermediate larger grains, which are anhedral- to subhedral in shape precede a final generation of coarse-textured, >5 mm, euhedral quartz.

Plagioclase compositions are dominantly oligoclase, and together with albite, the majority feldspar(s) in three of the C-type examples (two are magnetite varieties and one is tourmaline-bearing). The majority of oligoclase is amoeboid or rounded and included in microcline or interstitial to larger quartz and K-feldspars. Many of the plagioclase grains are albite rimmed, with twinning continuous across the zonation. Plagioclase distribution in some sections is distinctly bi-modal comprising compound grains >4 mm in size displaying multiple twinning, and singular, sparsely distributed, <2 mm near euhedral grains.

Biotite is scarce and in most thin sections, it occurs as skeletal blades and as fine disseminated inclusions. Occasionally it occurs in mm - scale booklets.

Magmatic, reaction textures are abundant in surface and hand specimens, particularly in the tourmaline-bearing varieties where sub solidus reactions produce vermicular and rune shaped quartz and quartz–tourmaline nests. Vermicular quartz is only rarely observed in plagioclase cores, contrasting with observations at Goanikontes by Nex (1997); and myrmekite has developed as solid state reactions between plagioclase and K-feldspar contacts. Accessories present include apatite (IDAG 19); zircon (IDAG 22); and muscovite (IDAG 22) (illustrated in Figure 4.15a, b and c, respectively).

*Ida Dome Magnetite C-types*

Thin sections of $C_m$-types show microcline to be the dominant mineral, with characteristic inclusions of flame textured albite and globular quartz. K-feldspars are coarse, centimetric, and more euhedral than the other phases. K-feldspar grain boundaries often have myrmekite replacement textures at plagioclase contacts (Figure 4.16a).

The overall rock texture is that of tartan-twinned microcline replacing- and surrounding plagioclase (Figure 4.16b). Chill margins usually contain schlieren of biotite from the host schists and gneiss. Microscopic observations show fine- and coarse-grained textures divided by biotite trains. HDD025 142.01-142.37 illustrates the grain size contrasts in a leucogranite chill margin, with a skeletal biotite train dividing distinct grain-size distributions (Figure 4.16c

and d). Significant amounts of mm- to cm-sized titaniferous magnetite define the $C_m$-types (Figure 4.16e). In addition to magnetite, common accessory phases are zircon, monazite, and apatite. Minor amounts of secondary U minerals occur in association with biotite in the C-types and secondary U phases associated with zircon and monazite occurs in fractured quartz (Figure 4.16f).

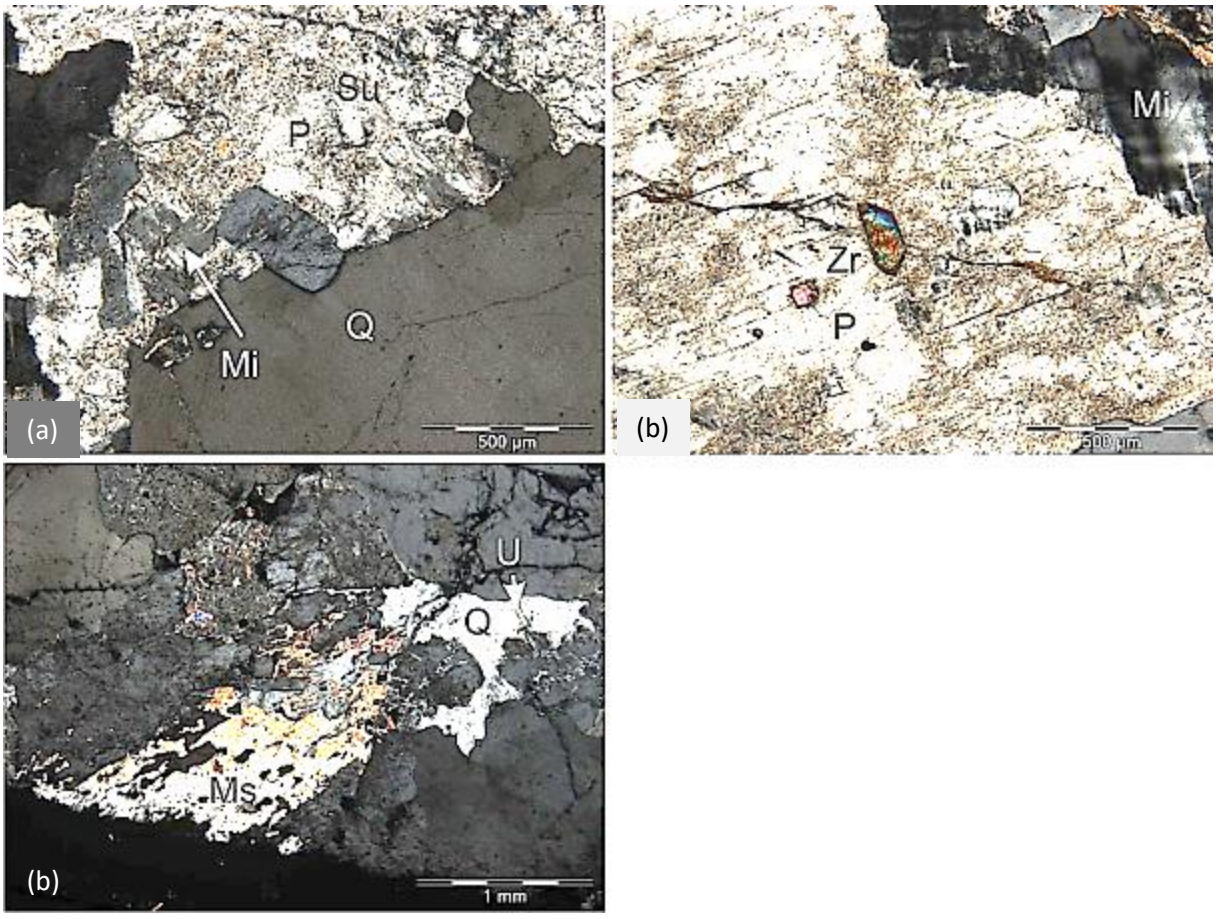



Figure 4.15 Ct-type Sheeted leucogranites at Ida Dome. (a) Apatite (Ap) is a frequent accessory phase in CZ granites. Microcline (Mi) is growing over plagioclase (Pl) IDAG 19, xpl. (b) Zircon is a common U repository in Sheeted leucogranites and occurs as singular and clustered grains, IDAG 22, xpl. (c) Skeletal muscovite is indicative of an entrained sedimentary lath IDAG 22, xpl.

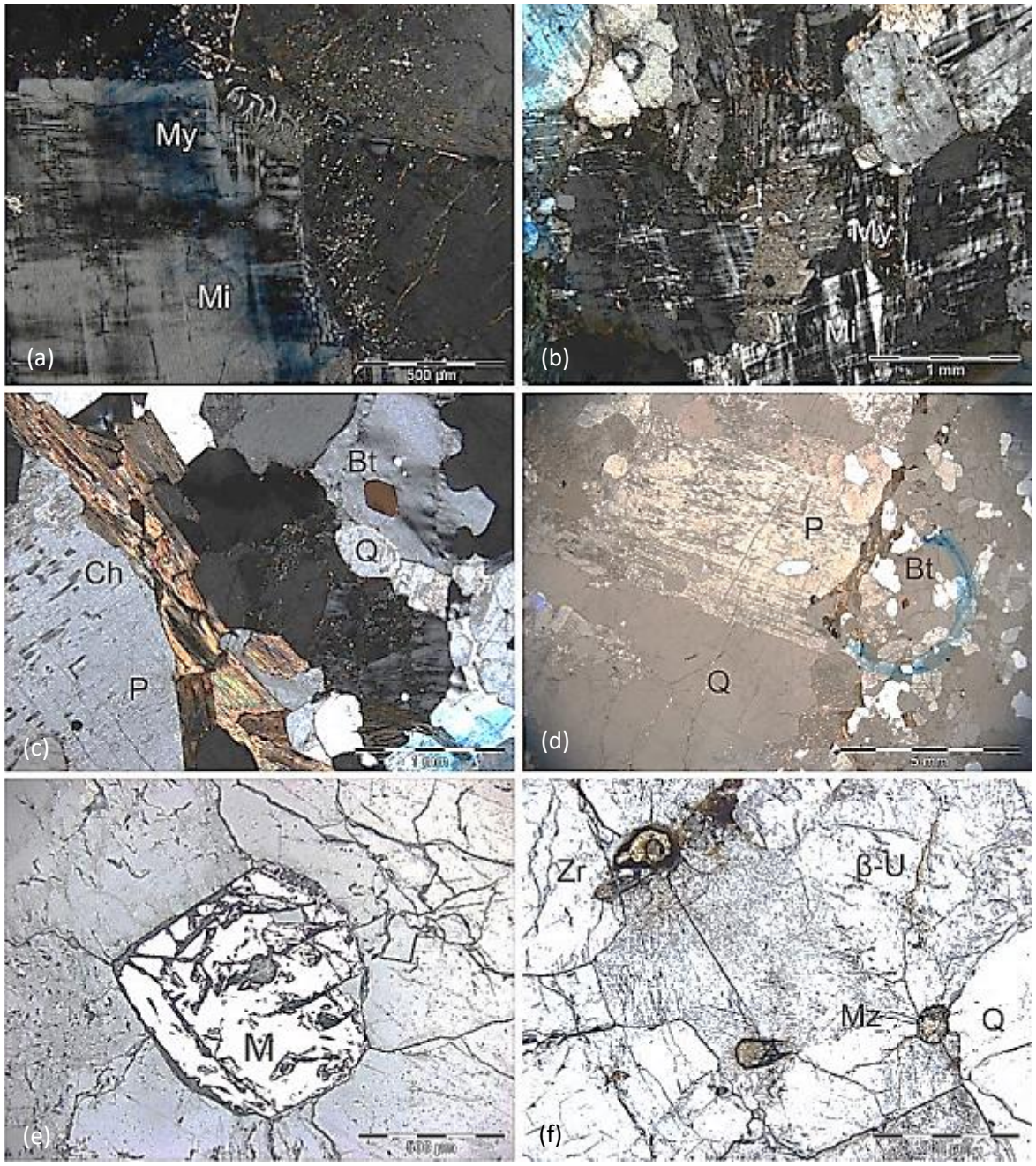



Figure 4.16 Photomicrographs of Cm type leucogranites from the Ida Central Area. (a) Myrmekite (My) is common in all samples and is developed interstitially to larger K-feldspar and quartz, IDAG 08, xpl. (b) Myrmekite has developed within inclusions of early plagioclase in K-feldspar, IDAG 15, xpl. (c) Biotite, included in K-feldspar, contains pleochroic halos. A second texture is partially skeletal and shows chloritisation interference colours. It is sandwiched between a large euhedral plagioclase (P) and equigranular quartz – K-feldspar – plagioclase, HDD027-142.31, 5X, xpl. (d) Euhedral plagioclase and quartz, in a pegmatitic veinlet that intrudes a finer-grained $C_m$ - type sheeted leucogranite. Biotite in the finer portion is fine and disseminated with pleochroic halos, HDD027-142.31, 1.25X, xpl. (e) Magnetite is typically ~1 mm in size and often euhedral and skeletal with exsolved ilmenite and radiating cracks resulting in volume expansion by metamictisation IDAG 08, rfl. (f) Accessory phases include phosphates (monazite-Mz) and silicates (zircon-Zr) which are often clustered and surrounded by radial cracks, IDAG 08, ppl.

### *Husab C-type leucogranite thin section petrography*

RDD008 284-285A is a combination of accessory-free granite and a later alaskite. The accessory-free granite has a distinctive pegmatitic texture and graphic - textured patches throughout. Thin section observations show that K-feldspar occurs in at least two generations; the older comprising finer grains surrounded by albite halos as inclusions in larger masses of microcline perthite. Micrographic quartz intergrowths mirror the macroscopic observations of the hand specimens (Figure 4.17a). The granites are relatively accessory free, but do contain fine-grained inclusions of oxides and sulphides, in the case of RDD008 284-285 a primary magnetite-ilmenite is clustered with pyrite (Figure 4.17b). The leucogranite contains fibrolite clusters, indicating a peraluminous source component, or simply entrainment of such rocks (Figure 4.17c).

Quartz is coarse-grained and occurs as runes and blebs in plagioclase, and as chains between K-feldspars. It shows strain in the coarser grain size fraction and in fractures around weakly metamict zircon inclusions. K-feldspars are observed in two varieties; dominant microcline-perthite and the less abundant tartan variety. Grain sizes are typically pegmatitic with an inhomogeneous distribution of fine (< 0.5 mm) and coarse (>5 mm) grain sizes.

Plagioclase is bimodal, with large grains (>10 mm) preserving albite twinning, overprinted with fine white mica. The smaller grains have corroded edges, albite halos and occur in broken chains between later K-feldspar. Myrmekite is well-developed in the cores of these grains, which also preserve twinning (Figure 4.17d).

Accessory tourmaline appears amorphous in hand specimen, and occurs in cluster with entrained mafics near metasedimentary contacts. The tourmaline is in fact in the form of very fine radiating needles, surrounding a zircon nucleus (Figure 4.17e and inset). The dominant alteration overprint is extensive microclinisation of the tartan microcline variety, and the sericitisation of the larger plagioclase feldspars (Figure 4.17f).

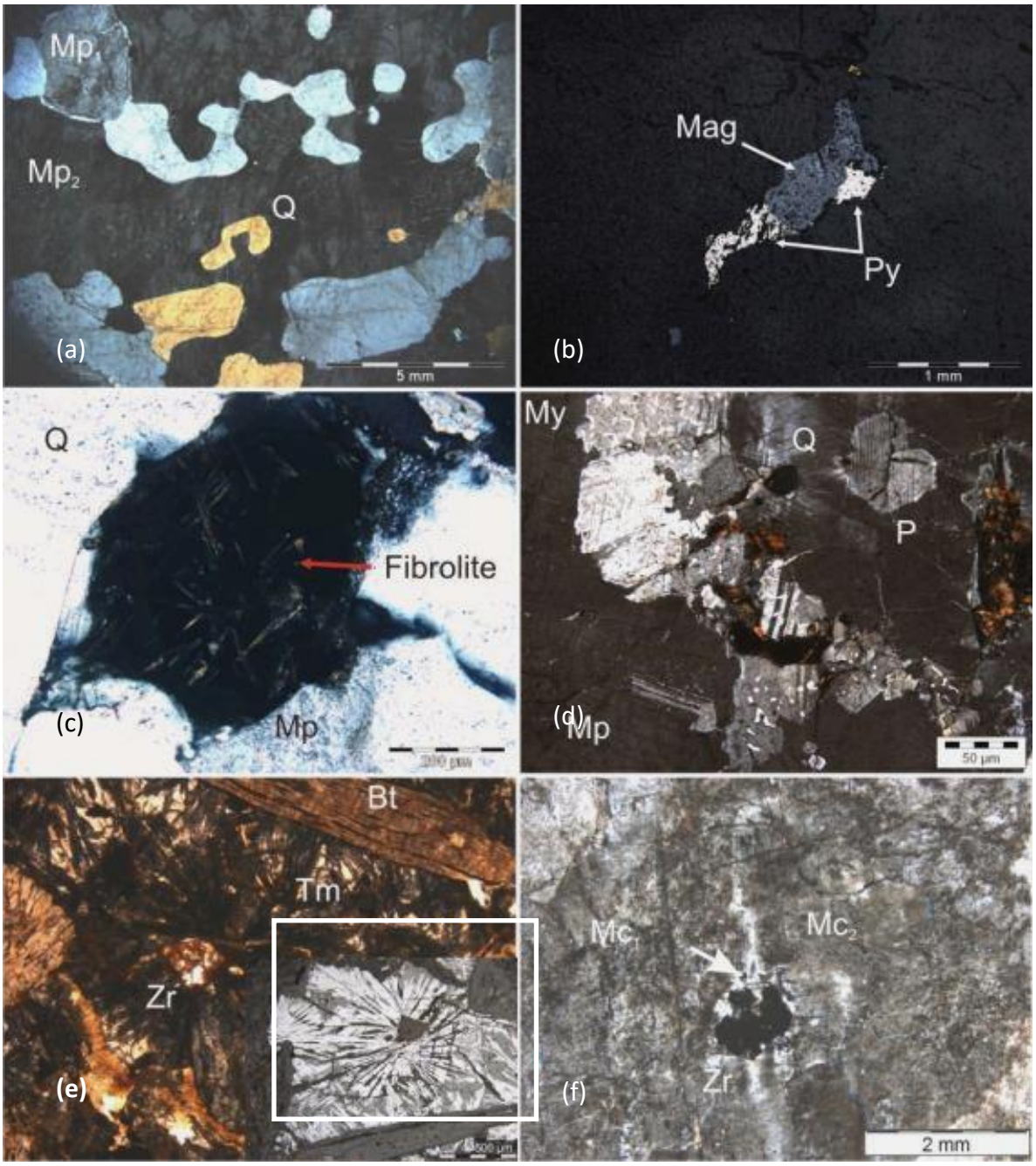



Figure 4.17 Examples of common sheeted leucogranites of the Husab Deposits. (a) Typically, the weakly mineralised granites are feldspar - dominated, and quartz tends to form as singular runes. Secondary processes have formed albite rims around older microcline-perthite feldspars (Mp1) RDD008 284-285 A, xpl. (b) Accessory phases include sulphides and iron oxides in disseminated microscopic clusters and singular crystals, typically at grain boundary junctions, RDD008 284-285 m A, rfl. (c) Certain accessory phases indicate a metasedimentary source; mineral textures such as fibrolite occur in granites that intrude peraluminous metasediments, RDD004 154-155 m A, ppl. (d) Albite rims surround sodic feldspar (P) inclusions in strained quartz (Q) and myrmekite has developed in larger clusters of plagioclase, RDD373 115-116 m, xpl. (e) The distinguishing accessory phase, tourmaline occurs in clusters with mafic entrainments (biotite) with zircon at the nucleus of the radiating cluster, RDD373 115-116 m, ppl - xpl inset. (f) Extensive microclinisation (Mc2) of K-feldspars (Mc2) dominates the barren, tourmaline granites, the source of hydrothermal fluids are the intruding alaskites, and accessory phases include zircon clusters, RDD351 328-329 m, xpl.

### *Valencia C-types*

The C-type SLG distribution correlates with stratigraphy: the magnetite variety occurs within the Khan Formation; and the tourmaline-bearing sheets occur in the pelitic units of the Swakop Group, mostly in the Kuiseb Formation; and the accessory-free varieties occur throughout the lower Swakop Group. Table 4.9 summarises the C-type samples from Valencia.

Table 4.9 Petrographic characteristics of Valencia C- and F- type sheeted leucogranites (U and Th content by XRF, in ppm). A brick red - coloured pegmatite sample is included in the table as a unique specimen of the Valencia deposit within the context of this study.

| **Sample** | **Colour** | **Grain size** | **Texture** | **Biotite** | **Main Feldspar** | **Plag. Comp.** | **Th** | **U** | **Type** |
|---|---|---|---|---|---|---|---|---|---|
| VALG 02 | White | Pegmatitic | V. coarse | Minor, skeletal | Microcline-perthite | $An_{5-18}$ | 20 | 7 | $C_t$ |
| VALG 04 | Light pink | Pegmatitic | Inhomogeneous | Minor, skeletal | Oligoclase | $An_{18}$ | 27 | 8 | $C_t$ |
| VA26-141 89.82-90.75 | White | Pegmatitic | Inhomogeneous | Large laths | Oligoclase | $An_{11}$ | 9 | **42** | $C_t$ |
| J04 132.68-132.96 | Pink and white | Coarse - v. coarse | Pegmatitic | Sparse, laths | Oligoclase | $An_{12-17}$ | **42** | 21 | $C_m$ |
| VALG 06 | Pink and white | Coarse | Homogeneous | Minimal, skeletal | Microcline | $An_{8-15}$ | 9 | 7 | $C_m$ |
| VALG 10 | Light pink | V. coarse | Homogeneous | Sparse, booklets | Microcline | $An_{9-15}$ | 9 | 7 | $C_m$ |
| VALG 07 | Brick-red | Pegmatitic | Inhomogeneous | skeletal | Microcline | Seric. | 9 | 7 | F |

Oligoclase is the dominant feldspar in the pegmatitic textured C-type specimens (>50% of observed sections) and microcline is the dominant feldspar in the aplitic-textured example. Most plagioclases are large (some over 17 mm) and euhedral. There are two prominent textures within the euhedral plagioclase population; one unaltered, and one with albite rims. The former has higher measured $An_n$ than the rimmed plagioclases.

Skeletal textured and round-edged plagioclase is less-abundant than euhedral crystals and predominantly constitutes a population of inclusions within microcline. Quartz occurs as both globular inclusions in feldspars (plagioclase and microcline) and as large (> 4 mm) grains in ~30 % proportion in samples VALG 04 and Va26-141 89.92-90.35 (plagioclase dominated).

Quartz is the dominant mineral (~40 %) in VALG 02 (though microcline > plagioclase) and occurs as euhedral interstitial chains and as rims around anhedral K-feldspars.

Accessory phase assemblages in addition to zoned tourmaline (Figure41.8a) include biotite, muscovite, sillimanite, zircon, and a single, ~ 1 mm, titaniferous magnetite in sample VALG 04. Plagioclases in most $C_m$-types show alteration in the form of cleavage-controlled sericite and less abundant coarse saussurite (Figure41.8b). Some C-type thin sections contain skeletal muscovite and trains of sillimanite, or less commonly mm-scale sillimanite nests (Figure41.8c). Muscovite and sericite have also developed cleavage-parallel in microcline and plagioclase as retrogressive phases.

Microcline is the dominant mineral observed in thin sections of two of the three Valencia magnetite SLG samples. It is coarse-grained, predominantly euhedral (up to 20 mm in size) and anhedral where there are two varieties of K-feldspar (microcline and microcline-perthite). Sample J04 132.69-132.96 is oligoclase dominated (>50 %) and has inclusions of anhedral microcline (Figure 4.19a) suggesting it may not be a typical C-type SLG. Sample VALG 06 provides an example of microcline containing sericitised oligoclase inclusions (Figure 4.19a).

Reactions within the microcline grains include; perthite exsolution in deformed microcline-perthite (Figure 4.19b). Perthite has developed parallel to K-feldspar cleavages and this generation is crosscut by flame-textured mesoperthite (albite twinning is visible in some samples). Myrmekite occurs at plagioclase and K-feldspar grain contacts. In addition to myrmekite textures, globular quartz (<0.1 mm) has formed in the cores of partially sericitised plagioclase inclusions found in larger microcline-perthite (Figure 4.19c).

Quartz is subordinate to feldspars and occurs in two populations; the older is in fine-grained (<1 mm) inclusions and the younger coarse-grained anhedral to euhedral grains, interstitial to feldspars and in clustered grains, each up to 4 mm across. Strain extinction is common and varies in intensity from sample to sample.

Magnetite is titaniferous with prominent ilmenite exsolution. Some examples are pristine and euhedral, while others show evidence of alteration, an example is given by sample J04

132.69-132.96 (Figure 4.19d). The magnetite porphyroblasts' grain sizes range from <0.5 mm to over 2 mm. The most abundant accessory mineral is biotite, which occurs as skeletal entrained contaminants, and as centimetric blades books in the pegmatitic examples, but is also prominent as sub-millimetric blades in thin section. Most of the biotite observed in the thin sections contained pleochroic halos, often with visible zircon inclusions.

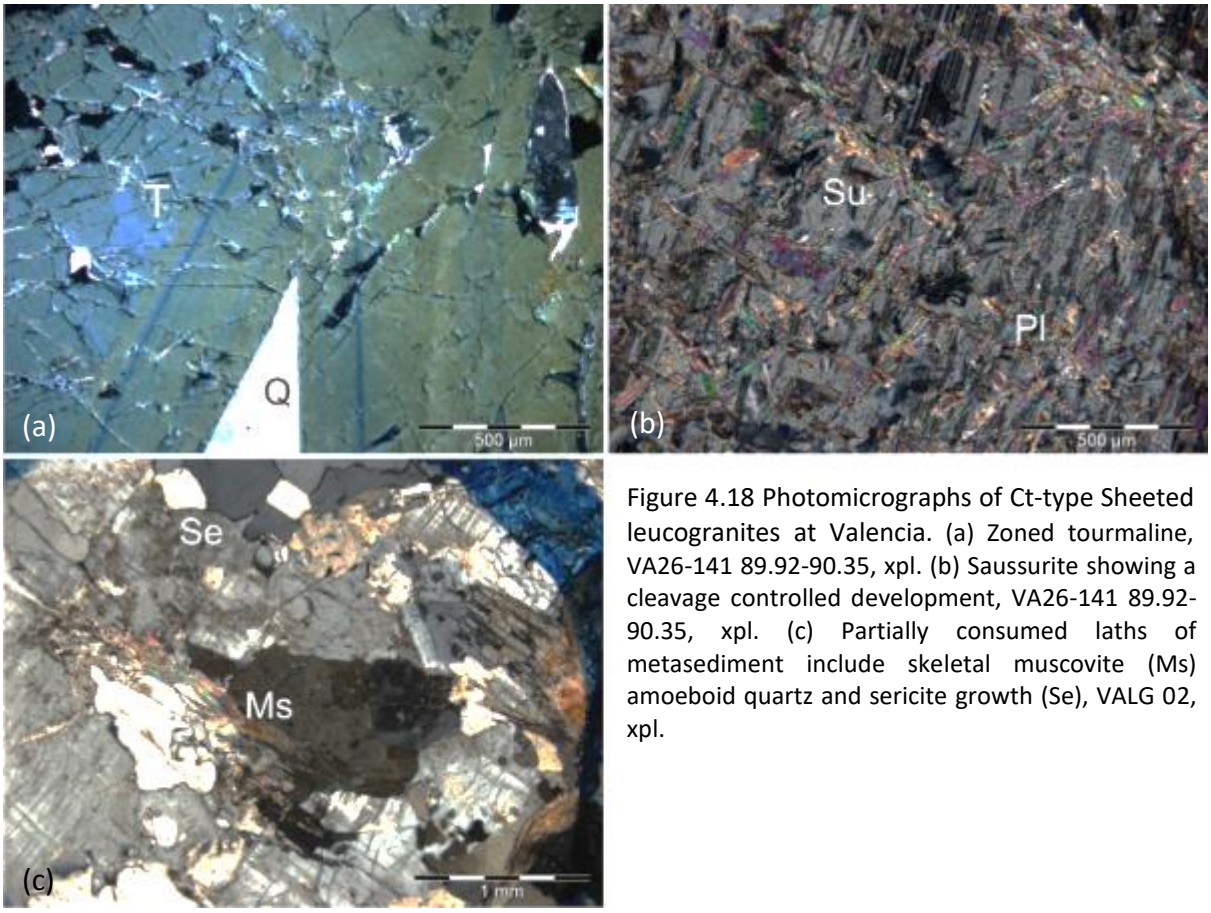



Figure 4.18 Photomicrographs of Ct-type Sheeted leucogranites at Valencia. (a) Zoned tourmaline, VA26-141 89.92-90.35, xpl. (b) Saussurite showing a cleavage controlled development, VA26-141 89.92-90.35, xpl. (c) Partially consumed laths of metasediment include skeletal muscovite (Ms) amoeboid quartz and sericite growth (Se), VALG 02, xpl.

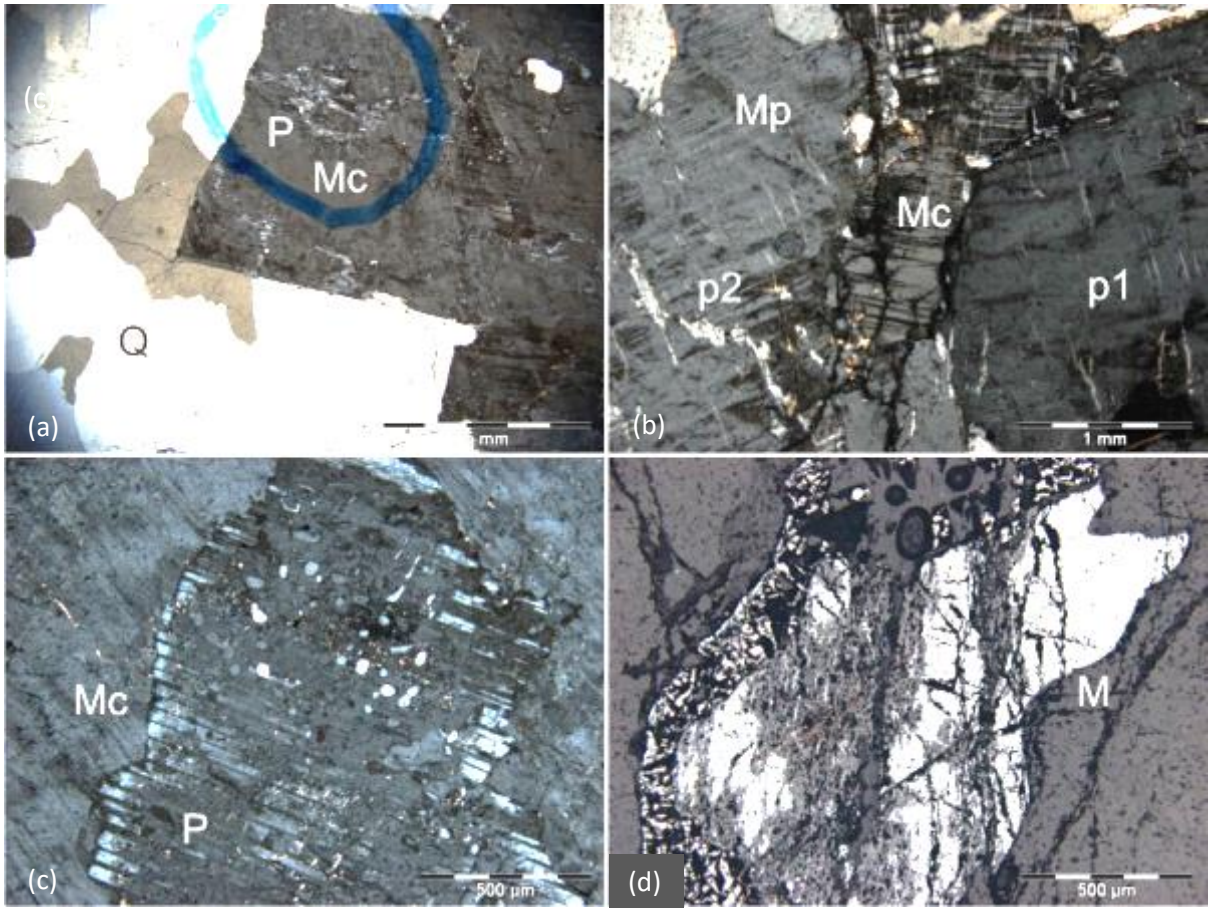



Figure 4.19 Petrographic features of Magnetite-type sheeted leucogranites at Valencia. (a) Euhedral microcline (Mc) with skeletal plagioclase inclusions (P) VALG 06, ppl. (b) Two generations of K-feldspar; an older tartan-twinned microcline (Mc) is sandwiched between two microcline-perthite grains (Mp). There are two generations of perthite exsolution (p1-cleavage-parallel exsolution and p2 - albite twinning in flame perthite) VALG 06, xpl. (c) Plagioclase inclusion in microcline with sericitised core and globular quartz inclusions, J04 132.69-132.96, xpl. (d) Magnetite is the most abundant accessory in the magnetite type sheeted leucogranites, J04 132.69-132.96, rfl.

## 4.9 Uraniferous Sheeted Leucogranites- The Alaskites

### *Rock-Forming and Accessory Minerals of Uraniferous Leucogranites*

The uraniferous leucogranites exhibit particular colour and texture in hand specimen, but comprise quartz and varying proportions of plagioclase and K-feldspars. Quartz does tend to be more abundant than in the non-uraniferous leucogranites, as does tartan-twinned microcline. Plagioclase feldspars are predominantly of oligoclase composition and the generally higher An content of the mineralised specimens relative to the barren or weakly uraniferous SLGs is observed fairly consistently in local comparisons. Biotite occurs in varying abundance and tends to be chloritised with prominent opaque mineral developments along cleavage (ilmenite and Fe-oxides). Biotite in uraniferous granites contains fluorite, zircon

inclusions, uraninite, coffinite, magnetite and pyrite. Accessory phases are also visibly more abundant and include apatite, betafite, boltwoodite, brannerite, monazite, thorite, uraninite, uranophane, xenotime, and zircon. The opaque, or the ore mineral, assemblages in the uraniferous leucogranites differentiate them from the weakly mineralised and early non-mineralised varieties.

### *Ore Mineral Petrography Samples*

Ore petrography studies utilised transmitted and reflected light microscopy, of polished thin sections and polished grain mounts. Petrographic microscope facilities were provided by the University of the Witwatersrand, and the Geological Survey of Namibia.

The study serves three main objectives, the first is to identify the primary and secondary uranium minerals, and the second is to describe the texture and major mineral associations of the mineralisation phases. The third objective is to identify suitable samples for the EPMA study, based on the textural and mineralogical context.

The primary tool in the ore mineral petrography study is to observe uranium mineral textures and relationships within the major- and accessory mineral assemblages. Placing the uranium minerals into the context of the host rock and the alteration overprints is an important component in establishing a representative paragenetic sequence for a given sample, or for a deposit. The strategy for thin section site selection thus, has a preferential bias toward positions of anomalous U concentration, finer grain sizes, and accessory mineral abundances.

In total 179 thin sections were available to this study, of which the majority are summarised in Appendix D1. The ore petrography section of this chapter however, preferentially describes and interprets thin sections of specimens with direct association to the QEMSCAN and EPMA studies of Chapter 7 and Chapter 8, respectively. Ore petrography notes from this study are in Appendix D2

Magmatic iron-titanium species, and subsequent alterations of the primary U-minerals, are the most abundant opaque phase along with haematite and ilmenite (Figure 4.20a). Magmatic magnetite occurs in both uraniferous and barren leucogranites, though the

coarsest porphyroblasts occur in Khan Formation-hosted $C_m$-type SLGs, which tend to be U-barren. Magnetite may reach centimetric sizes in the barren- and millimetric sizes in uraniferous leucogranites; a greater intensity of REDOX reaction and secondary Fe stains are usually accompanied by uranophane/boltwoodite species in the E-type examples. The presence of Fe in magnetite-ilmenite and in sulphides (pyrite-pyrrhotite) is an ovious indiation of the varied states of oxidation in the crystallising mineralised SLGs.

The variable REDOX conditions in the magma alone may be responsible for the ilmenite and magnetite intergrowth (Figure 4.20b). The relationship between the two oxides in the REDOX context in granite is primarily addressed in Ishihara (1977) and is quantified with respect to the I- and S-type classifications in Whalen and Chappell (1988). At the very least the alaskites may be considered as oxidised where magnetite is abundant and reduced where Fe is predominantly hosted in sulphides. Magmatic magnetite may appear later than pyrite and other sulphides in the sheeted leucogranites. Figure 4.20c and 4.20d illustrate corroded pyrite fragments of primary sulphide surrounded by magnetite in thin section, VALG08 at Valencia.

Contact metamorphism has produced magnetite at reactive margins between barren and uraniferous leucogranites and biotite schists of the Khan Formation. The secondary magnetite has possibly derived some iron from contact reactions with biotite in the metasediment host rocks, which also host magnetite porphyroblasts at some distance from the intrusives. The relationship is observed at all deposits in this study; sample DH019 146.77-147.00 at Goanikontes gives an example of the relationship between the SLG and the magnetite-bearing metasediments. Disseminated magnetite porphyroblasts defining the contact zone (Figure 4.21a and 4.21b). The magnetite in the host rock is euhedral, <0.2 mm across and evenly distributed throughout the fine–grained matrix.

Magnetite in the granite is fine-grained and euhedral, similar to that in the host but lacks any ilmenite exsolution, indicative of new magnetite with low degrees of oxidation. The most important feature is the coalescence of the magnetite in a 1-2 mm wide band at the contact between the gneiss and the granite with a tapering off in abundance in the metasediment, away from the granite (Figure 4.21c and 4.21d).

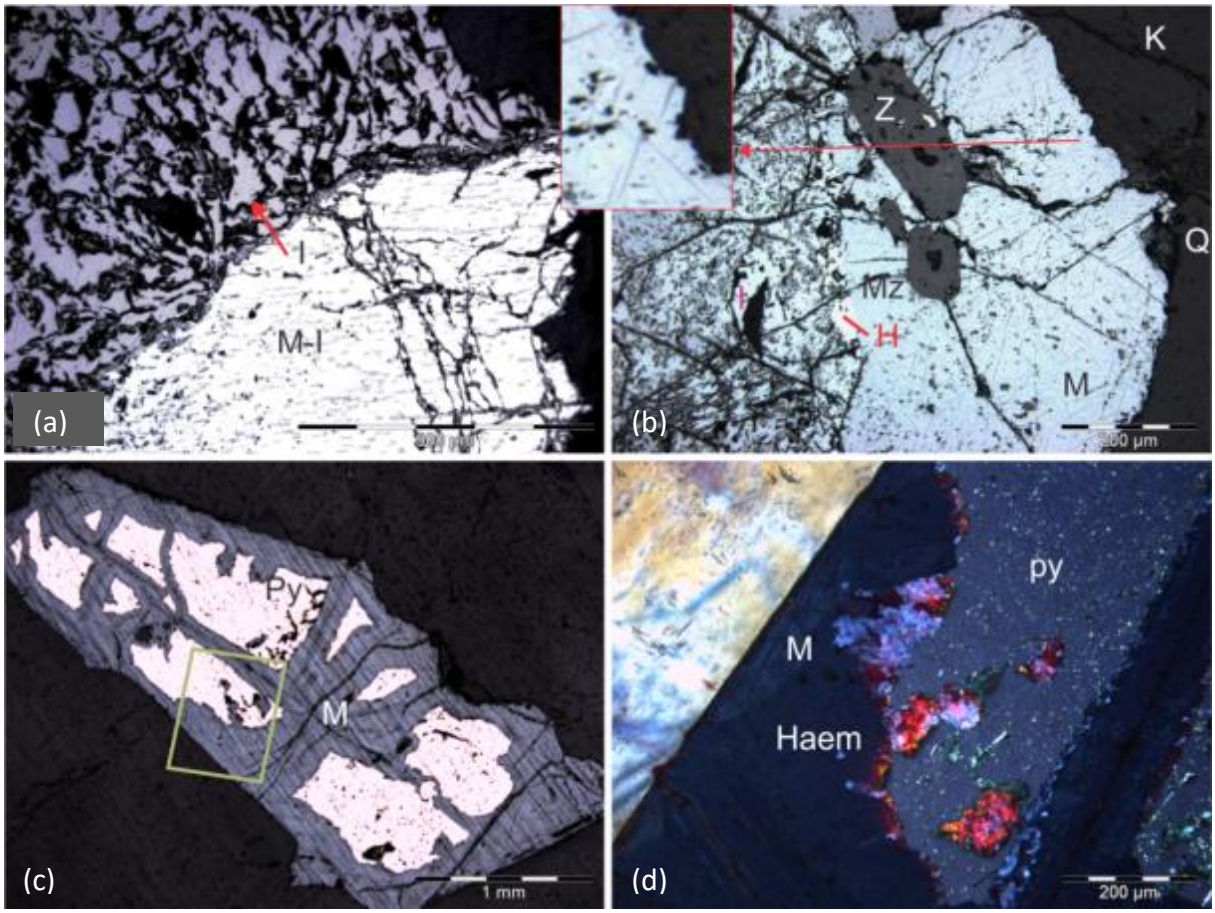



Figure 4.20 Magnetite-haematite-ilmenite and sulphide textures in Central Zone leucogranites. (a) Magnetite with ilmenite in a C-type leucogranite at Goanikontes: Note the exsolution lamellae are in a single orientation, parallel to {111}. The single direction is a result of resetting during deformation. Haematite has exsolved from ilmenite, and subsequently leached out, leaving deformed triangular voids. DH022 59-59.24 20 x ppl– rfl. (b) Ilmenite-haematite-magnetite oxidation replacement textures in uraniferous leucogranite: Note ilmenite in two directions in the undeformed magnetite (M) and the thickest part of the lamellae at the grain boundary. The replacement of ilmenite (I) by haematite produces high-Fe haematite (H) between the ilmenite- and magnetite-dominated grains. The magnetite-ilmenite compound hosts euhedral, primary zircon (Z) and monazite (Mz). DH019 71.74-72.18, 20 x ppl– rfl. (c) Fractured pyrite surrounded by magnetite-haematite, 10 x ppl - rfl). (d) Enlarged area of (c); magnetite and haematite, with prominent red, internal reflections, VALG 08, 20 x, xpl - rfl.

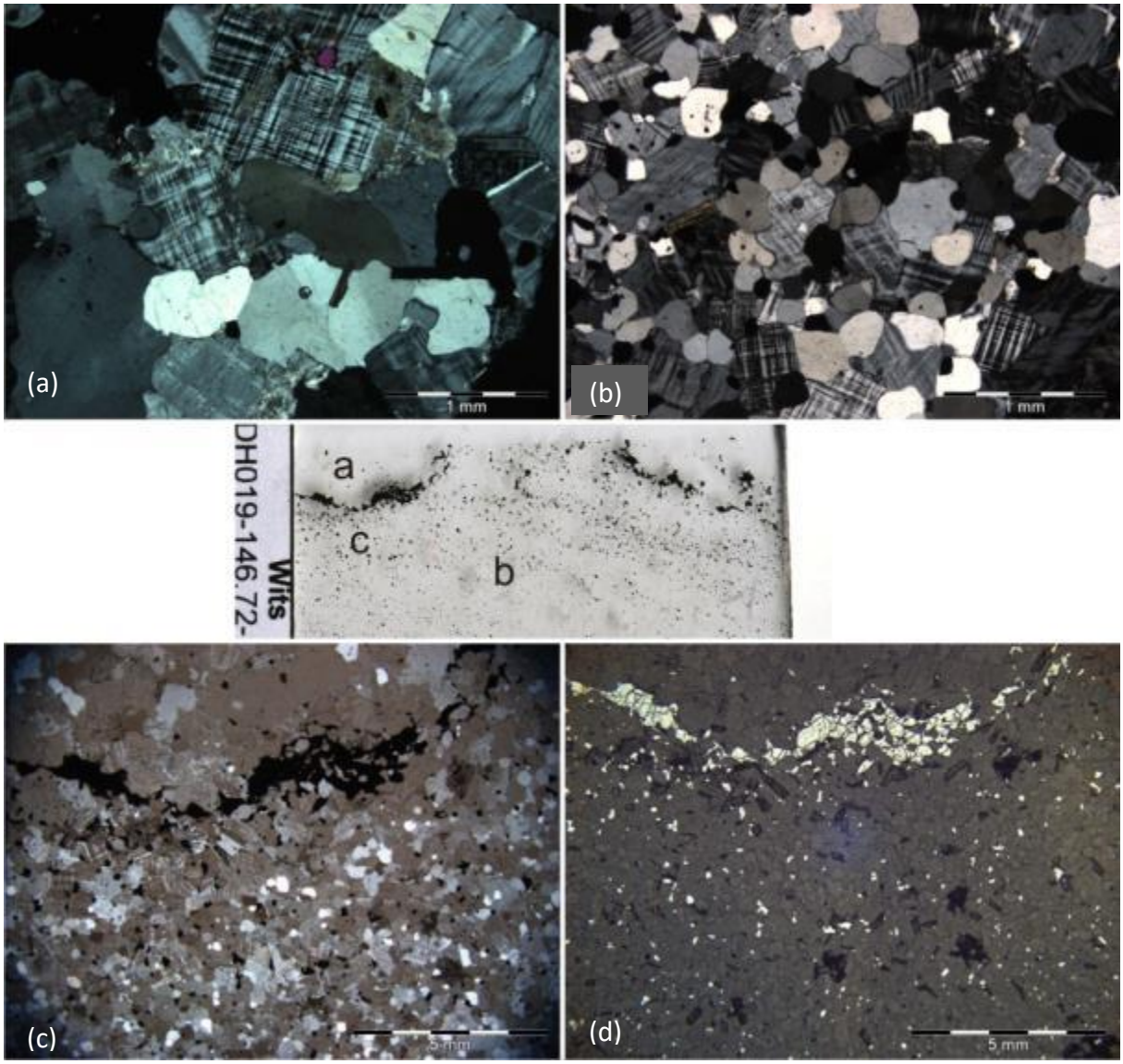



Figure 4.21 Magnetite at reaction contact between sheeted leucogranite and a metasediment. (a) The coarse-grained texture of the sheeted leucogranite is typical of a magnetite-bearing C-type, microcline is the dominant mineral with anhedral quartz clustering between larger feldspars, 5x, xpl. (b) Quartzo-feldspathic composition of the metasediment, with fin-grained disseminated magnetite, 5x, xpl. (c) The top of the image shows the sheeted leucogranite contacting the fine-grained Khan Formation biotite gneiss, 1.25 x, xpl. (d) Reflected light reveals extent of magnetite decreasing away from the intrusion contact. All images of DH019 146.72-147.00, Etango deposit, Goanikontes. Positions of slides are indicated on the slide at centre.

### *Mineralisation*

Uranium concentrations in the sheeted leucogranites are strongly associated with sulphide mineralisation. The uraniferous leucogranites and the intruded sediments each host two- to three generations of sulphide minerals, with evidence of formation before uraninite, in the metasediments, and after uraninite in the alaskite. The most abundant sulphide minerals are pyrite, pyrrhotite, and chalcopyrite in most of the sulphide-bearing specimens. Chalcopyrite

is particularly abundant at the Ida Central and Husab deposits, while Ni content over 1 000 ppm indicates pentlandite is present at Husab (Chapter 5).

Sulphide textures in the leucogranites are predominantly skeletal and often subtly aligned with entrained biotite (Figure 4.22a and 4.22b). The sulphide assemblages that are predominantly pyrite and pyrrhotite with subordinate chalcopyrite in the mineralised leucogranites are consistent with the magnetite series granites of Ishihara (1977); pyrrhotite exclusively hosts reduced Fe, while pyrite accommodates reduced and oxidised Fe.

Husab pyrite textures vary from thin section to thin section, and illustrate at least two generations of disseminated pyrite. Primary, euhedral pyrite (Figure 4.23a) and secondary pyrite halos around existing reduced phases such as uraninite (Figure 4.23b). Molybdenite appears late, and fills space between the clustered uraninite and cross-custs pyrite halos (Figure 4.23c).

The refractory uranium minerals, brannerite and betafite tend to be coarser, and >1 mm examples of each are observed at Husab, and betafite particularly well-known at the SH deposit of Rössing Uranium (Cuney, 1980a and b; Herd, 1996; Freemantle, 2006; Abraham, 2009).

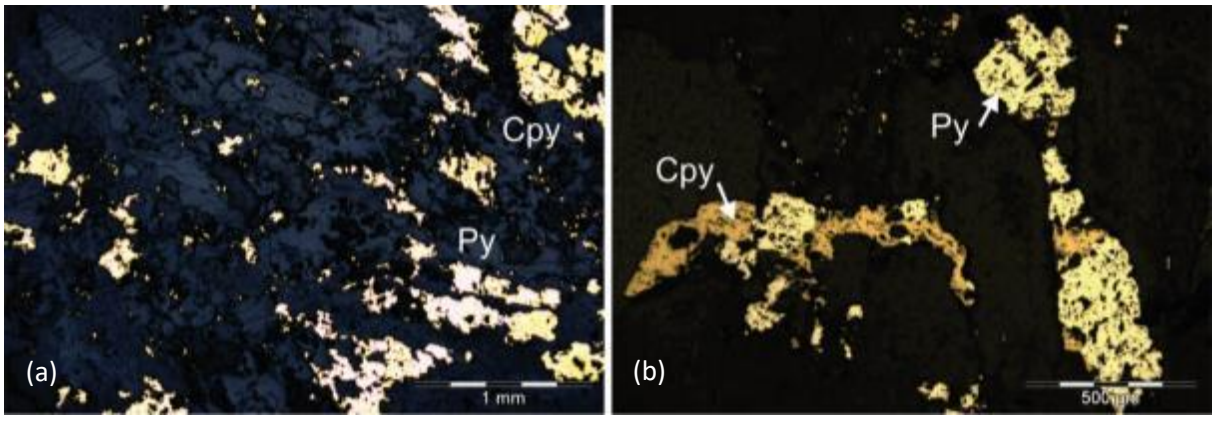



Figure 4.22 Entrained sulphides at Ida Central and Valencia. (a) Subtly-aligned skeletal pyrite-chalcopyrite grains at Ida Central, HDD27 122.90-123.22, rfl. (b) An example of hydrothermal sulphides; in this image, pyrite and chalcopyrite in fractures and at grain boundaries in Valencia leucogranite, VALG 16, rfl.

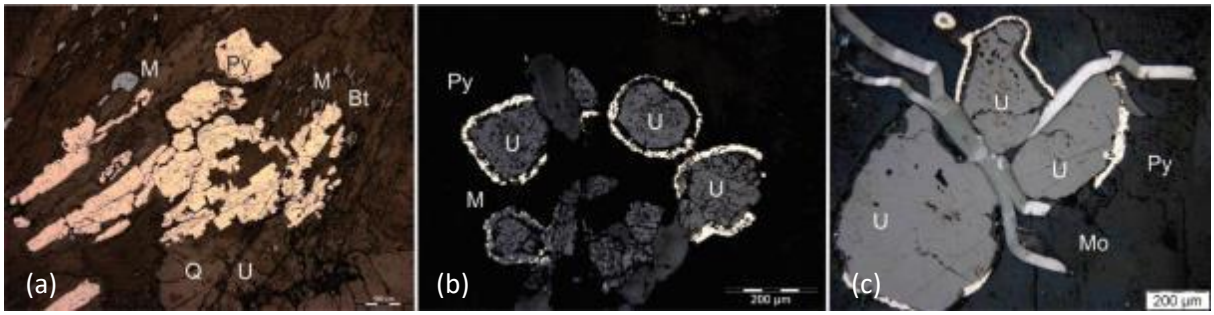



Figure 4.23 Two textures of pyrite and molybdenite younger than uraninite, in Husab alaskite. **(a)** Cubic pyrite clusters (Py) associated with biotite (b) nests in mineralised alaskite, rfl, ppl. Magnetite (M) occurs with biotite and uraninite (U) is included in quartz (Q) RDD373 93 m A, ppl rfl. (b) Rounded and subhedral uraninite (U) surrounded by compound halos of hydrothermal magnetite (M) and pyrite (P) RDD219 336 m, ppl rfl. (c) Uraninite cluster with pyrite halos which are cross – cut by molybdenite, RDD351 – 258 m, ppl rfl.

The identification of primary and secondary uranium minerals in their host rocks allows for a quantification of the uranium- and host - mineral relationships, as well as the relationship with other sulphide and oxide ore minerals, accessory phases. The radioactive phases, including silicate, phosphate, and oxide host minerals, show distinctive characteristics. The most distinctive of these include the following:

- Radial fractures in the host rock minerals form around radioactive minerals;
- Uranium and thorium minerals have high, positive relief and are opaque when unaltered;
- Secondary minerals tend to be yellow (occasionally green) in colour and translucent;
- Brannerite is opaque when unaltered, and brown-orange with variable translucence when altered;
- Betafite is dark brown-yellow in colour and displays some translucence;
- Primary U-phases occur between rock forming phases, and sometimes accompanied by jarosite halos in surrounding feldspar[36];
- Primary uranium phases can occur as inclusions, where pre-existing fluid pathways are available, microcline feldspar and biotite providing the most accessible sites for deposition;

[36] Identified and observed at Rössing Uranium Mine by Herd (1996).

- Uraninite inclusions in Fe-Ti oxides show dull reflectance relative to the host magnetite, and bright reflectance relative to titanite and rutile; and
- Biotite hosts inclusions of uranium-bearing minerals and primary uranium phases identified by dark - opaque pleochroic halos.

The radioactive oxides, silicates, and hydrated silicates however, do exhibit certain characteristics in reflected and transmitted light that aid positive identification. The most distinctive of these include radial fractures in the host rock minerals that form to accommodate volume expansion by metamictisation. Most primary uranium and thorium minerals show high positive relief, occur between the rock forming minerals, and rarely as inclusions within individual quartz or feldspar crystals. Biotite however, hosts uraninite in association with magnetite and ilmenite, where pairs and clusters of uraninite have formed parallel to disrupted mica cleavage. Primary uranium minerals exhibit dull reflectance relative to most Ti-Fe oxides with magnetite and haematite often showing secondary Fe alteration at the edges.

Alteration around uranium minerals is typically composed of jarosite[37] and clays where K-feldspar is one of the host phases, and haematite where magnetite, biotite are host or associated accessory minerals.

Brannerite is variably metamict, and shows highly variable alteration; the most intensely altered brannerite is metamict and semi-translucent with dense fracture networks hosting yellow alteration minerals. Euhedral, moderately altered brannerite is isotropic and occurs in multi-mineral clusters typically primary and secondary Fe-Ti minerals (titanite and rutile) with pyrite and chloritised biotite. Betafite is comparatively rare in hand and thin section specimens; a single 1.2 mm grain showed intense alteration and fracturing, semi-translucence and fits the description given for Rössing deposit examples in Herd (1996) and Nex *et al*. (2003).

[37] Jarocite $KFe^{3+}_3(SO_4)_2(OH)_6$ is a uraninite associated alteration mineral after K-feldspar and is described at Rössing in Herd (1996). The mineral is a hydrated sulphate has formed from pyrite-derived $S^-$ as an alteration of K-feldspar during oxidising hydrothermal conditions.

Reduced and oxidised secondary uranium minerals are typically silicate (coffinite) and calcium- or potassium silicate hydrates (Ca- uranophane and K- boltwoodite). The dominant secondary mineral is coffinite, which occurs in weakly-altered D- and E-type leucogranites, and predominantly formed as a replacement of primary uraninite in all the deposits of this study. Coffinite veins are comparatively rare but noted in some of the Husab samples. It has lower reflectance than uraninite and is identified best when in direct comparison to uraninite.

The hydrated secondary minerals are typically bright yellow and form along mineral cleavages, fissures, leached silicate cavities, and as coatings on fault planes. Berning (1986) and Nex (1997) describe the yellow secondary mineral β-uranophane[38] at Rössing and Goanikontes, respectively. They are variably abundant and most of the hydrate phase observations are in leucogranites from the near surface (or near the palaeo-surface in the case of samples from the Husab deposits which are 99 % concealed by Quaternary, Namib sediments) and in magmatic-hydrothermal altered specimens from depth.

There is a varied assemblage of mineralised leucogranites at each of the deposits in this study all of which are presumed to be of a similar age and generally having been emplaced as a result of a protracted single deformation event, $D_3$ in the chronology of Miller (1983a). Nex (1997) gives two distinctive textural varieties or uraniferous leucogranite, the D- and E-type; Each is described as being the results of close, but temporally different events. Each deposit has examples of a ubiquitous, primary mineralised variety, the D-type, and a range of secondary textures and alterations of the original D type which are classified as the E-type. The E-type is utilised exclusively as a descriptive term for uraniferous leucogranites that exhibit variably intense alteration, and are not recognised as an independent generation of leucogranite sheets in this study.

[38] $Ca(UO_2)_2(SiO_3OH)_2.1.5H_2O$

### *Alteration of the Uraniferous Sheeted Leucogranites*

The mineralisation processes at Rössing have been described by Jacob (1974b, 1975); Cuney (1980a); Berning (1986) and Herd (1996) among others, as an important factor in the mineralisation processes that produced and 'upgraded' the uranium deposits of the Central Zone (~45 % of uranium at Rössing is in secondary phases).

The sheeted leucogranites at Goanikontes, Ida Dome, Valencia, and Hildenhof have undergone three recognisable alteration episodes listed from oldest to youngest below:

1. Alteration by a late-stage magmatic fluid, similar to the processes described at Rössing, is particularly evident at Goanikontes and the Ida Dome deposits. Sodic alteration involves, chessboard albite textures, albite rims around K-feldspars and albite growth in microcline (Figure 4.52a); rimmed plagioclases with myrmekite development and mesoperthite exsolution in microcline is prevalent in the mineralised samples from all the deposits in this study (e.g. Figure 4.52b).

   The growth of fine K-feldspar, present in a number of samples, represents slightly lower T° potassic - alteration in the Central Zone leucogranites. Sub-solidus redistribution of magnetite (magmatic or entrained), forms euhedral- and amorphous crystals that are interstitial to euhedral quartz and feldspars (Figure 4.52c). Silicification and de-silicification (corroded quartz boundaries) are evident in quartz-rich, and feldspar dominated samples, respectively.

   $F^-$ is the most electronegative element, as such $F^-$-complexes in the fluids substantially increase quartz solubility (Abdalla *et al.*, 1996) and the presence of such complexes in the sub-solidus environment is indicated by the presence of fluorite veins in many of the mineralised samples (Figure 4.52d) particularly at Husab. The partially oxidised environment also resulted in the corrosion of magnetite and uraninite, producing β-uranophane and associated haematite along grain boundaries (Figure 4.52e).

2. A second, distinctive phase of high temperature alteration has to have taken place sometime after the alteration that produced coffinite from uraninite

corrosion. This event would have taken place well after the last crystallisation of the granites. Palaeomagnetic studies by Corner (1982, 1983) show that a hydrothermal event of significant magnitude erased the thermo-remnant magnetism in the oxidised sheeted leucogranites.

The oxidised sheeted leucogranites are distinctive from the unaltered varieties when observed in thin section. Distinctive characteristic features include:

- Further oxidation of uraninite to β-uranophane and subsequent redistribution of these oxidised minerals along fractures and existing grain boundaries (Figure 4.53(a);
- New euhedral- and anhedral quartz-veinlet development at the expense of feldspars and intensive alteration of biotite to chlorite (Figure 4.53b); and
- Remobilisation of- and development of botryoidal haematite, minor albitisation of oligoclase (chess-board albite, Figure 4.53c) albite rim growth and zonation of plagioclases, and new mesoperthite development at the expense of tartan-twinned microcline (Figure 4.53d).

The oxidation phase that generated the halos is discussed in Nex (1997) and recognises the halos as being more likely to be magmatic features. The large halos in considerably thick and impermeable sheeted granites at Garnet Valley support a magmatic, or auto-hydrational, fluid-derived alteration, rather than a separate, and/or later hydrothermal event which should have overprinted the more permeable host metasediments as well.

3. The final stage of alteration is by low T° alteration, possibly facilitated by the percolation of meteoric fluids via brittle fractures, faults, and joint planes. This type is most prominent in surface and near-surface samples. This is interpreted to be similar to the process in uraniferous granites in Egypt, presented by El-Naby (2009).

4. The later stage of alteration includes new mica growth, sericite, saussurite, and coarse muscovite in feldspar cleavage, Figure 4.53e and 4.53f). Clays and calcite develop in surface samples and fracture zones at a range of depths are characterised by chlorite and epidote development.

5. Mesozoic magmatism in southern Gondwana and the subsequent Cretaceous break-up resulted from the rise of the Tristan Plume (Pirajno et al. 2000) and the extent of these episodes is present throughout the Damara. The most prominent representatives of this time-period include the Etendeka flood basalts and examples of granite intrusions such as at Brandberg and at Erongo. The following authors present a number of detailed petrologic and chronologic descriptions and interpretations:

    - Erlank et al. (1984) for the Mesozoic magmatism;
    - Deihl (1990) for the Brandberg;
    - Harris (1995) for both the Etendeka- and the Karoo igneous provinces; and
    - Trumbell et al. (2003) for the Brandberg and Erongo.

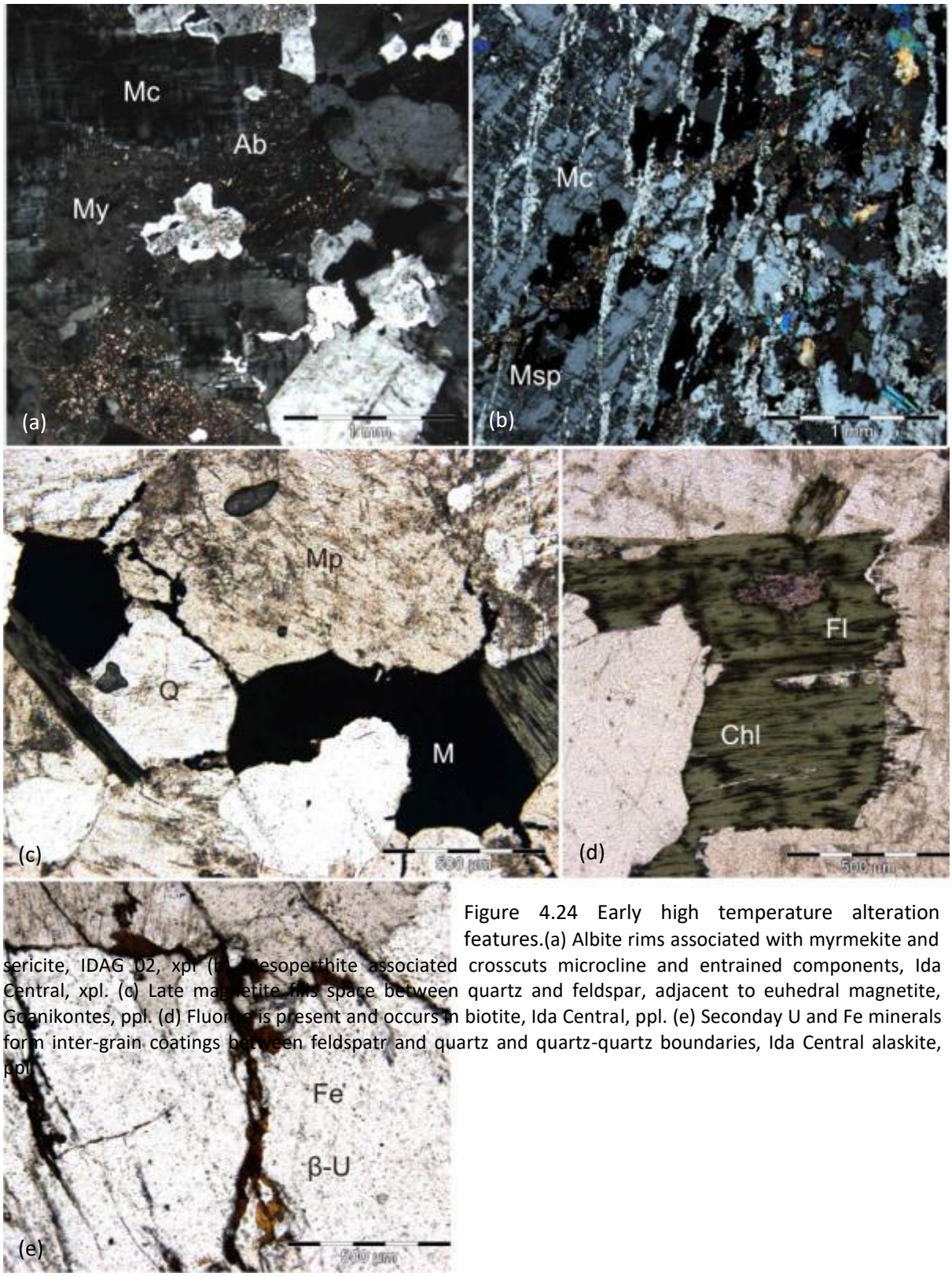



Figure 4.24 Early high temperature alteration features.(a) Albite rims associated with myrmekite and sericite, IDAG 02, xpl (b) Mesoperthite associated crosscuts microcline and entrained components, Ida Central, xpl. (c) Late magnetite fills space between quartz and feldspar, adjacent to euhedral magnetite, Goanikontes, ppl. (d) Fluorite is present and occurs in biotite, Ida Central, ppl. (e) Seconday U and Fe minerals form inter-grain coatings between feldspatr and quartz and quartz-quartz boundaries, Ida Central alaskite, ppl.

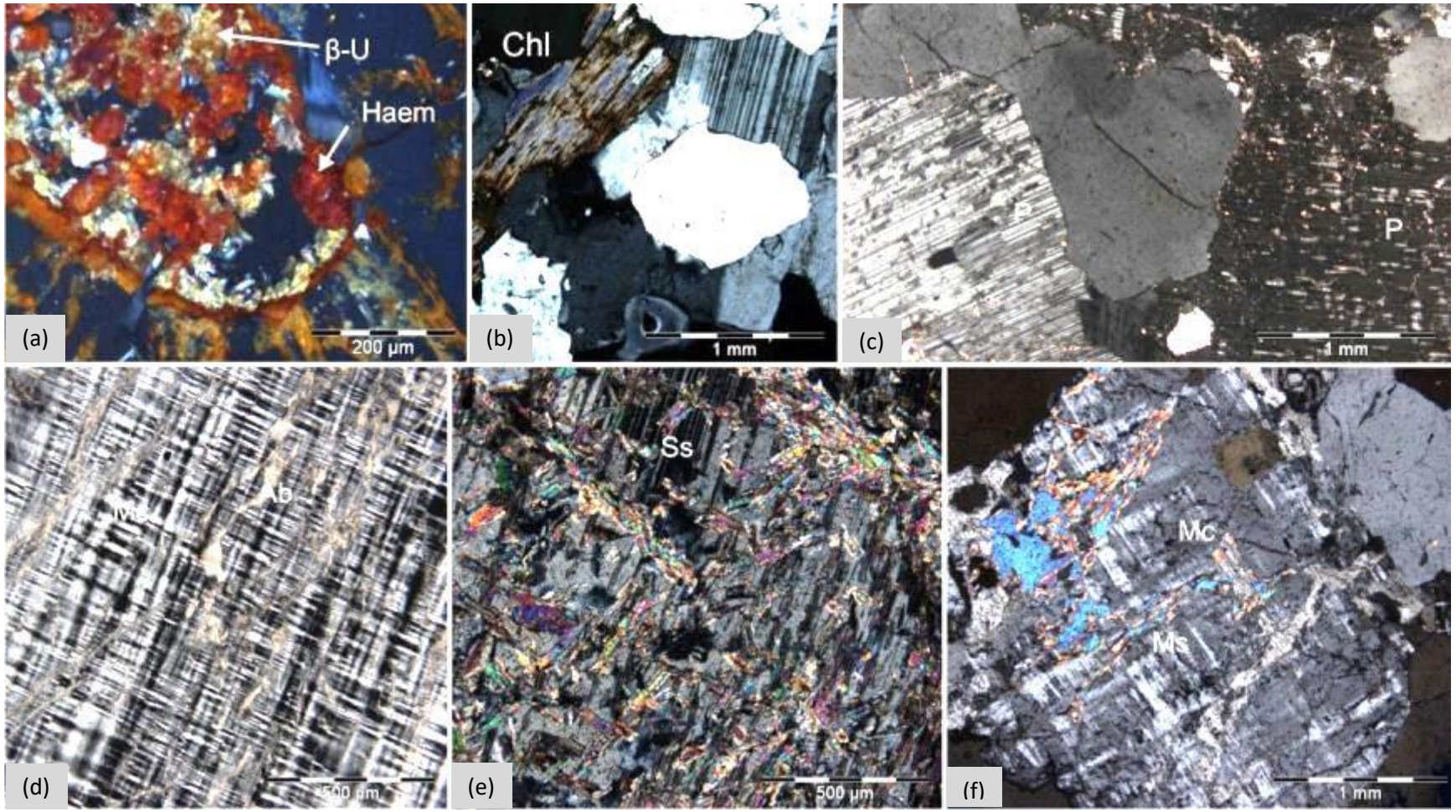



Figure 4.25 Late high temperature and low temperature alteration features. (a) Partially disintegrated, botryoidal, haematite and associated β-uranophane. (b) Chlorite lath, after biotite, HDD27 89.47-89.95, xpl. (c) Chess board albite (Pl) and albite over-growing tartan-microcline, DH012 127.72-128.04, xpl. (d) Mesoperthite (Ab) in tartan microcline, DH19 100.50-100.93, xpl. (e) Saussurite in oligoclase, VA26-141 89.92-90.35, xpl. (f) Coarse mica (muscovite, Ms) on microcline, Va26-111 157.44-157.82, xpl.

### *D- and E-type Sheeted Leucogranites at Goanikontes*

The most U-enriched sheeted leucogranite type at Goanikontes is the D-type, as described in Nex (1997). These are recognisable without the aid of a scintillometer or spectrometer as the granites are composed of distinctive jet-black smoky quartz and white coloured feldspar. Textures and grain sizes are variable; the coarser-grained samples tend to be inhomogeneous and finer-grained samples tend to have uniform grain size distributions. Quartz is often the dominant phase but proportions of feldspar can be highly variable in the coarse-grained varieties.

D-types have undergone numerous varieties of alteration, dominated by red-orange Fe-staining, which is present on surface and at depth in drill core. Thin section petrography is undertaken on eleven alaskites, including a surface sample from the Rabbit Valley test pit and ten samples from two NQ diamond boreholes. Three core samples are unaltered D-type sheeted leucogranite and seven represent the various alterations of the D-type, including the E-type. There are two types of alteration classification; those with the typical E-type Fe-oxidation discoloration. Table 4.10 summarises the features of the uraniferous samples at Goanikontes.

Thin sections of unaltered D-types show that the granite comprises approximately 30% quartz with variable plagioclase or tartant-twinned microcline dominance. In thin sections of typical E-types, both plagioclase and microcline-after-plagioclase are the main feldspars, which are usually subordinate to the chains and clusters of euhedral polycrystalline quartz. Polycrystalline veins of straight-edged quartz (>4 mm grains) surround feldspars and earlier quartz (Figure 4.26a) while subhedral to anhedral fine-grained quartz (<2 mm) tends to fill interstitial spaces with similar-sized plagioclase and less-abundant tartan-twinned microcline.

Cleavage-controlled finer-grained quartz inclusions occur in micrographic intergrowth with plagioclase and with microcline. Minor strain extinction is evident in the larger quartz grains but is rarely as intense as in the non-mineralised SLGs. Oligoclase ($An_{15}$ to $An_{17}$) is the dominant plagioclase phase (up to >30 % modal in most samples). It occurs as large euhedral crystals between similar-sized quartz and occasional, smaller microcline.

The majority of accessory phases such as zircon, xenotime (Figure 4.26b) and magnetite have characteristic radiating cracks surrounding them, indicative of their radioactive inclusions. Some magnetite, particularly in sample DH025 353.60-304.03, contains uraninite inclusions/replacements.

Xenotime and monazite appear to be a characteristic pair of phosphate minerals in the Goanikontes SLGs; Chapter 5 illustrates relatively anomalous Y in whole-rock geochemistry of Goanikontes samples, which reflects a Y host.

Table 4.10 Petrographic characteristics of D- and E-type leucogranites from the Goanikontes area. Plagioclase compositions are optically determined, with high An usually corresponding to high U content, e.g. DH025 353.60-354.03. $E_{alt}$ – Sericitised sheeted leucogranite, may or may not have been a D-type prior to alteration, these have sericite and limonite alteration. $E_{con}$ – Oxidation associated with metasedimentary contact. $E_r$ – Oxidised portion of an E-type. $E_c$ – The unaltered portion of an E-type. $D_{sc}$ – D-type with prominent sericitisation (U and Th content by XRF, in ppm).

| Sample | Type | Colour | Grain size | Texture | Biotite | Plag. | Th | U |
|---|---|---|---|---|---|---|---|---|
| DH012 127.72-128.04 | D | Black and white | Coarse | Inhomogeneous | Minor, gneissic streaks | $An_{15}$ | **428** | 613 |
| DH012 342.47-342.84 | $D_{sc}$ | Black and white | Coarse with fine patches | Inhomogeneous | Minor, disseminated | $An_{16}$ | 219 | 562 |
| DH025. 353.60-354.03 | D | Black and white | V. coarse | Pegmatitic | Interstitial booklets | **$An_{17}$** | 92 | **922** |
| DH012 42.38-42.75 | E | Pink, orange | V. coarse | Inhomogeneous | Sparse booklets | $An_{16}$ | 137 | 378 |
| DH019 13.75-14.15 | $D_{sc}$ | Light grey | Medium-coarse | Homogeneous | Fine, disseminated | $An_{15}$ | 80 | 100 |
| DH019 71.74-72.18 | $E_r$ | Oxidised orange | Medium | Homogeneous | Fine, disseminated | $An_{16}$ | 331 | 247 |
| DH019 71.74-72.18B | $E_c$ | Grey | Medium | Homogeneous | Fine, disseminated | $An_{6-17}$ | 29 | 39 |
| DH025 235.81-236.14 | E | White, red | Fine-medium | Inhomogeneous, foliation | Minimal, disseminated | $An_{15}$ | 92 | 496 |
| DH025 334.91-335.25 | $E_{con}$ | Pink, red, grey | Fine-coarse | Pegmatitic | Entrained laths and streaks, prominent | $An_{12}$ | 168 | 519 |
| DH025 496.03-496.38 | $E_{alt}$ | Grey, light green | Fine-coarse | Inhomogeneous, high % alteration | Disseminated streaks, chloritised | $An_5$ | 80 | 310 |
| CZ7-1 | E | Red, | Coarse | Inhomogeneous | Minimal | $An_{15}$ | 43 | 248 |

Sample DH025 353.60-354.03 is particularly coarse-grained. Tartan-twinned microcline is the largest feldspar (~20 mm) and has embayed contacts with surrounding quartz (Figure 4.26c) whereas tartan-twinned microcline is the subordinate feldspar in two other sections. Note in Figure 4.26d that quartz is heavily fractured, and microcline is not. Subordinate

microcline occurs as rounded, <4 mm crystals and is often included in plagioclase as well as in quartz. One of these samples, DH012 127.72-128.04, is illustrated in Figure 4.26e. There is no myrmekite at plagioclase K-feldspar contacts or in plagioclase inclusions in microcline (Figure 4.26f). This sets the D-type apart from the barren sheeted leucogranites and some of the E-types, which tend to have myrmekite development to varying degrees.

Cleavage-controlled sericitisation is the most prolific alteration in the D-types and particularly in the near-surface sample DH019 13.75-14.15. Minor albite rims have formed around plagioclase and some of the more anhedral quartz grains. Accessory muscovite is associated with skeletal, chloritised biotite or occasionally parallel to cleavages in feldspars.

Magnetite is prevalent in DH025 353.60-354.03 and some porphyroblasts have prominent β-uranophane association. Alteration processes that mobilised and deposited the secondary uranium minerals do not appear to have oxidised the magnetite. This sample is illustrated and discussed in the Goanikontes-specific sections of Chapter 7 and Chapter 8 as it has important implications for the nature of mineralisation in the Goanikontes ores. Magnetite is also present as a minor accessory in the other D-type samples.

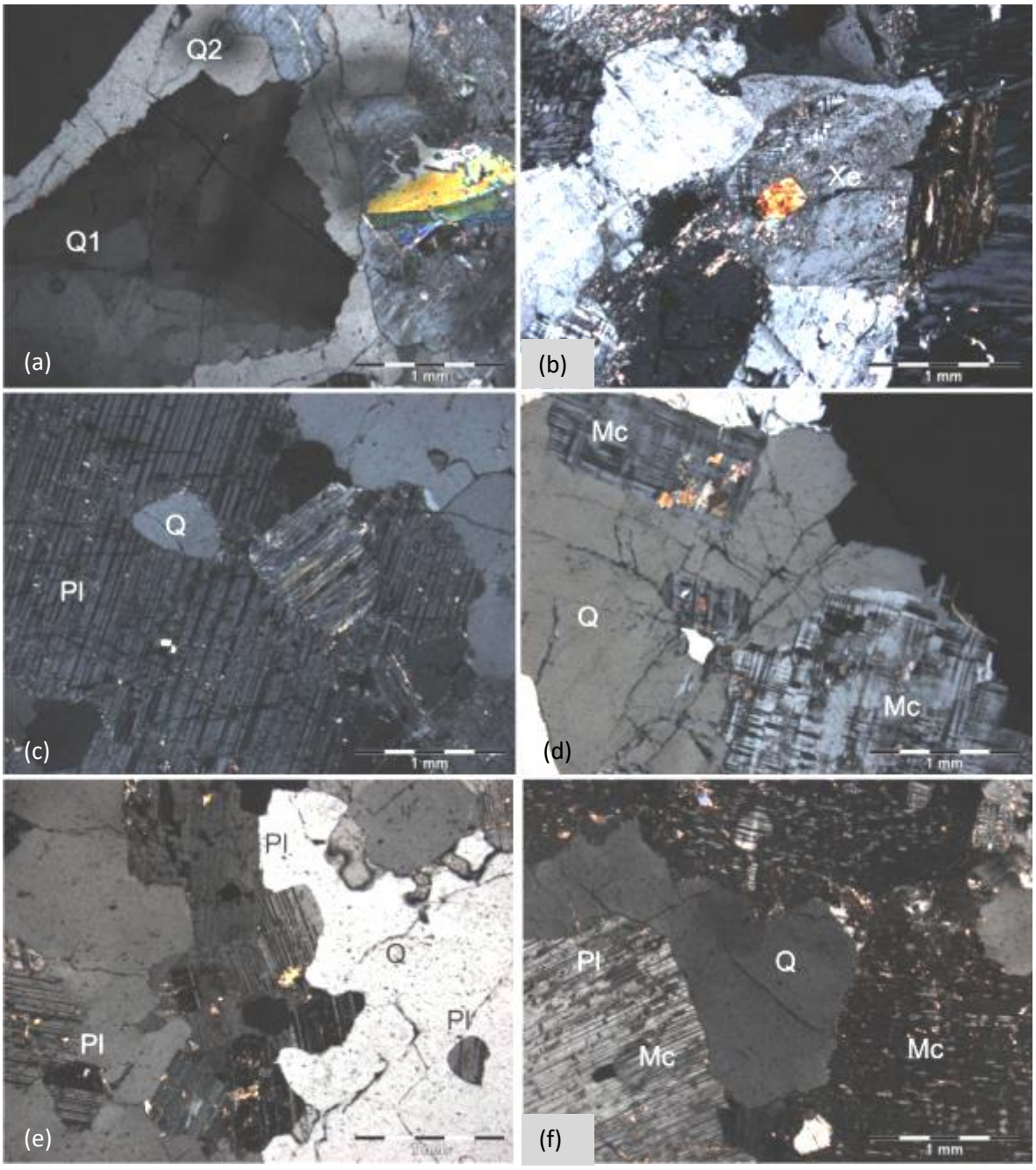



Figure 4.26 Petrographic characteristics of Goanikontes D-type sheeted leucogranites. (a) Quartz may be the dominant rock-forming mineral and is often in at least two generations, new quartz (Q2) grows between K-feldspar and an older quartz grain (Q1). Strain extinction is present in both quartz generations and the feldspars. DH025 353.60-354.03, xpl. (b) Accessory phases such as xenotime (Xe) contribute to anomalous Y concentration in many D and E-type Goanikontes sheeted leucogranites, DH012 342.47-342.84, xpl. (c) Plagioclase is the dominant feldspar in the D-type sheets and often contains inclusions of quartz and occasional biotite (always chloritised) DH019 13.75-14.15, xpl. (d) Microcline is the subordinate phase in most samples and has embayed contacts with quartz grains as well as typical globular quartz inclusions, DH025 353.60-354.03, xpl. (e) Anhedral quartz (Q) surrounds euhedral and anhedral plagioclase (Pl) DH012 127.72, xpl. (f) Microcline (Mc) development after plagioclase (Pl) with strained quartz veinlet (Q) DH012 127.72-128.04, xpl.

***Goanikontes E-Type Sheeted Leucogranites***

Quartz shows strain extinction, which may result from processes associated with post-$D_3$ geological activity. In addition to extensive chains and clusters, quartz is also present as fine- to medium-grained (<2 mm) rounded inclusions in larger microcline and occasionally in plagioclase. In the oxidised portions of samples (e.g. DH019 71.74-72.18) microcline is the dominant phase, but in the unaltered portion, plagioclase is far more abundant (>4 mm in size) and often euhedral.

Tartan-twinned microcline (Figure 4.27a) shows mesoperthite cross-cutting fine, cleavage-parallel microperthite. It is the most abundant K-feldspar in most samples and overgrows plagioclase, and is especially abundant in samples where quartz is rounded and distributed in discontinuous chains. The composition of plagioclases in the E-types is predominantly oligoclase and occasionally albite, though singular amoeboid inclusions may be up to $An_{36}$ (andesine) in composition. Oligoclase, for example, in sample DH025 235.81-236.14 is particularly sparse and <2 mm in size, is strongly sericitised and occurs as inclusions in quartz (Figure 4.27b) and tartan-twinned microclines.

Magnetite, the most abundant Fe accessory phase after biotite, is skeletal, with variable ilmenite exsolution, and is associated with zircon (Figure 4.27c and 4.27d). Magnetite in E-types is however, intensely oxidised and fracture-fill is often a combination of haematite and limonite. The severely altered sheeted leucogranite is included in this section because it is moderately mineralised (300 ppm U) and observations suggesting that it may be an altered C-type as the dominant feldspar is microcline.

Plagioclase in the D and E-types is a significant proportion of the rock; and graphic quartz-feldspar intergrowth textures are visible at low magnification, a textural feature that is absent in most uraniferous leucogranites. β-uranophane occurs in association with haematite that surrounds magnetite clusters in the E-types.

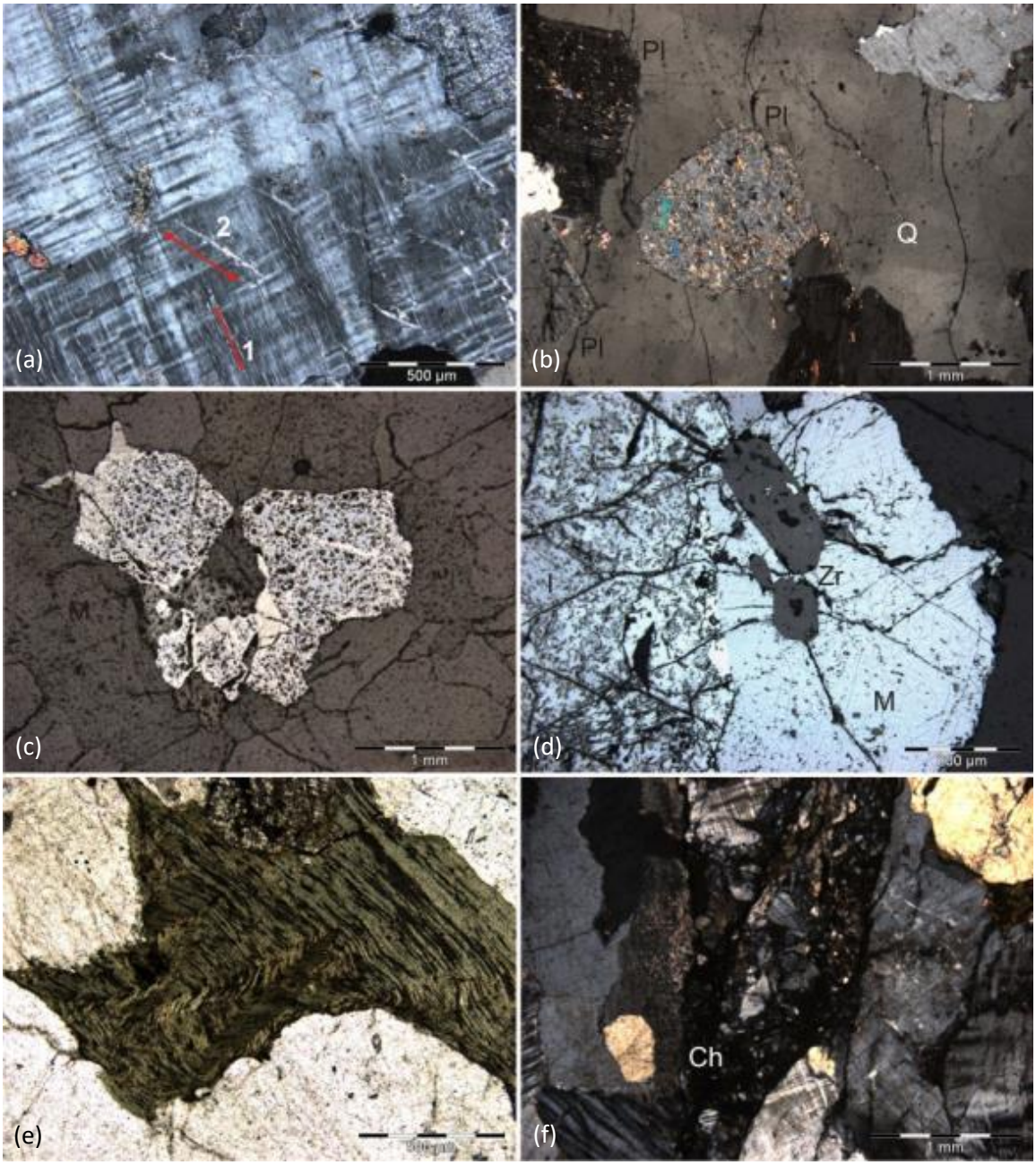



Figure 4.27 Features of altered D and E-type sheeted leucogranites. (a) Perthite in microcline is developed cleavage-parallel first (1) and then as flame perthite (2) oblique to the twinning directions, DH025 235.81-236.14, xpl. (b) Plagioclase (Pl) as anhedral inclusions within later quartz (Q) and in clusters of euhedral grains adjacent to quartz. The inclusion has well-developed sericite compared to the euhedral examples, DH019 71.74-72.18, xpl. (c) Euhedral magnetite is a common accessory in E-type sheets at Goanikontes, alteration by oxidation has resulted in pock–marked textures, DH025 334.91-335.25, rfl. (d) Accessory zircon occurs in clusters, with occasional double termination; zircon is most closely associated with phosphates and magnetite – ilmenite clusters, DH019 71.74-72.18, rfl. (e) The sample is from a fault zone and the deformation evident in the biotite is unique to this particular sheeted leucogranite, DH025 496.03-496.38, ppl. (f) An example of highly altered sheeted leucogranite with a zone of micro-fractures and breccia. Chlorite and epidote are prominent alteration products. DH025 496.03-496.38, xpl.

Biotite is more prevalent than in the other mineralised varieties. Blades are skeletal and often deformed (Figure 4.27e). A strongly sericitised sample illustrates chlorite replacement veins that cross-cut magnetite and surround it on most sides, *DH025 496.03-496.38 (Figure 4.27f). Despite high cps in hand-specimen, secondary uranium phases are not prevalent.

Magnetite is distinguishable from uraninite primarily by ilmenite exsolution lamellae; uraninite also lacks red internal reflections, which are more common in partially oxidised magnetite; D- and E-types do not appear to have finite differences in primary uraninite and secondary uranophane relationships.

### *Hildenhof Uraniferous Sheeted Leucogranite Petrography*

Ten thin sections represent ten of the hand specimens collected at surface on EPL3345 of Bannerman Resources. Table 4.11 presents a summary of the samples, which highlights the range in uranium and thorium concentrations in the sheeted leucogranites. As at all deposits, the sheets incorporate wall rock material at the margins. Petrographic observations show that of the ten samples observed, K-feldspar is the dominant feldspar in nine, and tartan-twinned microcline is dominant in six of these.

Quartz is the main mineral in sample HILG 35, and in this sample, the dominant feldspar is oligoclase. Quartz is a major component in the mineralised sheeted leucogranites (>40 %) and tends to occur, interstitial to K feldspars, in discontinuous vermicular clusters up to 3 cm long. Veinlets (5 mm) of new, euhedral, polycrystalline quartz with highly variable strain cut older anhedral grains, a feature characteristic of Goanikontes E-types. Quartz inclusions in feldspars are scarce; however, in quartz-rich samples, quartz contains inclusions of anhedral K-feldspars. Graphic quartz feldspar growth is common in both pegmatitic textured and coarse-grained samples.

Tartan-twinned microcline constitutes >40 % in most samples and appears to be growing at the expense of plagioclase (Figure 4.28a). The K-feldspar crystals, including microcline-perthite, range in size from <1 mm to over 5 mm. Oligoclase accounts for <10 % in nine of the

sections, and in all but two samples (HILG 12 and HILG 15- where oligoclase is >3 mm up to 8 mm), Oligoclase occurs as remnant ~1 mm inclusions in microcline (Figure 4.28a). Myrmekite is a prominent texture in samples- HILG 07, 12, 19 and 35; the majority occurs in uniform grains with no zonation. This is in contrast to the observations of Nex (1997) at Goanikontes where myrmekite was observed in the cores of zoned plagioclases. In the Hildenhof samples, myrmekite is abundant in tartan-twinned microcline-dominated samples, particularly where oligoclase is an inclusion in K-feldspar, HILG 19 is characterised by grains composed entirely of myrmekite texture (Figure 4.28(b).

Table 4.11 Petrographic characteristics of mineralised sheeted leucogranite thin sections from Hildenhof.The red blocks highlight samples with the highest U and Th content. (U and Th content by XRF, in ppm)

| Sample | Type | Colour | Grain size | Texture | Biotite | Main Feldspar | Plag. | Th | U |
|---|---|---|---|---|---|---|---|---|---|
| HILG 01 | E | White, with red staining | Very Coarse | Inhomogeneous | Cm scale laths | Microcline-perthite | $An_{12}$ | 102 | 847 |
| HILG 07 | E | Light Pink | Coarse | Inhomogeneous | Sparse mm scale laths | Microcline | $An_{12}$ | 18 | 85 |
| HILG 12 | D | White | Very Coarse | Inhomogeneous | Sparse cm scale books | Microcline | $An_{10-15}$ | 27 | 186 |
| HILG 13 | E | Pink | Medium | Homogeneous, subtle foliation | Fine, fabric, disseminated | Microcline | N/S | 46 | **1967** |
| HILG 15 | E | White | Very Coarse | Inhomogeneous | Large cm scale clumps | Microcline-perthite | $An_{15}$ | 9 | 95 |
| HILG 19 | E | Pink, stained red | Very Coarse | Inhomogeneous | Cm scale laths | ~Microcline | $An_{12}$ | 81 | 623 |
| HILG 21 | E | Light Pink | Very Coarse | Inhomogeneous | Sparse cm scale laths | Microcline-perthite | $An_{11}$ | **211** | 1339 |
| HILG 29 | E | Light green, grey | Medium - coarse | Homogeneous, subtle foliation | Sparse, fine, disseminated | Microcline | $An_{15}$ | 51 | 77 |
| HILG 34 | E | Light Pink | Medium - coarse | Homogeneous | Sparse, fine, disseminated | Microcline | $An_{15}$ | 12 | 53 |
| HILG 35 | D | White | Very Coarse | Inhomogeneous | Sparse, cm scale books | Oligoclase-andesine | $An_{0-1}$ | 31 | 137 |

Oligoclase is interstitial and anhedral in quartz-rich SLGs, with 1 mm to 2.5 mm grain sizes to most feldspar crystals. Albite rims surround the majority of oligoclase grains, and twinning tends to be continuous from core to rim. Sericite development is moderate, but variably present in the majority of grains.

Biotite is predominantly red-brown to tan-green in colour depending on the degree of chloritisation and is ~1 mm-3 mm long, bladed, and well cleaved with ragged edges,

occasional skeletal grains are also present, indicative of entrainment from other sources (wall rocks). Pleochroic halos around zircon and uraninite inclusions are abundant and most prominent in the chloritised biotite blades.

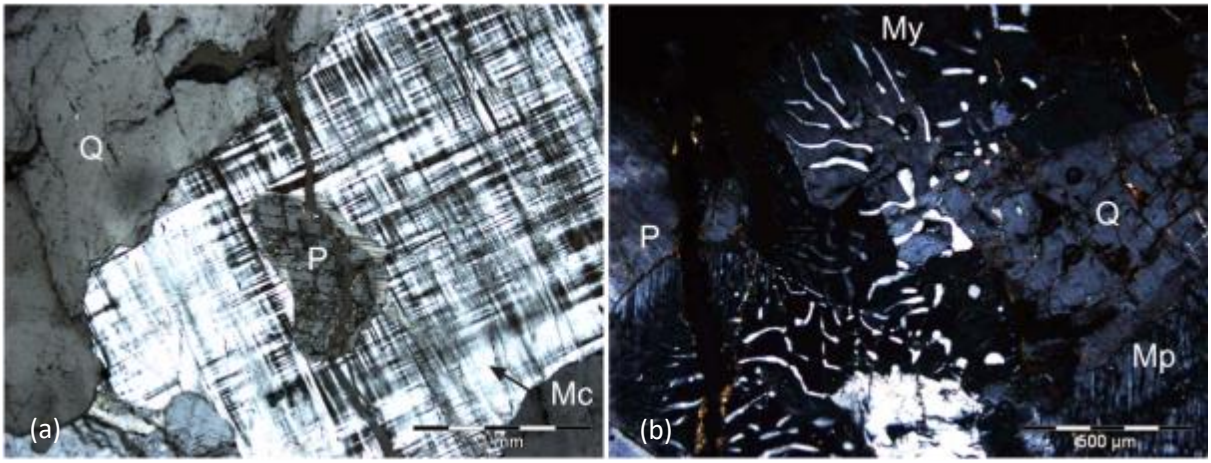



Figure 4.28 Features common to the majority of mineralised sheeted leucogranites at Hildenhof. (a) Albite-rimmed Oligoclase in microcline, as in the pre-$D_3$ sheets quartz exhibits strain extinction, HILG 12, xpl. (b) At least four mineralised samples contain myrmekite; it occurs in cores of plagioclase but rarely in the rims. Plagioclase without cores and little sericite tend to have the best-developed quartz intergrowths, HILG 19, xpl.

### *Goanikontes and Hildenhof Ore Mineral Petrography*

The samples described in this section include an Etango surface sample (CZ14-1) an E-type core specimen from within the supergene envelope (~43 m depth) and two samples from depth (~330 m depth) in hole DH025. The samples described in this section are relatively high-grade (where an average grade of ~350 ppm or 500 ppm U is mined at Rössing or Husab, respectively). HILG 21 has 847 ppm U, DH025 334.99-335.45 has 519 ppm U, and DH025 353.60-354.03 has 922 ppm U. CZ14-1 is a lower-grade sample with 248 ppm U. Hand specimen photographs are in Digital Appendix 3 and the full complement of thin section descriptions for all Goanikontes and Hildenhof specimens are in Appendix D1.

The selection of mineralisation samples from the Goanikontes - Hildenhof areas includes five samples that are investigated by QEMSCAN for semi-quantitative U-mineral deportment.

Uraninite and other uranium phases of the Hildenhof sample HILG 21, and the core sample DH025 353.60-354.03 were analysed by EPMA.

Sample HILG 29 has distinctly green biotite with considerably more halos than the biotite in the other Hildenhof samples. Accessory phases in the Hildenhof mineralised samples include magnetite-ilmenite (Figure 4.29a) zircon, monazite (Figure 4.29c) and fluorite-uranophane crystallisation along grain boundaries (Figure 4.29b). Uraninite is scarce and difficult to distinguish from magnetite when characteristic ilmenite exsolution or haematite are not present.

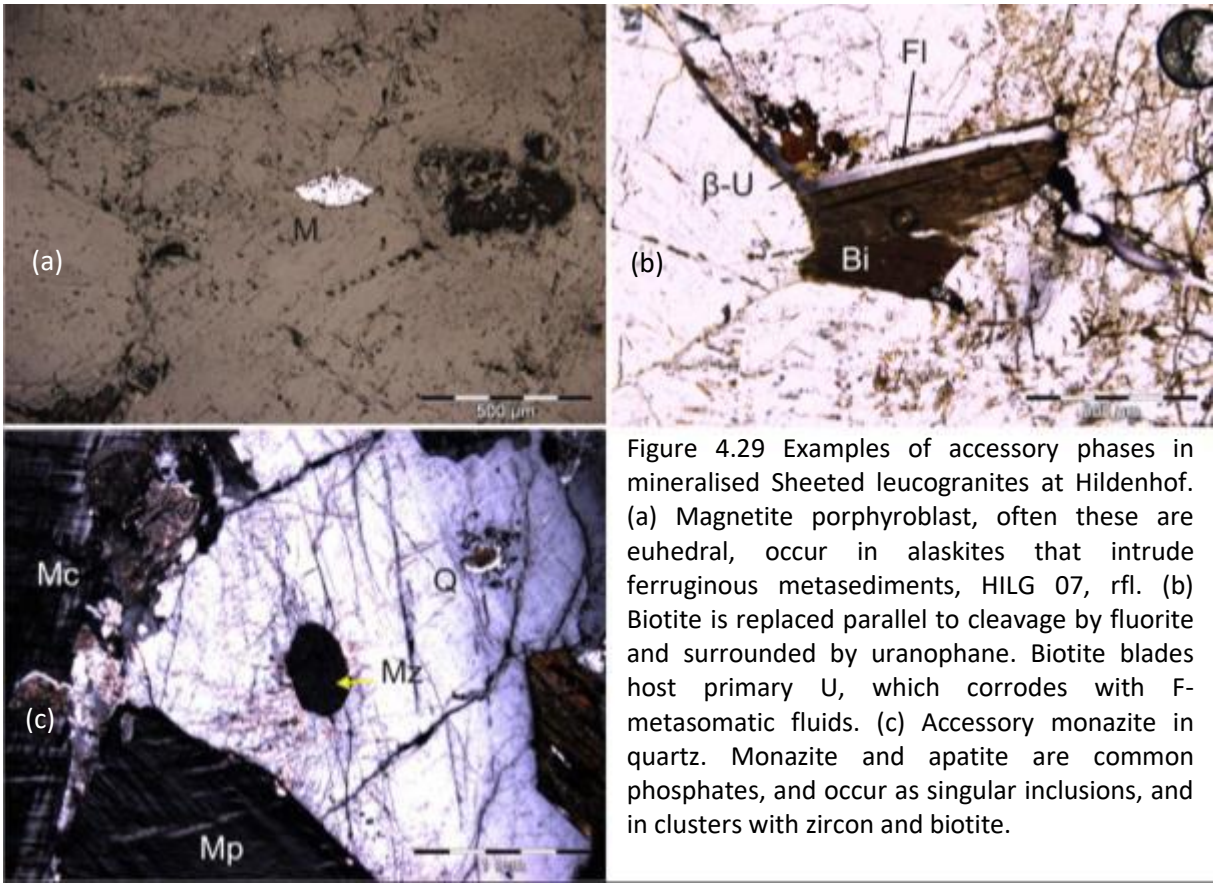



Figure 4.29 Examples of accessory phases in mineralised Sheeted leucogranites at Hildenhof. (a) Magnetite porphyroblast, often these are euhedral, occur in alaskites that intrude ferruginous metasediments, HILG 07, rfl. (b) Biotite is replaced parallel to cleavage by fluorite and surrounded by uranophane. Biotite blades host primary U, which corrodes with F-metasomatic fluids. (c) Accessory monazite in quartz. Monazite and apatite are common phosphates, and occur as singular inclusions, and in clusters with zircon and biotite.

Uranium is present in uraninite; and in uraninite inclusions hosted in magnetite and biotite. It appears that the uraninite may simply be a replacement texture in magnetite, given the

altered nature of the Fe-oxides in the alaskites; and probably as a replacement along biotite cleavages. Zircon inclusions within biotite contain their own radioactive inclusions, as evident in the pleochroic halos that surround them. Uranophane is a common observation in thin sections of mineralised samples, and shows a particular association with uraninite-hosting magnetite grains in the DH025 samples. Figure 4.30a through 4.30c illustrates the relationships between uranium and Fe-minerals in the D-type textured sheeted leucogranites at Goanikontes, which are often visible in hand specimen.

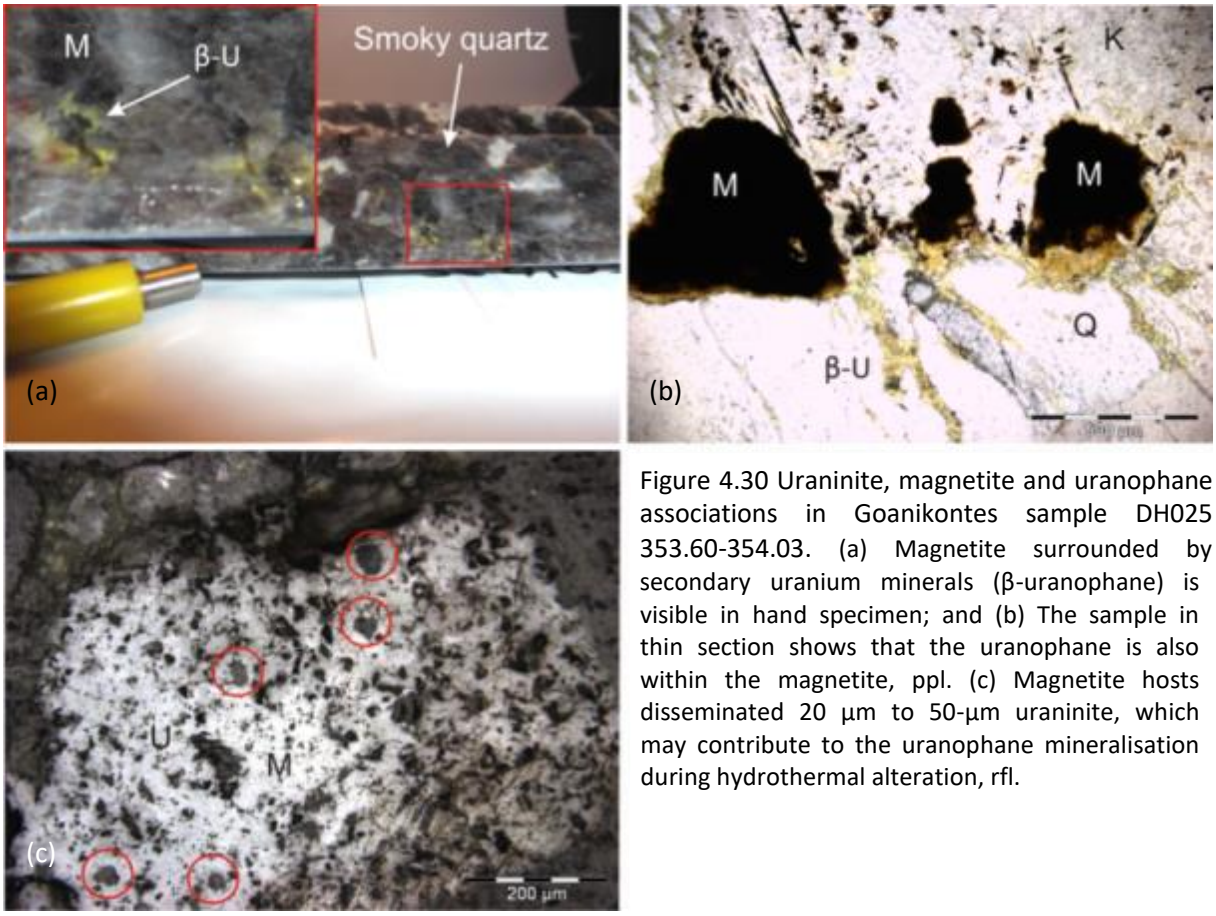



Figure 4.30 Uraninite, magnetite and uranophane associations in Goanikontes sample DH025 353.60-354.03. (a) Magnetite surrounded by secondary uranium minerals (β-uranophane) is visible in hand specimen; and (b) The sample in thin section shows that the uranophane is also within the magnetite, ppl. (c) Magnetite hosts disseminated 20 µm to 50-µm uraninite, which may contribute to the uranophane mineralisation during hydrothermal alteration, rfl.

The D-type ore has the typical colour contrast between black quartz and white feldspar. There is some evidence of alteration, which has mobilised and deposited secondary U, but has not mobilised Fe from magnetite (Figure 4.30b). This relationship indicates that reduced

Fe in magnetite remains unchanged in the presence of late $U^{6+}$-bearing fluids, which do not contain $Fe^{3+}$. The source of U for uranophane I would be the proportion of oxidised U that remains in the magmatic fluids; however, some magnetite contains fine-grained inclusions of uraninite which implies that the magnetite is a site for U reduction by reaction with the $Fe^{2+}$ component of the magnetite (Figure 4.30c).

Figure 4.31a is of an E-type sample from ~330 m depth and shows secondary Fe-minerals staining the K-feldspar at the top right of the photomicrograph. The image in Figure 4.31b is an example of alteration that has deposited yellow secondary uranium minerals (uranophane) and not secondary iron. The uranophane fills spaces between quartz and feldspar. Alteration has also contributed to the breakdown of K-feldspar and in some of these spaces uranophane grows as acicular crystal clusters (Figure 4.31c). The halos of uranophane around magnetite may also have formed from liberating $U^{6+}$ from uranium-bearing inclusions in the magnetite itself. The magnetite-uraninite relationship is common in the nearby Goanikontes leucogranites, it is unconfirmed at Hildenhof.

Magnetite in the Goanikontes ores is variably oxidised and contains ilmenite lamellae and alteration halos of red staining visible in hand specimen and in transmitted light. Primary magnetite occurs in two main textures; primary magnetite as euhedral spinel-shaped crystals between quartz and feldspar, and secondary magnetite that occurs as a product of biotite breakdown, forming lenses between biotite sheets with ilmenite and haematite. Hydrothermal alteration has altered the crystals of magnetite leaving anhedral edges with red oxide halos around many grains.

Uranium minerals occur as fine-grained masses within cavities between the main rock-forming minerals (Figure 4.32a) where the radiating fractures are the best identifying feature of radioactivity. There is a common association with Fe-Ti phases such as titanite and magnetite – haematite (Figure 4.32b and c). The high magnification in Figure 4.30c illustrates the fine-grained uranophane and amorphous mobile iron phases that lend the E-type granite its red-pink hue. Biotite is variably chloritised, with Fe-Ti phases forming opaque, cleavage-parallel by-products of deuteric alteration (Figure 4.32d).

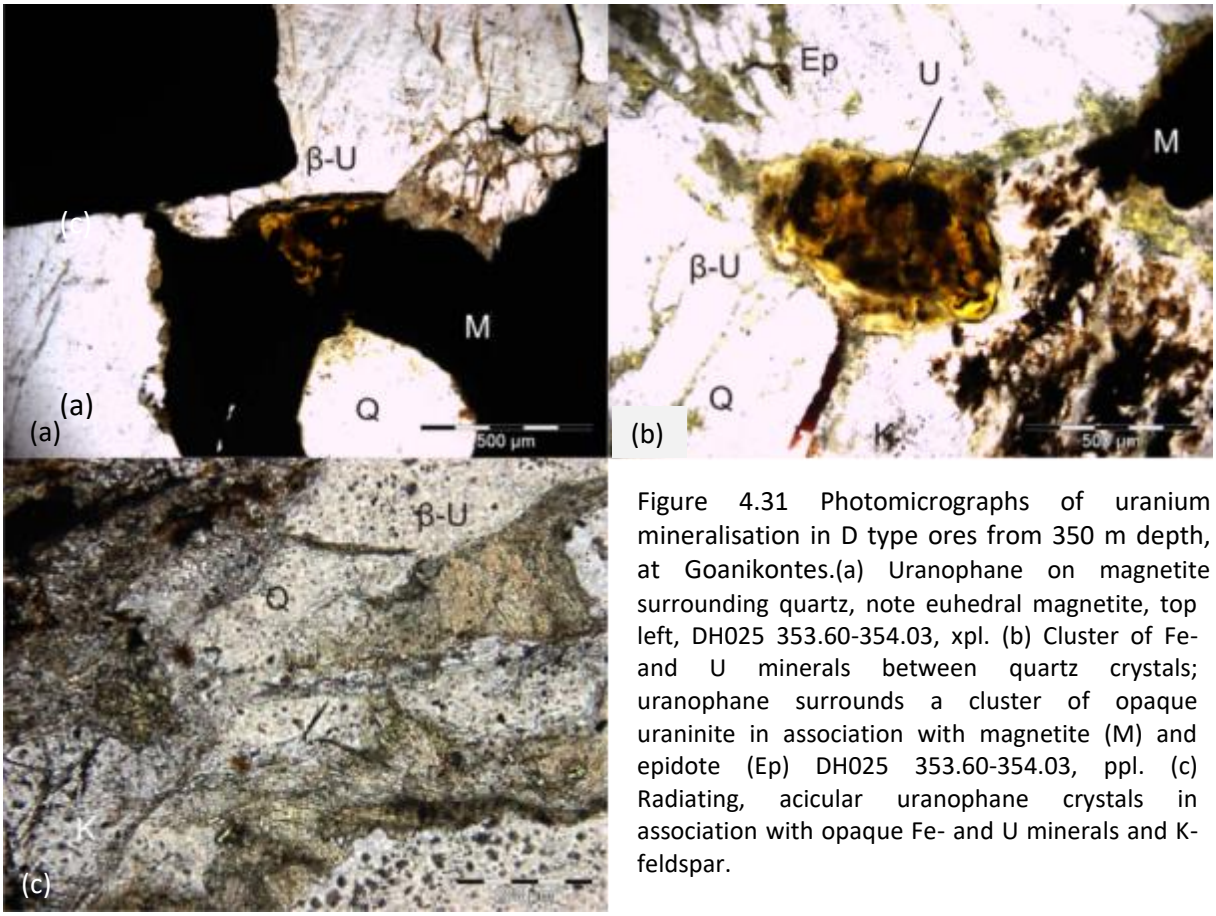



Figure 4.31 Photomicrographs of uranium mineralisation in D type ores from 350 m depth, at Goanikontes.(a) Uranophane on magnetite surrounding quartz, note euhedral magnetite, top left, DH025 353.60-354.03, xpl. (b) Cluster of Fe- and U minerals between quartz crystals; uranophane surrounds a cluster of opaque uraninite in association with magnetite (M) and epidote (Ep) DH025 353.60-354.03, ppl. (c) Radiating, acicular uranophane crystals in association with opaque Fe- and U minerals and K-feldspar.

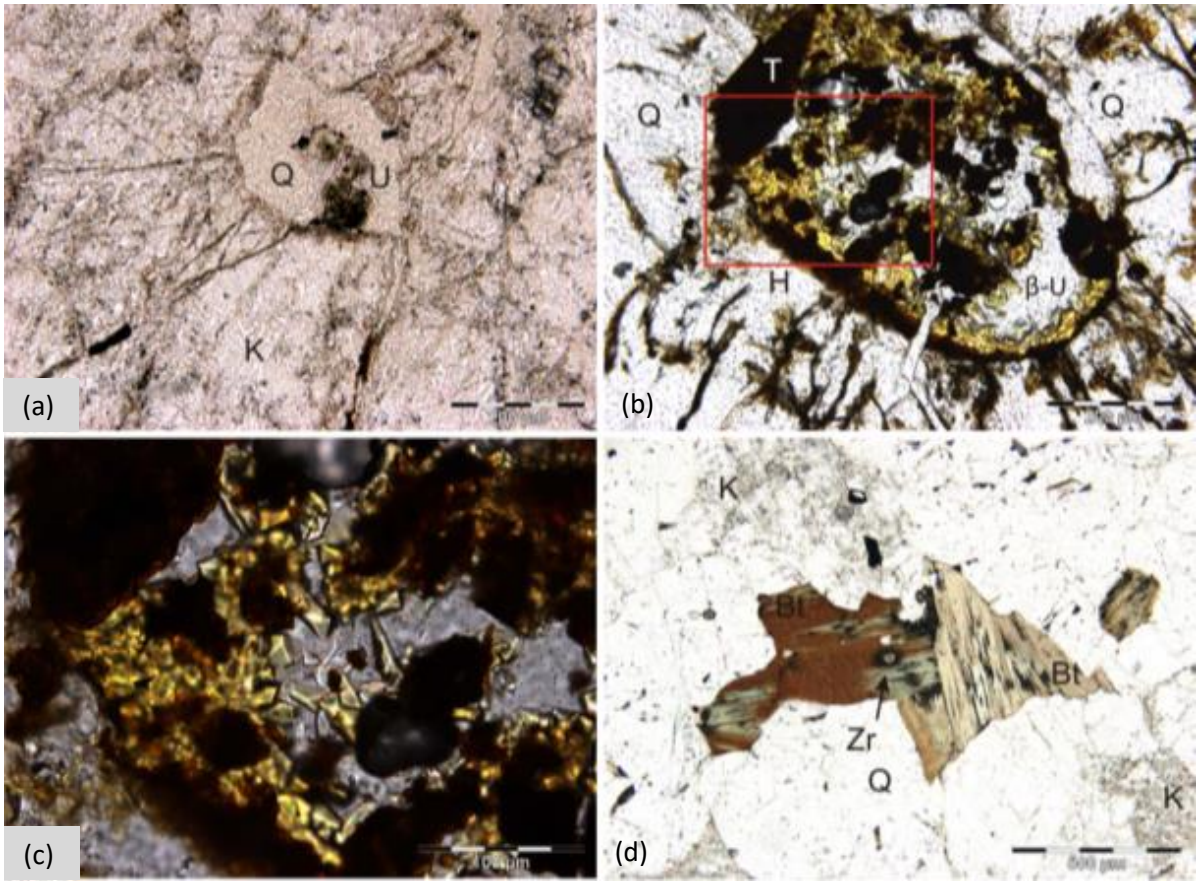



Figure 4.32 Uranium mineral features in the surface sample HILG21 from the Hildenhof anomaly. (a) A complex arrangement of opaque uraninite (U) crystals surrounded by a halo of secondary U minerals that is surrounded by quartz (Q). Radiating fractures in feldspar (K) are a result of metamictisation by radiation damage, HILG 21, ppl. (b) Corroded cluster of magnetite and titanite (T) haematite (H) and yellow uranophane (β-U) filling the voids, HILG 19, ppl. (c) High magnification reveals well-formed crystal terminations of β-uranophane amongst amorphous Fe and U hydroxides and silicates, HILG 19, ppl. (d) Skeletal and bladed biotite clusters are abundant in the sample and host uraniferous inclusions, including zircon (Zr).

### *Ida Dome Uraniferous Sheeted Leucogranite Petrography*

Uraniferous leucogranites were sampled at Garnet Valley, Holland's Dome, and Ida Central, and at a location within the Abbabis Gneiss of the Ida Dome core (IDAG 34 - 500559E 7487162N). Petrographic studies were performed on Ida Central and the Holland's Dome samples; Table 4.12 summarises characteristics observed in the thin section samples of Ida Dome area.

Table 4.12 Petrographic characteristics of alaskite thin sections cut from core samples from Ida Central and hand specimen from the Holland's Dome deposit. Type abbreviations: $D_{oxi}$ -oxidised D-type with no halo (corona); E –mineralised sample with typical oxidation halo (corona); and E'-mineralised sample with discoloration by sediment interaction. Area abbreviations: C -Ida Central; and HD -Holland's Dome (U and Th by XRF). IDAG 10 is the lowest-grade sample in the set, IDAG 16 is the most U-enriched and IDAG 46 has lost U relative to Th during hydrothermal alteration.

| Sample | Area | Type | Colour | Grain size | Texture | Biotite | Feldspar | Plag. | Th | U |
|---|---|---|---|---|---|---|---|---|---|---|
| HDD027 104.36-104.70 | C | D | Light Pink | Coarse | Pegmatitic | Minimal | Oligoclase | $An_{17}$ | 15 | 303 |
| HDD027 122.90-123.22 | C | $D_{alt}$ | Light pink | Fine-coarse | Inhomogeneous | Entrained laths | Microcline | $An_{12}$ | 9 | 91 |
| HDD027 89.47-89.97 | C | $D_{alt}$ | Light pink | Fine-coarse | Inhomogeneous | Disseminated streaks | Oligoclase | $An_{12}$ | <12 | 119 |
| IDAG 03 | C | D | White | Coarse | Pegmatitic | Disseminated sparse | Oligoclase | $An_{12}$ | <12 | 155 |
| IDAG 05a & b | C | E | Red | Medium-Coarse | Inhomogeneous | Disseminated variable dist. | Oligoclase | $An_{17}$ | 74 | 624 |
| IDAG 10 | C | D | White | Medium-Coarse | Inhomogeneous | Disseminated fine | Microcline-perthite | $An_{17}$ | 9 | 31 |
| IDAG 16 | C | $D_{alt}$ | Light green-grey | V. coarse | Pegmatitic | Disseminated fine | Plagioclase | N/S | 111 | **1087** |
| IDAG 21 | C | $D_{alt}$ | White, red stained | Medium-coarse | Inhomogeneous foliated | Disseminated | Oligoclase | $An_{15}$ | 126 | 398 |
| IDAG 29 | C | E' | Light brown | Bimodal, fine, coarse | Inhomogeneous | Coarse, books | Oligoclase | $An_{17}$ | 85 | 155 |
| IDAG 34 | Ida Dome | D | Light green-grey | Fine-coarse | Pegmatitic | Fine, disseminated | Oligoclase | $An_{18}$ | 60 | 269 |
| IDAG 43 | HD | E' | Pink | Medium | Homogeneous, foliated | Prominent | Oligoclase | $An_{16}$ | 101 | 883 |
| IDAG 44 | HD | C | White | Medium-coarse | Inhomogeneous | Large laths | Microcline | $An_{14}$ | 49 | 32 |
| IDAG 46 | C | $D_{alt}$ | Orange | Coarse | Pegmatitic | Minor, entrained | Microcline | $An_{12}$ | **369** | 428 |

D-type sheeted leucogranites, as well as an assortment of altered samples that lack the typical halos that characterise the E-type (as described for Goanikontes/Etango by Nex, 1997, for example). Labelling follows D, $D_{alt}$, or E-type: Where $D_{alt}$ refers to an altered D-type and E refers to the typical uraniferous SLG with prominent oxidation halos. Further descriptive tables are in Appendix D1. The samples from the HDD027 hole resemble D-types; but in thin-section, textures and accessory assemblages suggest significant host rock interaction, and are therefore described as altered, or $D_{alt}$-type.

Plagioclase feldspars dominate the feldspar populations of the uraniferous Ida Central and Holland's Dome samples (Figure 4.33a). They account for >35% - 40% of feldspars in section

are primarily of oligoclase composition. It is coarse-grained, average ~4 mm, euhedral, and only occasionally show anhedral textures where quartz grains are in direct contact.

Quartz grain sizes vary from 0.2 mm - 2.5 mm in the Ida Dome alaskites, and larger grains occasionally dominate (IDAG 03), with minor embayed and globular fine grains (<0.5 mm) included in feldspars and shows strain extinction in most samples. It is predominantly straight-edged and arranged in chains and clusters (Figure 4.33b). Quartz occurs in at least two generations. The oldest generation occurs as inclusions in feldspar and the younger occurs as vein and clusters that replace and envelop sub-rounded inclusions of plagioclase and microcline, IDAG 29 and IDAG 34 (Figure 4.33a and c), respectively. Polycrystalline quartz is rare and observed as an entrained contaminant.

Two D-type samples, IDAG 10 and IDAG 44, from Ida Central and Holland's Dome, respectively, have minimal U enrichment (Table 4.14) both samples have extensive sericite and saussurite developed cleavage-parallel in plagioclase (IDAG 10) and microcline (IDAG 44). Myrmekite is poorly developed and scarce in the Ida mineralised sheets in general (but is present in HDD27 104.36-104.70 (illustrated in Figure 4.33c). Microcline is subordinate and is later than plagioclase, replacement textures are common (Figure 4.33d) and are associated with intense sericitisation of the plagioclase. K-feldspar is between 2 mm and 5 mm in size, and coarser than 20 mm in some hand specimens.

Biotite is scarce and not present in some sections. It is generally fine - grained and blades rarely exceed 2.5 mm and is most often disseminated or in subtle stringers when present. Grain textures range from bladed to amoeboid and skeletal; most are chloritised with minor fluorite and associated pleochroic halos and Fe-stained cleavage planes. Accessories include clinopyroxene (entrained diopside) skeletal muscovite, zircon (Figure 4.33e) and a host of metamict, high - relief accessory phases, most with characteristic radiating fractures.

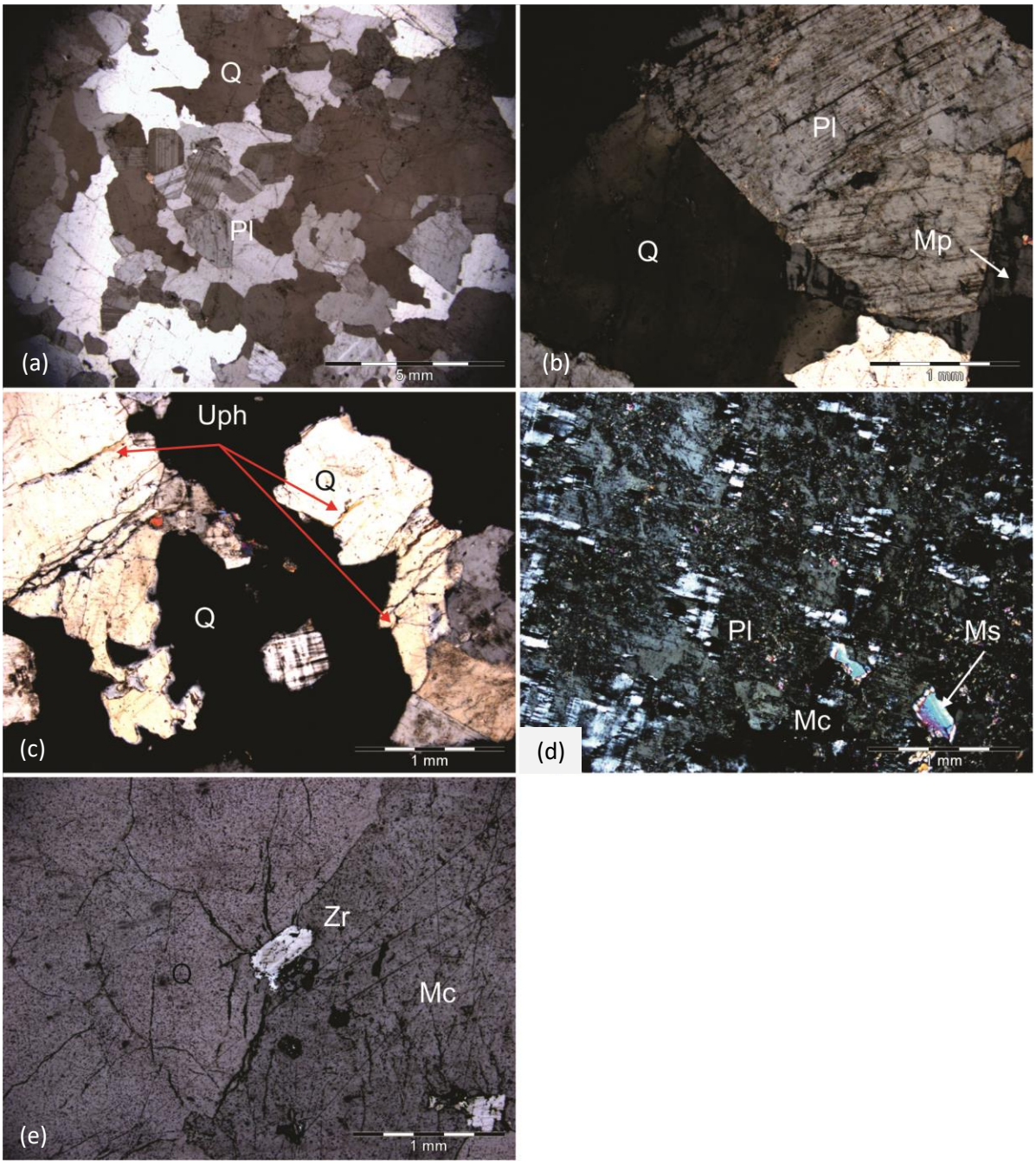



Figure 4.33 Features of mineralised sheets from the Ida Dome area. (a) Amoeboid quartz with sub-rounded plagioclase (Pl), xpl. (b) Euhedral plagioclase, in planar contact with quartz and irregular contact with microcline-perthite (Mp), IDAG 34, xpl. (c) Anhedral embayed quartz (Q) surrounds microcline and has planar boundaries with plagioclase (bottom left) and fractures in some quartz are filled with U secondary phases (top left) IDAG 34, xpl. (d) Alteration of plagioclase (Pl) to microcline (Mc) in a D-type, the accessory microcline is common to altered samples, IDAG 03, xpl. (e) Accessories such as zircon (Zr) are common in most Ida Dome samples, particularly those with biotite. Zircons are often zoned and surrounded by radiating fractures and are often in clusters, IDAG 46, rfl.

Quartz is the main constituent in most E-type leucogranite thin sections and occurs in polycrystalline clusters, chains and veinlets of grains with sizes averaging 0.1 to 5 mm. Inclusions of globular quartz are also common in K-feldspars and are predominantly <500 µm in size. Quartz tends to show less intense strain in the unaltered section (Figure 4.34a). Strain extinction appears more intense in quartz of the altered portion of the E-type (Figure 4.34b). Plagioclase grain sizes and textures are bimodal and range from fine-grained anhedral inclusions in microcline to large (>5 mm) euhedral crystals in clusters or chains (IDAG 29, Figure 4.34c). Plagioclase occasionally has embayed edges with amoeboid quartz. Albite twins dominate with only minor occurrences of pericline and carlsbad twinning. Myrmekite growth on plagioclase is also very sparse.

The granites, although altered from meteoric water ingress, preserve strain twinning, which suggests conditions were not hot enough to reset the quartz structure. The strain in quartz is variable; older fractured quartz most often has prominent strain, the polycrystalline clusters and chains of more euhedral quartz show more-subtle strain (Figure 4.34d), while the amoeboid and globular quartz show little to no strain, suggesting late formation.

Microcline in most other samples is a minor constituent despite very coarse grain sizes, often larger than 5 mm. However, microcline is the dominant feldspar in IDAG 43, from Holland's Dome; it is mostly subhedral and forms a matrix of 1-3 mm grains, occasionally exceeding 5 mm. Biotite is prominent in some samples and averages <2 mm in size. Booklets occur in samples with interactive contacts with the host metasediments (for example, IDAG 29). Individual laths may be >5 mm in size and most show a skeletal texture. All biotite is chloritised with pleochroic halos and fluorite is occasionally included. Biotite aligns in a subtle fabric in thin sections of samples that show deformational features in hand-specimen, such as IDAG 43.

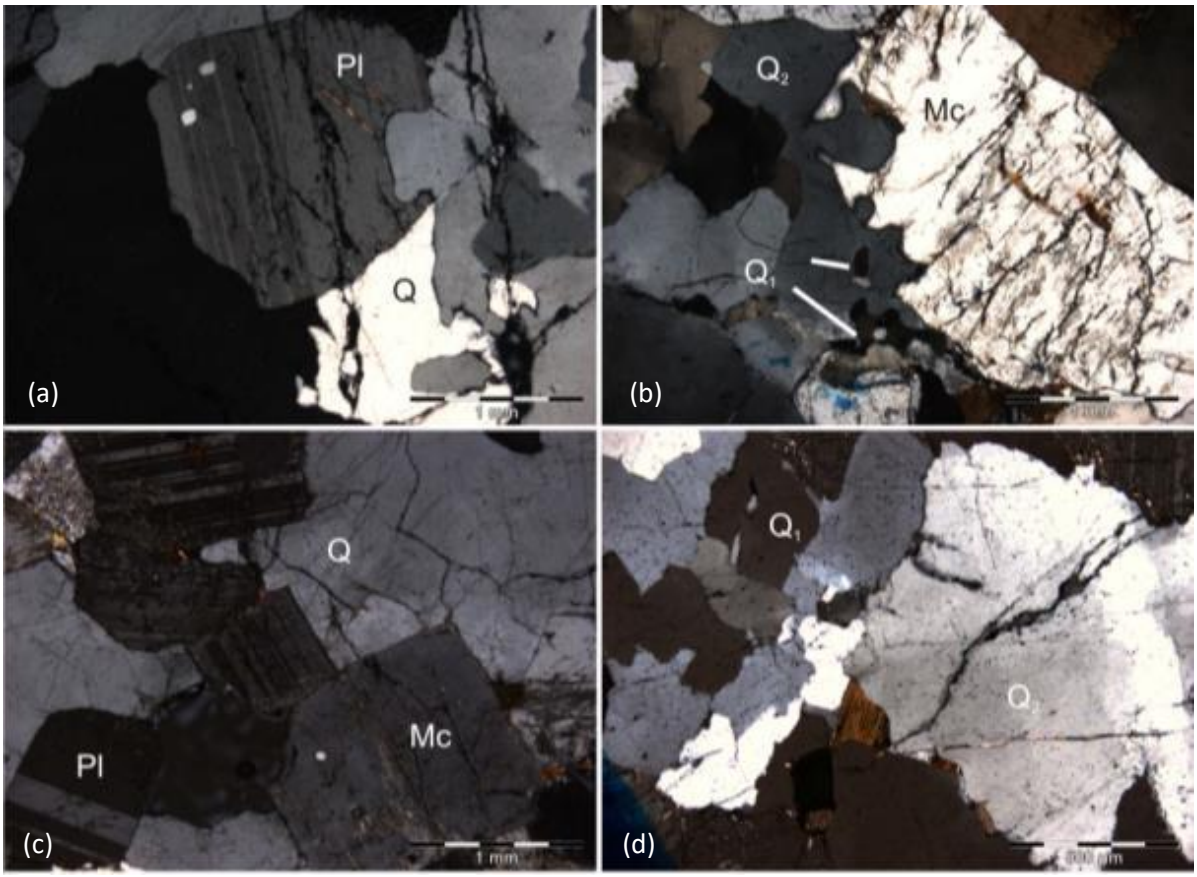



Figure 4.34 Features in oxidised and unaltered portions of E-type leucogranite at Ida Dome. Sample is the unaltered portion of IDAG 05a: (a) Quartz displays weak strain extinction, plagioclase is relatively unaltered and secondary U is minimal (b) Altered portion IDAG 05b: Quartz (Q2) shows stronger strain extinction, embays microcline (Mc) and surrounds older quartz globules (Q1). Embayed K-feldspar has secondary U minerals along cleavage-parallel fractures, xpl. (c) Euhedral plagioclase and microcline occur in interstitial chains and clusters, surrounded by, younger, anhedral, strained quartz, Unaltered sample IDAG 29, xpl. (d) Polycrystalline, euhedral quartz (Q2) cluster has formed adjacent to a larger, earlier fractured quartz crystal (Q2) IDAG 43, xpl.

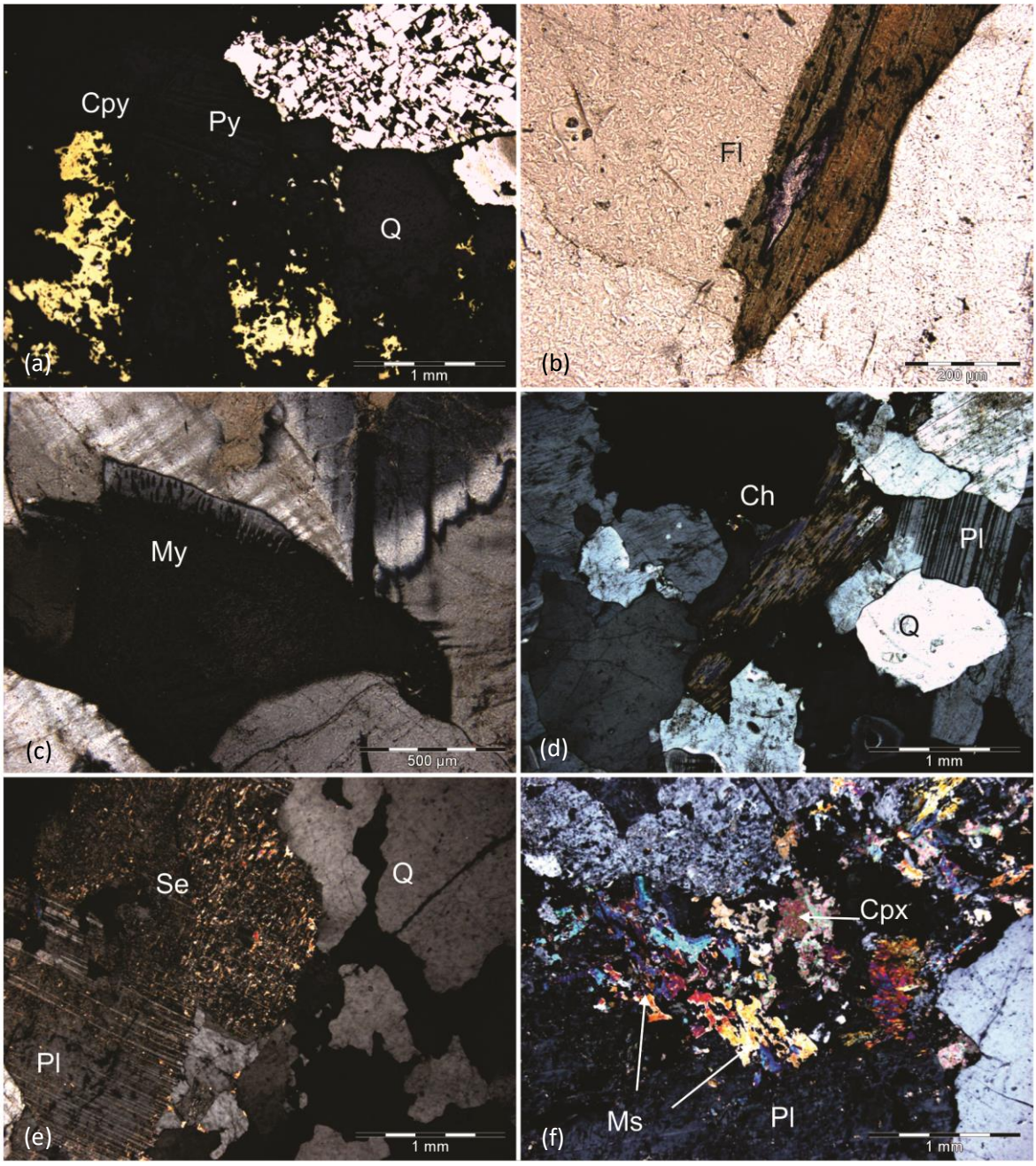



Figure 4.35 Features of mineralised samples with skarn and host rock interaction. (a) Large clusters of skeletal chalcopyrite (Cpy) and inclusion-rich pyrite (Py) are common minerals in sheets that intrude the upper Khan Formation, HDD027 122.90-123.22, rfl. (b) Fluorite is present in skarns (Husab) and is only present with biotite in thin section, HDD27 104.36-104.70, ppl. (c) Myrmekite growth at plagioclase rims is a common feature in the barren sheeted leucogranites but significantly less so in the mineralised sheets. Fluid interaction between skarns and sheets at the Ida Dome would provide suitable conditions for its growth, HDD027 104.36-104.70, xpl. (d) Anhedral quartz and plagioclase are not unusual in altered sheeted leucogranites, this sample also has entrained, chloritised biotite (Ch) HDD027 89.47-89.95, xpl. (e) Variable temperature alteration episode(s) results in sericite growth (Se) in plagioclase (Pl) adjacent to a euhedral quartz veinlet, IDAG 10, xpl. (f) CPX is scarce but present in the samples with skarn interaction, IDAG 03, xpl.***Ida Dome Ore Mineral Petrography***

The Ida Dome sheeted leucogranites at Ida Central are proximal to an Abbabis basement core, and invade a package of Khan- and Rössing Formation rocks that is <750 m thick. The sheets host accessory minerals that may be entrained components from the source(s) of the silicate partial melt such as anhedral zircon with radioactive inclusions (Figure 4.36a). In addition to entrained minerals, there is a significant contribution of Cu-sulphide from the host Khan Formation biotite schists, chalcopyrite for example in HDD027 122.90-123.22 (Figure 4.36b).

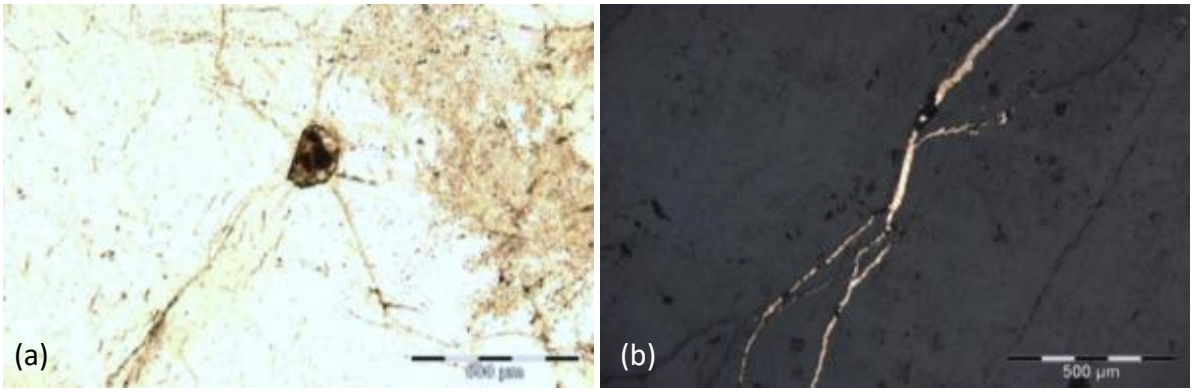



Figure 4.36 Uranium mineral associations in core specimens from HDD025. (a) Zircon is a common accessory mineral in sheeted leucogranites and many examples host uraniferous inclusions. The anhedral crystal may be an entrained component rather than a primary phase. Radioactive decay results in metamictisation and volume expansion, which is accommodated by the surrounding radiating fractures, HDD27 104.36-104.70, ppl. (b) The Khan Formation is locally cupriferous. Chalcopyrite veins that crosscut the leucogranites preserve the resulting Cu-sulphide mobilisation during granite emplacement, HDD027 122.90-123.22, rfl.

IDAG 43 is a typical uraniferous leucogranite, coarse-grained and with smoky quartz (Figure 4.37a). It has a red hue, which places it in the E-type category of Nex (1997). The sample also has a well-developed foliation and therefore precedes at least one deformation period, or is diachronus with a period of deformation and strain. It is therefore potentially a syn- $D_3$ or $D_2$ intrusive. Uranium and copper mineralisation at the Ida Copper Mine is described in Söhnge (2001) and the exposed Cu workings and trenches provide samples of uraniferous sheeted leucogranite with prominent alteration features, reflecting the role of magmatic fluids mobilising metals from the reactive, cupriferous biotite schists of the Khan Formation

(Figure 4.37b). Primary uranium is in uraninite and secondary uranium occurs as uranophane coatings on quartz and feldspar surfaces (Figure 4.37c). IDAG 46 has abundant radioactive minerals visible in thin section, all surrounded by prominent radial fractures (Figure 4.37d and e). The fracture network is so extensive that the dense network is visible in the hand specimen.

IDAG 08 is a low-grade, homogenous textured sheeted leucogranite; it has 128 ppm U and shows typical alteration features such as sericite replacement of plagioclase, and variably-haematised K-feldspar. The sample hosts uraninite with euhedral edges (Figure 4.38a). Uraninite tends to be cubic, and is primarily replaced by coffinite. The example in IDAG 05 (Figure 4.38b) shows the contrast in reflectance between U-oxide and U-silicate and internal reflections identify haematite and uranophane in the alteration halo that surrounds the uraninite. The ~400 µm crystal has grown at the junction of biotite and quartz grains. Uranophane replaces coffinite at the left and top centre of the uraninite-coffinite compound grain. Highly mobile $U^{6+}$ forms secondary minerals (uranophane) that coat the surfaces of quartz inclusions in altered K-feldspar (Figure 4.38c) and along quartz-microcline grain boundaries, (Figure 4.38d).

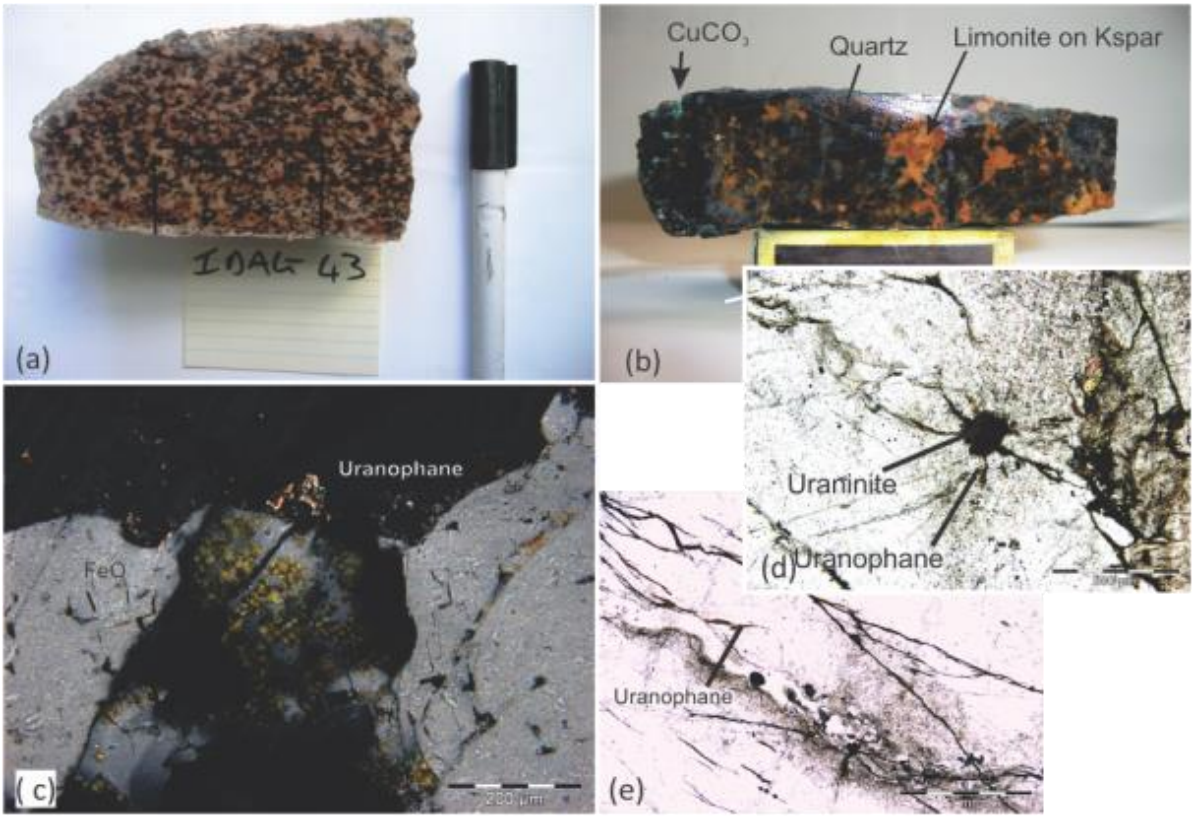



Figure 4.37 Alteration features of mineralised granites at Ida Dome. (a) Red-pink coloration typify E-type sheeted leucogranites, the IDAG 43 example also shows a subtle alignment of quartz and feldspar, a response to deformation suggesting the granite is younger than $D_3$. (b) Mineralised SLG that has undergone intensive oxidation during metasomatism. The feldspars have been altered to limonite stained sericite and Cu carbonates have filled spaces made available by feldspar alteration to clays, IDAG 46. (c) Uranophane on quartz, it is associated with the red, amorphous Fe-phases that give the rock its pink coloration, IDAG 43, xpl. (d-e) In thin section the IDAG 46 sample is highly fractured, metamict primary phases are visible and fractures throughout the sample have uranophane precipitation, IDAG 46, xpl and ppl.

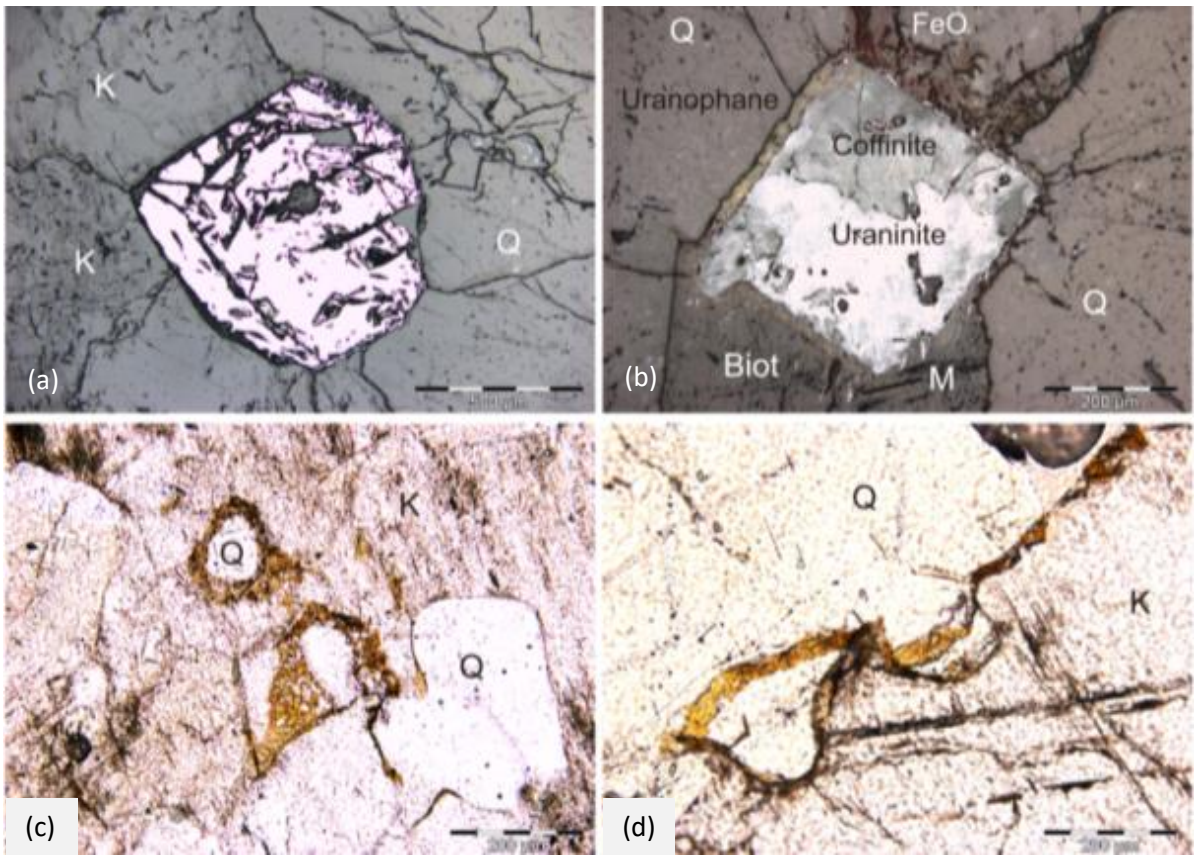



Figure 4.38 Uraninite and uranophane in Ida Dome Leucogranites. (a) Uraninite with radiating cracks in sample IDAG 08. (b) Pyrite/uraninite in an E-type sample IDAG 05; the sample may be pyrite or uraninite or a combination of both. Note FeO denotes a variety of potential hydrated iron oxides, uranophane occurs in the surrounding metamict halo and radiating fractures. (c) Uranophane surrounding globular quartz crystals within altered K-feldspar. (d) Uranophane in a sample from depth (HDD027 104.36-104.70); the secondary mineral permeates along grain boundaries where quartz has intergrown with K-feldspar.

### *Husab Alaskite Petrography*

The Husab Deposits at Zone 1 and Zone 2 cover a large area; economic ore bodies extend ~5.4 km N-S, ~2 km across, and are over 200 m in true thickness in certain areas. Sampling these large ore zones therefore provides a great variety of uraniferous leucogranite textures, colours, grain sizes, ore mineralogy, host rock interactions, and alteration overprints. All of which vary considerably within such a spatial context. Much like the other primary deposits, the main contribution to the variation in alteration and texture is the variation of interaction with the reactive units of the Rössing Formation, proximity to

meteoric fluid ingress, faulting and original oxidation state of the crystallising granite magma.

Approximately 90 % of the uraniferous SLG is hosted in Rössing Fm. Schists between carbonate packages. Table 4.13 summarises the petrographic characteristics of the Husab alaskites and includes description of typically D-type leucogranites and of alaskites that host uranium-bearing refractory minerals.

Table 4.13 Petrographic characteristics of the Husab alaskites. Samples are NQ ¼ core, U assay in ppm, ICP-MS. E/beta or brann indicates leucogranites that host uranium-bearing refractory minerals, namely betafite (beta.) and brannerite (brann.).

| Sample | Type | Colour | Grain size | Texture | Biotite | Dominant Feldspar | U |
|---|---|---|---|---|---|---|---|
| **RDD145 412-413m** | D | White, smoky quartz | Very Coarse | Pegmatitic | Minor, coarse books, partial chloritisation | Plagioclase, some silicification | **1031.5** |
| **RDD141 244-245m** | D | White, smoky quartz | Coarse | Consistent, coarse | Minor, disseminated | Microcline-perthite | 493.1 |
| **RD006 171-172m** | D | White, smoky quartz | Coarse | Pegmatitic | Coarse centimetric books, weak chloritisation | Microcline-perthite | 2439.0 |
| **RDD193 315-316m** | D | Light pink-grey quartz | Coarse | Pegmatitic | Clusters at metased. contacts | Plagioclase | 325.5 |
| **RDD373 63-64m** | $E_{brann.}$ | Orange-light pink | Very Coarse | Pegmatitic | Minor booklets (<1cm) all chloritised | Microcline perthite, minor tartan twinned grains | 299.5 |
| **RDD373 93-94m** | $E_{brann.}$ | Light pink - orange | Coarse - <7 mm ave. | Pegmatitic | Clustered booklets, all chloritised, at metased. contact | Tartan microcline dominant with intense microclinisation. | 561.6 |
| **RDD373 116-117m** | $E_{beta.}$ | Light orange | Very Coarse – centimetric | Pegmatitic | Fine books in clusters, chloritised | Tartan microcline, microclinisation on all grains | 359.1 |
| **RDD373 117-118m** | $E_{brann.}$ | Light orange-pink | Very Coarse | Pegmatitic with mineralisation in fine-grained patches | Fine blades in chains and clusters | Microcline-perthite-intense clay alteration | 262.6 |
| **RDD373 124-125m** | $E_{brann.}$ | Dark orange-grey - high mafic content | Very Coarse | Pegmatitic with fine-grained patches | Blades in nests with mafics, FeO and chloritisation of most. | Tartan microcline, microclinisation on all grains | 447.4 |

The Husab uraniferous leucogranite suite contains roughly three prominent varieties; unaltered alaskite with minimal accessories, relatively high smoky quartz content, minimal

contamination from wall rock entrainment – analogous to the Goanikontes D-type; alaskite with prominent pegmatitic textures and prominent single-phase segregations, the most notable being metre-scale biotite clusters; and altered alaskites, some with uranium-bearing refractory mineralisation and prominent wall rock contamination are the closest approximations to the E-type, but lack distinctive alteration halos. The colour, texture, and the relatively low abundances of mafic accessory phases in the Husab leucogranites, as with most Ida Dome, Valencia, and Goanikontes uraniferous leucogranite populations, are more or less consistent with the alaskite definition given in Johannsen (1931).

The unaltered Husab alaskites resemble the typical D-types observed at any of the other deposits in the surrounding region; feldspars are typically white, most are smoky quartz–dominant, with oligoclase and microcline-perthite feldspar compositions. Plagioclase usually shows variable coloration due to sericite replacement. Textures are typically coarse-grained to pegmatitic, with chill margins and schlieren of biotite typifying most sedimentary contact margins.

Quartz forms unbroken chains around feldspars and coarse clusters (over 10 cm - 15 cm across). Biotite of all textures and grain sizes typically occurs at or near the margins of schist and gneiss contacts in most samples. The drill core sections in Figure 4.39a through 4.39e illustrate typical, unaltered, uraniferous sheeted leucogranites of the Husab Deposit. The black and white coloration, definitive smoky quartz and particular coarse-grained texture of the samples correspond to the D type of Nex (1997) described at Goanikontes.

The Husab uraniferous sheeted leucogranites tend to contain variably coarse biotite books, which are over 10 cm in length in some examples. The biotite volumes as well as coarse textures appear to be characteristic of the Husab alaskite that differentiates the deposit to a certain degree from the other deposits. Uranium minerals are rarely visible and often do not exceed 1 mm.

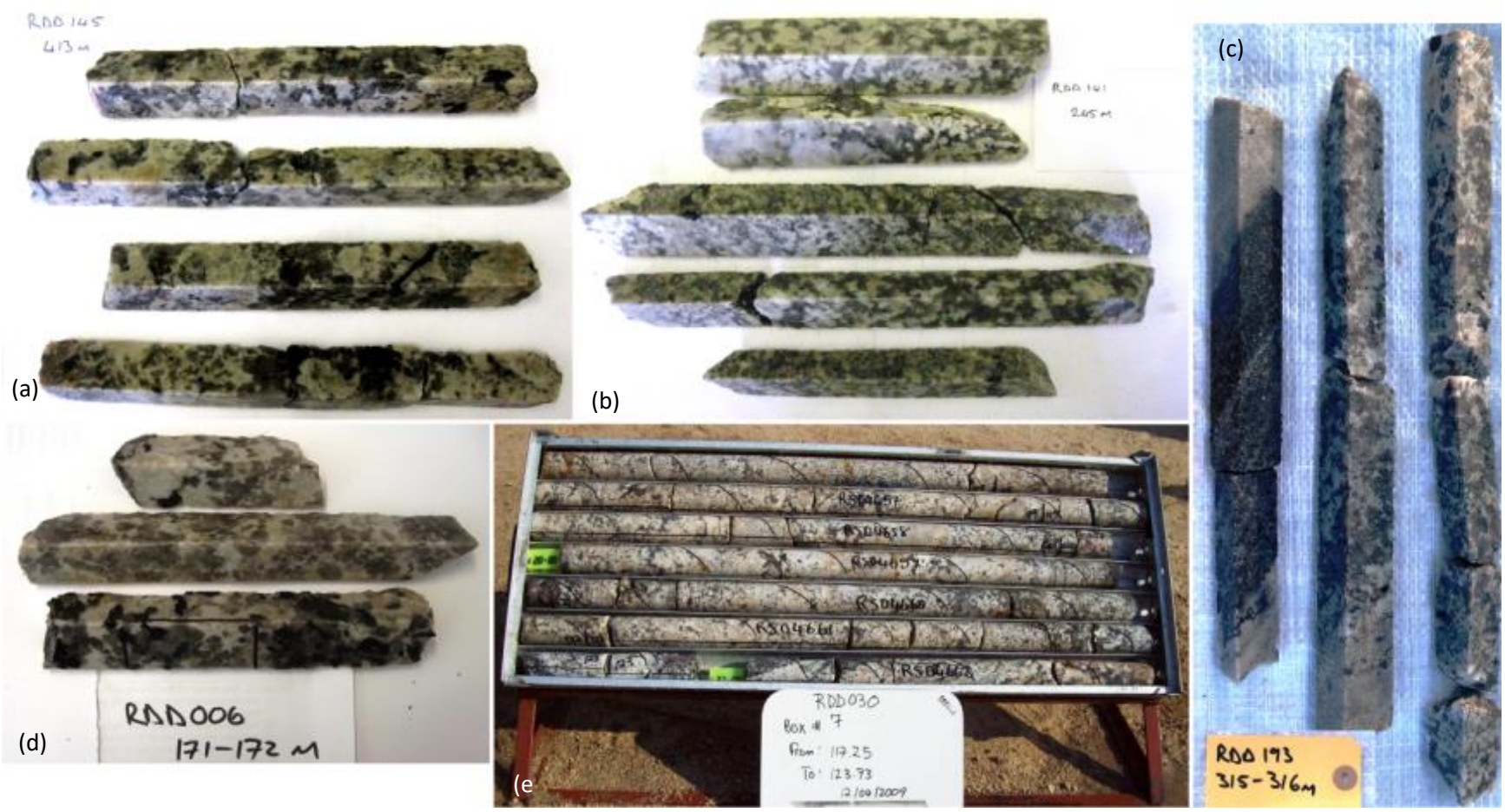



Figure 4.39 Examples of primary uraniferous sheeted leucogranite at the Husab Deposits. (a) Typical uraniferous sheeted leucogranite texture of coarse-grained granite with high % of smoky quartz and white - coloured feldspar, RDD145, Zone 1 Deposit. (b) Primary uraniferous sheeted leucogranite showing metasomatic alteration (fuzzy edges to feldspars) RDD141, Zone 1 Deposit. (c) A primary uraniferous sheeted leucogranite from the southern end of Zone 1 Deposit; A fine- grained chill margin has formed at the contact with Rössing cordierite gneiss, RDD193. (d) An example of coarse-grained uraniferous sheeted leucogranite with coarse biotite books. Quartz occurs in globules and in centimetric clusters, RDD006, Zone 2 Deposit. (e) Uraniferous sheeted leucogranite intervals are tens of metres thick, the example in RDD030 illustrates the tendency for smoky quartz to form clusters, and segregations within feldspar-dominated granites.

The altered alaskites of the Husab deposit tend to be coarse or pegmatitic, pink- or orange in colour, indicative of at least one phase of oxidised/acidic fluid flux that remobilised Fe. The granites have an inhomogeneous mineralisation distribution, which shows an affinity for contact margins and clustered mafics (chloritised biotite enclaves). Potassic feldspars are the dominant mineral component, and indicative quartz colour ranges from milky to jet-black smoky. Some of the pegmatitic alaskites host uranium-bearing refractory phases in certain locations, most of these granites occur within the upper cordierite gneiss units of the Rössing Formation.

Zones of pegmatitic texture are abundant and recorded in most drill logs. These zones are tens of metres in extent and characterised by coarse, centimetric biotite books; individual books are centimetres thick (Figure 4.40a). Biotite books may accumulate in metre scale clusters much like a typical pegmatite; this variety hosts uranium mineralisation up to 0.1- to 1 wt. % metal on average (Figure 4.40b).

The distribution of grade within the pegmatitic alaskites is inhomogeneous; the quartz and biotite segregations host very nearly the entire U budget within what are relatively U-barren pegmatites. The pegmatite-textured alaskites contain the highest known grades of uranium in the Zone 1 and Zone 2 of the Husab Mine. One hundred and twenty-nine drill core samples exceed 10 000 ppm, eighty-four of which contain over 20 000 ppm (>2% U). Patches of quartz-biotite segregation occur throughout the deposits, and these tend to form along- or near metasediment contacts. The smoky quartz forms centimetric veins with associated Fe-staining that overprints the usually white-coloured feldspars (Figure 4.40b - top section of core tray).

Quartz forms metre-scale pods, usually within metasediments but always within close proximity to uraniferous sheeted leucogranite, and are thus a feature associated with the intrusives. These pods comprise quartz and biotite entirely. These portions of the pegmatitic variety may host in excess of five weight percent U metal; the single highest-grade metre-length of core at the deposit, sample RDD307 465-466 m, contains twenty weight percent U metal (Figure 4.40c). Uraninite is the primary ore mineral and occurs in two prominent

textures, an early euhedral one and a later anhedral generation of interstitial blebs (Figure 4.40d and e).

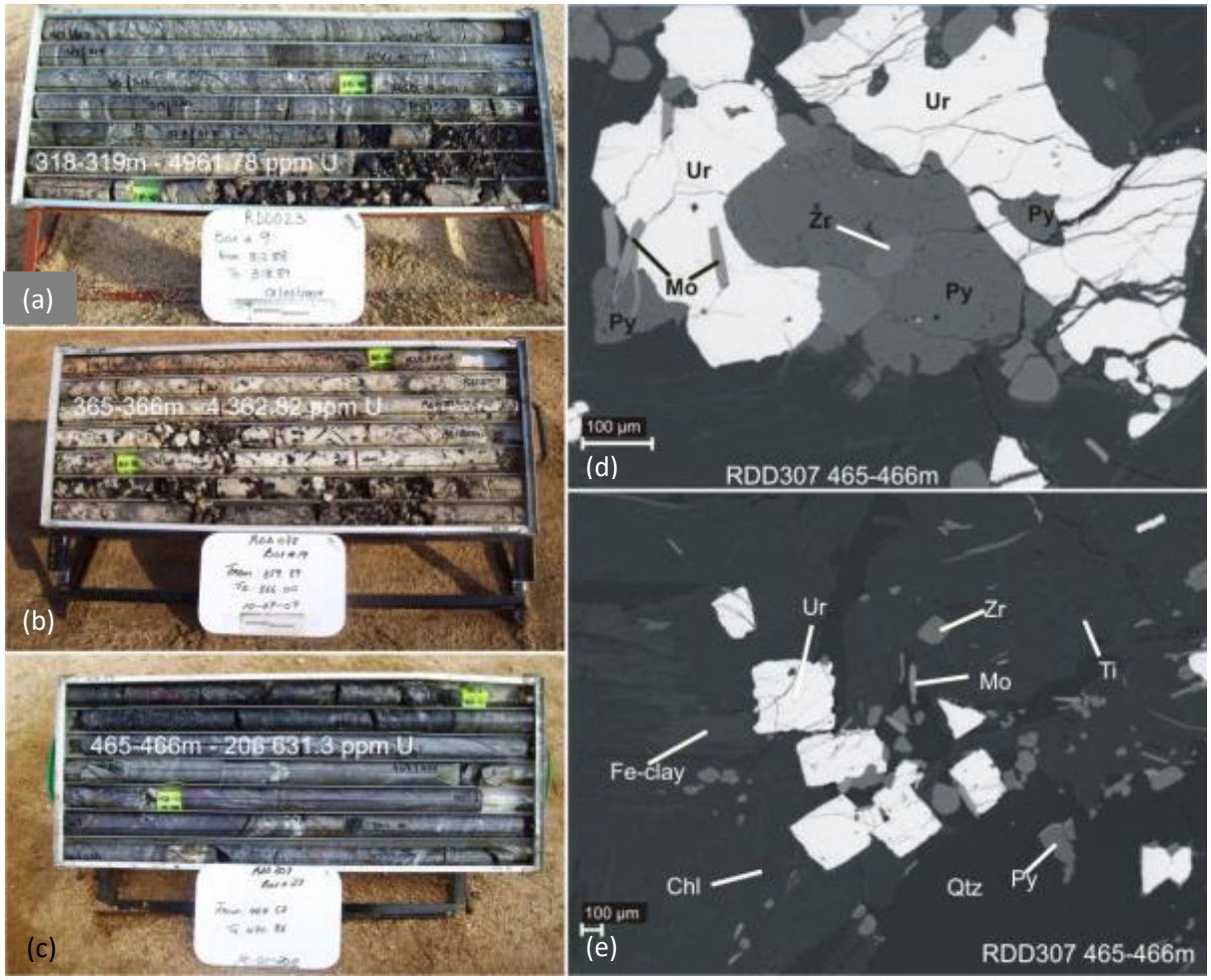



Figure 4.40 Pegmatitic uraniferous sheeted leucogranites at the Husab Deposit, Zone 1. (a) Coarse-grained biotite books, occupy 20 to 30 cm spaces within the pegmatite and host the majority of the U. The intrusion is ~5 m thick and intrudes mottle-textured cordierite gneiss of the Rössing Formation in drill hole RDD023. (b) Similarly, a centimetric - scale patch of very coarse biotite books hosts significant U in a 29-m thick interval of uraniferous sheeted leucogranite. The biotite clusters occur within 80 cm of the footwall contact with intercalated gneiss and calcsilicate of the Rössing Formation, RDD078. (c) The highest-grade sample from Husab occurs in Zone 1 and comprises almost entirely biotite with subordinate quartz. The biotite is entirely chloritised, with interstitial spaces between books and clusters filled by smoky quartz, RDD307. (d) and (e) Backscatter images of the RDD307 465 m interval: The host phase is almost entirely uraninite which occurs in two distinct textures. The primary uraninite is euhedral and cubic, 100 µm to 500 µm across and assembled in clusters with sulphides between biotite (chloritised) books. The secondary texture fills spaces between the gangue phases and contains inclusions of earlier - crystallised minerals (pyrite in Figure d).

The dominant feldspars in the unaltered and pegmatitic alaskites appear to be microcline and other K-feldspar derivatives, plagioclase is determined as subordinate by the relatively sparse distribution of sericitised feldspar crystals. Quartz grains are coarse and exceed 5 mm to 10 mm in some samples (Figure 4.41a). Quartz also occur as inclusions in feldspars and as a later phase replacing the K feldspar crystals. Strain extinction is evident in some quartz but with far less intense strain than in the altered D-type SLGs, or the weakly mineralised and barren SLGs.

Plagioclase feldspars occur in two prominent textures; either as the dominant feldspar in coarse-grained, near euhedral grain sizes (Figure 4.41b) or as the subordinate primary feldspar replaced by, and enclosed in later K feldspar (Figure 4.41c). Twinning is predominantly albite, which is cross cut by albite rims in the included grains. The cores of plagioclase inclusions in microcline are sericitised and rarely include myrmekite development; thus, representing primary plagioclases. Microcline is dominant with respect to plagioclase and is coarse-grained, most observations are of >5 mm grains. Microcline-perthite varieties are subordinate to tartan-twinned grains, and each type displays some form of perthite or meso-perthite exsolution. Microcline is later than plagioclase and is replaced itself- or included in the youngest generations of quartz (Figure 4.41d).

The accessory assemblage includes bladed and skeletal biotite, which hosts radioactive inclusions as well as uraninite in variable abundances along with cleavage-parallel lenses of purple fluorite. The biotite is variably altered to chlorite, distinctly less so than in the altered (and refractory mineral-bearing) and pegmatitic varieties. Biotite blades vary in size from a few mm to > 20 mm in length. The dominant phosphates are apatite (Figure 4.41e) and monazite, which occur in clusters and in close association with zircon (Figure 4.41f). Zircons and monazites are radioactive and show prominent zoning, occurring in clusters associated with entrained mafic phases. Yellow secondary U minerals or secondary, amorphous Fe phases fill the cracks in zircon crystals. Feldspars that surround the zircons and phosphates show intense alteration textures associated with the radial fractures surrounding the accessories.

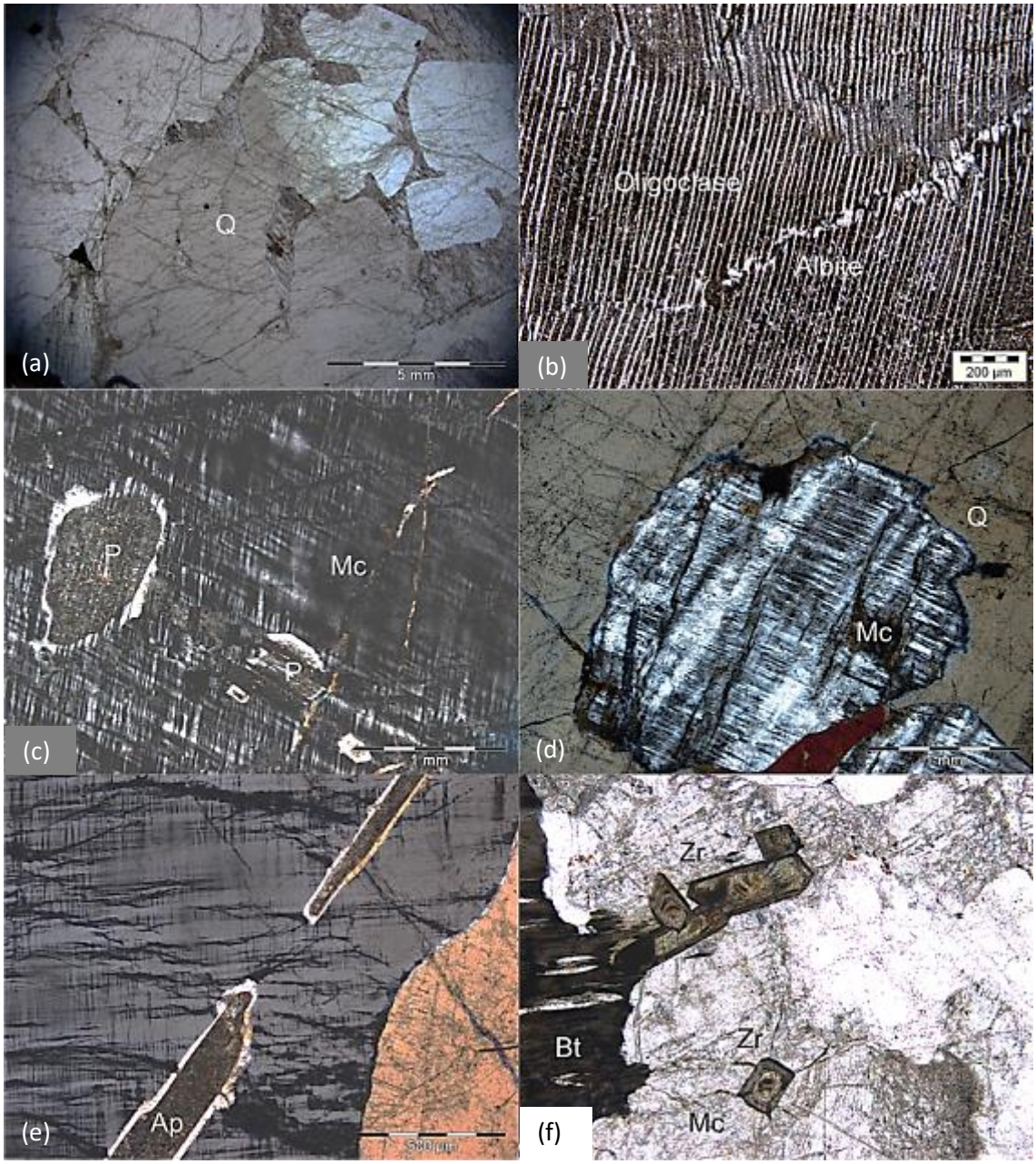



Figure 4.41 Petrographic features of typical D-type alaskites at Husab. (a) Coarse-grained quartz replaces microcline-perthite in RDD006 171-172m, xpl. (b) Husab uraniferous sheeted leucogranites show some evidence of deformation in hand specimen fabric; distortion of crystallised mineral twins (P - plagioclase) reflect some post intrusive event(s) in thin section. Metasomatic activity produced the fine clays in disseminations and hairline fracture-fill, RDD141 244-245m, xpl. (c) Sub-solidus textures include albite rims around primary plagioclase inclusions with sericitised cores, surrounded by tartan microcline, RDD145-413m, xpl. (d) Microcline grain with embayed edges, completely surrounded by quartz, clay alteration preferentially occurs parallel to one of the cleavage planes, RDD145 - 413m, xpl. (e) Apatite is the most abundant phosphate observed in the study, RDD006 - 172m, xpl. (f) Zircon clusters are perhaps the most abundant accessory phases observed, here, in long- and cross-section orientations within K-feldspar. Zircons (Zr) often occur in

association with biotite (often as pleochroic inclusions within the mica) the radiating fractures are ubiquitous with radioactive mineral inclusions, RDD006 - 172m, ppl.

A certain number of SLGs within the Zone 1 and Zone 2 deposits contain uranium hosted in refractory minerals, namely brannerite and betafite. The leucogranites tend to be coarse to pegmatitic textured, quartz is variably smoky, and biotite is coarse and most often chloritised. Most of the observed examples show some evidence of metasomatism (predominantly fine-grained Fe-mineral staining). Figure 4.42 illustrates five refractory mineral-bearing alaskite intersections of drill hole RDD373, which was bored specifically to investigate geological controls on brannerite and betafite distribution at the deposit. Betafite and brannerite-bearing SLG distribution appears to be within the upper portion of the Rössing Formation.

For this study; drill hole RDD373 provides all the samples of leucogranites that host uranium-bearing refractory minerals. The drill hole intersects a near complete interval of the Rössing Formation, from just below the Chuos Formation to the diopside-bearing gneiss of the Khan Formation. The lithological profile places the refractory mineral-bearing leucogranites within the upper units of the Rössing Formation. There are two packages of refractory mineral-bearing leucogranite, for the purposes of this study the upper package occurs immediately above and between the upper carbonate succession, the lower package of leucogranite intrudes units within the cordierite gneiss succession between the carbonates (essentially in the upper portion of the lower pelitic gneiss described by Anderson and Nash, 1997). The labels 'A, B, and C' in Figure 4.42 identify the locations of thin section samples cut from the refractory mineral-bearing core samples from hole RDD373.

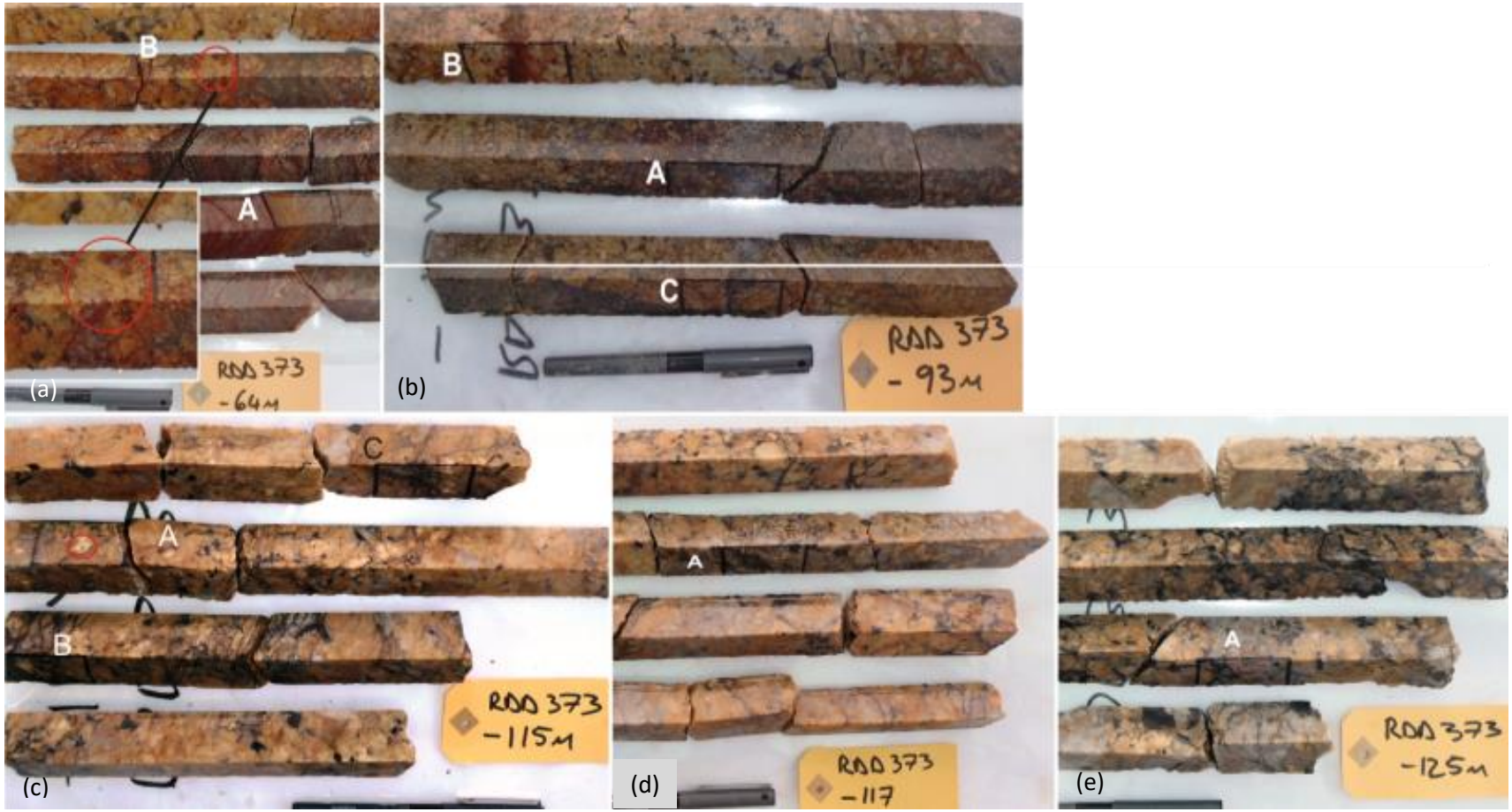



Figure 4.42 Brannerite- and betafite-bearing uraniferous leucogranite samples from drill hole RDD373. The granites in this hole all display some alteration, predominantly oxidation that discolours the feldspars. Some sample display two phases of alteration, the earlier being chlorite- and sericite- dominated and the younger haematite-dominated. (a) Brannerite (circled) is millimetric in most leucogranite samples. (b) Brannerite-bearing leucogranite with a ~250 mm xenolith of metasediment. Chloritisation of biotite, Fe-oxide, and sericitisation of feldspars dominate the alteration assemblages. Sulphide blebs occur in both the intrusive and in the xenolith of metasediment host rock. (c) Betafite occurs between feldspars and quartz in pegmatitic uraniferous sheeted leucogranite, note the milky quartz. (d) Uraniferous sheeted leucogranite with mafic clusters comprising predominantly chlorite, biotite, and titanite. The chlorite clusters host fine-grained brannerite. (e) A - brannerite crystal between quartz grains in coarse-grained uraniferous leucogranite. Chloritised biotite forms broken chains space between the feldspars and quartz.

Quartz is coarse-grained and occurs as individual crystals and as clusters and chains, singular quartz crystals are empirically more abundant in the betafite and brannerite bearing SLGs. Typical grain sizes are millimetric up to 10 mm or more in the coarser portions of the rock. Quartz records a number of solid-state deformation features in thin section; Figure 4.43a illustrates chessboard strain extinction and sutured boundaries, in this case accentuated by chlorite veins. Quartz replaces feldspars or fills voids within larger crystal structures (Figure 4.43b).

Coarse-grained plagioclase (>1 mm) appears to be the dominant feldspar. Crystals are typically albite twinned with euhedral edges (Figure 4.43c). Less-common, anhedral grain boundaries are present where quartz has crystallised at the expense of feldspar, and where plagioclase occurs as an inclusion phase in K-feldspar. Myrmekite and albite rims are the dominant reactions of the plagioclase inclusions, sericite is less apparent. The mineral also records the strain history in displaced twinning along micro-fractures, and sub-solidus reaction features such as lenticular twinning and cross-cutting albite exsolution.

K-feldspar is observed in two textures; tartan twinned microcline being dominant over microcline perthite crystals. Both textures are coarse-grained, and appear to grow at the expense of plagioclase. Microclinisation occurs throughout most samples, and almost completely replaces some microcline crystals with fine-grained cloudy texture (Figure 4.43d).

The accessory mineral assemblage is dominated by titanite, apatite, monazite, xenotime, and zircon. Opaque Fe phases tend to cluster between coarse feldspars and quartz and occur in association with chloritised biotite. Certain minerals are entrained from the skarn and cupriferous schists of the Khan Formation and include calcite and Mg- and Fe-rich diopside, and chalcopyrite-bornite (Figure 4.43e and f).

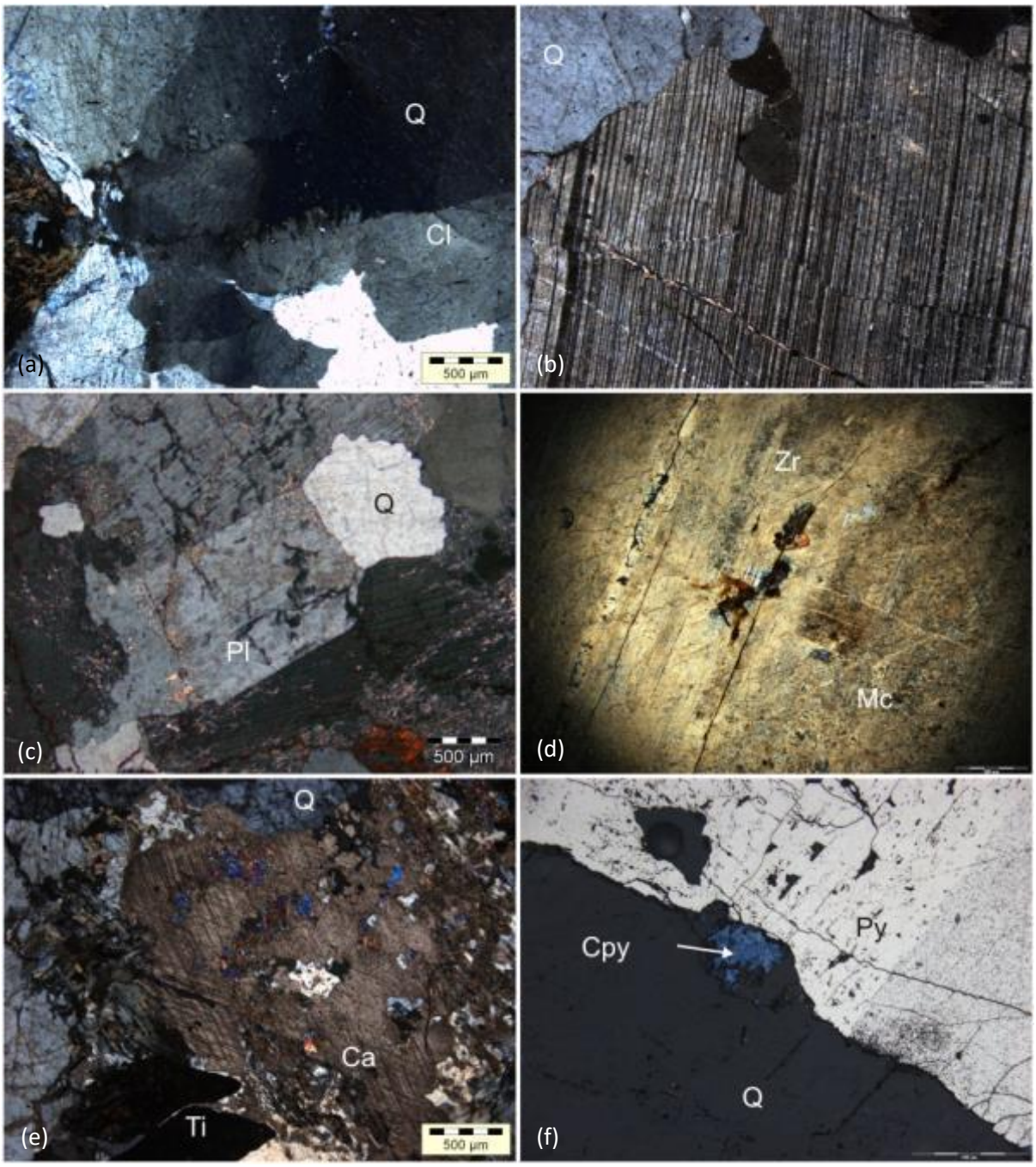



Figure 4.43 Petrographic features of brannerite- and betafite-hosting sheeted leucogranites. (a) Coarse-grained quartz grains with chloritised biotite (left) and chlorite veins along a suture. The worm - like suture and chessboard extinction in the quartz reflect solid - state strain (from deformation). (b) Plagioclase twins with displacement along micro fractures and a quartz rune comprised of multiple crystals (scale bar is 500 µm). (c) A euhedral plagioclase (Pl) with irregular, sutured boundaries shared with later quartz (Q). (d) Hydrothermal alteration of tartan - twinned microcline, (e) Accessory titanite (Ti) in quartz, with later calcite that has filled a void. The high interference minerals are clinopyroxene. (f) Sulphides are present in coarse pyrite (millimetric) and subordinate chalcopyrite/bornite.

### *Alteration of the Husab Uraniferous Sheeted Leucogranites*

Husab sheeted leucogranites occur in pristine and altered variations, in both the oxidised and the reduced settings. A deposit-wide alteration process' has produced a minor population of yellow boltwoodite and uranophane minerals. Which must have formed similarly to the syn- to post-intrusive fluid flux that produced the significant secondary mineral population at the Rössing SJ deposit. Supergene alteration from pre-Quaternary exposure at and near surface and along steep fault planes, emphasise pre-existing oxidation features which manifest in pervasive haematite and limonite staining, prominent clay alteration of the potassic feldspars and widespread calcite vein- and cavity-fill.

Alteration from magmati fluids is pervasive and appears to have affected the intrusives and metasediments regardless of depth from surface, and at some point, after granite crystallisation. Highly acidic, $F^-$-bearing fluids have leached silicates from granitic and pelitic rocks, with preferential fluid pathways through the gneiss and schistose units of the upper Khan Formation. The acidic fluid composition is not determined, but it must have contained a hydrofluoric component because fluorite is always present in hairline veins and in centimetric breccia veins that cross-cut the intrusives and metasediments. Fluorite is also present along biotite cleavage plains in seemingly unalterd D-type SLGs.

The supergene alteration is found throughout the deposits and has altered the alaskites in three, prevalent ways. Figure 4.44a illustrates the supergene alteration of the Husab alaskites in association with brittle faulting and $F^-$-bearing fluid flux. Fe-dominated alteration in the near palaeo-surface envelope, primarily by oxidised fluids, has left prominent iron-staining on the host and intrusive lithologies; Sericite-dominated alteration occurs at depth in the deposits, usually in association with prominent fault zones. K-feldspars have altered to clay minerals with a prominent chlorite overprint typifying the breakdown of biotite. Figure 4.44b illustrates the effect of highly acidic and oxidising magmatic fluids on the reduced Rössing metasediments at a contact margin. $Fe^{2+}$ minerals are altered to haematite and red secondary staining, and silicates in the sediment are leached as the magmatic fluids permeate away from the granite.




Figure 4.44 Fluorite and F-associated alteration. (a) Fluorine was mobile at some point after/during uraniferous sheeted leucogranite crystallisation. In this example a brittle fracture has cross-cut a uraniferous granite (see smoky quartz); whereas in (b) A coarse-grained pegmatoidal alaskite is less affected than its host rock, a banded gneiss of the Rössing Formation. The acidic fluid has attacked the granite leaving a front stained by mobile iron.

***Husab Ore Mineral Petrography***

The uraninite specimens tend to be euhedral and cubic and occur between the rock-forming minerals, and occasionally within a single phase, such as microcline. Most of the primary uraninite shows some evidence of alteration, which may vary from minor coffinite replacement at the rim of a grain to complete U(IV)-silicate replacement, or near-complete leaching of uranium from uraninite. Sulphide association with uraninite at Husab is considerably more apparent than in other deposits; the sulphides in the Husab leucogranites illustrate a combination of interaction with reduced metasediments during granite emplacement and uraninite crystallisation, and the circulation of $S^-$ in the system after granite and uraninite-coffinite crystallisation. The late generation of sulphides includes Cu- and Fe species, dominated by pyrite veins. The uranium-bearing refractory minerals show evidence of alteration and metal leaching as they are more prevalent in the altered zones of

the deposits. Tabulated descriptions of the Husab deposit thin sectioned samples are in Appendix D1 and photographs of the core specimens are in Digital Appendix 3. Uranium mineralisation occurs in five variations, of which two appear to be primary textures:

1. Euhedral crystals that form early between quartz and feldspar (Figure 4.45a); and
2. Euhedral crystals that grow from sub-100 µm to millimetric cubes within biotite, distorting biotite cleavage planes in the process (Figure 4.45b).

Uraninite inclusions form in Fe-Ti phases, predominantly in titanite associated with intrusives at skarn and carbonate contacts (Figure 4.45c); clusters or pairs of fine-grained euhedral uraninite crystals, deposited from fluids that chloritised the biotite (Figure 4.45d), constitute the later uraninite. Some uraninite forms semi-euhedral crystals completely included within feldspar (Figure 4.45e) and therefore represent the oldest generation of the primary uraninite. A potential sixth texture is identified. Fine-grained, euhedral uraninite crystals formed in cavities and pore spaces within the leucogranite; these primary minerals altered to uranophane/boltwoodite in association with fluorite at some time after the alaskite crystallised (Figure 4.45f).

The Rössing metasediments at the Husab deposits contain abundant sulphides The most abundant sulphide is pyrite, which occurs in two main textures; as hydrothermal veins that pervade the sediments and the granites (Figure 4.46a) and as replacements to the damaged halos in host minerals that surround the uraninite crystals; as replacements in multi-mineral clusters (Figure 4.46b); in cross-cutting relationships with pyrrhotite and with chalcopyrite (Figure 4.46c); and surrounding clusters of older, sub-rounded uraninite (Figure 4.46d). Molybdenite is late relative to uraninite and cross-cuts pyrite (Figure 4.46e), suggesting that fluids remain oxidised enough to mobilise Mo, after the reduction reaction of iron and uranium that forms uraninite. Sulphide minerals fill casts left by the complete leaching of uraninite (Figure 4.46f) exploiting fracture networks that formed in the host mineral around

metamict uraninite. Molybdenite and chalcopyrite are rarely observed together, more often molybdenite and pyrite occur in the same thin sections (Figure 4.43e).

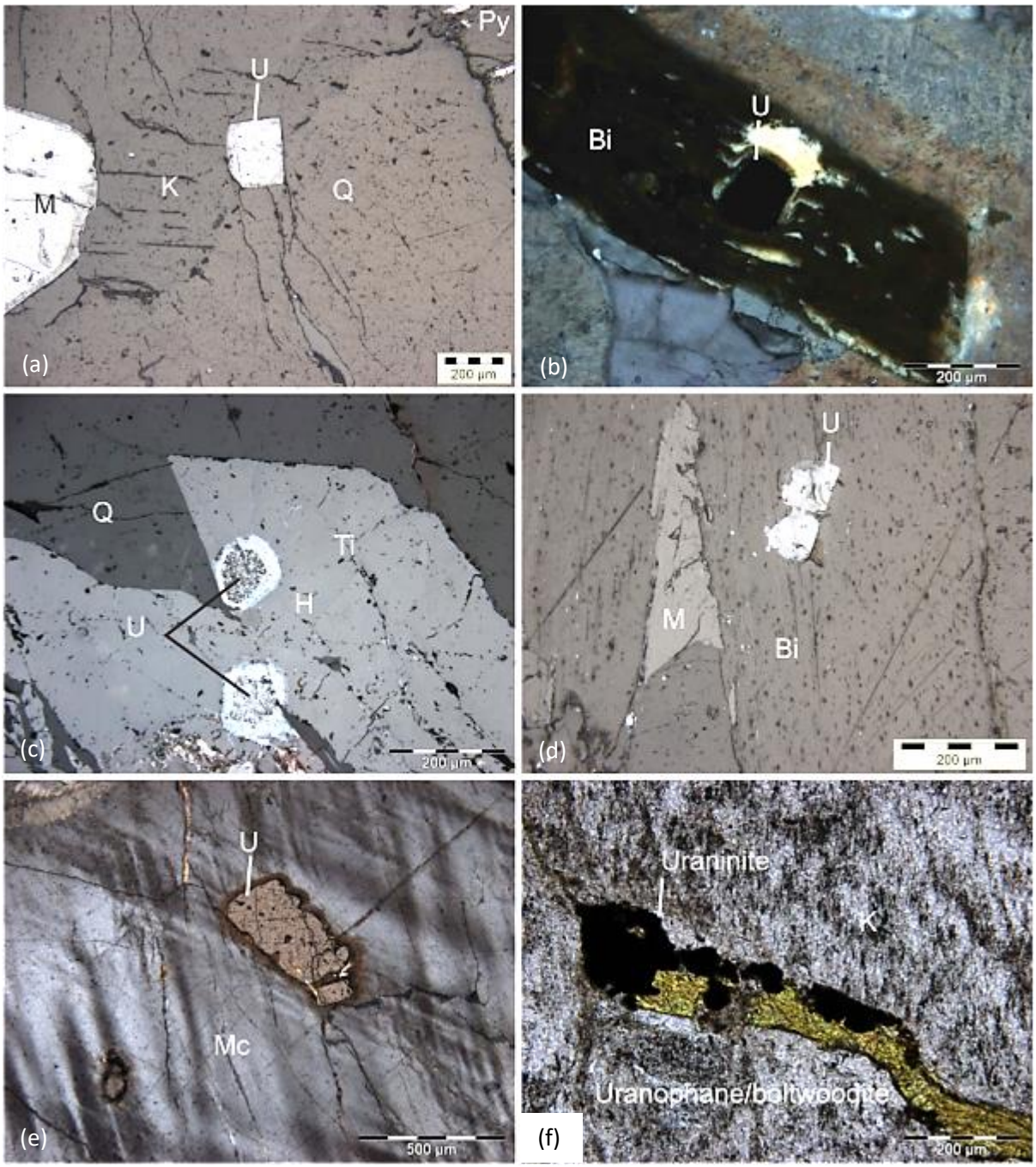



Figure 4.45 Primary uraninite textures and mineral relationships at the Husab deposits. (a) A cubic uraninite crystal, formed between quartz and feldspar. Coffinite replacement is visible at all four edges, RDD373-125 m, rfl. (b) Cubic uraninite grains in biotite, surrounded by a halo of clay replacement in biotite, RDD102 318 m, xpl. (c) Titanite-hosted, corroded uraninite surrounded by haematite halos, RDD219 336 m, rfl. (d) Euhedral uraninite grains associated with magnetite in biotite, RDD373-125 m, rfl. (e) Euhedral uraninite in microcline, note the distorted microcline structure at each end of the elongate grain, RDD078 363

m, rfl. (f) Cubic uraninite grains in a fracture-fill. The coarse, opaque masses at the interface between uranophane/boltwoodite and K-feldspar are fluorite, RDD102 318 m, ppl.

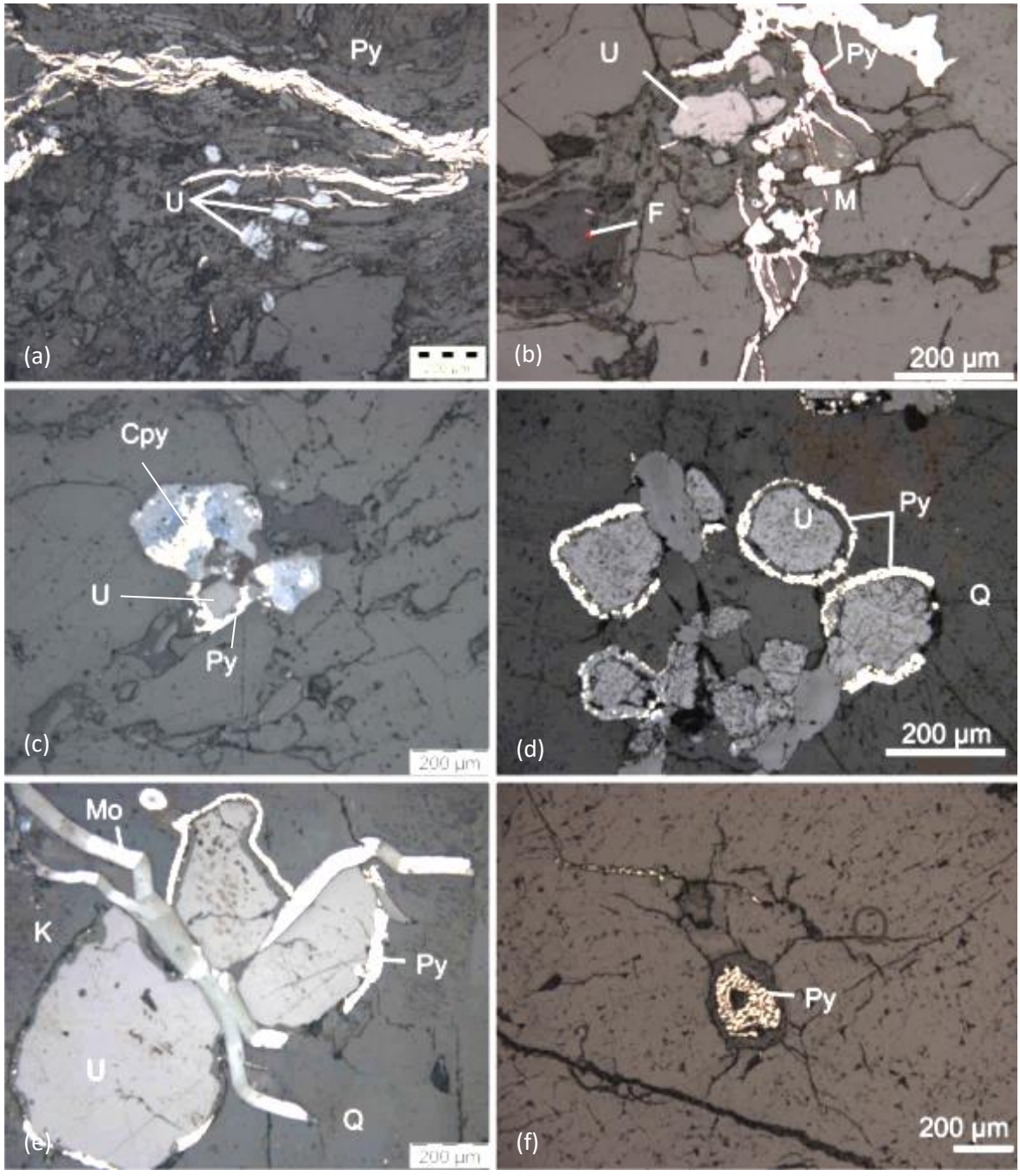



Figure 4.46 Sulphide and uraninite textures in the Husab sheeted leucogranites. (a) Pyrite veins cross cut a nest of coarse biotite that hosts a cluster of euhedral uraninite, RDD373 154-155C, rfl. (b) Net-texture pyrite veins propagate into inter-granular spaces and through fractures in quartz. Late fluorite, chlorite, and epidote surround the uraninite, RDD373 92-93A (c) Chalcopyrite is often in solid solution with bornite. A halo of coffinite (dull reflectance) surrounds the immediate edges of the uraninite, and pyrite surrounds the coffinite, RDD193 267-268b, rfl. (d) A cluster of altered uraninite with rounded edges surrounded by pyrite halos; some uraninite is in direct contact with pyrite, while coffinite and iron-oxides occur between uraninite and pyrite in others, indicating multiple episodes of alteration, RDD219 335-336 m, rfl. (e) Uraninite, some with coffinite-

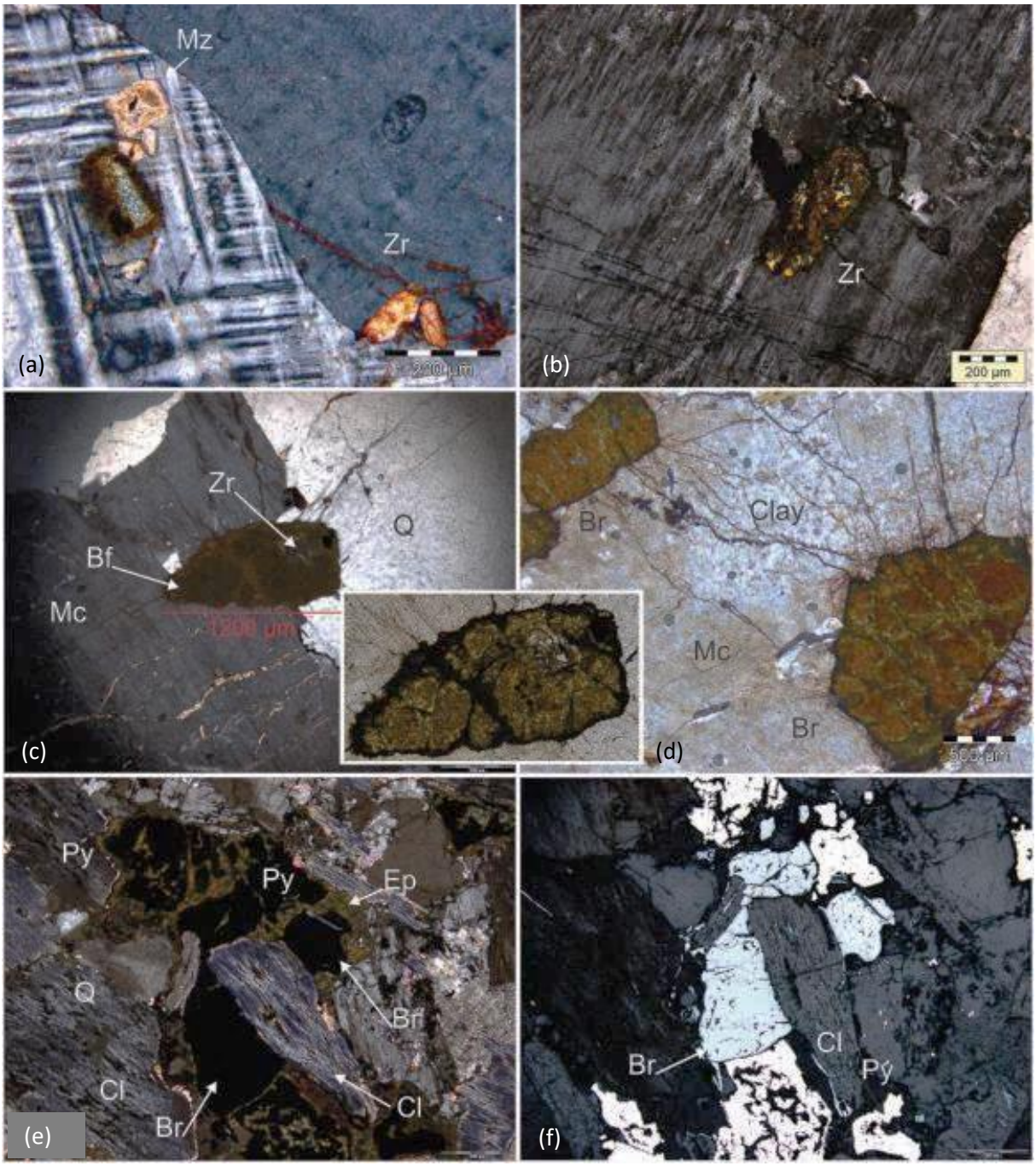
pyrite and some with pyrite-only halos, occur in a cluster bisected by coarse molybdenite, RDD351 257-258b (f) Pyrite crystallisation in a cast of leached radioactive phase (assume uraninite), RDD373 92-93A, rfl.

Alaskite at Husab hosts brannerite in two textural-mineralogical relationships and betafite fitting similar description to the Rössing deposit occurrences described in detail in Herd (1996). Accessory minerals appear to be abundant in the uraniferous leucogranites relative to the Salem, Grey, and other pre-$D_3$ leucogranites. The brannerite and betafite bearing alaskites at Husab contain comparably more accessory phosphates, oxides and silicates than the average alaskites observed in this study. Titanite, magnetite zircon, monazite, and apatite dominates the accessory mineral assemblages; sulphides other than minor pyrite and very fine-grained chalcopyrite are absent from the brannerite- and betafite-bearing SLGs (Figure 4.47a and 4.47b).

Brannerite and betafite occur in relatively coarse-grained form and tend to be sub-millimetric, whereas uraninite rarely exceeds 1 mm; while both betafite and brannerite hosted between coarse-grained quartz and feldspars show intensive alteration features, weakly-altered brannerite is most often observed in mafic mineral clusters. This petrographic study identifies a single, typically coarse (>1.2 mm) betafite crystal for detailed description, it has crystallised early in the rock-forming sequence between quartz and feldspar, with subsequent alteration resulting in embayed edges and metal leaching along internal fractures. Characteristic radial fractures permeate into the surrounding quartz and feldspar, and are visible in hand specimen. The sample is anhedral and is semi-translucent, which is contrary to the ideal cubic or octahedral shape described for the type locality Betafo, Madagascar, or even some Rössing samples (Herd, 1996).

Figure 4.47c shows the 1.2 mm betafite with a zircon inclusion, the dark red-brown portions are the least altered and are in fact isotropic. Hydrothermal alteration has leached uranium metal at the grain edges and along the prominent internal fracture planes (illustrated in Figure 4.47d). Altered brannerite is red-orange relative to betafite in transmitted light. Samples are variably dull in reflected light, showing anisotropy in crossed polarised light. Comparably unaltered brannerite appears less abundant than the coarse-grained, altered variety and occur in mafic enclaves. The unaltered brannerite specimens show less fracturing and even-textured surfaces relative to the singular quartz-feldspar hosted specimens. The mafic enclaves comprise primary biotite (always partially- to fully replaced by chlorite) titanite, rutile, and pyrite. Epidote, fluorite, chlorite, and fine-grained Fe-mineral veins and replacement constitute the later alteration assemblage. Figure 4.47e and 4.47f illustrate the same slide of the typical mafic enclave hosting euhedral brannerite in plane- and crossed polarised light. A strong textural contrast between the euhedral brannerite and skeletal pyrite is apparent, showing evidence of corrosion by calcium, silica and fluorine-bearing fluids. The enclave comprises chloritised biotite, rutile, ilmenite, and pyrite in two generations. Hydrothermal pyrite, epidote, and fluorite fill spaces between the entrained mafic minerals, skeletal pyrite and the brannerite crystals.

Figure 4.47 Accessory mineral textures in Husab alaskites. *following page* (a) An example of accessory mineral associations; where monazite and apatite crystals with pyrite occur in microcline, and zircon in the quartz, RDD373 - 63A, xpl. (b) Zircon in microcline perthite, a polycrystalline quartz grain is included in the K-feldspar, RDD373 - 115 - 116A, xpl (c) Large, 1.2 mm, betafite between quartz and microcline perthite. The betafite has a 200 µm zircon inclusion and displays intense corrosion along fracture planes, RDD373 - 115-116A, xpl. (d) Two, anhedral brannerite crystals between microcline grains with prominent corrosion along internal fracture planes. Feldspars have altered to clay in the fractured area between the two radioactive mineral grains, RDD373 63-64B, ppl. (e) An assembly of mafic minerals clustered between quartz and feldspars in alaskite. Biotite shows interference colours typical of chlorite alteration, epidote, fluorite and chlorite has replaced pyrite and the brannerite grains. Brannerite has retained its euhedral edges and is relatively fracture-free, RDD373 92 - 93C, xpl. (f) The same assemblage in reflected light highlights the skeletal pyrite adjacent to the intact brannerite, which also occurs between sheets of biotite (x).




The alteration overprint that has had a variable effect on the conditions of the refractory minerals has resulted in the complete replacement of uraninite and formed prominent $U^{4+}$ and $U^{6+}$ silicates in altered alaskites throughout the deposits. Clay and secondary Fe minerals (Figure 4.48a) replace cubic uraninite. The specimen is a coarse-grained uraninite hosted

between quartz and biotite and is surrounded by a halo of haematite, which may have replaced the more common pyrite halo that surrounds many uraninite grains. Herd (1996) identified jarosite[39] in the sheeted leucogranites of the SH area, which forms a halo around uraninite hosted in K-feldspar. Similar examples were observed at Husab, where jarosite is a replacement of sulphide halos around uraninite and forms preferentially in feldspar over quartz (Figure 4.48b). Jarosite is a common by-product of oxidation of pyrrhotite, which is a common sulphide in the cordierite schist at Rössing, and at Husab.

Coffinite is the most abundant uranium silicate in the Husab deposit, it is a replacement mineral and would have formed while high residual Si-bearing fluid flux altered the primary rock forming minerals soon after emplacement and often exceeds uranium deportment in uraninite. Husab uraninite seldom hosts U-silicate inclusions and any coffinite replacement always appears from grain edges inward. Coffinite surrounds a cluster of uraninite in a sample from drill hole RDD337; while K-feldspar hosts the uranium minerals and the surrounding halo of clay alteration (Figure 4.48c). The Husab deposit SLGs have a prominent overprint of fluid-type alteration, which is characterised by fluorite and intensive silicate leaching. Feldspars alter to clays and leave dissolution vugs, which fill with secondary uranium (Figure 4.48d and e). The well-developed acicular/fibrous crystals signify a prolonged period of fluid circulation.

[39] Jarosite is a typical alteration phase in sulphide-bearing rocks and has the formula $KFe_3^{3+}(SO_4)_2(OH)_6$

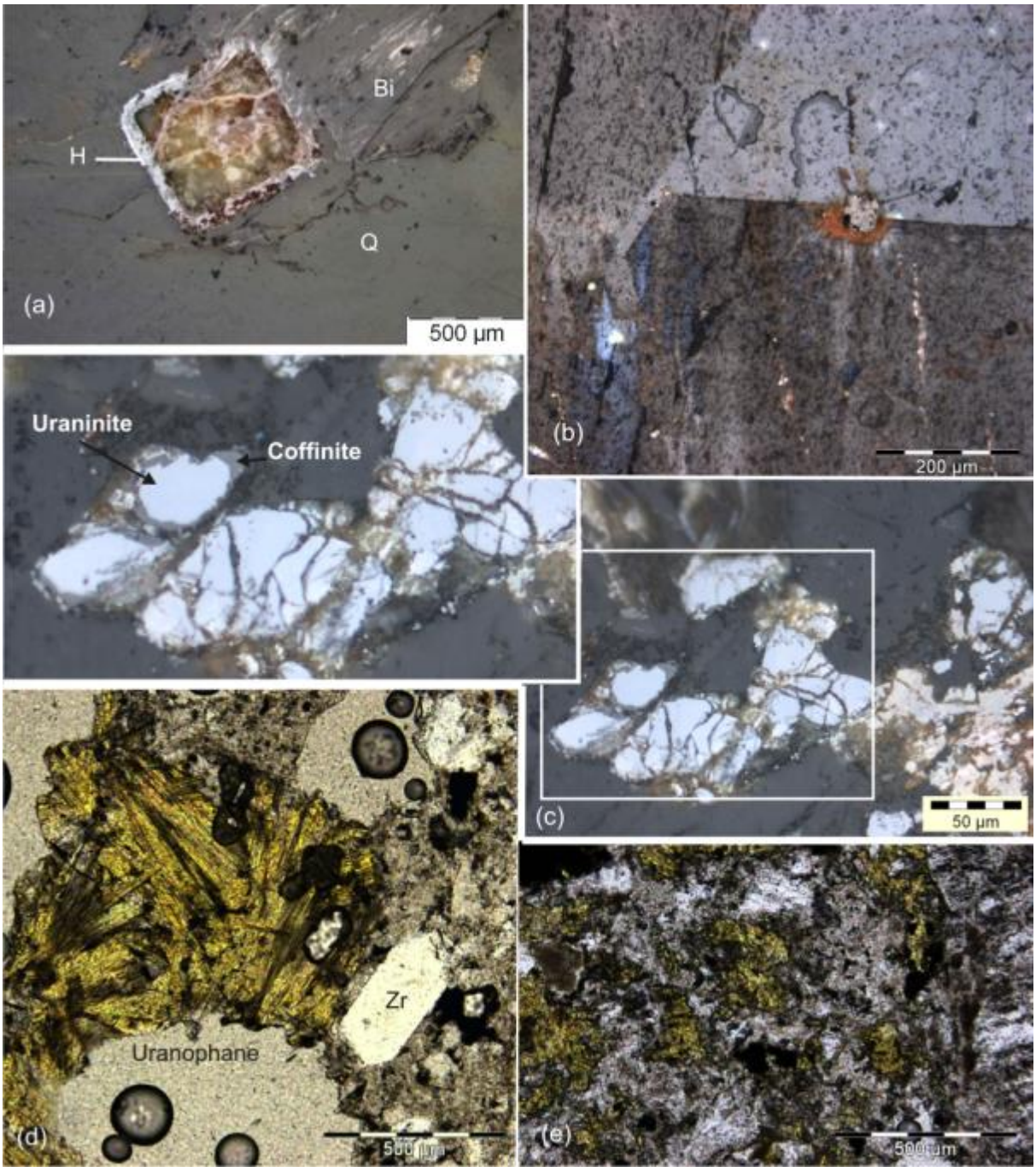



Figure 4.48 Alteration and remobilization of uranium at Husab. (a) Euhedral uraninite cast surrounded by haematite, RDD351 328-329, rfl. (b) Uraninite at a quartz - K-feldspar boundary, jarosite forms as a replacement of feldspar breakdown, associated with radioactive damage, quartz is more resilient, RDD219 335-336m, xpl. (c) Cluster of fractured uraninite surrounded by alteration minerals from the breakdown of the host feldspars. Coffinite forms halos around some of the uraninite (inset). RDD373 116-117A, rfl. (d-e) Boltwoodite and uranophane fills pore spaces created as feldspars are leached during hydrothermal fluid circulation. Hiemstra (1968) and Berning (1986) describe β-uranophane in Rössing mine leucogranites; Townend (2009) identified boltwoodite at Husab, discrimination performed with the aid of XRD.

### *Valencia Uraniferous Sheeted Leucogranite Petrography*

The prominent antiform located on the north limb of the Khan Syncline hosts D-type SLGs in a saddle reef type emplacement geometry. The hinge plunges ~30° to 40° southeast, and mineralisation continues on this same trend at depth. Older tourmaline- and magnetite-bearing SLGs also occur within the mass of uraniferous leucogranite. The uraniferous sheets at Valencia are typically alaskite in appearance with distinctive low-percentages of mafic minerals. The alaskite sheets, uniquely, intrude lithologies of the Khan, Rössing, Chuos, Karibib and Kuiseb Formations; Table 4.14 presents summarised petrographic characteristics.

Table 4.14 Thin section characteristics of uraniferous sheeted leucogranites from the Valencia deposit. Key: D- D-type, $D_{oxi}$- altered D-type, Apoph. - alaskite melt intruding Salem granite (U and Th content by XRF, in ppm).

| Sample | Type | Colour | Grain size | Texture | Biotite | Main Feldspar | Plag. | Th | U |
|---|---|---|---|---|---|---|---|---|---|
| VALG 11 | D | White and black | Medium-coarse | Homogeneous | Minimal, disseminated | Microcline | $An_{10}$ | 43 | 257 |
| VALG 12 | D | White | Medium | Homogeneous, Foliated | Minimal, disseminated | Microcline-perthite | $An_{12}$ | 93 | 62 |
| VALG 15 | D | White and black | Fine and coarse | Inhomogeneous | Prominent laths | Microcline-perthite | $An_{12}$ | 88 | 139 |
| VALG 16 | D | White and black | Medium | Homogeneous | Prominent booklets | Microcline-perthite | $An_{15}$ | 94 | 552 |
| VALG 20 | D | White and grey | Coarse | Inhomogeneous | Prominent laths | Microcline | $An_{12}$ | **97** | 38 |
| VALG 24 | $D_{oxi}$ | v. light pink | Coarse | Homogeneous | Minimal, disseminated | Oligoclase | $An_{15}$ | 41 | 29 |
| VALG 26 | D | White and black | Medium-coarse | Homogeneous | Fine, disseminated | Microcline-perthite | **$An_{17}$** | 45 | **564** |
| VA26- 111/ 157.49-157.82 | $D_{oxi}$ | Light pink and black | Coarse | Inhomogeneous | Minimal, disseminated | Microcline | $An_{15}$ | 31 | 486 |
| Va26-141/ 259.57-260.00 | $D_{oxi}$ | Light red, white | Coarse | Inhomogeneous | disseminated booklets | Microcline-perthite | $An_{12}$ | 9 | 138 |
| Va26-141/ 261.69-262.00 | $D_{oxi}$ | Red-pink and cream white | Medium to coarse | Inhomogeneous with quartz-rich patches | Minimal | Microcline | Seric. | 14 | 315 |
| Va26-141/ 301.29-301.60 | D | White | Medium | Homogeneous, foliated | Streaks | Microcline | $An_{7}$ | 18 | 101 |
| VALG 08 | Apoph. | Pink | Coarse | Inhomogeneous | Minimal, skeletal | Microcline | $An_{13}$ | 22 | 85 |

Hand-specimens show medium- to coarse-grained textures, white to cream coloration, with distinctive grey- to jet-black smoky quartz. Sparsely spread veinlets and clusters of quartz are often associated with fine-grained xenoliths of older granites (Figure 4.49a) and form centimetric, localised patches in outcrop (Figure 4.49b). Biotite is the only accessory mineral

of significant proportion (<5 %) and occurs predominantly in fine disseminations- to cm-scale laths at contact margins with the pelitic metasediments or as disseminated blades and clusters (1 mm - 5 mm in size). These contact zones are unanimously characterised by elevated cps.

The set of altered D-type sheeted leucogranites included in this study comprises a single surface sample and three oxidised samples taken from 47 mm NQ diamond core, from over 150 m depth (Figure 4.49c). Surface expressions of the Valencia alaskite are characterised by even textured, coarse granite with localised radioactivity (Figure 4.49d). The pavements of oxidation halos so prevalent at Goanikontes and the Ida Dome are largely absent at Valencia. Thus, the Valencia samples retain the D-type name in this section, rather than include the E-type where some form of metasomatism is evident, a suitable subscript is included; sample VALG24 is a $D_{oxi}$ for example.




Figure 4.49 Typical post D3 sheeted leucogranites at Valencia. (a) The D-types have a distinctive homogeneous, coarse-grained texture which is peppered with quartz-rich patches of elevated grade. 524260E 7528859N (b) D-type comprises white-cream coloured feldspar and black smoky quartz on fresh surfaces. VALG 26, 522060E 7528836N. (c) Altered mineralised granite at Valencia. The sample has the appearance of a C-type with typical accessory tourmaline; a quartz-rich veinlet has however enhanced the U content in an alteration halo of haematite staining, Va26-141 261.69-262.00. (d) Typical even textured Valencia alaskite

texture, the scintilometer reads ~1300 cps which proved to equate to 564 ppm U by XRF. VALG 26, 522060E 7528836N.

The thin section sample set for mineralised Valencia sheeted leucogranites consists of; six surface-sampled D-types and one core-sampled D-type, one altered surface D-type and three altered core-sampled D-types. The set also includes a sample of the mineralised apophysis from the Joly Zone (now Namibplaas). Two samples, VALG 12 and Va26-141 301.29-30.160 show a subtle fabric highlighted by biotite alignment.

Tartan twinned microcline and microcline-perthite are the dominant feldspars in most of the samples (VALG 11 ~70% of observed thin sections) and in VALG 16; plagioclase (~35 % of observed thin sections) is roughly equal in proportion to K-feldspar. Microcline-perthite is the dominant K-feldspar variety (~35-60 % of observed thin sections) in four samples, and is subordinate in three samples (tartan twinned microcline occupies up to 70% of some slides). It forms a matrix of 1 mm - 5 mm, subhedral to euhedral grains with highly variable micro-perthite component (Figure 4.50a). The tartan twinned microcline crystals tend to be finer-grained than the microcline-perthite (average observed between 1 mm and 3 mm), has variable proportions of mesoperthite exsolution, and occasionally has micrographic intergrowth with quartz.

Quartz occurs in three varieties: as globular inclusions in feldspars and as micrographic intergrowths; as anhedral to subhedral, interstitial, singular, clusters or chains of variably strained grains and as euhedral new quartz veinlets with only weak strain (Figure 4.50b). Grain sizes range from 0.05-0.5 mm inclusions to >10 mm chains and clusters. Quartz is predominantly ≤40 % and is usually subordinate to the dominant feldspar.

Plagioclase is of albite- to oligoclase composition and modal distribution is sub-30 % in all but one sample. Grain sizes are up to 6 mm and textures range from coarse millimetric euhedral grains, some with ragged edges, to sporadic skeletal, or rounded and zoned inclusions, the latter constitutes the plagioclase component when modal distribution is ~sub-10 % of a section. Twinning varies and is predominantly of albite type (lenticular twins occur in strained samples) but carlsbad and pericline twins are also present in samples with higher proportions of oligoclase. Sericite is present in all samples and when prominent it is associated with sub-solidus reactions- myrmekite rims and globular quartz inclusions in the plagioclase. Myrmekite texture occurs as wart-like growths into tartan-twinned microcline

and is associated with albite rims around the feldspars in the microcline-dominated samples (Figure 4.50c). Accessory phases are dominated by zircon which is often associated with biotite, monazite, and allanite (Figure 4.50d and 4.50e).

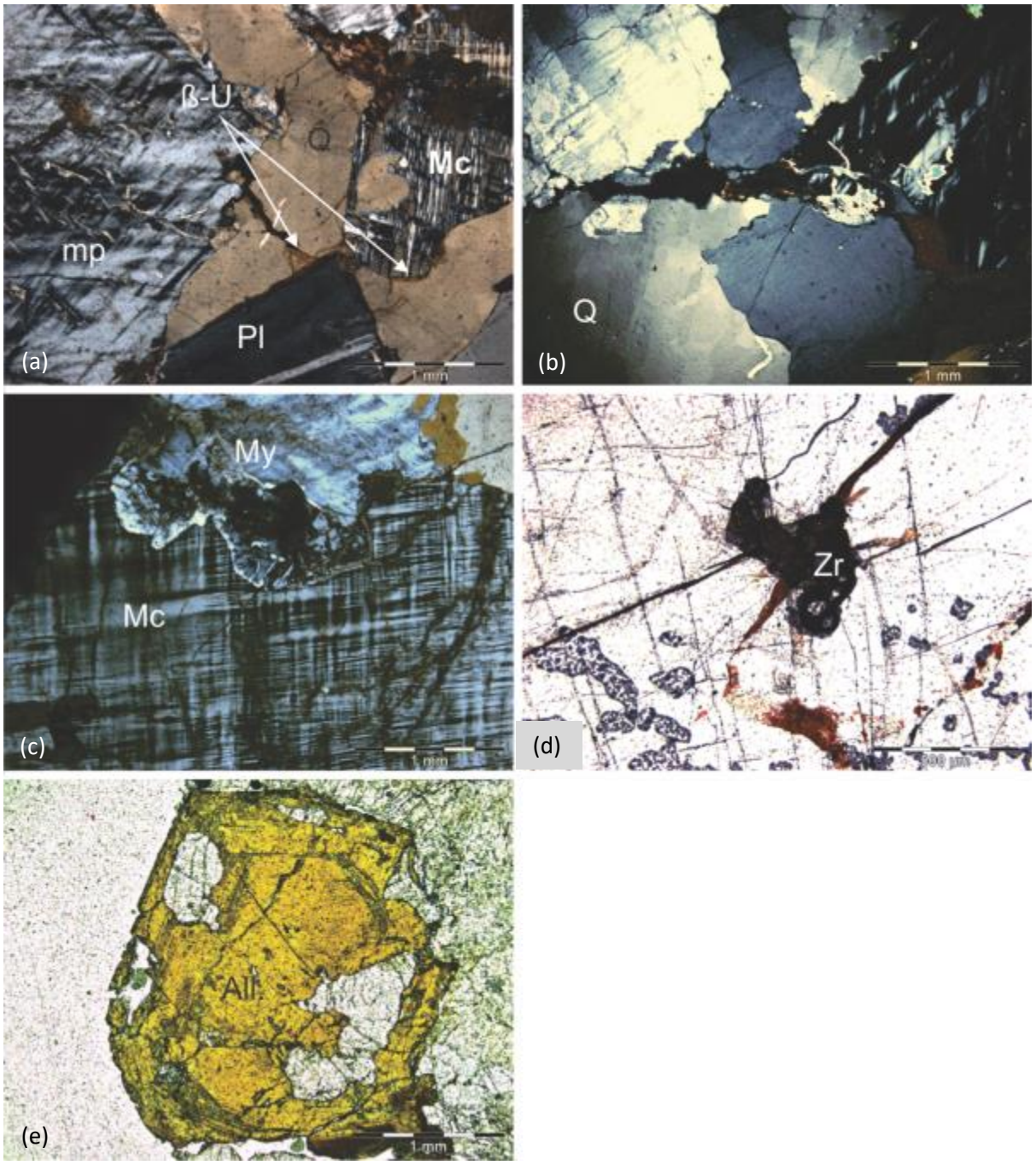



Figure 4.50 Unaltered D-type sheeted leucogranites and mineralised apophyses at Valencia. (a) Euhedral plagioclase (Pl) anhedral microcline (Mc) and uniformly extinct quartz veinlets with secondary U minerals (yellow stains in fractures) VALG 16, xpl. (b) Euhedral quartz with uniform strain cutting strained quartz (Q) VALG 26, xpl. (c) Myrmekite (My), in wart like growth at microcline (Mc) contact, is uncommon in mineralised sheets at most deposits, but is characteristic of the melt apophyses, VALG 08, xpl. (d) Zircon (Zr) is associated

with biotite in most samples, VALG 11, xpl. (e) Allanite is one of the less common accessories but may be substantial in size, VALG 12, ppl.

Thin sections of the melt apophyses in the Salem granites show tartan-twinned, euhedral microcline as the dominant rock-forming mineral. Grain sizes are up to 15 mm long and sporadic flame perthite occurs in the smaller, anhedral grains. Quartz is predominantly euhedral and up to 10 mm across, it occurs in extensive chains of euhedral grains displaying variably weak strain. Older quartz is included in microcline and varies in size from <0.1 mm to >3 mm.

Oligoclase is included in microcline and occasionally in quartz as skeletal and amoeboid grains ~2 mm across with variable degrees of sericitisation.

Biotite is bladed, disseminated and occasionally forms clusters of 2-3 mm in size; it contains zircon inclusions up to 0.2 mm across. Although zircon usually is a refractory mineral, fracturing has aided the release of U from the crystal for oxidation and redistribution as secondary phases in quartz and feldspars.

The altered D-types at Valencia are characterised by variably intense oxidised haematite-staining of quartz and feldspars. The granites also host quartz-dominated pods near metasediment contacts; a large fault at the western edge of the mineralised body has abundant quartz pods in the vicinity. Haematite staining is present in core samples at a range of depths and is analogous to the oxidation halos observed on surface at Goanikontes. Uranium mineralisation is associated with these quartz-rich patches. Biotite is present as a distinctive phase associated with the prominent Fe - staining in hand specimen, and in thin section, it shows variable chloritisation (Figure 4.51a).

Quartz is the main rock-forming mineral with modal estimates greater than 40% in observed thin sections, in the potassic feldspar-rich samples. It occurs as fine globular inclusions (<1 mm) in microcline and occasionally oligoclase and as interstitial euhedral veinlets and clusters of ~2 mm - 5 mm grains with prominent strain in most (Figure 4.51b).

Three of the thin sections show K-feldspars are dominant; two are microcline and one is microcline-perthite. Grain sizes are coarse and average 2 mm - 3 mm with more euhedral, larger grains up to 6 mm across. Microcline and microcline-perthite have extensive perthite exsolution with associated skeletal muscovite (Figure 4.51c). Very fine-grained new

microcline (microclinisation) is present in all the K-feldspar dominated samples observed at Valencia.

Oligoclase is scarce, anhedral and often rimmed (Figure 4.51d) with an average $An_{13}$ composition comparable to the unaltered varieties. It is a common inclusion in microcline, grains are anhedral and albite-rimmed with intermittent myrmekite growth into K-feldspar. An oligoclase-dominated sample (VALG 24) is characterised by very coarse textures; albite and carlsbad-twinned grains are up to 20 mm across and contain globular quartz inclusions. Variable sericitisation occurs in all oligoclase grains in this sample.

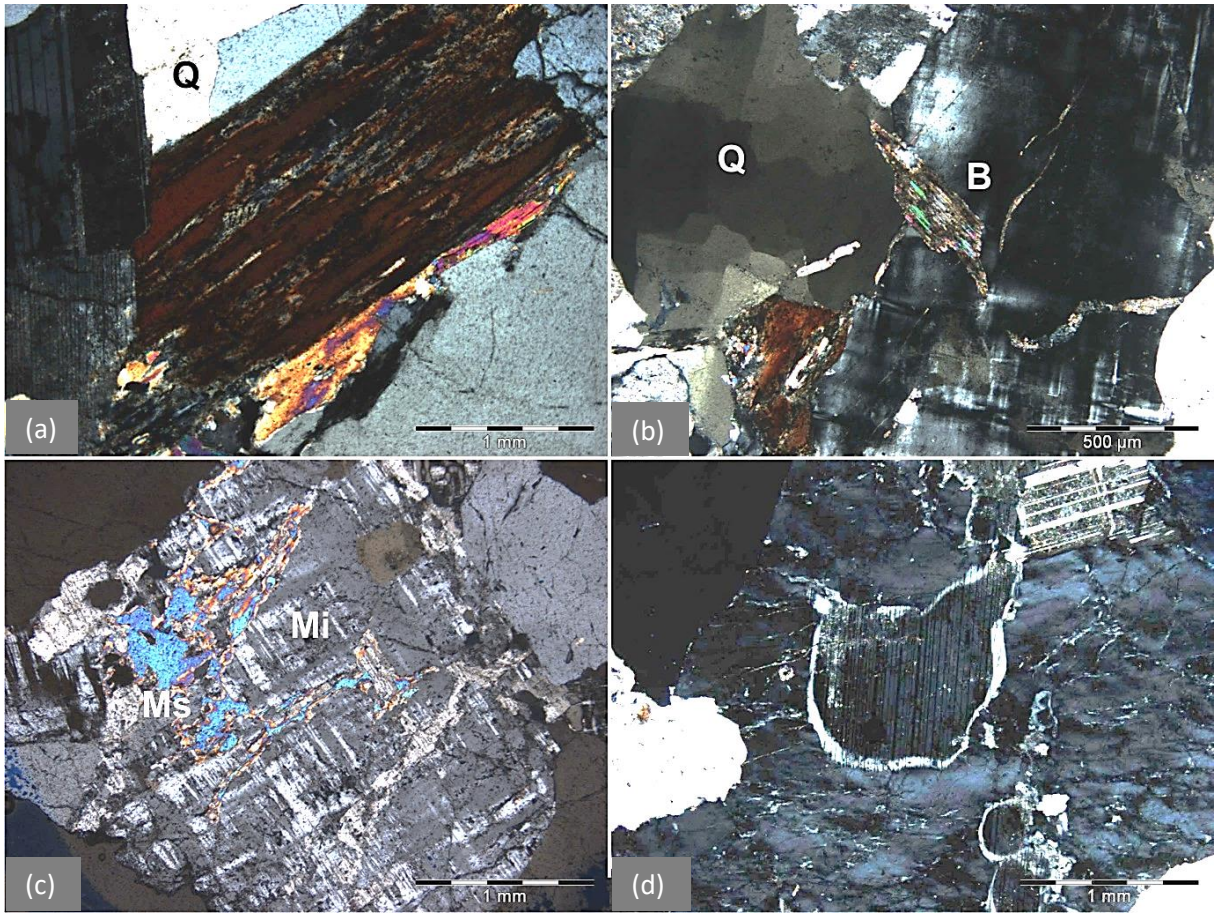



Figure 4.51 Oxidised D-type sheeted leucogranite from Valencia. (a) Va26-141 259.57-260.00, xpl; large biotite blade altering to chlorite. The euhedral quartz (Q) forms clusters and veinlets up to 10 mm in extent. (b) VA26-141 259.51-260, xpl; strained quartz (Q) and chloritised biotite are typical in the oxidised sheeted leucogranites at Valencia and the other deposits. (c) Va26-111 157.44-157.82, xpl; Anhedral microcline with perthite parallel muscovite development, in some microcline muscovite is cleavage-parallel. (d) Plagioclase is often surrounded by albite, thi sexample shows mesoperthite in the microcline that surrounds the plagioclase (P) Extinction angles seem to be consistent between the core and rim, typical of subsolidus type alteration.

Biotite is ragged- to skeletal, sparsely distributed, and chloritised with Fe-stained cleavages and punctuated by pleochroic halos surrounding zircon and uraninite. Some uraninite is as large as 300 µm.

The accessory assemblage includes abundant zircon and monazite; as well as less common magnetite-ilmenite; disseminated pyrite, which appears to be associated with biotite; and a single anhedral 0.75 mm tourmaline in VA26-141 261.69-262. Zircons are zoned, brown in colour and surrounded by radial fractures in the host minerals. Monazite grains do not exhibit prominent zoning, and have annealed deformation-related crystal defects. Prominent radial fractures surrounding the monazite crystals indicate radioactive inclusions.

### *Valencia Ore Mineral Petrography*

The samples represent a variety of uranium grades, from sub-100 ppm u to ~1 000 ppm U. The petrographic sample set includes examples from the suite of sampled uraniferous SLGs described in the previous section. The figures and descriptions in this section include some of the nine samples that are in the QEMSCAN study. The Valencia samples, like the Husab and Ida Dome specimens, host sulphide mineralisation. Uraninite is the dominant uranium mineral, with most observations made of fine-grained specimens (50 µm to 150 µm). Uraninite is common in skeletal- and bladed-textured biotite (all altered to a varying degree to chlorite). This suggests that it is a late phase that crystallises within permeable minerals, and potentially that skeletal biotite may be transporting uranium in inclusions (e.g. zircon) from the leucogranite partial melt source rock.

Sulphides remained in circulation for a time after granite and uraninite crystallisation; Figure 4.52a and 4.52b illustrate late pyrite around uraninite, and pyrite filling cavities between uraninite crystals. Magnetite is a common accessory mineral in leucogranites that intrude the Nosib Group, and it appears to crystallise before uraninite in the example given in Figure 4.52b. Haematite has formed at the edge of the magnetite as a result of oxidation.

There is a close association between biotite and uraninite, and at Valencia a similar relationship to the one at Husab is observed; uraninite occurs as fine-grained inclusions, often only visible by the pleochroic halos that surround the metamict inclusions; occasionally relatively coarse ~100 µm grains completely disrupt the mica structure. Coarse

uraninite inclusions tend to correspond to wide alteration halos (Figure 4.52c and inset). Uraninite has also crystallised in magma that contains skeletal biotite; Figure 4.52d illustrates a uraninite that shares a straight edge with biotite, supporting uraninite after biotite paragenesis. The exposed edges of the uraninite show signs of alteration and corrosion subsequent to crystallisation of the feldspar co-host.

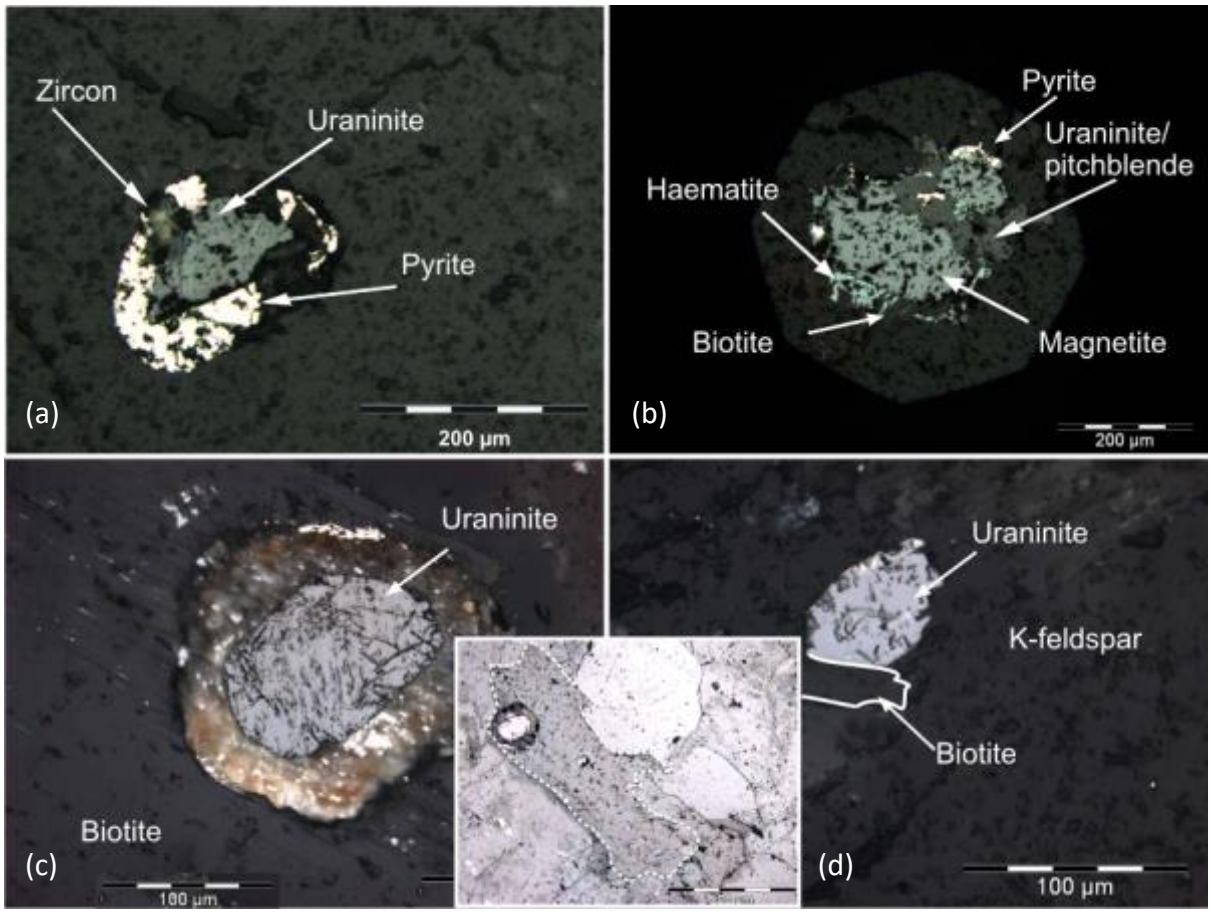



Figure 4.52 The common primary uranium mineralisation textures and ore mineral associations in Valencia alaskites. (a) Valencia leucogranites contain disseminated uraninite and zircon. Pyrite surrounds one of the uraninite grains and replaces the alteration halo that surrounds the uraninite in the host K-feldspar, Va26 111 157.44-157.82, rfl. (b) Uraninite and magnetite association in the Valencia sheeted leucogranites. Amorphous uraninite/pitchblende has formed between two magnetite porphyroblasts, surrounding a fine grain of pyrite. A second generation of pyrite-chalcopyrite overgrows the compound grain on one side, Va26 111 157.44-157.82, rfl (c) Uraninite is often hosted in biotite, in primary deposits throughout the Central Zone. Most radioactive inclusions are very fine-grained, occasionally coarse >100 µm grains form. Radiation damages the surrounding mica structure, facilitating pyrite-magnetite and clay replacement, Va26 141 301.29-60, rfl. (d) Uraninite is late in the crystallisation sequence at Valencia, in Va26 141 261-62 a uraninite shares a common edge with biotite, indicating the temporal relationship between biotite (if entrained, the biotite is older) and mineralisation (younger uraninite), rfl.

Secondary uranium minerals are visible in many surface samples and appear to be less abundant in core samples from depth than in the near-surface samples. Minerals such as

uranophane occur in varying abundances in the sheeted leucogranites at Valencia and in various associations with the host rocks (Figure 4.53). Uranophane and similar hydrous silicates have crystallised in fine-grained textures along mineral cleavage planes, as amorphous coatings on coarse rock-forming minerals, and as acicular crystal growths in dissolution vug- and leached silicate pore spaces in altered feldspars and carbonates.

Microcline, with fine-grained feldspar replacement, hosts uranophane in well-developed cleavage (Figure 4.53a). Fine-grained coatings between coarse, rock-forming minerals are likely the result of low-T°, meteoric (slightly acidic) fluid circulation (Figure 4.53b).

Well-developed, acicular uranophane crystal growth may have formed during sustained, high- and low-T° uranium-bearing fluid circulation to facilitate crystal growth (Figure 4.53c). The well-developed crystals would likely have grown at some point during or after silicate leaching in the host rock, associated with post emplacement fluid flux, comparable to the model presented for Rössing. The contrast in amorphous and well-developed uranophane textures is attributed to differing modes of uranium remobilisation and deposition;

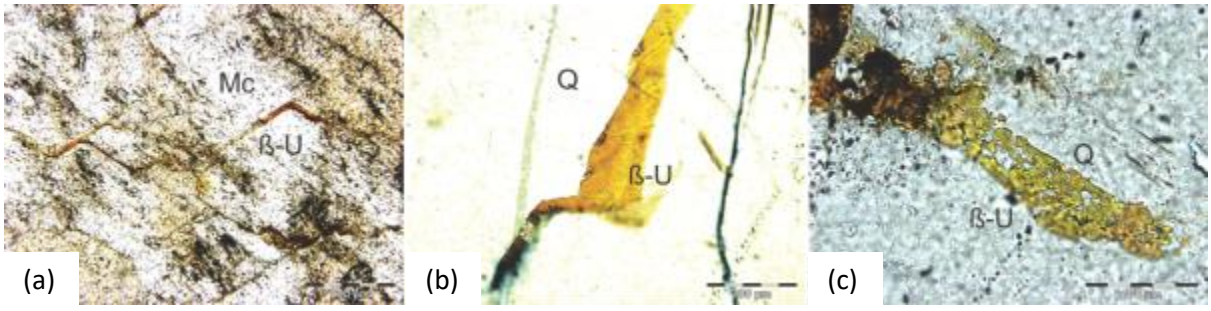



Figure 4.53 Secondary uranium mineral textures at Valencia. (a). Uranophane crystallisation along the cleavage planes of microcline feldspar. The feldspar has undergone sub solidus alteration, giving the cloudy appearance VALG 11, ppl. (b) Uranophane forms amorphous coatings on the surfaces of rock-forming minerals such as quartz, VALG 16 (c) Uranophane occasionally has space in altered feldspar, to grow crystals of acicular habit, VALG 15, ppl.

## 4.10 Petrography Summary

***Petrogenesis implications of the non-uraniferous leucogranites***

The sheeted leucogranites of the Central Zone host a number of prominent accessory phases, which allow for a relatively consistent means of identifying a granite in-situ or in hand specimen. The common, diagnostic accessory minerals in the sheeted leucogranites of the Central Zone include garnet and tourmaline in those that intrude the Rössing, Chuos, and Kuiseb Formations. Magnetite in sheeted leucogranites appears to be abundant, but limited to those that intrude the Khan- and occasionally the Rössing Formations. The sections that follow elaborate on these diagnostic accessory minerals.

*Garnet-bearing leucogranites (B-type)*

Compositional data for garnet in early leucogranites is not available in this study; however, Ward et al. (2007) and Ward *et al.* (2008) show that garnetiferous granites may be produced by melting cordierite-garnet-biotite schists of the Kuiseb Formation, at shallower depths and lower than expected T°, when in the presence of sufficient water.

Nex (1997) in contrast, shows that garnet compositions support granite production from dry deep crustal sources as well as at shallower depths. The garnets in B-types at Goanikontes show predominantly almandine (Fe) compositions with spessartine (Mn) at ~10%. Spessartine contents >10 % are usually considered to be indicative of garnets produced as late stage differentiates. The garnets produced by melting the Kuiseb have ~65 % almandine and >20 % pyrope (Ward et al., 2007) while those in the B-types near Goanikontes have >70 % almandine and <20 % pyrope (Nex, 1997) with the balance of spessartine, these are comparable compositions and suggest they formed from the same process in similarly pelitic rocks, albeit in different Formations.

The large volumes of garnet granite observed at the Valencia deposit in this study however, suggest that they are not simply Kuiseb melts filling local dilation sites, but should similar in origin to those discussed in Nex (1997). In other words variable volumes of partial melt have migrated and amalgamated Garnetiferous granites do appear limited to host rocks of the

Chuos- Rössing - and Kuiseb Formation pelitic-type schist and gneiss and are rarely observed in the Khan Formation.

*Tourmaline-bearing sheeted leucogranites ($C_t$-type)*

B, F, and Li all concentrate through fractionation; in the traditional sense of magmatic fractionation; from a wholesale melt or chamber such as in tin and lithium pegmatite systems; and by melt migration from a crystallizing pluton or set of sheeted intrusives.

The fractiontion process through melt migration is proposed as a potential mechanism for explaining chemical trends in granite magmas in Clemens *et al*. (2010) and Clemens and Stevens (2012). Indeed, there is little evidence of large plutonic chambers mentioned for the Damara. As is shown in numerous works Jacob (1974a); Berning (1986); Oliver (1994); Nex (1997); Longridge (2012); Longridge *et al.* (2014) melt migration is the most important mechanism by which the sheeted leucogranites are emplaced, thus, migrateion driven fractionation should be particularly evident in sheets that are located furthest from the basement and supposed melt sources at depth.

The migration is largely a mechanical process facilitated by periods of pronounced deformation outlined in Miller 1983b. However, the role of migration on the geochemical and petrographic character of the leucogranites is less well-documented. The most comprehensive local-scale interpretation is perhaps Ward *et al.* (2009) who describe the roles of source composition, metamorphism, and melt migration through existing structural pathways in the formation of the garnetiferous leucogranites, though these sheets appear to be products of Damaran metasediment melt rather than derived from some depth, i.e. the basement.

The tourmaline-bearing sheets that invade the Swakop group may also be a result of mechanical fractionation as described in Clemens and Stevens (2012). What role the metasedimentary rocks have played in affecting granite magma composition along the magma pathways, and at the emplacement sites, is not well-constrained. It is clear though at most sites of tourmaline-bearing sheeted leucogranites that wall rock interaction is rather limited.

*Magnetite-bearing leucogranite ($C_m$-type)*

One of the key observations related to leucogranites within the Basement, Etusis, Khan, and Rössing Formations is the relative abundances of magnetite and ilmenite. The Basement, Etusis, and portions of the lower Khan Formation host leucogranite-pegmatites with visibly abundant mafic accessory minerals. These are predominantly ilmenite and magnetite. Within the basement-hosted pegmatites ilmenite is often radioactive, and thus assumed to contain a significant proportion of the mineral davidite. The magnetite-bearing leucogranites seem to be influenced by the host rocks, although wall-rock interaction is often limited, with clean boundaries and weakly apparent chill margins suggesting high temperatures of the metasediments at the time of emplacement at most localities, an observation presented in Jacob (1974) for Rössing. More likely, the granites are oxidised to an extent that garnet cannot sequester Fe, instead the dominat Fe-phase is magnetite and mag-ilmenite where Ti is available. The Khan Formation is not reducing enough to influence the formation of Fe-sulphides either.

These sheets are roughly parallel to $S_1$ and the transposed bedding and fold axes; and in certain location have influenced the growth of magnetite porphyroblasts in the metasediments. It is clear that they are oxidised melts and therefore must have been generated from oxidised source regions. Whether they are extracted from a chamber or the more likely scenario, as migrated melts the REDOX state should remain fairly stable as discussed in Blevin and Chappell (1995); Ishihara and Wang (1999); Carmichael (1991); and Takagi and Tsukomura (2007). Any further work would require sulphur isotope studies to establish the role of $S^-$ in the granite system.

*Accessory Minerals*

Accessory phases such as monazite and zircon will remain as small crystals in the melt, as evidenced by concentric growth zones on these minerals. Clusters of monazite and zircon further support an inherited interpretation for some of these accessories. To a certain extent, the anhedral shape of some Fe-Ti oxides such as magnetite suggests that these minerals may have been transported. The coarser nature of magnetite in the C type

suggests the Fe- Ti-oxides are metastable or even soluble in the C-type sheeted leucogranite melts, nucleation mechanisms are uncertain but the type of granite is consistently limited to the Khan Formation at all deposits of this study, where the invading melts crystallise in an oxidised state. Numerous locations show that the biotite schists of the Upper Khan Formation have developed magnetite porphyroblasts in response to contact metamorphism. These granites have very low abundances of REE and low abundances of accessory minerals. Biotite is variably altered but not to the same degree of chloritisation as in the uraniferous sheets, and is considerably less abundant. Reaction with the metasediments is nearly absent in many locations suggesting that the melts have migrated passively into already hot rocks but at lower T° than the uraniferous sheets.

***Summary of petrographic characteristics of the sheeted leucogranites***

Petrographic observations show that certain traits are unique to particular groups of sheeted leucogranite. The uraniferous granites in particular show pervasive alteration, which must be dominantly internally driven as the host rocks most often only show hydrothermal or contact metamorphism in the vicinity of the post-$D_3$ leucogranites. The key features identified in this study are listed below:

- The plagioclase in the Grey granites is substantially less calcic ($An_{8-12}$) than that of the Salem monzogranite which ranges from $An_{36-to}$ $An_{44,}$ and lower than the younger porphyritic (megacrystic) types (plagioclase composition $An_{27-35}$) of Jacob (1974a);

- SLG plagioclase has the lowest An content of the granites at the CZ deposits investigated in this study, and is comparable to the Grey granites. There is some distinction in the uraniferous sheets, which average about 3% lower An than the pre-$D_3$ group of sheeted leucogranites;

- Biotite content decreases with successive generations of Grey granite;

- Significant entrainment of sedimentary-sourced biotite booklets and laths masks a systematic estimation of the magmatic biotite proportions;

- Garnetiferous B-type samples at Valencia are conspicuous in the amounts of peraluminous minerals such as garnet and entrained sillimanite trains in the pegmatitic varieties; Sillimanite is observed only in sheeted leucogranites that intruded the Kuiseb schists (Figure 4.12b).

- Myrmekite is most often associated with metasomatism and reaction between feldspars (Hippert, 1998), the prevalence of these textures in the C-types throughout the Central Zone, corresponds to the pre-$D_3$ timing of the SLGs, where the reaction may be a response to subsequent metamorphism/deformation;

- Magnetite-bearing C-types appear to be confined to the Khan Formation, $Fe^{2+}$ is in magnetite-ilmenite and $Fe^{3+}$ occurs in botryoidal haematite (hydrothermal/magmatic fluid flux) after magnetite and in the structure of K-feldspars;

- Mineralised granites exhibit peraluminous K-feldspar textures (well-developed tartan twinning) and metaluminous textures (dominantly perthite);

- The mineralised granites are predominantly K-feldspar dominant, but plagioclase is prominent in samples from all of the deposits;

- Albite exsolution has developed in K-feldspars and in sodic-feldspars of the mineralised granites;

- Valencia and Hildenhof mineralised samples are dominated by tartan-twinned microcline and vermicular quartz in more than two generations.

- Ida Dome, Husab, and Goanikontes samples are dominated by albite-oligoclase with variably subordinate K-feldspars and at least 2 generations of quartz;

- All biotite in the mineralised samples is chloritised to a certain degree and most contain pleochroic halos associated with uranium-silicates, oxides, zircon and purple fluorite inclusions;

- The E-type halos that are present at Goanikontes and Ida Dome, are poorly developed at Valencia, Hildenhof, and Husab, where Fe-alteration appears to be limited to metasedimentary contacts. The abundance of the well-developed halos at the Ida Dome and Goanikontes areas coincides with the location of much of the mineralised leucogranites in the Khan Formation at these two locations:- below the Chuos Formation at Goanikontes and below the Rössing Formation at the Ida Dome.

- Potentially one or two stages of alteration have occurred, most notably soon after intrusion as recognised at Rössing and probably in a Central Zone-wide Cretaceous event; and

- Modification of the A to F classification of Nex (1997) is necessitated by the wide variety of sub types in the C-type generation, and textural/ore mineral variation identified in D-type/E-type SLGs at other Central Zone uranium deposits.

***Origins of the sheeted leucogranites***

Leucogranites described elsewhere in the Central Zone are interpreted as highly-fractionated S- and A-type granites, with a wide variety of sedimentary ± igneous sources, in summary they are derived from a mixed source, broadly, the metamorphic complex that is the Abbabis Complex (Haack et al., 1982; Marlow, 1983; McDermott, 1986; McDermott et al., 1996; McDermott et al, 2000; Nex, 1997; Jung *et al.* 2000a, and references therein; Tjimunee, 2009; Longridge, 2012).

Uraniferous and non-uraniferous sheets contain remnants of peraluminous minerals, most notably muscovite, garnet, and tourmaline, and occasionally cordierite, though this may be an entrained component, the source material would likely contain metasedimentary rock in the uraniferous and non-uraniferous populations. Whether or not the pre-mineralisation leucogranites (SLG and Grey) and mineralised SLGs come from the same or similar sources has been a contentious question since the discovery of the Rössing deposits and in more

recent times the detailed classification of Nex (1997) supports different source rocks for the pre- and post-$D_3$ SLGs.

The abundance in late generations of sheeted leucogranite suggests that a more U-rich source, with protolith compositions that support high U-solubility in the magma and associated fluids, during a period in which P-T° conditions facilitated low-degrees of partial melt.

If the lower Khan and Etusis Formation rocks are melting to produce leucogranites as is proposed in McDermott *et al*. (1996) then a oxidised-type magnetite>ilmenite series granite is produced, with capacity to transport oxidised U. Comparably, if the granites are derived from a source with heavy sulphur, as described in Sasaki and Ishihara (1979) then a magnetite series, oxidised granite is produced. The Damaran uraniferous leucogranites are therefore derived from source rocks that promote an oxidised melt, thus potentially ruling out the source being partial melt of Khan Formation metasediments. The Etusis rocks however may produce oxidised melts, being shallow water sediments.

The role of wall rock interaction is the most influential of the mineralisation trigger mechanisms, and would in effect produce locally reduced-type granites.

The widespread distribution of uraniferous sheets, their proximity to basement-dominated inliers and the variation metasedimentary populations across the western Central Zone suggests that peak metamorphic conditions, which would be comparable parallel to the NE-SW Damara fabric in the western Central Zone (after Goscombe et al., 2003a; Longridge, 2012; and Longridge et al., 2014) were key drivers in generating uraniferous melt, and that source rock composition may account for the variable texture, composition and U-content of alaskite populations at each deposit. In other words, the nature of the alaskites at each deposit must be a reflection of the local crustal composition that melt was produced from.

The bulk of the alkali-feldspar melt would probably be derived from K, Th, and U-bearing hydrous minerals such as biotite and to lesser degree halogen-bearing minerals such as hornblende. The high concentrations of U would also require that other U-bearing phases such as monazite, xenotime and zircon be present and soluble, but the occurrence of these

in magmatic and entrained clusters and textures suggest that not all melts were in full equilibrium with the U-host minerals at the source.

The leucogranites within the upper Khan Formation and within the Rössing Formation are also host to mafic minerals, most of which are uraniferous, where the uranium concentration corresponds to the abundance of iron, as evidenced by typically red haematite staining. These mafic mineral assemblages are dominated by biotite, ilmenite, and magnetite. There is an apparent contrast in magnetite and ilmenite abundances which is relatively consistent between deposits, with ilmenite abundances noted at Valencia, Ida Dome, Goanikontes, and basement-Damara sequences from east of the Ida Dome to the west of the Husab mine. Ishihara (1977) described the granites of the Japanese arc in terms of modal magnetite abundances, although quantified modal abundances are not available to this study, field observations show consistency over a broad area, and over 290 thin sections confirm abundant magnetite in uraniferous leucogranites, with variable ilmenite content.

The oxidation state of the parent magma to the leucogranites and alaskites is critical because it plays the primary role of converting U into a soluble valence state. Furthermore, magnetite is present in the pre-$D_3$ and in the uraniferous SLGs, and in both varieties, there are examples of ilmenite exsolution. Ilmenite also occurs as an independent phase and more abundant exsolution lamellae in the younger leucogranites help distinguish the more oxidised uraniferous leucogranites from the pre-mineralisation varieties.

The Damaran leucogranite were not formed in an ocean arc-type setting, however the metasedimentary sequence of the Damara is deposited in an evolving rift, culminating with a deep-water setting (after Henry 1992; de Kock, 2001). However, the deep-water sediments of the Kuiseb Formation produce garnet-bearing melt, not magnetite granites. Additionally, the abundance of carbonates and amphibolite within the basement complex may represent similar deep water sediment precursors, allowing for heavy sulphur to influence melt $fO_2$ during partial melting.

The detailed assessment of the granite varieties present at the primary uranium deposits of the Central Zone provides an empirical means of comparing and contrasting the granites and the deposits that host them. The information allows for qualitative investigations and discussion of topics such as hand specimen texture, stratigraphic interaction and temporal

and spatial location. Microscopic comparisons are possible for mineral textures, alteration assemblages and trends, accessory mineral assemblages, uranium mineral and sulphide mineral relationships, and add further criteria to the qualitative appraisal of the granite populations.

Although there is ample evidence of alteration in the mineralised SLG's or alaskites, it is localised around accessory and ore- assemblages and is largely limited to the granites themselves. The only evidence of anatexis in the host rocks occurs at contacts to the sheets and in the most pelitic units of the Swakop Group. In this regard the interpretations of auto-hydration driven alteration in the Namaqua metamorphic complex granitoids and charnokites, and high-grade metamorphic rocks (Robb *et al*., 1986; Andreoli et al., 1992; and Andreoli *et al*., 2003, respectively) seem to be the most applicable comparisons.

The onset of $D_3$ deformation coincident with peak metamorphism at 510 is too close temporally to the intrusion of the alaskites not to infer a near-direct relationship. The alteration assemblages of the alaskites do however, show that the granites were altered in the presence of high T° fluids. These could easily be derived from the carbonate-silicates in the upper Rossing and lower Swakop Group assemblages, certainly the wollastonite-scapolite assemblages that occur at all of the deposits are evidence of some external fluid contribution on a local level. In large deposits that are relatively free of true marble and abundant calc-silicate, for example at Goanikontes (after Nex, 1997) the breakdown of hydrous phases such as biotite would be an important source of internal alteration fluids.

Modification of the original A- to F- classification of Nex (1997) is required to accommodate sub-varieties in the voluminous C-type sheets and to remove the E-types as a separate granite type. The new classification should include the A- and B-types; the C-types (C, Cm and Ct); the D-types and the late sporadic F-type and is presented in Table 4.15.

Although there is ample evidence of alteration in the alaskites, it is localised around accessory and ore- assemblages and is largely limited to the granites themselves. The only evidence of anatexis in the host rocks occurs at contacts to the sheets and in the most pelitic units of the Swakop Group. In this regard the interpretations of auto-hydration driven alteration in the Namaqua metamorphic complex granitoids and charnokites (Robb *et al.,*

*1986, and* Robb *et al.,* 1999; and Andreoli *et al*., 2003, respectively) seem to be the most applicable comparisons.

Table 4.15 Revised Central Zone sheeted leucogranite classification after Nex (1997). Goanikontes refers to the location on farm Goanikontes of the Etango Deposit, Husab refers to the Zone 1 and Zone 2 deposits within ML171, Ida Dome refers to the area that encompasses the Ida Central (EPL3138), Garnet Valley and Holland's Dome Deposits (both EPL3439), Hildenhof refers to the portion of the anomaly on Farm Hildenhof that lies within EPL3345 (Bannerman Resources, 2014).

| Type | Description | Locations | CPS vs. BG |
|---|---|---|---|
| A-type | Thin, very light pink to white, bedding parallel, very little accessories, often folded and boudinaged within Damaran Metasediments, limited extent. | Goanikontes, Valencia | low |
| B-type | White as well as light pink, medium grained and homogeneous often bedding parallel, folded and boudinaged. Garnet is a distinctive accessory and is found in clusters or as disseminated grains mostly < 1 cm in size. Examples at Valencia may be anatectic granites from Kuiseb Formation melt, as described in Ward *et al*. (2008). | Goanikontes, Ida Dome, Valencia (Husab – not certain) | low |
| C-type (accessory-free) | Extensive sheets or coalescences of sheets, predominantly in upper Nosib and Swakop Groups, white to light pink in colour, variably coarse-grained, minimal accessories except entrained biotite. May be a B-type at Valencia, as they are cross-cut by tourmaline SLG's. | Throughout CZ | low |
| $C_m$-type (magnetite) | Distinctive pink and white colour, medium to coarse as well as pegmatitic in patches, accessory magnetite clusters or disseminated throughout. These may also have accessory tourmaline accompanied by clear quartz. Recognisable by being parallel to bedding/cleavage/foliation. | Goanikontes, Hildenhof, Husab, Ida Dome, Valencia, | Low-high in patches |
| $C_t$-type (tourmaline) | May be light pink or white, mostly fairly coarse-grained with clusters of massive tourmaline, often in clusters. The massive tourmaline can often be as large as 5 - 6 cm across. Occur as parallel to bedding sheets in Kuiseb and Khan schists and gneisses. | Ida Dome, Valencia | low |
| D-type | White, medium to medium - coarse-grained, smoky quartz (black) and very little accessory biotite. May have yellow uranium secondary phases on exposed surfaces and on joint planes | Goanikontes, Husab, Ida Dome, Valencia | very high |
| Altered form- | Highly oxidised deep pink amorphous veins and fingers of granite intruding a range of other granites. These have a high biotite content and smoky quartz. Hydrothermal alteration of D-types has resulted in the colour and texture seen as the E-type. | Goanikontes, Hildenhof, Husab, Ida Dome | High- very high |
| F-type | Deep red pink, pegmatitic, milky quartz, cross cuts most features and granites | Goanikontes, Valencia, Ida Dome | low |

The onset of $D_3$ deformation coincident with peak metamorphism at 510 is too close temporally to the intrusion of the alaskites not to infer a near-direct relationship. The alteration assemblage of the alaskites does however, show that the granites were altered in the presence of fluids. These could easily be derived from the carbonate-silicates in the

upper Rossing and lower Swakop assemblages, certainly the wollastonite-scapolite assemblages that occur at all of the deposits are evidence of some external fluid contribution on a local level, however in large deposits such as Goanikontes, which are relatively free of true marble and abundant calcsilicate (after Nex, 1997) the breakdown of biotite would have to be the primary source of internal alteration fluids.

A systematic and quantitative assessment and comparison of the primary uranium deposits requires more statistically acceptable data and interpretation. Such data includes whole rock geochemistry, including rare earth element analyses. Geochemical data, to be meaningful, requires context, thus most of the samples that are described in this Chapter, were submitted for geochemical analyses. The results of the geochemistry follow in Chapter 5 and Chapter 6.

## 4.11 Concluding Remarks

One of the primary aims of this study was to test the Central Zone-wide application of the leucogranite classification scheme of Nex (1997); which was derived from detailed study at the Goanikontes area. Of the six varieties described at Goanikontes, most are represented at the other deposits in the region, the Valencia deposit in particular hosts at least 5 sheeted leucogranites that can be separated on cross-cutting relationships alone. Further subdivision is possible at all the deposits of this study with the aid of petrography. There is a remarkable consistency in the field relationships of the pre-mineralisation leucogranites:

Dominant accessory mineral assemblages are indicative of:

- The REDOX nature of the granite source, e.g. the magnetite-bearing sheets;
- The prevalence of granite fractionation, e.g. the boron concentration of tourmaline-bearing sheets; and
- The equilibrium state with peraluminous phases, e.g. the garnet-bearing granites.

All of the above essentially represent the main repositories of Fe in the various leucogranites. In the case of the mineralised sheets the interaction with the reduced

metasediments results in pyrrhotite and pyrite hosting Fe, or a combination of sulphides and Fe-oxides at the Goanikontes locations.

The consistent positions of the leucogranite types within the stratigraphic sequences across the western Central Zone implies that if the granites are derived from sources of similar composition, certain melts have travelled further than others, a process that may have influenced the ability to crystallise or dissolve certain phases. Fe content is high in the Khan Formation-host granites, hence magnetite, while in the granites higher up in the sequence garnet and tourmaline tend to be the main Fe hosts in the accessory assemblages.

The interpretation of observations presented in this study motivates, with consideration of previous work, that the E-type of Nex and Kinnaird (1995) and Nex (1997) are not a separate generation of sheeted leucogranite to the D-type. Rather a product of variably influenced metasomatic alteration of the D-type and possibly magnetite-bearing C-type sheeted leucogranites. The C-type leucogranites, usually cross-cut by D-type, are separated into three main sub-types, the magnetite, tourmaline, and accessory-free varieties. The B-type, the garnetiferous sheets, are observed at all deposits and in the vicinity of the subsurface Husab deposits, there is potential to subdivide these sheets into older foliated and later pegmatoidal subtypes based largely on observations at the Valencia Deposit.

The highly variable uranium content is primarily the result of uranium leaching, and redistribution of secondary uranium minerals. The metasomatic alteration varies from localised haematisation around entrained- and magmatic-derived Fe phases to the characteristic halos around unaltered cores of D-type leucogranite. The proposal takes into consideration the following observations:

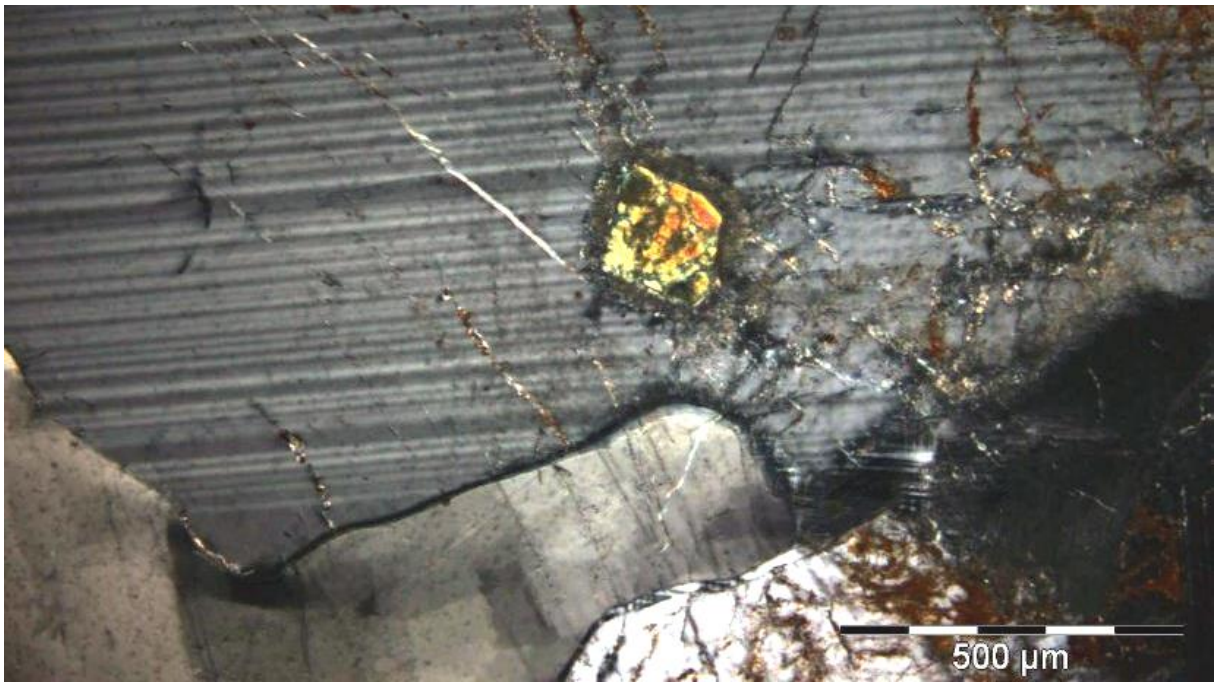
- Halos (coronas) are not restricted to mineralised sheeted leucogranites, there is therefore a process that has cross cut the sheeted leucogranite sequence both spatially and temporally, and must post-date barren and mineralised varieties;
- Palaeomagnetic studies by Corner (1981 and 1983) show that the unaltered granite in the cores of oxidation halos have retained magnetism similar to the negative ~500 my Damara anomaly retained in titaniferous magnetite in the

Khan Formation. The granite outside the halos, is in fact the altered portion and has been reset (chemically in Ti-magnetite) by a more recent event;

- Oxidation stains at Valencia are most prevalent in samples adjacent or in the vicinity of Cretaceous-aged fault zones and dolerite dykes, where mobilised fluids are most likely to alter the granite;
- Oxidation halos of the kind described at Ida, Goanikontes and Rössing do not occur at mineralised localities such as Valencia and Hildenhof;
- At Valencia, the entire sheeted leucogranite sequence is present as described in Nex (1997) with the exception of the E-type. If the E-type is a successive generation of sheeted leucogranite it should be present rather than absent considering the number of sheeted leucogranite types at present at the deposit; and
- In the Central Zone, the earliest metasomatism of the sheeted leucogranites, particularly the mineralised varieties, involves a late stage magmatic fluid flux that upgraded the SJ deposit by remobilising and depositing secondary U-phases shortly after granite crystallisation.

A systematic and quantitative assessment and comparison of the primary uranium deposits requires more statistically acceptable data and interpretation. Such data includes whole rock geochemistry, including rare earth element analyses. Geochemical data, to be meaningful, requires context, thus most of the samples that are described in this Chapter, were submitted for geochemical analyses. The results of the geochemistry follow in Chapter 5 and Chapter 6.

# CHAPTER 5 GEOCHEMISTRY OF THE GRANITIC ROCKS AT THE PRIMARY-HOSTED URANIUM DEPOSITS




A euhedral monazite crystal inclusion is hosted by albite-twinned plagioclase feldspar (oligoclase $An_{27}$) in a uraniferous sheeted leucogranite. The sample is IDAG05 (624 ppm U, XRF) from the Ida Dome area. Monazite is a common accessory in the uraniferous sheeted leucogranites and is either Ce- or La-rich and the ratio of these two elements shows systematic behaviour relative to Th across the Central Zone deposits. Clusters of such accessories may indicate inherited enclaves of a weakly radioactive source. Radioactive inclusions in the mineral are responsible for the pleochroic patches, prominent at two opposing ends of the crystal. Fe and Ca, in secondary minerals, are introduced to the system through alteration processes after granite crystallisation. The abundances of accessory minerals and the variable degrees of secondary alteration help characterise the trace elemental chemical traits of the granite populations at each of the individual primary uranium deposits.

## 5.1 Introduction

Geochemical data are presented for a range of granite types and granite generations at the Central Zone primary uranium deposits. The analytical results are discussed with respect to those made for Damaran equigranular-textured granites and sheeted leucogranites at Goanikontes by Nex (1997). The study showed that despite their observable contrasts, the Goanikontes leucogranite whole rock geochemistry does not consistently highlight strong

differences within the pre-$D_3$ leucogranite varieties. Nex (1997) did however, show that geochemistry is able to discriminate between the equigranular-textured Grey granites, the pre-$D_3$ sheeted leucogranites, and the post-$D_3$ uraniferous leucogranites (alaskites).

Nex (1997) described detailed field and petrographic observations) as a valid and acceptable means of classification and that chemistry of the granites may be used as a support for- and/or confirmation of many of the field and petrographic observations of Goanikontes granitoids. The broad characteristics such as stratigraphic position, accessory assemblages, U content, colour and texture and above all, cross-cutting relationships are the most pertinent in this regard. Petrographic studies show certain trends in the pre- and post-$D_3$ populations, particularly the abundances of accessory minerals in the uraniferous varieties. Sub-solidus reaction is relatively uncommon in the pre-$D_3$ sheets and is variably widespread in the uraniferous granites. These differences should translate into variations in major and trace element abundances.

This chapter presents and discusses the analytical results of samples from the following granite suites:

- Three varieties of Grey granite from Hildenhof (Chapter 3, Figure 3.3);
- Two varieties of Salem granites from Valencia (Chapter 3, Figure 3.3); and
- At least six textural and temporal varieties of the sheeted leucogranites (sheeted leucogranites) together with several minor sub-varieties sourced from Etango (Goanikontes) Hildenhof, Husab, Ida Dome and Valencia (Chapter 3, Figure 3.3).

## 5.2 Methodology

The primary motivation for geochemical analyses and classification of the leucogranite and older Grey (and Salem) granites is to produce a quantifiable, and consistent, correlation between petrographic and field observations that classify the intrusive suites at the southern Central Zone primary-hosted uranium deposits.

The geochemical dataset comprises whole rock X-Ray Fluorescence for Major and Trace Element abundances, Hand-held X-Ray Spectrometry for detailed chemical assessment of mineralised leucogranites (to characterise refractory-bearing alaskites) and ICP-Mass Spectrometry for Rare Earth abundances:

- The laboratories and the equipment employed are listed in Appendix E1.
- Sample preparation procedures for the sample suites in this study are detailed in Appendix E2 for whole rock XRF; Appendix E3 for hand-held XRF; and E4 for whole-rock ICP-MS.
- Calibration standards for the XRF and ICP-MS laboratories are detailed in Appendices E5 and E6, respectively.

A number of independent accuracy and precision tests are facilitated by blind repeats and duplicates; the results show that the results between two different XRF laboratories are within an acceptable difference of each other. A standard sample of known composition was submitted with each batch of XRF samples as a means of monitoring consistency, the sample is sourced from Rössing Mine drill core.

- Hand Held XRF: - Repeats, time-interval and comparative assays were employed to test the accuracy and precision of the hand - held XRF which utilises its own auto-calibration feature, the results are compared to conventional XRF and to ICP-MS data.
- The REE samples are tested by comparing whole – rock geochemical data and ICP-MS data from a historical U assay database (Husab samples only). Two samples were also submitted as independent repeats.
- Accuracy and precision testing is detailed in Appendices E7, E8 and E9 for XRF, hand – held XRF and ICP-MS, respectively.
- Raw data are presented in Appendices E10, E10, E11 and E12.
- Appendix E13 contains normalised REE samples (McDonough and Sun, 1995).
- Appendix E14 contains descriptive summary of the REE samples specimens.

### *Major Elements*

Major elements oxide analysis and reporting by XRF: $Al_2O_3$; CaO; $Cr_2O_3$ (Husab only); $Fe_2O_3$; FeO (Husab only); $K_2O$; MgO; MnO; $Na_2O_3$; NiO (Husab only); $P_2O_5$; $SiO_2$; and $TiO_2$. Loss on ignition value is reported for all samples and average 0.71 wt.%, with a range of 0.00 to 3.87. $Fe_2O_3$ was measured; normative FeO was calculated using an $Fe^{3+}$/total Fe of 0.3 of typical rhyolite magma, as advised by the CIPW macro[40]. Table 5.1 summarises major element abundance statistics for the full data set of this study:

Table 5.1 Summary statistics of 244 major element XRF analyses of Central Zone granite and metasediment samples.

| Wt% | $SiO_2$ | $Al_2O_3$ | $Fe_2O_3$ | FeO | MnO | MgO | CaO | $K_2O$ | $Na_2O$ | $P_2O_5$ | $TiO_2$ | NiO | $Cr_2O_3$ | LOI | Total |
|---|---|---|---|---|---|---|---|---|---|---|---|---|---|---|---|
| Min | 24.34 | 0.42 | 0.01 | 0.00 | 0.00 | 0.00 | 0.09 | 0.09 | 0.13 | 0.00 | 0.01 | 0.13 | 0.03 | 0.00 | 62.34 |
| Max | 96.77 | 23.89 | 22.61 | 1.81 | 0.71 | 11.84 | 32.15 | 9.92 | 5.61 | 2.50 | 4.19 | 0.20 | 0.06 | 3.87 | 103.54 |
| Ave. | 73.26 | 12.74 | 1.38 | 0.42 | 0.04 | 1.08 | 1.83 | 5.42 | 2.67 | 0.12 | 0.20 | 0.17 | 0.04 | 0.71 | 98.76 |

Geochemical data are presented systematically with plots that utilise the common major element ratios and CIPW normative calculations to:

- Classify the rock types (An-Ab-Or of Barker, 1979); and
- Classify the rock sub type (Q'-ANOR of Le Maître, 1989).

Molar abundances are calculated from the whole rock data and applied to classification diagrams such as:

- Ternary, rock system diagrams (Q-Ab-Or of Tuttle and Bowen, 1958);
- Aluminium Saturation (Chappell and White, 1974a and 1974b); and
- Major element rock discrimination diagrams (MALI, Fe- and Mg-based schemes of Frost *et al.*, 2001 and P-Q plots of Debon and le Fort, 1983).

The diagrams show some trends that prove useful in classifying the individual granite varieties within the local area of a deposit, as well as showing consistencies and contrasts that help classify the deposit suites within the Central Zone as a region.

[40] CIPW calculator Excel macro of Professor K. Hollocher, Union College, New York.

### *Trace Elements*

The variation in trace element abundances assayed by XRF in this study are summarised in alphabetical order in

. Trace element ratios essentially reflect concentrations of accessory phases, transport from source in restite and xenolith components, in refractory mineral inclusions, and substitute for major elements in rock-forming phases. The trace element section splits the observations between: high-field strength elements; mobile, low-field strength elements; transition metals; and radioactive elements.

Table 5.2 Trace elements summary of the granitic samples collected for this study, all values in ppm, analysed by XRF fusion

| | Ag | As | Ba | Bi | Cd | Ce | Co | Cr | Cu | Eu | Ga |
|---|---|---|---|---|---|---|---|---|---|---|---|
| Min | 4.0 | 3.0 | 4.0 | 2.1 | 10.0 | 5.0 | -0.6 | 0.9 | -0.2 | 2.0 | 6.4 |
| Max | 24.0 | 38.8 | 149958.0 | 10.0 | 59.3 | 3050.9 | 80.6 | 311.1 | 2167.0 | 18.4 | 38.0 |
| Ave. | 5.7 | 13.3 | 1421.8 | 5.9 | 11.4 | 81.3 | 6.4 | 62.0 | 40.8 | 2.4 | 16.1 |
| | **La** | **Mo** | **Nb** | **Ni** | **Pb** | **Rb** | **Sb** | **Sc** | **Se** | **Sn** | |
| Min | 0.9 | 0.9 | 0.0 | 0.9 | 9.0 | 6.7 | 10.0 | -0.7 | 3.0 | 10.0 | |
| Max | 1614.5 | 339.7 | 116.0 | 1311.3 | 3304.0 | 702.7 | 10.0 | 335.1 | 5.5 | 82.1 | |
| Ave. | 48.4 | 26.2 | 14.3 | 47.9 | 81.9 | 276.4 | 10.0 | 24.0 | 3.2 | 11.8 | |
| | **Sr** | **Ta** | **Th** | **U** | **V** | **W** | **Y** | **Yb** | **Zn** | **Zr** | |
| Min | 6.8 | 18.0 | 8.0 | 5.9 | 4.0 | 10.0 | 1.7 | 8.0 | 0.0 | 3.0 | |
| Max | 1365.0 | 57.7 | 921.3 | 4761.8 | 742.4 | 18.4 | 896.8 | 158.3 | 1325.0 | 1022.2 | |
| Ave. | 102.0 | 21.4 | 65.8 | 374.8 | 56.3 | 10.3 | 46.6 | 11.7 | 31.5 | 135.9 | |

### *Hand - Held XRF Assay*

The Husab deposit, like Rössing, hosts a minor proportion of the known uranium budget in the accessory minerals, betafite and brannerite. Historically, the distribution of the minerals is known from intensive investigation of satellite deposits to the Rössing Mine open pit. Numerous historical investigations have attempted, with variable success, to determine the geochemical controls on betafite and brannerite distribution.

At Husab there are localised alaskite intervals with significant uranium concentration in refractory minerals, particularly in brannerite. Analyses using a hand-held XRF on a 10 cm - 15 cm sample spacing interval were undertaken to identify major and trace element

patterns associated with the accessory minerals. The close-spaced sampling is designed to overcome the fine-grained and sometimes disseminated nature of the brannerite and betafite crystals within the granite. Results of the investigation are presented in their own section with observations, interpretations and discussion points that reconcile the XRF assays with observable macroscopic and microscopic textural-mineralogical-alteration traits. The elements of interest to the study are Cl, Nb, Th, Ti, and U and these are analysed and reported in ppm.

***Rare Earth Elements***

A total of 41 samples spread across the Valencia, Husab, Goanikontes, and Ida Dome deposit areas were analysed by ICP-MS in the Earth Labs at the Bernard Price Institute, University of the Witwatersrand, Johannesburg. Analyses for 40 elements including the full suite of REE are given in Table 5.3. The results are presented and discussed in Chapter 6.

Table 5.3 Rare-earth, trace-, and major elements analysed at the Bernard Price Institute ICP-MS laboratory.

| | | | | | | | | |
|---|---|---|---|---|---|---|---|---|
| Ce | La | Pr | Nd | Sm | Eu | Gd | | Y included because of lanthanide affinity |
| Tb | Dy | Ho | Er | Tm | Yb | Lu | Y | |
| As | Ba | Co | Cr | Cs | Cu | Ga | Hf | |
| Li | Nb | Ni | P | Pb | Rb | Sc | Sn | |
| Sr | Ta | Th | Ti | U | V | W | Zn | Zr |

## 5.3 Sampling andAims

The intention of the sampling programs was to collect representative material, where possible, of all the varieties of leucogranite and Grey granites present at the individual Central Zone deposits. A total of 244 samples were analysed; 11 Grey granites; 200 sheeted leucogranites (includes U-mineralised samples) 2 red granites; 6 quartz-pegmatites; and 16 assorted country rocks, skarns and xenoliths. The sample suites are summarised in Table 5.4. The samples were analysed by XRF in four batches split between two different laboratories.

Duplicate samples and a control- sample, a Rössing sample obtained from EGRI (included in all batches) were included in order to monitor accuracy and precision. A standard CIPW norm macro was used to calculate molar mineral compositions[41].

Table 5.4 Summary total of samples analysed for major and trace elements by XRF fusion and/or pressed pellet analyses. The number of core samples is in parentheses in the totals column. *Husab skarns comprise two gneissic rocks with veins of alaskite and a sample of Rössing quartzite.

| Rock / Area | Salem | Grey | Red | sheeted leucogranites | Quartz-pegmatites | Calcsilicates | Skarns | Skarn xenoliths | Total |
|---|---|---|---|---|---|---|---|---|---|
| Goanikontes (Etango) | | 1 | | 40 | | | | | 41 (39) |
| Hildenhof | | 5 | 2 | 20 | 2 | 1 | | | 30 |
| Ida Central (I) | | | | 27 | 1 | | | | 28 (4) |
| Garnet Valley (GV) | | | | 7 | | | | | 7 |
| Holland's Dome (HD) | | 3 | | 18 | | 4 | 2 | 1 | 28 |
| Valencia | 9 | 1 | | 55 | 2 | | | 2 | 69 (25) |
| Husab Fluorite | | | | | | | 1 | | 1 |
| Namib Pb-Zn | | | | 1 | | | | | 1 |
| Control Standards (Rössing) | | | | 5 | | | | | 5 |
| Husab* | | | | 15 | 1 | 1 | 3 | | 20 |
| Duplicates | | 1 | | 12 | | | 1 | | 14 |
| Total | 9 | 11 | 2 | 200 | 6 | 6 | 7 | 3 | 244 |

The mandate at the Goanikontes area was to collect samples from depth, as previous studies by Mouillac *et al.* (1986); Nex and Kinnaird (1995); and Nex (1997) comprised predominantly surface samples. The Ida Dome area provided surface samples at Ida Central, Garnet Valley and Holland's Dome. At the time of field mapping, drill core was available from Ida Central, where a single hole was sampled. Swakop Uranium provided samples from the Husab deposits as part of their internal mineralogical study program which permits a limited set of results to be presented in this study. Geologists at Extract Resources selected samples from Zone 1 and Zone 2, to represent a variety of alaskite textures. A deposit-wide sampling program, conducted during the present study, has focussed on modelling the distribution of

[41]CIPW Norm Calculator Microsoft Excel® Macro written by Kurt Hollocher, Geology Department, Union College, Schenectady, NY, 12308, hollochk@union.edu.

refractory phases since 2011. Selected findings from this study are presented in this chapter. The Valencia sample suite provides the most comprehensive data set of the different sheeted leucogranites as described by previous authors (Nex and Kinnaird, 1995; Herd, 1996 and Nex, 1997) and for this reason, some geochemical plots include only Valencia samples.

The F-types were only sampled on surface at Valencia and from Goanikontes a sample from core that resembles an F-type is included in the data set. Classification by whole-rock chemistry is the ideal starting point and the least complicated of schemes is the Q'-ANOR diagram of Le Maître (1989) as the fields correspond to those of the ternary IUGS Streckeisen Diagram.

Geochemistry of major and trace elements by XRF is limited to 15 Husab samples, while hand–held XRF assay accounts for 390 sample points across mineralised zones. Uranium and thorium plots are described separately prior to the mineralisation chapter (Chapter 6). The majority of diagrams include data from Rössing samples. Detailed analytical data is available from the Economic Geology Research Institute, School of Geosciences, Wits University, including analyses in Freemantle (2006).

This data is included for the following reasons:

- The SJ Rössing deposit is considered the type locality for primary U-mineralisation in the Central Zone;
- Metasomatic features present in mineralised samples necessitate the comparisons to the hydrothermally altered Rössing samples;
- To compare with the geochemistry of other sheeted leucogranites, with respect to their location (deposit, and regional) and type (A-F) of Nex (1997);
- Highlight contrasts and trends between mineralised sheeted leucogranites with respect to their localities and alteration;
- Show that high-T (metasomatic) and low T surface- and near-surface alteration has had some influence on major and mobile trace element distribution within the mineralised suites; and
- That interaction with reactive host rocks has sometimes, profound effects on certain trace element, and major element abundances.

## 5.4 Major Element Trends

The average compositions of the Grey and Salem suite granites at the Central Zone deposits have a lower $SiO_2$ content than the leucogranite suites. The pre-and post-$D_3$ leucogranites all contain >70 wt.% $SiO_2$ on average, Al, Ca, and Fe of the leucogranites at all deposits average less than the Grey and Salem suites. Na, and K tend to be comparable, though it may be argued that K is slightly more abundant in the leucogranite sheets. The major element averages of individual deposit leucogranite populations, the Central Zone Salem and Grey granite collections of this study, and some comparative skarn and xenolith samples are summarised in Table 5.5.

Major element data shows limited compositional differences between weakly mineralised and mineralised sheeted leucogranites (Figure 5.1). The plots show the ranges of Si, Al, K, Na, Ca, and P. The major element abundances and ranges provide a simple means of discriminating between the leucogranite groups, in terms of the six-fold classification of Nex (1997) and the earlier Salem and Grey granite suites. Narrow ranges of Si, Al, and P abundances characterise the A and B type sheets; K ranges are comparable with only the A and B type, and the magnetite-bearing $C_m$-type sheets stand out with narrow ranges and low abundances. Na and Ca show the greatest variance in the D-types, while P is only abundant above 0.5 wt.% in the E type. The maxima of Si, Na, and Ca of the Grey and Salem granites are consistently lower than the leucogranite populations.

The major element abundances and ranges of the individual deposits constitute a large dataset. The granites of primary interest to this study are of course the uraniferous varieties. The compositions of these granites are expected to vary given the variable degree of interaction with the host sediments at each deposit. Figure 5.2 shows the range and abundances of Si, Al, K, Na, Ca and Fe for the uraniferous populations (D-and E-types combined). The Husab deposit sample-set stands out with the greatest range in Si, Al, K, Na, and Fe. The Hildenhof samples, which are all variably weathered surface material, show the greatest range and abundance of Ca. Na and Ca ranges and abundances are low in the Valencia samples and distinguish the D-and E-types of the deposit from the others. Ca, Fe,

and Al maxima of all the deposits exceed the corresponding maximum values in the comparative Rössing samples. Consideration is given to any local host rock influence that has resulted in variable major element proportions within individual deposit localities, particularly with regard to mobile elements; Ca, K and Na.

Table 5.5 Major Element averages of Central Zone granites in this study (all XRF fusion). Leucogranite suites for each deposit include U-mineralised and weakly mineralised leucogranites. Ida includes Central, Garnet Valley and Holland's Dome. The Rössing sample is a control sample of known composition submitted with every batch of XRF powders. Appendix 5.2 details sample preparation and laboratory procedures.

| Area / Oxide | Grey | Salem | Goa. Leuco. | Hildenhof Leuco. | Ida Dome Leuco. | Husab Leuco. | Valencia Leuco | Skarn Xenoliths | Skarns |
|---|---|---|---|---|---|---|---|---|---|
| **Samples** | **9** | **11** | **40** | **20** | **52** | **15** | **55** | **3** | **3** |
| %$SiO_2$ | 68.10 | 66.06 | 73.68 | 71.33 | 76.57 | 77.42 | 74.37 | 64.90 | 46.53 |
| %$TiO_2$ | 0.43 | 0.84 | 0.08 | 0.20 | 0.06 | 0.25 | 0.10 | 0.11 | 0.27 |
| %$Al2O_3$ | 14.52 | 14.79 | 13.06 | 13.68 | 12.43 | 11.02 | 13.04 | 12.70 | 11.57 |
| %$Fe_2O_3$ | 3.02 | 5.24 | 1.18 | 1.36 | 0.71 | 1.22 | 1.28 | 8.77 | 8.24 |
| %MnO | 0.04 | 0.08 | 0.02 | 0.02 | 0.01 | 0.03 | 0.03 | 0.08 | 0.29 |
| %MgO | 1.90 | 2.56 | 1.05 | 0.77 | 0.62 | 0.92 | 1.06 | 0.50 | 3.97 |
| %CaO | 2.63 | 2.49 | 1.34 | 1.04 | 1.29 | 1.15 | 0.85 | 2.94 | 19.41 |
| %$Na_2O$ | 2.89 | 2.82 | 2.18 | 2.46 | 3.30 | 2.19 | 2.80 | 2.82 | 1.88 |
| %$K_2O$ | 4.85 | 4.18 | 6.45 | 7.47 | 4.33 | 4.59 | 5.82 | 5.35 | 0.59 |
| %$P_2O_5$ | 0.10 | 0.20 | 0.07 | 0.30 | 0.07 | 0.05 | 0.13 | 1.92 | 0.32 |
| %LOI | 0.68 | 0.71 | 0.64 | 0.59 | 0.30 | 1.06 | 0.56 | 0.28 | 1.15 |
| **TOTAL** | **99.17** | **99.96** | **99.74** | **99.23** | **99.69** | **99.91** | **100.03** | **100.38** | **94.23** |

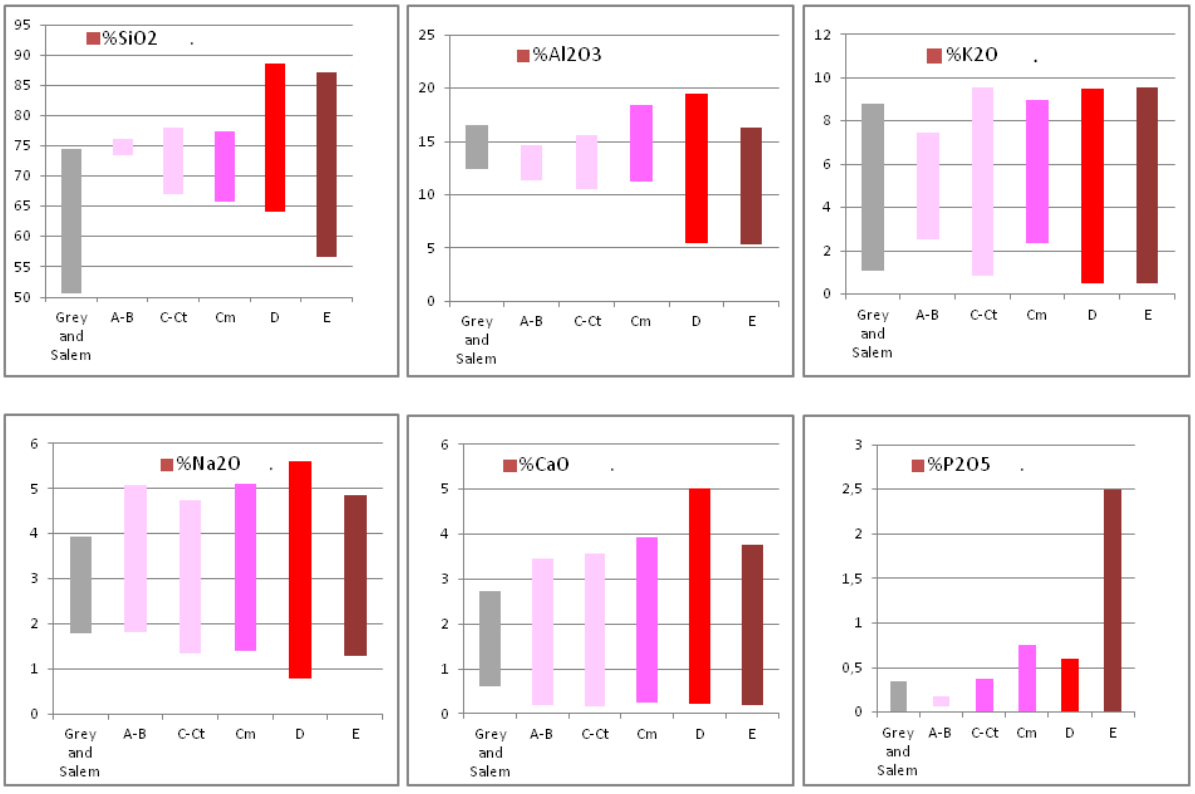


Figure 5.1 Major element wt.% ranges of the Central Zone leucogranites and equigranular Grey and Salem suite granites. An increase in normative quartz content is the most distinctive contrast between the mineralised and weakly mineralised leucogranites, as presented in Herd (1996) and Nex (1997). This observation appears to hold true for most of the samples from the Central Zone, particularly between the D-type and the magnetite-bearing $C_m$-type.

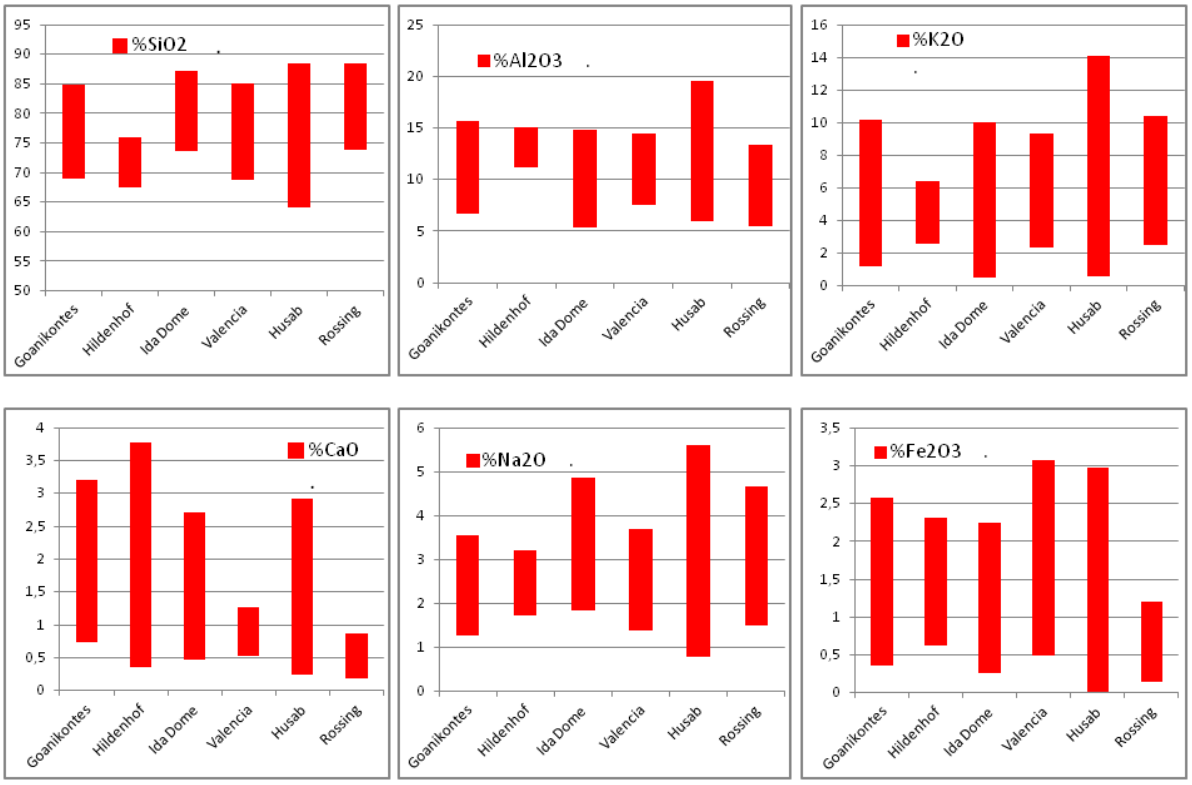



Figure 5.2 Major element abundances of the uraniferous leucogranite populations at the Goanikontes, Hildenhof, Ida Dome, Husab, and Valencia Deposits. Rössing data from Freemantle (2006).

The discrimination diagrams in the sections that follow show that the leucogranite types at Central Zone uranium deposits have distinct similarities despite their spatial separation. D-type SLGs from all the deposits, for example, plot in the alkali-feldspar field of Le Maître (1989). Certain suites of leucogranites, particularly the Valencia A, B, C, D and F types are chemically distinguishable from each other. Deposit specific diagrams are therefore, presented where chemical classification features are prominent.

## 5.5 Rock Classification using Major Elements

Major element data may substitute for modal analysis plots by normative composition calculations, typically the CIPW norm. The normative Or – An - Ab diagram in

Figure 5.3 shows diversity in plagioclase and K-feldspar content within the sample suite. The plot of normative An-Ab-Or with the rock classification fields of Barker (1979) is useful for illustrating the relative, normative An contents of the leucogranite samples as it has relatively large discrimination fields. Grey and Salem granites illustrate how successive generations of granite suites in the Central Zone evolve. They also plot within the same fields as sheeted leucogranites due to increased K-feldspar content in partial melts (Figure 5.3a). The leucogranites, have lower normative An than the older, less evolved Salem type and Grey granites, which conforms to the observations described in Miller (1983a) and illustrated in Figure 5.3b.

The Salem type granites show a successive shift to normative Ab with Or increase, the sheared varieties reflecting a partial melt component with very low An and distinctly high Or relative to the younger type 2 variety. The Grey granites appear compositionally to be tonalite, a single intermediate Grey granite is granodiorite. The youngest generation is the least mafic, and shows more evolved composition with low An and tending toward normative Or.

Another method of classification for overcoming the high silica content of granite is to use a modal analysis of the rock by point-counting feldspar and quartz proportions and plotting on a Streckeisen diagram (1976). A modal classification of samples is not ideal as the pegmatitic nature of the rocks hampers statistical consistency. Certain samples and indeed certain sampling areas are particularly prone to biased counting because of their coarse textures. The Q-ANOR diagram of Le Maître (1989) utilises CIPW normative proportions of quartz, orthoclase, anorthite and albite in place of modal abundances. The diagram is plotted by the proportion of normative quartz to the total of Ab + An + Or + Q as (Q') on the Y axis and the proportion of normative An to the total of normative An + Or on the X axis (ANOR). Splitting the Central Zone population by deposit reveals consistencies by deposit area. Mineralised

sample compositions from Rössing (Freemantle, 2006) have been included as a means of comparison in all diagrams.

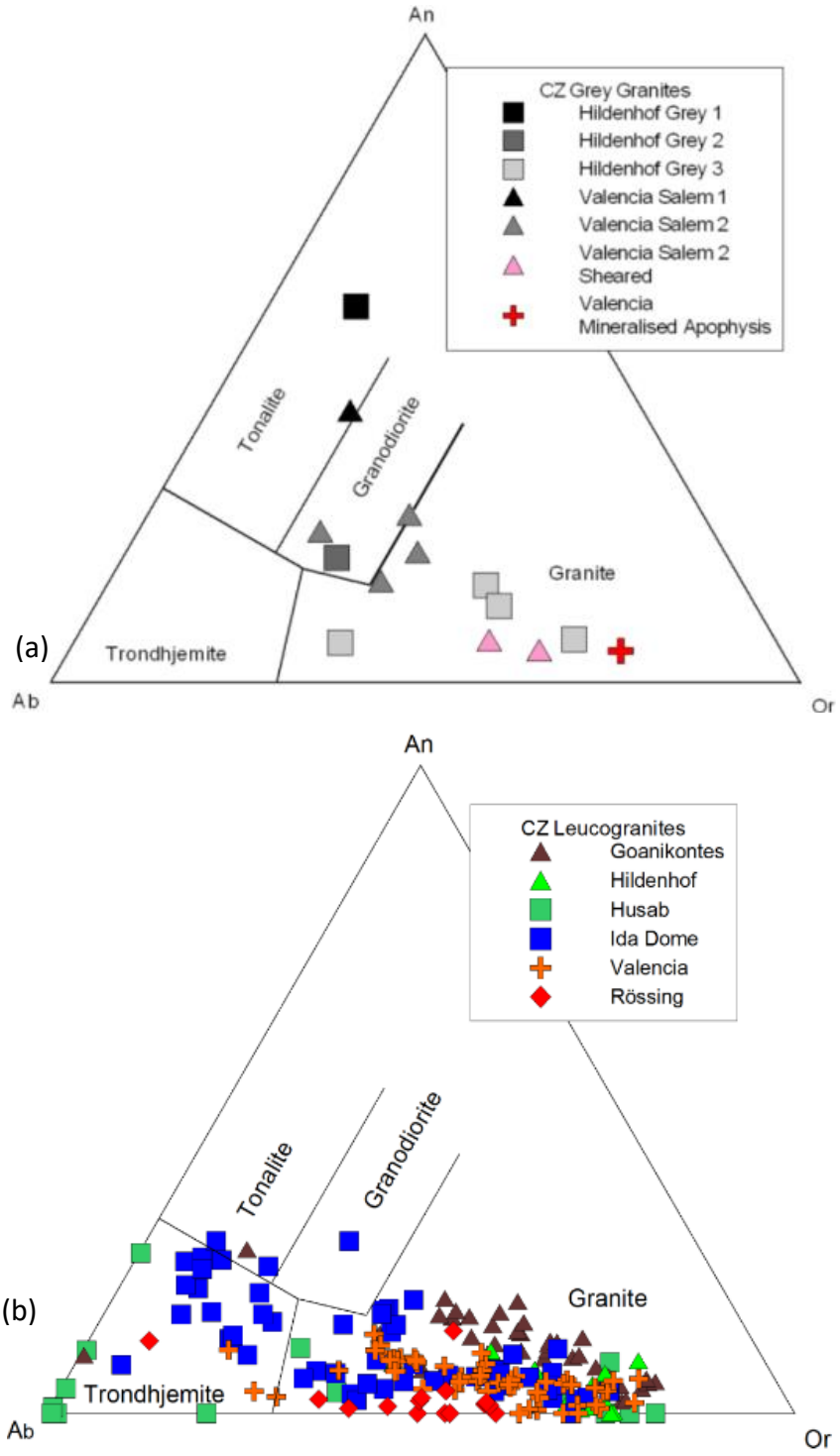



Figure 5.3 Or-An-Ab normative plots (after Barker, 1979) of Salem, Grey, and leucogranite suites of the Central Zone uranium deposits. (a) Or-An-Ab normative plots of Grey granites from Hildenhof and Salem Suite samples from Valencia. The diagram illustrates a compositional trend with age (type-1 are old and types 2 and 3 are successively younger, shearing and partial melting of Salem type-2 samples has resulted in higher normative Or proportions. The mineralised apophysis is a sample of mineralised leucogranite (alaskite) that intrudes megacrystic Salem granite near the Valencia deposit.
(b) Or-An-Ab normative plots of sheeted leucogranites from the Central Zone. All deposits plot within the granite field, except for the Ida Dome samples and some of the Husab alaskites. Goanikontes samples have elevated An composition relative to the average. Most of the samples in this study have greater Or than the comparative set from the Rössing SJ deposit. Rössing data are from Freemantle (2006).

***Q'-Anor***

The compositional discrimination diagram is a useful means of illustrating trends in successive generations of evolving granite compositions, and successfully shows the

systematic evolution from diorite to syenogranite composition, in line with petrographic observation of successively felsic grey granite generations at the Ida, Hildenhof and Valencia (Salem type granite) deposits. Within the Grey granites and Salem Suite textural change is particularly varied, from a fine and often foliated tonalite (older) and quartz diorite through to porphyritic granodiorite and monzogranite (younger) with feldspars often larger than the average 46 mm x 27 mm glass slide. Salem and Grey granites of Valencia and Hildenhof, respectively, reflect an evolution from diorite to increasingly granitic compositions with decreasing age (Figure 5.4).

*Q'-ANOR of Grey, Salem, and weakly-Mineralised Sheeted Leucogranites*

Grey and Salem granite sample quartz contents (Q') are highly variable and successively younger granites tend to increase in Q'. The Joly Zone melt apophysis sample from Valencia is an example of Salem granite-hosted uraniferous pegmatite. It is a K-feldspar-dominated granitoid, with typical low An and low Q' of a plagioclase-deficient partial melt.

With respect to leucogranites, Berning (1986); Cuney (1980a and 1980b); and Nex (1997) have shown that mineralised granites tend to be more alkali feldspar-rich than weakly-mineralised varieties. The compositional plots in this section illustrate to a certain extent that the uraniferous sheeted leucogranites are alkali feldspar in composition, but they are not necessarily more K-feldspar rich than most of the non-uraniferous varieties as shown in modal classification plots of Freemantle (2006) at the Rössing deposit. Most SLGs contain anomalous U content with respect to the earths crust, and to typical granite (from Plant *et al.*, 1999). Thus, those varieties that do not possess the typical petrographic characteristics as described in Chapter 4 are termed weakly-mineralised.

The weakly uraniferous sheeted leucogranites cluster in the alkali-feldspar field and show a positive relationship between Q' and ANOR (also An content). B-types have higher Q' than A-types and F-types have the lowest Q' value and plot close to the ANOR = zero axis. The plot reflects their low quartz content, and K-feldspar dominated composition. Deviation into the monzo- and syenogranite and granodiorite fields occurs for the C-types (Figure 5.5a). The Valencia sheeted leucogranite suite is divided into A, B, C, Cm (magnetite-bearing), Ct

(tourmaline-bearing), D, E and F types and plotted in Figure 5.5b, as an example of the compositional variety within a single deposit area.

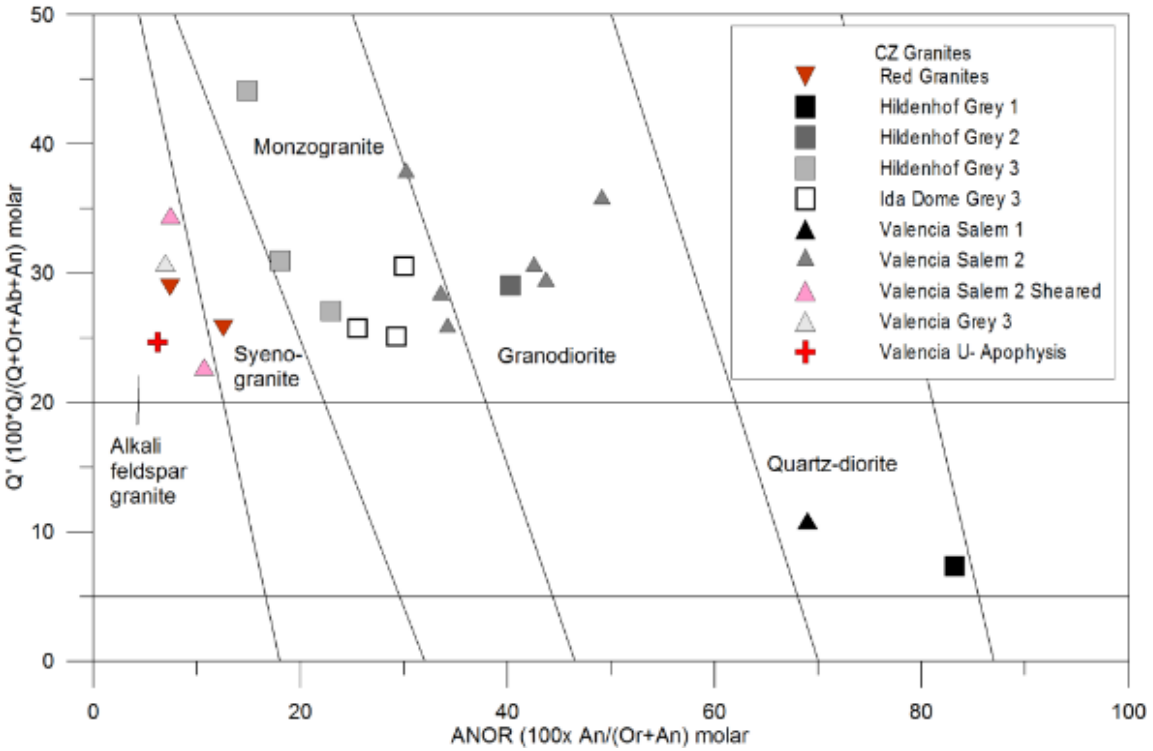



Figure 5.4 Q'-ANOR diagrams of Central Zone uranium deposit granites. Salem and equigranular (Grey and Red) granites at the Central Zone uranium deposits at Hildenhof, Ida Dome and Valencia. The trend from diorite to monzogranite is reflected in successively decreasing mafic content, and increasing K-feldspar proportion observed in petrographic and study.

Compositions range from monzogranite to alkali-feldspar granite; most of the weakly mineralised sheeted leucogranite types plot in the alkali-feldspar field. The quartz content (Q' axis) is highly variable; unaltered samples tend to cluster between Q'=30 and Q'=40. Weakly mineralised varieties predominantly lie below Q'=35. Figure 5.5b illustrates the trends that characterise the weakly mineralised and mineralised sheets at the Valencia deposit. The diagram includes the E 'or oxidised D-types' which have a Q' range from Q'=25 to Q'=48.

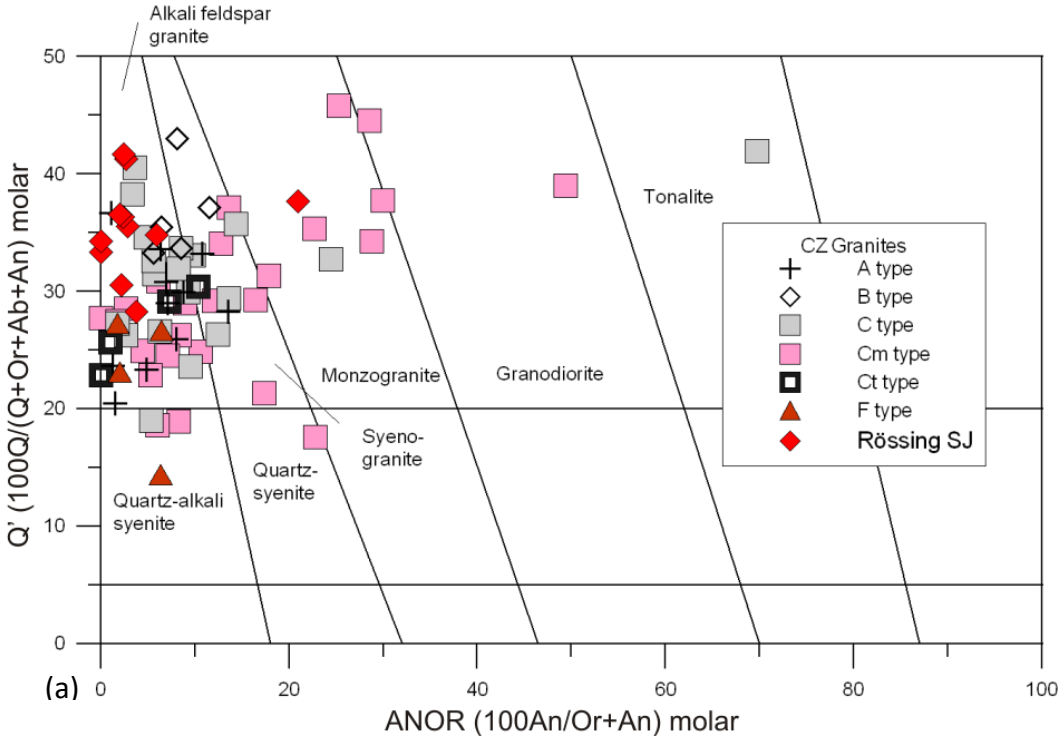



Figure 5.5 Q'-ANOR of the pre- and post-D3 leucogranite type populations of the Central Zone U deposits. (a) Q'-ANOR diagram of pre-D3 sheeted leucogranite from the Central Zone U-deposits. The plot also includes late pegmatite F-type sheets. The majority of the samples are alkali-feldspar granite in composition, exceptions that plot in the monzogranite to tonalite fields are predominantly Ida Dome samples. Rössing sample data: Freemantle (2006).

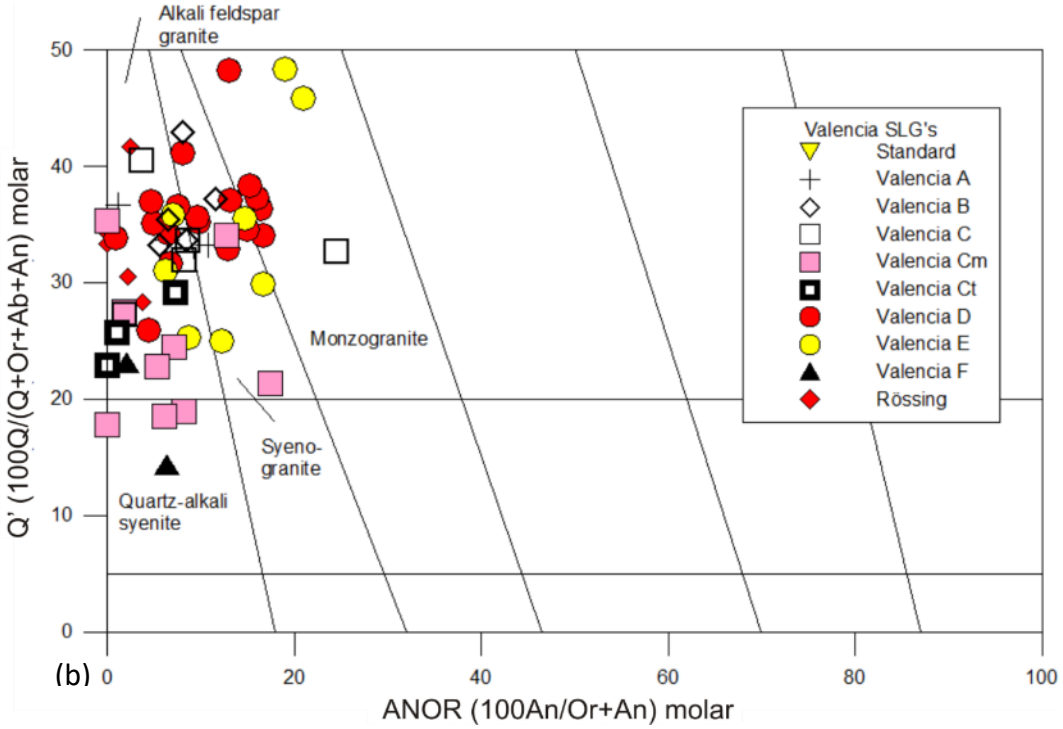



Figure 5.5(b) Q'-ANOR diagram of the sheeted leucogranite suite at the Valencia deposit. Sheeted leucogranite show a wide range of Q' values, which do distinguish between magnetite C types (low Q') and C types (intermediate Q'). Oxidised D-types show a greater variability in Q' than the unaltered D-types. Rössing sample data: Freemantle (2006).*Q'-ANOR of uraniferous sheeted leucogranites*

Uraniferous samples from Goanikontes, Ida Dome, Valencia and Hildenhof are divided into the classic D- and E-types of Nex (1997) and include anomalously uraniferous C-types. The majority plot within the alkali-feldspar and syenogranite fields (Figure 5.6). There are a significant number though, that are in the fields corresponding to higher normative An.

The Hildenhof samples, all from surface, plot within a narrow ANOR range with respect to the nearby Etango deposit samples at Goanikontes. They have low Q' in comparison to the Rössing deposit and Goanikontes samples (Figure 5.7) and Hildenhof (Figure 5.8). The Ida Central, Garnet Valley and Holland's Dome areas highlight a variance in composition between reasonably close-spaced sampling areas (Figure 5.9).

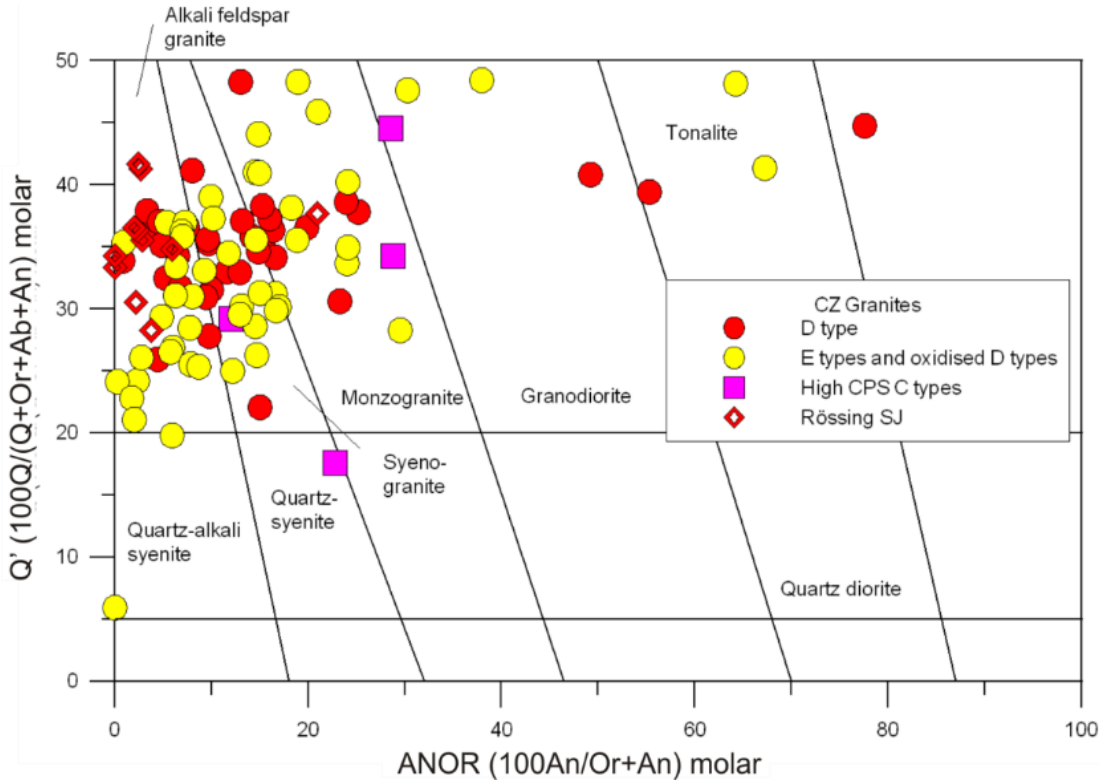



Figure 5.6 Q-ANOR of uraniferous leucogranites. Q'-ANOR of altered (E-type) and unaltered (D-type) alaskites from the primary uranium deposits. D-type samples tend to plot with higher normative quartz than the E-type, and anomalous C-type leucogranites plot with considerably lower normative anorthite.

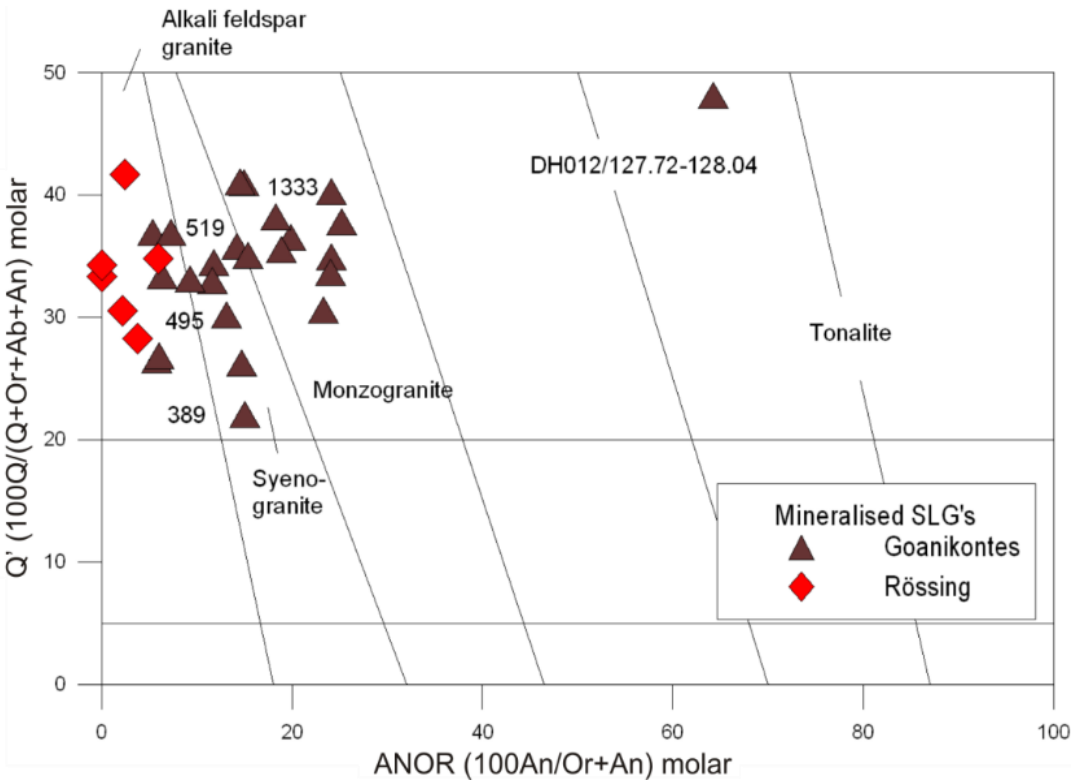



Figure 5.7 Q'-ANOR diagram for mineralised leucogranites from Etango deposit (on Farm Goanikontes) diamond drill core. Goanikontes samples have a range from monzogranite to alkali feldspar granite; the majority of samples have a syeno- to monzogranite composition. There is one plagioclase rich sample which plots accordingly in the tonalite field. The quartz content is higher than the samples from Rössing.

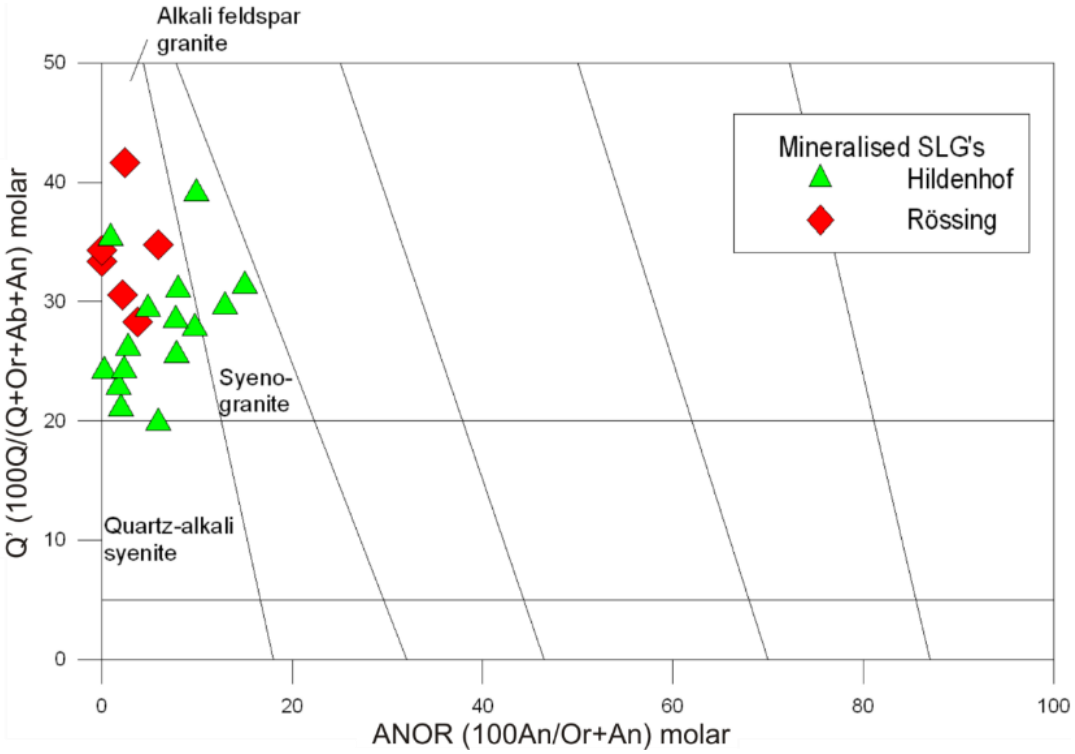



Figure 5.8 Q'-ANOR diagram of Hildenhof mineralised sheeted leucogranite. The majority of the Hildenhof samples are alkali – feldspar granite in composition, quartz content is slightly lower than those sampled at Rössing.

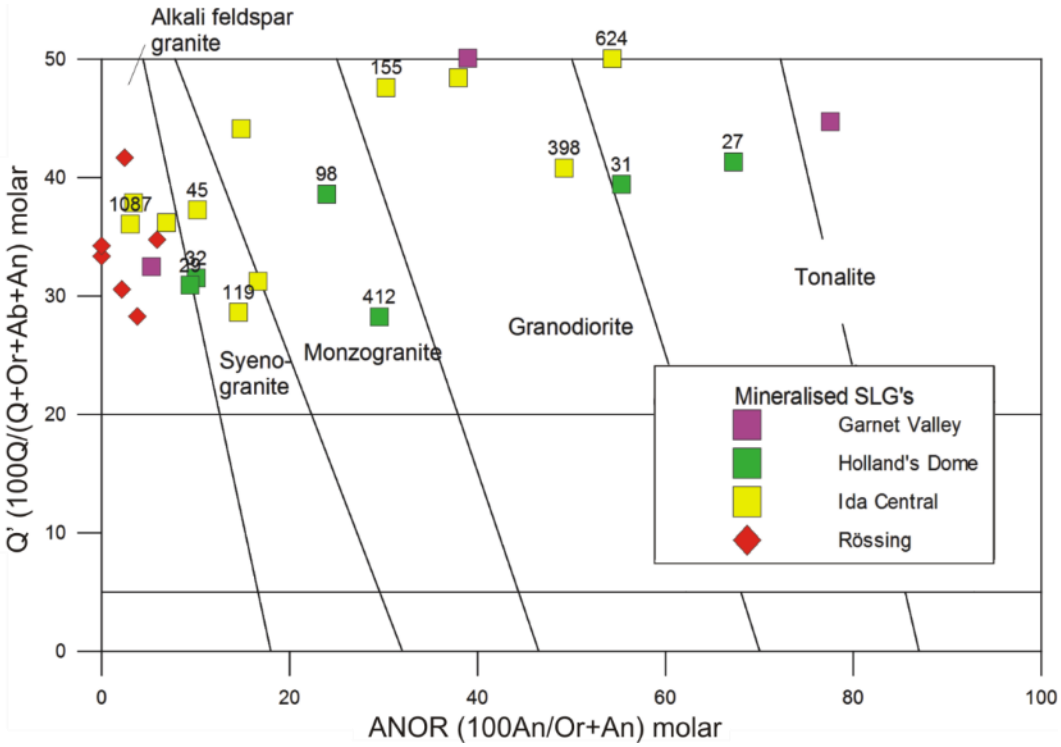



Figure 5.9 Samples from the Central, Garnet Valley and Holland's Dome deposits. The samples show variation in normative An content and relatively high quartz content compared to the Rössing samples. Plagioclase (albite-oligoclase) is present in all Ida Central thin sections. External Ca and Si is contributed to the system by reactive calcareous units of the Khan and Rössing Formations.

Q' and ANOR ratios are the most variable within the Ida Dome and Husab deposits sampled in this study, particularly the Ida Central and Holland's Dome sample sets. Husab samples were sourced from core at a variety of depths, and are presumed relatively free of any meteoric water interaction (Figure 5.10). The samples plot with highly variable Q' values, and An ratios similar to the Rössing reference samples. The great variation in Q' is interpreted as a reflection of differing sample compositions given their pegmatitic textures. Q' unlike ANOR, is less likely to be affected by meteoric water which may mobilise Ca.

The Valencia samples are similar to the compositions of Rössing samples and ANOR values only exceed 20 in one sample, Va26 113/ 225.64-225.89. The highest U content (997 ppm in Va26 139/ 104.50-104.78) is found in a sample with a composition similar to the Rössing samples (Figure 5.11). Plagioclase is present in some samples but not in the proportions observed in the Ida Central samples, which may explain low An ratios. Samples do not show the same amount of alteration observed at the Ida Central area. There is a distinct clustering of samples, with the more uraniferous specimens showing relatively low Q' and low ANOR.

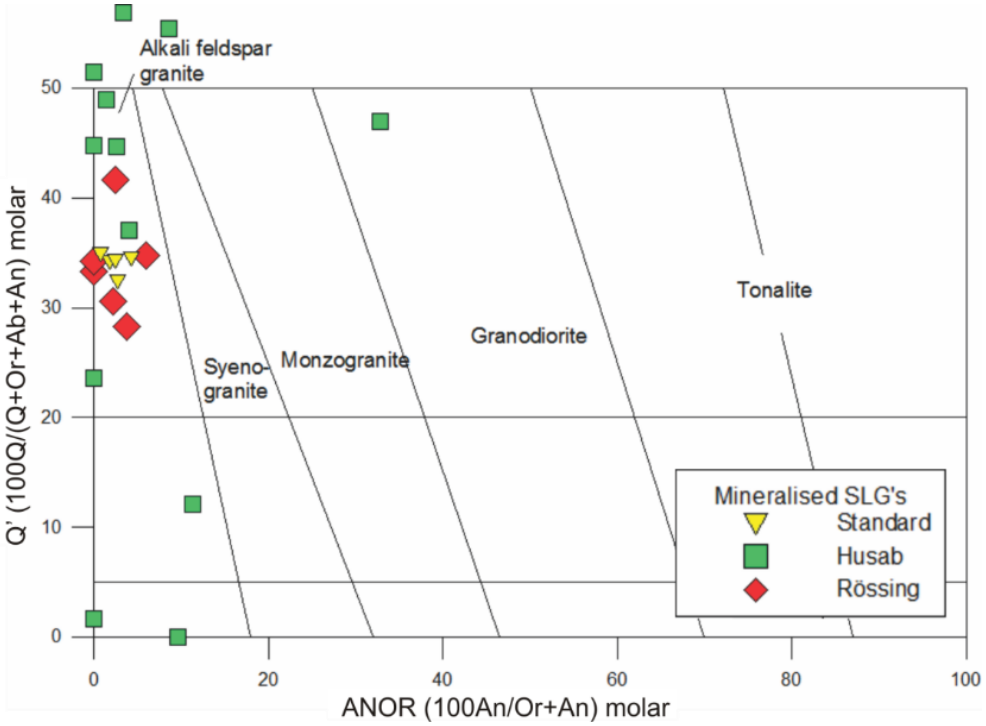



Figure 5.10 Q'-ANOR diagram of selected Husab mineralised leucogranites (alaskites). The Husab samples display a wide range of CIPW calculated mineral compositions, a product of wall rock and fluid interaction. Samples are all sourced from 'fresh' NQ core and are assumed free from prolonged meteoric weathering associated with surface - sourced samples at the other deposits.

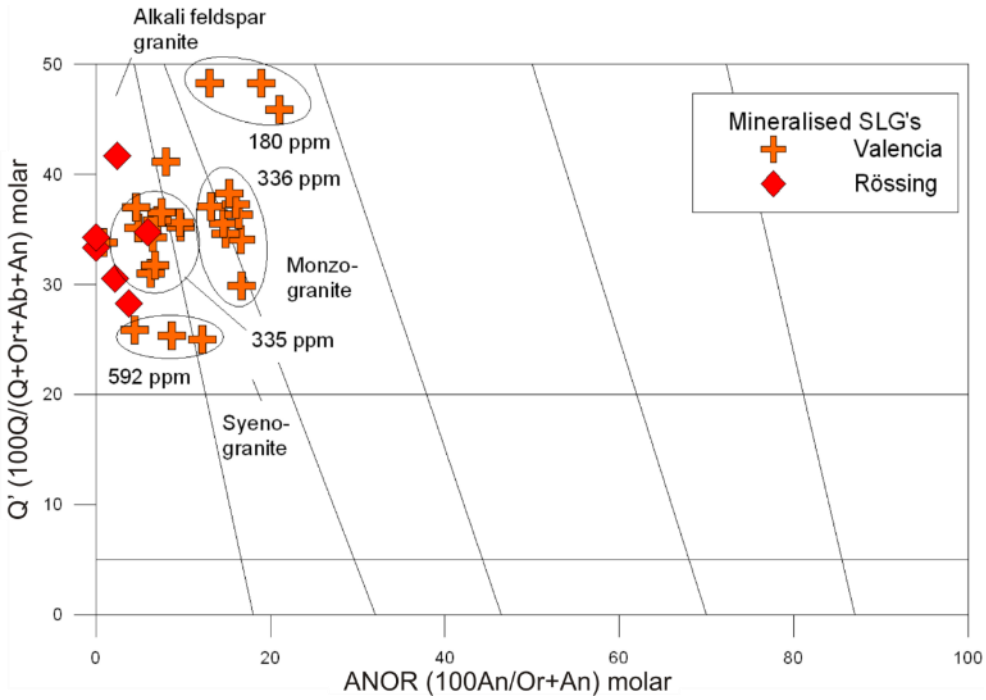



Figure 5.11 Valencia mineralised sheeted leucogranites. Samples tend to plot with Q' <40 and ANOR <20. The circled clusters highlight mean U values in ppm. The highest average grade samples from Valencia have similar Q' to the Rössing samples, and plot near the alkali-feldspar field. Rössing sample data: Freemantle (2006).

The plots on the Q'-ANOR diagrams of this study show that compositions calculated by major element molar proportions are varied from deposit to deposit. The relatively unaltered D-type leucogranites have a narrower range of Q' than the variably altered E-type leucogranites. The alteration may reflect the addition of new quartz through late Si-rich fluid circulation, and may include a component of feldspar replacement (albite rims and K- and plagioclase feldspar breakdown).

Uranium content is weakly related to Q' content, if at all, in unaltered D-types of the Etango deposit samples at Goanikontes, but are inconsistent in the Hildenhof and Valencia samples. The uraniferous Hildenhof population shows the least variance in ANOR values, despite being entirely sampled from surface locations, which might have resulted in K-feldspar breakdown or ingress of Ca from groundwater. While the uraniferous sheets are predominantly alkali feldspar granite in composition, in areas where there is skarn or carbonate-silicate rock interaction there is a broad, inconsistent compositional scatter in Q' and ANOR, as illustrated in the Ida Dome area, particularly at Holland's Dome.

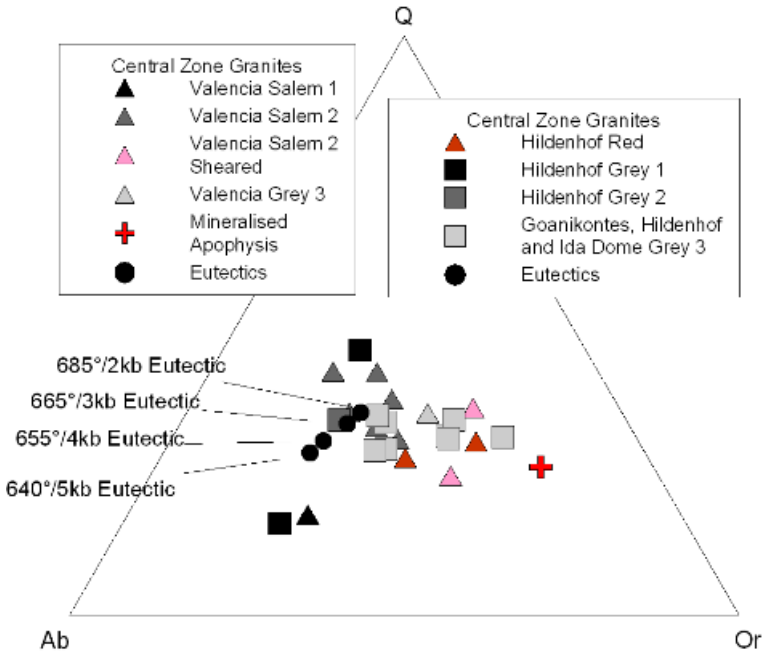
The Q'-ANOR diagrams are suitable for characterising the evolution of compositions of the equigranular-textured and Salem granite generations, but not for different varieties of leucogranite. Sample conditions have a profound influence on the CIPW norm calculations, and the great number of samples that are surface derived, and those that show prominent evidence of alteration, at depth, also plot with variable ANOR, but alteration is difficult to link to Q'. The diagram is thus only useful for interpreting the original compositions of pristine, unaltered granites, of which there are limited numbers at a given deposit

### *The Granite System Ternary Diagram*

The granite system diagram, devised by Tuttle and Bowen (1958), showed that magmas of granitic composition (normative albite, orthoclase and quartz) crystallised at a series of eutectics determined by the relationship between temperature and pressure. The diagrams that follow include four of the eutectics (from Rollinson, 1993) that are close to the conditions believed to have prevailed in the Central Zone. These conditions of metamorphism around the uranium deposits are described in Longridge *et al*. (2014);

Longridge, (2012); Ward *et al.* (2008); Goscombe *et al.* (2003a); Jung and Metzger (2003a); Nex *et al.* (2001b); and Tack and Bowden (1999). The sheeted leucogranites, when plotted on the granite system diagram, show deviation (with some consistencies) from these predicted eutectics. The Rössing samples from Freemantle (2006) for comparison seem follow the eutectic trend, potentially because they are limited within spatial context to a particular part of the Rossing SJ deposit.

Equigranular Red and Grey granites and the Salem samples cluster around the high T low P eutectics (Figure 5.12). The Grey granite samples of the Swakop River Deposits (Goanikontes, Hildenhof, Ida Dome) tend towards the Or apex with decreasing age. Sheared and partially melted Salem samples plot with higher Or proportions than undeformed samples.




(a)

Figure 5.12 Normative orthoclase-quartz-albite ternary plots of Grey and Salem granites of the CZ uranium deposits. Equigranular granites analogous to the type-3 grey granite at Hildenhof are included from the Ida and Goanikontes deposits. The trend with age toward the Q apex is apparent in the sheared and partially melted samples. Eutectics from Rollinson (1993).

Figure 5.13a shows that Goanikontes and Hildenhof mineralised samples plot with a narrow range of Q:Ab and a wider range of Or:(Ab + Q). E types reflect increased Q proportions associated with magmatic fluid alteration (new Q veins, silicate leaching/clay alteration/new Ca). In Figure 5.13b, the Husab alaskite population lacks linear trends or any consistency in distribution. The least altered Husab samples plot with low Ab with Q>Or, while one oulier

plots with lower Q than the Rössng samples because of interaction at the metasediment contact.

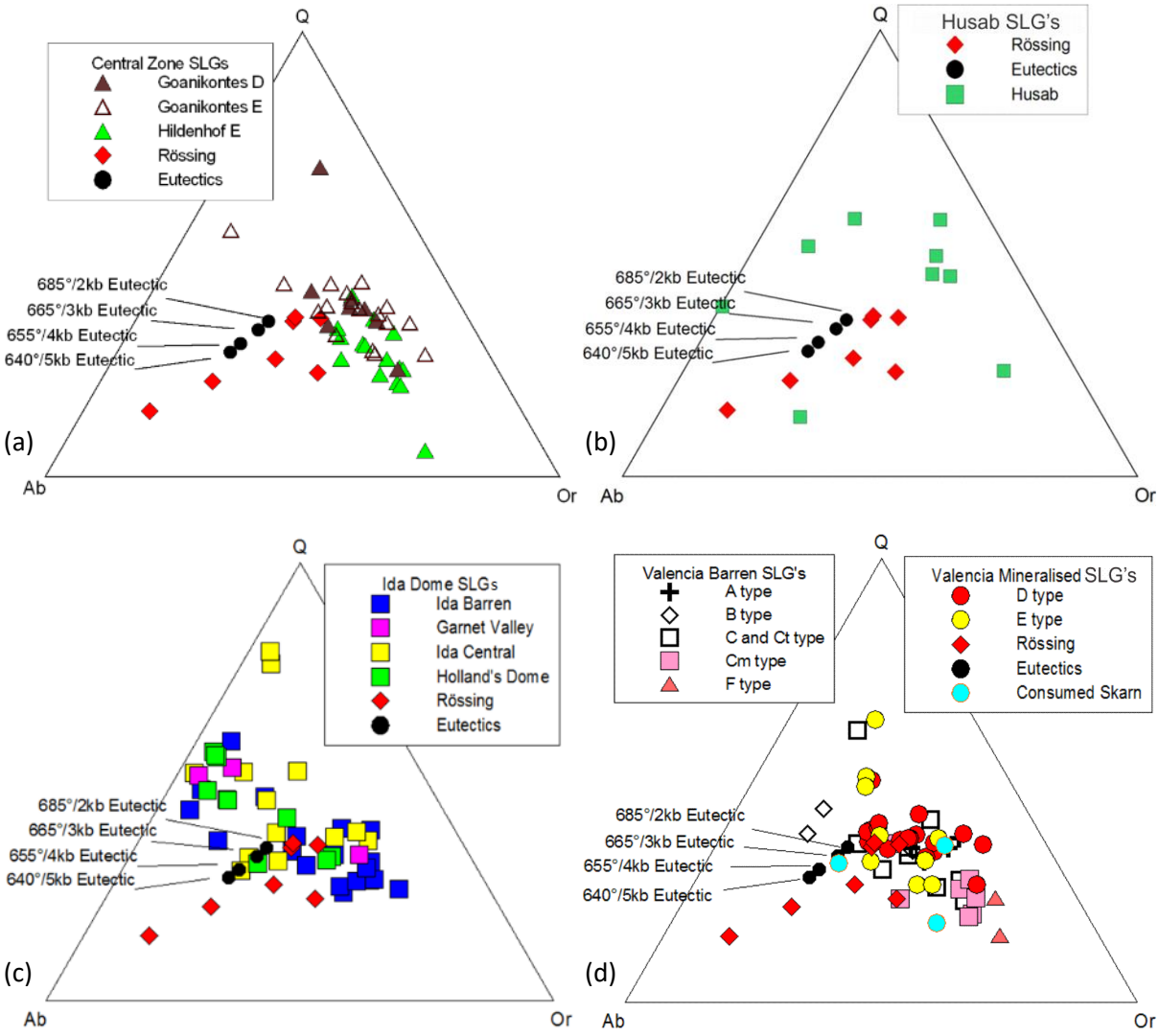



Figure 5.13 Normative orthoclase-quartz-albite ternary plots of sheeted leucogranites of the CZ uranium deposits. (a) Granite ternary system diagram of the Etango (Goanikontes) and Hildenhof mineralised sheeted leucogranites. Q is higher than the Rössing samples and oxidised (open triangles) samples, on average have higher, Q proportions. (b) Granite ternary system diagram of Husab alaskites. Q proportions are higher than the Rössing samples and plot with a broad range of Or. The poor correlation with the expected eutectics compares with the scattered plotting seen on the granite classification diagrams. (c) The granite ternary system diagram of the Ida Dome deposits; mineralised sheeted leucogranites are in colour and weakly mineralised varieties are in blue. The majority of the weakly mineralised samples plot below the eutectics (in terms of Q) with a relatively narrow Ab-Or range. The mineralised sample plot roughly into two groups; one group varies along Ab-Or with a narrow Q range, the other reflects inconsistent composition with very low Or, and have the highest Q content. (d) The granite ternary system diagram of Valencia granitoids. Trends in the successive sheeted leucogranite generations are not clear cut, but the F-type and Cm-type have the highest Or component and the mineralised varieties have higher quartz content overall.

Mineralised Ida Dome samples plot in roughly two groups, one group follows the eutectic trend, with an Or apex bias, the other represents the altered population with very low Or compositions (Figure 5.13c). The majority of the weakly mineralised samples plot toward the Or apex, with clustering reflecting lower degrees of host rock contamination, relative to the mineralised samples. Figure 5.13d shows the Valencia sample set, along with the Goanikontes and Hildenhof samples are more consistent than the Husab and Ida Dome deposits. C-types show lower Ab:(Q + Or) than the mineralised samples. The D- and E-type (oxidised) samples plot close to the high T low P eutectics. They also show much lower deviation and are therefore assumed to reflect lower degrees of host rock interaction and contamination.

***Discussion of the Granite Eutectics***

The leucogranite populations at each deposit vary considerably with respect to normative Or, and less so with respect to their An and Ab proportions. Ida Dome samples have low Or relative to the other deposits, but are higher in An with a noticeable cluster toward the Ab apex (Figure 5.13c). The sheeted leucogranite samples from all areas have on average higher An than the Rössing samples, which would be expected to have variable Ca given the marble abundance at the deposit.

Red granites with Ca enrichment are described and interpreted at Goanikontes as being a result of country rock assimilation, particularly where marble is present (Nex, 1997). Similarly, the deviations from the eutectics (Figure 5.12a) are attributable to the variations in country rock compositions into which the granites have intruded. Granite populations in the Ida Dome deposits show the widest ranges of major element compositions (Figure 5.9 and Figure 5.13c). Particularly reactive carbonate-bearing sediments are relatively abundant and form prominent hangingwalls above the Khan Formation, evidence of contact metamorphism is abundant in the extensive skarn outcrops and the availability of Ca has affected the whole-rock composition of the intrusives, particularly the uraniferous types. The weakly mineralised samples predominantly occur lower in the Khan succession (toward the core of the Holland's Dome antiform) or higher in the Rössing-Chuos, away from the reactive calcareous units near to, or at, the Khan-Rössing transition. Interactions with the

reactive host rocks are the most suitable explanations for the scattered plots that characterise the local Ida Dome, Husab and Goanikontes samples:

- The sheeted leucogranites at the Ida Dome have pooled beneath relatively thick (10 m to 100 m scale) marble packages, and interaction with attenuated metamorphosed evaporite units and calcsilicates units is likely to have contributed to inconsistent additions of Ca and Na to the intruding magma;
- Husab samples have highly variable ratios of Q-Ab-Or which reflect the degrees to which the alaskites have interacted with- and assimilated the reactive Rössing Formation units.
- Goanikontes and Hildenhof have significantly less calcareous metasediment to provide excess Na and Ca and therefore plots cluster with consistent Q:Ab, with most variation in K-feldspar content (Figure 5.12b). The low degrees of sediment interaction and assimilation at Valencia are reflected in close clustering of the uraniferous samples on ternary plots. Magnetite-bearing sheets cluster toward the Or apex, which compares consistently with the low ANOR values of the Valencia sheeted leucogranites.

## 5.6 Aluminium Saturation Index

The Aluminium Saturation Index, referred to as the ASI of Zen (1986), was defined as molar $Al_2O_3/(CaO+K_2O+Na_2O)$ by Shand (1927) and is an important and effective means of determining the granite types.

The ratio of molar Al/molar Na + K of Clarke (1981) also applies to all diagrams to follow. The fields of metaluminous and peraluminous (from Shand, 1927) are included as they are shown by Chappell and White (1974a) to be important, not only in assessing the composition, but also the inferred source of the granites (I-Type vs. S-Type). The modified ratio ASI = 1.1 described by Chappell and White (1974b, 1992), was used to discriminate between I- and S-Type granites of the Lachlan Fold Belt and are included in some of the

diagrams that follow. In the Lachlan context, S-types are peraluminous and I-types are metaluminous, as a generalisation.

It is possible to discriminate aluminium saturation and alkali index on a single diagram between granite populations, simply A/CNK vs. A/NK. The diagram however is not suitable for discriminating between I- or S-type granites in the case of the leucogranites, as the source rocks are not unequivocal and may include a range of mixed litho-types, especially if derived from a potential source such as the geologically complex Abbabis metamorphic complex. In addition, contamination from the pelitic host rocks and the abundant petrographic evidence of sub-solidus reaction textures, feldspar replacement and widespread alteration features, evident in observations presented in Chapter 4, further limit the aluminium saturation diagrams, and derivatives thereof, as robust tools for leucogranite source rock discrimination.

In the diagrams that follow, aluminium saturation plots are presented on A/CNK vs. A/NK diagrams. Plotting these two ratios against each other allows for an ASI line as well as an alkalinity line.

Despite the limitations described above, the diagrams are useful in highlighting the highly variable range of compositions in the granite suites of the Central Zone deposits. The Grey, Red, and Salem suites show a successive trend in decreasing Al saturation; where the high peraluminosity of the most mafic type reflects the abundant biotite and high proportion of oligoclase relative to the younger generations. The systematic trend supports an evolving suite with successively less plagioclase fractionating and increased K-feldspar content (Figure 5.14a).

The type 1 Salem and Grey granite samples plot within the metaluminous field, as the proportion of oligoclase is greatest in the primitive granites. An alternative classification parameter is presented by Ludington and Mossotti (2008)[42] in which the perpendicular distance of a sample from the A/CNK = A/NK is plotted against $SiO_2$ wt.%. The parameter is the Alkali- Alumina Index (AAI) and successfully shows a decreasing AAI value with increasing

[42] AAI is simply calculated 0.707*(PI-ASI) where PI is A/NK and ASI is A/CNK).

silica content as the Grey and Salem granites evolve from mafic-rich to felsic-dominated (Figure 5.14b).

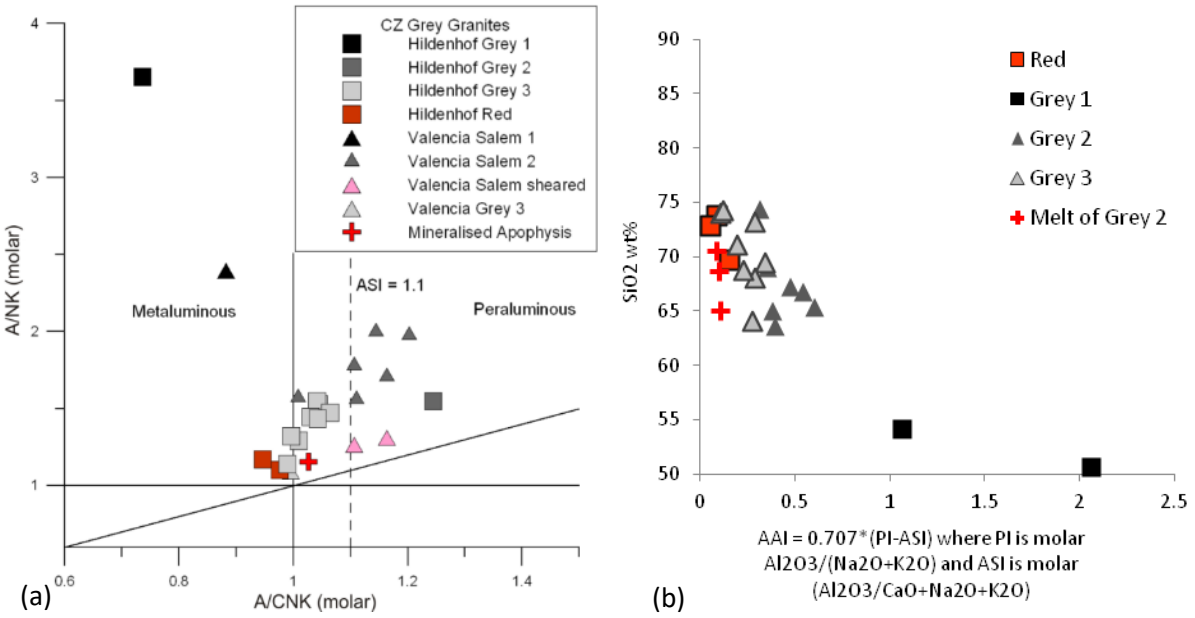



Figure 5.14 Aluminium saturation diagrams of the granite suites at the Central Zone primary uranium deposits. (a) The Grey and Salem type granites plot with successively decreasing peraluminosity between type 2 and type 3 generations. The diorite composition type 1 Grey and type 1 Salem samples plot within the metaluminous field; petrographic observation of abundant plagioclase with >20 % An is reflected in high A/NK and low A/CNK. (b) Alkali-alumina index vs. silica for the Grey and Salem suite samples. The diagram shows the successive decrease in AAI as silica saturation increases. Partial melt in the Salem granites comprise almost entirely K-feldspar and quartz, and plot with correspondingly low AAI.

The Grey and Salem samples are the least evolved, and have the higher $CaO:SiO_2$ values, consequently, normative anorthite may be as high as 35 % (HILG 02) and in the Salem granites An by optical determination is consistently higher than in sheeted leucogranite. The earliest generation Grey and Salem granites therefore plot as outliers, with high A/NK and low A/CNK. Husab Samples are included as the deposit lies between the Ida Dome and Rössing Mine, providing a spatially intermediate set for comparison. Most Husab samples plot on the peraluminous side, with the greatest variation between Al and (Na + K) ratios.

Leucogranites from the Hildenhof and Valencia deposits and some Ida Dome samples plot parallel to the A/CNK = A/NK line. A single Ida Dome sample plots well into the metaluminous field. The majority of Goanikontes, Ida Dome and Husab samples show a large variation in A/NK and do not fit into the metaluminous or peraluminous fields with any obvious consistency (Figure 5.15). Sources of calcium include contamination from calcareous

host rocks in addition to the Ca - rich plagioclases expected in the Salem granites. A summary of the $Al_2O_3$, CaO, $Na_2O$ and $K_2O$ wt.%, values for each of the outlying sample is given in

Table 5.6 and average molar proportions of the Ida Dome deposit samples are compared in Table 5.7. Holland's Dome samples in particular have high CaO, which is expected given the abundance of U mineralisation associated with skarns. IDAG 46 serves as an example of an altered sample with elevated CaO content.

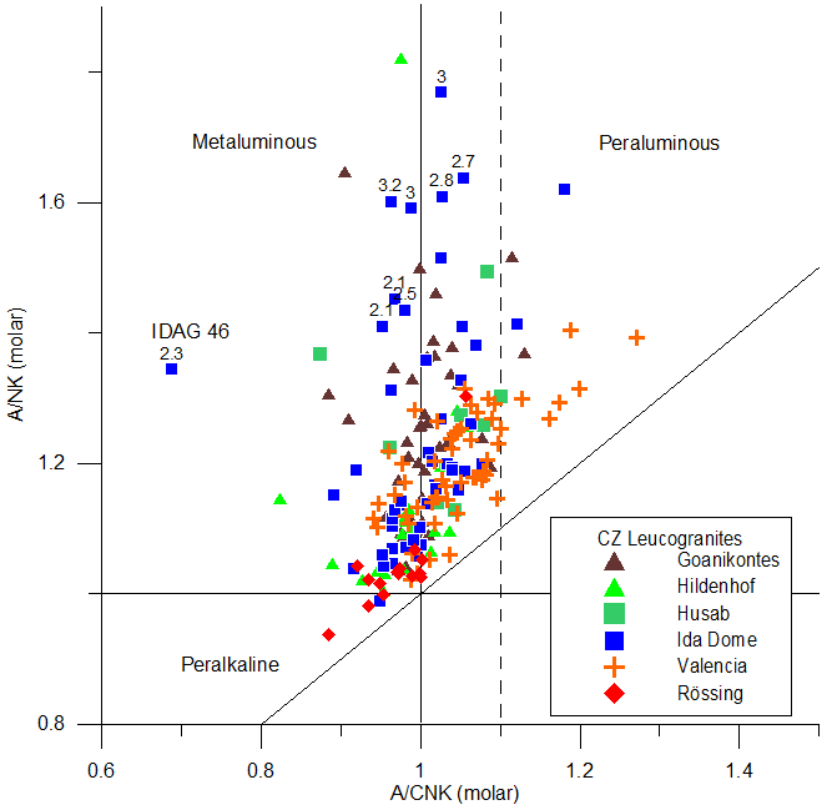



Figure 5.15 Aluminium saturation diagram of sheeted leucogranites from the Goanikontes, Hildenhof, Husab, Ida Dome and Valencia deposits. Rössing sample data: Freemantle (2006). Outliers- These samples are an illustration of how significantly CaO content affects the composition of the Central Zone granites and thus their position on some geochemical diagrams. For example, most of samples with >2 wt. % CaO are from the Ida Dome, and labelled as such.

Table 5.6 Summary of the $Al_2O_3$, CaO, $Na_2O$ and $K_2O$ wt.% values of the outlying sample, with U in ppm (XRF).

| Sample | Type | $Al_2O_3$ (wt.%) | CaO (wt.%) | $Na_2O$ (wt.%) | $K_2O$ (wt.%) | $K_2O/Na_2O$ | $CaO/(K_2O+Na_2O)$ | U (ppm) |
|---|---|---|---|---|---|---|---|---|
| **IDAG 46** | E | 5.33 | 2.3 | 1.83 | 0.88 | 0.48 | 0.77 | 428 |

Table 5.7 Molar proportions of Al, Ca, Na and K at the Ida Dome Deposits.

| **Molar Proportions (wt.%/Molar mass of oxide)** | | | | | | | |
|---|---|---|---|---|---|---|---|
| Ida Dome Area | An (Ca/(Ca+Na) | C/NK | Al/Ca | K/Na | A/NK | Al | Ca |
| Central | 0.27 | 0.17 | 14.28 | 1.7 | 1.19 | 12.38 | 1.1 |
| Garnet Valley | 0.29 | 0.22 | 15.55 | 1.64 | 1.31 | 13.08 | 1.39 |

| | | | | | | | |
|---|---|---|---|---|---|---|---|
| Holland's Dome | **0.34** | **0.26** | **9.55** | **1.38** | **1.35** | **13.41** | **1.7** |
| Average | 0.30 | 0.22 | 13.13 | 1.57 | 1.28 | 12.96 | 1.40 |

***Aluminium Saturation Indices of Uraniferous Leucogranites***

The mineralised sheeted leucogranite populations of the Central Zone deposits follow predictable trends, similar to those of the previous diagrams (Figure 5.17). Goanikontes samples plot with higher A/NK than Hildenhof samples, and in general greater variation in Al ratios. The outlying Goanikontes sample shows intense sericite alteration of plagioclase in petrographic observation (Figure 5.17a).

Holland's Dome samples in particular are all above or below the Ida Dome averages. The majority of the weakly mineralised Ida Dome samples plot close to the Rössing sample set, emphasising the inhomogeneity (contamination) of the composition of the mineralised samples (Figure 5.17). In hydrothermal-like environments such as skarn localities, where reactive rocks de-gas and provide fluids, the granites have lost Na and K relative to Ca (the process at Ida is similar to what is described in Barker (1998). The presence of calcite in microfractures of Ida samples (Chapter 4) also indicates Ca deposition in events subsequent to emplacement. This interpretation is somewhat equivocal given the polymetamorphic nature of the orogen, and the relatively late stage of uraniferous SLG intrusion.

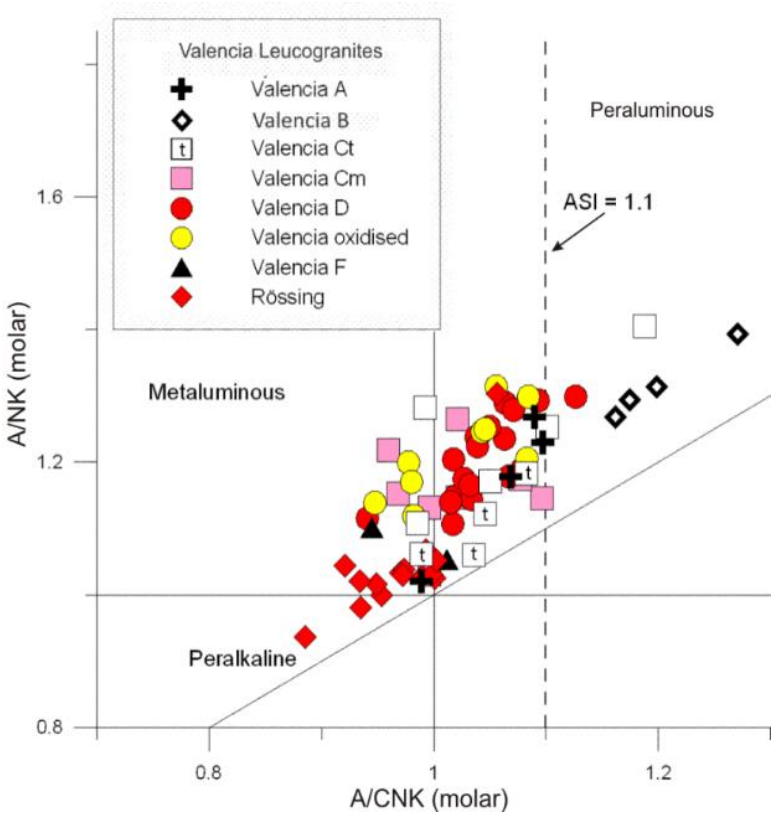



Figure 5.16 Aluminium saturation diagram of the Valencia leucogranite suite. The variety of leucogranites at Valencia cluster to the left of ASI = 1.1, the B types are the most peraluminous and the Ct-types follow the 1:1 line nearer than the other C types. The D-types are all more peraluminous than the oxidised varieties. Rössing sample data: Freemantle (2006).

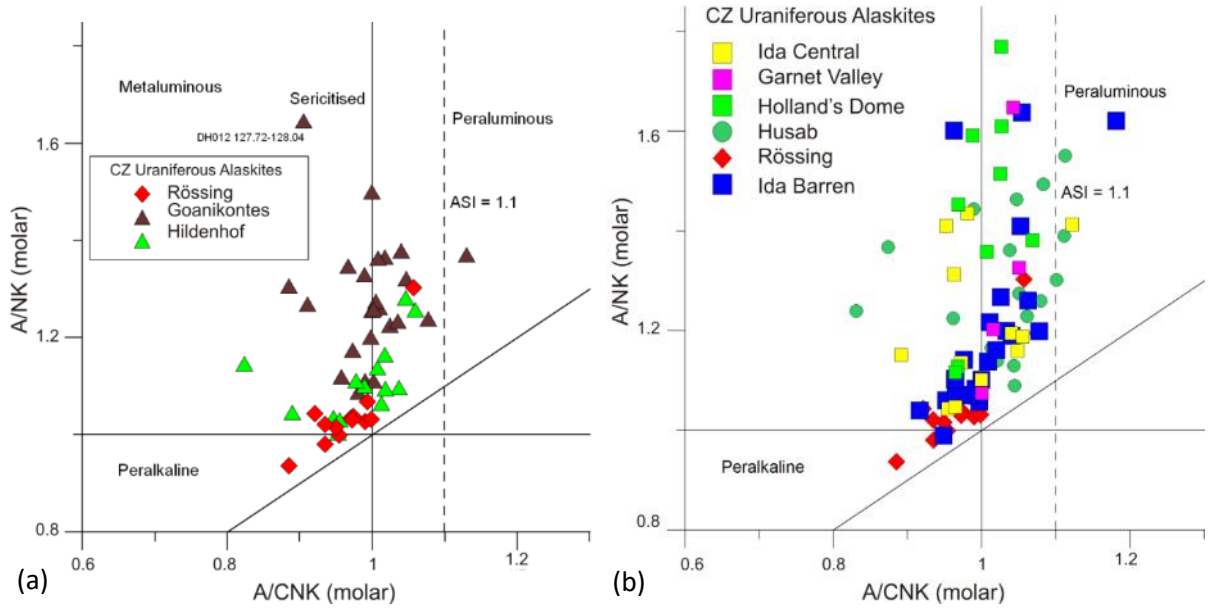



Figure 5.17 Aluminium saturation diagrams of uraniferous sheeted leucogranites. (a) Aluminium saturation diagram of Goanikontes and Hildenhof mineralised sheeted leucogranite. The variety of alteration in Goanikontes samples results in greater deviation from the Rössing trend than the Hildenhof samples, which are all surface samples. Rössing sample data: Freemantle (2006). (b) Aluminium saturation diagram of Ida Dome area and Husab mineralised sheeted leucogranite. Ca content contrasts significantly between the deposits at the Ida Dome. The Holland's Dome samples have the highest deviation from the Rössing sample trend as a result of Ca mobility during interaction with the numerous skarn pods at the deposit. The Ida Central samples have a closer fit to the Rössing samples. Rössing sample data: Freemantle (2006).

*Aluminium Saturation Index Discussion*

Granitic rocks typically have low Ca, so a slight variation in Ca content results in prominent deviations when plotting some discriminatory geochemical diagrams, particularly aluminium saturation diagrams. Because of the sensitivity with respect to Ca, quantifying how much skarn interaction has taken place is limited. The high- and low-T processes, responsible for adding calcite, are also responsible for removing K and Na, and in a low-T environment as Al is lost (after Barker, 1998). Considering this, the aluminium saturation diagrams when applied to the variably altered and weathered sheeted leucogranite suites at best can characterise individual sample areas with specific, consistent, traits.

*Alternative and Cationic Discrimination Diagrams*

The IUGS classification scheme modified in the Q'-ANOR diagrams of Le Maître (1989); the diagrams of Barker (1979) and the various cationic plots (e. g. De la Roche *et al.*, 1980) are not universally applicable to granitoids, primarily because they are genetic and do not account for variability in mafic phases (Frost *et al.*, 2001). Mafic-rich Central Zone granitoids (Red, Grey and Salem suites) may plot in the same fields as the leucogranites in diagrams such as the ANOR-Q' scheme of Le Maître (1989). Frost *et al.* (2001) present a series of binary classification plots that are more universally applicable to granites.

The preceding classification diagrams showed that samples, particularly from the Ida Dome areas deviate from compositional ranges shown for given pressure and temperature conditions (ternary Granite System diagram). Aluminium Saturation Index diagrams also produce highly erratic aluminium plots, where ratios vary a great deal with respect to normative Ca, K and Na. The variable compositional plots are influenced primarily by high-temperature alteration, near-surface weathering (and feldspar breakdown) and interaction with host rocks (mobile elements being incorporated into granites at reactive contact margins). Further plots were selected to emphasise that individual deposits have unique trends within their localised sheeted leucogranite suites.

Mineralised alaskites, in comparison to the other sheeted leucogranite varieties at Valencia, tend to have higher $SiO_2$ content (Figure 5.6). The high silica content reflects the

trend indicated in the Q'-ANOR diagrams, and the noticeably high quartz content typical of the mineralised sheets. The most aluminous granites at Valencia are the garnet-bearing B type sheeted leucogranite. They are also the only type that plot entirely to the right of the ASI = 1.1 line. Tourmaline-bearing sheeted leucogranite (Ct-type sheeted leucogranites, labelled- subscript 't') lie closer to the 1:1 line than the C and Cm-types. D-types are peraluminous while the majority of the oxidised varieties (E-type sheeted leucogranite) are metaluminous, relative to the 1:1 line.

### *The Modified Alkali-Lime Index - MALI*

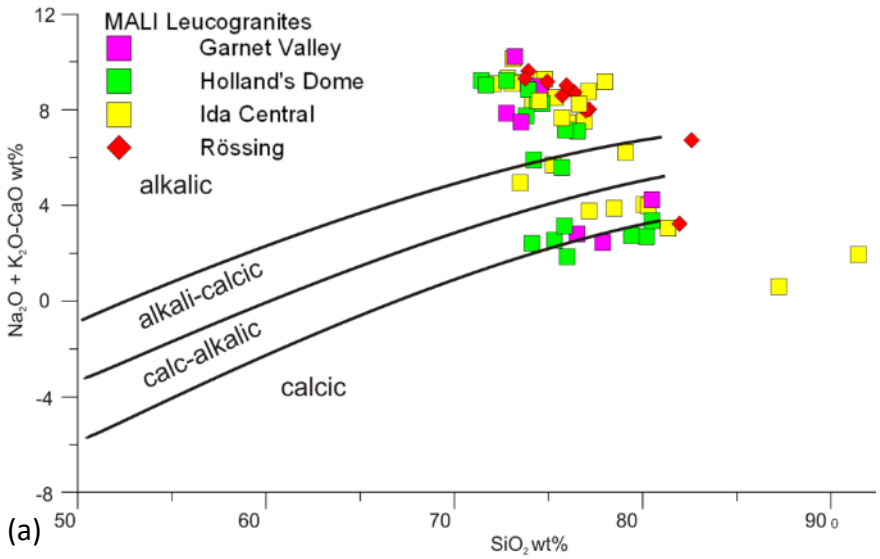
The modified alkali lime index or MALI is described in detail by Frost *et al.* (2001) and is applicable to granitoids over a wide range of silica values. It is calculated from weight percentages of $Na_2O + K_2O - CaO$, and is ideal for the mineralised granites where $SiO_2$ content is considerably variable. In theory, MALI should increase with increased wt.% $SiO_2$ in any given suite of unaltered granite.

The MALI index for the samples from the Ida Dome area plot with a bimodal distribution (Figure 5.18a). The upper cluster shows a similar plotting position to samples from the Rössing mine, while the lower one reflects elevated CaO in altered samples. The negative slopes with respect to silica are indicative of silica increase and Na and K loss relative to Ca during magmatic fluid activity (Figure 5.18a). The Husab deposit samples plot with a great range of Si and variable MALI range. Compared to mineralised Holland's Doem samples, the Husab samples show no relation or trend, and have probably incorporated high quantities of Ca relative to Na and K. Thus, all of the Husab samples should be treated as altered granites (Figure 5.18b).

The Etango samples (Goanikontes) plot largely within the alkalic field, there is no distinctive trend with respect to $SiO_2$ content (Figure 5.19a). The least-altered uraniferous samples plot close to the Rössing mine samples, whereas the remainder of the samples represent the altered uraniferous leucogranites, and the MALI indices of the weakly mineralised varieties. The majority of the Valencia samples plot close to the Rössing mine MALI indices, with low

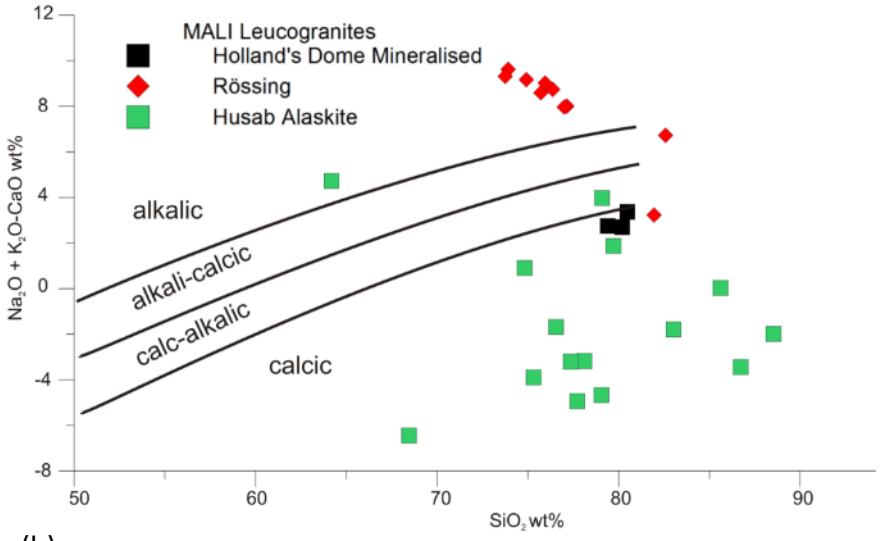
Ca samples plotting higher in the alkalic field, and a small number of altered, uraniferous samples plotting between the calcic and alkalic fields (Figure 5.19b).

The mineralised samples of the Valencia deposit cluster close to the Rössing sheeted leucogranite samples, and show the lowest variance in MALI and $SiO_2$, except for a few outlying plots. Some of the high-MALI weakly mineralised sheeted leucogranites from Valencia show a positive $SiO_2$ correlation, the only group of samples to display this trend. The tight clustering of the Valencia mineralised sheeted leucogranites is attributed to the relatively weak oxidation and low proportions of wall rock contaminants in the sample suite.




(a)

Figure 5.18 Modified alkali-lime index diagrams of the Ida Dome and Husab leucogranite suites. (a) Ida Dome sheeted leucogranite. Two clusters are apparent, the upper conforming to the Rössing trend and the lower following the expected positive MALI/$SiO_2$ trend.




(b)

Figure 5.18(b) Modified alkali-lime index diagram of Husab Alaskites showing a positive MALI/$SiO_2$ trend. Field lines from Frost *et al.* (2001) and Rössing sample data: Freemantle (2006).

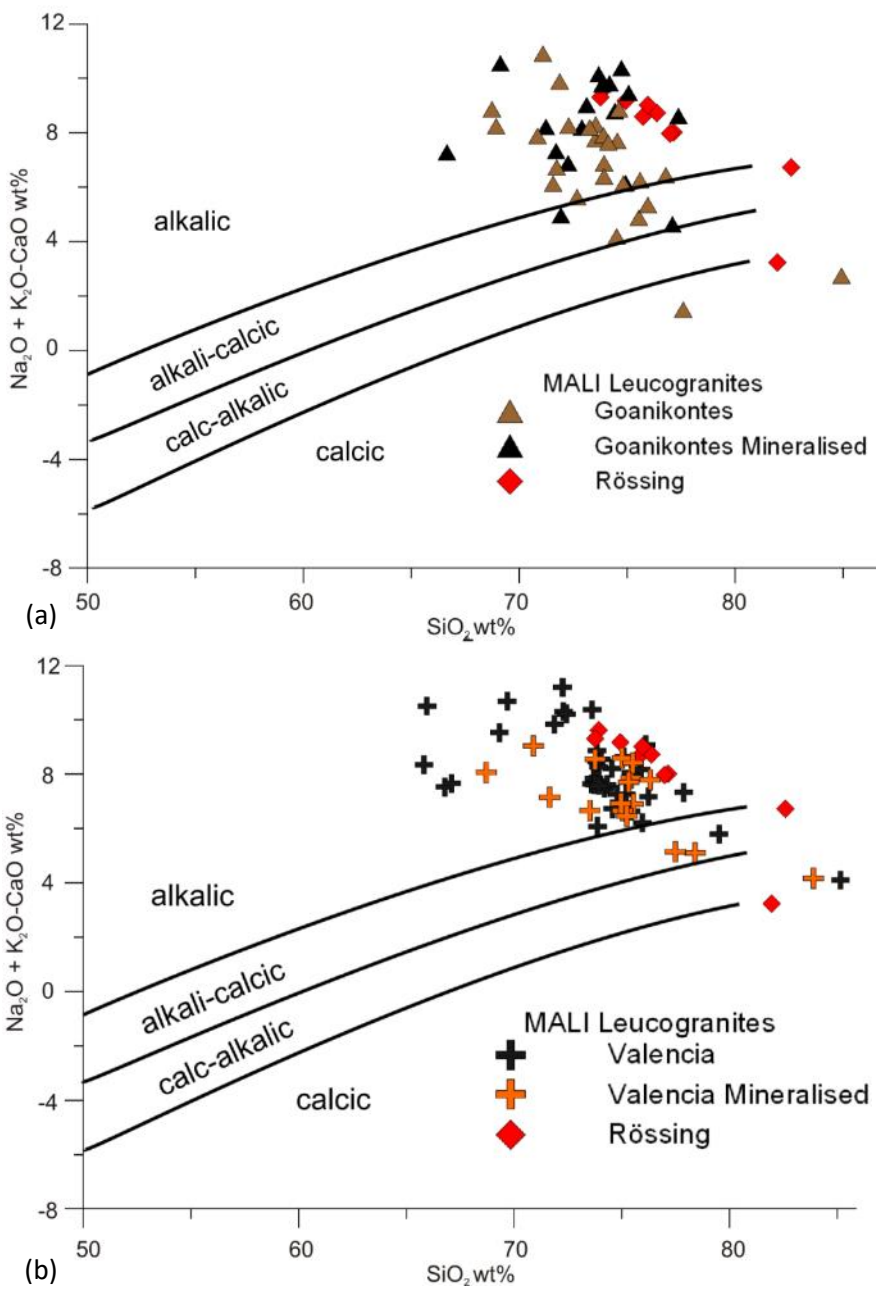



Figure 5.19 Modified alkali-lime index diagrams of the Goanikontes and Valencia leucogranite suites. (a) Modified alkali-lime index diagrams of Goanikontes sheeted leucogranite. Mineralised and weakly mineralised samples lie predominantly within the alkalic field.

(b) Modified alkali-lime index diagrams of Valencia sheeted leucogranites. The majority of samples cluster in the alkali field, with the densest grouping around the Rössing set. High MALI weakly mineralised samples (black +) follow a positive trend with $SiO_2$ but overall samples plot close to- and follow the Rössing sheeted leucogranite trend of decreasing alkali with increasing silica.

*Iron-based Classification Schemes: - Fe**

Fe-Mg silicate interaction is the main control on magnetite and/or ilmenite formation in granites (Frost *et al.*, 2001). This was shown by Miyashiro (1970) to correlate directly with FeO/(FeO + MgO) vs. $SiO_2$. Magnetite is the most prominent accessory in many of the C types and occurs in a large proportion of the mineralised sheeted leucogranites of the Goanikontes deposits. Magnetite often shows exsolved ilmenite, and is associated with magmatic-Imenite intergrowths. Considering the possible influence that interaction with the Khan and/or Rössing Formations have had on the crystallisation of magnetite in mineralised

and weakly mineralised sheets, binary diagrams such as the Fe* plot of Frost *et al.* (2001) may be useful to distinguish between different sheeted leucogranite types. Fe* is defined as ($FeO_{tot}/FeO_{tot}$ + MgO). Where magnetite is absent, sulphides in the D-types such as pyrrhotite and pyrite host the Fe along with ilmenite, if it is present.

The diagram that Frost *et al.* (2001) have proposed is a ferroan-magnesian classification for granitoids. Fe:Mg differs depending on the enrichment mechanism of Fe relative to Mg:

- In some systems Fe is enriched while Si is not abundant, and in others
- Si is enriched with minimal Fe enrichment (Nockolds and Allen, 1956).

In a granitic system, there is a proportion of ferric to ferrous iron that exists and the ferroan-magnesian plots ideally require FeO values as this helps eliminate any discrepancies caused by $Fe^{2+}$:$Fe^{3+}$ variation. This proportion is not known for the Central Zone samples as this was not determined analytically. Frost *et al.*, (2001) recommend the $SiO_2$ vs. Fe* ($FeO_{tot}/FeO_{tot}$ + MgO) plot using $FeO_{tot}$. $FeO_{tot}$ is defined for this diagram as the total Fe content analysed as an oxide, in this case the analysis by XRF is fro $Fe_2O_3$. This total Fe ratio is preferred as sub solidus oxidation creates highly variable $Fe^{3+}/Fe^{2+}$ ratios. The axis is simply expressed as FeO/FeO+MgO, calculated in wt.%. Deviation across the Fe* line tends to occur in samples with $SiO_2$ >70 wt.% and sub-solidus oxidation and entrainment of ferro-magnesian phases are the main components in the highly variable Fe* values.

An important consideration in using the discrimination diagram is that many of the sheeted leucogranites have Fe and Mg concentrations that were contributed to by external sources; such as entrained biotite and magnetite and other ferro-magnesian phases from the Khan Formation for example. It is also widely accepted that interaction with the metasediment is the chief proponent in uranium reduction and deposit formation, and thus mobile Fe may have been incorporated in the alaskites from sources in the reduced sediments.

### *Fe Classification of the Central Zone Leucogranites*

The Valencia deposit provides a range of sheeted leucogranites with which to test the suitability of the Fe* diagram for discriminating between sheeted leucogranite generations.

Typically A-type granites plot above the Fe* line (Frost *et al.*, 2001). The majority of the leucogranite samples however, plot below the Fe* line, apart from some surface-sampled D-type and some C-type sheets. The plot does not adequately discriminate between the empirically different A-, B- and C-types, but does show that most of the uraniferous samples have relatively low Fe* (Figure 5.19, Figure 5.20a). The comparative samples from the Rössing deposit tend to lie above and close to the Fe* line and weakly mineralised Rössing samples (red diamonds) lie below the Fe* line. The Goanikontes samples, pre- and post-$D_3$ uraniferous generations are comparable to the Valencia samples; the majority plot below Fe* and within the relatively narrow range of $SiO_2$ although it is possible that there is a very weak, positive relationship with Fe*. As with the Valencia population, most of the uraniferous samples have Fe* < 0.5 (Figure 5.20b).

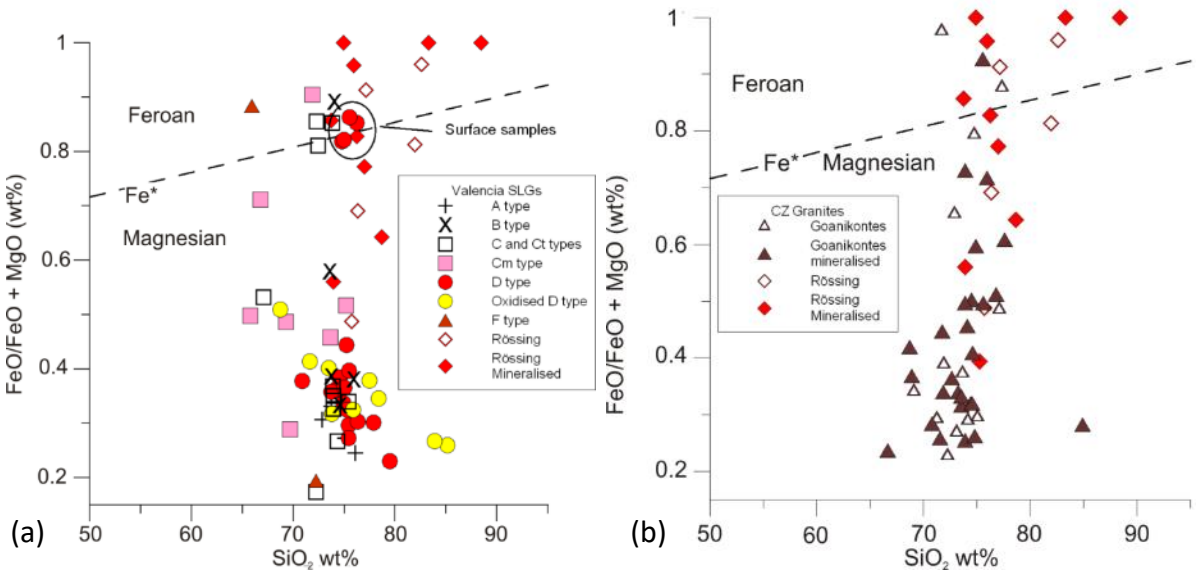



Figure 5.20 Fe* vs. $SiO_2$ diagrams of the leucogranite suite at Valencia and Goanikontes. (a) Fe* vs. $SiO_2$ diagram of mineralised and weakly mineralised Valencia sheeted leucogranite varieties. The majority of samples lie below the Fe* line, though some mineralised samples lie on or above it. If surface samples are removed the fresh Valencia mineralised samples do not plot above the Fe* line despite high $SiO_2$ content. The Fe* line is from Frost *et al.* (2001). (b) Fe* vs. $SiO_2$ diagram of mineralised and weakly mineralised Goanikontes sheeted leucogranite. A very subtle trend toward the Fe* line with increasing $SiO_2$ is apparent. The majority cluster below Fe*=0.4.

There is a stark contrast between the Ida Central and Holland's Dome samples. All Holland's Dome samples have low Fe* (<0.5) because of the consistently higher concentrations of Mg (Figure 5.21c). Diopside is abundant in the skarns and the margins of the granite sheets at Holland's Dome. The diopside ranges in colour from black to green, with the majority of

those observed in outcrop being of the green magnesium end members. The Husab sheeted leucogranites plot with consistently lower Fe* when compared to the Rössing mine samples. There appears to be two populations, with no relationship to $SiO_2$ or to the uranium content of the samples, with U-enriched samples plotting in both Fe* ranges (Figure 5.21d).

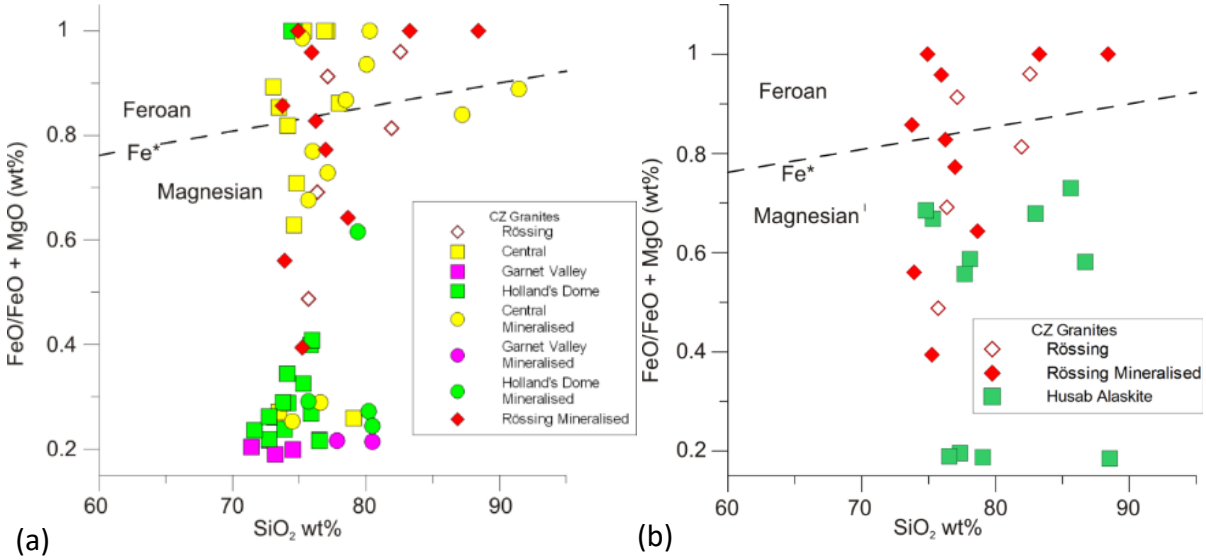



Figure 5.21 Fe* vs. $SiO_2$ diagrams of the leucogranite suite at the Ida Dome and Husab. (a) Fe* vs. $SiO_2$ diagram of mineralised and weakly mineralised Ida Dome sheeted leucogranites. There is a clear difference between the Ida Central, Garnet Valley and Holland's Dome samples; Ida Central samples plot close to Rössing samples with high Fe – Mg ratios. Holland's Dome samples have higher Fe-Mg ratios due to greater interaction with Fe and Mg skarn minerals. (b) Fe* vs. $SiO_2$ diagram of Husab alaskites. The Husab data set has a range of Fe* from <0.2 to ~0.7 and plots in two distinct populations, with no apparent relationship to U content.

### *Maficity*

Simply expressed, the mafic oxide weight percentages of the various granites of this study allow for differentiation between the biotite bearing Salem- and Grey granite suites, and the SLGs. $Fe_2O_3$ + MgO expressed as Total Fe + Mg (wt %) in Figure 5.22 is a representation of the degrees of maficity apparent in each variety of granite populations, by type, sampled in this study. The graph reflects a decrease in mafic phases with successive generations of the Salem- and Grey granite suites.

Maficity, expressed as the sum of molar Fe + Mg + Ti (Clemens *et al.*, 2011) is a simple and convenient measure of the evolution of partial melts as evolving granites are expected to contain decreasing mafic minerals (Fe- and Mg-containing phases) for the less evolved granites.

The leucogranites do not show any trend between old and young with respect to maficity, primarily because their maficity ranges are principally a reflection of the interaction with- and probable entrainment of Fe- and Mg-bearing accessory phases (as individual minerals or as constituents of metasedimentary or older granitic xenoliths). The B-types show slightly higher maficity than the accessory-free A-type sheets, as mineral contributors of Fe and Mg in the early leucogranites are biotite, Fe from almandine garnet and Mg from cordierite.

Variable biotite content has resulted in similar maficity ranges between magnetite -bearing and accessory-free C types. The tourmaline-bearing (Ct) varieties have minimal mafic accessory phases other than tourmaline on surface and in hand specimen. Unaltered alaskites or the D-types, are relatively accessory-free, with a low mafic mineral content.

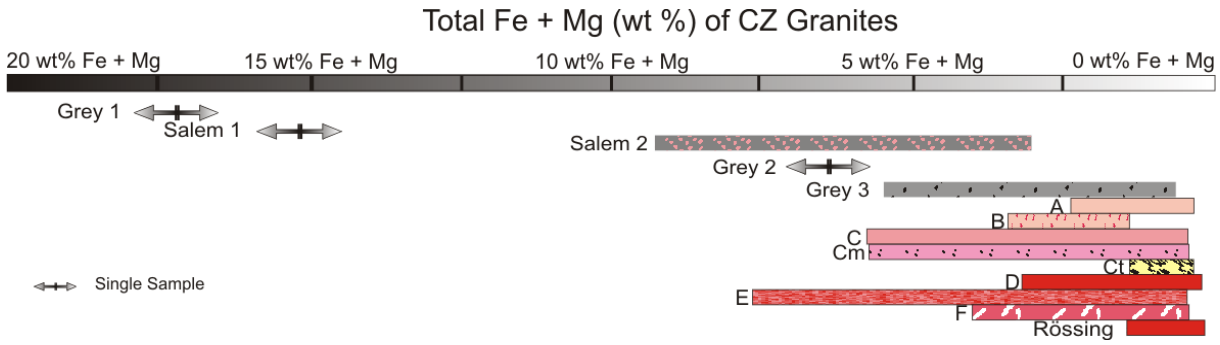



Figure 5.22 Total $Fe_2O_3$ + MgO (wt.%) of Central Zone granites. The Grey and Salem granites show a decrease in Fe and Mg with decreasing age. C type (except Ct varieties) and E-type (oxidised and haematite stained) sheets, have the broadest range of total Fe + Mg content.

The Goanikontes alaskites are somewhat of an exception as they contain accessory magnetite, with euhedral magmatic textures, oxidation of these phases often manifests as prominent, localised red staining. Maficity of most of the mineralised leucogranites is therefore an indication of the amount of magmatic Fe and Mg and variably entrained Fe- and Mg-bearing phases such as biotite, titanite, diopside, garnet, and cordierite. The oxidised E-type alaskites, show a broad range of maficity, reflecting variable degrees of Fe-dominated alteration.

The Grey granites and Salem granites should plot with maficity ratios that are nearer to those of the source rocks, at least with respect to the maficity values of the leucogranites.

The plots that follow distinguish the older more mafic grey varieties from the younger more leucocratic sheeted leucogranites.

Figure 5.23a illustrates that maficity and Ti content are the highest in the older, melanocratic generations of Grey and Salem granites. There is a progressive decrease in maficity with successive generations of Grey and Salem granites as they tend toward more peraluminous composition. The Red granites at Hildenhof, described as anatectic granites by McDermott (1986) show a low-mafic component, as would be expected from melts derived from the breakdown of biotite at source. Shearing of the Salem megacrystic monzogranite at Valencia has not affected the maficity, despite increasing the feldspar content in partial melt veins that form along the conjugate shear bands.

The leucogranites from the Goanikontes and Ida Dome deposits preferentially intrude biotite-rich pelitic metasediment that probably contributed biotite and/or magnetite at interactive contacts or as xenolithic components. Mineralised Goanikontes sheeted leucogranites plot in a distinct population of relatively elevated molar Fe + Mg. Holland's Dome and the majority of the Garnet Valley samples follow the same trend as the Goanikontes alaskites, being hosted predominantly in Khan Formation gneiss and schist units below the Rössing marbles (Figure 5.23b). The Ida Central samples tend to plot with lower maficity and show a similar erratic distribution within the low maficity range of the comparative Rössing samples. The Valencia leucogranite suite illustrates variable maficity in the B and C type samples, though they constitute a limited sample set, the A, D, E, and $C_m$ types plot with a positive correlation to Ti content (Figure 5.24). This reflects a single, or limited, phase distribution of Fe and Ti in ilmenite within the leucogranites.

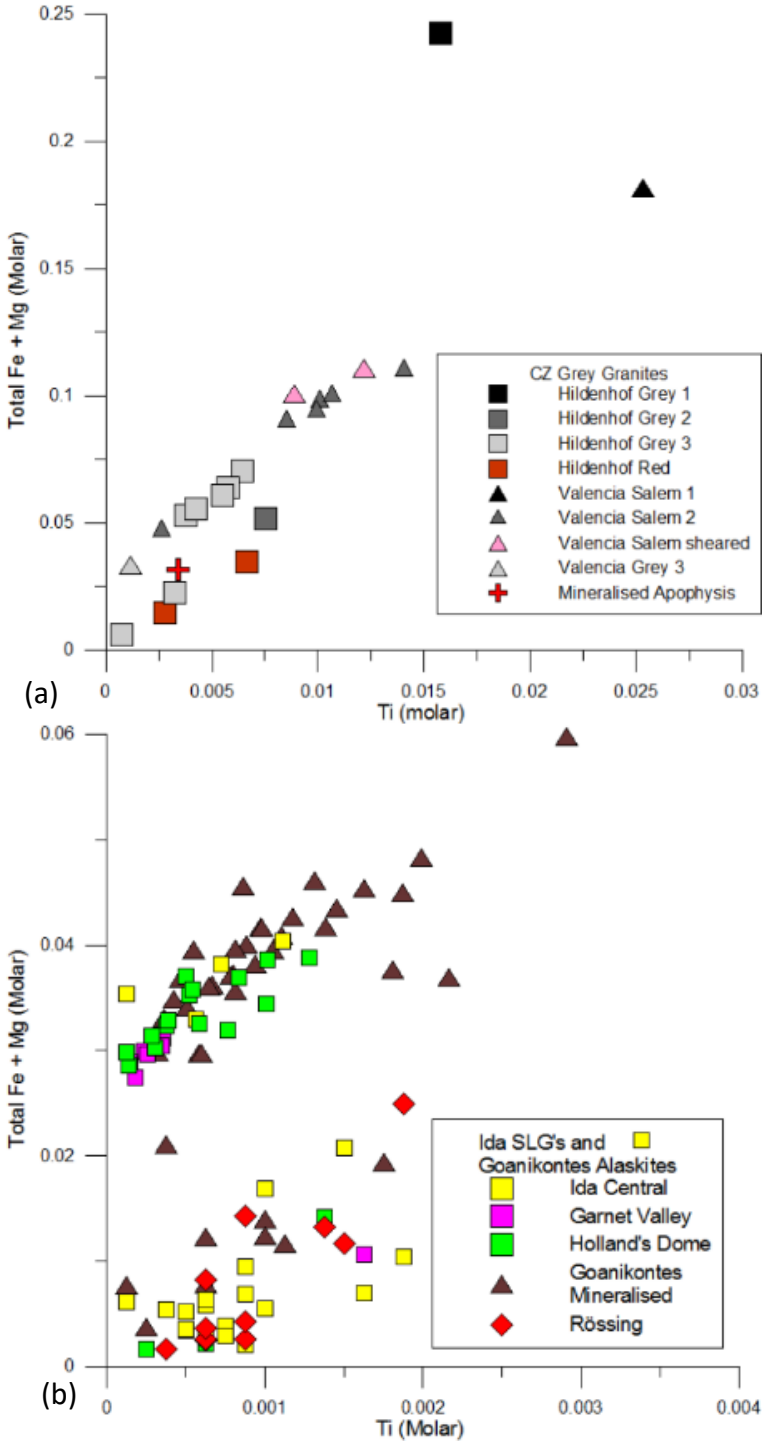



Figure 5.23 Maficity diagrams of Central Zone Grey, Red and Salem granites and sheeted leucogranites. (a) Maficity (Fe and Mg) and Ti contents are highest in the older, melanocratic, generations of Grey and Salem granites. There is a regression in maficity with successive generations of Grey and Salem granites.

(b) Maficity disparity between Ida Dome deposits and the Etango deposit at Goanikontes. Holland's Dome samples are elevated in maficity relative to Ida Central and Rössing. Rössing sample data: Freemantle (2006). Field observations of Goanikontes and Holland's Dome sheeted leucogranite indicate interaction with skarns and incorporation of phases such as titanite into weakly mineralised and mineralised sheeted leucogranite (alaskites). The Ti content of the Holland's Dome samples is comparable to the Goanikontes samples, which suggests that the selection of sampled material successfully avoided zones of wall rock contamination. Elevated Fe and Mg is contributed by contaminant phases such as clinopyroxene, titanite, biotite and magnetite.

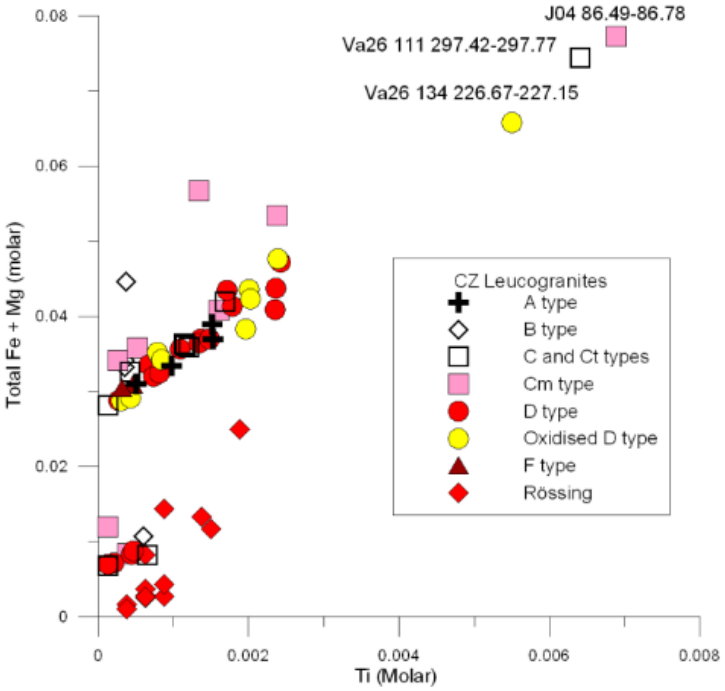



Figure 5.24 Maficity diagrams of Central Zone sheeted leucogranites at Valencia. The majority of the Valencia samples have elevated maficity in excess of Rössing, all oxidised D-types plot with excess Fe + Mg. A small population of low-biotite D-types plot in a cluster close to the Rössing sample composition highlighting the role of biotite in the plots. Rössing data from Freemantle (2006).

***Debon and Le Fort Binary Classification***

The A-B and P-Q diagrams of Debon and Le Fort (1983) are similar to the R1-R2 diagram of De La Roche *et al.* (1980) in that cationic proportions are the discriminating components. The A-B diagram plots the peraluminous index of granite rocks along the A axis (y) and the metaluminous index or differentiation index along the B axis (x). The P-Q diagram is constructed from cationic proportions of Ca, K, Na and Si and the A-B diagram from weight % of Al, Ca, Na, K **(A)** and Fe, Mg and Ti **(B)**.

The P-Q diagram represents the plagioclase – K-feldspar content relative to quartz content and the A-B diagram illustrates mafic content relative to the aluminium index. The millication A-B and P-Q diagrams are better suited to characterising the leucogranite types than the R1-R2 plot which is limited by silica content. Quartz textures in the sheeted leucogranites indicate multiple generations as illustrated in Chapter 4, suggesting addition or removal of silica by hydrothermal-like magmatic fluid processes. Thus, applying A-B and P-Q plots may provide a means of discriminating between granites and deposits where samples contain excess quartz/silica. Villaseca *et al* (2001) adds the I- and S-type discrimination after White and Chappell (1988) to the A-B plot. Petrographic investigations show that plagioclase

and microcline occur in varied proportions between sheeted leucogranite types and between deposits; Na and K variations should reflect on the diagrams.

The A-B diagrams in Figure 5.25a and Figure 5.25b reflect the patterns of the molar proportion aluminium saturation diagrams (A/CNK vs. A/NK) and show some contrasts between the Goanikontes and Valencia sheeted leucogranites. Peraluminous Goanikontes granites do not exceed B values of 60, and rarely plot above the superimposed I-S line of White and Chappell (1988).

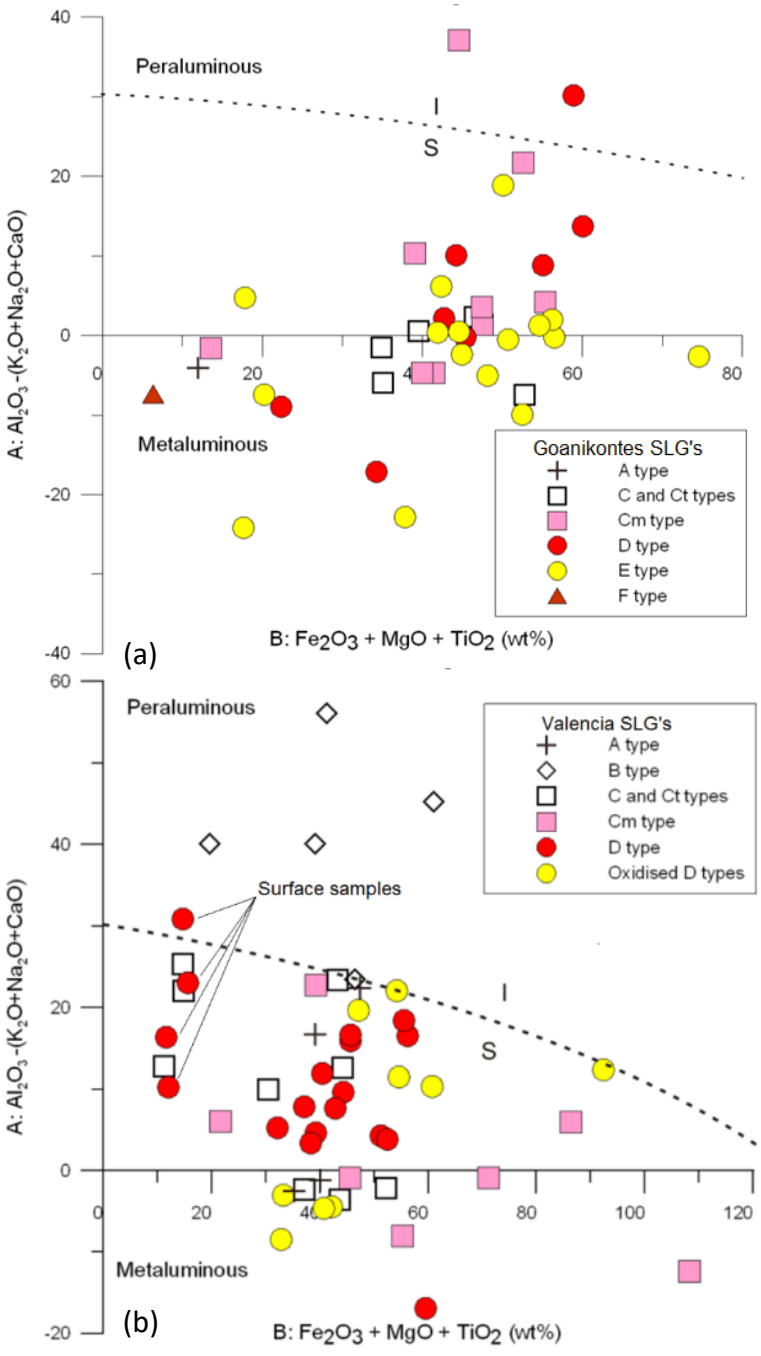



Figure 5.25 A-B diagrams of Debon and Le Fort (1983) of Central Zone sheeted leucogranites. (a) Goanikontes Cm granite varieties show an increase in mafic content with increasing peraluminosity. The majority of the samples plot below the I-S line of White and Chappell (1983). (b) A-B plots of Valencia sheeted leucogranites. D-types show a positive A-B trend and the majority of the samples lie below the ASI line. As in the aluminium saturation diagrams, the B types are strongly peraluminous and plot above the I-S line of White and Chappell (1983). The clustering of surface samples, with considerably lower 'B' from the fresh material illustrates the sensitivity of this diagram to weathering of mafic phases.

The P-Q diagram in Figure 5.26 discriminates between sub-types, separating the two textural varieties of the B-type at Valencia; one being distinctly pegmatitic with centimetric garnet in clustered porphyroblasts, and the other showing finer grain size with a persistent fabric and hosting generally smaller millimetric garnet in nests and disseminations. The foliated granite is interpreted as the older generation, while the pegmatitic variety is likely to be a similar generation of SLG as the $C_t$-type. A similar separation exists between the Ida A-type on the plagioclase side and Valencia A-type on the K-feldspar side. Supporting petrographic observations show that plagioclase is the prominent feldspar in two of the Ida samples and microcline-perthite is the most abundant in the single Valencia A-type thin section. The F-types from Goanikontes and Valencia consist almost entirely of K-feldspar and subordinate milky quartz (with accessory biotite) and correspondingly, they plot with high positive P values and low Q values.

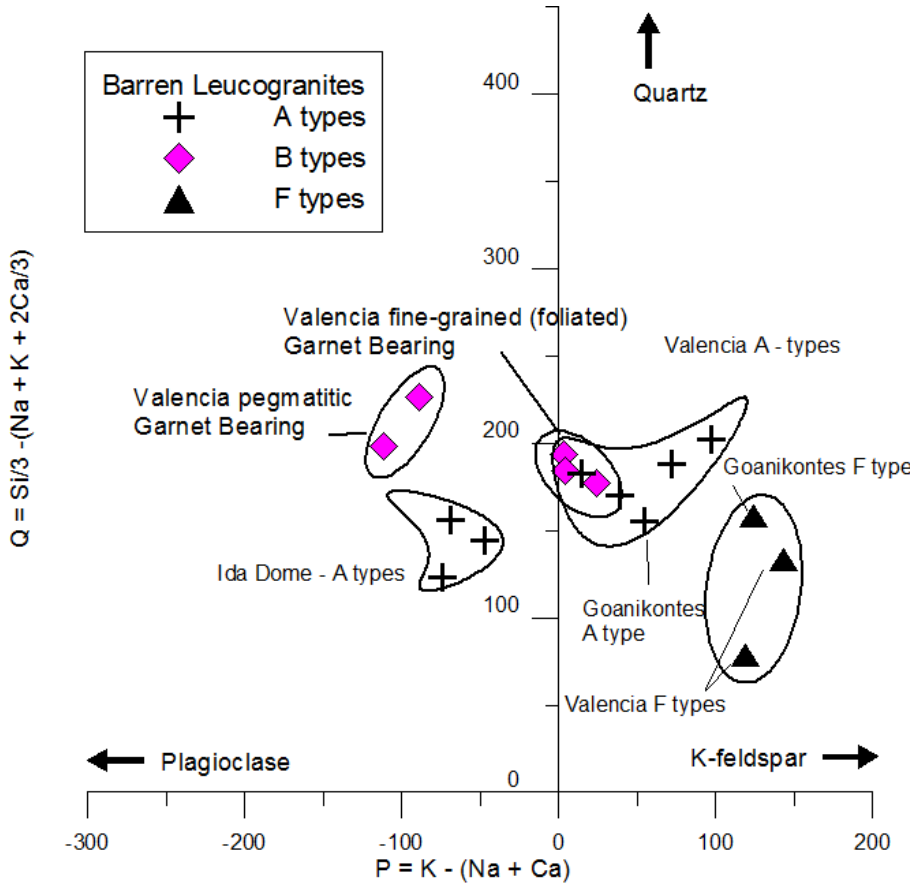



Figure 5.26 P-Q plot of Goanikontes, Ida and Valencia A, B, and F-types.Valencia A and F-types and the foliated B types plot on, or to the right of the K-feldspar line, the pegmatitic B type and the Ida A-types plot toward the plagioclase side of the P axis.

## 5.7 Major Element Summary and Discussion

The mineralised sheeted leucogranite intrude areas of diverse stratigraphic and structural setting, which directly influence interaction with reactive lithologies and therefore the compositions of some the granites. The Ida Dome deposits show the broadest variation of structural and stratigraphic parameters; where significant skarn development in some areas has resulted in variable whole-rock compositions, driven by the presence of accessory Ca phases such as titanite and diopside. Sheet orientations are governed by vertical NNE-SSW extensional fractures parallel to fold axial planes, and horizontal sheets, perpendicular to $\sigma_3$ in the vertical direction. Mineralisation in the leucogranites is controlled by interaction with reactive carbonate units, regardless of leucogranite dyke orientation. In contrast, the Etango and Valencia deposits host relatively thin marbles, if any, in the vicinity of the mineralised granites, and thus reflect much narrower ranges of Ca ratios than do the Ida Dome samples. The mineralised Husab geochemical samples presented for this study show major element inhomogeneity and therefore illustrate the influence of host rock interaction on mobile major element ratios. The aluminium saturation (ASI) ranges of the pre-$D_3$ granites are distinctly narrow (Figure 5.27) and only the B-type sheets plot with a completely peraluminous composition. This Central Zone-wide trend is consistent with the compositional trends identified by Nex (1997) for the Goanikontes pre- and post-$D_3$ populations.

The propensity for most samples to plot in the metaluminous field of Debon and Le Fort (1983), which corresponds with the Chappell and White (1974a, 1992) S-type field, reflects the source of the sheeted leucogranites. The only anomalies are the anatectic B types at Valencia which are peraluminous in all classification plots. The samples also show a positive A-B correlation overall. Isotope data by Jung *et al.* (2000a) show a crustal origin and therefore S-type affinity of the Central Zone sheeted leucogranites.

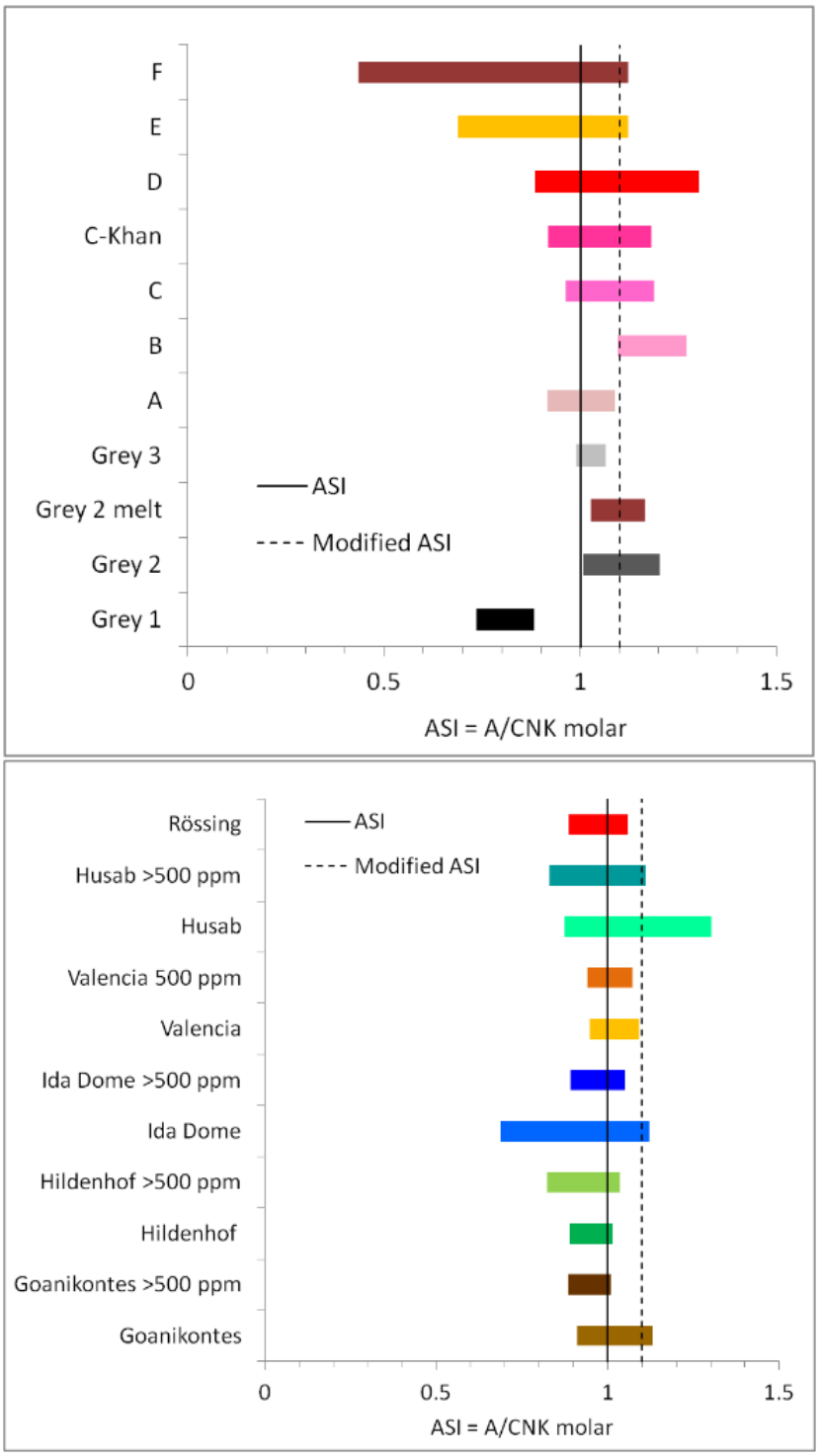



Figure 5.27 Bar graph plots of aluminium saturation of the sheeted leucogranites. The graphs illustrate narrow ASI ranges in the Salem and Grey granites, where Grey 1 and Grey 2 refer to first and second generation diorite and syenogranite varieties, and the pre-$D_3$ leucogranites. The most primitive granites (diorite) in the region are metaluminous; all of the felsic biotite granites are peraluminous in the modified ASI classification. The pre-$D_3$ leucogranites tend to be peraluminous, with the magnetite-bearing C-types (C-Khan) being the most metaluminous of the group. The D-types reflect the more accurate compositional range of the uraniferous and post-$D_3$ leucogranites, while the E-types, which are essentially altered D-types, give a metaluminous compositional range. There is some uncertainty in this study as to whether the F-types that are sampled are in fact the youngest leucogranites in the Central Zone, the broad range in a small sample set (n=3) limits any interpretation of the granites by ASI. (b) ASI plots of individual deposit uraniferous leucogranite populations. The range plots show the Husab samples with <500 ppm.

## 5.8 Trace Elements

Trace elements can be classified into groups in which all the elements within a group display similar chemical behaviour and thus similar predictable behaviour in geological processes (Rollinson, 1993). Trace elements in geological processes may concentrate in accessory

phases and substitute for major elements in rock-forming minerals, particularly Rb, Sr, and Ba (Rollinson, 1993). Thus, geological processes, such as partial melting (granite-forming) or alteration by residual magmatic fluids and assimilation (interaction with skarn localities or partial- to complete incorporation of pelitic host rocks) may be reflected in the various trace element abundances. For this reason, discrimination diagrams pertaining to source and melt mechanisms use trace elements.

The intention of this section is to use trace element trends and abundances of the more common elements, where possible, to fingerprint specific deposit suites (mineralised populations) and specific sheeted leucogranite types (A-F of Nex, 1997) and provide some reasoning as to why these trends may exist.

Mobile, or low field-strength trace elements Rb, Sr, and Ba may substitute for major elements as the Large Ion Lithophiles - K, Na or Ca in the rock-forming minerals- while elements such as Zr, La, Ce, and Y reflect accessory phase abundances, the latter three particularly in phosphates. The transition metals include the base metals found in the Khan, Kainkaghas, and Ida mines; diagrams that use these elements should therefore show country rock contamination trends in the sheeted leucogranites from the Ida Dome, Valencia, and potentially Husab given its proximity to the Khan Mine.

The discussion is focussed on the immobile, mobile and transition groupings. The differences in emplacement setting between deposits, and the uniqueness of each geological setting that must leave its subtle mark on the chemistry of the granites, should provide discrimination with mobile trace element abundances between deposits. In the same light, the robustness of high field strength trace element diagrams may show discrimination between the different generations of granite at the deposits, or at least be tested by the leucogranites of this study.

Since this thesis has a focus on uranium mineralogy and mineralisation, there is an emphasis on the behaviour of U and Th geochemistry. These elements preferentially partition into uraninite, coffinite and thorite but also into refractory mineral phases such as betafite (U), brannerite (U), allanite (Th), and into phosphates such as monazite (Th).

### *Low Field Strength Trace Element Trends*

#### *Rb, Sr and Ba*

Rb - Sr ratios distinguish between the different Damaran granitoids; particularly between the suites of Grey-, Red- and Salem granites, and the later leucogranites. Jacob *et al.* (1986), McDermott *et al.* (1996) and McDermott *et al.* (2000) show that the sheeted leucogranite compositions in terms of Na, K, and Ca reflect a combination of partial melting of a number of sources and/or wall-rock entrainment respectively.

The concentration of these elements is directly related to the proportions of the primary rock-forming minerals into which they substitute and their relative mobility in the magmatic, hydrothermal and meteoric environments. The varying emplacement settings between deposits, and the presence or lack of Ca lithologies of the Rössing Formation may contribute to the variable Rb, Sr, and Ba concentrations between different deposit areas.

#### *Rb*

K and Rb have a positive correlation in the Central Zone sheeted leucogranites, as shown in Figure 5.28a. The plot shows that Rb corresponds less systematically with increased $K_2O$ wt.%. The Rössing samples for comparison plot with relatively elevated Rb compared to samples from the other deposits. By removing the less uraniferous samples (those <100 ppm U are almost always A-, B-, or C-type, while D-types may have <100 ppm U, the pre-$D_3$ sheets seldom exceed 50 ppm U, in this study) and including the Husab samples, which are all above 100 ppm U, the sample sets show that above 4 wt.% $K_2O$, Rb concentration is variable and in a range of ~300 ppm to 520 ppm Rb whereas below 4 wt.% $K_2O$, Rb values are less than 200 ppm Rb (Figure 5.28b).

The Rössing samples for comparison show consistently elevated Rb for any given $K_2O$ value. The Husab and Hildenhof sample sets show particularly variable Rb:$K_2O$. The Hildenhof samples are all surface samples, while the Husab sample set represents a diverse collection of leucogranite textures and grades. The uraniferous leucogranite populations of each deposit also show distinguishable clusters of $K_2O$ vs. Rb.

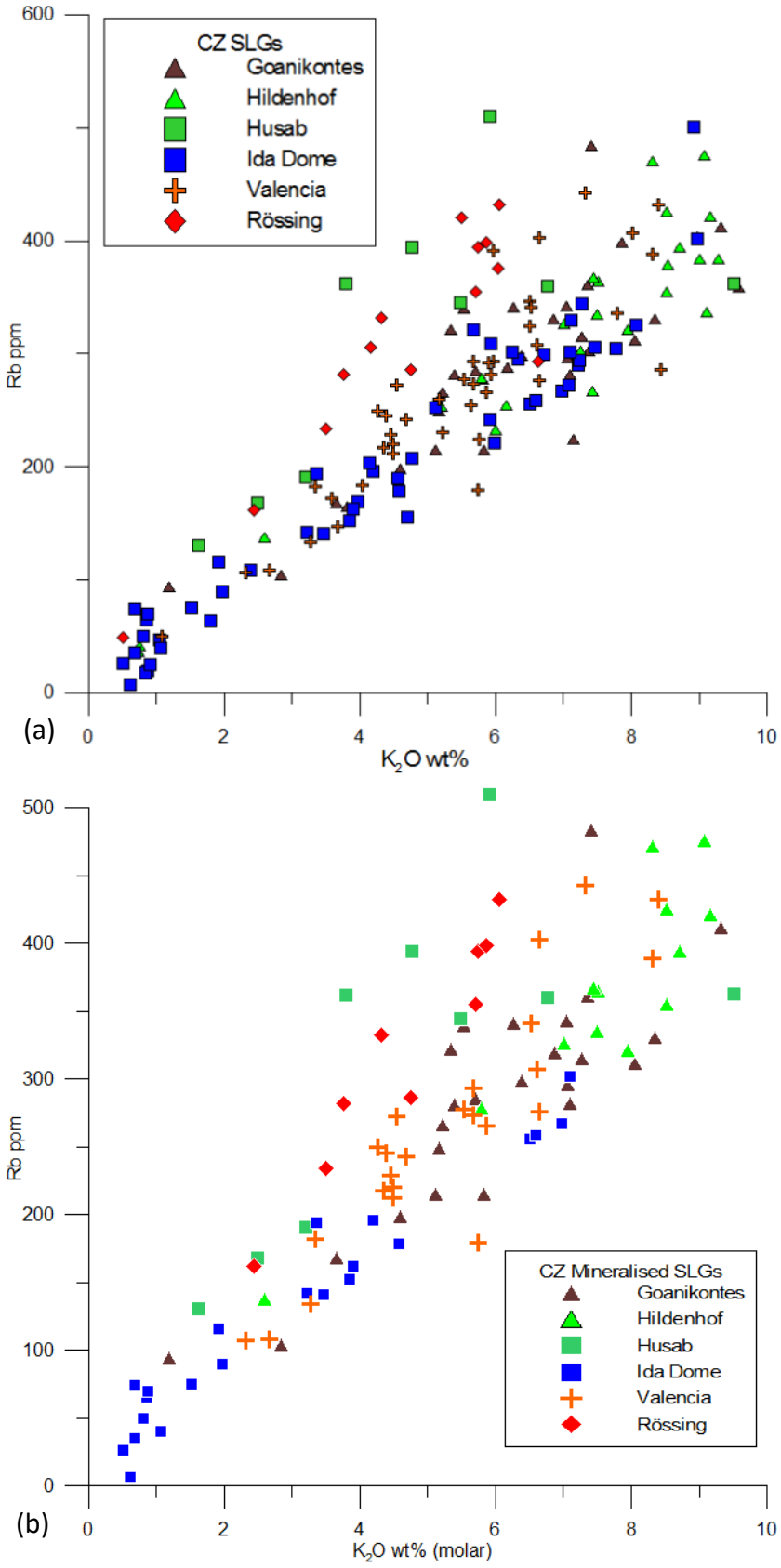



Figure 5.28 $K_2O$ wt.% vs. Rb ppm of Central Zone sheeted leucogranites. (a) Rb shows a positive correlation with $K_2O$ in all samples, but at high $K_2O$, the Rb content becomes erratic, especially in the Hildenhof samples. Rössing mineralised samples show distinctly elevated Rb for comparison. Rössing sample data: Freemantle (2006). (b) $K_2O$ wt.% vs. Rb ppm of mineralised sheeted leucogranites. The sample suites of individual deposits show some distinction relative to one another; Ida samples have depleted K, and just four samples exceed 200 ppm K. Goanikontes and Valencia samples plot with enriched K and Rb, relative to Ida Dome, with a less systematic trend; the Husab samples plot with erratic Rb:K and high Rb relative to the sample population; and Hildenhof samples have some of the highest K proportion, and correspondingly high Rb. Rössing sample data: Freemantle (2006).

The uraniferous Goanikontes samples show a positive Rb vs. K correlation over a wide range of Rb values (Figure 5.29a); The Husab sample suite is too small to highlight a confident trend but Rb values tend to exceed all other deposits for any given $K_2O$ value (Figure 5.29b) and seem quite similar to Rössing samples; The Hildenhof samples are the most potassic group in the sample set (Figure 5.29b); and many of the Ida Dome mineralised sheeted leucogranites are the least potassic, Holland's Dome samples, correspondingly cluster in a low-concentration Rb-$K_2O$ group and the Ida Central samples have a wide range of $K_2O$ and corresponding Rb (Figure 5.29c).

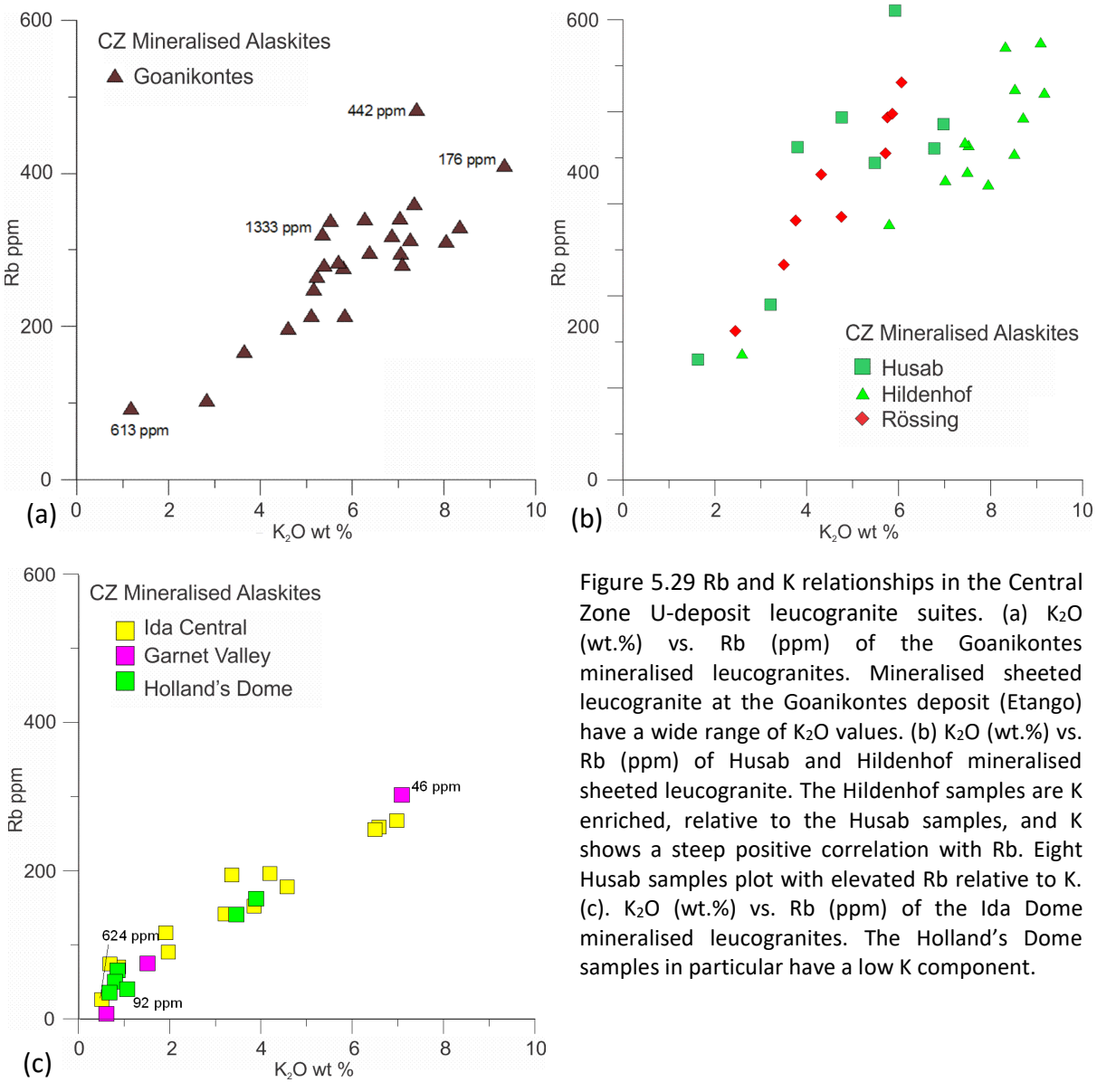



Figure 5.29 Rb and K relationships in the Central Zone U-deposit leucogranite suites. (a) $K_2O$ (wt.%) vs. Rb (ppm) of the Goanikontes mineralised leucogranites. Mineralised sheeted leucogranite at the Goanikontes deposit (Etango) have a wide range of $K_2O$ values. (b) $K_2O$ (wt.%) vs. Rb (ppm) of Husab and Hildenhof mineralised sheeted leucogranite. The Hildenhof samples are K enriched, relative to the Husab samples, and K shows a steep positive correlation with Rb. Eight Husab samples plot with elevated Rb relative to K. (c). $K_2O$ (wt.%) vs. Rb (ppm) of the Ida Dome mineralised leucogranites. The Holland's Dome samples in particular have a low K component.

*Sr*

Sr concentrations in the Central Zone granites are highest in the early Grey and Salem granites (>200 ppm to >350 ppm for the Salem type) and decrease to <160 ppm in the sheeted leucogranites.

Sr concentrations discriminate between sheeted leucogranite generations: Unaltered D-types have a narrow $SiO_2$ range relative to the altered E-types; the variability of $SiO_2$ in the altered alaskites (E) does not appear to have had any influence on the range of Sr content though; Cm-types have similar $Sr/SiO_2$ to the grey granites; and Ct-types have consistently lower Sr than the Cm-types (Figure 5.30). Sr and Ca relationships do not appear to be as linear as would be expected, but a weakly positive trend is apparent in the Cm and D-types. The most reasonable explanation is the considerable interaction between leucogranite and host rock. CaO abundance itself sets most D-types apart from the comparative Rössing mine samples (Figure 5.31).

Rb/Sr ratios were shown by Nex (1997) to increase with successive generations of granite at the Goanikontes area, where interpretation suggested separate sources for the pre- and post-$D_3$ granites. Rb/Sr is applied to this data set as the discriminatory variable. The ratio successfully distinguishes between the pre-$D_3$ Salem and Cm-types and the post-$D_3$ populations at Valencia, though there is some overlap between the C- and D-types (Figure 5.32a). The A-, B-, and C-type sheets show elevated Rb/Sr with comparable $SiO_2$ to the D-type (Figure 5.32a).

The ratio is also successful at distinguishing between the Ida Dome D-type and the D-types from theHusab and Rossing deposits. Visibly oxidised Ida Dome E-type samples plot with low ratios relative to the less-altered D-type (Figure 5.32b). The comparative Rössing samples plot with a ratio intermediate to the Ida Dome D- and E-type. The Husab samples, which tend to show a greatly variable degree of alteration and sub-solidus reaction textures plot with low ratios relative to the Ida Dome Area D type sheeted leucogranites.

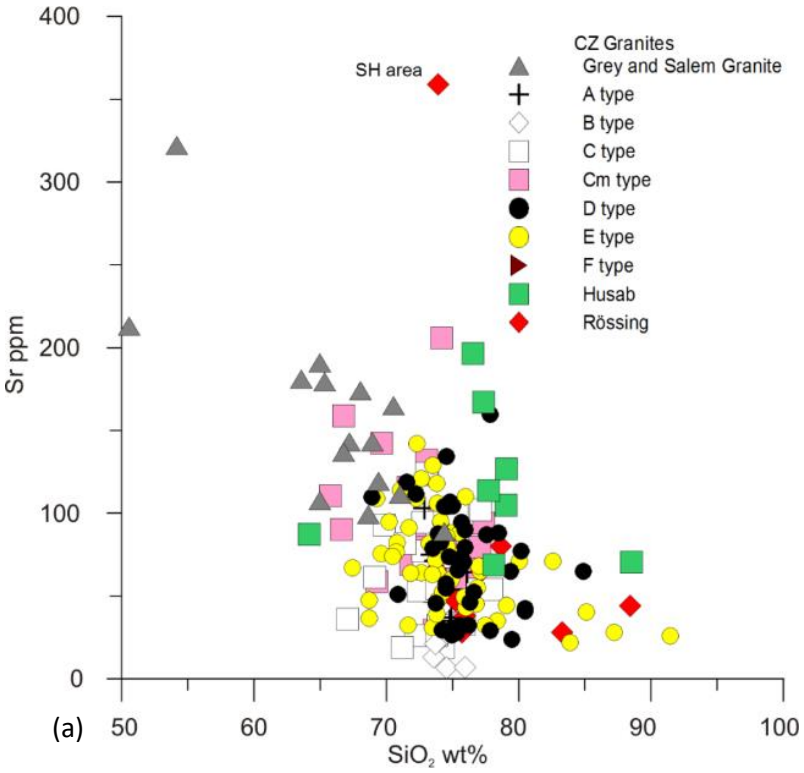



Figure 5.30 Sr content of Central Zone granites relative to $SiO_2$. Sr content decreases from the least evolved Grey and Salem granites to <30 ppm in the B type sheets and to <100 ppm in the majority of the mineralised sheet. The SH area is anomalous in Sr, which substitutes for Ca in phases such as betafite

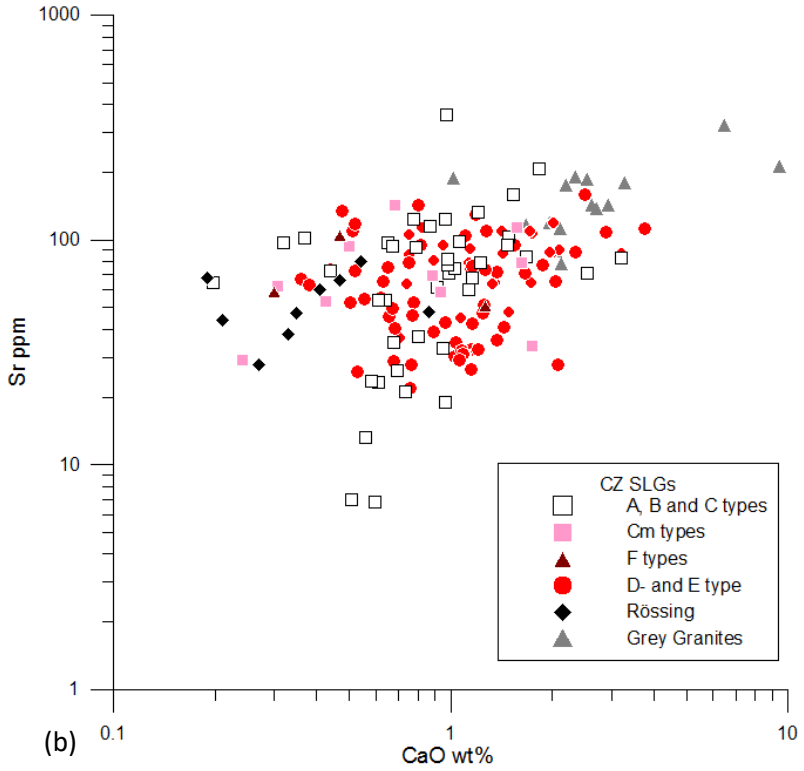



Figure 5.31 CaO vs. Rb/Sr of granites at the Central Zone uranium deposits. Sr and Ca are in lowest abundances in the pre-D3 leucogranites, but relatively enriched in the pre-D3 and older plagioclase-bearing equigranular granites. The Cm and D-types may share petrogenesis similarities as Sr/Ca is comparable between the populations.

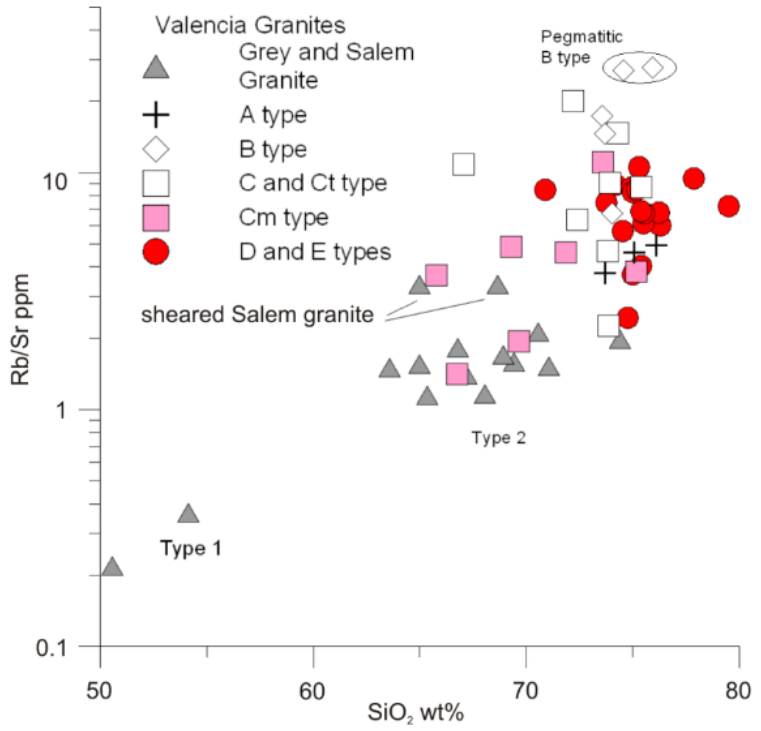
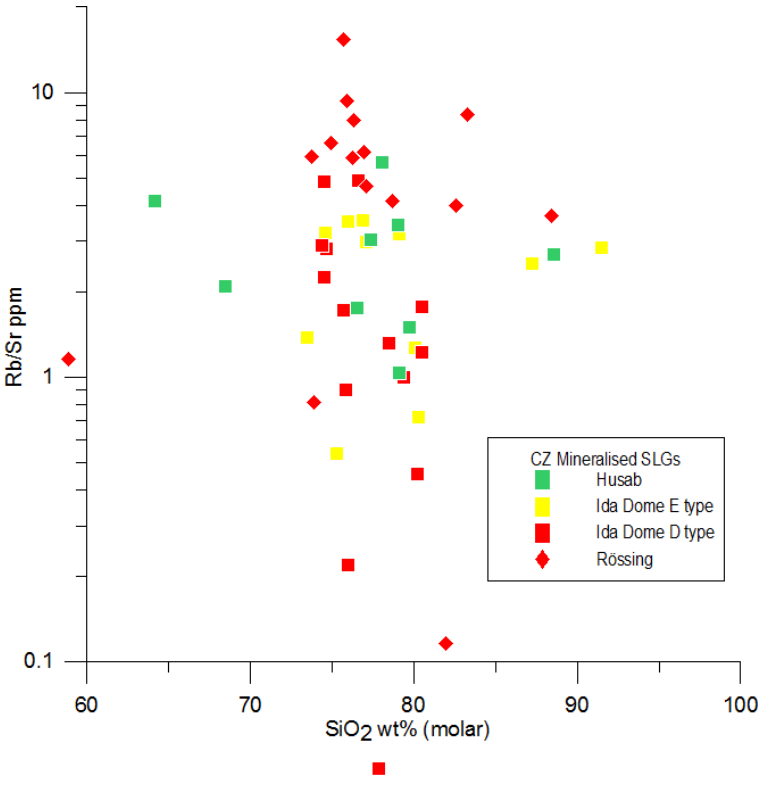



Figure 5.32 Plot of SiO2 vs. Rb/Sr ppm of Valencia and Goanikontes granites. (a) Rb/Sr plotted against Si content of the Valencia granite suites shows a systematic increase in Rb/Sr from Salem type syenogranite through Cm-type leucogranites to mineralised varieties. The garnet-bearing types within the Kuiseb Formation have high K-feldspar proportions and a correspondingly high Rb/Sr, overall the ratio increases with stratigraphic level of intrusion.




(b) $SiO_2$ vs. Rb/Sr in D and E-type samples from the Ida Dome and Husab deposits. Alaskite samples from the Rössing deposit are included for comparison. D-types show a slight negative Rb/Sr with Si increase. Husab samples show no relationship between the ratio and Si. E-types of the Ida Dome area seem to be in two groups, one with Rb:Sr>3 and the other with Rb:Sr<2. Both areas have Rb:Sr significantly depleted relative to the comparative samples at Rössing. Rössing sample data: Freemantle (2006).

Ba

Barium, together with elements such as V, is expected to be enriched in Ca-rich granites, however, the sporadic CaO distribution of some of the granites (Ida Dome in particular) on

the various major element classification plots may limit Sr/CaO and Ba/CaO plots. Ba is a highly mobile element and is saturated to % - scale concentrations in the fluorite and skarn deposits near the Ida Dome (up to 1.5% Ba). Ba and other low field strength-, large ion lithophiles such as Sr are identical in charge and very similar in size (Rollinson, 1993) and because of this Ba may substitute for Sr or Ca. The element however, did not show systematic relationships with CaO in the Valencia SLG suite. In Figure 5.33a, Ba and $K_2O$ show a weakly systematic possitive correlation in the Valencia suite; where data are available for all the types of sheeted leucogranite varieties. Magnetite C-type samples are enriched in Ba relative to mineralised samples and the comparative samples from Rössing.

In Figure 5.33b, Ba concentrations of the mineralised samples at Ida Dome and Valencia are depleted relative to their respective weakly mineralised sheeted leucogranite populations. The depleted (relative to sample suite) Ba mirrors the trend identified for Sr, which is depleted in the mineralised samples. Holland's Dome samples plot with erratic CaO and consistently low Ba, indicative of Ca mobilisation in the local, skarn-dominated, system.

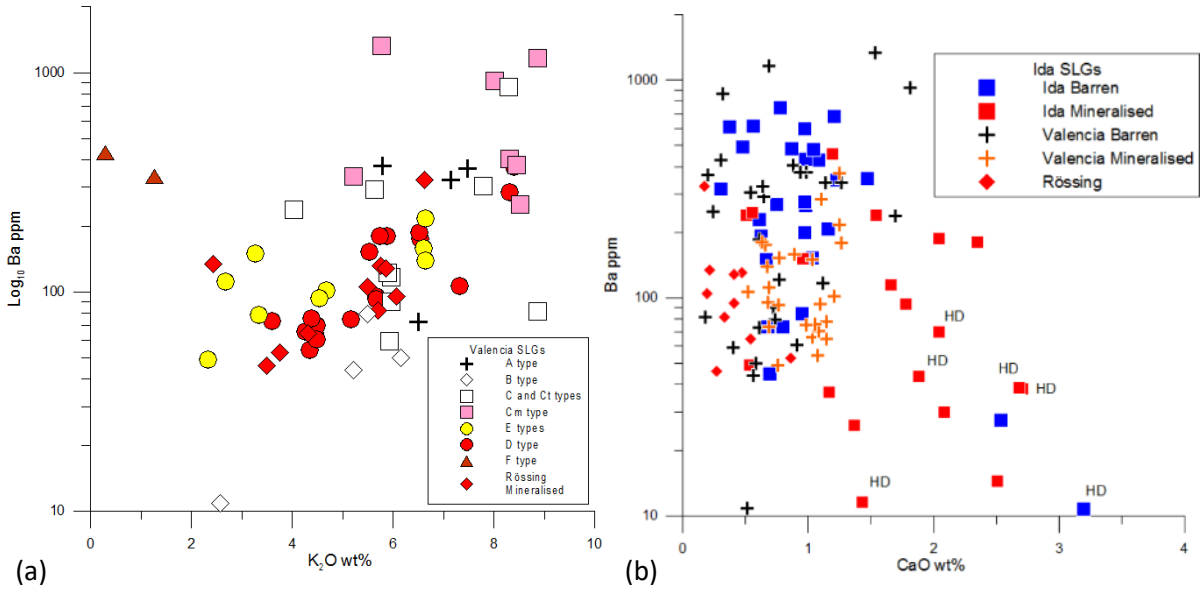



Figure 5.33 Relationships between Ba and $K_2O$, and Ba and CaO in Central Zone leucogranites. (a) There is no relationship between Ba and CaO for Valencia sheeted leucogranite types. Pre-D3 types on average show elevated Ba when compared to the post-$D_3$ uraniferous types. A-types have relatively high Ba compared to the B types and accessory-free and tourmaline-bearing C types have lower Ba than the magnetite varieties across the range of CaO values. The mineralised varieties have a higher CaO content but comparable Ba to (b) CaO vs. Ba of Valencia and Holland's Dome weakly-mineralised and mineralised sheeted leucogranites (labelled HD). Mineralised samples have consistently decreased Ba, and the Holland's Dome samples are the most calcareous with consistently lowest Ba. Ba and Sr have a systematic relationship in the

Central Zone granites (Figure 5.34). Holland's Dome and Garnet Valley samples, are relatively depleted in Ba, and plot to the extreme left and are relatively enriched in Sr. These outliers are surface samples from locations where considerable interaction between the calcareous wall rocks and the granites is observed in prominent outcrop.

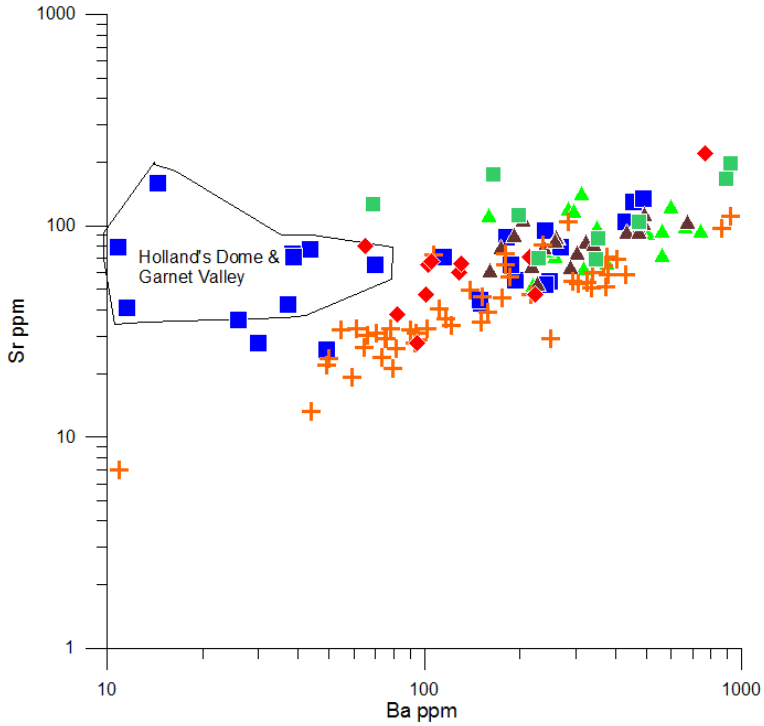



Figure 5.34 Ba vs. Sr in the SLGs. The majority of the samples conform to a shallow positive trend, where Goanikontes, Hildenhof and some Ida Dome samples tend to be Ba enriched. Holland's Dome and Garnet Valley samples are Ba depleted and some Valencia samples cluster in a low Sr cluster. Rössing sample data: Freemantle (2006).

### *Mobile Trace Element Discrimination Diagrams*

The relatively systematic behaviour of the mobile trace elements Rb, Sr, and Ba relative to major element substitutions allows for discrimination by the ratios of these elements at different deposits, and within granite populations at individual deposits (such as Valencia). Ba is generally an indication of the degree of partial melt as it partitions in early minerals, but remains available in the magma until the late stages of differentiation (Nockolds and Allen, 1956). Taylor *et al.,* (1960) showed that Ba/Rb is a more sensitive means of assessing differentiation than Rb/K for example because Ba abundance may reflect K-feldspar or plagioclase. And, Ba:Sr is expected to increase with increasing fractionation as Ba may substitute for K, essentially Ba:Sr reflects feldspar abundance and in the extracted partial

melt, K-feldspar is in greater abundance than plagioclase. Sr though, may subsititute for K or for Ca, and is shown for the SLGs to have a systematic relationship with K.

The uraniferous SLGs tend to plot parallel to the Rb-Ba axis, probably reflecting a low degree of partial melt, as Sr may be remaining in unmelted plagioclase at source (Figure 5.35a). In comparison, the Rössing samples plot closer to the Rb apex along with a cluster of Valencia sheeted leucogranite; indicative of lower degrees of partial melting and/or a component of fractionation.

Small proportions of the Husab deposit, Goanikontes, and Hildenhof samples plot within the 'Granite' field, which suggests higher volumes of partial melt, or less plagioclase – K-feldspar differentiation in these few samples (Figure 5.35a). Corresponding K-Na-Ca plots reflect the highly variable mobile trace element proportions of the Ida and Husab deposits, while in all other deposits, including Rössing, Na and K are the dominant variables, with K>Na, matching the generally high Rb:Sr and Rb:Ba ratios.

The Ida deposits in contrast have a highly variable Sr content, both in mineralised and in weakly mineralised sheeted leucogranite populations. The eratic plots on the ternary diagram (Figure 5.35a) are however, in some agreement with the highly variable Ca content (Figure 5.35b). The compositional variation and the lack of any systematic Rb-Sr-Ba trends similar to the other deposits' samples lends itself to an interpretation of significant country rock assimilation, and or Ca addition subsequent to deposit formation at the Ida Dome, and Holland's Dome in particular.

The ratios of the mobile trace elements do not appear to show any systematic relationships between successive generations of leucogranites, and may reflect different sources or melting conditions rather than successive melts of the same or similar sources (Figure 5.35c). The SLGs do show a fractionation or differentiation trend that seperates them from the less evolved Salem and Grey granites.

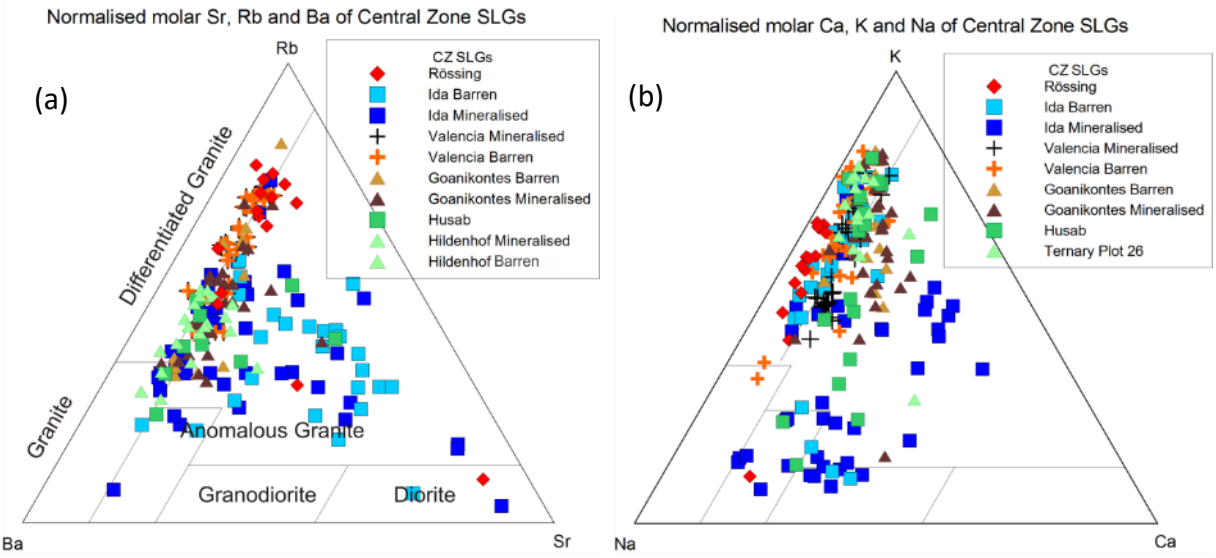
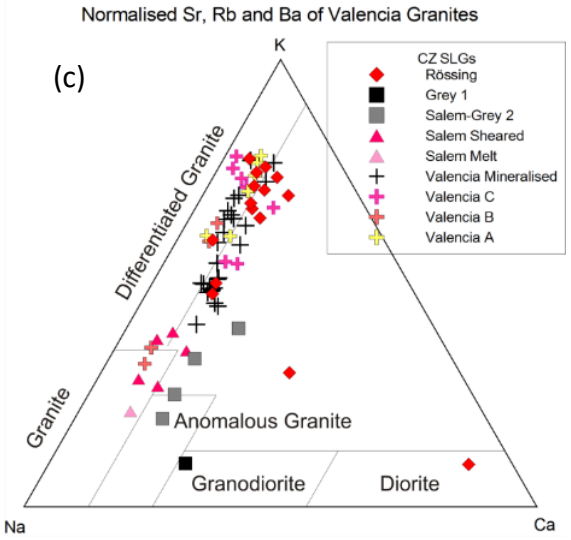



Figure 5.35 Ternary plots of Ba, Rb and Sr and Na, K and Ca proportions of the Central Zone deposits. (a) Sr-Rb-Ba ternary plot of the Central Zone pre- and post-$D_3$ leucogranite populations. The Ida Dome and Husab plot with very little systematic trend. The Hildenhof and Goanikontes samples are less-differentiated than the Valencia and comparative Rössing samples. (b) A comparison to Ca-K-Na plots most leucogranites within the differentiated field. Major elements of the Ida Dome and Husab samples show great Ca and Na variation. (c) Ca-K-Na ternary of Valencia granites. The leucogranites plot within the differentiated field and grouping of some A and C-type samples with K components comparable to the uraniferous granites illustrates the limitation of this major element discrimination diagram.




Rb is typically expected to successively increase relative to Sr in granitic rocks over time as partial melting results in successively less Sr being released from plagioclase. The expected increase in the ratio is inconsistent in the Ida Dome and Husab samples, but shows some systematic relationships in the Hildenhof, Goanikontes and Valencia samples. A number of trends with respect to mobile and major element relationships are summarised below:

- Rb:Sr increases with $SiO_2$ from type-1 Salem and grey granite to C type sheeted leucogranite;
- There is a poor Rb – $K_2O$ correlation at high concentrations of K results in some variation expected Rb:Sr in mineralised sheets;
- Low Sr in B types corresponds to the highest Rb:Sr;

- The lack of systematic Sr:Ca may be a result of Sr partitioning into K-feldspar, rather than in plagioclase;
- Country rock assimilation at the Ida Dome may be responsible for the a-typical Rb-Sr-Ba ternary plot in (Figure 5.35a);
- Magnetite bearing C types have lower Rb:Sr than accessory-free and tourmaline-bearing C types; and
- The B types from Valencia (Figure 5.35) only occur in the Kuiseb schists and have the highest Rb:Sr ratios, reflecting minimal plagioclase content. The Rb:Sr ratio increases with magmatic evolution.

The lower Rb/Sr ratios in the $C_m$- and D-types maybe due to the contribution of Ca to magmatic fluids from the reactive rocks in the lower Rössing and upper Khan Formations. The Cm-types occur in the Khan Formation proximal to the D-type sheeted leucogranites and would be affected by the same localised magmatic fluid alteration. Sub-solidus alteration has affected all of the Central Zone deposits (Corner, 1983; Nex, 1997), but other than the scattered large ion lithophile elements in the Ida Dome samples, the majority of SLG populations at each deposit plot coherently. In other words, there does not appear to be a fractionation trend in the SLG types, and variation between Ba and Rb is far greater than Rb and Sr because of Ba ability to substitute into K-feldsaprs. Ca from country rocks does not appear to have had such a dramatic effect on the composition of the SLGs, with the exception of Ida Dome area.

## 5.9 High Field Strength Elements

High field strength elements (HFSE) Ce, La, Y concentrate in common accessory minerals of the Central Zone granites, primarily in xenotime ($YPO_4$), monazite, $(Ce,La)PO_4$, and allanite, $(Ce,Ca,Y,La)_2(Al,Fe^{+3})_3(SiO_4)_3(OH)$, in leucogranites at Valencia. Zr concentrates in zircon, ($ZrSiO_4$), which may also retain uranium. The dominant phosphate in a sample with elevated Y is likely to be xenotime, and whereas if Ce and La exceed Y, monazite is likely to be the prominent phosphate phase. The following section presents and discusses systematic trends

between the HFSE in the sheeted leucogranites, with minimal emphasis placed on weakly mineralised sheeted leucogranite varieties.

Nex (1997) showed that Ce and La have a systematic relationship with respect to Th in the sheeted leucogranites at Goanikontes. The same systematic relationship holds true for most of the samples sourced from the other Central Zone deposits. Ce concentrations are roughly double La concentrations in all early sheeted leucogranite types.

Ce and La show less consistent ratios in the uraniferous leucogranites (Figure 5.36). A comparison to the REE sample group which was analysed by ICP-MS shows the ratio is relatively consistent across the range of equigranular and leucogranite types (Figure 5.36). Ce is in greater abundance than La in almost all samples, except in a small group of weathered specimens from the Hildenhof, Ida Dome, and Valencia deposits and is most likely an alteration feature of the surface environment.

The magnetite-bearing Cm types plot with relatively lower Ce and La concentrations than the uraniferous types, suggesting monazite is a restite phase in the source rocks, or is not in comparable equilibrium with the uraniferous granite melt. Y and Ce behave less systematically in the uraniferous SLGs. The relationship between the two elements does not distinguish between mineralised samples from the deposits of this study. The Goanikontes samples though, are in the more enriched category with regard to Ce, and the most enriched in Y, relative to the sample population (Figure 5.37). Most of the deposits host more Ce than Y, this contrast, though weak, either reflects contrast in the source material trace element abundances, or contrasts in HFS solubility.

Zircon is a common accessory phase in granitic rocks, occurring as a magmatic phase, or as an entrained phase from the precursor rock/s. Zircons in the granites of the Central Zone are often brown in colour, an effect of the radioactive inclusions that they host and in almost all observed examples they are prominently zoned. Zircon is able to host both uranium and uraninite. Atomic recoil as a result of radioactive decay results in metamict crystals, which subsequently expand in volume; the expansion is accommodated by radial cracks in the surrounding feldspar and quartz to form around the included zircons (Chapter 3 and Chapter 4). The trace element Zr is an indicator of the relative amount of zircon present in a sample, and a plot of U vs. Zr is therefore a crude indicator of any relationship between U content

and zircon abundance. Figure 5.38 illustrates a poor correlation between the U and Zr content of mineralised samples.

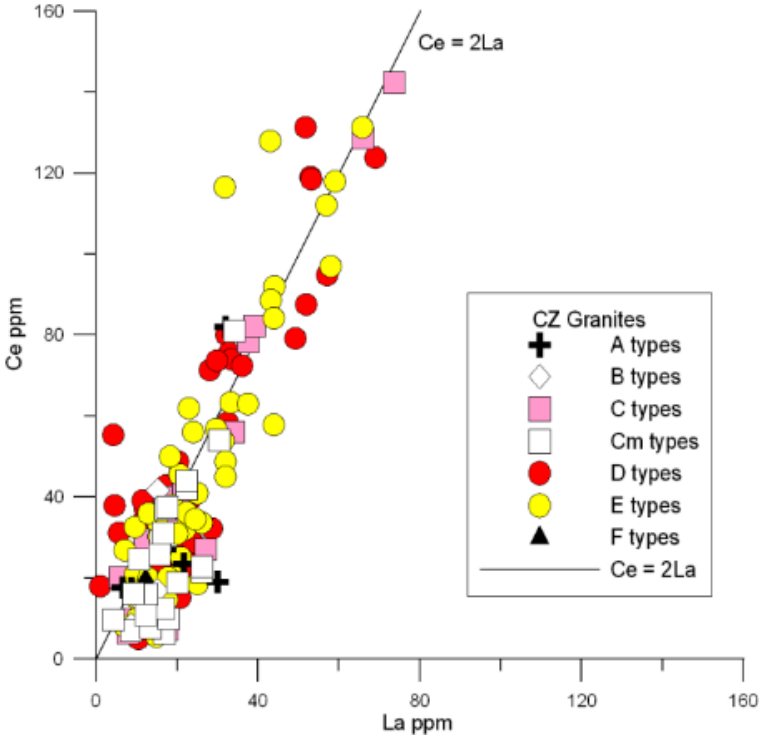



Figure 5.36 La vs. Ce in Central Zone sheeted leucogranite. (a) Ce and La show a systematic ~2:1 relationship overall in the Central Zone sheeted leucogranite, indicative of occurrence solely within monazite. D-type sheeted leucogranites tend to have higher Ce and La concentrations, while the majority of the weakly mineralised samples plot below the 2:1 line with Ce and La <40 ppm. Some of the magnetite-bearing C-type plot with a consistent ratio with concentrations comparable to mineralised sheeted leucogranite. Rössing sample data: Freemantle (2006).

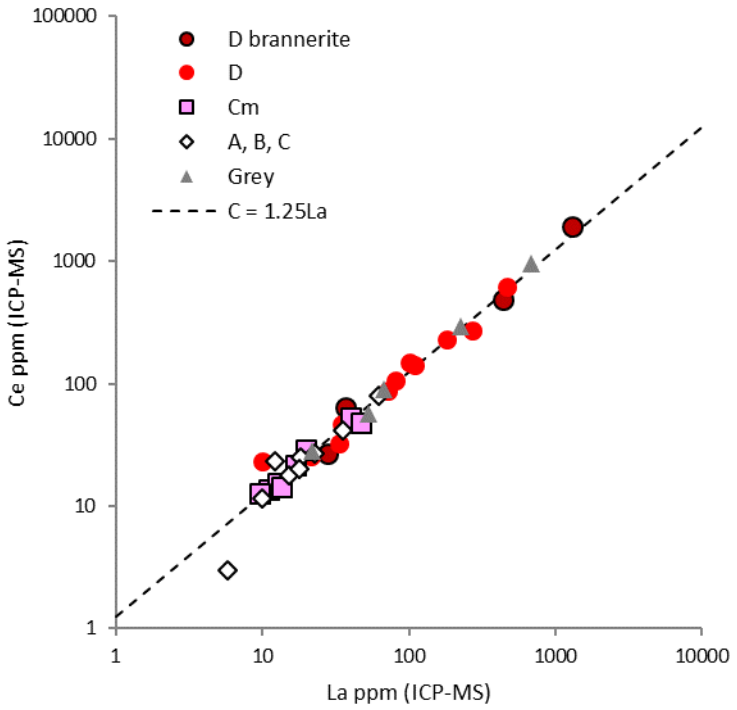



Figure 5.36 Ce vs La of 41 samples analysed by ICP-MS. Ce is consistently 1.25 x La, which is inconsistent with the average of 2:1 in the XRF dataset. A, B, and C types have low HFS abundance, as do the Cm types. The D-type SLGs show a range of HFS abundance but tend to be greater than in the pre-D3 leucogranites.

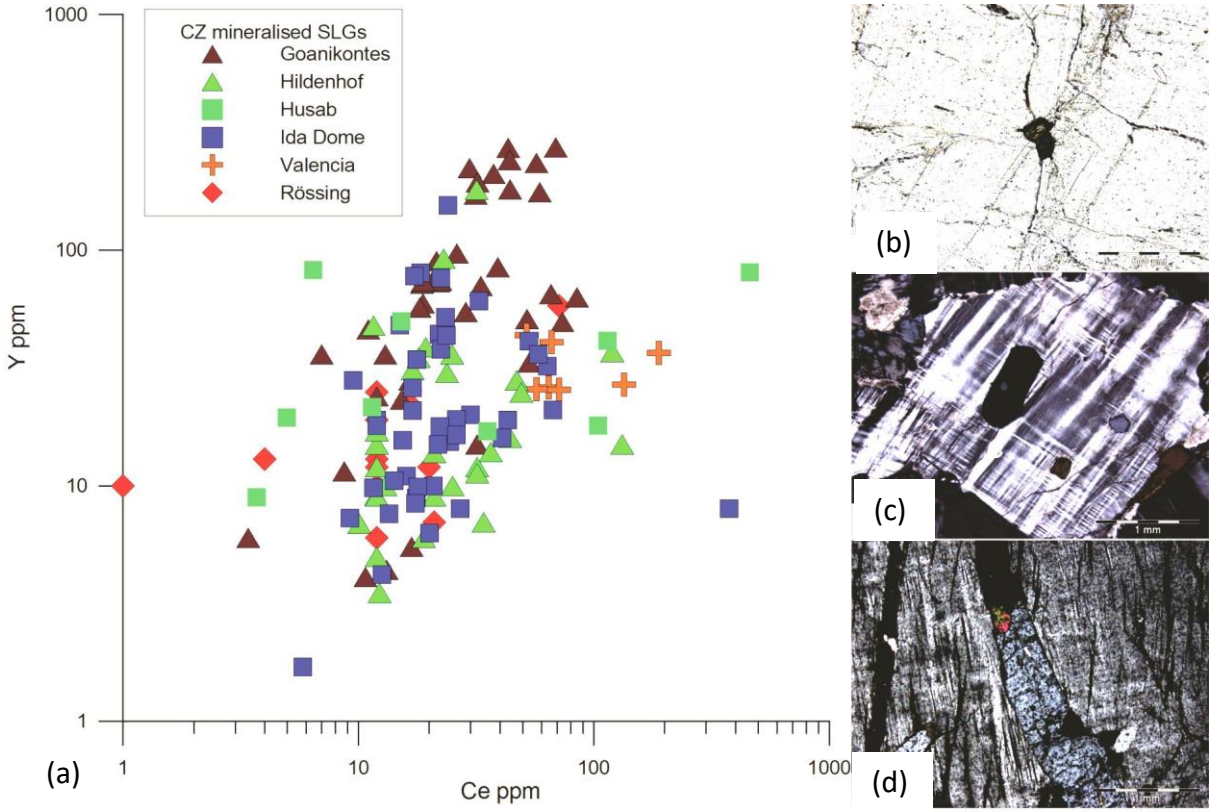



Figure 5.37 Ce and Y content of mineralised sheeted leucogranite and photomicrographs of phosphate minerals. (a) Y and Ce ratios are only weakly systematic, illustrating a variable abundance of monazite and xenotime. The relatively high Y/Ce ratio of the Goanikontes samples for example suggests xenotime is the dominant phosphate, in addition to apatite. Valencia contrasts with comparatively few samples hosting Y above 5 ppm. The weakly linear trend in the Ida Dome samples indicates that xenotime and monazite are present. (b) Xenotime and zircon between quartz and microcline, ppl, DH25 334.99-355.45. (c) Apatite is a prominent P-bearing phase and does not hold significant lanthanides or Y, xpl, HILG 22. (d) The Valencia deposit has samples of apatite >3 mm long but relatively little xenotime.

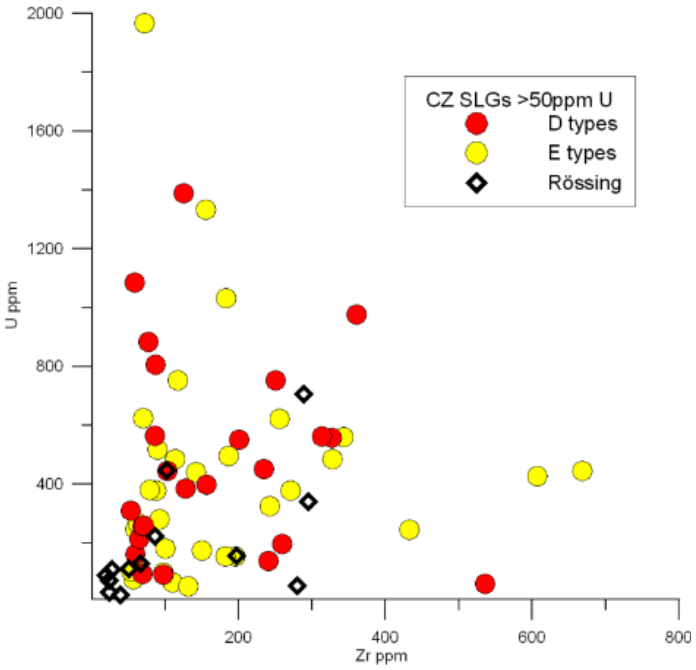



Figure 5.38 Graph of U vs. Zr of the Central Zone uraniferous SLGs. Uranium and zirconium both occur in zircon, which may co-exist with uraninite in phases such as biotite. Despite the co-existence there is no apparent relationship between the two elements in the Central Zone leucogranite suites.

In summary, Ce, La and Th show elevated abundances relative to those of the older weakly uraniferous sheeted leucogranites although the magnetite-bearing C-types show similar Ce and La trends and concentrations to those of the mineralised samples.

The weak correlation between decreasing La/Th and increasing U in the uraniferous samples from Goanikontes and Valencia probably reflects a variable La- and Ce-monazite population with Th and U content (Th may be hosted in uraninite and U-thorite) in a positive relationship reflected by the lower La/Th. The Y-rich samples appear to have a restricted distribution in the sampled boreholes, reflecting a lithological control/source within the Khan Formation at Goanikontes and for some Husab samples.

### *Trace Element Indicators of Granite Source Affinity*

Chappell and White (1974b) suggested that the bulk of granitic rocks tend to lie within one of two main categories; the I-type and S-type or, those derived from igneous dominated sources, or from sedimentary sources, respectively. Petrographic investigation of the sheeted leucogranites and the earlier Salem and Grey type granites at the deposits strongly support hydrous melting (Tuttle and Bowen, 1958), rather than anhydrous melting, which other than requiring considerably higher temperatures than the granulite facies of the Central Zone (Goscombe *et al*., 2003a; Longridge, 2012) would also produce granites with very little mica and amphibole.

The leucogranites and the biotite-bearing Grey- and Salem granites all host biotite of varying texture; some of the tourmaline- and garnet-bearing granites hosting sillimanite and muscovite, implying a metasedimentary (pelitic) source; and some of the older diorites host amphibole minerals (McDermott, 1986). Thus it is likely that most of the granites at the deposits are products of hydrous melting, involving biotite-breakdown among other minerals. Clemens (2014) suggests that certain trace element abundances and relationships may be useful indicators of source rock tenor, with the main implication that metasedimentary sources pass on their fabric-influenced elemental distributions to the resulting melts.

This principle is derived from work by Watt and Harley (1993). The discriminator, Ba is used as a proxy for partial melt, and compared to Zr and Y; Ba is an indicator of how much biotite has melted completely, and Zr is likely derived from biotite in metasedimentary protolith. This relationship is interpreted from linear Ba/Zr relationships in S-type granites (Clemens, 2014). Y and Ba relationships are also shown to be linear in S-type granites, because garnet as the main reservoir, transports Y as an entrained phase, in addition zircon and monazite may be progressively liberated as biotite melts, adding Y to the melt fraction. Ba, Y and Zr trends are illustrated in Figure 5.39a to Figure 5.39d, comparing the largely pre-$D_3$ sheeted leucogranites (Zr and Y in Figure 5.39a and Figure 5.39b, respectively) with the largely syn- to post-$D_3$ D and E-type alaskite varieties (Figure 5.39c and Figure 5.39d).

The A and B-type SLGs show the only real linear relationship, and this is between Ba and Zr, and therefore represent biotite breakdown to form S-type melts. Ba and Y however, do not show a linear relationship, implying that Y may be derived from minerals that are not inclusions in biotite, if biotite melting in the metasediments has indeed generated the melts. Zr and Y abundances distinguish some of the D-type SLGs from the pre-$D_3$ weakly uraniferous varieties, in comparison Y and Zr also show almost no relationship with Ba in the D-types just as in most of the pre-$D_3$ SLGs.

The implications of these plots are that the sheeted leucogranites, with the exception of B-types, are not likely to be derived from exclusively metasedimentary sources. Determining their source is also made equivocal by the compositions of the potential source rocks, the Nosib Group is derived predominantly from eroded Abbabis Basement as shown in $^{143}Nd/^{144}Nd$ and $^{87}Sr/^{86}Sr$ and Sm/Nd ratios (McDermott *et al.*, 1996).

The magnetite bearing sheets are exclusively sampled from the Khan Formation, these granites tend to be parallel to the foliation in the transposed bedding, and do not appear to be derived from within the Khan, at least not within the vicinity of the outcrop. Thus, they may be derived from the basement as similar textured, and magnetite bearing pegmatites also invade the gneissic rocks of the Abbabis inliers at the Ida Dome, Valencia and along the Khan and Swakop River valleys.

The basement had already developed a fabric prior to Damaran-age deformation (e.g. Sawyer, 1981) which may manifest S-type like elemental distribution in the partial melt

products. The uraniferous granites on the other hand must have been produced from either similar rock but at higher metamorphic conditions liberating zircon and monazite-bound elements; or, are derived from source(s) that have a less sedimentary affinity than the pre-$D_3$ sheets. In the case of the latter, McDermott *et al.* (1996) offer the anatectic Red and Grey granites as sources of the sheeted leucogranites. The lack of S-type affinity shown in the trace element plots (Figure 5.39) is in agreement, robust isotope data is required to support this hypothesis. In addition, the P-T conditions at peak metamorphism may be adequate to melt pelitic rock as shown in Ward *et al*. (2008) but may not be sufficient to melt rocks that are anhydrous. Haack *et al*. (1983) suggest that these source granites could have elevated the local T° by their internal radiogenic heat generation.

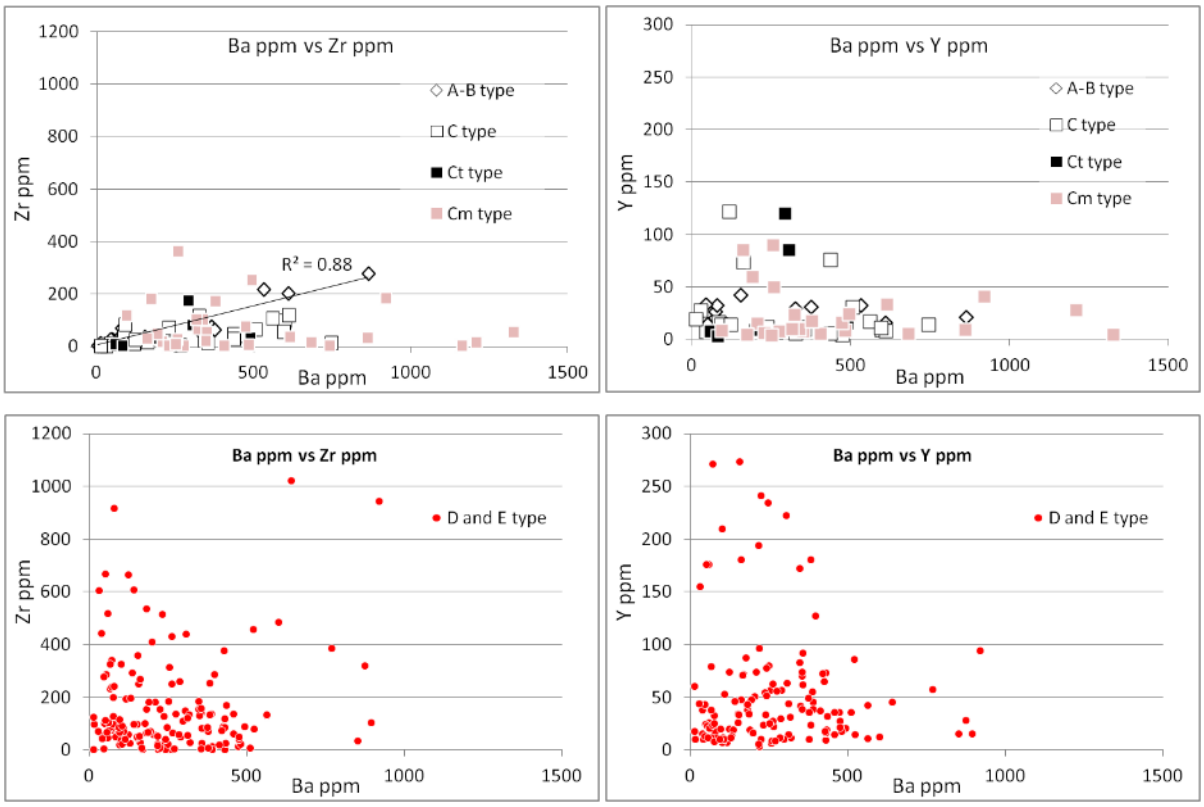



Figure 5.39 Trace element trends of pre-D3 sheeted leucogranites and uraniferous sheeted leucogranites as indicators of I- or S-type affinity. (a) Ba vs. Zr of pre-D3 leucogranites, there is an overall low abundance of Y and potentially a weak linear trend in the Cm type, but a strong correlation in the Kuiseb-Formation derived B-type as illustrated by the 0.88 R2 of the A- B-type group. (b) Ba vs Y is comparable to Zr, however only weak, low abundance relationships are apparent. (c) The uraniferous leucogranites do not show any correlation between Ba and Zr. (d) The relationship with Ba is similar with respect to Y, though with some imagination there is perhaps a positive correlation within some of the high-Ba samples.

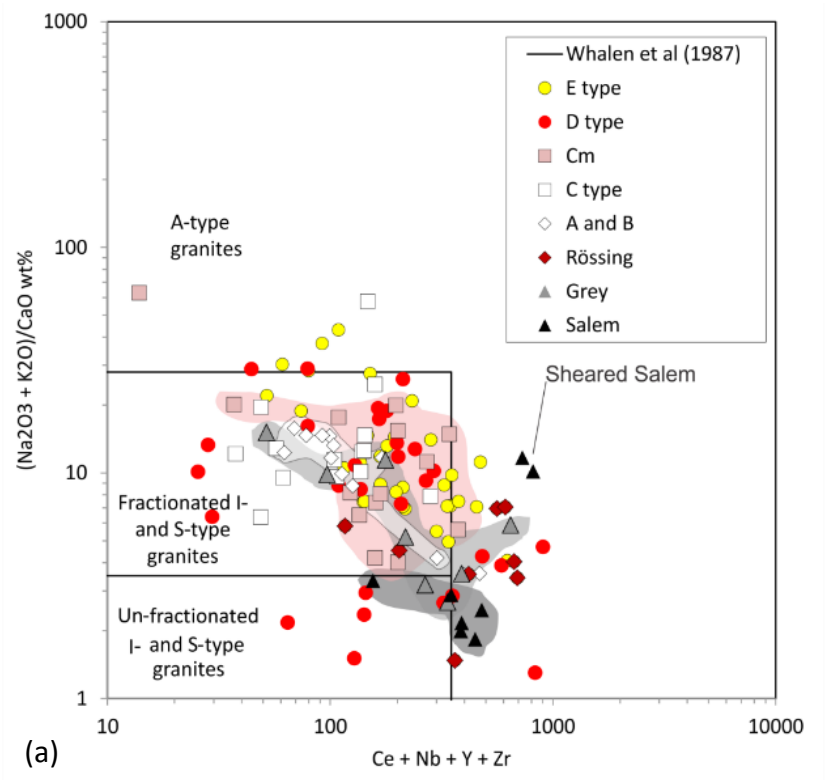
### *Discrimination Diagrams*

The high field strength elements are often used in granite classification schemes (I, S, and A type granites) and tectonic setting discrimination diagrams. In this section the hyphenated *A-type* refers to a sheeted leucogranite of specific description (from Nex, 1997) and unhyphenated *A type* refers to an anorogenic style granite. Typical discrimination diagrams compare concentrations of Ce, Nb, Ta, Y, Yb, and Zr, which reflect accessory mineral abundances, with ratios such as maficity or calc-alkali ratios. These elements have been shown to be relatively insensitive to alteration in granites (Pearce and Cann, 1973). Ga-Al ratios typically differentiate between A-type and I- or S-type.

The major and mobile trace elements plots of data from leucogranites in this study show systematic behaviour between Sr and Ba, and between Rb and K. Rb/Sr increases systematically in leucogranites intruded at higher stratigraphic levels. Maficity is less systematic but differentiates between pre- and post $D_3$ granites. The biotite-bearing Salem and Grey granites (the equigranular suites) that are weakly uraniferous and the uranium-enriched granites are all reasonably distinguishable by major and mobile element ratios. Mobile element discrimination ternary diagrams of El Bouseily *et al.* (1975) show with some limitation that the uraniferous granites are more differentiated than the weakly mineralised pre-$D_3$ granites. The discrimination diagrams of Whalen *et al.* (1987) and Pearce *et al.* (1984) that follow, compare the abundances of HFSE to the mobile and major trace elements, and may be considered as additional, more robust, discriminators because of the behaviour of the HFSE elements.

The high field strength element (HFSE) abundance plots (Ce+Nb+Y+Zr) in Figure 5.40 show relatively consistent trends with respect to total alkali-oxide/CaO ratios, where increasing abundances of HFSE correspond with A type granite concentrations (Figure 5.40a). The A- and B-type SLG samples plot with a strongly linear, negative relationship between calc-alkali and HFS element abundance. Total Fe ($Fe_2O_3$ as analysed) and MgO ratios expressed as $FeO_{tot}$/MgO ratios are inconsistent with the calc-alkali ratios, with most samples plotting within the undifferentiated field. There is a clear divide between the magnetite-bearing ($C_m$) and C type leucogranites; where the $C_m$ are relatively HFSE element-enriched and plot with abundances comparable to the D-type (Figure 5.40b).

The HFS abundances of some D and E types would suggest A-type affinity, but the $FeO_{tot}$/MgO ratio is low and more consistent with the un-fractionated granite field. The contrast in Alkali and Fe ratio plots is best explained by the low abundances of mafic minerals in the leucogranite populations.



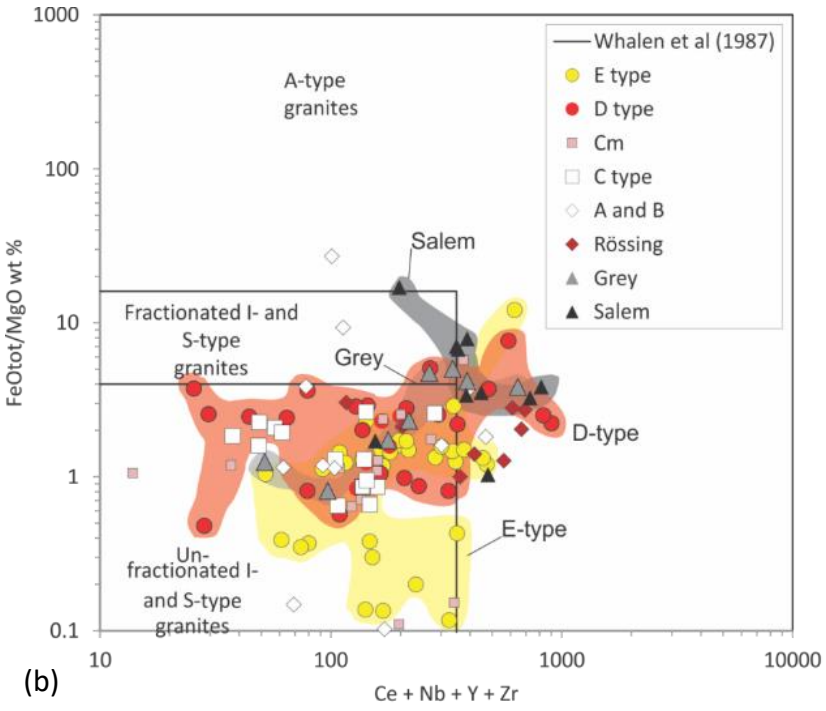




Figure 5.40 Discrimination plots of (Ce+Nb+Y+Zr) in CZ granite types, with fields from Whalen *et al*. (1987). (a) The majority of granites plot within the differentiated field for I- and S-type granites. The A and B type granites, which are hosted in the Chuos and Kuiseb Formations, show the closest correlation. The Grey and Salem suites also exhibit a close correlation. High fractionation ratios do not correspond with HFSE abundances. Rössing data from Freemantle (2006); data also contributed from Johnson (2011). Samples in which one or more HFSE analyses are missing are not plotted.

(b) The total Fe:Mg ratios of the leucogranites and Salem and Grey granite suites support an un-fractionated source. The maficity ratio differentiates between the D- and E-type leucogranite varieties somewhat. The Salem granites and the pre-$D_3$ sheeted leucogranites appear to have a negative maficity abundance with respect to HFS abundance. Only the Salem type granites have maficity ratios that imply some fractionation.

Ga/Al ratios tends to be low, rarely above 2 with none of the granite ratios plotting above the discrimination line of Whalen *et al.*, (1987) at 10 000*Ga/Al = 2.6 (Figure 5.41). Na+K/Al wt.%, K/Mg wt.%, or $Fe_{tot}$/Mg wt.%. ratios are equivocal; most of the samples plot within the 'other granite' field with limited distinction between the uraniferous populations (Figure 5.41a, Figure 5.41b, and Figure 5.41c). However, whereas the Rössing and Hildenhof samples approach the alkali-alumina discrimination line; the A, B- and $C_m$-types cluster with low Ga/Al and variable alkali: alumina, the younger $C_m$-type having the higher alkali ratios. The Husab sample set, which includes data from Johnson (2011) tends to low Ga:Al with increasing alkali ratios.

The $K_2O$/MgO ratios show a contrast between the Husab D-type and the comparative Valencia, Rössing, and Goanikontes D- and E-type samples (Figure 5.41b). Husab SLGs plot with low K/Mg and a negative trend with Ga/Al, while the other populations tend have variable, but high K/Mg (Figure 5.41b). The plot also shows distinct differences between the pre-$D_3$ leucogranites and equigranular granite populations; A, B, and $C_m$-types plot within the A-type field with high K/Mg, while most of the mafic-bearing equigranular granites plot with low ratios. There is a steep negative trend in $K_2O$/MgO with respect to 10K*Ga/Al. The sheeted leucogranites are partial melts, as such, plagioclase should retain some Al in the source, and the K and Ga ratios should both increase systematically with respect to Mg and Al, with increasing melt. The opposite is observed and indicates that the D- and E-type SLGs are produced from very low %age melting.

Iron- magnesium ratios tend to be low, with most samples plotting in the 'other granite field' with a few $C_m$ and B-type leucogranites plotting in the A-type granite field, and the Valencia samples plotting with distinctly low FeO/MgO ratios[43] (Figure 5.42). The ratio is diagnostic, with the Husab and Ida Dome SLG populations, showing distinct ranges of $FeO_{tot}$/MgO for the two populations. The Husab samples have a lower Fe:Mg, and a weak negative relationship with respect to 10K*Ga/Al. The Hildenhof and Goanikontes samples plot with intermediate ratios between the Husab and Ida Dome SLGs.

[43] The samples in the diagram are plotted from analyses in which MgO and $Fe_2O_3$ are above XRF detection limits.

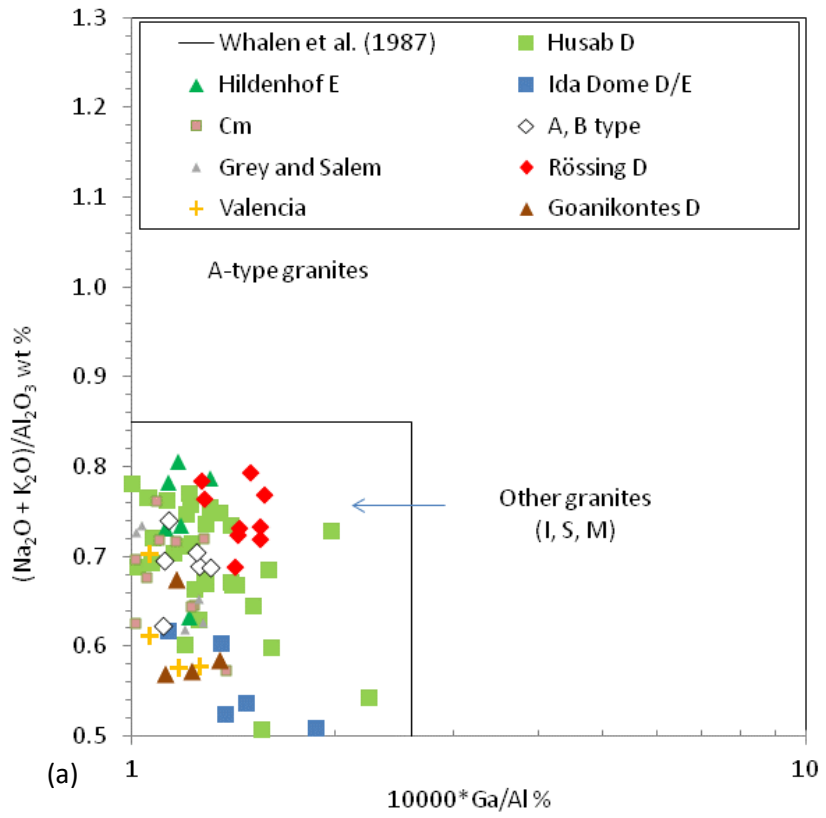



Figure 5.41 Ga/Al and major element discrimination plots of Central Zone leucogranites, Salem, and Grey granites. a) Ga/Al vs. $Na_2O+K_2O/Al_2O_3$ shows most leucogranites and grey granites fit in the field of 'other granites'. The Ida Dome samples plot with low total alkali, reflecting the effects of anomalously high CaO as seen in other classification and discrimination plots.

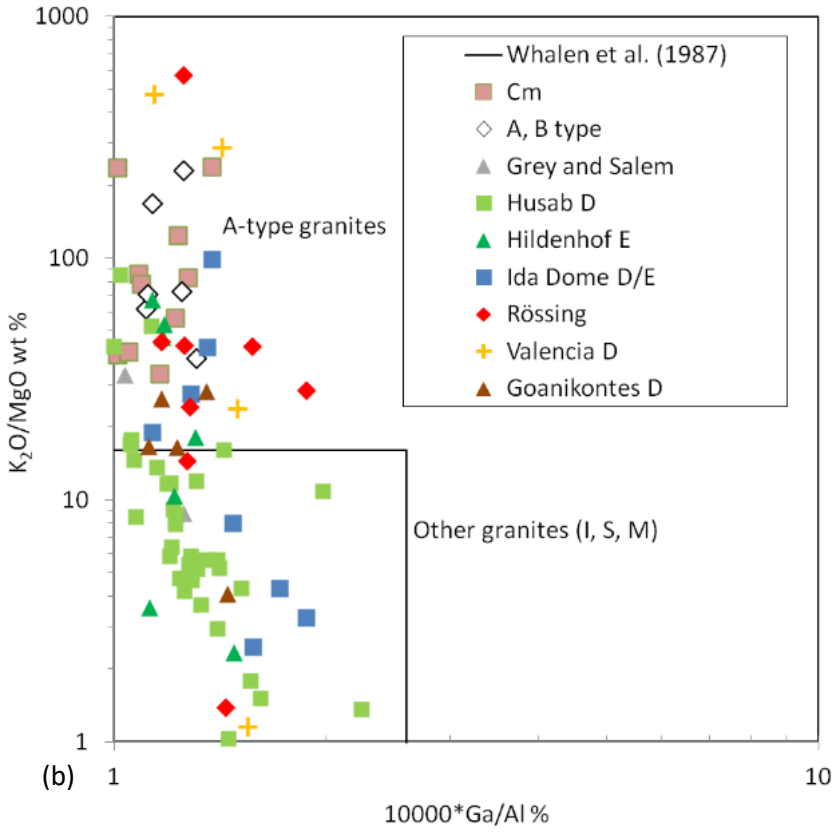



Figure 5.41 (b) $K_2O/MgO$ ratios show a far wider range with the Valencia, most Goanikontes, and Rössing samples plotting in the A-type field. Ida Dome, Hildenhof, Rössing, and the Salem and Grey granites plot in both discrimination fields. The Cm samples all show A-type ratios of K and Mg.

The $C_m$ samples plot in two distinctive populations, in which $FeO_{tot}$/MgO is either >- or <1 (Figure 5.42). The most reasonable explanation for the magnetite-bearing granites to have this bimodal distribution is the amount of interaction with diopside (Mg)-bearing lithologies of the Khan Formation that is observed at the Ida Dome and Valencia deposits. All but two of the comparative Rössing samples plot with lower FeO/MgO than the Husab population and only the Valencia samples show a positive relationship between the ratios, but the concentrations and number of samples are too low to draw any meaningful conclusions. $FeO_{tot}$/MgO may be elevated enough in some samples to be classified A-type, the bulk of the samples do not adhere to the trends outlined in Whalen *et al.* (1984) and do not plot within the required fields.

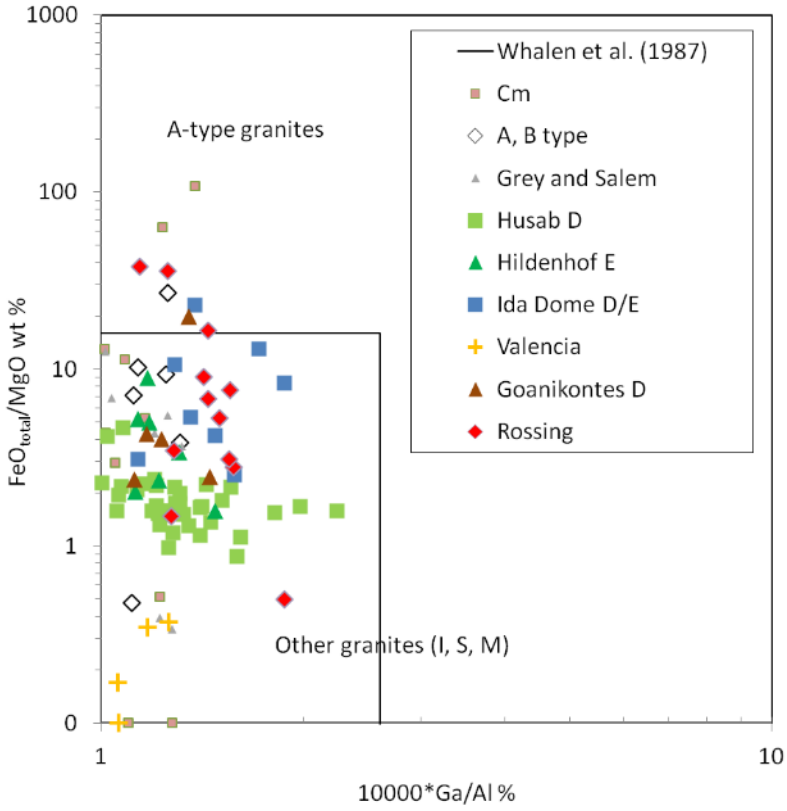



Figure 5.42 $FeO_{tot}$/MgO ratios of SLGs at the CZ primary U deposits. Fe/Mg ratios tend to be low, with most leucogranite samples plotting with ratios less than 2. The magnetite-bearing granites are oxidised and thus host accessory magnetite in variable abundances, reflected in high FeOtot/MgO ratios. The Goanikontes samples plot with relatively high FeOtot/MgO relative to the Husab and Valencia samples, while the Ida Dome uraniferous granites plot with the highest average FeOtot/MgO of the mineralised suit.

Whalen *et al.* (1984) show that in anorogenic A type granitoids, Fe/Mg tends to increase with increased fractionation, i.e. Al is retained in plagioclase. The overall trend in the Husab sample set is that of decreasing $FeO_{tot}$/MgO with respect to 10K*Ga/Al. The Ida Dome samples are comparable. Overall the plots do not support fractionation, and Ga ratios are too low in the SLG samples of this study to be considered as anorogenic, A type granites.

Another means of classifying the SLGs through their chemistry are tectonic discrimination diagrams, such as those of Pearce *et al*. (1984). The diagrams in Figure 5.43 and Figure 5.44 show a clustering of SLG compositional data at the intersection between the fields of syn-collision-, within-plate- and volcanic arc granitoids.

The D type granites show relatively high Rb with respect to all other samples, including for the most part the E-type samples (Figure 5.43a) and predominantly plot in the 'within plate' field. The magnetite-bearing $C_m$-type SLGs plot as syn-collision more than any ther field. The C-type, Salem, and Grey granite suites plot close to the junction between syn-collision and within plate fields. The individual suites of uraniferous SLGs at each deposit area show some discrimination between the deposits in Figure 5.43b:

- Goanikontes D-type and E-type sheeted leucogranites plot within plate, while the nearby Hildenhof samples plot as syn-collision; and
- The Ida Dome samples have comparatively low Rb enrichment, and so plot in the 'volcanic arc-within plate' compositions.

There is an even spread of 'within plate' and 'syn-collision' compositions in the Husab population and the comparative Rössing samples predominantly lie within the syn-collision field. Only the Valencia samples show a positive relationship between HFS abundance and Rb abundance. It may be argued that the linear relationship displayed in the Valencia leucogranite suite shows that the deposit has the least evidence of assimilation and extensive alteration that may have affected the Rb abundance.

Yb+Ta vs. Rb is shown in Figure 5.34a, and is limited to 41 ICP-MS samples from the REE dataset; Ta abundance is low and not detected in most of the XRF analyses. The plot successfully discriminates between the C type-dominated pre-$D_3$ samples and the brannerite-bearing samples from Husab. The trend of C-types being enriched in Rb with respect to the D-types in the XRF dataset is consistent with the ICP-MS dataset (Figure 5.44a). The ratios however, are equivocal with respect to discriminating the tectonic setting of the uraniferous granites. Y and Nb ratios show the most distinct difference between the pre-$D_3$ (C- and $C_m$-type) leucogranites and the uraniferous populations (Figure 5.34b). The equigranular granites plot between the two leucogranite groups. Both Nb and Y are

relatively enriched in the younger uraniferous populations, but relatively few contain Y in the 100's of ppm abundances normally expected for A-type granites or NYF pegmatites (e.g. Ercit, 2005b).

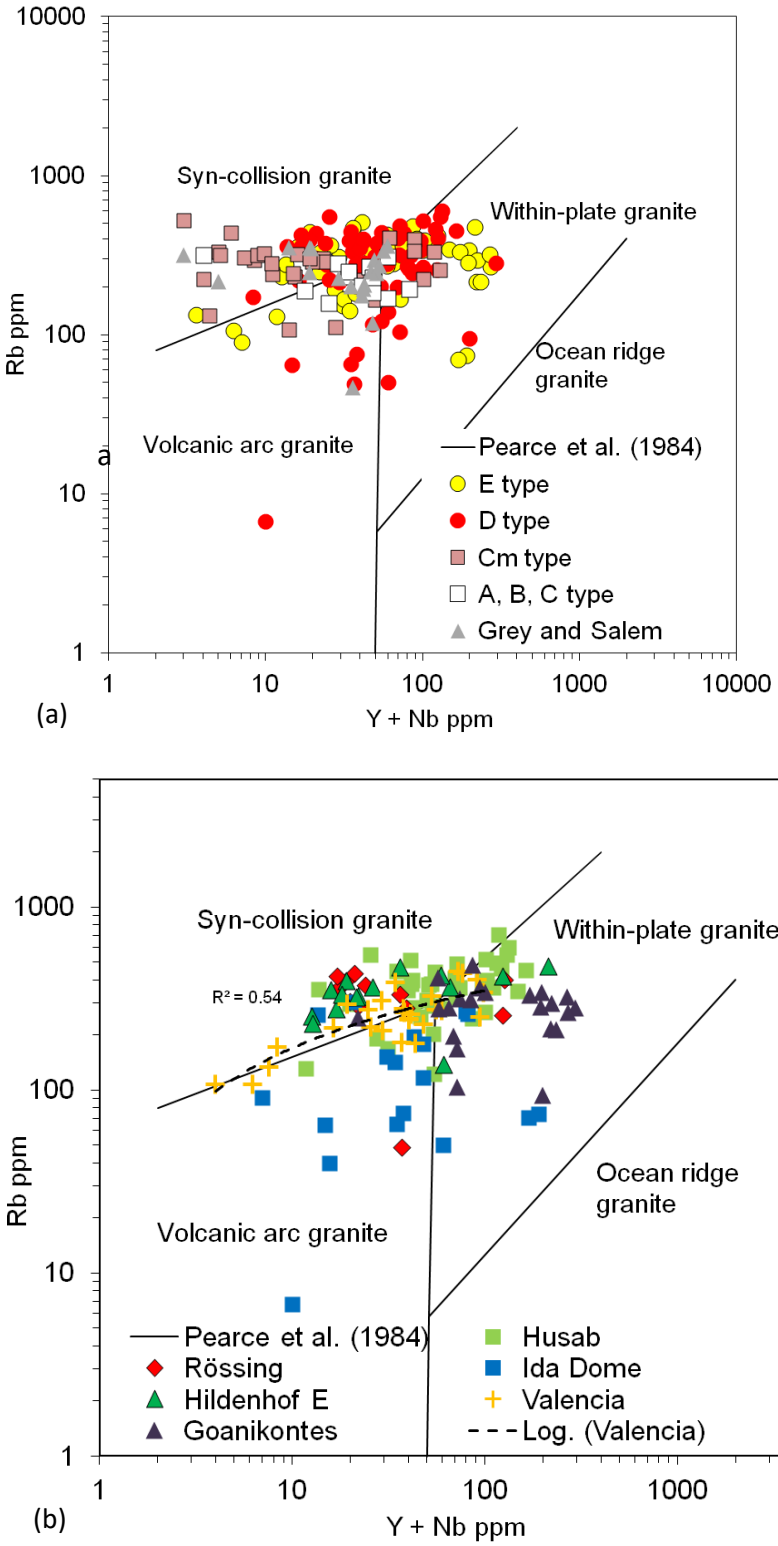



Figure 5.43 Y - Nb and Rb discrimination diagrams of Central Zone uranium deposit granites with fields from Pearce *et al.* (1984). (a) Central Zone A-C type, Cm-type, D- and E-type, and the Grey and Salem suites. the plots show a distinction between the uraniferous varieties (D, E) and the Cm samples; mineralised samples predominantly plot within and near the 'within-plate' field, and the un-mineralised samples plot from syn-collision through within-plate.

(b) The uraniferous sheets at the primary deposits show a number of trends; the CaO-rich Ida Dome samples plot with low Rb in the volcanic arc field, the Valencia samples show a systematic relationship with Y+Nb along the syn-collision volcanic arc line, the Goanikontes sample plot in the within plate field, and the Husab samples plot with relatively high Rb near- and in the within-plate field. The comparative Rössing samples tend to plot in the syn-collision field. The Valencia samples show the most obvious positive trend between Y+Nb and Rb. The trend is weakly apparent in the Husab samples, and less so, in the sample suites for the Ida Dome and Goanikontes deposits.

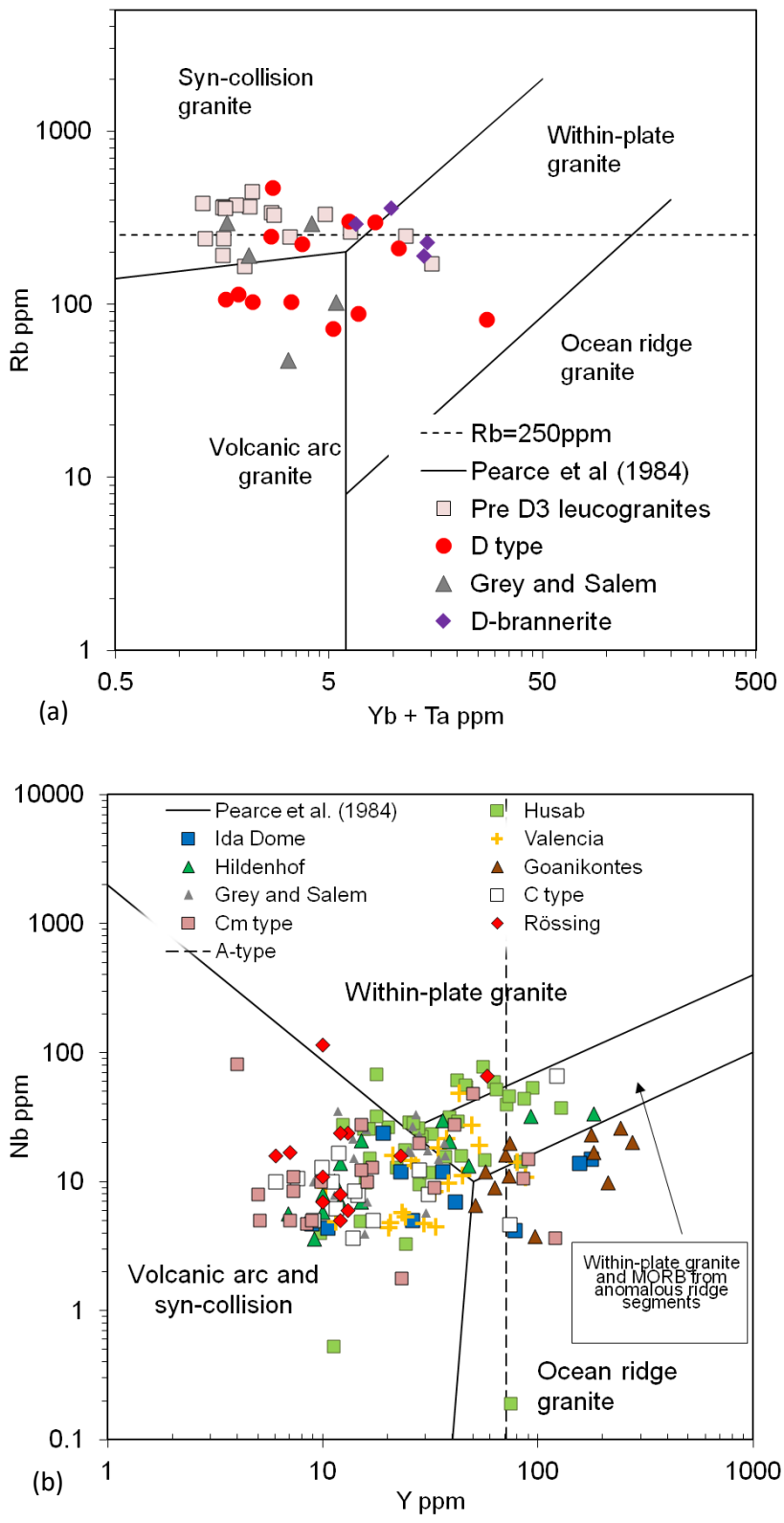



Figure 5.44 Y and Nb, and Yb - Ta and Rb discrimination plots with fields from Pearce *et al*. (1984). (a) Yb + Ta vs. Rb plot using ICP-MS analysis. The ICP-MS data set is limited to 37 leucogranite samples, of which 14 are classified as D-or E-type. Rb content of the pre- and post-$D_3$ leucogranites straddles the 250 ppm line of Chappell and White (1992); as with Figure 5.33a, Rb is elevated in the pre-$D_3$ granites relative to many of the D-type and E-type sheets. There is a bi-modal distribution with respect to the HREE (Yb and Ta abundances), with distinctly less spread in the pre-$D_3$ leucogranites. The brannerite and betafite-bearing samples are Yb and Ta enriched relative to most samples.
(b) C- and $C_m$-type leucogranites, and the Grey and Salem suites appear to be restricted to the syn-collisional field, while the uraniferous populations plot across the syn- and within-plate fields. The relatively high Y of the Goanikontes samples and the high Nb of the Husab samples adds to the diversity of the leucogranite sample distribution on the diagram. The majority of the Rössing mine samples plot within the syn-collisional field.

### *Transition Metals*

Base metal data is not available for all samples. Metals such as Cu-Pb and Zn occur in sporadic distribution throughout the Central Zone. Numerous skarn-associated deposits occur within the Khan Formation, characterised by titanite-diopside-spinel bearing pegmatites, with associated magnetite and base metal-sulphide mineralisation. The Khan Mine and Ida Mine are well known examples of copper mining and abandoned workings of the Kainkaghas Mine occur NE of the Valencia Deposit. Söhnge (2001) recounts a strong association of uranium mineralisation with Cu in the alaskites that invade the Khan Formation schists of the Ida Dome at the Ida Mine (now Ida Central uranium deposit). In addition, the newly discovered Husab deposits contain abundant examples of Mo disseminations and veinlets, and prominent pyrrhotite in massive- and blebby textures, particularly in samples that intrude skarns. Pentlandite occurs in some of the pyrrhotite, which is one of the Fe repositories with pyrite in the locally reduced leucogranites.

The leucogranites of the Central Zone contain trace zinc and lead, and instead are more copper molybdenite associated. Figure 5.45a illustrates total base metal concentrations in the sheeted leucogranites, discriminated against uranium abundance. Data from Johnson (2011) is included and plotted as Husab*. There is an overall positive correlation. The mineralised sheets that intrude the upper Khan Formation at the Ida Central deposit show elevated concentrations of Cu, supporting a high granite-metasediment fluid interaction during emplacement. Molybdenite occurs in skarn localities of the southern Central Zone, particularly at Goanikontes and the Rössing Mine; data are available for samples from all the deposits, but it only exceeds detection limit in the Valencia and Husab samples of this study.

The ore petrography study suggests that most of the sulphides crystallised in the SLGs as late features with respect to uraninite; Figure 5.45b shows fine-grained molybdenite surrounding uraninite within alaskite of the Husab deposit. Locally Mo abundance may be greater than Cu or Ni, but in most deposits observed in this study pyrrhotite or chalcopyrite are the next most abundant sulphides after pyrite. Figure 5.45c illustrates millimetric chalcopyrite-bornite in alaskite of the Ida Central deposit; a representation of the close U-Cu mineralisation at the Ida Mine location.

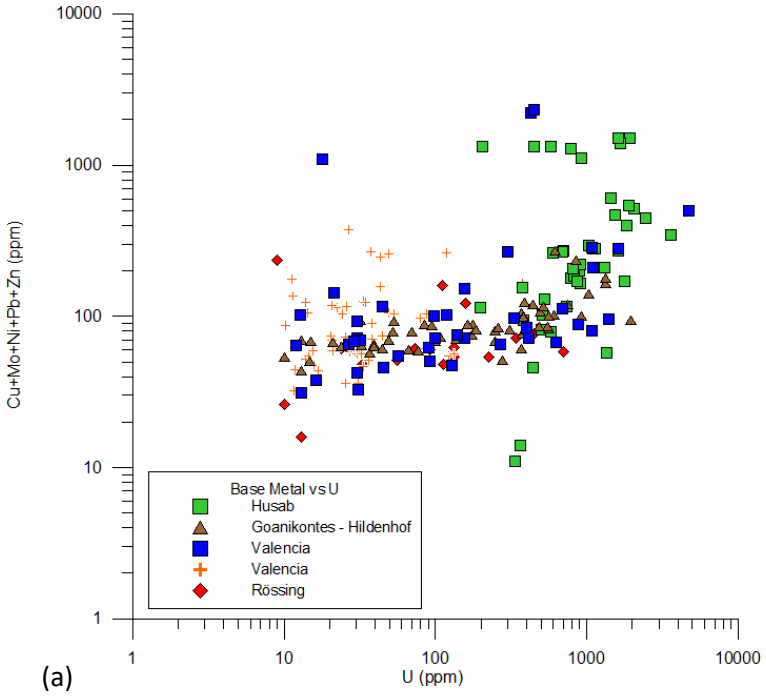



Figure 5.45 Transition metal trends in the Central Zone alaskites. (a) Plot of U vs. total base metals of Central Zone sheeted leucogranites. Total base metal content includes Co, Cu, Mo, Ni, Pb, and Zn in ppm. Numerous occurrences of molybdenite are found in the Rössing pit (Abraham pers comm., 2008). Alaskites have intruded sulphide-bearing skarn lithologies. at Valencia and the Ida Dome; samples from near the Cu workings at each host anomalous base metals. The Husab samples from this study show elevated base metals (Mo and Ni in particular) relative to the other deposits, Ni in particular is >1 000 ppm in some samples (Husab*: Johnson, 2011).

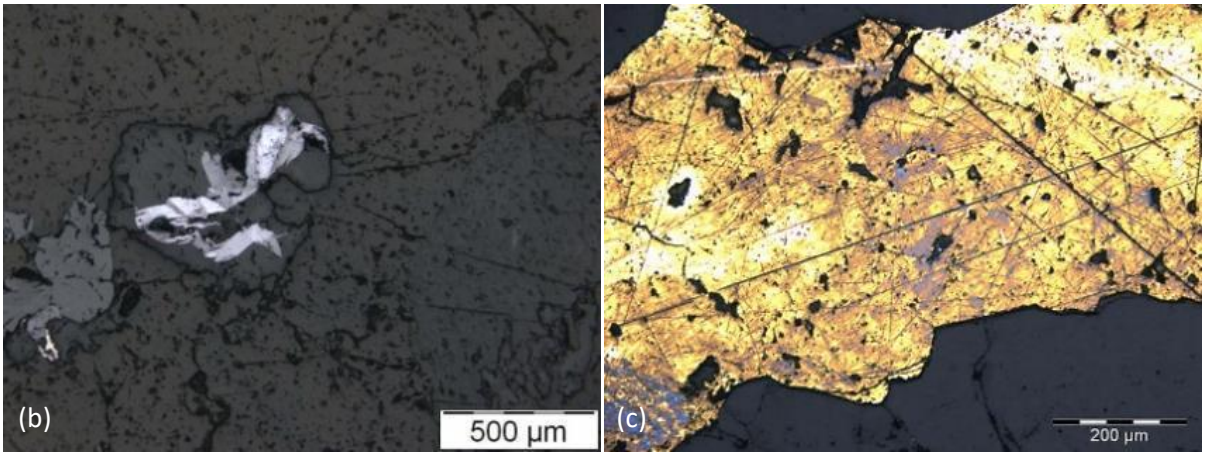



Figure 5.45 (b) Molybdenite surrounds uraninite in Husab leucogranite and (c) chalcopyrite is altered to bornite in an Ida Dome leucogranite. Rössing sample data: Freemantle (2006).

## 5.10 Uranium and Thorium

Uranium and thorium ions are large, very close in size (4.265 AU and 4.223 AU, respectively) and both are strongly incompatible in the major silicate minerals. Both elements exist with high valence states (4+) which further limit their ability to substitute into the common rock-forming minerals. U and Th are successively enriched in granitic rocks by crustal recycling processes; felsic rocks on average host ~4 ppm U (Rogers and Adams, 1969). This incompatibility of uranium and thorium results in the enrichment of these elements in

crustal rocks over time, as successive melting and recycling of crustal material partitions the elements into fractional and partial melts (from Cuney, 2010).

Key variables of U enrichment in peralkaline and peraluminous melts are the ratio of Na+K/Al and the availability of F, which increases the solubility of U in the melt (Peiffert *et al.*, 1996). The Central Zone leucogranites are essentially high-K metaluminous granites; some may be marginally peralkaline though this may be an effect of variable Ca. Ca content may or may not reflect host rock assimilation or highly variable source rock compositions. The diagrams in Figure 5.46 illustrate a poor correlation between U and A/NK and A/CNK. U concentration in the alaskites must also depend on additional controls other than bulk composition as is expected in peralkaline or peraluminous rocks (after Skirrow *et al.*, 2009).

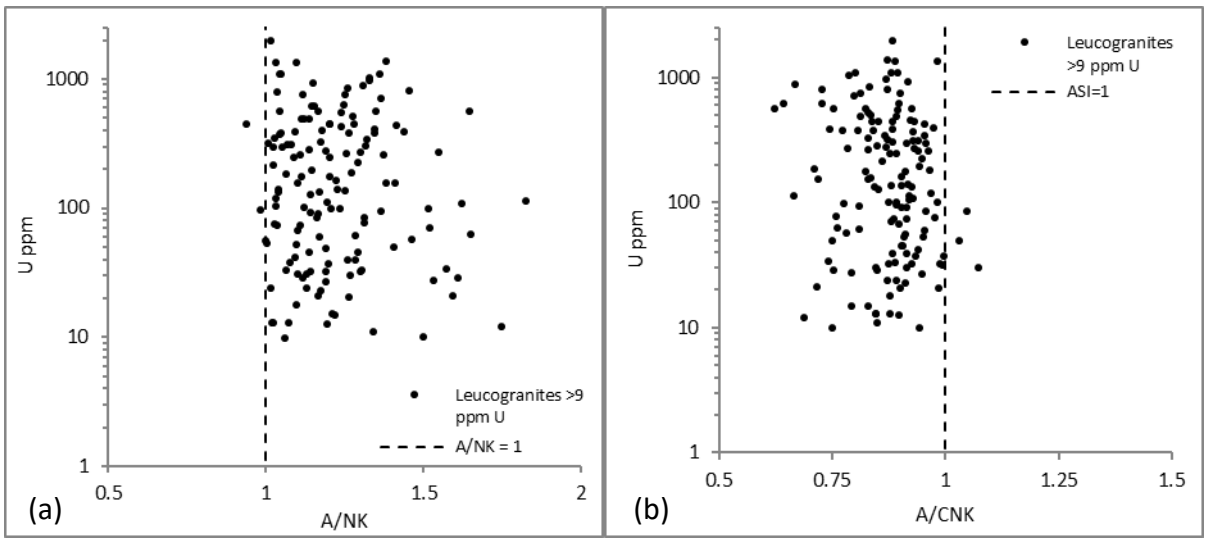



Figure 5.46 U vs. A/NK and U vs. A/CNK of the Central Zone sheeted leucogranites. (a) The Peralkaline index after Shand (1927) vs U. U abundance does appears to show some positive relationship with aluminium saturation, measured against the peralkaline index of Shand (1927) (b) The metaluminous - peraluminous index of Shand (1927) vs U does not show any such positive relationship.

Uranium differentiates from Th in the magmatic and hydrothermal environments because it is abundant in $U^{4+}$ and $U^{6+}$ valence states, and can change between the states if sufficiently oxidising, or reducing agents are available. In addition, melts that are not in equilibrium with Th repositories such as monazite should contain high U:Th. Thus, uranium can be transported and enriched in the ionic state and the dissolved-complex state in the fluid phase. The overwhelming majority of uranium preferentially partitions into uraninite late in

the granite crystallisation sequence (Cuney and Friedrich, 1987). Coffinite is the next most abundant uranium mineral and forms as a replacement of uraninite during residual magmatic fluid conditions; provided that dissolved silica is available.

Uranium tends to be limited to a few accessory phases because of its ionic radius and valence, the more abundant of these are zircon, apatite, monazite, allanite, titanite, xenotime, pyrochlore, brannerite, davidite and thorite. Zircon, monazite and pyrochlore are robust in most geological environments, thus treated as refractory phases, and monazite anneals the fractures that result from radioactive decay of uranium with time, hampering the escape of the metal over time. The local geological conditions at the time of emplacement influenced the potential volume of accumulated melt, incorporation of host rock schlieren, and amount of contact with reactive carbonates. As a consequence, the local physical and chemical environment at each deposit will vary. It is the aim of this section to present and discuss the trends recognised for U/Th in the leucogranite populations of the Central Zone primary deposits.

The Grey and Salem granitoids illustrate a successive enrichment in U and Th from the diorite composition type 1 generation through the intermediate type 2 and melts derived from shearing of the biotite-bearing rocks (Figure 5.47a). Any chemical or alteration process that was syn- or post granite emplacement, which involved external influences from reactive sediments or later uranyl-complex bearing fluids, will have changed the U/Th ratios of a given granite sample. Although the Grey and Salem granites are largely considered as S-type granites (Miller; 1983a, 2008) an example in McDermott *et al.* (2000) from the Swakop River is comparable to Damaran A-type granites, particularly because of HFS element abundances.

Nonetheless, the oldest varieties of granitoids at the deposits contain the lowest U and Th, with successive generations hosting greater enrichments of U and Th. Th is consistently greater than U in the Grey and Salem granites (Figure 5.47a). Two megacrystic Salem granites host U>Th, one contains 34 ppm U the other 278 ppm, the latter being predominantly uranophane derived from intruding apophyses of leucogranite. The high Th/U of the Grey and Salem granites represents a source with low U abundance, and the low totals of these elements relative to the leucogranites reflects a much lower degree of differentiation.

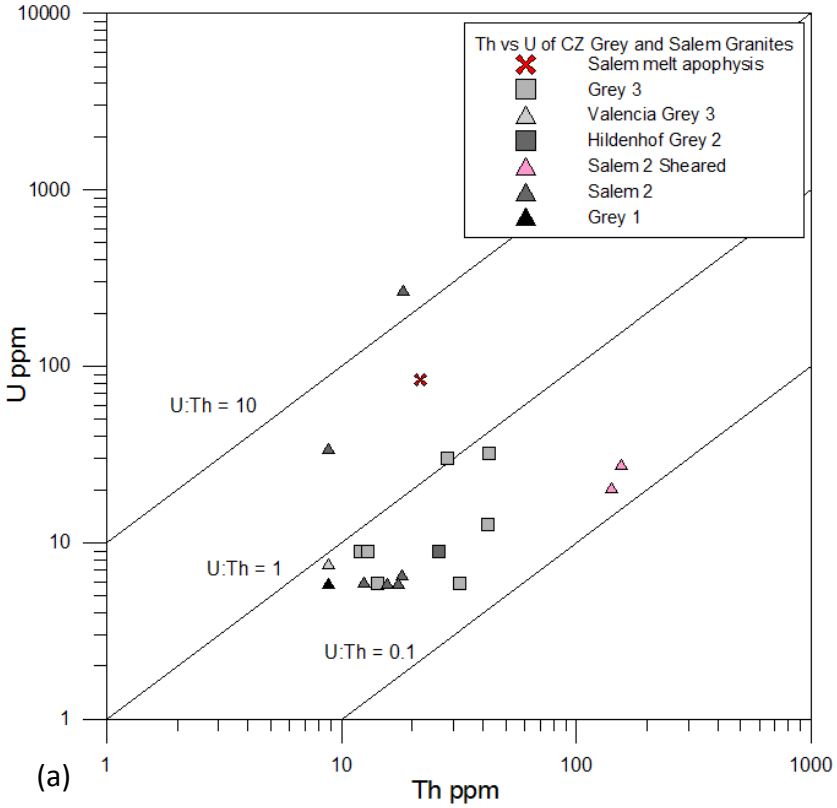
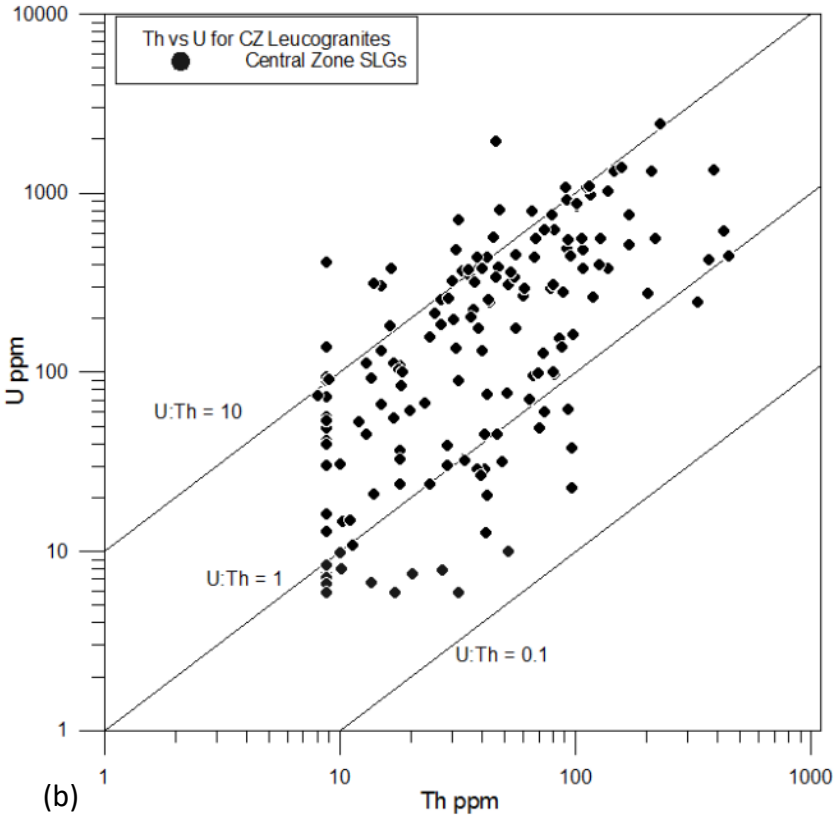



Figure 5.47 Plots of Th vs. U of Grey, Salem, and uraniferous leucogranite suites of Central Zone U deposits. (a) Th vs. U of Grey- and Salem granites. Most samples have little or no detectable U, but range from 10 ppm- to ~200 ppm Th. Some Salem granites are enhanced by secondary U in the Joly Zone and so plot in similar positions to the mineralised apophysis. Rössing mine sample data: Freemantle (2006). Data clipped to >9 ppm U and >9 ppm U.

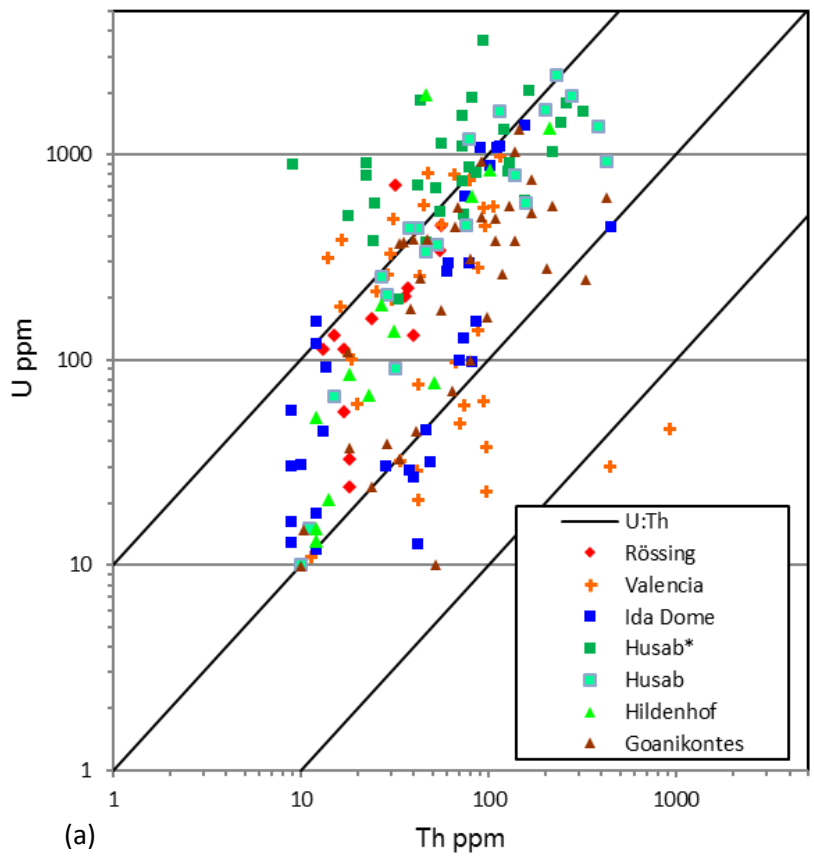



(b) The majority of Central Zone leucogranite samples plot with U:Th >1. This trend highlights the differentiated nature of the leucogranites as well as the contribution of uranium enrichment that is contributed from the dissolved U in the magmatic-fluid system. Data clipped to >9 ppm U and >9 ppm Th.

Uranium and thorium concentrations in uraniferous samples of the Central Zone granites are thus highly variable. The typical crustal ratio of U:Th is 1 - 2.7:10 (Plant *et al.*, 1999 and the

ratio of U to Th in typical granite is 1:3 (Plant *et al.*, 1999). The U:Th of the sheeted leucogranites predominantly lie between one- and ten for most granites analysed from the Central Zones as illustrated in Figure 5.47b. There is also a noticeable increase in U:Th with increasing U ppm in the plot. Samples with enhanced values of uranium (> 75 ppm U) tend to plot above the U/Th = 1 line, with uranium-rich samples that contain >500 ppm U the ratio is close to- or greater than 10:1. There is a considerable variation in local conditions that has affected the ratio; a significant proportion of the Ida Dome and Valencia samples plotting well above the 10:1 line, while at Husab some samples have ratios of up to 40:1 (Figure 5.48a). The majority of Goanikontes samples plot between U/Th = 1:1 and =10:1. U/Th of comparative Husab samples from Johnson (2011) show ratios that are consistently ≥10:1. The roles of surface- and near-surface U remobilisation and interactions with reactive metasediment are illustrated in Figure 5.48b and Figure 5.49, respectively. Core and surface samples from the Ida Dome area and the Valencia deposit show that comparatively fresh leucogranites sampled from core have consistently higher U/Th than the surface-sampled material. Although uranium does not readily oxidise in surface waters (Finch and Ewing, 1992) the impure nature of $UO_2$ with a proportion of $UO_3$ allows for U/Th ratios to change as soluble U is leached in the near-surface weathering environment.

A number of anomalously radiogenic samples from the Central Zone deposits were collected, and include anomalously radioactive xenoliths, garnet (andradite)-magnetite skarn, various calcsilicate and quartzite rocks and a grab sample of uraniferous fluorite from the Husab Fluorspar Mine, south east of the Husab Uranium Mine (Figure 5.49). The Holland's Dome skarns appear to have acted as a sponge for soluble U in the mineralisation system, where U enriched fluids derived from the crystallising leucogranites have infiltrated the brittle fracture networks of the calcsilicate-magnetite skarn boudins. Mineralisation is localised around these boudins and is in the form of uranophane in concentrations approaching 5 000 ppm to 40 000 ppm U. Similarly, quartz-rich segregations within pegmatitic leucogranites host U and Th in ratios of >20:1. The >110:1 U to Th ratio in the Husab fluorite sample further illustrates the solubility contrast between U and Th and the solubility of U in $F^-$-bearing solutions. At the other end of the spectrum, radioactive xenoliths of phosphate-bearing skarn at Valencia illustrate how Th may be enriched in apatite and monazite-bearing material (441-921 ppm Th vs. 30-46 ppm U).



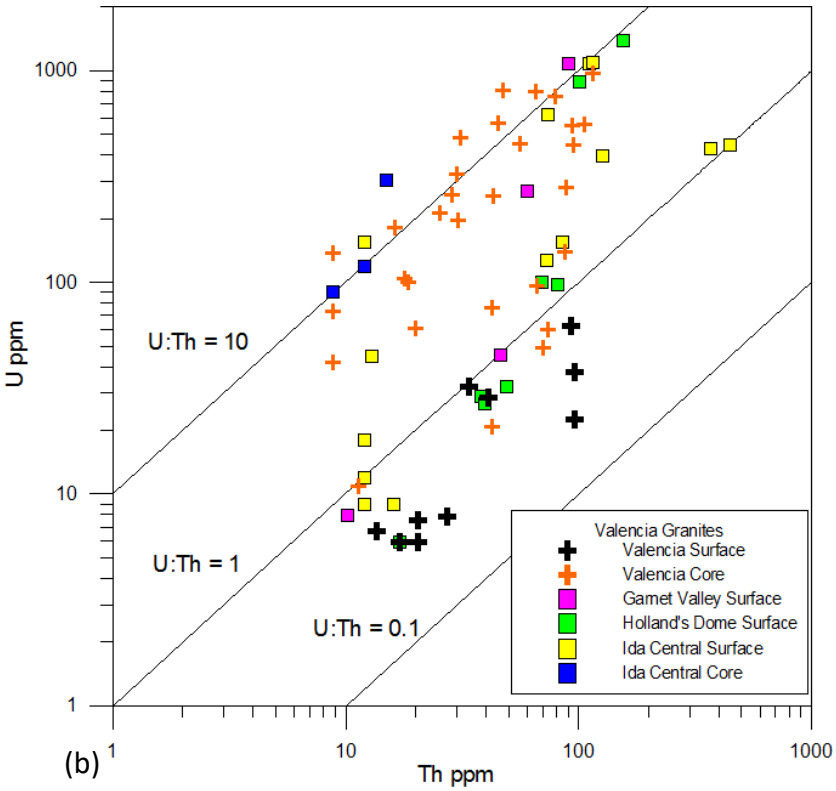




Figure 5.48 Uranium and thorium concentrations in Central Zone leucogranites and associated metasediments. (a) Th vs. U of Central Zone U-bearing sheeted leucogranites. Valencia samples plot in two groups, one has predominantly U>Th, the other is U<Th. All but two outliers from Goanikontes and Hildenhof plot below the U/Th=1 line. Overall, U/Th tends to increase with increasing U. Rössing mine sample data: Freemantle (2006); Husab* data: Johnson (2011). Data clipped to >9 ppm U and >9 ppm U.

(b) Th vs. U of surface vs. core sample U and Th ratios at Ida Central and Valencia. Core samples, that show little to absent evidence of surficial leaching tend to have retained original, high U:Th. Data clipped to >5 ppm U and >9 ppm U. Five of the Holland's Dome samples and three Valencia samples contain <9 ppm Th, and so plot with 'equal' Th abundances.

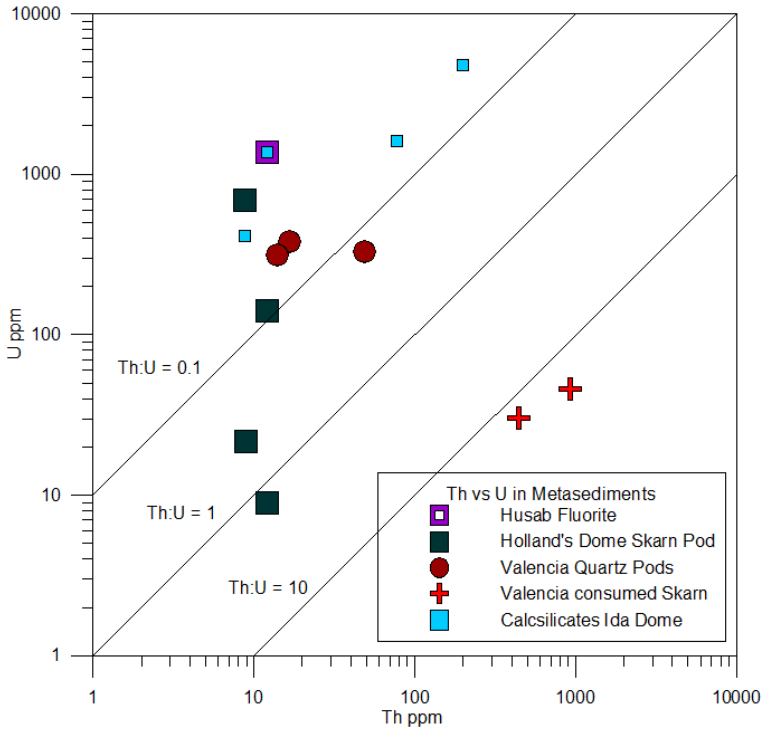



Figure 5.49 Graph of Th vs. U of Central Zone skarn and country rock xenoliths. The consumed skarns of Valencia are the exception and have high 100's- to low 1000 ppm Th, a result of U migration in hydrothermal-like conditions, and the deportment of Th into monazite.

### *U, Nb, and Ti Discrimination Plots*

The Rössing Uranium deposit and the Husab deposit both report uranium deportment in refractory minerals, particularly betafite at Rössing, and brannerite at Husab. The most convenient chemical difference between betafite-bearing and uraninite-coffinite dominant leucogranites is the relative abundance of Nb in the refractory mineral-bearing samples. Brannerite is less obvious as it does not contain appreciable Nb, if at all. It is a Fe-Ti oxide and thus may be identified by proxy if granite hosts above average Ti. ICP-MS analyses of samples from the Central Zone show clear trends between uranium mineralogy and trace element (and Ti) abundance. The ratios of Nb/U, Nb/Ta, and Ti/U show trends within- and between the pre- and post-$D_3$ leucogranites. The ratios are particularly important with respect to the geochemical identification of uranium-bearing refractory mineral abundance.

*Chapter 7 presents automated scanning electron microscope data (QEMSCAN) for selected uraniferous SLGs from the Central Zone primary-U deposits. This data is primarily intended to provide semi-quantitative comparisons of the uranium mineral populations at the deposits.*

Husab samples with QEMSCAN-quantified U-deportment statistics (10 wt.% to >40 wt.% U in brannerite) are compared to uraninite-dominated leucogranites and to Grey granite

samples from the Central Zone deposits. Nb abundances tend to be <100 ppm in the leucogranites and Grey granites of the Central Zone (Figure 5.50a). However, the brannerite-bearing samples from Husab (green squares) plot with relatively enriched Nb content that is coincident with U enrichment (400 - ~2 000 ppm U).

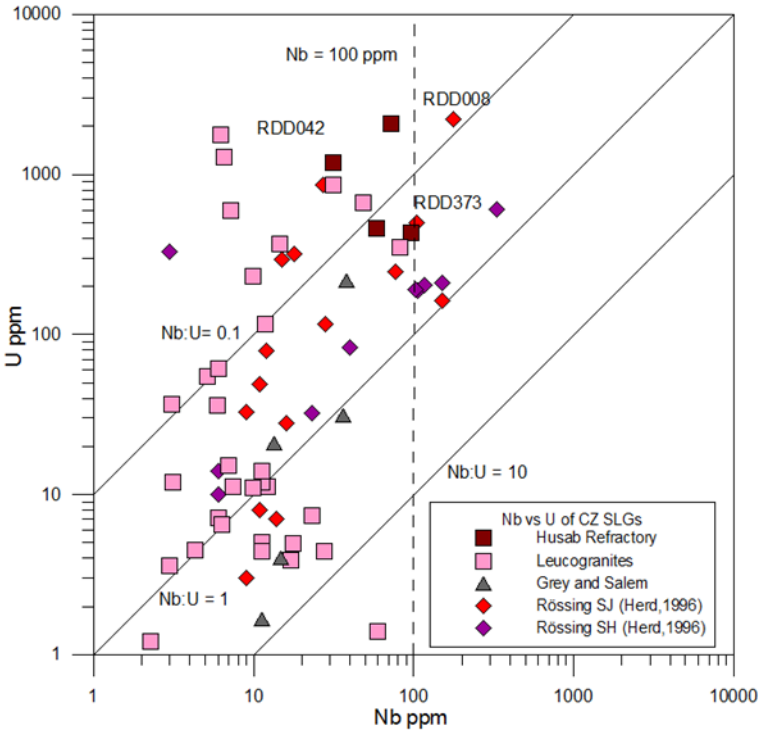



Figure 5.50 Nb vs. U for ICP-MS samples. The plot shows that Nb is a reasonable diagnostic tool for the identification of refractory – bearing alaskites. The four brannerite (+betafite) bearing samples (Husab Refractory) plot with higher Nb relative to the leucogranite and grey granite sample set. Though the majority of samples plot with <25 ppm Nb, the known refractory samples all contain >25 ppm Nb. All data are obtained by ICP-MS.

The ratio of Ti and U also appears to be diagnostic; the brannerite-bearing samples host up to 4 000 ppm Ti with correspondingly high U. Ti is enriched in some of the Grey granites as well as a small number of the sheeted leucogranites, but U is in comparatively low abundances (Figure 5.50b). Betafite may host trace amounts of Ta; the element is in low concentrations in the Rössing deposit betafite (Herd, 1996) but does show a comparative enrichment in brannerite- and betafite-bearing Husab leucogranites. Despite the low abundance, Ta in the whole rock, Ta and Nb show a systematic relationship, and likely being hosted in the same phase. Nb/Ta shows a consistent 10:1 ratio in the uraniferous samples (Figure 5.39c). The brannerite-bearing Husab samples plot with enriched Nb and Ta relative to the uraniferous-, and un-mineralised leucogranites, and the Grey granites.

A simple explanation is that betafite and brannerite may occur in the same rocks, as both are complex U minerals, with U predominantly in the hexavalent state. In addition, the

conventional indicators for betafite mineralisation such as Nb enrichment and elevated Ta are coincident with Ti enrichment. Nb and Ta are also enriched in brannerite-bearing samples of the Husab deposit, relative to the other CZ granites.

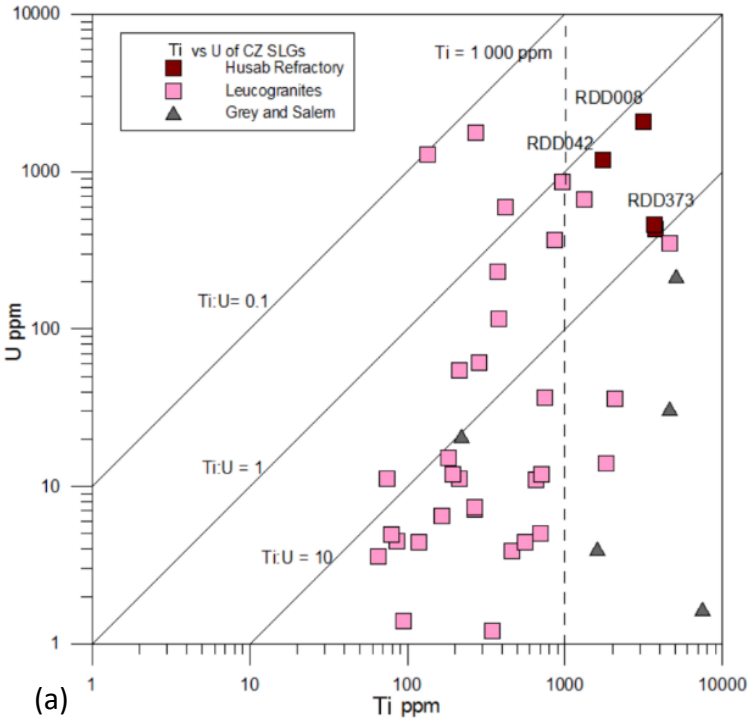



Figure 5.51 Plots of Ti vs. U and Ta vs. U for the ICP-MS samples. (a) Twelve samples contain >1000 ppm Ti; four are early, mafic -bearing grey and Salem granites, and four are leucogranite/alaskite. The remaining four are all betafite-brannerite bearing leucogranites from the Husab Zone 1 deposit. Ti is always >U and ratios range from ~2:1 to ~5 000:1 for Grey granites or ~200:1 for leucogranite.

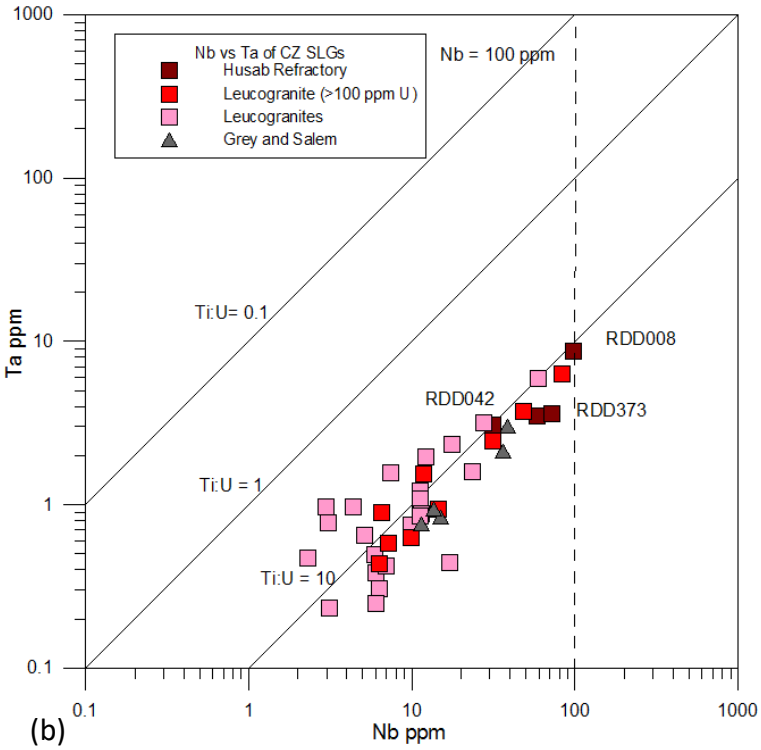



Figure 5.51 (b) Ta vs. U shows that four of the seven most Ta–enriched samples are refractory mineral-bearing. Th

## 5.11 Alternative Geochemical Techniques: Hand-Held XRF

### *Background*

The primary uranium-bearing refractory minerals betafite and brannerite occur in relative abundance at the Rössing Mine SH area, southwest of the main pit at the SJ area (Cuney, 1980; Herd, 1996; Nex *et al.*, 2003) and at the SK anomaly to the east (Abraham, 2009).

Rössing Uranium identifies potential refractory mineral-hosted uranium by assaying for Nb, Ti and U, which concentrate in betafite in certain pegmatites; there is a positive correlation between betafite abundance and Nb and Ti concentrations and so the assay serves as a chemical proxy for assessing mineral abundances. Swakop Uranium recognised brannerite in abundances that approached 40 wt.% of the U budget in what appeared to be localised occurrences. This observation is in contrast to Rössing, where betafite appears to the dominant uranium-bearing refractory host.

The compositions of betafite and other pyrochlore species at Rössing are given by Herd (1996) and further investigated with respect to granite fluid inclusion and extraction studies in Nex *et al.* (2003). Brannerite however, is a complex Fe-Ti-U oxide which may also host appreciable quantities of REE. The uraniferous leucogranites contain highly-variable, sub-weight percentage concentrations of Fe and Ti, concentrated in variable abundances of magnetite, ilmenite, titanite, rutile, sulphides, and biotite (structurally, or as exsolved alteration constituents). Given the abundances of monazite, xenotime, and zircon associated with uranium, the REE abundances are limited as a means of positively identifying brannerite by chemical proxy. Thus, it would seem that the composition of brannerite limits the use of whole-rock geochemistry of major-, trace, and rare earth elements for detecting the mineral. Traditional metallurgical approaches such as acid-leach testing and semi-quantitative mineral analysis are not expected to be viable short-term options either, given the length of time and high cost of sample preparation and data acquisition.

The Husab mine project was thus presented with a challenge of finding a cost-effective, efficient means of detecting brannerite and/or betafite in the Husab ore bodies. Betafite

and brannerite, however, are oxidised minerals, and would likely form under similar conditions, with the availability of A and B site cations to determine the species. The effectiveness of handheld XRF assay as a means of determining mineralogical populations was therefore investigated, with the assumption that betafite and brannerite occur together, the findings of which are described in the sections that follow.

### *Drill Hole RDD373 Geochemical Profile*

A diamond drill hole was bored into an area of known brannerite mineralisation in 2011, for the purposes of petrographic, geochemical, and mineralogical scrutiny. The core intercepted the local Rössing Formation, which includes two distinct carbonate-calcsilicate packages, sulphide-bearing cordierite-garnet gneiss, and garnet schist packages. The pelitic rocks in particular, are intruded by pegmatoidal leucogranites that contain mafic enclaves; the enclaves are characterised by strongly chloritised biotite with clustered rutile-titanite assemblages, all of which are variably replaced by epidote-pyrite-fluorite veining. The granite intrusions bear strong textural resemblance to the betafite-bearing pegmatites that constitute the SH area southwest of the Rössing open pit; and betafite visible in hand specimen further adds to the similarity. Brannerite is not as easily recognisable and in many ways, resembles rutile not only to the unaided eye but also in reflected and transmitted light. The petrography in Chapter 4 details the occurrences of the two phases within the RDD373 core.

### *Evaluation of Geochemical Data from a Portable XRF Profile of RDD373 Drill Core*

Sampling intervals total 390 readings were roughly evenly spaced over 45 m of intermittent mineralisation throughout the RDD373 drill hole, with the majority of assays performed on the uraniferous leucogranites and pegmatites. A further 141 readings were taken across mineralised intervals at 10 cm to 15 cm spacing on five drill cores. The XRF assessment identified sites of anomalous, coincident U, Th, Ti, and Nb in several segments of the RDD373 drill core. The results of three mineralised intervals at 63-64 m, 92-94 m, and 124-125 m are presented in the sections that follow.

***Uranium Mineralisation in the RDD373 Drill Hole***

Uranium mineralisation between 55$^{th}$ m and 70$^{th}$ m downhole (47 m to 61 m below surface in the -60° on 270° angled hole) occurs in pegmatitic leucogranite, with intermittent D-type textures, and within a halo of alteration and granite intrusion into the host cordierite schist. The lithological symbols used in the study are given in a legend in Figure 5.52.

The 64$^{th}$ m to 65$^{th}$ m interval contains uraninite, coffinite, uranothorite and brannerite in speciation proportions of 29.6 wt.%, 10.1 wt.%, 4.5 wt.%, and 43.1 wt.%, respectively. The relatively low content of U metal in the brannerite structure (~43 wt.%) translates to 27.4 wt.% of the metal being hosted in the brannerite component of the uranium mineral population. There are two distinct textural varieties of brannerite as described in the petrography chapter. Figure 5.53a and Figure 5.53b illustrate a 1 mm and 2.5 mm brannerite crystal from sample RDD373 64 m in altered microcline. A cluster of euhedral, unaltered brannerite occurs within a mafic cluster in sample RDD373 93C (chloritised biotite, magnetite, rutile). Pyrite is late and fills cavities between the altered biotite Figure 5.53c, brannerite was identified by traditional optical techniques, and confirmed by SEM with WDS; the mineral is present in two forms, semi-translucent and opaque crystals. While some brannerite specimens were identified by optical technique, and confirmed by SEM, many of the thin section sample sites were identified by the hand held XRF survey. Betafite does not appear to be present in the sample, and was not identified in mineralogical study.

Nb abundances increase with depth as the lithology changes from leucogranite- to cordierite schist (Figure 5.54). Nb abundances tend to be low, but are detected in most analyses; Ti concentration is in the tens of thousands of ppm range; thus, Nb is factored up by 5, and Ti is factored down by 10 in all graphs in Figures 5.42, 5.43, and 5.44. The 85 m to 98 m interval is characterised by leucogranite and pegmatite, with laths of consumed cordierite schist. The alteration assemblage is dominated by intensive chloritisation of the schist and mobile Fe staining in the schist and granite components.

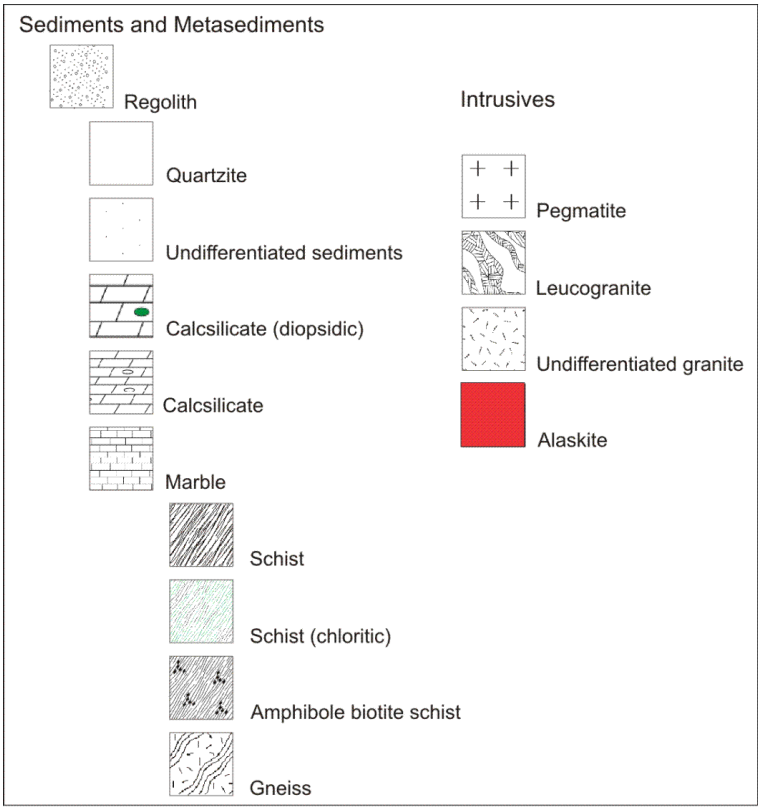



Figure 5.52 Key to lithology codes used in the RDD373 geochemical- and petrographic collages. The key lithologies in the drill hole are the carbonate, quartzite, and calcsilicate packages, which form impermeable hanging walls, or ceilings to the intrusions, and the pelitic schists and gneiss units that host the majority of the intrusions.

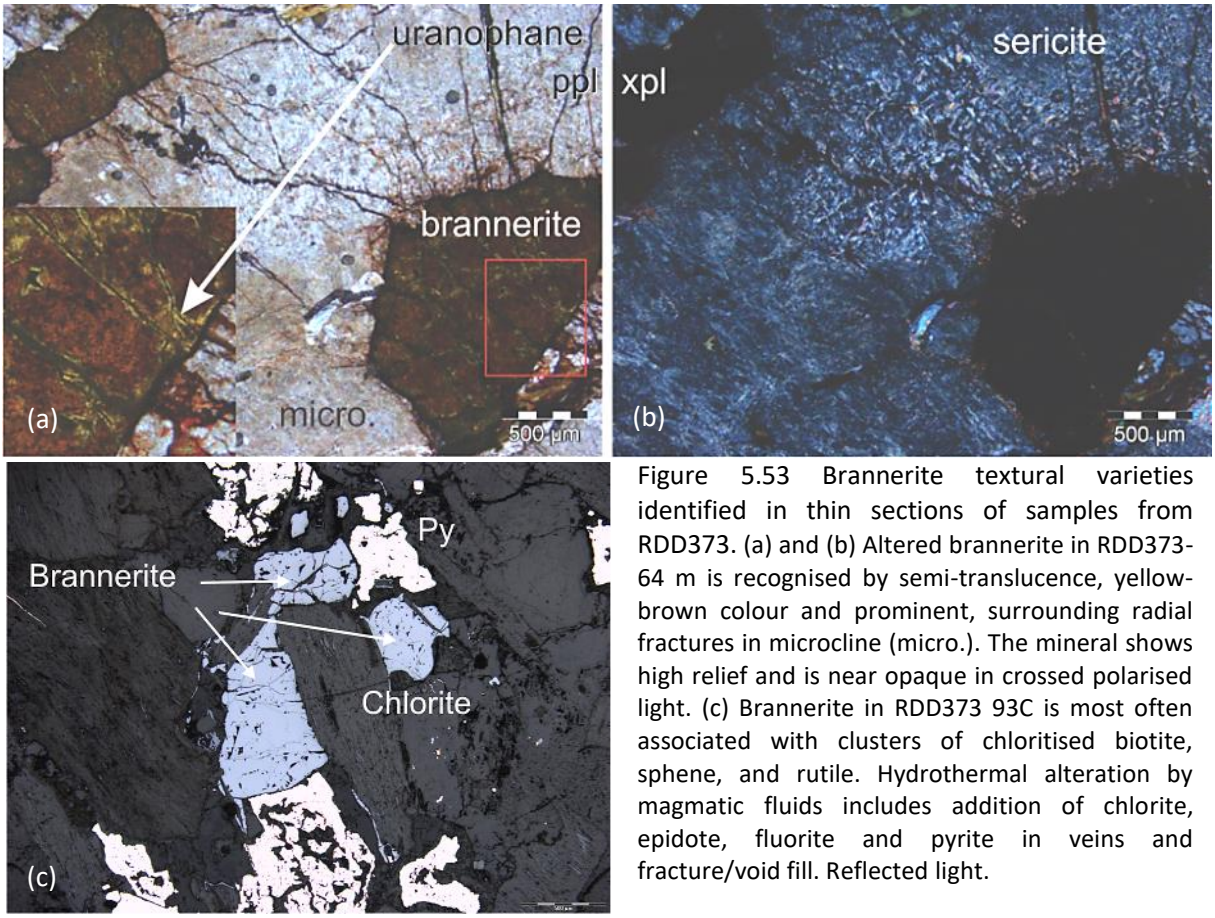



Figure 5.53 Brannerite textural varieties identified in thin sections of samples from RDD373. (a) and (b) Altered brannerite in RDD373-64 m is recognised by semi-translucence, yellow-brown colour and prominent, surrounding radial fractures in microcline (micro.). The mineral shows high relief and is near opaque in crossed polarised light. (c) Brannerite in RDD373 93C is most often associated with clusters of chloritised biotite, sphene, and rutile. Hydrothermal alteration by magmatic fluids includes addition of chlorite, epidote, fluorite and pyrite in veins and fracture/void fill. Reflected light.

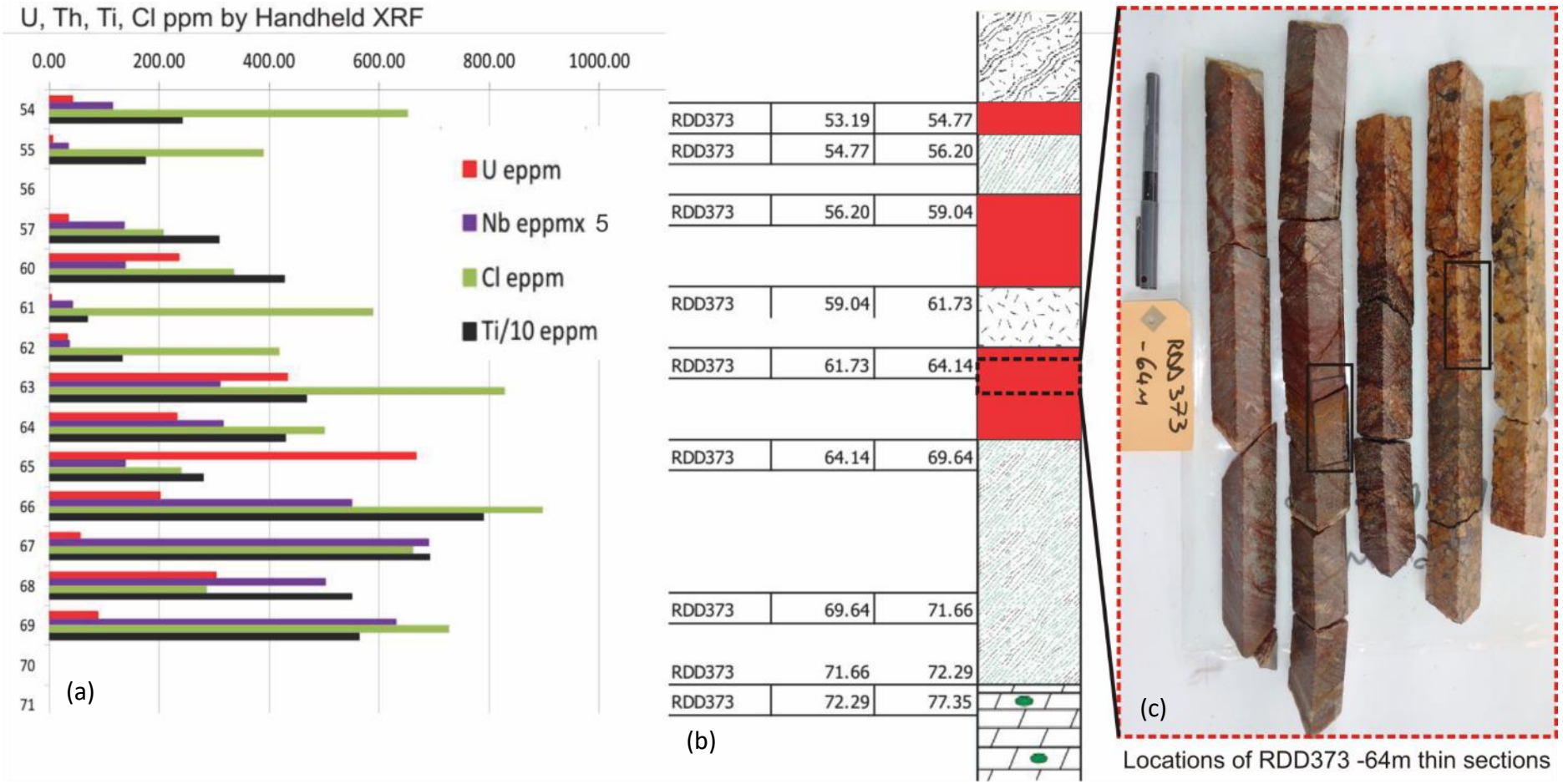



Figure 5.54 RDD373-64 m specimens in hand sample with thin section localities. The footwall is heavily fractured, chlorite schist. Primary mineralisation occurs in the alaskite and in a contact halo that extends ~36 cm into the schist. Mineralisation in the schist is hosted by quartz-calcite veins, and along the cleavage planes of the schist. Mineralisation in the schist is in the form of coffinite and a yellow secondary phases. Boltwoodite and uranophane were identified as the main secondary phase by Townend (2009) in a commissioned study report.

Figure 5.55 illustrates two alaskite intrusives, one at 85 m to 86 m, and another between 92 m and 94 m; the upper granite is located above a ~7 m carbonate-quartzite package, the lower leucogranite has the carbonate as a hanging wall contact. Both of the granite packages contain appreciable Nb and Ti, however, U is less than 50 ppm, as detected by hand held XRF. Figure 5.55a and Figure 5.55b illustrate the metre-by-metre XRF assay averages, and the individual decimetre-spaced assays of U, Nb, Cl, and Ti, respectively. The lithological strip log illustrates the relative positions of the intrusives and the carbonate and schist packages in Figure 5.55c. Three thin sections shown in d were cut where Nb, Ti, and U assays were in highest coincident concentrations; section C hosts euhedral brannerite, which is described in detail in Figure 5.57.

Figure 5.56 illustrates a slightly different assemblage in the 124 m to 125 m sample interval; the mafic enclave-bearing leucogranite is hosted within a low-U pegmatite which intrudes a mottled textured cordierite-chlorite gneiss package. The 124 m to 125 m sample hosts 10 wt.% U in betafite and 4.5 wt.% U in brannerite; which corresponds to XRF analyses of ~200 ppm Nb. Most of the anomalous Nb readings occur within the 124 m to 125 m interval.

The euhedral brannerite is hosted in a mafic enclave of chloritised biotite and rutile. The enclave is overprinted by chlorite-epidote-pyrite, which all appear to be variably replaced by fluorite. SEM backscatter (Figure 5.45) illustrates pyrite replacement of the euhedral brannerite, and the wavelength dispersive spectra of the analytical points show U leaching along the fracture network of the crystal.

Brannerite and the associated rutile and ilmenite are the most obvious hosts of anomalous Ti concentrations. It is not clear which mineral hosts the elevated Nb, it may be in fine-grained betafite, or in cordierite. The halogen Cl is associated with F which is a common constituent of biotite in granitic systems.

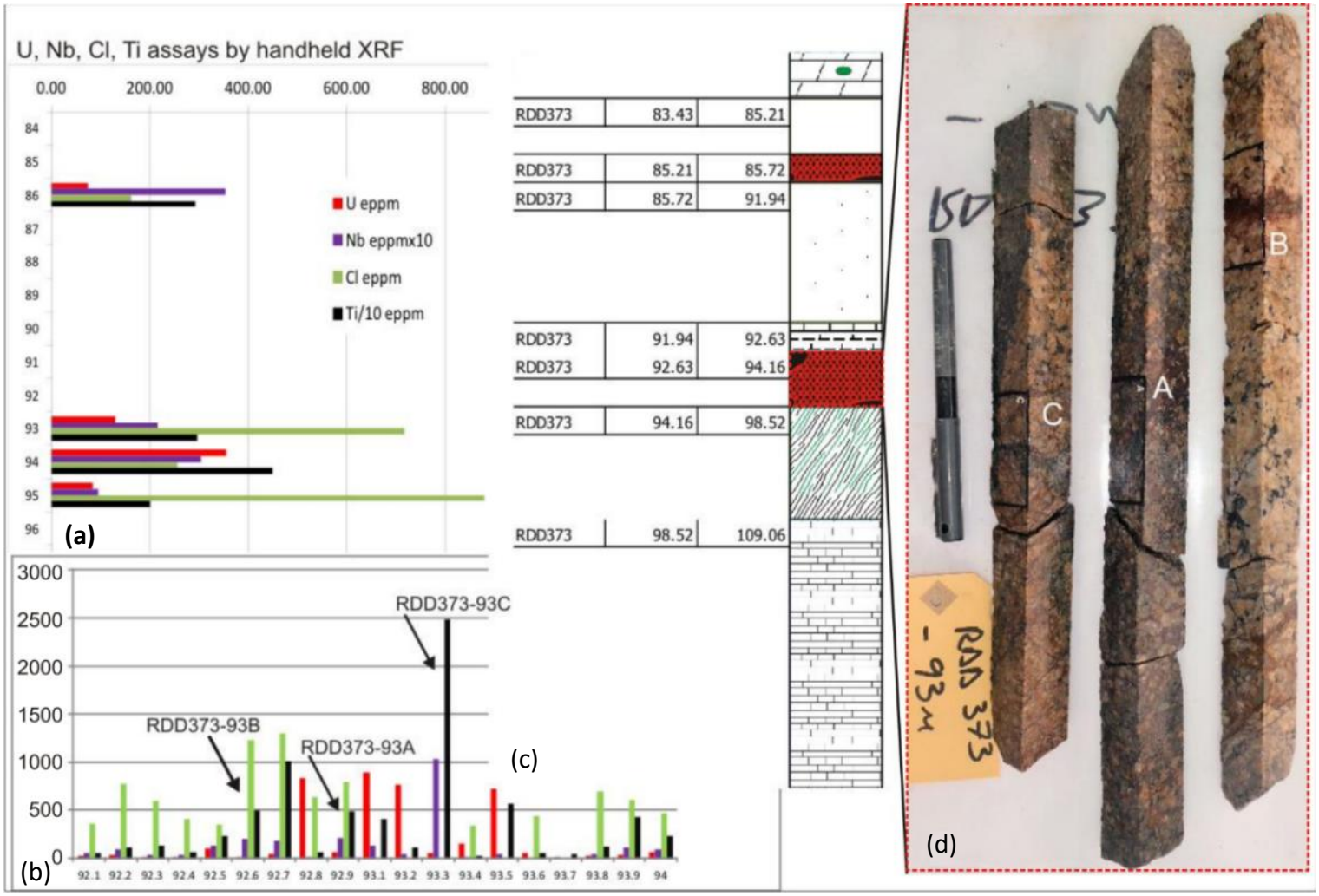



Figure 5.55 The RDD373 124-125 m sample with thin section locality and handheld XRF assay data. (a) Bar chart illustrating the abundances of selected elements as per hand-held XRF assay. (b) Gives a 10cm resolution of the handheld XRF assay spots. (c) Representative lithological section showing the RDD373-93m alaskite intruding a carbonate-calcsilicate-schist package. (d) The actual section of sample submitted for U-deportment analyses at the CSIRO, Perth.

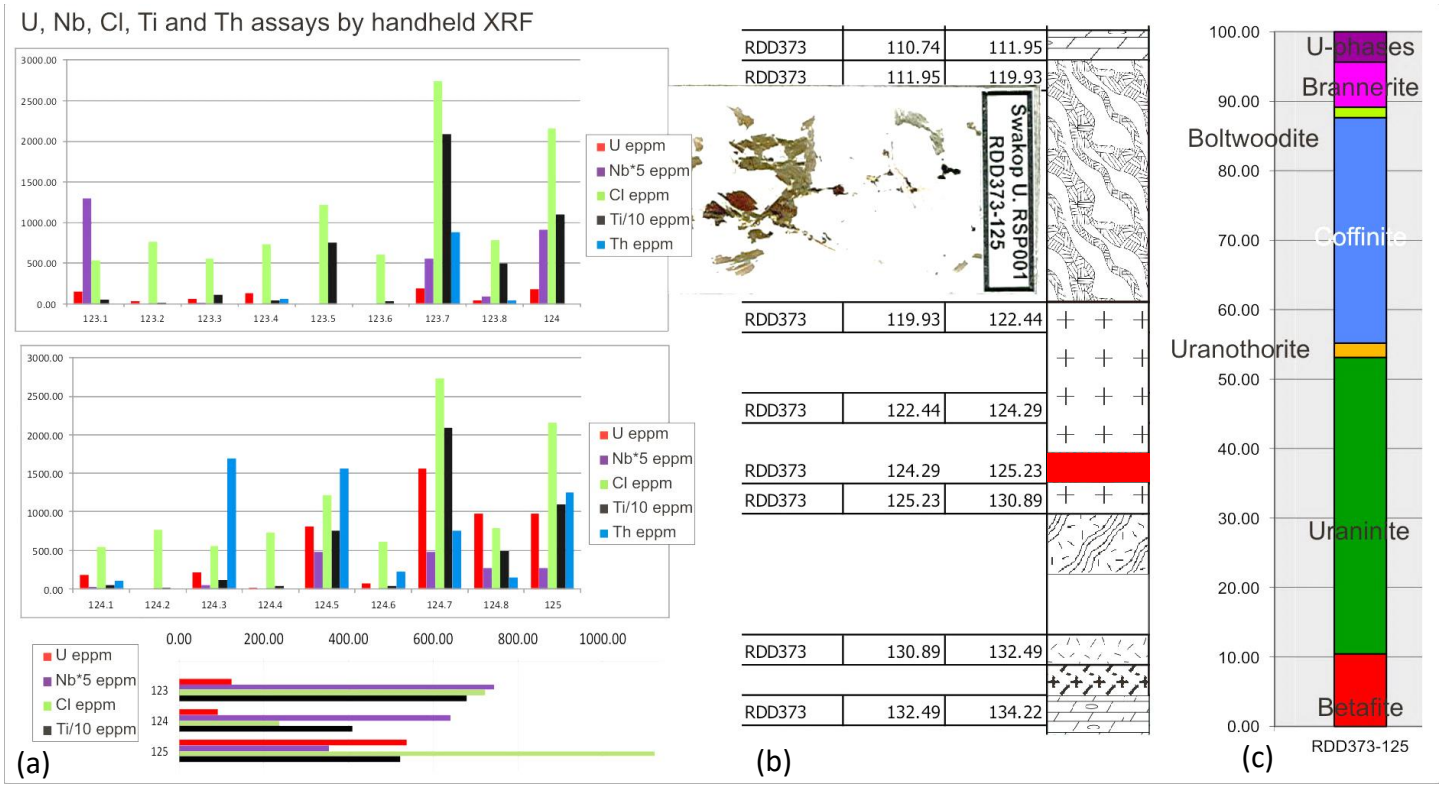






Figure 5.56 The RDD373 124-125 m sample with thin section locality and handheld XRF assay data. The sample is an altered alaskite with prominent biotite content and pervasive fracturing throughout the mineralised interval. High cps readings are localised over biotite clusters. (a) A systematic 10 cm assay scheme with handheld XRF values highlights discrete sites of elevated Nb with corresponding elevated Ti. (b) The sample is situated in an 8-m thick pegmatite-alaskite with prominent coarse-grained biotite. (c) The deportment study by QEMSCAN reveals 10 wt.% U in betafite combined with brannerite for 16.94 wt.% U in refractories. This sample in particular shows that potential exists for XRF analyses as a means of identifying refractory-bearing targets. (d) Illustration of the distinctive alaskite texture.

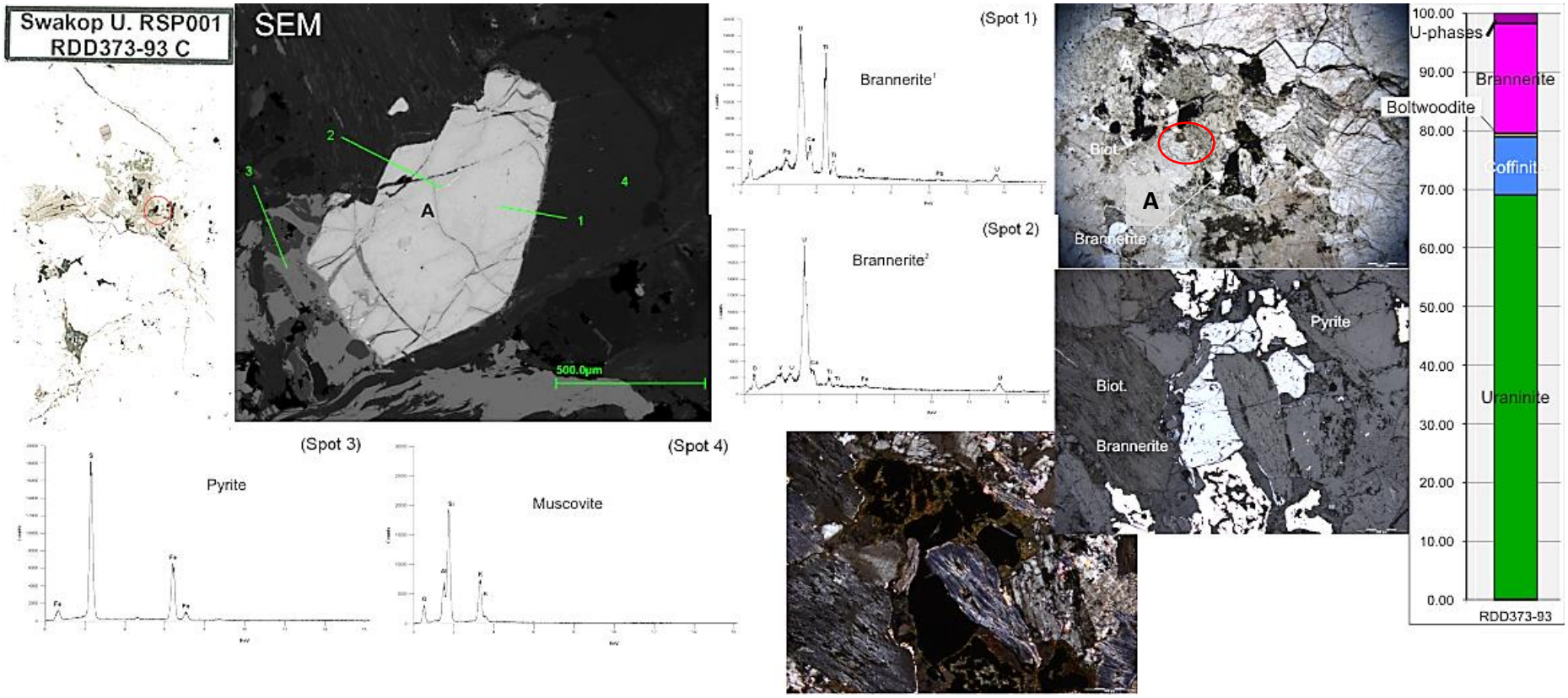



Figure 5.57 Thin section and SEM imagery of sample RDD373-93C. Brannerite occurs as free grains (SEM image labelled A) within biotite clusters and is closely associated with pyrite and muscovite. A secondary brannerite-phase occurs in fractures of the brannerite with a composition similar to uraninite, without any Pb. The SEM image illustrates important mineral textures and relationships. Pyrite (3) is inter-leaved with chloritised biotite indicative of its late magmatic nature. Brannerite occurs as a primary euhedral phase, and as a secondary product of mineral weathering (1 and 2). Muscovite occurs with biotite and is in contact with the brannerite. The primary brannerite is also illustrated in the photomicrograph, top right of the collage. A mixture of secondary U- (coffinite) and Fe-minerals occur in the interstitial spaces of the brannerite-biotite clusters, illustrated in the photomicrograph at bottom centre. QEMSCAN deportment results show a prominent brannerite constituent in the total U-mineral budget. The brannerite occurs in alaskite in this particular sample.

### *Discussion of Handheld XRF Survey Results*

A total of 391 scans were performed on RDD373: 276 detected uranium, 251 detected Nb, 307 detected Th and 208 detected Cu. This translates to ~70% of all scans in mineralised intervals detecting uranium. Similarly, Nb and Th detection rates are 64.2% and 78.5%, respectively. The accuracy of the XRF is compared to the metre intervals of ICP-MS assay for the 50 m to 250 m interval of RDD373 in Figure 5.58a; the elevated readings by XRF coincide with some acceptable deviation from the ICP-MS benchmark assays. Figure 5.58b and 5.58c illustrate the 54 m to 72 m interval of the hole in detail; where b shows each individual 10 cm or 15 cm sample interval, and Figure 5.58c compares ICP and XRF assays, with sample spacing averaged metre-to-metre.

Uraninite is a small and comparatively rare accessory phase in the leucogranites; Thus, detecting geochemical trends associated with the disseminated distribution of mineral such as brannerite or betafite may be limited by sampling intervals of 1 m. Assessing the geochemical signatures over narrow intervals greatly increases the probability of identifying markers such as elevated Ti or Nb, in this regard the handheld XRF is a well-suited tool. Data and assessment exercise findings are in Appendix E11. Table 5.8 summarises the XRF study, and compares drill core from intervals that contain betafite and brannerite, with those that do not host refractory minerals. Utilising a hand held XRF to identify chemical trends of known refractory-bearing intervals shows that where refractory phases occur, Nb, Ti and Cl are abundant relative to the average analyses of all the mineralised intervals in the same diamond drill hole (RDD373).

Table 5.8 Summary of handheld XRF chemical analyses. Key element abundances for brannerite and betafite-bearing RDD373 alaskite intervals.

| RDD373 - Summary of 390 Analyses over 45 m of mineralised Alaskite. Spacing 10cm - | | | | RDD373 Refractory - bearing Intervals | | | | | 141 Mineralised Samples | | |
|---|---|---|---|---|---|---|---|---|---|---|---|
| Element | Ave. | Std Dev. | Max | 63-64m | 65-66m | 93-94m | 115-116m | 124-125m | Ave. | Std Dev. | RDD009 (46); RDD200 (61); RDD197 (9); RDD195 (16); RDD211 (9) |
| U | 181.87 | 8.43 | 2850.00 | 154.80 | 92.20 | 356.30 | 72.63 | 537.44 | 370.82 | 12.68 | |
| Nb*5 | 29.41 | 1.62 | 690.00 | 322.50 | 350.50 | 152.00 | 63.13 | 177.22 | 18.79 | 1.65 | |
| Th | 79.90 | 5.21 | 1740.00 | 45.00 | 22.50 | 39.00 | 156.13 | 639.11 | 36.85 | 5.87 | |
| Cl/10 | 65.52 | 17.79 | 867.00 | 71.73 | 85.25 | 50.08 | 256.01 | 112.33 | 111.85 | 21.49 | |
| Ti/10 | 374.37 | 7.24 | 42895.00 | 816.75 | 705.47 | 430.96 | 256.01 | 522.97 | 286.08 | 7.51 | |
| U/Th | 6.18 | 5.21 | 4.13 | 3.44 | 4.10 | 9.14 | 0.47 | 0.84 | 10.06 | 2.16 | |

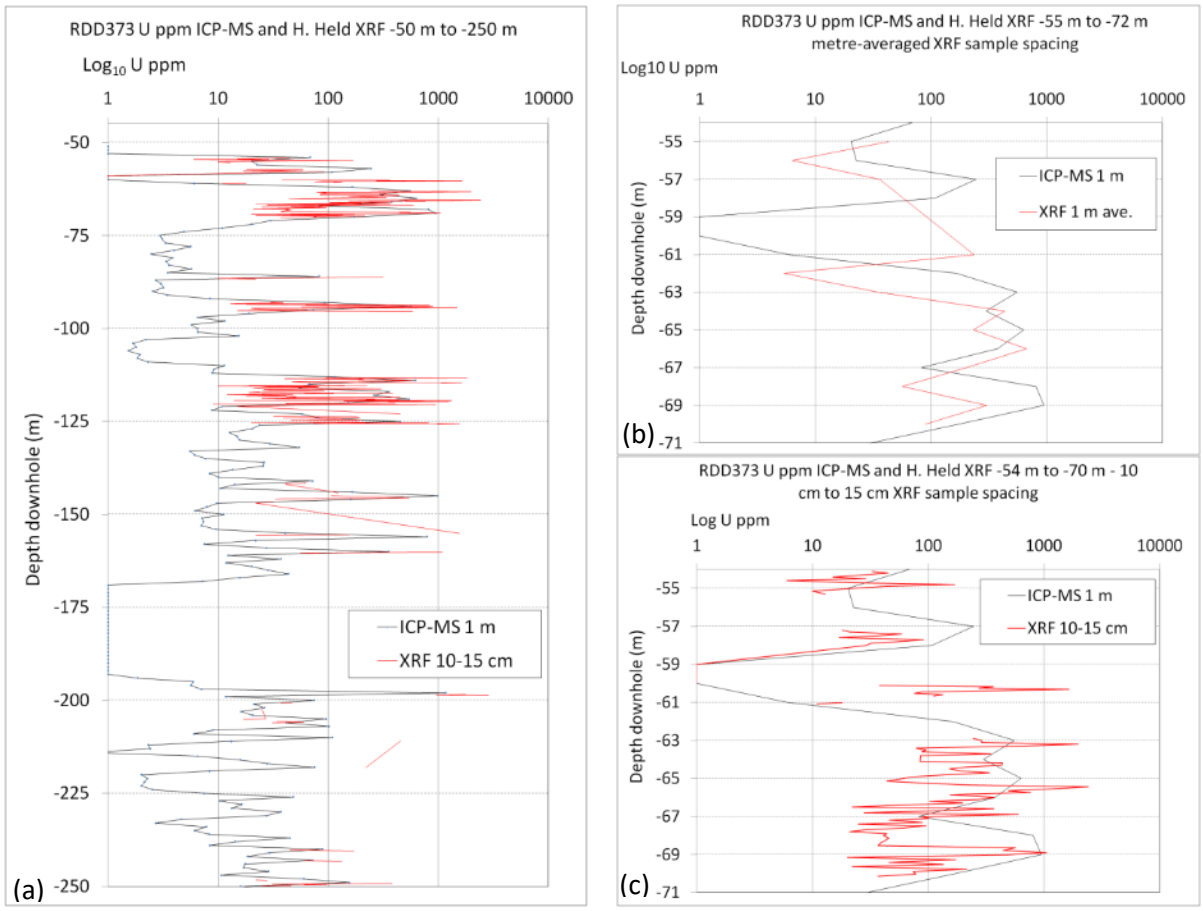



Figure 5.58 Uranium assay by ICP-MS comparison with hand held XRF assay. (a) Uranium assays by ICP-MS are sampled at 1-metre intervals; the hand held XRF is sampled at 10 cm to 15 cm intervals because the analysis spot is ~1 cm2 and the leucogranite is coarse-grained. (b and c) Two mineralised intervals in detail from -53 m to -70 m. Brannerite is present at -68 m downhole; and the same interval with the XRF analyses averaged to match the metre interval of the ICP-MS samples.

Elevated Ti and Cl represent areas where mafic phases are concentrated. Nb and Ti show a systematic positive relationship in the refractory mineralised samples (Figure 5.59). This indicates that there is at least one common phase that concentrates both elements, or that Nb-bearing minerals have an association with titaniferous minerals, which include titanite, rutile, and brannerite. From these qualitative XRF data and the petrographic observations, the following summarise the handheld XRF and refractory uranium mineral associations:

- Combining anomalous Ti and Nb, with indicators of late-magmatic fluid alteration (U/Th values) provides a means of confidently identifying potential sites of brannerite-betafite mineralisation.

- Although Nb and Ti show a positive correlation overall, the elements also show anomalous concentrations that are independent of each other, thus a cautious approach with other sources of information is recommended.

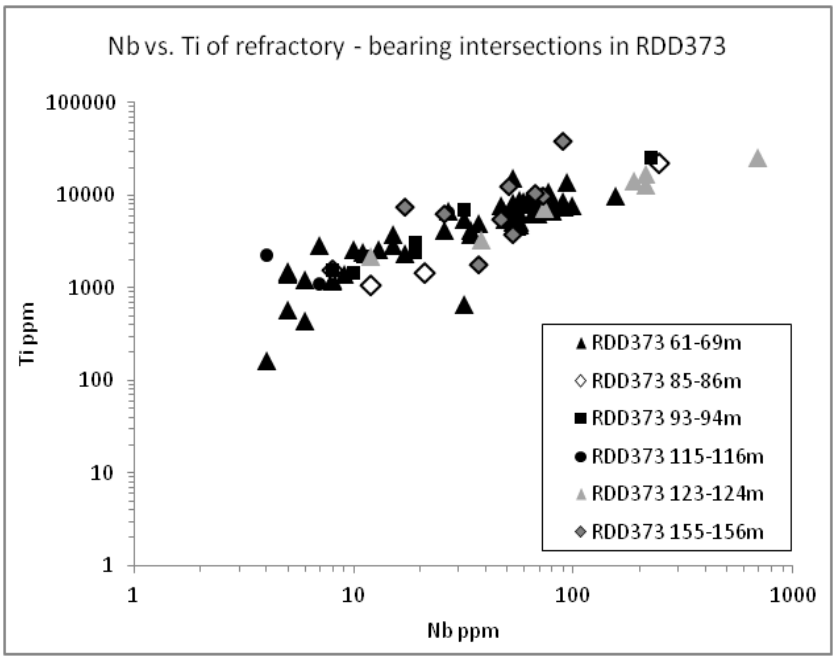



Figure 5.59 Nb (ppm) vs. Ti (ppm) of brannerite- and betafite-bearing intervals in drill hole RDD373. Each point represents a spot on a 10-15 cm interval spacing in given mineralised intervals. The overall correlation between the elements in these intervals is positive. Nb reflects betafite, columbite, or cordierite; while Ti reflects rutile, titanite, ilmenite or brannerite or leucoxene abundances. although, the positive correlation may reflect a single-phase distribution.

## 5.12 Geochemistry Results Discussion and Petrogenesis Implications

It is possible to differentiate between the pre- and post-$D_3$ leucogranite populations at the Husab, Ida Dome, Goanikontes, Hildenhof and Valencia using geochemical data. The samples are divided roughly into three groups, essentially following the divisions of Nex (1997); pre-$D_3$ equigranular granites (in this study all biotite-bearing, Salem suite and Grey granites); pre-$D_3$ leucogranites (all A-, B-, $C_{t/m}$- type leucogranites); and the post-$D_3$ uraniferous leucogranites (D and E type). Basic observations of major element abundances show that the uraniferous group is the most silica enriched, which is consistent with the observations of Nex (1997). Simple normative mineral calculations on ternary (Barker, 1979) and normative ratio (Le Maître, 1989) diagrams successfully classify the granites, and for the most part classification by geochemistry agrees with petrographic observations. The leucogranites are alkali feldspar

dominated, with quartz being visibly more abundant in the later, uraniferous varieties, which explains the high Q and Q' content on classification diagrams.

### *Major Elements Discussion*

The normative plots of Tuttle and Bowen (1958); Barker (1979); and Le Maître (1989) are suitable for discriminating between the biotite-bearing Grey and Salem suite granites (the equigranular group (Figure 5.3 and Figure 5.4) and the leucogranites, as well as between certain pre-$D_3$ and post-$D_3$ populations (e.g. Figure 5.5).

The post-$D_3$ leucogranites (the D- and E-type) show the greatest variance in normative composition, particularly on diagrams in which CaO is a variable. The variation in normative composition does not appear to be systematic with respect to uranium content, but individual deposit populations tend to show similar trends, sufficient to divide the deposits into two groups with respect to the uraniferous leucogranite populations. The uraniferous samples from the first group show the least variance in normative composition and in some Ab-Q-Or diagrams show systematic trends. The samples from the second group show the greatest variation in normative composition, showing far more limited indications of systematic trend or clustering on the conventional normative plots (Figure 5.12). In this division scheme, the Goanikontes, Hildenhof and Valencia Deposits are in the first, less-variable group; and the Husab and Ida Dome deposits are in the second, less-predictable group.

Aluminium Saturation Index (ASI) diagrams show that most of the leucogranites are metaluminous (if ASI = 1.1 is the boundary, as suggested in Chappell and White, 1974b) or weakly peraluminous if ASI = 1.0 (Shand, 1927). The Valencia sample set shows that individual generations of sheeted leucogranite have characteristics identifiable in major element plots, particularly in the aluminium saturation diagrams. The garnetiferous B-type SLGs in particular are the most peraluminous granites, ASI is >1.1, whereas the majority of the leucogranites plot between ASI = 1 and 1.1. A/NK is highly variable in the sheeted leucogranites, and limits the application of the index in discriminating the sheeted leucogranite generations (Figure 5.16).

Alkali-alumina indices show a systematic evolution from the most mafic equigranular granites through to the leucocratic varieties. Partial melts of the Salem granites and the Red granites correspondingly plot with the lowest alkali-alumina index. The B type at Valencia may in fact be the same type of anatectic melts of the Kuiseb Formation described in Ward *et al.* (2008). However, there are at least two generations of B-type; the pegmatitic type clearly cross-cuts the older foliated type in some locations and may be the same type of granite as the tourmaline-bearing C type. The pegmatitic type plots on the plagioclase side of the P-Q diagram of Debon and La Fort (1983).

The modified alkali-lime index of Frost *et al*. (2001) reiterates the division into two groups of deposits; where the first group of Goanikontes and Valencia deposits plot above the alkali line, the second group of Husab and Ida Dome samples span all four fields (Figure 5.19). The Husab samples all plot below the calc-alkalic line and show a great variation in alkali-lime index. The role of reactive skarn and calcareous metasediment in the final composition of the crystallising leucogranites is the most likely cause.

Fe/Mg ratios appear to be an important discrimination tool; certainly, macroscopic observation allows for the consistent discrimination of magnetite-bearing leucogranites from sulphide-bearing varieties. There are only a few samples that plot above the A-type granite discrimination line or Fe* line of Frost *et al.* (2001). With only a few exceptions, most Rössing mine samples plot above Fe*, the only comparable population is at Ida Central. The low Fe/Mg ratio may be explained by the entrainment of Mg-bearing diopside from the Khan Formation. Maficity plots show an evolving trend in the mafic to leucocratic equigranular granite generations, but only weak linear consistency is apparent in the A to F generations of the Valencia Deposit. The high Mg content of the Holland's Dome samples discriminates this population from the Ida Central and Garnet Valley populations, and shows that the maficity diagrams may be applied with some success if considered with sufficient field and petrographic observation. Cationic plots of Debon and Le Fort (1983) highlight the differences between weakly mineralised sheeted leucogranites at Goanikontes, Valencia and the Ida Dome and between the A-F- types of sheeted leucogranite (Figure 5.25).

Very few of the leucogranites follow the eutectic trend of Tuttle and Bowen (1958), the pre-$D_3$ samples tend to plot toward the Or apex and the uraniferous samples toward the Q apex, and the least few samples plot toward the Na apex, reflecting a low degree of sub solidus albite reactions (Figure 5.12). These observations are consistent with the observations of Nex (1997) at Goanikontes. Trace element abundances are therefore likely to have had equally little change since granite crystallisation.

***Trace Elements Discussion***

Rb/K is probably the most useful mobile element ratio, as Sr and Ba do not show any linear relationship with respect to Ca content. This is interpreted as a result of Ca mobility in the sub-solidus and later stages of deposit formation and where marble is present Ca contamination is inevitable. Applying Ca, K, and Na ratios to major element discrimination plots and mobile trace elements Rb, Sr, and Ba to similar ternary plots, shows a tendency for the mineralised granites to be differentiated and the majority of these contain >250 ppm Rb which is a characteristic of most differentiated granites (Whalen *et al.*, 1987). However, it is only at the Valencia deposit that major element and mobile element abundances can be used to discriminate a consistent difference between weakly differentiated C types and differentiated D types (Figure 5.35). The explanation may be the thin marbles at Valencia and the weak evidence of assimilation and wall rock interaction at the deposit.

The abundances of Ba, Y and Zr in the pre-$D_3$ SLGs seem to suggest an S-type affinity, where a strong linear relationship between Zr and Ba reflect the trends and interpretations of S-type granites in Clemens (2014) while the Y and Ba relationship does not because garnet is a major accessory phase in the leucogranites, and in the source metasediment. The D-types in contrast, do not show any linear relationships between Ba and Zr or Ba and Y implying a different source for these sheeted granites. High field strength (HFS) elements are the most diagnostic geochemical tool, although are not good discriminators for Ida Dome and Husab leucogranites (Figure 5.40).

The tectonic discrimination diagrams of Pearce *et al.* (1984) appear *et al*. to be more consistent in discrimination between the pre- and post-$D_3$ leucogranites (Figure 5.43). C- and D-type SLGs cluster in groups apart from each other, with some minor overlap so that the pre-$D_3$ leucogranites plot within the syn-orogenic field, on the various discrimination plots, while the uraniferous populations tend to lie in the within-plate field. The consistent contrast in composition in the HFS populations supports the interpretation of different sources, or at the very least, of different conditions of melt formation. But perhaps more importantly, trends are apparent for individual deposit populations of D-type leucogranite, with the Valencia samples showing a linear relationship between the different discriminators.

Transition metals (Figure 5.45) highlight the influence of calcareous Khan Formation on the metal content of the sheets; Cu, Mo, and Ni are mobile in hydrothermal environments, especially if S is abundant. The leucogranites have reacted with the metasediments; it is apparent that as granite crystallisation progressed, residual fluid ingress mobilised base metal sulphides from the country rocks at local contacts. Sulphide abundance with uranium mineralisation has become a characteristic of certain deposit areas. Some Ida Dome samples for example, host elevated Cu (up to 0.1 %) which is inherited from the cupriferous schist units of the Khan Formation. Similarly, the Valencia samples contain up to 100 ppm Ni, which is also inherited from the Khan Formation. The Husab deposit hosts over 1 000 ppm Ni in some samples, which suggests that pentlandite is associated with the abundant pyrrhotite within the granite - sulphide system. There is a positive Mo-U relationship in the leucogranite population at Valencia; similarly, at Rössing molybdenite is associated with uraninite. Freemantle (2006) using SEM imagery of Rössing concentrates showed that uraninite is attached to molybdenite in some samples. The presence of Mo in such close association with U suggests a magmatic source for the base metal, as opposed to a metasedimentary source of Cu as inferred for Ida Central.

### *Classification Schemes*

*A-, I-, and S- type*

A number of authors (e.g. Jung *et al.*, 2000a) describe some Central Zone leucogranites as A - type granites (leucogranites), these studies however, do not refer specifically to the sheeted leucogranite suites of the various U deposits. The sheeted leucogranites conform, in some diagrams, to the S- or I type criteria of Chappell and White (1974b). Also, in the HFS element diagrams of Whalen (1987) certain pre-$D_3$ granites plot within the A-type fields, while in others the abundance of Ce+Nb+Y+Zr suggest A-type affinity, but is contradicted by low Ga/Al. There is a contrast between the major element and HFS element discrimination plots. The Cm type lies in the A-type field if K/Mg is a discriminator, however, this is an unreliable parameter as uraniferous types have entrained diopside and thus have elevated Mg. If Nb and Zr abundances are a discriminator, the high concentrations of these elements show an inverse relationship, where the Husab samples in particular lie within the A-type field and the Cm type are in the 'other granite' box.

The leucogranites are oxidised, as is typical of calc-alkali magma series, and if fractionation has taken place Fe/Mg ratios should be higher. The low Fe/Mg but high K/Mg of the leucogranites does pose a problem. The low Mg relative to K supports an anorogenic granite type, whereas the low Fe/Mg appears to contradict this interpretation. The magnetite-ilmenite series classification of Ishihara (1977) may be applicable simply from petrographic observation. In addition, Whalen and Chappell (1988) show that I- and S- type granites are roughly distinguishable by the opaque mineral assemblages; where S-types are characterised by magnetite + ilmenite. The magnetite and ilmenite series classification of Ishihara (1977) is based upon magmatic arc granites, where *f*O is controlled primarily by the ratio of C combustion, without supporting sulphur isotope data no further interpretation can be made.

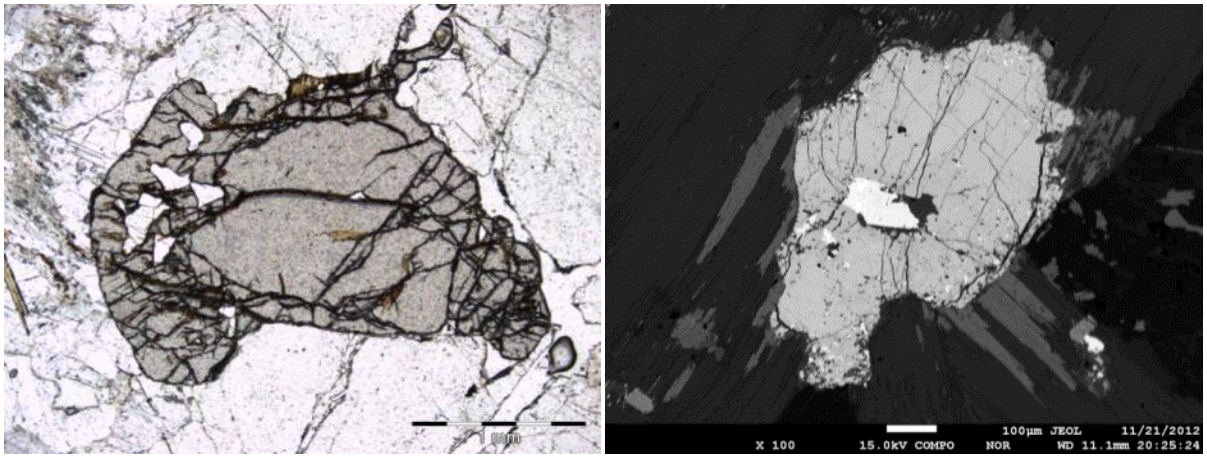
## 5.13 Geochemical Conclusions

The mineralised granites clearly come from a different source to the pre-$D_3$ intrusions as indicated by high field strength- and incompatible element abundances, and discrimination of the two leucogranite populations on more than one tectonic discrimination diagram. Different conditions of granite generation and melt migration and interaction with the host rocks must have taken place. This is supported by mobile and immobile trace element trends. There is less discrimination with respect to major element abundances and ratios, except where the garnet and tourmaline leucogranites are concerned, as these are more peraluminous than the other leucogranites, and consistently plot apart on most of the other cationic discrimination plots. Mobile trace elements are also fairly limited as discriminators; Rb for example is in comparable abundances in weakly mineralised and mineralised leucogranites, suggesting that they are all variably differentiated, and probably subject to similar alteration.

Placing the leucogranites into either A-, M-, I-, or S-type is not clear cut. Certainly, the peraluminous A and B type sheets are probably more S-type than any other SLG grouping in this study. The Cm and D type have some interesting comparisons; the Cm type is restricted more or less to the Khan Formation, and unlike the A and B type, are too oxidised to crystallise garnet. Instead they contain variably abundant magnetite. The D-type also contain comparable Fe, but not necessarily in magnetite. Instead pyrite, pyrrhotite and chalcopyrite host Fe, reaffirming the oxidised-reduced contrast that corresponds to U-mineralisation. HFS (Y in particular) abundance in the D type discriminates these from the Cm type, as does the K/Mg ratio, and Nb abundance. The magnetite – pyrrhotite contrast is purely a result of host rock influence, but the HFS and K/Mg contrast supports different sources.

The rare-earth elements in Chapter 6 show that abundances of HREE and LREE are able to discriminate between leucogranite groups and that the uraniferous granites in this study agree with a fractionated source as interpreted in Tjimunee (2009).

# CHAPTER 6 RARE EARTH ELEMENT GEOCHEMISTRY




Garnet porphyroblast (left) in a B-type granite located within the Kuiseb Formation at the Valencia Deposit. The ability of garnet to host heavy rare earth elements and Y allows for REE data to discriminate between SLG's with some consistency to petrographic observations. Similarly, the abundance of phosphates in the mineralised SLG's is reflected in elevated light rare earth abundances, differentiating the mineralised from weakly mineralised sheets chemically (Husab, hole RDD373). The backscatter image illustrates a uraninite inclusion, surrounded by fractured monazite, in turn included within a cluster of biotite books (right).

## 6.1 Introduction

The rare-earth elements usually provide a useful geochemical tool because of the systematic way in which the elements from La to Lu on the periodic table decrease in ionic radius, and generally retain a steady $3^+$ valence state. Rare earth elements (REE) tend to behave as incompatible elements in felsic melts because of their large ionic radii.

Those elements that are heavier than Eu display the so-called lanthanide contraction, in which the larger nucleus pulls the outer electron shell inward; as such there exists a compatibility contrast between the light and heavy rare earth elements (from Rollinson, 1993). The tendency for Eu to partition in the source plagioclase is also a useful tool that may be applied to characterisation of the fractionated melts that produce the Central Zone leucogranite suite. The data are compared to existing REE analyses of sheeted leucogranites

at the Goanikontes area, specifically the Etango deposit, (Tjimunee, 2011) and Central Zone alaskites (McDermott *et al.*, 1996).

The REE patterns of felsic rocks are most strongly influenced by the accessory assemblage of the given sample, and REE patterns tend to reflect the abundances of the phosphates, monazite and xenotime, aluminium silicates, and zircon. Ce and La, for example, concentrate in the phosphate, monazite and Ce in allanite. Zircon and garnet host the heavy rare earths and the element Y is hosted by garnet and the phosphate, xenotime[44].

The LREE concentrations in fractionated leucogranite melts should display enrichment, concurrent with enrichment in other incompatible elements, especially uranium. The abundances of LREE may be used as an indicator of peraluminous melt temperature, or to infer relative differences in the conditions of partial melting between successive generations of sheeted leucogranites (Miller *et al.*, 2003; and Chappell *et al.*, 2004). In low-T partial melts, monazite may retain REE in the source, while zircon and garnet may introduce transported HREE to a leucogranite sheet. Since, REE trends reflect the accessory mineral assemblages of the leucogranites, which in turn is dependent on the solubility, distribution within the source, and degree of partial melt; it should be possible to differentiate between the uranium deposits regionally. Clemens (2014) suggested that trace element abundances, which may include REE, are related not only to melt percentage, but also to the nature of the source rock and distribution of accessory minerals. REE plots should in theory differentiate between leucogranites with stronger S- or I type affinity.

The aim of this chapter is therefore to determine whether REE analyses are an effective tool for discrimination between the fractionated SLG suites within deposit areas and regionally; and whether REE consistently distinguish between leucogranites that were emplaced at different stratigraphic levels. Additionally, do the REE trends correspond with the empirical observations of accessory assemblages in the various leucogranite sheets at each deposit area?

[44] Y is included as there are useful trends identified in this sample set.

Key features of the field observations and petrographic evidence in the sheeted leucogranite types to be considered in the comparison of REE abundances include:

- B-type sheets should show field-evidence that they predate the tourmaline-bearing leucogranites, as they contain accessory garnet, which the tourmaline varieties do not (Chapter 4);
- Magnetite-bearing C-types predominantly intrude the Khan Formation (Chapter 3, Chapter 4);
- Tourmaline-bearing sheets intrude the Khan-, Rössing- and Kuiseb Formations (Chapter 3);
- The D-types and E-types are uranium-bearing and it should also be possible to distinguish refractory mineral-bearing types from weakly mineralised sheeted leucogranites because brannerite is defined as having Ce and Y (and potentially HREE) in the A-site (Hewitt *et al.*, 1957; Frondel, 1958) and betafite is associated with REE-bearing allanite and zircon.;
- All subdivisions within the SLG samples are determined by field and petrographic characteristics alone. U content is a secondary consideration, where applied, 100 ppm is used to be consistent with the convention established in Chapter 5.

***Samples***

In order to confirm whether it is possible to distinguish these different types of sheeted leucogranites from the various areas, samples were collected from major uraniferous areas at Husab, Valencia, Etango and Farm Goanikontes (including a single diorite from Hildenhof); and the Ida Dome area (Garnet Valley, Holland's Dome and Ida Dome). At Husab it was possible to sample material with known, significant refractory U mineral-bearing phases so four refractory uranium mineral hosts, from three boreholes, were analysed.

The total suite of samples comprises 41 granitic rocks, all analysed by Inductively Coupled Plasma – Mass Spectrometry (ICP-MS) at the Bernard Price Institute of the University of the

Witwatersrand, Johannesburg. Two samples were repeated for quality control, and the net dataset is therefore of 39 individual samples. Sample preparation procedures for the sample suites in this study are detailed in Appendix E4, and descriptions of the each of the REE samples are given in Appendix E12. Individual sample descriptions, locations and whole-rock geochemistry are also given in Appendix D1, D2 and Appendix E10.

The surface samples and their locations in UTM (WGS84) are summarised in Table 6.1 and the collar positions of sampled diamond drill core in Table 6.2.

Table 6.1 Collar positions of diamond holes sampled for REE analyses. X and Y are in UTM (WGS84- 33S). Samples represent 1 m intervals of granite (alaskite).

| Hole ID | X | Y | Deposit | Area | Sample Intervals (m down-hole) |
|---|---|---|---|---|---|
| RDD008 | 507165 | 7507204 | Husab | Zone 1 | 296-297(D alaskite); 297-298 (D alaskite); |
| RDD011 | 506765 | 7506801 | Husab | Zone 1 | 380-381 (Cm) |
| RDD042 | 506206 | 7505202 | Husab | Zone 1 | 237-238 (D - refractory) |
| RDD373 | 506530 | 7506402 | Husab | Zone 1 | 65-66 (D - refractory); 125-126 (D - refractory); 160-161 (D - alaskite); 201-202 (D - leached alaskite) |
| GOADH0012 | 482372 | 7488695 | Etango | Goanikontes | 127.72-128.04 (D - alaskite) |
| GOADH0022 | 482708 | 7488903 | Etango | Goanikontes | 200.42-200.72 (D - alaskite) |
| GOADH0034 | 482068 | 7488097 | Etango | Goanikontes | 261.71-262.00 (Cm) |
| J04 132.68 | 523948 | 7529985 | Joly Zone | Valencia | 132.68-132.96 (Cm) |
| VA 26 139_104 | 524088 | 7528841 | Valencia | Valencia | 104.50-104.78 (D- alaskite) |

Table 6.2 Positions of surface samples submitted for REE analyses. X and Y are in UTM (WGS84- 33S).

| Name | x | y | Variety | Name | x | y | Variety |
|---|---|---|---|---|---|---|---|
| **Ida Dome Area** | | | | **Valencia** | | | |
| CZ7-1 | 501315 | 7484263 | D | VALB 01 | 523092 | 7530183 | Sheared Salem |
| IDAG 64 | 501850 | 7484922 | D | VALB 03 | 523092 | 7530183 | Salem Megacrystic |
| IDAG 70 | 502290 | 7482272 | Cm | VALG 01 | 524768 | 7530557 | B |
| IDAG 1(b) | 502993 | 7486813 | C | VALG 02 | 524768 | 7530557 | Ct |
| IDAG 09 | 503114 | 7487076 | C | VALG 06 | 523502 | 7529135 | Cm |
| IDAG 92 | 501555 | 7481794 | Grey 3 | VALG 07 | 523502 | 7529135 | F |
| **Hildenhof** | | | | VALG 11 | 524002 | 7528840 | D |
| HILG 02 | 489186 | 7489596 | Grey 2 diorite | GRA 74 | 524260 | 7528859 | D |
| | | | | GRA 83 | 524365 | 7528560 | B |
| | | | | LVA 01 | 523981 | 7529088 | D leached |
| | | | | VALG 13 | 523904 | 7528727 | B |

## 6.2 REE Analysis Results

All data are chondrite normalised to the abundances presented in McDonough and Sun (1995) and the raw and normalised data are given in Appendix F.1 tables (Calibration standards of the ICP-MS laboratory are in Appendix E6.

The first approach to interpreting the REE data is to plot the three main categories of granite; namely the early generation Grey and Salem types, the intermediate sheeted leucogranites in their various 'types' and the late mineralised granites. Each category was then sub-divided into specific deposits. The plot of five samples of Grey and Salem types from Hildenhof, the Ida Dome, and Valencia highlights two clear trends (Figure 6.1).

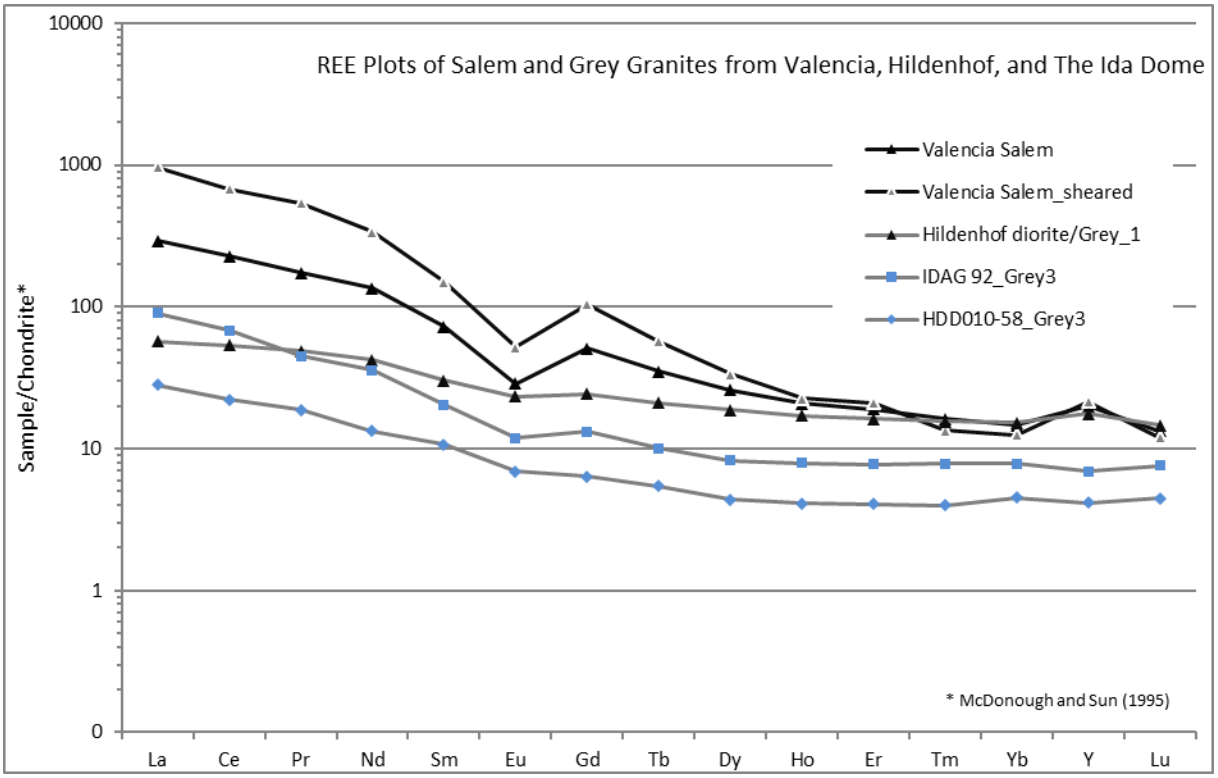



Figure 6.1 REE plots for Grey and Salem Suite granites at Valencia, Holland's Dome and Hildenhof. Salem granites are relatively REE enriched, and show minor -ve Eu anomalies. The Grey granites are less enriched than the Salem granites, do not show a pronounced Eu anomaly and Y is <Lu in two samples, and slightly >Lu in one of the surface samples (HILG 02 - a Hildenhof surface sample).

The Salem type granites are relatively enriched in LREE with an Eu anomaly, and have normalised Y > normalised Lu. The Grey granites, in contrast, do not show the same Eu anomaly and the shallow negative slope continues through Y < Lu. The two Salem granite samples plot with 1000 ppm and 300 ppm normalised La, while the Grey varieties plot with <100 ppm normalised La. A nominal value of 100 ppm has been chosen to distinguish between 'weakly mineralised' and 'mineralised' sheets, to be consistent with the geochemistry chapter. REE data for A-, B-, and C-type sheeted leucogranites plot with relatively flat, depleted slopes compared to the Grey and Salem granites (Figure 6.2).

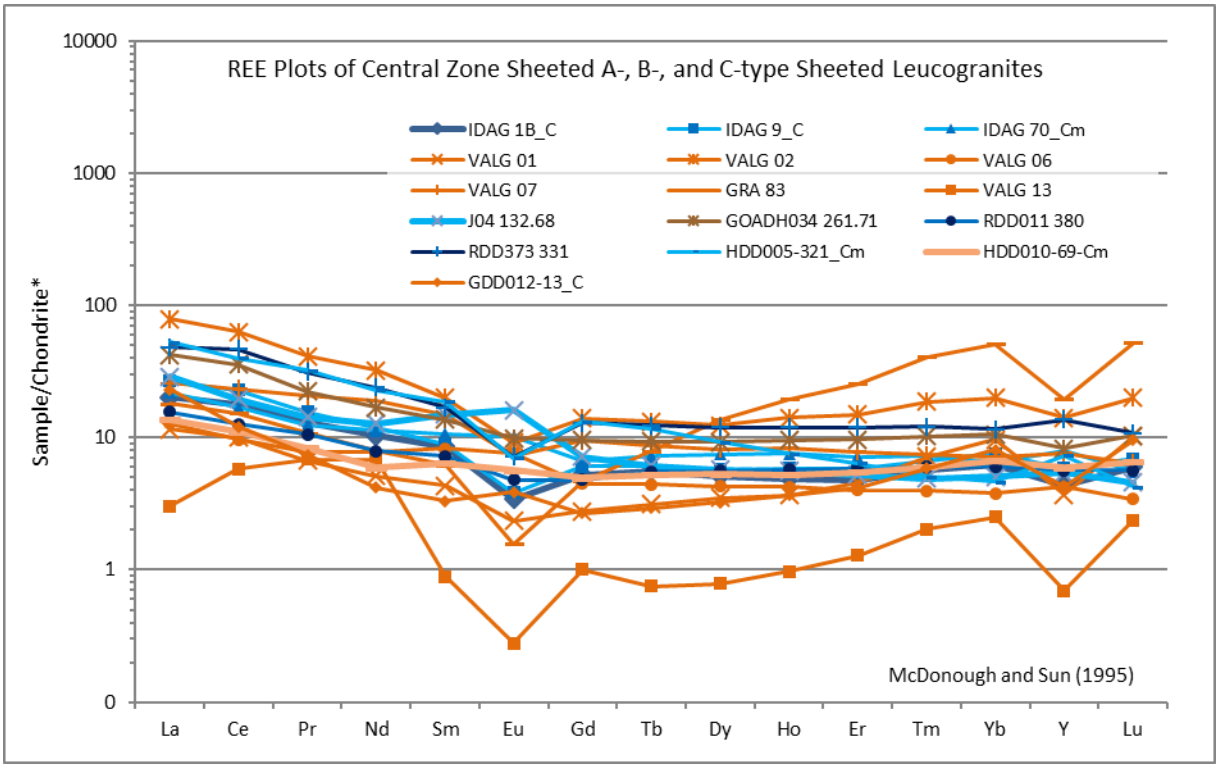



Figure 6.2 REE plots for sheeted leucogranites from Etango, Husab, Ida Dome and Valencia. The samples show a combination of -ve Eu anomalies, and relatively flat or shallow negative slopes. Y is included as a measure of host rock/phosphate interaction, where samples with elevated Y are interpreted as being contaminated by phosphates (xenotime).

There is a great variety of REE slopes in the SLG suites. Some samples are LREE enriched with negative slopes and -ve Eu anomalies; some show +ve Eu with flat HREE and Y>Lu; and some show pronounced HREE enrichment, with Y<<Lu. Slightly elevated Eu occurs in some

samples, indicating plagioclase enrichment. All samples plot with <100 ppm normalised La. The uraniferous samples consistently plot with -ve Eu anomalies, some more pronounced than others (Figure 6.3).

REE Slopes range from steeply negative, LREE enriched samples to relatively flat slopes in low REE-enrichment samples. Y is >Lu in five samples, including two of the four refractory mineral-bearing samples. The mineralised samples can be separated into those with positive, HREE enrichment and those with a negative HREE abundance slope. There is an overall positive correlation in comparing total HREE abundances and U content. However, U and HREE abundances are inconsistent within individual granite populations from each deposit (Figure 6.4).

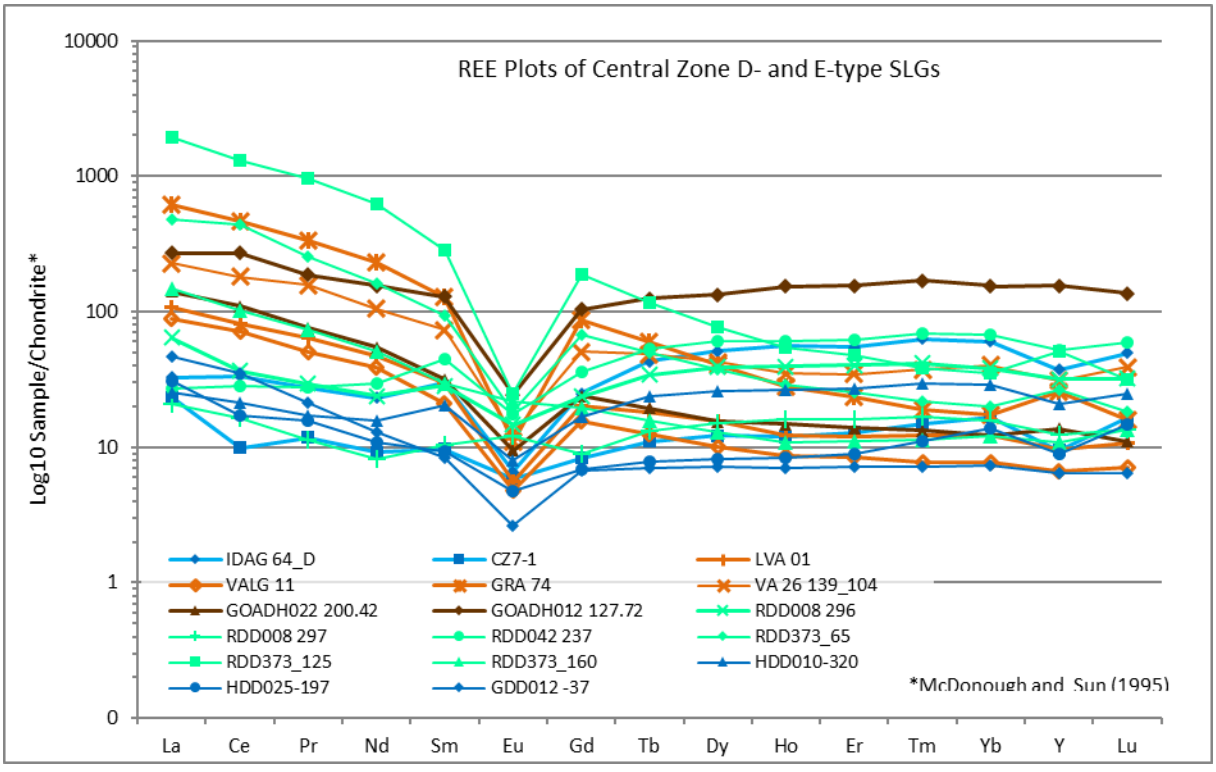



Figure 6.3 REE plots of mineralised leucogranites/ alaskites from Etango, Husab, Ida Dome and Valencia.The mineralised samples consistently plot with -ve Eu, and with highly variable HREE. As with the leucogranites, the mineralised samples appear to show either HREE enrichment relative to Gd abundance, with Lu>Y, or with negative- to flat HREE slopes relative to Gd. A single mineralised alaskite from Goanikontes displays normalised HREE above 100 ppm, for all elements.

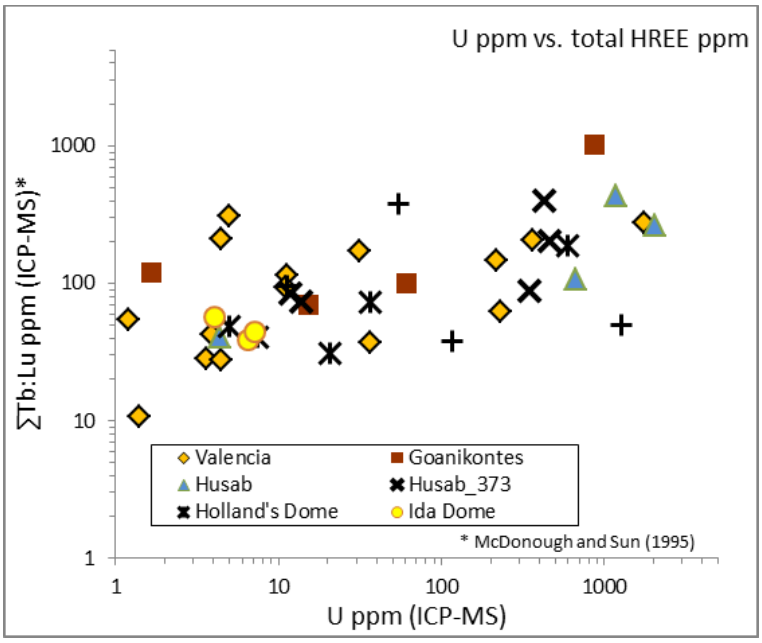



Figure 6.4 Uranium content vs. ∑HREE from Tb through Lu. The plot shows a strong positive trend between U and HREE. Heavy rare earth enrichment occurs in low grade Valencia samples, which host prominent quantities of garnet porphyroblasts.

## 6.3 REE Trends of the Goanikontes Sheeted Leucogranites

The REE study presented by Tjimunee (2009) comprised a suite of 20 granites; 8 relatively high grade samples (>500 ppm U, two of which are >1000 ppm); 1 weakly mineralised sample (<200 ppm U); 10 C-type leucogranites (<25 ppm U) and 1 diorite from the nearby Hildenhof anomaly. The sample set of this thesis comprises 2 mineralised leucogranites, a single C type and Grey granite (diorite) from Hildenhof and is essentially a test of consistency between the 2009 data and the 2013 data of this study. As with the Tjimunee samples, the mineralised granites show a relative enrichment in LREE, with a negative slope, a pronounced -ve Eu and convex HREE. In contrast to the 2009 results, Y>Lu distinguishes the uraniferous samples of this study (Figure 6.5).

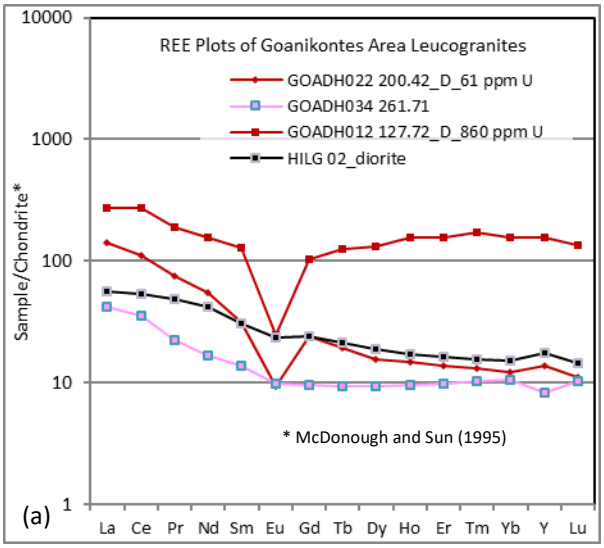



Figure 6.5 REE plots of leucogranite samples from the Etango Deposit at Goanikontes. (a) Data of samples of the Etango deposit core, and a single hand specimen from Hildenhof. Two alaskite samples, one with a high grade (860 ppm U) and the other low grade (61 ppm U) both show pronounced -ve Eu anomalies. The higher-grade sample is enriched in LREE and HREE relative to the other samples. The sample from hole 034 is a Khan Formation - hosted magnetite Cm-type, and shows a negative slope of low concentration REE's. The diorite sample from Hildenhof shows a consistent, shallow negative slope.

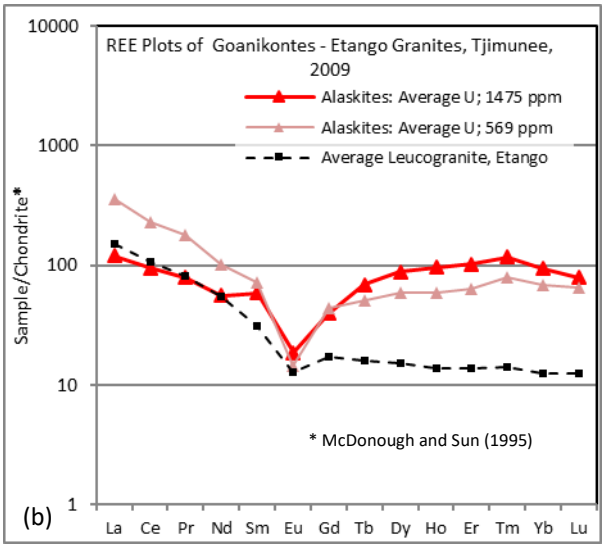



Figure 6.5(b) Comparison with existing data from Tjimunee (2009) shows pronounced -ve Eu in the mineralised samples. Samples show a positive correlation between HREE and U; high-grade samples (>1000 ppm U) for example plot with elevated HREE relative to the average of all the leucogranite samples. Similarly, the Cm-type sample shows near identical REE composition to the Tjimunee (2009) data.

REE plots of three Etango Deposit sheeted leucogranites and a diorite composition Grey granite, all from near farm Goanikontes show strong contrasts between weakly mineralised- and U-enriched alaskites, and the Khan Formation-hosted $C_m$-type (magnetite-bearing (Figure 6.5a). The U-enriched sample contains the highest concentration of HREE of any sample in this study, and exceeds even the most HREE enriched Etango sample from the more comprehensive Tjimunee (2009) data set. Heavy rare earth elements tend to have high D values in accessory phases such as zircon, titanite, xenotime, and apatite; and such phases observed, in the Etango samples have provided the sites for the HREE to accumulate in anomalous concentrations, xenotime in particular.

## 6.4 REE Trends of the Husab Sheeted Leucogranites

The deposits at the Husab Mine present an opportunity to assess the REE content of whole rock material from refractory mineral-bearing and uraninite- and coffinite- dominated sheeted leucogranites. Samples are sourced from Zone 1 of the Husab Mine, where refractory minerals are known from four isolated diamond drill holes, samples in this study are sourced from three of these. Table 6.3 summarises the REE plots of the Husab sample set. The sample suite comprises:

- Two uraniferous leucogranites that intrude mottled cordierite gneiss from the Rössing Formation;
- Four refractory mineral-bearing leucogranites that intrude mottled cordierite gneiss from the Rössing Formation, above the lower carbonates;
- Two Khan Formation - hosted leucogranites; and
- One leucogranite leached of silicates by hydrothermal fluid(s).

Table 6.3 Summary of REE trends of refractory-bearing and uraniferous sheeted leucogranites at the Husab Zone 1 deposit.

| Samples | Category | LREE shape | Eu | HREE shape | Y vs. Lu |
|---|---|---|---|---|---|
| RDD373 160 m; RDD008 297m | Mineralised | Flat | Flat | Flat | Y slightly < Lu |
| RDD008 296 m; RDD042 237m | Mineralised, refractory | Flat to weak negative | Negative | Elevated convex after Gd | Y<Lu |
| RDD373 65m; RDD373 125m | Altered mineralised, refractory | Enriched, negative | Pronounced negative | Negative after Gd | Y>>Lu |
| RDD373 201; | Mineralised, but severely altered | Enriched, negative | Negative | Strong negative after Gd | Y>>Lu |

REE abundances of uraniferous leucogranites hosted in the Rössing Formation show steeply negative slopes for LREE and HREE in all samples; with a wide range of LREE concentrations (Figure 6. 6). The refractory mineral-bearing samples show two contrasting HREE slopes; The RDD373 samples show a negative slope with Y>Lu, while the samples from RDD008 and

RDD042 show HREE enrichment from Gd to Lu, with Y<Lu. The RDD008 and RDD042 samples contain appreciably more brannerite than the two RDD373 samples. Since brannerite concentrates Y, elevated HREE content may be an indicator of the refractory mineral in a given sample. The consistently high LREE abundances of the RDD samples relative to the RDD008 and RDD042 samples, and consistent Y>Lu suggest that phosphates (monazite and xenotime) may be relatively abundant in the RDD sheeted leucogranites.

The RDD373 samples are visibly altered and Fe-stained, and each contain <500 ppm U; while RDD042-237 m contains 1190 ppm, and RDD008-296 over 2060 ppm. HREE tends to be elevated in samples with high U content, while in the less uraniferous samples LREE show considerable enrichment over the sheeted leucogranites at Husab. The 295 m - 296 m interval contains 2062 ppm U, and the 296 m - 297 m interval contains 669 ppm U. The latter is correspondingly less enriched in REE, but shows the same HREE enrichment relative to Gd, and Y<Lu. RDD373-65, RDD373-125, and RDD373-201 are variably altered and discoloured, each displaying some evidence of alteration (Fe staining and chlorite veins).

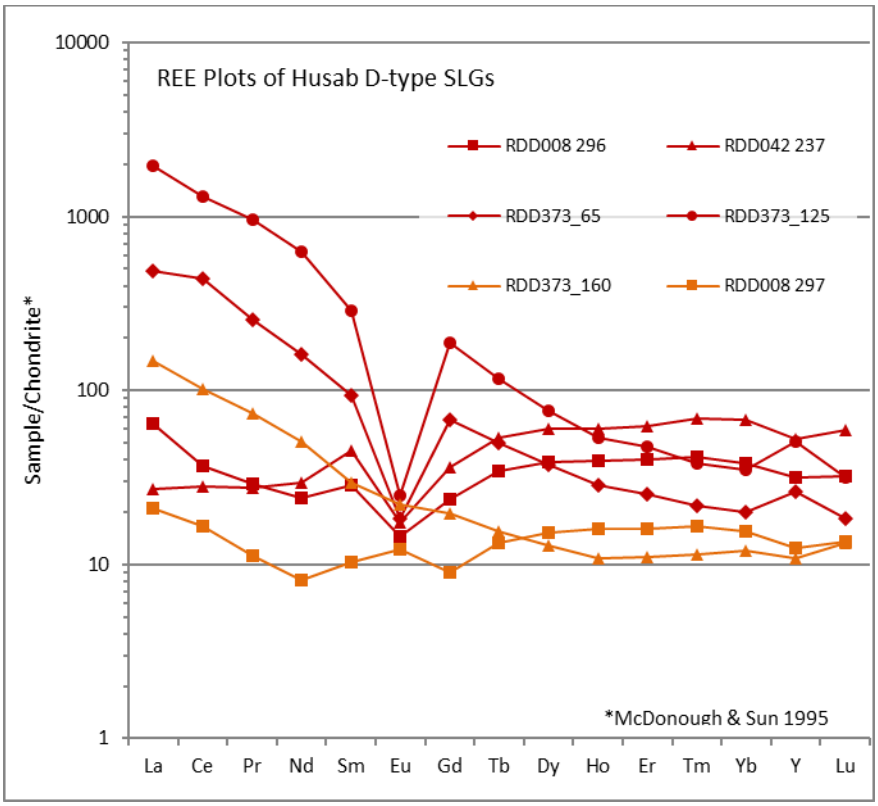



Figure 6.6 REE plots of Rössing Formation-hosted alaskites from the Zone 1 deposit at Husab. The uraniferous samples with refractory uranium minerals from RDD008, RDD042 and RDD373 show distinctly -ve Eu anomalies. (deep red plots). The refractory mineral-bearing samples of RDD373 also have a steep -ve LREE trend, Gd enrichment, -ve HREE slopes and Y>Lu. All four characteristics distinguish the refractory-bearing RDD373 samples from the D-type SLGs (orange plots).

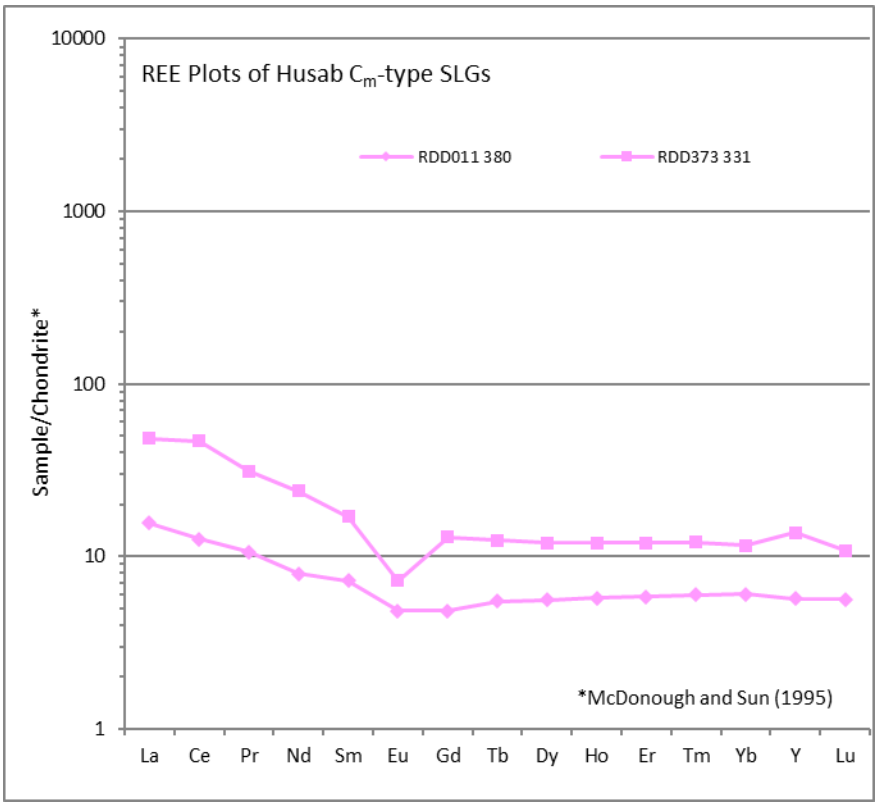



Figure 6.7 REE plots of magnetite C-types from Zone 1, Husab. The RDD373 sample shows a strong -ve Eu, flat HREE and Y>Lu. The RDD011 sample displays a negative slope to Eu, with all REE less abundant than in the RDD373 sample. Ce and La- and Y-phosphates are known to host uraniferous inclusions, and may explain the observations in the plot.

RDD373-201 shows silicate leaching in hand specimen, as the sample has a sponge-like network of cavities caused by acidic fluid circulation. The samples are depleted U in comparison to the RDD008 and RDD042 samples. The altered leucogranites show a negative, concave HREE slope with Y>Lu while the unaltered samples show a positive, concave HREE enrichment, with Y<Lu (Figure 6.6).

For sheeted leucogranites hosted in the Khan Formation, two samples are from diamond holes RDD373 and RDD011; RDD011 is ~400 m north along strike and both samples come from comparable host rocks. The two samples show contrasting HREE content, where the RDD373 sample has consistent REE abundance relative to the RDD011 sample, with distinctive Y>Lu (Figure 6.7). Both samples show negative LREE slopes and the RDD373 sample contains slightly more U (11 ppm vs. 4 ppm) consistent with relative LREE enrichment over the less uraniferous RDD011 sample (Figure 6.7).

## 6.5 REE Trends of the Ida Dome Granites

The Ida Dome area samples are divided into three sets, the Grey granites (2 samples,

Figure 6.8); the Khan-Formation hosted leucogranites, which either host accessory magnetite, or are considered free of diagnostic accessory phases (Figure 6.9); and the uraniferous sheeted leucogranites (Figure 6.10). Table 6.4 summarises the defining REE trends. The alaskites at Garnet Valley and Holland's Dome have pronounced –ve Eu anomalies, and compare with the other alaskites in the CZ. The most mineralised sample has HREE enrichment relative to the other samples and all of the mineralised samples have a negative LREE slope with a pronounced +ve Sm accentuating the -ve Eu. Mineralised samples tend to be less LREE enriched than counterparts at the Valencia, Etango and Husab deposits.

Table 6.4 of REE trends of Grey granites, leucogranites and mineralised leucogranites (alaskite) of the Ida Dome area sample set.

| Samples | Category | LREE shape | Eu | HREE shape | Y vs. Lu |
|---|---|---|---|---|---|
| IDAG 64; CZ7-1; GDD012 37m; HDD010 320m. | Mineralised | Negative, inconsistent slope | Strong negative | Strong convex after Gd | Y<Lu to Y<<Lu |
| HDD025 197m; | Mineralised, altered (E type) | Negative | Moderate negative | Convex after Er | Y<<Lu |
| IDAG01; IDAG09; GDD012 13m; IDAG70 | C type in Khan Fm. | Negative and flat | Inconsistent, strong negative and weak positive | Negative, $C_m$ are flat After Gd, two samples convex after Er | $C_m$ Y≥Lu; Garnet Valley (GDD012-13m) Y<<Lu; Others Y=Lu |
| HDD010 58m; IDAG92 | Khan – Hosted Grey | Negative, consistent | Weak negative | Flat | Y≤Lu |

The Khan Formation-hosted leucogranites, predominantly of the $C_m$ type, have low concentrations of REE; LREE do not exceed, normalised 55 ppm, and HREE only exceed 10 ppm in a magnetite-bearing sample from the Holland's Dome area (Figure 6.9). The $C_m$-types have relatively flat to negative low abundance REE curves, with -ve Eu and weakly +ve Eu anomalies reflect variable plagioclase content (Figure 6.9). Y is also inconsistent, and is either just <Lu or anomalously enriched, which is attributed to variable phosphate and zircon content and/or garnet restite. There is potentially a weak component of HREE mobility in the alteration environment. Drill core sample GDD012-13 m contains anomalous Lu and other HREE relative to the other samples. The sample is sourced from below a carbonate package known to host accessories such as zircon, titanite and apatite, all of which host HREE.

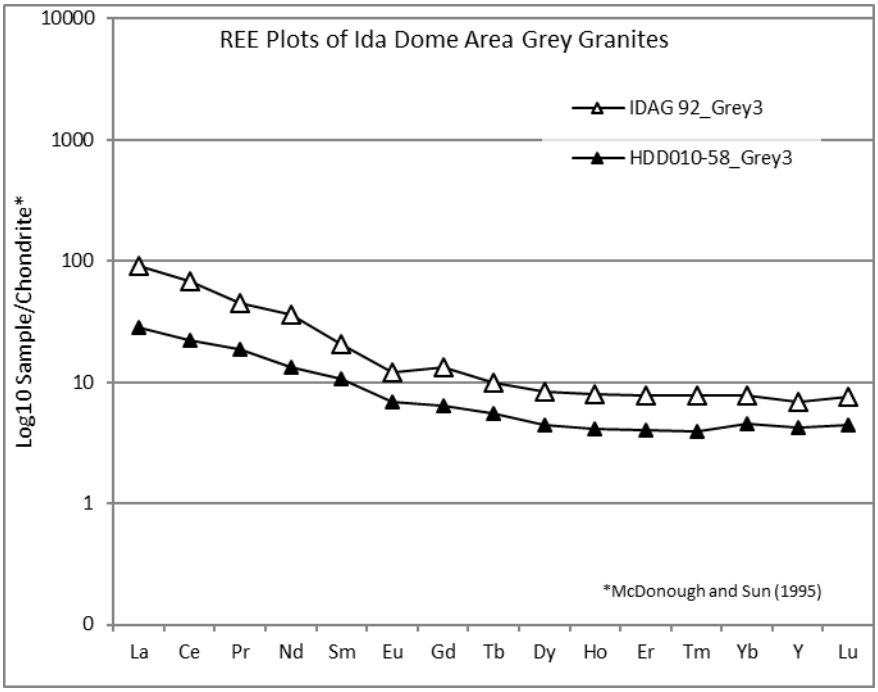



Figure 6.8 REE abundances of Ida Central and Holland's Dome Grey granites. The Grey granites have a negative slope from LREE to HREE, with only a weak -ve Eu anomaly in the Holland's Dome sample.

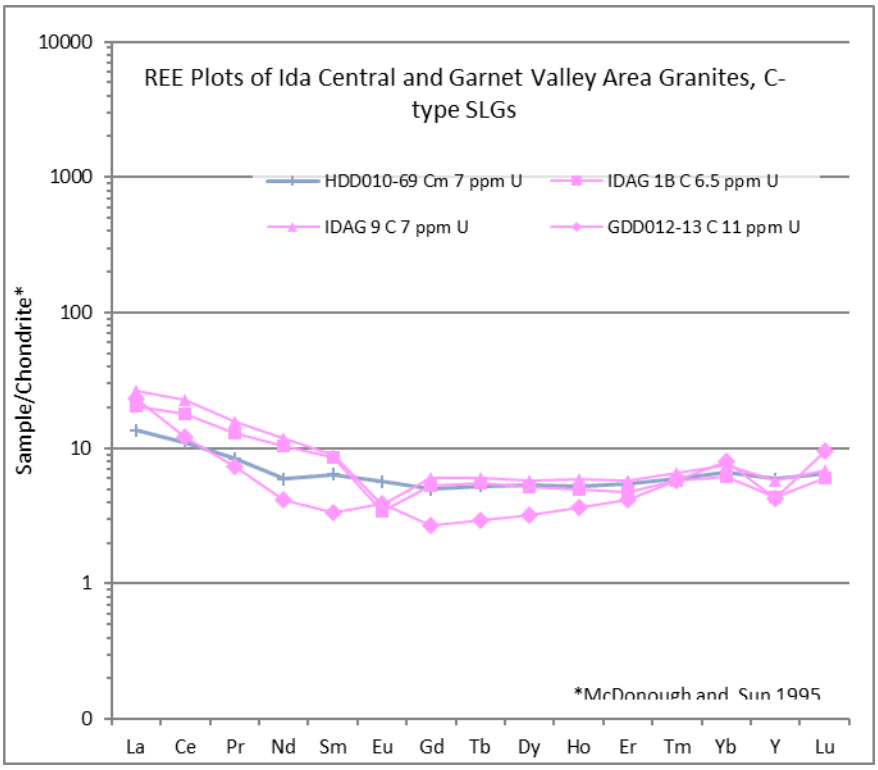



Figure 6.9 REE abundances of the Ida Central and Garnet Valley C-type, and Cm-type sheeted leucogranites. The C-type sheets plot in two distinct populations; one has a distinctive, -ve Eu anomaly, and the other with a slightly +ve anomaly. There is no consistent difference between the magnetite-bearing ($C_m$) and accessory-free (C) varieties. All of the granites are sampled from within the Khan Formation, and contain uniformly low abundances of REE.

The uraniferous alaskites at Garnet Valley and Ida Central have pronounced -ve Eu, with comparable patterns and abundances with the other uraniferous samples in the CZ (Figure

6.10). The most mineralised sample has ΣHREE enrichments of between 50 ppm and 70 ppm. The mineralised samples have a negative LREE slope with a pronounced +ve Sm anomaly accentuating the -ve Eu. LREE of uraniferous Ida Dome samples tend to be less abundant than counterparts at the Etango and Husab deposits. HREE are abundant relative to the LREE and Y is consistently less enriched than Lu.

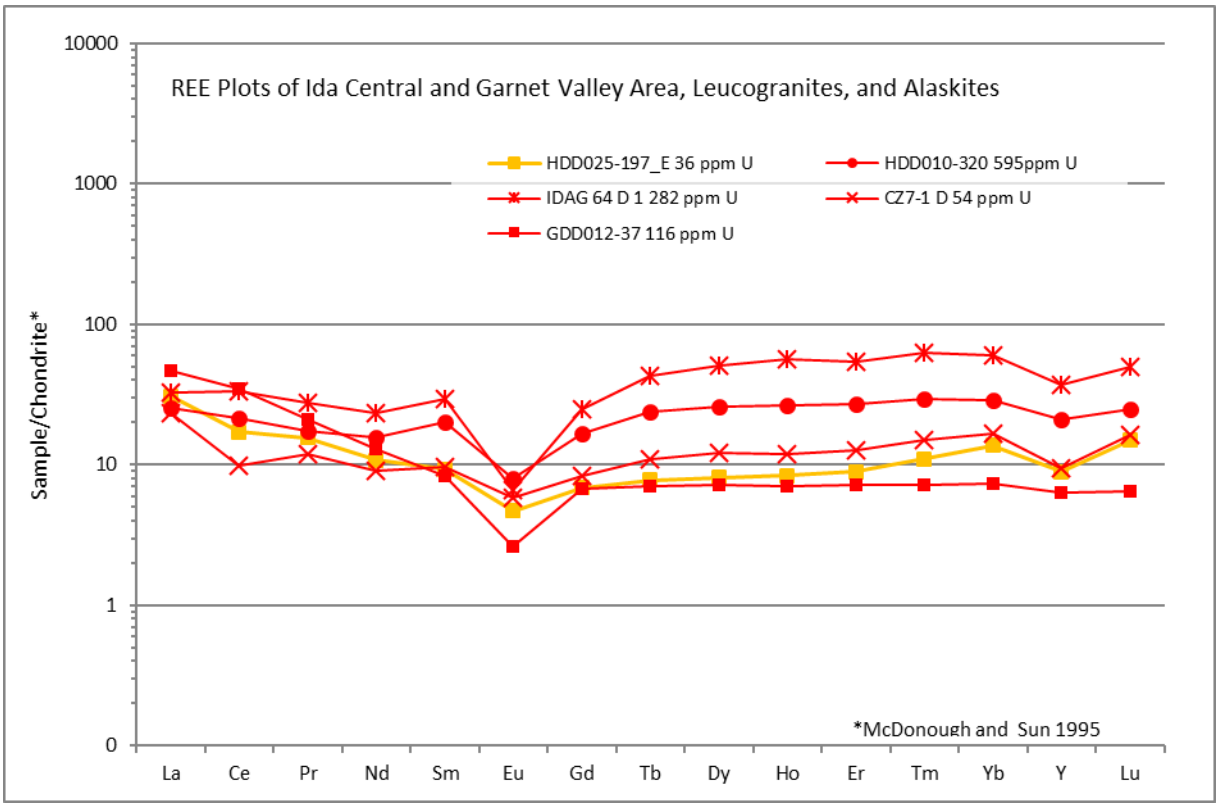



Figure 6.10 REE plots of Ida Dome Area leucogranite and alaskite. The mineralised samples show enriched HREE, with consistent Y<Lu at Garnet Valley. The Garnet Valley-Ida Central C-types show negative slopes with -Eu and weakly +Eu (IDAG09) and the uraniferous alaskites contrast with pronounce -ve Eu anomaly and gull wing type patterns of HREE enrichment.

## 6.6 REE Trends of the Valencia Sheeted Leucogranites

The samples from Valencia comprise the most comprehensive assemblage of leucogranite varieties analysed for this study. The sheeted leucogranites at Valencia show distinctive

physical differences when compared with respect to their location within the Damaran stratigraphic sequence. Accessory mineralogy in particular shows a consistent zonation with regard to the host-rock position in the stratigraphic sequence. Magnetite-bearing sheets tend to be confined to the Khan Formation and lower Rössing Formation, while the garnet- and tourmaline-bearing sheets occur in the Rössing-, Chuos-, and Kuiseb Formations.

Tourmaline-bearing sheeted leucogranites are noted in the Khan Formation, but are rare and minor in comparison to the magnetite variety. Uraniferous sheets predominate within the Rössing Formation, but have invaded higher up to the Kuiseb Formation at fold hinges (particularly at the main ore body). There are sporadic occurrences of pegmatites within the Khan- and Rössing Formations, which appear to fit the description of the F-type leucogranite described at Goanikontes by Nex (2007).

Thus, the REE comparisons are described with respect to the stratigraphic location. Table 6.5 summarises the REE plots of the Valencia sample set, which comprises:

- Pre D3 diorite: – 2 Salem suite diorites, 1 megacrystic textured, one sheared with partial melt and anomalous U (>200 ppm);
- Pre D3 sheeted leucogranites: – 3 Kuiseb Formation-hosted garnet varieties and 1 tourmaline-bearing SLG;
- Syn-post D3: - Khan Formation-hosted pegmatites - 2 magnetite-bearing alkali feldspar granite sheets; and
- Uraniferous leucogranites.

The plots of REE concentrations in the Valencia samples illustrate consistent trends in the mineralised samples; low abundances of REE in the Khan Formation-hosted C-types; and HREE enrichment in the garnetiferous B-types (Figure 6.11)

Table 6.5 Summary of REE trends of Grey granites, leucogranites and mineralised leucogranites (alaskite) of the Valencia sample set.

| Samples | Category | LREE shape | Eu | HREE shape | Y vs. Lu |
|---|---|---|---|---|---|
| VALB01; VALB03 | Salem Granites | Convex negative, sheared sample is enriched | Negative | Negative after Gd | Y>>Lu |
| VALG06; J04 132.68 | Khan Fm.-hosted $C_m$ | Concave to Eu | Positive | Flat | Y>Lu (slight) |
| VALG01; VALG13; GRA83 | Garnet granites in Kuiseb Fm. | Negative, weak enrichment | Negative | Strong positive, | Y<<Lu |
| GRA74; VALG11; LVA01; Va26-139 | D type, mineralised | Enriched, relationship with U content; negative, weakly convex | Pronounced negative in high grade U samples | Negative after Gd; enrichment corresponds to Zr | Y≤Lu |

The Salem granites intrude the lower and upper Khan Formation immediately west of the main deposit, and towards the north, the diorite intrusives also invade the Rössing Formation at the Joly Zone, ~220 m north of the deposit. The Salem granites and the Khan Formation are intruded by an assemblage of accessory-free, magnetite-bearing, and uraniferous sheeted leucogranite dykes and sills (~parallel to $S_1$). The granites have preferentially fractionated LREE from their source, and show a strong negative slope and slight -ve Eu anomaly, not unlike some of the mineralised leucogranites at most other sample areas (Figure 6.12).

The $C_m$-type in contrast, has low REE abundances, as does the later generation F-type pegmatite sample (Figure 6.12
Figure 6.12). Both of the $C_m$ samples have +ve Eu and are therefore comparable to the $C_m$ types at the Ida Dome area, and Holland's Dome in particular. Kuiseb Formation-hosted leucogranites include an assemblage of variably textured relatively enriched HREE and a shallow negative LREE slope, with a weak -ve Eu anomaly. The samples have comparable REE patterns to the garnet - cordierite granites described by Jung *et al* (2000a) and therefore probably also represent a collection of moderately fractionated granites.

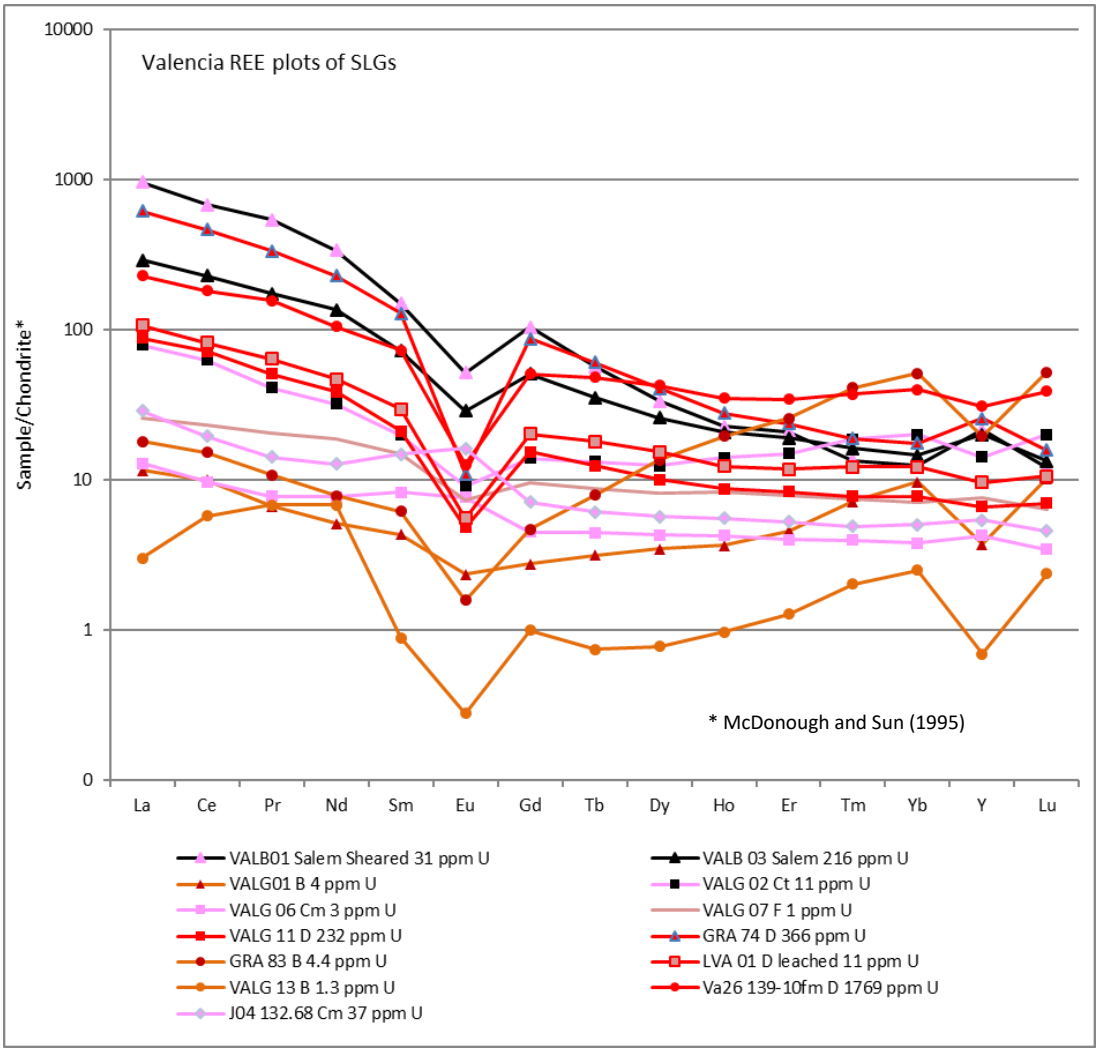



Figure 6.11 Rare earth element plots of sheeted leucogranite and Salem granites at the Valencia deposit. The data show negative slopes for all samples from LREE to Eu, but at least five samples plot with relative HREE enrichment. Samples with flat HREE slopes, plot with Y>Lu; and in samples with positive HREE slopes, Y<Lu. Types: B- garnet-bearing leucogranite; Cm- Khan Formation-hosted magnetite leucogranite; Ct- Kuiseb Formation-hosted tourmaline leucogranite; D- uraniferous sheeted leucogranite (alaskite); F- K-feldspar pegmatite.

The garnet-bearing samples represent three prominent textures; VALG 01 is a fine-grained leucogranite with fine (<0.75 cm) garnet porphyroblasts throughout, VALG 13 is a pegmatite with sporadic, coarse (> 1-2 cm) garnet porphyroblasts, and GRA 83 is a sample from an extensive, coarse-grained sheeted leucogranite body, swamped with fine <4 mm garnet. Granite GRA 83 has the highest concentration of HREE, followed by VALG 01. The HREE content, of relative Yb and Lu abundance, in these samples appears to be a reflection of garnet abundance (Figure 6.13). The tourmaline-bearing sample is the most LREE enriched in

the group, although all REE abundances are below 100 ppm (normalised) in the non-mineralised, pre-$D_3$ SLGs. There is a weak -ve Eu anomaly, and the HREE curve is flat. All three of these characteristics distinguish the granite from the various garnetiferous samples.

The uraniferous sheeted leucogranites plot in two groups, those with REE enrichment, and those with lower REE fractionation (Figure 6.14). All four samples show enriched LREE with steep negative slopes and pronounced -ve Eu anomalies. HREE show shallow -ve slopes, with one sample GRA 74 containing Y>>Lu. GRA 74 is twice as enriched in LREE compared with the most uraniferous sample from 104 m in diamond drill core Va26 139, but contains less abundant HREE. This type of pattern, with GRA 74 containing 0.09 wt.% $P_2O_5$ compared to <0.6 wt.% for the other three samples, suggest monazite and xenotime are more abundant in this sample. The most U-enriched sample at Valencia (Va26 139 104m) has the greatest HREE abundance, which is similar at the other CZ deposits. The LVA 01 sample shows visible evidence of a weak degree of alteration, and low REE abundance. It is assumed the sample is a primary, weakly uraniferous sample, as the alteration does not appear intense enough to have removed appreciable uranium. A comparison of the most Zr-rich of the samples shows that those samples with the most abundant HREE correspondingly contain the most Zr (Figure 6.14).

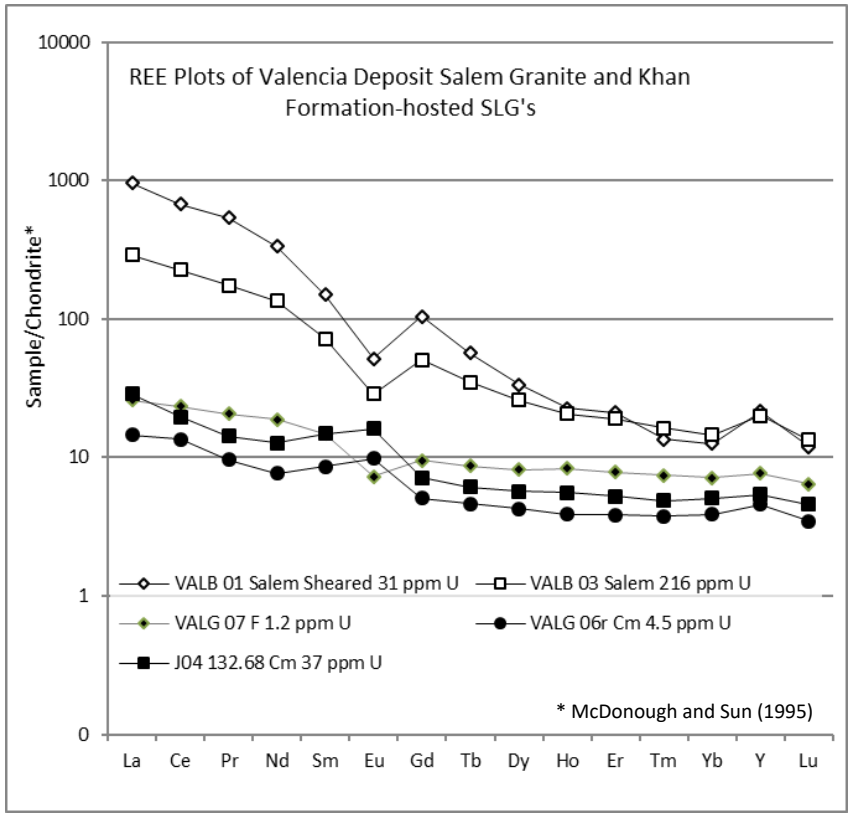



Figure 6.12 The Khan Formation-hosted Salem suite and leucogranites at Valencia. The collection comprises two Salem suite granites, two magnetite-bearing pre- syn-$D_3$ C-type sheets, and an F-type pegmatite. The more primitive Salem samples are relatively enriched in LREE, the sheared sample (VALB01) is the most enriched, where incompatible LREE partition into melt bands along conjugate shear sets.

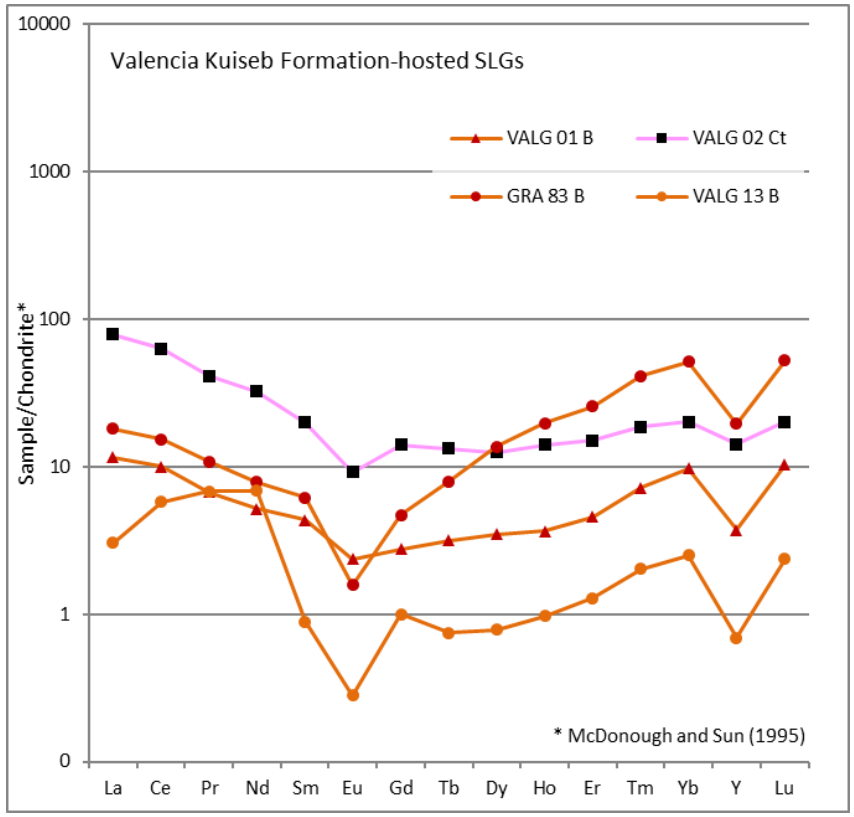



Figure 6.13 The Kuiseb Formation-hosted sheeted leucogranites at Valencia. Garnet- and tourmaline-bearing varieties have enriched HREE abundances, relative to the Khan Formation-hosted leucogranites. The garnet-bearing samples have distinct convex HREE curves, reflecting the garnet abundances in a given sample. The tourmaline sample has -ve slope, relatively enriched LREE and a weak -ve Eu anomaly. The low LREE and Y abundance, in comparison to the Salem granite, reflects low phosphate abundance.

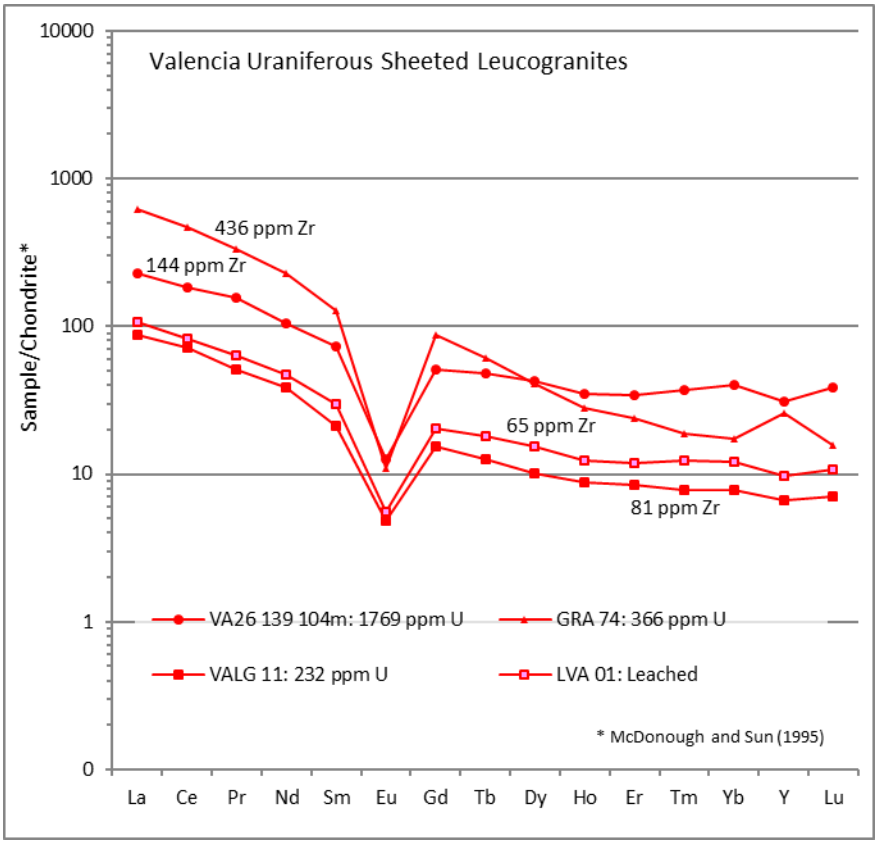



Figure 6.14 Uraniferous sheeted leucogranites at Valencia. The HREE enriched sample VA26 139 is correspondingly the most Zr enriched.

The REE sample set at Valencia thus allows for a classification of the leucogranite suites into 4 categories, which mirror the classification scheme of Nex (1997) and the geochemical and petrographic observations made in this study. The metasedimentary position does not appear to have had any influence on the actual REE content. Magnetite-bearing SLGs are restricted to the Khan Formation, the garnetiferous and tourmaline SLGs within the Kuiseb Formation, with minor volumes of these intrusives in the Rössing Formation, and, the uraniferous SLGs are predominantly restricted within the Rössing Formation stratigraphy. The four leucogranite rare earth element groups are as follows:

- Khan Formation-hosted Salem, Grey, and $C_m$-type sheeted leucogranites;
- Rössing Formation-hosted leucogranites (minor C- and B-types);
- Kuiseb-Formation-hosted leucogranites (B- and C-types); and
- Uraniferous sheeted leucogranites (D- and E-types).

## 6.7 REE Discussion

### *Rare Earth Element Fractionation*

The HREE tend to concentrate in certain accessory phases; xenotime for example is able to host elements similar to Y, while zircon and garnet are common hosts to HREE (after Rollinson, 1993). Note that the HREE-enriched B-type contains more Y than most samples (

Figure 6.15) but a very low concentration of Zr, which suggests that xenotime may concentrate some HREE, but zircon is in low abundance. The abundant garnet is therefore the dominant HREE host in the B-type samples.

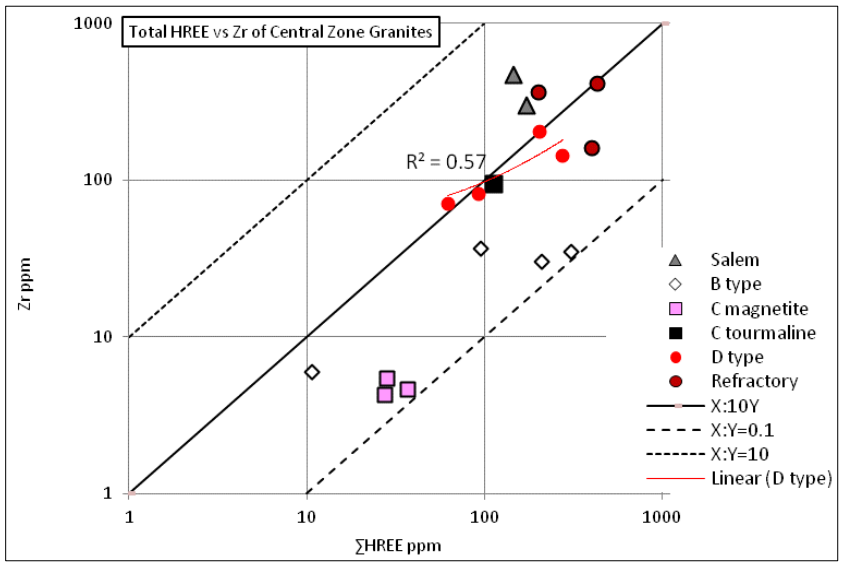



Figure 6.15 X-Y plot illustrating systematic behaviour of HREE abundances vs. Zr. There is a weak positive relationship between Zr and total HREE of the D-type sheets; however, none of the other leucogranites populations, or equigranular granites are similar. The high HREE content of the B-type is concentrated in garnet, while in the brannerite-bearing leucogranites, phosphates and brannerite may host the HREE and Y.

Y and HREE show a positive correlation in the sheeted leucogranite populations of the Central Zone uranium deposits, as a general trend (Figure 6.16). The outliers in the trend come from all deposits, and represent samples that may be derived from the metasediments, where garnet is a restite phase, while others that follow the trend contain single phase Y hosts, such as xenotime. The four uraniferous samples show a systematic

relationship between HREE and Y, but only weakly so with HREE and Zr, where the most HREE enriched contain elevated Zr.

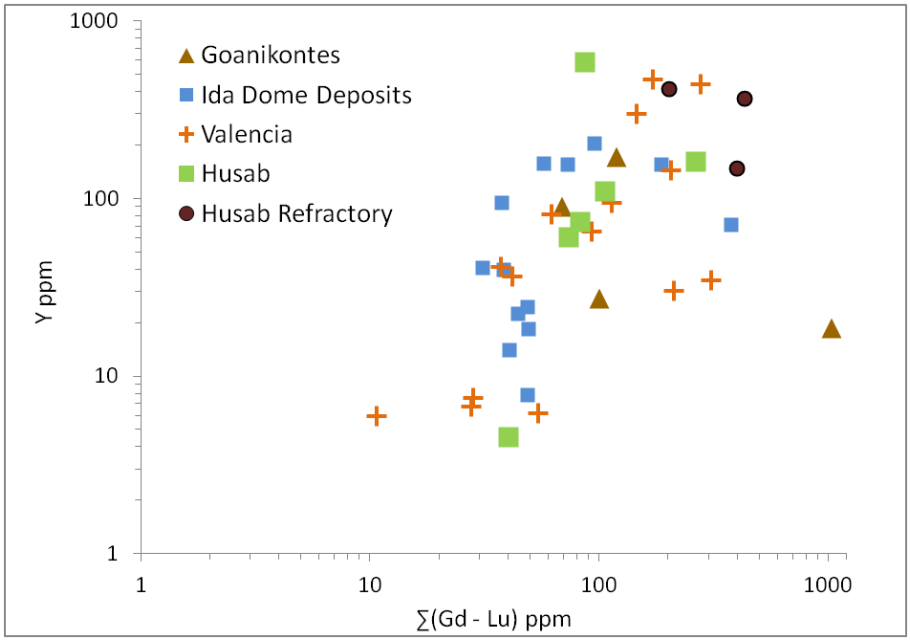



Figure 6.16 HREE vs Y of Central Zone sheeted leucogranites. HREE and Y show a systematic, positive relationship, in which the Valencia samples illustrate a wide range of concentrations, the refractory-bearing samples cluster with similar ratios to the Ida Central samples. On average, HREE = ~6Y.

Light rare earth fractionation tends to increase with increasing REE content, the bivariate plot of normalised La/Yb vs. normalised Ce of the CZ leucogranites and syn-tectonic granites illustrates this in Figure 6.17. The B-type, C-type and Cm-type leucogranites all plot with relatively low abundances, but LREE/HREE fractionation in the group ranges from 0.3 to 10. There is considerable overlap between the uraniferous group and the C-types, where about half the D-type samples show low-degrees of REE fractionation (<10) and half plot with LREE/HREE between 10 and 100. The Grey granites are comparable to the Cm-type in terms of REE content, and those described in this study are consistent with descriptions of Grey granites and sheeted leucogranites in the Khan Formation near the Ida Dome in Longridge *et al*. (2011) and Longridge (2012). The Salem diorites from Valencia show strong LREE/HREE fractionation and are more comparable to the D-type in terms of REE abundances in this regard.

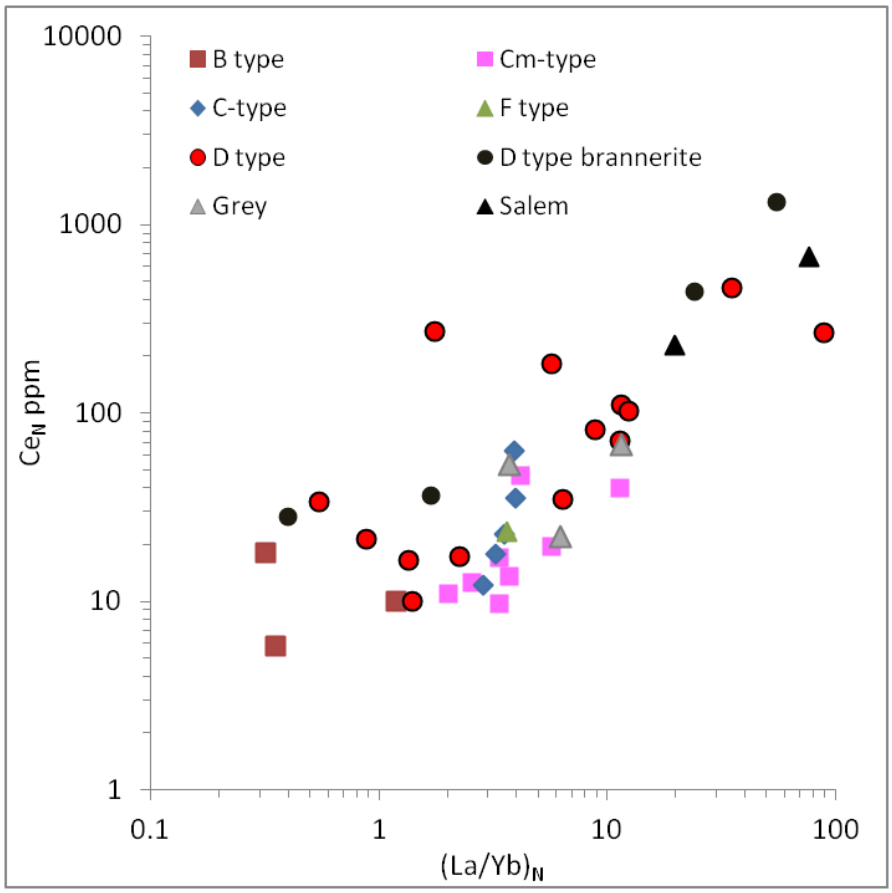



Figure 6.17 LREE fractionation trends of selected CZ granites. The B-, C-, and Cm-types host relatively depleted Ce, but a marked contrast in light-rare earth fractionation exists for B-types, and more oxidised Cm-types. The Grey granites are potentially related to the Cm-types on the basis of similar Ce abundances and light - heavy rare earth fractionation.

Fractionation trends within the heavy rare earth elements of the CZ leucogranites and syn-tectonic granites in Figure 6.18 show that the pre-D3 leucogranites and Grey granite samples tend to cluster within a 0.7 to 3 range for normalised Gd/Yb; The B-type show the lowest degree of HREE fractionation, typical for the partial melt of a garnetiferous, pelitic source rock (Kuiseb Formation). Within the group the C-type and magnetite-bearing Cm-type samples plot in distinct groups (circled, Figure 6.18). One group is comparable to the Cm-type with higher Yb concentration; the other group has stronger HREE fractionation and considerably enriched Yb. The brannerite-bearing D-types from Husab plot within the HREE-enriched group.

LREE are relatively enriched in the Salem suite, with HREE abundances tending toward relatively flat patterns. The uraniferous leucogranites have on average 5 times the LREE abundances of the pre-$D_3$ leucogranites (

Figure 6.15); HREE abundances tend to be similar, but abundances relative to element number show no linear relationships. Eu in uraniferous samples has a negative anomaly in conventional REE diagrams; the actual abundance of Eu in the uraniferous variety though is still greater than in the pre-$D_3$ leucogranites. Figure 6.18 also illustrates a consistent trend in LREE abundances between the uraniferous and weakly uranifeorus SLGs (B-, C, Cm-types). The HREE do not show any systematic relationship, other than the HREE abundance of uraniferous samples being greater than the U-weakly mineralised samples.

The magnetite- bearing C-type sheeted leucogranites hosted in the Khan Formation have depleted LREE with respect to the uraniferous- and Kuiseb Formation-hosted varieties. Abundances are relatively flat between LREE and HREE, with some Husab, Ida Dome and Valencia deposit samples showing a +ve Eu anomaly, which is unique amongst sheeted leucogranites. The only accessory mineral observed in these samples of any significance is magnetite and no indication of phosphate abundance is shown in whole-rock geochemistry.

The pre-$D_3$ SLGs are likely to have been derived from a lower temperature partial melt that retained insoluble phosphates, garnet and zircon, and therefore retained REE at the source; whereas the uraniferous SLGs, with relatively enriched REE compared to the pre-$D_3$ SLGs have either been derived from partial melt conditions capable of dissolving REE host minerals such as monazite, or were derived from source material inherently more enriched in REE-host minerals than the source material that produced the C-types for example. The lack of consistent -ve Eu also favours a partial melt model over simple fractionation from a chamber.

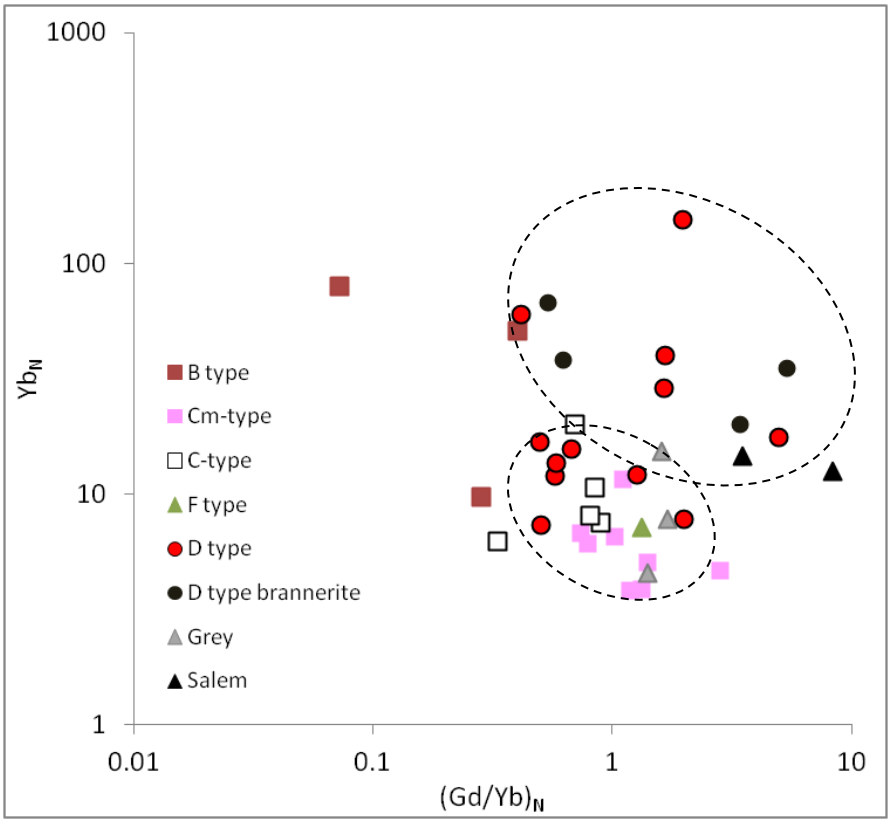



Figure 6.18 HREE fractionation trends of selected CZ granites. Most pre-$D_3$ granites host <10 ppm $Yb_N$ with the syn-tectonic Salem type perhaps the most Yb enriched. The brannerite-bearing alaskites also have high concentrations of HREE, Yb in particular sets these mineralised granite samples apart from the more abundant D-type alaskite.
.

The Kuiseb Formation-hosted leucogranites contain highly variable garnet abundances, some appear entrained at granite margins and others appear to be poikiloblasts. The elevated HREE reflects the relative abundances of garnet in each of the samples. The tourmaline sheets that crosscut the garnet leucogranites may have migrated from below the Kuiseb Formation as the sample (VALG 02) has REE abundances that resemble the Khan Formation-hosted samples. The pegmatitic variety displays pronounced -ve Eu, but also LREE enrichment relative to the HREE. All of the Kuiseb Formation samples show low abundances of REE relative to the uraniferous samples. HREE abundances are enriched relative to LREE in most samples. Garnet is the primary host of the HREE, and the abundances of the peraluminous phases supports a partial melt that has not migrated a great distance from source. Ward *et al.* (2008) showed that such a melt may migrate from a fertile source such as the Kuiseb Formation, where biotite will melt in the presence of water at metamorphic grades that existed in the Central Zone.

The larger ionic radius of Nd vs. Sm causes preferential enrichment of Nd in successively differentiated rocks (Rollinson, 1993). This property allows for a comparison of the potential sources of the granites at the uranium deposits. Sm/Nd ratios of the whole rock fill a narrow, but systematic positive range of ratios and support S-type affinity of the Grey granites with low Sm/Nd, and the very-low ratios of the B-type, support Sm retention in garnet in the metapelite source rock. Most of the uraniferous D-type specimens have Sm/Nd that are >0.3 and imply a slightly less-fractionated, crustal source(s) relative to the earlier granites Figure 6.19.

Simplistically, the pre-$D_3$ leucogranites have low totals of rare-earth elements, and the Salem type of this study, the A type granites (Sorris-Sorris, Dachsberg, and Horebis River of McDermott *et al.*, 2000), and the uraniferous SLGs of this study host greater concentrations of Sm and Nd, but critically also have greater Sm:Nd. This is an important property because the uraniferous leucogranites are interpreted to be derived from partially melted calc-alkaline rocks (McDermott *et al*., 2000).

Figure 6.20 illustrates the relative size of the Eu anomaly with respect to LREE fractionation, and successfully distinguishes between the strongly oxidised Cm-type leucogranites, the Grey granites, the Central Zone A type and the uraniferous alaskites. The HREE and LREE fractionation trends show distinct differences between the granite groups of this study (Figure 6.17 and Figure 6.18) and the ratios of $(La/Yb)_N$ and $(Gd/Yb)_N$. More-specifically, a comparison is made between the early Grey and Salem granites, the pre-$D_3$ sheeted leucogranites, and the post-$D_3$ alaskites. The uraniferous leucogranites, including those with prominent brannerite-betafite mineralisation and the Salem type diorites have REE enrichment, and far more pronounced LREE/HREE fractionation (Table 6.6).

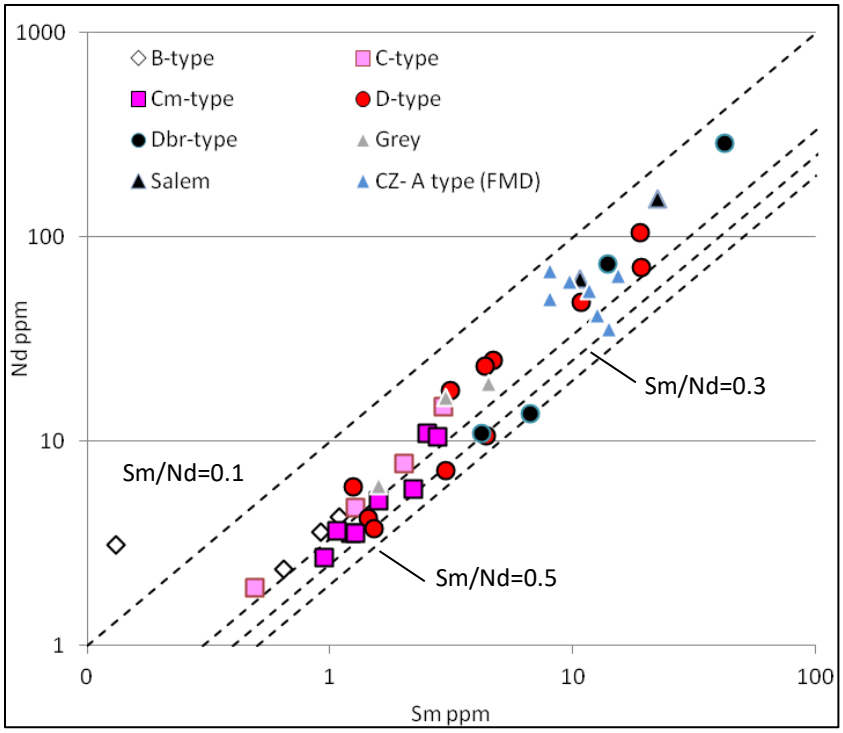



Figure 6.19 REE ratios as discriminators between sheeted leucogranite types. Sm and Nd ratios appear to distinguish between the uraniferous and non-uraniferous sheets; The B-types host Sm/Nd of ~0.3; the $C_m$-type host Sm/Nd between 0.3 and 0.4, while the relatively enriched alaskites host Sm/Nd close to 0.2. The comparative A type granites of the Central Zone (Sorris-Sorris, Dachsberg, and Horebis River granites) host a range of Sm/Nd and do not show the systematic relationship observed in the sheeted leucogranites (data from McDermott *et al.*, 2000).

Table 6.6 REE fractionation summary of the SLGs, Grey-, and Salem granites in this study.

| Granite | Total REE | Eu/Eu* | $La_N/Yb_N$ |
|---|---|---|---|
| D- and E-type | **29 ppm to 664 ppm** | 0.46 | **13.5** |
| Refractory-bearing D-type | **88 ppm to 1759 ppm** | 0.33 | **20.5** |
| B-type | 9 ppm to 52 ppm | 0.38 | 0.8 |
| C-type | 20 ppm to 93 ppm | **0.74** | 4.5 |
| $C_m$-type | 19 ppm to 68 ppm | **0.99** | 4.5 |
| Grey Granite | 34 ppm to 95 ppm | 0.8 | 7.2 |
| Salem Granite | **323 ppm to 911 ppm** | 0.44 | **48** |

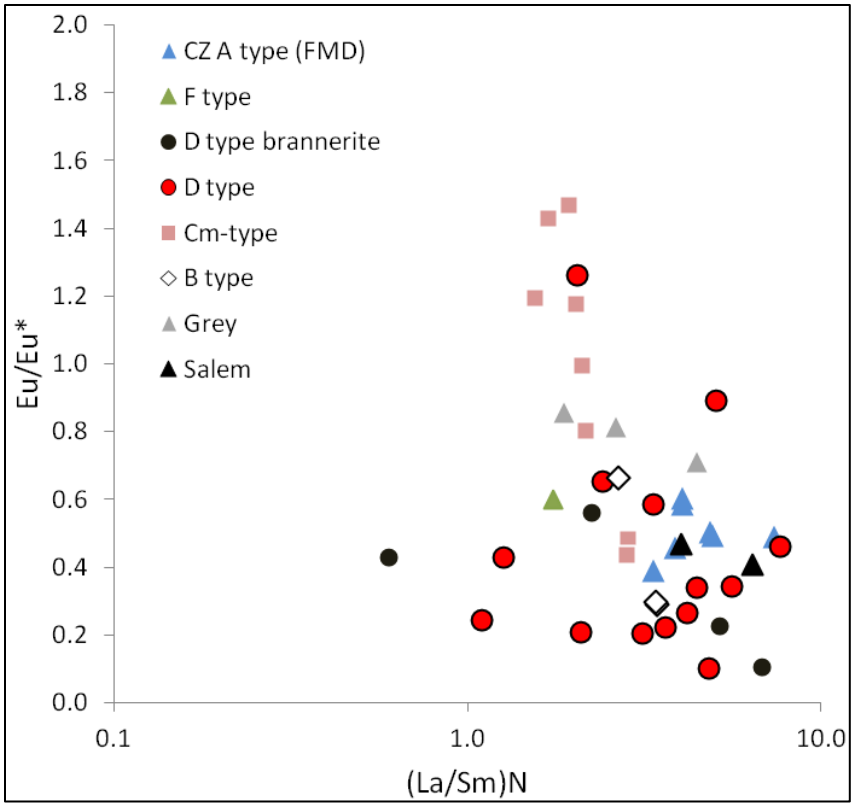



Figure 6.19 La/Sm vs. Eu/Eu* of the CZ granites and SLGs. The uraniferous alaskites have strongly negative Eu anomalies, as do the Salem type diorites at Valencia (this study); and the A type Sorris-Sorris, Dachsberg, and Horebis River granites (data from McDermott *et al.*, 2000). The strong negative Eu (Eu/Eu*) is indicative of a plagioclase-bearing source in which Eu is in a similar oxidation state to Ca, and is preferentially retained during partial melting.

The presence of fluorite in relative abundance in the mineralised samples (Chapter 4) which is observed in close association with the mineral brannerite in some of the Husab samples, often surrounding the brannerite as a late-stage vein. The nature of fluorite is probably a combination of a co-genetic and entrained component, where late-stage veins crystallise from $F^-$-bearing residual magmatic fluids, and entrained fluorite is hosted in biotite. Bau and Dulski (1995) show that in fluorine-rich hydrothermal systems Y and Ho may fractionate, with a negative non-chondrite Y/Ho correlation with fluorite-precipitating hydrothermal fluids. Though there is little evidence of hydrothermal fluids, there is abundant evidence of magmatic-derived fluid alteration in the uraniferous granites, particularly those that host abundant brannerite. The mean Y/Ho of the granites at the uranium deposits of the Central Zone is 27.07 from forty analyses; all but one of the brannerite dominated samples plot below the mean and follow a negative trend with respect to increasing U abundance (Figure 6.20). There is considerably more scatter in the uraninite-coffinite dominated D-types, with some negative correlation with respect to increasing U. All of the Cm-type leucogranites

contrast and plot above the mean. The implications of this observation highlight the relationship between uranium mineralisation and fluorite veins. If Y/Ho is an indication of relative abundance of co-genetic fluorite veining in the crystallising granites, then the trends in Figure 6.20 serve to reiterate the role of F in the alaskite mineralisation model. The comparatively low Y/Ho in the most uraniferous samples suggests that F is more abundant in these samples.

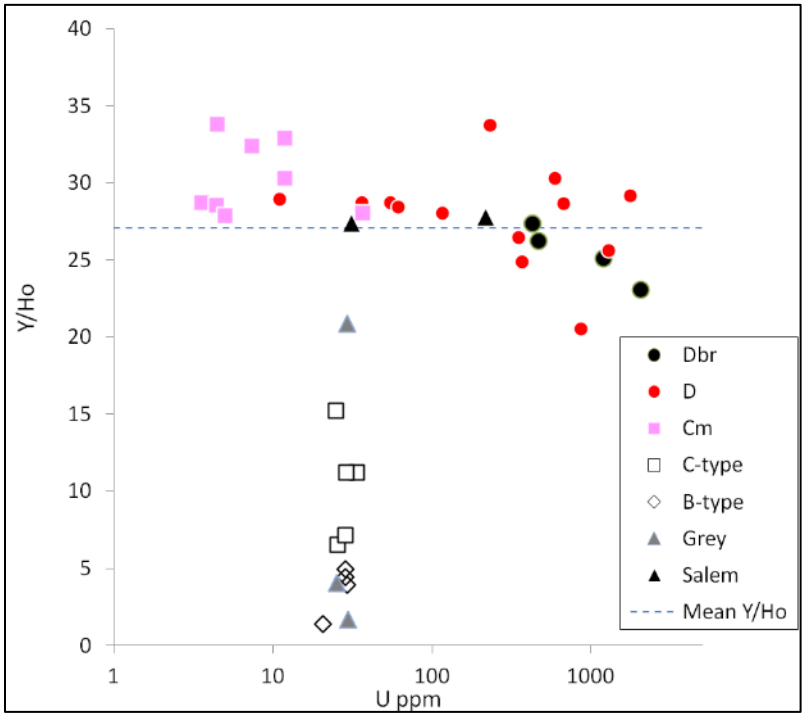



Figure 6.20 U in ppm vs. Non-chondritic Y/Ho of CZ granites. The Cm types plot above the mean for the sample group, while the D-type show considerable scatter, there appears to be a negative trend with respect to U. The brannerite-bearing samples ($D_{br}$) plot with a systematic negative Y/Ho relationship with respect to increasing U, with 3 of 4 samples below the mean. The Grey granites, B-type and the C-type SLGs are considerably different to the $C_m$ and D-type SLGs.

The uraniferous samples occur almost exclusively within the upper Khan Formation and throughout the pelitic and semi-pelitic units of the Rössing Succession. The uraniferous leucogranites plot with highly variable LREE enrichments and depletion relative to the HREE, a reflection of highly variable accessory mineral assemblages. The samples generally plot with -ve LREE slope and pronounced -ve Eu anomalies. HREE plot either as enriched, exceeding LREE content, or continue on a similar negative slope from Gd to Lu. The brannerite/betafite-bearing samples show a particular HREE enrichment relative to their LREE abundances.

The Goanikontes samples display both LREE and HREE enrichment with a strongly pronounced -ve Eu as shown in Tjimunee (2009). The Etango samples are considerably enriched in HREE compared to granites from all other deposits, with one of the samples being the only leucogranite with >100 ppm normalised HREE. The Ida Dome area samples plot with the lowest LREE concentrations of the uraniferous samples, at abundances comparable to the Khan- and Kuiseb Formation-hosted leucogranites. The Husab samples plot with variable LREE and HREE, the brannerite/betafite-bearing samples show a relative HREE enrichment. There is also a positive correlation between uranium content and REE abundance.

Petrographic observations identify abundant monazite, xenotime, apatite, and zircon in the uraniferous SLGs. Single-grain phosphates tend to be hosted between quartz and feldspars, while zircons occur as inclusions in biotite and in K-feldspar, as well as clustered grains in many of the observed samples. Clustered crystals of phosphate minerals and zircon were also observed fairly regularly within the quartz-feldspar matrix of the mineralised SLGs, and in enclaves of entrained mafic minerals (usually in SLGs that intruded skarns). The phosphates and zircons often displayed zonation, in the clusters, in single grains and in the inclusion-types. Clustered- and biotite inclusion-type phosphate mineral and zircon grains suggest that they were inherited, while singular grains in the quartz-feldspar matrix should be magmatic; the prominent zonation across the textural range suggests that even the matrix-hosted grains may be inherited, and that the history of these REE hosts is complex, and may explain the great ranges in REE abundances.

Two prominent REE patterns occur for the refractory mineral-bearing alaskite samples from Husab. The visibly hydrothermally altered and oxidised refractory mineral-bearing samples show LREE enrichment relative to HREE and pronounced -ve Eu. HREE follow a negative slope, and Y is consistently enriched relative to Lu. The more pristine D-type alaskites, those with much less visible signs of alteration, show less enriched LREE relative to HREE, similarly pronounced -ve Eu, and convex, enriched HREE curves, where Y<Lu. The difference may be ascribed to inherent differences in HREE host phase concentrations, and

also to differences in mobility/solubility between the HREE and LREE phases during alteration that tends to characterise the refractory U-mineral-bearing SLG samples.

Inconsistent HREE ratios across the SLG populations at the deposits may be a symptom of the variable uranium content; as is shown by Mercadier *et al.* (2011), HREE may approach 1 000 ppm in uraninite. Therefore, if uraninite is crystallising from magma and associated fluids, the REE abundances will reflect the REE fractionation of the silicate melt, given the capacity of uraninite to incorporate LREE and HREE without preference at temperatures above 350 °C. It is also plausible that some of monazite was in equilibrium with some of the melts considering the granulite facies conditions between 520 Ma and 510 Ma, resulting in relatively consistent LREE abundances and ratios. Alternatively, HREE hosts such as zircon and garnet may have been in more variable states of solubility, this is particularly true for garnet if there is a hydrous component to the melt, potentially explaining the less consistent HREE abundances and ratios. The relative abundances of accessory minerals contrast between the mineralised (post-$D_3$) and non-mineralised (pre-$D_3$) populations, reflecting a combination of the following:

- LREE were released into the uraniferous melt because temperatures were sufficient to dissolve monazite and other LREE hosts; and
- HREE are variably retained in the sources of the uraniferous and weakly mineralised leucogranites, with conditions suiting HREE mobilisation in the uraniferous melt.

The uraniferous sheets show the most consistent and pronounced -ve Eu, which indicates that there is some degree of fractionation during melt generation. This is the accepted mode of incompatible-enrichment in silicate melt systems, provided they are released from refractory phases in the source. The most likely repository of HREE in all samples are the garnet porphyroblasts in the B types, with xenotime, titanite, zircon, rutile and apatite as potential HREE hosts in other types. The HREE values may simply therefore reflect the variability of the accessory mineral abundances (Figure 6.16). The systematic relationship

between HREE and Y shows that xenotime (as the primary Y mineral) is also a dominant HREE host mineral.

### *Monazite Geochemistry*

The light rare earth elements show a strong systematic relationship in monazite, where all of the Valencia and Husab monazite analyses show a decrease from the most abundant element, Nd, through Ce, La and Pr. Forty-five EPMA analyses were performed on monazite crystals; one from the Etango deposit in the Goanikontes area, one from the Valencia deposit and three from Husab. Compositional zoning is not apparent in BSE imagery (Figure 6.21), and analyses confirm little difference between core and rim regions of the three Husab specimens.

The ratios of Nd : Ce : La : Pr are comparable as follows where Nd is normalised to 1:

- 1 : 0.78 : 0.57 : 0.009 for Husab monazite, and
- 1 - 0.71 - 0.45 - 0.009 for Valencia monazite.

The two samples from each deposit are therefore of comparable provenance. LREE (Ce,La,Pr,Nd) in the Husab monazites range between 53 wt.% and 56 wt.% and ~44 wt.% in the Valencia sample, Pr and Nd data are not available for the Goanikontes sample. Nd is consistently enriched relative to the other REE, 20.6 wt.%- and 23.4 wt.% $Nd_2O_3$ for Valencia and Husab, respectively.

Ce and La ratios are different in the whole rock when compared to those in the few monazite analyses by EPMA. Whole rock Ce:La = 2.1:1 (Chapter 5, Figure 5.36) and in monazite from the nine analyses (3 analysis points on 3 specimens) gives Ce:La = 1.39:1. Comparison of core and rim Ce/La shows that Ce is not mobile from some monazite. However, the high Ce/La in the whole rock would suggest that Ce is hosted in other accessory phases. Appendix E14 contains a table of monazite analyses.

Figure 6.22 illustrates the compositional variation on a binary plot of Ca + Th vs REE. The U content in the monazite is typically low in the Husab and Valencia monazite, <1 wt.% $UO_2$ and ~1.4 wt.% $UO_2$, respectively. U in the Goanikontes specimen is considerably enriched at ~6 wt.%. Systematic substitution for LREE by Ca and Th is evident in the molecular abundances in Figure 6.23

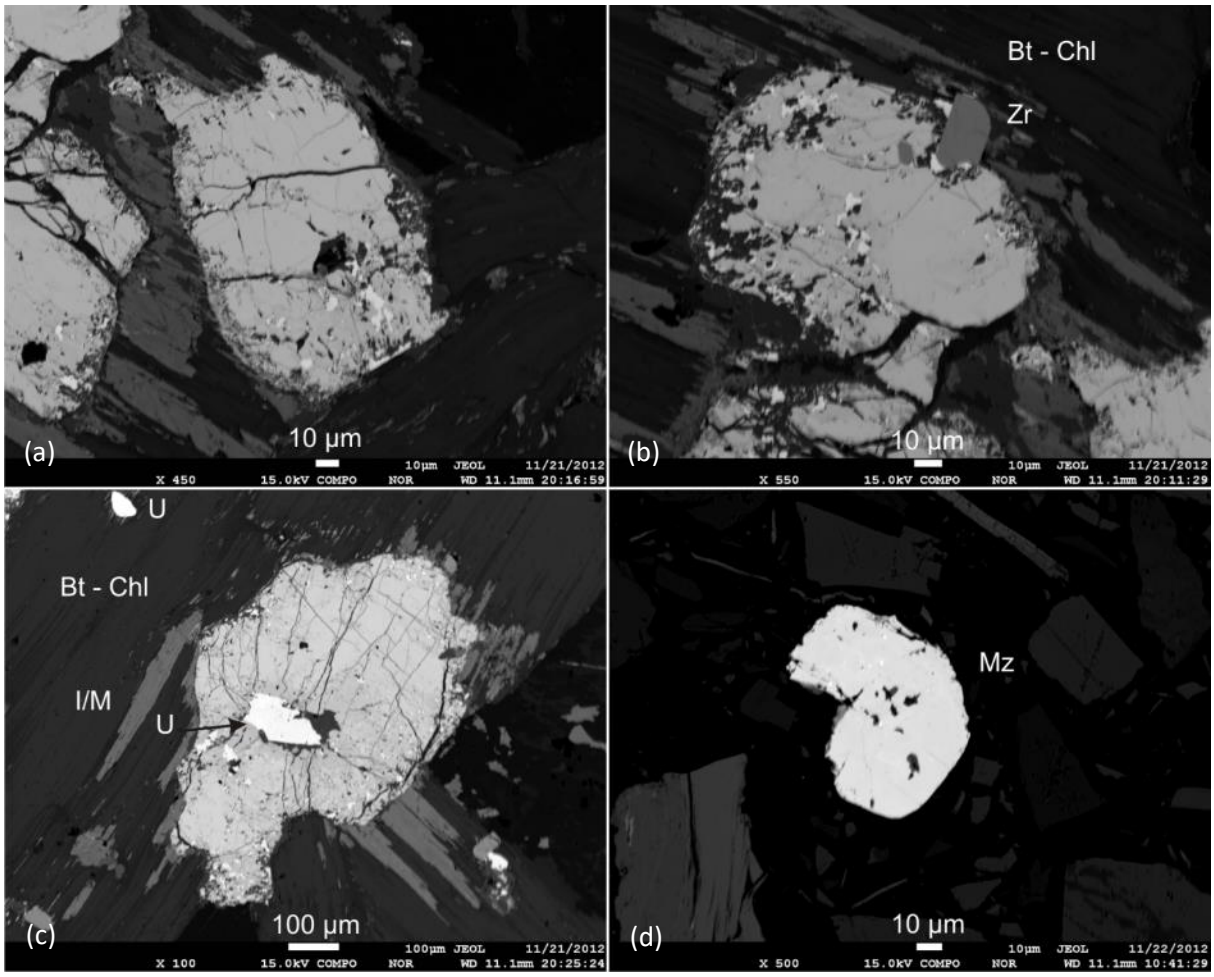



Figure 6.21 Monazite specimens in backscatter imagery. (a) Monazite # 4 from Husab core sample RDD373 125 m; the sample shows alteration toward the rim and is hosted in biotite with a zircon inclusion. (b) Monazite #4B from the same Husab core sample, note the bright inclusion of a U-Ti phase (assumed to be brannerite) indicating later crystallisation of the particular monazite. The monazite is hosted in a cluster of biotite-chlorite (Bt-Chl), and is compound with a fine-grained zircon (Zr). (c) The embayed edges and prominent fracturing suggest mobile elements may have been lost to alteration from the sample. The monazite hosts uraninite (U) and occurs at the junction of perpendicular biotite-chlorite (Bt-Chl) books that also host uraninite inclusions (U). Typical magnetite and or ilmenite is exsolved from biotite as a product of propylitic alteration to chlorite. (d) Monazite compound grain from a Valencia deposit heavy mineral separate, Va26 141-290 m. The BSE image is of relatively low resolution but the grain does not appear to have prominent zoning.

The monazite populations of the CZ alaskites plot in the Th-rich monazite field of Ward *et al*., (1992); where the Valencia specimen analyses exhibit particular Th enrichment and Ca replacement patterns (Figure 6.23). The Valencia sample has the highest Ca and Th abundances with the substitution approaching 50 % of the LREE content. There is very little difference between the core and rims of most Husab samples, except in sample monazite 10 which shows more fractures than the other Husab monazite specimens, potentially losing Ce to the alteration environment (Figure 6.21).

Normative Ce-Nd-La plots cluster tightly but close inspection shows a consistent Nd enrichment in the Valencia specimen over the Husab population (Figure 6.24). A normative molar plot of Y-Th-Ce with fields of Gratz and Heinrich (1997) suggest relatively low temperature monazite. The metamorphic history of the Central Zone is complex though, and monazite analyses by Longridge (2012) for example shows that monazite underwent resetting sometime after peak metamorphism.

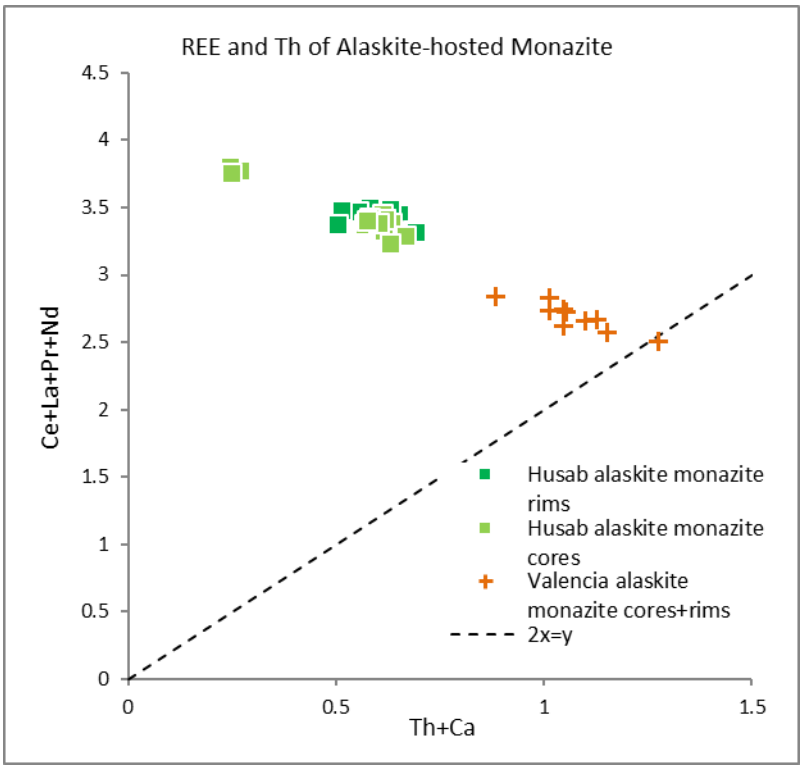



Figure 6.22 Compositional variation of monazite from Valencia and Husab. Th and Ca abundances increase systematically at the expense of the detected LREE. This relationship is not easy to explain, but may simply imply preferential REE retention in the melt or melt source relative to Th.

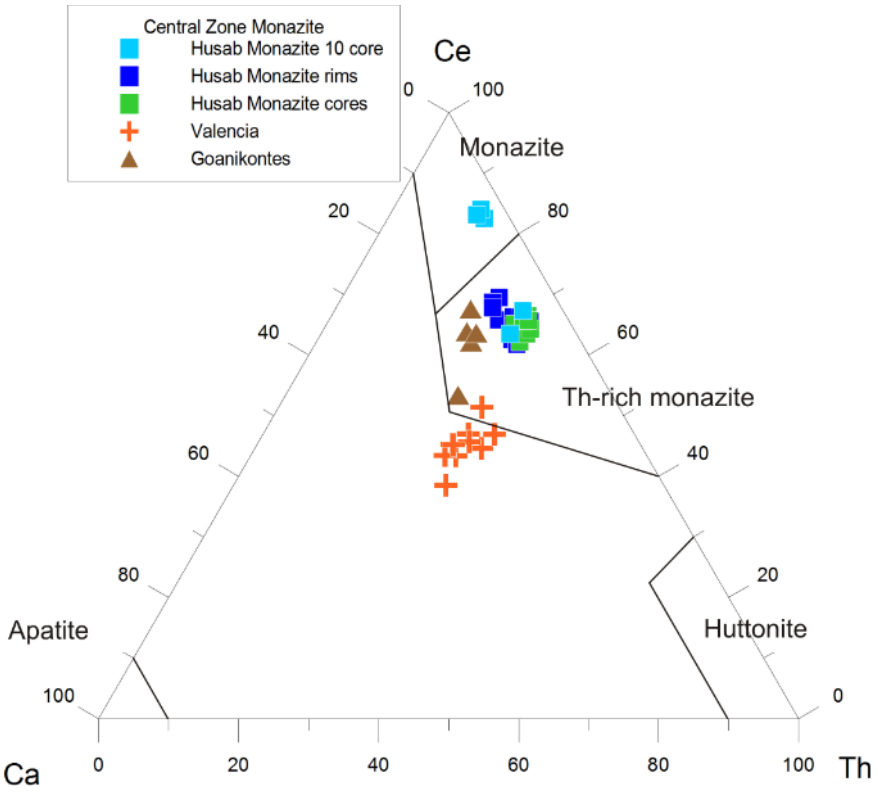



Figure 6.23 Ce-Ca-Th ternary plot of CZ monazite. Ternary compositional plot with fields of Ward *et al*. (1992) place the alaskite-hosted monazite in the high-Th field, which also supports an REE retention hypothesis.

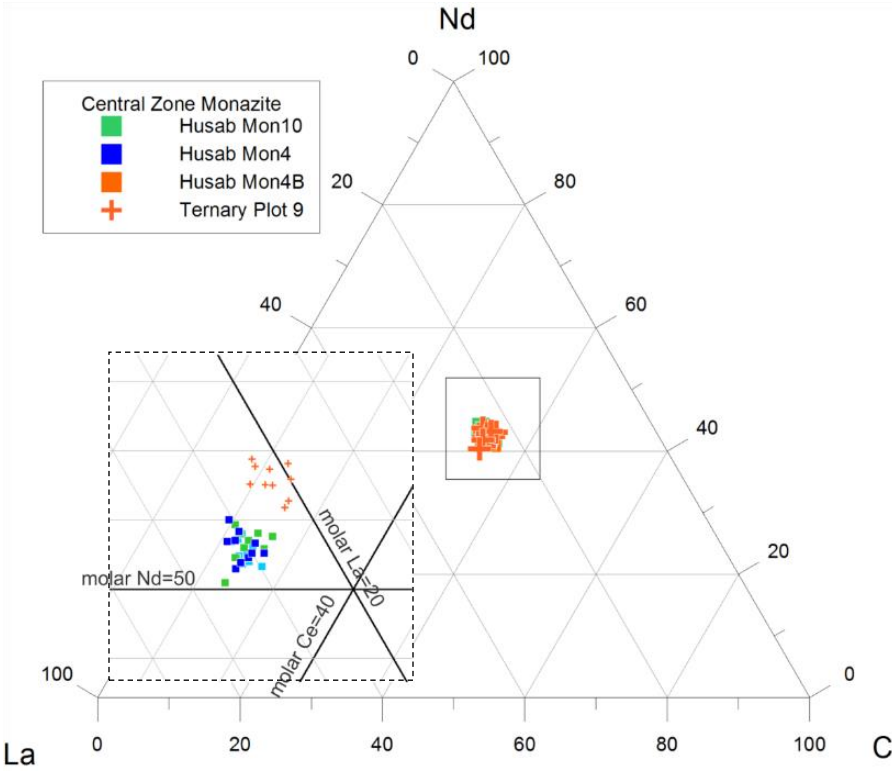



Figure 6.24 Nd-Ce-La ratios of the Valencia and Husab monazite samples. The analyses cluster tightly, although the Valencia samples consistently plot with Nd-dominated REE abundance relative to Husab.

Although the Nd:Ce ratio in the monazite is not readily explained, the monazite is Nd-enriched relative to most monazite, which tends to be Ce-dominated. The relative enrichment of Th may be explained by the nature of the alaskite melt, which is likely to be the result of partial melt of a biotite-rich source, given the abundance of fluorite in the Husab alaskites for example. Watt (1995) explains how F-bearing melt would inhibit to a certain degree the partitioning of REE into monazite, if biotite is not available for F to partition into, a condition satisfied by the melt migration model (Jacob *et al*., 1986; Nex, 1997) generally accepted for the uraniferous alaskites. Implying simply that Ce is lost to the alteration environment is difficult to explain with the most Ce-enriched monazite being monazite #10 from Husab also being the most fractured and thus susceptible to alteration effects (Figure 6.25).

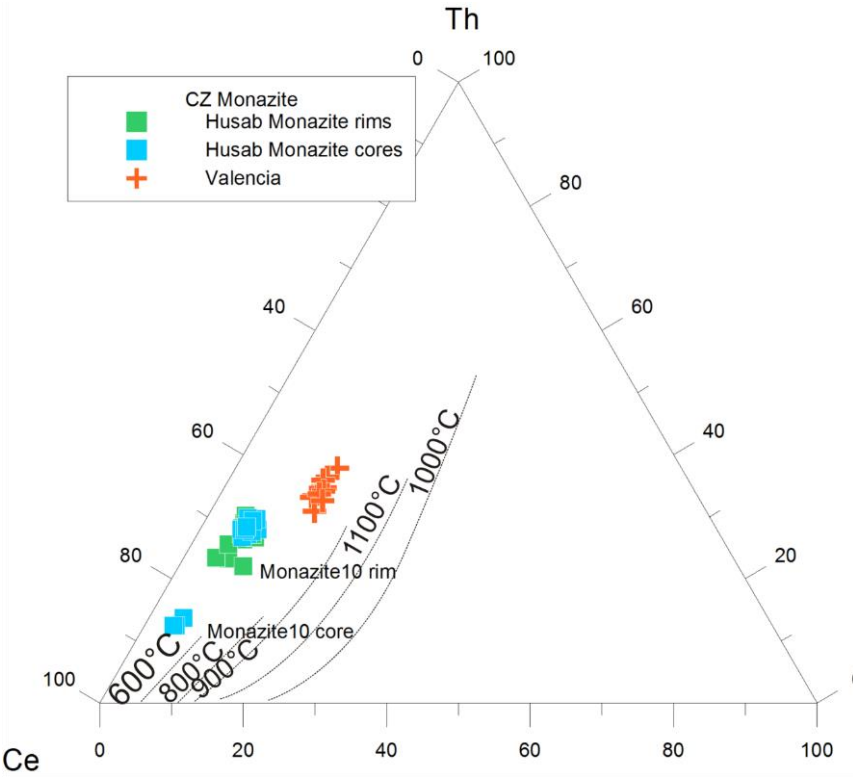



Figure 6.25 Monazite compositions on a ternary diagram of Y-Th-Ce with temperature fields of Gratz and Heinrich (1997). The plots imply comparable T to the peak metamorphic conditions that are widely accepted during alas kite emplacement (e.g. Longridge, 2012; Longridge *et al*., 2014).

## 6.8 Summary of The REE Trends of The Central Zone Uranium Deposits

- The Holland's Dome Grey granites are REE depleted in comparison to the other pre-leucogranite granites such as the diorite at Hildenhof and the Salem granites at Valencia. The low concentration of REE in the B types suggests they are not representative of the primary melt and the prevalence of garnet reflects an Al - rich source of crustal material, as would be expected of a pelitic Damaran sediment source rock.
- Strong correlation between mineralised samples and La, Ce, Y is reflected in the relative abundance of monazite and xenotime, respectively. HREE enrichment reflects titanite, apatite, garnet, and zircon occurrence.
- Khan Formation-hosted samples have the lowest average REE concentrations.
- Mineralised Ida Dome samples are hosted by the Khan Formation, and also show lower REE content than comparable samples from other deposits.
- LREE show a negative slope in all samples from all areas.
- Husab alaskites appear to be depleted in REE relative to mineralised samples from other deposits.
- Husab brannerite/betafite– bearing samples are LREE and HREE enriched, relative to other Husab samples.
- Goanikontes U-enriched samples are HREE enriched relative to other deposits
- Valencia mineralised samples are LREE enriched and high HREE corresponds positively with Zr and U.
- Valencia D sheeted leucogranites show shallow negative HREE slope with Y>Lu
- High grade (>1 200 ppm U) samples at the Ida Dome area show convex, enriched HREE curves with consistent Lu>Y.

The REE abundances, relative enrichments of HREE and LREE are effective geochemical tools for discrimination between uraniferous and pre-$D_3$ leucogranites. Simple quantification of the degree of REE-fractionation by Eu anomaly shows that the pre- and post-$D_3$ SLGs are derived from sources where partial melt is at a lower percentage for the uraniferous leucogranites. Whether the LREE/HREE fractionation is a function of the partial melt, or of

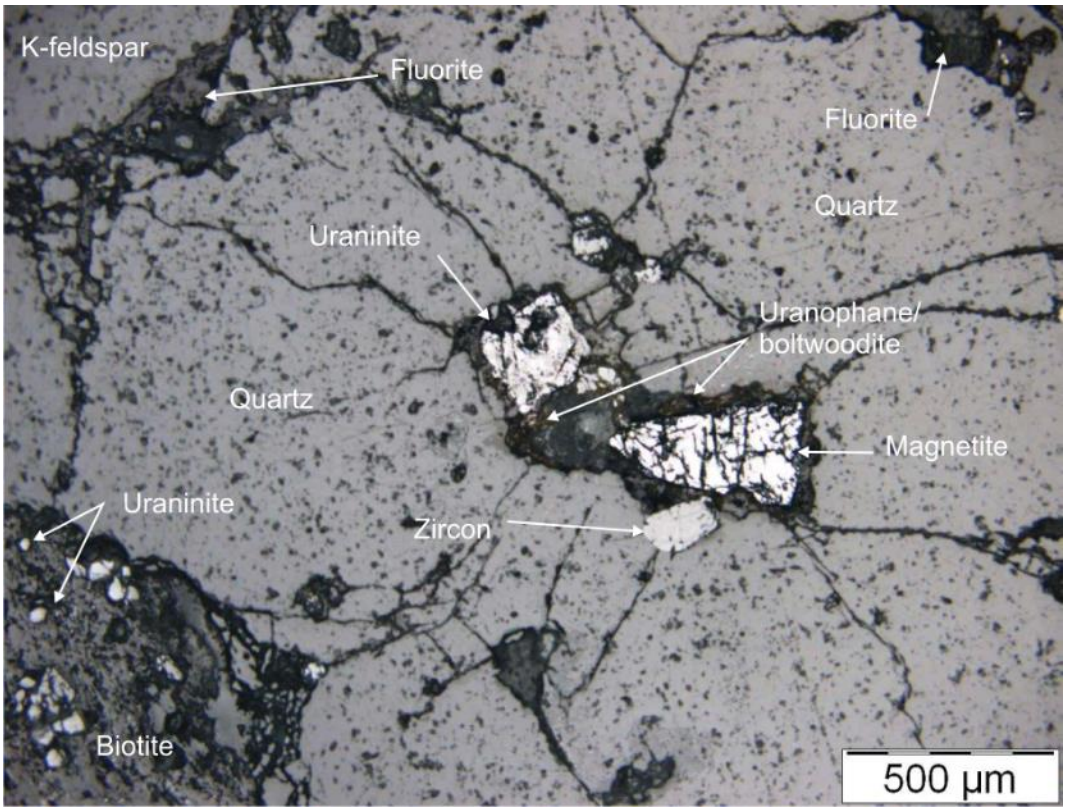
fractionation during melt migration is not constrained at this stage. However, the degree of REE fractionation in the uraniferous varieties is considerably greater than in the pre-$D_3$ leucogranites. It may be argued that the greatest REE fractionation is in the brannerite-bearing alaskites, which seems acceptable considering the strong partitioning of Y and REE content of brannerite and betafite.

The uraniferous leucogranites predominantly plot with steep -ve REE curves, with overall low abundances. Exceptions to this trend are located at Goanikontes and at the Ida Dome area (Ida Central and Garnet Valley). Typically, a steeply -ve curve indicates that phases such as garnet are in equilibrium with the partial melt and remain as residual phases. The enriched LREE abundances in some uraniferous samples are indicative of the incompatibility contrast that exists between the light and heavy lanthanides. All of the other leucogranite varieties are less enriched in REE than the mineralised granites, which suggest that melt-forming conditions of these granites did not liberate LREE from monazite at source if they are derived from similar sources, or that the granites have entrained, and possibly assimilated garnet. The lower abundances in the pre-$D_3$ granites may also support a model where the two pre- and post-$D_3$ populations are from different sources. Samples with peritectic garnet show HREE enrichment relative to LREE, but the abundances are not comparable to those in the uraniferous examples. The abundance of phosphate may be directly related to the amount of reaction with wall rock and associate fluids during deposit formation, and thus U concentration corresponds positively with REE abundance at all deposits. The low LREE and comparably more enriched HREE in the Ida samples suggests lower abundance of phosphate minerals and HREE is hosted in phases such as zircon and garnet rather than xenotime. Titanite-magnetite-diopside skarns are abundant at the Khan-Rössing transition at the Ida Dome, and are also noted at Goanikontes and Valencia. The skarns, and similar lithologies, host anomalous phosphate relative to the other country rocks and interaction between these and the magma and associated fluids could contribute varying LREE and Y to the uraniferous leucogranites.

Chapter 7 presents the findings of semi-quantitative ore mineralogical studies by the QEMSCAN method.

.

# CHAPTER 7 URANIUM MINERALISATION AND URANIUM MINERALOGY OF THE PRIMARY DEPOSITS




Primary uraninite is cubic and has formed within a quartz cluster with magnetite and zircon (centre). Later uraninite has formed within the cleavage planes of hydrothermally altered biotite. Residual magmatic fluids have permeated along mineral grain boundaries and deposited fluorite. The alteration has replaced uraninite and magnetite with secondary U-silicates, uranophane and boltwoodite, and Fe hydroxides.

## 7.1 Introduction

Large low-grade uranium deposits characterise the Central Zone, in which petrographic investigation suggests the dominant primary uranium mineral is uraninite, certainly Rössing uranium mine reports uraninite as the dominant primary phase in much of the SJ deposit, in studies conducted prior to mining (e.g. Hiemstra *et al*. 1968, Berning *et al*., 1976, von Backström and Jacob, 1978). The map segment in Figure 7.1 shows the locations of the deposits that provided the mineralogical samples for this study.

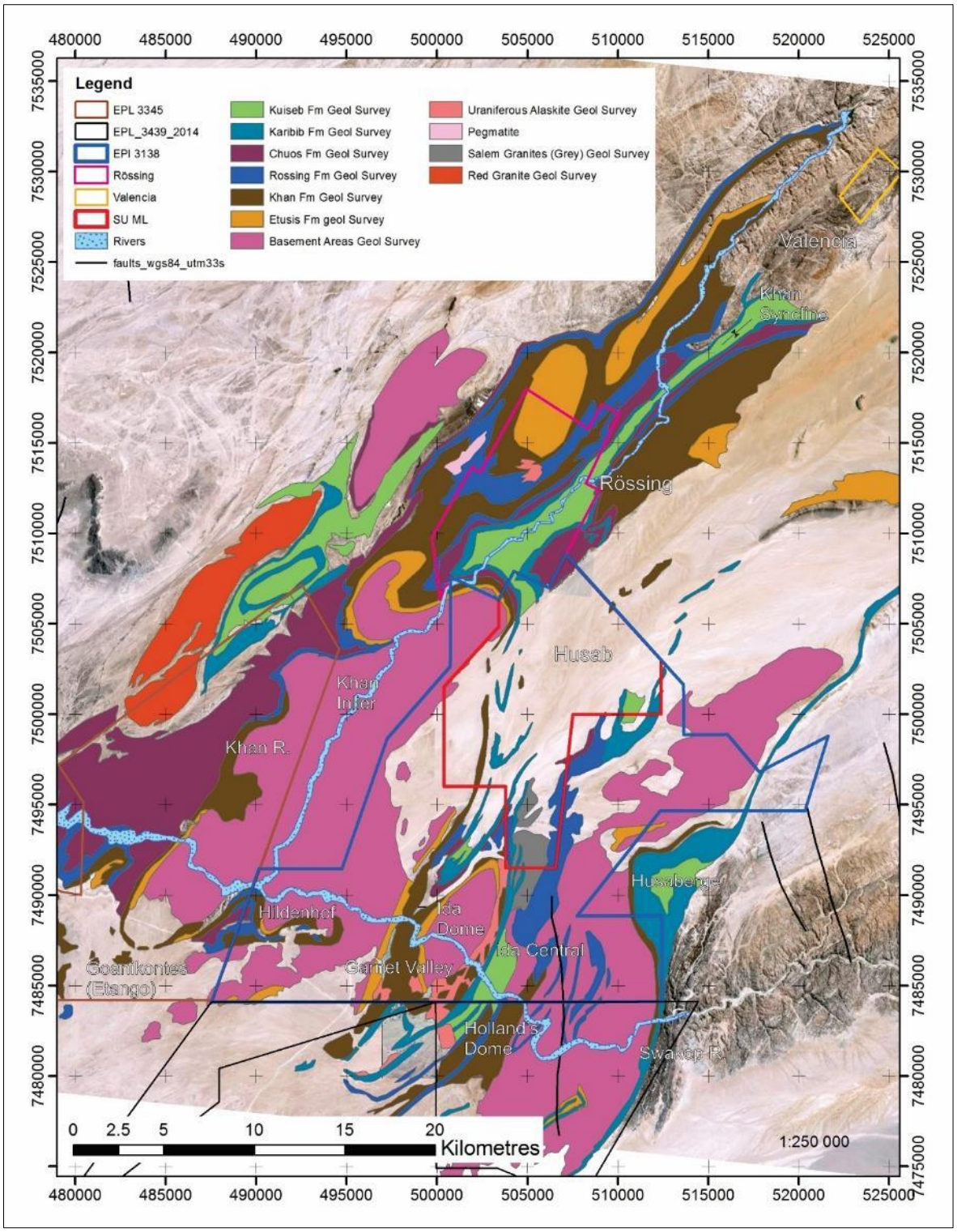



Figure 7.1 Summary map of the Central Zone geology and locations of the study areas. Goanikontes and Hildenhof samples sourced from EPL3345 of Bannerman Resources; Ida Dome area samples sourced from the Ida Central and Holland's Dome deposits of Swakop Uranium; the Husab samples are from the Husab Mine, also Swakop Uranium; and the Valencia samples are from the Valencia mine project of Norassa Namibia. The red, green, and orange polygons delineate the uranium mining licence areas of Husab (red) Rössing (green) and Valencia (orange).

The primary uranium deposits within the Central Zone are also expected to contain predominantly uraninite-hosted uranium. However, the presence of significant proportions of the pyrochlore mineral betafite and to a lesser extent brannerite (a complex Ti-Ca-U oxide) in deposits that surround the Rössing Mine are cause for concern. These two minerals behave as refractories in conventional acid leach processing, thus rendering the deposits complicated to exploit economically. The nature and abundances of the refractory minerals at Rössing are discussed in detail in Cuney (1980a, 1980b), Herd (1996), Nex *et al.* (2003), and Abraham (2009).

Given the potential for refractory mineral-hosted uranium mineralisation, the deposits in the surrounding Central Zone were studied during the 2008 and 2010 period, where samples selected by the prospect owners and in this study, were the subjects of petrographic, geochemical, and mineralogy studies by automated scanning electron microscope studies (QEMSCAN). The primary aim of these studies was to establish if there is sufficient uranium deportment in refractory minerals to warrant further investigation.

### *Previous Uranium-Bearing Mineral Studies in The Central Zone*

Hiemstra (1968) and Hiemstra *et al.* (1968) conducted detailed mineralogical investigations of the Rössing deposit ores, which included uranium mineral compositional analysis by microprobe. Since then, Herd (1996) and Nex *et al.* (2003) presented detailed mineralogical analyses on betafite from the Rössing Mine's SH area, including compositional analyses of betafite and pyrochlore specimens. A limited amount of mineral deportment investigations by Freemantle (2006); Kinnaird and Nex (2007) at the SJ Pit; and Abraham (2009) at the SK deposit, assessed the mineral population statistics and place the findings into geological context, but do not include mineral composition analysis at Rössing. Townend (2009) identified boltwoodite, $HK(UO_2)(SiO_4).1.5H_2O$, as an abundant secondary U-phase at Husab.

Previous studies by Cuney (1980a, 1980b); Nex *et al*. (2003); Kyser and Cuney (2008) suggest that uranium mineral speciation is strongly controlled by the REDOX conditions in the melt and fluid phase, derived primarily from variation in local metasedimentary composition. The relationship between magmatic fluid and $CO_2$ and Na concentration is described as a possible control on melt temperature and $fO_2$ mechanisms which directly

influences the local U speciation. The role of soluble and insoluble iron concentrations in the melt and host metasediment is however, a topic that requires further investigation. It is therefore important to understand the controls of such mineral formation with consideration of the composition of the local, reactive metasediments.

Comparatively little work has been undertaken on uranium deportment statistics outside of the Rössing Mine area; This chapter thus, aims to focus on the distribution of U-bearing refractory minerals with the intent of identifying any areas that should be of concern to potential uranium-producing companies.

Swakop Uranium identified the refractory phase brannerite at the Husab Deposit in early 2009, when 'oxidised facies' ore samples from ~64 m to 125 m below surface were sent for leach test work and returned poor results. A confidential report compiled by SGS, Australia, highlighted U-recovery results as low as 61 % in isolated samples. Follow-up mineralogical studies by semi-automated SEM (QEMSCAN) confirmed that the main refractory phase in the Husab samples is in fact brannerite, a marked contrast to the betafite-dominated ores near the Rössing uranium mine. Subsequently, brannerite has been reported in localised occurrences throughout the two main deposits at Zone 1 and Zone 2, hosting up to 47 wt.% of U-oxide in given samples of 1- to 10-metre drill core composites. The distribution and abundance of brannerite appears to be minor with respect to the deposit as a whole but remains an important geological consideration. Most of the brannerite-bearing ore samples occur within 30 m to 100 m of the Rössing - Chuos Formation contact, essentially within the upper Rössing[45] succession. There are however, eleven notable intersections identified throughout the two deposits; in which uranium deportment in brannerite and betafite exceeds 15 wt. % of the measured metal budget. Previous investigations of refractory mineral distribution and uranium mineralisation are described for the northern sector of Husab Zone 1 in Johnson (2011). The refractory mineral deportment of U in the Husab samples ranges between 17 wt. % and 68 wt. % U in the analysed samples.

[45] Freemantle (2012) identified refractory bearing ore in an ~8 000 sample bottle roll leach test campaign, and shows the spatial distribution be largely related to the position of the intrusives within the upper Rössing succession.

### *Uranium in Refractory Minerals in the Central Zone*

Several minerals have been noted in the Central Zone, where uranium forms a significant component. These include, in addition to uraninite, coffinite, and uranophane as the major species, localised abundances of betafite and pyrochlore variants, davidite, brannerite, and leucoxene (Cuney, 1980; Herd, 1996; Nex *et al*., 2003; Freemantle, 2006; Abraham, 2009; Johnson, 2011).

Betafite is a rare mineral, although it can be locally abundant, as at the SH and SK deposits west and east of the main pit at Rössing, respectively. It typically has the formula $(Ca,REE,U)_2(Ti,Nb,Ta)_2O_6(OH)$ and may host up to 34 wt. % U, thus Namibian betafite has U in excess of REE (Herd, 1996 and Nex *et al.*, 2003).

Brannerite, commonly given as $(U^{4+},REE,Th,Ca)(Ti,Fe^{3+},Nb)_2(O,OH)_6$ may host 26- to 33 wt.% $UO_3$ and in addition, up to 10 wt. % $UO_2$, combined the U oxide mass proportion must be greater than $TiO_2$ (Hewitt *et al.*, 1957). Davidite $(Fe^{2+},REE,U,Ca,Zr,Th)_6(Ti,Fe^{3+},V,Cr)_{15}(O,OH)_{36}$, a complex Ti-Fe hydrated oxide may host up to 7.7 wt. % $UO_2$, but Whittle (1959) reports lower values for davidite hosted in pegmatites of between 1- and 3 wt. % which is probably also applicable to Central Zone examples.

Davidite is found in relative abundances with magnetite and ilmenite in pegmatite melts within gneissic blocks of the basement granite-gneiss rocks of the Abbabis Complex. Notable locations identified in this study are found along the Swakop River, and include the Ida Dome and the basement inlier between the Holland's Dome antiform and the upper Damara succession of the Husabberg.

All of the above minerals are refractory in conventional sulphuric acid leach extraction processes and thus, do not release uranium. So, if any of these minerals occur in abundance, without constraint on their distribution, then predictable or expected uranium recoveries may prove challenging in the ore processing environment.

## 7.2 Uranium Mineral Speciation and Deportment Study - QEMSCAN

Uranium mineral deportment assessments are important in project exploration, evaluation, and feasibility studies. Although betafite and brannerite are comparatively rare in the Central Zone with respect to uraninite, in areas of marginal ore grades it is vital to be able to accurately estimate the U-extraction potential of a given target. This is because the uranium-bearing refractory minerals are locally, and potentially predictably, abundant. The understanding of controls on the distribution of refractory minerals will in future play a role in mine planning activities as lower prices for uranium and competition from low-cost in-situ leach operations drives conventional open pit mining operations to greater levels of efficiency. A key objective in this regard is to quantify the relative abundances of primary and secondary uranium mineral species. Table 7.1 summarises the QEMSCAN sample collection of this Central Zone study. Appendix F1 gives an abridged history and description of the QEMSCAN system and Appendix F2 gives a list of sample distributions for this study. The QEMSCAN is an automated, high-speed, scanning electron microscope which generates micron-resolution bitmap images of ore minerals and associated gangue phases. Each pixel in the bitmaps represents an analysis point of roughly 1 $\mu m^2$. These data from the bitmap analyses are processed to produce semi-quantitative mineral statistics.

Relative uranium mineral proportions, the uranium deportment within the mineral population, mineral association, particle size distribution, and mineral liberation quantification are all reported to required specifications. Prepared samples typically consist of resin mounts of the prepared material, which are polished and carbon coated, as for scanning electron microscopy. Mineral speciation and deportment statistics, and gangue mineral associations are pertinent to this study primarily for processing concerns. It is important to consider that particle size distribution, mineral liberation and to a certain extent mineral associations may be a product of sample preparation, all samples are milled and sieved to a +90 µm - 125 µm size fractions, the fine portion were discarded and if a coarse fraction remained after 30 seconds of milling it was recombined.

Table 7.1 Summary of QEMSCAN study samples and locations

| Deposit/Area | Surface Samples | Core Samples |
|---|---|---|
| Etango and Hildenhof - 5 samples | 1 at Etango, CZ-14-1; 1 x Hildenhof | 3 x 1/4 NQ core sections, Hole DH025 @ 43 m, 334 m, and 353 m. |
| Ida Dome - 5 samples | 1 at Ida Central, IDAG08; 1 Holland's Dome, IDAG43. | 3 x 1/4 NQ core sections; Hole HDD027 @ 89 m, 104 m, and 122 m. |
| Husab Zone 1 - 13 samples | | 13 x 1/4 NQ core sections, 8 Holes: **RDD004**, 154 m; **RDD008**, 284 m; **RDD060**, 289 m; **RDD078**, 360 m; **RDD141**, 244 m; **RDD145**, 413 m; **RDD219**, 336 m; **RDD373**, 64 m, 68 m, 93 m, 125 m, 155 m, and 159 m. |
| Husab Zone 2 - 9 samples | | 9 x 1/4 NQ core sections, 5 Holes: **RDD005**, 284 m (1 alaskite, 1 metasediment); **RDD006**, 119 m, 146 m, 171 m, 245 m; **RDD072**, 268 m; **RDD102**, 318 m; **RDD157**, 344m. |
| Valencia - 9 samples | 2 Samples; Goldfields test pit, VALG11; ~centre of the exposed ore body, VALG26. | 7 x core sections, 2 Holes: **Va26 113**, 81 m, 155 m, and 225 m; and **Va26 141** 259 m, 261 m, 290 m, and 301 m. |

The sampling and sample preparation process' are described in Appendix F3, and Appendix F4 summarises and tabulates the data validation and bulk mineral analyses statistics. This QEMSCAN study has two key objectives; firstly, to quantify the relative proportions of uranium minerals within the sample collection, and secondly to illustrate the main uranium mineral relationships in the alaskite, by means of digital mineral maps. Analyses were undertaken on specimens from the Etango deposit at Goanikontes, Hildenhof on EPL3345 (Bannerman Resources) the Husab deposits, the Ida Dome deposits, and the Valencia deposit. Location maps of the QEMSCAN surface samples and collar positions are given in the individual deposit subsections of this chapter.

## 7.3 QEMSCAN Results

The mineral maps in this thesis were generated over a period of 2.5 years, during which the SGS laboratory provided two colour codes and updated the reference mineral database. A set of six samples were submitted to the CSIRO in Perth, Australia, who employ their own

colour scheme. Bar graphs in Figures 7.2 and 7.3 summarise mineral speciation and deportment statistics of all the Central Zone samples of this study. Deportment statistics of the QEMSCAN samples are given in Appendix F5 and detailed summaries of the sample sets from each deposit are given in Appendix F6. A collection of all sampled material photographs is in Appendix F7 and QEMSCAN derived digital mineral maps are collated Appendix F7 and utilise the mineral keys in Figure 7.4. The QEMSCAN mineral maps illustrate important relationships between uranium phases and the rock-forming-, accessory-, and opaque minerals in each sample. Certain relationships appear to be unique to some sample areas while others are ubiquitous. Uraninite overall, has an affinity for Fe-Ti oxides, phyllosilicates, sulphides, and accessory silicates and phosphates. Mineral cleavage and fracture planes in feldspars host uraninite and secondary uranium silicates. Fractures in uraninite are defined by fine-grained coffinite and uranophane replacement, and fine-grained uranium minerals occur along internal feldspar mineral cleavages, as confirmed in thin section observations.

Table 7.2 Common abbreviations used in Chapter 7.

| | | | |
|---|---|---|---|
| EPMA | Electron Probe Micro Analyser | U | Uranium/uraninite |
| WDS | Wave-length Dispersive Spectra / Spectrometer | β-U | Beta-uranophane |
| QEMSCAN | Automated Quantitative Electron Microscope | Th | Thorium/thorite |
| HMS / HMC | Heavy Mineral Separate / Concentrate | M/Mg | Magnetite |
| TS | Thin Section | $U_{tot}$ | Weight percentage ($UO_2$+$UO_3$) |
| ppl | Plane polarised transmitted/reflected light | P | Phosphate |
| xpl | Crossed-polarisers transmitted/reflected light | Ti | Titanium/titanite |
| rfl | Reflected light | Bt | Biotite |
| HT / HP | Hydrothermal or High-Temperature / High-Pressure | Fl | Fluorite |

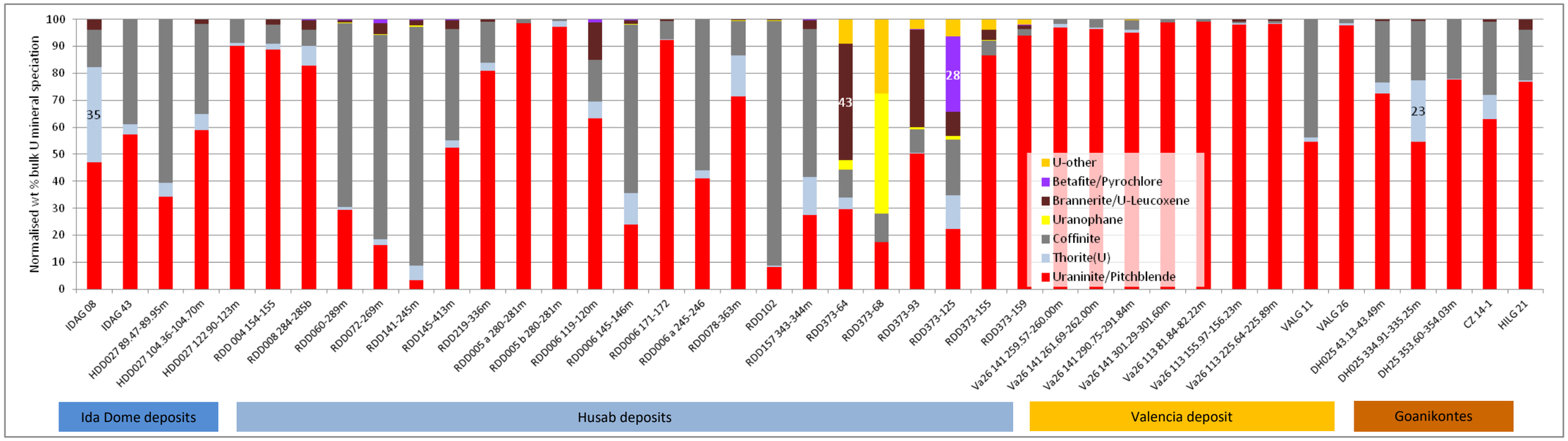



Figure 7.2 Uranium-mineral speciation charts of samples from the Central Zone primary uranium deposits. Uraninite is the dominant phase at most deposits. Thorite is present in all samples, as are coffinite and trace proportions of uranium-bearing refractory minerals (betafite and brannerite). Secondary uranium silicates (boltwoodite and uranophane) are not recorded in some analyses, thus their proportion is unknown, however, secondary U-silicates are always present in sample analyses that included secondary U calibration. In some sample analyses, the laboratory excluded coffinite/uranophane differentiation in speciation analyses, but discriminated between the two in the deportment calculations (The Goanikontes, Ida Dome and Valencia sample sets for example).

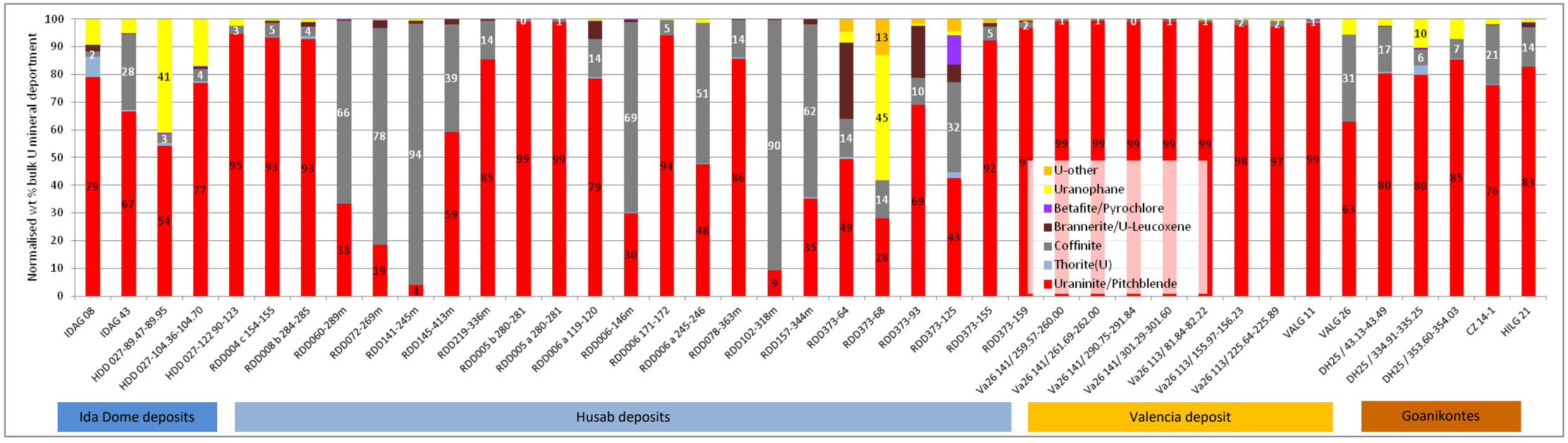



Figure 7.3 Uranium-mineral deportment statistics chart. Uranium dominates the deportment statistics in this Central Zone sample set. Uranophane occurs in shallow and deep downhole intersections at Ida Central and Goanikontes, but not in any significance at Valencia. High proportions of uranophane occurs in the supergene zone samples; at Husab (RDD373 64 m and 68 m) at Ida Central (HDD027 89.47-89.95 m) and in hydrothermally altered samples from depth at Goanikontes (DH025 334.91-335.25 m, and 353.60-354.03 m) Four of the Husab samples contain appreciable proportions of brannerite, with a single sample reporting >10 wt.% betafite.

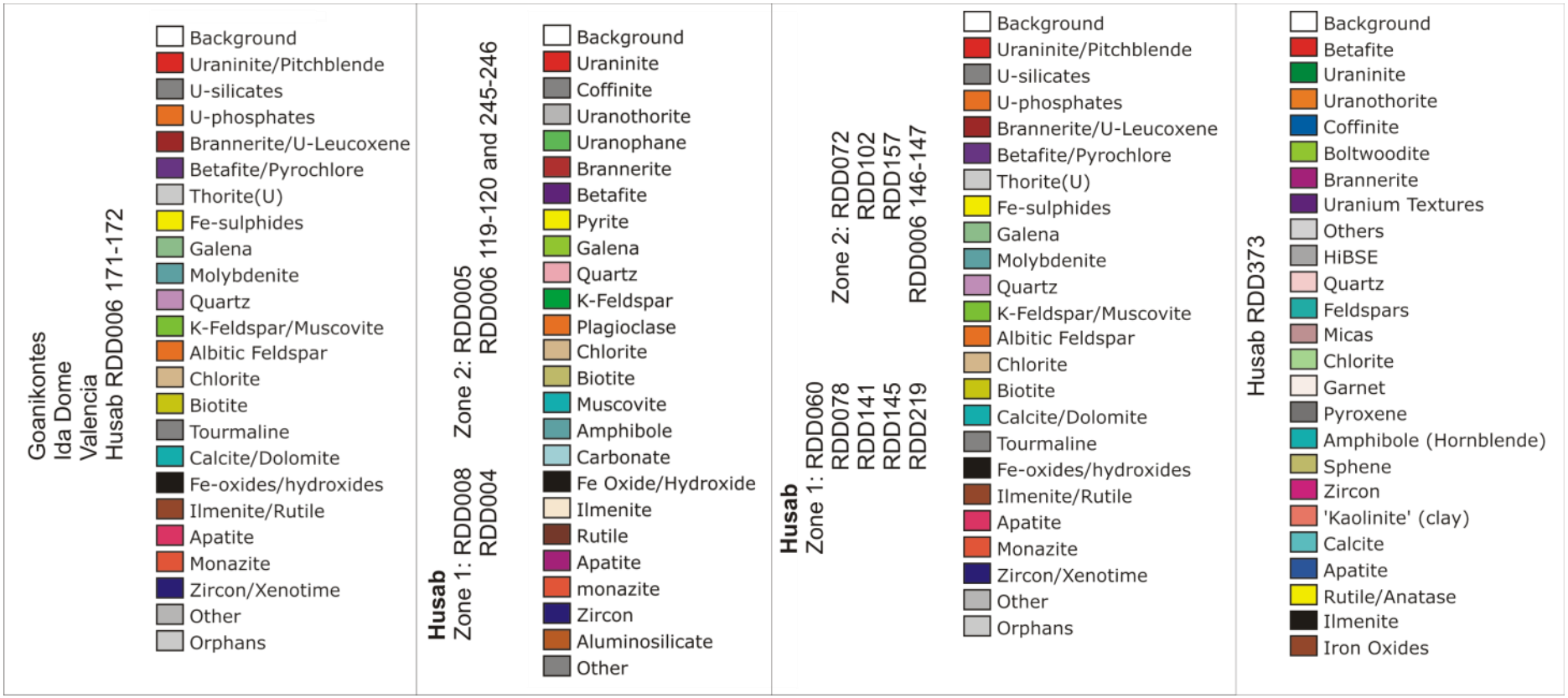



Figure 7.4 Key to mineral particle maps in the QEMSCAN section. The particle maps of the Goanikontes, Ida Dome, Valencia and Husab samples were generated by SGS in Johannesburg; and the particle maps for the RDD373 samples, from Husab, were produced at the Australian CSIRO in Perth.

## 7.4 QEMSCAN Mineral Maps of Central Zone Deposits

QEMSCAN-derived mineral maps presented in this section illustrate uranium mineral textures and relationships with quartz, feldspar, and mica phases of the host rock as well as key relationships with the accessory assemblages. The images show replacement uranium mineral trends which contribute to the individual deposit paragenesis interpretations. The following subsections highlight the key features that define the primary uranium mineralisation of the Central Zone deposits.

### *Goanikontes and Hildenhof Mineral Maps*

The Etango deposit on Farm Goanikontes is represented in three diamond drill core intervals of hole DH025, and a single surface sample, CZ14-1, from Rabbit Valley[46]. Surface sample HILG 21 sample comes from Hildenhof, on the Bannerman Resources license EPL3345. The surface samples represent oxidised leucogranites, the Rabbit Valley sample being a typical E-type, and the Hildenhof sample a pink-red, biotite-bearing pegmatite. Uranium deportment in uraninite is ≥80 wt.% in all the core samples from DH025 as well as in the Hildenhof surface sample, the Rabbit Valley E-type hosts 21 % U in coffinite, and 76 % U in uraninite.

The near-surface drill core sample, DH025 43.13-43.49, hosts two textures of uraninite; primary, euhedral uraninite which is relatively coarse (>200 µm) and late uraninite-calcite replacements of magnetite, with the calcite association and the vermicular texture suggesting mineralisation is associated with post deposition alteration (Figure 7.5).

Uranium deportment in coffinite exceeds ~15 wt.% in the surface samples and in the near surface core sample (DH025 43.13-43.49 m) but is significantly less abundant in the two samples from depth. Uranophane is detected in all samples, and is host to 10 wt.% of the U in DH025 334.91-335.25 m.

[46] Rabbit Valley is described in Nex (1997) and is a steeply incised creek bed flowing northward from the Namib peneplain to the Swakop River. The area is known for exposures of the E-type sheeted leucogranites.

Brannerite is detected in four of the samples, but only >1-wt.% of the U in the surface sample from Hildenhof. Betafite is not detected in any samples above 0.2 wt.% U deportment. It occurs as a minor constituent with uraninite, coffinite, and brannerite in complex replacements of ilmenite. The drill core samples are described as follows:

- DH025 43.13-43.49 m is from the near surface within the supergene alteration envelope (Figure 7.5);
- DH025 334.91-335.21 m (Figure 7.6) is of an E-type leucogranite with fine-grained haematite and other oxidised Fe-minerals throughout; and
- DH025 353.60-354.03 m, (Figure 7.6) represents a typical D-type sheeted leucogranite, with a secondary uranophane.

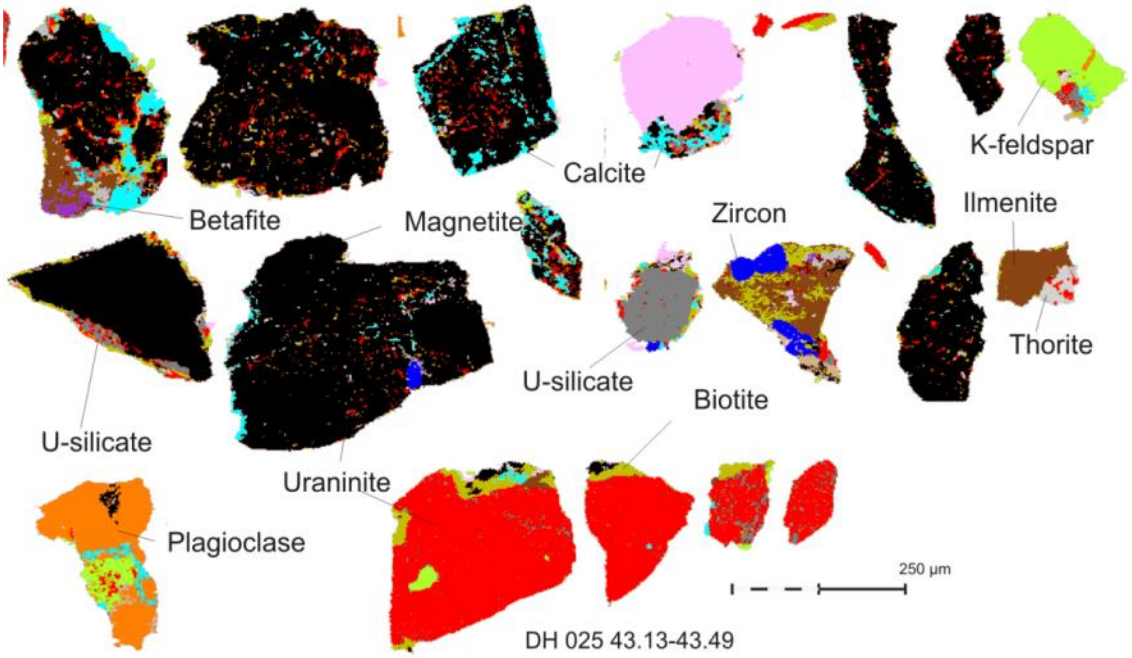



Figure 7.5 Mineral map features of DH025 43.13-43.49 from the Etango Deposit at Goanikontes. Note the coarse-grained, euhedral primary uraninite and fine-grained uraninite replacement of Fe-oxides. There are two textures; one of uraninite-calcite replacing the mobile Fe constituent of magnetite, the other of uraninite forming coatings with coffinite on magnetite surfaces.

The mineral maps of the samples from >300 m depth, also contain magnetite, but there are no examples of uraninite replacement or inclusions within magnetite, rather of uraninite

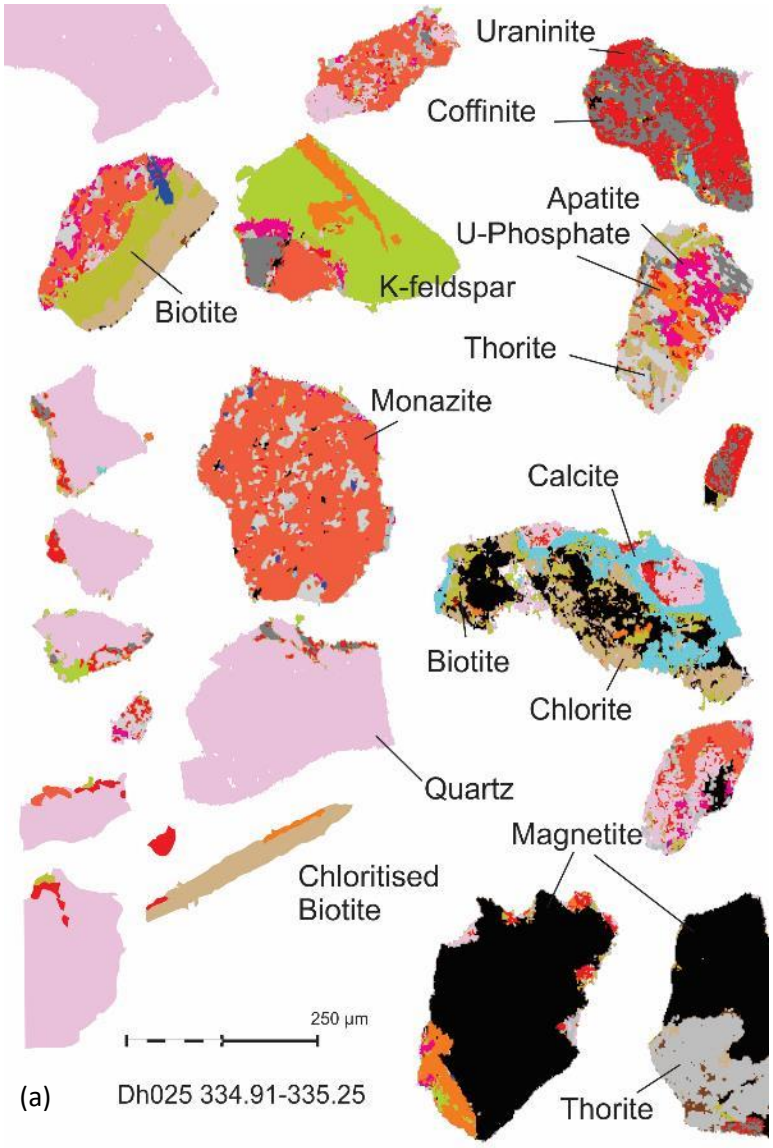
and coffinite adhered to Fe-oxide surfaces. This observation is in contrast to the observations of uraninite inclusions within magnetite in polished thin section.

Magnetite is a site for uranium crystallisation in the samples from depth; Figure 7.6(a) and (b) illustrate primary, euhedral magnetite with uraninite on the surfaces, and complex uraninite-quartz-biotite (chlorite)-calcite clusters. Fine-grained uraninite with coffinite has crystallised between quartz and feldspar and along biotite cleavages. The surface sample CZ14-1 illustrates a contrast in uraninite grain sizes and associated mineral populations.

There are three textural-mineral associations of uraninite; relatively fine uraninite-monazite, very fine grained <10 µm uraninite inclusions in primary rock-forming minerals (plagioclase) and fine-grained uraninite associated with Fe-Ti minerals, namely coarse euhedral magnetite and fine-grained anhedral ilmenite (Figure 7.7).

The QEMSCAN statistics show that over 75 wt. % of the CZ14-1 uraninite is within the <25 µm in size fraction. Prominent associations with fine-grained uraninite include; brannerite-betafite and magnetite-pyrite within chloritised biotite; and uraninite-betafite-brannerite-pyrite within- and attached to ilmenite/rutile[47].

[47] QEMSCAN does not distinguish ilmenite and rutile in the Goanikontes sample set analyses.



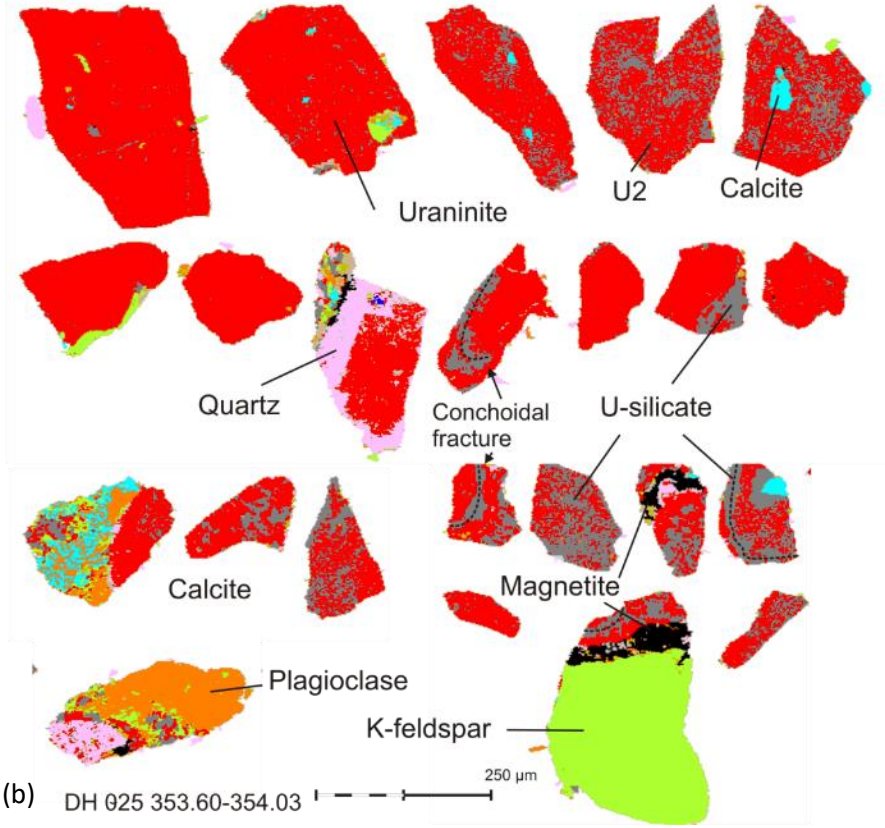




Figure 7.6 Mineral map of DH025 334.91-335.25 and DH025 353.60-354.03 from diamond hole 25 at the Etango deposit, Goanikontes. There are two contrasting styles of uranium mineralisation. (a) The 334.91 m sample contains uraninite as fine-grained inclusions in monazite, and as adhered components of euhedral magnetite. The sample also contains coarse uraninite, with variable coffinite replacement. (b) Uraninite is coarse and shows varying degree of replacement by coffinite. The coarse grains also show conchoidal fracture, along which coffinite is a replacement texture. Conchoidal fracture is typical of magmatic, crystalline uraninite. (Grain U2 is analysed by EPMA).

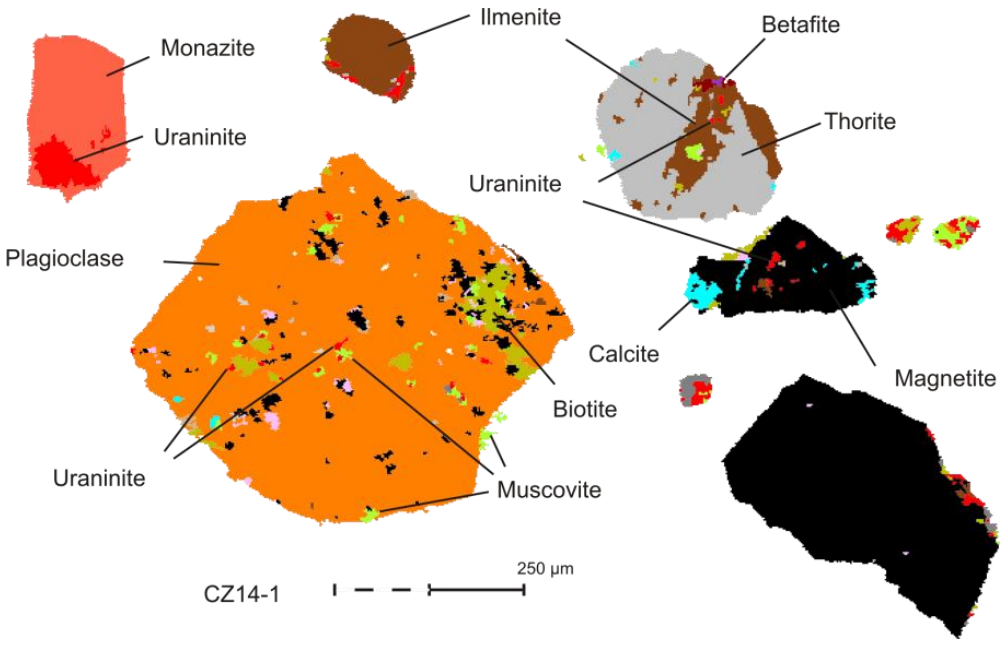



Figure 7.7 Mineral map features of CZ14-1, surface sample E-type from Rabbit Valley. Uraninite in the Ida Central sample is a secondary crystallisation phase that adheres to magnetite and ilmenite/rutile. It also occurs as large inclusions (or as compound grains) in euhedral monazite, and as fine inclusions associated with biotite and magnetite in plagioclase feldspars.

The mineral maps of the HILG21 sample in Figure 7.8 illustrate three uranium mineralisation styles: primary, euhedral uraninite, with coffinite replacement at edges and along fracture planes; uraninite-brannerite-magnetite precipitation along cleavage planes of chlorite (after biotite); and uraninite-coffinite-brannerite-betafite replacement in fractured ilmenite/rutile. Figure 7.9 illustrates the uranium deportment statistics for the Goanikontes-, and the Hildenhof samples. Key textural and mineralogical associations identified by QEMSCAN analyses of the Goanikontes and Hildenhof samples include:

- Coarse-grained (>100 µm) uraninite with variable proportions of uraninite replacement by coffinite, highlighting conchoidal fracture planes (DH025 353.60-354.03 m);
- Fine-grained uraninite inclusions in major and accessory elements (plagioclase and K-feldspar, quartz, biotite, magnetite, ilmenite, and monazite);
- Remobilised uraninite associated with brannerite-betafite occurs in biotite cleavages and within altered ilmenite;

- Uraninite-, calcite-, and coffinite- replace Fe-oxides in magnetite, and adhere to magnetite and ilmenite surfaces (DH025 43.13-43.94 m, and 353.60-354.03 m); and
- Thorite is coarse-grained, anhedral and is associated with magnetite and ilmenite.

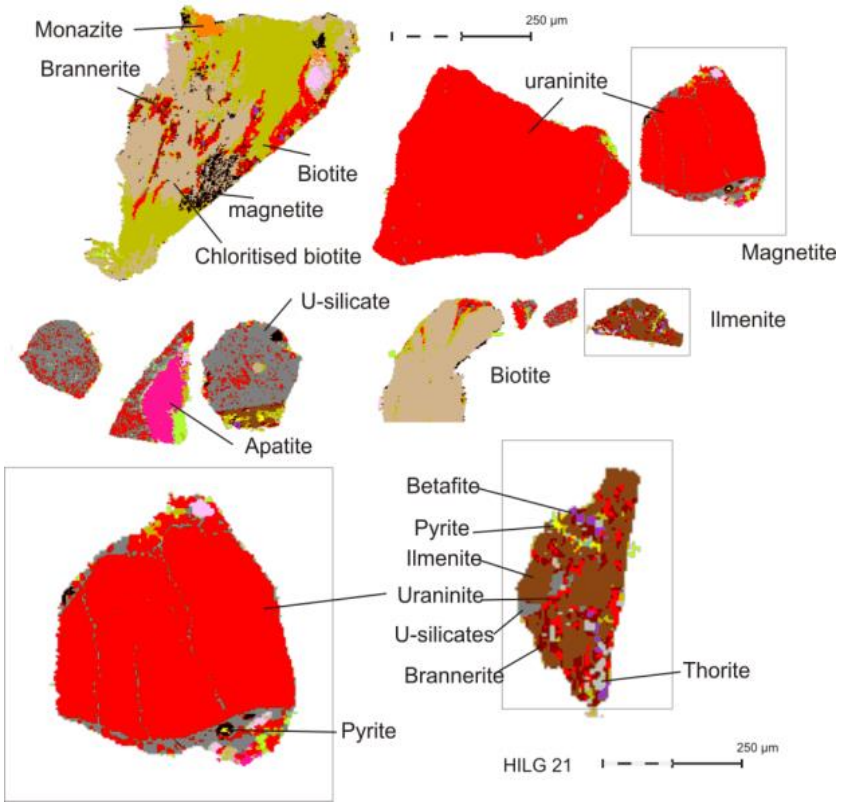



Figure 7.8 Mineral map features of HILG 21. Brannerite, betafite, uraninite and coffinite, and thorite deposit as secondary in rutile/ilmenite. Apatite is surrounded by uraninite-coffinite, indicating a secondary crystallisation around the phosphate. The sample shows primary uraninite in variable stages of coffinitisation, with some grains nearly completely altered to U-silicate.

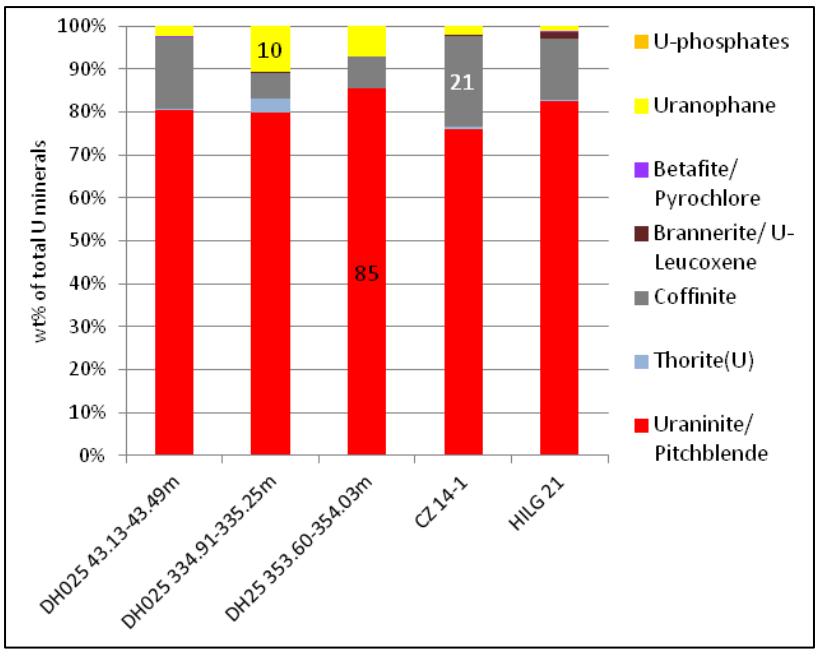



Figure 7.9 Uranium deportment statistics of Goanikontes and Hildenhof samples. Uraninite is the dominant mineral, followed by coffinite as the dominant secondary mineral in two of the core samples and both of the surface samples

### *Ida Dome Mineral Maps*

The Ida Dome area is represented by five mineralogical samples; three samples are collected in angled diamond drill hole HDD027 at Ida Central at 89 m, 104 m, and 122 m downhole; a single surface sample, IDAG08 at Ida Central; and one surface sample, IDAG 43, is from the Holland's Dome deposit.

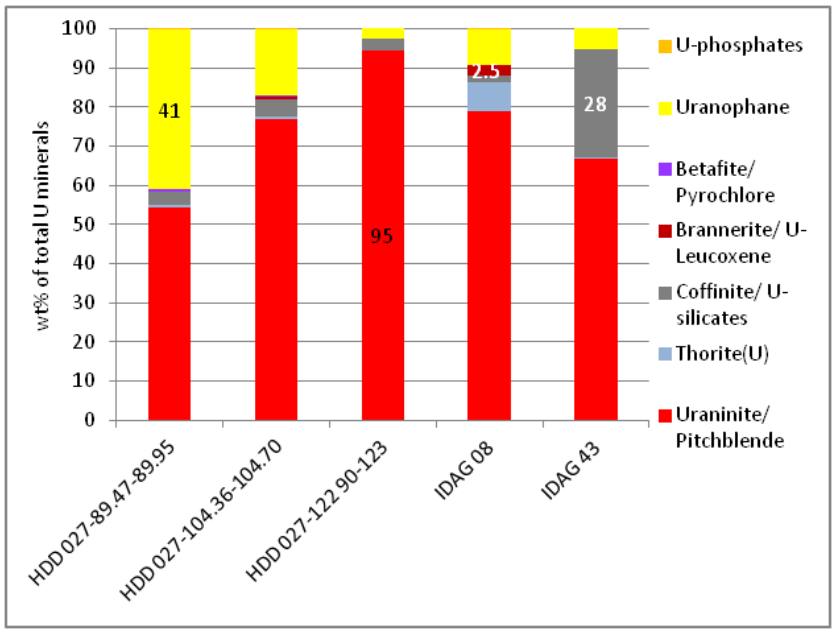



Figure 7.10 Uranium deportment of the Ida Dome QEMSCAN samples. The core samples show a systematic decrease of uranophane/ uraninite with depth. Brannerite is detected in the two deeper Ida Central core samples, and the surface sample (IDAG08) which hosts a maximum of 2.5 wt.% U. The compositions of uraninite-, coffinite-, and thorite are determined by EPMA analyses for samples from IDAG 43.

Uraninite is the dominant uranium mineral in the Ida Dome sample set. Coffinite is present in all samples and is subordinate to uranophane in all except IDAG 43. The uranium deportment statistics are presented in graphical form in

Figure 7.10. Uranophane hosts a significant proportion of uranium in the three samples from the Ida Central diamond drill core HDD027, with uraninite hosting ~55 wt.% to >90 wt.% of the uranium. The majority of uranium is in uraninite in the surface samples from Holland's Dome and Ida Central. Brannerite is the only uranium-bearing refractory mineral detected in the Ida Dome sample set and hosts a maximum of 2.5 wt. % of the uranium budget in the Ida Central sample. Results also show that for the Ida Central core samples the proportion of secondary uranium phases decreases with depth.

Surface and core samples host two generations of uraninite mineralisation: primary, magmatic uraninite, which is usually euhedral; and fine-grained uraninite-coffinite crystallisation along rock-forming- and accessory mineral surfaces and micro-fractures. Uranium minerals show some association with Fe-Ti oxides and biotite, where replacement type textures characterise the Fe-Ti mineral relationship and fine-grained uranium minerals occupy the spaces between mica sheets in biotite. The Fe-Ti association is particularly apparent in the surface samples. Plagioclase, K-feldspar, and zircon host sub-10 µm uraninite inclusions in all five QEMSCAN samples.

The core samples from Ida Central contain uraninite and coffinite predominantly as inclusions, while U-silicate coatings on quartz, feldspar, and Fe-oxide surfaces are not categorised, it is reasonable to assume that uranophane is dominant, given the statistics in Figure 7.10. U has also been deposited along mineral cleavages of biotite and feldspars. Free grains of uraninite show minimal alteration to coffinite, and are relatively fine-grained, with all visible grains <75 µm. Accessory minerals such as zircon, apatite and monazite host fine-grained uraninite-coffinite inclusions, while magnetite hosts U-minerals and has coatings or adhesions of uraninite-coffinite.

The mineral maps of HDD027 89.47-89.95 m (Figure 7.11a) show that uraninite occurs with U-silicates, either as a secondary phase, or as remnants within complete silicate-replacement. Plagioclase hosts inclusions of uraninite and biotite, surrounded by

alteration halos of muscovite (interpreted as sericite) and secondary magnetite, which permeated into fractures surrounding the uranium phase. Zircon is coarse-grained (>200 µm) anhedral and hosts inclusions of quartz and uraninite. The sample is the only specimen with coarse-grained pyrite, which hosts uraninite-coffinite on its surface (Figure 7.11a).

Fine-grained veins and coatings of uraninite-coffinite-Fe oxides are distributed along grain boundaries and along internal fractures of quartz and feldspars in HDD027 104.36-104.70 (Figure 7.11b). The textural relationships of feldspars in thin section show K-feldspar replaces plagioclase; in the mineral map Fe-U-Si minerals infill the cavities and fractures in the K-feldspar and the plagioclase, while the relationship with quartz appears to be more of a surface coating between coarse grains. Examples of euhedral uraninite are scarce; a single, 130 µm example of complete uraninite replacement by coffinite being the only free grain of any size (Figure 7.11b). HDD027 122.90-123.22 has the coarsest uraninite crystals of the Ida Central core samples; some are >50 µm in size. The grains are anhedral in shape and show little evidence of coffinitisation. The fine-grained uraninite occurs as cavity-fill in large altered feldspars and quartz (Figure 7.11c). The euhedral nature of some of the fine, <50 µm grains that occur with coarser anhedral specimens suggest at least two size distributions in addition to the fine-grained late uraninite.

There is an abundance of unattached, fine-grained (<20 µm) uraninite in all three of the core samples; these are interpreted as liberated fragments of uraninite coatings and fracture-fill, as well as being part of the brittle magmatic uraninite component. The fine-grained nature of the uraninite suggests that fluids were cooled too quickly to allow for coarse-grained crystal growth. The proportion of secondary uranium minerals (coffinite and uranophane) is clearly less abundant in the core sample from ~122 m depth, as reflected in the speciation and deportment statistics.

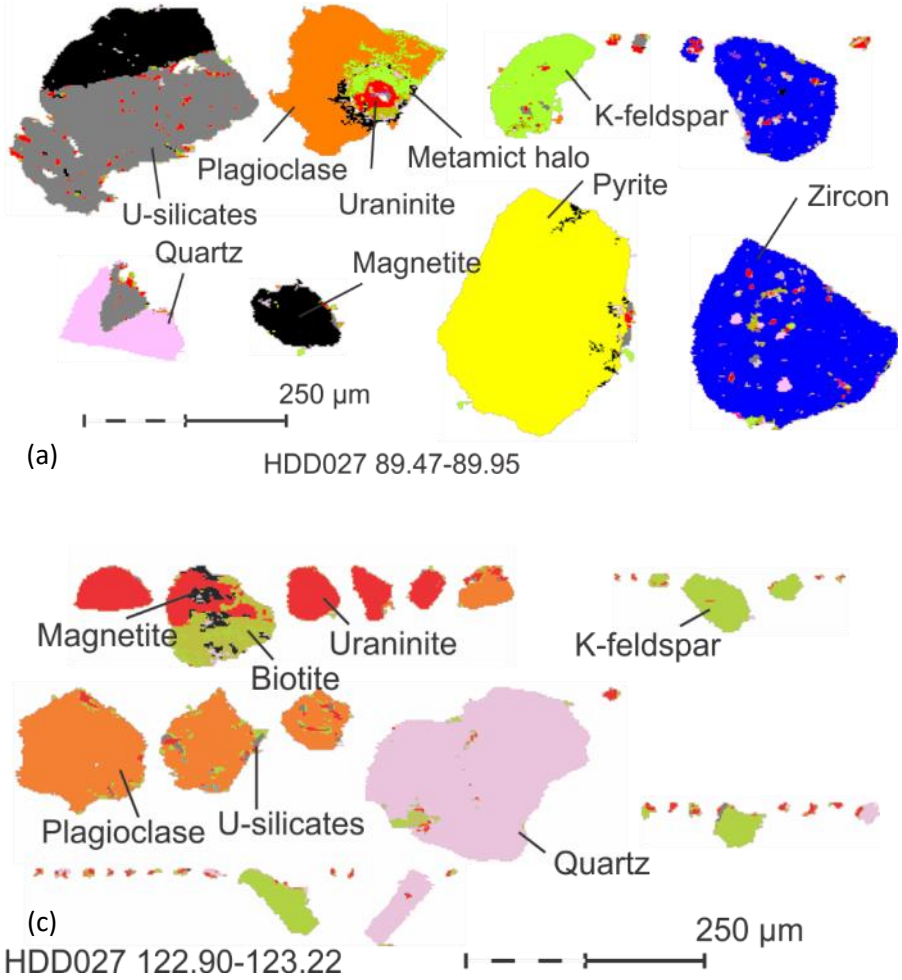



Figure 7.11 Mineral map features of HDD027 samples. (a) 89.47-89.95 from Ida Central. The coarse pyrite reflects the abundant pyrite and Cu-sulphides observed in thin section. The relationship in this example is of uraninite-coffinite

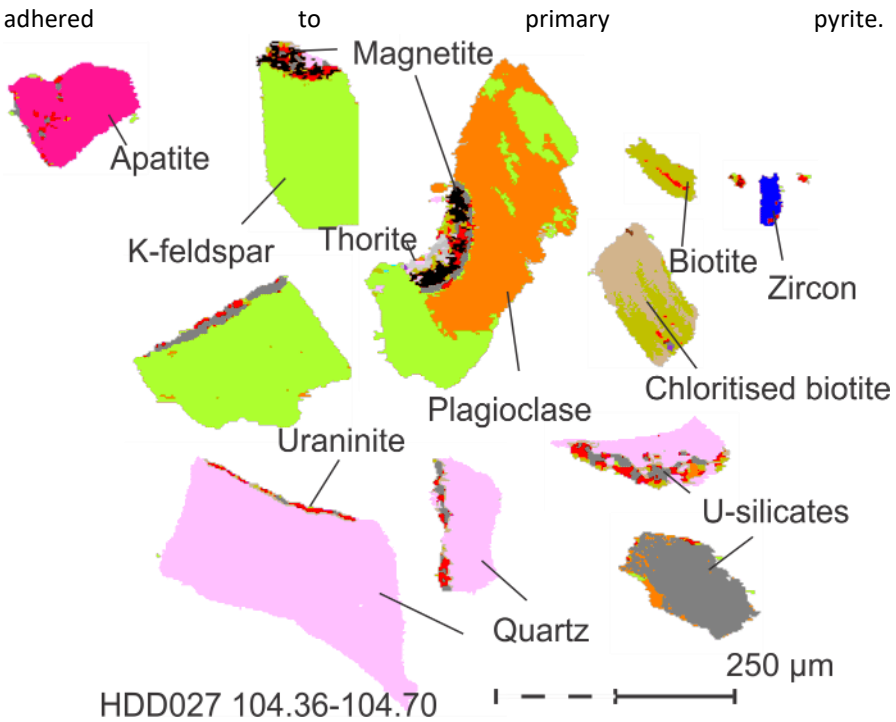



Figure 7.11 (b) 104.36-104.70. Uranium occurs in uraninite inclusions hosted by zircon, apatite, biotite and Fe-phases (magnetite). Uraninite is also on the surfaces of rock-forming minerals with uranium silicates (coffinite). Uraninite has also crystallised on the surfaces of coarse-grained coffinite. (c) Mineral map features of HDD 122.90-123.22 from Ida Central. Note that U-silicates may refer to uranophane or coffinite, as the analysis at the SGS laboratory does not discriminate between the two on the mineral maps.

### *Ida Dome and Holland's Dome Surface Sample Mineral Maps*

The two surface samples, IDAG 08 from Ida Central and IDAG 43 from Holland's Dome illustrate the relationship between entrained and magmatic Fe-Ti phases. Many of the calcareous metasediments have reacted to contact metamorphism and are characterised by coarse diopside, magnetite and titanite porphyroblasts in the host, and localised pegmatoidal textures in the intrusives. The magnetite and titanite show contrasting relationships with respect to uranium mineralisation; uraninite-coffinite is adhered to the surfaces of magnetite, but forms complex replacement networks ± brannerite and betafite in coarse titanite-rutile grains (IDAG08 – Figure 7.12). Quartz, feldspar and zircon host uraninite on grain boundary surfaces, while thorite hosts uraninite inclusions.

The sample from Holland's Dome (Figure 7.13) contains four distinct examples of uranium distribution: unaltered primary uraninite, altered primary uraninite, Fe-mineral replacement by uraninite, and secondary coatings on U-silicates and rock-forming minerals. Primary unaltered uraninite is cubic in shape, which is typical of magmatic growth, whereas altered primary uraninite is surrounded by a halo of secondary calcite in the IDAG 43 example. Uraninite replaced the mobile iron constituents on an altered, anhedral magnetite, and is also present as <5 µm vermicular replacements in altered magnetite. Feldspars and quartz host fine-grained uraninite-coffinite replacement along internal fractures (Figure 7.13).

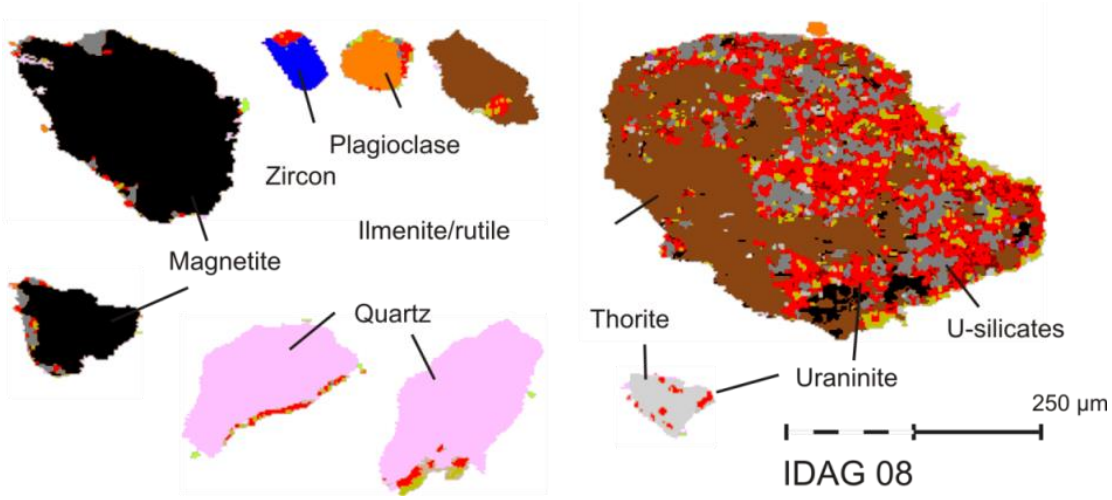



Figure 7.12 Mineral map features of IDAG 08 from Ida Central. Note the coarse-grained ilmenite with uraninite-coffinite replacement. Fine-grained, uraninite-coffinite forms coatings on quartz and magnetite surfaces. The textures in this sample reflect late crystallisation of uranium minerals on the surfaces of the rock-forming and accessory Fe-Ti oxides.

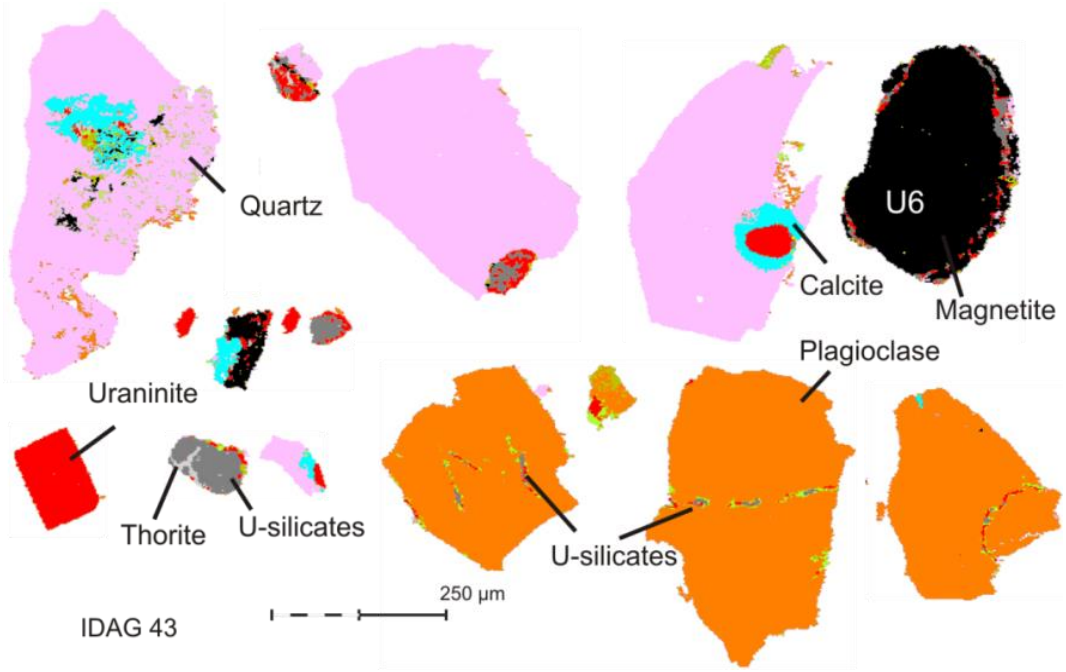



Figure 7.13 Mineral map features of IDAG 43 from Holland's Dome. Key textures are the replacement of the rim of magnetite by uraninite-coffinite (specimen U6 is analysed by EPMA), coffinite deposition along feldspar cleavage planes, euhedral uraninite, and calcite replacement of uraninite rims. This sample is an example of euhedral magmatic uraninite, and secondary uranium-mineral crystallisation within microstructures of the rock-forming minerals.

The Ida Dome samples in many ways reflect the same relationships between uranium and Fe, in particular the coatings and surface replacements of magnetite by uraninite-coffinite. The replacement textures that characterise the near-surface and surface samples at Goanikontes appear to be absent from the Ida samples set. The samples from depth at Goanikontes and Ida Dome only show uraninite-coffinite on magnetite surfaces. The Ida Dome samples contain ilmenite-rutile, which host uraninite-coffinite ± brannerite-betafite replacements; Ti phases appear to be absent, at least with respect to uraninite relationships, in the Goanikontes samples. The contrast between the two sample sets is further exacerbated by the coarse-grained nature of uraninite in the Goanikontes alaskites, compared to the fine-grained, inclusion and coating style of uraninite distribution in the Ida Dome samples.

### *Husab Deposit Mineral Maps*

The Husab QEMSCAN data set is the most comprehensive in this study and comprises a total of twenty-two individual sample analyses; thirteen samples from eight diamond drill holes in

the Zone 1 deposit, and nine samples in five diamond drill holes in the Zone 2 deposit. The diamond drill hole RDD373 samples provide examples of uranium-bearing refractory mineralisation, locally abundant in leucogranites intruding below calcsilicate units of the upper Rössing Formation in Zone 1; while the RDD006 drill-hole samples provide a cross-section of uranium mineralisation trends in leucogranites that intruded the local Rössing succession at Zone 2.

Ten of the twenty-two Husab deposit QEMSCAN samples host <50 wt.% of the U in uraninite, nine contain >30 wt. % U in coffinite (Figure 7.14). The U-silicate is the dominant replacement phase, and ranges from micro fracture-fill to complete replacement of primary uraninite. This widespread abundance of coffinite replacement of uraninite sets the Husab alaskite apart from the other deposits and reflects a more intense late fluid alteration phase of the mineralisation model.

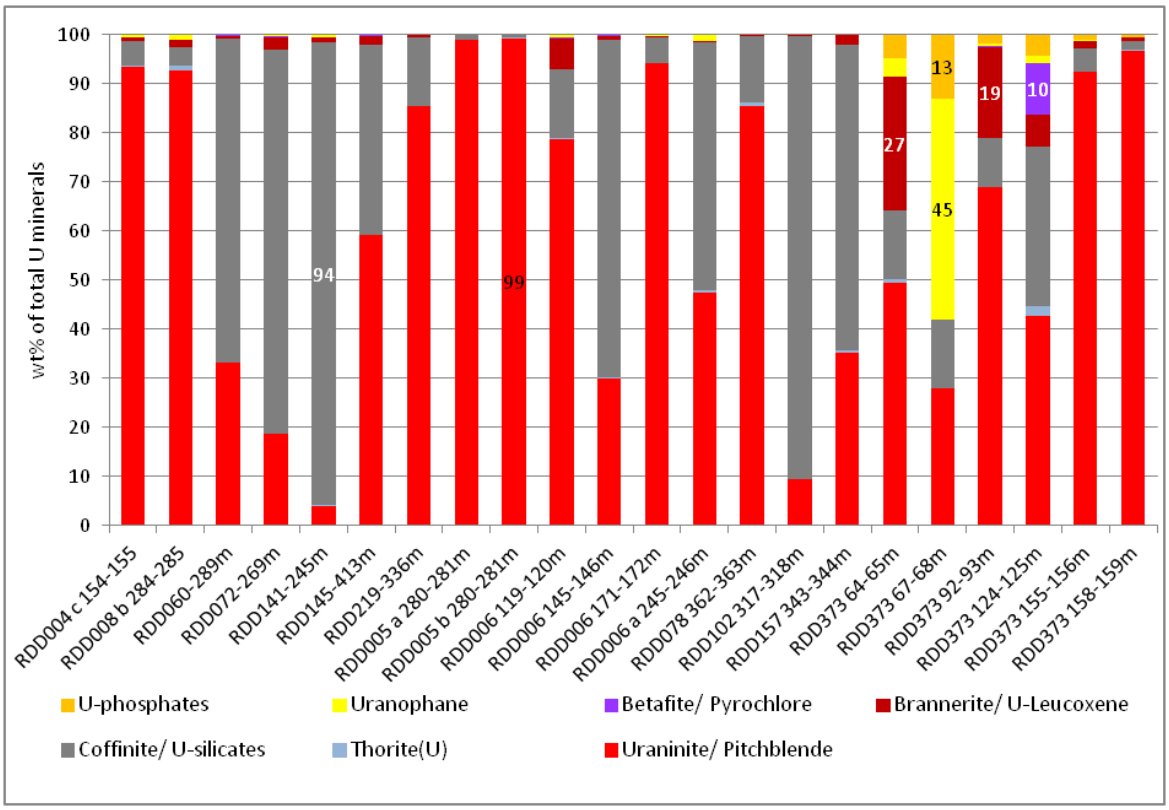



Figure 7.14 Uranium deportment of the Husab QEMSCAN samples from Zone 1 and Zone 2. Seven of the samples have U-deportment in coffinite > uraninite, with appreciable uranophane in a single sample, RDD373 67-68 m. Uranium mineral compositions are determined by EPM in samples RDD006 171-172; RDD008 284-285 m; RDD373 64-65 m, 92-93 m, 124-125 m.

The abundance of coffinite over uranophane is especially important when comparing the deposit to the type locality at Rössing, where up to 45 % of the U minerals occur as hexavalent beta-uranophane (after Berning, 1986).

Brannerite is reported in all samples, but only exceeds 5 wt.% in four samples. Three of these samples are from drill hole RDD373. Betafite is detected in most samples and only exceeds 1 wt.% in one sample, RDD373 124-125 m (10.45 wt.%). Thorite is comparably scarce and only exceeds 1 wt.% in two samples, the maximum being 2.5 wt.% in RDD373 155-156 m.

The summarised characteristics of the Husab sample set as determined by QEMSCAN analyses are as follows:

- Uraninite is the most abundant uranium mineral;
- Uraninite is replaced by coffinite in varying proportions in all samples;
- Coffinite is most abundant mineral in 6 samples, and uranophane in 1 sample;
- Brannerite is the most abundant uranium-bearing refractory mineral in 21 samples, betafite is the dominant refractory phase in 1 sample; and
- The RDD 373 drill hole contains the most diverse uranium mineral population and contains examples of uraninite, coffinite, thorite, uranophane, coffinite, brannerite, betafite, and U-phosphates (autunite).

Major textural and mineralogical relationships in the Husab samples include:

- Euhedral, magmatic uraninite up to 600 µm in size;
- Biotite-, quartz-, and feldspar-hosted euhedral uraninite,
- Secondary uraninite, and coffinite and uranophane crystallisation in biotite and feldspar mineral cleavages;
- Uraninite hosted in betafite, and uraninite-betafite compound grains; and
- Backscatter imagery shows evidence of uranium leaching from brannerite and betafite specimens of the RDD373 samples.

### *Uranium Mineral Textures of The Husab Deposits*

Uraninite and coffinite are abundant and present in every sample analysis, thus mineral grain maps are often overwhelmingly represented by the two minerals, the images that follow are selected to highlight the relationship between these two minerals and the less abundant U- and Th-phases, and the relationships between the uranium-bearing oxides and silicates and the host- and accessory assemblages. Sulphides are abundant, with the most common association being pyrite, radiogenic lead may be the source of galena, and iron mineral textures suggest variable degrees of Fe-mobilisation during alteration.

Compound uranium mineral clusters that consist of combinations of fine-grained uraninite, brannerite, pyrite, galena, Fe-oxides, and calcite all support uranium and mobile metal circulation post-emplacement (Figure 7.15a). Uraninite in a single sample such as RDD078-363 m may show multiple textures from relatively unaltered, euhedral uraninite, to completely coffinitised grains, and fine-grained inclusions within thorite (Figure 7.15b).

As with the example in Figure 7.15a, galena and pyrite occur as inclusions in the coffinite replacement. Coffinite/uranophane fills the micro fractures within uraninite, showing that uraninite is older than at least one generation of coffinite RDD102-318 m (Figure 7.15c). Coffinite is the dominant mineral in the sample and it has completely replaced uraninite, and is essentially a pseudomorph. In some examples, coffinite has completely replaced euhedral uraninite (Figure 7.15c). Coarse-grained, euhedral uranothorite and similar sized uraninite show contrasting alteration, where the thorite species is euhedral and unaltered and uraninite is anhedral (Figure 7.15d).

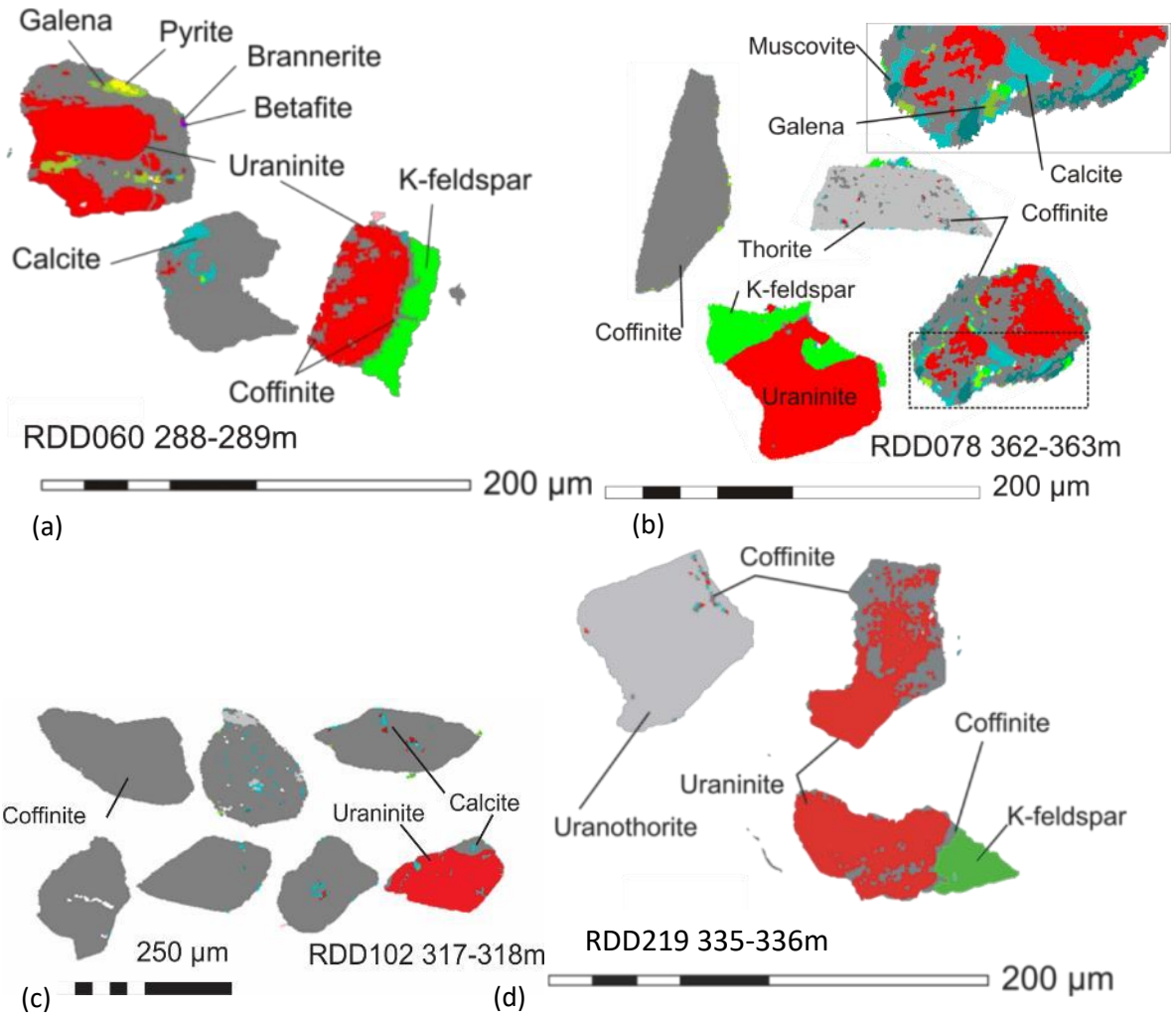



Figure 7.15 QEMSCAN mineral maps of uraninite and coffinite textures in Husab Zone 1 and Zone 2 samples. (a) Compound grains of uraninite replacement by coffinite with associated brannerite and sulphides. Galena is likely to be a product of radiogenic lead mobilisation from altered uraninite. Coffinite forms as inclusions in impure uraninite and at contact margins with K-feldspar. (b) Compound grains and fractured uraninite, illustrating aggressive replacement of uraninite with accessory sulphides. Thorite hosts uraninite and coffinite inclusions, and uraninite fills cavities at a K-feldspar contact RDD078 362-363 m. (c) Examples of coffinite in sample RDD102-318m. Uraninite is a minor phase, and is variably- to completely replaced by coffinite. The coffinite also contains thorite inclusions, potentially remnants of solid solution. (d) Primary uraninite overgrown- and replaced by coffinite, and primary uranothorite with coffinite fill in fractures, RDD219-336 m. Coffinite occurs as a replacement mineral and as a fill in fractured uranothorite as well as at the contact between uraninite and K-feldspar.

The uranium-bearing refractory minerals tend to occur together. Most samples that host primary betafite also contain brannerite, of varying textural relationships. RDD145-413 m contains coarse-grained uraninite, many of which are euhedral and ~75-100 µm in size. Betafite appears to be primary and subhedral. Betafite/brannerite contacts with uraninite are characterised by coffinite rims around the refractory minerals (Figure 7.16a) while betafite – coffinite contacts are characterised by quartz rims (also Figure 7.16a). Brannerite

is secondary and shows replacement texture along uraninite grain edges and with uraninite fractures. Remobilised uranium is most often coffinite, which fills cavities in altered rock-forming minerals and halos around primary uraninite (Figure 7.16a). Betafite in RDD141 244-245 m is replaced by brannerite and coffinite fills cavities in quartz clusters (Figure 7.16b). Brannerite is widespread as a fine-grained inclusion/replacement within rock-forming minerals and accessory minerals such as pyrite (Figure 7.16c). It occurs with primary uraninite which shows some alteration/replacement by coffinite. The brannerite occurs with secondary uraninite and coffinite, and replacement calcite. Brannerite may also be replaced, in the RDD157 343-344 m sample the relationship shows coffinite intensely replacing brannerite along preferred fracture orientations. Coffinite also replaces rutile/ilmenite and is associated with secondary calcite. As in most samples, betafite is present and shows a reaction texture with a thorite grain; uraninite has formed between the two primary minerals and along the edge of the altered thorite (Figure 7.16d).

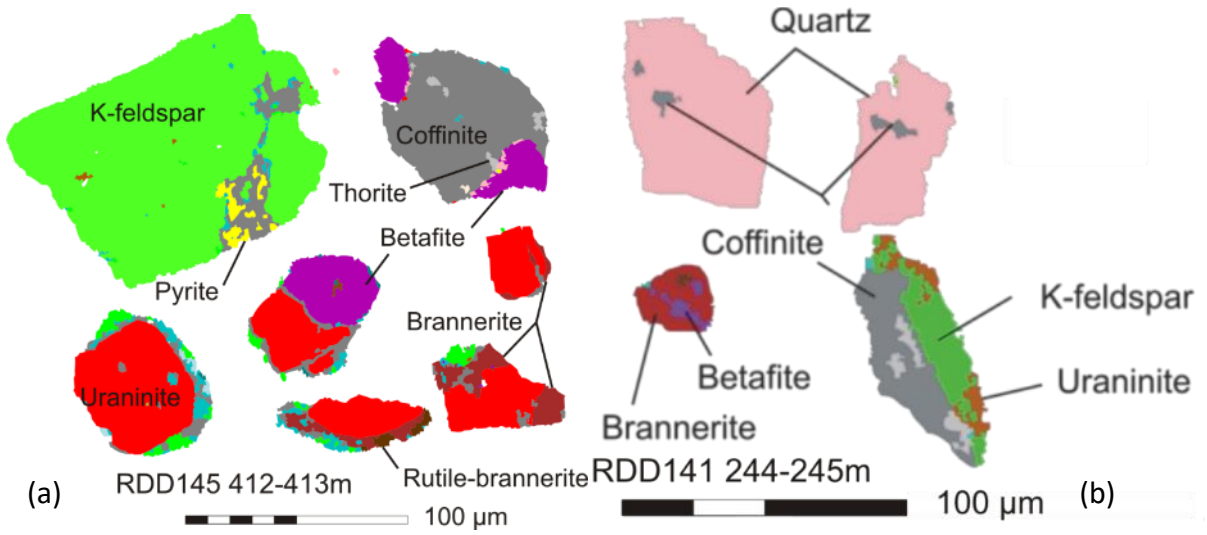



Figure 7.16 QEMSCAN mineral maps of uranium mineral textures in Husab Zone 1 and Zone 2 samples.(a) Betafite relationships with coffinite and uraninite in sample RDD145 412-413 m. Betafite occurs with coffinite and has quartz at the contact margins. Coffinite surrounds betafite and uraninite, replacing the contact margin between the two minerals. In the same sample, euhedral uraninite may exceed 100 µm across. (b) Brannerite replaces betafite with associated calcite; coffinite replaces thorite, potentially in solid solution along a K-feldspar grain contact, RDD141 244-245 m.

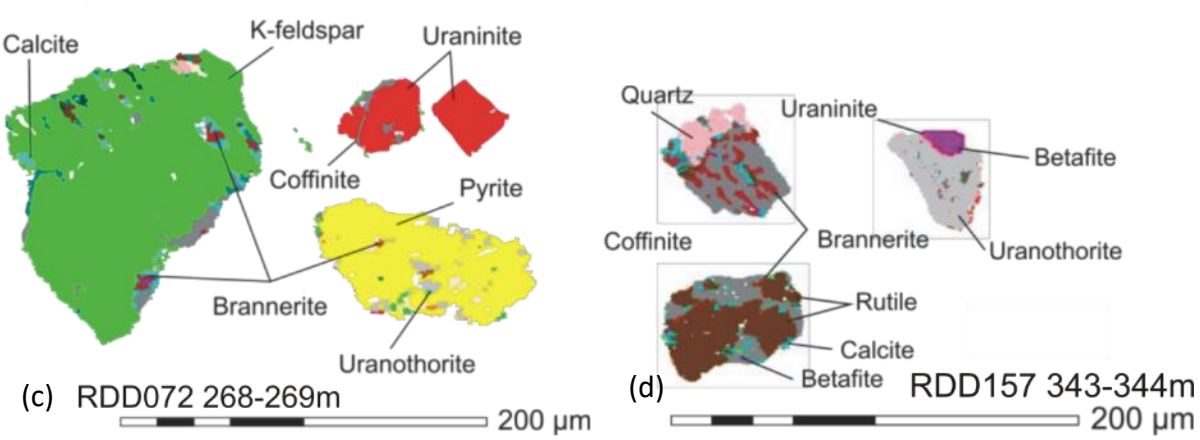



Figure 7.16 (c) Examples of U-remobilisation in RDD072 268-269 m. Altered K-feldspar hosts cleavage-controlled coffinite-brannerite-calcite and skeletal pyrite hosts brannerite and uranothorite-coffinite inclusions. Coffinite fills fractures within uraninite- note euhedral shape of the primary uraninite. (d) Ti oxide relationships with coffinite in the RDD157 343-344 m sample. Brannerite is replaced by cleavage-controlled coffinite, and coffinite replaces anhedral rutile/ilmenite. Betafite occurs in contact with thorite, with associated secondary uraninite.

### *Uranium-Bearing Refractory Minerals and Textures In Husab Drill Core RDD373*

Petrographic observation shows that primary brannerite and betafite exhibit variable degrees of alteration, as does uraninite. Accessory mineral associations with betafite and brannerite are potentially less varied with respect to uraninite, limited by the refractory nature of the minerals. Certain textural examples are shown in backscattered imagery, where the resolution and spectral signals confirm accessory mineral relationships. Prominent mineral associations are dominated by the Fe-Ti phases, ilmenite/rutile, titanite, while phosphates and sulphides appear to be late and crosscut betafite, brannerite and uranothorite, whereas in some examples brannerite, or Ca-Ti-U phases that resemble it, appear to be replacing earlier replacements of monazite (Ce).

The RDD373 borehole intersects uraniferous sheeted leucogranites that contain appreciable proportions of the uranium-bearing refractory minerals betafite and brannerite. The betafite and brannerite are more abundant, relatively, in the near surface intervals where alteration has leached soluble U from uraninite, coffinite and uranophane. The 64 m and 93 m depth intervals host appreciable brannerite, 29 wt.% and 19 wt.% of the U budget, respectively. The 125$^{th}$ m downhole interval contains the most betafite of the analysed samples at 10 wt.%. Other examples of refractory mineral-hosted uranium associations occur in the 115$^{th}$ m downhole interval and include uraninite-betafite, thorite-phosphate,

and brannerite; the relationships of these minerals illustrate portions of the paragenetic sequence of deposit: -

Betafite is euhedral when unaltered, with evidence of hydrothermal alteration accompanying anhedral or irregular grain edges. Fracture planes in the crystal are filled by a secondary mineral; the spectra show that it is depleted in Nb, Ta and Y relative to the primary phase, but comparable in U proportions, highlighting U mobility relative to the other constituents (Figure 7.17a). Betafite has crystallised late in the sequence and some examples contain primary uraninite and zircon inclusions (Figure 7.17b). Brannerite occurs in complex associations with Ce-phosphate, titanite and ilmenite. The brannerite example in Figure 7.17c has undergone hydrothermal leaching, where the secondary brannerite/ leucoxene contains more metal (mobile U) as indicated by brighter contrast in the backscatter image.

The original brannerite is a replacement texture within the ilmenite. A portion of the grain gives the impression of brannerite-ilmenite zonation within the crystal, if true, this supports coeval crystal growth. U-bearing thorite (uranothorite) occurs in a compound phosphate grain, with apatite and Ce-monazite (Figure 7.17d). The compound grain may be an entrained apatite as it has anhedral shape and irregular grain boundaries. The thorite, monazite and apatite are crosscut by late sulphide.

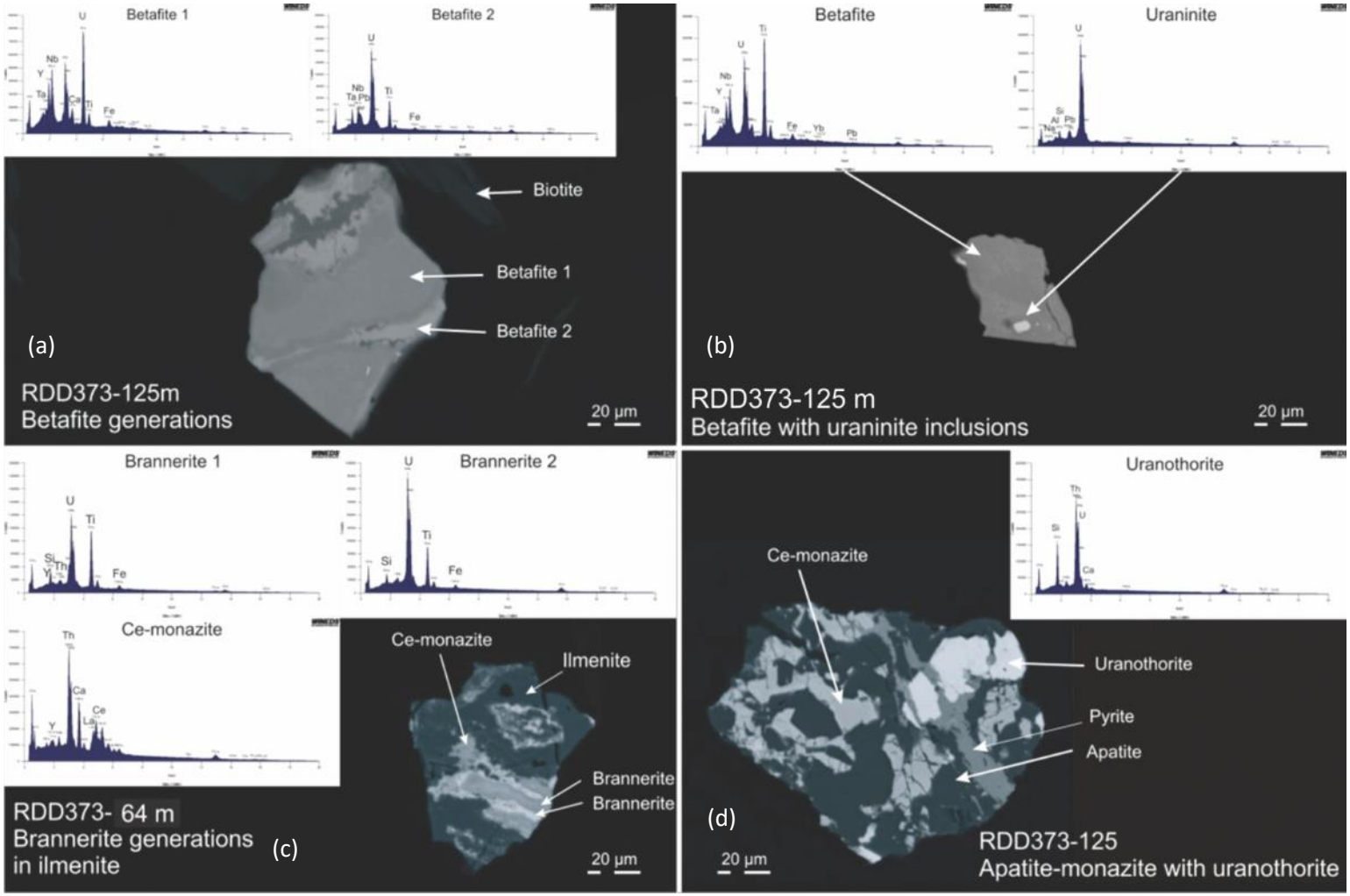



Figure 7.17 Uranium-bearing refractory mineral textures in samples from hole RDD373, Husab. (a) Brannerite alteration in RDD373-125m. Brannerite occurs as a secondary mineral, crystallising in fractures of the primary mineral. The secondary mineral has a higher metal content, as it comprises mobile U (b) Betafite (20 µm) with uraninite inclusion, RDD373-125 m. The sample is a backscatter image of a compound mineral grain identified in a QEMSCAN sampling study of core from RDD373, Zone 1, Husab deposit. (c) First- and second-generation pyrochlore (betafite) in the RDD373-64m sample. Relatively euhedral betafite crystallised late in the granite crystallisation sequence. Later fractures (from radiation damage generated from within the crystal) are filled by a Nb pyrochlore-like secondary mineral (d) Entrained compound, apatite-monazite grain with uranothorite inclusion in RDD373-125m. The compound phosphate has corroded, irregular edges, and pyrite crosscuts the phosphates and the thorite.

The RDD006 hole is located in the central eastern portion of the Zone 2 ore body. The samples provide an abridged representation of ~125 m of uranium mineralisation within relatively flat-lying Rössing Formation in the hinge of the open antiform that hosts the Zone 2 deposit. The core section serves as a type-example to compare uranium mineral populations relative to stratigraphic position (Figure 7.18).

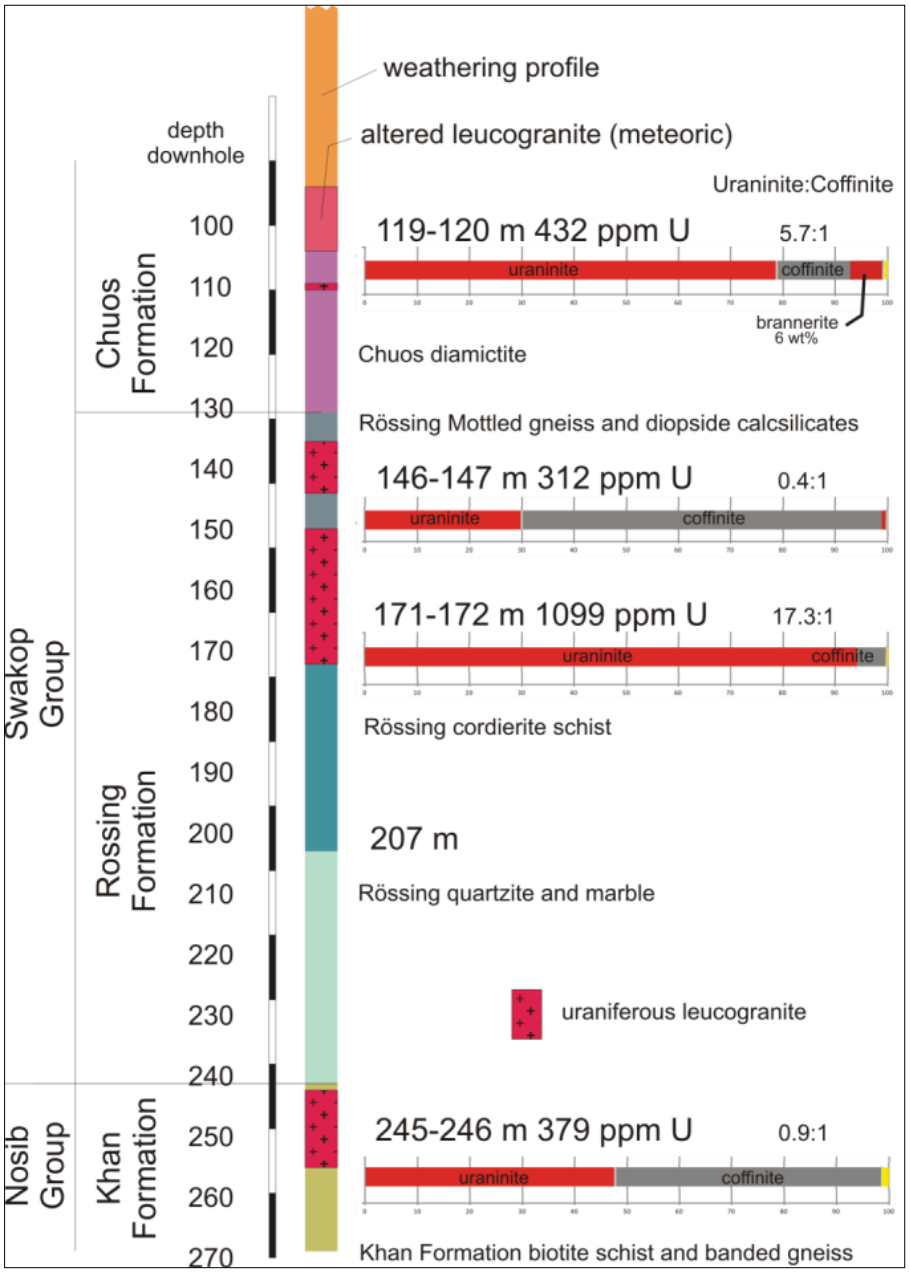



Figure 7.18 Graphical representations of the RDD006 sample intervals. Uraninite/coffinite ratios vary with depth and show a pattern with respect to host rock; the two leucogranites that intrude below the carbonate-calcsilicate units at -147 m and -246 m downhole host coffinite ≥ uraninite. The two samples sampled from within intervals of gneissic/schistose host-rock have uraninite as the dominant U mineral. The shallow sample, at -120 m downhole, also hosts appreciable U in brannerite (6 wt.%).

The local succession essentially comprises a footwall package of amphibole biotite schist and locally migmatised gneiss with prominent feldspar-pyroxene compositional banding of the Khan Formation. The top of the Khan Formation is marked by ~8 m of metasomatised (chlorite-dominated) biotite schist, capped by a ~1.25 m-thick meta-conglomerate. This is succeeded by a ~35 m intercalated package of quartzite, calcsilicate and marble units, analogous to the lower Rössing marble package of Anderson and Nash (1997). The lower marble package is succeeded by intercalated impure quartzite and mudstone (schists). There is at least 50 m of pelitic schist and mottled-textured gneiss (cordierite and garnet-bearing) succeeding the marble, and above this a ~25 m-thick calcsilicate-quartzite package (analogous to the upper marble units described at the Rössing deposit). The carbonates are succeeded by banded, fine-grained quartzite, which appears to be a remnant of original deposition. A ~20 m succession of pelitic gneiss and schists occurs between the carbonate-siliciclastic and the diamictite dominated Chuos Formation. Locally the Rössing Formation is capped by a narrow (<10 m) limestone which has metamorphosed to a marble with well-crystallised, centimetric calcite rhombs.

From shallow to deep the QEMSCAN samples, with U ppm by ICP-MS, are as follows; RDD006 -120 m, moderate grade (432 ppm U); RDD006-146 m, a moderate-low grade (312 ppm U by ICP-MS combined with metasediment contact); RDD006-172 m, is from a 7-m thick D-type leucogranite, it is high-grade with 1099 ppm U; and RDD006-246 m, an oxidised alaskite (E-type) with moderate- to low-grade (379 ppm U). Figure 7.18 graphically represents a simplified core log of the RDD006 hole, and distinctive mineral textures of the four specimens are in Figures 7.19a to 7.19d. Appendix F6 lists photographs of all the Husab core specimens.

The leucogranite at 120 m intrudes the upper pelitic gneiss package, and is characterised by a relatively homogenous texture, medium to coarse grain sizes, with fine-grained relatively abundant biotite (Figure 7.19). Uraninite is bimodal, occurring as >100 µm euhedral cubic crystals, and as fine-grained inclusions in altered biotite, associated with brannerite. Coffinite is the dominant replacement of uraninite, and occurs as a rim and near-complete replacement texture, but is not identified within biotite. Rutile/ilmenite crystals contain fine-

grained uraninite and brannerite inclusions as well as adhesions of uraninite on surfaces. Calcite occurs as a replacement texture in biotite, and rutile/ilmenite.

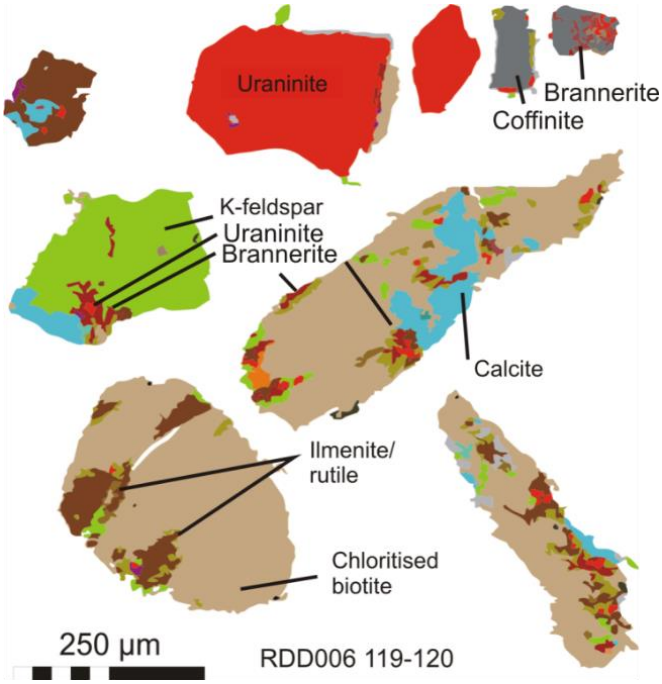



Figure 7.19 QEMSCAN derived mineral maps illustrating uranium mineral textures of RDD006 specimens. RDD006 119-120 m, euhedral uraninite with examples of unaltered-, full- and partial coffinite replacement. Uraninite, ilmenite and brannerite occur between biotite sheet, and within K-feldspar.

The abundance of titaniferous minerals associated with uranium is coincident with >6 wt.% U deportment in brannerite. The leucogranite at 146 m depth has intruded below the upper carbonate package; within the upper chloritised pelitic schist and gneiss units, that contain intercalated calcareous material (Figure 7.20a). There are prominent, metre-thick Fe-reaction margins at the sediment contacts, which have discoloured the white feldspars to a light orange. The dominant mineral is coarse uraninite (200 - 600+ µm) which shows variably intense degrees of replacement by coffinite. Although the sample contains 100 µm-scale betafite crystals, just 0.06 wt.% of the uranium is hosted in the refractory mineral, ~98 wt.% of U minerals are uraninite and coffinite (29.8 % and 68.5 %, respectively).

The 171-172 m sample is from a 1.5 m thick, pegmatitic textured leucogranite with coarse, centimetric biotite near the lower cordierite gneiss contact (Figure 7.20b). The sample is from within a ~20 m thick, variably textured D-type leucogranite intrusion, potentially a stack of

multiple sheets, within the lower pelitic gneiss. The pegmatitic texture appears to be reflected in >750 µm uraninite crystals. The sample also appears to have been spared alteration by siliceous fluids, with only 5.4 wt.% U in predominantly fracture-fill coffinite veining.

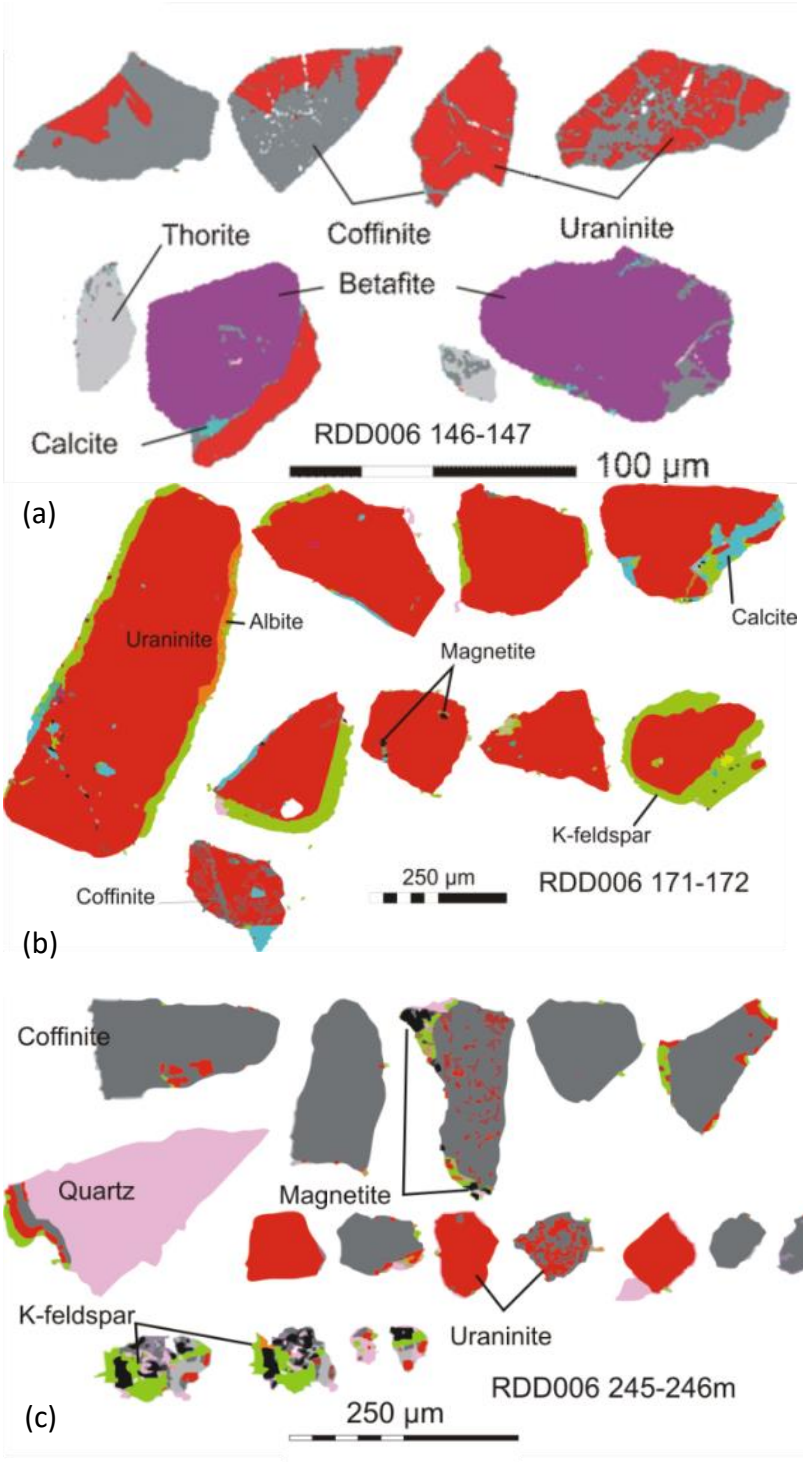



Figure 7.20 QEMSCAN derived mineral maps illustrating uranium mineral textures of RDD006 specimens continued. (a) RDD006 146-147 m, euhedral uraninite with all uraninite showing variable coffinitisation. Coffinite forms along fracture networks within the uraninite. Betafite is coarse, with secondary U-silicates in fractures. (b) Sample RDD006 171-172 m is characterised by coarse-grained uraninite, most grains are >150 µm across. Albite rims indicate that uraninite crystallised before sub solidus reactions were complete. Some of the uraninite has coffinite alteration along fine internal fracture planes. Calcite is in replacement texture along the rims of some uraninite. The largest, labelled, coarse-grained uraninite is analysed by EPMA. (c) Sample interval RDD006 245-246 m illustrates a population of near-complete coffinite replacement of uraninite, euhedral uraninite, and compound grain clusters of K-feldspar, coffinite-uraninite, thorite, quartz and magnetite. Euhedral unaltered uraninite suggests that alteration is localised in patches within the 1 metre sample.

The 245 m sample is from a 1.5 m thick E-type leucogranite that intrudes the uppermost schist and gneiss units of the Khan Formation (Figure 7.20c). There is a reactive margin within the hanging wall rocks, which comprise a package of quartzite-calcsilicates of the lower marble package. Acidic fluids, potentially F-bearing and magmatic, associated with the granite have leached silicates from the metasediment, over 1m away from the intrusive contact.

The uranium mineral population comprises near equal proportions of coffinite and euhedral uraninite with ~1.5 wt. % uranophane. Coffinite is coarse-grained (>150 µm) and appears to be coated by uraninite in some specimens and has completely replaced uraninite in others. Coffinite-uraninite veins have formed along quartz grain boundaries, while uraninite has crystallised along replacement coffinite grain edges. The highly variable uraninite-coffinite textures are indicative of a dynamic system in which uranium is mobile intermittently for a period after granite crystallisation.

***Valencia Uranium Mineral Maps***

The main ore zone of the Valencia deposit comprises a mass of amalgamated sheeted leucogranites that occupy the hinge zone of a secondary $D_2/D_3$ antiform. The granites transgress the Khan-, Rössing-, Chuos-, Karibib-, and Kuiseb Formations via brittle structures.

QEMSCAN analysis samples are sourced from two NQ drill cores (three intervals in hole 113, and four in hole 141) and two surface locations (VALG 11 and VALGE 26). The samples have variable uranium concentrations, the highest approach 1 000 ppm U and occur in leucogranites that have intruded the reactive units of the Khan- and Rössing Formations. Surface sample VALG 11 is from stratigraphically below the marble and VALG 26 is from leucogranite that invades the Kuiseb Formation above. The location is within the hinge zone of the antiform that hosts the deposit and the metasediments dip southward at ~50°. The core samples are from drill intersections of Rössing Formation at the eastern and central sectors of the deposit (Figure 7.22). The core samples from diamond drill hole Va26 113 samples represent the main granite body, characterised by a low proportion of metasediment throughout the drill intersection.

Diamond drill hole Va26 141 is located on the eastern end of the deposit; it has a higher proportion of entrained metasediment, and consequently a greater variation in granite texture.

The textural variation shows no bearing on the overall uraninite character between the sample sets of the two drill holes, apart from a compound betafite-brannerite in Va26 141 at 301.19 m to 301.60. Magmatic uraninite is dominant and has primary mineral associations with quartz, feldspar, biotite, monazite, apatite, and zircon (Figure 7.21). Secondary associations are dominated by Fe-Ti minerals and pyrite. Monazite is coarse, anhedral and hosts uraninite and thorite inclusions, zircon does not host U inclusions of any significance. Thorite is particularly scarce in the Valencia samples. Valencia samples overall, show little variation in uraninite texture and speciation between samples. Uraninite is the dominant U-host mineral in the samples and bimodal, with coarse-grained, euhedral uraninite crystals more abundant than fine-grained inclusions and fracture-fill type uraninite-coffinite crytallisation. Clustered zircon, anhedral monazite, and fine-grained poly-mineralic clusters suggest a component of entrained material. The zircon and monazite textures appear to be unique to the Valencia samples.

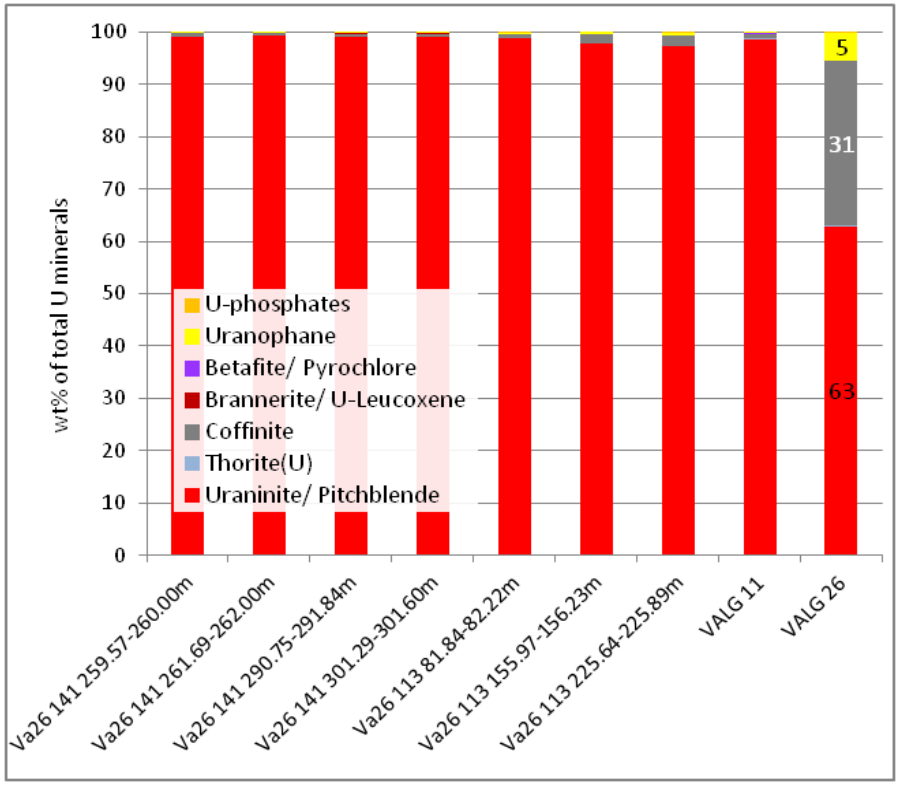



Figure 7.21 Uranium deportment statistics of the Valencia QEMSCAN samples. The dominant mineral is uraninite, which accounts for over 90 % of the uranium budget in all but one sample, VALG26. VALG26 is a surface sample collected at a location stratigraphically above the Karibib Formation marble, and hosts ~30% of the U in coffinite.

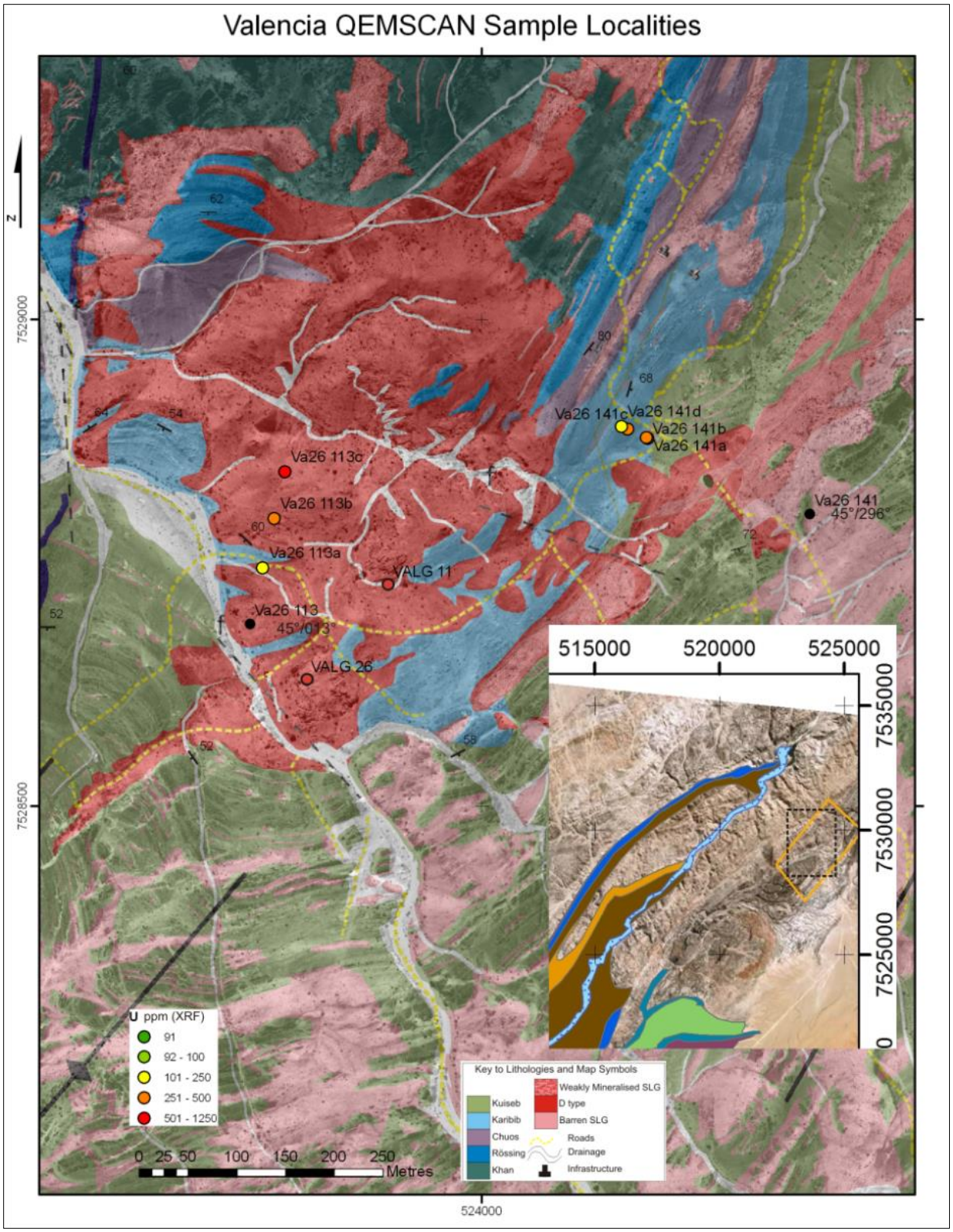



Figure 7.22 Ortho-photo with lithological overlay at Valencia with localities of samples submitted for QEMSCAN analyses. Drill hole collars are labelled with plunge and azimuth, samples with suffix (a-d) are projections to surface of the position of the sample downhole.

Uraninite is dominant in all nine samples, and only one surface sample contains any uranophane of significance. Coffinite is also rare, and is predominantly a fine-grained fracture replacement at coarse uraninite edges. VALG 26 hosts 31 wt.% U in coffinite and is the only sample that exhibits near complete uraninite replacement by coffinite. Mineral maps compiled from the Va26 113 samples show that the uraninite population comprises relatively unaltered uraninite in three distinct sizes and textures; coarse, sub-rounded, occasionally euhedral 100- to 250 µm grains; intermediate-sized grains, <100 µm, are angular and the straight edges imply fragmentation of larger brittle grains during sample preparation and fine-grained inclusions within rock-forming and accessory minerals are rare and suggest a low degree of soluble U circulation during granite crystallisation. Very-fine uraninite forms chains and veinlets along internal cleavage fractures in coarse K-feldspars. Monazite occurs in two textural varieties, one is anhedral and characterised by fine-grained uraninite and thorite inclusions, with secondary apatite at the rims of the grains (Figure 7.23a). The second texture is euhedral and does not contain inclusions, but does have some uraninite association (Figure 7.23b). U-silicate replacement within uraninite is rare; some coarse uraninite has fine-grained coffinite/uranophane replacement in microfractures at grain edges. U-silicate almost completely replaces some uraninite in the sample Va26 113 225.64-225.80 m, shown in Figure 7.23c. The replacement occurs within a sample set that illustrates prominent calcite replacement of uraninite. The main alteration/secondary mineral is calcite, forming rims around some uraninite-quartz contacts in samples from the three sampled depths (Figure 7.23c). The calcite replacement fills brittle, occasionally conchoidal, fractures in coarse-grained uraninite.

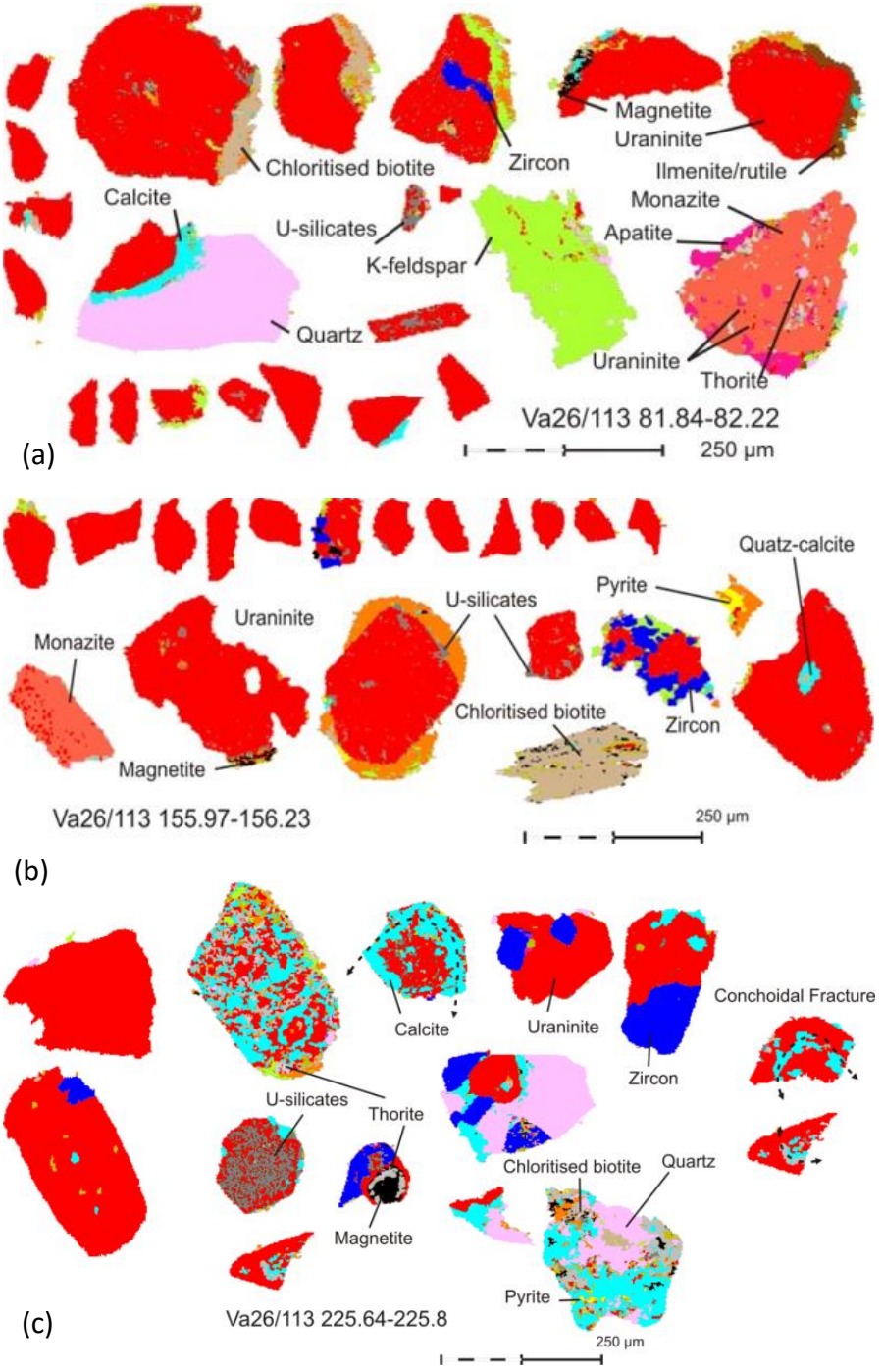



Figure 7.23 Mineral maps of samples from the Va26 113 diamond drill hole at Valencia. (a) Uranium mineral features of Va26 113 81.84-82.22 m. Uraninite is rarely euhedral and has calcite at grain edges. Monazite has inclusions of uraninite and thorite and fine uraninite fills fractures in feldspar. (b) Mineral map features of Va26 113 155.97-156.23. Uraninite occurs as disseminated inclusions in monazite and along biotite cleavages. U-silicates are restricted to fractures towards grain edges. Clustered zircon forms a site for uraninite nucleation. (c) Mineral map features of Va26 113 225.64-225.80. Calcite fills spaces in a large proportion of uraninites, occasionally highlighting the conchoidal fracture. Large (up to ~100 µm) inclusion-free zircon is attached to uraninite. Composite fine-grained clusters include quartz, calcite, plagioclase, biotite and disseminated uraninite, magnetite and pyrite. U silicates after uraninite are scarce.

Samples from drill hole Va26 141 show similar uraninite textures and grain size-distribution to the Va26 113 samples; coarse-grained uraninite crystals exceed 200 µm and are occasionally euhedral; intermediate-sized grains comprise, almost exclusively, angular fragments formed during sample preparation. The sample set is roughly divided into two groups; one is slightly shallower with two samples between 259 m and 262 m downhole, the other is deeper with two samples, at ~290 m and ~301 m downhole. Fine-grained, disseminated uraninite inclusions in major and accessory mineral phases are scarce, contrasting with abundances observed in the Va26 113 samples. The most common mineral association in the shallower samples is with quartz (Figure 7.24a and b) where euhedral and anhedral uraninite occurs within single or clustered quartz, often accompanied by secondary magnetite/Fe-oxides, abundant pyrite, and coarse-grained zircon.

The granite in the 261.69 m -262.01 m interval is metasomatised with quartz-rich patches and haematite staining and magnetite visible in hand specimen. Uraninite in the deeper intersections appears to be more feldspar- and biotite associated than with quartz. The lack of a uraninite-quartz association is emphasised by the graphic textured quartz-feldspar cluster in Figure 7.24c. Secondary U-minerals and brannerite fill the internal fractures near uraninite grain edges (Figure 7.24d). Biotite hosts uraninite inclusions up to 120 µm across and these are accompanied by cleavage parallel magnetite/Fe-oxide as a by-product of biotite alteration to chlorite. Clay minerals (illite) fill the alteration halos and surrounding radiating cracks in uraninite-hosted in biotite and plagioclase (Figure 7.24d).

Radiation damage around uraninite within biotite has led to clay alteration and a rim of jarosite. The Valencia example at 301 m in hole 141 illustrates how fine-grained brannerite, 5–10 µm in size, crystallised late in the paragenetic sequence, subsequent to alteration of the feldspar that hosts the primary uraninite (Figure 7.24d). Zircon crystals occur both as attachments to- and inclusions within uraninite. Zircon is finer-grained than in the Va26 113 samples, but is free of any detectable uraninite inclusions. The uraninite in the deeper samples contains inclusions of zircon and of biotite (Figure 7.24c and 7.24d).

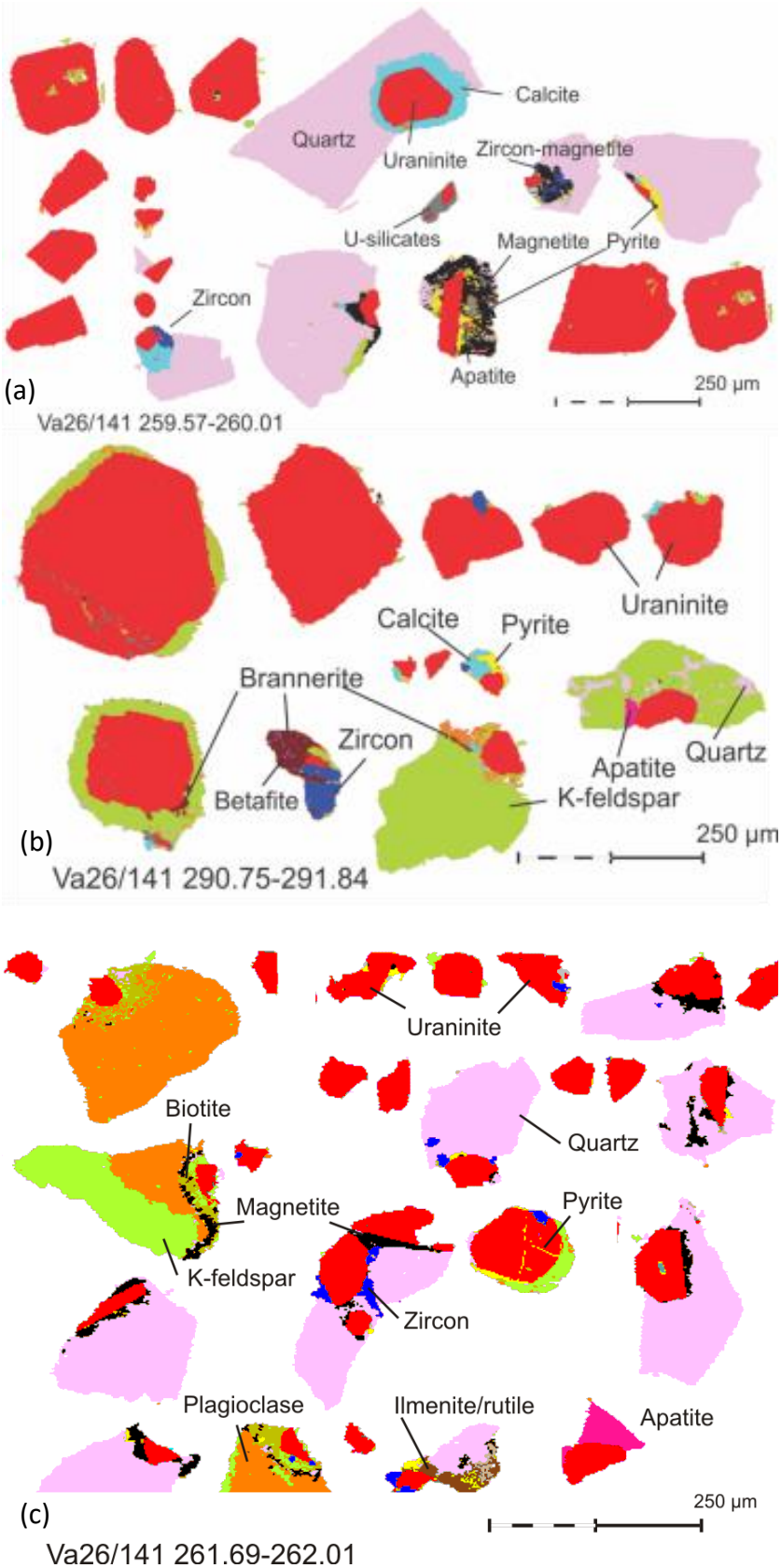



Figure 7.24 Mineral map features of Va26 141 diamond drill hole at Valencia. (a) 259.57-260.01 m. Coarse 100-200 µm uraninite grains are often euhedral, predominantly in cubic form. A single crystal face has five sides and may be from a dodecahedron. Most are free grains, with common attachments being quartz and Fe-oxides. Uraninite is late in the crystallisation sequence and hosts inclusions of biotite, feldspar, Fe-oxides and pyrite.
(b) Uranium mineral features of Va26 141 261.69-262.01 m. Euhedral uraninite is associated with Fe-Ti oxides at junctions of quartz clusters. Secondary Fe fills cavities that result from mineral degradation adjacent to the radioactive uraninite inclusions. Secondary pyrite surrounds euhedral uraninite, and fills internal fractures within U- and Fe-Ti minerals.
(c) Mineral map features of Va26 141 301.29-301.60. Uraninite is coarse-grained (>200 µm) and euhedral, in cubic and octahedral forms. The uraninite occurs as free grains, and as inclusions within feldspar, and at clustered feldspar grain junctions.

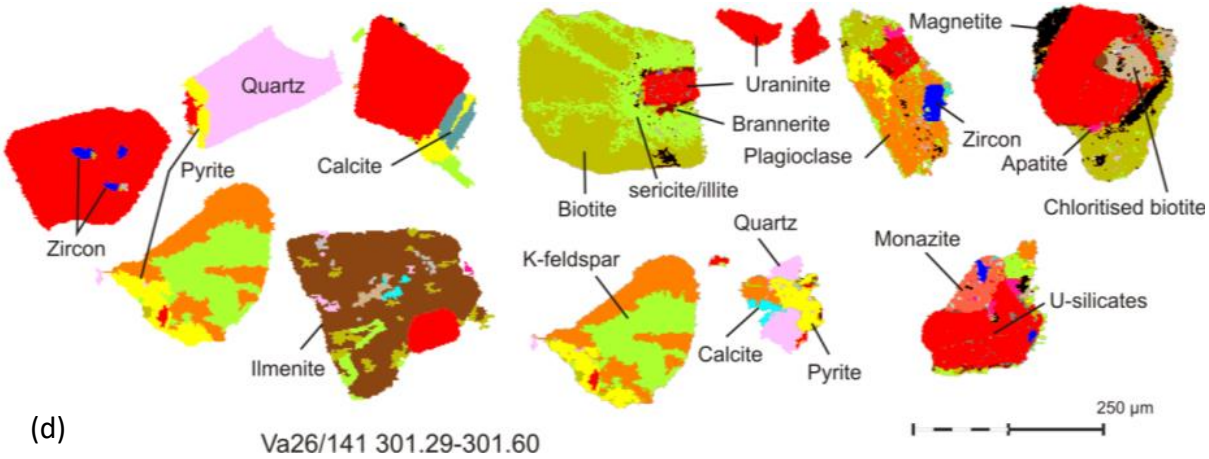



Figure 7.24 (d) Uranium mineral textures and associations of Va26 141 301.29-301.60. Uraninite is euhedral and is associated with biotite, chlorite, phosphates (monazite) ilmenite and zircon. Sulphides are particularly abundant in this leucogranite sample hosted by banded - mottled Rössing Formation gneiss. Pyrite is the major sulphide, and is accompanied by molybdenite in one of the specimens. An early generation of uraninite occurs as euhedral inclusions in feldspar, while a later generation of uraninite contains inclusions of zircon and biotite. Degradation of the host phases surrounding uraninite alters K-feldspar and biotite to clay, voids surrounding the uraninite have been filled with Fe-oxides.

### *Valencia Surface Samples*

The VALG 11 and VALG 26 samples represent leucogranites that were emplaced into the Rössing- Chuos Formations and Karibib-Kuiseb Formations, respectively. However, the mass of granite limits the ability to pinpoint the specific stratigraphic unit. The two samples exhibit contrasting uranium mineralogy. The VALG 11 sample is dominated by euhedral uraninite, hosted in plagioclase (interpreted as albite rims around uraninite) while the VALG 26 sample contains an appreciable proportion of coffinite. Both samples contain uraninite as inclusions in accessory phosphates and in compound mineral clusters of Fe-Ti oxides with biotite.

There is some alteration in the VALG 11 sample, signifying that sub solidus reactions may be taking place after uraninite crystallisation. U-silicates replace uraninite, and magnetite fills the cavities in the alteration halos that surround the radioactive minerals. Coarse-grained, anhedral monazite hosts apatite, zircon, thorite, and uraninite inclusions (Figure 7.25). VALG 26 has a very high proportion of U-silicates compared to the Valencia sample set; coffinite has nearly completely replaced uraninite and thorite in some mineral grains. The sample also contains anhedral monazite and compound grains of magnetite-pyrite-uraninite-coffinite-biotite. The compound grains are fragments of hydrothermally altered

portions of the rock. Another prominent alteration feature includes calcite inclusions in uraninite.

Replacement textures appear to be related to two events. One in which coffinite replaces uraninite/thorite, followed by Fe-oxides (magnetite) filling cavities in the altered uraninite-coffinite grains. Uraninite and U-silicates fill cleavage fractures in large feldspars, which show coarse albite exsolution textures (orange streaks on coarse K-feldspar, Figure 7.26).

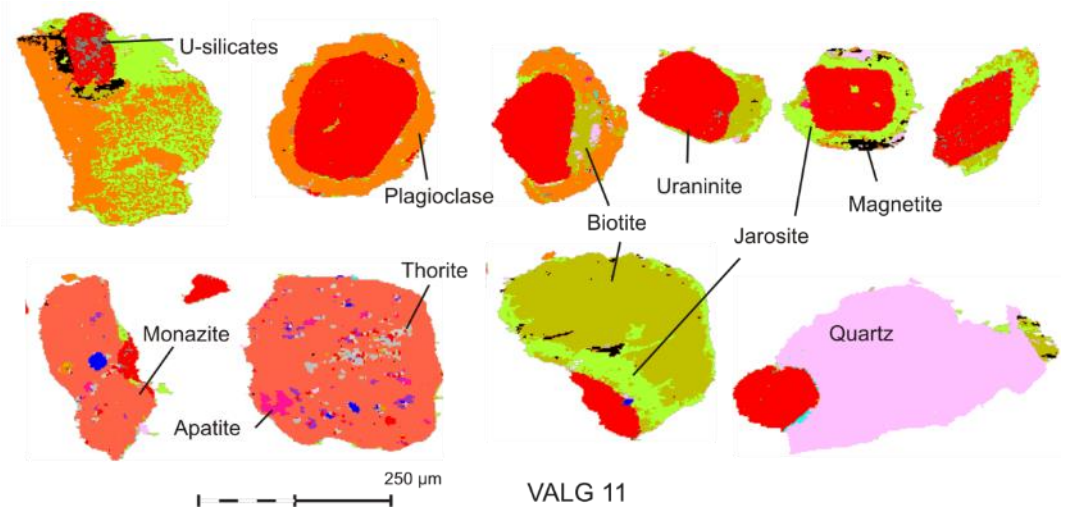



Figure 7.25 Mineral map features of VALG 11. Uraninite is coarse-grained (>100 µm) and is hosted in K-feldspar, quartz and biotite. Alteration of the biotite and feldspars results in albite and clay halos, respectively, around the radioactive minerals. Anhedral monazite hosts fine-grained uraninite, zircon and thorite.

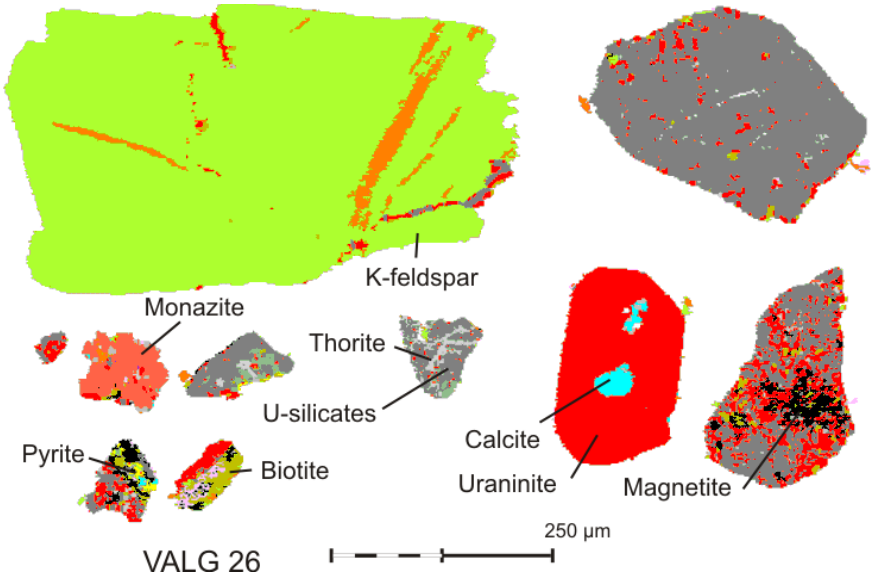



Figure 7.26 Mineral map features of VALG26. Uraninite tends to be fine-grained, and large grains have mostly altered to coffinite/uranophane. Albite, and secondary uraninite and coffinite/ uranophane fill the cleavage planes of K-feldspar. Unaltered uraninite shows evidence of cavities, which are filled with calcite.

## 7.5 QEMSCAN Discussion

### *Mineralisation Trends*

$S^-$ plays an important role in reducing hydrothermal U into insoluble state and is discussed in detail by Cuney and Kyser (2008). The prevalence of sulphide in the Husab ores may therefore be the evidence of the primary role of sulphur interaction with the invading leucogranite and fluids; the reduced sulphides providing $Fe^{2+}$ and promoted uraninite crystallisation in localised abundances near metasedimentary contacts.

Where sulphide is absent or in low abundances, Fe tends to accompany uranium mineralisation. Oxidised Fe is the most obvious indicator of uranium mineralisation in the leucogranites, as Fe is the most likely reducing agent of soluble U in magmatic U systems (after Cuney and Kyser, 2008). Magnetite is particularly abundant in the Goanikontes ores, and relationship between Fe and mineralisation may be investigated further by geochemical study. There are however, multiple Fe-bearing minerals in the leucogranites which may limit any conclusive findings.

*Biotite and mineralisation*

The uraniferous sheeted leucogranites host chlorite and epidote, which is not stable under granulite conditions (Waters, 1989; Moore and McStay, 1990). These minerals typically form from the breakdown of biotite, and their textural relationship with primary ore suggests that fluid flux perpetuated for some time after granite crystallization and at least the formation of the first generation of uraninite brannerite and betafite crystallization. The abundance of epidote also supports the interpretation that most of the mineralised leucogranites underwent some form of alteration after emplacement, and therefore after peak metamorphism.

Biotite and uraninite are closely associated at all of the Central Zone primary deposits:

- Biotite in uraniferous granites is almost always chloritised as a result of late fluid alteration;

- Biotite textures such as skeletal blades and irregular grain boundaries, biotite nests/enclaves occur in many uraniferous leucogranites;
- Altered biotite hosts exsolved magnetite-ilmenite, which may be indicators of relative oxidation-reduction conditions;
- Biotite hosting uraninite inclusions are observed in samples from all the deposits in this study; and
- Fluorite is particularly abundant as an inclusion in biotite, with the Husab deposits potentially hosting the highest concentrations.

The above observations indicate that biotite is in variable equilibrium with the melt, that a significant component is entrained, and that biotite may provide an important source of Fe to the REDOX system as a result of alteration. Fluorite abundance may be seen as a relative indicator of the capacity of the melt to host dissolved uranium, and as an indicator of the abundance and melt-equilibrium of halogen-bearing minerals in the source rocks. At the same time, the relative paucity of biotite also indicates low degrees of partial melt, and relatively dry magma.

The brannerite and betafite-bearing leucogranite samples from the Husab deposit resemble the textures and coloration described at locations around the Rössing deposits. The granites typically host entrained mafic components, and visibly abundant Ti minerals. The location of the intrusives within the upper cordierite gneiss package is also consistent with observations in Cuney (1980b), Herd (1996), Nex *et al*. (2003) and Abraham (2009). Further investigation requires systematic geochemical analyses to measure the abundances of indicator elements such as Nb (in betafite); Y (in brannerite) and Ti.

*Primary and Secondary Uranium Mineralisation*

Uraninite is the dominant primary mineral, it occurs as relatively coarse (>200 μm) euhedral crystals in all of the primary deposits. The Husab uraninite is the most coarse-grained in the study set, followed by the Valencia samples. The coarse-grained, predominantly euhedral uraninite is probably of magmatic origin, however, euhedral uraninite is also present in secondary textures in biotite and in fractures and voids (Figure 4.43, Chapter 4). Euhedral

uraninite is also closely associated with pyrite veins, which are more than likely late in the paragenetic sequence, given the pyrite's crosscutting nature in the granitic and metasedimentary host rocks (e.g. Figure 4.44, Chapter 4). The textures observed in the petrographic study (section 4.4, Chapter 4) are largely reflected in the QEMSCAN mineral maps. Fine-grained cubic uraninite occurs in replacement veins, along biotite cleavages and within cavities in the major silicate minerals, and is thus a secondary phase derived from magmatic fluid circulation.

The other primary phases, thorite, betafite, and brannerite are comparatively rare, and coarser-grained than the primary uraninite. Thorite is particularly rare in the Valencia samples, and in general occurs with coffinite as a solid solution series, or as relatively coarse-grained primary crystals (occasionally with ordered uraninite and coffinite inclusions).

Petrographic observation identified uranophane as a widespread mineral in the uraniferous leucogranites, an observation that is not uniformly reflected in the QEMSCAN datasets. Uranophane and boltwoodite fill silicate cavities, form halos around uraninite and coffinite, coat crystal faces, and fill mineral cleavage planes. The most likely explanation for the paucity of uranophane is attributed to sample preparation, which pulverised the material followed by heavy liquid separation techniques, which mechanically and chemically remove friable and soluble U(VI) phases. Where it is present, uranophane (and boltwoodite) tends to be more abundant in the near- or on-surface samples. The occurrence of the mineral at variable depths is attributed to the circulation of magmatic-hydrothermal fluids in the deposits, as is described for the Rössing deposit in Berning *et al.* (1986).

Certain mineral observations made with the aid of the SEM-derived graphics characterise the different deposits, as well as supporting petrologic interpretations. The primary minerals uraninite and brannerite occur with coffinite as secondary minerals in fractures, cavities, along cleavage planes, and along mineral surfaces. The presence of secondary uranium minerals within mineral cleavages, along grain boundaries, and across rock types indicates that uranium was in solution for some time after the host rocks crystallised. The uranium crystallised in either locally reduced-dominant (uraninite-coffinite>brannerite) or oxidised-dominant (brannerite>uraninite-coffinite) forms. The preference for which assemblage

formed was primarily affected by the localised conditions, which may vary within an individual sample at the mineral interface level. FeO-bearing minerals such as biotite and magnetite provide a source of reductants in soluble iron, promoting reduced type uranium minerals. These reactions are taking place at the fluid circulation stage and the role of REDOX control may be enhanced by pH at lower temperatures (as described in Cuney and Kyser, 2008). Given that FeO magnetite is an effective agent in reducing uranium in ground waters (Ervanne, 2004; Scott *et al*., 2005; Latta, 2010) the relationship between altered magnetite in the near surface samples at Goanikontes appears to be one where mobile U is trapped by $Fe^{2+}$-reduction in magnetite, at lower temperatures.

Magnetite appears to play an important role in uranium deposition in the Etango deposit; where fine-grained uraninite has crystallised in weathered magnetite in the near surface sample, and at depth less-altered magnetite does not show replacement textures with uraninite, instead uraninite-coffinite occurs as surface adhesions. The relationship is likely to have been a REDOX driven reaction of substitution in the presence of oxygen, where U(VI) and soluble Fe(II) on the magnetite surface react, simplified as such:

$$UO_3 + 2FeO = Fe_2O_3 + UO_2$$

The reaction above is a gross simplification and does not show the complex role of hydroxyl phases in uranium solubility, and is instead given as an example of $U^{6+}$ in ionic form reacting with Fe, at the expected high temperatures of deposit formation. The reaction of uranium as an oxidant with iron may explain why haematite-red staining is so much more abundant in the uraniferous leucogranites than in the earlier generations, particularly at Goanikontes where magnetite only shows oxidised alteration in the mineralised intervals of the upper Khan Formation and not in the banded gneiss hosted $C_m$-type leucogranites in the lower Khan. The presence of sulphides in the deposits, at Husab and the Ida Dome in particular, are likely to have had a weak effect on uranium solubility in the high temperature phases, although pyrite and pyrrhotite indicate abundant soluble Fe that would have reacted with the oxidised uranium-bearing fluids and thus promote $UO_2$ formation.

The alteration reaction of biotite to chlorite is a well-known alteration feature in granitic rocks and is quantified by Ferry (1985) in granites of Maine, USA, and by Eggleton and Banfield (1985) in southeast Australia. The reaction is coupled with the alteration of

plagioclase to sericitie, which is a dominant feldspar alteration feature of the mineralised leucogranites (alaskites) from all of the deposits of this study. FeO content of biotite in the Central Zone leucogranites is not quantified, however, Parry and Downey (1982) show that biotite contains approximately 14 wt.% FeO and in hydrothermal chlorite replacement of biotite FeO content is up to 23 wt.% or more. The reaction of Parry and Downey (1982) also contributes $F^-$ and $Ti^+$ in comparable mass to $Fe^{2+}$ and up to 6 mols $Cl^-/m^3$ of rock. The example is given for a quartz monzonite in Utah, USA.

Perhaps, a more applicable comparison, though not quantified chemically, is the alteration textures and mineralogy described for leucogranites in Namaqualand Metamorphic Complex in Robb *et al.* (1986) in which biotite to chlorite reactions are attributed to autohydration reactions during- or subsequent to granite crystallisation. Thus, it is asserted that the biotite is altered to chlorite in the Central Zone host rocks, as a reaction to the regional metamorphism prior to the intrusion of the sheeted leucogranites. While chlorite in the alaskites themselves may be the result of similar autohydration process', this si supported by the widespread subsolidus reaction textures that characterise the mineralised SLGs across the study region.

The chloritised biotite that characterises the pelitic units of the Rössing Formation show this alteration independently of the presence of alaskite intrusions, therefore the chlorite has likely formed prior to the post-$D_3$ intrusives, and is not a contact metamorphism feature. The chlorite in theory should have FeO available to react with the dissolved $U^{6+}$ complexes in the fluids associated with the alaskites. In addition, sphene and Fe-oxides that form as products of the chlorite reaction would provide additional reagent in the form of Ti and Fe, respectively. There is certainly good evidence of uraninite and brannerite association with Fe and Ti oxides in all the deposits of this study as evidenced in the QEMSCAN mineral maps of this chapter.

A simplified paired reaction that describes the biotite-chlorite and plagioclase-sericite assemblage of the alaskites is given in Parry and Downey (1982) as follows:

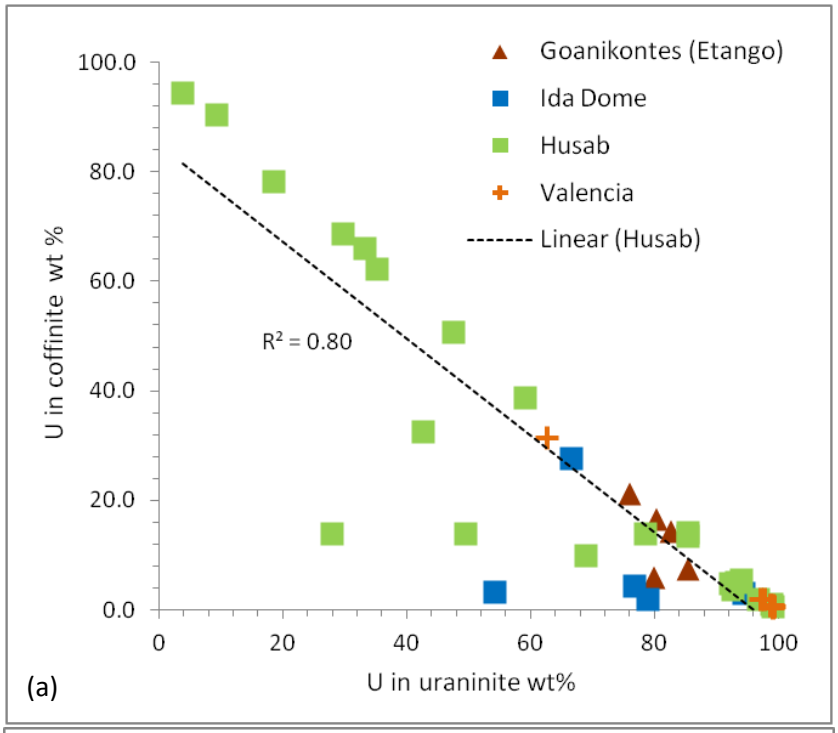
1 biotite + 0.21 anorthite + 1.64 $H_2O$ + 1.46 $H^+$ + 0.08 $O_2$ → 0.46 chlorite+ 0.11 sphene + 0.10 epidote + 0.56 muscovite* 0.63 quartz+ 0.02 (Fe-Ti oxides) + 1.46 $K^+$

### *Secondary Uranium Minerals*

There are two main generations of coffinite in the Central Zone leucogranites; one is that of replacement of primary uraninite; the other is the co-crystallisation of secondary uraninite and coffinite. Most uraninite is partially replaced by coffinite, at mineral rims, along internal fracture and cleavage planes and in net-textures, which occasionally render a specimen with a coffinite>uraninite composition. Fine-grained <µm coffinite is visible in backscatter imagery, and may illustrate inherent coffinite/silicate contamination in the primary uraninite.

The Husab deposits contain the most prevalent coffinite replacement of uraninite, where uranophane only exceeds coffinite in one of the twenty-two samples. Coffinite abundance is systematic with uraninite in most samples, with exceptions only where U in uranophane exceeds 1.5 wt.%. The strong trend shown in Figure 7.27a suggests that coffinite at Husab is primarily a result of uraninite replacement, and therefore this study presumes only a small proportion of coffinite crystallised from the magma, and that at some stage after the crystallisation of uraninite replacement by coffinite took place.

The relationship between U in coffinite and U in uraninite is less apparent in the other Central Zone deposits. Thorite and coffinite are in solid solution in certain environments, and may have a relationship in the Valencia samples, where Th and U partition into thorite and coffinite, respectively. The abundances of the two minerals show a systematic correlation only in the Valencia QEMSCAN dataset (Figure 7.27b).



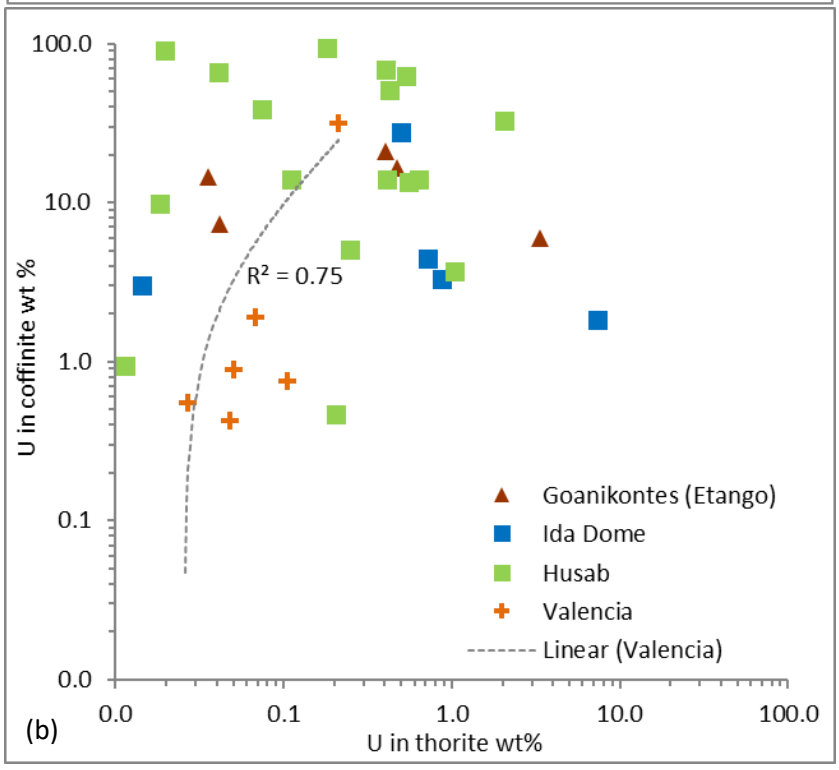




Figure 7.27 Uraninite, coffinite, and thorite phase distribution and relationships of the Central zone primary deposits. (a) Uraninite and coffinite show a systematic, negative correlation, coffinite replaces uraninite in Goanikontes and Husab samples. Husab samples deviate from the trend where uranophane hosts >1.5 wt.% of the U budget.

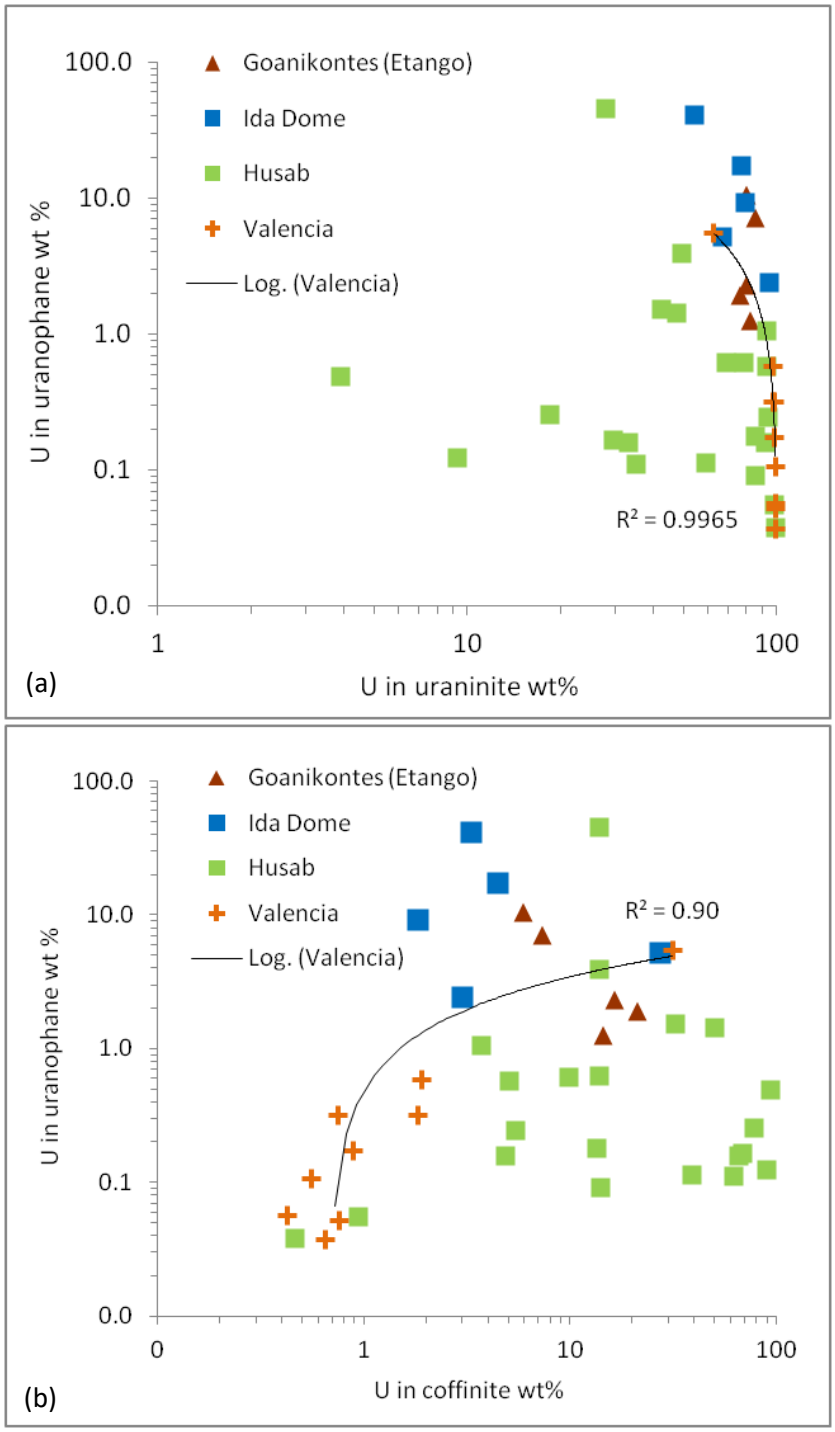
(b) Coffinite and thorite share a solid solution series but show no correlation in the sheeted leucogranites; and have formed independently.

Uraninite does not readily oxidise in ground water (Janeczek and Ewing, 1992b) thus the prevalence of uranyl oxy-hydroxides (e.g. uranophane) in the near supergene environment is the result of recirculation of already-oxidised uranium, which was present in highly mobile uranyl complexes during initial deposit formation (after Cuney (1980b). The process in the near surface environment is described in Youlton (2014) and the nature of oxidised secondary uranium formation at the Rössing deposit as an example for the Central Zone is described in Berning *et al*. (1986).

Thus, the systematic decrease in uranophane and boltwoodite abundances is attributed to decrease in acidic meteoric fluid flux with successive depth. U deportment in uraninite does not correspond well with U in uranophane, as coffinite is a major component in most U-deportment assessments.

The Valencia samples contain some of the lowest proportions of coffinite and uranophane, while the Ida Dome samples contain some of the highest proportions of uranophane. Both sets of samples show a strong negative correlation of U-deportment between uraninite and uranophane (Figure 7.28a). This suggests that the uranophane is a replacement of uraninite at these deposits. U distribution between uranophane and coffinite shows a positive correlation between the two minerals in the Valencia samples, and a negative relationship in the Goanikontes samples (Figure 7.28b).

The paucity of secondary uranium minerals in the Valencia samples is attributed to the attenuated nature of the marble packages and the geometry of the deposit. The granites have punched through the Valencia antiform and invaded the Kuiseb Formation. The schist and gneissic rocks tend to be more permeable than the calcsilicates and marbles which have tended to pond magma and fluids at the Rössing and Ida Dome deposits.




uraninite and uranophane shows a systematic negative relationship in Valencia and Ida Central samples, but less so in Husab and Goanikontes samples.

(b) U-deportment between coffinite and uranophane shows a positive relationship in the Valencia samples, and a negative relationship in Goanikontes samples.

Figure 7.28 Uraninite, coffinite, and uranophane phase distribution and relationships of the Central zone primary deposits. (a) U-deportment in

### *Betafite and Brannerite Occurrences at Husab*

Brannerite and betafite both contain an appreciable $UO_3$ content. Herd (1996) showed that Rössing betafite may host over 30 wt.% U. Samples from Husab tend to have brannerite dominant over betafite, and the relative proportions of either of the refractory minerals

being in the sub-percentage range at all the other sampled deposits. There is however, a strong positive relationship between the minerals. This is because both are predominantly oxidised phases, U is in $^{6+}$ valence state in the ideal composition of each mineral, thus, SLGs crystallising in oxidised conditions could conceivably produce bith minerals if sufficient Ti is available. Both minerals are titaniferous oxides and host appreciable REE, betafite hosts Nb, but brannerite does not. It appears that both minerals occur together in relatively uniform ratios (Figure 7.29) but where concentrations are in excess of 1 wt.% samples are either betafite, or brannerite dominant. This may be directly related to the abundances of key elemental components, such as Nb.

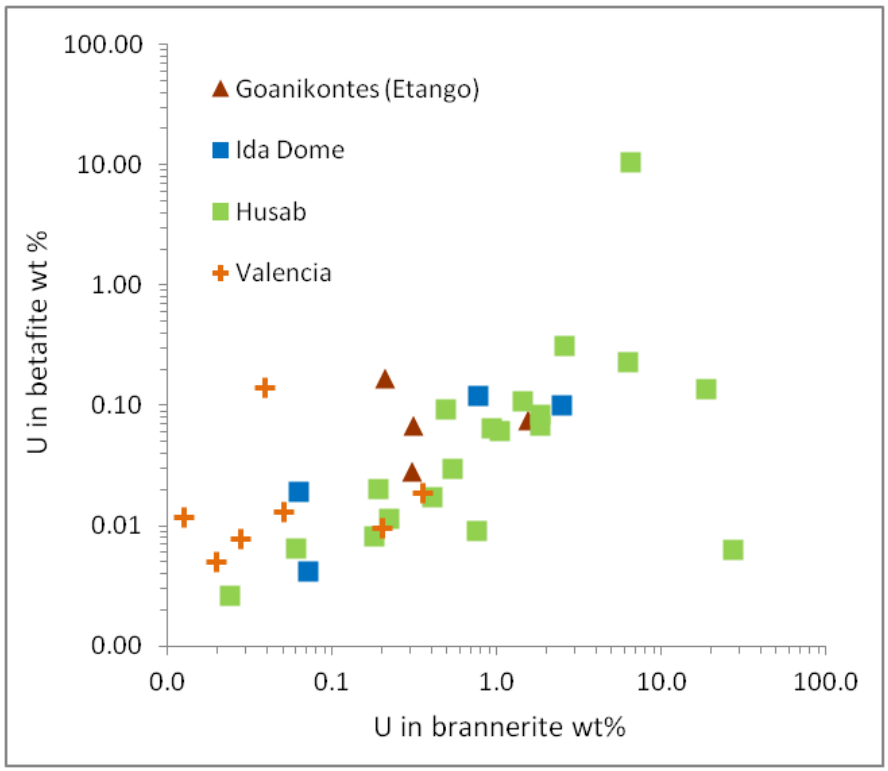



Figure 7.29 U-deportment between brannerite and betafite. The minerals have a positive relationship in the Husab and Valencia leucogranites. Three Husab samples host >10 wt.% of U in one of the refractory mineral species. Petrological Indicators.

Zircon, monazite, and xenotime textures and relationships show that the sheeted leucogranite melts are in variable states of equilibrium with the uranium-bearing silicate and phosphate minerals in the source rocks. Coarse-grained anhedral zircon hosts uranium minerals and quartz inclusions in the Ida Dome samples, whereas zircons are relatively inclusion-free in the Valencia samples. The abundance of zoned zircon (e.g. Chapter 4, Figure 4.39), and the variation in metamictisation in petrographic observations show that

the melt is locally variable; well-zoned zircons are magmatic, while zircons that contain abundant inclusions and show anhedral grain edges are more likely inherited. The inclusion of inherited zircons is in some ways supported by the low degree of partial melt evident in the pronounced -Eu of the alaskites, throughout the Central Zone (this study).

In addition, QEMSCAN mineral maps of Valencia samples contain abundant zircon with uraninite attached and clustered, anhedral zircon with uraninite 'cement' support a melt with entrained zircon serving as a nucleation site for new uraninite crystallisation. Inherited monazite is anhedral, and contains inclusions of thorite and uraninite, and are likely a source of Th other than $Th^{+}$ transported in the melt.

The Valencia sample group contains the only specimens with coarse-grained, anhedral monazite that hosts uraninite, thorite-coffinite, and zircon inclusions, as monazite in the other deposits tends to be inclusion-free. Thus, the monazite at Valencia has acted much like the zircon at Ida Dome, as a transport medium for entrained U and Th. The low proportion of thorite in the Valencia samples (0.1 wt. % vs. 0.65 wt.% group average) is attributed to Th being locked in monazite in the source rocks.

### *Speciation and Refractory Mineral-Hosted Uranium*

Uranium-bearing minerals fall into two categories in the alaskite-hosted deposits of the Central Zone, the first is the uraninite dominated occurrences, where dissolved U is reduced and bonds with $O^{-}$ as a function of REDOX change during wall rock assimilation (as is given for the type example at Rössing, e.g. Jacob, 1974b); the second are the occurrences in which betafite and/or brannerite are the dominant accessory mineral hosts of U; and the third are the category of hydrated uranium silicates, which are either in $U^{4+}$ or $U^{6+}$ coordination as in coffinite or uranophane and boltwoodite, respectively. In the latter of the three, textures in hand specimen and outcrop invariably indicate that the minerals have formed after granite crystallisation (Chapter 4) and in microscopic observation coffinite appears to be predominantly if not solely a replacement of uraninite. Betafite and brannerite mineralisation requires $U^{6+}$ oxygen coordination and therefore dissolved uranium in the melt is either predominantly $U^{6+}$, or dissolved $U^{4+}$ is converted to predominantly $U^{6+}$ by

reaction with Fe and/or Ti during host-rock interaction. More likely a combination of U valence states exists in the magma and only $U^{6+}$ is incorporated into betafite and brannerite while $U^{4+}$ is incorporated into uraninite.

The starkest contrast between the brannerite-dominated mineralisation occurrences and those that are uraninite-coffinite dominated is the oxidation state of U. In brannerite and betafite U is in $6^{+}$ coordination, whereas in uraninite $UO_2$ usually is in excess of $UO_6$ (e.g. Korzeb *et al*., 1997; Janeczek and Ewing, 1992a and 1992c, this study Chapter 8).

What the oxidation state of U was in the alaskite magma is probably a combination of $U^{6+}$ and $U^{4+}$, as $Th^{4+}$ is also soluble. Th is presumed soluble because concentrations approaching 500 ppm Th cannot be attributed to accessory monazite alone, and the abundance of thorite immediately implies Th was transported in the magma. Given the abundance of magnetite visible in hand specimen and in microscopic scale (Chapter 3 and Chapter 4) and the relative paucity of nickel sulphides the following is implied for the silicate melts that form the alaskite deposits:

> *"…haematite-magnetite or $Cu_2O$-CuO buffered silicate melts, carry up to 3 times more $U^{6+}$ than corresponding NiO-buffered melts in which uranium is in the $U^{4+}$ state"* (after Peiffert *et al*., 1994, 1996, in Skirrow *et al*., 2009).

The prevalence of centimetric, crystalline fluorite veins, and microscopic fluorite in association with alaskites and uranium minerals, respectively, at all of the Central Zone Primary U deposits (this study), the peraluminous-metaluminous composition of the alaskites and the uranium concentrations that may reach sub-percentage levels suggests that fluorine has played a significant role in the solubility of the uranium in the melts. In addition, it is well appreciated that country rock interaction and indeed assimilation have played the prominent role of focussing the uranium mineralisation within a relatively narrow stratigraphic window (e.g. Jacob 1974b; Cuney, 1980a; and Nex, 1997), however, this role is heterogeneous within the deposits because there are $U^{6+}$ coordinated minerals such as betafite and brannerite detected in numerous samples (this Chapter). Betafite is present in abundance at the SH area at Rössing (Cuney, 1980a and 1980b; Herd, 1996; and Nex *et al*., 2003) and brannerite abundances are comparable to uraninite within parts of the Husab deposits. The causes of betafite prevalence over uraninite are addressed through

fluid inclusion studies in Cuney (1980b) and fluid extraction studies (Nex *et al*, 2003) for the Rössing deposit, but to date the nature of brannerite-dominant mineralisation within locations of the Husab deposits remains open to interpretation. According to the models of Peiffert *et al*. (1994) and (1996) the concentrations of uranium in the alaskite melts exceed the capacity of peraluminous melts with magnetite-haematite buffers, thus HF or NaF fluid compositions are required to attain the 1 000 to 10 000 ppm U-concentration ranges present in the alaskite.

The QEMSCAN study identifies a close association with Fe-Ti minerals, particularly rutile, and petrographic observations (Chapter 4) highlight the prevalence of fluorite in association with brannerite-dominated mineral enclaves (also Chapter 4). It appears that $U^{6+}$ may become complexed in the presence of Fe and Ti and form compounds in conjunction with, or even before the crystallisation of $UO_2$ which would be a product of metasediment driven REDOX buffers (as is the model for the Rössing deposit). What remains uncertain, is whether or not the presence of fluorine solutions inhibits or promotes the preferential crystallisation of uraninite over brannerite. What is clear in the textural analysis of the QEMSCAN images is that uraninite and betafite may replace, or crystallise along mineral cleavage and fracture planes of brannerite, but there is no evidence of brannerite crystallising along uraninite mineral cleavages and fracture planes. Sample RDD008 284-285 m from Zone 1 (Figure 7.30) shows primary euhedral uraninite, with K-feldspar and clay alteration halos. The uraninite is also a site for localised Fe-oxide deposition as magnetite-haematite and coffinite, it is interpreted in this study as a reaction between reduced U in $UO_2$ and soluble Fe, to form $FeO.Fe_2O_3$. Though the presence of oxygen and carbonate may result in ferrous hydroxides and limonite which may not be discerned adequately by the QEMSCAN.

Betafite appears to be replacing brannerite along two cleavage directions, these two minerals are not in solid solution, but the image shows betafite crystallising at the brannerite grain edges (lower left, Figure 7.30) In another grain, uraninite is crystallising along preferred cleavages in brannerite (centre right, Figure 7.30), and within the same grain betafite has also formed along the cleavage planes. It appears that brannerite is early in this sample and has undergone alteration, where mobile U, Nb, Ti, and Fe fill fracture planes within the mineral. Uraninite or betafite may represent the dominant U-mineral

species in a given sample. This is largely dependent on the local oxidising conditions. Where reducing conditions prevail $U^{4+}$ will dominate and preferentially crystallise $(U^{4+},U^{6+})O_2$ in the absence of external influences. Where oxidising conditions prevail $U^{6+}$ may concentrate in more complex minerals such as betafite and brannerite. Supergene processes my leach $U^{6+}$, through the oxidation of uraninite, artificially increasing the proportions of 'primary' betafite and/or brannerite.

Primary thorite contains cleavage-parallel inclusions of uraninite exsolution, the lack of uraninite replacement at the margins support an interpretation of uraninite as an immiscible phase in a crystallising silicate. Thorite, uraninite, betafite, and brannerite inhomogeneity textures in petrographic and QEMSCAN observation necessitate analysis of the compositions of the U and Th-bearing phases by electron microprobe, the results of which are presented in Chapter 8. An example of varied uranium mineral mineralogy is given in Figure 7.29 and is intended to pre-empt the detailed mineral composition study given in Chapter 8.

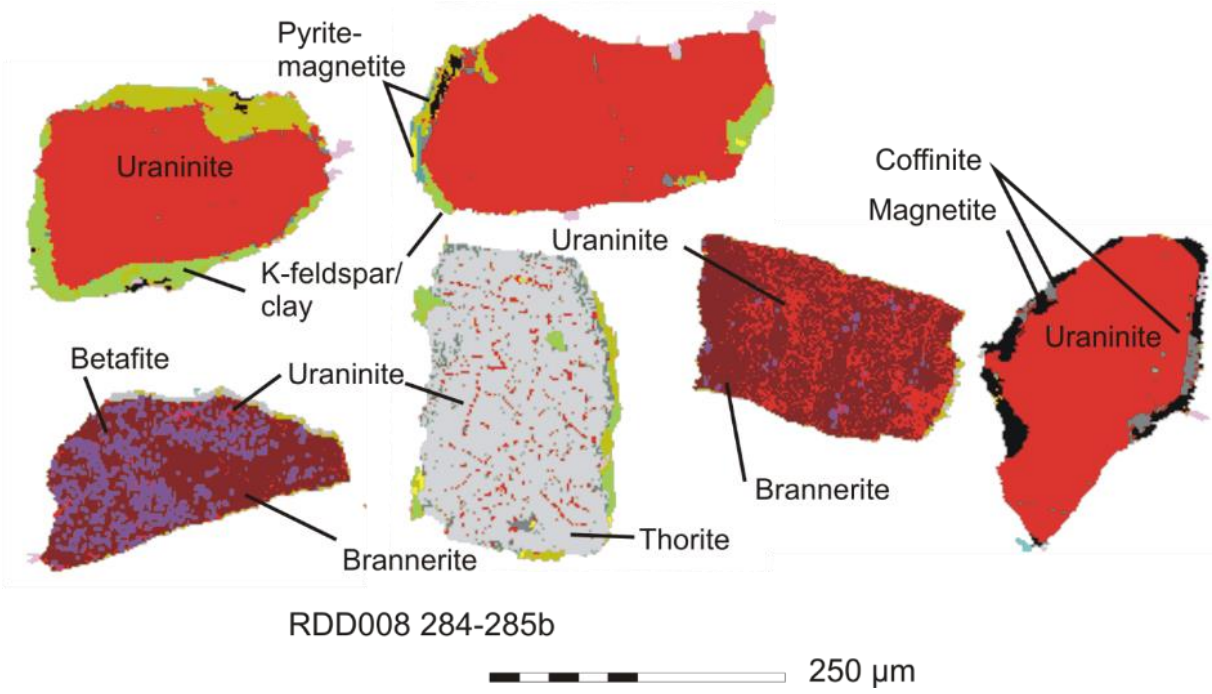
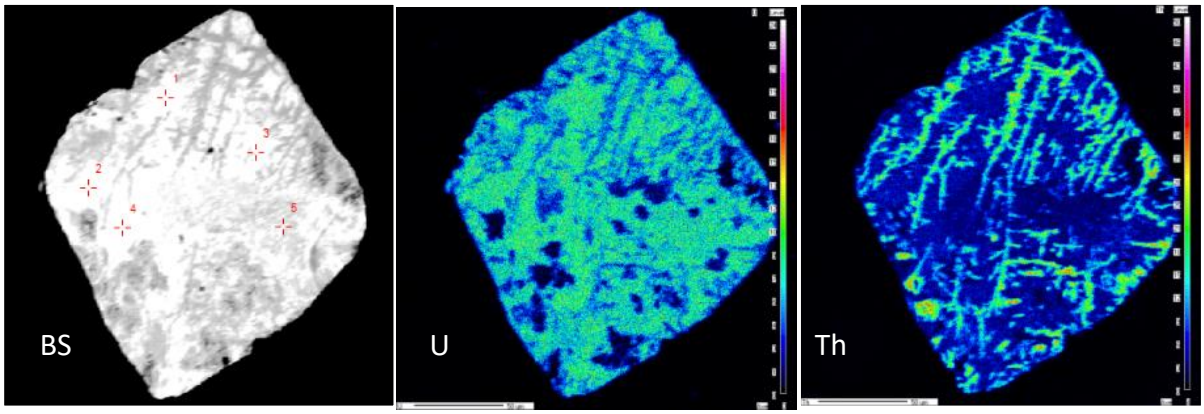



Figure 7.30 Primary uraninite-thorite-brannerite-betafite relationships with mobile U. Primary uraninite is euhedral and of magmatic origin, it is usually hosted within feldspar or quartz, and rarely within a single-phase host. Secondary uraninite occurs within primary brannerite and betafite, showing cleavage or fracture-controlled distribution from the outside inward. Uraninite in thorite however, is a product of solid solution, where excess U forms uraninite within thorite, with no uraninite at the grain boundaries.

# CHAPTER 8 URANIUM MINERAL DESCRIPTION AND COMPOSITONS AT THE PRIMARY DEPOSITS




Backscatter electron image of 120 µm uraninite-coffinite grain from the Valencia deposit (left). The inhomogeneous backscatter reflectance shows the densest U-metal distribution is toward the centre of the specimen (centre). Coffinite has replaced uraninite at the edges; however, the ordered network of dull reflectance corresponds to the Th channel on a WDS scan (right). It is interpreted as a primary feature of uraninite and thorite intergrowth since Th is immobile and less likely to crystallise as a replacement texture from a dissolved state in a hydrothermal solution.

## 8.1 Introduction

Uraninite is the most abundant uranium mineral in the samples of uraniferous sheeted leucogranites from granite-hosted deposits of the Central Zone. In granitic systems, it crystallises primarily from silicate melts and associated fluids, where a change in REDOX of the host fluid/magma is the main driver for $U^{6+}$ reduction and uraninite crystallisation. The uranium deposits of the Central Zone host uraninite, coffinite, uranophane, betafite, brannerite, monazite and thorite species; coffinite is almost always a product of uraninite alteration by Si-rich hydrothermal fluids and is itself a $U^{4+}$ mineral. Uranophane however, forms from $U^{6+}$ which may come about by oxidation of uraninite in the late sub solidus environment; Circulation of residual fluids shortly after granite crystallisation and remobilisation of highly soluble $U^{6+}$ complexes in the near surface environment being the chief mobilisation agents of U redistribution.

The primary uraninite shows evidence of variable composition; inhomogeneous optical and backscatter electron (BSE) reflectance; pitted surfaces; inclusions; and reaction textures at the grain edges all reflecting alteration during late Si-rich fluid flux. The unaltered portions of a uraninite therefore represent the best possible sample material for analysis of primary uraninite compositions. Coffinite and uranophane (and other uranyl-complexes) are the predominant alteration phases of uraninite, formed under reducing and oxidising conditions, respectively (Janeczek and Ewing, 1992b) and are observed in samples from all the deposits of this study. Certain deposits host a minor population of uranium-bearing refractory minerals, which may dominate over uraninite in certain localities.

Modern, hard-rock uranium mining continues to refine efficiencies, from employing large-capacity mining equipment to investigating more than one mineral processing circuit for different ore categories. Supporting the drive to efficient extraction not only requires an understanding and quantification of the nature, variability, and distribution of the uranium-bearing phases, but also a description and quantification of the compositional variations within the uranium minerals. Greater environmental awareness and responsibility add to the need for mineral population analysis when exploiting increasingly lower grade, high tonnage deposits (after Bhargava *et al.*, 2015).

$U^{4+}$ in uraninite does not readily oxidise to $U^{6+}$ in meteoric conditions, and it is in fact the inhomogeneity of the primary uraninite that is responsible for the availability of $U^{6+}$ to the system (Frondel, 1958; Janeczek and Ewing, 1992a, 1992c; and Korzeb *et al.*, 1997, describe the process). The formation of uraninite under oxidising conditions was proposed by Frondel (1958) while investigating impure natural uraninite and thorite.

The presence of trivalent and divalent cations in uraninite is given as supporting evidence that uraninite hosts $U^{4+}$ and $U^{6+}$ in its structure. Thus, the compositions of the uraninite at each deposit may be a key influence on the abundance of uranophane in a system. Given the diversity of geological settings among the deposits, the efficiency of the primary mineralising mechanism, the REDOX barriers and the composition of uraninite at each deposit may also be deposit-specific. This chapter specifically addresses the implications of uraninite composition in terms of uraninite genesis and subsequent alteration within each deposit.

***Previous Work***

Publicly available chemical composition of the primary uraninite in Central Zone deposits is however, limited to a small number of studies.

A limited number of microprobe analyses were conducted between 1968 and 1969 at the National Institute of Mining, South Africa and given in a now-declassified report of uranium mineralogy by Hiemstra *et al.* (1968)[48]. Two studies of uraninite compositions were undertaken in recent time; Cross *et al.* (2009) analysed a uraninite population from metallurgical feedstock of the Husab mine, for the purposes of geochronological investigation of uraninite; and Mercadier *et al*. (2011) and Mercadier *et al.* (2013) included Rössing uraninite for REE content as part of a global uraninite composition study, specifically for REE content.

A recent example of a study of uraninite composition in granite-hosted uranium deposits is described by McKechnie (2012) at the Fraser Lakes and Moore Lakes properties in the Bancroft District, Canada; that also summarises relevant previous work in the area. The uraninite compositions given in McKechnie (2012) formed at ca. 1.8 Ga, during Hudsonian orogenic events. The uranium mineralisation of the ca. 310 Ma Hercynian-age Erzgebirge metallogenic province of Germany and the Czech Republic is described Förster *et al.* (1995) and Förster (1999) and serve as a younger example of orogenic primary uranium deposit types. Other granite-hosted uranium studies include ca. 230 Ma Indosinian-age two-mica granites of the Liueryiqi deposit in China (Min *et al.*, 2005); the ca. 603 Ma thorite-bearing anorogenic granites of the Egyptian Shield (El-Naby., 2009); the Devonian sediment-hosted ca 304 Ma Ruggles pegmatite New Hampshire, U.S.A. Korzeb *et al.* (1997); and granites described by Rafalskiv (1963) in Russia.

Compositions of uraninite from a metallurgical composite at Husab are given in Cross *et al.* (2009). Studies that examined the compositions of natural uraninite include, but are not limited to, Janeczek and Ewing (1992a, 1992b, 1992c); Alexandre and Kyser (2005); Cuney and Brisbin (2009); Cuney (2010); Mercadier *et al.* (2011); and Mercadier *et al*. (2013).

[48] The de-classified reports are available to the public at the Namibian Ministry of Mines and Energy Library in Windhoek.

### *Approach*

The systematic analysis of uraninite compositions of specimens from the Central Zone deposits provides some indication of the probable conditions during and subsequent to mineralisation:

- Euhedral, relatively unaltered uraninite presumably forms under magmatic, or even hydrothermal conditions, euhedral uraninite within the quartz-feldspar matrix potentially represents the least altered of the early generation mineralisation. Euhedral uraninite in clearly altered quartz-feldspar matrices would represent mineralisation subsequent to the granite emplacement at the deposits. Thus, the closest approximations to relative $U^{4+}$ and $U^{6+}$ abundances in the mineralising fluids during initial formation of the deposits are preserved in the compositions of the least-altered primary uraninite specimens, hosted in the quartz-feldspar matrices of the alaskites;
- U:Th in unaltered primary uraninite indicates relative U and Th abundances mobilised from the source material(s) if the volume of Th hosts such as monazite, thorite and coffinite are negligible;
- U:Th of uraninite is not necessarily an indication of the state of equilibrium of predominantly U-bearing or Th-bearing minerals with the melt, but it is a useful ratio to assert U:Th of the source rocks; similarly
- The various contaminant elements in uraninite reflect to some degree the presence of typical accessory minerals in the system, for example, Y in uraninite would suggest the phosphate xenotime may be a component of either the source material or represent evidence of alaskite interaction with Y-bearing host rocks.

### *The Significance of Uraninite Composition in The Granite-Hosted Mineral Systems*

Petrographic and automated SEM studies in Chapters 4 and 7 showed that uraninite and coffinite are the dominant uranium minerals in the Central Zone deposits. Common primary uranium-bearing phases also include thorite, brannerite, and betafite, which appear to have a

minor distribution in all samples from all deposits in this study, and share a systematic relationship in relative abundances. The refractory mineral betafite, which hosts ~30 wt.% U or more, is described at the Rössing deposits in variable context in Cuney (1980b); Herd (1996); Nex *et al.* (2002); Nex *et al.* (2003); Kinnaird and Nex (2007); and Abraham (2009). The researchers describe in detail the nature and distribution of the refractory phases and offer possible explanations for the existence of the mineral at the other deposits of the Central Zone.

In contrast, the nearby Husab deposit reports brannerite as the dominant uranium-bearing refractory mineral, and that it is present in rare, but significant proportions in certain leucogranites that invade the semi-pelitic, upper Rössing Formation.

Uraninite compositional data may have useful implications in the exploration, mining, and processing industries for the following reasons:

1. Impurities in uraninite are shown by Finch and Ewing (1992) and Alexandre and Kyser (2005) to have an influence on the stability of uraninite in natural systems, and thus affect the distribution of primary and secondary uranium ore minerals in hydrothermally altered deposits;
2. Impurities in uraninite are reported by Grandstaff, (1976); Casas *et al.* (1998); Ring (1979); and more recently in Bhargava *et al.* (2015) to influence uraninite leach susceptibility in commercial applications;
3. Ram *et al.* (2013) show that lead impurities within uraninite preferentially leach during processing then precipitate as sulphate, which inhibits further reaction extraction. The Pb content of the Central Zone uraninite is variable, because the uraninite is old, radiogenic Pb proportions may approach 10 wt.% while alteration subsequent to crystallisation may preferentially leach Pb from a given ore sample.
4. Compositional data of pristine uraninite specimens should reflect the REDOX conditions during crystallisation from the magma and associated fluid phases. Compositions of altered uraninite represent subsequent late-magmatic and/or metasomatic conditions.

### *Replacement and Contamination Trends in Uraninite*

Uraninite is rarely pure $UO_2$ in nature and contains impurities of cationic substitution of Pb, Th, Ca, Y and REE which take place during crystallisation, alteration, and in the case of Pb, through radiogenic decay. Bhargava *et al.* (2015); Mercadier *et al.* (2010); Deditus *et al.* (2007); Förster (1999); and Janeczek and Ewing (1992a and 1992b) describe the substitutions in various settings.

Certain other elements, Al, Fe, K, P, and Si are quantified in uraninite specimens of this study and reported as uraninite contaminants in McKechnie *et al.* (2013); Cross *et al.* (2009); Alexandre and Kyser (2005); and Finch and Ewing (1992). The composition of natural uraninite is so varied that Janeczek and Ewing (1992b) give the formula:

x is the amount of excess oxygen equal to $U^{6+}$, y is the number of trivalent cations (typically Y and REE), z is the number of divalent cations such as Pb and Ca, and v is the number of uranium vacancies in the formula unit:

$$(U_1\text{-}U^{6+}\text{-}REE\text{-}Pb,Ca\text{-}v^{4+}U_x^{6+}REE_y^{3+}Mz_z^{2+4-v})O_{2+x-(0.5y)-z-2v}$$

With the above formula in mind, representative samples of the uraninite populations of the Goanikontes, Hildenhof, Husab, Ida Dome and Valencia deposits were investigated by electron probe micro-analyser or EPMA. The EPMA study employs a stoichiometry calculation macro in Microsoft Excel to recalculate $UO_2$ and $UO_3$ ratios in charge balanced analyses of uraninite, coffinite, thorite, betafite, and brannerite. Uraninite, as the primary ore accounts for the bulk of the analyses and interpretation and discussion.

### *Industrial Application*

The uranium mining industry processes uraninite more than any other mineral, and the primary deposits of the Central Zone include some of the lowest-grade uranium deposits that process the mineral (after Cuney and Kyser, 2008). Bhargava *et al.* (2014) provide the most concise and recent summary of the knowledge base on the subject of uranium leaching from uraninite. Alexandre and Kyser (2005) and Finch and Ewing (1991, 1992) show that uraninite

stability in natural systems is affected by the nature and amount of impurities, while Ram *et al.*, (2013) and (2014); and Ring (1979) have reported that uraninite composition influences uranium leaching in commercial applications.

Thus, acquiring the compositions of the uraninite populations of the Central Zone primary uranium deposits serves two objectives:

1. To quantify the uranium compositional variations;
    - Derive interpretations of the conditions for uraninite genesis; and
    - subsequent alteration trends which took place at each deposit; and
2. Provide quantitative uraninite compositional data for samples from each deposit, which may have application in refining and improving uranium-leach test performances. Especially where marginal grade ores are investigated as part of conventional mining and processing operations.

## 8.2 Samples and Methodology

The sample specimen collection of this study consists of polished grain mounts and polished thin sections of Husab specimens, and polished grain mounts of the Goanikontes, Hildenhof, Ida Dome, and Valencia Deposit specimens. All of the polished grain mounts are from the same collection utilised in the QEMSCAN study of Chapter 7. In summary, the EPMA sample collection comprises:

- Four thin sections from the Husab Deposit, all from the RDD373 drill hole;
- Two sets of polished grain mounts from the RDD008 drill hole from Husab Zone 1 and RDD006 drill hole from Husab Zone 2;
- Two polished grain mounts of mineral separates of core from the Va26 113 and Va26 141 diamond drill holes, sampled at 225 m and 290 m, respectively at the Valencia deposit;
- One polished grain mount each of heavy mineral concentrates from surface samples sourced at Hildenhof (HILG 21); Ida Dome (IDAG 43); and Valencia (VALG 11).

There are certain limitations in collecting and analysing representative mineral specimens; the size of deposits such as those at Husab and at Goanikontes each have strike lengths of granite-hosting metasediments of three- or more kilometres. The diversity of granite and metasedimentary interactions at each deposit adds to the complexity of sampling uraninite expected to be representative of a deposit. Thus, the samples of this study were selected for the following reasons:

- The two Goanikontes core samples represent alaskites that intrude the Chuos- and Khan Formations. A sample in the supergene zone within the Chuos (~43 m downhole, or 37 m from surface) and a sample from a depth of ~353 m downhole, (or 305 m from surface) within the Khan Formation;
- The Ida Dome core samples represent uranium mineralisation in alaskites intruded into the lower Rössing- and upper Khan Formation at Ida Central;
- Five individual uraninites were analysed for the Hildenhof deposit from a single grain mount of heavy mineral separates;
- Thirteen Husab drill holes and twenty-two QEMSCAN samples represent a selection of the more abundant alaskite textures at the deposit. The EPMA samples are from Zone 1 (hole RDD008); Zone 2 (hole RDD006); and a uraninite specimens from the RDD373 hole (also Zone 1). The uraninite from RDD373 intersections comes from alaskite that hosts abundant uranium-bearing refractory minerals (up to 40 wt.% of U mineral population); and
- The Valencia uraninite specimens are sourced from two drill holes (Va26- 113 and 141) and a surface sample (VALG 11).

***Uranium Mineral Compositions By EPMA***

Mineral composition studies provide an opportunity to compare the primary U deposits in microscopic detail. It also provides a means of comparing the primary mineralogy and contribute to paragenetic interpretations. Quantification of textural and compositional variation between the primary U phases and secondary U phases of the deposits are possible with the use of a quantitative analyser. The Electron Probe Micro-analyser at the Department of Geology at Rhodes University provided all of the analytical data for this thesis. The

extensive database of petrographic and SEM data available for all samples provided an effective basis for EPMA. Samples were pre-selected prior to arriving at the Electron Probe Micro-analyser Laboratory. The EPMA at Rhodes University is a JEOL JXA 8230 Superprobe, which operates with five wavelength energy-dispersive crystal detectors. Appendix G1 describes the EPMA standards, calibration and operating procedure of the probe.

### *Stoichiometry Formulae Recalculation*

One of the principal aims of this chapter is to assess the ratios of oxidised and reduced uranium in the ore mineral phases. As is outlined in Janeczek and Ewing (1992b) natural uraninite is comprised of an appreciable proportion of $UO_3$ which is related to the environment in which the uraninite crystallises. In addition, the ratios of $U^{4+}$ and $U^{6+}$ may also be interpreted as indicators of sub solidus alteration conditions. $U^{6+}$ may be preferentially leached from uraninite under oxidised conditions at a range of temperatures, and in high temperature conditions fluids may oxidise $U^{4+}$ in uraninite, a process described for New Hampshire, USA, and pegmatites in detail by Korzeb *et al*. (1997). The interpretation of alteration of uraninite through U ratios of course can only be done in context, with suitable 'pristine' uraninite compositions serving as benchmarks of original composition. High resolution BSE imagery is another essential dataset for any meaningful interpretation.

An Excel macro was provided by the EPMA laboratory at the Rhodes University Department of Geology and is compiled by Dr G. Costin. The conditions of calculation are the same for all uraninite and summarised in Appendix G2. Essentially uraninite is normalised to two oxygen and the ratios of $UO_2$ and $UO_3$ weight percentages adjusted to achieve a cation charge balance sum of ~1. An example of a recalculated formula for uraninite and coffinite is given in Appendix G2. Tables of raw EPMA analyses are given in Appendix G3, and in Digital Appendix 5. The partial collection of re-calculated mineral formulae for each deposit is given in Appendix G4 and a full collection of recalculated formulae is given in Digital Appendix 5.

## 8.3 EPMA Analysis Results

Uraninite analyses total 196 individual spots across 43 specimens, the average compositions of the 43 uraninite grains are given in Table 8.1. $UO_2$ wt.% averages are dominant over $UO_3$ wt.% except in the Goanikontes samples. $ThO_2$ content ranges from ~5 wt.% to ~8 wt.% and exceeds PbO wt.% in Husab (8.22 wt.% $ThO_2$/5.87 wt.% PbO) and Goanikontes uraninite ($ThO_2$ 8.09 wt.%/PbO 5.29 wt.%). The Valencia samples contain the highest average Pb, while the Goanikontes specimens have the least, and the highest standard deviation, indicating highly variable Pb and therefore prevalent uraninite alteration. Contaminant elements include Ca, Fe, K and P, while lanthanides and Y are detected in only a few Goanikontes samples, which also host the most P.

Recalculated stoichiometric proportions of $UO_2$, $UO_3$, and $ThO_2$ constitute ≥85 wt.% of the mass of magmatic uraninite and the ratios of these three oxides serve as the primary discrimination tools to compare uraninite within- and between deposit populations. Figure 8.1 represents a ternary plot of normalised uraninite compositions, all ratios are derived from stoichiometric formulae calculations. The uraninite populations plot in distinct groups; Husab specimens have low normative Th, the Goanikontes specimens plot with different $UO_2/UO_3$ each consistent with the sampling depth in the same drill hole (DH025 at 43 m and 353 m); and the Hildenhof samples plot with the lowest normative Th. The Valencia specimens have consistent U ratios in the two core sample populations. The Husab and the Valencia surface sample (VALG 11) have outliers along the $UO_2$-$UO_3$ axis, representing individual specimen compositional variation.

Compositional variations of uraninite appear to be deposit-specific. Figure 8.1 illustrates the narrow $ThO_2$ range in the uraninite populations, and a wide distribution of $UO_2$ and $UO_3$. The range in composition of uraninite with respect to major contaminant elements Th, Pb, Si and Ca are illustrated in graphical form in **Error! Reference source not found.** Uraninite from most d eposits contains ≤90 wt.% U oxides, with most containing >75 wt.% minimum.

The Etango and Hildenhof samples represent the exceptions, with Hildenhof uraninite containing >90 wt.% U oxide and the Etango uraninite hosting the lowest maximum U oxide and lowest minimum.

- Etango deposit samples in the supergene zone (DH025 43 m) have lower $UO_3$ than the samples from depth (DH025 353 m);
- The Hildenhof uraninite has near 50/50 $UO_2$ and $UO_3$;
- The Zone 1 and Zone 2 uraninite populations from Husab plot with discrete $UO_2/UO_3$ grouping, Zone 2 being $UO_2$ dominant; and
- All the Valencia uraninites plot with a similar U ratio and the lowest overall $ThO_2$.

This study presents compositional data of 43 individual uraninite specimens with formulae recalculated to account for $U^{4+}$ and $U^{6+}$ ratios in minerals. The results of the analyses and recalculation summarised in Table 8.1, and in Figure 8.1 and Figure 8.2. Mineral formulae recalculation from EPMA data is based on stoichiometry and charge balance. The results show that calculated $UO_2$ and $UO_3$, and charge-balanced U/Th for uraninite populations is both varied and deposit-specific.

Since the averages of individual grains may disguise certain trends, plots of all 196 of the uraninite analyses are shown in the bivariate diagrams of Figure 8.3. All of the plots use oxide percentages from the same stoichiometric recalculation. $UO_2$ vs. $UO_3$ ratios of uraninites tend to cluster with more or less equal proportions, Figure 8.3a. The Husab and Goanikontes populations have some outliers. Husab uraninite occurs in two populations, one is $UO_2$ dominated while the other set is comparable to the general composition of the other deposit uraninites. The Goanikontes near surface and deep samples plot with comparatively low $UO_2$ but $UO_3$ is similar between 35- and 45 wt.%. Total U vs. Th + REE + Y in Figure 8.3b shows a linear substitution relationship in comparative samples from the older Bancroft district uraninites from McKechnie *et al.* (2012) and in the younger Variscan age uraninite samples of Förster (1999). The relationship is clearly linear in the Goanikontes samples, which contain an average of 2.2 wt.% $Y_3O_3$. The other uraninite data sets do not have REE data.

$UO_2/UO_3$ vs. CaO shows a linear relationship where $U^{4+}$ is probably replaced by Ca, Figure 8.3c. The Goanikontes samples contain the most CaO, the Hildenhof, and Etango uraninite show the strongest indication of systematic Ca replacement of U, while the Husab and Valencia samples show the least. Si and $UO_2$ have a weakly negative correlation in the Central

Zone uraninite. The Valencia uraninite samples show the most systematic U:Si relationship, reflecting a coffinite-dominated replacement trend (Figure 8.3d).

The best explanation for the low $UO_2$ in some Goanikontes uraninite may be the relatively low totals in some of the original analyses; however, these totals were normalised to resemble the higher totals of the rest of the group, yet $UO_3$ + $UO_2$ totals remain below the Central Zone average for this study. A less direct explanation is that the samples come from an interval of alaskite characterised by an overprint of uranophane, and the uraninite may have been oxidised, or simply crystallised with above average $UO_3$ proportions.

The outliers of high $UO_2$ uraninite from Husab, Figure 8.3a, come from a sample with a very low proportion of coffinitisation, <5 wt.% of the U deportment as shown in Figure 7.3, Chapter 7, sample RDD006 171-172 m. These relatively high-$UO_2$ specimens may be examples of uraninite that crystallised in particularly reducing conditions with a low degree of subsequent alteration and low total $UO_3$ in circulation. The trends identified above show that individual deposits, and individual uranium mineral specimens contain variable ratios of $U^{4+}$, $U^{6+}$, Th, Si, Ca, Pb, REE, Y and other contaminants. The following section summarises some of the unique uranium mineralisation features at each of the deposits.

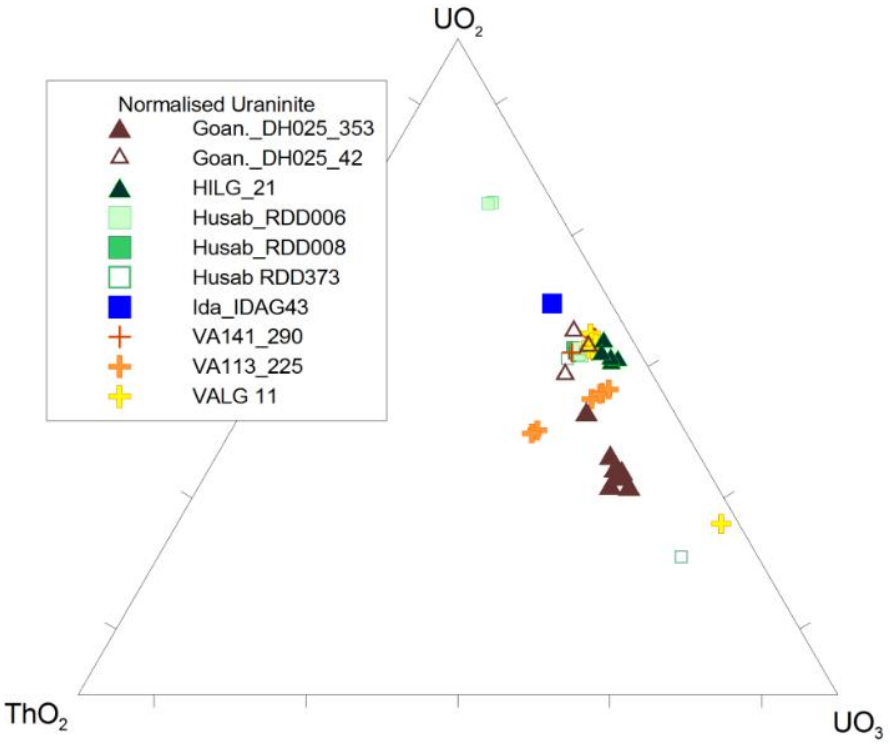



Figure 8.1 Uranium and thorium ternary diagram of 43 uraninite specimens from selected Central Zone primary deposits. $U^{4+}/U^{6+}$ varies between deposit areas; Etango samples from DH353 and from Holland's Dome have the highest $UO_3$ ratios, most of the specimens have ~10 wt.% $ThO_2$ and 40 wt.% to 50 wt.% $UO_3$. Valencia specimens returned the lowest average $ThO_2/U_{tot}$ analyses of the sample set. All data are normalised from calculated oxide proportions.

Table 8.1 Average compositions of Central Zone primary uranium deposit uraninite, as determined by EPMA analyses. $UO_2$ and $UO_3$ determined by stoichiometry calculation, normalised to two oxygens.

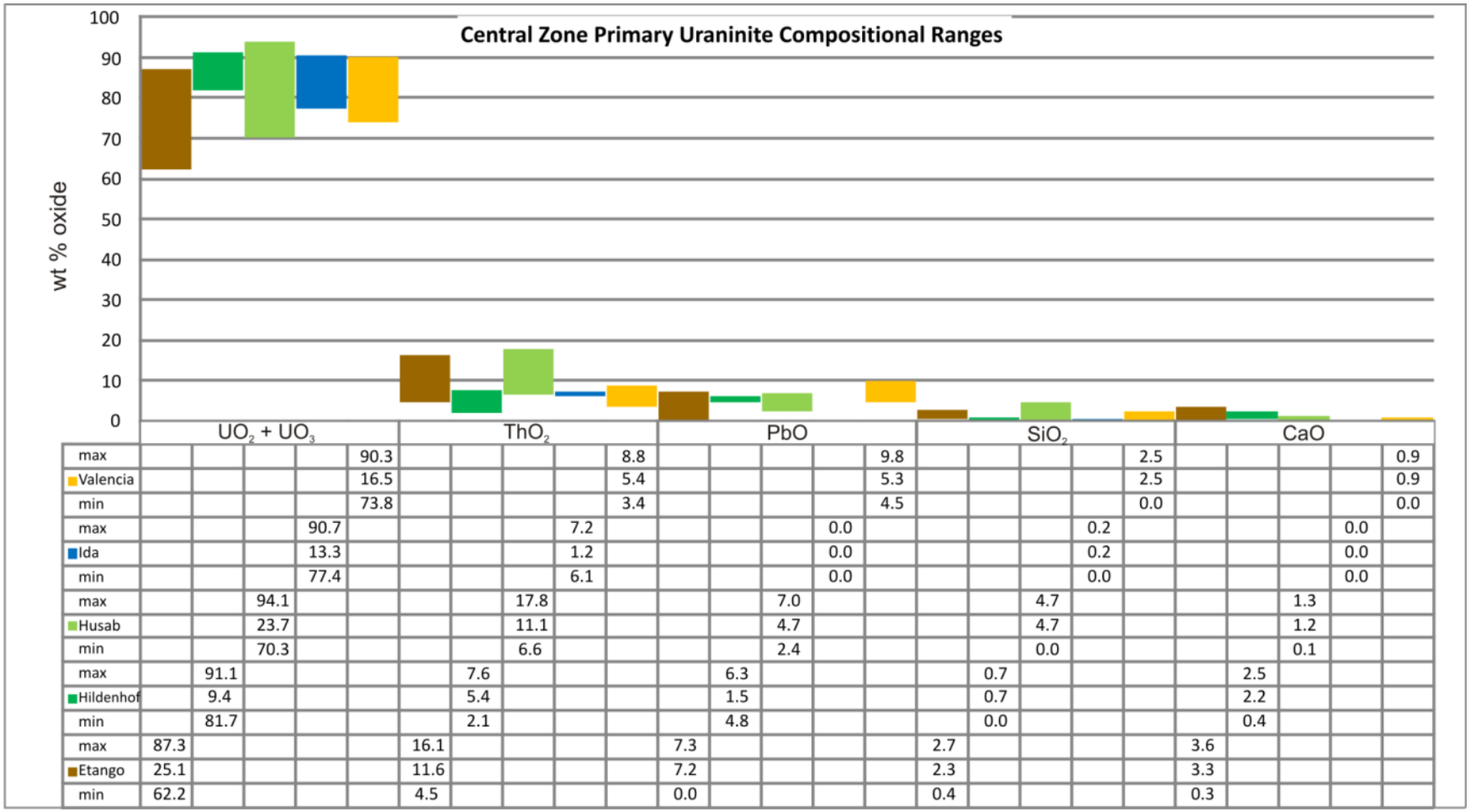
| **Deposit** | **Valencia** | | **Ida Dome** | | **Husab** | | **Hildenhof** | | **Goanikontes (Etango)** | | **Total** |
|---|---|---|---|---|---|---|---|---|---|---|---|
| specimens | 15 | | 1 | | 13 | | 5 | | 9 | | **43** |
| analyses | 64 | | 4 | | 69 | | 22 | | 35 | | **196** |
| | ave. | Σ | ave. | σ | ave. | σ | ave. | σ | ave. | σ | Average CZ uraninite |
| $UO_2$ | 47.423 | 3.220 | 47.423 | 4.234 | 52.757 | 8.147 | 47.703 | 1.711 | 31.815 | 10.820 | **44.924** |
| $UO_3$ | 36.999 | 1.430 | 36.999 | 2.309 | 33.911 | 7.308 | 40.266 | 1.820 | 38.193 | 2.904 | **37.342** |
| $ThO_2$ | 5.396 | 1.427 | 5.396 | 0.511 | 8.222 | 1.715 | 3.692 | 1.288 | 8.089 | 1.396 | **6.350** |
| PbO | 6.544 | 1.163 | nd | | 5.866 | 0.874 | 5.563 | 0.415 | 5.289 | 1.588 | **5.573** |
| $SiO_2$ | 0.360 | 0.640 | 0.360 | 0.084 | 0.297 | 0.971 | 0.226 | 0.238 | 1.473 | 0.655 | **0.589** |
| $Al_2O_3$ | 0.000 | 0.000 | 0.000 | 0.000 | 0.000 | 0.000 | 0.000 | 0.000 | 0.000 | 0.000 | **0.000** |
| CaO | 0.404 | 0.196 | nd | | 0.466 | 0.233 | 1.365 | 0.495 | 2.241 | 1.255 | **1.357** |
| $Fe_2O_3$ | 0.021 | 0.026 | 0.021 | 0.025 | 0.019 | 0.041 | 0.080 | 0.056 | 0.034 | 0.032 | **0.038** |
| $K_2O$ | 0.087 | 0.231 | 0.087 | 0.000 | 0.019 | 0.126 | 0.000 | 0.000 | 0.071 | 0.188 | **0.044** |
| $P_2O_5$ | 0.008 | 0.011 | 0.008 | 0.012 | 0.007 | 0.009 | 0.009 | 0.016 | 0.011 | 0.015 | **0.009** |
| $Ce_2O_3$ | nd | | nd | | Nd | | nd | | 0.197 | 0.408 | **0.197** |
| $La_2O_3$ | nd | | nd | | Nd | | nd | | 0.031 | 0.112 | **0.031** |
| $Y_2O_3$ | nd | | nd | | Nd | | nd | | 2.255 | 0.203 | **2.255** |
| **Total** | **97.241** | | **90.293** | | **101.563** | | **98.904** | | **89.697** | | **87.516** |

All analyses normalised to two oxygens.

nd = not detected in wave length dispersive scan, thus not analysed for in point analyses.

High Husab totals are corrected analyses, corrections performed at Rhodes University by Dr. G. Costin.

Goanikontes- 2 core samples; Hildenhof- 1 surface sample; Ida Dome- 1 surface sample; Husab- 4 core samples; Valencia- 3 core samples, 1 surface sample.




| | $UO_2 + UO_3$ | | | | | $ThO_2$ | | | | | PbO | | | | | $SiO_2$ | | | | | CaO | | | | |
|---|---|---|---|---|---|---|---|---|---|---|---|---|---|---|---|---|---|---|---|---|---|---|---|---|---|
| max | | | | | 90.3 | | | | | 8.8 | | | | | 9.8 | | | | | 2.5 | | | | | 0.9 |
| Valencia | | | | | 16.5 | | | | | 5.4 | | | | | 5.3 | | | | | 2.5 | | | | | 0.9 |
| min | | | | | 73.8 | | | | | 3.4 | | | | | 4.5 | | | | | 0.0 | | | | | 0.0 |
| max | | | | 90.7 | | | | | 7.2 | | | | | 0.0 | | | | | 0.2 | | | | | 0.0 | |
| Ida | | | | 13.3 | | | | | 1.2 | | | | | 0.0 | | | | | 0.2 | | | | | 0.0 | |
| min | | | | 77.4 | | | | | 6.1 | | | | | 0.0 | | | | | 0.0 | | | | | 0.0 | |
| max | | | 94.1 | | | | | 17.8 | | | | | 7.0 | | | | | 4.7 | | | | | 1.3 | | |
| Husab | | | 23.7 | | | | | 11.1 | | | | | 4.7 | | | | | 4.7 | | | | | 1.2 | | |
| min | | | 70.3 | | | | | 6.6 | | | | | 2.4 | | | | | 0.0 | | | | | 0.1 | | |
| max | | 91.1 | | | | | 7.6 | | | | | 6.3 | | | | | 0.7 | | | | | 2.5 | | | |
| Hildenhof | | 9.4 | | | | | 5.4 | | | | | 1.5 | | | | | 0.7 | | | | | 2.2 | | | |
| min | | 81.7 | | | | | 2.1 | | | | | 4.8 | | | | | 0.0 | | | | | 0.4 | | | |
| max | 87.3 | | | | | 16.1 | | | | | 7.3 | | | | | 2.7 | | | | | 3.6 | | | | |
| Etango | 25.1 | | | | | 11.6 | | | | | 7.2 | | | | | 2.3 | | | | | 3.3 | | | | |
| min | 62.2 | | | | | 4.5 | | | | | 0.0 | | | | | 0.4 | | | | | 0.3 | | | | |

Figure 8.2 Compositional ranges of primary uraninite specimens from the Etango, Hildenhof, Husab, Ida Dome, and Valencia localities. As with the ternary diagram a few subtle compositional variations suitably discriminate between the uraniniie populations at each deposit. Total U content is relatively low in the Goanikontes samples. Th in the Goanikontes samples is comparable to Husab, while Valencia, Hildenhof and Ida all have narrow ranges. High relative Pb content sets Valencia apart. High Si in some Husab samples sets the population apart from the other deposit' uraninites. Ca is relatively low in all sample populations. The narrow ranges of U, Th, Pb, Si, and Ca of the Hildenhof specimens shows that the individual uraninite grains are all very similar or have been altered to the same extent in the particular sample set.

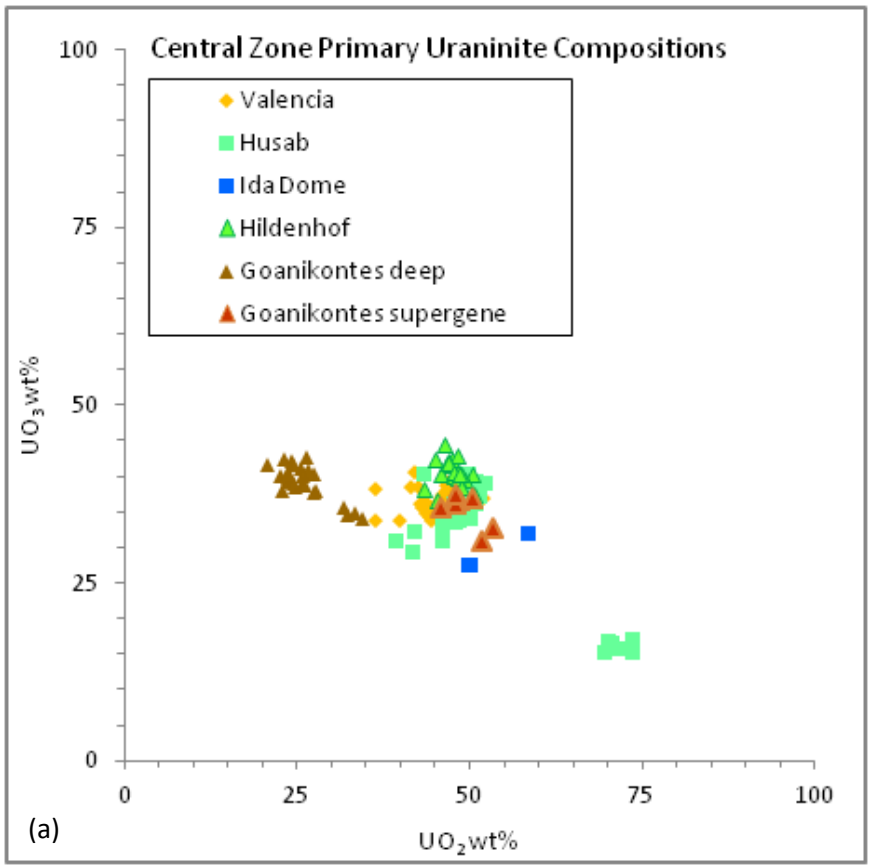
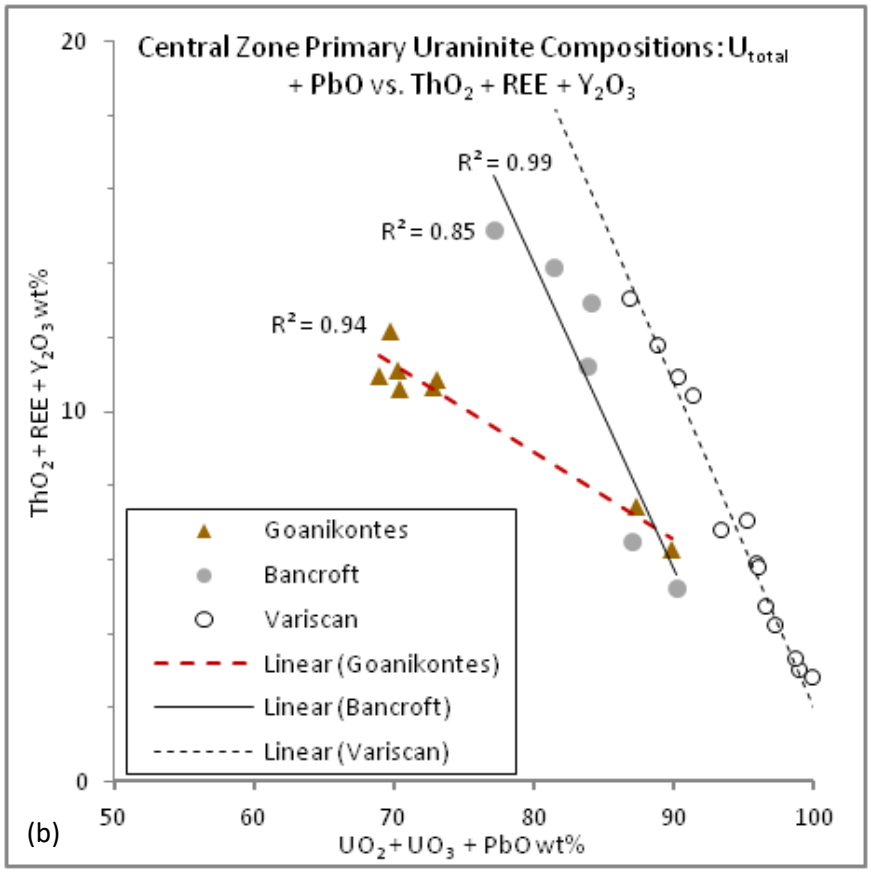



Figure 8.3 Four binary plots of uraninite compositional variables, U oxides, Th, REE and Y, Ca, and Si. (a) Calculated $UO_2$ vs. $UO_3$. The plot highlights a range in $UO_2$ of 35 wt.% to 65 wt.% for most samples whereas the Goanikontes samples plot with lower $UO_2$, and comparable, slightly higher $UO_3$ content. The anomalies with high $UO_2$ are from hole RDD008, and the particular uraninite is fractured.




(b) Calculated U oxide total + PbO vs. $ThO_2$ + REE + Y: The Central Zone uraninite populations (except Goanikontes) show a weaker indication of systematic substitution by Th REE and Y. Comparative samples from the Variscan and Bancroft studies of Förster (1999) and McKechnie (2012) respectively.

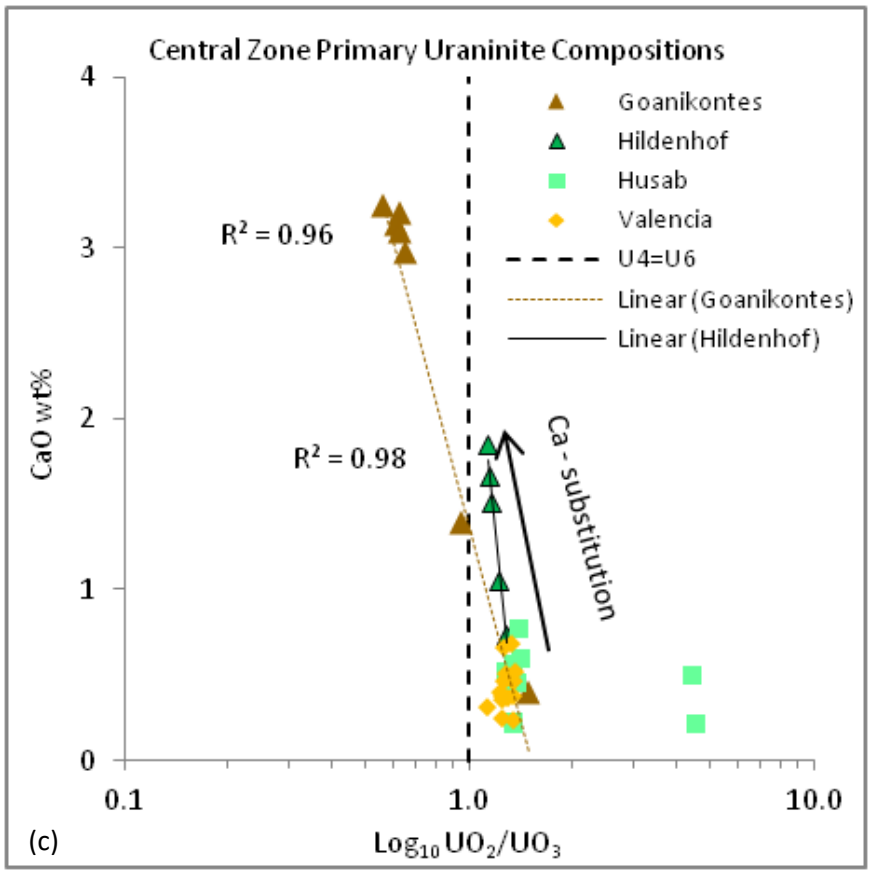
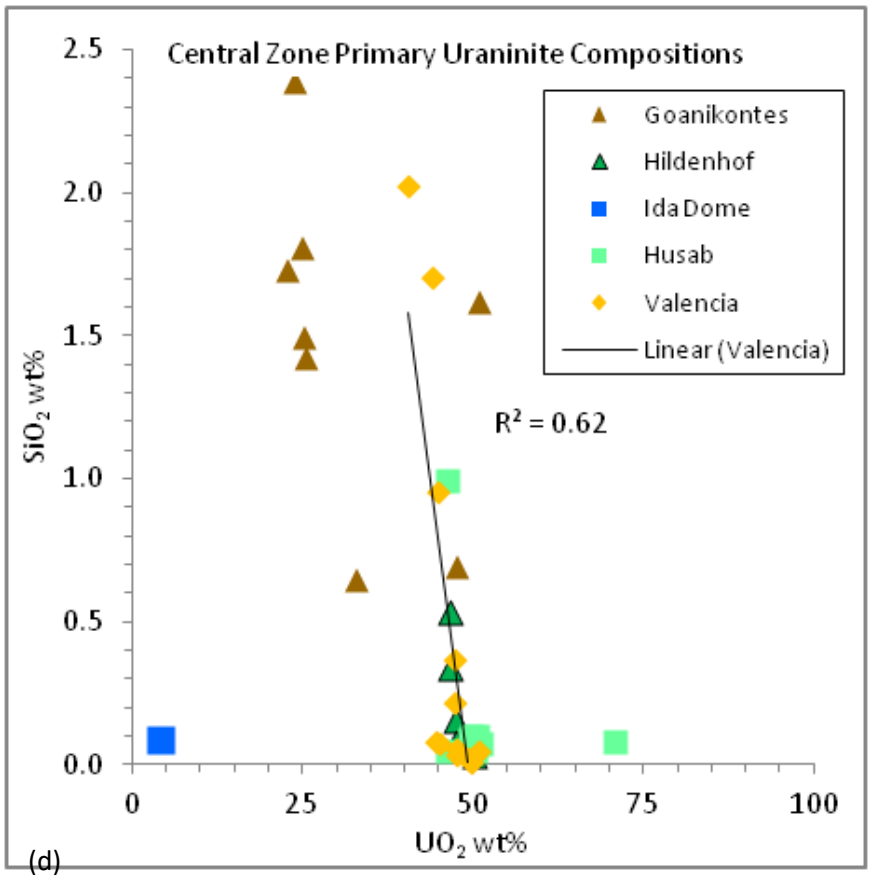



Figure 8.3 (c) Plot of UO2/UO3 vs. CaO contents of the uraninite populations. Ca and U show a systematic negative relationship in the Etango, Hildenhof, and Valencia samples and most of the Husab uraninite. Ca and and UO2/UO3 is particulalry systematic in the Goanikontes and Hildenhof samples.




(d) Si occurs in all forty-three uraninite specimens in this study. Key trends are the contrasts in Si abundances between most of the Valencia samples and most of the Husab uraninite (which have low Si) compared to the Goanikontes uraninite.

## 8.4 Goanikontes U-Mineral Compositions

Petrographic studies of polished thin sections and polished grain mounts identified compound mineral grains of uraninite, magnetite, and phosphates (xenotime, monazite and apatite) in the drill core specimens from the Etango deposit at Farm Goanikontes. QEMSCAN analyses provided detailed qualitative textural analyses of the uranium mineral populations of four specimens, three of core DH025 from 43 m-, 334 m and 353 m, and a surface sample. The EPMA provided the opportunity for a qualitative assessment of the elemental distribution, and therefore, by inference the mineral phase distribution of selected uraninite-magnetite compound grains. Ore petrography studies identified inclusions of uraninite in larger magnetite grains. In sample DH025_43, which is confirmed, in low-resolution, by the SGS QEMSCAN. Two generations of uranium mineralisation are visible in hand specimen and in thin sections of DH025_353. Thus these two specimens were selected as textural variants of the Etango deposit.

- The shallow sample is a typical alaskite of medium- to coarse texture, homogenous, dominated by smoky quartz and K-feldspar with accessory biotite; and
- The deeper sample is similar, but with a coarser, pegmatitic texture, with a lesser abundance of biotite.

The two samples both show evidence of hydrothermal alteration in hand specimen and in thin section, notably sericitisation of feldspars, quartz veining, chloritisation, and corrosion of magnetite with secondary Fe halos. The shallower intersection shows prominent near surface-derived Fe staining. The deeper sample has retained a white colour to the feldspars and the quartz is distinctly black. Yellow secondary uranium minerals indicate at least one episode of late fluid flux in the deeper sample.

A summary list of analyses that were obtained:

- WDS spectra for positive identification of mineral phases
- One positive identification by WDS and multi-spot quantitative analysis of a uranophane grain in DH025_353;

- Multi-spot quantitative analyses of 3 uranium mineral grains in DH025_43;
- Multi-spot quantitative analyses of 10 uranium mineral grains in DH025_353;
- 1 multi-element mineral map of a uranium-phosphate cluster in DH025_353; and
- 1 multi-element mineral map of a magnetite grain hosting uraninite in DH025_43.

### *Goanikontes Uraninite and Coffinite*

Uraninite formula recalculations were applied to uraninite specimens from two populations, one from DH025 43 m, and the other from DH025 353 m. Coffinite replacement of uraninite is analysed for DH025 43 m specimen U7. Figure 8.4 illustrates the textures of the uraninite specimens from the Etango DH025 drill hole. Uraninite appears to have a uniform metal distribution when viewed under low magnification; however, inspection at high magnification reveals uneven surfaces and uneven metal distribution.

The dull patches on most uraninite specimens correspond to coffinite replacement, where U content may be < 60 wt.%. Sample DH025 43 m- U5 is an example of a primary uraninite with euhedral edges, and relatively homogenous U distribution. It contains inclusions that were likely to have been removed during polishing. Specimen U6 is an example of secondary uraninite, where soluble U has crystallised in a uraninite vein. The uraninite has a conchoidal fracture and inhomogeneous metal distribution; and U7 is a high silica uraninite (16.4 wt.% $SiO_2$) which is probably completely replaced by coffinite, facilitated by the network of coarse fractures. Sample DH025 363- U1 illustrates mostly homogeneous reflectance; the coarse surface texture is a result of polishing.

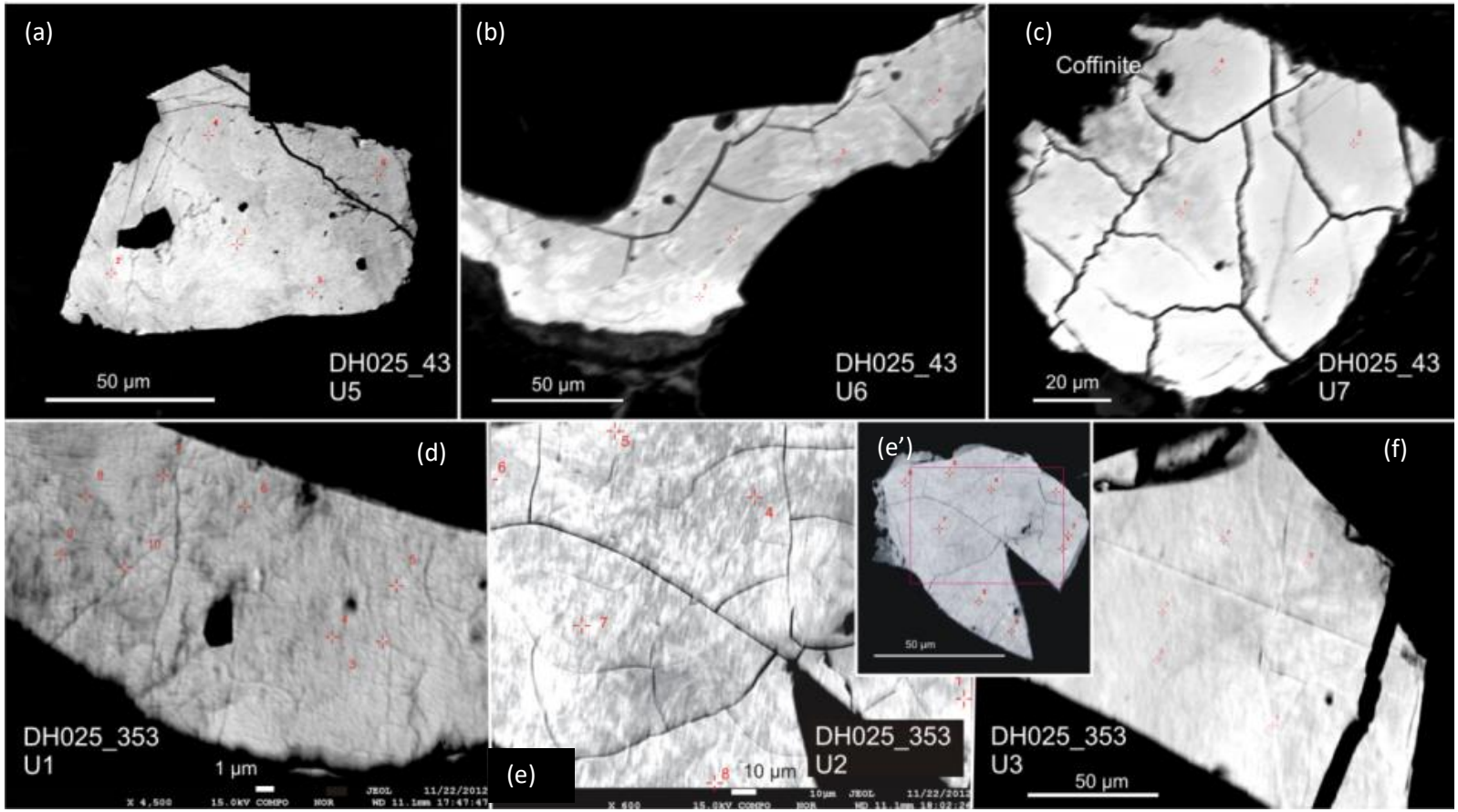



Figure 8.4 Uraninite and coffinite in sample DH025-43m and DH025-353m. (a) Secondary uraninite fills a fracture and is itself altered at one of the edges (bottom). The uraninite is less uniformly dense than U7 DH25-43m: (b) U6 shows fairly uniform density, and is slightly brighter surrounding a void (left). Hairline fractures surround the void, suggesting a metamict, radioactive mineral occupied it and expanded and fractured the host. (c) U7 is an anhedral uraninite, completely replaced by coffinite. It has conchoidal cleavage linked by radial pattern fractures. The grain has particularly uniform reflectance. Backscatter images of selected Etango deposit uraninites. DH025-353m: (d) U1 has a relatively uniform reflectance and is crosscut by a network of hairline fractures. QEMSCAN studies show that calcite predominantly replaces the voids within the Valencia uraninite crystals. (e and e') U2 displays well-developed conchoidal cleavage, typical of crystalline, magmatic uraninite. The grain is coffinitised throughout (dark grey). The missing segment was likely lost during sample preparation. (f) U3 is a euhedral uraninite, which appears to have been octahedral. The reflectance is uniform, with some metal-dense patches showing bright.

The dark spots represent low U content, while the voids represent inclusions of low-density minerals; U2 illustrates a clear example of conchoidal fracture, with detail revealing that reflectance is not homogenous; and U3 illustrates micrometric and fine, hairline fractures across a relatively homogenous uraninite. All of the uraninite recalculations are balanced to 2 oxygen, with $UO_2$ and $UO_3$ wt.% adjusted such that the cation totals = ~1. The formulae for the two populations show the main contrast in U content between the two sample intervals is between the $U^{4+}$ proportions; where the DH025 353 m samples contain about half the weight percentage of $UO_2$ that the DH025 43 m samples do.The DH025 353 m samples also contain significantly more Ca, while the high average Si content in the DH025 43 m sample population, Figure 8.3d, is attributed to one of the three uraninites containing >15 wt.% $SiO_2$ (which suggests the specimen is extensively replaced by coffinite).

Uraninite compositions between the two sample populations show contrasts in U ratios, Ca content, Si abundance and REE + Y abundances. CaO and $UO_2$ show a systematic, substitution relationship within the DH025 353 m population, which is also consistent within the analyses of individual uraninite specimens, Figure 8.5a. The DH025 43 m samples do not contain Y, at detectable limits. The specimens contain Ce>La, with a maximum $Ce_2O_3$ content of 1.6 wt.%. The DH025 353 m sample contains 0.0 wt.% to >0.05 wt.% $Ce_2O_3$ but host up to 2.7 wt.% $Y_2O_3$, Figure 8.5b. The contrast in Y content of uraninite between the two populations, however, does not reflect the whole-rock geochemical assays, where DH025 43 m hosts 210 ppm Y vs. 72 ppm Y for DH025 353 m.

Average non-stoichiometric formulae for DH025 43 uraninite specimens

Normalised to 2 Oxygen including DH025 43_U7 analysed as uraninite: 3 uraninite/13 analyses

$$(U^{4+}_{0.409}U^{6+}_{0.419}Th_{0.060}Pb_{0.033}Ca_{0.023}Fe_{0.001}Si_{0.173}La_{0.002}Ce_{0.009}P_{0.001})_{\sum=1.13}O_2$$

Average formula recalculation for DH025 353 uraninite specimens

Normalised to 2 Oxygen: 7 uraninite/26 analyses

$$(U^{4+}_{0.253}U^{6+}_{0.335}Th_{0.086}Pb_{0.062}Ca_{0.120}Fe_{0.001}Si_{0.091}Y_{0.052})_{\sum=1}O_2$$

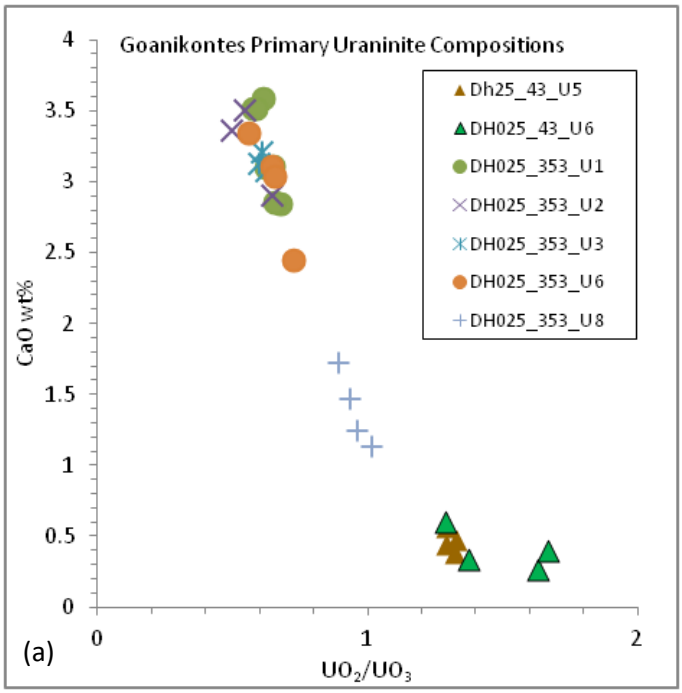
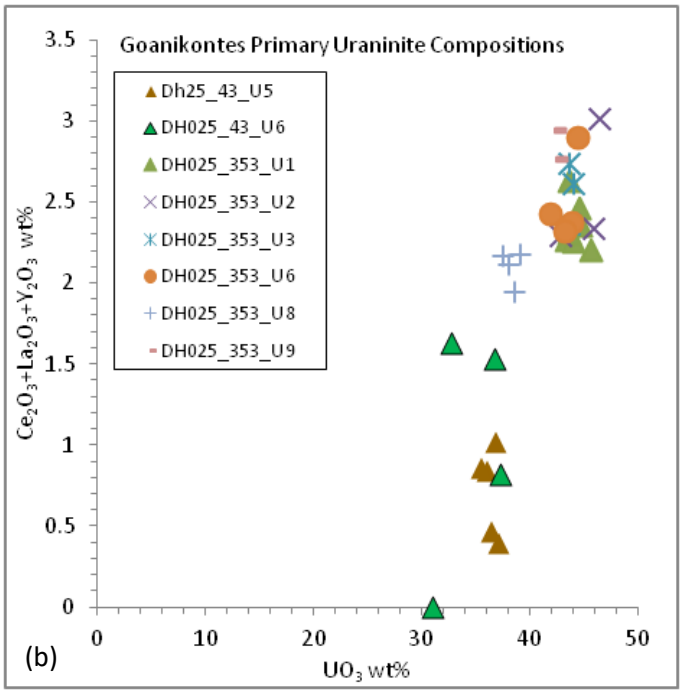



Figure 8.5 Uraninite compositional variation in the Etango DH025 drill hole samples. (a) The uraninite specimens from the two depth intervals contrast in $UO_2/UO_3$ and in CaO content, where the 353 m samples host consistently more CaO to a maximum of 3.5 wt.%. The consistent negative trend (within individual uraninite specimens) suggests Ca substitution of $U^{4+}$.




(b) The 353 m samples also host appreciably more REE and Y, specifically Y. There is an overall positive correlation with $UO_3$ and REE + Y, which support a substitution of $U^{6+}$.

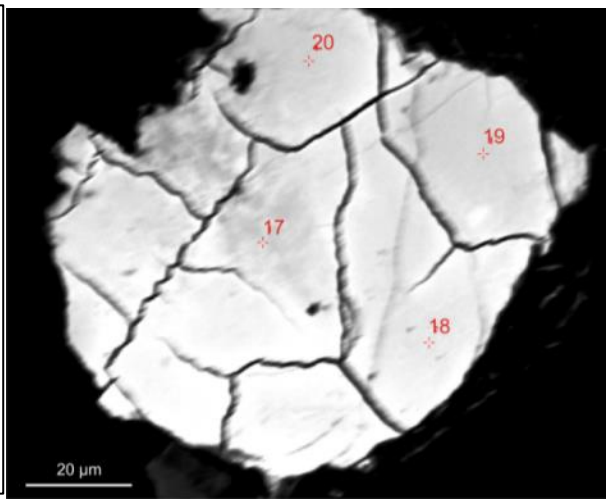
*Coffinite in sample DH025 43_U7*

Stoichiometric recalculation of coffinite compositions requires balancing of two variables; $UO_2$ and $UO_3$ and solving for 'x' such that the formula $(U,Th)(SiO_4)_{1-x}.(OH)_{4x}$ is satisfied. Of the three analysis points on DH025 43_U7, only point (U7-18) returned suitable values when inserted into the mineral formula recalculation macro. Thus the compositions as produced

by the EPMA analysis of the specimen are tabulated below without a coffinite formula recalculation, Table 8.2.

Table 8.2 Composition of coffinite specimen U7 of sample DH025_43m. Water is estimated by balancing U and Th such that U+Th = 1 and Si <1 with an oxygen normalisation of 3.

| DH25_43 Point<br>Wt % oxide | U7-18 | U7-19 | U7-20 |
|---|---|---|---|
| $UO_2$ | 55.890 | 62.340 | 66.470 |
| $ThO_2$ | 11.271 | 8.109 | 4.665 |
| $SiO_2$ | 16.588 | 16.370 | 17.156 |
| $La_2O_3$ | 0.000 | 0.000 | 0.050 |
| $Fe_2O_3$ | 0.030 | 0.001 | 0.000 |
| $P_2O_5$ | 0.050 | 0.053 | 0.019 |
| CaO | 0.983 | 0.865 | 0.904 |
| PbO | 0.024 | 0.200 | 0.107 |
| $Ce_2O_3$ | 0.000 | 0.000 | 0.000 |
| $K_2O$ | 0.390 | 0.608 | 0.715 |
| $UO_3$ | | | |
| $H_2O$ | 9.4 | 9.4 | 9.4 |
| Total | 94.626 | 97.946 | 99.476 |




### *Goanikontes Uranophane-, and Monazite-Hosted Uranium Mineralisation*

Uranophane[49] was analysed by EPMA in six samples. Backscatter image analyses identified two distinctive textures of the mineral, one is an amorphous coating/vein fill type, the other is of acicular, clustered prisms, as illustrated in Figure 8.6a and 8.6b. Uranophane forms an amorphous (at 600x magnification) fill in fractures of coarse rock forming phases such as feldspar, Figure 8.6a; and Crystalline uranophane has grown in voids between coarse minerals (common where silicates are leached) and forms acicular crystals in larger voids (Figure 8.6b).

Uraninite inclusions are common in phosphates. The monazite in Figure 8.6c hosts uraninite and thorite. The typically rounded inclusions are very fine-grained, 10-15 µm across. The host mineral often occurs in association with apatite, and the cluster in the example shows some euhedral edges, but also evidence of alteration in the fractured edges. Cuney and Kyser (2008) suggest that inclusions hosted in entrained phosphates may have contributed

49 Ca was erroneously left off the EPMA recipe at the time of analysis. The results, with CaO calculated as 100 wt% composition - (12.8 wt% H2O + existing oxides). 12.8 % is approximate to analyses in Viswanathan and Harneit (1986). The results are tabulated in Appendix F9.

some of the U budget in the products of weakly peraluminous silicate melts, the rounded nature of the inclusions suggest that uraninite was incorporated into monazite prior to leucogranite formation, potentially at the source.

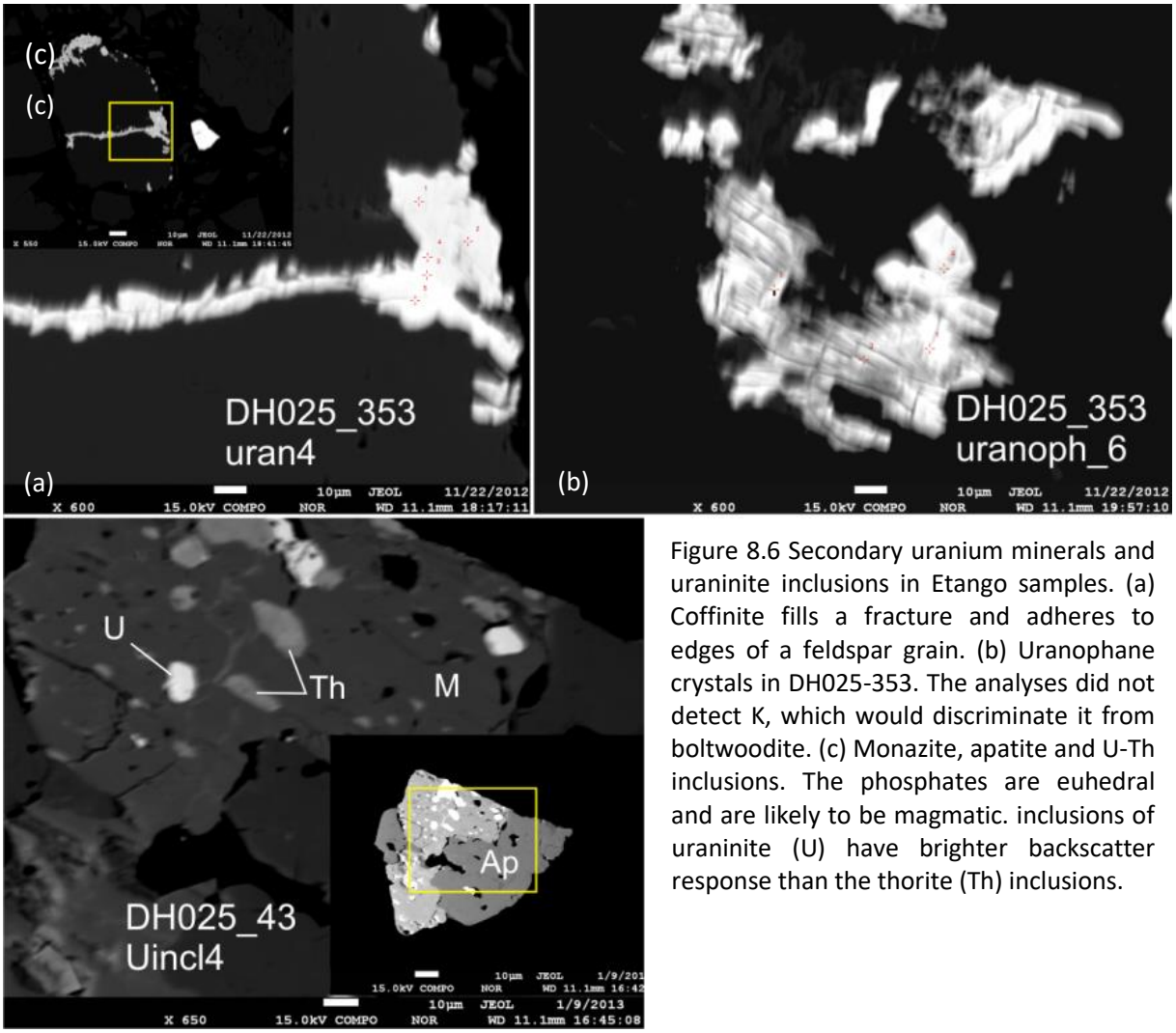



Figure 8.6 Secondary uranium minerals and uraninite inclusions in Etango samples. (a) Coffinite fills a fracture and adheres to edges of a feldspar grain. (b) Uranophane crystals in DH025-353. The analyses did not detect K, which would discriminate it from boltwoodite. (c) Monazite, apatite and U-Th inclusions. The phosphates are euhedral and are likely to be magmatic. inclusions of uraninite (U) have brighter backscatter response than the thorite (Th) inclusions.

The collages in Figure 8.7 show that magnetite is an early phase and is subject to at least two phases of alteration; the first phase took place during $fO_2$ conditions that removed mobile Fe, leaving vermicular voids in the magnetite crystal. The second phase deposited U into these voids. Subsequently, calcite formed around the corroded magnetite edges. This relationship is present in samples from a range of depths. Figure 8.7a and 8.7b illustrate the near surface sheeted leucogranite of DH025_43 m and the vermicular uraninite replacement in magnetite in electron backscatter image, respectively. The element maps of

the same magnetite porphyroblast show an inverse U and Fe distribution, thus the two elements are independent of each other in the sample. Coincident U-K-Si probably represents boltwoodite rather than uranophane, Figure 8.7c: Ca, not shown, is not coincident with U or K in the sample, which would otherwise have indicated uranophane. Y is present in fine phosphates, as are Ce and La but in lesser concentration, indicating monazite solubility in the sub solidus environment. Figure 8.7d illustrates a hydrothermally altered magnetite with vermicular voids left by leaching of Fe and other impurities in the DH025 353 m sample. Uranium minerals fill the voids toward the periphery and do not penetrate to the core of the grain. Figure 8.7e shows a secondary relationship, where mobile U was deposited as yellow secondary phases boltwoodite ± uranophane in the surrounding fractures.

The simplest compound grain represents a high temperature interaction between Fe and U in DH025 43 m, in which U oxides are included in a large magnetite (Figure 8.7). Complex mineral clusters comprise various combinations of uraninite, thorite, apatite, monazite, xenotime, boltwoodite and/or uranophane, and zircon, the example given is from DH025 353 m in Figure 8.8.

The images of a complex cluster of minerals in Figure 8.8 give an indication of the paragenetic sequence between the phases, (backscatter image and accompanying element maps). K-feldspar surrounds the cluster. A xenotime-apatite crystal forms the nucleus of the cluster and uranium minerals occur in three dominant textures:

1. Subhedral uraninite with even edges and partial coffinite replacement;
2. Anhedral uraninite with irregular edges; and
3. Fractured uraninite replaced by coffinite; and uranophane, which forms a skeletal mass between coffinite, thorite and the host feldspar.

Thorite forms around the uraninite, and between uraninite and xenotime. The youngest phases appear to be the fibrous secondary U minerals between uraninite, K-feldspar and xenotime. Thorite forms around the uraninite, and in the space between two uraninites and the xenotime.

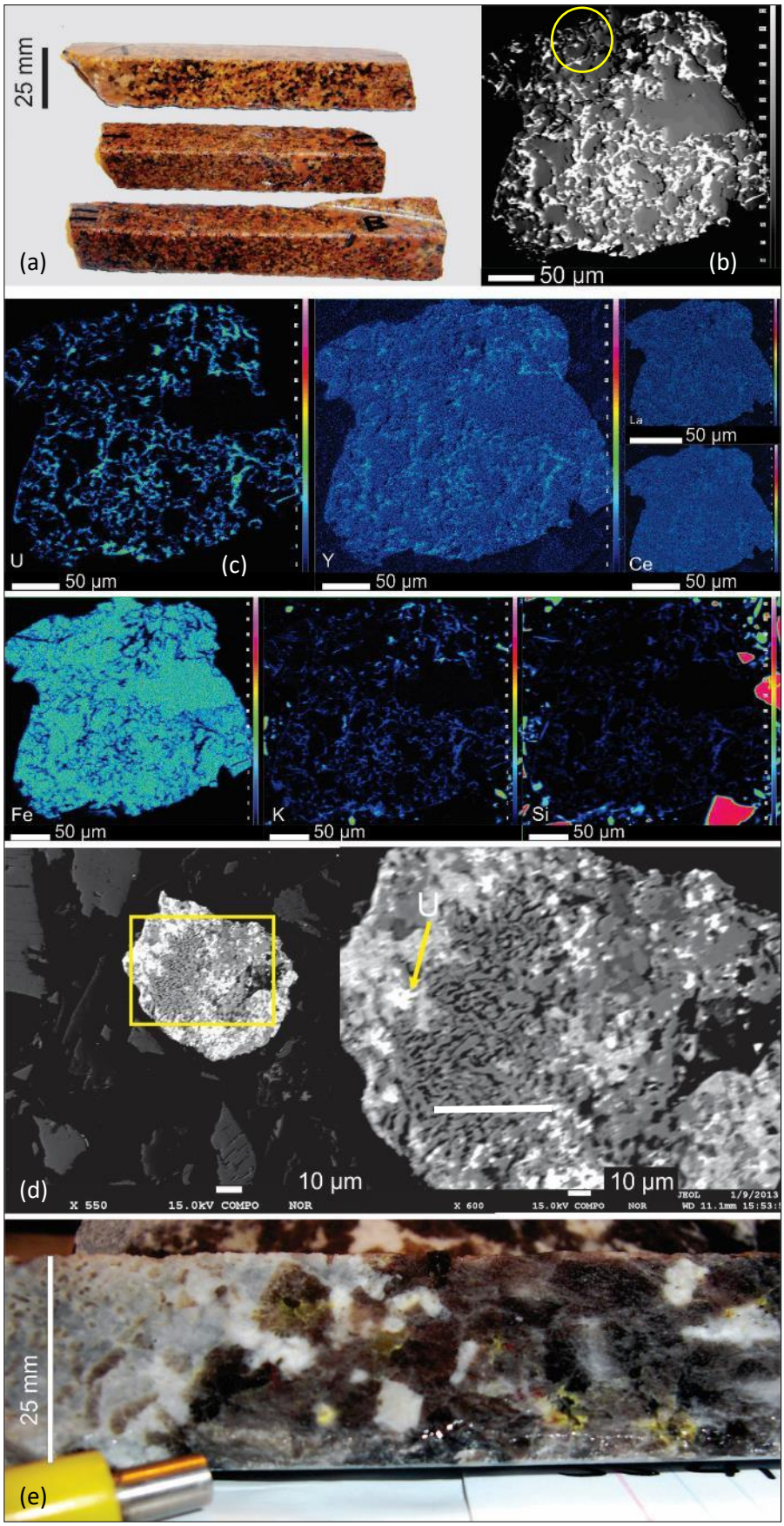



Figure 8.7 Uranium and magnetite relationships in Etango drill hole DH025 samples at 43 m and 353 m. (a) The shallow intersection of alaskite at 43 m, shows pervasive Fe - staining from limonite and siderite. Feldspars are all altered and original colour appears to have been white. (b) Backscatter image of a corroded magnetite. Secondary uranium minerals fill vermicular voids, which register their higher density (metal-content) as bright shades.
(c) A collage of U, Y, La, Ce, Fe, K and Si element maps of the magnetite grain. U, Y, K and Si correspond, suggesting boltwoodite. Ce, La, and Y are coincident, supporting phosphate mobilisation in the subsolidus environment.
(d) Backscatter image of a corroded magnetite with vermicular voids partially filled by uranium minerals at the rim of the grain.
(e) The yellow halos of uranophane/ boltwoodite that surround the magnetite porphyroblasts appear to be the product of magnetite-hosted uraninite corrosion. Their composition is likely to be a combination of boltwoodite and uranophane, given the presence of K in the surface sample.

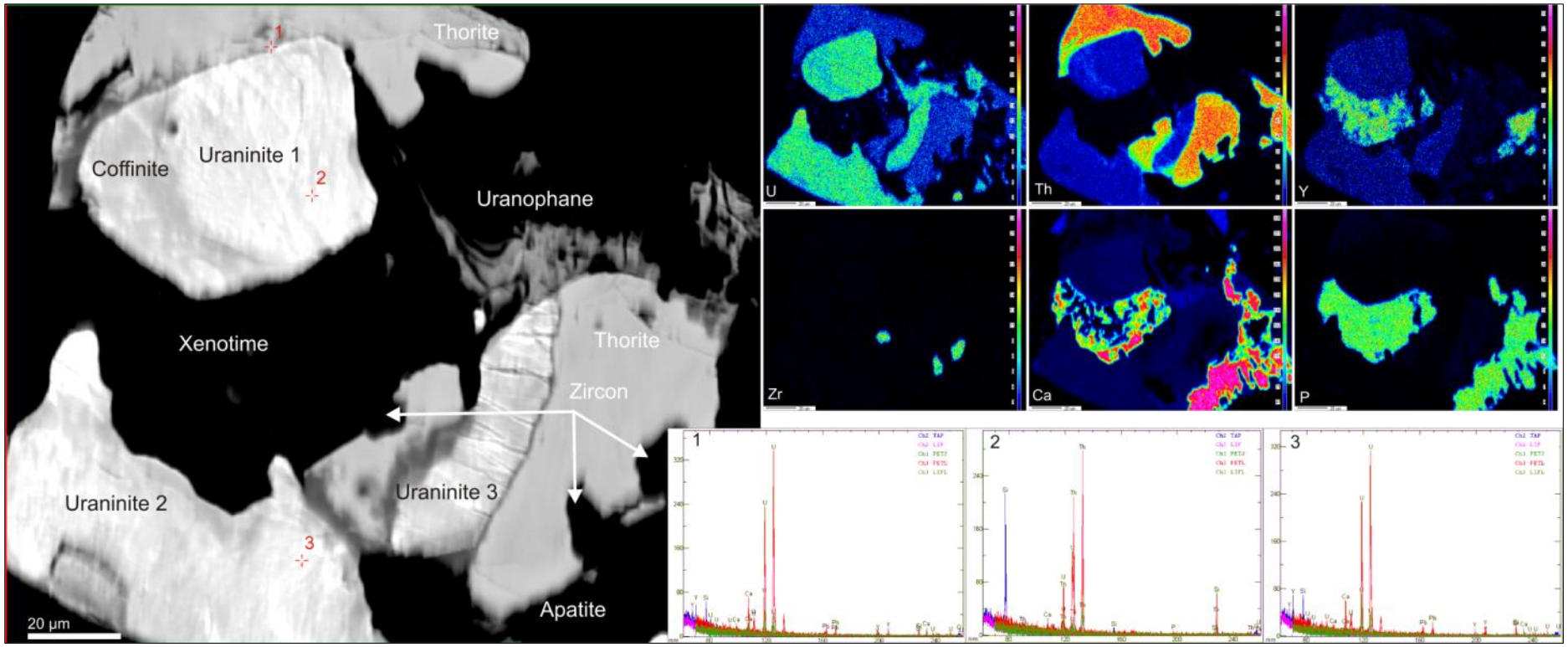



Figure 8.8 Composite mineral grains from sample DH025_353 m. The composite grain in backscatter shows a clear density contrast between thorite and uraninite. WDS scans at positions 1 through 3 confirm the two minerals. The mineral maps of U, Th, Y, Zr, Ca and P identify the following phases in the cluster; Uraninite in two textures, one as a euhedral grain '1' and as a replacement grain '2'; Thorite as anhedral grains, after zircon; and Xenotime, which appears to have inter-grown with apatite (co-incident P and Ca vs P and Y).

## 8.5 Hildenhof Uraninite Compositions

The mineralisation at Hildenhof is a continuation of the sheeted leucogranites that intrude around the southern lobe of the Khan inlier at the Etango deposit at Goanikontes. The uranium-bearing minerals of the Hildenhof sample HILG 21, however, do not necessarily show the same textural and mineralogical associations observed in the Etango samples. Polished grain mounts were prepared from heavy mineral separates and thus represent the primary and insoluble uranium mineral compositions of the uraninite population. The results of the element map and mineral analyses include element maps of a uraninite that hosts Ce-monazite (Figure 8.9a to Figure 8.9i). Four of the five specimens are shown in Figure 8.9j to Figure 8.9m in backscatter image. In summary, the images of the mineral element maps in Figure 8.9 show a uniform distribution of U, and ingress concentration of Fe and Ca into the characteristic fractures. The monazite is a Ce end member, and shares the void it occupies with apatite. The uraninite backscatter images in the collage illustrate the corroded nature of the minerals.

The EPMA study produced twenty-two point analyses of oxide wt.% across five individual uraninite grains. Analyses point positions were selected from the least altered portions of the uraninite specimens. The results show that $U^{4+}$ is dominant by ~8 wt.% over $U^{6+}$ and the minor components (Al, Ca, Fe, K, P and V) comprise, on average, < 1.5 wt.% of the uraninite mass (Figure 8.10a). Ca substitution has taken place in the Hildenhof uraninite, as illustrated by a systematic Ca correlation with $UO_2$ abundance (Figure 8.10b). The uraninite formula recalculation is coordinated with two oxygen and the proportions of $UO_2$ and $UO_3$ are determined for each analytical point such that the cation total in the stoichiometric calculation macro sum to ~1. The average non-stoichiometric composition of the HILG21 uraninite is:

Oxygen coordination: 2

22 analyses, 5 specimens

$(U^{4+}_{0.463}U^{6+}_{0.361}Th_{0.035}Pb_{0.063}Ca_{0.065}Fe_{0.003}Si_{0.010})_{\sum=1}O_2$

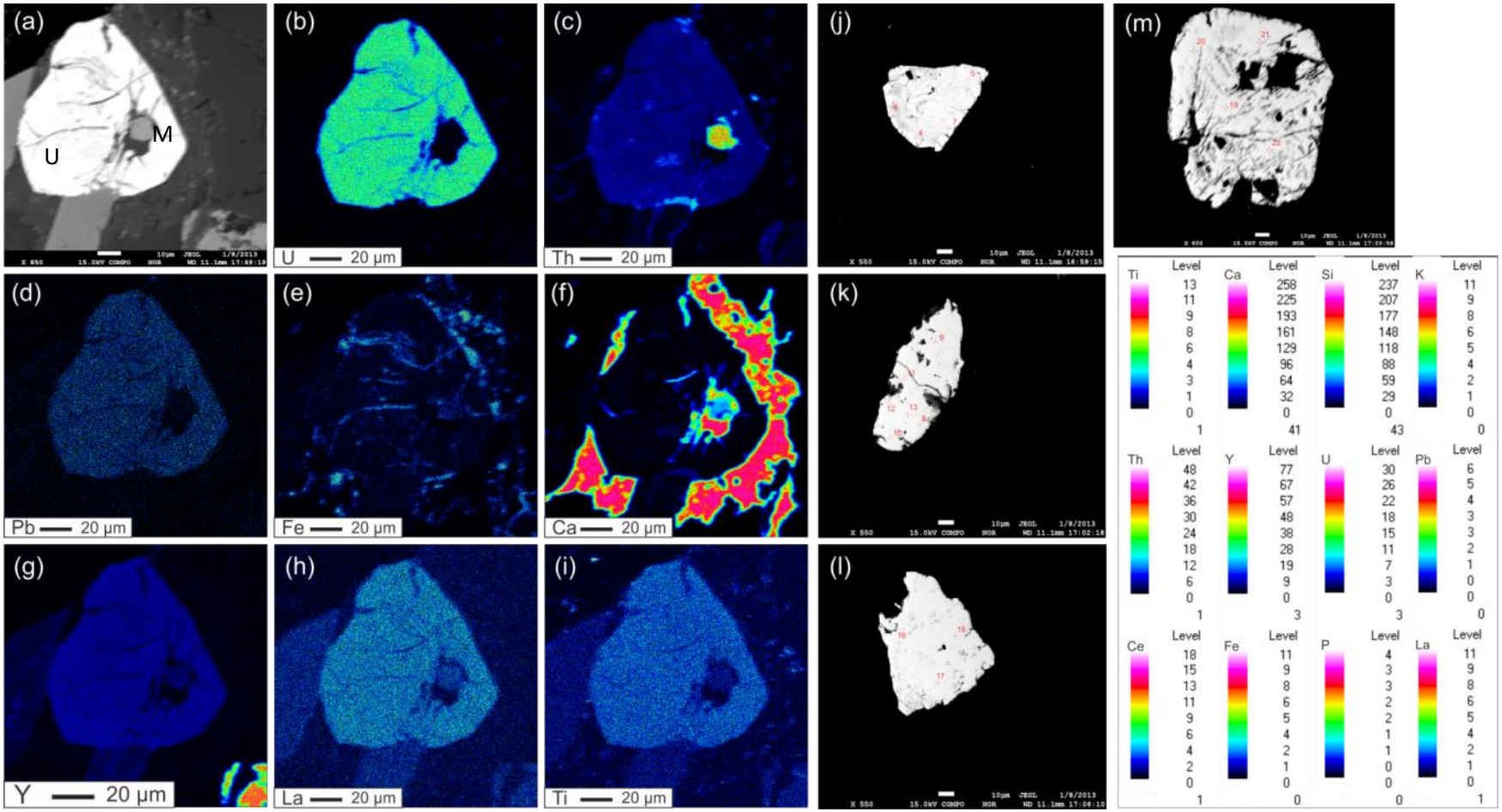
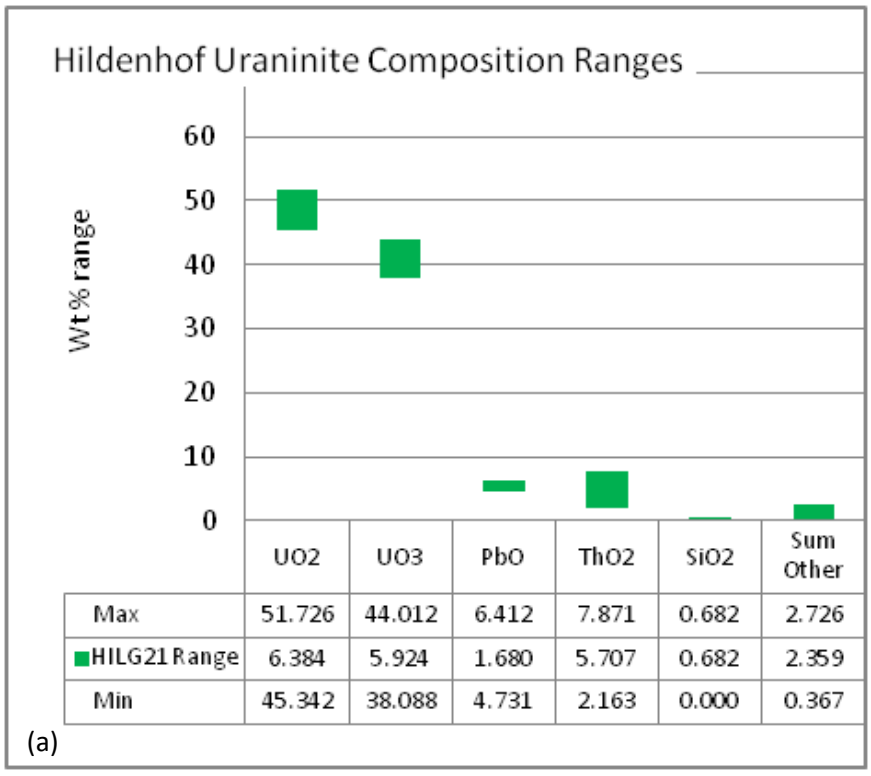



Figure 8.9 Backscatter and element map imagery of Hildenhof uraninite specimens from surface sample HILG21. (a) Backscatter image of a uraninite (U) with a Ce-monazite inclusion (M): (b) U is evenly distributed in the crystal; (c) Th occurs in the monazite inclusion and in patches within the uraninite; (d) Traces of Pb occur throughout the uraninite and (e) Fe fills the prominent fractures throughout the crystal. (f) Ca (as calcite) surrounds the uraninite, and fills fractures and surrounds the monazite inclusion halo; (g)(h) Y and La occur throughout the uraninite in 'above - background' concentrations; La is less concentrated in the monazite than in the uraninite; and (i) Ti shows some concentration in the host minerals. j - m) Uraninite specimens and their analytical point locations. (j) U2 is a near euhedral specimen with fractured edges. (k) U3 is an altered, euhedral specimen. (l) U4 is a near euhedral uraninite with coarse fracture networks propagating from the edges. (m) U5 is an intensely altered and fractured uraninite that hosted coarse inclusions.



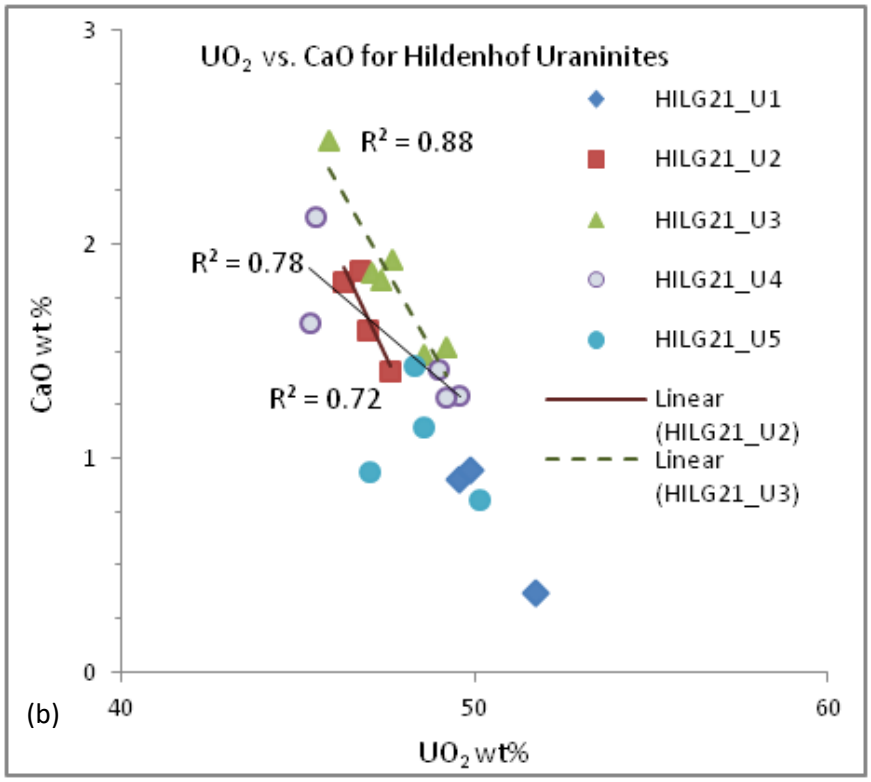




Figure 8.10 Compositional summaries of 5 uraninite specimens in Hildenhof sample HILG 21. (a) $U^{4+}$ is dominant in the uraninite, with radiogenic Pb and Th making up the major contaminant elements.

(b) The systematic relationship between $U^{4+}$ and Ca shows that Ca substitution has taken place in the Hildenhof uraninite.

## 8.6 Ida Dome U-Phase Compositions

The sample IDAG 43 (Holland's Dome deposit) is the only sample submitted for uranium mineral analyses from the Ida Dome area. Uranium minerals are few in number and fine-grained. WDS spectra positively identified specimens of thorite, coffinite, and uraninite and compositional maps were obtained of examples of each phase. Coffinite occurs as a replacement/coating on a magnetite grain (U6, Figure 8.11). The uraninite and thorite specimens are singular grains, labelled U7 and U8, respectively.

### *Ida Dome U- and Fe-Mineral Relationships and Coffinite andThorite Compositions*

Magnetite is an abundant mineral in the Khan Formation and the invading leucogranite sheets. Magnetite porphyroblasts up to 1 cm across occur in the granite and metasediments at contact zones at the Holland's Dome deposit. The specimen IDAG43-U6 is a ~500 µm long magnetite with a ~10-15 µm thick, near-continuous rim of coffinite Figure 8.11a). The magnetite has irregular edges as a result of hydrothermal alteration. The rim of coffinite appears to have replaced Fe-oxide along a conchoidal fracture plane at the mineral edge, rather than as a coating.

QEMSCAN data of IDAG 43 from the Holland's Dome prospect show that the sample contains uraninite, thorite and U-silicates (coffinite) and minor thorite. Analyses are limited, with one specimen of coffinite, uraninite, and thorite providing suitable results for interpretation. Element mapping by EPMA results are presented for each of the three specimens and the analytical results summarised and presented in Figure 8.11. Compositional data for each of the specimens is summarised as follows:

IDAG 43 - U6 **Coffinite**, Figure 8.11. Coffinite formula is recalculated calculated as (U,Pb) $(SiO4)_{1-x}.(OH)_{4x}$.

Oxygen: 2.7; specimens: 1; sample points: 3

$(U^{6+}_{0.055}U^{4+}_{0.384}Pb_{0.005})_{\Sigma=0.444}(Si_{0.456}Al_{0.002}Fe_{0.058}K_{0.009})_{\Sigma=0.525}(OH)_{1.9}$

IDAG 43 - U7 **Uraninite** ( Figure 8.11b). The specimen has rounded edges and shows signs of alteration and corrosion with fine hairline fractures at all edges, and a larger fracture that bisects the crystal. The composition of the specimen is calculated from 3 sample points, with oxygen coordination set at 2, and $UO_3$ and $UO_2$ adjusted to achieve a cation total ~1. The non-stoichiometric formula is as follows:

Oxygen: 2, specimens: 1, sample points: 4

$(U^{6+}_{0.306}U^{4+}_{0.609}Th_{0.082}Si_{0.002})_{\sum=0.999}O_2$

IDAG 43 - U8 **Thorite replaced by coffinite** (Figure 8.11c). The sample is an inhomogeneous mix of thorite with patches of elevated U and coffinite. The sample thus provided analyses of intermediate U-Th silicate compositions and a single analysis spot that approximates to coffinite. There is solid solution between thorite and coffinite, thus the availability of U or Th in the local system will have determined the dominant phase (Förster, 2001). The compositions presented below are the best possible combinations obtained from the data.

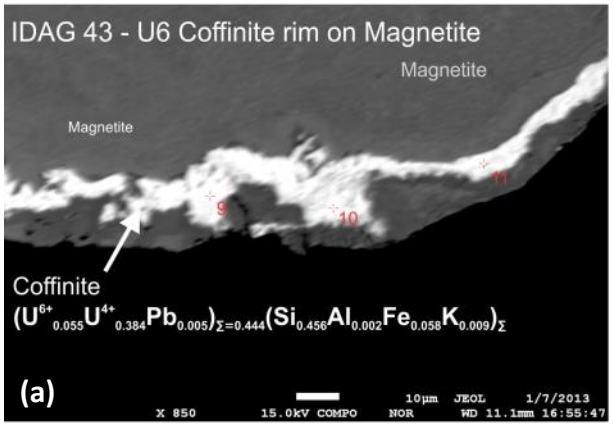
Coffinite:- single spot analysis

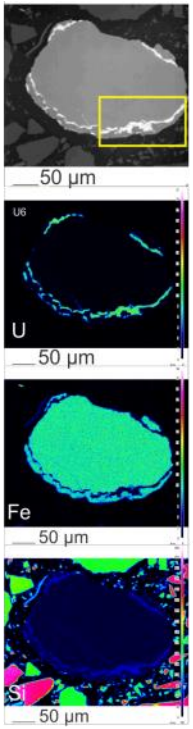
$(U^{6+}_{0.037}U^{4+}_{0.276}Th_{0.037}Pb_{0.0})_{\sum=0.35}(Si_{0.456}Al_{0.002}Fe_{0.058}K_{0.009})_{\sum=0.525}(OH)_{1.9}$

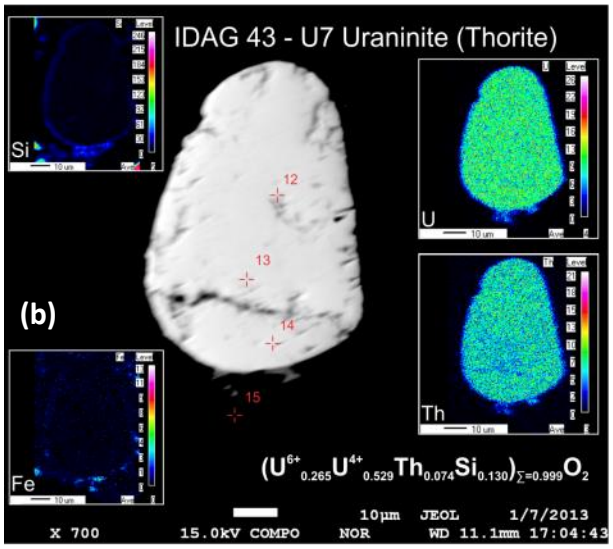
Thorite:- 2 analyses

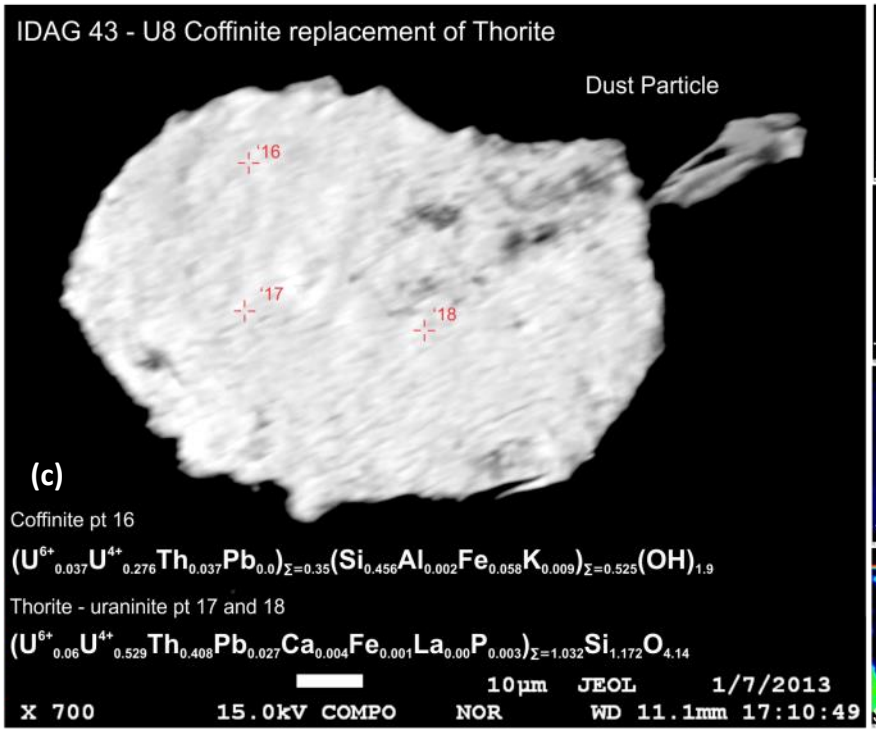
$(U^{6+}_{0.06}U^{4+}_{0.529}Th_{0.408}Pb_{0.027}Ca_{0.004}Fe_{0.001}La_{0.00}P_{0.003})_{\sum=1.032}Si_{1.172}O_{4.14}$

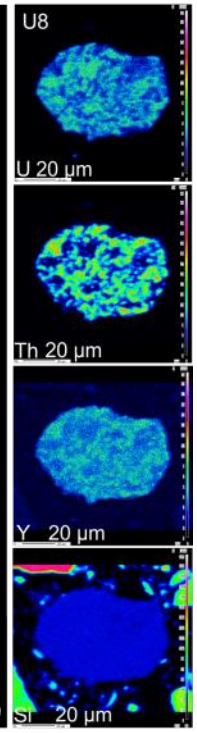
Figure 8.11 N*ext page*. Mineral maps of Holland's Dome U phases: Mineral maps of thorite, uraninite, and coffinite in sample grains U6, U7 and U8 show elemental distributions. (a) IDAG 43 U6: Secondary coffinite forms a rim around a corroded magnetite grain. The coffinite has an inhomogeneous texture and has precipitated with variable metal distribution as an amorphous fracture fill. (b) IDAG 43 U7: Uraninite with ~6.5 wt.% Th. The uraninite is corroded to a sub rounded shape, with cracks facilitating leaching of mobile U at grain boundaries. (c) IDAG 43 U8, the inhomogeneous distribution of Th and U in this specimen results in low compositional totals. U:Th and UO3:UO2 are inconsistent across the three measured points. Spot 16 is coffinite as Si = ~15 wt.% which is consistent for both coffinite and thorite, but Th is just ~7 wt.%, too low for thorite.




| Spot | $UO_2$ | $UO_3$ | $ThO_2$ | $SiO_2$ | $Al_2O_3$ | $K_2O$ | $Fe_2O_3$ | $P_2O_5$ | $V_2O_3$ | Total |
|---|---|---|---|---|---|---|---|---|---|---|
| IDAG43_U7-12 | 50.20 | 27.442 | 6.788 | 0.000 | 0.000 | 0.000 | 0.017 | 0.026 | 0.000 | 84.47 |
| IDAG43_U7-13 | 50.00 | 27.373 | 7.241 | 0.005 | 0.000 | 0.000 | 0.009 | 0.009 | 0.000 | 84.64 |
| IDAG43_U7-14 | 50.20 | 27.495 | 6.084 | 0.169 | 0.000 | 0.000 | 0.056 | 0.000 | 0.000 | 84.00 |
| IDAG43_U7-15 | 58.60 | 32.054 | 7.078 | 0.000 | 0.000 | 0.000 | 0.000 | 0.000 | 0.000 | 97.73 |

| Spot | $UO_2$ | $UO_3$ | $ThO_2$ | $SiO_2$ | $Al_2O_3$ | $Fe_2O_3$ | $K_2O$ | $P_2O_5$ | PbO | $V_2O_3$ | $H_2O_{calc.}$ | Total |
|---|---|---|---|---|---|---|---|---|---|---|---|---|
| IDAG43_uran-coff6-9 | 56.750 | 10.691 | 0.000 | 15.442 | 0.089 | 2.162 | 0.561 | 0.001 | 0.591 | 0.000 | 13.713 | 86.287 |
| IDAG43_uran-coff6-10 | 67.300 | 6.273 | 0.000 | 17.369 | 0.031 | 2.465 | 0.153 | 0.000 | 0.709 | 0.000 | 5.700 | 94.300 |
| IDAG43_uran-coff6-11 | 53.800 | 12.307 | 0.000 | 16.035 | 0.070 | 3.821 | 0.116 | 0.005 | 0.611 | 0.000 | 13.235 | 86.765 |
| Average | 59.283 | 9.757 | 0.000 | 16.282 | 0.063 | 2.816 | 0.277 | 0.002 | 0.637 | 0.000 | 10.883 | 89.117 |

| Spot | $UO_2$ | $UO_3$ | $ThO_2$ | PbO | $SiO_2$ | CaO | $Fe_2O_3$ | $La_2O_3$ | $P_2O_5$ | $H_2O_{calc}$ | Total |
|---|---|---|---|---|---|---|---|---|---|---|---|
| **Coffinite** | | | | | | | | | | | |
| IDAG43_uran-coff8-16 | 52.6 | 7.72104 | 7.104 | 0 | 15.972 | 0 | 0 | 0 | 0 | 16.60296 | 83.39704 |
| **Thorite** | | | | | | | | | | | |
| IDAG43_uran-coff8-17 | 25.8 | 0 | 30.243 | 0 | 16.007 | 0.05 | 0.037 | 0 | 0.023 | | 72.15576 |
| IDAG43_uran-coff8-18 | 37.4 | 8.2309 | 17.608 | 0.287 | 15.684 | 0.039 | 0 | 0 | 0 | | 79.2489 |

## 8.7. Valencia Uraninite and Coffinite Compositions

The uranium mineral assemblage of the Valencia deposit samples is dominated by uraninite. Uranophane and coffinite comprise <5 wt.% of the uranium mineral population in eight of the nine samples; VALG 11 hosts 31.4 wt.% U in coffinite and 5.4 wt.% U in uranophane. Of the nine samples, two are surface, and seven are core samples (Table 8.3). Mineral chemistry data and formula recalculation for six uraninite specimens in one surface sample (VALG 11) and for six uraninite specimens in core Va26 113_225 m and five uraninite from core Va26 141_290 m. The core specimens are shown in Figure 8.12 and three BSE images of uraninite are presented in Figure 8.13. Table 8.3 presents a summary of the EPMA analyses of uraninite, coffinite and thorite grains from the Valencia sample set, recalculated mineral formulae from the analyses are given in Table 8.4. The two core samples represent two common uraniferous leucogranite textures at Valencia, one analogous to the E-type and one fitting the D-type description of Nex (1997).




Figure 8.12 Core samples from Va26 113 and Va26 141 NQ drill holes at Valencia. (a) The 225 m interval in hole 113 is dominated by a secondary Fe overprint, analogous to the typical E-type described at Goanikontes by Nex (1997). Quartz veining and cloudy-textured feldspars are indicative of high temperature metasomatism. (b) The 290 m interval in hole 141 contains a typical Valencia sheeted leucogranite, with smoky quartz and accessory biotite indicating uranium mineralisation. Alteration is present but far less intense than in the Va26 113 sample.

Seventeen uraninite mineral grains were analysed in total, with seventy individual analysis point locations. The minimum count per uraninite specimen is three points, and the maximum is seven.

The uraninite population in the Valencia samples shows consistent ratios in $U^{4+}/U^{6+}$ of between 1 and 1.4. The uraninite textures reflect fine grain sizes of <200 µm. Three anhedral crystals in Figure 8.13 illustrate inhomogeneous reflectance of the uraninite in the VALG 11 U7 image (Figure 8.13a); Subhedral uraninite, with extensive coffinite replacement from altered leucogranite in Va26 113_225 m (Figure 8.13b); and homogeneous reflectance in euhedral uraninite from the weakly altered Va26 141_290 m sample (Figure 8.13c).

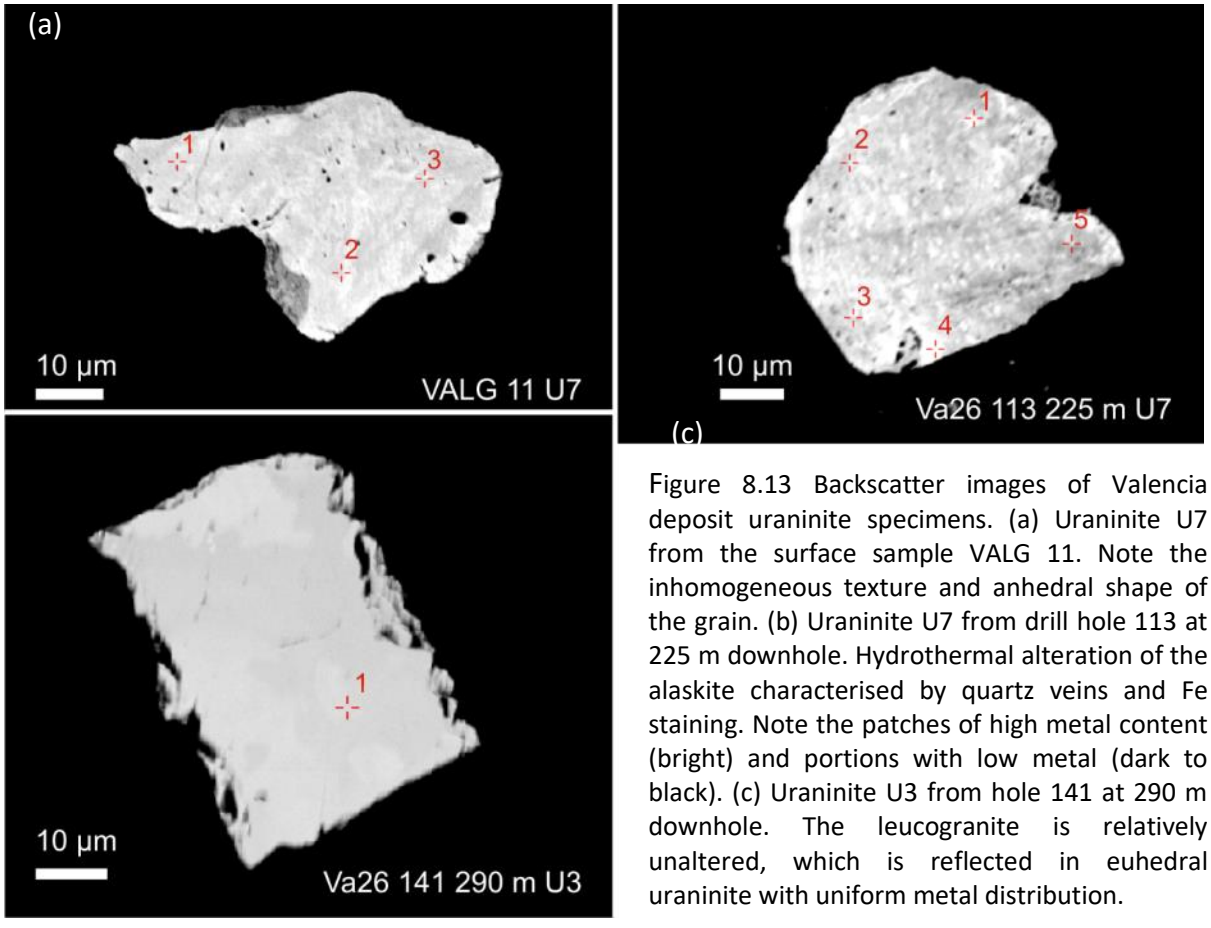



Figure 8.13 Backscatter images of Valencia deposit uraninite specimens. (a) Uraninite U7 from the surface sample VALG 11. Note the inhomogeneous texture and anhedral shape of the grain. (b) Uraninite U7 from drill hole 113 at 225 m downhole. Hydrothermal alteration of the alaskite characterised by quartz veins and Fe staining. Note the patches of high metal content (bright) and portions with low metal (dark to black). (c) Uraninite U3 from hole 141 at 290 m downhole. The leucogranite is relatively unaltered, which is reflected in euhedral uraninite with uniform metal distribution.

Alteration of the whole-rock is reflected in slightly elevated concentrations of Ca, Fe, Si, and K, with slightly depleted Pb (Figure 8.14a). The surface sample and the weakly altered Va26 141_290m sample have comparable ranges of $UO_2$ and $UO_3$ with the surface sample hosting

about half as much $ThO_2$ as the sample from core (Figure 8.14b and c). The samples have a wide range in $UO_2$ but a narrow $UO_3$ which may reflect preferential, but consistent leaching of $U^{6+}$. Certain uraninite specimens display prominent coffinite replacement, necessitating analyses and formula recalculation for coffinite domains within individual grains. Coffinite and thorite analysis and formula recalculation are presented for a coffinitised uraninite specimen (Va26 113_225 m U7) in Table 8.3.

Table 8.3 Summary of uraninite analyses undertaken by EPMA on 11 uraninite specimens from Valencia. Samples are from 2 NQ drill cores and 6 specimens from a surface sample at the Valencia Deposit.

| Sample and Specimen | Pts. | Max $U_{total}$ (wt.%) | Max $UO_2$ wt.% | Max $ThO_2$ wt.% | Max $SiO_2$ wt.% | Max CaO wt.% |
|---|---|---|---|---|---|---|
| VALG11 - 6 grains | 24 | 89.642 | 51.00 | 6.013 | 0.397 | 0.776 |
| Va 26 113-225 m - 6 grains | 22 | 87.081 | 50.30 | **21.038** | **12.455** | **1.073** |
| Va26 141-290 m - 5 grains | 24 | **90.288** | **52.12** | 8.474 | 0.797 | 0.685 |
| Total uraninite :17 grains | **70** | | | | | |
| Va26 113-225 m Coff. | 2 | 68.5 | 19.3 | 20.5 | 13.38 | 7.41 |
| Va26 113-225 m Thorite* | 1 | 25.4 | 14.40 | 40.37 | 13.86 | 3.43 |

### *Coffinite and Thorite Calculations*

Sample Va26 113_225 m U7 (Figure 8.13b) is calculated as coffinite on two of the five analysis points (indicated as points 2 and 5 in Figure 8.13b) because thorite and coffinite may form solid solution, point 5 is also calculated as thorite, as the Th content at the point is relatively high, at 40.38 wt.% $ThO_2$. Points 2 and 5 on Va26_113_225 m U7 recalculated as replacement coffinite - $U(SiO_4)_{1-x}(OH)_{4x}$:

Oxygen: 3.04, specimens: 1, sample points: 2

$$(U^{6+}_{0.221}U^{4+}_{0.064}Th_{0.070}Pb_{0.004})_{0.358}(Si_{0.291}Al_{0.001}Ca_{0.097}Fe_{0.001}K_{0.021})_{\Sigma=0.411}(OH)_{1.677}$$

Point 5 calculated as thorite returned the following formula:

$$(U^{4+}_{0.202}U^{6+}_{0.142}Th_{0.563}Pb_{0.013}Al_{0.004}Ca_{0.225}P_{0.001})_{\Sigma=1}SiO_4$$

The most acceptable compositional calculations for uraninite on specimen Va26 113_225 m U7 is limited to point number 4 (position is illustrated on the backscatter image Figure

8.13c). The majority of the grain appears to be uraninite, and analysis at Point 4 is calculated assuming uraninite with an oxygen coordination of 2.

The recalculation returns a balanced non-stoichiometric formula as follows:

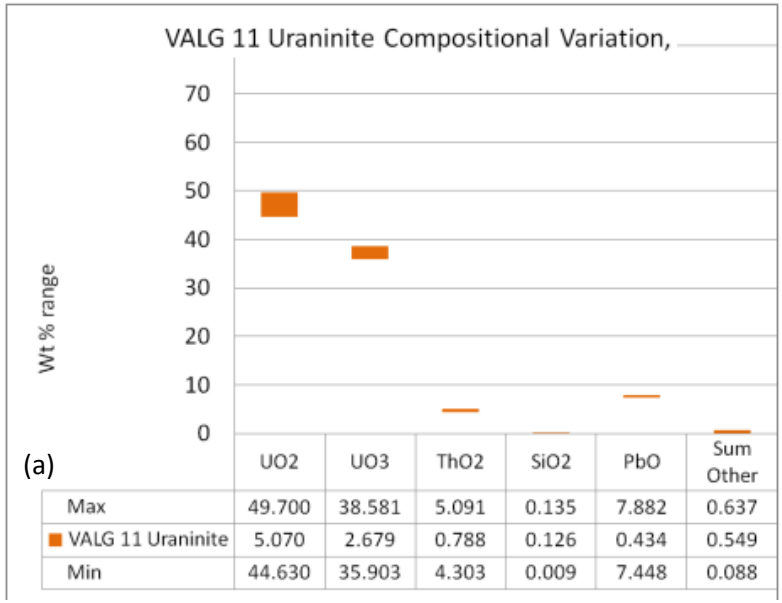
Oxygen: 2, specimens, 1: analyses: 1

$(U^{4+}_{0.363}U^{6+}_{0.310}Th_{0.046}Si_{0.177}Pb_{0.038}Ca_{0.016}K_{0.05})_{\sum=0.99}O_2$

Table 8.4 The recalculated non-stoichiometric formulae of uraninite, coffinite and thorite from the Valencia deposit.

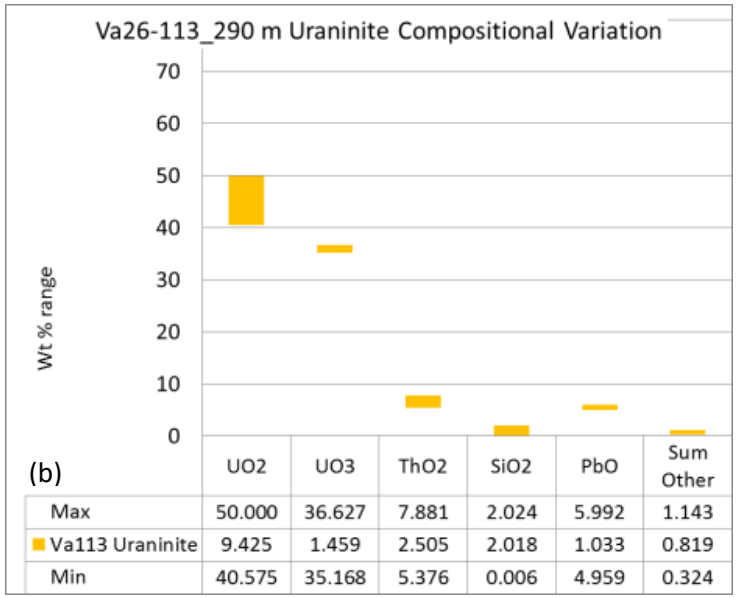
| Valencia uraninite formula recalculations summary | |
|---|---|
| VALG11 | $(U^{4+}_{0.495}U^{6+}_{0.351}Th_{0.046}Pb_{0.084}Si_{0.004}Ca_{0.019})_{\sum=0.998}O_2$ |
| VA141-290 m | $(U^{4+}_{0.506}U^{6+}_{0.35}Th_{0.043}Pb_{0.072}Ca_{0.022}Y_{0.004})_{\sum=0.998}O_2$ |
| VA113-225 m | $(U^{4+}_{0.37}U^{6+}_{0.30}Th_{0.08}Si_{0.13}Pb_{0.05}Ca_{0.05}K_{0.02})_{\sum=1.0}O_2$ |
| VA113-225 m coff. | $(U^{6+}_{0.221}U^{4+}_{0.064}Th_{0.070}Pb_{0.004})_{0.358}(Si_{0.291}Al_{0.001}Ca_{0.097}Fe_{0.001}K_{0.021})\sum=_{0.411}(OH)_{1.677}$ |
| VA113-225 m thorite | $(U^{4+}_{0.202}U^{6+}_{0.142}Th_{0.563}Pb_{0.013}Al_{0.004}Ca_{0.225}P_{0.001})_{\sum=1}SiO_4$ |

A mineral map was produced of uranium specimen U1 from diamond hole Va26 113 at 225 m. The probe study obtained five analyses of the specimen; two returned low totals and were rejected for compositional calculations. Coffinite is the likely replacement phase, and an attempted formula recalculation using points 1 and 5 returned an un-balanced formula recalculation for the replacement coffinite (inserted into Figure 8.15). The element map of the sample shows that it has an inhomogeneous texture, with Pb distributed in discrete patches (galena) and Y-bearing thorite filling prominent fracture networks (thorite solid solution). The presence of K suggests that there is boltwoodite in the mineral. Ca correlates with Pb and may be in a phase of unknown composition.



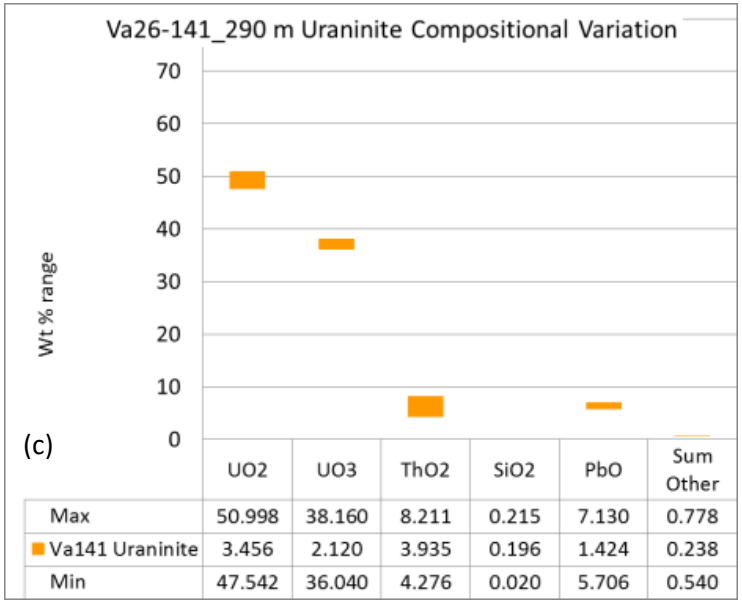

(a)

| | UO2 | UO3 | ThO2 | SiO2 | PbO | Sum Other |
|---|---|---|---|---|---|---|
| Max | 49.700 | 38.581 | 5.091 | 0.135 | 7.882 | 0.637 |
| VALG 11 Uraninite | 5.070 | 2.679 | 0.788 | 0.126 | 0.434 | 0.549 |
| Min | 44.630 | 35.903 | 4.303 | 0.009 | 7.448 | 0.088 |




(b)

| | UO2 | UO3 | ThO2 | SiO2 | PbO | Sum Other |
|---|---|---|---|---|---|---|
| Max | 50.000 | 36.627 | 7.881 | 2.024 | 5.992 | 1.143 |
| Va113 Uraninite | 9.425 | 1.459 | 2.505 | 2.018 | 1.033 | 0.819 |
| Min | 40.575 | 35.168 | 5.376 | 0.006 | 4.959 | 0.324 |




(c)

| | UO2 | UO3 | ThO2 | SiO2 | PbO | Sum Other |
|---|---|---|---|---|---|---|
| Max | 50.998 | 38.160 | 8.211 | 0.215 | 7.130 | 0.778 |
| Va141 Uraninite | 3.456 | 2.120 | 3.935 | 0.196 | 1.424 | 0.238 |
| Min | 47.542 | 36.040 | 4.276 | 0.020 | 5.706 | 0.540 |

Figure 8.14 Uraninite compositional variations in specimens of drill core and from surface.(a) The six surface sample uraninites show a narrow range in UO3 and UO2 ratios. Th, Pb, Si, and other contaminants abundances compare similarly to those in the Va26 141 290 m uraninite population. (b) The Va26 113 225 m sample hosts a population of uraninite with variable composition. UO2 ranges between 40.5- and 50 wt.% while UO3 is constant and close to 36 wt.% in all four specimens. Si shows a greater range than the Va26 141 and VALG 11 samples. (c) The five uraninite specimens from hole Va26 141 290 m represent weakly-altered sheeted leucogranite. Th and Pb show a slightly wider range in abundance than in VALG 11.

.

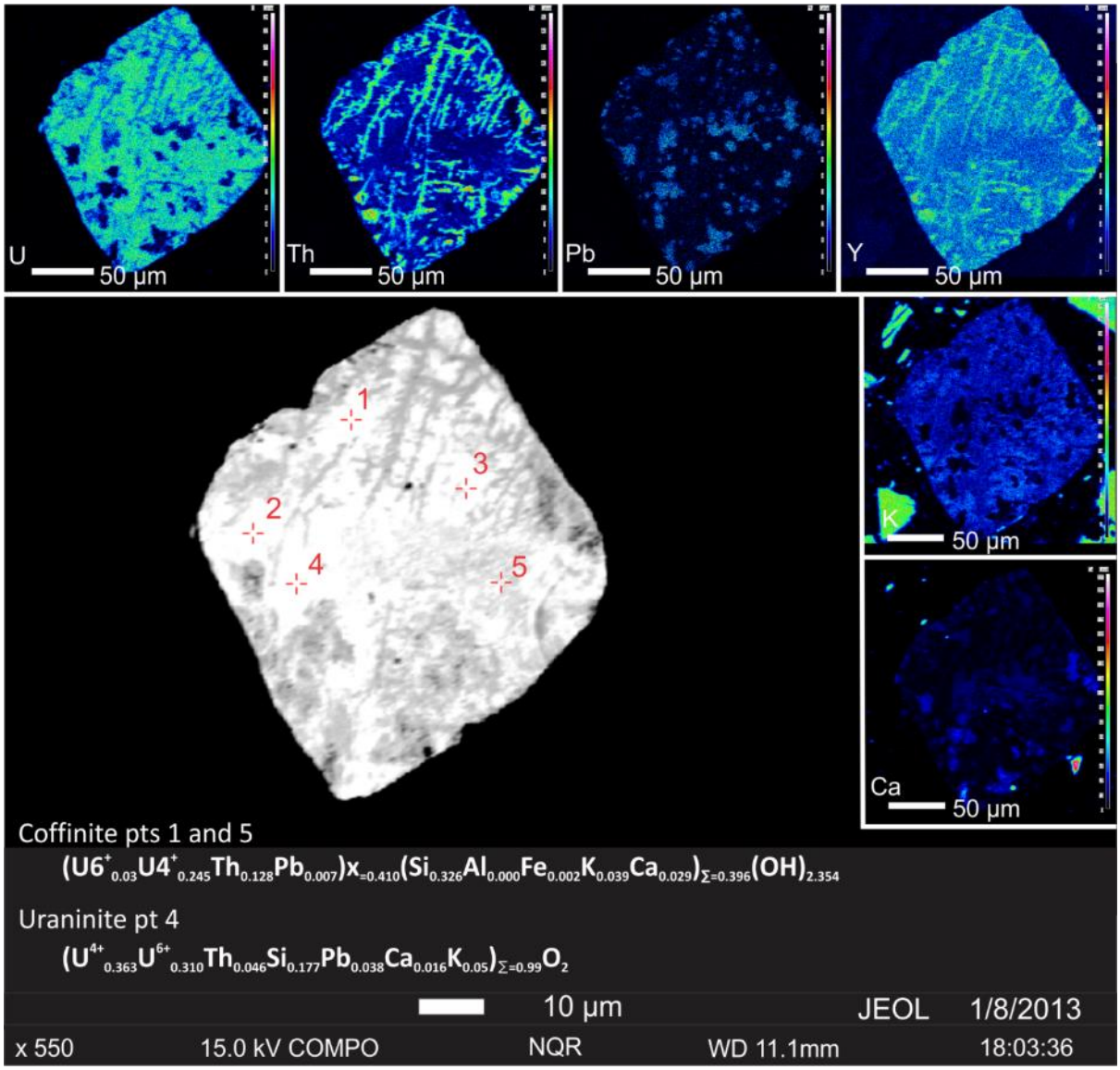



Figure 8.15 Coffinite replacement of uraninite U1 from Va26 113 225m. The backscatter image at centre is of a euhedral uraninite with clear leaching of metal along preferred fracture pathways, with highest density, U-rich material somewhat preserved in the core of the specimen. The fracture pathways have lost U6+ and Th remains as a relatively concentrated component. Y is coincident with Th and may be concurrent with new phosphate deposition (potentially monazite with xenotime. Pb and U are inversely abundant, and represent Pb deposition (galena). K correlates with U abundance and is the most common impurity after Si at points 1 and 5.

## 8.10. Husab Uranium Mineral Compositions

The Husab deposits constitute the largest assembly of granite-hosted uranium mineralisation in Namibia, and thus, also the largest collection of sampling material available to this study. The Husab sheeted leucogranites host three primary uranium phases; these are dominant uraninite, with accessory proportions of betafite and brannerite. Brannerite

and betafite appear to be trace components of the uraninite-coffinite-uranophane/boltwoodite assemblages, but may be locally significant (Johnson, 2011).

Coffinite is late, and in most examples, involves the partial- to complete replacement of uraninite, almost always from the outside in. Fine-grained coffinite veins that fill radial fractures in aluminosilicates and quartz around primary uraninite and hairline seams in the surrounding metasediments constitute a very small proportion of U-silicates. Mineral formulae recalculations were applied to the uraninite, coffinite, brannerite and betafite specimens, according to the methodology given in Appendix G2.

### *Husab Uranium Mineralogy Sample Descriptions*

The RDD008 and RDD006 holes (Zone 1 and Zone 2, respectively) provide five and six uraninite specimens, respectively for a total of 51 analysis points (23 and 28, respectively) Averages of the compositions are given as cation-corrected non-stoichiometric formulae in Table 8.5. The RDD373 hole (Zone 1) provides three uraninite specimens (two at 64 m and one 125 m); three brannerite specimens at 64 m and 93 m (); and one which is not true brannerite (leucoxene) at 125 m. A single betafite specimen at 115 m downhole in RDD373 is analysed at 15 positions.

The RDD006 and RDD008 drill holes contain fairly typical examples of the D-type uraniferous leucogranites that are coarse-grained, quartz-dominant, with white feldspars and variably coarse biotite. The RDD008 sample contains a portion of quartz-biotite segregation. The RDD373 leucogranite samples represent hydrothermally altered leucogranite, alternating between limonite-haematite discoloration in the near surface environment and sericite-chlorite-epidote dominated alteration at depth.The uraninite specimens from the three drill holes, each drilled -60° on 270°, represent a variety of textures and characteristics:

- RDD008 and RDD006 specimens are euhedral specimens, which are likely to be magmatic;
- Uraninite specimens from RDD373 64 m are sourced from the same leucogranite that hosts brannerite; and

- The RDD373 125 m uraninite represents a biotite-hosted uraninite with well-defined replacement at the rim.

Table 8.5 Husab uraninite, coffinite, brannerite, and betafite composition summary.

| Samples | Zone 1 RDD008 U1-U5 Uraninite | Zone 2 RDD006 U2-U6 Uraninite | Zone 1 RDD373 64 m U8-U9 Alt. uraninite | RDD373 125 m U7 Uraninite core | RDD373 125 m U7 Uraninite rim | RDD373 125 m U5 Coffinite | RDD373 115 m Betafite | RDD373 Brannerite |
|---|---|---|---|---|---|---|---|---|
| specimens/ Analyses | 5/23 | 6/28 | 2/8 | 2/10 | 1/3 | 1/4 | 1/15 | 3/35 |
| $UO_2$ | 50.074 | 47.728 | 48.010 | 47.884 | 41.089 | 40.825 | | 8.205 |
| $O_3$ | 36.984 | 40.784 | 33.988 | 34.700 | 30.767 | 15.78658 | 34.995 | 35.811 |
| $ThO_2$ | 8.432 | 7.681 | 9.107 | 7.672 | 15.682 | 11.89875 | 3.666 | 7.008 |
| PbO | 5.880 | 5.558 | 4.685 | 5.433 | 2.787 | 0.022 | 1.798 | 1.630 |
| $SiO_2$ | 0.063 | 0.411 | | 0.151 | 4.055 | 15.2285 | | |
| $Al_2O_3$ | 0.000 | 0.000 | | | | 0 | | |
| CaO | 0.397 | 0.550 | 0.214 | 0.339 | 1.021 | 0.35175 | 3.998 | 3.956 |
| $Fe_2O_3$ | 0.018 | 0.013 | 0.078 | | | 0.19625 | 1.344 | 1.003 |
| $K_2O$ | 0.000 | 0.037 | | | | 1.2775 | | |
| $Na_2O$ | | | | | | 0.03275 | | |
| $MoO_3$ | | | | 0.007 | 0.213 | | | |
| $P_2O_5$ | 0.007 | 0.007 | | | | | | |
| $SO_3$ | | | | 0.027 | 0.000 | | | |
| $TiO_2$ | | | 0.052 | | | | 27.531 | 36.985 |
| $V_2O_3$ | 0.000 | 0.000 | | | | | | |
| $Nb_2O_5$ | | | | | | | 12.523 | |
| $Ta_2O_5$ | | | | | | | 0.459 | |
| $Ce_2O_3$ | | | | | | | | |
| $La_2O_3$ | | | | | | | | |
| $Y_2O_3$ | | | 0.297 | | | | 6.081 | 1.219 |
| $ZrO_2$ | | | 0.021 | | | | | |
| **Total** | **101.987** | **102.768** | **96.450** | **96.212** | **95.613** | **85.61908** | **100.000** | **95.817** |
| Water (calc.) | | | | | | 14.38092 | 7.604 | |
| REE + $Y_2O_3$ | 0.000 | 0.000 | 0.297 | 0.000 | 0.000 | 0.000 | 6.081 | 1.219 |
| $U^{4+}/U^{6+}$ | 1.358 | 1.472 | 1.414 | 1.381 | 1.338 | | | |
| Ti/Fe | | | 0.673 | | | | 22.201 | 58.025 |
| $U_{tot}$ | 87.191 | 88.478 | 48.123 | 82.584 | 71.855 | | 32.179 | 44.015 |
| U:Th | 10.325 | 11.523 | 9.004 | 10.765 | 4.582 | 4.758 | 9.545 | 6.280 |

The RDD373 sampling interval (64 m to 125 m) represents a ~60 m interval of intercalated calcsilicates, marble lenses, mottled-textured cordierite gneiss, quartzite, and garnet-bearing schists. The interval constitutes the upper Rössing Formation as described in Anderson and Nash (1997). Unique petrographic, geochemical and REE attributes of the RDD373 leucogranites in this interval are described in chapter 4, chapter 5, and chapter 6, respectively. Backscatter reflectance in the sample collection tends to be uniform, reflecting high-density uraninite with low ratios of replacement by coffinite.

## 8.11. Husab Uraninite Composition Analysis

### *Weakly Altered Uraninite*

Four of the eleven samples are presented in Figure 8.16a to Figure 8.16d; two samples from RDD008 (284 m DH) and two from RDD006 (171 m DH):

- RDD006 U3a and U3b represent a compound grain, with one portion showing slightly dull BSE and therefore a slightly lower metal density;
- RDD008 U3 likely represents more than one phase of cubic uraninite growth with low-density mineral inclusions;
- RDD006 U6 is a large grain, ~ 1 mm long, and is given as an example of primary uraninite mineralisation at Husab, the large size effectively means analyses toward the core represent uraninite of an original composition; and
- RDD008 U5 represents a fine-grained cubic uraninite with evidence of U replacement and dissolution at the grain boundaries.

Each of the eleven weakly-altered uraninite grains is analysed at between three and six points, with a total of 51 compositional analyses constituting the whole population. The recalculated oxide proportions show that uranium proportions range from 81.3 wt.% to 89.8 wt.% U-oxide ($UO_2$ + $UO_3$). $ThO_2$ proportions range from 7.3 wt.% to 9.4 wt.% and $SiO_2$ is relatively low, from 0.04 wt.% to 1.83 wt.%. PbO is fairly consistent and ranges from 4.7 wt.% to 6.6 wt.% while CaO replacement in all samples is relatively low, between 0.2 wt.% and 0.8 wt.%. The average Zone 1 uraninite specimens contain more Th, more Pb and have a lower $UO_2/UO_3$ ratio than the Zone 2 specimens; while the Zone 2 specimens contain more total U-oxide, more CaO and more $SiO_2$ (0.4 wt.% vs. 0.06 wt.%). Overall the low Ca, Si and consistent U/Pb ratios reflect uraninite that has undergone relatively low degrees of alteration.

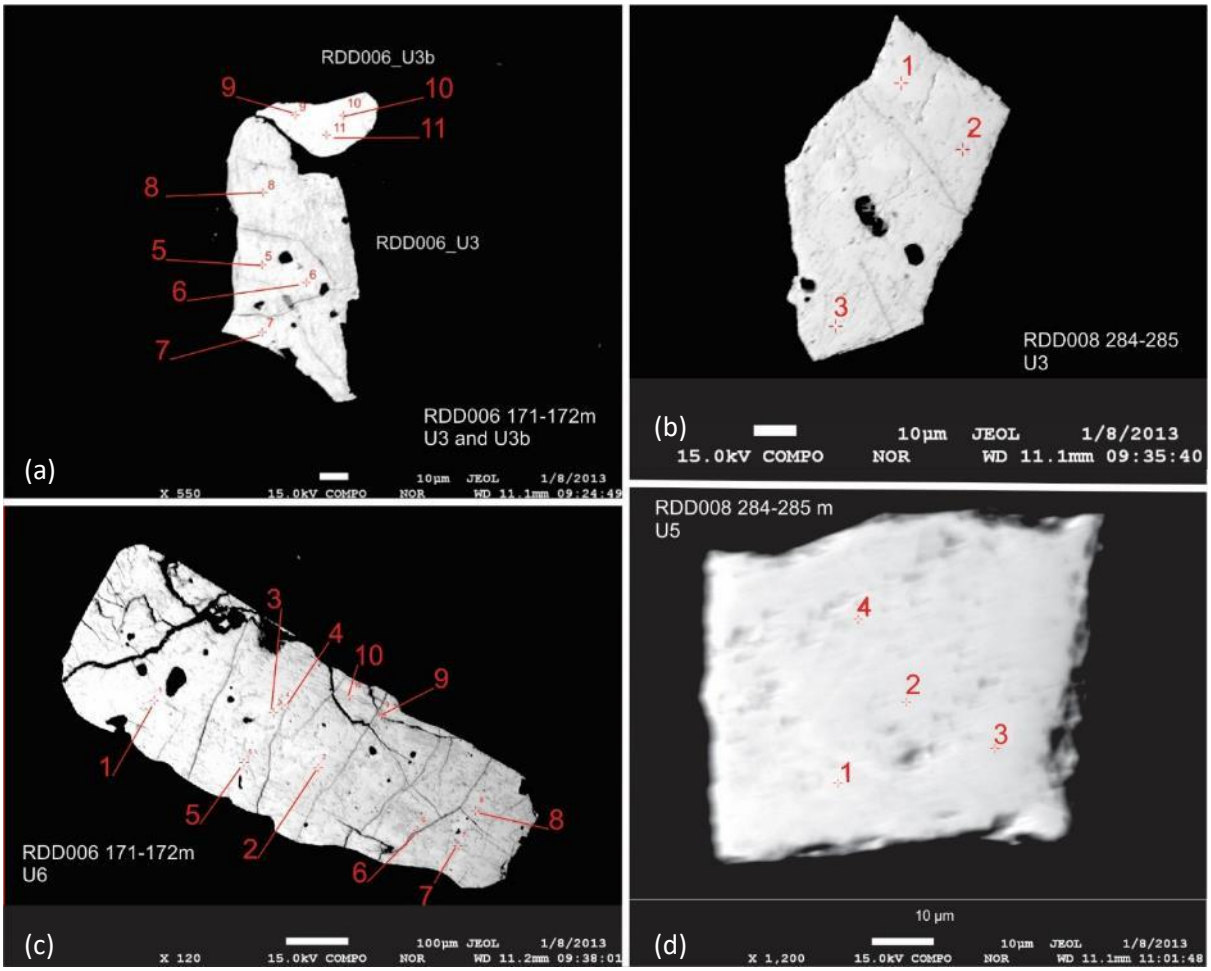



Figure 8.16 Uraninite specimens from the Husab Zone 1 and Zone 2 deposits. (a) U3 is a compound grain with variable metal content; U3b contains a denser U concentration than U3. (b) RDD008 284-285 m U6 is a euhedral uraninite with calcite inclusions. (c) RDD006 171-172 m U3 is one of the largest uraninite grains analysed. It shows relatively uniform density and the large size allows for analyses that are independent of the influence of prominent fractures. (d) RDD008 284-285 m U5 is a euhedral uraninite, ~60 µm across. It appears to be uniformly dense and has a finely pitted surface.

### *Altered Uraninite*

The altered uraninite specimens are represented by five individual grains analysed at 21 sampling points. All five examples come from the RDD373 hole and the specimens include a pair of >100 µm, euhedral uraninite crystals hosted in altered biotite with cleavage-parallel magnetite exsolution lenses (Figure 8.17a).

This relationship is particularly common in the Husab samples, where variably chloritised biotite nests host coarse-grained biotite in association with zircon, fluorite, pyrite, and magnetite. The RDD373 125m U7 specimens have replacement/metal leaching at one of the rims, indicated by low backscatter reflectance. Compositional ranges of the RDD373 125m

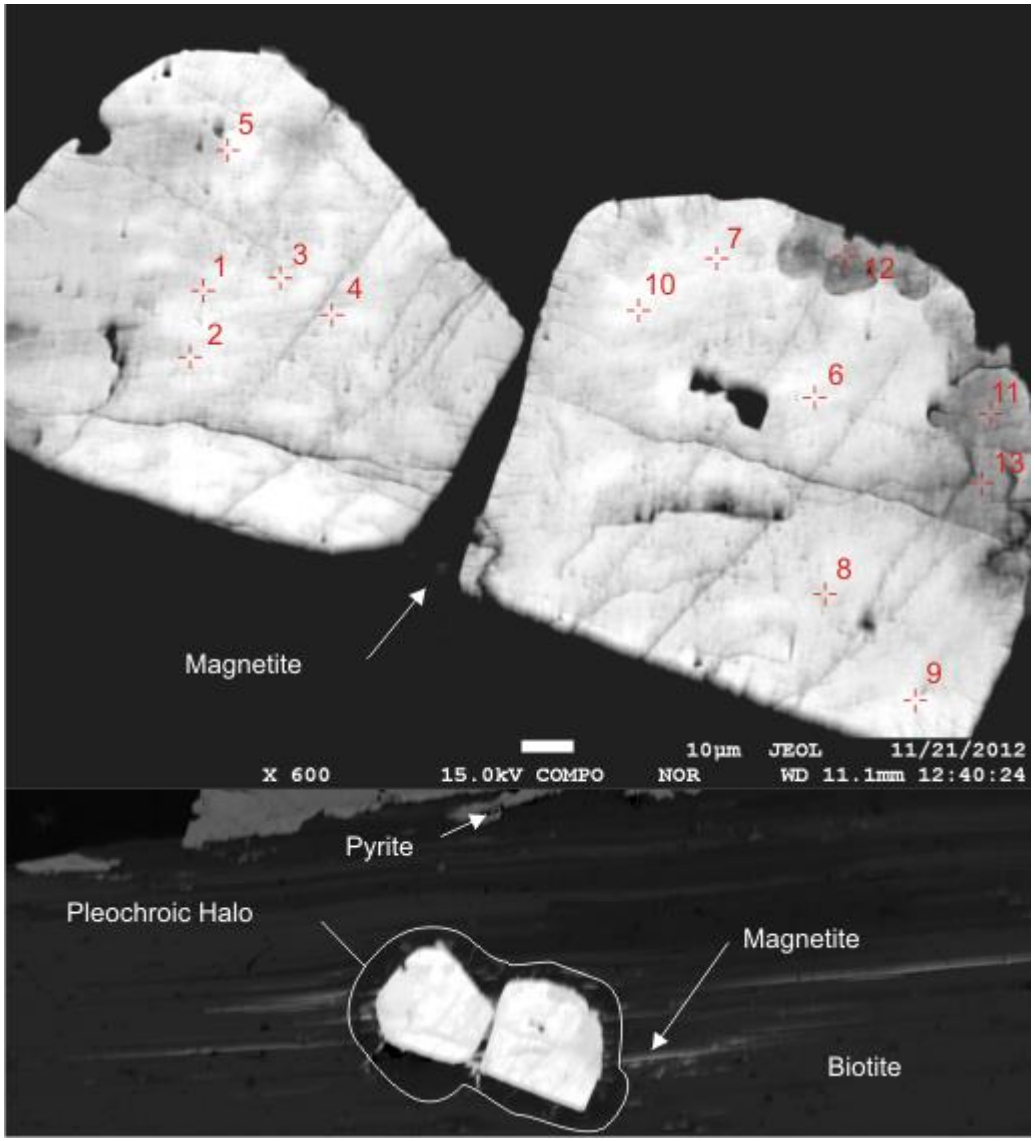
U7 uraninite analyses; $UO_2$+$UO_3$, $ThO_2$, PbO, $SiO_2$, and CaO + $SO_3$ + $MoO_3$ proportions help distinguish the less-altered U7 uraninite core from the altered rim (points 11, 12, and 13 in Figure 8.17a).

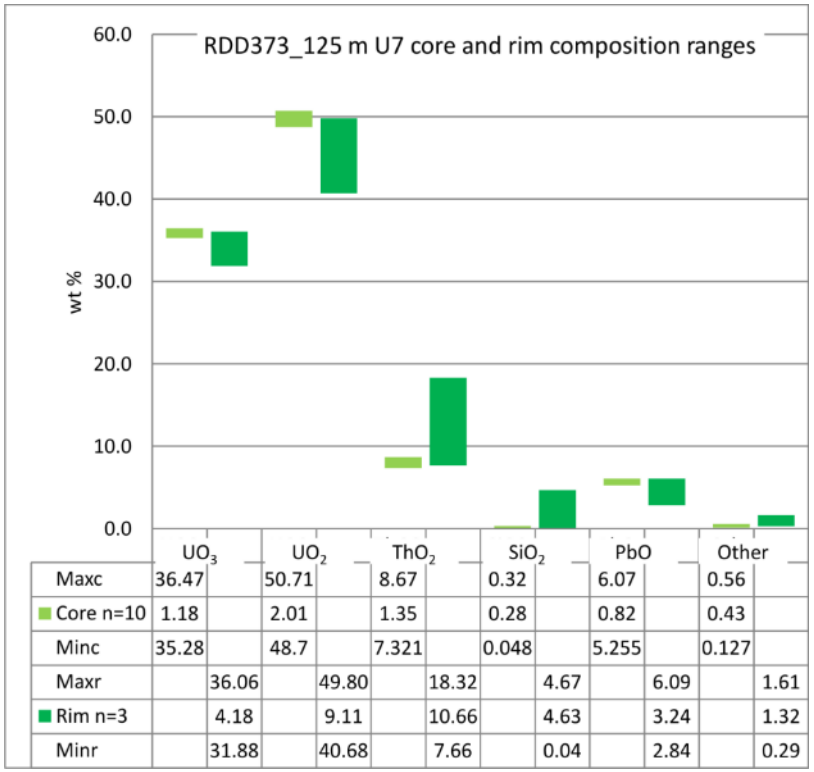
U totals are lower at the rim, with greater ranges in all oxide abundances; the low Pb and U minima reflect U and Pb mobility. Trace amounts of Mo at the uraninite rim (max. 0.3 wt.% at point 13 (Figure 8.17a) in the U7 uraninite reflects late sulphide mineralisation, prevalent in a high proportion of the Husab mineralised zones.

A comparative table of non-stoichiometric uraninite compositions is given in Table 8.6. The uraninite specimens from hole RDD373 are considered more altered than the specimens from the RDD006 and RDD008 holes.

Table 8.6 Recalculated mineral formulae for Husab uraninite specimens.

| **Area/mineral** | **Recalculated formula** |
|---|---|
| Zone 1 RDD008 284 m uraninite | $(U^{4+}_{0.488}U^{6+}_{0.337}Ca_{0.020}Pb_{0.073}Th_{0.078}Si_{0.003})_{\Sigma=1.000}O_2$ |
| Zone 2 RDD006 171 m uraninite | $(U^{4+}_{0.333}U^{6+}_{0.303}Th_{0.133}Pb_{0.042}Ca_{0.082}K_{0.008})_{\Sigma=0.998}O_2$ |
| Zone 1 RDD373 64 m altered uraninite | $(U^{4+}_{0.501}U^{6+}_{0.325}Th_{0.094}Pb_{0.057}Ca_{0.011}Fe_{0.003}Ti_{0.002}Y_{0.007})_{\Sigma=0.999}O_2$ |
| Zone 1 RDD373 125 m uraninite core | $(U^{4+}_{0.499}U^{6+}_{0.331}Th_{0.079}Pb_{0.066}Ca_{0.016}Si_{0.007})_{\Sigma=1.000}O_2$ |
| Zone 1 RDD373 125 m uraninite rim | $(U^{4+}_{0.371}U^{6+}_{0.254}Ca_{0.043}Pb_{0.030}Th_{0.140}Si_{0.159})_{\Sigma=1.000}O_2$ |




| | $UO_3$ | | $UO_2$ | | $ThO_2$ | | $SiO_2$ | | PbO | | Other | |
|---|---|---|---|---|---|---|---|---|---|---|---|---|
| Maxc | 36.47 | | 50.71 | | 8.67 | | 0.32 | | 6.07 | | 0.56 | |
| Core n=10 | 1.18 | | 2.01 | | 1.35 | | 0.28 | | 0.82 | | 0.43 | |
| Minc | 35.28 | | 48.7 | | 7.321 | | 0.048 | | 5.255 | | 0.127 | |
| Maxr | | 36.06 | | 49.80 | | 18.32 | | 4.67 | | 6.09 | | 1.61 |
| Rim n=3 | | 4.18 | | 9.11 | | 10.66 | | 4.63 | | 3.24 | | 1.32 |
| Minr | | 31.88 | | 40.68 | | 7.66 | | 0.04 | | 2.84 | | 0.29 |

Figure 8.17 Composition and texture of uraninite U7, hosted in biotite of sample RDD373-125 m. (a-b) The uraninite grains are euhedral and surrounded by a halo of alteration in the host biotite. Grain sizes are ~100 µm across. (c) Si, Th, Pb and contaminant phases ($MoS_2$) contrast between core and rim; U and Pb ranges in the core are ~4 x greater in the rim, Th range is ~8 x greater in the rim, Si range is ~16x greater in the rim, and total contaminants are ~3 x greater in the rim.

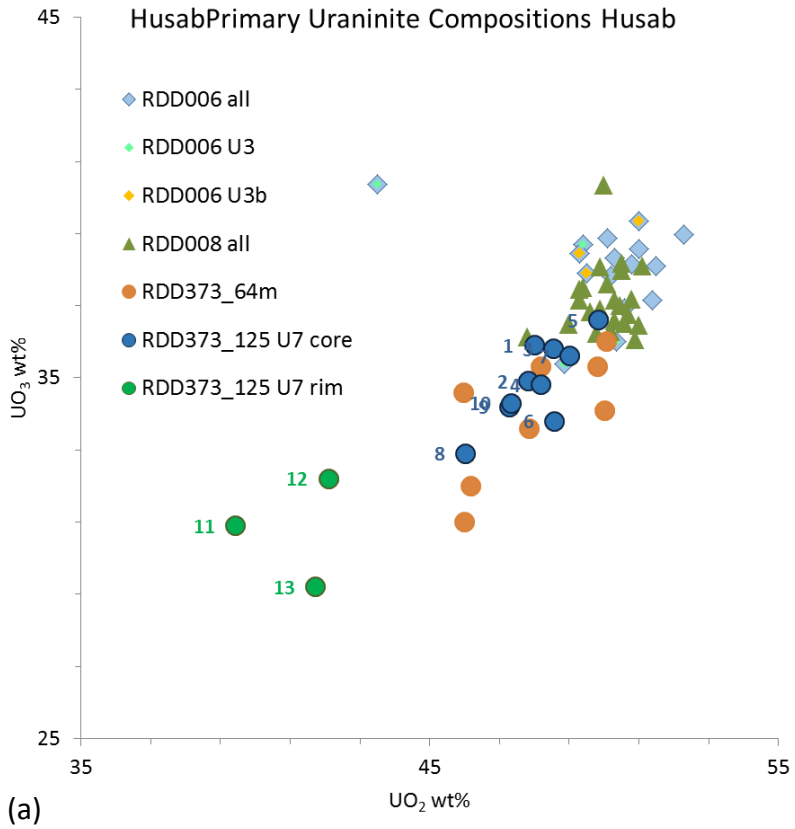
### *Husab Uraninite Compositional Variation*

Binary plots of U oxide proportions show that the EPMA analysis of uraninite populations discriminates between the Zone 1 (RDD008 and RDD373 holes) and Zone 2 (RD006 hole) uraninite groups (Figure 8.18). Weakly altered uraninite from Zone 1 (RDD008) and Zone 2 (RDD006) tend to cluster with relatively high U content; the compound grains RDD006 (U3 and U3b) and RDD373 (U7 core and rim) show consistent contrasts in $U^{4+}$ and $U^{6+}$ abundances, with the rim of the grain reflecting low relative U (Figure 8.18a).

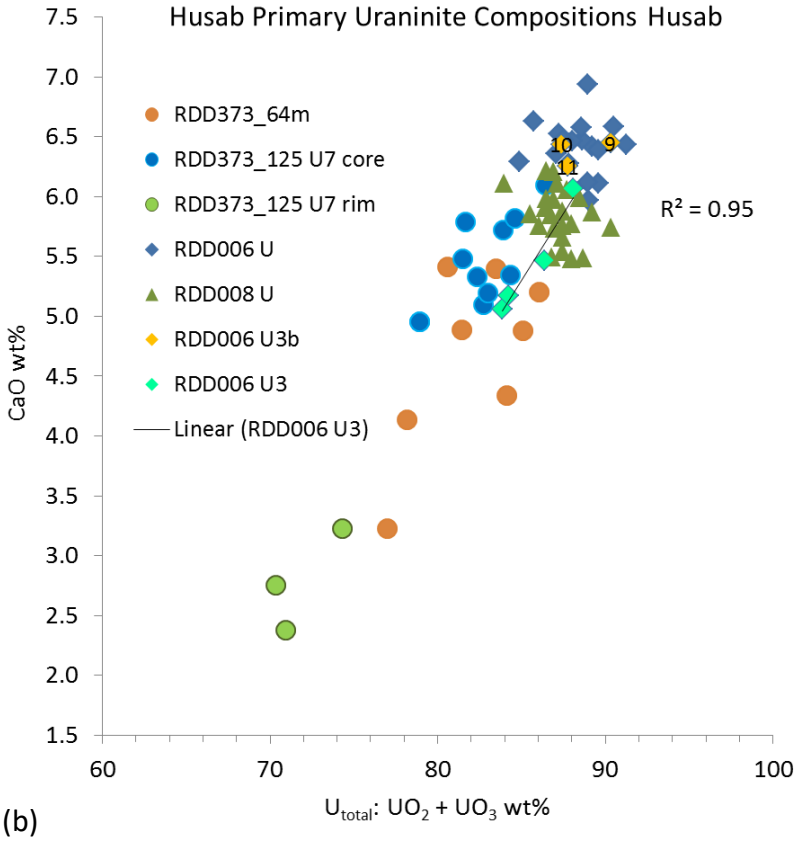
CaO content in the altered uraninite (RDD373 - 64 m and 125 m) contain lower CaO than the less altered RDD006 and RDD008 specimens. There is a contrast in U vs. Ca in the RDD006 U3 and U3b specimens; the U3b specimen is bright and contains higher proportions of U, while U3 is dull, and has an inhomogeneous reflectance, yet shows a linear relationship between U and Ca, perhaps due to systematic Ca replacement of U

The major trends in the Husab uraninite populations are summarised as follows:

- Uraninite RDD373 64 m is in oxidised leucogranite, and has less U and Ca than the weakly altered RDD006 and RDD008 uraninite;
- The rim of RDD373 U7 uraninite and the dull uraninite in RDD006 U3 have consistently lower U and Ca abundances than their bright BSE counterparts, the RDD373 $U7_{core}$ and bright RDD006 U3b specimens, respectively;
- The strong correlation between U and CaO in RDD006 U3 suggests Ca may be substituting, and/or that calcite is systematically replacing uraninite (Figure 8.18b); and
- The Zone 2 uraninite (RDD006 population) contains U and Ca in greater abundances than the other Husab uraninite populations of this study (Figure 8.18b).




(a)




(b)

Figure 8.18 Uraninite specimens from the RDD008 and RDD006 drill cores, Zone 1 and Zone 2, respectively. (a) $UO_2$ vs. $UO_3$ of selected Husab RDD006 and RDD008 uraninite specimens; The RDD006-U6, RDD006 U3b and RDD008-U5 samples plot with the closest cluster, reflecting uniform metal distribution. The numbers adjacent to the U7 symbols correspond to the labels in Figure 8.17a.

(b) U-oxide wt.% vs. CaO wt.% of the Husab uraninite populations. The biotite-hosted and altered uraninite from hole RDD373 have lower overall U content than the weakly altered Zone 1 and Zone 2 populations from holes RDD008 and RDD006, respectively. Labels 9, 10, and 11 correspond to the analyses points on RDD006 U3b, in Figure 8.55(a), and highlight the contrast in U and Ca content between the bright reflectance of U3b and the comparatively dull U3 specimen. CaO and $U_{total}$ show poor correlation in most of the analyses populations which indicates that Ca-phases replace altered uraninite. RDD006 U3, however, has a strong correlation which may instead represent direct Ca substitution for U, or simply that uraninite replacement by calcite is a systematic process.

## 8.12. Primary Uraninite Compositional Variation - Discussion

The primary comparative tool for uranium mineral compositions is the U and Th, U and Pb, and $U^{4+}$ and $U^{6+}$ ratio. The U valence ratios require non-stoichiometric recalculation. Magmatic uraninite will invariably crystallise with a Th component among other contaminants such as Ca, REE, and Si (after Janeczek and Ewing, 1992a and 1992b). The $UO_2$:$ThO_2$ should be fairly consistent in the magmatic uraninite population in individual alaskite deposits with variations in composition attributed to one or more of the following factors:

a. The bulk ratio of U:Th in the partial melt of the source rock, and the degree to which U and Th host minerals of the source are in equilibrium with partial melt.
b. If the silicate melt component is in equilibrium with common Th host minerals such as monazite or thorite, Th may partition into these phases first, and not be available to late-crystallising uraninite;
c. Ratio of $U^{4+}$ and mobile uranyl complexes in the melt associated fluids and thus also the degree to which REDOX buffering has reduced $U^{6+}$;
d. The concentration of $U^{6+}$ in the oxidised magmatic fluids and the efficiency at which U is reduced by wall-rock interaction;
e. Abundances of phosphate and silicate into which Th may preferentially partition, which may be a function of country-rock assimilation (particularly skarns); and
f. The degree to which leaching of $U^{6+}$ has removed U from uraninite.

The last point necessitates the formula recalculation in order to assess the proportions of insoluble $UO_2$ and $UO_3$ in a specific uraninite. The non-stoichiometric ratio gives some indication of how effectively the soluble uranium ions were removed from altered uraninite by reactive fluids. The local REDOX conditions of uraninite crystallisation may be inferred when the ratio is calculated for unaltered uraninite analyses.

The Central Damara primary uraninite populations are compared with two comparable granite-hosted uraninite from collisional settings; namely, the Trans-Hudsonian Orogeny in

the Fraser Lakes District (EPMA data from McKechnie, 2012) and late- to post-collisional granites of the Variscan Orogeny in the Erzgebirge (Förster, 1999). Figure 8.19 is a comparison of $UO_2$ wt.% with $ThO_2$ of the data from the comparative orogenic granite-hosted uraninite, and all non-stoichiometric recalculations were performed with the same Excel macro as the Damara specimens. The granites described for the Bancroft District comprise similar, late-orogenic, highly evolved intrusives, while the Variscan sample set comprises biotite- and biotite-muscovite-Li-mica- bearing granites, in which the micas host significant quantities of uraninite. The Variscan granite samples are described as S-type as they contain two micas and the high biotite content described for the samples in Förster (1999) suggest they are less-evolved than the sheeted leucogranites in Namibia and Canada. The compositional ranges of uraninite in the *ca*. 310 Ma Variscan granites of the Erzgebirge show a relatively uniform trend of Th substitution into uraninite (Werner and Lippolt, 1998b; Werner et al., 1997; and Förster, 1999). The Damaran and Bancroft specimens show a wide range of $UO_2$ and $ThO_2$ values and poor correlation between the two elements.

Most granites plot with $UO_2$:$ThO_2$ between 5 and 20, the older Bancroft samples have considerably lower U/Th ratios; possible explanations include:

1. **Age of granites**: U decay to radiogenic Pb is greatest in the *ca* 1.8 Ga, Trans-Hudsonian Bancroft granites that contain up to 17 wt.% PbO; and lowest Pb content is in the Hercynian-age, Variscan granites (~4 wt.% PbO). The Pan African, Damara samples in comparison average 5.9 wt.% PbO;
2. **Sub solidus reactions**: Interaction with residual oxidising fluids, converting $UO_2$ to mobile $UO_3$;
3. **Th in source minerals**: High-percentages of Th host minerals in equilibrium with the silicate melt; and/or
4. **Equilibrium**: Co-crystallisation of uranothorite and uraninite at high T (after Cuney and Friedrich, 1987);

All four explanations should be applicable to primary uraninite composition discussions; certainly, a significant component of uraninite populations is secondary, as shown by textures in the QEMSCAN study, while the ages of the three comparative deposit groups

(Trans-Hudsonian, Pan African, and Variscan) correspond with successively low Pb content. The source of the mobilised U is the residual dissolved constituent that partitions into the fluids as initial crystallisation takes place, as well as the oxidation of $U^{4+}$ and the leaching of $U^{6+}$ from uraninite. The process is comparable to the paragenetic sequence of the Devonian-aged Ruggles pegmatite U-deposit in New Hampshire, USA, described in detail by Korzeb *et al*. (1997).

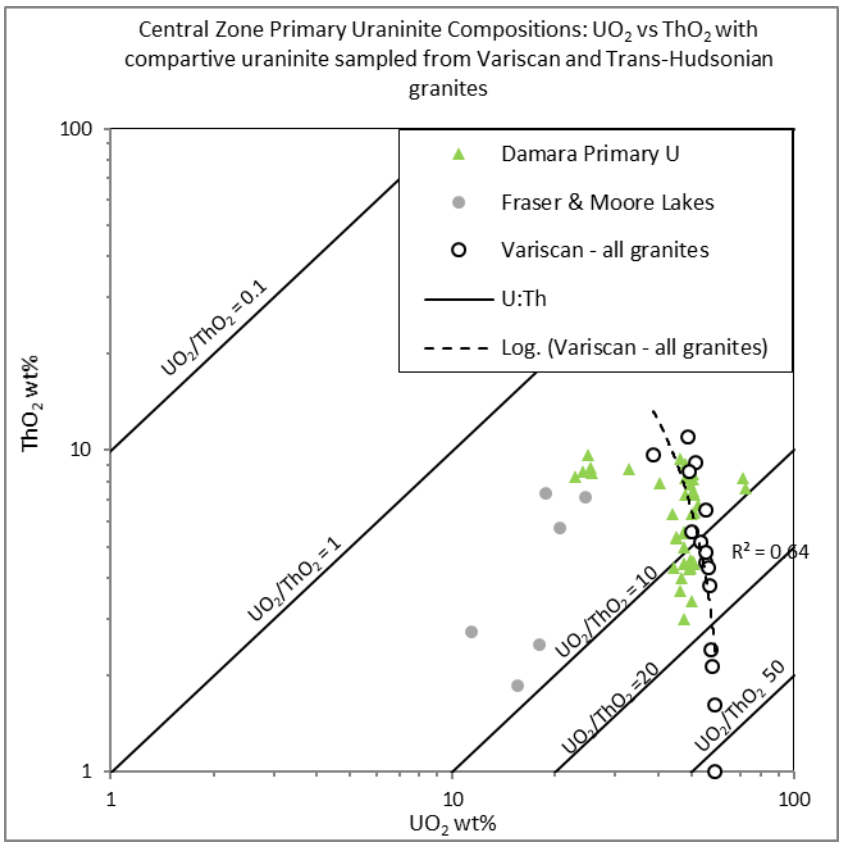



Figure 8.19 $UO_2$ vs. $ThO_2$ of granite-hosted uraninite. Samples from the Damara Orogen compare with uraninite specimens from the Moore and Way Lakes prospects, Bancroft District, Canada and granite-hosted uraninite from the Erzgebirge in the Variscan Belt, Germany-Czech Republic. The Variscan uraninite has the highest average U content (92.2 wt.%, 18 samples n is not disclosed) the Damara primary uraninite are intermediate (82.6 wt.% U, 43 samples n=194) while the Bancroft district specimens average ~66 wt.% U (7 samples, 320 analyses). Bancroft data from McKechnie, (2012); Variscan data from Förster (1999).

The total U and Th ratios of the uraninite populations provide a means of discriminating the mineral populations between the individual deposits (Figure 8.20b). Comparing $ThO_2$ with $UO_2$ provides a more accurate assessment of the deposition conditions, as lower average $UO_2$ in the Goanikontes samples and relatively high average $ThO_2$ suggest that the Goanikontes uraninite populations have crystallised under different (more oxidising) conditions compared with the populations at the other Central Zone deposits. The high relative Th also infers co-crystallisation of uranothorite (hosting the bulk of the Th) and potentially reflects that the melt was not in equilibrium with monazite and thorite to the

same degree as the other deposits. The Hildenhof, Husab, Ida Dome and Valencia deposits contain comparable $UO_2$ (40- to 50 wt.%) with Hildenhof uraninite containing the least Th.

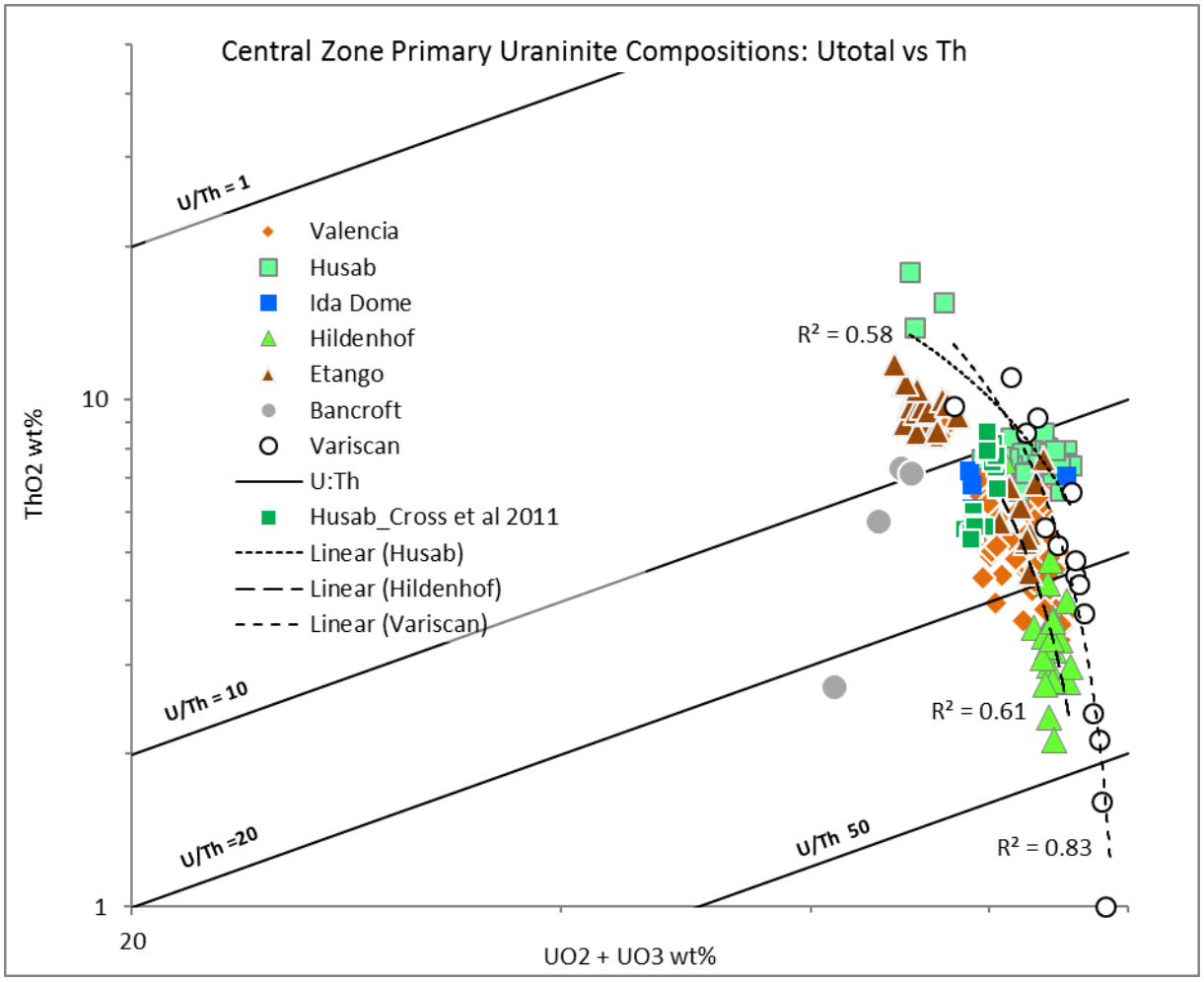



Figure 8.20 $U_{tot}$ vs. $ThO_2$ wt% in uraninite of the Central Zone primary uranium deposits, with comparative orogenic granite-hosted uraninites. (a) U total vs. Th of the Central Zone (CZ) deposits, Fraser and Moore Lakes prospects near Bancroft, Canada, and Variscan uraninite populations from the Czech Republic. U:Th ratios in the Etango samples, most of the Husab, Ida Dome, and Valencia samples plot with comparably low U/Th ratios, close to $U_{tot}$/Th = 10. Although U totals in the Bancroft district specimens are relatively low, the $U_{tot}$/Th is comparable to the CZ. The Variscan sample set shows a strong linear relationship of decreasing Th/U with increasing $U_{tot}$, spanning a full range of ratios from U:Th = 10 to U:Th = 96. The Hildenhof uraninites have the highest U/Th of the CZ groups; the Valencia specimens cluster with ratios between 10 and 20, while the samples from Etango have bimodal distribution on either side of the U:Th = 10 line.

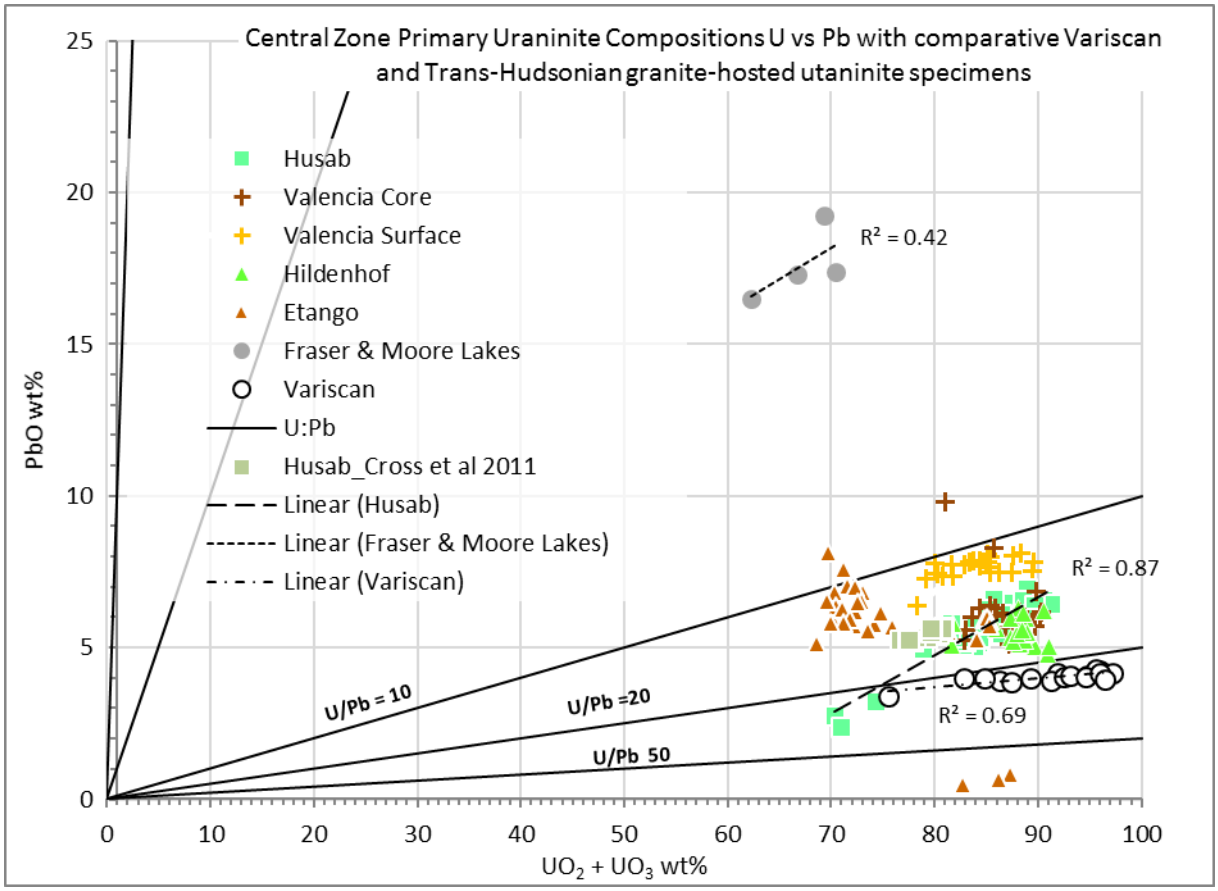



Figure 8.20 (b) $UO_2$ + $UO_3$ vs PbO wt% of the Fraser and Moore Lakes area, Central Zone deposits, and Variscan uraninite specimens. Pb content appears to be relatively constant in the Variscan and Bancroft specimens, and positively systematic with respect to U. The relationships are less systematic in the Central Zone deposits. Valencia data shows compositional differences between surface and core populations, with the surface samples having the highest Pb content. The relatively high Pb content of the Bancroft samples, intermediate Central Zone, and low Pb of the Variscan uraninite is consistent with the relative ages of the Hudsonian, Damaran, and Variscan orogenies.

Whole-rock U and Th content of the host leucogranites of selected uraninites show that the leucogranites rarely exceed U/Th >10. The uraninite populations predominantly plot between U/Th = 10 and U/Th = 50 with the exception of the Husab and Goanikontes specimens. However, whole-rock U and Th content cannot be compared directly with uraninite, given the diversity of uranium and thorium minerals present in the rocks (Figure 8.21a). Most of the samples plot with $U:Th_{mineral}$ about 4 times greater than in the whole-rock. The U:Th in uraninite is greater than in the corresponding whole rock sample analyses, at all of the deposits except Husab. However, at Husab Th:U tends to be greater in the whole rock and in uraninite than the other Central Zone deposits. This is viewed as a reflection of a

greater magmatic uraninite component at Husab; in systems where fluid-derived uraninite dominate Th/U ratios should be low because of low Th solubility.

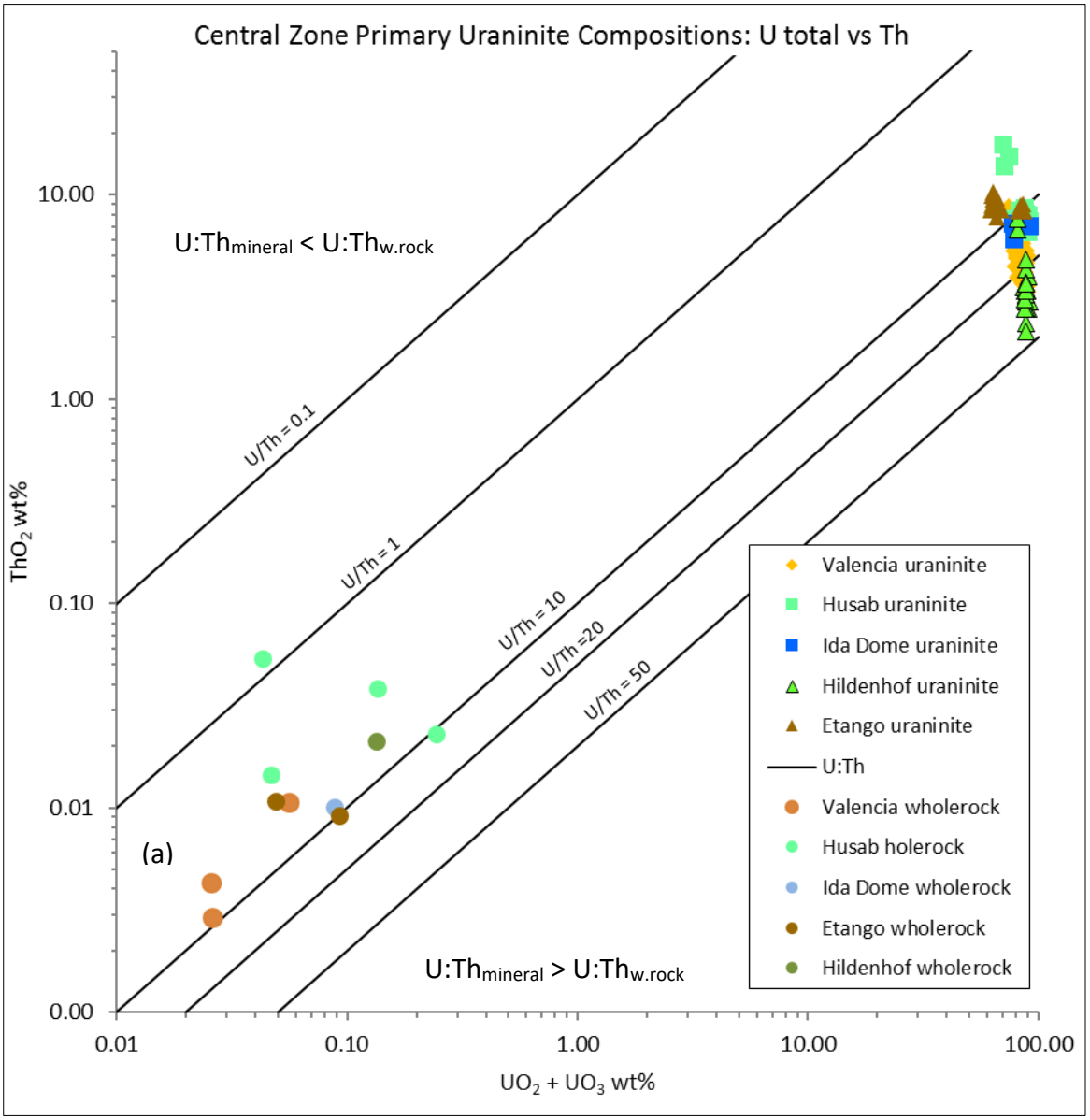



Figure 8.21 Uranium and thorium concentrations in uraninite and in corresponding whole-rock samples (e.g. Valencia WR). The Etango samples have the lowest $UO_2/ThO_2$ ratios, this is not necessarily because of high Th content, but low $UO_2$. The Valencia uraninite hosts the widest range of Th abundances, while the Husab and Goanikontes samples plot with a wide range of $UO_2$+$UO_3$:$ThO_2$.

### *Rare Earth- and Trace Element Abundances in Uraninite*

Uraninite is able to incorporate variable quantities of trace elements during crystallisation, which Janeczek and Ewing (1992a) describe as a reflection of the diversity of the

mineralisation conditions, particularly of the metal-bearing fluids. In addition, simple substitution of Ca for U, or sub-µm replacement of uraninite by coffinite may influence uraninite trace element abundances. The post granite-crystallisation conditions in the Damara alaskite are dominated by sub-solidus fluid flux, and may involve highly acidic fluorine-bearing fluids, or episodes of pervasive sulphide-bearing late magmatic fluid flux (pyrite is usually earlier than molybdenite at Husab, for example). These higher temperature alteration episodes may have played some role in alteration and subsequent compositional variation of the uraninite crystals.

Alexandre and Kyser (2005) describe the substitution and replacement mechanisms in post-depositional environments, and conclude that alteration limits the accuracy of certain analytical interpretations. Mercadier *et al.* (2010) describe how REE substitution for U is a potentially powerful tool for characterising U deposit styles, and therefore also a tool for determining the origins of a particular deposit.

The REE tend to be less sensitive to REDOX changes than uranium, and therefore less susceptible to influences of post-crystallisation processes. In addition to REE incorporation, the uraninite structure is able to accommodate a number of contaminant elements at high temperatures (Skirrow *et al.* 2009). This implies that the available contaminants in the late-crystallising environment at each Central Zone deposit may be reflected in uraninite, and could characterise individual deposits, while REE may be used to characterise deposits with respect to pre-alteration, or the original deposit-forming conditions.

Wavelength dispersive spectrometry of specimens in this study, prior to initialising quantitative analyses, identified the following rare earth- and trace elements in uraninite populations from the Goanikontes area (Etango deposit) Husab, and Valencia deposits, Y is included as it behaves in a similar way to the heavy rare earth elements in magmatic environments (Rollinson, 1993):

- Etango - Ce, La and Y;
- Husab - Y and Zr; and
- Valencia - Ce, La and Y.

Comparison of uraninite contamination in the primary Damara samples is effectively a comparison of the availability of light rare earth elements (LREE - Ce and La) and elements with heavy rare earth affinity (Zr and Y) to the crystallising uraninite. As is shown in Chapter 6, rare earth abundances in the leucogranites tend to be low, thus uraninite is not expected to contain significant abundances fo these minerals; in addition, a certain proportion of the bulk REE would be hosted in entrained phosphates, garnet, and zircon. Figure 8.22 illustrates the relationships between $UO_2$ Ce, La, and Y for selected uraninite samples of the Central Zone deposits.

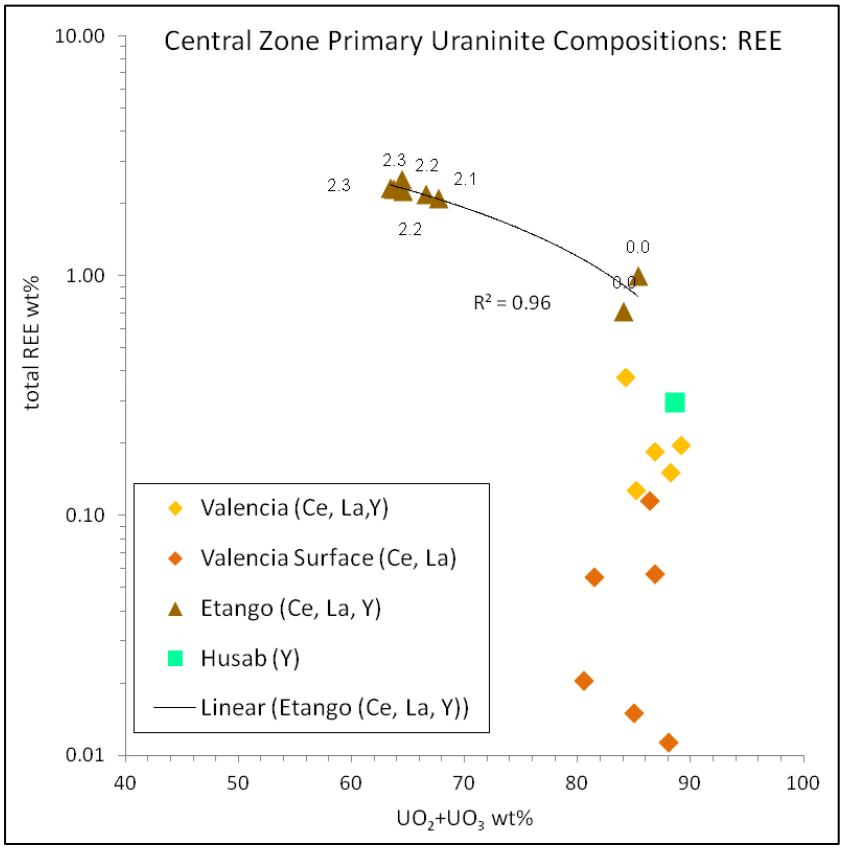



Figure 8.22 Uranium vs. total REE wt.% for primary uraninite. REE are detected in the Goanikontes (Ce, La, and Y) Husab (Y) and Valencia uraninite specimens (Ce, La, and Y). The high concentration of REE and Y in the Goanikontes samples correlates with anomalous Y content of the whole-rock. Y and U show systematic negative correlation, suggesting Y substitution for U. The REE content of the Valencia samples is between 0.01 and 0.4 wt.%. The low overall REE and Y abundances in the uraninite are indicative of silicate melt equilibrium with monazite and xenotime. In addition, uraninite crystallises in more than one episode, and is subject to at least one prominent alteration event. As such Ce, La, and Y were not available to the late-crystallising phase.

Y is the most abundant contaminant phase, although HREE were not detected in the uraninite of this study. Goanikontes uraninite from the DH025 353 m sample contains over 2 wt.% $Y_2O_5$ which reflects anomalous Y in the whole-rock analyses in leucogranites that invade certain units of the Khan Formation (Chapter 4 and Chapter 5). Y and U abundance in

the Goanikontes display a distinctly linear relationship, implying a magmatic relationship during the earlier crystallisation of uraninite relative to xenotime. Ce and La occur in low abundances in the Goanikontes, Husab, and Valencia samples, all of which host appreciable abundances of monazite (Ce, La) and xenotime (Y). Mercadier *et al.* (2010) describe how REE concentrations in uraninite undergo only minor change during uraninite alteration, thus the low concentration is attributed to greater REE abundance in the entrained mineral population, such as monazite, not as a function of uraninite degradation.

## 8.13. Other Primary Uranium Phases – The Husab Betafite and Brannerite Examples

Brannerite is the most abundant uranium-bearing refractory phase in the Husab samples and is present in trace amounts in all the analysed samples of the QEMSCAN study. This contrast with the betafite-dominated locations near the Rössing Mine is not fully understood. The main contrast appears to be the availability of Y and Nb, which appear as anomalous concentrations in brannerite-, and betafite-bearing granites, respectively.

### *Betafite*

An anhedral specimen ~1.25 mm on its longest axis was sampled from an altered leucogranite at 115 m down hole in diamond core RDD373 (~100 m below surface) at Husab Zone 1. It occurs between a microcline-perthite and quartz grain within a 6 m-wide, light pink-orange leucogranite (alaskite). The interval of leucogranite occurs within a zone of pervasive alteration; the facies is represented primarily by secondary iron staining of the feldspars, and haematite-red stains that overprint predominantly chlorite alteration of the host Rössing Formation schists and gneiss.

Swakop Uranium submitted the sample for SEM analyses in late 2011 at SGS, Johannesburg who confirmed the mineral species by wavelength-dispersive spectrometry using an SEM. The specimen was analysed at 15 points, one was discarded, and subject to stoichiometric cation correction calculations (Table 8.7). Metal leaching is evident along fracture plains

within the crystal, as shown by lower BSE reflectance along the fissures in the backscatter image of Figure 8.23a. Figure 8.23b illustrates WDS spectra of 10 of the elemental constituents in the specimen, the fractures in the betafite reflect as variably prominent troughs in the profiles of the respective element spectra, The Figure 8.23c collage illustrates a fracture junction within the betafite that hosts secondary uraninite and Fe-Ti phases.

The element mapping study and line spectra analysis of the betafite identified complex element distribution within the altered, fractured portions of the mineral. The line spectra in Figure 8.23b show that Ce and Th are elevated in the altered portion adjacent to the zircon inclusion, probably indicating fine-grained monazite. Y, Ti, Nb and U concentrations are relatively consistent across the unaltered portions of the mineral, with troughs in U spectra over fractures supporting a predominantly soluble $U^{6+}$ mineral composition. The detailed element maps, are taken over a specific area of the betafite specimen, at a junction of internal crystal fractures; Figure 8.23c is a collage of 9 elements, and shows Ti and Si concentration in the fracture junction (secondary titanite) while low abundances of U, Th, and Nb define the less-altered portions of the betafite, while high U abundances highlight mobilisation along the fractures. Concurrent Ca and Y distribution probably reflects a complex substitution within the crystal during formation while Ti abundance is relatively consistent in the crystal. Fe is almost absent and concentrates in secondary phases in the fractures.

The final sample formula calculation uses the results of fourteen spot analyses taken on the grain. Eight are located within the brightest BSE reflectance positions, and six on the dull, altered portions of the mineral. The results of the recalculated formula are shown in Table 8.7. Table 8.8 details each of the compositional analyses at the EPMA spots on the betafite grain. The general non-stoichiometric mineral formula is $X_2Y_2O_6(OH)$. Dr Gelu Costin at Rhodes University advised that the formula should be balanced such that Y cation total = 2 on condition that the X cation total is <2. $U^{4+}$ is set at 0 in order to simplify the calculation, which requires normalisation of two variables, OH and O (O is >6). Thus, the general formula for the Husab betafite is given as a combined average of formulae calculated for the unaltered and altered portions of the mineral specimen.

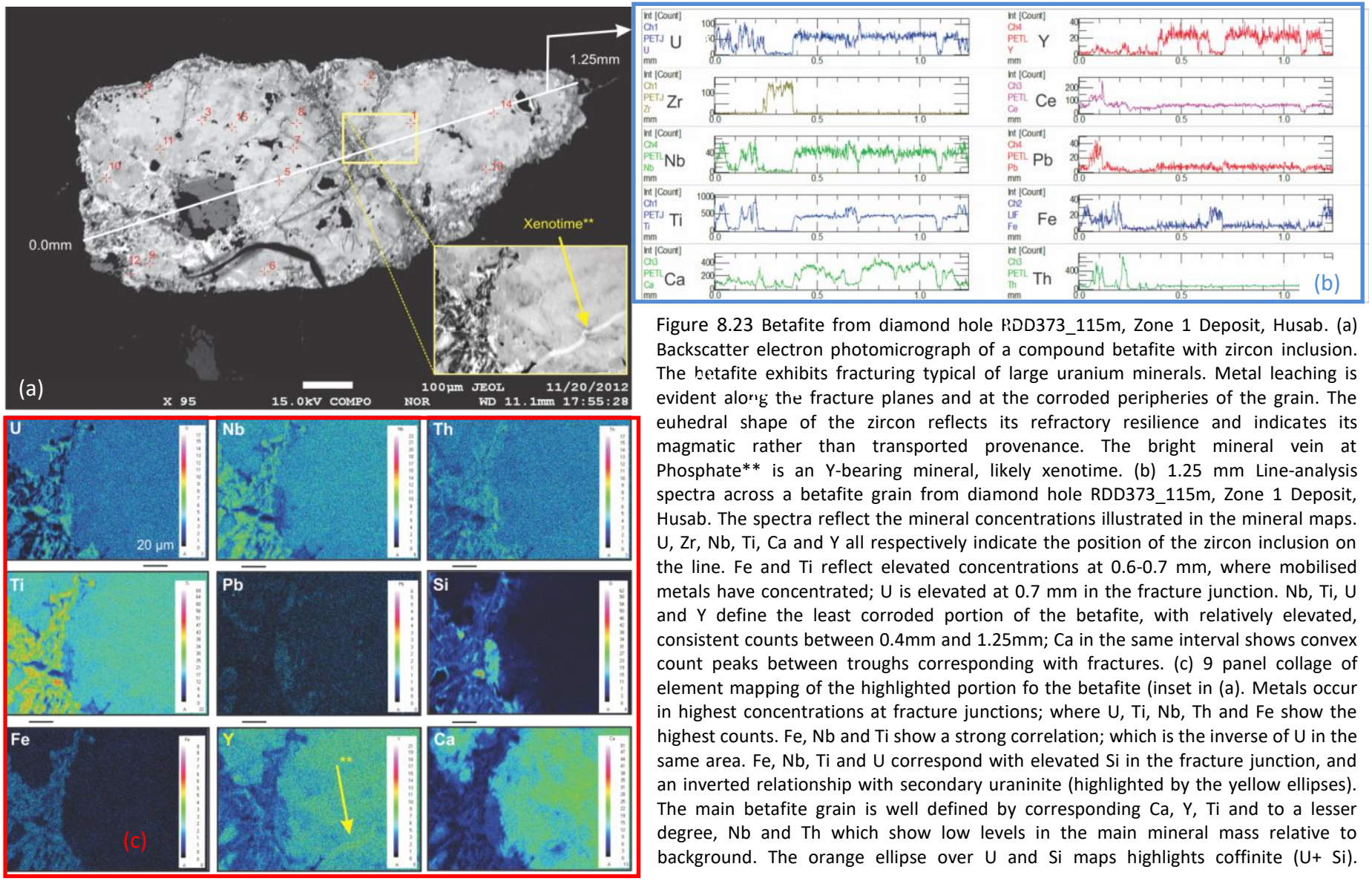



Figure 8.23 Betafite from diamond hole RDD373_115m, Zone 1 Deposit, Husab. (a) Backscatter electron photomicrograph of a compound betafite with zircon inclusion. The betafite exhibits fracturing typical of large uranium minerals. Metal leaching is evident along the fracture planes and at the corroded peripheries of the grain. The euhedral shape of the zircon reflects its refractory resilience and indicates its magmatic rather than transported provenance. The bright mineral vein at Phosphate** is an Y-bearing mineral, likely xenotime. (b) 1.25 mm Line-analysis spectra across a betafite grain from diamond hole RDD373_115m, Zone 1 Deposit, Husab. The spectra reflect the mineral concentrations illustrated in the mineral maps. U, Zr, Nb, Ti, Ca and Y all respectively indicate the position of the zircon inclusion on the line. Fe and Ti reflect elevated concentrations at 0.6-0.7 mm, where mobilised metals have concentrated; U is elevated at 0.7 mm in the fracture junction. Nb, Ti, U and Y define the least corroded portion of the betafite, with relatively elevated, consistent counts between 0.4mm and 1.25mm; Ca in the same interval shows convex count peaks between troughs corresponding with fractures. (c) 9 panel collage of element mapping of the highlighted portion fo the betafite (inset in (a). Metals occur in highest concentrations at fracture junctions; where U, Ti, Nb, Th and Fe show the highest counts. Fe, Nb and Ti show a strong correlation; which is the inverse of U in the same area. Fe, Nb, Ti and U correspond with elevated Si in the fracture junction, and an inverted relationship with secondary uraninite (highlighted by the yellow ellipses). The main betafite grain is well defined by corresponding Ca, Y, Ti and to a lesser degree, Nb and Th which show low levels in the main mineral mass relative to background. The orange ellipse over U and Si maps highlights coffinite (U+ Si).

Table 8.7 Cation corrections for all betafite analysis spots from sample RDD373_115m. The cation proportions of the leached and pristine analysis spots on average do not deviate substantially from the combined average. This illustrates that even under hydrothermal alteration; U, Pb and Fe are not susceptible to leaching from the refractory phase

| |
|---|
| Combined Analyses (14) |
| $(U^{6+}_{0.446}Ca_{0.295}Y_{0.227})_{\Sigma=0.968}(Ti_{1.423}Nb_{0.397}Fe^{3+}_{0.079}Th_{0.059}Pb_{0.033}Ta_{0.009})_{\Sigma=2.00}O_{4.67}(OH)_{3.588}$ |
| Pristine/unaltered Spots (8) |
| $(U^{6+}_{0.452}Ca_{0.300}Y_{0.224})_{\Sigma=0.976}(Ti_{1.425}Nb_{0.398}Fe^{3+}_{0.076}Th_{0.059}Pb_{0.034}Ta_{0.009})_{\Sigma=2.00}O_{4.330}(OH)_{3.511}$ |
| Leached/altered Spots (6) |
| $(U^{6+}_{0.449}Ca_{0.261}Y_{0.229})_{\Sigma=0.938}(Ti_{1.420}Nb_{0.394}Fe^{3+}_{0.076}Th_{0.060}Pb_{0.036}Ta_{0.009})_{\Sigma=2.00}O_{4.203}(OH)_{3.677}$ |

Observations of a polished thin section, supporting backscatter SEM imagery and EPMA element mapping (Figure 8.23) show at least three stages in the history of the betafite grain; The grain grew around an earlier-formed zircon. The zircon is of magmatic origin, shown by well-defined, euhedral grain boundaries and clear zonation. The crystal of betafite grew into the available space between quartz and K-feldspars, assuming an irregular elongate shape. Siliceous hydrothermal fluids leached U, Fe, Ti, Y and Pb along fracture planes in the crystal. A complex mix of remobilised Fe - Ti minerals, uraninite and Y-phosphate form veins (xenotime) along the fractures and at fracture junctions. The timing of hydrothermal alteration is not constrained, it may be soon after crystallisation while fluids were still in circulation, but has also definitely exploited the internal fracture network which would have needed some time to form.

Table 8.8 Cation proportions of the RDD373_115A Betafite, normalised to 8.31 oxygen. The mineral formula recalculation is balanced with 0 wt $UO_2$ and thus calculated with all U in the oxidised state. Analyses are split into two groups, one of bright reflectance spots, and the other of dull reflectance where metal has leached. U varies from 25 wt.% to 34 wt.% with an average of 32.1 wt.%. $Nb_2O_5$ averages 13.2 wt.% and $Ta_2O_5$ is < 1 wt.%.

| Sample point | 1_1 | 1_2 | 1_3 | 1_4 | 1_5 | 1_6 | 1_7 | 1_8 | 2_10 | 2_11 | 2_12 | 2_13 | 2_14 | 2_15 | **Bright** | **Dull** | Ave. |
|---|---|---|---|---|---|---|---|---|---|---|---|---|---|---|---|---|---|
| Ca+U4+U6+Y | 1.258 | 0.911 | 1.227 | 1.115 | 1.048 | 0.633 | 1.230 | 1.147 | 1.065 | 1.041 | 1.049 | 1.098 | 1.045 | 0.796 | 1.083 | 1.136 | 1.047 |
| Ti+Nb+Ta+Fe+Th+Pb | 2.314 | 2.000 | 2.197 | 2.162 | 2.115 | 1.944 | 2.267 | 2.193 | 2.161 | 2.194 | 2.120 | 2.149 | 2.114 | 1.936 | 2.142 | 1.985 | 2.133 |
| 2Ti/(Nb+Ta) | 7.335 | 6.858 | 7.190 | 6.445 | 6.148 | 8.236 | 7.125 | 7.447 | 7.307 | 7.162 | 7.168 | 6.296 | 7.599 | 6.675 | 7.047 | 8.125 | 7.071 |
| Oxygen to normalise | 8.310 | 8.310 | 7.570 | 7.690 | 7.860 | 8.550 | 7.330 | 7.580 | 7.69 | 7.58 | 7.84 | 7.73 | 7.86 | 8.58 | 7.925 | 7.770 | 7.891 |
| $UO_2$ | 0.000 | 0.000 | 0.000 | 0.000 | 0.000 | 0.000 | 0.000 | 0.000 | 0.000 | 0.000 | 0.000 | 0.000 | 0.000 | 0.000 | 0.000 | 0.000 | *0.000* |
| $TiO_2$ | 29.128 | 28.197 | 28.468 | 28.542 | 27.658 | 28.328 | 29.168 | 28.677 | 28.588 | 29.052 | 28.233 | 27.828 | 28.840 | 28.580 | 28.590 | 28.429 | *28.521* |
| FeO | 1.388 | 1.847 | 1.009 | 1.323 | 1.553 | 1.262 | 1.104 | 1.479 | 1.947 | 1.364 | 1.538 | 1.314 | 1.295 | 1.470 | 1.393 | 1.458 | *1.421* |
| CaO | 4.931 | 4.715 | 5.169 | 4.391 | 4.047 | 1.312 | 5.149 | 4.643 | 4.059 | 3.781 | 4.194 | 4.271 | 4.398 | 3.762 | 4.602 | 3.668 | *4.202* |
| $ThO_2$ | 3.843 | 3.810 | 3.606 | 3.123 | 3.709 | 5.291 | 3.878 | 3.813 | 3.932 | 3.807 | 4.065 | 3.663 | 4.151 | 3.893 | 3.838 | 3.980 | *3.899* |
| $Nb_2O_5$ | 12.954 | 13.424 | 12.883 | 14.427 | 14.644 | 11.150 | 13.388 | 12.523 | 12.716 | 13.253 | 12.829 | 14.362 | 12.371 | 13.990 | 13.272 | 13.123 | *13.208* |
| $Y_2O_3$ | 7.834 | 3.659 | 6.983 | 8.336 | 7.843 | 3.307 | 7.572 | 6.542 | 6.773 | 5.981 | 6.134 | 8.296 | 5.847 | 6.182 | 6.558 | 6.471 | *6.521* |
| PbO | 1.651 | 1.242 | 1.639 | 1.440 | 1.494 | 4.402 | 1.517 | 1.549 | 1.183 | 1.475 | 1.585 | 2.087 | 1.731 | 2.900 | 1.715 | 2.029 | *1.850* |
| $Ta_2O_5$ | 0.432 | 0.428 | 0.487 | 0.516 | 0.542 | 0.491 | 0.390 | 0.483 | 0.505 | 0.407 | 0.461 | 0.574 | 0.428 | 0.429 | 0.452 | 0.492 | *0.470* |
| $UO_3$ | 33.578 | 32.004 | 34.324 | 30.938 | 30.533 | 31.280 | 32.894 | 34.133 | 33.040 | 34.161 | 33.285 | 30.369 | 33.095 | 25.475 | 32.004 | 32.179 | *32.079* |
| $H_2O$ | 4.261 | 10.674 | 5.432 | 6.964 | 7.977 | 13.177 | 4.940 | 6.158 | 7.257 | 6.719 | 7.676 | 7.236 | 7.844 | 13.319 | 7.576 | 8.171 | *7.831* |
| Total | 100 | 100 | 100 | 100 | 100 | 100 | 100 | 100 | 100 | 100 | 100 | 100 | 100 | 100 | 100 | 100 | *100* |
| Ti | 1.670 | 1.407 | 1.596 | 1.530 | 1.461 | 1.384 | 1.640 | 1.583 | 0.988 | 1.537 | 1.579 | 1.511 | 1.496 | 1.534 | 1.530 | 1.506 | *1.350* |
| Fe | 0.088 | 0.102 | 0.063 | 0.079 | 0.091 | 0.069 | 0.069 | 0.091 | 0.026 | 0.116 | 0.082 | 0.091 | 0.079 | 0.077 | 0.082 | 0.086 | *0.077* |
| Ca | 0.403 | 0.335 | 0.413 | 0.335 | 0.304 | 0.091 | 0.413 | 0.365 | 0.094 | 0.311 | 0.293 | 0.320 | 0.327 | 0.333 | 0.352 | 0.280 | *0.253* |
| Th | 0.067 | 0.058 | 0.061 | 0.051 | 0.059 | 0.078 | 0.066 | 0.064 | 0.013 | 0.064 | 0.063 | 0.066 | 0.060 | 0.067 | 0.062 | 0.063 | *0.056* |
| Nb | 0.446 | 0.403 | 0.434 | 0.465 | 0.465 | 0.327 | 0.453 | 0.415 | 0.138 | 0.411 | 0.433 | 0.413 | 0.464 | 0.396 | 0.426 | 0.419 | *0.397* |
| Y | 0.318 | 0.129 | 0.277 | 0.316 | 0.293 | 0.114 | 0.301 | 0.255 | 0.008 | 0.258 | 0.230 | 0.232 | 0.315 | 0.220 | 0.250 | 0.244 | *0.207* |
| Pb | 0.034 | 0.022 | 0.033 | 0.028 | 0.028 | 0.077 | 0.031 | 0.031 | 0.030 | 0.023 | 0.029 | 0.030 | 0.040 | 0.033 | 0.033 | 0.038 | *0.049* |
| U | 0.000 | 0.000 | 0.000 | 0.000 | 0.000 | 0.000 | 0.000 | 0.000 | 0.000 | 0.000 | 0.000 | 0.000 | 0.000 | 0.000 | 0.000 | 0.000 | *0.000* |
| Ta | 0.009 | 0.008 | 0.010 | 0.010 | 0.010 | 0.009 | 0.008 | 0.010 | 0.008 | 0.010 | 0.008 | 0.009 | 0.011 | 0.008 | 0.009 | 0.009 | *0.007* |
| U | 0.538 | 0.446 | 0.537 | 0.463 | 0.450 | 0.427 | 0.517 | 0.526 | 1.438 | 0.496 | 0.519 | 0.497 | 0.456 | 0.492 | 0.480 | 0.476 | *0.336* |
| H | 2.167 | 4.725 | 2.700 | 3.311 | 3.736 | 5.711 | 2.464 | 3.014 | 2.933 | 3.461 | 3.239 | 3.642 | 3.449 | 3.701 | 3.511 | 3.802 | *5.579* |
| Total | 5.739 | 7.635 | 6.124 | 6.588 | 6.898 | 8.287 | 5.961 | 6.353 | 5.677 | 6.687 | 6.474 | 6.811 | 6.697 | 6.860 | 6.735 | 6.924 | *8.312* |
| Oxygen in Formula | | | | | | | | | | | | | | | | | 4.67 |

### *Brannerite*

Petrographic investigations show that brannerite occurs within enclaves of biotite-titanite-chlorite (after biotite) as well as between quartz and feldspar within the sheeted leucogranites[50]. Two specimens from diamond core RDD373, at 64 m and 93 m down hole represent anhedral, altered brannerite. The former is hosted between quartz and feldspar (64 m); and the euhedral weakly altered brannerite is hosted in a biotite-titanite-chlorite enclave (93 m).

Mineral formulae are recalculated with parameters that include the general stoichiometric formula of $XY_2O_3$ where X:Y = ~2 and O = ~6, where X is (U, Th, Ca, Y, Pb) and Y is (Ti, Fe). Manipulation of $UO_2$, $UO_3$ and O quantities such that Y = ~2 is satisfied first and then X = ~1, with the final cation balancing of X + Y as close to 3 as possible. The non-stoichiometric formulae that result from $UO_2/UO_3$ adjustments are detailed below.

### *Specimen Descriptions and Analyses*

The altered brannerite (64 m) shows intense fracturing and low backscatter reflectance indicative of metal leaching between 10 µm and 20 µm along either side of the fracture lines. The unaltered portions show relatively uniform BSE reflectance (Figure 8.24). It was analysed at fifteen spots, nine targeting the brightest uniform reflectance, and six on the areas of low reflectance associated with the internal fracture network. Ca, Pb, and U contents are lower in the dull analyses and Fe and Ti show relatively consistent abundances in the dull- and bright reflectance analyses.

The euhedral brannerite specimen at 93 m down hole is not entirely free of alteration features, and uniform bright and variably dull reflectance occurs within the fragmented mineral portions and along the prominent fractures, respectively. The specimen however, shows straight edges, and the BSE contrast range is relatively low, it is thus presented as a type specimen of primary brannerite at the Husab deposit. Recalculation parameters are similar to those for the 64 m specimen.

[50] Chapter 4 and Chapter 7 describe the nature and occurrence of the brannerite in the 64 m and 93 m intervals of RDD373. Detailed Description of the mineral and geochemical signal are given in Freemantle, 2011.

Eleven analysis spots provided the oxide weight percentages; X:Y is lower in the euhedral 93 m brannerite, 1.653 vs. 1.982 in the altered specimen. For this specimen, Y = ~2 was satisfied first and then X = ~1, with $UO_2$, $UO_3$ and O adjusted. In order to achieve Y:X = 1.958 in the unaltered portions oxygen coordination was set to 6.2 anions, this value was then applied to all recalculations. The eleven calculations of cation proportions are split into two groups; Five with Y:X > 1.7 and six with Y:X < 1.7. X and Y cation totals vary by ~10 % from ideal Brannerite ( $XY_2O_6$).

Table 8.9 gives calculated formulae for the brannerite specimen at 64 m down hole, and Table 8.10 gives formulae recalculated from the five best analyses, the six analyses with Y:X <1.7 and the combined average of all eleven analyses of the brannerite from 93 m down hole. Interestingly calculated $U^{4+}$ and $U^{6+}$ abundances appear to be very similar in the altered and unaltered specimens.

Table 8.9 Brannerite formulae from EPMA analyses of sample RDD373 – 64m. The relatively altered and unaltered portions of the specimen have variable backscatter reflectance, which are spot analysed as 'bright' and 'dull' analysis sets.

| | |
|---|---|
| Average Y:X = 1.982, Cation Total = 2.999 n = 15 | $(U^{4+}_{0.125}U^{6+}_{0.432}Ca_{0.216}Y_{0.079}Pb_{0.035}Th_{0.136})_{\sum=1.017}(Fe_{0.067}Ti_{1.915})_{\sum=1.982}O_{6.068}$ |
| Bright- Y:X = 1.920, Cation Total = 3.006 n = 9 | $(U^{4+}_{0.129}U^{6+}_{0.443}Ca_{0.223}Y_{0.074}Pb_{0.038}Th_{0.126})_{\sum=1.030}(Fe_{0.065}Ti_{1.903})_{\sum=1.967}O_{6.048}$ |
| Dull- Y:X = 1.980, Cation Total = 2.990 n = 6 | $(U^{4+}_{0.120}U^{6+}_{0.417}Ca_{0.204}Y_{0.086}Pb_{0.030}Th_{0.1349})_{\sum=1.003}(Fe_{0.067}Ti_{1.926})_{\sum=1.986}O_{6.002}$ |

Table 8.10 Brannerite formulae from EPMA analyses of sample RDD373 – 93m. The Brannerite shows consistent reflectance in backscatter imagery, indicative of uniform metal distribution. Spot analyses by EPMA returned variable composition.

| | |
|---|---|
| Good Y:X = 1.742, Cation Total = 3.082 n = 5 | $(U^{4+}_{0.124}U^{6+}_{0.544}Ca_{0.309}Y_{0.040}Pb_{0.022}Th_{0.085})_{\sum1.124}(Fe_{0.104}Ti_{1.812})_{\sum1.958}O_{6.200}$ |
| Poor Y:X = 1.583, Cation Total = 3.087 n = 6 | $(U^{4+}_{0.161}U^{6+}_{0.541}Ca_{0.350}Y_{0.031}Pb_{0.024}Th_{0.087})_{\sum1.195}(Fe_{0.044}Ti_{1.848})_{\sum1.891}O_{6.200}$ |
| Average Y:X = 1.653, Cation Total = 3.085 n = 11 | $(U^{4+}_{0.144}U^{6+}_{0.543}Ca_{0.332}Y_{0.035}Pb_{0.023}Th_{0.086})_{\sum1.163}(Fe_{0.067}Ti_{1.855})_{\sum1.921}O_{6.200}$ |

## 8.14. Mineral Element Mapping

Element mapping of a fracture junction on the brannerite shows that the uniform reflectance over the unaltered portions does not reflect uniform U or Th distribution, with distinct, zoned areas dominated by one or the other element (Figure 8.24). U, Th, and Fe show denser concentrations in the fracture networks than in the uniform or unaltered mineral areas; while Y, Ti, and Ca are relatively uniform within the unaltered areas. Th is anomalous in fractures where it is hosted in secondary phosphates, such as Ce-monazite. The anomalous Ti showing on the mineral map represents a void in the mineral, not a Ti-phase. Ta is elevated at the grain boundary and may represent a phase similar to betafite. Fe and Si are more abundant along fractures and may represent secondary Fe-Ti-Si phases.

Figure 8.25 illustrates the relatively uniform backscatter reflectance of the 93 m brannerite and presents element maps to illustrate compositional variation. Dull reflectance is apparent along the fracture lines, but less so, relative to the 64 m specimen. Ti, Y, and Ca are relatively uniform, while U and Th show distinct inverse zonation, which was not apparent in the altered sample. This zonation may reflect preferential thorite/coffinite relationships, except Si abundance is not consistent with Th or U. The texture confirms that brannerite has a magmatic origin much like the zoned zircon.

Pb concentrates as galena along the fracture lines, and may have its source as a radiogenic product of the U in the brannerite. Secondary Fe fills the fracture planes, and may be sourced from associated pyrite, biotite or potentially a small proportion from the brannerite itself. Biotite is adjacent to the brannerite in RDD373-93C and the chloritisation process has exsolved titaniferous phases (ilmenite) along the cleavage planes (Figure 8.24). Summary Table 8.11 and Table 8.12 provide the recalculated oxide proportions and cations of two brannerite specimens.

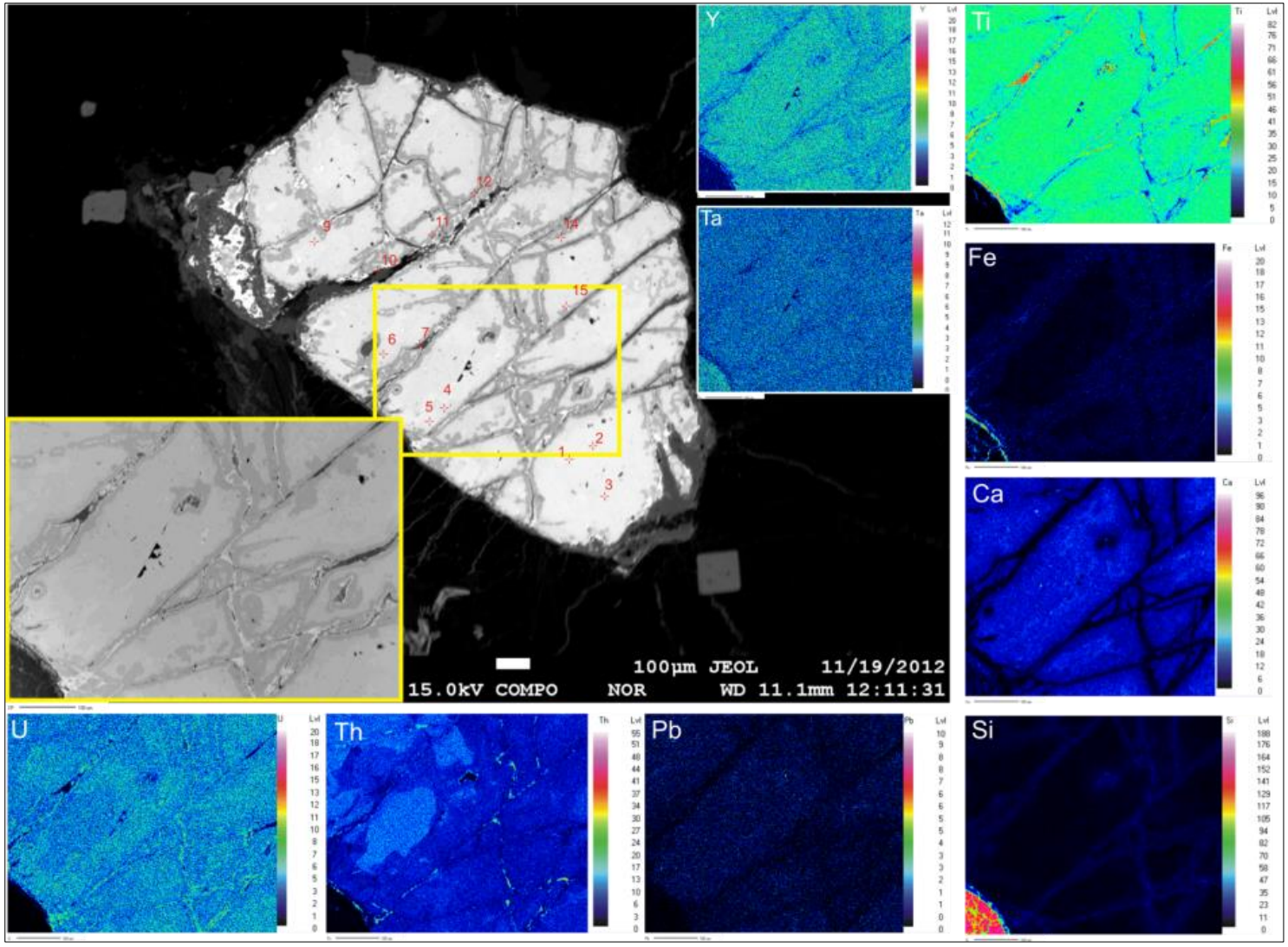
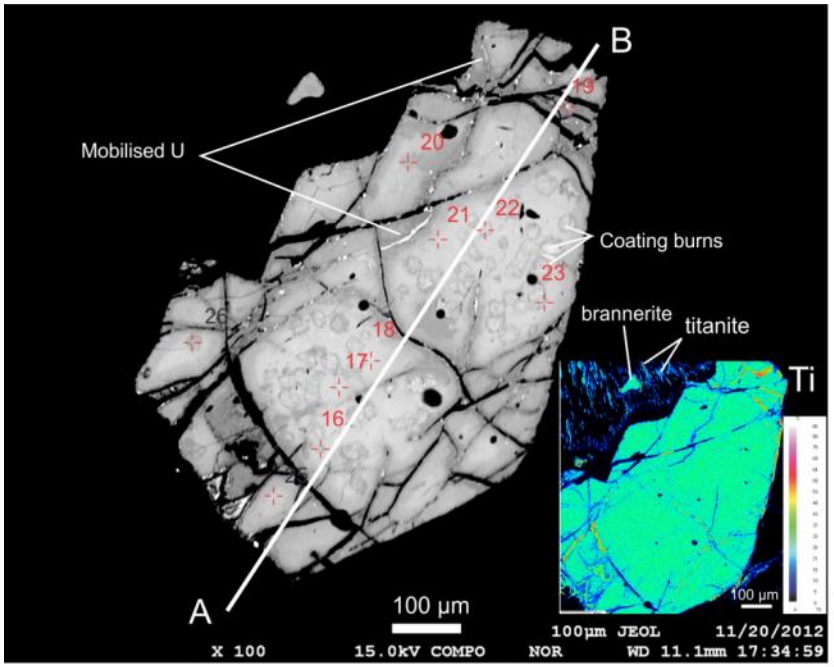
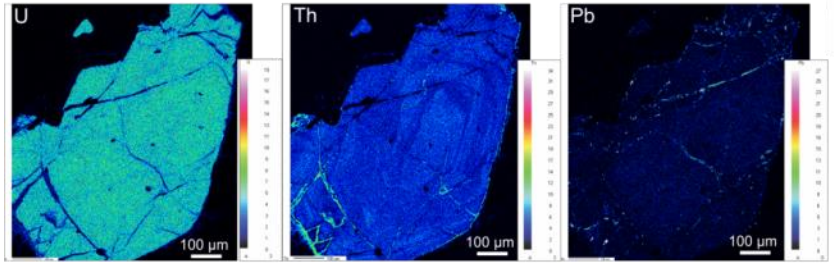
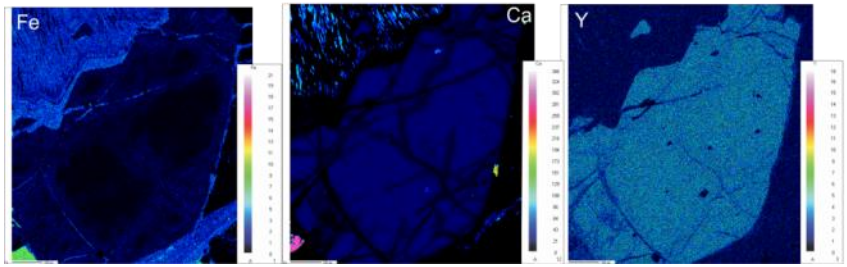



Figure 8.24 Mineral map of a detailed area in an altered brannerite specimen. Backscatter brightness shows metal leaching along the grain edges and along the prominent fracture network, which served as the fluid pathways. U in brannerite is predominantly $U^{6+}$ thus soluble in a high T environment. Uranium shows an inverse distribution, though faint, U appears to concentrate in the fractures, as a secondary precipitate. Correspondingly, Th shows an inverse distribution to U. Si and Fe concentrate along the fractures, while Ca does not appear in the fractures, and concentrates in variable concentration in the less disturbed portions of the specimen. Y shows a fairly uniform distribution in the undisturbed portions of the mineral, but is leached along some edges.



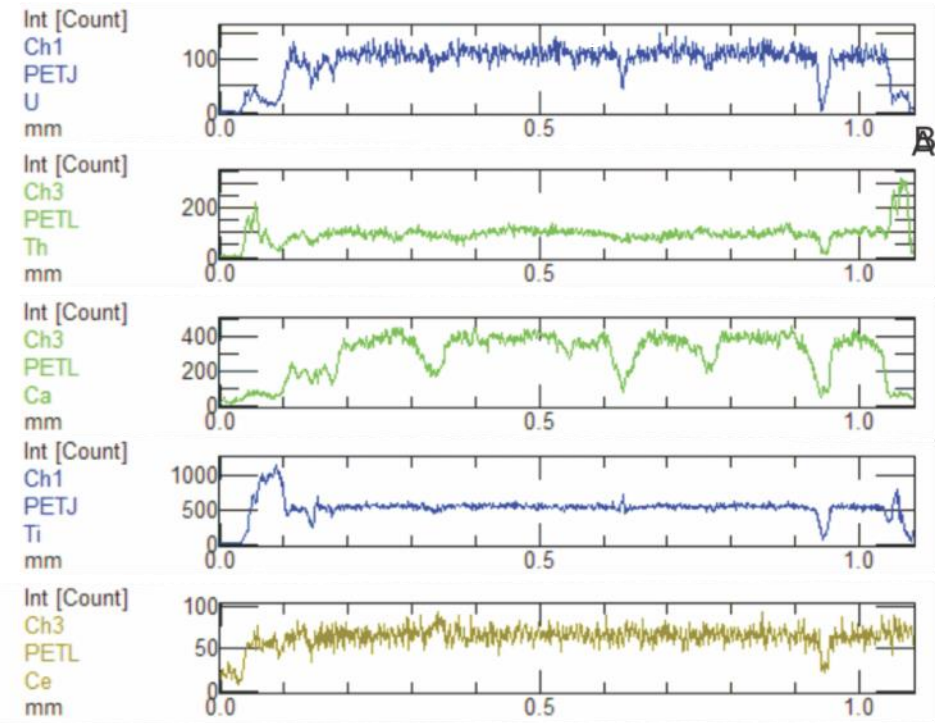




Figure 8.25 Mineral map with line scan spectra for selected major and trace elements of euhedral brannerite from 93 m in hole RDD373. The mineral shows uniform distribution for U, Ti, and Y. Th displays some zonation, and the concentric pattern probably represents stages of mineral growth, in which U4+ may be substituted for by Th. Ca shows some leaching at the edges of the mineral, and Fe is present as a replacement, concentrating at the edges and along a major fracture set that bisects the specimen. Pb is mobile, and is concentrated along fracture planes. The line scan spectra reflect minor U depletion at fracture positions. Ca is the most mobile constituent in brannerite and is reflected in pronounced plateau and trough profile of the line scan. The Ti line scan reflects high concentration of Ti, an edge effect, and a uniform concentration across the specimen with troughs corresponding to large fractures.

Table 8.11 Results of formula recalculation of the RDD373 64 m brannerite specimen. The mineral has clear areas of metal leaching (dull reflectance) and areas where alteration is minimal (bright reflectance) and is analysed at 15 spots (Figure 8.24). The low reflectance spots returned lower average U, Ca, and Pb. Ti, which is less mobile in the hydrothermal environment returned similar abundances in the dull and bright analyses. Uranium is marginally lower in the dull spots, ~2.1 wt.% less, which reflects the refractory nature of the mineral, even within the hydrothermal environment.

| Sample point | Brann_ 64B 1-1 | Brann_ 64B 1-2 | Brann_ 64B 1-3 | Brann_ 64B 1-4 | Brann_ 64B 1-5 | Brann_ 64B 1-6 | Brann_ 64B 1-7 | Brann_ 64B 1-8 | Brann_ 64B 1-9 | Brann_ 64B 1-10 | Brann_ 64B 1-11 | Brann_ 64B 1-12 | Brann_ 64B 1-13 | Brann_ 64B 1-14 | Brann_ 64B 1-15 | **Bright** | **Dull** | **Average** |
|---|---|---|---|---|---|---|---|---|---|---|---|---|---|---|---|---|---|---|
| Oxygen in Brannerite Formula | | | | | | | | | | | | | | | | | | **6.2** |
| (U, Th, Pb, Ca,Y,Ce)/Y | 1.958 | 1.894 | 1.875 | 1.923 | 2.001 | 1.982 | 1.918 | 2.041 | 1.820 | 1.979 | 1.950 | 2.001 | 2.049 | 1.892 | 1.974 | **1.930** | **1.981** | **1.951** |
| Y: (Ti+Fe) | 1.998 | 2.001 | 1.940 | 1.932 | 1.999 | 1.994 | 1.972 | 2.013 | 1.936 | 1.993 | 1.983 | 2.000 | 2.016 | 1.963 | 1.991 | **1.979** | **1.986** | **1.982** |
| UO3 | 33.316 | 34.503 | 32.162 | 34.443 | 32.185 | 30.517 | 30.613 | 27.061 | 33.600 | 32.107 | 30.009 | 26.461 | 23.743 | 25.848 | 33.251 | **31.294** | **29.547** | ***30.655*** |
| UO2 | 8.200 | 6.950 | 8.400 | 7.500 | 9.000 | 4.250 | 9.500 | 10.100 | 8.000 | 8.200 | 8.950 | 8.500 | 9.400 | 9.900 | 5.250 | **8.288** | **7.800** | ***8.140*** |
| PbO | 2.200 | 2.410 | 1.990 | 1.868 | 2.611 | 2.010 | 2.626 | 1.837 | 2.185 | 1.814 | 1.315 | 1.266 | 1.687 | 1.388 | 1.692 | **2.041** | **1.660** | ***1.927*** |
| TiO2 | 38.478 | 37.170 | 37.237 | 37.335 | 36.783 | 38.760 | 37.483 | 37.871 | 37.546 | 38.075 | 37.612 | 39.050 | 38.880 | 38.304 | 38.421 | **37.814** | **38.285** | ***37.934*** |
| Fe2O3 | 0.733 | 1.151 | 0.906 | 1.227 | 2.842 | 0.836 | 1.283 | 1.878 | 0.584 | 1.362 | 1.071 | 0.549 | 1.498 | 0.830 | 1.315 | **1.085** | **1.091** | ***1.204*** |
| CaO | 3.025 | 3.200 | 3.449 | 3.261 | 2.857 | 2.670 | 3.109 | 2.527 | 3.498 | 2.885 | 3.178 | 2.484 | 2.641 | 3.384 | 2.885 | **3.135** | **2.853** | ***3.004*** |
| ThO2 | 7.595 | 7.174 | 7.656 | 6.818 | 6.441 | 11.859 | 6.193 | 9.963 | 9.028 | 7.513 | 8.076 | 12.026 | 12.463 | 11.868 | 8.647 | **8.516** | **9.793** | ***8.888*** |
| Y2O3 | 1.709 | 1.757 | 1.781 | 1.629 | 1.724 | 2.826 | 2.531 | 2.331 | 1.405 | 1.991 | 1.967 | 3.003 | 3.034 | 2.797 | 2.585 | **2.112** | **2.408** | ***2.205*** |
| $U_{tot}$ | | | | | | | | | | | | | | | | ***39.582*** | ***37.347*** | |
| Total | 95.256 | 94.315 | 93.581 | 94.081 | 94.443 | 93.728 | 93.338 | 93.568 | 95.846 | 93.947 | 92.178 | 93.339 | 93.346 | 94.319 | 94.046 | **94.284** | **93.437** | ***93.956*** |
| Oxygen | 6.100 | 6.100 | 6.050 | 6.100 | 6.030 | 6.075 | 6.010 | 6.000 | 6.081 | 6.080 | 6.040 | 6.039 | 5.950 | 5.950 | 6.110 | **6.050** | **6.047** | ***6.048*** |
| Ti | 1.936 | 1.893 | 1.897 | 1.898 | 1.854 | 1.946 | 1.898 | 1.916 | 1.895 | 1.925 | 1.925 | 1.974 | 1.939 | 1.907 | 1.928 | **1.909** | **1.935** | ***1.915*** |
| Fe | 0.037 | 0.059 | 0.046 | 0.062 | 0.143 | 0.042 | 0.065 | 0.095 | 0.029 | 0.069 | 0.055 | 0.028 | 0.075 | 0.041 | 0.066 | **0.055** | **0.055** | ***0.061*** |
| Ca | 0.217 | 0.232 | 0.250 | 0.236 | 0.205 | 0.191 | 0.224 | 0.182 | 0.251 | 0.208 | 0.232 | 0.179 | 0.188 | 0.240 | 0.206 | **0.225** | **0.206** | *0.216* |
| Th | 0.116 | 0.111 | 0.118 | 0.105 | 0.098 | 0.180 | 0.095 | 0.152 | 0.138 | 0.115 | 0.125 | 0.184 | 0.188 | 0.179 | 0.131 | **0.130** | **0.149** | *0.136* |
| Y | 0.061 | 0.063 | 0.064 | 0.059 | 0.061 | 0.100 | 0.091 | 0.083 | 0.050 | 0.071 | 0.071 | 0.107 | 0.107 | 0.099 | 0.092 | **0.075** | **0.086** | *0.079* |
| Pb | 0.040 | 0.044 | 0.036 | 0.034 | 0.047 | 0.036 | 0.048 | 0.033 | 0.039 | 0.033 | 0.024 | 0.023 | 0.030 | 0.025 | 0.030 | **0.037** | **0.030** | *0.035* |
| $U^{4+}$ | 0.126 | 0.108 | 0.130 | 0.116 | 0.138 | 0.065 | 0.147 | 0.156 | 0.123 | 0.126 | 0.140 | 0.131 | 0.143 | 0.150 | 0.080 | **0.128** | **0.120** | *0.125* |
| $U^{6+}$ | 0.468 | 0.491 | 0.458 | 0.489 | 0.453 | 0.428 | 0.433 | 0.382 | 0.474 | 0.453 | 0.429 | 0.374 | 0.331 | 0.359 | 0.466 | **0.441** | **0.417** | *0.432* |
| Sum U | 0.594 | 0.599 | 0.588 | 0.605 | 0.591 | 0.493 | 0.580 | 0.538 | 0.597 | 0.580 | 0.568 | 0.505 | 0.474 | 0.510 | 0.546 | **0.569** | **0.537** | *0.558* |
| Cation Tot. | 3.019 | 3.057 | 2.975 | 2.937 | 2.999 | 3.001 | 3.000 | 3.000 | 2.999 | 3.000 | 3.000 | 3.000 | 3.000 | 3.000 | 3.000 | **3.006** | **2.990** | *2.999* |

Table 8.12 Results of formula recalculation of the RDD373 64 m brannerite specimen. The brannerite represents a euhedral crystal, with uniform reflectance. The analysis numbers correspond to the sampling positions in Figure 8.25. U content ranges from 43 wt.% oxide to 49.6 wt.%. The euhedral brannerite contains less Ti, Pb, Th, and Y than the altered specimen in RDD373 64 m. It does, however contain greater proportions of U, Ca, and F.

| Point | Brann_ 93C_2-16 | Brann_ 93C_2-17 | Brann_ 93C_2-18 | Brann_ 93C_2-19 | Brann_ 93C_2-20 | Brann_ 93C_2-21 | Brann_ 93C_2-22 | Brann_ 93C_2-23 | Brann_ 93C_2-24 | Brann_ 93C_2-25 | Brann_ 93C_2-26 | Average |
|---|---|---|---|---|---|---|---|---|---|---|---|---|
| (U,Ca,Y,Ce)/ (Ti,Fe) | 1.554 | 1.823 | 1.503 | 1.771 | 1.598 | 1.762 | 1.694 | 1.618 | 1.592 | 1.637 | 1.664 | 1.656 |
| Y: (Ti,Fe) | 1.878 | **1.985** | 1.854 | 1.965 | 1.895 | 1.972 | 1.941 | 1.909 | 1.896 | 1.916 | 1.928 | 1.922 |
| UO3 | 38.592 | 42.956 | 38.731 | 42.547 | 41.366 | 32.363 | 36.819 | 35.771 | 36.994 | 36.612 | 36.393 | 38.216 |
| TiO2 | 36.377 | 34.913 | 36.024 | 35.841 | 35.912 | 37.734 | 37.470 | 35.881 | 36.577 | 36.662 | 36.551 | 36.502 |
| FeO | 0.481 | 3.555 | 0.285 | 2.861 | 1.534 | 0.378 | 0.757 | 0.846 | 0.705 | 0.772 | 0.878 | 1.686 |
| CaO | 5.086 | 3.920 | 5.283 | 4.575 | 5.386 | 3.845 | 4.514 | 4.107 | 4.655 | 4.448 | 4.436 | 4.258 |
| ThO2 | 4.903 | 5.048 | 5.803 | 5.148 | 5.972 | 6.336 | 4.105 | 5.676 | 5.965 | 5.601 | 6.708 | 5.469 |
| Y2O3 | 0.890 | 0.688 | 0.843 | 0.872 | 0.832 | 1.087 | 1.237 | 0.897 | 0.902 | 0.830 | 1.634 | 1.104 |
| PbO | 2.017 | 1.662 | 2.434 | 0.947 | 0.928 | 0.935 | 0.940 | 0.925 | 0.454 | 1.101 | 1.664 | 1.230 |
| UO2 | 9.500 | 3.700 | 8.600 | 3.700 | 5.200 | 13.500 | 11.300 | 13.900 | 12.800 | 12.100 | 7.500 | 7.940 |
| | | | | | | | | | | | | 46.156 |
| Total | 97.846 | 96.442 | 98.003 | 96.491 | 97.130 | 96.178 | 97.152 | 98.003 | 99.052 | 98.126 | 95.764 | 96.403 |
| O | 6.200 | 6.200 | 6.200 | 6.200 | 6.200 | 6.200 | 6.200 | 6.200 | 6.200 | 6.200 | 6.200 | 6.200 |
| Ti | 1.851 | 1.783 | 1.838 | 1.805 | 1.809 | 1.950 | 1.899 | 1.860 | 1.857 | 1.873 | 1.877 | 1.863 |
| Fe | 0.027 | 0.202 | 0.016 | 0.160 | 0.086 | 0.022 | 0.043 | 0.049 | 0.040 | 0.044 | 0.050 | 0.095 |
| Ca | 0.369 | 0.285 | 0.384 | 0.328 | 0.387 | 0.283 | 0.326 | 0.303 | 0.337 | 0.324 | 0.325 | 0.309 |
| Th | 0.075 | 0.078 | 0.090 | 0.078 | 0.091 | 0.099 | 0.063 | 0.089 | 0.092 | 0.087 | 0.104 | 0.085 |
| Y | 0.032 | 0.025 | 0.030 | 0.031 | 0.030 | 0.040 | 0.044 | 0.033 | 0.032 | 0.030 | 0.059 | 0.040 |
| Pb | 0.037 | 0.030 | 0.044 | 0.017 | 0.017 | 0.017 | 0.017 | 0.017 | 0.008 | 0.020 | 0.031 | 0.022 |
| $U^{4+}$ | 0.147 | 0.058 | 0.134 | 0.057 | 0.080 | 0.213 | 0.175 | 0.220 | 0.198 | 0.188 | 0.117 | 0.124 |
| $U^{6+}$ | 0.548 | 0.613 | 0.552 | 0.598 | 0.582 | 0.467 | 0.521 | 0.518 | 0.524 | 0.522 | 0.522 | 0.544 |
| Cation total | 3.087 | 3.073 | 3.087 | 3.076 | 3.081 | 3.091 | 3.087 | 3.089 | 3.088 | 3.087 | 3.086 | 3.082 |

## 8.15. Compositional Variation and Trends in Betafite and Brannerite

The mineral betafite is well known at the SH, SK and SJ deposits of the Rössing Uranium mine area. The mineral was studied intensively by Herd (1996) and Nex *et al.* (2003) who provide the most comprehensive mineral chemistry for Namibian betafite, and pyrochlore. The database of Rössing type pyrochlore includes compositional data of two coloured varieties of SK area betafite, SH betafite, SJ betafite, and a collection of Nb-pyrochlore samples. According to Hogarth (1977, 1989) the pyrochlore group betafite is defined as having 2Ti> Nb + Ta, in the case of the Husab betafite sample, this is satisfied where 2Ti (2.846) > Nb (0.397) + Ta (0.009). Figure 8.26defines the Ti-Ta-Nb classification on a ternary plot. Cation - corrected and normalised compositional data of Husab and Rössing samples place the betafite and pyrochlore specimens within their respective groups (all analyses are normalised to 6 oxygens). The binary plots in this section use $UO_3$ or total U as some of the brannerite analysis points are balanced with both $UO_2$ and $UO_3$ components. The plots include all the analytical point data, rather than averaging the multiple analyses of a single betafite and three brannerite species. The collection compares elements common to betafite and brannerite, elements such as Nb effectively discriminate between betafite and brannerite, while REE and Y occur in relative abundance in both mineral species. The data points are also split into groups, differentiating between analyses on altered and relatively unaltered portions of the specimens. A complex Fe-Ti-Ca-U mineral, labelled as leucoxene[51] is included for comparison

A second means of comparing betafite compositionally is the binary Cv1 vs Cv2 plot of Ercit (2005), Figure 8.27 where:

***Cv1*** *= 0.233Na + 0.104Ca – 0.115Fe* + 0.405Pb + 0.174Y* + 0.261LREE + 0.096U* + 0.301Ti + 0.095Nb + 0.107Ta* – 12.22 (oxide wt.%) and*

51 An alteration product and mixture of Fe-Ti oxides, including titanite, perovskite, titanian magnetite, but especially ilmenite. Most 'leucoxene' is anatase or rutile. ww.mindat.org/min-6174.

***Cv2*** *= = 0.119Na – 0.126Ca – 0.334Fe* – 0.172Pb – 0.361Y* – 0.287LREE – 0.197 U* – 0.105Ti – 0.182Nb – 0.116Ta* + 18.54 (oxide wt.%).*

Table 8.13 The A site cation proportions of the Husab betafite.

| **Sample** | **U** | **Ca** | **Y** | **Hogarth (1977, 1984) Name** |
|---|---|---|---|---|
| Husab RDD373-115 m. Betafite (15 analyses of large grain) | **46.1 %** | 30.5 % | 23.4 % | Betafite, U is dominant |

| **Sample Analysis Group** | **CV1** | **CV2** | **Ercit (2005a) Classification** |
|---|---|---|---|
| Husab leached average | 2.764 | 1.102 | Euxenite-Aeschynite (range does not cover Pyrochlore group) |
| Husab pristine average | 2.433 | 0.928 | Euxenite-Aeschynite (range does not cover Pyrochlore group) |
| Rössing SH, Nex *et al.* (2003) average. | 1.856 | 1.395 | Euxenite-Aeschynite (range into Pyrochlore group) |

The Husab betafite is comparable to the Rössing betafite, where Ta constitutes only trace proportions, and variation is largely between Ti and Nb. SK betafite has roughly equal Ti and Nb, while at SH and SJ Ti:Nb ranges from 2:1 to 3:2. The Husab betafite has Ti:Nb of ~4:1. Speciation within the betafite subgroup is then defined by the dominant A site cation, which it is either Ca, Pb, U or REE (Y). The most abundant A - site cation conditionally names the subspecies. If Ca and Na are the only cations, the mineral is calciobetafite. If other cations are present, then they name the mineral, if they account for >20 % of the total A site.

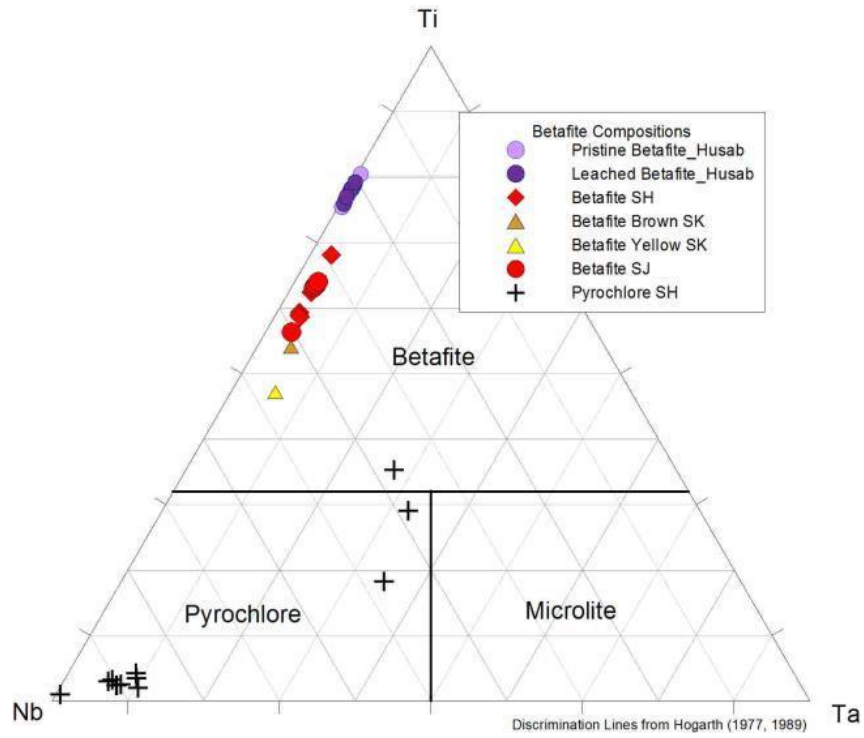



Figure 8.26 Normalised cationic proportions of Husab betafite and Rössing Mine betafite. The Husab data are sourced from 7 spot analyses on 'pristine', unaltered zones of a 1.2 mm betafite (lavender circles), and 6 spot analyses of leached zones of the same mineral grain (purple circles). Ta is low in both populations and no differentiation is possible for Nb:Ti between leached and pristine portions of the RDD373-115m specimen. Rossing Data: Herd (1996) and Nex et al. (2003).

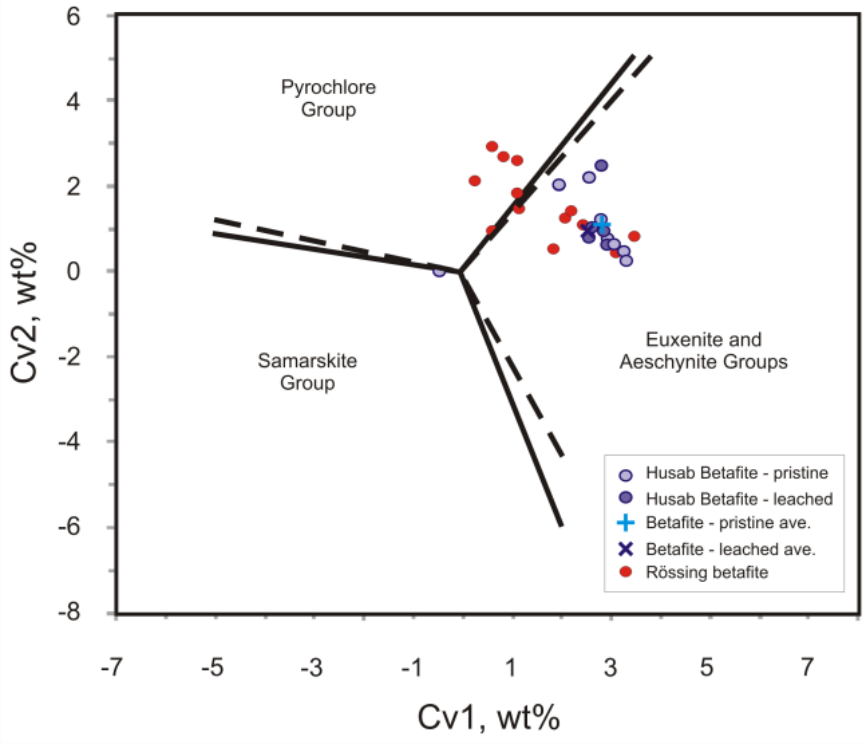
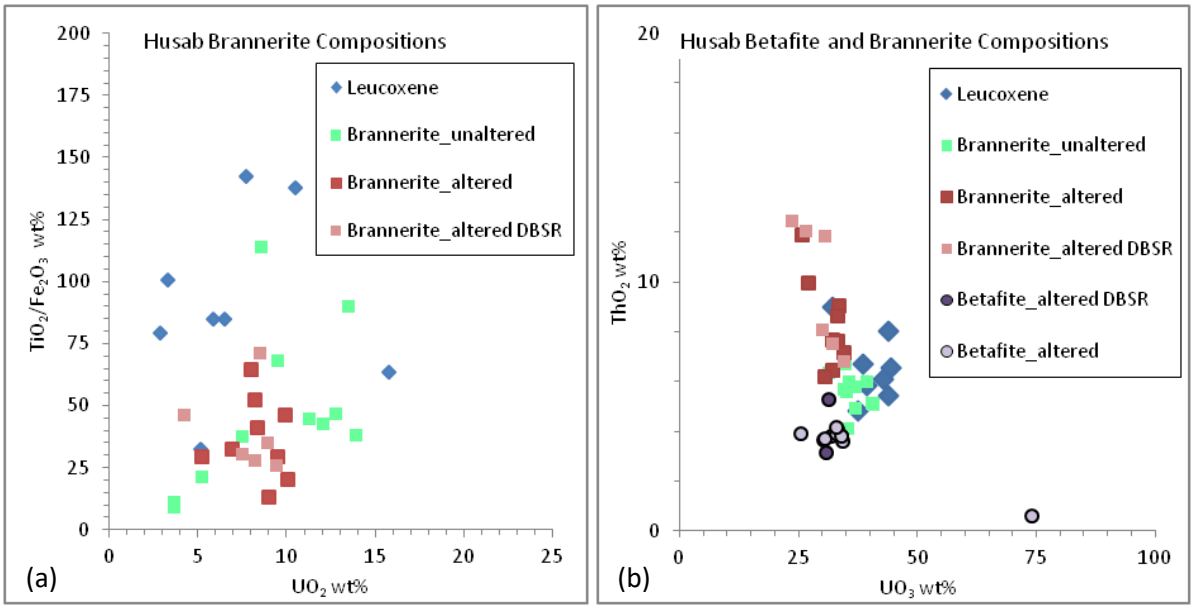



Figure 8.27 Binary plot of Husab RDD373-115m betafite (purple) data points pyrochlore-euxenite-samarskite mineral group classifications. The Rössing betafite (red) by comparison host slightly elevated Ta (Cv2) and a wider range of Nb:Ti (Cv1). Rössing Data from Herd (1996) and Nex *et al*. (2003). Discrimination fields from Ercit (2005a).

*Betafite and Brannerite composition Variation*

Fe, Ti, Th, and Y are the major trace consitruents that are common to both betafite and to brannerite. Binary plots of U content, as UO3 wt%, on the x-axis offer a means of direct comparison between specimens from the Husab deposit. $TiO_2/Fe_2O_3$ ratios for betafite are in the range of 5;1 to 25:1, while the brannerite analysis populations plot with a greater range, with $TiO_2/Fe_2O_3$ >75 in two sample points of the unaltered RDD373_93 m brannerite. There does not appear to be any relationship between $TiO_2/Fe_2O_3$ and $UO_3$ content, or a relationship between the leached and unaltered portions of the brannerite. The leucoxene phase is characterised by slightly higher $UO_3$ and a greater Ti/Fe ratio (Figure 8.28a). Formatting issues here



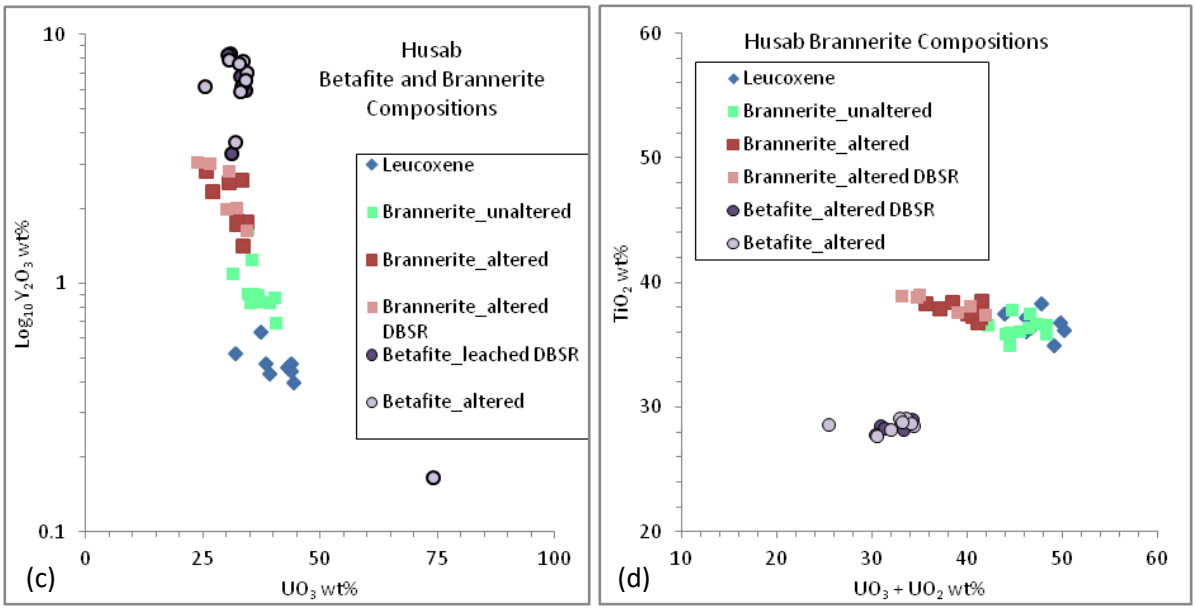



Figure 8.28 Bivariate plots of betafite and brannerite compositions. Plots represent individual sample points on single specimens of each mineral. Key: DBSR = dull backscatter reflectance, (a) UO2 vs. Ti/Fe of brannerite and leucoxene. Although leucoxene is not a recognised mineral structure, high Ti low U phases are relatively common in the brannerite-bearing samples. The Ti/Fe ratio is comparatively high with respect to the ratios in the altered and pristine brannerite. (b) U and Th abundances in brannerite, leucoxene and betafite are mineral-specific; relative Th abundance is higher in the altered brannerite than in the unaltered variety, calculated UO3 is comparatively higher in leucoxene than in other minerals. The refractory nature of betafite is evident in the clustered plots of altered and unaltered portions of the specimen. (c) Y abundance in the betafite grain discriminates it from the brannerite. Y is also more abundant in the altered brannerite than the unaltered specimen; the linear correspondence with UO3 suggests a substitution relationship. This is also apparent in the unaltered specimen. (d) Utotal vs. TiO2 of Husab betafite and brannerite; the two minerals show contrasting relationships between U and Ti abundance, betafite is positively correlated while the altered brannerite in particular shows a Ti increase with corresponding U decrease.

Plots of total U vs. $TiO_2$ show that the leached brannerite has a systematic negative correlation between U and Ti, and that the Ti content decreases with increasing U between the leached and unaltered brannerite and the leucoxene. The betafite and altered brannerite plot with relatively constant U and Ti, reflecting the insolubility of Ti and the nature of the mineral to retain U (Figure 8.28b).

$Y_2O_3$ content is highest in the betafite specimen and relatively high in the altered brannerite, and comparable to the Goanikontes uraninite in this study. The unaltered brannerite and leucoxene have lower concentrations of Y, between 0.4 and 1.5 wt.% oxide (Figure 8.28c). The Y trend indicates systematic substitution for U in the altered brannerite specimen, the relationship is less pronounced but still apparent in the leucoxene and

unaltered brannerite. The betafite analyses show no relationship between U and Y, despite the relatively elevated Y content of the mineral.

Total $UO_3$+ $UO_2$ vs $TiO_2$ is also a diagnostic ratio for discriminating between brannerite and betafite, which may appear quite similar when metamict. Comparing total U also helps overcome complicated formulae recalculation required to determine $UO_2/UO_3$ (Figure 8.28d). U and Ti show a weakly positive correlation and in the Husab sample, constitute lower abundances than in the brannerite. The altered brannerite and, to a less obvious degree, the leucoxene samples show a weakly negative relationship between U and Ti.

## 8.16. Alteration of Primary Uranium Minerals

The simplest measure of uraninite alteration is the ratio of Pb to uranium, where the premise that all Pb that is detected is the result of radiogenic decay of uranium and potentially of thorium ($^{206}Pb$ and $^{208}Pb$, respectively). Simplistically there should be a linear regression of U with respect to Pb, assuming most Pb is a product of U decay and that none is lost to alteration. Deviation from a linear trend thus implies alteration.

The binary plot of $U_{total}$ -oxide wt.% vs. PbO wt.% illustrates some characteristics of the uraninite alteration history at each deposit (Figure 8.29a and Figure 8.30). The relatively high Pb content of the Valencia surface samples is hard to reconcile with the lower Pb of the core samples; the best explanation is the evidence of fluid-present alteration in the core samples, which is absent from the surface material. Although the $R^2$ values for U and Pb in the Valencia samples is low, the analyses plot with a relatively consistent trend. Overall the $U_{total}$ relationship with PbO is linear and positive in the Husab samples, where $R^2$ is the highest of any uraninite group. The Hildenhof and Goanikontes samples, which incidentally have the highest- and lowest $U_{total}$ abundances, respectively show no relationship between U and Pb. Thus, the high and low totals may be the result of secondary processes on the uraninite populations at these deposits. The U:Pb is highest in the Variscan granites of Förster (1999) and lowest in the Bancroft district samples of McKechnie (2012) the youngest and oldest

uraninite populations, respectively. U and Pb data from EPMA analyses of Husab uraninite is included from Cross *et al.* (2011), with a caution that the specimens selected were purposefully chosen to represent the least altered uraninite for U-Pb dating purposes.

Comparison of Pb with immobile U(IV) and Th(IV) ratios reflects the $U_{total}$ and Pb relationships (Figure 8.30). Low $UO_2$ contents are reflected by low U:Th in the Goanikontes area samples which suggests that U content of the uraninite population has changed relatively soon after crystallisation. The Etango uraninite specimens have on average 10 wt% less $U_{tot}$ than uraninites sampled in the region, Pb content though is comparable with the other deposits. This may indicate that the uraninite had comparable $U_{tot}$ and has lost $UO_3$ during subsequent process' such as those that produced the E-type SLGs described in Nex (1997). Conversely, the comparable Pb content suggests otherwise, since Pb is also mobile the Etango specimens should have depleted Pb if alteration has leached $U^{6+}$. The comparatively narrow range and high ratios of U:Th of the Valencia surface samples relative to the core samples suggests that the altered core samples have lost $UO_2$ through oxidation to $UO_3$. The relatively elevated PbO of the Valencia surface samples is not easily explained, as mobile Pb should really be more susceptible to leaching at surface. The high PbO of the samples from the Bancroft district reflects their chemical age (Trans-Hudsonian of ~1.8 Ga) in which U has had a longer period of time to decay to Pb. The high Pb also suggests that comparatively little leaching has taken place.

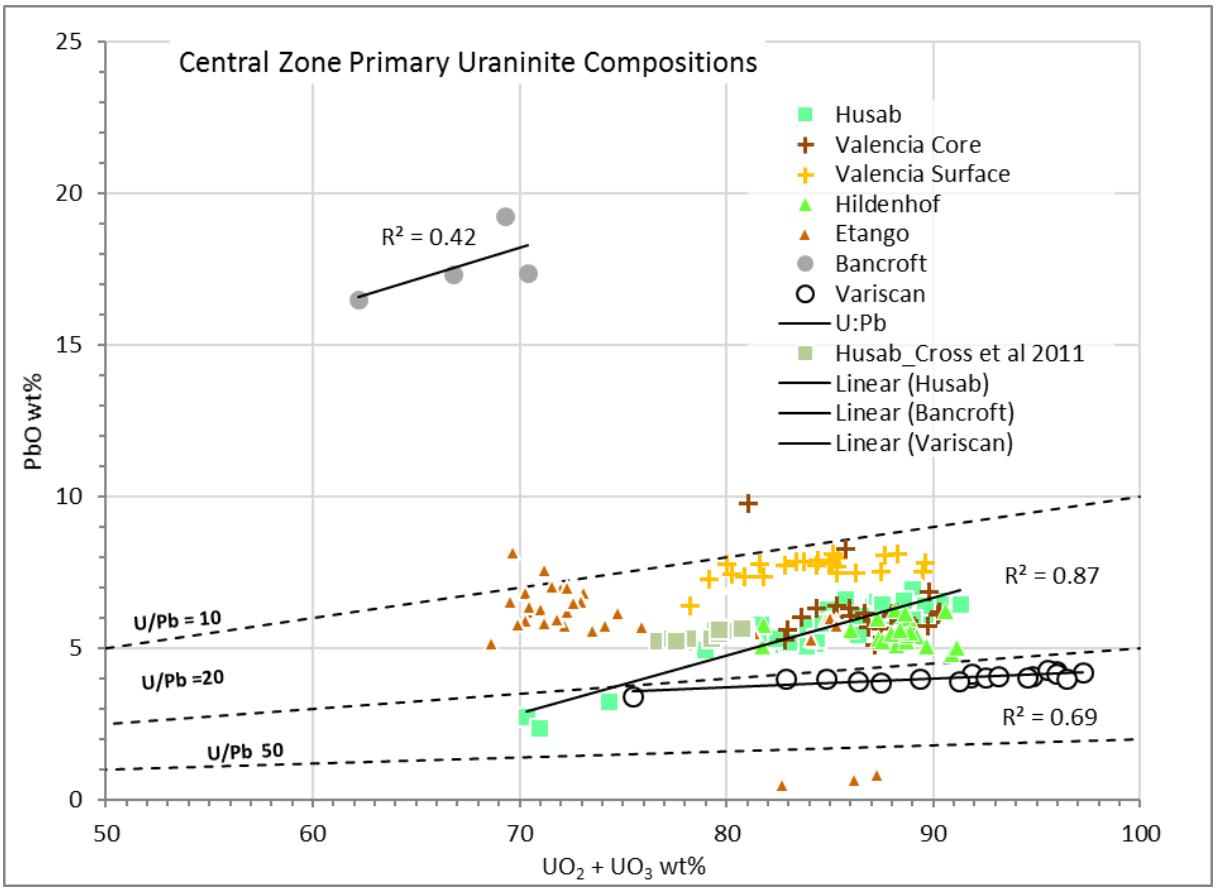



Figure 8.29 Uranium vs PbO wt.% for the Central Zone uraninite. The Husab uraninite population shows the strongest positive correlation between U and Pb, which indicates that sampled uraninite specimens have not lost significant Pb to secondary processes. The Valencia sample population has bimodal distribution, where the surface samples have retained the highest proportion of Pb; and the samples from depth have lost Pb, during hydrothermal alteration episodes (E-type leucogranite). The Hildenhof samples comprise a set of altered uraninite with prominent fractures, thus a poor Pb and U correlation. The Etango uraninite shows evidence of Ca, REE and Y substitution of U, prominent fracturing and coffinitisation, which contribute to a weak Pb and U correlation.

The uraninite specimens of Cross *et al.* (2011) have a relatively narrow range of $UO_2$:$ThO_2$ and an equally narrow PbO, reflecting careful sample selection for the intended purpose of age dating. Uraninite is dated at ~496 Ma in Cross *et al.* (2011) which is considerably younger that the ~506 Ma U-Pb zircon of the Valencia alaskite to the north (Longridge, 2012) or the ~508 Ma U-Pb zircon age of Goanikontes alaskite to the south (Briqueue *et al*., 1980). The age difference is somewhat equivocal, Cross *et al*. (2011) assert the age of the uraninite is accurate, having directly compared to a uranium standard age, however, Pb and U mobilisation is challenging to estimate accurately given the nature of the specimens; and,

uraninite appears to be late with respect to quartz and feldspar, but not necessarily zircon and could have crystallised at some point after initial rock formation and zircon. Uraninite for example is stable at a greater range of temperatures and can crystallise in fluids at temperatures as low as 20 °C in granites (Min *et al.,* 2005).

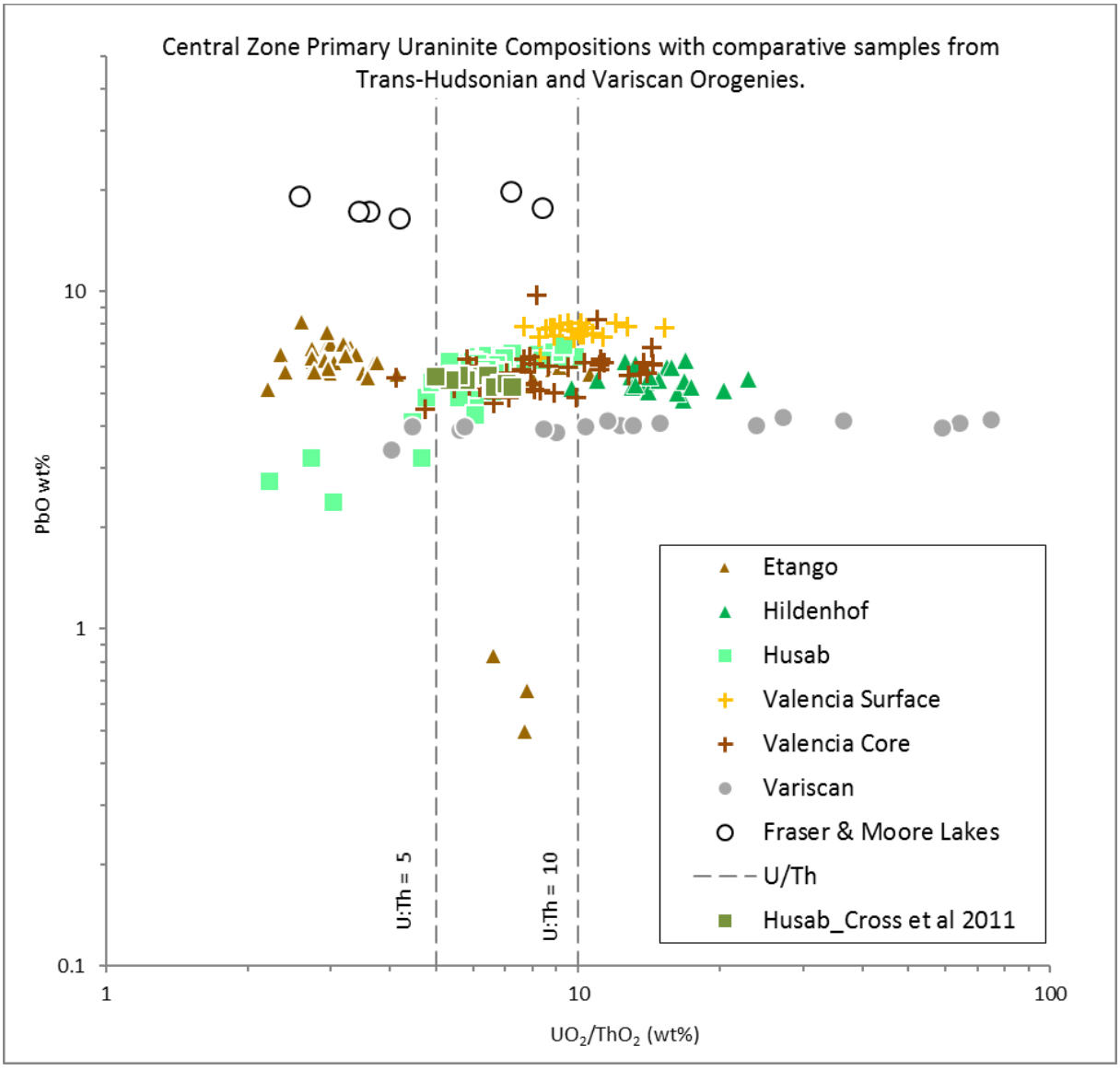



Figure 8.30 $UO_2/ThO_2$ vs. PbO of Central Zone uraninite. The ratio should remain fairly constant unless alteration affects REDOX conditions and oxidises immobile U(IV) to U(VI). The U/Th ratio shows similar trends of increasing Pb with increasing U/Th in the Damara and Bancroft district samples, except in the Goanikontes samples. The Valencia core samples have a great range in $UO_2/ThO_2$ which may reflect oxidation of immobile U and subsequent leaching during alteration.

The distribution of Ca, Pb, and Si in uraninite is unequivocal; both elements have smaller ionic radii, and all much smaller than U, thus ruling out U substitution. However, Pb is a product of U decay, and is also mobile within the magmatic-hydrothermal environment during granite crystallisation (after Alexandre and Kyser, 2005). Figure 8.31 illustrates Pb, Si, and U distribution in a Valencia uraninite. Pb concentrations are erratically distributed throughout the mineral and show a roughly inverse relationship with U and with Si. Si and U however, correspond, implying a coffinite component. The higher density Pb may coincide with original uraninite, which has decayed, while low Pb concentration corresponds with less U-dense coffinite.

The ranges of Pb concentration in uraninite may be indicative of the alteration that uraninite has undergone. A narrow Pb range represents a uraninite population with uniform alteration (low level of Pb leaching), wide ranges with low minimum Pb represent uraninite populations that are altered (i.e. high variable %age of Pb is leached). Ca may substitute for U (106 Å vs. 105 Å, respectively) or as is evident in petrographic and SEM observation, it may simply represent replacement by uranyl silicates such as uranophane, $Ca(UO_2)_2(SiO_3OH)_2{}^2{}_5H_2O$.

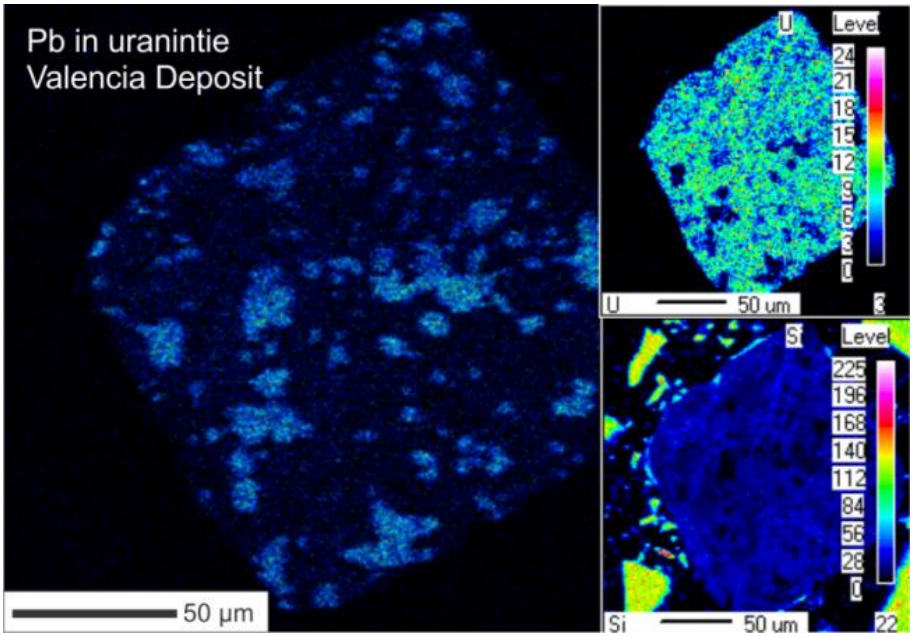



Figure 8.31 Pb distribution in Valencia uraninite. The specimen illustrates Pb distribution is in discrete patches, which implies it is a replacement texture rather than substitution. The patchy distribution is also more evident of Pb-mineral replacement than U-Pb decay. Si in contrast has a more uniform distribution and represents coffinite where it is coincident with U.

Ca is an important component in betafite and in brannerite, and is found in concentrations of over 12 wt.% in Rössing betafite. The least altered brannerite specimens and the least-altered portions of the Husab betafite have a maximum of 5.5 wt.% CaO. The mobility of Ca relative to U in the refractory phases is compared with reference to Th, which is relatively immobile regardless of what phase it is hosted in.

Figure 8.32 plots total $U_{oxide}/ThO_2$. The Ca and U relationship is positive, which may represent substitution, given that U and Ca are the main A site cations. Herd (1996) and Nex *et al* (2003) showed that Ca was mobile and leached from betafite in the surface environment. The trends in the Husab brannerite and betafite show that although Ca is leached and in lower concentration in altered specimens, U/Th ratios do not show any systematic trend between altered and un-altered analyses of betafite. The altered brannerite however, shows lower U and Ca in the analyses of the more altered mineral portions.

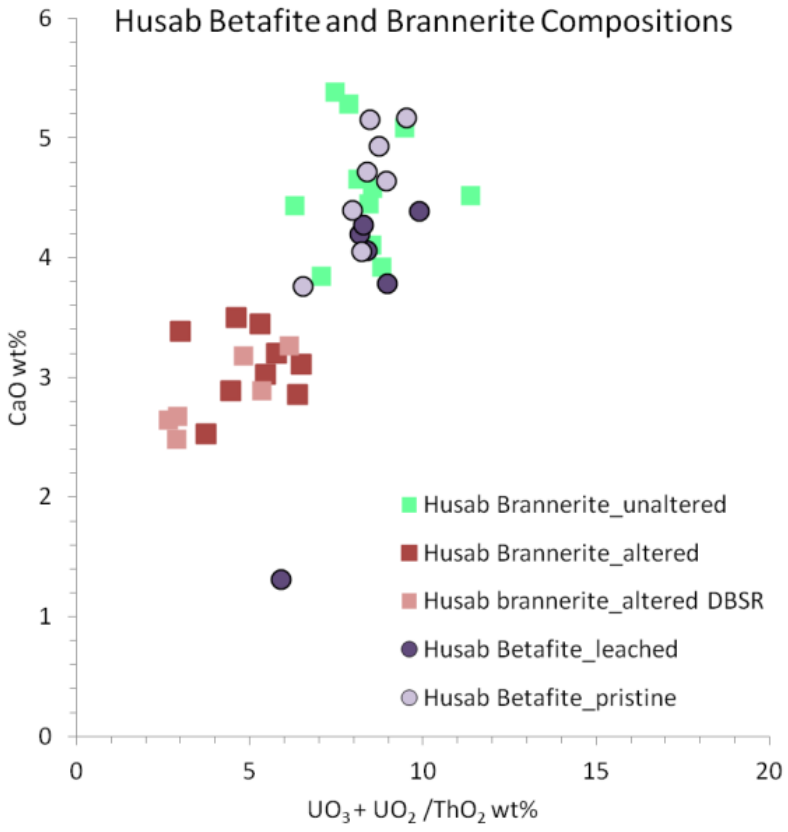



Figure 8.32 $UO_3$ +$UO_2$/$ThO_2$ vs. CaO wt.% from analyses of betafite and brannerite from drillhole RDD373. CaO tends to be in lower abundance in the altered portions of the betafite. The altered brannerite at 64 m has lower CaO relative to the unaltered specimen at 93 m. The leached portions of the altered brannerite host the lowest concentrations of CaO. (DBSR:- dull backscatter reflectance). Overall there is a positive correlation between U content and CaO, and this trend is consistent when comparing analyses of altered and unaltered specimens.

## 8.17. Concluding Remarks on Composition Analysis Findings

The Central Zone uraninite populations show greater variation in total U + Pb vs Th + REE, Y than the comparative samples from the Variscan and Bancroft granites (Förster, 1999; and McKechnie, 2012, respectively). The samples plot with an overall negative correlation, suggesting there is some systematic substitution of U, however, mobile $U^{6+}$ and Pb content are the likely major cause for deviation from an expected systematic trend.

The primary alteration of uraninite is replacement by coffinite, which occurs under reducing conditions (Janeczek and Ewing, 1992a, 1992b). Coffinite replacement is common to samples from all deposits in this study, and is the dominant uranium mineral in seven of the twenty-two Husab samples. It forms at the rims of uraninite and along mineral cleavage and fracture planes; and some uraninite samples contain thorite with coffinite in solid solution (Valencia as an example at the start of this chapter). Uranophane and other uranyl oxy-hydroxides appear confined to the supergene portions of deposits, and decrease in abundance but do not necessarily disappear with depth. They are present at depths of over 300 m downhole (>150 m vertically from surface) and are associated with localised late magmatic and fault associated hydrothermal alteration.

1. The primary uraninite textures subdivide into four key categories:
    a. Early magmatic uraninite is coarse-grained and occurs as near-euhedral inclusions most often in microcline or quartz;
    b. Intermediate magmatic uraninite is the most abundant variety and occurs as singular or clustered euhedral cubic crystals between quartz and feldspar crystals, often in association with other accessory minerals such as zircon, monazite, xenotime, and thorite;
    c. Late magmatic uraninite predominantly occurs along preferred fluid pathways such as biotite cleavages, and forms euhedral crystals that disrupt the host mineral structure. Examples such as in hole RDD373 at 125 m show a pair of 100 µm uraninite, arranged parallel to the biotite cleavage (the biotite is altered to chlorite with magnetite filling lenses between mica sheets); and

d. Inclusions of uraninite tends to be fine-grained, and occur in accessory minerals, such as monazite, biotite, zircon, and magnetite (specifically at Goanikontes). The textures of some of the host minerals suvch as biotite, monazite, zircon, and thorite, suggest that they constitute an entrained component from the source or assimilation from the country rocks (particularly the skeletal micas). Other examples such as zoned zircon and uraninite-hosting magnetite (Goanikontes) support a model of early uraninite incorporation into melt-derived accessory minerals. Uraninite inclusions also occur in skarn assemblage minerals, such as titanite, but are localised to sporadic occurrences at Husab and Holland's Dome.

2. Secondary uraninite

e. Late uraninite crystallises as a fine-grained or amorphous vein and fracture-fill, replacing voids in minerals following leaching of silicates and oxides. Type examples include uraninite in vugs within feldspars at Husab, and uraninite in a vermicular texture filling voids in altered magnetite-haematite crystals at Goanikontes.

The formation of uranium mineralisation is a complex process that has taken place in more than one episode, firstly the formation of primary uraninite within the quartz-feldspar matrix, uraninite formation along biotite cleavages, within cavities and on the surfaces of altered Fe oxides, and within enclaves of inherited accessory minerals, at some point after initial formation a generation(s) of hydrated $U^{6+}$ and $U^{4+}$ silicates formed. The silicates occur as stand-alone phases such as uranophane on fracture planes, and as direct replacements of uraninite such as coffinite. Coffinite Pb content is very low compared to uraninite, with almost all sample specimens reporting less than 1 wt.% PbO compared to the >5 wt.% PbO of all the uraninite analyses.

There are three events in which U mobilisation may have taken place; the first is the initial mineralisation phase at the time of magma generation and subsequent migration through to mid-crustal levels. The process is interpreted to have focussed incompatable elements in the melt that migrated toward the final emplacement sites, thus large ions like U and Th

may preserve a steady ratio throughout. For some time after the initial emplacement of the granites a period of residual magmatic fluid flux (Jacob, 1974b; Berning *et al.*, 1986) and fluids derived from decarbonation reactions with the metasediments (Cuney, 1980b; Herd, 1996; Kinnaird and Nex, 2007) would have facilitated the recirculation of oxidised uranium, which crystallised as uraninite where it encountered reducing agents, and as complex Nb-Ta-Ti-Ca oxides in the upper units of the Rössing Formation (Cuney, 1980b; Herd, 1996; Kinnaird and Nex, 1997; this study).

The interpretation of uranum mineralisation subsequent to granite crystallisation is supported by K-Ar cooling ages such as *ca*. 440 Ma of Haack and Hoffer (1976), which suggests sufficient heat was available for some time. This period of cooling is sufficiently hot to mobilise U and crystallise secondary generations of U(IV) and U(VI) minerals. A comparative such as the Dalonshan granites of China have been shown by Zhao *et al*., (2003) to have mobilised U and crystallised uranium minerals in periods that post-date alkali-feldspar granite intrusions by ~8 Ma and took place at temperatures as low as 250 °C to 300 °C. U would also be liberated from now-metamic accessory minerals such as biotite,

zircon, and monazite. Figure 8.33

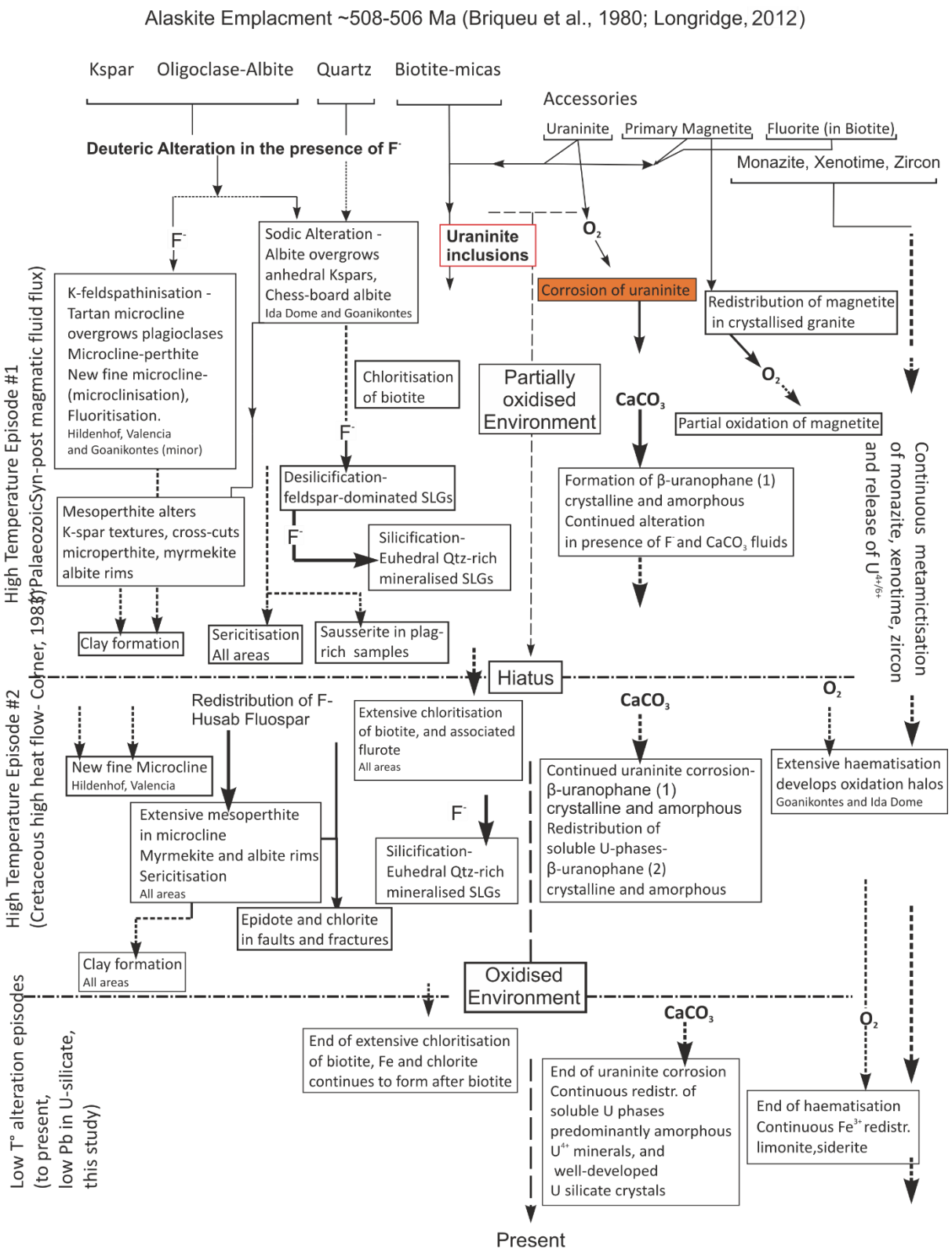



Figure 8.33 illustrates a simiplified mineralisation sequence for the primary-hosted deposits.

The break-up of Gondwana is a well-known period of heat flow in the Damara and the western Central Zone is punctuated by numerous dolerite dykes, and at locations around

the Rössing Mine and the Goanikontes deposits host uranophane and boltwoodite mineralisation in chert veins that appear to be parallel to the orientations of the Cretaceous dolerite dykes. In more recent times, the coating of joint and mineral surfaces in the near surface and palaeo-surface environments (Husab, Goanikontes, this study) suggest that highly soluble uranium (VI) complexes were mobilised in the groundwater environment, some of which is evident over 200 m below surface along steep-dipping fault planes (Husab, Ida Central, this study).

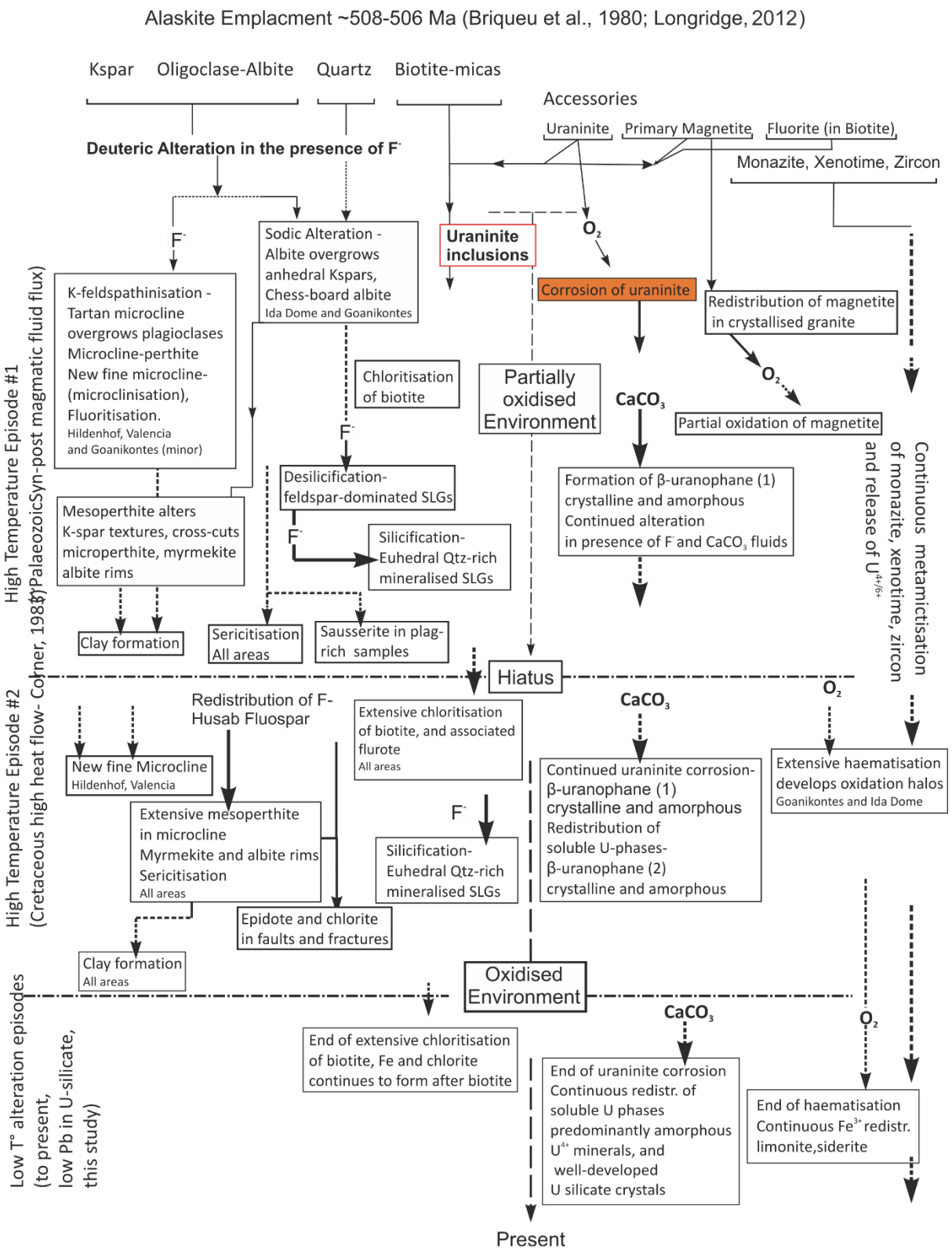



Figure 8.33 Simplified mineralisation sequence for the primary uranium deposits. The scheme splits the sequence into three episodes, the first is initial formation, the intermediate is a period of high heat flow in the Cretaceous and the third is the last period which includes recent geologic time where deposits exposed at the surface are perceived to be altered by oxidising meteoric fluids.

***Betafite and brannerite compositions***

The betafite from Husab chemically plots within the betafite field of Hogarth (1977) but not within the pyrochlore field when using the Ercit (2005a) criteria. The trends on the latter suggest that the alteration of the mineral has affected the composition. In most bivariate discrimination plots the altered and unaltered betafite show little difference between populations. Altered and unaltered brannerite and leached and non-leached portions of altered brannerite do show distinct trends with respect to U, Th, Fe and Y. The presence of leucoxene and the close association between brannerite and other Ti minerals suggests that a great range of brannerite-like phases may exist (leucoxene) in a given sample.

The Husab specimen contains comparably low Ta abundance but is otherwise quite distinct compositionally from the betafite at the Rössing deposits. Brannerite and betafite host appreciable concentrations of Ca, and relationships of Ca and U indicate that substitution may be taking place, but for the most part Ca is preferentially leached with respect to U in both refractory mineral species. The presence of these refractory minerals at Husab will require further investigation; the conclusions of this study, with reference to internal studies by Guy Freemantle at Swakop Uranium are as follows:

- Brannerite and betafite are comparable in texture and chemistry and are likely to have formed in similar conditions;
- Both host appreciable Y, but REE tend to be in very low abundance both species of refractory U-mineral;
- Nb is the most effective discriminator between the minerals at Husab, with betafite hosting ~11-15 wt.% $Nb_2O_5$ and brannerite hosting in-detectable concentrations;
- Ta and Nb abundances tend to be much lower than in the Rössing Deposit betafite, which host over 20 wt.% $Nb_2O_5$;
- The abundances of betafite and brannerite appear to be associated , as is expressed in QEMSCAN study and SEM analyses; and
- Although compositions are different the major components of U, Ca, and Ti and textural relationships support magmatic crystallisation, relative timing of betafite and brannerite crystallisation are not established.

Certain compositional and petrographic observations support an interpretation of crystallisation from weakly reduced U-rich fluids; the crystals are larger than uraninite, and in the case of betafite crystallise between quartz and feldspar, but after magmatic zircon. Zircon may have acted as a nucleus in the particular example of this study as illustrated in Figure 8.23. The non-stoichiometric formulae for brannerite and betafite require $U^{6+}$ in order to balance, implying that the magma and fluids were oxidised, or at least local conditions allowed for dissolved $U^{6+}$. Conditions were locally not conducive to uraninite ($U^{4+}$) dominant mineralisation. The reasons for this at Husab may be similar to those proposed for Rössing by Cuney (1980a, b); Herd (1996); Nex *et al*. (2003) and Abraham (2009).

The influence of the intruded sediments on the magmatic fluid chemistry has promoted lower temperature crystallisation and largely oxidising conditions. However, the abundance of brannerite overprinted by sulphides at Husab would suggest that it crystallised in reduced conditions. The euhedral brannerite is also consistently associated with biotite-titanite-rutile enclaves that appear to be entrained and uniformly chloritised with cleavage-parallel Fe-Ti oxide exsolution. The euhedral shape and zoned growth of the brannerite imply a magmatic origin, and the abundance of fluorite in association with brannerite in the Husab alaskite suggests that sufficient U is retained in the oxidised melt for sunsequent uranophane/boltwoodite crystallisation, or crystallisation of brannerite as an alteration of rutile. (F promotes $U^{6+}$ solubility in silicate melts, Pieffert *et al.,* 1994). Where suitable amounts of Ti (potentially from biotite-exsolved ilmenite) are available the $U^{6+}$ in the melt may then crystallise in more complex phases such as brannerite.

Betafite is comparatively rare at Husab, and where observed it always accompanies brannerite, in greater abundance. It has lower Nb and Ta and the most likely explanation is that Nb from cordierite in the Rössing schists may not be as accessible as in the SH and SK areas at Rössing.

The refractory phases occur in units of the upper Rössing Formation, with the most prominent occurrence hosted in pegmatitic alaskites that invade chloritic, cordierite-bearing schists and gneissic rocks. These are succeeded by quartzite-carbonate packages that constitute the upper Rössing Formation marble of Nash (1971) and Anderson and Nash (1997). Brannerite is sporadically present throughout the Husab deposits and is invariably

found in leucogranites invading upper Rössing Formation schists, stratigraphically within 50 m to 100 m of the Chuos Formation diamictite and schists. In this light, promotion of brannerite crystallisation appears to mirror that of betafite mineralisation at the SH area, where the upper Rössing Formation is dominated by the refractory phase, rather than uraninite.

# CHAPTER 9 SUMMARY AND CONCLUSIONS

## 9.1 Introduction

The aims of this thesis were to investigate the granite populations at each of the major primary uranium deposits of the western Central Zone, with particular emphasis on the sheeted leucogranites and the relationship(s) between the non- or weakly-uraniferous (nominally ≤50 ppm U) and the uranium-enriched varieties (100's to 1 000's of ppm U). The benchmark studies of the Central Zone sheeted leucogranites are those of Nex (1997); Nex *et al*. (2001); and Kinnaird and Nex (2007) against which much of the comparative observations are made. The deposits of this study were investigated at outcrop level (Chapter 3); by thin section and petrography (Chapter 4); major and trace element whole rock geochemistry (Chapter 5); rare earth element whole rock geochemistry (Chapter 6); uranium mineralisation statistics (semi-quantitative electron microscope – Chapter 7); and uranium mineral speciation and compositional analysis (electron microprobe – Chapter 8).

## 9.2 Geological Context

The primary uranium deposits of the Central Zone occur at structural anomalies within the otherwise extensive northeast to southwest striking tectonic fabric of the Damara Orogen. They are usually close to a relatively competent Abbabis Basement inlier or dome structure, although Smith (1965) and more recent findings by Longridge (2012) and Longridge *et al.* (2014) suggest that the basement inliers usually contain a significant component of in-folded Damaran rock in this part of the southern Central Zone. Each deposit is characterised by multiple generations of sheeted leucogranite dykes and extensive $S_1$-parallel sills. The emplacement of the leucogranites are described in terms of temporal, metamorphic, and structural setting in Nex and Kinnaird (1995); Nex (1997); Basson and Greenway (2004); and Kinnaird and Nex (2007) with emphasis on the Goanikontes and Rössing areas, respectively.

The granites of the Central Zone essentially fall into three broad categories given by Marlow (1981) and Brandt (1987); the earlier group are the syn- to post tectonic granites, these tend to be mafic, calc-alkaline granites and coincide with the onset of the collision between the Congo and Kalahari Cratons at *ca.* 560 Ma. The primary members of the early- to syn-tectonic granites include the *ca.* 580 Ma - 560 Ma Goas Intrusive Suite (Lehtonen *et al.*, 1995; Miller, 2008; Milani *et al*., 2014) which are followed by the *ca.* 560 Ma - 540 Ma Salem-type diorite granites and anatectic Red Granites from *ca.* 534 Ma to 530 Ma (Smith, 1965; Jacob, 1974; Sawyer, 1981; Marlow, 1981; Longridge, 2012). The third group are described as late- to post-tectonic granites and primarily constitute the various leucogranite varieties (Marlow, 1981; Brandt, 1985; Oliver, 1994; Nex and Kinnaird, 1995; Jung *et al.*, 2000; McDermott *et al.*, 2000; and Longridge, 2012).

McDermott (1986) simplifies the various granite groups into calc-alkaline (the Goas suite); crustal melt granitoids (the Salem and Red granite suites); and the within-plate granites (the sheeted leucogranites and uraniferous alaskite/leucogranites). Within the leucogranite field, Miller (2008) and Longridge (2012) include the Grey granites, which are relatively abundant in the western part of the southern Central Zone. They are not strictly leucocratic and have variable biotite content, but even the melanocratic varieties are chemically distinct from the Salem suite, and considerably younger, having intruded at *ca.* 520 Ma (age- Longridge 2012, geochemistry- this study- Chapter 5, Longridge, 2012).

The late post-tectonic leucocratic granites intrude between *ca.* 526 and 488 Ma (e. g. Briqueue et al., 1980; Marlow, 1983; McDermott, 1986; Jung *et al*., 2000a). These include voluminous leucocratic sheeted granites that occur in the Southern Zone (Bloedkoppie and Donkerhuk, e.g. Kukla *et al*., 1991) and Central Zone (Oetmoed granite, Jung *et al*., 2000a).

However, many of these are muscovite and garnet-cordierite-tourmaline-bearing rocks, which are not appreciably enriched in uranium. The Stinkbank leucogranites intruded at *ca.* 549 Ma (Johnson *et al*. 2006) well before the peak western Central Zone metamorphic age of c*a.* 510 Ma and *ca.* 510-490 Ma $D_3$ range of Longridge (2012) and Longridge *et al*. (2014); but within range of 540 Ma timing of the cessation of $D_3$ as interpreted by Jacob *et al*. (2000),

Kisters *et al*. (2004) and Miller (2008). Nex (1997) recognised a tectono-metamorphic divide between the weakly mineralised and uraniferous varieties, this divide is of profound importance as the intrusion of the uraniferous leucogranites, *ca.* 508 Ma. to 506 Ma is within one standard deviation of peak metamorphic conditions of the Central Zone between ca. 520 Ma to 510 Ma (Jung *et al*., 2001; Jung *et al.*, 2001; Jung and Mezger, 2003a; 2003b; Goscombe *et al.,* 2003a; Longridge *et al.*, 2011; and Longridge, 2012). The variably foliated uraniferous leucogranites intruded during- and/or after the third major Damaran deformation episode. Petrographic and geochemical contrasts between the weakly-uraniferous and uraniferous leucogranites were recognised by Nex (1997), who also suggests that they are derived from different sources.

The broader study in this thesis shows that the leucogranites of the Central Zone show many comparisons with the Goanikontes leucogranites of Nex (1997) although the larger study area highlights some additional features. The following section discusses the granites at each deposit of this study and places the geochemical discussion that follows into context with the existing descriptions and classifications.

Salem type granites are sampled at the Valencia deposit, and are largely absent at the other deposits of the Central Zone. An extensive megacrystic to porphyritic Salem granite partially outcrops between the Ida Dome and Husab, but is not included in this study as it is not in the vicinity of a major U-deposit. Equigranular-textured Grey granites tend to be the oldest granites at the deposits and occur in at least three successively leucocratic generations at the Ida Dome, Hildenhof, and Goanikontes areas, and at least one variety of Grey granite is present in drill core at the Husab deposit. Nex (1997); Nex *et al*. (2001b); and Longridge (2012) show that the Grey granites and the pegmatitic leucogranites are not genetically related at any of the deposits of this study.

Sheeted leucogranites predominantly invade:

- Abbabis basement orthogneisses;
- Etusis Formation meta-clastic package;
- Gneisses, calcsilicates, skarn, and schistose units of the Khan Formation; and

- in the cyclic carbonate-clastic packages and the intermittent pelitic and semi-pelitic metasediments of the Rössing Formation.

Where the Rössing Formation is thin or absent, the leucogranites also invade the Chuos Formation as at the Hildenhof anomaly, the Goanikontes deposits (Etango in particular) the Valencia deposits, and at the Husab Deposit. Significant uraniferous leucogranite intrusions are rare above the Chuos Formation and are limited to the Z19 deposit of Rio Tinto and Z21 deposit held by Zonghe[52] to the east of the Rössing mine.

There are isolated alaskite intrusions above the Rössing Formation at the Husab deposits, but erosion in the palaeo-environment has removed much of the host rock above the Chuos Formation. At these levels the Karibib marbles formed an impermeable barrier to invading sheets, which reacted with the cyclic carbonate, calcsilicate and pelitic units of the Arandis Formation. It is only at the Valencia deposit and reportedly the Z21 anomaly near Rössing, that syn- to post-orogenic sheeted leucogranites have invaded above the Karibib Formation and emplaced within the Kuiseb Formation schists. All of the deposits in this study host at least two to three distinct varieties of leucogranite that pre-date the uraniferous generation, which compares well with the Nex (1997) model at Goanikontes.

The earliest, A-type sheets are limited in occurrence in this study to the Valencia deposit, and are in equally limited in volume (Chapter 3).

Garnetiferous B-type sheets are abundant at the Valencia and Ida Dome areas and there are at least two generations of the garnet-bearing granite at Valencia. The older foliated generation has clear contact margins, with little evidence of interaction with the metasediments, while the younger generation is very similar in sheet size and geometry to the pegmatitic tourmaline- and magnetite-bearing C-type leucogranites. Both show evidence for the magma having been derived from a distal source. Ward *et al.* (2008) show that many of the peraluminous sheets in the Kuiseb Formation could be the products of

[52] Former Z26 deposit of Rio Tinto, now owned by China National Nuclear Corporation.

localised, lower-temperature, water-present partial melts. Garnet is a peritectic mineral in this environment, having migrated within the host rock via pre-existing structures.

Thus, not all 'B-type' leucogranites, as described in this study, may be the sheeted leucogranites derived from a deeper source. Many of the garnetiferous leucogranite sheets described in this study have large volumes over hundreds of metres in lateral extent and are thus difficult to explain by accumulation of Kuiseb schist-derived partial melt alone. The large volume sheets, proximity to the Basement, and the strongly attenuated succession imply a source from below the Damara succession.

The C-type leucogranite is widespread, and sheets are recognisable by the large size and generally pegmatitic texture. Although the temporal relationship between these leucogranites and the mineralised generation is well-defined at Goanikontes, it is less so at Valencia and the Ida Dome. Crosscutting relationships at the latter are ambiguous in some outcrops, and many locations exhibit small uraniferous pegmatitic patches within otherwise weakly mineralised granites. Figure 9.1a illustrates an example of ambiguity in crosscutting relationships, and Figure 9.1b shows how host rock composition may have had a profound effect on granite composition in certain localities.

This relatively isolated example contrasts with observations in Jacob *et al*. (1986); Nex (1997); Nex *et al*. (2001b), who remarked on the distinctly sharp contacts between the leucogranites and the host rocks, but is not widely observed in the pre-$D_3$ leucogranites. Nex *et al*. (2001) proposed that they intruded prior to peak metamorphism. Relationships at Valencia and the Ida Dome area support pre-$D_2$ intrusion (Figure 3.48 and 3.49, Chapter 3). The timing of intrusion originally prior *ca.* 571 Ma (Nex, 1997 after Kroner *et al*., 1991) is possibly later but prior to the onset of $D_2$ between *ca.* 540-560 Ma (Longridge *et al*., 2009; Longridge, 2012).

The C-type sheets are relatively easily subdivided on the basis of accessory mineral assemblage, texture, and stratigraphic level of intrusion:

Magnetite-bearing, oxidised sheets ($C_m$-type) occur almost exclusively within the Khan Formation and lower Nosib Group lithologies. Contact metamorphism with

these sheets occasionally develops magnetite porphyroblasts in the mafic schists of the Khan Formation, and is occasionally marked by entrainment of mafic host rock phases such as clinopyroxene.

Tourmaline-bearing sheets ($C_t$-type) in contrast, are limited to the pelitic and semi-pelitic units of the Rössing-, Chuos-, and Kuiseb Formations and thus more distal from the perceived lower Nosib or Abbabis basement source. A third variety of pegmatitic C-type lacks any distinguishing accessory assemblage; it may simply represent a slight variation in composition or host rock interaction of the more abundant magnetite and tourmaline varieties.

Accessory-free leucogranites are particularly abundant at Garnet Valley and the Ida Dome area. They are recognisable by the distinct paucity of accessory minerals, other than skeletal and entrained biotite at contact margins. They are observed at all deposits in varying proportions and tend to occur above the Khan Formation intruding the least-reactive units of the Rössing Formation.

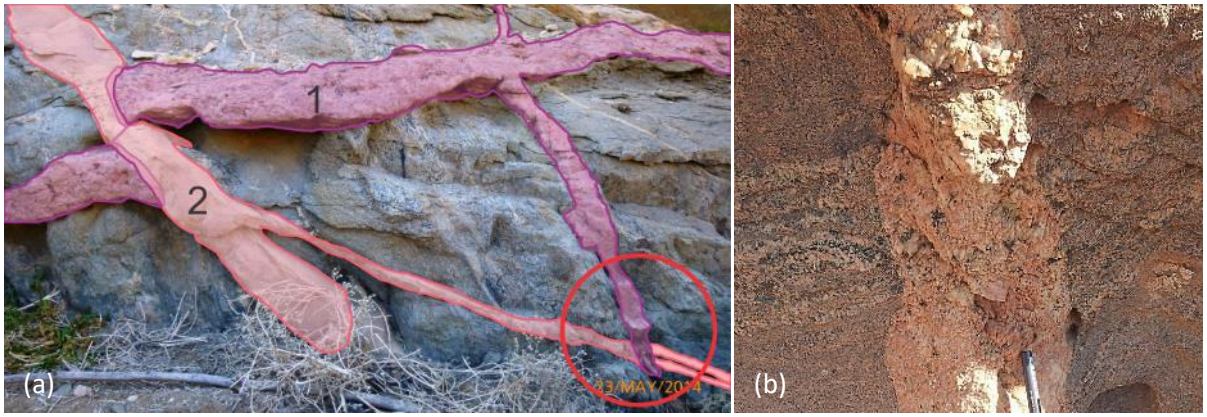



Figure 9.1 Textural and compositional inhomogeneity in the leucogranites. (a) Ambiguous crosscutting relationships between two texturally different sheeted leucogranites at the Ida Dome. 1 is cut by 2 at top left, but 2 is cut by 1 at bottom right. Textural relationships suggest 1 is an F type, and 2 is probably a B or C type. (b) Leucogranites that crosscut compositional banding in the Khan Formation inherit diopside from the host rock.

The uraniferous D type sheets are widespread and show a wide range of textures and sizes. They exhibit clear crosscutting relationships with older sheets at some locations, while at others they may show a prominent foliation, parallel to pre-$D_3$ sheets. The sheets can vary in

size from centimetric stringers to massive dykes hundreds of metres in length to massive amalgamations hundreds of metres across, such as the main deposit at Valencia. Prominent Fe-dominated discoloration tends to occur at contact halos with the reactive metasediments, and may pervade through several metres of leucogranite thicknesses. Although mafic phases are in low abundance, biotite is significantly more altered (sometimes near-complete chloritisation) than biotite in the pre-mineralisation leucogranites; it contains abundant pleochroic halos around zircon and uraninite inclusions, and is very often host to cleavage-parallel fluorite. The uraniferous sheets are also distinguishable from the weakly mineralised varieties by the relative abundances of accessory phosphate minerals, fluorite-bearing biotite, sulphides, and distinctly zoned and metamict, zircon varieties. The magmatic magnetite that defines the Khan-Formation hosted C-types appears to be more abundant in the Goanikontes D- and E-types, while tourmaline and garnet are rare in the mineralised samples from all the primary deposits.

Monazite, apatite, thorite, zircon, and titanite occur as magmatic crystals, often zoned indicating episodic/prolonged growth. Although there are abundant examples of singular crystals of zircon, thorite, and monazite, clusters of these minerals suggest some my be inherited. McKechnie (2012) interprets the clustered accessory minerals as representatives of entrained source components in similar orogenic sheeted leucogranites of the Trans-Hudsonian Orogeny. Five unzoned monazites were analysed by EPMA in this study, and findings show consistent Ce > La ratios, with Nd consistently more enriched than Ce (Nd:Ce in ratios of 1.2 to 1.5). The weak zoning supports a predominantly magmatic origin to the monazite and it is classified as monazite (Nd) on account of the LREE abundance. Ore mineral populations are dominated by uraninite, which is abundant and easily recognised as sub-millimetric magmatic crystals between quartz and feldspar, or as micrometric inclusions in biotite, magnetite, titanite, and zircon.

Leucogranites within the Rössing Formation tend to host sulphides, which in most examples appear to have crystallised late, often surrounding and sometimes replacing primary uraninite. The sulphide populations are dominated by pyrite, but at the Ida Central, Valencia and Husab deposits Cu-sulphides and molybdenite are abundant and associated

with the cupriferous Khan Formation. The contribution of the copper-bearing sediments is not quantified. Molybdenite appears to be the youngest sulphide and may be used as a means to confine uraninite mineralisation ages in the future.

The altered D-tyep SLGs (analogous to the E-type of Nex, 1997) occur throughout the Ida Dome area, in limited distribution at Valencia whilst at Husab, Fe-alteration seems to be limited to contact margins or around entrained host rock xenoliths. The E-type sheets are characterised by prominent Fe-oxide halos. Nex (1997) regarded the haloes as most likely being the result of alteration by residual magmatic fluids rather than a later metasomatic feature as described in Corner (1982). The fact that Nex (1997) concludes that the E-type texture is a result of magmatic alteration, and that clear crosscutting relationships are not apparent at the other deposits in the region suggests that the E-type is a variant of the same generation of magma as the D-type.

Uraniferous granite-pegmatite melts (the D-type), were emplaced into $D_2$ and $D_3$ structures in semi-permeable pelitic gneisses of the Khan Formation and lower Nosib Group, and the lower Swakop Group. The pegmatite-granite melts at the Rössing deposit formed sheeted dykes and $S_1$-parallel sills that coalesced below a relatively impermeable marble cap in the lower Rössing Formation (Jacob, 1974; Berning, 1986; Herd, 1996; Nex *et al*, 2001a and 2001b; Nex *et al.*, 2002; and Kinnaird and Nex, 2007).

Elsewhere in the Central Zone, Nex (1997) describes uraniferous sheets within the Khan and Chuos Formations at Goanikontes, and Marlow (1983) and Tack *et al.* (2002) describe the timing (Rb-Sr and U-Pb, respectively) and emplacement of Khan- and Rössing Formation-hosted alaskites at the eastern flank of the Ida Dome. SHRIMP ages of *ca.* 520 Ma for grey granites that are cross cut by Ida Dome alaskites suggest the *ca.* 540 Ma Rb-Sr and U-Pb ages for the Ida Dome alaskites may be too old. Transposed Rössing Formation marble and pelitic units form an impermeable barrier to the alaskites, and the 'pooling' of sheets against the marble hanging wall is clearly visible along the Swakop River section. Garnet Valley and Ida Central represent clear examples of melt migration from the basement into the upper Khan- and lower Rössing Formations via predominantly cleavage-controlled pathways. This location is perhaps the closest impermeable marble cap analogy to the type locality at

Rössing. Table 9.1 summarises the deposits of this study and includes Rössing as the primary uranium type-locality comparative.

The Husab deposit alaskites are hosted almost entirely within the Rössing Formation pelitic units, between lower- and upper-quartzite-carbonate packages. The assemblage of the packages is highly variable, with the low percentages of true marble perhaps the most consistent feature across the strike length. Some sheets have invaded into the lower portions of the Chuos diamictite and within the upper banded-textured gneiss package of the Khan Formation.

Similarly, at the Valencia deposit the alaskites have transgressed the stratigraphy of the local Damara succession through to the Kuiseb Formation. Uraniferous sheets predominate over other sheets within the Rössing Formation and upper Khan Formation.

At Rössing, Basson and Greenway (2004) noted that the late development of brittle structures facilitated pressure shadows allowing for melt migration into low strain zones to form the present deposit. Reactions primarily driven by REDOX process reduce soluble $U^{6+}$ into $U^{4+}$ and uraninite crystallised from the magma and associated fluids (Cuney, 1980).

The Etango- and associated deposits at Goanikontes are the result of uraniferous granitic melt concentration in $D_2$ and $D_3$ structures. Nex (1997) describes, in detail, the role of brittle-ductile transition structures within a high strain zone along a Damara Sequence-Abbabis basement contact, comparable to certain areas around Rössing. The Holland's Dome deposit occupies a relatively upright $D_3$ box fold, with leucogranite sheet orientations strongly controlled by axial planar cleavage, and northeast-southwest extension in response to the overall southeast to northwest compression direction. Husab alaskites occupy cleavage-parallel structures in a regional scale upright- to northwest-verging anticline. The available drill core information strongly suggests a combination of S1-parallel sheets linked by dykes at a variety of angles to the overall dip and strike of the metasediments. The bulk of mineralisation is within the Rössing Formation, but uranium-bearing sheets also intrude the Khan- and Chuos Formations.

Table 9.1 Central Zone uranium deposit geological characteristics

| Deposit | Stratigraphic Formations | Stratigraphic Location of Mineralised SLG's | Prominent Structures and Emplacement Characteristics | Nex (1997) SLG types | Other Granites |
|---|---|---|---|---|---|
| **Etango** | Etusis, Khan ± Rössing, Chuos | Etusis-Khan and Khan ± Rössing, most mineralised sheets intrude the Khan Formation. | High-strain Zone (Nex, 2007) brittle-ductile transition. Goanikontes lobe of Palmenhorst Dome. | A, B, C, D, E, F | Grey, Red |
| **Hildenhof** | Khan, Rössing, Chuos | Khan-Chuos and Khan-Rössing contacts. | Roughly parallel to bedding and D2 verging fold hinges. Antiform is infolded between lobes of the Palmenhorst Dome. | C, D, E, F | Grey, Red |
| **Husab** | Khan, Rössing, Chuos, (Arandis) Karibib, Kuiseb | Rössing Formation with minor volumes of sheets in the Chuos- and Khan Fms. | Antiform, possibly overturned, verging northwest and adjoins the Welwitschia Syncline of Smith (1965). Hinge Zone of a regional antiform (Husab Anticline). | C, D, E | Grey, Salem Suite, pegmatite |
| **Ida Central** | Khan, Rössing | Upper Khan-Rössing, Rössing marble hanging wall. | Cleavage-controlled, oblique to bedding, coalescence below marble. Steeply dipping Marble and gneiss package on east flank of the Ida Dome structure. | A, B, C, D, E | Grey |
| **Garnet Valley** | Khan, Rössing | Upper Khan-Rössing, duplicated Rössing marble hanging wall. | Cleavage-controlled, oblique to bedding, coalescence below marble. Steeply dipping Marble and gneiss package on east flank of the Ida Dome structure. | B, C, D, E | Grey, pegmatites |
| **Holland's Dome** | Khan, Rössing | Upper Khan-Rössing, prominent skarn influence on mineralisation in the Khan Formation | Upright anticline between Garnet Valley and the Basement to the east. Axial planar, oblique to bedding and occasionally bedding-parallel. Extension in two directions creates space. | C, D, E | Grey, pegmatites |
| **Valencia** | Minor Etusis, Khan, Rössing, Chuos, Karibib, Kuiseb | Upper Khan-Rössing-Chuos-Karibib-Kuiseb, mineralisation prominent at Khan-Rössing transition. | Secondary antiform on a limb of the Khan Syncline– saddle reef type. Narrow folded basement inlier, Localised disharmonic hinges of secondary folds. | A, B, C, D, F | Salem, Grey-diorite, pegmatites |
| **Rössing** | Etusis-Khan-Rössing-Chuos. Kuiseb-Karibib at satellite deposits | Khan-Rössing contact strongly influenced by thick marble units and distinctly zoned either side of biotite-amphibole-garnet schist. | Dome rotation and shearing against southeast of dome (Basson and Greenway, 2004). Etusis-cored Rössing Dome. | C, D, E | Grey |

Although uranium-bearing sheets have invaded the entire local stratigraphy at Valencia, magma emplacement was primarily facilitated by the axial planar cleavage of a local-scale anticline within the northern limb of the regional Khan Syncline. The leucogranites form a saddle-reef linked by cleavage-parallel dykes. Figure 9.2 , as presented in the Chapter 3 discussion section, illustrates the deposits of this study in a schematic style with reference to emplacement in a stratigraphic location. Although uranium-bearing sheets have invaded the entire local stratigraphy At Valencia, magma emplacement was primarily facilitated by the axial planar cleavage of a local-scale anticline within the northern limb of the regional Khan Syncline. The leucogranites form a saddle-reef linked by cleavage-parallel dykes.

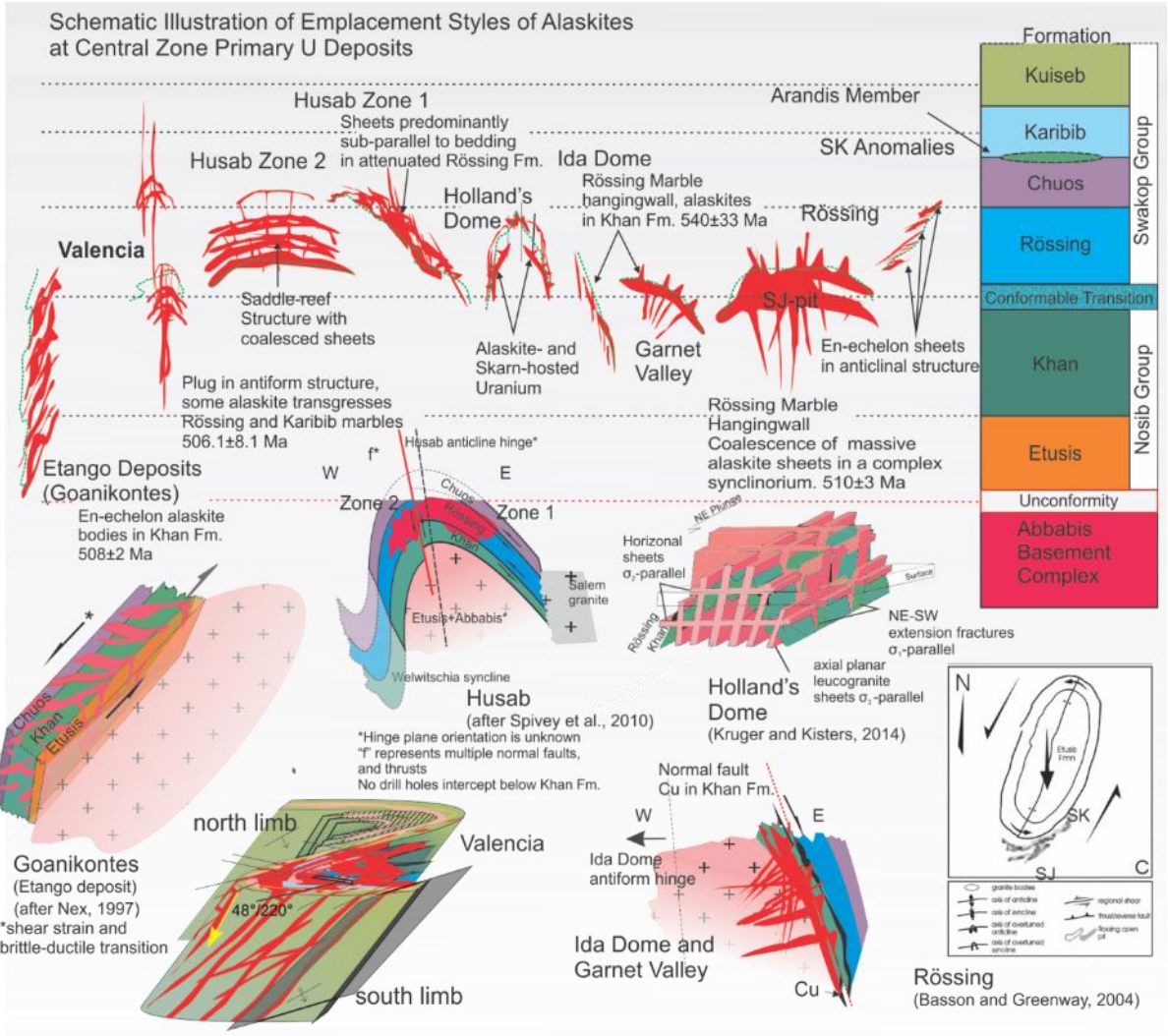



Figure 9.2 Schematic diagram of the Central Zone deposits within the context of the Damara stratigraphic succession. Tectonic processes have prepared certain sites within the Central Zone where relatively ductile sediments occur at an unconformable contact with relatively competent basement rocks. Local-scale rheological contrasts produce pressure shadows within shears, primary- and secondary folds, and associated extensional features, into which regionally significant volumes of leucogranite have invaded, in a more or less passive fashion. Interaction between U-bearing granite contact margins and reactive, predominantly reduced, metasedimentary rocks has played the most crucial role in deposit formation. The interaction zone between the granites and sediments is essentially a REDOX boundary, promoting $U^{6+}$ reduction to insoluble $U^{4+}$ and resultant uraninite precipitation. The cyclic carbonate sequences at most deposits have provided a physical barrier to retain a granite mass within focussed areas, leading to an increased tonnage of uranium ore.

The Holland's Dome deposit occupies a relatively upright $D_3$ box fold, with leucogranite sheet orientations strongly controlled by axial planar cleavage, and northeast-southwest extension in response to the overall southeast to northwest compression direction. Husab alaskites occupy cleavage-parallel structures in a regional scale upright- to northwest-

verging anticline. The available drill core information strongly suggests a combination of S1-parallel sheets linked by dykes at a variety of angles to the overall dip and strike of the metasediments. The bulk of mineralisation is within the Rössing Formation, but uranium-bearing sheets also intrude the Khan- and Chuos Formations.

## 9.3 Discussion of Petrographic, Geochemical and Rare Earth Element Findings

The Salem type diorite and monzogranite at Valencia host amphibole and abundant biotite, indicating melt temperatures below biotite and amphibole dehydration. The biotite-bearing equigranular and porphyritic textured Grey and megacrystic Salem granites plot with variable An-Ab proportions and on Or-An-Ab plots the earliest generations plot in the tonalite field, while successive generations systematically tend toward the Or apex in the granite field with increased K content. Normative Q-Ab-Or plots support a sub-700 °C, partial melt generation of the leucocratic Grey granite varieties, which is within the realm of metamorphic conditions at the time of emplacement (Jung *et al*, 2001, Jung and Metzger, 2003a; Longridge, 2012; and Longridge *et al*., 2014).

The early A-type leucogranites, that are discontinuous and sinuous, are probably generated from localised partial melts. The discontinuity of the sheets and relatively small volumes do not support melt migration over the same distances interpreted for the more voluminous C- and D-type sheets that predominate at the deposits.

The garnet-bearing B-type leucogranites host Fe in almandine garnet and are thus derived from melt regimes with REDOX conditions quite distinct from the magnetite-bearing $C_m$-type and Fe-sulphide-bearing D-type leucogranites. Additionally, the garnetiferous leucogranites at Valencia occur in two distinctive groups, an older foliated variety and a younger pegmatitic generation, the latter being the more abundant and voluminous in outcrop. Figure 9.3 illustrates the two granites. The compositions of almandine examples from Goanikontes are given in Nex (1997) and shown to be distinctly different to the garnet in the

host schist. Nex (1997) also shows that based on the spessartine component differentiating between a deep or shallow crustal source is equivocal at Goanikontes. Ward *et al.* (2008) describe the formation of extensive garnetiferous sheeted granites as being the product of water-present biotite breakdown of the Kuiseb Formation. The latter study concluded that it is possible to form garnet-bearing melt, with a spessartine component, within relatively shallow crust and that the large volumes of melt may be facilitated by ladder structures of melt migration through the existing brittle deformation fracture network.

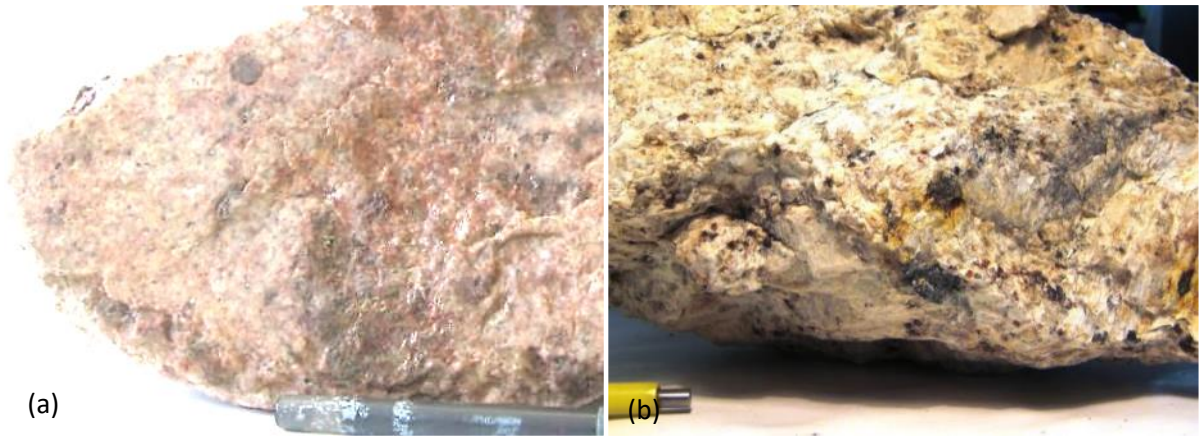



Figure 9.3 Textural varieties of garnetiferous leucogranite. It is not absolutely certain if the two varieties represent the same anatectic melts of the Kuiseb schist described by Ward *et al.* (2008) but the two types (foliated, left, and pegmatitic, right) have distinctive temporal-, petrographic-, and consistent geochemical contrasts.

The garnet-bearing granites in this study plot in two geochemically distinct groups: older foliated garnet-bearing granites plot on the potassic side of the P-Q discrimination plot, while garnets from the more extensive younger pegmatitic sheets, plot on the plagioclase side of the diagram because of the greater Na content and low K content (Chapter 4). The two textural varieties clearly intruded on either side of a major deformation event, the older foliated variety is pervasively altered, while the pegmatitic type, sampled at the same location is largely unaltered (Figure 9.3). The pegmatitic variety has 2.56 wt.% $K_2O$ and 5.03 wt.% $Na_2O$ + CaO, compared to 5.62 wt.% $K_2O$ and 3.65 wt.% $Na_2O$ + CaO of the foliated type. The foliated type may be derived from a similar upper Swakop Group protolith but

were deformed and probably formed under different conditions. Given the P-T-t history given in Longridge (2012) the foliated type would have formed at lower temperatures, but conclusive evidence in this regard is not available. REE profiles show that the late, pegmatitic variety is LREE and HREE depleted relative to the foliated type, but display a strongly -ve Eu anomaly, the Eu profile suggests they are not comparable to the uniformly REE-depleted Cm-type.

The $C_m$ leucogranites contain accessory magnetite and very little if any biotite, apart from schlieren and partially consumed xenoliths. These sheets represent highly oxidised melts and occur almost exclusively within the Khan Formation, almost directly below the mineralised sheets (Chapter 3). These granites do not represent potentially uraniferous sheeted leucogranites that did not happen to invade the 'right' kind of metasediment, and U content tends to be close to XRF detection limits. Although the magnetite granites occur in proximity to D-types, crosscutting relationships tend to be common, empirical evidence shows the older $C_m$ sheets to contain far less abundant accessory minerals, limited biotite, predominantly milky quartz and an overall K-feldspar over quartz-dominated composition. All of which contrast with the uraniferous sheets quite distinctly. Microscopic textures show that the Cm-type is relatively free of the pervasive magmatic fluids that are responsible for the extensive sub-solidus alteration of the D-types. They are therefore derived from sources suited to dry magma.

Whole rock, major element compositions may overlap considerably between the two types, but high field strength- and rare earth element abundances distinguish the two types quite distinctly. The uraniferous sheeted leucogranites exhibit the greatest variety in textural variation and in petrographic analysis; plagioclase feldspar tends to be more oligoclase than albite, sub solidus alteration features may be pervasive, and characterised by locally intensive development of sericite after plagioclase, new fine-grained K-feldspar, predominance of tartan-twinned microcline, and intensely chloritised biotite. The greatest variation in accessory mineral species occurs in the mineralised leucogranites, fluorite is particularly abundant at some deposits and the major Fe-repositories after biotite are pyrite,

pyrrhotite, and chalcopyrite. They are always anomalous in U content relative to other granites, except where intensive alteration has leached the metal along with other silicates. Typically, their varied appearance is the result of alteration and/or deformation during and after crystallisation. Mafic mineral distributions appear to be limited to schlieren and skeletal biotite laths at contact margins suggest a restite component, but there is evidence of magmatic biotite to a lesser degree, in thin section.

Tourmaline and magnetite-bearing sheets are both considered as pre-$D_3$ generations and the temporal relationship between these two sheets is inconsistent from deposit to deposit. Their distribution is however, fairly consistent relative to each other; the magnetite-bearing sheets overwhelmingly in the Khan Formation and the tourmaline-bearing variety almost exclusively invade the lower and upper Swakop Group metapelites. This spatial separation may be a function of the distance from the perceived source, the Abbabis basement; the magnetite-bearing sheets fit the description of the basement-derived, Khan Formation-hosted granites of Jung *et al.* (2003b); while the tourmaline-bearing sheets may be the result of fractionation of light elements by melt migration, particularly light elements such as boron. This concept is explored as a mechanism for explaining certain chemical trends in granitic magmas in Clemens and Stevens (2012) and may have application in further explaining the nature and origin of these granites. What role the metasedimentary rocks have played is not well-constrained, as wall rock interaction and contact aureoles around these leucogranite at most localities are rather limited, at least with respect to the type of interaction that characterises many of the D-types.

Trace and rare earth geochemistry analyses from this study reveal a few key differences between the pre-$D_3$ and the uraniferous syn- to post-$D_3$ leucogranites, most notably the abundances of incompatible elements and rare metals. Table 9.2 highlights some of these differences. Major elements show some difference, particularly in Na and K abundance, Si is comparable between the two populations of pre-$D_3$ and the uraniferous varieties.

The high Rb content suggests that the $C_m$ is more differentiated than the D-type and should therefore contain uranium, but they are in fact relatively depleted in incompatible elements (Figure 5.33a, Chapter 5).

Table 9.2 Major and trace element abundances in the pre-D3 and the uraniferous leucogranites. All trace element averages are in ppm. Major elements are comparable, but on average high-field strength, REE, and incompatible elements are enriched in the post-$D_3$ alaskites.

| SLG | Ce | Nb | Rb | Sc | Ta | Th | U | Y | Yb | Zr |
|---|---|---|---|---|---|---|---|---|---|---|
| D type | **120.62** | **30.93** | 195.80 | **4.95** | **2.37** | **159.32** | **658.73** | **49.02** | **5.51** | **218.60** |
| pre-D3 | 13.52 | 14.29 | **292.98** | 4.2 | 1.50 | 10.20 | 8.72 | 13.01 | 2.38 | 102.82 |
| | **%$SiO_2$** | **%$Na_2O$** | **%$K_2O$** | | | | | | | |
| D type | **75.33** | 2.68 | 5.36 | | | | | | | |
| pre-D3 | 73.10 | **3.27** | **6.04** | | | | | | | |

There are a number of observations that support a change in source rock composition, particularly the negligible U content of the C-type leucogranites. Although it is not possible to differentiate the melt-generating conditions between C and D type leucogranites, the relative age difference suggests that the D-types are closer to being coincident with peak metamorphism. The skeletal biotite and the high-enriched incompatible element content of some leucogranites support a partial melt model of mixed sources, with melt generation close to, but below biotite dehydration temperatures of ~760 °C and well-below biotite melting of 800 ˚C to 850 ˚C (Vielzeuf and Montel, 1994; Stevens *et al.*, 1997).

### *Conclusions on Sheeted Leucogranite Classification*

The preceding discussion of petrographic and field relationships lends itself to the following conclusions regarding the pre-$D_3$ sheeted leucogranites; the A-type sheets are limited in extent and volume and could not have migrated far from source, the B-type sheets may be derived from distal sources, but geochemical composition, accessory assemblage, and the limited occurrences within garnet-cordierite metapelites of the Rössing and Kuiseb Formations implies a predominantly Damaran metasedimentary source, as described in Ward *et al*. (2008) and Longridge (2012) and this study. The voluminous accessory-free and tourmaline-bearing sheets have a closer affinity to the large-volume garnet-bearing

pegmatites than to the magnetite-bearing Cm-type, but are geochemically distinct being considerably less peraluminous. The Cm-type sheets of this study are only observed within Khan Formation gneiss, and are always within proximity to Abbabis basement inliers/domes. Vielzeuf and Montel, (1994) have shown that small amounts of biotite remain stable between 900 °C - 950 °C at 6 kbar to 8 kbar in the presence of quartz, this is important when considering the conditions required to liberate U and Th from minerals such as zircon and monazite in the source rocks. Also, quartz will be present in a crustal source, but not necessarily in a mantle-derived source rock. The fact the biotite is present in the alaskites, as skeletal entrained blades, may not discount melting of a source rock at higher temperatures, if the source rock is composed of quartz-bearing lithologies, i.e. the gneissic lower crust. It must also be reiterated that the conditions of melting at the source of the sheeted leucogranites do not necessarily have to be the same.

This study presents the first systematic assessment in the southwestern Central Zone of pre- and post-$D_3$ leucogranite rare earth element abundances. The sampled area spans the triangular region between the northernmost deposit at Valencia and the western- and easternmost deposits at Goanikontes and the Ida Dome, respectively.

The following section aims to present and discuss the results of the district-wide REE analyses of the leucogranites at the four major deposits of this study; and expands from some of the field-based, petrologic and geochemical observation points of the previous section. Comparisons to existing whole-rock REE analyses include Salem-type, Red Granite, post-tectonic leucogranite and sheeted leucogranite data, the bulk of which are from McDermott *et al*., (1989); McDermott *et al*. (1996); and Longridge (2012). Igneous rock REE chemistry is invariably a reflection of the source rock and the clear contrasts in REE abundances and heavy and light REE ratios between the pre- and post-D3 leucogranites is an immediate indicator of differing source rock provenance (Figure 9.4, and Figure 6.3, Chapter 6).

The early or syn-tectonic Salem and Red granites tend to have strong LREE fractionation and all samples show a pronounced –ve Eu anomaly in the historical data. The Salem type

diorite sampled at Valencia in this study compares with a near match in most REE abundances and LREE fractionation to the available data for comparable early-generation, calc-alkaline rocks elsewhere in the Central Zone. The Grey granite samples, which include melanocratic and leucocratic variants of the homogeneously fine-grained, foliated biotite granites at the Ida Dome and Hildenhof display uniformly, depleted REE trends with very little light- and heavy rare earth differentiation. Their occurrence mainly within the Nosib Group is consistent at these deposits. The most obvious contrast between the Cm- and D-type are in the several-orders of magnitude differences in LREE and HREE abundances (Figure 6.2 and 6.3, Chapter 6; and Figure 9.4).

The garnetiferous leucogranites, as described in Chapter 4, Chapter 5 and Chapter 6, appear to be relatively unique among the sheeted leucogranite types. The REE plots of these granites show the strongest relative depletion in LREE and pronounced HREE enrichment, relative to the LREE. The relative HREE enrichment is easily explained by the abundance of garnet porphyroblasts, and the overall REE depletion is in agreement with observations made in Jung *et al.* (1995) and thus the interpretation of leucosomes derived from anatectic melting of the Kuiseb Formation near the Valencia deposit. These granitoids typically show low degrees of REE fractionation.

The C-type and $C_m$-type leucogranites have comparably flat, uniformly depleted REE curves, occur primarily within the Nosib and lower Swakop Groups, and as suggested in Longridge (2012) may be related in some way to the foliated Grey granites. Samples of the Grey- and C-types display little if any -ve Eu. Longridge (2012) records slight LREE enrichment and small to large –ve Eu in the Grey granites, with one sample reporting no Eu anomaly. The paucity of accessory minerals apart from magnetite (Chapter 4) is reflected in strongly depleted REE profiles, relative to the rest of the Central Zone sheeted leucogranite suite (Chapter 6).

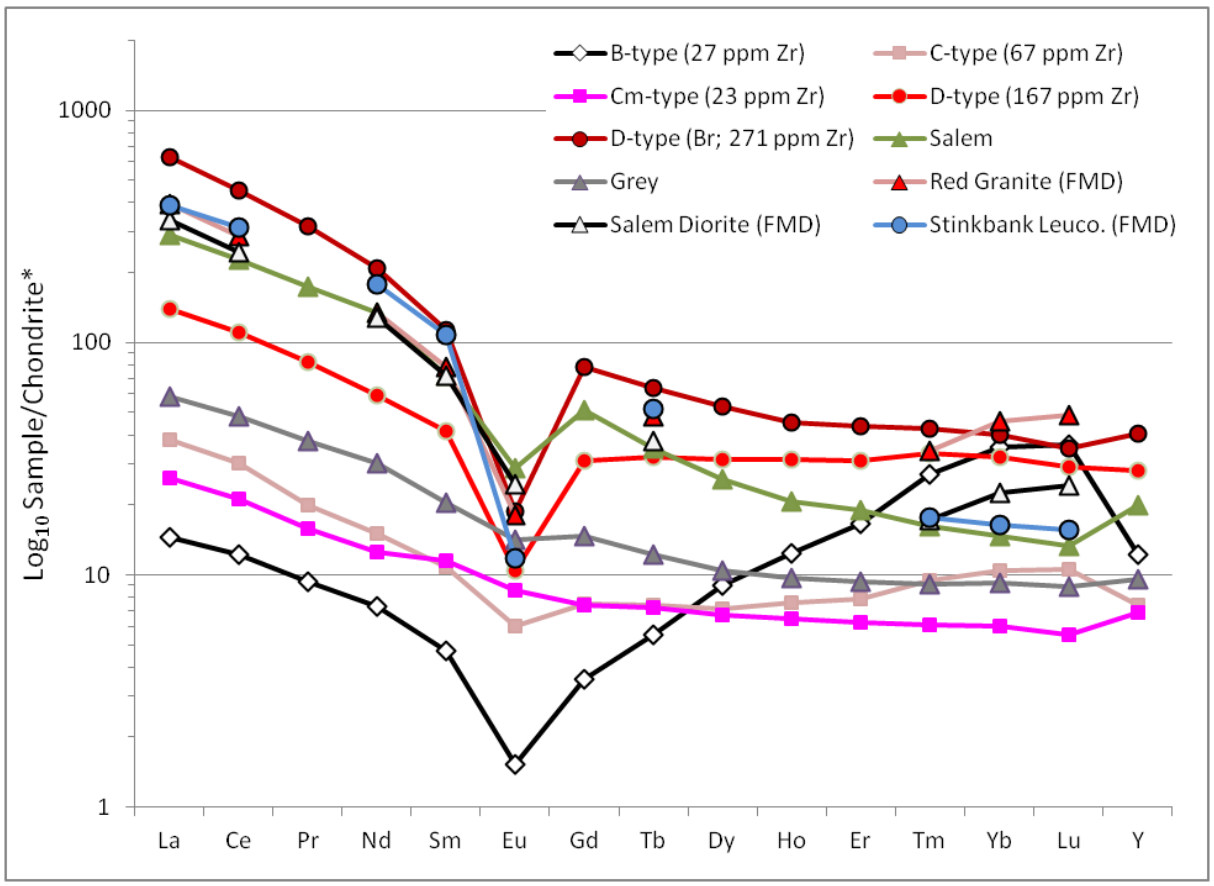



Figure 9.4 Average REE abundances of selected Central and Southern Zone granite groups. The pre-$D_3$, B- and C-type samples have contrasting HREE enrichment; where the C-type is weakly depleted and the B-type is strongly enriched. The post-$D_3$ leucogranites have been split into two varieties; one with uraninite dominated mineralisation, and the other brannerite-dominated (D-type, Br). HREE and LREE fractionation are comparable, as is the -ve Eu anomaly, but the overall REE abundance is consistently enriched in the brannerite-bearing type. Samples with (FMD) are sourced from McDermott *et al.* (1989) and McDermott *et al.* (1996). All data normalised to McDonough and Sun (1995).

McKechnie (2012); Mercadier *et al*. (2010); Cross *et al*. (2009); and Förster (1999) show that granite hosted uraninite may host up to 10 wt.% total REE. None of the uraninite analyses in this study detected REE + Y above 3 wt.%, despite acceptable analysis totals and checking prior to analysing a group of uraninite a WDS scan was performed to check which elements were present in a specimen. It appears that REE abundances in the Central Zone uraninite are low, but a more focussed study may reveal deposit-specific trends, considering the high REE content of the uranium-bearing granites and the findings of Mercadier *et al*. (2011). The low REE abundances of the pre-$D_3$ sheeted leucogranites and the grey granites correspond with the low HFS element abundances of these granites (Chapter 5 and previous section). The geochemical and REE trends place them in the crustal granite category of McDermott *et*

*al.* (1986) and are classified in this study as moderately fractionated. The relatively weak LREE fractionation of these granites suggests that the magma did not undergo significant fractionation, and is inferred not to have migrated a great distance from source, at least relative to the Salem type and uraniferous leucogranites.

The B-type leucogranites that are exclusively sampled from locations within the Kuiseb Formation fit the descriptions of the anatectic melts described in Ward *et al.* (2008) and Longridge *et al*. (2009). A single tourmaline-bearing leucogranite was analysed and shows HREE enrichment, with a typical wing-shaped REE pattern nearly identical in shape and overall REE abundance to the B-type sheets. These abundances and REE patterns place these granites within the anatectic leucosomes derived from Damara metasediments described in Jung *et al.* (1995). The fractional process of melt migration and the composition of the Kuiseb Formation are interpreted as the main influences on concentrating boron thus tourmaline formation in the particular C-type leucogranite. Garnet in both the $C_t$ type and in the B-type has preferentially enriched the HREE fraction. Overall low abundances are typical of such migmatised and associated melts (Jung *et al.*, 1995; Jung *et al.*, 1998; and Ward *et al.*, 2008).

Three general models are proposed for the source rock of the uraniferous leucogranites; Jacob *et al*. (1986) propose melting of the Abbabis basement, McDermott *et al*. (1996) suggest that basal Damaran metasediments have partially melted, and McDermott *et al*. (2000) propose melting of Damaran calc-alkaline intrusives. The third model would derive a granite with an A type affinity, but requires preparation of the lower crust by fenitisation, as outlined in Martin (2006). The first and second models are equally plausible from a geochemical perspective, as McDermott *et al*. (1996) show that the basal Damara rocks are derived from basement erosion, and thus partial melts from the two sources are indistinguishable. Certain limitations exist and include the large volumes of sheeted leucogranite crosscutting basement and basal Damaran rocks at Goanikontes (Nex, 1997); at the Ida Dome (Smith, 1965; Barnes, 1981; Longridge, 2012, this study –Figure 3.23, Chapter 3): and in the Khan River gorge near Valencia and Husab (this study – Figure 2.3, Chapter 2). Trace element abundances tend to be a robust means of geochemical comparison between

similar rock types and the following section includes A type granites and the sheeted leucogranites to compare the temporally similar suites.

The first scenario is most likely, as the $D_3$ period is shown to be of profound significance in the tectono-thermal evolution of the southern Central Zone, and in particular for preceding or being coincident with of large volumes of uranium-bearing melt. The second scenario is less likely; if the perception that the same material is simply subject to increased metamorphic conditions the first melts would leave behind a dehydrated residual which would not be as susceptible to partial melt by incongruent biotite breakdown. However, if a new source material gains access to the crust, and suitable conditions such as the granulite facies metamorphism and decompression facilitated by existing brittle-ductile structures, under higher grade metamorphic conditions, species such as garnet, apatite, monazite, xenotime, and zircon may play less of a role as residual minerals.

The latter interpretation may be supported by inferring that granulite facies conditions at peak metamorphic conditions were suitable for garnet, monazite, and zircon equilibrium with the silicate melt, while prior to this the P-T conditions did not allow the melt to sequester REE from monazite, garnet, and zircon. And, that the temporal spacing between uraniferous and non-uraniferous leucogranites is too close to expect a drastic change in source rock composition, without the advent of a significant tectonic/structural regime change, such that $D_3$ would have to account for a new magma source having access to shallower crust to emplace REE-enriched D-type leucogranites. The role of composition on the solubility of REE is potentially important, as the D-type granites clearly contain more $F^-$ than the pre-$D_3$ granites, the availability of F in the melt and associated fluids allows for transport of zircon (Rubin *et al.* 1989); $F^-$ also complexes with REE and with Ti (Barsukava *et al*, 1979; and Ayers and Eggler, 1991)

The model of partial melting of a mixed metasedimentary and igneous assemblage, with melt transport via pre-existing structural pathways, as the primary source of uraniferous and associated sheeted leucogranites is supported by, among others: Jacob *et al.* (1986); Cuney (1980); Berning (1986); Nex (1997); Jung and Hellebrand (2006); and Cuney and Kaiser

(2008). Most authors give petrographic observation and petrological interpretation, and geochronology; citing evidence such as skeletal biotite, muscovite, entrained mafic minerals, zircon ages, geochemical trends, and accessory assemblages in support of this model. This model essentially supposes the partial melting of an orthogneiss (e.g. the Abbabis basement) where plagioclase retains Eu. However, the consistently pronounced -ve Eu in the uraniferous samples of this study is somewhat contradictory, it implies divalent Eu, while U is most likely in the oxidised state given the concentration in the D-type. The magnetite-bearing leucogranites are strongly oxidised and the lack of -ve Eu anomaly in these granites, at all deposits, implies an oxidised source where trivalent Eu was not retained to the same degree in plagioclase. The similarities between the uraniferous leucogranites, the Salem granites (this study) and the A type granite suites of the Central Zone that exist in REE content, discriminating REE ratios, and the pronounced -ve Eu anomaly suggest some relationship between these suites. They are temporally diverse *ca.* 540-560 Ma for the Salem and other calc-alkaline granites, 508 - 506 Ma for the uraniferous leucogranites, and ~495 ± 15 Ma for the Sorris-Sorris A type granite (Hawkesworth *et al*., 1983). The rare-earth patterns, ratios and trends of the Salem granites and the A type granites are comparable to the uraniferous alaskites, across a range of discrimination diagrams (this Chapter).

## 9.4 Classification of The Central Zone Sheeted Leucogranites

*The following section will discuss the leucogranites in terms of the broader Central Zone and tectonic setting, where the alphabet-type classification becomes relevant; in order to avoid ambiguities, the hyphenated 'A-type' refers to the early-generation sheeted leucogranite of Nex (1997) Nex et al. (2001b) and the un-hyphenated 'A type' refers to the anorogenic type granite of the alphabetised classification.*

The granites are most likely transitional, as in post-orogenic, however, they intrude during $D_3$ at the Ida Dome, and may thus by derived from anatexis of the lower crust, rather than simple decompression melting. The following discussion will show that certain trace and

major element discriminators of the sheeted leucogranites are comparable with confirmed A type granitoids of the Damara Orogen, but invariably an I type classification best suits the uraniferous sheets, while the pre-D3 sheets show mixed I type and S type affinity on the typical discrimination diagrams.

Various attempts have been made to pigeon-hole the sheeted leucogranites of the Central Zone into various granite classification schemes. Independent of alphabet-type classification, Cuney and Kyser (2008) describe the uraniferous sheeted leucogranites in terms of three groups; a plagioclase-rich group, a granitic group with near eutectic composition, and a K-feldspar-rich group. One of the major discussion points regarding the sheeted leucogranites is the so-called alphabet classification of the sheeted leucogranites, whether they are I-, S-, or A-type remains uncertain. McDermott *et al*. (2000) suggest the leucogranites are derived from Damaran calc-alkaline rocks and are analogous to anorogenic granites of the Central Zone; Nex (1997) in a comprehensive assessment of the sheeted leucogranites showed, through petrographic and geochemical study, that the sheeted leucogranites are not all the same, and that some pre-$D_3$ verities are simply S types, being derived from the Damaran metasediments; while Nex (1997) and Nex *et al*. (2001b) caution that the uraniferous varieties bear similarity to HFS element-rich, anorogenic granitoids, but are also compositionally indistinguishable from I type uraniferous leucogranites of the ~1.1 Ga Namaqua Metamorphic Complex.

The uraniferous alaskites, or D-types, are somewhat less obvious; Nex (1997) and Nex *et al*. (2001) show that the post-$D_3$ leucogranites have low Ga/Al ratios and Y/Nb abundances more akin to syn-collisional granites, thus limiting an A type granite classification as defined by Eby (1992). Nex (1997) and Nex *et al*. (2001) regard the sheeted leucogranites as crustal-derived, as was established for a number of other Damaran granite suites by isotope analyses (Hawkesworth *et al*., 1986; McDermott, 1986; McDermott *et al*., 1996). In addition to the igneous, sedimentary and anorogenic granite classifications, the magnetite and ilmenite classifications of Ishihara (1977) are particularly relevant because the contrast between Khan Formation-hosted leucogranites, and the uraniferous sheets is particularly

stark, despite the close spatial relationship. The Khan Formation leucogranites are magnetite-bearing, clearly akin to the magnetite-series, too-oxidised to crystallise garnet, and thus host low concentrations of REE. Immediately adjacent (and crosscutting) to these granites the uraniferous sheets host Fe in sulphides, and are thus reduced and more akin to the ilmenite-series. They do not host garnet but, empirically, host the greatest abundances of zircon and phosphates (apatite, monazite, xenotime). The absence of abundant magnetite may suggest an ilmenite-series affinity. This study will attempt to place the uraniferous granites into the correct magnetite - ilmenite series context.

In this thesis, deposit-specific populations of uraniferous leucogranites may be characterised petrographically, where one or more of the rock-forming assemblage-; accessory assemblage-; dominant alteration feature(s)-; or secondary mineral texture(s) may define the individual deposits. In this regard, the simplified classification of Cuney and Kyser (2008) is applicable.

The Hildenhof and Goanikontes alaskites are K-feldspar-rich, magnetite-ilmenite bearing and tend to plot with a tight grouping and systematic clustering on most geochemical diagrams. The Ida Dome alaskites tend to be oligoclase dominated, thus of a plagioclase-rich grouping, which is reflected in normative geochemical diagrams, especially those with Ca as a discriminator. The Husab granites appear to be K-feldspar dominant, with a comparatively high fluorite content and abundant secondary sulphides, they also show geochemical variation comparable to the Ida Dome alaskites; The Valencia samples are K-feldspar-dominated, contain comparatively low abundances of accessory phases, though they are the only alaskites in which allanite was observed (Figure 4.47, Chapter 4). The Ida Dome area is the only example in this study, outside of Rössing, where duplicated Rössing Formation marbles have formed a continuous and impermeable barrier to the intrusives. Almost all of the alaskites show evidence of sub solidusreactions, with many Goanikontes, Husab, and Valencia alaskites plotting near typical granite eutectics (Or-Q-Ab plots, Figure 5.7b, Chapter 5) but very few Ida Dome samples do. The interpretation of this study is that most if not all of the uraniferous leucogranites are typical alkali-feldspar granites, with a small percentage

spanning the compositional range from tonalite through monzo- and syenogranite as shown by Briqueu *et al*. (1980); Marlow (1981); Nex (1997); Nex *et al*. (2001). Most of the exceptions are samples from the Ida Dome where reactive country rock is considerably more abundant, and from Husab, where the alaskites display considerably more secondary minerals such as crosscutting sulphide and fluorite veining.

The broad geochemical scope of this study primarily compares the geochemistry of over 270 sheeted leucogranites and pre- and post-$D_2$ granitoids. One of the more comprehensive, recent assessments of A type granites of the Damara Orogen are those of McDermott *et al*. (2000), who include the data for the Swakopmund Salem Granite with '*unequivocally A type*' Horebis-river, Sorris-Sorris, and Dachsberg granites. McDermott *et al*. (2000) assert that the A-type granites of the Central Zone exhibit typical HFS element enrichment and high $FeO_{tot}/(FeO_{tot} + MgO)$ and high $TiO_2/MgO$ ratios, but low CaO and $Al_2O_3$. The high field strength element abundances and timing of emplacement are considered strong evidence but the interpreters caution that zircon abundance may be a result of Zr solubility enhanced by abundant fluorine, still these are all typical features of anorogenic- or A type granites. This is an important consideration as the sheeted leucogranites have highly variable Zr and abundant, biotite-associated fluorite.

The generation of anorogenic, or A type granites often involves a complex history which includes fenitisation of the lower crust to produce suitable melt precursors for the distinctive enrichment patterns of these intrusives and extrusives (after Martin and De Vito, 2005 and Martin, 2006). There is no constraint on the source(s) but they may also require some mantle-derived influence. The sheeted leucogranites exhibit S- and I type granite features, as well as low Ga/Al which is typically high in A type granites. However, there is merit in assessing whether the sheeted leucogranites, particularly the alaskites are A type granites; Ercit (2005a and 2005b) for example, has concluded that A type granites need not necessarily be plutons, but may also derive from pegmatite-forming magma, if anatexis of a suitable, metamorphosed source rock takes place in the deep crust. In this regard, the granulite-facies Central Zone may have achieved higher-grades of metamorphism below the

currently-exposed crust. The exotic nature of the uraniferous sheets, being emplaced at *ca.* 508 to 496 Ma in mid-crustal rocks that were exhumed between 530 Ma and 510 Ma during north Central Zone $D_2$ deformation, high field strength element abundances and K/Mg ratios (Figure 5.41, Chapter 5) also suggest A-type affinity. Whether the sheeted leucogranites are true A type granites or not, they are post collisional and the uraniferous sheets are definitely anorogenic in the temporal and structural sense, thus classification based on feldspar composition and texture is appropriate. It is only in the uraniferous sheets, that pervasive, late magmatic fluids have altered the rock-forming minerals. In many examples the uraniferous sheets may be seen as two-feldspar granites as some samples are dominated by albite-oligoclase rather than orthoclase or microcline. Perthitic exsolution, abundant sulphides and albite rims surrounding older feldspars potentially support a hypersolvus classification. In addition, the intrusion of the granites into low-pressure zones may also support the same. The emplacement is at mid-crustal levels and the melts likely have been derived from below their emplacement position (Longridge, 2012; Jung *et al*., 2000; McDermott *et al*., 2000; Nex, 1997; Oliver, 1994). Overwhelmingly, petrographic observations show distinct K-feldspar and albite-oligoclase crystals, with relatively few perthite textures normally associated with hypersolvus granites. The exsolution textures may also be a product of the emplacement of lower-crust derived magma that is emplaced into zones of localised lower pressure, such as at the nose of the rotated Rössing Dome (Basson and Greenway, 2004) or in the high strain zone at Goanikontes (Nex, 1997).

Addition of geochemical data of the Horebis-river, Sorris-Sorris and Dachsberg Granites, and certain Swakopmund Salem Granites allows for classification of the leucogranites of this study with respect to their post orogenic emplacement setting and type - classification. The element ratios and discrimination fields of Whalen *et al.* (1987) provide the type-classification (Figure 5.40 and Figure 5.42) and Pearce *et al*. (1984) determine the tectonic setting (Figure 5.43a and 5.43b). The diagrams successfully show that the pre-and post-$D_3$ leucogranites are geochemically distinct, and are also distinguishable from the A type granitoids from Horebis-river, Sorris-Sorris, and Dachsberg. The high field strength element abundances suggest that some of the uraniferous leucogranites and the Valencia Salem

granites are directly comparable with A type granites of the Central Zone if HFS elements are compared alone. Fe/Mg ratios seem to suggest lower degrees of fractionation and stronger I- or S type affinity than the largely A type classification of the Sorris-Sorris, Horebis River and Dachsberg group (labelled CZ A type / Anorogenic types, Figure 9.5).

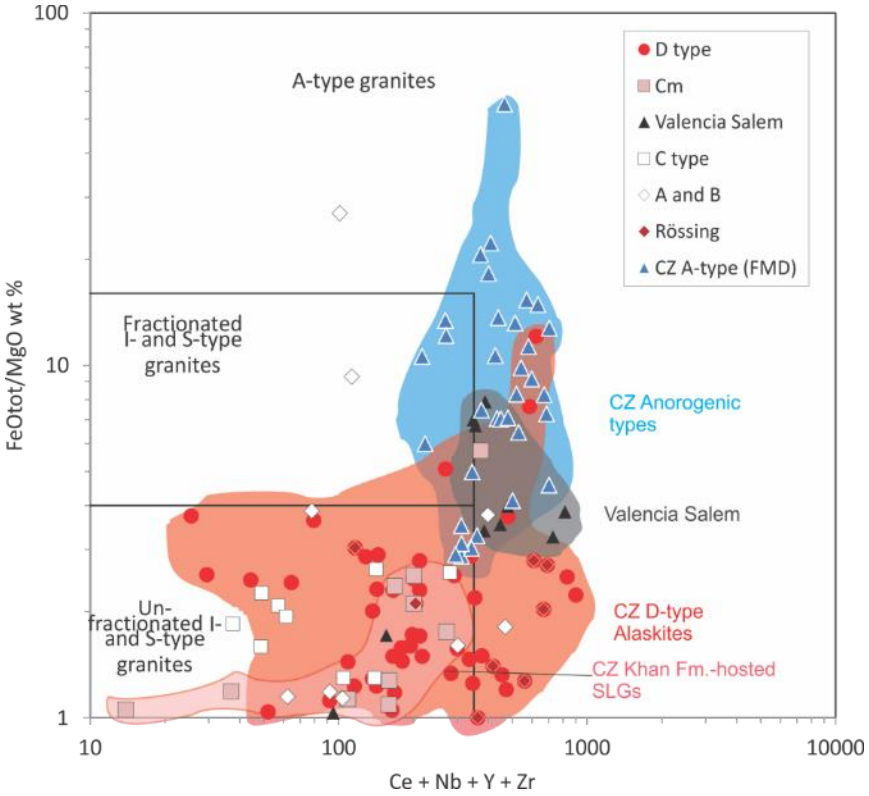



Figure 9.5 HFS elements vs. FeOtot/MgO wt.% granite- discrimination plot. The Valencia Salem granites, the A- and B-type SLG's, the C- and $C_m$-type leucogranites and the D-types are compared to the anorogenic granite suites of the Central Zone (CZ A-type, FMD). The bulk of the pre-$D_3$ sheeted leucogranites plot within the un-fractionated field, while the uraniferous sheets and the Valencia Salem diorites tend to plot outside because of HFS element abundance. CZ A-type (FMD) data from McDermott *et al*. (2000).

Ga data are not available for the anorogenic Sorris-Sorris, Horebis-river, and Dachsberg granites, but the Ga/Al ratio vs. $K_2O$/MgO ratios in the leucogranites of this study show that the samples are largely I type or S type granites (Figure 9.8). A proportion of the $C_m$-type leucogranites may be compositionally A type but this assertion contrasts with the un-fractionated classification that the HFS element and Fe/Mg abundances imply for these granites. The $FeO_{tot}$/MgO and $K_2O$/MgO ratios of the sheeted leucogranites of the Central Zone show a consistent difference between pre- and post-D3 granites, but plot the clearly S type garnetiferous (B-type) leucogranites in the A type granite field with respect to K/Mg, but contradict this classification with low, un-fractionated Fe/Mg ratios (Figure 9.6). The low Fe/Mg, un-fractionated classification also contradicts the generally high $SiO_2$ content of the

uraniferous sheets (Figure 5.1, Chapter 5). Additionally, Ga/Al ratios are relatively low and none of the SLG's of this study plot outside of the undifferentiated S- and I type fields of Whalen *et al*. (1987).

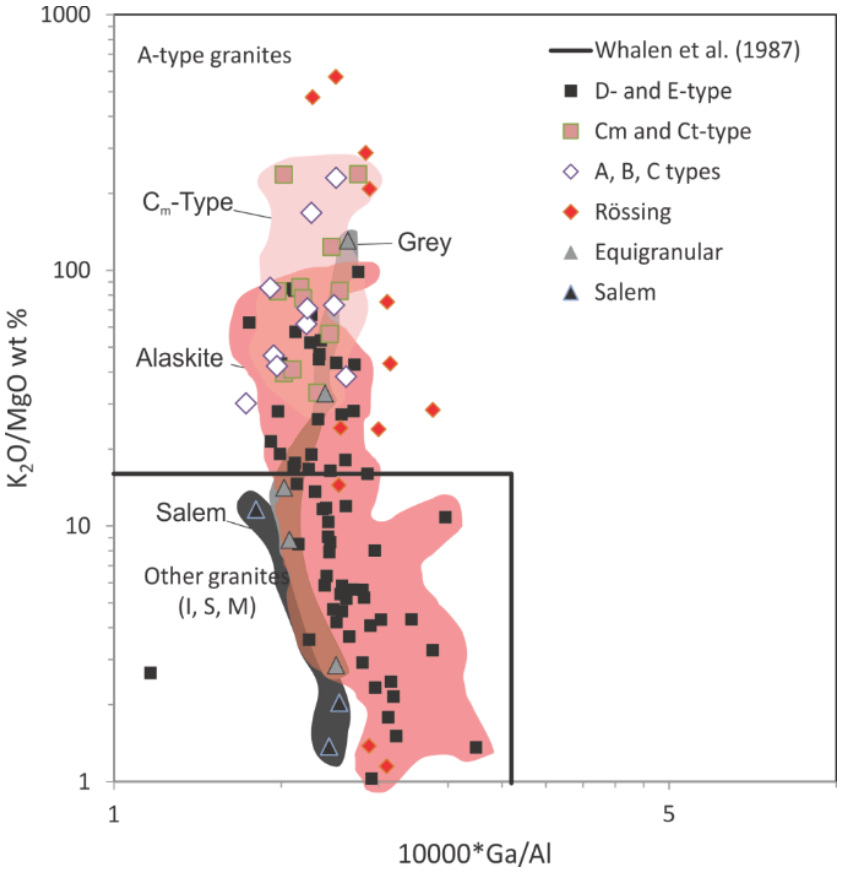



Figure 9.6 10000*Ga/$Al_2O_3$ wt.% vs $K_2O$/MgO plot with discrimination fields of Whalen *et al*. (1984). Most of the pre-$D_3$ leucogranites plot with high K/Mg, typical of anorogenic granite, as do the Rössing alaskites, half of the Ida Dome alaskites and most of the Goanikontes alaskites. The bulk of the Husab samples however plot within the 'other granites' field. This may be attributed to the altered nature of the Husab alaskites resulting from metasedimentary interaction.

Major and trace element ratios place the sheeted leucogranites into contrasting discrimination categories. Thus, the degree of fractionation that has taken place within the leucogranite suits is not easily determined from whole rock geochemistry. According to the criteria and boundaries given in Whalen *et al.* (1987) the uraniferous leucogranites may have A-type affinity if K, Na, and Ca ratios are considered, however low Fe and Mg content is not an A type characteristic. One of the more robust geochemical tools for interpretation of the leucogranite source material, and therefore also supporting interpretations of the tectonic models, are the REE elements. From

Figure 9.5 and Figure 9.6 it is clear that whilst some sheeted leucogranites plot in the A-type field of Whalen *et al.* (1987) some compositions plot in the field of I, S or M types, and there is inconsistency between different discriminating ratios. Anorogenic granites are restricted to the post-collisional and continental-rifting tectonic settings, while I type and S type granites span the continental arc, collision-, and anorogenic settings, with I type granites also occurring in island arc settings. True A type granites should thus lie within plate on tectonic discrimination diagrams. Typically, the granites of the Damara Orogen should reflect a change from syn-collision setting through within plate, where the older I type and S type granites are syn- to post-collisional, and the younger A type granites are essentially limited to the within plate, post-orogenic setting. The tectonic discrimination diagrams of Pearce *et al.* (1984) discriminate between the pre- and post-$D_3$ sheeted intrusives. The abundances of Y and Nb place pre-$D_3$ leucogranites in the syn-collision field, while the mineralised samples plot more towards the within-plate field (Figure 9.7a).

A similar distribution for the mineralised granites is shown based on the discriminators Y + Nb vs. Rb (Figure 9.7b). As is observed in the discrimination diagrams of Figure 9.5 and Figure 9.6, the uraniferous leucogranites straddle the fields usually occupied by I type and S type granites and the A type granites. The pre-$D_3$ leucogranites tend to be syn-collision more than within-plate, which is consistent with their temporal-structural setting. The Salem type granites of this study are also consistently excluded from the within-plate field, reflecting their relatively early emplacement in the collision sequence. Certainly, some of the sheeted leucogranites were sourced from the Abbabis Basement complex, or the unconformable meta-volcanic and metasedimentary units of the Etusis Formation and possibly the lower Khan Formation rocks (Jung *et al*., 2003b; McDermott *et al*., 1996). Thus, the nature of the source rocks may strongly influence the S type affinity of some of the weakly mineralised sheeted leucogranites, with sedimentary source indicators particularly garnet, sillimanite, and cordierite.

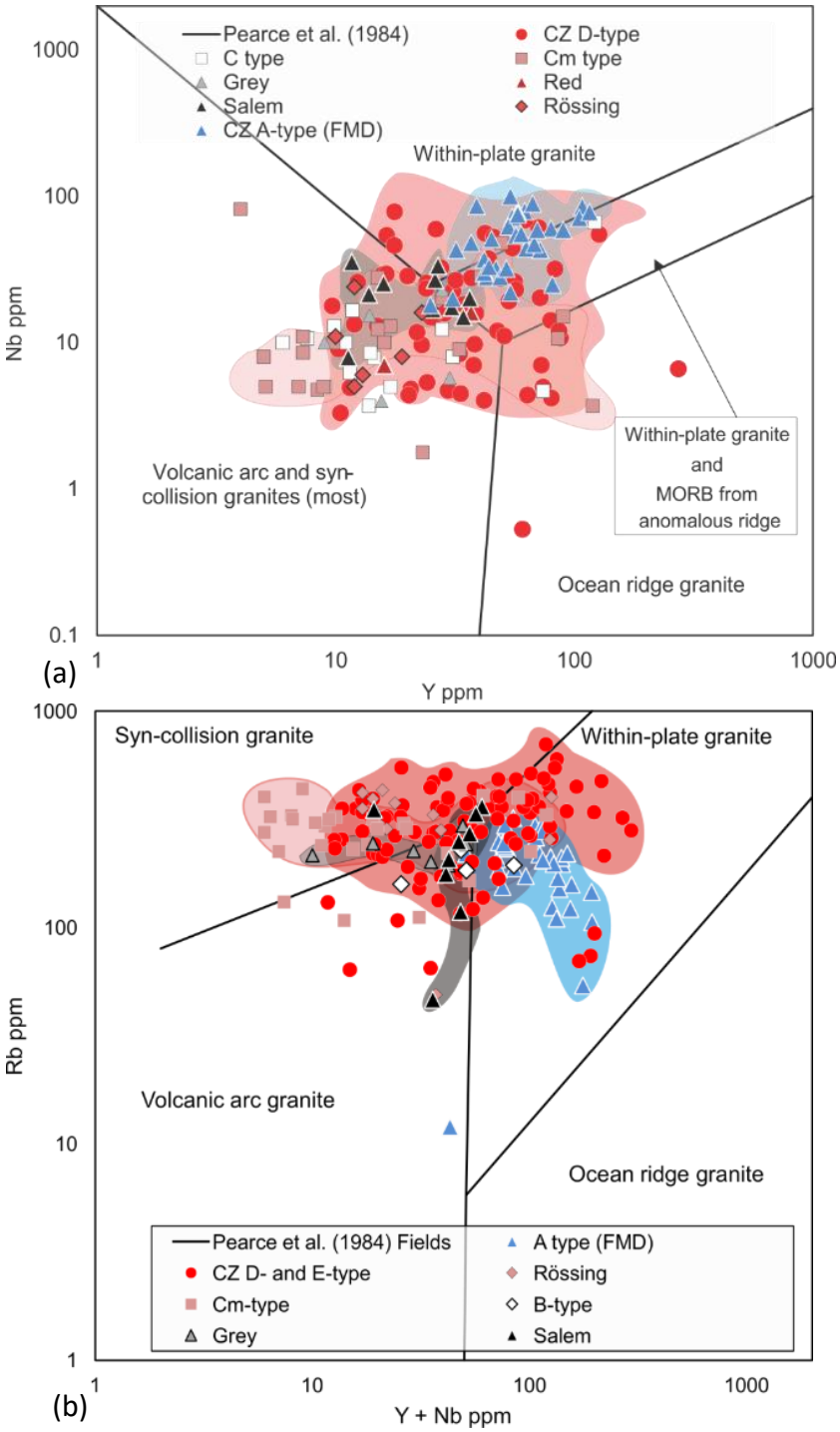



Figure 9.7 Tectonic discrimination diagrams of the Central Zone granites. (a) Y vs. Nb shows a distinct difference between the pre-$D_3$ and the mineralised granites. Although the source is not constrained, the difference in HFS element abundances is considered strong evidence for different source material between the populations. The Rössing comparative samples plot within the volcanic arc - syn-collisional field, which supports a calc-alkaline affinity proposed by McDermott *et al.* (2000).

(b) Y + Nb vs. Rb of selected Central Zone granites. The Grey granites and Cm-type SLG's have low HFS element abundance but have comparable Rb to the uraniferous sheets. The narrow Y+Nb range of the Salem diorites reflects the limited extent of the sampling locality at Valencia. The D-types plot with wide-ranging Y+Nb abundance and appear to bridge the gap between the I-type Cm sheets and the A type granites. The Rössing comparative samples are unique, and unanimously plot within the syn-collision field. Rössing data from Freemantle (2006) and A type data from McDermott *et al.* (2000). Discrimination fields from Pearce *et al.* (1984).

The high Rb and variable HFS element abundances of the uraniferous leucogranites and the Khan Formation-hosted $C_m$-types suggest the two SLG subtypes are derived from different source material, or formed in different conditons (contrasting monazite solubility would

affect REE and HFS abundances). HFS abundances in the garnetiferous B-type are comparable to the C-type and D-type SLGs, but Rb is relatively depleted, and K/Mg in the B-type is significantly higher than in the C- and D-type, as would be expected from a partial melt of metapelites.

Milani *et al.* (2014) show that even the Goas suite calc-alkaline intrusives, which might be expected to show a mantle input, were derived from within crust (possibly by mantle magma underplating). Crustal thickening that took place during orogenesis (Milani *et al.*, 2014; Longridge *et al.*, 2014; Longridge, 2012; Miller, 2008; Gray *et al.*, 2008; Goscombe *et al.*, 2003b; Miller, 1983a and 1983b) should ensure that the sheeted leucogranites be crustally-derived, and therefore within-plate. The Rb content would appear to be the most convincing element to show this (Figure 9.7b).

The $C_m$ type sheets in the Khan Formation, the uraniferous sheets in the Khan - Rössing - Chuos succession and the late A type granites appear to conform to an evolving orogenic system, where the older Khan-hosted granites are syn-collision, the uraniferous sheets are syn-collisional to within-plate, and the A type granites are almost exclusively within-plate.

Considering the trends on the geochemical diagrams in Figure 9.5, Figure 9.6, and Figure 9.7, the uraniferous sheets are not convincingly A type, and are perhaps best described as I type granites. The sheeted leucogranites are weakly peraluminous and as a whole the uraniferous populations at each deposit are more metaluminous than peraluminous in comparison to the pre-$D_3$ sheeted leucogranites on ASI = 1.1 discriminator plots. The original magma composition may have been peraluminous in some cases, given that (Na+K)/Al averages between 0.61 and 0.66, requiring a significant Ca content in order to exceed Al. As is visible at most locations around the Ida Dome; entrained country rock schlieren, interaction with reactive carbonates, and evidence of subsequent hydrothermal alteration (hairline- to centimetric quartz-calcite veining) in uraniferous leucogranites are all external influences on CaO content.

The abundance of magnetite in leucogranites that intrude the Khan Formation, and the prerequisite that the melts are oxidised enough to mobilise soluble uranium shows that the

granites are derived from a high *f*O environment. In the magnetite-ilmenite series classification of Ishihara (1977) the pre- and post-$D_3$ leucogranites are easily differentiated because of the REDOX contrast between magnetite-bearing Khan Formation-hosted leucogranites and the pyrrhotite and pyrite-bearing Rössing Formation hosted alaskites, regionally. The Goanikontes sheeted leucogranites do not invade any sulphide-bearing Rössing Formation lithology, this may be an important consideration, as the dominant iron host in most of the uraniferous alaskites in the Central Zone is pyrite, chalcopyrite, and pyrrhotite, but at Goanikontes magnetite is particularly abundant in the samples of this study. Whalen and Chappell (1988) suggest that most S type granites of the Lachlan Fold Belt are ilmenite series, and most of the corresponding I type granites are magnetite-series. It is not certain whether this observation is applicable to the Central Zone granites, or if it is applicable to classifying the uraniferous sheets. The primary control on the oxidation state of the sheeted leucogranites at emplacement appears to be the reactions that take place with the host rocks.

The sheeted leucogranites are variously pegmatitic and can also be considered in terms of the classifications that rely on the trace element content to subdivide pegmatites into NYF types and LCT types. It has been suggested that NYF types were emplaced during extension whereas LCT types were intruded during compression. However, this concept doesn't work in several parts of Africa (Kinnaird and Nex, 2013) and in Namibia both occur within the same time frame with the same structural setting at around 500 Ma as the classic Rubicon LCT pegmatites is post-tectonic. The occurrence of fluorite in the uraniferous sheets especially at Husab together with the relatively enriched Nb and Y abundances supports an NYF pegmatite classification. The extensional nature of the structural setting suggested by the NYF classification above could also be argued to suggest an A type nature for the sheeted leucogranites, but is limited by the inconsistency of other common chemical discrimination plots.

### *Conclusions on Sheeted Leucogranite Classification*

Classification of the sheeted leucogranites is essentially a two-part discussion: First, the six-fold classification of Nex (1997) is essentially a sub-division of a certain group of granitoids and is limited to the syn to late orogenic sheeted leucogranites. The scheme preceded by comprehensive field work by Oliver (1994); Nex and Kinnaird (1995); Oliver and Kinnaird (1996) and comprehensive studies at Rössing by Herd (1996). Nex *et al.* (2001) and Kinnaird and Nex (2007) use the classification, and caution that it is applicable at Goanikontes and to a certain extent at Rössing, but not necessarily at all the uranium deposits of the Central Zone. The second classification is the source rock and orogenic context which governs the so-called alphabet classification. Whether the five to six varieties of sheeted leucogranite are genetically related, or a consecutive sequence is not easily demonstrated by field observation or petrographic study alone.

Some sheeted leucogranites are clearly S type and others are clearly I type, and aanorogenic A type. The B- and C-types may be further subdivided with consistency; the garnetiferous B-type occurs in at least two, geochemically distinctive generations, which are easily distinguished by prominent foliation of the older variety. Field relationships and textures of these sheets are consistent with the descriptions of leucosomes and granite melt migration models presented in Longridge (2012); Ward *et al.* (2008); Jung *et al.* (2003a); Jung *et al.* (2001) and Jung *et al.* (2000b). Thus, all of the A-type and B-type sheets of this study are classified as S type on account of their ASI values, low HFS abundance and trace element patterns. The three-part C-type leucogranite sub-division (Table 3.1 Chapter 3) divides the most abundant and widespread of the sheeted types. The $C_t$ sheets with abundant tourmaline may be derived from within the metasediments, and are thus likely to be genetically related to the garnetiferous sheets. Boron may be contributed by specific units within the metapelites, and was further concentrated by fractionation that was enhanced by melt propagation through the $D_2$-prepared Damaran host rocks. The tourmaline sheets, which succeed the garnetiferous sheets at most locations, are thus also S type on account of their peraluminous ASI index and trace element trends. The magnetite-

bearing sheets are almost exclusively hosted by the Khan Formation, and have been linked to the equigranular Grey granites described in Longridge (2012). Miller (2008) classifies the Grey granites as part of the leucogranite suite and geochronology in Longridge (2012) seems to support this classification. Perhaps the most relevant work on the magnetite-bearing sheets is by Jung *et al.* (2003b) who show the provenance of the Khan Formation-hosted leucogranites to be the Abbabis basement through Sr, Nd, Pb, and O isotopes. They are thus I type granites and any S type traits that may be apparent are interpreted as relicts of pre-existing compositional banding in the migmatised Abbabis source rocks.

The D-type leucogranites, or alaskites, appear to be distinct not only temporally (508-506 Ma vs. ~520 Ma for the Grey granites, and ~514 Ma for the $C_m$-type) but show remarkably consistent REE and HFS element trends that serve to confirm that they are different to all the leucogranites that precede them. Nex (1997) showed that they are temporally and thus tectonically separated by a major deformation event at Goanikontes. Adjacent to the Ida Dome the uraniferous sheets have intruded in a rather passive manner and have invaded structures normal to and at low angles to the major compressive axis. They should at the very least be considered as transitional and late- to post-orogenic, but not A type in the anorogenic sense.

The fifth type of leucogranite in the Nex (1997) classification is the E-type, characterised by iron-stained halos, which are determined to be magmatic in origin by Nex (1997). These halos are particularly abundant at the Ida Dome are, but are rare in the deposits to the north at Husab and Valencia. The typical halo texture is absent, but red iron-staining is apparent in leucogranite at all deposits with no evidence that the stained granites belong to a separate magma generation. The distinctive E-type halo-texture is thus determined to be a local feature at the Goanikontes and Ida Dome areas. Geochemical trends in this study consistently illustrate evidence of alteration and in some cases assimilation (abnormal Ca for example, ASI section, Chapter 5). The F-type sheets were rarely observed and only one clear example was sampled at Valencia.

Conclusive summary of sheeted leucogranite classification

- The predominance of magnetite over ilmenite (Chapter 4), low Na+K/Al ratios (Figure 5.41, Chapter 5) abundance, and low Ga/Al (Figure 9.6) suggest that the leucogranites are not true A type granites.
- The abundant high field strength elements (Chapter 5, pages 355 through 370); and the within plate tectonic setting of many of the uraniferous leucogranites may support an anorogenic granite classification. However, mineralised granites from different deposits seem to plot within these fields simply because of anomalously high Y while hosting comparatively low concentrations of Nb (Figure 5.43b, Chapter 5).
- There is more evidence that the uraniferous sheets are I type in character than they are S- or A type. They have geochemical and petrographic traits -K/Na, $SiO_2$ content, magnetite>ilmenite, propylitisation of biotite, fluorite etc.- that are directly comparable in many aspects to the uraniferous leucogranites of the Namaqua Metamorphic Complex. These granites must therefore have been derived from orthogneiss precursors (as suggested in Robb *et al.,* 1986) under conditions that were relatively homogeneous across the region, given the closely comparable geochemical- and rare earth element trends.
- The A-type, the garnetiferous B-type, and a great deal of the C-type sheets are weakly to strongly peraluminous S type granites, derived from predominantly Damaran metapelites. The $C_m$-type sheets are I type on the basis of ASI <1.1 and magnetite dominance over ilmenite, they are crustally derived, but transgress the predominantly orthogneissic Abbabis basement and the psammitic lower to upper pelitic Nosib Group; they therefore cannot be derived from a metasedimentary-dominated source.
- Table 9.3 concludes the classification of five sub-divisions of the sheeted leucogranite populations from this study; with the A-type, B-type, and accessory-free and tourmaline C-types classified as predominantly S type granites on account of ASI index and low abundance of HFS elements; the Cm-

and D-types are I type, with the uraniferous sheets tending toward an A type affinity. The E-type is omitted as it is considered as simply a local variation of the D-type (this concurs with findings of Nex, 1997). The F-type pegmatites are omitted on account of the paucity of convincing examples identified in the field and sampled for this study.

Table 9.3 Revised classification scheme for the sheeted leucogranites. The temporal-tectono-metamorphic divide between the pre-D3 and post D3 leucogranites is characterised by a change from predominantly peraluminous, garnetiferous S type granites through to metaluminous-tending I type, magnetite and sulphide-bearing I type granites.

| SLG | Aluminium Saturation | REE | 10000* Ga/Al | Ce+Nb + Y+Zr | U ppm (n) | Fe-bearing minerals | Alpha-bet | Mag./Ilm |
|---|---|---|---|---|---|---|---|---|
| A | weakly peraluminous | low | ND | | ~10 | Minimal biotite | S | |
| B | strongly peraluminous | HREE> LREE | >2.5 | Moderate, 60-400 ppm | ~6 | Garnet (spessartine) | S | |
| $C/C_t$ | metaluminous< peraluminous | low | <1 | Low, 40-300 ppm | ~27 (22) | Minimal biotite | S to I | Ilm |
| Cm | metaluminous> peraluminous | low | <1 | Low, 20-350 ppm | ~42 (32) | Magnetite-ilmenite | I | Mag |
| D | metaluminous> peraluminous | most LREE>> HREE | >1 | Wide-range, 20-1100 ppm | ~565 (144) | Pyrite, pyrrhotite, magnetite | I to A | Mag., locally reduced by Rössing Fm. |

## 9.5 Mineralisation

This study has shown through quantitative mineral deportment and compositional analysis of ore-bearing material from the four major deposits that uranium mineralisation essentially occurs in three main phases. The primary phases have crystallised as a direct result of chemical interaction between the host metasediments and the intruding magma and fluids, with evidence of early crystallisation (inclusions within quartz, feldspar, and biotite) and during the final stages of crystallisation (uraninite crystallises between crystals of altered feldspar and quartz). Uraninite, uranothorite, impure thorite, betafite and brannerite constitute the first or primary uranium mineralisation phase, with uraninite in the overwhelming responsible for U-deportment. The model and mineralisation characteristics

are covered in detail at Rössing (Jacob, 1974b; Cuney, 1980a; Berning *et al*., 1986; Herd, 1996; Nex *et al*., 2003; Abraham, 2008) and Goanikontes (Nex and Kinnaird, 1995; Nex, 1997; Kinnaird and Nex, 2007). This study has added the mineralisation characteristics of the Ida Dome, Valencia, and Husab deposits, and has increased the understanding of mineralisation at Goanikontes. The study covers a total of nine individual areas at these deposits and is the first assessment at such a scale in the Central Zone.

Paragenetic Sequence:

Subsequent to crystallisation of primary/magmatic uraninite, thorite, brannerite, and betafite, a second phase(s) of uranium mobilisation and mineral crystallisation took place before final granite cooling. A final phase of uranium remobilisation, characterised by the hydrated uranyl-silicates uranophane (β-) and boltwoodite, appears to have taken place throughout the near-surface ore zones- and in association with prominent, deep-penetrating fault structures.

There is local variation in primary, intermediate and secondary uranium mineral proportions at the deposits of this study and in summary the three main mineralisation phases are as follows:

1. Within the primary phase there are two styles of mineralisation, uraninite-dominant and brannerite/betafite-dominant;
2. The intermediate phase comprises two dominant U(IV) species, one is uraninite the other is coffinite; and
3. The third phase comprises predominantly hydrous U(VI) minerals and is dominated by uranophane and/or boltwoodite.

It is clear from the ore petrography and QEMSCAN studies (Chapter 4 and Chapter 7, respectively) that uraninite and the other primary U-minerals occur in varied size distributions. Where relatively coarse-grained, sub-millimetric uraninite tends to occur between rock-forming minerals and fine-grained, micrometric uraninite occurs as inclusions

along mineral cleavages or within accessory minerals such as monazite, zircon and magnetite. The fine-grained inclusion-type uraninite must be an early phase, if not older as part of the entrained portion of peritectic phases.

Coarse-grained (millimetric) uraninite, betafite, and brannerite have crystallised for some time during and after the bulk of quartz and feldspar, with some uraninite showing clear evidence of alteration at grain boundaries while others seem to have retained a near perfect cubic shape, perhaps spared from late Na-Si fluid flux. Betafite and brannerite are very rare, and petrographic observations of each in this study are limited to a few samples from Husab. Crystallisation of brannerite and betafite is early as evidenced by the mineral occurrence at quartz-feldspar junctions, and the extensive alteration at the rims and along the fractures indicating the crystals had formed before fluids ceased to circulate through the granites. There are also examples of late-formed brannerite in the QEMSCAN textural analyses, which shows brannerite formation that is closely associated with Ti-present alteration of biotite (Figure 8.25, Chapter 8) and appears to post-date or be unaffected by fluorine-, sulphide-, and chlorite-bearing magmatic fluids.

The intermediate uranium mineral assemblage comprises coffinite, brannerite and uraninite, with the former the result of two mechanisms, being substitution and replacement. Secondary uraninite is present as adsorbed components on magnetite, along biotite-chlorite cleavage planes and in vug-like cavities within the leucogranites. This style is simply the result of FeO availability on the exposed surfaces and cavities in altered magnetite and biotite-chlorite. The prevalence of uraninite and coffinite have crystallised in secondary textures rather than oxidised uranyl species shows that the reduced conditions prevailed during and after granite crystallisation and thus, at a range of successively lower temperatures, some potentially much lower than those of the primary stages of mineralisation. The primary and secondary uraninite may be as young as ca. 484 Ma, as implied by uraninite age dating by Cross et al. (2009) at Husab. Secondary brannerite on the other hand must be a product of slightly different processes, and as with the primary brannerite, it appears to be restricted to mineralisation within the upper portion of the

Rössing Formation at Husab. There is a clear affinity for titanium minerals as the only examples of secondary brannerite texture are hosted in ilmenite, rutile and titanite.

The presence of titanite does not seem to guarantee the formation of brannerite, and it seems that a number of conditions need to be met for the formation of the mineral. It is more likely that where conditions suited the formation of prismatic rutile, and Ca, U and Y (monazite-xenotime) are present prismatic brannerite is likely to have formed. Brannerite however, is not observed simply as a substitution reaction of rutile in any of the samples of this study, which is not surprising considering the stability of rutile over a range of temperatures. Rather, where Ti-phases are altered, sites of reaction with U-bearing fluids will preferentially have crystallised brannerite over uraninite as $Fe^{2+}$ is simply not available for U-reduction (Figure 7.17, Chapter 7). Brannerite and betafite also appear to be in a dynamic relationship, with examples of each mineral hosted as an inclusion in the other, or as a replacement (Figure 7.29, Chapter 7).

Contrasts in fluid chemistry and REDOX state are seen as major controls on primary uranium mineral speciation, and the controls on the fluid chemistry are generally accepted as directly related to host rock influence. $CO_2$ is derived from the host metasediments (Cuney, 1981; Herd, 1996; Nex *et al.*, 2003) but is not essential to uraninite crystallisation, as is shown at the largely carbonate-absent Goanikontes area deposits. Fluid extraction analysis showed that high $CO_2$ ratios in certain deposit areas correlate with high ratios of uranium deportment in betafite. The discussion of the role of $H_2O$ and $CO_2$ fluid compositions is elaborated on in Cuney, 1980a; Herd, 1996; Nex *et al.*, 2003; Kinnaird and Nex, 2007; and Abraham, 2009). Mitchell and Kjarsgaard (2003) show that $H_2O$, $F^-$-free fluids may promote perovskite over pyrochlore formation, however, it is not quite clear why a $CO_2$ fluid in fluorite-bearing leucogranites may inhibit uraninite formation.

The youngest phase of uranium mineralisation is dominated by uranophane at Ida Dome, Husab and Valencia and by boltwoodite at Husab (Townend, 2009, this study) and these minerals are products of $U^{6+}$ leaching from primary phases and remobilisation of dissolved uranyl phases during granite emplacement. U(IV) minerals may be as young as the recent

geological past; Leucogranites are shown to host ~ 1 Ma uraninite in the Namaqua Metamorphic Complex (Robb *et al.*, 1986) which also suggests local reducing conditions may promote uraninite crystallisation at low temperatures, but no such evidence is yet shown for the Central Zone. The abundance of sulphides that are particularly oxidised in the near-surface environment in the Rössing Formation, also implies that meteoric fluids would be acidic, and thus suited to leaching and redistributing soluble $U^{6+}$ compounds. Moreover, the high heat flow in the Damara at some point after granite emplacement (Corner, 1982) and the consistent trend of high ratios of uranophane: uraninite in near surface leucogranites support at least two discreet episodes of $U^{6+}$-type mineralisation in the distant- and recent geological past.These trends are shown in studies at Rössing (Kinnaird, 2007; Abraham, 2008) and across the Central Zone as a region (this study) Field observations in this study recognised boltwoodite and uranophane mineralisation in chert veins and fault sets. Quantitative mineral deportment shows that uranophane distribution is greatest in surface to near-surface alaskites and decreases successively with depth, a trend recognised at Rössing (Kinnaird and Nex, 2007; Abraham, 2008).

The Goanikontes alaskites seem to have remained sufficiently oxidised to crystallise magnetite, y*et al*so contain sufficient uranium and an FeO source (most likely magnetite, sulphides, and to a lesser extent biotite) to reduce U(VI) and crystallise uraninite. Elsewhere in the Central Zone, the uraniferous SLGs of this study contain comparatively little magnetite but abundant pyrite-pyrrhotite-chalcopyrite, and thus are considered to have crystallised in comparatively more reduced environments (e.g. Figure 4.46, Chapter 4). The Husab deposits host patches of brannerite-dominated uranium mineralisation. The location of these sheets is within the upper pelitic gneiss units of the Rössing Formation, a comparable stratigraphic level to that described for the SH area near the Rössing mine. Carbonate-bearing rocks are present in the overlying packages. The role of the host rocks on fluid composition is not well-constrained. However, mineral compositions and non-stoichiometric calculations show that U is overwhelmingly in $U^{6+}$ coordination in brannerite and betafite. Observations also show that titanite is in relative abundance in the samples and often hosts secondary textures of U-Ti-oxide within crystal fractures. Across the Central Zone titanite-bearing leucogranites occur

within proximity to skarn units in the upper Khan Formation and within the Rössing formation. The paragenetic sequence is complex and a gross simplification is presented in Figure 9.8.

Composition calculations of the uranium-bearing refractory mineral phases show that betafite and brannerite contain predominantly $UO_3$ thus the minerals have formed where reduction of U has not been efficient. In addition, the association with Ti minerals and the location of the refractory mineral-bearing granites toward the top of the Rössing Formation at Husab is consistent with observations at the Rössing Mine's SH and SK deposits. Hand held XRF analyses show that Cl- is anomalous over the brannerite-betafite-dominated intervals of leucogranite; as Cl favours U portioning in the fluid phase it is reasonable to suggest that elevated Cl had a role in inhibiting U reduction to form uraninite by retaining elevated quantities of dissolved U. The host rock is cordierite schist, which would account for the Nb required to form betafite assuming contact metamorphism aided Nb mobilisation from the metapelite. Further to this, the reduction of $U^{4+}$ may be seen as less efficient at Goanikontes because of the absence of reactive Rössing Formation material, and thus the leucogranites at the deposit should also contain refractory minerals, considering that they also host significant Y, which is concentrated in brannerite. However, it is apparent that the Ti and Nb are essential to the formation of the refractory minerals. With the upper Rössing all but absent, these elements were not available at Goanikontes. A local trap, such as the Rössing quartzite package also promoted magmatic fluid retention, allowing the granite to crystallise while U concentrated in the fluid phase which interacted with the Nb-bearing schist. In addition, abundant magnetite in the Goanikontes alaskites would have provided soluble Fe to promote U reduction and uraninite precipitation, oxidising Fe in the process.

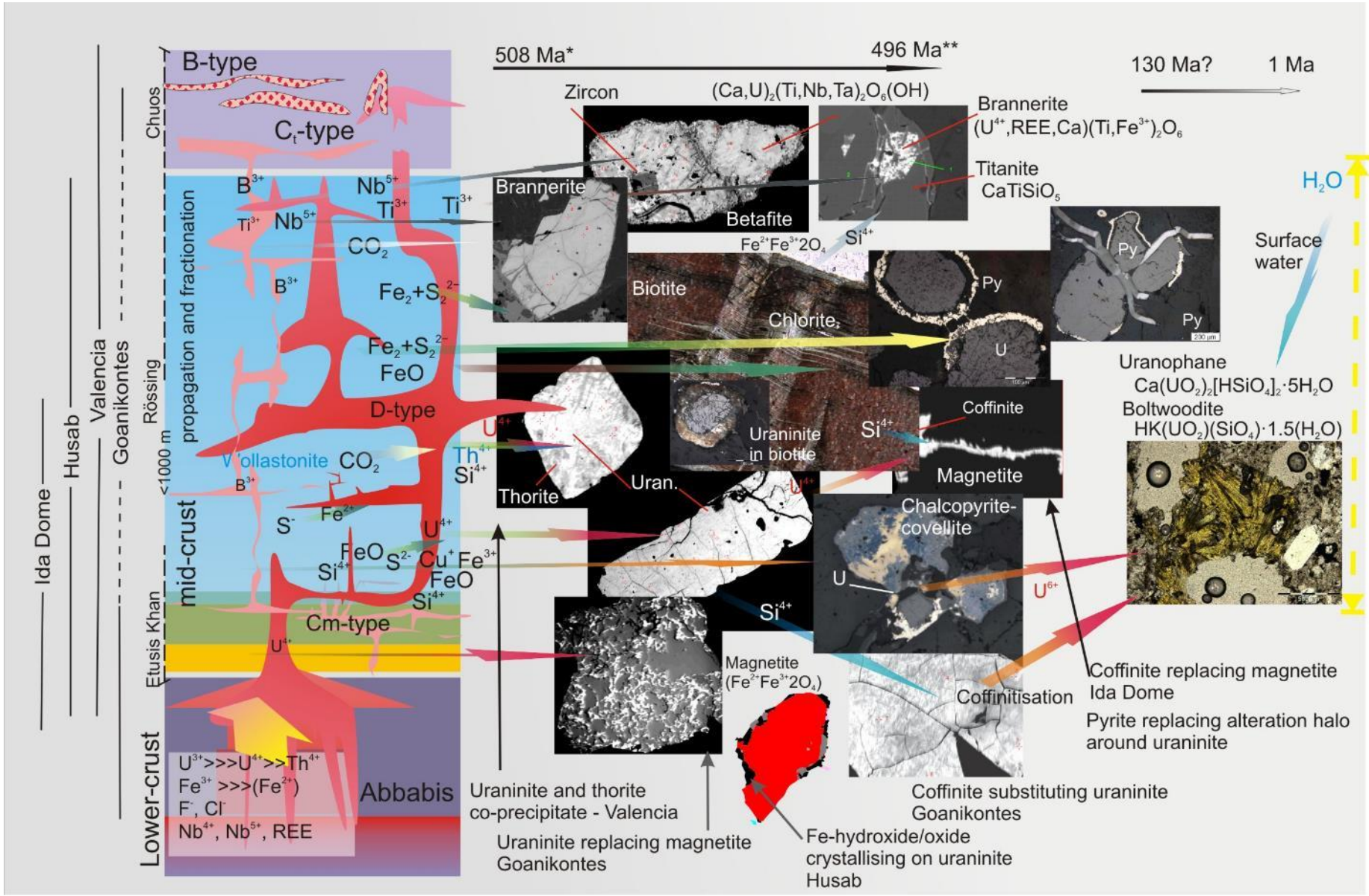

508 Ma*
496 Ma**
130 Ma?
1 Ma
Ida Dome
Husab
Valencia
Goanikontes
Chuos
Rössing
Etusis Khan
<1000 m
B-type
Ct-type
propagation and fractionation
mid-crust
Lower-crust
Cm-type
D-type
Wollastonite
Abbabis
U3+>>>U4+>>Th4+
Fe3+ >>>(Fe2+)
F-, Cl-
Nb4+, Nb5+, REE
Zircon
(Ca,U)2(Ti,Nb,Ta)2O6(OH)
Brannerite
(U4+,REE,Ca)(Ti,Fe3+)2O6
Titanite
CaTiSiO5
Betafite
Brannerite
Biotite
Chlorite
Fe2+Fe3+2O4
Py
U
Surface water
H2O
Uranophane
Ca(UO2)2[HSiO4]2·5H2O
Boltwoodite
HK(UO2)(SiO4)·1.5(H2O)
Coffinite
Magnetite
Uraninite in biotite
Thorite
Uran.
Chalcopyrite-covellite
Coffinitisation
Coffinite replacing magnetite Ida Dome
Pyrite replacing alteration halo around uraninite
Uraninite and thorite co-precipitate - Valencia
Uraninite replacing magnetite Goanikontes
Coffinite substituting uraninite Goanikontes
Fe-hydroxide/oxide crystallising on uraninite Husab

Figure 9.8 Simplified schematic diagram of the mineralisation sequence in the Central Zone primary deposits. *previous page* The primary reducing agent is $Fe^{2+}$ which oxidises to $Fe^{3+}$ in the reaction with $U^{6+}$. THe simplified sequence is: Uraninite - Coffinite - uranophane. Concurrently uranothorite and thorite probably form at the same time as uraninite; the timing of brannerite and betafite is also relatively early, with at least one late generation of secondary brannerite that replaced altered titanite. Sulphides from the metasediments recrystallised in the latter stages of emplacement/mineralisation often forming halos around primary uraninite. Molybdenite appears to be later than pyrite, and chalcopyrite may form from the $Fe^{3+}$ and Cu remobilised from the upper Khan Formation. * Briqueu *et al*. (1980), ** Cross *et al*. (2011).

Betafite compositions of samples from the SH Area (Herd, 1996) and Husab deposit (this study) are substantially different but plot within the betafite field of the Hogarth (1977, 1989) classification. In fact, the alternative pyrochlore classification scheme of Ercit (2005a) suggests a euxenite composition for the Husab betafite. This observation highlights a marked difference in betafite composition between Rössing and Husab specimens; which is due to the near-absence of Ta from the Husab betafite specimen. Samples at the type localities in Madagascar rarely exceed > 1 wt.% $Ta_2O_5$, similarly the Husab and Rössing analyses rarely exceed 4 wt.% $Ta_2O_5$ and the Husab samples do not exceed 1 wt.% $Ta_2O_5$. The low Ta abundance in betafite is reflected in the whole rock analyses by ICP-MS of selected alaskites, where Nb/Ta ppm is in the range of ~3 to 38, typically in peraluminous melts this ratio is <1 in peraluminous melts (Linnen and Keppler, 1997). The influences that T, $F^-$, and aluminium saturation indices have on the solubilities of Nb and Ta in granitic melts are quantified in Chevychelov *et al*., (2010), who also determine that minerals such as columbite-tantalite $(Fe,Mn)(Ta,Nb)_2O_6$ are soluble above 800 °C and do not crystallise at the liquidus of peralkaline and peraluminous melts. This property may explain the paucity of the mineral, if it is present at all in the alaskites. If the Nb in betafite is sourced from the melt then Ta should be in comparable concentrations to Nb in the mineral. However, Nb is in greater abundance than Ta, and this ratio is not comparable between deposits. Nb:Ta in Husab betafite is ~28:1 (this study) and in the Rössing betafite it averages 6.6:1 (Herd, 1996). This leads to the interpretation that the Nb is probably sourced from outside the melt, bearing in mind that the granites are probably high temperature (coincident within ca. 10 Ma of ≥800 °C peak metamorphism, Longridge, 2012) and fluorine-bearing (increases Nb-Ta solubility). The mineralised SLGs also contain appreciable Y, and so the normal rules that

apply to LCT type pegmatites that host columbite (Anderson *et al*., 2013) are less suitable than interpretations of NYF (Nb -Y-F) pegmatite formation.

Although peraluminous melt and fluid systems favour U partitioning into the fluid in the presence of $Cl^-$ (Peiffert *et al.*, 1994, 1996), the Central Zone leucogranites appear to have been reduced efficiently enough to crystallise uraninite from the melt, as most uraninite is euhedral, and is occasionally included in other magmatic phases. Cl and F may have been sourced from the amphibolite in the Abbabis Basement Complex, and/or the reduced schists of the Khan Formation. Halogens must have played a role in the system, whether early in magma generation, or simply as a by-product of substantial biotite alteration in the sub solidus environment and it is evident in the abundant fluorite veins that occur at Husab and are observed in varying abundances in the other deposits of the region.

### *Uranium Mineralisation Conclusions*

$U^{4+}$ is soluble in silicate melts as a function of K/Na, where U is less soluble in K-rich melts (Domine and Velde, 1985 and Pieffert *et al.,* 1994). Thus, considering the high K/Na ratios and the K-feldspar dominated compositions, it is logical that the majority of the U in the leucogranite melts is dominated by $U^{6+}$ because fluorite is abundant and promotes solubility of hexavalent uranium. Thus, at each deposit it is well known that the metasediments have played a role in reducing the uranium to promote uraninite crystallisation. What is not unequivocally clear is what is reacting with hexavalent uranium and which elements are being oxidised to donate electrons to the dissolved $U^{6+}$? Where marble is present, graphite may be expected to be such a reducing component, however, the Rössing marbles are highly attenuated, if present at all, at the Central Zone deposits, thus this study proposes that Fe and more specifically sulphides have played the key role of reducing U to form the bulk of U mineralisation at the deposits.

Locally the Goanikontes and certain samples from the Ida Dome and Valencia areas contain relatively little sulphide but do host magnetite, which is the most likely source of mobile iron required for reduction of the soluble uranium. Halogens, carbonate, and sulphate anions within the magma promoted dissolution and transport of U, and the abundance of fluorite, and anomalous Cl as noted in portable XRF assays of mineralised granites, indicates the abundance of halogens in the magmas. Abundant sulphides (as indicated by Ni and Cu exceeding 1000 ppm) at Husab suggest the reduced sulphide-bearing Rössing Formation units promoted the bulk of U mineralisation.

In localised contrast though, abundant fluorite at Husab, Rössing and elsewhere together with $CO_2$ mobility provided from de-gassing of carbonate rocks have all enhanced the mobility of uranium. Much as the formation of betafite at Rössing appears to be a function of the availability of Ca, Ta, Nb and the influence of certain reactive metasediments on the $fO_2$ in the alaskites (Cuney, 1980b; Herd, 1996, Nex *et al*., 2003a) brannerite at Husab seems to occur where Ti, Ca, and Nb are in relative abundance (Figure 5.42, Chapter 5). It is also clear that the composition of the reactive host rocks plays a critical role in determining the speciation of the primary uranium minerals. A simplification of the distribution of the primary phases is as follows:

- Primary uraninite crystallises as $(U^{4+}, U^{6+}, Th^{4+})O_2$ throughout the mineralised interval that spans the upper Khan- Rössing and lower Chuos Formations, with each deposit occupying a limited interval within this stratigraphic range;
- Uraninite and magnetite formed intimate associations in alaskites that invaded the lower-Rössing and upper-Khan transition at the Goanikontes, Ida Dome, and Valencia deposits. Where uraninite occurs as inclusions in magnetite and as replacements of altered magnetite there is usually a magnetite-titanite-diopside skarn within the vicinity, particularly at Goanikontes. At Valencia and the Ida Dome QEMSCAN mineral texture maps predominantly show that uraninite is a site for Fe oxides to form rims and replacements, such that uraninite is a mineral-scale reducing site;

- Uraninite predominates over all uranium phases throughout the lower- to mid Rössing and in the lower Chuos Formation at Husab, Valencia and the Ida Dome (no Chuos -level mineralisation at Ida Dome); and
- The Husab deposits are unique in that brannerite and minor betafite may constitute over 50 % of local uranium deportment in alaskites that intrude the upper pelitic metasediments of the Rössing Formation.

Mineral compositions, of uraninite, with stoichiometric calculations of $UO_3/UO_2$ confirm variation of REDOX conditions, and thus variation of uranium-bearing fluid-melt interaction with individual deposits. Perhaps equally so, the abundant evidence of post-magmatic alteration shows that the ratio is susceptible to external influences as $UO_3$ preferentially leaches. In order to assert the true REDOX condition at the initial formation only the least altered uraninite may be considered for further study. The variable ratios of $UO_2$ and $UO_3$ in the uraninite populations of individual deposits plot as groupings when compared to other deposits. Thus, the regional variation in deposit-forming REDOX conditions is reflected in the clustering of uraninite populations on the compositional plots.

Ore petrography of chapter 4 shows that many phases post-date the uraninite and are typical of hydrothermal alteration, but the lack of pervasive alteration of the host rocks rules out substantial alteration by an externally derived hydrothermal fluid. Alteration is most prevalent at the contacts with the alaskite intrusives. The sub-solidus alteration within the alaskites is probably driven by fluids that either immediately accompany the alaskites at contact margins with reactive metasediment and derived from paired propelytic reactions within the granites themselves (as described in Robb *et al*., 1986).

This combined model is perhaps the most suitable as many clusters of uranium mineralisation occur with biotite that is completely chloritised and surrounded predominantly by epidote, a typical product of propylitisation of biotite, the timing of biotite alteration to chlorite is unclear, but probably occurred soon after emplacement, as chloritisation has taken place in alaskites at great depths, well-below any depths of

supergene influence. The source of sulphur-bearing fluid is probably driven by contact metamorphism of the host metasediments, which occur in a widespread base metal-bearing interval of the Damaran stratigraphic succession. Copper prospects in the lower Damara succession of the southern Central Zone were exploited from the Ida Dome to as far northwest as Karibib.

The fluids that maintain the high U content of the system are also responsible for the deuteric alteration, as is evidenced by extensive oligoclase breakdown to sericite and albite rims around feldspar that characterise the alaskites.

The uranium-bearing refractory minerals occur at a variety of depths at Husab, up to 17 wt.% of U deportment at depths exceeding 290 m down hole (Johnson, 2011) with most occurrences however, being recorded in the supergene envelope between 0 m and 150 m, and within the upper units of the Rössing Formation. The proportion of refractory mineral-hosted uranium in the supergene environment is enhanced by the following factors:

- A high percentage of U partitioned into oxidised magmatic fluids;
- Late crystallisation as a function of solubility change rather than REDOX, producing high $UO_3$ ratios in uraninite;
- Low percentages of U in the melt, evidenced by the low percentage of uraninite in refractory mineral-bearing granites; and
- In the supergene environment, uraninite is preferentially leached, enhancing the proportion of U deportment in the more resilient refractory minerals.

Fluid inclusion studies by Cuney (1980b), Herd (1996) and Nex *et al*. (2003) have shown temperatures of at least 220 °C. Comparatively Zhao *et al*., (2003) show that uranium mineralisation post-dates alkali-feldspar granite intrusions at Dalonshan, China by ~8 Ma and took place at temperatures as low as 250 °C to 300 °C. Cooling ages for the Central Zone as young as 440 Ma are shown by Haack & Hoffer (1976) and which is concurrent with granite pegmatite intrusives in the vicinity of primary uranium deposits at ca. 434 Ma (after

Longridge, 2012; Nex and Kinnaird, 1995; this study). Temperatures at this cooling stage pass through 500 °C to 300 °C (Miller, 2008). This is consistent with Corner (1983) who suggests temperatures above 500 °C in a regional event taking place at some point after crystallisation, resetting magnetism in Ti-Fe oxides. With these conditions, it is entirely possible that the mineralisation age at Husab of 496 ± 4.1 Ma (Cross *et al*,. 2009) may in fact not represent the youngest age of uraninite, coffinite, brannerite, or betafite mineralisation.

## 9.6 Comparisons with Other Orogenic Belts and Uranium Mineralisation Provinces

Damaran-age uranium deposits that are hosted by late- to post-orogenic granites are poorly represented outside of the economic occurrences of the southern Central Zone. The uraniferous sheeted leucogranites are relatively unique and do not occur in comparable concentrations elsewhere in the Damara Orogen. The immediate geological comparisons that one makes with the inland branch of the Damara Orogen are with the two nearest, comparably-aged continental suture zones, the Kaoko and Gariep belts. The mobile belts host leucogranites, but not in the volumes or varieties that characterise the west southern Central Zone, and there are no known occurrences of uraniferous leucogranite deposits in these parts of the Damara Orogen (after Miller, 1983a; Durr and Dingledey, 1996; Frimmel and Frank, 1998; Miller, 2008). Why this is so may be explained by the contrast in tectono-stratigraphic setting that of each of these parts of the Damara Orogen have to the Inland Branch or Damara Belt. The Namaqua Metamorphic Complex is essentially the basement to the Gariep Belt, where the granulite facies Gordonia sub-province in the north is in juxtaposition onto low grade metavolcanics of the Richtersveld sub-province by an 85-km displacement along the Tantalite Valley shear zone. (Waters, 1989). The Port Nolloth Zone (PNZ) is the closest Central Zone comparative of the Gariep Belt as it was deposited in a passive rift graben setting; shelf carbonates prevailed and were followed by thick glacial sediments and deep water greywacke and turbidites, below the shelf carbonates the psammitic, and rheologically competent units that characterise the Nosib in the Central

Zone are less well-represented in the Gariep. In this context, the PNZ is comparable to many aspects of the Swakop sequence in the Central Zone, but less so with the Nosib-Swakop combination. The most recent interpretation of continent-continent collision with respect to these belts is in Gray *et al.* (2008). Key features of these belts are the sinistral transpressional styles of collision in the Kaoko Belt (Durr and Dingledey, 1996; Maloof, 2000; Passchier *et al.*, 2002; Goscombe *et al.* 2003a) and in the Gariep Belt (Davies and Coward, 1982; Miller, 1983a; Porada *et al.* 1983 Franz *et al.,* 1999; Stanistreet and Charlesworth, 2001; Goscombe *et al.*, 2003a). The Gariep and Kaoko belts have imbricate thrust structures, with mylonitic zones and inferred décollements along north west- and west-dipping detachment planes (after Gray *et al.*, 2008) who also suggest that the Northern and Southern Marginal assemblies on either side of the granite-dominated Central Zone must have similar detachments. The merits of these interpretations are discussed in Longridge (2012). Essentially the Gariep and Kaoko belts may be viewed as one half of an inland branch. This is comparable to the Southern Zone, but not the Central Zone where upright folding occurs in the later stages and steep structures facilitate melt migration from lower crystal levels to the mid-crust representing a significant contrast to the low angle thrusting in the Gariep and Kaoko Belts.

Metamorphic conditions reached granulite facies in the Kaoko Belt (Goscombe *et al*, 2003; Frimmel and Frank, 1998) and is characterised by higher pressures and lower temperatures (Frimmel, 1995) than the Damara Belt. Whereas the Central Zone experienced uplift and relaxation in the Damara, the Port Nolloth Zone is thrust over-, from the west by the Marmora Terrane. A P/T of 500-550 °C and 6 Kbar at peak also contrast with the 4-5 Kbar and >800 °C of the Central Zone. The low-pressure high-temperature metamorphism is concurrent with voluminous granite intrusions near metamorphic peak in the southern Central Zone of the inland branch (the Damara Belt). It appears unique among the Namibian metamorphic belts. Post-orogenic granites in the Kaoko Belt intruded between *ca.* 530 Ma (Allsopp *et al*., 1983) and *ca.* 521 Ma (Frimmel and Frank, 1998) which is 15 Ma to 25 Ma later than peak metamorphism (Frimmel, 1995; da Silva *et al*., 1997). The Damara Belt in comparison appears to have peak metamorphism very close to emplacement age of the

uraniferous leucogranites. Longridge (2012) gives a ca. 510 Ma metamorphic peak vs. ≤508 Ma alaskite emplacement (Briqueu *et al.*, 1980). Longridge (2012) gives a detailed appraisal of the tectono-thermal, deformational, and igneous history of the Central Zone of the Damara inland branch and suggests a more Himalayan-style affinity than an Alpine type.

In the Orange River area, crustal shortening led to the assembly of terranes each with a distinct history (Dewey *et al* 2006). In summary:

- Richtersveld Terrane ~1900 Ma greenschist with U <3·4 ppm, Th 20·1 ppm;
- Aggeneys/Steinkopf Terranes ~1100 Ma, amphibolite U<10 ppm, Th 52 ppm; and
- The Okiep Terrane which contains the more incompatable element enriched granites (U<17 ppm; Th 66 ppm).

Most U-enriched rocks occur in the 1030 Ma granulite-facies core of the Namaqua belt, quartzo-feldspathic gneisses (U ≤ 46 ppm; Th = 90 ppm) and charnockite (U<52 ppm; Th = 400 ppm) both from Andreoli *et. al.* (2006). Note that the U:Th ratios are the inverse of typical Central Zone SLGs. Trans-tensional constriction was probably dextral and bounded to the NE by the dextral Tantalite Valley Shear Zone, adjacent to which there is substantial clockwise rotation of structural trends (Dewey *et al.*, 2006). The Namaqualand Metamorphic Complex hosts a number of uraniferous leucogranite bodies, which have invaded the 1199 ± 12 Ma Modderfontein augen gneiss, which correlates to the 1197 ± 55Ma Nababeep granite gneiss (Clifford *et al*., 2004). The leucogranites are thus comparable in many ways to the CZ alaskites, being hosted in a structurally complex granulite facies setting. The descriptions and interpretations of Robb *et al*. (1986) are the most comprehensive accounts of the granites on the South African side of the Orange River, and may be directly compared to similar alaskitic bodies near Warmbad, Namibia.

The uraniferous leucogranites (alaskites) are classified as I type on the basis of low A/CNK, as are the predominantly metaluminous CZ alaskites; they are highly fractionated with high $SiO_2$, as are the CZ alaskites. The anorogenic granites of the Namaqua Metamorphic Complex (NMC) are dated at *ca.* 920 Ma by Allsop *et al* (1979) and have thus intruded post

tectonically (at ca. 1.1 Ga). These anorogenic granites though have potentially formed at lower grade conditions (lower amphibolite, Frimmel, 1995). The conditions would not therefore not have been in equilibrium with U-bearing accessory phases such as monazite and zircon. This observation of the Namaqua belt granites is a suitable explanation for the lower uranium grades when compared to the Central Damara.

Considering the deposits of this study are more like the Rössing deposit than the NMC leucogranites, the mineralisation styles are probably a combination of closely linked processes rather than discreet episodes as proposed for the NMC leucogranites. Uraninite is bimodal in biotite of the Central Zone alaskites; it is hosted as euhedral inclusions and as mineral cleavage-parallel replacement precipitates in chlorite after biotite. In this sense the mineralisation with respect to biotite involvement has much similarity to the mechanism described for the uranifeorus leucogranites of the Namaqua Metamorphic Complex.

A comparative example outside of the southern African context is the ca. 1.9- to 1.8 Ga Trans-Hudsonian Orogen in Canada. The setting shares many similarities with the Central Zone. The backdrop of Laurentian assembly by the suturing of Archaean cratons is directly comparable with Pan African assembly of Gondwana by Congo and Kalahari Craton collision. The starkest contrasts between the Luarentian and Pan African examples being that the tectono-stratigraphically zoned Trans-Hudson Orogen is the largest Palaeoproterozoic orogen in the world and the underlying basement rocks are characterised by Archaean greenstones, whereas the Damara is a smaller component of a Gondwana assembly, significantly younger palaeoproterozoic basement.

The Fraser Lakes area leucogranites occupy a fold and thrust portion of the Trans-Hudsonian Orogen known as the Wollaston Domain, which comprises a comparable sequence of psammitic and calcsilicate units to those of the Central Zone, Namibia. The depositional environment of the Wollaston Domain, presented in Annesley *et al*. (2005) describes rift, passive margin, and foreland basin environments, where rifting margins, succeeded by calcareous metasediments and calcsilicate-gneiss units compares well with the in the Central Damara succession. Thus, the stratigraphic succession satisfies the

sedimentary conditions, where REDOX contrasts exist in the sequence; the structural setting is dominated by fold and thrust belts (Annesley *et al*., 2005) and although upright folds are the dominant late structural feature of the Central Zone, it is not devoid of prominent thrusts. The Wollaston Domain is tectonically bound by a dome and basin dominated zone to the west, the Mudjatik terrane (Lewry and Sibbald, 1977) and an Archaean granite greenstone basement to the west, the La Ronge Domain.

The east to west profile of the Trans Hudson Orogen is thus comparable, but perhaps not identical to the south to north profile of the Damara Orogen south of the Northern Zone. McKechnie (2012) postulates that the peritectic phases, biotite, monazite, allanite and zircon indicate that some of the less-evolved, U-poor pegmatites are more likely to have been sourced from the mid-crust, this interpretation ties in well with the interpretation of the $C_m$-type sheeted leucogranites of the Central Zone, which host low abundances of U (<50 ppm) but also hosts comparably scarce accessory minerals. The C-type SLGs of the sCZ precede the uraniferous sheets, but are most likely derived from different source rocks, or from similar rocks but with greater degrees of partial melt diluting any expected U enrichment (this study). This compares with the assertion that the uraniferous alaskites of the sCZ are generated at lower crust levels, on the basis that preceding leucogranites would have already depleted the source rocks prior to the formation of the late, uraniferous sheets (after Nex, 1997; Nex *et al*., 2001a; Nex *et al*., 2001b; Kinnaird and Nex, 2007, this study). In essence this study agrees that the uraniferous SLGs or alaskites are the product of a different source material to the preceding SLGs, and that the REE evidence in this study confirms low degrees of partial melt in the pronounced -ve Eu anomalies seen in alaskites from all the deposits of this research.

Table 9.4 attempts to cover the major geological features that compare the Namaqua Metamorphic Complex, the Trans Hudson Orogeny and the Damaran contexts of uraniferous leucogranites.

Table 9.4 Comparative table of uraniferous sheeted leucogranites and their respective geological settings in the Trans Hudson Orogen, Kibaran Orogen - Namaqua Metamorphic Complex and the Central Zone of the Damara Orogen.

| **Orogenic Deposits** | **Fraser Lakes District, Saskatchewan, Canada** | **Namaqua Metamorphic Complex, southern Namibia, South Africa** | **Western Central Zone, Damara Orogen, west central Namibia** |
|---|---|---|---|
| (a) General setting | Trans-Hudsonian Orogeny - Himalayan-style craton – craton collision. | Kibaran Orogeny; area Gordonia sub province in the N, and the Richtersveld sub province in the S. Transpressional with subduction and thrusting | Damaran Orogeny - Himalayan style craton-on-craton collision with some Alpine affinity |
| (b) Basement Rocks | *ca.* 2.6 Ga Archaean quartz-diorite to granitic orthogneiss inliers. | ~1.9 Ga Richtersveld Terrane: Predominantly granitic gneisses of the potentially 1.7 Ga Gorrasis-and Garub Group rocks, Sinclair Supergroup and Gordonia sub province, respectively. | Un-clear 1.1 Ga most likely *ca.* 2 Ga. Meta-igneous dominated with paragneiss and metasediments, amphibolites, and carbonates. |
| (c) Metasedimentary sequence | *ca.* 2.07 Ga Palaeoproterozoic, locally in two groups, upper is Giekie River Grp. calcsilicate dominated, lower is Wollaston Grp. psammitic and pelitic metasediment dominated. | Garub Group to the S, metavolcanics, quartzite, carbonates and amphibolitic rocks; Mixed and banded Gaidip Fm. gneiss and carbonates of the Guadom Fm. of the Pella Terrane. | Two Neoproterozoic Groups; lower- meta-volcanic, meta-clastic, and semi-pelitic Nosib Group *ca.* 752 Ma and upper- Swakop Group *ca.* 635 Ma. |
| (d) Peak metamorphic conditions | Upper amphibolite to granulite facies; *ca.* 1.86 to 1.78 Ga; fabric precedes peak T; 850 °C/9 kbar. | Gordonia - 780-850°C/5-8 kbar; Richtersveld inferred <650°C/5-6 kbar. Deformation and granite emplacement concomitant with deformation at ~1.01 Ga. Area is dominated by the ESE-WNW Tantalite Valley Shear Zone; | Upper amphibolite to granulite facies; 800 °C to 850 °C/4-5 kbar. Peak metamorphic fabric precedes the uraniferous leucogranites. |
| (e) U-bearing granites | Two groups: Older is U-deficient, intrudes as discordant dykes, rarely cross the calcsilicates; Younger group is alaskitic is radioactive, and either U- or Th-mineral dominant. | Leucocratic pegmatites, highly variable in size and U-content, tend to host U in biotite. Occupy antiformal structures in vein and stock-like amalgamations. | Two groups: Older is U-deficient, precedes major deformation event ($D_3$) subdivides into three varieties; Younger alaskite is syn- to post-$D_3$, U-enriched, Th is minor, may subdivide into two or three groups based on U-mineralogy and alteration facies |
| (f) Major accessory minerals | Titanite, magnetite, ilmenite, garnet, apatite, monazite, zircon, Nb-rich mineral(s). | Predominantly biotite and magnetite-hosted uranium/uraninite. Regional pegmatites host Nb-Ta phases, tantalite and columbite, betafite, monazite, Sn and Cu mineralisation | Magnetite, ilmenite, titanite, apatite, monazite, zircon, betafite, brannerite, allanite. |
| (g) Sulphides | Pyrite in host rocks and in alaskites. | Sulphides are not reported | Pyrite, chalcopyrite, pyrrhotite, molybdenite, pyrite and chalcopyrite in host rocks. |
| (h) Alteration | Sericite, chlorite, clays, radiogenic galena? Fluorite and carbonate veins, haematite staining. | Little information, locally other pegmatites may have greisen. High grade assemblages are markedly retrograded. | Sericite, chlorite, clays, radiogenic galena and wulfenite, fluorite and carbonate veins, haematite staining (E-type alaskites). |

Sources: (a) (Hoffman, 1990; Ansdell, 2005; Corrigan *et al.*, 2009); (after Longridge, 2012). (b) (Hamilton and Delaney, 2000); (Clifford, 1970; Toogood, 1976; Miller (2008); (Kroner *et al.*, 1991) and (Jacob *et al.*, 1978; Jacob *et al.*, 2000; De Kock *et al.*, 2000; Tack *et al.*, 2002; Longridge *et al.*, 2014). (c) (Ansdell *et al.*, 1999) and (McKechnie, 2012); (Beukes, 1973; Jackson, 1976; Toogood, 1976); (de Kock *et al.*, 2000) and (Hoffmann *et al.*, 2004). (d) (Tran *et al.*, 2008; McKechnie, 2012); (Jackson, 1976, Dewey *et al.*, 2006); (Longridge, 2012, Longridge *et al.*, 2011; Jung *et al.*, 2001; Goscombe *et al.*, 2003a; Jung and Metzger, 2003a and 2003b) and (Longridge, 2012, this study). (e) (McKechnie, 2012; McKechnie *et al.*, 2013); (Xemplar Energy Corp.); (Herd, 1996; Nex, 1997; Kinnaird and Nex, 2007; Nex and Kinnaird, 1995; this study). (f, g, h) (McKechnie, 2012); (Miller, 2008); (this study).

## Conclusions

All four of the deposits areas of this study exhibit some combination of aspects of each of the five features summarised below. It is only where at least one aspect of each of these features is present that a significant volume of granite at economic grades occurs. Elsewhere in the Damara Orogen conditions were either too high-pressure (7-9 kbar, Kaoko Belt) or structurally and tectonically unsuited to form suitable melt compositions (subduction in the Gariep Belt). The ~1.1 Ga I type granites of the Namaqua Metamorphic Complex are thorium-over-uranium enriched, and intrude migmatised host rocks. Without the input of significant quantities of reduced Fe from reactive metasediments, the reduction of uranium was not facilitated to the same degree and the resultant mineralisation is focussed at the only available FeO hosting sites, chloritised biotite and magnetite porphyroblasts. Thus, the key requirements for economic granite-hosted uranium deposits of exploitable size must include the following:

1. Tectono-metamorphic: Existing age-dating at three deposits places the alaskites or mineralisation within 2 Ma to 14 Ma of peak metamorphism, and syn- to post-$D_3$ upright fold-dominant, deformation. This is important because older granites may coincide within error with previous metamorphic peaks, but it was not until ca. 510 Ma that metamorphism reached granulite facies, potentially releasing U from accessory phases.

2. Structural: all of the deposits of this study occur at what can best be summarised as structural anomalies in an otherwise northeast – southwest striking tectonic fabric. Each of these anomalies is a pressure shadow of some form and may include a combination of shearing in a brittle-ductile transition zone, saddle-reef accumulation in disharmonic $D_3$ related fold hinges, axial-planar and conjugate fracture plane intrusion, and pooling at competent and ductile rheological boundaries. Invariably the intrusion of the uraniferous sheets, though voluminous, appears to be passive and a reaction to local geometric variation in

the regional scale deformation domain. Prior to $D_3$ upright folding was limited, thus pathways from the lower crust would also be restricted.

3. Physical: The overwhelming focusing mechanism is that of melt propagation along fracture sets in relatively competent psammitic and metapelitic Damaran metasediments. Eventual pooling of the magma beneath a less-competent, but more impermeable carbonate-siliciclastic barrier is not essential, but does facilitate voluminous sheet aggregation as at Rössing (Jacob *et al*, 1976), the Ida Dome and Husab (this study); the key contrasts in the region would be the Ida Dome and Rössing deposits with tectonically thickened marble units of the Rössing Formation compared to the Goanikontes (Nex, 1997) and Valencia deposits where marble is thin and often absent.

4. Compositional: The uraniferous sheeted leucogranites are likely more I type, potentially S-type. They are metaluminous to weakly peraluminous, highly fractionated, and alkali-feldspar dominated with high K:Na. They are most likely derived as fractionated anatectic melts from the metamorphosed lower crust, which partially explains the indistinction between the classic alphabet classification. The uraniferous sheets have near identical REE profiles to other, less-fractionated granites derived from the lower crust. They are relatively REE-enriched among the Damaran leucogranite suite, with pronounced plagioclase fractionation, HFS- and $F^-$ -enrichment. The combination of the aforementioned compositional characteristics can be used to distinguish the uraniferous generations from all the preceding sheeted granite varieties. The REE compositions confirm that the uraniferous sheets are genetically distinct within the sheeted types of the Central Zone. They appear to bridge a compositional- and tectonic-setting gap between voluminous, Khan-Formation and upper Abbabis Basement-hosted U-deficient, magnetite-bearing sheets and slightly younger anorogenic type granites elsewhere in the CZ (e.g. -type granites described in McDermott *et al*., 2000).

5. Chemical: Uranium mineralisation coincides with Fe reactions, and in almost all deposits reduced iron minerals occur with uraninite, these minerals in particular are pyrite and pyrrhotite. Reaction facilitated by the strong affinity that exists between Fe and Ti has resulted in distinctive secondary Fe coloration that often characterises mineralised zones. The source of $Fe^{2+}$ is not unanimously certain but deuteric alteration features that are very nearly identical to those described for uraniferous leucogranites of the Namaqua Metamorphic Complex (Robb *et al*., 1986, Kinnaird, pers. comm.) and the Bancroft District (McKechnie, 2012; McKechnie *et al*., 2013). It is certain that uraninite occurs in more than one textural relationship with biotite and magnetite, as an inclusion and as a reaction replacement mineral, and in the case of Fe-oxides, uraninite appears to be a mineral-scale site for $Fe^{2+}$-deposition. Uraninite appears to have crystallised before some of the sulphides which occur in the metasediments and were incorporated in the granites. This study concludes that the primary source of reduced iron must be pyrite and pyrrhotite in the metasediments at Husab, pyrite and chalcopyrite in the metasediments at the Ida Dome and Valencia deposits, and potentially a combination of Mo- and Fe-sulphides and magnetite at Goanikontes. Although it must also be stated that the reducing conditions would also facilitate the crystallisation of reduced Fe minerals within the crystallising granites.

With the above in mind, the most likely targets for primary hosted uranium mineralisation would be the western Central Zone, which is also aided by the oblique east to west erosion profile. The syn-tectonic granite-hosting Coastal Terrane of the Kaoko Belt has comparably low pressures regimes to the Central Zone but does not satisfy the granulite facies metamorphic grade with peak temperatures at 565 °C (Miller, 2008). Comparably the Port Nolloth Zone of the Gariep Belt would be best suited to uraniferous leucogranite hosted deposits, as the Port Nolloth Zone contains a similar sequence of variable-energy

siliciclastics, shelf carbonates, unconformities, diamictites and turbidites. A sequence which overlies a ~ 2 Ga basement of Namaqua Complex metamorphics (after Frimmel, 2000; Frimmel, 1995; Frimmel and Frank, 1998). The Gariep belt is well-endowed with mineral deposits and prospects, most notably the Skorpion and Rosh Pinah mines, both of which are the result of sedimentary exhalative and in the case of Skorpion, post-Gariep supergene enrichment (Frimmel *et al*., 2004). The sulphide-bearing units would be well-suited to interaction with uranium-bearing granites, however, the Gariep Belt is host to a limited number of post-orogenic intrusives, whose composition is not well-constrained and are dominated by alkali granite and alkali-seynites. Perhaps most telling is the subduction type orogenesis of the Gariep that would not have promoted incompatible rich, hydrous mineral-poor sheeted leucogranites that characterise the late orogenic suites of the Central Zone.

## 9.7 Recommendations for Further Work

As is often the case with economic geology, there is a continued shifting of research priority between academic interest and economic suitability. One of the more important considerations of the uranium deposits of the Central Zone, notwithstanding the recent discovery of the super large Husab deposit, is that the largest and therefore most economically viable deposits of the Central Zone have not necessarily all been discovered. There is potential for new large deposits, though regional aeromagnetic surveys do not suggest any promising targets in the immediate region of Husab, the Ida Dome, or Rössing.

In this sense, geological priority of the Central Zone should see a shift from a combination of brown- and greenfields dominated exploration to one of predominantly brownfield investigation and resource definition. Essentially existing targets need to be as well-understood as possible to take maximum advantage at the very onset of a commodity price upswing, for which uranium surely is due as the global community slowly moves away from carbon-intensive fossil fuels.

Although many new insights into uranium mineralisation of the primary deposits have been brought forward in this study, there remains considerable room for improvement in a few areas. In no order of importance, the following topics require more investigation:

**Age(s) of Mineralisation**: - It is clear that the leucogranites are about 508 Ma in age, but the time at which uranium mineralisation ceased is not absolutely certain. Uraninite may be forming at these deposits for a considerable period after emplacement, given the high heat flow of the region. The ca. 469 Ma uraninite age of Cross *et al*. (2011) constrains the age of primary uraninite. The very low Pb content (<1 wt.%) of coffinite suggests the secondary uranium minerals are geologically young, as radiogeic Pb as not accumulated.

**Isotope Geochemistry**: - Certain isotope ratios have been applied to the granitic suites of the Central Zone and have shown profound differences between the suites of intrusives, particulary with respect to time of emplacement and provenance. A systematic study of the uraniferous sheets from across the Central Zone is however, lacking.

**Sulphide Tenor:** - This study proposes that the sulphides must be derived from the metasediments, and are circulated through the systems by fluids derived from the magma and from the immediate reaction with the sediments at the contacts. What is not certain is whether the S is also present in the intruding granites. Determining whether the sulphides in the alaskites is of magmatic or metasedimentary origin may shed new light on the nature of the source rocks, and the contribution of $S^-$ to the mineralisaton process.

**Local Structural Controls**: - The very nature of the Central Zone deposits, large and low-grade, limits the extraction to high tonnage open pit operations. This lends itself to limited selectivity of ore as 100 tonnes ore more of ore are scooped at a time. As large deposits are exposed, such as at the Husab Mine, geologists can anticipate the exposure of a prime candidate for increasing the understanding of structural controls on alaskite geometry and consequently metal distribution within the deposits.

The first three fields of interest are perhaps more geologically significant, while the fourth is of particular interest to existing operations from a more economic perspective.

***References***

Note: This select list of sources consulted in the compilation of the thesis has been arranged according to the South African Journal of Geology method.

Abd El-Naby, H. H. (2009). "High and low temperature alteration of uranium and thorium minerals, Um Ara granites, south Eastern desert, Egypt." Ore Geology Reviews **35**: 436-446.

Abdalla, H. M., Ishihara, S., Matsueda, H., Abdel - Monem, A. A., 1996. On the albite - enriched granitoids at Um Ara area, Southeastern Desert, Egypt: I. Geochemical, ore potentiality and fluid inclusion studies. *Journal of Geochemical Exploration*, 57, 127–138.

Abraham, I.M., 2009. The nature, geology and spatial distribution of uranium minerals in the SK anomaly area, Rössing Mine, Namibia. MSc. Thesis, Univeristy of the Witwatersrand. 180pp.

Alexandre, P. and Kyser, T. K., 2005 Effects of Cationic Substitutions and Alteration in Uraninite, and Implications for the Dating of Uranium Deposits. *The Canadian Mineralogist*. 43, 1005 - 101.

Allsopp, H. L., Barton, E. S., Kröner, A., Welke, H. J. & Burger, A. J., 1983. Emplacement versus inherited isotopic age patterns: a Rb---Sr and U---Pb study of Salem-type granites in the central Damara Belt. In: Miller, R. McG. (ed.) *Evolution of the Damara Orogen. Special Publication of the Geological Society of South Africa* **11**, 281---287.

Anderson, H. and Nash, C., 1997. Integrated lithostructural mapping of the Rössing area, Namibia using high resolution aeromagnetic, radiometric Landsat data and aerial photographs. *Exploration Geophysics*, 28, 185–191.

Andreoli, M. A. G., Ashwal, L. D., Hart, R. J., Smith, C. B., Moore, J. M. and Stevens, G., 1992. Th - REE - U enriched charnockites of Namaqualand, South Africa: implications for granulite petrogenesis. Abstracts, Geocongress '92. Bloemfontein: *Geological Society of South Africa*, pp. 8–10.

Andreoli, M. A. G., Coetzee, H., Hart, R., Ashwal, L. D., Huizenga, J. M., Smit, A. and Brandl, G., 2003. The Erlank paradox: high - U granulites, low U - amphibolite - facies gneisses in the mobile belts of southern Africa. In: Cuney, M. (ed.) Extended Abstracts, Conference on Uranium Geochemistry, April 2003. Nancy: France, University of Nancy, pp. 47–50.

Andreoli, M. A. G., Hart, R. J., Ashwal, L. D. and Coetzee, H., 2006. Correlations between U, Th Content and Metamorphic Grade in the Western Namaqualand Belt, South Africa, with Implications for Radioactive Heating of the Crust. *Journal of Petrology*, 47, 1095 - 1118.

Andrew, M.C., 2009. Valencia Uranium Pty Ltd: Valencia Project, Namibia – Resource Update. *Technical Report*, Snowden Group.

Annesley, I.R., Madore, C., Kusmirski, R. & Bonli, T., 2000. Uraninite-bearing granitic pegmatite, Moore Lakes, Saskatchewan: petrology and U–Th–Pb chemical ages. *In* Summary of Investigations 2000, **2**. *Saskatchewan Geological Survey, Regina, Saskatchewan,* 201-211.

Annesley, I.R., Madore, C. & Portella, P. (2005): Geology and thermotectonic evolution of the western margin of the Trans-Hudson Orogen: evidence from the eastern sub-Athabasca basement, Saskatchewan. *Canadian Journal of Earth Sciences,* **42**, 573-597.

Ansdell, K.M., 2005. Tectonic evolution of the Manitoba– Saskatchewan segment of the Paleoproterozoic Trans-Hudson Orogen, Canada. *Canadian Journal of Earth Sciences*, **42**, 741-759.

Ansdell, K., Corrigan, D., Stern, R., and Maxeiner, R., 1999. Shrimp U-Pb geochronology of complex zircons from Reindeer Lake, Saskatchewan: implications for timing of sedimentation and metamorphism in the northwestern Trans-Hudson Orogen (abstract). Geological Association of Canada, Mineralogical Association of *Canada Joint Annual Meeting*, May 26-28, Sudbury, p3.

Ayers, J.C. and Watson, E. B., 1991. Solubility of Apatite, Monazite, Zircon, and Rutile in Supercritical Aqueous Fluids with Implications for Subduction Zone Geochemistry. *Philosophical Transactions of the Royal Society of London* **05**, 335:365-375.

Ayers, J.C. and Eggler, D. D., 1991. Saline aqueous fluids in equilibrium with silicate melt at mantle conditions: trace element partition coefficients and evidence for ionic behaviour. Geochimica et Cosmochimica Acta. (Submitted.)

Badenhorst, F.P. (1992). *Lithostratigraphy of area 2215 B and D of the Central Zone of the Damara orogen with emphasis on facies changes and regional correlation*. M.Sc.-thesis (unpublished), University of Port Elizabeth, Port Elizabeth, South Africa, 124p.

Barbour, E.A., 1983. Swakop Project, Prospecting Grant M46/3/600. Unpubl. rep., Western Mining Group (Pty), Ltd, 6pp.

Barbour, E.A., 1980. Report on prospecting activities for the period 9th April 1977 to 8th April 1980 - Prospecting Grant M46/3/600. Unpubl. rep., Western Mining Group (Pty) Ltd.

Barker, A. J., 1998. *Introduction to Metamorphic Textures and Microstructures*. 2nd Edition, Stanley Thornes, Cheltenham, p 92 - 95.

Barker, F., 1979. Trodhjemite: Definition, environment and hypotheses of origin. In: Barker F. (ed.) 1979 *Trondhjemites, dacites and related rocks*. Elsevier. pp 1 - 12.

Barnes, J. F. H., 1981. Some aspects of the tectonic history of the Khan-Swakop region of the Damara Belt, Namibia. Unpublished Ph.D. thesis, University of Leeds, 466 pp.

Barnes, S. J. and Sawyer E. W, 1980. An alternative model for the Damara mobile belt: ocean crust subduction and continental convergence. Precambrian Research, **13**, 297–336.

Basson, I, J. and Greenway, G., 2004. The Rössing uranium deposit: a product of late - kinematic localisation of uraniferous granites in the Central Zone of the Damara Orogen, Namibia. Journal of African Earth Sciences. 38, p 413–435.

Barsukova, M. L., Kuznetov, V. A., Dorofeyeva, V. A. and Khodakovskiy, L. I., 1979. Measurement of the solubility of rutile $TiO_2$ in fluoride solutions at elevated temperatures. *Geokhimiya*, **7**, 1017-1027.

Bau, M. and Dulski, P., 1995. Comparative study of yttrium and rare-earth element behaviours in fluorine-rich hydrothermal fluids. *Contributions to Mineralogy and Petrology*. **119- 2**, 213-223.

Berning, J., 1986. The Rössing uranium deposit, South West Africa / Namibia. In C. R. a. M. Anhaeusser, S. Johannesburg (Eds.) 1986 *Mineral Deposits of Southern Africa*. Geological Society of South Africa. II: 1819 - 1832.

Berning, J., Cooke, R., Hiemstra, S.A. and Hoffman, U., 1976. The Rössing Uranium Deposit, South West Africa. *Economic Geology*, 71. pp 351 - 368.

Bertram, N.G.E., 1982b. *Report in support of the application for renewal of Prospecting Grant M46/3/449*. Trekkopje Exploration and Mining Company (Pty) Limited, Prospecting Grant M46/3/449., 20 July, 1982

Bhargava, S. K., Rama, R., Pownceby, M., Grocott, S., Ring, B., Tardio, J. and Jones, L., 2015. A review of acid leaching of uraninite. Hydrometallurgy, **151,** 10–24.

Blevin, P. L., and Chappell, B. W., 1995. Chemistry, origin, and evolution of mineralized granites in the Lachlan fold belt, Australia: the metallogeny of I- and S-type granites: Economic Geology, **90**, 1604–1619.

Bons, D. P., Druguet, E., Hamann, I., Carreras, J., Passchier, C. W., 2005. Apparent boudinage in dykes. Journal of Structural Geology 26, 625–636.

Bowden, P., Herd, D. and Kinnaird, J.A., 1995. "The significance of uranium and thorium concentrations in pegmatitic leucogranites (alaskites), Rössing Mine, Swakopmund, Namibia." *Communications of the geological Survey of Namibia*. 10: 43 - 49.

Brandt, R., 1987. Granitic magmatism in the Damaran orogenic belt, Namibia. *Revista Brasileira de Geociências*, **17**, 459–463.

Brandt, R., 1985. Preliminary report on the Stratigraphy of the Damara sequence and the geology and geochemistry of Damaran granites in an area between Walvis Bay and Karibib. *Communications of the Geological Survey of Namibia* **1**. 31 - 43.

Briqueue, L., Lancelot, J.R., Valois, J. - P. and Walgenwitz, F., 1980. Géochronologie U - Pb et genèse d'un type de minéralisation uranifère: les alaskites de Goanikontès (Namibie) et leur encaissant, *Bulletin Centre Research Exploration et Production. Elf. Aquitaine*, **4**, 759 - 811.

Brookins, D.G., 1975. Coffinite–uraninite stability relations in the Grants Mineral Belt. *American Association of Petroleum Geologists Bulletin* 59, 905. (Appendix F1

Brynard, H. J. and Andreoli, M. A. G., 1988. An Overview of the Regional Geological setting of The Uraniferous Granites in the Damara Orogen, Namibia. Proceedings of the Technical Committee Meeting on Recognition of Uranium Provinces Organised by the IAEA in London, Sept., 1985.

Carmichael, I. S. E., 1991, The redox states of basic and silicic magmas: a reflection of their source regions?: Contributions to Mineralogy and Petrology, v. 106, p. 129–141.

Casas, I., de Pablo, J., Gimenez, J., Torrero, M.E., Bruno, J., Cara, E., Finch, R.J., Ewing, R.C., 1998. The role of $pe^-$, pH, and carbonate on the solubility of UO2 and uraninite under nominally reducing conditions. *Geochimica et Cosmochimica Acta*, **62** (13), 2223–2231.

Cesbron, F., Ildefonse, P. and Sichere, M - C., 1993. New Mineralogical Data on Uranophane and β - Uranophane; Synthesis of Uranophane. *Mineralogical Magazine*, **57**, no. 387, 301 - 308.

Chappell, B.W. and White, A.J.R., 1974a. Two contrasting granite types. *Pacific Geology,* **8**, 173 - 4.

Chappell, B.W. and White, A.J.R., 1974b. I-and S- type granites of the Lachlan Fold Belt. *Transactions of the Royal Society of Edinburgh: Earth Sciences*, **83**, 1-26.

Chappell B. W. and White A. J. R., 1992. I- and S-type granites in the Lachlan fold belt. Transactions of the Royal Society of Edinburgh: *Earth sciences* **83**, 1–26.

Chappell, B.W., White, A.J.R., William, I.S., Wyborn, D., 2004. Low and high-temperature granites. *Transactions. of the Royal. Society of Edinburgh. Earth Science*. **95**,125-140.

Chevychelov, V.Yu., Borodulin, G.P., and Zaraisky, G.P., 2010. Solubility of columbite, (Mn, Fe)(Nb, Ta)$_2O_6$, in granitoid and alkaline melts at 650–850°C and 30–400 MPa: An experimental investigation. *Geochemistry International*, 48, 5, 456-464. *Original Russian Text © V.Yu. Chevychelov, G.P. Borodulin, G.P. Zaraisky, 2010, published in Geokhimiya, 2010, Vol. **48**, No. 5, pp. 485–495*

Clarke, D. B. (1981). The Mineralogy of Peraluminous Granites: A Review." *Canadian Mineralogist*, **19**: 3-17.

Clemens, J.D. 2014. Element concentrations in granitic magmas: ghosts of textures past? *Journal of the Geological Society of London*, **171**, 13-19.

Clemens, J. D., and Steven G., 2012. What controls chemical variation in granitic magmas? Lithos, **134-135**, 317-329.

Clemens, J. D., Helps, P. A., Stevens, G., 2010. Chemical structure in granitic magmas - a signal from the source? Earth and Environmental Science Transactions of the Royal Society of Edinburgh, **100** (1-2), 159-172.

Clemens, J. D., Stevens, G., and Farina, F., 2011. The enigmatic sources of I-type granites: the peritectic connexion, *Lithos*, **126**, 174–181.

Clifford, T. N., Barton, E. S., Stern, R. A., and Duchesne, J-C, 2004. U-Pb zircon calendar for Namaquan (Grenville) crustal events in the granulitefacies terrane of the O'Okiep Copper District of South Africa. *Journal of Petrology*, **45** number 4 pages 669–691

Corner, B., 1983. An Interpretation of the Aeromagnetic Data Covering the Western Portion of the Damara Orogen in South West Africa/Namibia. *Special Publications of the Geological Society of South Africa*, **11**,339 - 354.

Corner, B., 1982. An Interpretation of the Aeromagnetic Data Covering Portion of the Damara Orogenic Belt, With Special Reference to the Occurrence of Uraniferous Leucogranite. *Per - 95*, Atomic Energy Corporation of South Africa.

Corner, B., 1981. '*An interpretation of the aeromagnetic data covering portions of the Damara Orogenic Belt with special reference to the occurrence of uraniferous granite'*, PhD thesis, University of the Witwatersrand, Johannesburg, South Africa.

Corrigan, D., Pehrsson, S., Wodicka, N. and De Kemp, E., 2009, The Paleoproterozoic Trans-Hudson orogen: a prototype of modern accretionary processes. *Geological Society of London, Special Publication*, **327**, 457-479.

Coward, M. P., 1983 The history of The Damaran Belt. In Miller, R. McG. (Ed.) *Evolution of the Damara Orogen of South West Africa/Namibia*. Special Publication of the Geological Society of South Africa, **11**, 515pp.

Cross, A., Jaireth, S., Rapp, R. and Armstrong, R., 2009. Reconnaissance-style EPMA chemical U–Th–Pb dating of Uraninite. Australian Journal of Earth Sciences: An International Geoscience Journal of the Geological Society of Australia, 58:6, 675-683.

Cuney, M., 1980a. Preliminary results on the petrology and fluid inclusions studies of the Rössing uraniferous alaskites. *Transactions of the Geological Society of South Africa,* 83, 39–45.

Cuney, M., 1980b. Petrography geochemistry and fluid inclusion studies of the Rössing alaskites and surrounding gneisses. *Nancy, Centre de Recherches sur la Geologie de l'uranium*. 58.

Cuney M., 2014. Felsic magmatism and uranium deposits. *Bulletin de la Société Géologique de France*, **185**, vol 2, 75-92.

Cuney, M., 2010. Evolution of Uranium Fractionation Processes through Time: Driving the Secular Variation of Uranium Deposit Types. *Economic Geology.* 105, 553–569.

Cuney, M., 2009. "The extreme diversity of uranium deposits." Mineralium Deposita **44**: 3-9.

Cuney, M. and Brisbin, D., 2009. "*SEG Uranium Deposit Models Course*" Society of Economic Geologists U2009 Conference, Keystone, Colorado Short Course.

Cuney M. and Friedrich M., 1987. Physicochemical and crystal-chemical controls on accessory mineral paragenesis in granitoids. Implications on uranium metallogenesis. - *Bull. Mineral*., **110**, 235-247.

Cuney, M., and Kyser K., 2008. Recent and not-so-recent developments in uranium deposits and implications for exploration: Mineralogical Association of Canada Short Course Series, v. **39**, 258 p

Da Silva, L.C., McNaughton, N.J., Hartmann, L.A., Fletcher, I.R., Gresse, P.G. and Scheepers, R., 1997. U-Pb (SHRIMP) isotopic constraints for the evolution of Southern Brazilian granitic province, and some correlated South African, Pan-African plutons.

*2nd International Symposium on Granites and Associated Mineralization, Salvador*, 24-29 August, 276-277.

Dana, E.S., 1892. *Dana's system of mineralogy,* (6th edition), 488-490.

Debon, F. & Le Fort, P., 1983. A chemical–mineralogical classification of common plutonic rocks and associations. *Transactions of the Royal Society of Edinburgh, Earth Sciences,* **73**, 135–149.

Deditius, A., Utsunomiya, S., Ewing, R., 2007. Alteration of $UO_{2+x}$ under oxidizing conditions, Marshall Pass, Colorado, USA. Journal of Alloys and Compounds, **444**, 584–589.

De Kock G. S., 2001. A reappraisal of the Namibian Damara stratigraphy in part of the Southern Swakop Terrane and its implications to basin evolution. South African Journal of Geology, **104**, 115 - 136.

De Kock, G.S., Eglington, B.E., Armstrong, R.A.., Harmer, R.E. and Walraven, F., 2000. U - Pb and Pb - Pb ages on the Naauwpoort rhyolite, Kawakeup leptite and Okongava diorite: implications for the onset of rifting and orogenesis in the Damara belt, Namibia. *Geological Survey of Namibia Communications. Henno Martin Special Publication*

De Kock, G.S. and Botha, B.J.V. (1989). Depositional environment and basin evolution of the Etusis Formation in the central Damara orogen. *South African Journal of Geology*, **92**, 183-196.

De la Roche, H., Leterrier J., Grande Claude, P. and Marcheal M., 1980 A classification of volcanic and plutonic rocks using R1 - R2 diagrams and major element analysis – its relationships and current nomenclature. *Chemical Geology,* **29**, 183 - 210. In Rollinson, H., 1993. *Using geochemical data: evaluation, presentation, interpretation*, 61 - 63.

Department of Economic Affairs., 1988. Application for extension of Prospecting Grant M.46/3/1496: Trekkopje Exploration and Mining. *Letter from Department of Economic Affairs* to The Chief Geologist, Gold Fields Prospecting, Windhoek. Dated 25 October 1988.

Dewey, J.F., Robb, L., Van Schalkwyk, L., 2006. Did Bushmanland extensionally unroof Namaqualand? Precambrian Research, **150** (3), 173–182.

Diehl, B. J. M., 1990. Geology, mineralogy, geochemistry and hydrothermal alteration of the Brandberg Alkaline Complex, Namibia. *Memoirs of the Geological Survey of Namibia*, 10, 55 pp.

Domine, F. and Velde, B., 1985, Preliminary investigation of the processes governing the solubility of uranium in the silicate melts. *Bulletin de Mineralogie*, **108**, 755-765.

Downing, K.N., 1983. The stratigraphy and palaeoenvironment of the Damara Sequence in the Okahandja Lineament zone. In: Miller, R.McG. (Ed.), *Evolution of the Damara Orogen of South West Africa*, Special Publication of the Geological Society of South Africa **11**, 37–41.

Downing, K. N. and Coward, M. P., 1981. The Okahandja Lineament and its significance for Damaran tectonics in Namibia. *Geologisch Rundschau,* **70**, 972–1000.

Dreissig, I., Weiss, S., Hennig C., Bernhard, G., Zänker H., 2011. Formation of uranium(IV)-silica colloids at near-neutral pH. Geochimica et Cosmochimica Acta, **75**, issue 2, 352-367.

Durr, S. B. and Dingledey, D. P., 1996. The Kaoko Belt (Namibia): part of a late Neoproterozoic continental-scale strike-slip system. *Geology*, **24**, 503-506.

Eberle, D., Andritzky, G., Wackerle, R., 1995. The new magnetic data set of Namibia: its contributions to the understanding of crustal evolution and regional distribution of mineralization. *Communications of the Geological Survey of Namibia,* **10**, 141–150.

Eby, G. N. and Charnley, N., 2009. Using apatite and biotite as monitors for the fluorine and chlorine concentrations of alkaline felsic magmas. *Geological Association of Canada – Mineralogical Association of Canada, Joint Annual Meeting, Ottawa 2009, Program with Abstracts* **34**, p.28.

Eby, G.N., 1992. Chemical subdivision of the A-type granitoids: petrogenetic and tectonic implications. *Geology,* **20**, 641–644.

Eby, G.N., 1990. The A-type granitoids: a review of their occurrence and chemical characteristics and speculations on their petrogenesis. *Lithos,* **26**, 115–134.

Eggleton, R. A. and Banfield, J. F., 1985. The alteration of granitic biotite to chlorite. *American Mineralogist*, **70**, 902-910.

El Bouseily, A. M., & El Sokkary, A. A., 1975. The relation between Rb, Ba and Sr in granitic rocks. Chemical Geology, **16**, 207–219.

El-Naby, H. H. A., 2009. High and low temperature alteration of uranium and thorium minerals, Um Ara granites, south Eastern Desert, Egypt. *Ore Geology Reviews,* **35**, 436–446.

Ellis, A. J. & Mahon, W. A. J., 1977. Chemistry and geothermal systems. Academic Press, New York. 403pp.

England, P. C. & Thompson, A. B., 1984. Pressure-temperature-time paths of regional metamorphism I. Heat transfer during the evolution of regions of thickened continental crust. *Journal of Petrology*, **25**, 894-928.

Ercit, T. S., 2005a. Identification and alteration trends of granitic-pegmatite-hosted (Y,REE,U,TH)–(Nb,Ta,Ti) oxide minerals: a statistical approach. *The Canadian Mineralogist*, **43**, 1291-1303.

Ercit, T.S., 2005b. REE-enriched granitic pegmatites. In: Linnen, R., Samson, I. (Eds.*), Rare Element Geochemistry and Mineral Deposits*. Geological Association of Canada, Short Course Notes, **17**, pp. 175–199.

Erlank, A. J., Marsh, J.S., Duncan, A. R., Miller, R. McG., Hawkesworth, C. J., Betton, P. J. and Rex, D. C., 1984. Geochemistry and petrogenesis of the Etendeka volcanic rocks from SWA/Namibia, 195 - 245. In Erlank, A. J. (Ed) Petrogenesis of the volcanic rocks of the Karoo Province. Special Publication of the Geological Society of South Africa, **13**, 395 pp.

Ervanne, H., 2004. Oxidation state analyses of uranium with emphasis on chemical speciation in geological media. PhD thesis, the Faculty of Science, University of Helsinki, 50 pp.

Extract Resources., 2009 Husab Zone 1 initial resource. Australian Stock Exchange Media Release, January 2009.

Ferry, J. M.,1985. Reaction mechanisms, physical conditions and mass transfer during hydrothermal alteration of mica and feldspar in granitic rocks from south-central Maine. *American Journal of Science*, **278**, 1025-56.

Finch, R.J., Ewing, R., 1991. Alteration of natural uranyl oxide hydrates in Si-rich groundwaters: implications for uranium solubility. *Materials Research Society Symposium Proceedings*, **257** (1).

Finch, R.J. and Ewing, R.C., 1992. The corrosion of uraninite under oxidising conditions. *Journal of Nuclear Materials*, **190**, 133 - 156.

Finch, R.J., Hanchar, J.M., 2003. Structure and chemistry of zircon and zircon group minerals. In: Hanchar, J.M., Hoskin, P.W.O. (Eds.), Zircon. *Review in Mineralogy*, **53**, 1–26.

Finnemore, S. H., 1978. The geochemistry and origin of the Matchless amphibolite belt, Windhoek District, South West Africa. *In*: Verwoerd, W. J., (Ed) *Mineralisation in metamorphic Terranes.* Special Publication of the Geological Society of South Africa, 4, 433-477.

Förster, H.-J., 2001. *Thorite-zircon-coffinite-xenotime solid solutions: Composition and origin*., 11th Meeting of the EUG (Strasbourg, France).

Förster, H. -J., 1999. The chemical composition of uraninite in Variscan granites of the Erzgebirge, Germany. Mineralogical Magazine, **63**(2), 239-252.

Förster, H.-J., Seltmann, R. and Tischendorf, G., 1995. High-fluorine, low-phosphorus A-type (post-collision) silicic magmatism in the Erzgebirge. *Terra Nostra*, 7, 32-35.

Franz, L., Romer, R. L. and Dingeldey, D. P., 1999. Diachronous Pan-African granulite-facies metamorphism (650Ma and 550 Ma) in the Kaoko belt, NW Namibia. *European Journal of Mineralogy*, **11**, 167-180.

Fredrickson, J.K., Zachara, J.M., Kennedy, D.W., Duff, M.C., Gorby, U.A., Li, S-M.W., and Krupka, K.M., 2000. Reduction of U(VI) in goethite (α-FOOH) suspensions by a dissimilatory metal-reducing bacterium. *Geochimica et Cosmochimica Acta, **64**, 3085-3098.*

Freemantle, G., 2012. *Results of a multi-disciplined investigation of uranium mineralisation in two refractory bearing, Husab Zone 1 drill holes*. Swakop Uranium Internal Report GF020 v003, 69pp.

Freemantle, G., 2011. *Field Testing of Innovx Delta Premium™ hand held XRF Spectrometer Report.* Swakop Uranium Internal Report, GF008 v003, 34pp.

Freemantle, G. G., 2006. *Investigation of the Accessory Mineral Assemblages of Sheeted Leucogranites from the Rössing Uranium Mine, Namibia*. BSc. Honours Research Project, University of the Witwatersrand, unpublished.

Friedrich, M., Cuney, M. and Poty, B., 1987, Uranium geochemistry in peraluminous leucogranites. *Uranium*, **3**, 353-385.

Frimmel, H. E., 1995. Metamorphic evolution of the Gariep Belt. *South African Journal of Geology*, **98**, 176-190.

Frimmel, H. E., 2000. The Pan-African Gariep Belt of southwestern Namibia and western South Africa. *Communications of the Geological Survey of Namibia*, **12**, 197-209.

Frimmel, H. E. and Frank, W., 1998. Neoproterozoic tectono - thermal evolution of the Gariep Belt and its basement, Namibia and South Africa. Precambrian Research 90, 1 - 28.

Frimmel, H. E., Jonasson, I. and Mubita, P., 2004. An Eburnean base metal source for sediment-hosted zinc-lead deposits in Neoproterozoic units of Namibia: Lead isotopic and geochemical evidence. *Mineralium Deposita*, **39**, 328-343.

Frondel, C., 1950a. Studies of uranium minerals. 1. Parsonsite and randite. *American Mineralogist*. 35, 245 - 250.

Frondel, C., 1958. Systematic mineralogy of uranium and thorium. *U.S. Geological Survey Bulletin*. 1064.

Frondel, C., 1950b. Mineral composition of gummite. *American Mineralogist*. 41, 539 - 568.

Frost, B. R., Barnes, C. G., Collins, W. J., Arculus, R. J., Ellis, D. J. and Frost, C. D., 2001. A Geochemical Classification for Granitic Rocks. *Journal of Petrology*, 42, no. 11, 2033.

Frost, M. T., O'Hara, K., Suddaby, P., Grant, G., Reid, A. F. W, and Zuiderwyk, M., 1976. A Description of Two Automated Control Systems for the Electron Microprobe. *X - Ray Spectrometry*. 5, 180 - 187.

Gauthier - Lafaye, F., Stille, P. and Bros, R., 2004. The Nuclear Fuel Cycle: Special cases of natural analogues Gieré, P. Stille, P. (Eds). The Gabon and Cigar Lake U ore deposits. *Geological Society, London, Special Publications*. 236, 123 – 134

GSN - 1. Labuschagne, A. N., 1975 Communication between Gold Fields (PTY.) Limited and Trekkopje Mining and Exploration Company Limited, Geological Survey of Namibia Archives.

GSN - 2. Divisional Secretary Anglo American Corporation South Africa Limited., 1975. Communication between Swakop Exploration (PTY.) Limited and Trekkopje Mining and Exploration Company, Geological Survey of Namibia Archives.

Gorman D.H. and Nuffield E. W., 1955 Studies of Radioactive Compounds: VIII - Uranophane and Beta - Uranophane. *American Mineralogist*. 40, 634 - 645.

Goscombe, B.D., Gray, D. and Hand, M., 2003a. Variation in Metamorphic Style along the Northern Margin of the Damara Orogen, Namibia. *Journal of Petrology*, **45**. *no.* 6, 1261-1295.

Goscombe, B. D., Passchier, C. W. and Hand, M., 2003b. Boudinage classification: end - member boudin types and modified boudin structures. *Journal of Structural Geology* **26**, 739-763.

Graeser, S. and Schwander H., 1987. Gasparite-(Ce) and monazite-(Nd): two new minerals to the monazite group from the Alps. *Schweizerische Mineralogische und Petrographische Mitteilungen.,* **67**, 103–113.

Grandstaff, D. E., 1976. A kinetic study of the dissolution of uraninite. *Economic Geology* **71**(8): 1493-1506.Greenaway, G., 2007. Valencia Uranium Pty Ltd: Valencia Project, Namibia – Resource Update. *Technical Report*, Snowden Group

Gray, T., 2015, *The Geological Setting of Uranium Mineralisation in the Rössing Area, Namibia* PhD thesis, University of the Witwatersrand, Johannesburg, South Africa, unpublished.

Gray, D. R., Foster, D. A., Meert, J. G., Goscombe, B. D., Armstrong, R., Trouw, R. A. J. And Passchier, C. W., 2008. *A Damara Orogen perspective on the assembly of southwestern Gondwana*. Geological Society, London, Special Publications, 294; p. 257-278.

Gratz, R. and Heinrich, W., 1997. Monazite-xenotime thermobarometry: experimental calibration of the miscibility gap in the binary system $CePO_4$-$YPO_4$. American Mineralogist, **82**, 772-780.

Guillaumont, R., Fanghanel, T., Fuger J., Grenthe, I., Neck, V, Palmer, D. A. and Rand, M. H., 2003, Update on the chemical thermodynamics of Uranium, Neptunium, Plutonium, Americium and Technecium. NEA-OECD, **5**.

Haack U. and Hoffer E., 1976. K/Ar ages of biotites from the Damara orogen, South West Africa. Transactions of the Geological Society of. South Africa, **79**, 213–216.

Haack, U., Gohn, E. and Klein, J. A., 1980. Rb/Sr ages of granitic rocks along the middle reaches of the Omaruru River and the timing of orogenetic events in the Damara Belt (Namibia). *Contributions to Mineralogy and Petrology* 74, 349 - - - 360.

Haack, U., Hoefs, J. and Gohn, E., 1982. Constraints on the origin of Damaran granites by Rb/Sr and ð18O data. *Contributions to Mineralogy and Petrology* 79, 279 - 289.

Haack, U., Gohn, E. and Hartmann, O., 1983 'Radiogenic heat generation in Damaran rocks', in 'Evolution of the Damara Orogen of southwest Africa/Namibia,' (ed. R. McG. Miller), Special Publication 11, 225–231. Geological Society of South Africa.

Hambleton-Jones, B. B., 1984, Surficial uranium deposits in Namibia, in Toens, D., project leader, Surfical uranium deposits. Report for the working group on uranium geology organised by the International Atomic Energy Agency: Vienna, Austria, Report IAEA-TECDOC-322, p. 205-216.

Harris, C., 1995. The Oxygen Isotope Geochemistry of the Karoo and Etendeka Volcanic Provinces of Southern Africa. *South African Journal of Geology.,* 98, 126 - 139.

Hartmann, O., Hoffer, E., Haack, U., 1983. Regional metamorphism in the Damara orogen: interaction of crustal motion and heat transfer. In: Miller, R.McG. (ed.) *Evolution of the Damara orogen of South West Africa/Namibia*. Special Publication of the Geological Society of South Africa., **11**, 233–241.

Hawkesworth, C.J. and Marlow, A.G., 1983, Isotope evolution of the Damara Orogenic Belt, 397-407. In: Miller, R.McG. (ed.) *Evolution of the Damara orogen of South West Africa/Namibia*. Special Publication of the Geological Society of South Africa., **11**, 515 pp.

Hawkesworth, C.J., Gledhill, A.R., Roddick, J.C., Miller R. McG. and Kröner, A., 1983, Rb-Sr and 40Ar/39Ar studies bearing on models for the thermal evolution of the Damara Belt, Namibia, 323-338. In: Miller, R.McG. (ed.) *Evolution of the Damara Orogen of South West Africa/Namibia.* Special Publication of the Geological Society of South Africa., **11**, 515 pp.

Halverson, G. P., Maloof, A. C. and Hoffman, P. F., 2004. The Marinoan glaciation (Neoproterozoic) in northeast Svalbard. *Basin Research*, 16, 297-324.

Hambleton-Jones, B. B., & Toen, P.D., 1978. The geology and geochemistry of calcrete/gypcrete uranium deposits in duricrust, Namib desert, South West Africa. *Economic Geology*, **73**, 1407-1408.

Hamilton, M.A. and Delaney, G., 2000. New U–Pb geochronological constraints on the age of basement and cover in the eastern Wollaston Domain, Saskatchewan, and evolution of the SE Hearne Province. Geological Association of Canada. – Mineralogical Association of Canada, Program Abstracts. **25**, 1103.

Hansley P. L. and J. J. Fitzpatrick 1989. Compositional and Crystallographic Data on REE - bearing Coffinite from the Grants Uranium Region & Northwestern New Mexico. *American Mineralogist*. 74, 263 - 270.

Hemingway, B.S., 1982. Thermodynamic properties of selected uranium compounds and aqueous species at 298.15 K and 1 bar and at higher temperatures. Preliminary models for the origin of coffinite deposits. *United States Geology Survey Open - File Report.* 82 - 619, 90 pp.

Henry, G., 1992 *The sedimentary evolution of the Damara Sequence in the lower Khan River valley, Namibia*. PhD thesis, University of the Witwatersrand, Johannesburg, South Africa.

Herd, D. A., 1996. *Geochemistry and mineralisation of alaskite in selected areas of the Rössing Uranium Mine, Namibia.* M.Sc. dissertation (unpubl.), University of St. Andrews, Scotland. 144pp.

Hewett, D. F., Stone, J. and Levine, H., 1957 Brannerite from San Bernardino County, California. *American Mineralogist*. 42, 30 - 38.

Hiemstra, S.A., 1968. The determination of the relative amounts of uraninite and secondary uranium - bearing minerals in nine samples from the underground

workings at Rössing. *Confidential Research Report for Rössing Uranium Ltd.,* 384, National Institute of Mining.

Hiemstra, S. A., 1967. Rössing: Uranium Prospect in South West Africa. *Confidential Research Report,* 220, National Institute of Mining.

Hiemstra, S.A. and Beukes G.J., 1969. A Petrological Study of Forty Rock Specimens from Rössing, South West Africa. *Confidential Research Report for Rössing Uranium Ltd.,* 431, National Institute of Mining.

Hiemstra, S. A., Simpson, A. B. and Grote, E. W., 1968. Mineralogical examination of uraniferous concentrates from borehole RD2, Rössing, South West Africa. *Confidential Research Report For Rössing Uranium Ltd*., 387, National Institute of Mining.

Hippert, J. F., 1998. Myrmekite; constraints on the available models and a new hypothesis for its formation. *European Journal of Mineralogy*, 10, 317-331.

Hoernes, S. and Hoffer, E., 1979. Equilibrium of prograde metamorphic mineral assemblages. A stable isotope study of rocks of the Damara Orogen from Namibia. *Contributions to Mineralogy and Petrology.* 68, 377 - 389.

Hoffer, E., 1977. *Petrologische Untersuchungun zur Regionalmetamorphose Al - reicher Metapelite im südlichen Damara - Orogen (Südwest - Afrika).* Habilitationsschrift, University Göttingen, 150pp.

Hoffer, E., 1975. The reaction sillimanite+biotite+quartz⇌cordierite +K - feldspar+H2O and partial melting in the system K2O - FeO - MgO - Al2O3 - SiO2 - H2.

Hoffmann, K.H., 1990. Sedimentary depositional history of the Damara Belt related to continental breakup, passive to active margin transition and foreland basin development. *Abstracts. Geocongress '90, Geological Society of South Africa, Cape Town, South Africa*, 250-253.

Hoffmann, K. – H., 1987(a). application of tectonostratigraphic terrane analysis in the Damara Province central and northern Namibia, 25-27. *In*: Hartnady, C. J. H. (Ed.). *Proc. Abstr. Alex L. du Toit Golden Jubilee Conference on tectonostratigraphic strain analysis*. 17 October, Cape Town, Precambrian Research Unit, University of Cape Town (South Africa), 69 pp.

Hoffman, K. - H., 1983. Lithostratigraphy and facies of the Swakop Group of the southern Damara Belt, SWA/Namibia. In Miller, R. McG. (Ed.) *Evolution of the Damara Orogen of South West Africa/Namibia*. Special Publication of the Geological Society of South Africa, 11, 515pp.

Hoffmann, K.H., Condon, D.J., Bowring, S.A., and Crowley, J.L., 2004. A U-Pb zircon date from the Neoproterozoic Ghaub Formation, Namibia: Constraints on Marinoan glaciation: Geology, **32**, p. 817–820.

Hoffman, K.-H., Hawkins, D.P., Isachsen, C.E., Bowring, S.A., 1996. Precise U–Pb zircon ages for early Damaran magmatism in the Summas Mountains and Welwitschiainlier, northern Damara belt, Namibia. *Communications of the Geological Survey of Namibi*a 11, 47–52.

Hoffmann, K.-H., Prave, A. R., 1996. A preliminary note on a revised subdivision and regional correlation of the Otavi Group based on glaciogenic diamictites and associated cap dolostones. Communications of the Geological Survey of Namibia, 11, p 77 - 82.

Hoffman, P.F., 1990. Subdivision of the Churchill province and extent of the Trans-Hudson Orogen. In: *The Early Proterozoic Trans-Hudson Orogen of North America* (J.F. Lewry & M.R. Stauffer, eds.). Geological Association of Canada. Special Paper, **37**, 15-39.

Hoffman, P. F., 2005. 28th DeBeers Alex Du Toit Memorial Lecture, 2004. On Cryogenian (Neoproterozoic) ice - sheet dynamica and the limitations of the glacial sedimentary record. *South African Journal of Geology*, 108, 557 - 577.

Hoffman, P. F., 2002. Carbonates bounding glacial deposits:P Evidence for Snowball earth episodes and greenhouse aftermaths in the Neoproterozoic Otavi Group of northern Namibia. *16th international Sedimentological Conference, Excursion Guide*, Auckland Park, 39 pp.

Hogarth, D.D., 1989. Pyrochlore, apatite and amphibole: distinctive minerals in carbonatite. *In:* Bell, K. (Ed.), *Carbonatites, Genesis and Evolution.* Unwin Hyman, London, 105 - 148.

Hogarth , D. D., 1977. The Pyrochlore Group. *American Mineralogist,* 62, 430 - 410.

Hudleston, P. J., 1973. Fold morphology and some geometrical implications of theories of fold developed. *Tectonophysics*, v. 16, pp. 1-46.

Hanly, A. (Ed), 2014. *Uranium 2014: Resources, Production and Demand. A Joint Report by the OECD Nuclear Energy Agency and the International Atomic Energy Agency* English, 504 pages, published: 09/09/14 NEA#7209 Volume of the series: Nuclear Development Available online at: http://www.oecd-nea.org/ndd/pubs/2014/7209-uranium-2014.pdf.

Inwood, N., 2011. National Instrument 43-101 Technical Report Ida Dome - August 2008 Resource Update. Coffey Mining

Ishihara, S., 1977. The magnetite - series and ilmenite - series granitic rocks. *Mining Geology*. 27, 293–305.

Ishihara, S., 1971. Modal and chemical composition of the granitic rocks related to the major molybdenum and tungsten deposits in the inner zone of southwest Japan. *The Journal of the Geological Society of Japan*. 77, 441–452.

Ishihara, S., and Ulriksen, C. E., 1980. The magnetite-series and ilmenite-series granitoids in Chile. *Mining Geology*, **30**, 183–190.

Ishihara, S., and Wang, P. A., 1999. The ilmenite-series and magnetite-series classification of the Yanshanian granitoids of South China: Bulletin of Geological Survey of Japan, **50**, 661–670.

Jacob, R.E., 1975. Granite Genesis and Associated Mineralisation in Part of the Central Damara Belt. In Verwoerd, W.J., 1975 (Ed*.) Mineralisation in Metamorphic Terranes - 'Papers presented at "Geokongres 75*", the Sixteenth Congress of the Geological society of South Africa held at the University of Stellenbosch, 30 June - 4 July, 1975*. no.* 27, 417 - 432.

Jacob, R.E., 1974(a). Geology and metamorphic petrology of part of the Damara Orogen along the lower Swakop River, South West Africa. Bulletin 17 Chamber of Mines, Precambrian Research Unit, University of Cape Town.

Jacob, R. E., 1974(b). The radioactive mineralisation in part of the central Damara Belt, South West Africa, and its possible origin. Report PIN - 234(BR), Pelindaba, Atomic Energy Board, South Africa.

Jacob, R. E., Corner, B., Brynard, H.J., 1986. The regional structural and geological setting of the uraniferous granitic provinces of Southern Africa. In: Anhaeusser, C.R., Maske, S. (Eds.), Mineral Deposits of Southern Africa, vol. II. Geological Society of South Africa, Johannesburg, 1807–1818.

Jacob, R.E. and Kerber, P., 1997. Geology of the area around the main tailings dam, Rössing Uranium Mine. Unpublished Report, *Rhodes University*, 28 pp.

Jacob, R.E., Moore, J. M. and Armstrong, R. A., 2000. Zircon and titanite age determination from igneous rocks in the Karibib District, Namibia: implications for Navachab vein – style gold mineralisation. *Communications of the Geological Survey of Namibia,* 12, 157 - 166.

Janeczek, J. and Ewing, R.C., 1992a. Coffinitisation — a mechanism for the alteration of $UO_2$ under reducing conditions. Materials Research Society Symposium Proceedings 257, 497–504.

Janeczek, J. and Ewing, R. C., 1992b. The structural formula of uraninite. Journal of Nuclear Materials, 190, 128-132.

Janeczek, J. and Ewing, R.C., 1992c. Dissolution and alteration of uraninite under reducing conditions. Journal of Nuclear Materials., 190, 157–173.

Jasper, M. J. U., Stanistreet, I G. and Charlesworth, E. G., 1992/1993. Preliminary results of a study of the structural and sedimentological evolution of the Late Proterozoic/Early Palaeozoic Gariep Belt, southern Namibia. *Communications of the Geological Survey of Namibia*, **8**, 99-118.

Jasper, M. J. U., Stanistreet, I G. and Charlesworth, E. G. 2000. Neoproterozoic inversion tectonics, half-graben depositories and glacial controversies, Gariep fold-thrust belt southern Namibia. In: Miller, R. M. (ed.) *Henno Martin Commerorative Volume*. Communications of the Geological Survey of Namibia, Windhoek, 1887-1896.

Jeppe, J.F.B., 1952. *The Geology of the area along the Ugab River, West of the Brandberg.* Ph.D. thesis (unpubl.), University of the Witwatersrand, Johannesburg, 224 pp.

Johannsen, A., 1931, A Descriptive Petrography of the Igneous Rocks, Volume 1 (p.88 - 92. *University of Chicago Press, Chicago*. 267p.

Johnson, P. R., Andresen, A., Collins, A.S., Fowler, A.R., Fritz, H., Ghebreab, W., Kusky, T., and Stern, R.J. 2011. "Late Cryogenian-Ediacaran history of the Arabian-Nubian Shield: A review of depositional, plutonic, structural, and tectonic events in the closing stages of the northern East African Orogen." Journal of African Earth Sciences **61**: 167-232.

Johnson, R., 2011. *Heavy mineral assemblage of the granites in the Rössing South uranium deposit, Namibia*. BSc. Honours research dissertation, University of the Witwatersrand, Johannesburg, unpublished.

Johnson, S. D., Poujol, M. and Kisters, A. F. M., 2006. Constraining the timing and migration of collisional tectonics in the Damara Belt, Namibia: U - Pb zircon ages for the syntectonic Salem - type Stinkbank granite. *South African Journal of Geology*, 109, 427–440.

Jung, S. and Mezger, K., 2003a. U - Pb garnet chronometry in high - grade rocks - case studies from the central Damara Orogen (Namibia) and implications for the interpretation of Sm - Nd garnet ages and the role of high U - Th inclusions. *Contributions to Mineralogy and Petrolog*y, 146, 382–396.

Jung, S., Mezger, K. and Hoernes, S, 1998. Petrology and geochemistry of syn - to post - collisional metaluminous A - type granites - a major and trace element and Nd - Sr - Pb - O isotope study from the Proterozoic Damara Belt, Namibia. *Lithos*, 45, 147–175.

Jung, S., Hoernes, S. and Mezger, K., 2000a. Origin of some Pan - African syn - tectonic S - type and post - tectonic A - type granites (Namibia) - products of melting of crustal sources, fractional crystallisation and wall rock entrainment. *Lithos,* 50, 259– 287.

Jung, S., Hoernes, S. and Mezger, K., 2000b. Geochronology and petrology of stromatic and nebulitic migmatites from the Proterozoic Damara Belt— importance of episodic fluid - present disequilibrium melting and consequences for granite petrology. *Lithos,* 51, 153–179.

Jung, S., Mezger, K. and Hoernes, S., 2001. Trace element and isotopic (Sr, Nd, Pb, O) arguments for a mid-crustal origin of Pan - African garnet - bearing S - type granites from the Damara Orogen (Namibia). *Precambrian Research,* 110, 325–355.

Jung S, Hoernes S, Mezger K, 2003b. Petrology of basement-dominated terranes: II. Contrasting isotopic (Sr, Nd, Pb, and O) signatures of basement-derived granites and constraints on the source region of granite (Damara orogen, Namibia). *Chemical Geology*, **199,**1–28

Jung, S., Mezger, K., Masberg, P., Hoffer, E., and Hoernes, S., 1998. Petrology of an intrusion - related high - grade migmatite— implications for partial melting of metasedimentary rocks and leucosome - forming processes. *Journal of Metamorphic Geology*, 16, 425– 445.

Jung, S., Hoffer, E., Masberg, P. and Hoernes, S., 1995. Geochemistry of granitic *in-situ* low-melt fractions— an example from the Central Damara orogen, Namibia*. Special Publications of the Geological Survey of Namibia,* **10,** 21–31.

Kasch, K. W., 1983b. Continental collision, suture progradation and thermal relaxation: a plate tectonic model for the Damara Orogen, 423-429. *In:* Miller, R. McG. (Ed.) Evolution of the Damara Orogen of South West Africa/Namibia. Special Publication of the Geological Society of South Africa, **11**, 515 pp.

Kennedy, W. Q., 1964. The structural differentiation of Africa in the Pan-African (± 500 m.y.) tectonic episode. *Annual Report - Research Institute of African Geology* **8**, 48-49, Leeds.

Kinnaird, J. A. and Nex, P.A.M., 2007, A review of geological controls on uranium mineralisation in sheeted leucogranites within the Damara Orogen, Namibia. *Transactions of the Institute of Materials, Minerals and Mining,* **116** no. **2**, 68-85.

Kinnaird, J. A. and Bowden, P., 1991. Magmatism and Mineralisation Associated with Phanerozoic Anorogenic Plutonic Complexes of the African Plate, 410 - 485. In Kampunzu, A. B. and Lubala, R.T. (Eds.) *Magmatism in Extensional Structural Settings.* Springer Verlag, Berlin. 637 pp.

Kinnaird, J. A. and Freemantle, G., 2009 *Field Guide to the Central Zone Uranium Occurences*. SEG U - 2009 Conference Field Trip, Namibia.

Kinnaird, J. A., Nex, P. A. M. and Freemantle, G., 2008 *Field Guide to the Central Zone Uranium Occurences*. SEG - GSSA: Africa Uncovered Conference Field Trip, Namibia.

Kinny, P. D., McNaughton, N. J., Fanning, C. M. and Maas, R., 1994 '518 Ma sphene (titanite) from the Khan pegmatite, Namibia, Southwest Africa: a potential ion microprobe standard', *Proceedings of the 8th International Conference* on 'Geochronology, Cosmo chronology and Isotope geology', US Geological Circular, Berkeley, CA, USA, 1107pp.

Kisters, A. F. M*.,* Smith Jordaan, L. and Neumaier, K., 2004.Thrust - related dome structures in the Karibib district and the origin of orthogonal fabric domains in the south Central Zone of the Pan - African Damara belt, Namibia. *Precambrian Research,* 133, 283–303.

Klein, J.A., 1980. 'Geological report on area 2115(a).' *Geol. Surv. S.W. Afr./Namibia* (unpubl.)

Klemme, S., Günther, D., Hametner, K., Prowatke S., Zack, T., 2006. The partitioning of trace elements between ilmenite, ulvospinel, armalcolite and silicate melts with implications for the early differentiation of the moon. Chemical Geology, **234**, 251-263.

Klemme, S., Prowatke, S., Hametner, K., Günther, D., 2005. The partitioning of trace elements between rutile and silicate melts: Implications for subduction zones. *Geochimica et Cosmochimica Acta*, **69**, 2361–2371

Kohn, S. C., Dupree, R., Mortuza, M. G. and Henderson, C. M. B., 1991. NMR evidence of five- and six-coordinated aluminium fluoride complexes in F-bearing alumino-silicate glasses. *American Mineralogist*, **76**, 309-312.

Korzeb, S.L., Foord, E.E. and Lichte, F.E., 1997. The chemical evolution and paragenesis of uranium minerals from the Ruggles and Palermo granitic pegmatites, New Hampshire. *The Canadian Mineralogist* 35, 135–144.

Kröner, A., 1984. *Dome structures and basement reactivation in the Pan - African Damara belt of Namibia*, 191 - 206. In Kröner, A and Greiling, R., 1984. (Eds) Precambrian tectonics illustrated, Stuttgart, Nagele u. Obermiller.

Kröner, A. and Hawkesworth, C., 1977. Late Pan - African emplacement ages for Rössing alaskitic granite (Damara belt) and Rooi Lepel bostonite (Gariep belt) in Namibia and their significance for the timing of metamorphic events, 20th Annual Report, Research Institute of African Geology, Leeds University, Leeds, UK, 14–17.

Kröner, A., Reteif, E. A., Compston, W., Jacob, R. E. and Burger, A. J., 1991. Single grain and conventional zircon dating of remobilised basement gneisses in the central Damara belt of Namibia. *South African Journal of Geology,* **94**, 379–387.

Kruger, T. M., 2016. *Controls of melt migration and emplacement around the Ida Dome, Damara Belt, and its bearing on uranium mineralization.* M.Sc. dissertation Stellenbosch University (unpublished)

Kruger, T. M. and Kisters, A. F. M., 2016. Magma accumulation and segregation during regional-scale folding: The Holland's dome granite injection complex, Damara belt, Namibia. *Journal of Structural Geology* **89**, 1-18.

Kukla, P. A. (1992). Tectonics and sedimentation of a Late Proterozoic Damaran Convergent Continental Margin, Khomas Hochland, Central Namibia. *Geological Survey of Namibia Memoirs*, **12**.

Kukla, P. A. & Stanistreet, I. A. (1991). Record of the Damaran Khomas Hochland accretionary prism in central Namibia: Refutation of an “ensialic” origin of a Late *Proterozoic orogenic belt. Geology*, **19**, 473-476.

Kukla, C., Kramm, U., Kukla, P. A. and Okrusch M., 1991. U-Pb monazite data relating to metamorphism and granite intrusion in the northwestern Khomas Trough, Damara Orogen, central Namibia. *Communications of the Geological Survey of Namibia*, **7**, 49–54.

Kyser, K. and Cuney, M., 2008. In Raeside, R. (Series Ed.) Geochemical Characteristics of Uranium and Analytical Methodologies. *Recent and Not - so - recent Developments in Uranium Deposits and Implications for Exploration*. Mineralogical Association of Canada Short Course Series, **39**, pp 23 - 55.

Labuschagne, A. N., 1979. The Anomaly 26 Uranium Prospect and its Environments Valencia 122. Prospecting *Grant M46/3/449. Unpublished Report*, Trekkopje Exploration and Mining Co. (Pty) Ltd, 68 pp.

Lacroix, A., 1912. Sur un groupe de niobo - tantalites cubiques (radioactifs) des pegmatites de Vakinankaratra. *Bulletin Societé Francais Minéralogie*, **35**, 84 - 92.

Langmuir, D., 1978. Uranium solution - mineral equilibria at low temperatures with applications to sedimentary ore deposits. *Geochimica et Cosmochimica Acta*, **42**, 547–569.

Latta D. E., 2010. *A geochemical investigation of heterogeneous REDOX reactions between Fe(II), Fe(III), and uranium.* PhD thesis, University of Iowa., 194 pp.

Le Maitre, R. W., 1989. A Classification of Igneous Rocks and Glossary of Terms: Recommendations of the International Union of Geological Sciences, Sub commission on the Systematics of Igneous Rocks. Oxford: Blackwell, 193 pp

Lehtonen, M. I., Manninen, T.E.T., and Schreiber, U.M. (1996). "Report on the lithostratigraphy of the area between the Swakop, Khan and lower Omaruru Rivers, Namib Desert." Communications of the Geological Survey, Namibia 11: 65-76.

Lewry, J.F. and Sibbald, T.I.I., 1977. Variation in lithology and tectonometamorphic relationships in the Precambrian basement of northern Saskatchewan. *Canadian Journal of Earth Sciences*. **14**, 1453-1467.

Lindskog, L. and Inwood, N., 2009. National Instrument 43 - 101 Technical Document - Etango Project, Namibia. Coffey Mining Technical Report 9512 - 090326.

Linnen, R.L., Keppler, H., 1997. Columbite solubilty in granitic melts: consequences for the enrichment and fractionation of Nb and Ta in the Earth's crust. *Contributions to Mineralogy and Petrology*. **128**, 213–227.

Loiselle, M.C. and Wones, D.R., 1979. Characteristics and origin of anorogenic granites. *Geological Society of America Abstracts with Programs*, **11**, 468pp.

Longridge, L., Kinnaird, J. A., Gibson, R. L. and Armstrong, R. A., 2014. Amphibolites of the Central Zone: New Shrimp U-Pb Ages and implications for the evolution of the Damara Orogen, Namibia. *South African Journal of Geology*, **117**, 67-86.

Longridge, L., 2012. *Tectonothermal evolution of the southwestern Central Zone, Damara belt, Namibia.* PhD Thesis. University of the Witwatersrand, Johannesburg. 524pp.

Longridge L., Gibson. R. L. and Kinnaird, J. A., 2009. Dome formation Mechanisms in the southwestern Central Zone of the Damara Orogen, Namibia. Trabajos de Geología, Universidad de Oviedo, **29**, 440 - 444.

Lovley, D.R., Phillips, E., 1992. Reduction of uranium by *Desulfovibrio desulfuricans*. *Applied Environmental Microbiology*, **58** (3), 850–856.

Ludington S. and Mossotti, V. G., 2008. Aluminium Saturation, alkalinity, and magma series. Abstract series, International Geological Congress, Oslo, 2008.

Lumpkin, G.R. and Ewing, R.C., 1996. Geochemical alteration of pyrochlore group minerals: betafite subgroup. *American Mineralogist,* **81**, 1237 - 1248.

Luth, W.C., Jahns, R.H. and Tuttle, O.F., 1964. The granite system at pressures of 4 - 10 kbar. *Journal of Geophysical Research*, 69, 759 - 773.

Maloof, A. C., 2000. Superposed folding at the junction of the inland and coastal belts, Damara Orogen, Namibia. In: Miller, R. McG. (Ed.), Henno Martin Commemorative Volume, **12**. *Communications of the Geological Survey of Namibia*, 89-98.

Manning, D. A. C., 1981. The effect of fluorine on liquidus phase relationships in the system Qz-Ab-Or with excess water at 1 kbar. *Contributions to Mineralogy and Petrology*, **76**, 257-262.

Mazzi, F. and Munno, R., 1983. Calciobetafite (new mineral of the pyrochlore group) and related minerals from Campi Flegrei, Italy; crystal structures of polymignyte and zirkelite: comparison with pyrochlore and zirconolite. *American Mineralogist*, **68**, 262-276.

Marlow, A. G., 1983. Geology and Rb - Sr geochronology of mineralised and radioactive granites and alaskites, Namibia. 289 - 298. In Miller, R. McG. (Ed.) *Evolution of the Damara Orogen of South West Africa/Namibia*. Special Publication of the Geological Society of South Africa, 11, 515pp.

Marlow, A. G., 1981. *Remobilisation and primary uranium genesis in the Damaran Orogenic Belt, Namibia.* Unpublished Ph.D. thesis, University of Leeds, 277 pp.

Martin, H., 1983. Overview of the geosynclinal, structural and metamorphic development of the intracontinental branch of the Damara Orogen. In: Martin, H., Eder, F.W. (Eds.), *Intracontinental Fold Belts*. Springer, Berlin, pp. 473–502.

Martin, H. and Porada, H. 1977. The intracratonic branch of the Damara Orogen in South West Africa. Discussion of geodynamic models. *Precambrian Research*, **5**, 311-338.

Martin, H., Porada, H., and Wittig, R., 1983. The root zone of the Naukluft Nappe Complex: Geodynamic implications, 679-698. In: Martin, H., and Eder, F.W. (Eds) *Intracontinental Fold Belts - Case Studies in the Variscan Belt of Europe and the Damara Belt in Namibia*. Springer-Verlag, Berlin, 945 pp.

Martin, R. F. (2006). A-type granites of crustal origin ultimately result from open-system fenitization-type reactions in an extensional environment. *Lithos*, **91**, 112-136.

Masberg, H. P., 2000 Garnet growth in medium - pressure granulite facies metapelites from the central Damara Orogen: igneous versus metamorphic history. Communications of the Geological Survey of Namibia. 12. 115–124.

Masberg, H. P., Hoffer, E. and Hoernes, S., 1992. Microfabrics indicating granulite - facies metamorphism in the low - pressure central Damara Orogen, Namibia. *Precambrian Research*, 55, 243–257.

McDermott, F., 1986 Granite petrogenesis and crustal evolution studies in the Damara Pan - African orogenic belt, Namibia. Ph.D. Thesis, Open University, Milton Keynes (unpublished).

McDermott, F., Harris, N.B.W. and Hawkesworth, C.J., 1989. Crustal reworking in southern Africa: constraints from Sr-Nd isotope studies in Archaean to Pan-African terrains. *Tectonophysics*, **161**: 257-270.

McDermott, Harris, N. B. W. and Hawkesworth, C. J., 1996. Geochemical constraints on crustal anatexis: a case study from the Pan - African Damara granitoids of Namibia, *Contributions to Mineralogy and Petrology.* 123, 406–423.

McDermott, F., Harris N. B. W. and Hawkesworth, C. J., 2000. Geochemical constraints on the petrogenesis of Pan - African A - type granites in the Damara Belt, Namibia. *Communications of the Geological Survey of Namibia*. 12, 139–148.

McDonough, W. F. and Sun, S. –s., 1994. The composition of the Earth. Chemical Geology, **120**, 223-253.

McKechnie, C. L., 2012. The Fraser lakes Zone B U-Th-REE deposit and its host rocks: Implications for pegmatite- and leucogranite-hosted U-Th-REE deposits in northern Saskatchewan, Canada. Department of Geological Sciences. Saskatoon, University of Saskatchewan**:** 301.

McKechnie, C. L., Annesley, I. R. and Ansdell, K. M., 2012. Medium to low-pressure pelitic gneisses of Fraser Lakes Zone B, Wollaston Domain, northern Saskatchewan, Canada: mineral compositions, metamorphic p–t–t path, and implications for the genesis of radioactive abyssal granitic pegmatites.

Mercadier, J., Annesley, I. R., McKechnie, C. L., Bogdan, T. S., and Creighton, S., 2013. Magmatic and Metamorphic Uraninite Mineralization in the Western Margin of the Trans-Hudson Orogen (Saskatchewan, Canada): A Uranium Source for Unconformity-Related Uranium Deposits? *Economic Geology,* 108, 1037–1065.

Mercadier, J., Cuney, M., Lach, P., Boiron, M.-C., Bonhoure, J., Richard, A., Leisen, M., and Kister, P., 2011. Origin of uranium deposits revealed by their rare earth element signature: *Terra Nova*, **23**, 264-269.

Michel - Lévy, A. and Lacroix, A. 1890. Compte Rendus Acad. Fr.61, 846.

Milani, L., Kinnaird, J. A., Lehmann, J., Naydenv, K. V., Saalmann, K., Frei, D. and Gerdes, A., 2014. Role of crustal contribution in the early stage of the Damara Orogen, Namibia: new constraints from combined U-Pb and Lu-Hf isotopes from the Goas Magmatic Complex. *Gondwana Research*, in press, corrected proof.

Miller, R. McG., 1983a. 'The Pan - African Damara Orogen of South West Africa/Namibia, 431 - 515. *In* Miller, R. McG. (Ed.) *Evolution of the Damara Orogen of South West Africa/Namibia*. Special Publication of the Geological Society of South Africa, 11, 515pp.

Miller, R. McG., 1983b. Tectonic implications of contrasting geochemistry of Damara mafic volcanic rocks, South West Africa/Namibia. E*volution of the Damara Orogen of South West Africa/Namibia*. Special Publication of the Geological Society of South Africa, 11, 115-138.

Miller, R. McG., 2008. The Geology of Namibia. The Geological Survey of Namibia Special Publication. Vol. II

Miller, C.F., McDoweH, S.M., Mapes, R.W., 2003. Hot and cold granites? Implications of zircon saturation temperatures and preservation of inheritance. *Geology.* **31** , 529-532.

Min, M., Fanga, C. and Fayek, M., 2005 Petrography and genetic history of coffinite and uraninite from the Liueryiqi granite - hosted uranium deposit, SE China. *Ore Geology Reviews.* 26, 187–197

Mitchell, R. H. and Kjarsgaard, B. A., 2003. Solubility of niobium in the system CaCO3-$Ca(OH)_2$-$NaNbO_3$ at 0-1 GPa pressure', *Contributions to Mineralogy and Petrology*, **144**, 93–97.

Miyashiro, A., 1970. Volcanic rock series in island arcs and active continental margins. *American Journal of Science.* 274, 321 - 355.

Montel, J.M., 1986. Experimental determination of the solubility of Ce-monazite in SiO2-Al2O3-K2O-Na2O melts at 800°C, 2 kbar, under H2O- saturated conditions: Geology, v. 14, 659-662.

Moore, J. M. and McStay, J. H., 1990. The formation of allanite- (Ce) in calcic granofelses, Namaqualand, South Africa. *Canadian Mineralogist,* **28**, 77-86.

Mossman D. J., 1985. Davidite: A Review of Canadian Occurences and Report on a Recent Find at Kommes Lake, Saskatchewan. *The Canadian Mineralogist.* 23, 495 - 500.

Mouillac, J.L., Valois, J - P. and Walgenwitz, F., 1986. The Goanikontes Uranium Occurence4in South West Africa/Namibia. In Anhaeusser, C.R. and Maske, S. (Eds.) 1986. *Mineral Deposits of Southern Africa.* Volume II. 1833 - 1843.

Munoz, J. L., 1992. Calculation of HF and HCl fugacities from biotite compositions: revised equations. *Geological Society of America, Abstract Programs* **24**, A221.

Munoz, J. L., 1984. F-OH and Cl-OH exchange in mica with application to hydrothermal ore deposits. *Reviews in Mineralogy*., 13, 469-493.

Nield, T., 2002. Mining uranium the Namibian way. *Geoscientist.* 12*,* 1 - 7*.*

Nagel, R., 1999. *Eine Milliarde Jahre geolgischer Entwicklung am NW-Rand des Kalahari Kratons.* Dr. Rer. Nat. Thesis, University of Göttingen, 171 pp.

Nash, C.R., 1971. Metamorphic petrology of the SJ area, Swakopmund District, South West Africa. *Bulletin of the Precambrian Research Unit,* 9. *University of Cape Town*.

Nesbitt, H.W. and Young, G.M., 1984. Prediction of some weathering trends of plutonic and volcanic rocks based upon thermodynamic and kinetic considerations. *Geochimica et Cosmochimica Acta*. 48, 1523 - 1534.

Nesbitt, H.W. and Young, G.M., 1989. Formation and diagenesis of weathering profiles. *Journal of Geology*, 97, 129 - 147.

Nesse, W.D., 2000. *Introduction to Mineralogy.* Oxford University Press, USA. 438 pp.

Nex, P.A.M., 1997. *Tectono - metamorphic setting and evolution of granitic sheets in the Goanikontes area, Namibia.* Ph.D. Thesis (Unpubl.). National University of Ireland.

Nex, P.A.M. and Kinnaird, J.A., 1995 Granites and their mineralisation in the Swakop River area around Goanikontes, Namibia. *Communications of the Geological Survey of Namibia.* 10, 51 - 56.

Nex, P. A. M., Herd, D. and Kinnaird, J., 2002. Fluid extraction from quartz in sheeted leucogranites as a monitor to styles of uranium mineralisation: an example from the Rössing area, Namibia. *Geochemistry: Exploration, Environment, Analysis.* 2, 83 - 96.

Nex, P. A. M., Kinnaird, J. and Herd, D., 2003. The occurrence, mineralogy and chemistry of betafite and pyrochlore from sheeted leucogranites of the Rössing area, Namibia: Implications for the composition of ceramics for radioactive waste disposal. *Economic Geology Research Institute Research Circular,* 374, 24pp. University of the Witwatersrand, School of Geosciences.

Nex, P.A.M., Kinnaird, J.A. and Oliver, G.J.H., 2001(a)) Petrology, geochemistry and uranium mineralisation of post collisional magmatism around Goanikontes, southern Central Zone, Namibia. *Journal of African Earth Sciences*. 33, 481 - 502.

Nex, P. A. M., Kinnaird, J.A. and Oliver, G. J. H., 2001(b)). Spinel bearing assemblages and PT - t evolution of the Central Zone of the Damara Orogen, Namibia. Journal of African Earth Sciences. 32, 471–498.

Nockolds, S. R. and Allen, R., 1956. The geochemistry of some igneous rock series_III. *Geochimica et Cosmochimica Acta*, 9, 34 - 77.

Oliver, G.J.H., 1994. Mid - crustal detachment and domes in the central zone of the Damaran Orogen, Namibia. *Journal of African earth Sciences,* 19, *no.* 4, 331 - 344.

Oliver, G. J. H., 1995. The Central Zone of the Damara Orogen, Namibia as a deep metamorphic core complex. *Communications of the Geological Survey of Namibia.* 10, 33–41.

Oliver, G. J.H. and Kinnaird, J. A., 1996. The Rössing SJ Dome, Central Zone, Damara Belt, Namibia: an example of mid - crustal extensional ramping, *Communications of the Geological Survey of Namibia*, 11, 53–64.

Page D. C., and Watson, M., D., 1976. The Pb-Zn deposit of Rosh Pinah Mine, South West Africa. *Economic Geology,* vol. 71 no. 1 306-327

Palache, C., Berman, H., and Frondel, C., 1944. *Dana's system of mineralogy*. (7th edition), v. I, 542.

Parry, W. T. and Downey, L. M., 1982. Geochemistry of hydrothermal chlorite replacing igneous biotite. *Clays and Clay Minerals*, **30**, No. 2, 81-90.

Paschier, C.W. and Goscombe, B.D 2008 Pseudo - boudins in Pegmatite, Arunta, Australia. *Journal of Structural Geology*. 30, p. 273.

Pearce J. A. and Cann J. R., 1973. Tectonic setting of basic volcanic rocks using trace element analysis*. Earth and Planetary Sciences Letters*, **19**, 290-300,

Pearce, J.A., Harris, N.B. and Malpas, J., 1984. Trace element discrimination diagrams for tectonic interpretation of granitic rocks. *Journal of Petrology*, **25**, 956-983.

Piccoli, P., Candela, P., 1994. Apatite in felsic rocks: a model for the estimation of initial halogen concentrations in the Bishop Tuff (Long Valley) and Tuolumne intrusive suite (Sierra Nevada Batholith) magmas. *American Journal of Science,* **294**, 92-135.

Peiffert, C., Cuney, M. and Nguyen-Trung, C., 1994. Uranium in granitic magmas. Part I: Experimental determination of uranium solubility and fluid-melt partition coefficients

in the uranium oxide-haplogranite-H2O-$NaCO_3$ system at 770°C, 2 kbar. *Geochemica et Cosmochemica. Acta* 58, 2495-2507.

Peiffert, C., Nguyen-Trung C. and Cuney, M., 1996. Uranium in granitic magmas. Part II: Experimental determination of uranium solubility and fluid-melt partition coefficients in the UO2 - haplogranite - $H_2O$-halides system at 720-770°C, 200 MPa. *Geochemica et Cosmochemica. Acta* 60, 1515-1529.

Petford, N., Kerr, R.C., Lister, J.R., 1993. Dike transport of granitoid magmas. *Geology.* 21, 845–848.

Petford, N., Cruden, A.R., McCaffrey, K.J.W., Vigneresse, J. - L., 2000. Granite formation, transport and emplacement in the Earth's crust. *Nature.* 408, 669–673.

Pirajno, F., Phillips, D. and Armstrong, R. A., 2000. Volcanology and eruptive histories of the Erongo Volcanic Complex and the Paresis Igneous Complex, Namibia: implications for mineral deposit styles. *Communications of the Geological Survey of Namibia*, 12, 301 - 312.

Pirrie, D., Butcher, A. R., Power, M. R., Gottlieb, P. and Miller, G. L., 2004. Rapid quantitative mineral and phase analysis scanning electron microscopy (QemSCAN); potential forensic geoscience. In: Pye, K. and Croft, D. J. (eds) *Forensic Geoscience: Principles, Techniques and Applications.* Geological Society, London, Special Publication. 232*,* 123 - 136.

Plant, J.A., Simpson, P.R., Smith, B., Windley, B.F., 1999. Uranium ore deposits - products of the radioactive earth. In: Burns, P.C., Finch, R.J. (Eds.), Uranium: Mineralogy, Geochemistry and the Environment. Reviews in Mineralogy, 38. pp. 255–319.

Pointeau, V., Deditius, A. P., Miserque F., Renock, D., Becker, U., Zhang, J., Clavier, N., Dacheux, N., Poinssot, C. and Ewing, R.C., 2009. Synthesis and characterisation of coffinite. *Journal of Nuclear Materials.* 393, 449 - 458.

Poli, L., 1997. *Mid - crustal geodynamics of the Southern Central Zone, Damara Orogen, Namibia*. Ph.D thesis, St Andrews University, UK, 233 pp.

Poli, L. C. and Oliver, G. J. H., 2001 Constrictional deformation in the Central Zone of the Damara Orogen, Namibia. *Journal of African Earth Science*. 33, 303–321.

Porada, H. and Wittig, R., 1983. Turbidites and their significance for the geosynclinal evolution of the Damara Orogen, South West Africa/Namibia. In: R.McG. Miller (editor), *Evolution of the Damara Orogen of South West Africa/Namibia*. *Geological Society of South Africa Special Publication*, 11, 21 - 36.

Prior, L. L. and Robin, P. –Y. F., 1995. Retrograde metamorphic reactions in deforming granites and the origin of flame perthite. *Journal of Metamorphic Geology.* 13, 645 - 658.

Rafalskiv, R.P., 1963. Physicochemical investigation on forming conditions of Uranium ores. *Science Press*, Moscow, 165–182. (in Russian).

Rainaud, C., Master S., Armstrong, R. A., Robb, L.J., 2005. Geochronology and nature of the Palaeoproterozoic basement in the Central African Copperbelt (Zambia and the Democratic Republic of Congo), with regional implications. *Journal of African Earth Sciences*. **42**, 1–31.

Ram, R., Charalambous, F., McMaster, S., Pownceby, M., Tardio, J., Bhargava, S., 2013. An investigation on the dissolution of natural uraninite ores. Miner. Eng. 50, 83–92.

Ring, R.J., 1979. Leaching characteristics of Australian uranium ores. Australasian. Institute of. Mining and Metallurgy. **272**, 13–23.

Ritter, O., Weckmann, U., Vietor, T. & Haak, V., 2003. A magnetotelluric study of the Damara Belt in Namibia 1. Regional scale conductivity anomalies. *Physics of the Earth and Planetary Interiors*, **138**, 71-90.

Robb, L.J., 2005. '*Introduction to Ore - Forming Processes*'. p 1 - 74.

Robb, L. J., Thiel, K. and Vorwerk, R., 1986. Uraniferous leucogranites from the Namaqualand Metamorphic Complex: Part parallel—Uranium distribution and mineralisation processes. In: Anhaeusser, C. R. and Maske, S. (eds) *Mineral Deposits of Southern Africa,* Vol. II. Geological Society of South Africa, 1629–1650.

Robb, L. J., Armstrong, R. A. and Waters, D. J., 1999. Nature and duration of mid crustal granulite - facies metamorphism and crustal growth: evidence from single zircon U - Pb geochronology in Namaqualand, South Africa. *Journal of Petrology.* 40, 1747–1770.

Robit - Pointeau, V., Poinssot, C., Vitorge, P., Grambow, B., Cui, D., Spahiu, K. and Catalette, H., 2006 Assessment of the relevance of Coffinite formation within the near - field environment of spent nuclear fuel geological disposals, *Materials Research Society Symposium Proceedings,* **932,** 489–496pp.

Rösener, H. and Schreuder, C.P., 1994. 'Nuclear and Fossil Fuels - Uranium' in *Mineral Resources of Namibia.* Ch. 7.1, p. 1 - 59.

Rogers, J.J.W. and Adams, J.A.S., 1969. *Uranium*. In: K.H. Wedepohl (Editor*),* Handbook of Geochemistry. Springer, Berlin, Heidelberg, New York.

Rollinson, H., 1993. *Using geochemical data: evaluation, presentation, interpretation*. Longman Geochemistry Series. Longman Group, United Kingdom. 352 pp.

Rössing Uranium Limited 1988. Aspects of the regional, detailed and applied geology of the Rössing Uranium Mine. Internal Report (unpublished) Rössing Uranium Limited pp 50.

Rubin, J.N., Henry, C. D. and Price, J. G., 1989. Hydrothermal zircons and zircon overgrowths, Sierra Blanca Peaks, Texas. *American Mineralogist*, **89**, 865-869.

Sasaki, A., and Ishihara, S., 1979. Sulfur isotopic composition of the magnetite-series and ilmenite-series granitoids in Japan. *Contributions to Mineralogy and Petrology*, **68**, 107–115.

Sawyer, E.W., 1978. *Damaran structural and metamorphic geology of an area southeast of Walvis Bay, S.W. Africa/Namibia*. M.Sc. Thesis (Unpubl.). University of Cape Town.

Sawyer, E. W., 1981. Damaran structural and metamorphic geology of an area south-east of Walvis Bay, South West Africa/Namibia. *Memoirs of the Geological Survey, South West Africa*, **7***,* 83 pp.

Scaillet, B., Macdonald, R., 2003. Experimental constraints on the relationships between peralkaline rhyolites of the Kenya Rift Valley. Journal of Petrology, **44**, 1867–1894.

Schmidt A, Wedepohl K.H., 1983. Chemical composition and genetic relations of the Matchless amphibolite (Damara orogenic belt). Special Publication of the Geological Society of South Africa, **11**, 139–145.

Scott, T. B., Allen, G. C., Heard, P. J., Lewis, A. C., and Lee, D. F., Lee, 2005. The extraction of uranium from groundwaters on iron surfaces. *Proceedings of the Royal Society*, A, **461**, 1247–1259.

Shand, S. J., 1927. *Eruptive Rocks*. Murby, London.

Shand, S. J., 1943. Eruptive Rocks. Their Genesis, Composition, Classification, and Their Relation to Ore-Deposits with a Chapter on Meteorites. John Wiley & Sons, New York.

Sherman, D.M., Peacock, C.L. and Hubbard, C.G., 2008. Surface complexation of U(IV) on goethite (α-FeO.OH). *Geochimica et Cosmochimica Acta*, **72**, 298-310.

Skirrow, R. G., Jaireth, S., Huston, D. L., Bastrakov, E. N., Schofield, A., E. van der Wielen, S. E. and and Barnicoat, A. C., 2009. Uranium mineral systems: Processes, exploration criteria and a new deposit framework. Onshore *Energy and Minerals Division. Geoscience Australia,* Record 2009/20. 34 pp.

Skirrow, R.G., Jaireth, S., Huston, D.L. and Barnicoat, A., 2008. Uranium mineralising systems: a continuum of deposit styles? *Geological Society of Australia, Abstracts,* **89**, 228-229.

Smith, D.A.M., 1965. The geology of the area around the Khan and Swakop Rivers in South West Africa. *Memoir of the Geological Survey of South Africa* 1, 113pp.

Smith, D. A. M., 1961. *The Geology of the Area Around the Khan and Swakop Rivers in South West Africa.* PhD thesis, University of the Witwatersrand.

Smith, D.K., 1984: Uranium mineralogy. In *Uranium Geochemistry, Mineralogy, Geology, Exploration and Resources* (Vido, B. D., Ippolito, F, Capaldi, G. and P.R. Simpson, eds.). Institution of Mining and Metallurgy, London U.K. 43 - 71.

Smits, G., 1989. (U,Th) - bearing silicates in reefs of the Witwatersrand, South Africa. *The Canadian Mineralogist*, **27**, 643–655.

Söhnge, G., 2001. Journal of a Geologist. Geology Department, Stellenbosch University, 197 pp.

South African Committee for Stratigraphy (SACS), 1980. Stratigraphy of South Africa. Kent, L.E. (Comp); Part 1. *Lithostratigraphy of the Republic of South Africa, South West Africa/Namibia and the Republics of Bophuthatswana, Transkei, and Venda*. Handbook of the Geological Survey of South Africa, **8**.

Spivey, M., Penkethman, A. and Culpan, N., 2010. Geology and Mineralisation of the Recently Discovered Husab Uranium Deposit, Namibia. Society of Economic Geologists, Inc. Special Publication, **15**, 729 - 746.

Stanistreet, I.G., and Charlesworth, E.G., 2001. Damaran basement-cored fold nappes incorporating precollisional basins, Kaoko Belt, Namibia, and controls on Mesozoic supercontinental break-up. *South African Journal of Geology*, **104**, 1-12.

Stanistreet, I. G., Kukla, P. A. and Henry, G. 1991. Sedimentary basinal response to a Late Precambrian Wilson cycle: the Damara orogen and Nama foreland, Namibia. *Journal of African Earth Sciences*. **13**, 141-156.

Stieff, L.R., Stern, T.W. and Sherwood, A.M., 1956. Coffinite, a uranium silicate with hydroxyl substitution: a new mineral. *American Mineralogist,* **41**, 675– 688.

Streckeisen, A., 1976. To each plutonic rock its proper name. Earth Science Review, **12**, 1-33.

Streckeisen, A. and Le Maitre, R. W., 1979. A chemical approximation to the modal QAPF classification of the igneous rocks. *Neues Jahrbuch fur Mineralogie Abhandlung,* 136, 169–206. In Nesse, W.D., 2000. *Introduction to Mineralogy, pages* 186 - 188.

Tack, L. and Bowden, P., 1999. Post - collisional granite magmatism in the central Damaran (Pan African) Orogenic Belt, western Namibia. *Journal of African earth Sciences,* **23**, *no.* 3, 653 - 674.

Tack, L., Williams, I. and Bowden, P., 2002. SHRIMP constraints on early post - collisional granitoids of the Ida Dome, central Damara (Pan African) Belt, western Namibia. Abstract 11th IAGOD *Quadrennial Symposium and Geocongress, Windhoek, Namibia.* Geological Survey of Namibia.

Takagi, T. and Tsukimura, K., 1997. Genesis of oxidized - and reduced - type granites. *Economic Geology*, 92, 81–86.

Taylor, S.R., Heier, K.S. and Sverdrup, P.L., 1960. Contribution to the mineralogy of Norway, **5**. Trace element variations in three generations of feldspars from the Landsverk I pegmatite, Evje, southern Norway. *Norsk Geologisk Tidsskrift.,* 40: 133--156.

Taylor, S. R. and McClennan, S. M., 1985. The continental crust: its composition and evolution', 312pp. Oxford, Blackwells.

Tjimunee, D. (2009). Variation of rare earth elements in mineralised and unmineralised sheeted leucogranites of the Etango Project, Namibia. Johannesburg, University of the Witwatersrand**:** 92.

Toch B., 2013. Emplacement controls of leucogranite sheets in the Swakop River, Damara Belt, Namibia. BSc. Honours research thesis, University of Stellenbosch, Western Cape, South Africa, unpublished.

Toogood, D.J., 1976. Structural and metamorphic evolution of a gneiss terrain in the Namaqua belt near Onseepkans, South West Africa. *Bulletins Precambrian Research Unit,* Cape Town, **19**, 189 pp.

Townend, R., 2009. Preparation of one polished thin section of one drill core and examination (optical/SEM) for uranium minerals. Concentration of heavy minerals from part crushed drill core in TBE liquid and XRD identification (RDD023-362m). Confidential report prepared for Extract Resource by Roger Townend and Associates Consulting Mineralogists, ref 22600. 7 pp.

Tran, H.T., Ansdell, K.M., Bethune, K.M., Ashton, K., and Hamilton, M.A., 2008. Provenance and tectonic setting of Paleoproterozoic metasedimentary rocks along the eastern margin of Hearne craton: Constraints from SHRIMP geochronology, Wollaston Group, Saskatchewan, Canada. *Precambrian Research*, **167**, 171-185.

Trumbull, R. B., Bühn, B., Romer, R. L. and Volker, F., 2003. The petrology of basanite - tephrite intrusions in the Erongo complex and implications for a plume source of Cretaceous alkaline complexes in Namibia. Journal of Petrology, **44**, 93 - 112.

Tuttle, O.F. and Bowen, N.L., 1958, The origin of granite in the light of experimental studies in the system $NaAl_2Si_3O_8$ - $KalSi_3O_8$ - $SiO_2$ - $H_2O$. *Memoirs of the Geological Society of America*, *No.* **74**.

Vielzeuf, D., Montel, J.M., 1994. Partial melting of metagreywackes. Part I. Fluid-absent experiments and phase relations. Contributions to Mineralogy and Petrology, **17**, 375–393.

Villaseca, C., Romera, C.M. and Barbero, L., 2001. Melts and Residua Geochemistry in Low to Mid Crustal Section (Central, Spain), *Physics* and *Chemistry* of the *Earth (a) 26, No. **4** - **5**, 273 - 280.*

Viswanathan, K. and Harneit, O., 1986. Refned crystal structure of beta-uranophane, $Ca(UO_2)_2(SiO_3OH)_2.5H_2O$: Amer. Mineral., **71**, 1489-1493.

Vogel, T. A., 1964. Optical - Crystallographic Scatter In Plagioclase. *The American Mineralogist*, 49, 614–643.

von Backsröm, J.W., 1970. The Rössing uranium deposit near Swakopmund, South West Africa. A preliminary report. *Uranium Exploration Geology,* IAEA Report, IAEA –PL - **391/12**, Vienna, 143 - 150.

Von Backström, J.W. and Jacob, R.E. (1978). Uranium in South Africa and South West Africa. Philosophical Transactions of the Royal Society A, **291**, pp. 307–319.

Waite, T.D., Davis, J.A., Payne, T.E., Waychunas, G.A. and Xu, N., 1994. Uranium(VI) adsorption to ferrihydrite – application of a surface complexation model. *Geochimica et Cosmochimica Acta*, **58**, 5465-5478.

Walker, K.R., Shanmugam, G. and Ruppel, S.C., 1983. A model for carbonate to terrigenous clastic sequences. *Geological Society of America Bulletin,* **94**, 700-712.

Ward, C.D., McArthur, J.M. and Walsh, J.N., 1992. Rare earth element behaviour during evolution and alteration of the Dartmoor Granite, SW England. *Journal of Petrology*, **33**, p 785-815.

Ward, R., Stevens, G. and Kisters, A., 2008. Fluid and deformation induced partial melting and melt volumes in low - temperature granulite - facies metasediments, Damara Belt, Namibia. *Lithos,* **105**, 253–271.

Ward, R.A., Kisters, A.F.M. and Stevens, G., 2007. Structural controls of melt formation, melt extraction and transfer in mid - crustal meta - psammites of the Damara belt, Namibia. Hutton Symposium on Granites. Stellenbosch, South Africa.

Waters, D. J., 1989. Metamorphic evidence for the heating and cooling path of granulites: *Geological Society of London Special Publication*, **43**, p. 357-363

Watson, E.B., and Harrison, T.M., 1983. Zircon saturation revisited: temperature and composition effects in a variety of crustal magma types: Earth and Planetary Science Letters, **64**, pp. 295-304.

Watt, G. R., 1995. High-thorium monazite-(Ce) formed during disequilibrium melting of metapelites under granulite-facies conditions. *Mineralogical Magazine*, December 1995, **59**, pp. 735-743

Watt, G.R. and Harley, S.L., 1993 Accessory phase controls on the geochemistry of crustal melts and restites produced during water-under saturated partial melting. *Contributions to Mineralogy and Petrology*, **11**, 550–566.

Webster J. D., 1997, Exsolution of magmatic volatile phases from Cl-enriched mineralising granitic magmas and implications for ore metal transport. *Geochemica et Cosmochimica Acta*, **61**, 1017-1029.

Werner, O., and Lippolt, H. J., 1998b. Datierung von postkinematischen magmatischen Intrusionsphasen des Erzgebirges: thermische und hydrothermale Überprägung der Nebengesteine. In: *Terra Nostra;* Beitragszusammenfassungen des 7. *Koll. im DFG-Schwerpunktprogramm Orogene Prozesse*; 16–17.04.1998; Gießen. **2**, 160-163.

Werner, O., Lippolt, H. J., Hess J. C., 1997. $^{40}Ar/^{39}Ar$- and Rb–Sr-investigations of the cooling-history of metamorphic and plutonic rocks in the Erzgebirge (Mid-European Saxothuringian). *Terra Nova*, **9**, Abstract Supplement 1:106-107.

Whalen, J. B. and Chappell, B. W., 1988. Opaque mineralogy and mafic mineral chemistry of I- and S-type granites of the Lachlan Fold Belt, southeast Australia. *American Mineralogist* **73**, 281–296.

Whalen, J.B., Currie, K.L., and Chappell, B.W., 1987. S-type granites: geochemical characteristics, discrimination and petrogenesis. Contributions to Mineralogy and Petrology, **95**, 407-419.

White, A. J. R. and Chappell, B. W., 1988. Some supracrustal (S - type) granites of the Lachlan Fold Belt. *Transactions of the Royal Society of Edinburgh: Earth Sciences* 79, 169–181.

White, A. J. R. and Chappell, B. W., 1983. Granitoid types and their distribution in the Lachlan Fold Belt, southeastern Australia. *In:* Roddick J. A. (ed). *Circum - Pacific Plutonic Terranes*, 21–34. Geological Society of America Memoir, 159.

Whittle, A. W. G., 1959. The nature of davidite. *Economic Geology*, 54, No. 1, 64 - 81.

Youlton, B.J., 2007. *Controls on Uranium Mineralisation at the Klein Trekkopje Prospect, Namibia*. Hons. Thesis (unpubl). University of the Witwatersrand, Johannesburg, 1-68.

Youlton, B., 2014. *The Role of Quantitative Mineralogy in Predicting the Leach Response of Karoo-aged Uranium Ores.* PhD thesis, University of the Witwatersrand.

Youlton B. J., and Coetzee L. L., 2012. XRD and SEM Petrographic Examination of High Grade Uranium Sample. Mineralogical Report No: MIN0512/091. Prepared for Swakop Uranium, Confidential.

Youlton, B., Kinnaird, J., 2013. Gangue–reagent interactions during acid leaching of uranium. Minerals Engineering. **52**, 62–73.

Zen, E., 1986. Aluminium enrichment in silicate melts by fractional crystallisation: some mineralogic and petrographic constraints. *Journal of Petrology.* 27, 1095–1117.

Zhang, Y., Lumpkin, G.R., Li, H., Blackford, M.G., Colella, M., Carter, M.L. and Vance E.R., 2006. Recrystallisation of amorphous natural brannerite through annealing: the effect of radiation damage on the chemical durability of brannerite. *Journal of Nuclear Materials*, **350**, 293-300.

Zoellner, T., 2009. *Uranium; War, Energy, and the Rock That Shaped the World*. Penguin Books, 368 pp.

Website References

www.bannermanresources.com
www.forsysmetals.com
www.Swakopuranium.com
www.worldnuclear.org
www.iaea.org

CIPW Norm Calculator

CIPW Norm Calculator Microsoft Excel® Macro written by Kurt Hollocher, Geology Department, Union College, Schenectady, NY, USA, hollochk@union.edu.

EPMA Stoichiometric Formula recalculation

Calculation macro written in Microsoft Excel® by Dr. Gelu Costin, Department of Geology, Rhodes University, Grahamstown, South Africa. Presently employed at the Department of Earth Science at Rice University, Houston, Texas, USA; g.costin@rice.edu.